

T. Pradeep
Publications 2012

A Journal of the Gesellschaft Deutscher Chemiker

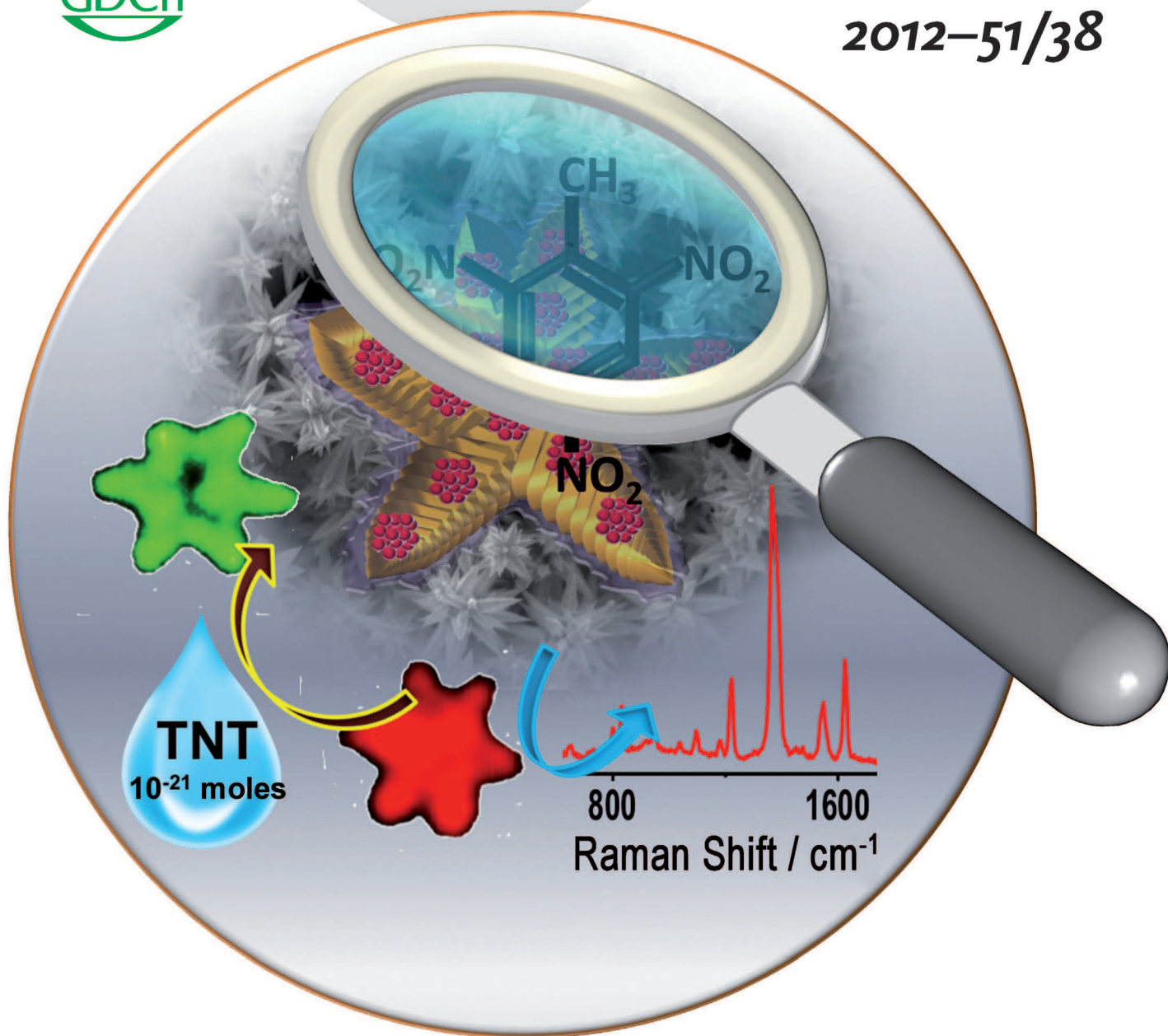
Angewandte Chemie

International Edition

GDCh

www.angewandte.org

2012–51/38



Realizing the limits ...

... of sensitivity, while maintaining selectivity, is an ongoing quest. In their Communication on page 9596 ff., T. Pradeep et al. report a technique that allows for the detection of tens of molecules of trinitrotoluene (TNT) by uniquely shaped anisotropic particles called mesoflowers, which enhance the luminescence of silver clusters bound on them. TNT interacts with the bovine serum albumin protecting the clusters, leading to luminescence quenching, and thus allowing detection.

 WILEY-VCH

Contents

1. Books

2. Book chapters

3. Journal papers

4. Patents

5. Technologies

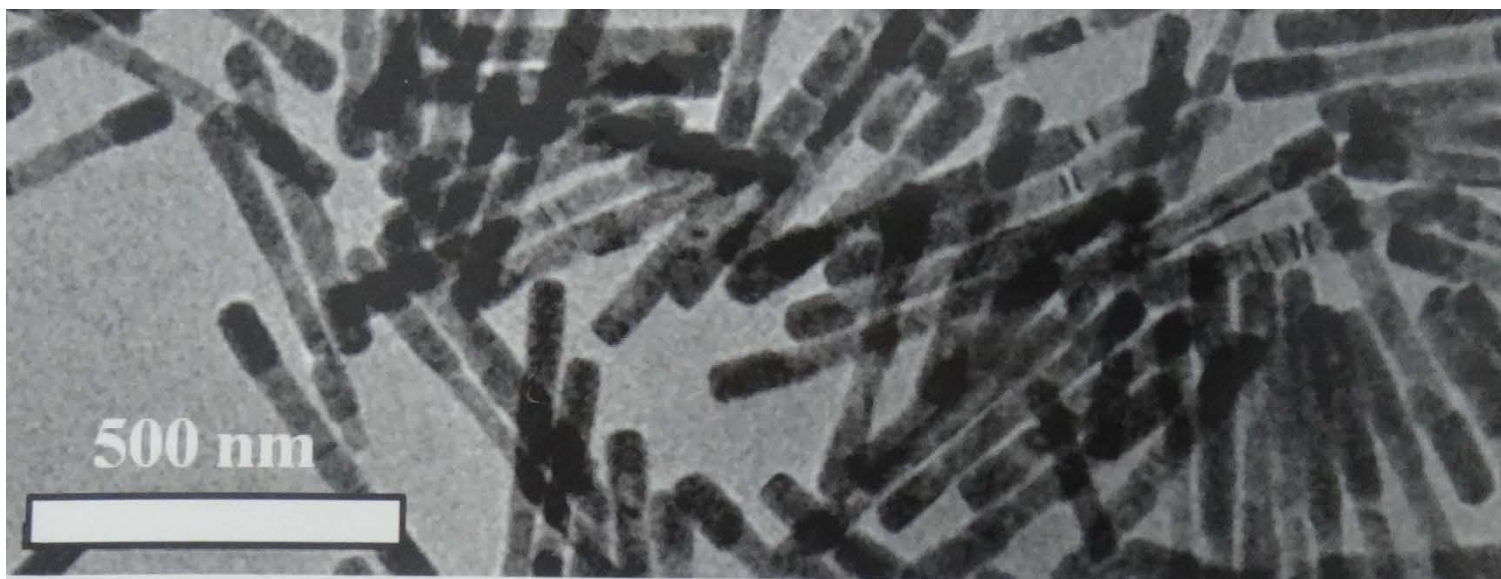
6. Media reports

1. Books

Only cover pages are attached

A Textbook of Nanoscience and Nanotechnology, 949 pages, McGraw-Hill Education, New Delhi, 2012.

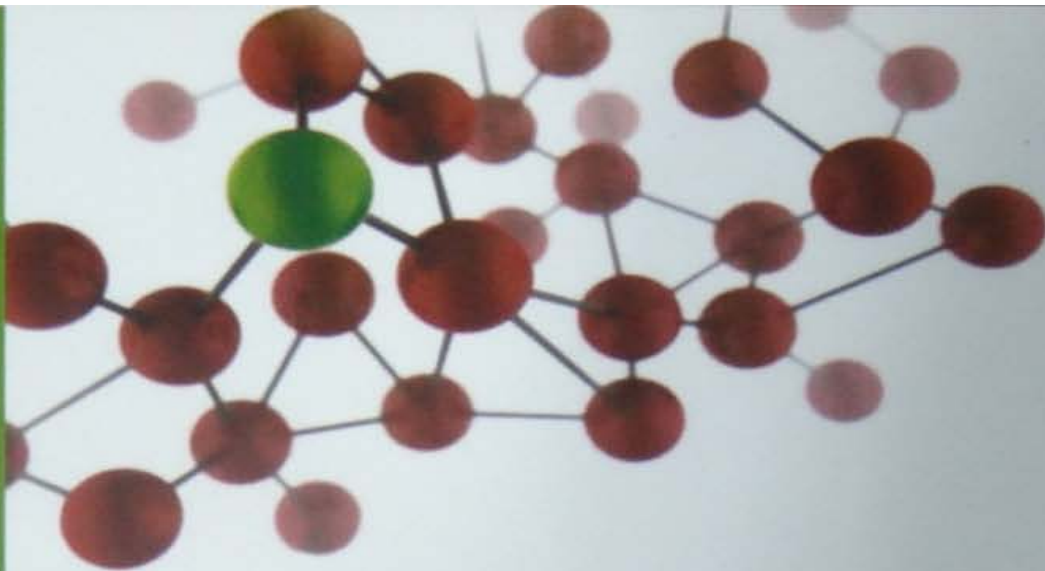
Kunjukanangalku Vasantham (2nd Edition), 144 pages, DC Books, Kottayam, 2012.



A Textbook of NANOSCIENCE AND NANOTECHNOLOGY

T. Pradeep

With: A. Ashokreddy | B. R. Buergi | A. Chainani | J. Chakrabarti | S. K. Das
N. DasGupta | P. A. Joy | M. A. H. Muhammed | G. U. Kulkarni | K. Manzoor | R. Mukhopadhyay
A. S. Nair | T. Pal | S. K. Pati | G. V. P. Kumar | V. K. Pillai | E. Prasad | R. Philip
V. R. R. Kumar | P. R. Sajanlal | A. K. Samal | E. S. Shibu | T. S. Sreeprasad | C. Vijayan



കേരള സാഹിത്യ അക്കാദമി അവാർഡ് നേടിയ കൃതി

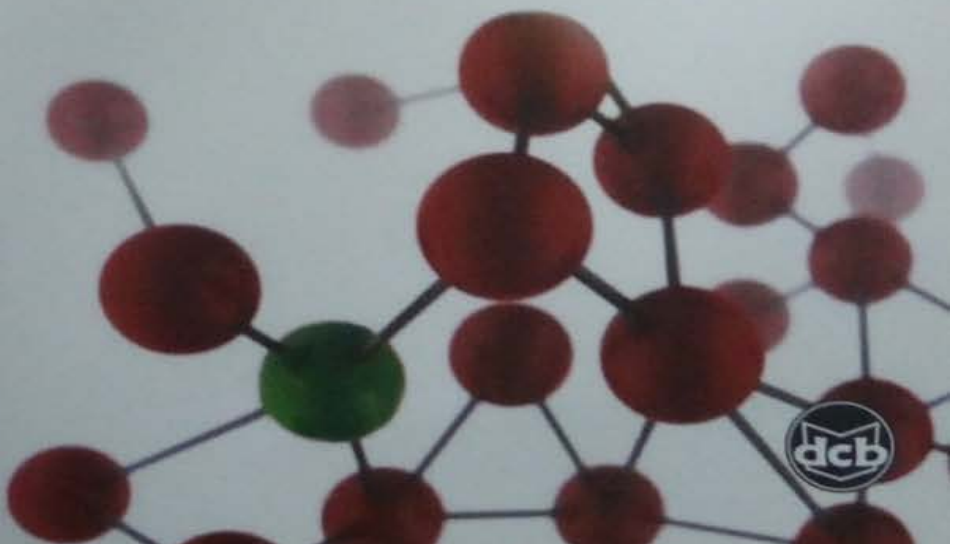
കുഞ്ഞുകണങ്ങൾക്ക് വസന്തം



An Introduction to
technology

നാനോടെക്നോളജിക്ക് ഒരാമുഖം

ടി. പ്രദീപ്



2. Book chapters

1. Gold nanoparticles, P. R. Sajanalal and T. Pradeep, Kirk-Othmer Encyclopedia, Published Online: 13 JAN 2012, DOI: 10.1002/0471238961.goldpard.a01.

Website: <http://onlinelibrary.wiley.com/doi/10.1002/0471238961.goldpard.a01/abstract>

2. Noble metal nanoparticles, T. S. Sreeprasad and T. Pradeep, Springer Handbook on Nanomaterials, 2012. Chap. 9. Noble Metals, Vajtai, Robert (Ed.) ISBN 978-3-642-20594-1

Website: <http://www.springer.com/materials/nanotechnology/book/978-3-642-20594-1>

3. Journal Papers

1. Conversion of double layer charge-stabilized Ag@citrate colloids to thiol passivated luminescent quantum clusters, L. Dhanalakshmi, T. Udayabhaskararao and T. Pradeep, Chem. Commun., 48 (2012) 859-861 (DOI: 10.1039/C1CC15604G). [Pdf File Supporting Information](#)
2. Ag₇Au₆: A 13 atom alloy quantum cluster, T. Udayabhaskararao, Yan Sun, Nirmal Goswami, Samir Kumar Pal, K. Balasubramanian and T. Pradeep, Angew. Chem. Int. Ed., 51 (2012) 2155-2159 (DOI: 10.1002/anie.201107696). [Pdf File Supporting Information](#)
3. Luminescent sub-nanometer clusters for metal ion sensing: A new direction in nanosensors, Indranath Chakraborty, T. Udaya Bhaskara Rao and T. Pradeep, J. Hazard. Mater., 211-212 (2012) 396-403 (DOI:10.1016/j.jhazmat.2011.12.032). [Pdf File Supporting Information](#)
4. Protein-protected luminescent noble metal quantum clusters: An emerging trend in atomic cluster nanoscience, Paulrajpillai Lourdu Xavier, Kamalesh Chaudhari, Ananya Bakshi and T. Pradeep, Nano Reviews, 3 (2012) 14767 (DOI: 10.3402/nano.v3i0.14767). [Pdf File](#)
5. Luminescent, freestanding composite films of Au₁₅ for specific metal ion sensing, Anu George, E. S. Shibu, Shihabudheen M. Maliyekkal, M. S. Bootharaju and T. Pradeep, ACS Appl. Mater. Interfaces, 4 (2012) 639-644 (DOI: 10.1021/am201292a). [Pdf File Supporting Information](#)
6. Understanding the degradation pathway of the pesticide, chlorpyrifos by noble metal nanoparticles, M. S. Bootharaju and T. Pradeep, Langmuir, 28 (2012) 2671-2679 (DOI: 10.1021/la2050515). [Pdf File Supporting Information](#)
7. Functional hybrid nickel nanostructures as recyclable SERS substrates: Detection of explosives and biowarfare agents, P. R. Sajanlal and T. Pradeep, Nanoscale, 4 (2012) 3427-3437 (DOI:10.1039/C2NR30557G). [Pdf File](#)
8. Luminescent, bimetallic AuAg alloy quantum clusters in protein templates, Jyoti Sarita Mohanty, Paulrajpillai Lourdu Xavier, Kamalesh Chaudhari, M. S. Bootharaju, Nirmal Goswami, S. K. Pal and T. Pradeep, Nanoscale, 4 (2012) 4255-4262 (DOI:10.1039/C2NR30729D). [Pdf File Supporting Information](#)
9. High temperature nucleation and growth of glutathione protected ~Ag₇₅ clusters, Indranath Chakraborty, T. Udaya Bhaskara Rao and T. Pradeep, Chem. Commun., 48 (2012) 6788-6790 (DOI: 10.1039/C2CC33099G). [Pdf File Supporting Information](#)
10. Heterojunction double dumb-bell Ag₂Te-Te-Ag₂Te nanowires, Anirban Som and T. Pradeep, Nanoscale, 4 (2012) 4537-4543 (DOI: 10.1039/C2NR30730H). [Pdf File Supporting Information](#)

11. Luminescent silver clusters with covalent functionalisation of graphene, Aditi Chandrasekar and T. Pradeep, *J. Phys. Chem. C*, 116 (2012) 14057-14061 (DOI: 10.1021/jp304131v). [Pdf File Supporting Information](#)
12. Protein directed synthesis of NIR-emitting, tunable HgS quantum dots and their applications in metal ion sensing, Nirmal Goswami, Anupam Giri, Shantimoy Kar, M. S. Bootharaju, Robin John, Paulrajpillai Lourdu Xavier, T. Pradeep and Samir Kumar Pal, *Small*, 8 (2012) 3175-3184 (DOI: 10.1002/sml.201200760). [Pdf File Supporting Information](#)
13. Selective visual detection of TNT at the sub-zeptomole level, Ammu Mathew, P. R. Sajanlal, and T. Pradeep, *Angew. Chem. Int. Ed.*, 51 (2012) 9596-9600 (DOI: 10.1002/anie.201203810). [Pdf File Supporting Information](#) (***Highlighted as cover page***)
14. Graphene from sugar and its application in water purification, Soujit Sen Gupta, T. S. Sreeprasad, Shihabudheen M. Maliyekkal, Sarit. K. Das and T. Pradeep, *ACS Appl. Mater. Interfaces*, 4 (2012) 4156-4163 (DOI: 10.1021/am300889u). [Pdf File Supporting Information](#)
15. One-step route to luminescent Au₁₈SG₁₄ in the condensed phase and its closed shell molecular ions in the gas phase, Atanu Ghosh, T. Udaya Bhaskara Rao and T. Pradeep, *J. Phys. Chem. Lett.*, 3 (2012) 1997-2002 (DOI: 10.1021/jz3007436). [Pdf File Supporting Information](#)
16. Low-energy ionic collisions at molecular solids, Jobin Cyriac, T. Pradeep, R. Souda, H. Kang and R. G. Cooks, *Chem. Rev.*, 112 (2012) 5356-5411 (DOI: 10.1021/cr200384k). [Pdf File](#)
17. Graphene for environmental and biological applications: Review, T. S. Sreeprasad and T. Pradeep, *Int. J. Mod. Phys. B*, 26 (2012) 1242001 (1-26) (DOI: 10.1142/S0217979212420015). [Pdf File](#)
18. Rapid identification of molecular changes in tulsi (*ocimum sanctum linn*) upon ageing using leaf spray ionization mass spectrometry, Depanjan Sarkar, Amitava Srimany and T. Pradeep, *Analyst*, 137 (2012) 4559-4563 (DOI: 10.1039/C2AN35655D). [Pdf File Supporting Information](#)
19. Graphene: A reusable substrate for unprecedented adsorption of pesticides, Shihabudheen M. Maliyekkal, T. S. Sreeprasad, Deepti Krishnan, Summayya Kouser, Abhishek Kumar Mishra, Umesh V. Waghmare and T. Pradeep, *Small*, (2012) In press (DOI: 10.1002/sml.201201125). [Pdf File](#)
20. Real time plasmonic spectroscopy of the interaction of Hg²⁺ with single noble metal nanoparticles, M. S. Bootharaju, Kamallesh Chaudhari and T. Pradeep, *RSC Adv.*, 2 (2012) 10048-10056 (DOI: 10.1039/C2RA21384B). [Pdf File Supporting Information](#)
21. Nanoscience in India: a perspective, Anirban Som, Ammu Mathew, Paulrajpillai Lourdu Xavier and T. Pradeep, *Nanoscience, Volume 1: Nanostructures through Chemistry*, Paul O'Brien (Ed.), Royal Society of Chemistry, London, (2012) (DOI:10.1039/9781849734844-00244).

22. Probing molecular solids with low energy ions, Soumabha Bag, Radha Gobinda Bhuin, Ganapati Natarajan and T. Pradeep, *Ann. Rev. Anal. Chem.*, 6 (2013). In press.
23. Atomically precise silver clusters for efficient chlorocarbon degradation, M. S. Bootharaju, G. K. Deepesh, T. Udayabhaskararao and T. Pradeep, *J. Mater. Chem. A*, 1 (2013) 611-620 (DOI:10.1039/C2TA00254J). [Pdf File Supporting Information](#)
24. The superstable 25-kDa monolayer protected silver nanoparticle: Measurements & interpretation as an icosahedral $\text{Ag}_{152}(\text{SCH}_2\text{CH}_2\text{Ph})_{60}$ cluster, Indranath Chakraborty, Anuradha Govindarajan, Jayanthi Erusappan, Atanu Ghosh, Bokwon Yoon, Robert L. Whetten, Uzi Landman and T. Pradeep, *Nano Lett.*, 12 (2012) 5861-5866 (DOI: 10.1021/nl303220x). [Pdf File Supporting information](#)
25. Low temperature thermal dissociation of Ag quantum clusters in solution and formation of monodisperse Ag_2S Nanoparticles, Remya Kadamkotte Puthenveetil, T. Udayabhaskararao and T. Pradeep, *J. Phys. Chem. C*, 116 (2012) 26019-26026 (DOI: 10.1021/jp306736s). [Pdf File Supporting information](#)
26. Emergence of multicolor photoluminescence in $\text{La}_{0.67}\text{Sr}_{0.33}\text{MnO}_3$ nanoparticles, Anupam Giri, Nirmal Goswami, M. S. Bootharaju, Paulrajpillai Lourdu Xavier, Robin John, T. Pradeep, Nguyen Thanh, Barnali Ghosh, Arup Raychaudhuri and Samir Kumar Pal, *J. Phys. Chem. C*, 116 (2012) 25623-25629 (DOI: 10.1021/jp308606a). [Pdf File Supporting information](#)
27. Immobilized graphene-based composite from asphalt: Facile synthesis and application in water purification, T. S. Sreepasad, Soujit Sen Gupta, Shihabudheen M. Maliyekkal and T. Pradeep, *J. Hazard. Mater.*, (2012). Just Accepted.
28. Protein-encapsulated gold cluster aggregates: The case of lysozyme, Ananya Baksi, Paulrajpillai Lourdu Xavier, Kamalesh Chaudhari, Nirmal Goswami, Samir Kumar Pal and T. Pradeep, *Nanoscale*, (2012). Just Accepted.
29. Evolution of atomically precise silver clusters to superlattice crystals, K. S. Sugi, Indranath Chakraborty, T. Udayabhaskararao, Jyoti Sarita Mohanty and T. Pradeep, *Particle & Particle Systems Characterization*, (2012). Just Accepted.

Cite this: *Chem. Commun.*, 2012, **48**, 859–861

www.rsc.org/chemcomm

Conversion of double layer charge-stabilized Ag@citrate colloids to thiol passivated luminescent quantum clusters†

L. Dhanalakshmi, T. Udayabhaskararao and Thalappil Pradeep*

Received 9th September 2011, Accepted 10th November 2011

DOI: 10.1039/c1cc15604g

A red luminescent silver cluster was synthesized in milligram quantities by the direct core reduction of the most widely studied class of large silver nanoparticles, namely silver@citrate of tens of nanometres diameter. No byproducts such as thiolates were detected, unlike in the case of typical methods of making such clusters. The route provides nearly pure clusters. The possibility to make diverse clusters from large nanoparticles expands the scope of cluster research.

One of the most studied families of nanomaterials is noble metal nanoparticles (NPs)¹ or colloids. A well known synthetic methodology to make noble metal nanoparticles is the citrate route, originally proposed by Turkevich *et al.* in 1951.² These charge stabilized nanoparticles, commonly described as M@citrate (M = Au, Ag) and their variants, exhibiting intense surface plasmon resonance (SPR) have been the most extensively used materials on which several unusual phenomena at the nanoscale have been explored. Typical Ag@citrate NPs are 30–70 nm in diameter while the gold analogues made under identical conditions are smaller, 15–20 nm in diameter. Diverse applications of such materials in catalysis,³ spectroscopy,⁴ water purification⁵ and a number of other areas became possible with various forms of these NPs. Such NPs are different from the more recent thiol and phosphene monolayer protected NPs in terms of their stability. In the former case, stability is based on the electrical double layer and in the latter, it is due to ligand passivation. The most recent addition to noble metal nanoparticles is their sub-nanometre size analogues, known as quantum clusters (QCs) composed of a few metal atoms in the core and a protecting ligand shell. Quantum clusters exhibit intense luminescence and associated physicochemical properties. Diverse methodologies have been employed to create clusters such as Au₂₅,⁶ Au₁₅,⁷ Au₂₃,⁸ Ag₉,⁹ Ag₇,¹⁰ *etc.* Typically, many clusters are formed together and versatile synthetic routes to create specific clusters in pure form are desired. While smaller monolayer protected nanoparticles of 2–3 nm or smaller diameter have been converted to clusters, particularly Au₂₅, by a core etching protocol,^{6c,e} the conversion of large, plasmonic NPs to clusters has not

been demonstrated. In this communication, we show that luminescent silver clusters can be made in one step from the most extensively studied family of nanomaterials, namely citrate protected nanoparticles. The formation of few atom clusters starting from M@citrate may enable the exploration of properties of a range of nanomaterials, from the largest to the smallest.

The process of synthesis involves making Ag@citrate NPs of average diameter 30–70 nm by boiling 5 mM, 50 mL AgNO₃ and adding aqueous sodium citrate (75 mg in 1 mL water) to it and continuing boiling for 10 min. Reduction in core dimension occurs by adding excess mercaptosuccinic acid (MSA, in solid form; 73.5 mg, details are in S1, ESI†) and maintaining a temperature of 70 °C, the temperature being critical. The as-synthesized Ag@citrate NPs show a SPR at 420 nm (Fig. 1Aa). During the reaction, there is a disappearance of the plasmon feature at 420 nm (Fig. 1Ab) implying that no

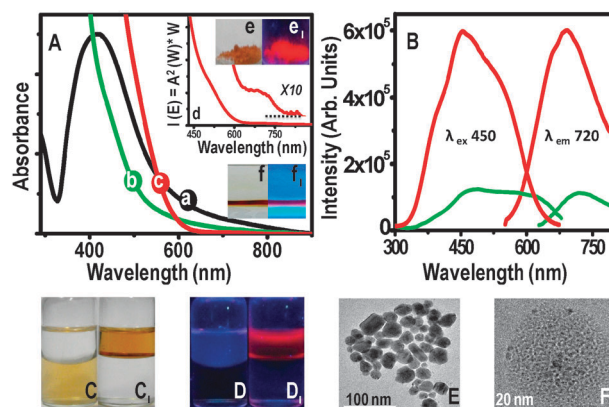


Fig. 1 (A) Spectral variation during the conversion of silver nanoparticles to quantum clusters. (a), (b) and (c) Spectra of parent Ag@citrate nanoparticles, that after 1 h and 24 h after adding MSA, respectively. Insets: (d) Jacobian corrected spectrum of the red trace as described in S1 (ESI†), (e) photograph of the crude cluster in visible light, (e₁) the same in UV light, (f) photograph of PAGE separated cluster in visible and (f₁) the same in UV light. (B) Luminescence spectra of the cluster before (green trace) and after (red trace) phase transfer. Excitation and emission wavelengths are marked. C and C₁ are the photographs before and after phase transfer in visible light and D and D₁ are in UV light. TEM images of (E) Ag@citrate and (F) phase transferred cluster protected with tetraoctylammonium bromide. Clusters are faintly visible. The larger particles are due to electron beam induced aggregation.

DST Unit of Nanoscience (DST UNS), Department of Chemistry, Indian Institute of Technology Madras, Chennai 600 036, India.
E-mail: pradeep@iitm.ac.in

† Electronic supplementary information (ESI) available. See DOI: 10.1039/c1cc15604g

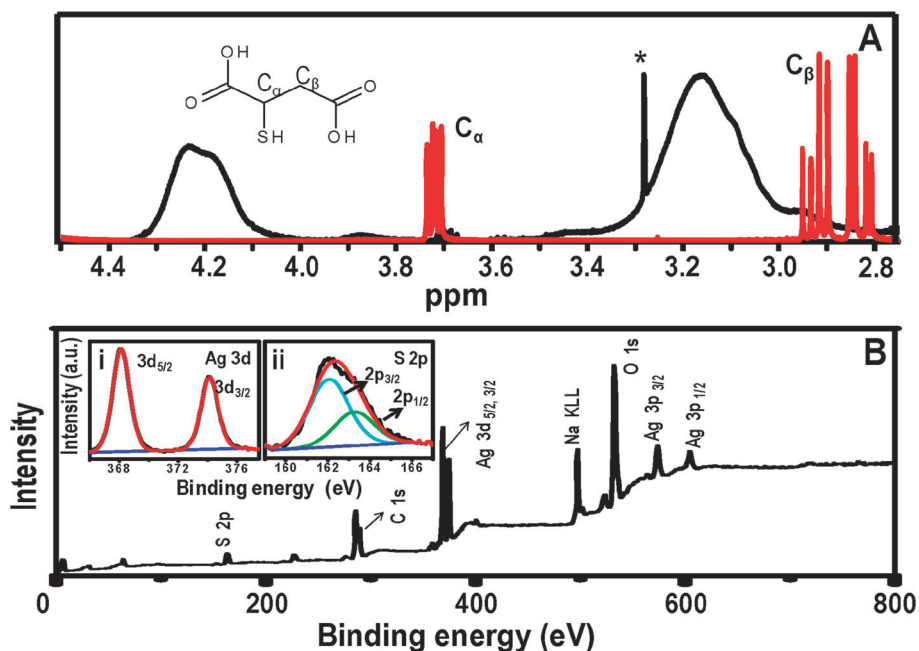


Fig. 2 (A) ^1H NMR spectrum of the $\text{Ag}_{\text{QC}}@\text{MSA}$ cluster in D_2O along with that of MSA. The peak labeled with * is due to methanol used in washing, which could not be removed despite freeze-drying. (B) XPS survey spectrum of $\text{Ag}_{\text{QC}}@\text{MSA}$ cluster. Inset (i) and (ii) are corresponding to Ag 3d and S 2p. Their components are fitted.

gradual but direct core reduction happens, unlike in the core-etching methods where the conversion is slower, taking hours.^{6c,e} Spectra collected at various times such as 5 and 10 minutes after adding MSA show this drastic decrease in plasmon features (Fig. S2, ESI[†]). The cluster formed has no apparent optical features (Fig. 1Ac). The step-like behavior and specific features are clear after the Jacobian correction (Fig. 1A inset, trace d). During the reaction, the color of the solution changes from golden yellow to orange with no observable precipitation due to thiolates or nanoparticles, unlike in the case of core etching. The solution upon precipitation and washing gave an orange powder (Fig. 1A, inset e) which shows red luminescence in the solid state (Fig. 1A, inset e₁). Extensive literature on quantum clusters¹¹ suggest that this luminescence is indicative of their formation. To know the monodispersity of the clusters, we separated the crude clusters by polyacrylamide gel electrophoresis (details are in S1, ESI[†]) which shows the presence of a single band. The photograph of the gel with this band was collected at room temperature in visible light and at 5 °C in UV light (Fig. 1A, inset (f and f₁)). The pink luminescence of the clusters is evident from the image. The band upon extraction gives an optical absorption spectrum resembling the crude (details in Fig. S3, ESI[†]) indicating that the parent material has no visible impurities. As a result, subsequent measurements were done with the crude. The luminescence spectrum of the as-prepared $\text{Ag}_{\text{QC}}@\text{MSA}$ shows excitation at 450 nm and emission at 720 nm. The quantum yield of the as-prepared cluster in water at 10 °C was found to be 6×10^{-3} using rodamine6G. The cluster can be easily phase transferred (details are in S1, ESI[†]) and luminescence shows an increase in intensity in the organic medium as shown in Fig. 1B. Photographs of the cluster before and after phase transfer in visible light (Fig. 1C and C₁) and the same in UV light

(D and D₁) show the expected characteristics. The cluster is not visibly luminescent at room temperature in water (Fig. 1D). From our previous studies of silver and gold QCs, it is known that water quenches luminescence.¹⁰ However, a toluene solution is visibly luminescent at room temperature (RT, 23 °C). The parent citrate NPs are polydisperse with a size in the range of 30–70 nm (Fig. 1E) while the clusters are too tiny (~1 nm) to be seen under the electron beam (Fig. 1F) and are also extremely beam sensitive, resulting in large particles upon longer term irradiation (Fig. S4, ESI[†]).¹² The yield of the cluster is 44%, in terms of the metal used.

The ^1H NMR spectra of MSA and $\text{Ag}_{\text{QC}}@\text{MSA}$ clusters were measured in D_2O and are shown in Fig. 2A. Two strong multiplets at 2.8 and 3.7 ppm in the ^1H NMR spectrum are from CH_2 and CH protons of MSA, respectively. These multiplets are broadened in the QC due to fast relaxation. Both CH and CH_2 protons are shifted downfield, but CH protons are shifted more because of the proximity to the silver core. The data presented suggest the formation of MSA protected silver clusters. Although detailed mass spectrometry (MS) was attempted both by electrospray ionization (ESI) and by matrix assisted laser desorption ionization (MALDI), no characteristic features were obtained; however, the presence of silver, sulfur and some Ag–MSA complexes was seen due to the decomposition of the cluster at higher capillary temperatures (Fig. S5 and S6, ESI[†]). This is not surprising as many clusters are not stable even under soft ionization conditions. Therefore, in the absence of MS, a detailed elemental analysis was performed to arrive at the cluster composition. The total organic fraction estimated was 47.1% (15.3% C, 20.4% O, 10.2% S, 1.2% H) and Inductively Coupled Plasma-Optical Emission Spectrometry (ICP-OES) gave 53.2% weight of silver. All the results were checked for reproducibility. These suggest a cluster compound

composed of ~ 38 Ag atoms and ~ 24 MSA ligands. The calculated silver and organic fraction for $\text{Ag}_{38}(\text{MSA})_{24}$ is 53.4% Ag and 46.6% MSA. Slight changes are attributed to water included in such a dicarboxylic acid incorporated structure, despite long freeze-drying as suggested by infrared spectroscopy (see below). Thermogravimetric (TG) analysis of the as-prepared cluster (Fig. S7, ESI†) gives 38% of the organic fraction as the remaining material was largely silver with some sulfur. This is in agreement with Ag–S and S–C bond cleavages in such clusters.¹⁰ Further support for the structure was obtained from energy dispersive analysis of X-rays (EDAX) and X-ray photoelectron spectroscopy (XPS). The silver to sulfur atomic ratio in EDAX was 0.62 (calculated 0.63). The EDAX spectrum and images of Ag, S, and C are shown in Fig. S8, ESI†. XPS gave a silver to sulfur atomic ratio of 0.65. All these quantitative analyses support the tentative formula of $\text{Ag}_{38}(\text{MSA})_{24}$. We are, however, continuing our efforts on the MS analysis to confirm the composition.

The XPS survey spectrum shows all the expected elements (Ag, C, O and S). High resolution XPS of silver shows Ag in the Ag(0) state (Fig. 2B, i). A binding energy (BE) of 368.0 eV for Ag $3d_{5/2}$ is similar to those of other silver clusters.^{10,13} S $2p_{3/2}$ appears at 162.0 eV due to S^- (Fig. 2B, ii). Both these are characteristic of thiolate protected silver quantum clusters. Expanded XPS spectra in the C 1s and O 1s regions are shown in Fig. S9 (ESI†). The MSA protection is confirmed by the IR spectrum which shows features corresponding to MSA ($\text{C}=\text{O}_{\text{str}} \sim 1579 \text{ cm}^{-1}$, $\text{C}-\text{O}_{\text{str}} \sim 1388 \text{ cm}^{-1}$, $\text{C}-\text{H}_{\text{str}} \sim 2929 \text{ cm}^{-1}$) and the disappearance of the S–H proton (Fig. S10, ESI†) in the cluster is due to thiolate binding. The presence of water is also clear from the IR data. X-Ray diffraction for $\text{Ag}@$ citrate gives features at 38° , 44° , 64° , 77° and 80° , but a broad peak around $2\theta \approx 37^\circ$ was obtained for $\text{Ag}_{\text{QC}}@$ MSA clusters (Fig. S11, ESI†). This kind of large broadening of the peaks is seen in gold¹⁴ and silver¹⁵ QCs.

The same method was tried with glutathione (SG) by changing some experimental conditions (details are in S1, ESI†). $\text{Ag}_{\text{QC}}@$ SG clusters in powder form as well as in organic phase show red luminescence. Absorption profiles of $\text{Ag}@$ citrate and $\text{Ag}_{\text{QC}}@$ SG clusters upon reaction and the luminescence spectrum of the phase transferred $\text{Ag}_{\text{QC}}@$ SG cluster are shown in Fig. S12, ESI†.

In conclusion, we report direct conversion of the most studied class of nanoparticles to the most emerging category

of sub-nano materials by a simple one step route. This methodology with various ligands and experimental conditions may give diverse clusters with varying properties. Access to a range of cluster sizes from tens of nanometres to sub-nanometres, as in clusters, allows diverse properties to be examined.

We thank the Department of Science and Technology, Government of India for financial support. Thanks to SAIF, IIT Madras for NMR and ICP-OES.

Notes and references

- (a) C. Burda, X. Chen, R. Narayanan and M. A. El-Sayed, *Chem. Rev.*, 2005, **105**, 1025; (b) P. V. Kamat, *J. Phys. Chem. B*, 2002, **106**, 7729.
- J. Turkevich, P. C. Stevenson and J. Hillier, *Discuss. Faraday Soc.*, 1951, **11**, 55.
- M. C. Daniel and D. Astruc, *Chem. Rev.*, 2004, **104**, 293.
- U. Kreibitz and M. Vollmer, *Optical properties of metal clusters*, Springer, Berlin, 1995.
- T. Pradeep and Anshup, *Thin Solid Films*, 2009, **517**, 6441.
- (a) T. G. Schaaff, G. Knight, M. N. Shafiqullin, R. F. Borkman and R. L. Whetten, *J. Phys. Chem. B*, 1998, **102**, 10643; (b) Y. Shichibu, Y. Negishi, T. Tsukuda and T. Teranishi, *J. Am. Chem. Soc.*, 2005, **127**, 13464; (c) Y. Shichibu, Y. Negishi, H. Tsunoyama, M. Kanehara, T. Teranishi and T. Tsukuda, *Small*, 2007, **3**, 835; (d) M. A. Habeeb Muhammed and T. Pradeep, *Chem. Phys. Lett.*, 2007, **449**, 186; (e) E. S. Shibu, M. A. Habeeb Muhammed, T. Tsukuda and T. Pradeep, *J. Phys. Chem. C*, 2008, **112**, 12168; (f) M. A. Habeeb Muhammed, A. K. Shaw, S. K. Pal and T. Pradeep, *J. Phys. Chem. C*, 2008, **112**, 14324; (g) M. Zhu, E. Lanni, N. Garg, M. E. Bier and R. Jin, *J. Am. Chem. Soc.*, 2008, **130**, 1138; (h) M. W. Heaven, A. Dass, P. S. White, K. M. Holt and R. W. Murray, *J. Am. Chem. Soc.*, 2008, **130**, 3754.
- E. S. Shibu and T. Pradeep, *Chem. Mater.*, 2011, **23**, 989.
- M. A. Habeeb Muhammed, P. K. Verma, S. K. Pal, R. C. Arun Kumar, S. Paul, R. V. Omkumar and T. Pradeep, *Chem.–Eur. J.*, 2009, **15**, 10110.
- T. U. B. Rao, B. Nataraju and T. Pradeep, *J. Am. Chem. Soc.*, 2010, **132**, 16304.
- T. U. B. Rao and T. Pradeep, *Angew. Chem., Int. Ed.*, 2010, **49**, 4218.
- (a) J. T. Petty, J. Zheng, N. V. Hud and R. M. Dickson, *J. Am. Chem. Soc.*, 2004, **126**, 5207; (b) J. G. Zhang, S. Q. Xu and E. Kumacheva, *Adv. Mater.*, 2005, **17**, 2336; (c) Z. Shen, H. Duan and H. Frey, *Adv. Mater.*, 2007, **19**, 349; (d) S. N. Narayanan and S. K. Pal, *J. Phys. Chem. C*, 2008, **112**, 4874.
- P. Ramasamy, S. Guha, E. S. Shibu, T. S. Sreeprasad, S. Bag, A. Banerjee and T. Pradeep, *J. Mater. Chem.*, 2009, **19**, 8456.
- Y. Negishi, R. Arai, Y. Niihori and T. Tsukuda, *Chem. Commun.*, 2011, **47**, 5693.
- M. Zhu, H. Qian and R. Jin, *J. Am. Chem. Soc.*, 2009, **131**, 7220.
- A. Ledo-Surez, J. Rivas, C. F. Rodriguez-Abreu, M. J. Rodriguez, E. Pastor, A. Hernandez-Creus, S. B. Oseroff and M. A. Lopez-Quintela, *Angew. Chem., Int. Ed.*, 2007, **46**, 8823.

Supplementary information for the paper:

Conversion of double layer charge-stabilized Ag@citrate colloids to thiol passivated luminescent quantum clusters

L. Dhanalakshmi, T. Udayabhaskararao, Thalappil Pradeep *

DST Unit of Nanoscience (DST-UNS), Department of Chemistry, Indian Institute of Technology Madras, Chennai 600 036, India

*E-mail: pradeep@iitm.ac.in

Table of contents

S.NO	Description	Page number
1	Experimental Section & Analytical procedures	2-4
2	Time dependent UV-Vis spectra	5
3	UV spectrum of Ag _{QC} @MSA after PAGE separation	6
4	HRTEM images and size distribution diagram	7
5	ESI-MS	8
6	MALDI MS	9
7	TGA	10
8	SEM and EDAX	11
9	XPS	12
10	FT-IR	13
11	XRD	14
12	UV spectrum of Ag _{QC} @GSH	15

S1. Supplementary information 1

Experimental Section

Synthesis of Ag@citrate nanoparticles

Silver nanoparticles were prepared by the well-known Turkevich method. 5 mM solution of silver nitrate in 50 mL deionized water was heated until it began to boil. 75 mg of sodium citrate dissolved in 1 mL deionized water was added drop-wise to the boiling silver nitrate solution and the boiling was continued. The color of the solution slowly turned into pale yellow, indicating the reduction of the Ag⁺ ions. Heating was continued for an additional 10 min. These nanoparticles show surface plasmon resonance peak at 420 nm which is characteristic of silver nanoparticles.

Synthesis of MSA protected silver quantum clusters

As prepared silver nanoparticle suspension was kept in ice cold water. 73.5 mg of MSA in powder form was added to this solution and kept for stirring at 70 °C for 24 h. The color of the solution changes from golden yellow to orange. Solution was freeze dried to yield a sticky paste which upon addition of water gave a concentrated solution. The cluster was precipitated from it by the addition of methanol. The precipitate was repeatedly washed by 90% methanol to remove unbound MSA and citrate ions. The product was dried under vacuum and was stored in the laboratory atmosphere. Yield of crude Ag_{QC}@MSA was 25 mg, starting from the above method, corresponding to 44% in terms of silver.

Purification by polyacrylamide gel electrophoresis (PAGE): PAGE separation of the clusters was performed as per the procedure given below.

A gel electrophoresis unit with 1 mm thick spacer (Bio-rad, Mini-protein Tetra cell) was used to process the PAGE. Total contents of the acrylamide monomers were 28% (bis(acrylamide:acrylamide) = 7:93) and 3% (bis(acrylamide:acrylamide) = 6:94) for the separation and condensation gels, respectively. The eluting buffer consisted of 192 mM glycine and 25 mM tris(hydroxymethylamine). The crude mixture of Ag_{QC}@MSA clusters, as an orange powder, obtained from the reaction was dissolved in 5% (v/v) glycerol-water solution (1 mL) at a concentration of 60 mg/mL. The sample solution (1.0 mL) was loaded onto a 1 mm gel and eluted for 4 h at a constant voltage of 100 V to achieve separation shown in Fig. 1A (f, f₁). The gel fractions containing the clusters were cut out, ground, and dipped in distilled water (2 mL) for 10 min. Subsequently, the solutions were centrifuged at 15,000 rpm for 15 min at -10 °C, followed by filtering with filter paper having 0.22 μm pores to remove the gel lumps suspended in the solution. The samples were freeze dried to get the Ag_{QC}@MSA powder. This was dispersed in water and UV spectrum was collected (Fig. S3).

Even without PAGE, the clusters are rather pure, the excess MSA was removed by washing with methanol many times.

Procedure for phase transfer

Clusters were phase transferred to toluene layer by using tetraoctylammonium bromide as phase transfer agent. Procedure is as follows: 2 mL of cluster in water was phase transferred to 2 mL of toluene by using 5 mg of tetraoctylammonium bromide

Synthesis of Ag_{QC}@SG

Citrate capped silver nanoparticles were prepared by taking 1mM silver nitrate in 50 ml deionized water in a synthesizer tube and was heated until it began to boil (100 °C). 1 mL of 47 mM sodium citrate was added dropwise to the silver nitrate solution and boiling was continued for 15 min to get the nanoparticle. Synthesizer tube containing

nanoparticle suspension was kept in ice-cold water. Cluster formation was preferable at basic conditions obtained by the addition of 1 mL of 0.15 M NaOH. To get the clusters 30.7 mg of glutathione in solid form was added and the solution was kept for stirring at 70 °C for 48 h. The color of the solution changes from yellow to orange. The Ag_{QC}@SG powder was obtained by following the same procedure used for Ag_{QC}@MSA. Powder in visible light appears as orange and it can be stored at laboratory conditions.

Method of Jacobian correction

To amplify the less-intense absorption features, the data have been corrected with the Jacobian factor. For this, the experimentally obtained absorbance values as a function of wavelength [$I(\omega)$], were converted to energy-dependent numbers [$I(E)$], using the expression,

$$I(E) = \frac{I(\omega)}{\partial E/\partial \omega} \propto I(\omega) * \omega^2$$

where $\partial E/\partial \omega$ represents the Jacobian factor.

Analytical procedures

A. UV-vis spectroscopy

UV-vis spectra were recorded using Perkin Elmer Lambda 25 UV-vis spectrometer. Spectra were typically measured in the range of 190-1100 nm.

B. Fourier-transform infrared (FT-IR) spectra

Perkin Elmer Spectrum One instrument were used for measuring FT-IR spectra. KBr crystals were used as the matrix for sample preparation.

C. Luminescence spectroscopy

The photoexcitation and luminescence studies were carried out using HORIBA JOBIN VYON Nano Log spectrofluorimeter with 100-W xenon lamp as excitation source. The band pass for both excitation and emission was set as 5 nm.

D. Transmission electron microscopy (TEM)

TEM images were collected using a JEOL 3010 microscope. A diluted solution of phase transferred cluster was spotted on carbon coated copper grid and was dried in laboratory ambience.

E. ESI MS

Mass spectrometric studies were conducted using an electrospray system, MDX Sciex 3200 QTRAP MS/MS instrument having a mass range of m/z 50-1700. As prepared clusters were dissolved in 1:1 water/methanol mixture in ppm concentration. The samples were electrosprayed at a flow rate of 10 μ L/min and ion spray voltage of 5 kV.

F. Matrix assisted laser desorption ionization time of flight mass spectrometry (MALDI TOF MS)

The mass spectrometric studies were also conducted using a Voyager DE PRO Biospectrometry Workstation (Applied Biosystems) MALDI TOF MS instrument. A pulsed nitrogen laser of 337 nm was used (maximum firing rate: 20 Hz, maximum pulse energy: 300 mJ) for desorption ionization and TOF was operated in the delayed extraction mode. The mass spectra were collected in negative mode and were averaged for 100 shots. The spectra were simulated using the Data explorer version 4.0.0.0 software provided by Applied Biosystems Inc. which uses the isotope database of IUPAC.

G. SEM and EDAX analyses

Scanning electron microscopic (SEM) and energy dispersive X-ray (EDAX) analyses were done in a FEI QUANTA-200 SEM. For measurements, clusters were drop-casted on an indium tin oxide coated conducting glass and dried in vacuum.

H. X-ray photoelectron spectroscopy

XPS measurement was done using an Omicron Nanotechnology spectrometer with polychromatic Al K α X-rays. As prepared clusters in water were spotted on a Mo plate and allowed to dry in vacuum. The X-ray flux was adjusted to reduce beam induced damage of the sample. The spectrometer was operated in the constant analyzer energy mode. Survey and high-resolution spectra were collected using pass energies of 50 and 20 eV, respectively. The binding energy was calibrated with respect to C 1s at 285.0 eV.

I. X-ray powder diffraction

Powder XRD patterns of the samples were recorded using PANalytical X'pertPro diffractometer. The powder samples of parent silver nanoparticles and clusters were taken on a glass plate and the X-ray diffractogram was collected in the 2θ range of 5 to 100 degrees.

J. Thermogravimetry (TG)

TG analyses of the as-prepared clusters were carried out with a Perkin Elmer TGA 7 at a heating rate of 20 °C per min in N₂ atmosphere.

K. NMR

¹H NMR spectra were measured with 500 MHz Bruker AVANCE III spectrometer. 20 mg/ 0.5 mL D₂O was used for ¹H NMR analyses.

L. Inductively Coupled Plasma-Optical Emission Spectrometry (ICP-OES)

ICP-OES measurements were done using Perkin Elmer Optima 5300 DV. As prepared cluster was dissolved in distilled water in ppm concentrations.

S2. Supplementary information 2

Time dependent UV-Vis spectra

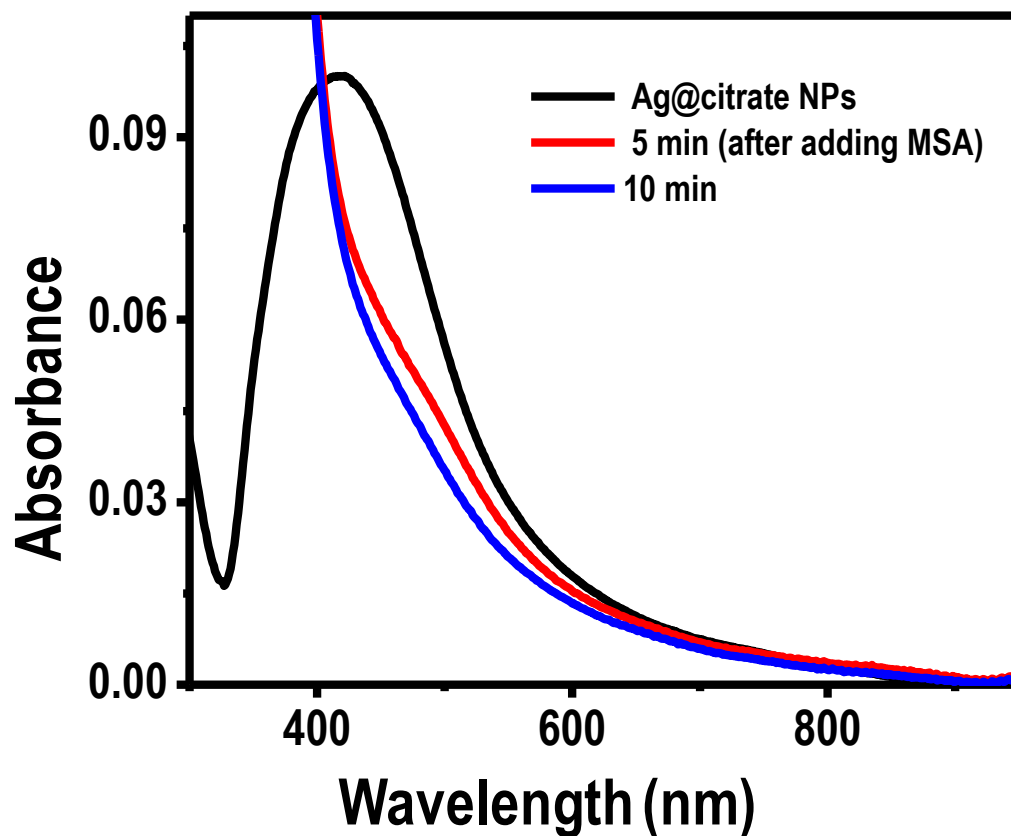


Fig S2. Spectral variation of Ag@citrate NPs after the addition of MSA followed by heating at 70 °C. After adding MSA, SPR peak of Ag@citrate NPs disappears after 10 minutes. The data at 5 and 10 minutes show a weakening shoulder due to the plasmon resonance.

S3. Supplementary information 3

UV-Vis of Ag₄₀@MSA after PAGE

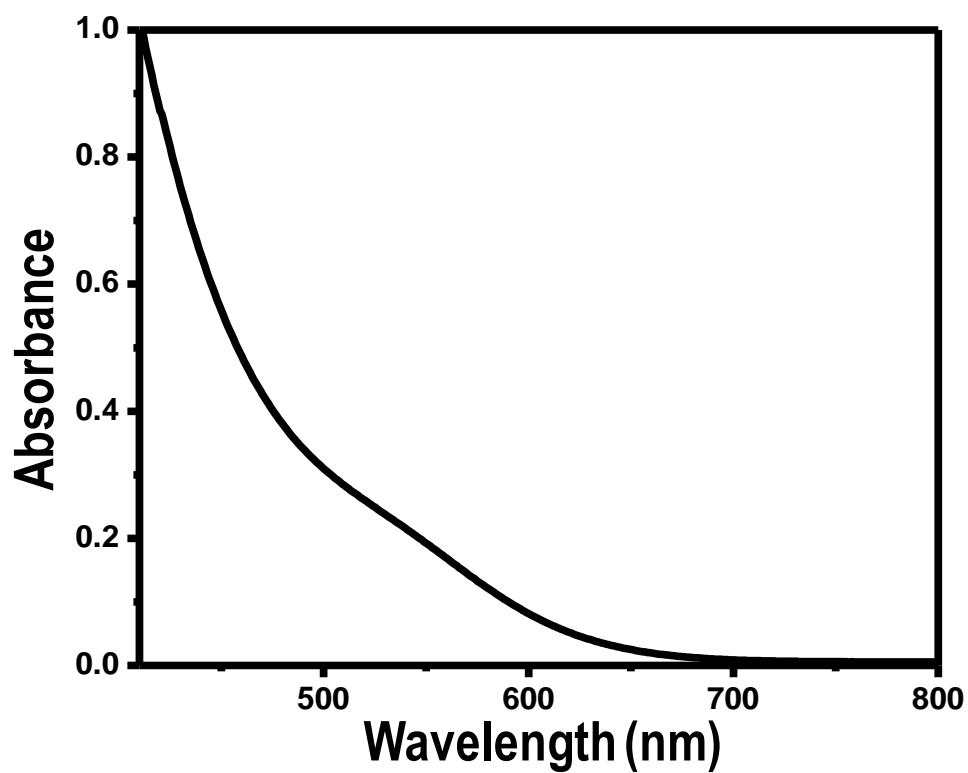


Fig S3. UV spectrum of Ag₄₀@MSA cluster after PAGE separation, showing the similar feature corresponding to as-synthesized cluster.

S4. Supplementary information 4

TEM, effect of electron beam irradiation

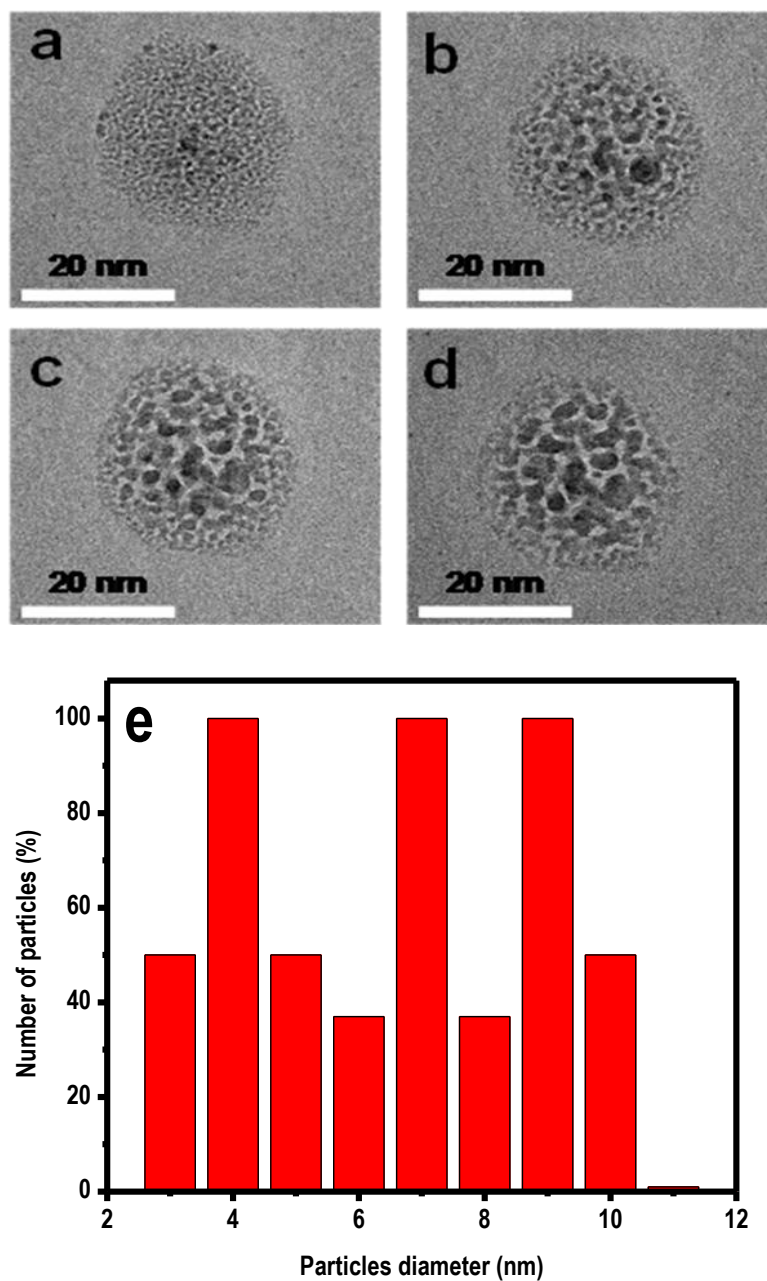


Fig S4. TEM image of phase transferred Ag_{QC}@MSA cluster aggregates upon continuous electron beam irradiation. The same regions of the grid are shown in images a, b, c and d. Image 'a' is at the start of the irradiation showing small clusters, image 'b' is after 30 sec. In 'c' the irradiation time was 60 sec. It was 90 sec in 'd'. Diagram 'e' is the particle size distribution corresponding to the TEM image 'd'. Various size distributions from 3 to 11.5 nm are due to Ag_{QC}@MSA cluster aggregates, upon electron beam irradiation.

S5. Supplementary information 5

ESI MS of as-prepared Ag_{QC}@MSA cluster

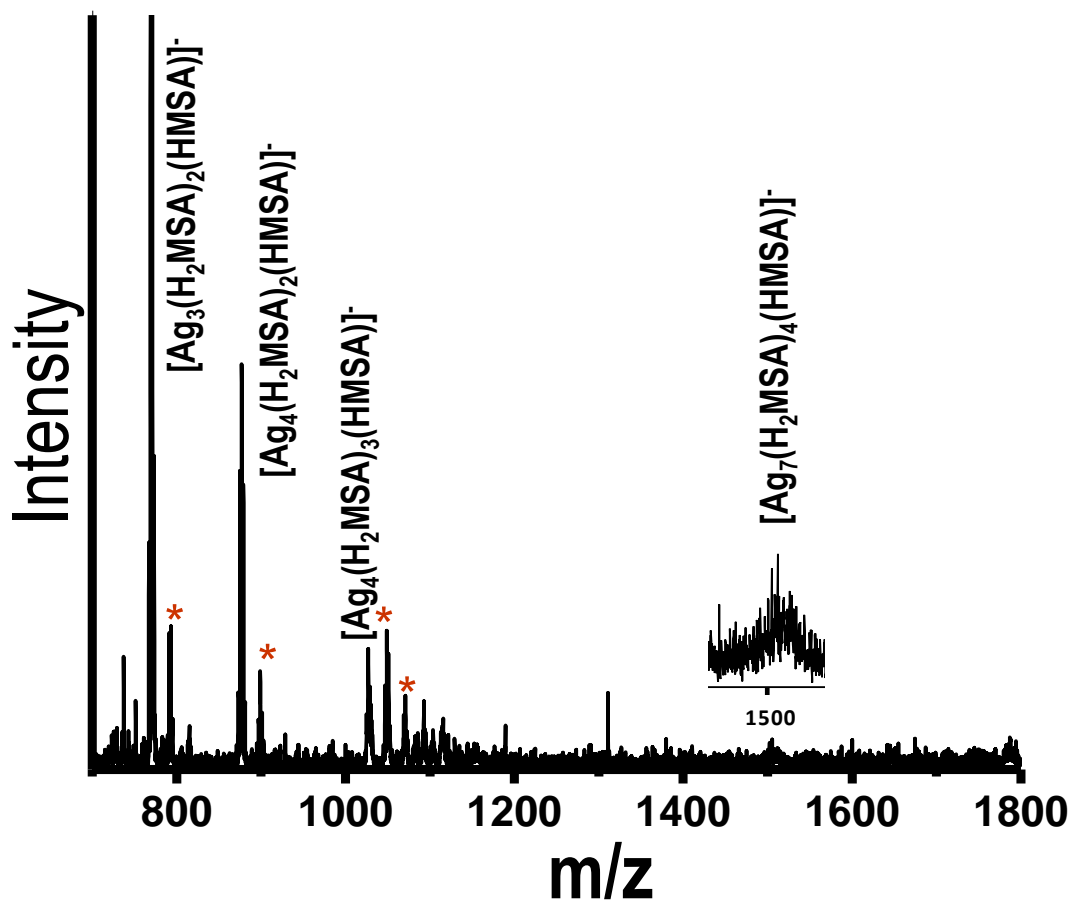


Fig S5. ESI MS of the Ag_{QC}@MSA cluster collected in the negative mode. Peaks with * show the Na adducts of the preceding formula. These appear to be decomposition products.

S6. Supplementary information 6

MALDI MS

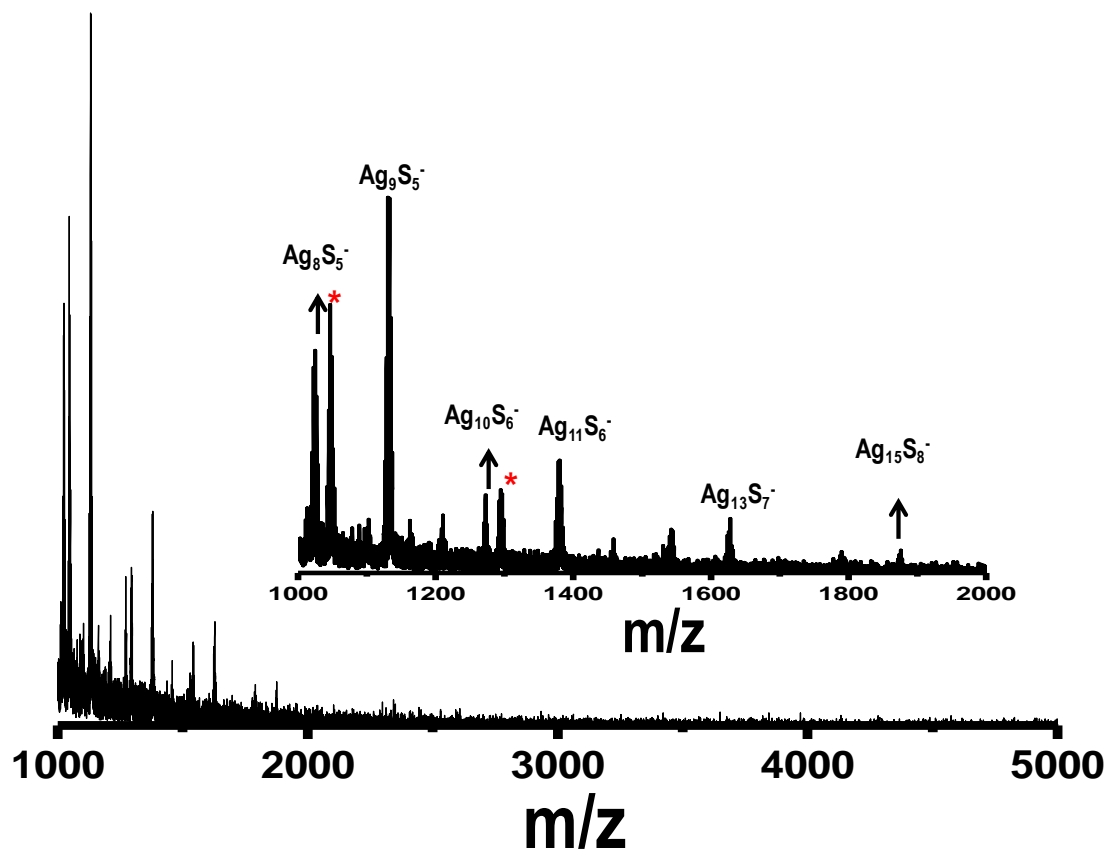


Fig S6. MALDI MS of Ag_{90c}@MSA cluster in negative mode. The Ag_nS_m⁻ series is labeled with their corresponding molecular formulae. Peaks with * show the Na adducts of the preceding formula. Inset shows expanded view of the MALDI MS.

S7. Supplementary information 7

TG analysis

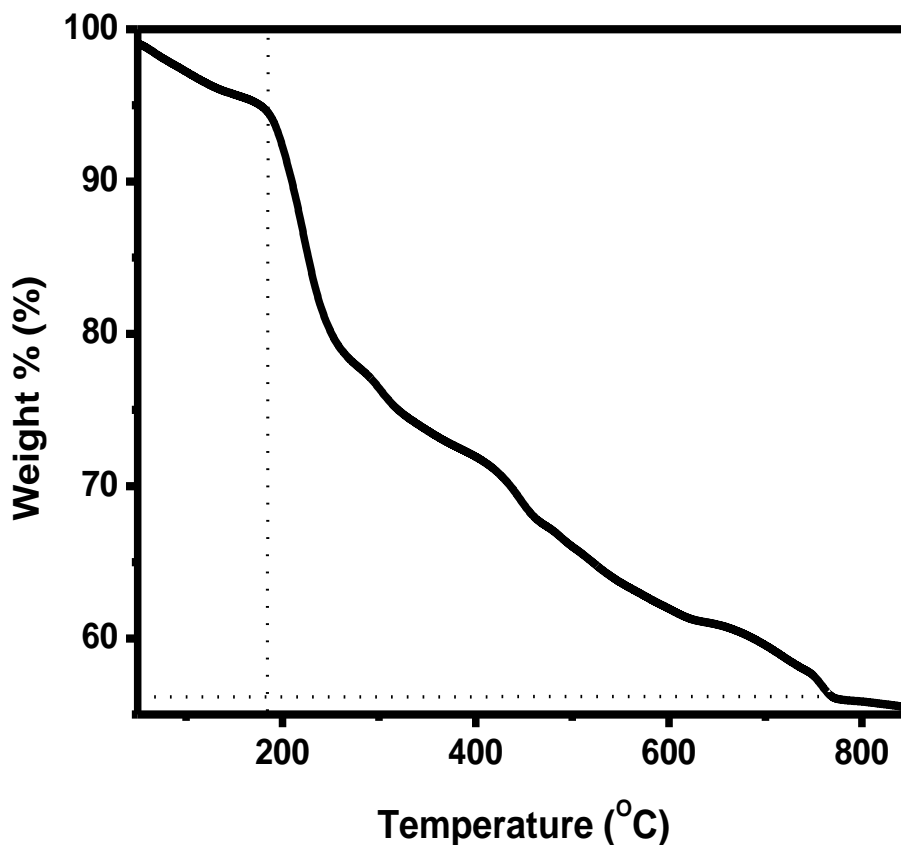
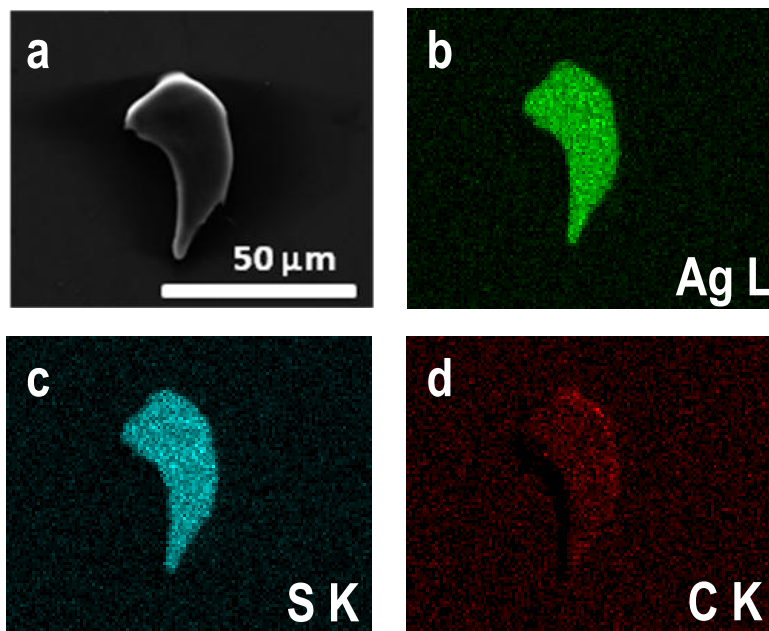


Fig S7. Thermogravimetric (TG) analysis of $\text{Ag}_{\text{QC}}@ \text{MSA}$ clusters performed under N_2 . A detailed analysis of the data was not attempted as such clusters decompose leaving Ag_2S as well as Ag . Several organic species are observed in thermal decomposition of such clusters. Both Ag-S and S-C bond cleavages are observed (unpublished data).

S8. Supplementary information 8

SEM/EDAX

A)



B)

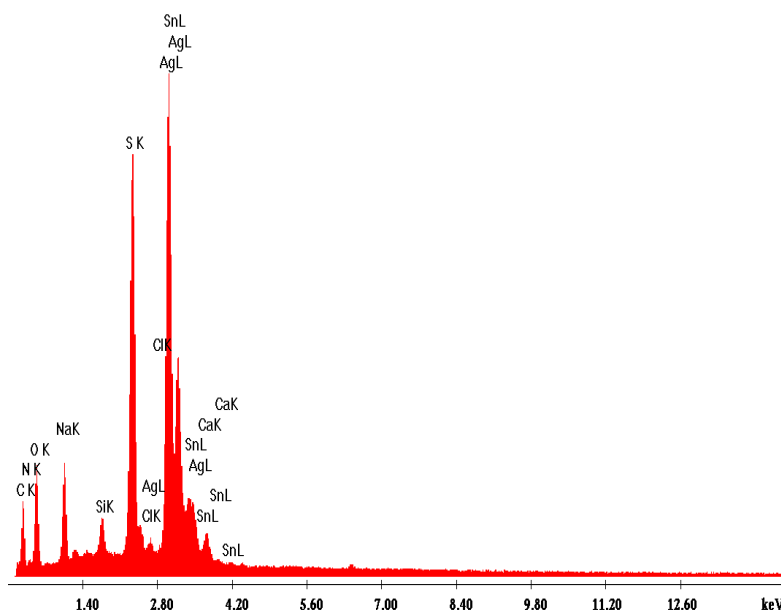


Fig S8. A) SEM and EDAX images of the cluster. EDAX maps using C K_α, Ag L_α, and S K_α are shown. B) EDAX spectrum of AgQC@MSA cluster.

S9. Supplementary information 9

XPS

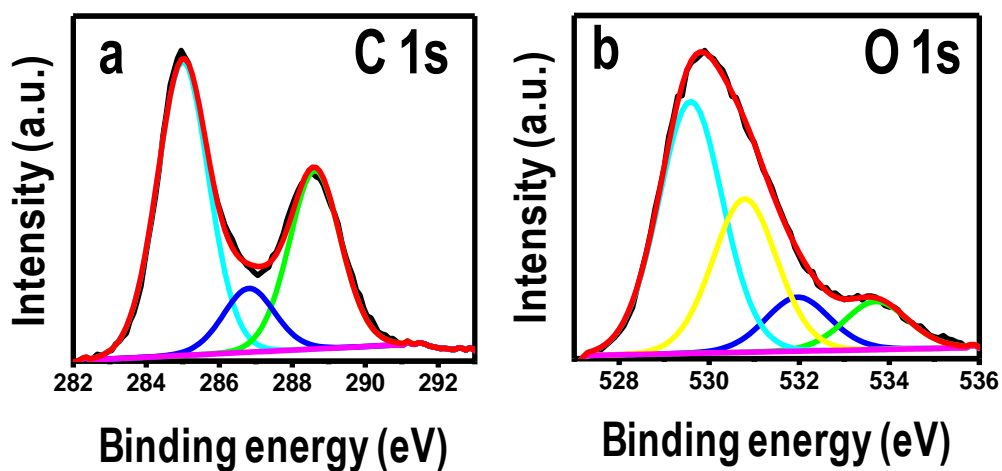


Fig S9. a) and b) C 1s and O 1s XPS spectra, respectively. C 1s region shows three peaks at 285.0, 286.8 and 288.3 eV, corresponding to the CH/CH₂, C-S and COO⁻ groups respectively. O 1s shows peaks at 529.6, 530.8, 532.0 and 533.5 eV corresponding to various species such as hydroxyl group, carboxylate oxygens and adsorbed H₂O. The Ag:S atomic ratio is 1:0.65 whereas the expected value is 1:0.63. The C:O ratio is not reliable in view of potential surface contamination.

S10. Supplementary information 10

FT-IR

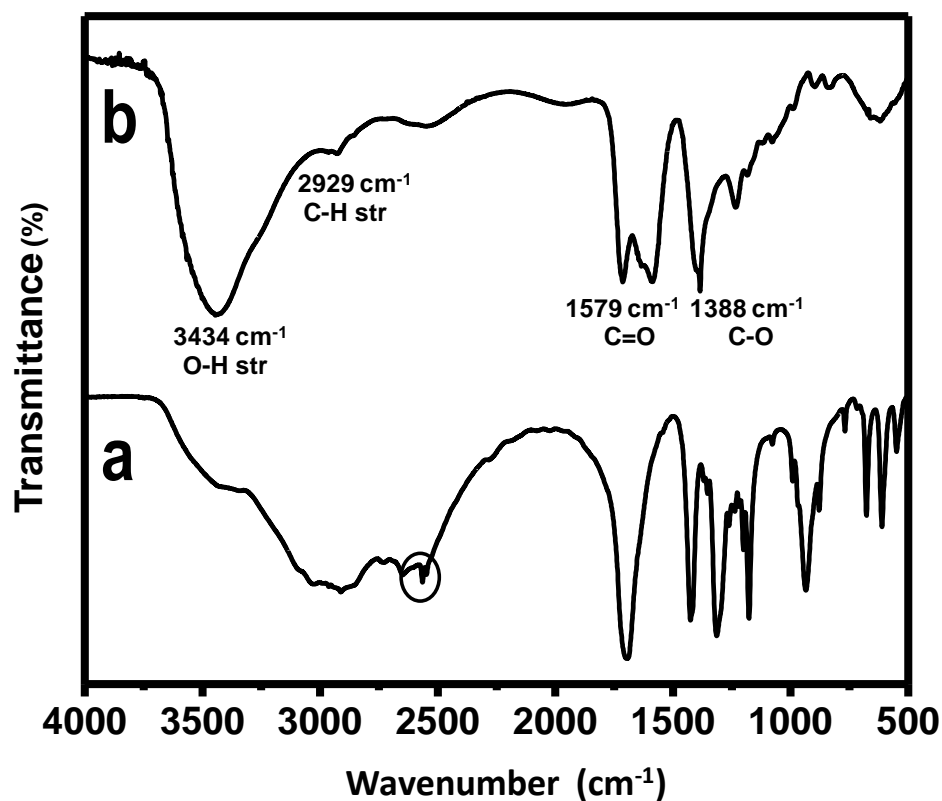


Fig S10. FT-IR spectra of (a) MSA (b) as-prepared Ag_{QC}@MSA. The -SH stretching feature at 2575 cm⁻¹ in H₂MSA is marked by a circle in (a) which is absent in Ag_{QC}@MSA cluster. H₂MSA features in the region of 2000-500 cm⁻¹ confirm the presence of MSA in the cluster. The strong band at 3434 cm⁻¹ in FT-IR of Ag_{QC}@MSA is due to hydrated water.

S11. Supplementary information 11

XRD

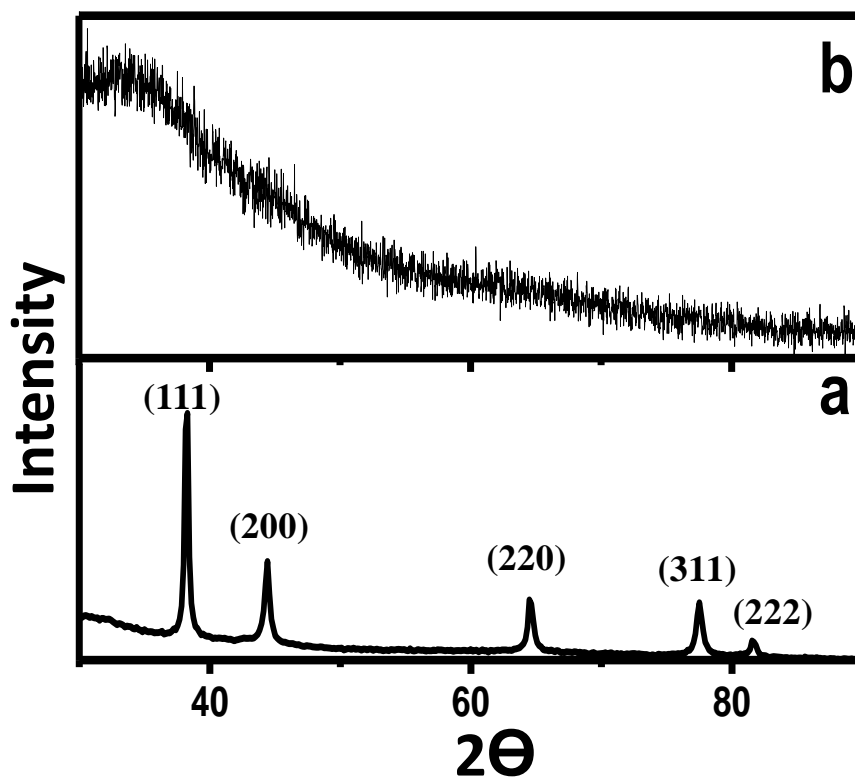


Fig S11. Comparing the X-ray diffraction patterns of (a) Ag@citrate (b) Ag_{QC}@MSA.

S12. Supplementary information 12

Ag_{QC}@SG quantum cluster

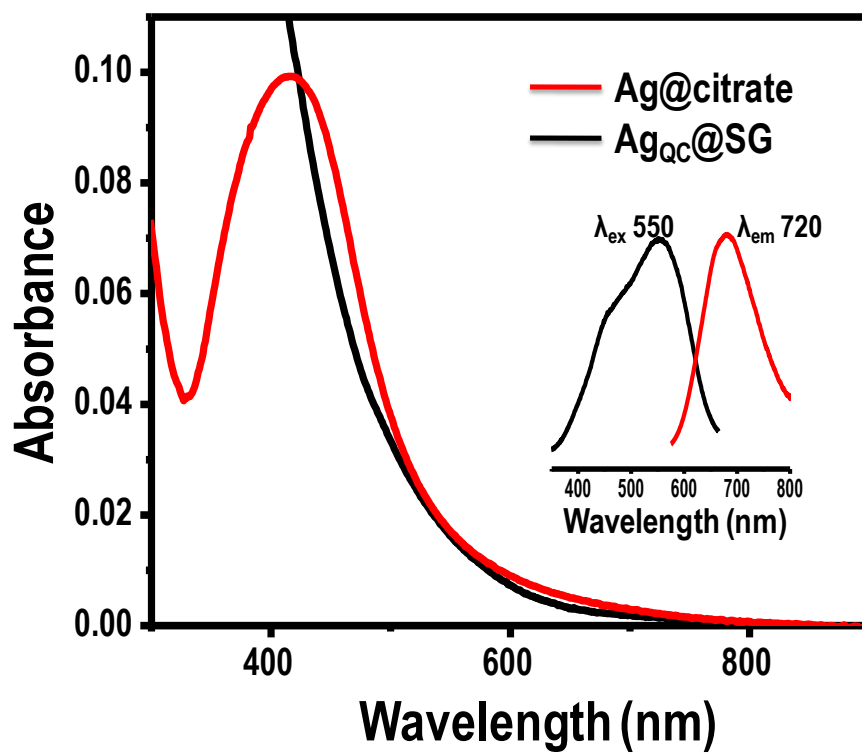


Fig S12. Absorption profile of Ag@citrate and Ag_{QC}@SG cluster upon reaction. Inset shows the luminescence spectrum of the phase transferred Ag_{QC}@SG cluster.

Ag₇Au₆: A 13-Atom Alloy Quantum Cluster**

Thumu Udayabhaskararao, Yan Sun, Nirmal Goswami, Samir K. Pal, K. Balasubramanian, and Thalappil Pradeep*

Dedicated to Professor R. Graham Cooks on the occasion of his 70th birthday

Stable gold cluster molecules of the type Au₁₁,^[1a] Au₁₃,^[1b,c] and Au₅₅,^[1d] have been fascinating and were some of the early molecular nanosystems synthesized. Quantum phenomena such as Coulomb blockade were demonstrated with them.^[2] Unusually intense luminescence and chemical reactivity of molecular clusters or quantum clusters (QCs) of noble metals, for example gold^[3a–e,h] have attracted intense interest in areas such as nanophotonics,^[4] bioimaging,^[5] catalysis,^[6] and others.^[7] In the past several years, some of these clusters have been characterized thoroughly, both theoretically^[8] and experimentally.^[9] Several reports of various core sizes of silver clusters are also known.^[10] However, synthesis of atomically precise alloy QCs of various compositions is a challenge.^[11] Murray et al. synthesized Pd@Au₂₄(SR)₁₈ which was further studied by Negishi et al.^[11b] Negishi et al. isolated PdAu₂₄(SR)₁₈,^[11b] Ag_nAu_{25–n}(SR)₁₈, and (AuAg)₁₄₀(SR)₆₀ (R = organic soluble alkyl/aryl groups) were obtained by simultaneously reducing metal salts in suitable conditions.^[11c,d] There is also a family of well-characterized Ag/Au/Cu cluster complexes^[12] that are different from the metal

core clusters discussed herein. We present the very first experimental investigation of the water-soluble AgAu alloy system belonging to the 13-atom family of clusters by a new synthetic route that reveals a category of materials of structural and electronic complexity that is expected to attract interest in the coming years.

The bimetallic 13-atom QC Ag₇Au₆, which is protected with mercaptosuccinic acid (H₂MSA, or its dianion MSA upon ionization in solution), exhibits well-defined transitions in the absorption profile. This QC is prepared from the Ag_{7,8} cluster (containing a mixture of Ag₇ and Ag₈).^[10d] Synthesis of alloy QCs involves three steps (for details, see the Supporting Information, S1). The various stages of synthesis are shown in Figure 1. First step is the synthesis of polydisperse Ag@H₂MSA nanoparticles followed by the synthesis of Ag_{7,8} clusters by interfacial etching in the second step, as reported previously.^[10d] Addition of an appropriate amount of 10 mM HAuCl₄ to the as-synthesized Ag_{7,8} cluster in the third step yields the alloy cluster (for details see the Experimental Section).

[*] T. Udayabhaskararao, Prof. T. Pradeep
DST Unit of Nanoscience (DST UNS), Department of Chemistry
Indian Institute of Technology, Madras, Chennai 600036 (India)
E-mail: pradeep@iitm.ac
Y. Sun, K. Balasubramanian
College of Science, California State University
East Bay, Hayward, CA 94542 (USA)
N. Goswami, S. K. Pal
Department of Chemical, Biological & Macromolecular Sciences
S. N. Bose National Centre for Basic Sciences
Block JD, Sector III, Salt Lake, Kolkata 700 098 (India)
K. Balasubramanian
Chemistry and Material Science Directorate Lawrence Livermore
National Laboratory, Livermore, CA 94550 (USA)
K. Balasubramanian
Lawrence Berkeley National Laboratory
Berkeley, CA 94720 (USA)

[**] We thank the Department of Science and Technology, Government of India for constantly supporting our research program on nanomaterials. This research was supported in part by the U.S. Department of Energy under grant number DE-FG02-05ER15657 and in part by the Department of Homeland Security's collaborative academic research program. The work at LLNL was performed under the auspices of the U.S. Department of Energy. The authors would like to acknowledge computational support on Lawrence Berkeley Lab's National Energy Research Supercomputers (NERSC).

Supporting information for this article is available on the WWW under <http://dx.doi.org/10.1002/anie.201107696>.

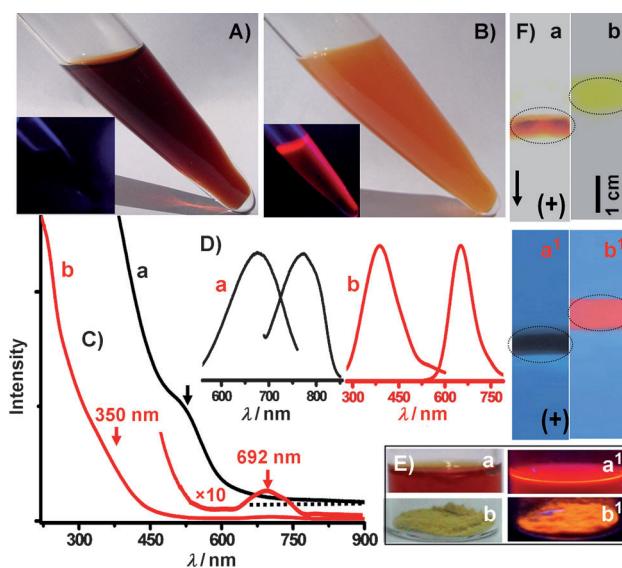


Figure 1. Changes observed during synthesis. A,B) Solutions of Ag_{7,8} (A) and the alloy QC (B) after synthesis under visible light. Insets: the same samples under UV light. C) UV/Vis profile of a) Ag_{7,8} and b) Alloy QC measured in water; arrows indicate the well-defined optical features of the cluster. D) Luminescence spectra of a) Ag_{7,8} and b) alloy QC in water at 300 K. E) Photographs of a,a') alloy QC in water and b,b') in the solid state under visible and UV light. F) Comparison of the PAGE of a,a') Ag₈ and b,b') alloy QC. Photographs of gel in visible (a, b) and UV (a', b') light. Band positions are marked with circles on the gels.

Photographs of $\text{Ag}_{7,8}$ clusters and the alloy QC product after synthesis are shown in Figure 1. During the reaction, the solution becomes turbid and the color changes from reddish brown to orange, indicating the completion of the reaction. A yellowish-white precipitate was removed upon centrifugation and the supernatant appears as a clear reddish yellow solution. The precipitate formed during the reaction is AgCl , as confirmed from XRD and EDAX (Supporting Information, S2). Note that both the thiolate and AgCl are insoluble in water. Finally, the supernatant was lyophilized and a powder sample was obtained for analyzing the cluster in detail. The as-synthesized clusters are stable for months in aqueous phase by storing at low temperatures (below 283 K) and in solid state at room temperature.

The absorption peak from the as-synthesized $\text{Ag}_{7,8}$ cluster at 530 nm (2.34 eV) disappeared within a short reaction time (1 min) and new optical absorption features appear in the next 15 min of reaction with features at 350 (3.54 eV) and 692 nm (1.79 eV). Figure 1C gives the plot of the natural logarithm of the Jacobian factor (details in the Supporting Information) versus wavelength of these clusters, to show the molecular features more clearly. Well-defined absorption features are marked with arrows. Note that Au_{13} cluster also exhibits the peak around 700 nm.^[13] Furthermore, changes in luminescence were observed before and after the reaction, which were attributed to the modifications of the core. For $\text{Ag}_{7,8}$, the excitation and emission maxima are at 670 and 770 nm, whereas for alloy QCs the values are at 390 and 650 nm, respectively (Figure 1D, a,b). Although $\text{Ag}_{7,8}$ cluster emission is weak (quantum yield (QY) of 8×10^{-3}) at room temperature (300 K), for Ag_7Au_6 , the emission intensity is enhanced and the QY was 3.5×10^{-2} . The materials, in both solution and solid states, show bright emission that can be photographed (Figure 1E). Polyacrylamide gel electrophoresis (PAGE) of Ag_8 QC (pre-separated^[10d] sample from $\text{Ag}_{7,8}$) and alloy QC are compared in Figure 1F. They moved to different extent, but as single bands with different mobilities. The mobility of alloy QCs is less than that of Ag_8 QCs, indicating the increase in cluster size. The presence of a single band indicates the formation of one type of cluster in the synthesis. The Ag_8 band does not luminesce brightly at room temperature,^[10d] whereas the alloy QC band shows visible red luminescence under UV light at room temperature (Figure 1F, a¹, b¹). Alloy QCs extracted from the band to water does not show observable shift in the luminescence peak position compared to the crude but there is a slight increase in the intensity (Supporting Information, S3), indicating that both the samples are the same. The cluster appears faintly in TEM but aggregates upon longer electron beam irradiation (Supporting Information, S4) as seen in such clusters.^[3g,10d]

The molecular formula and nature of the monolayer binding are supported by XPS, FTIR, and EDAX (Supporting Information, S5–S7). XPS survey spectrum of Ag_7Au_6 shows the expected elements. The $\text{Au} 4f_{7/2}$ peak at 84.7 eV supports a state intermediate to Au^{I} thiolate (86.0 eV) and Au film (84.0 eV) (Figure 2A, a). There is a slight binding energy (BE) shift of 0.7 eV compared to bulk gold, it is expected for monolayer protected QCs owing to $-\text{S}-\text{Au}-\text{S}-$ staples.^[3] A lower binding energy compared to Au^{I} thiolate is due to the

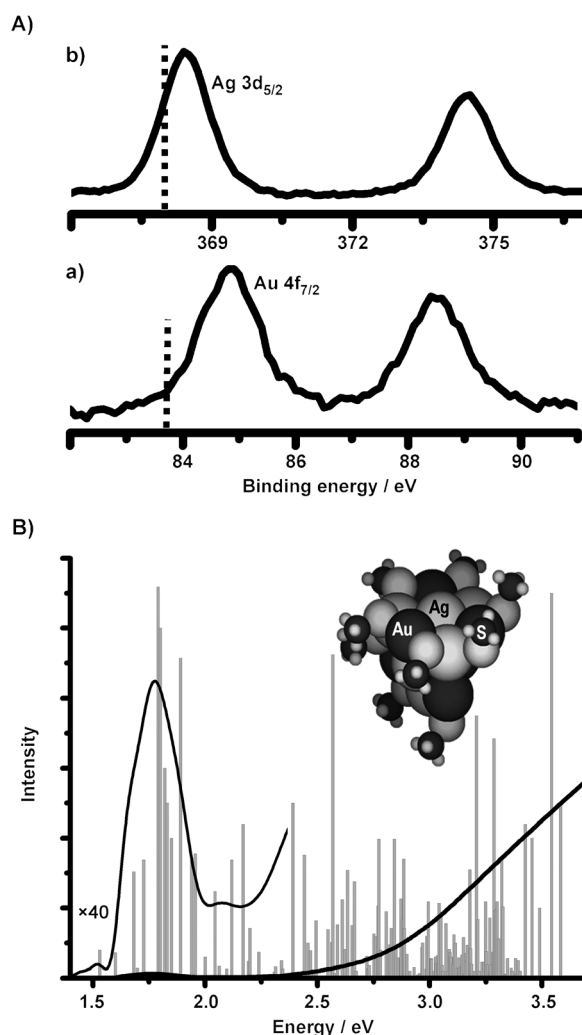


Figure 2. A) XPS spectra in the a) Au 4f and b) Ag 3d regions of $\text{Ag}_7\text{Au}_6(\text{H}_2\text{MSA})_{10}$. Dotted lines indicate the $\text{Au} 4f_{7/2}$ and $\text{Ag} 3d_{5/2}$ positions of the Au^0 and Ag^0 metallic films. B) Simulated absorption spectrum using time-dependent density functional theory (TDDFT). The data are compared with the experimental spectrum (full line). The region in between 1.4 to 2.3 eV is expanded. Inset: One of the optimized structures of the model cluster, $\text{Ag}_7\text{Au}_6(\text{SCH}_3)_{10}$, with which the spectrum was simulated. Ag large light gray, Au black, S small dark gray, CH_3 small light gray.

smaller extent of electron donation from the Au core to thiol ligands in QCs. $\text{Ag} 3d_{5/2}$ (BE of 368.1 eV) supports the Ag^0 state (Figure 2A, b). Note that there is not much difference in BE between Ag^0 and Ag^{I} states, unlike in the case of Au. The $\text{S} 2p_{3/2}$ BE is thiolate-like and a value of 162.0 eV is observed (Supporting Information, S5). An additional $\text{S} 2p_{3/2}$ peak at 164.1 eV observed upon peak fitting may be due to other ligand binding sites or X-ray induced damage.^[14] The total area of the both peaks was used for the estimation of sulfur. An XPS study confirms that a cluster composed of Au and Ag was formed with thiolate protection. ¹H NMR of the cluster is similar to $\text{Ag}_{7,8}$ ^[10d] and Ag_9 ^[10h] clusters protected with MSA, but extent of chemical shift and line broadening are different.

Several direct and indirect methods were used to know the composition of the alloy QC. All the results (discussed

below) compelled us to assign a formula of $\text{Ag}_7\text{Au}_6(\text{MSA})_{10}$ to the cluster. The Ag/Au/S atomic ratio measured in EDAX and XPS were 1:0.82:1.42 and 1:0.84:1.40, respectively in agreement with the ratio expected from the composition of $\text{Ag}_7\text{Au}_6(\text{MSA})_{10}$, namely, 1:0.86:1.43 (normalized with respect to Ag). Elemental analysis showed that the cluster contains an organic fraction of about 43.7% (C 14.03, H 1.76, O 18.68, S 9.34%), in good agreement with calculated value of 43.4%. Au and Ag were independently estimated by ICP AES and were found to be 35.2% and 23.4%, respectively (expected 34.4 and 22.0%, respectively).

We have investigated the geometric and electronic structures of the model system, $\text{Ag}_7\text{Au}_6(\text{SCH}_3)_{10}$ theoretically (for details, see the Supporting Information, S1). The Ag_7Au_6 core was fully optimized without any symmetry restrictions and then the ligands were added, yielding $\text{Ag}_7\text{Au}_6(\text{SCH}_3)_{10}$; the structure was optimized again. One of the possible structures is presented in Figure 2B, which originated from the Ag_7Au_6 core of C_{2v} symmetry, with the thiolates bonded in a bridged form, $-\text{Au}/\text{Ag}-\text{SR}-\text{Au}/\text{Ag}-$. The structure has a distorted icosahedral core. The simulated absorption spectra of this structure obtained by time-dependent density functional theory (TDDFT) agreed well with the experimental results, showing several excited states with relatively strong oscillator strengths coinciding with the experimentally measured values of 350 and 692 nm. There are a few other structures of similar energies as well (Supporting Information, S8).

Electrospray ionization mass spectrometry (ESI-MS) measurements of the as-prepared cluster does not show characteristic peaks owing to its decomposition at capillary temperatures. This is not surprising as the cluster in aqueous medium starts degrading to thiolates around 313 K. Similar degradation was also observed for Ag_9 QCs.^[10b] To create charged droplets at minimum capillary temperatures in ESI, we performed partial ligand exchange and transferred the cluster to the organic medium (Supporting Information, S1). The exchanged product in toluene shows absorption peaks at 350 and 690 nm that match with the absorption profiles of the MSA protected cluster, thus indicating that the cluster core is the same under ligand exchange.^[3b] Luminescence spectra also did not show change, suggesting the same (Supporting Information, S9). It was important that the ligand exchange was partial so that some H_2MSA ligands are also present on the cluster that could yield carboxylate ions upon ionization.

A mass spectrum of PET⁻ (phenylethanethiol) exchanged clusters in toluene/methanol (1:1, v/v) mixture (Figure 3) showed characteristic signatures that correspond to these clusters. Several aspects of the mass spectrum support a chemical composition of $\text{Ag}_7\text{Au}_6(\text{ligand})_{10}$ for the cluster. First, the observed isotope pattern matches perfectly with the theoretical prediction. Second, the peak positions of the ions are in perfect agreement, and third, the mass spectral series terminate exactly after six tropylium losses, as only six PET ligands are exchanged and they only can show these losses. The spectrum is seen only in the negative-ion mode, as H_2MSA is a dicarboxylic acid (giving MSA dianion after complete ionization). This assignment also matches well with the HT exchanged cluster (Supporting Information, S10). The

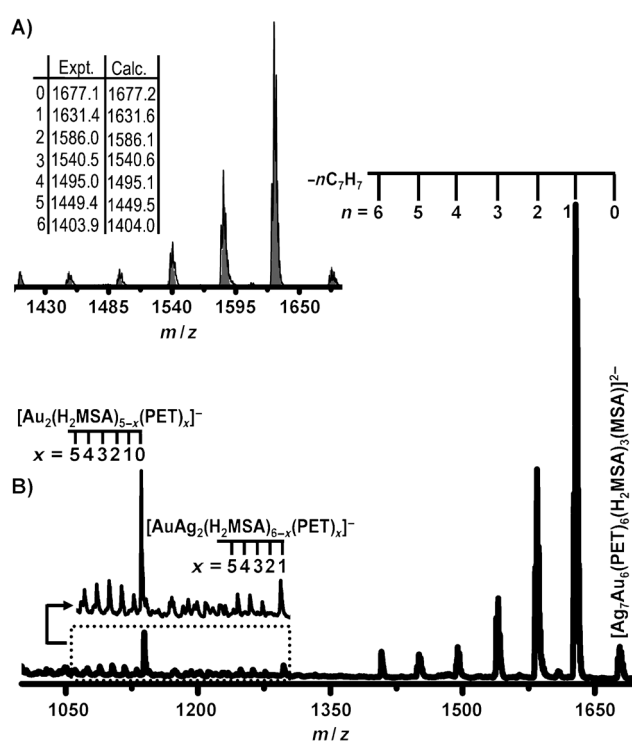


Figure 3. ESI MS spectrum of the PET-exchanged cluster in the negative-ion mode and in the region m/z 1000–1700. Sequential loss of tropylium ($n=0, 1, 2, \dots, 6$) was seen in ionization. The clusters show substitution of six ligands. The calculated isotope pattern is shown as gray under the experimental peak envelope in inset A. Inset B shows fragments.

lower-mass (m/z 1000–1300) peaks are from the smaller fragments owing to fragmentation. The peaks in the series are separated by m/z 12 and are due to the exchange of PET (MW 138.20) for H_2MSA (MW 150.15), as shown in Figure 3B.

Several experimental results^[3b,17] suggest that the position and intensity of the emission depends on the type of the protecting ligand. The luminescence intensity was a function of ligand protection; it followed the trend $\text{PET} > \text{OT} > \text{HT}$. The ligands influence the luminescence emission as observed in the Au_{25} system.^[3c,15] $\text{Ag}_7\text{Au}_6(\text{MSA})_{10}$ shows enhancement in luminescence upon phase transfer to toluene using phase transfer agent TOABr (Supporting Information, S11).^[3c,10k] The average luminescence lifetimes for these samples before and after phase transfer were 1.0 and 10.0 ns, respectively. The percentage of the faster component decreased by 30% after phase transfer; this is a consequence of reduction in non-radiative decay.^[3b] This kind of reduction is also observed for ligand-exchanged products (excitation at 409 nm and detection at 650 nm) of $\text{Ag}_7\text{Au}_6(\text{PET})_x(\text{H}_2\text{MSA})_{10-x}$, $\text{Ag}_7\text{Au}_6(\text{HT})_x(\text{H}_2\text{MSA})_{10-x}$, and $\text{Ag}_7\text{Au}_6(\text{OT})_x(\text{H}_2\text{MSA})_{10-x}$. Their average luminescence lifetimes are in the order $\text{PET} > \text{OT} > \text{HT}$ (11.9 > 7.9 > 4.8 ns). All of the samples exhibit a tri-exponential decay. There seems to be a pattern of average lifetime that may depend on the electron-donating property of the ligands.^[15] Lifetimes of the cluster before and after phase transfer and ligand exchange are given in the Supporting Information, S12.

From our previous reports, QCs undergo decomposition in presence of free metal ions, especially Au^{3+} .^[3f] It is also known that a metal-core galvanic exchange reaction was successful when Ag/Pd/Cu nanoparticles were treated with $\text{Au}^{\text{I}}\text{SR}$ instead of Au^{3+} .^[16] We propose that the mechanism of formation of the bimetallic clusters involves the reaction of Au^{3+} with unbound H_2MSA or Ag thiolate, forming Au^{I} -thiolate, which reacts with the $\text{Ag}_{7,8}$ clusters to form the alloy cluster. Indeed, the addition of Au^{I} thiolate to pure PAGE-separated Ag_8 clusters also forms the desired product. The addition (of more than the optimized amount) of HAuCl_4 to crude $\text{Ag}_{7,8}$ clusters produces plasmonic nanoparticles, and further addition leads to charge neutralization according to the Schultz–Hardy rule,^[18] resulting in coagulation and settling. This residue was analyzed using TEM, SEM, and a luminescence image, which shows the presence of tubular arrangement of nanoparticles (Supporting Information, S13). It is expected that thiolate acts as a template for this arrangement of nanoparticles (note that thiolate structures are layered).^[17] Several systematic control experiments were carried out to improve the yield of the alloy cluster and to arrive at this simplified procedure (Supporting Information, S14).

It is important to have various specific ingredients to form the cluster. Direct addition of HAuCl_4 to Ag^{I} thiolate or to PAGE-purified Ag_8 separately did not produce the desired product. In the former case, it is understood that there is no driving force for the reduction of Au^{3+} . In the latter case, the addition of HAuCl_4 to pure Ag_8 leads to the decomposition of the cluster and simultaneous reduction of Au^{3+} . This results in the formation of differently shaped gold–silver plasmonic nanomaterials (Supporting Information, S15, S16). This kind of decomposition reaction was observed in purified crude mixture of clusters (in the absence of thiolates + unbound H_2MSA ; for details see the Supporting Information, S1), indicating that both the clusters are playing a similar role in the reaction. However, a detailed mechanism of the formation of alloy clusters requires extensive investigations.

Similar experiments were carried out by taking glutathione-protected clusters. For this case, interfacial etching of polydisperse Ag@MSA was carried out with glutathione to produce Ag@SG QCs. The addition of HAuCl_4 to crude Ag@SG gives a red luminescent alloy QC with a distinct absorption profile. The protection of glutathione was confirmed by NMR spectroscopy (Supporting Information, S17). The extent of reaction to other kinds of silver QCs was also checked. For that we selected well-characterized, atomically pure $\text{Ag}_9(\text{MSA})_7$.^[10b] There are changes in the absorption profile during the reaction between $\text{Au}^{\text{I}}\text{MSA}$ and Ag_9 QCs. Reactions are very sensitive to the concentrations of reactants, and diverse clusters of varying properties can be prepared (Supporting Information, S18). Detailed experimental characterization of the clusters is beyond the scope of this work and will be reported separately.

In summary, a new 13-core Ag_7Au_6 QC was synthesized by a galvanic exchange reaction, starting from $\text{Ag}_{7,8}$ precursor. It exhibits quantum confinement in the absorption profile. The cluster is pure as confirmed by PAGE and was characterized by UV/Vis, FTIR, luminescence, TEM, XPS, SEM/EDAX,

and ESI MS. Possible structures have been investigated theoretically. The extension of this reaction to produce various alloy QCs was carried out by taking $\text{Ag}_{\text{QC}}@\text{SG}$ and $\text{Ag}_9(\text{MSA})_7$ as examples.

Experimental Section

Synthesis of alloy QCs: To of as-synthesized crude $\text{Ag}_{7,8}$ cluster (3.0 mL reddish brown solution in water containing $\text{Ag}_8 + \text{Ag}_7 + \text{thiolate}$) without washing, containing 10.0 mg of clusters, HAuCl_4 (6.0 mL, 10 mM) was added and stirred for 15 min at 293 K. The formation of the cluster was checked by the appearance of luminescence under UV light which was absent at 300 K for the parent clusters. The resultant solution was centrifuged to remove AgCl and thiolate. The reaction product was precipitated by the addition of excess methanol and washed to remove dissolved reactants such as H_2MSA or other ions. The cluster product was obtained by solvent evaporation using a rotary evaporator and the material was stored in the laboratory atmosphere. Analytical and computational methods are described in the Supporting Information, S1.

Received: November 1, 2011

Published online: January 20, 2012

Keywords: alloy clusters · ESI-MS · luminescence · quantum clusters · silver

- [1] a) P. A. Bartlett, B. Bauer, S. J. Singer, *J. Am. Chem. Soc.* **1978**, *100*, 5085; b) C. E. Briant, B. R. C. Theobald, J. W. White, C. K. Bell, D. M. P. Mingos, A. J. Welch, *J. Chem. Soc. Chem. Commun.* **1981**, 201; c) J. W. A. van der Velden, F. A. Vollenbroek, J. J. Bour, P. T. Beurskens, J. M. M. Smits, W. P. Bosman, *Recl. J. R. Neth. Chem. Soc.* **1981**, *100*, 148; d) G. Schmid, R. Pfeil, R. Boese, F. Bandermann, S. Meyer, G. H. M. Calis, J. W. A. Van der Velden, *Chem. Ber.* **1981**, *114*, 3634.
- [2] L. F. Chi, M. Hartig, T. Drechsler, T. Schwaack, C. Seidel, H. Fuchs, G. Schmid, *Appl. Phys. A* **1998**, *66*, S187.
- [3] a) R. Jin, *Nanoscale* **2010**, *2*, 343, and references therein; b) P. L. Xavier, K. Chaudhari, P. K. Verma, S. K. Pal, T. Pradeep, *Nanoscale* **2010**, *2*, 2769; c) M. A. Habeeb Muhammed, P. K. Verma, S. K. Pal, R. C. Arun Kumar, S. Paul, R. V. Omkumar, T. Pradeep, *Chem. Eur. J.* **2009**, *15*, 10110; d) E. S. Shibu, B. Radha, P. K. Verma, P. Bhyrappa, G. U. Kulkarni, S. K. Pal, T. Pradeep, *ACS Appl. Mater. Interfaces* **2009**, *1*, 2199; e) H. Qian, Y. Zhu, R. Jin, *J. Am. Chem. Soc.* **2010**, *132*, 4583; f) M. A. Habeeb Muhammed, T. Pradeep, *Chem. Phys. Lett.* **2007**, *449*, 186; g) P. Ramasamy, S. Guha, E. S. Shibu, T. S. Sreeprasad, S. Bag, A. Banerjee, T. Pradeep, *J. Mater. Chem.* **2009**, *19*, 8456; h) E. S. Shibu, M. A. Habeeb Muhammed, T. Tsukuda, T. Pradeep, *J. Phys. Chem. C* **2008**, *112*, 12168.
- [4] C. L. Haynes, A. D. McFarland, L. L. Zhao, R. P. Van Duyne, G. C. Schatz, L. Gunnarsson, J. Prikulis, B. Kasemo, M. Kall, *J. Phys. Chem. B* **2003**, *107*, 7337.
- [5] a) A. M. Gobin, M. H. Lee, N. J. Halas, W. D. James, R. A. Drezek, J. L. West, *Nano Lett.* **2007**, *7*, 1929; b) A. Verma, O. Uzun, Y. H. Hu, Y. Hu, H. S. Han, N. Watson, S. L. Chen, D. J. Irvine, F. Stellacci, *Nat. Mater.* **2008**, *7*, 588.
- [6] Y. Zhu, H. Qian, B. A. Drake, R. Jin, *Angew. Chem.* **2010**, *122*, 1317; *Angew. Chem. Int. Ed.* **2010**, *49*, 1295.
- [7] a) G. Ramakrishna, O. Varnavski, J. Kim, D. Lee, T. Goodson, *J. Am. Chem. Soc.* **2008**, *130*, 5032; b) J. I. Gonzalez, T.-H. Lee, M. D. Barnes, Y. Antoku, R. M. Dickson, *Phys. Rev. Lett.* **2004**, *93*, 147402; c) M. A. Habeeb Muhammed, A. K. Shaw, S. K. Pal,

- T. Pradeep, *J. Phys. Chem. C* **2008**, *112*, 14324; d) N. Sakai, T. Tatsuma, *Adv. Mater.* **2010**, *22*, 3185.
- [8] H. Häkkinen, *Chem. Soc. Rev.* **2008**, *37*, 1847.
- [9] a) P. D. Jadzinsky, G. Calero, C. J. Ackerson, D. A. Bushnell, R. D. Kornberg, *Science* **2007**, *318*, 430; b) M. W. Heaven, A. Dass, P. S. White, K. M. Holt, R. W. Murray, *J. Am. Chem. Soc.* **2008**, *130*, 3754.
- [10] a) O. M. Bakr, V. Amendola, C. M. Aikens, W. Wenselers, R. Li, L. D. Negro, G. C. Schatz, F. Stellacci, *Angew. Chem.* **2009**, *121*, 6035; *Angew. Chem. Int. Ed.* **2009**, *48*, 5921; b) Z. Wu, E. Lanni, W. Chen, M. E. Bier, D. H. Ly, R. Jin, *J. Am. Chem. Soc.* **2009**, *131*, 16672; c) N. Nishida, H. Yao, T. Ueda, A. Sasaki, K. Kimura, *Chem. Mater.* **2007**, *19*, 2831; d) T. Udaya Bhaskara Rao, T. Pradeep, *Angew. Chem.* **2010**, *122*, 4017; *Angew. Chem. Int. Ed.* **2010**, *49*, 3925; e) H. Yao, M. Saeki, K. Kimura, *J. Phys. Chem. C* **2010**, *114*, 15909; f) K. V. Mrudula, T. Udaya Bhaskara Rao, T. Pradeep, *J. Mater. Chem.* **2009**, *19*, 4335; g) N. Cathcart, V. Kitaev, *J. Phys. Chem. C* **2010**, *114*, 16010; h) T. U. B. Rao, B. Nataraju, T. Pradeep, *J. Am. Chem. Soc.* **2010**, *132*, 16307; i) S. Kumar, M. D. Bolan, T. P. Bigioni, *J. Am. Chem. Soc.* **2010**, *132*, 1314; j) I. Díez, R. H. A. Ras, *Nanoscale* **2011**, *3*, 1963; k) I. Díez, H. Jiang, R. H. A. Ras, *ChemPhysChem* **2010**, *11*, 3100; l) I. Dez, M. Pusa, S. Kulmala, H. Jiang, A. Walther, A. S. Goldmann, A. H. E. Muller, O. Ikkala, R. H. A. Ras, *Angew. Chem.* **2009**, *121*, 2156; *Angew. Chem. Int. Ed.* **2009**, *48*, 2122.
- [11] a) C. A. Fields-Zinna, M. C. Crowe, A. Dass, J. E. F. Weaver, R. W. Murray, *Langmuir* **2009**, *25*, 7704; b) Y. Negishi, W. Kurashige, Y. Niihori, T. Iwasa, K. Nobusada, *Phys. Chem. Chem. Phys.* **2010**, *12*, 6219; c) Y. Negishi, T. Iwai, M. Ide, *Chem. Commun.* **2010**, *46*, 4713; d) C. Kumara, A. Dass, *Nanoscale* **2011**, *3*, 3064; e) H. Qian, E. Barry, Y. Zhu, R. Jin, *Acta Phys. Chim. Sin.* **2011**, *27*, 513.
- [12] a) G. M. Concepcion, A. Laguna, *Chem. Soc. Rev.* **2008**, *37*, 1952; b) A. Laguna, T. Lasanta, J. M. López-de-Luzuriaga, M. Monge, P. Naumo, M. E. Olmos, *J. Am. Chem. Soc.* **2010**, *132*, 456.
- [13] L. D. Menard, S.-P. Gao, H. Xu, R. D. Twisten, A. S. Harper, G. Wang, A. D. Douglas, J. C. Yang, A. I. Frenkel, R. G. Nuzzo, R. W. Murray, *J. Phys. Chem. B* **2006**, *110*, 12874.
- [14] M. S. Bootharaju, T. Pradeep, *Langmuir* **2011**, *27*, 8134.
- [15] Z. Wu, R. Jin, *Nano Lett.* **2010**, *10*, 2568.
- [16] a) Y.-S. Shon, G. B. Dawson, M. Porter, R. W. Murray, *Langmuir* **2002**, *18*, 3880; b) T. Huang, R. W. Murray, *J. Phys. Chem. B* **2003**, *107*, 7434.
- [17] a) N. Sandhyarani, M. P. Antony, G. Panneer Selvam, T. Pradeep, *J. Chem. Phys.* **2000**, *113*, 9794; b) I. G. Dance, K. J. Fisher, R. M. H. Banda, M. L. Scudder, *Inorg. Chem.* **1991**, *30*, 183.
- [18] W. Nowicki, G. Nowicka, *J. Chem. Educ.* **1994**, *71*, 624.

Supporting Information

© Wiley-VCH 2012

69451 Weinheim, Germany

Ag₇Au₆: A 13-Atom Alloy Quantum Cluster**

*Thumu Udayabhaskararao, Yan Sun, Nirmal Goswami, Samir K. Pal, K. Balasubramanian, and Thalappil Pradeep**

anie_201107696_sm_miscellaneous_information.pdf

Table of contents

Number	Description	Page number
S1	Experimental section, analytical and computational procedures	2-4
S2	Confirming AgCl using SEM/EDAX and XRD	5-6
S3	Comparison of crude and PAGE separated clusters	7
S4	TEM, effect of electron beam irradiation	8
S5	XPS spectrum	9
S6	FT-IR spectrum	10
S7	EDAX spectrum and images	11
S8	Another possible structures of the model cluster, $\text{Ag}_7\text{Au}_6(\text{SCH}_3)_{10}$	12
S9	Luminescence spectra of ligand exchanged products	13
S10	Mass spectrum of HT exchanged cluster	14
S11	Luminescence spectra of before and after phase transfer	15
S12	Life time measurements	16
S13	TEM, SEM and luminescence studies on tubular arrangement of nanoparticles	17
S14	Effect of various amounts of HAuCl_4	18
S15	Blank reactions	19
S16	TEM of gold-silver plasmonic nanomaterials	20
S17	^1H NMR of $(\text{Ag}_m\text{Au}_n)_{\text{QC}}@SG$ QCs	21
S18	Photographs of various alloy QCs from $\text{Ag}_9(\text{MSA})_7$	22

S1. Supporting information 1

Experimental Section

Synthesis of Ag_{7,8}: About 85 mg of AgNO₃, dissolved in 1.7 mL water, was added to 448.9 mg of H₂MSA in 100 mL methanol under ice-cold conditions with vigorous stirring. Silver was reduced to the zero-valent state by slow addition of freshly prepared aqueous NaBH₄ solution (0.2 M, 25 mL). The reaction mixture was stirred for 1 h. The resulting precipitate was collected and repeatedly washed with methanol by centrifugal precipitation. Finally, the Ag@(H₂MSA) precipitate was dried and collected as a dark brown powder. Interfacial etching was performed in an aqueous/organic biphasic system. Ag@(H₂MSA) (100 mg in 100 mL H₂O) was dispersed in the aqueous phase. An aqueous solution of the as-synthesized Ag@(H₂MSA) nanoparticles was added to an excess of H₂MSA in toluene (1/2 water/toluene ratio). A weight ratio of 1:3 was used (Ag@(H₂MSA):H₂MSA). The resulting mixture was stirred for 48 h at room temperature (ca. 300 K). Initiation of interfacial etching is indicated by the appearance of a blue layer at the interface after 0.5–1 h. As the reaction proceeds, the color of the aqueous phase changes from reddish brown to yellow, and finally to orange. After centrifugation, thiolate got precipitated and gives a reddish brown solution which contains Ag₈, Ag₇, smaller amounts of thiolate and unbound H₂MSA. This solution is mentioned as crude Ag_{7,8} cluster solution. For further purification the solution was concentrated using freeze dry. The concentrated sample was centrifuged at 18,000 rpm, 278 K for 20 min to remove of thiolates. By the addition of methanol to supernatant, cluster product was precipitated from it and the precipitate was repeatedly washed with 90% methanol to remove excess H₂MSA. The final precipitate contains both clusters and free from thiolates and H₂MSA.

Ag₇Au₆ clusters were prepared as mentioned in the main text.

Ligand exchange reactions: Exchange reaction was done with phenylethanethiol (PET), hexanethiol (HT) and octanethiol (OT). 0.01M of these thiols were taken in 2.0 mL of toluene on top of 3.0 mL (3.3 mg/mL) of Ag₇Au₆(H₂MSA)₁₀ cluster solution. The mixture was gently stirred for 3 hours at 273 K. Exchange can be observed directly by visible color change of the toluene phase from colorless to reddish yellow. This was subjected to solvent evaporation to yield a paste-like material, which was washed with water several times and the final precipitate was soluble in toluene. Analytical and computational methods are described in S1.

Synthesis of Ag_{qc}@SG: Ag@H₂MSA nanoparticles and glutathione were taken (weight ratio of 1:3) in aqueous/toluene biphasic system. The resulting mixture was stirred for 48 h at room temperature (~300 K). As the reaction proceeds, the reddish brown color of the aqueous phase gradually disappears and finally it converts to orange. The separated aqueous phase is freeze dried and was washed with methanol to remove excess GSH. The product in powder form was obtained by solvent evaporation using rotavapor and stored in closed container since it is hygroscopic.

Phase transfer of Ag₇Au₆(H₂MSA)₁₀: 10 mg of alloy clusters was dissolved in 50 mL of distilled water. 5 mL of 3 mM TOABr [tetraoctylammonium bromide {CH₃(CH₂)₇]₄N Br] in toluene was added to make an immiscible layer above the water phase. Toluene got colored upon stirring the mixture for 2 min, indicating the transfer of cluster from aqueous to organic phase. Phase transfer occurred due to the electrostatic interaction of anionic carboxylic group of MSA to quaternary nitrogen group of TOA⁺.

Purification by polyacrylamide gel electrophoresis (PAGE): PAGE separation of the clusters was performed as per the procedure given below.

A gel electrophoresis unit with 1 mm thick spacer (Bio-rad, Mini-protein Tetra cell) was used to process the PAGE. The total contents of the acrylamide monomers were 28% (bis(acrylamide:acrylamide) = 7:93) and 3% (bis(acrylamide:acrylamide) = 6:94) for the separation and condensation gels, respectively. The eluting buffer

consisted of 192 mM glycine and 25 mM tris(hydroxymethylamine). The crude mixture of Ag@(H₂MSA) clusters, as a reddish brown powder, obtained in the reaction was dissolved in 5% (v/v) glycerol-water solution (1.0 mL) at a concentration of 60 mg/mL. The sample solution (1.0 mL) was loaded onto a 1 mm gel and eluted for 4 h at a constant voltage of 120 V to achieve separation shown in Figure 1. During the gel electrophoresis, PAGE setup was kept at ice cold temperature. The gel fractions containing the cluster were cut out, ground, and dipped in ice cold distilled water (2 mL) for 10 min. Subsequently, the solutions were centrifuged at 20,000 rpm for 5 min at -263 K, followed by filtering with filter paper having 0.22 μm pores to remove the gel lumps suspended in the solution. The samples were freeze dried to get reddish yellow powders. Same procedure was used to separate Ag₈ cluster from Ag_{7,8}.

We also performed high resolution electrophoresis using increased contents of acrylamide monomers of 35% for the separation gel. However, we did not observe any additional bands.

Analytical procedures

A. UV-vis spectroscopy

Perkin Elmer Lambda 25 UV-vis spectrometer was used for the measurements. Spectra were typically measured in the range of 190-1100 nm. The experimentally obtained spectral data, $I(\lambda)$, which are functions of wavelength, were converted to the energy dependent data, $I(E)$, according to the following relation, $I(E) = I(\lambda) / (\lambda^2 E^2)$ where $d\lambda/dE$ represents the Jacobian factor.

B. Fourier-transform infrared (FT-IR) spectra

FT-IR spectra were measured with a Perkin Elmer Spectrum One instrument. KBr crystals were used as the matrix for sample preparation.

C. Luminescence spectroscopy

Luminescence measurements were carried out using HORIBA JOBIN VYON Nano Log instrument. The band pass for excitation and emission was set as 3 nm.

D. Transmission electron microscopy (TEM)

TEM images were collected using a JEOL 3010 microscope. A diluted solution was spotted on carbon coated copper grid and was dried in laboratory ambience. Images were collected at 200 keV, to reduce beam induced damage of the clusters. Our earlier studies had shown that small clusters are highly sensitive to electron beam and they coalesce to yield nanoparticles on the grid.

E. Electrospray ionization (ESI) mass spectrometry (MS)

The ESI MS measurements were done in the negative mode using an MDX Sciex 3200 QTRAP MS/MS instrument having a mass range of m/z 50-2000. A 50% (v/v) methanol/toluene cluster solution (0.1 mg/mL) was electrosprayed through a stainless steel needle biased at ca. -3 kV. The solution was delivered by a syringe pump at a typical flow rate of 8 μL/min. Under an optimized capillary temperature (ca. 353 K), evaporation of the solvents from the droplets proceeds efficiently so that only the desolvated cluster ions in the intact form were formed at maximum yield. We observed dissociation of the intact clusters into small fragments, at higher capillary temperatures.

G. SEM and EDAX analyses

Scanning electron microscopic (SEM) and energy dispersive X-ray (EDAX) analyses were done in a FEI QUANTA-200 SEM. For measurements, samples were drop-casted on an indium tin oxide coated conducting glass and dried in vacuum.

H. X-ray photoelectron spectroscopy

The photoelectron spectra of the samples were obtained using an ESCA probe/TPD of Omicron Nanotechnology. Sample in water was spotted on a Mo plate and allowed to dry in vacuum. The size of the analyzed area was about 3 mm². In view of the sensitivity of the sample, surface cleaning was not attempted. Al K_a radiation was used for excitation; a 180° hemispherical analyzer and a seven-channel detector were employed. The spectrometer was operated in the constant analyzer energy mode. Survey and high-resolution spectra were collected using pass energies of 50 and 20 eV, respectively. The pressure in the analyzer chamber was in the low 10⁻¹⁰ mbar range during spectrum collection. Binding energies of the core levels were calibrated with C 1s BE, set at 284.7 eV.

I. Luminescence imaging

A Witec GmbH confocal Raman spectrometer, equipped with a Nd:YAG laser frequency doubled laser at 532 nm was used as the excitation source to collect the luminescence images. The laser was focused onto the sample using a 100X objective with the signal collected in a back scattering geometry. The signal, after passing through a super notch filter, was dispersed using a 150 grooves/mm grating onto a Peltier-cooled charge coupled device (CCD), which served as the detector. The sample mounted on a piezo stage was scanned with signals collected at every step. For the images displayed, the scan area was divided into 100X100 pixels for spectral image acquisition. Spectral intensities acquired over a predefined area were automatically compared to generate color-coded images. In the images, regions coded yellow are regions with maximum fluorescence intensities and regions shown in black are with minimum signal intensities.

J. Quantum yield

The quantum yield (QY) of the cluster was measured using rhodamine 6G (in water) as a reference.

K. Computational methods

The structure for Ag₇Au₆(SR)₁₀ was determined theoretically by performing density functional calculations with the Gaussian 09 software^[1] using Perdew-Burke-Ernzerhof (PBE) exchange-correlation (XC) functional,^[2] together with relativistic effective core potentials (RECP) that kept the outer valence 4d¹⁰5s¹ shells of silver atom, 2s²2p² for carbon atom, and 3s² 3p⁴ for sulfur atom, replacing the rest electrons by RECP.^[3] After obtaining the optimized ground state structures of Ag₇Au₆ core by global optimization method Taboo Search in Descriptor Space (TSDS),^[4] we passivated 10 methanethiolate (SCH₃) ligands on the optimized Ag₇Au₆ core and re-optimized these Ag₇Au₆(SCH₃)₁₀ structures, followed by single point calculations for triplet states of Ag₇Au₆(SCH₃)₁₀ based on the structures of the ground states. The simulated absorption spectra of this structure obtained by time-dependent density functional theory (TDDFT).

L. Life time measurements

Picosecond resolved photoluminescence transients of Ag₇Au₆(SR)₁₀ cluster were measured using a commercially available spectrophotometer (LifeSpec-ps, Edinburgh Instruments, UK) with a 409 nm excitation laser having

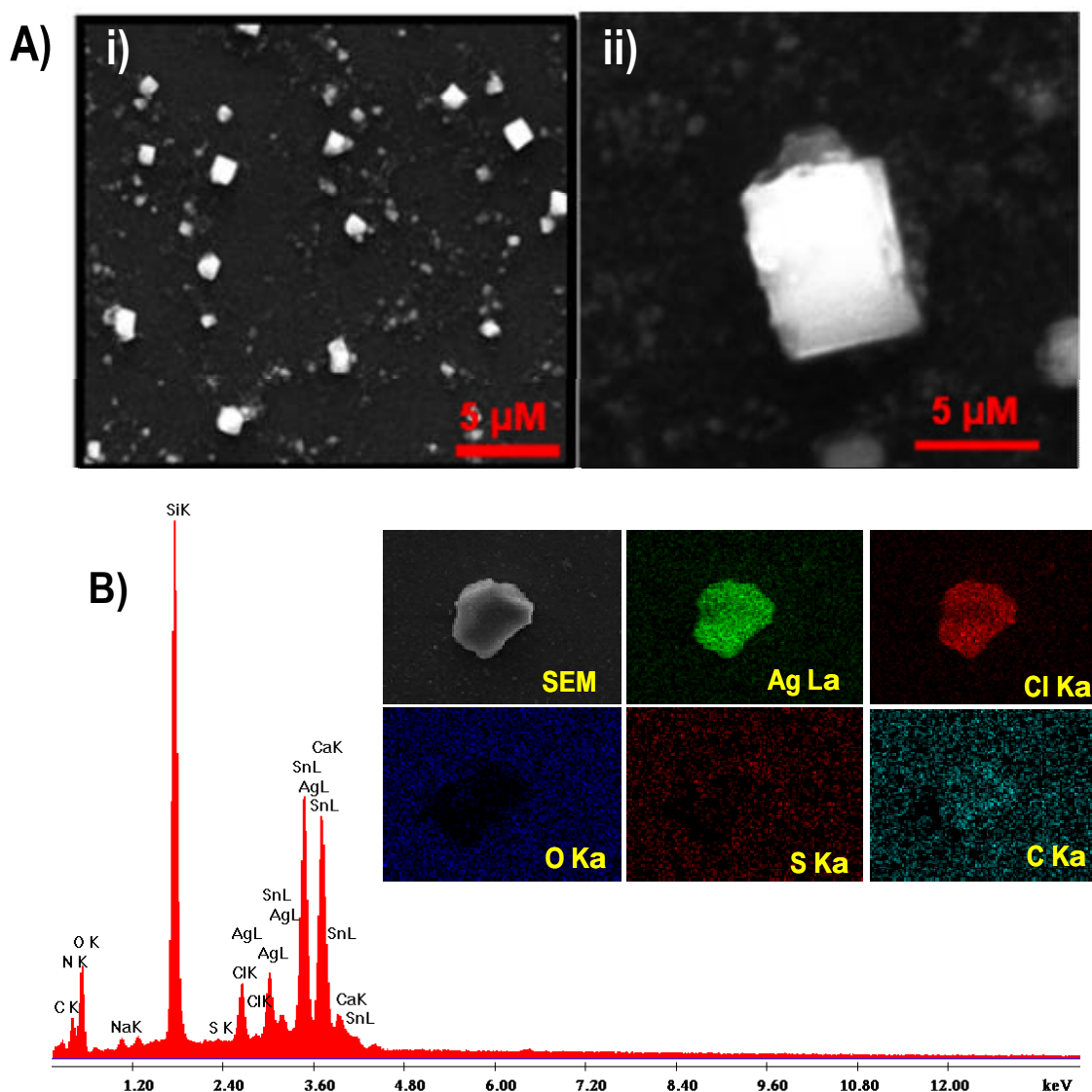
instrument response function (IRF) of 60 ps. The picosecond-resolved fluorescence transients have been fitted with tri-exponential function, $\sum_{i=1}^3 A_i \exp(-t/\tau_i)$, where, A_i 's are weight percentages of the decay components with time constants of τ_i . The relative change in the overall excited state lifetime is expressed by the equation $\tau = \sum_{i=1}^3 A_i \tau_i$, when $\sum_{i=1}^3 A_i = 1$. It has to be noted that with our time resolved instrument after deconvolution, we can resolve at least one fourth of the instrument response time constants.

References:

- [1] Gaussian 09, Revision A.1, Frisch, M. J. et al.
 [2] Perdew, J. P.; Burke, K.; Ernzerhof, M.; *Phys. Rev. Lett.* **1996**, *77*, 3865; **1997**, *78*, 1396 (E).
 [3] Ross, R.B.; Powers, J. M.; Atashroo, T.; Ermler, W.C.; LaJohn, L. A.; Christainsen, P. A.; *J. Chem. Phys.* **1990**, *93*, 6654.
 [4] Cheng, J.; Fournier, R.; *Theor. Chem. Acc.* **2004**, *112*, 7.

S2. Supporting information 2

Confirmation of AgCl from SEM/EDAX and XRD



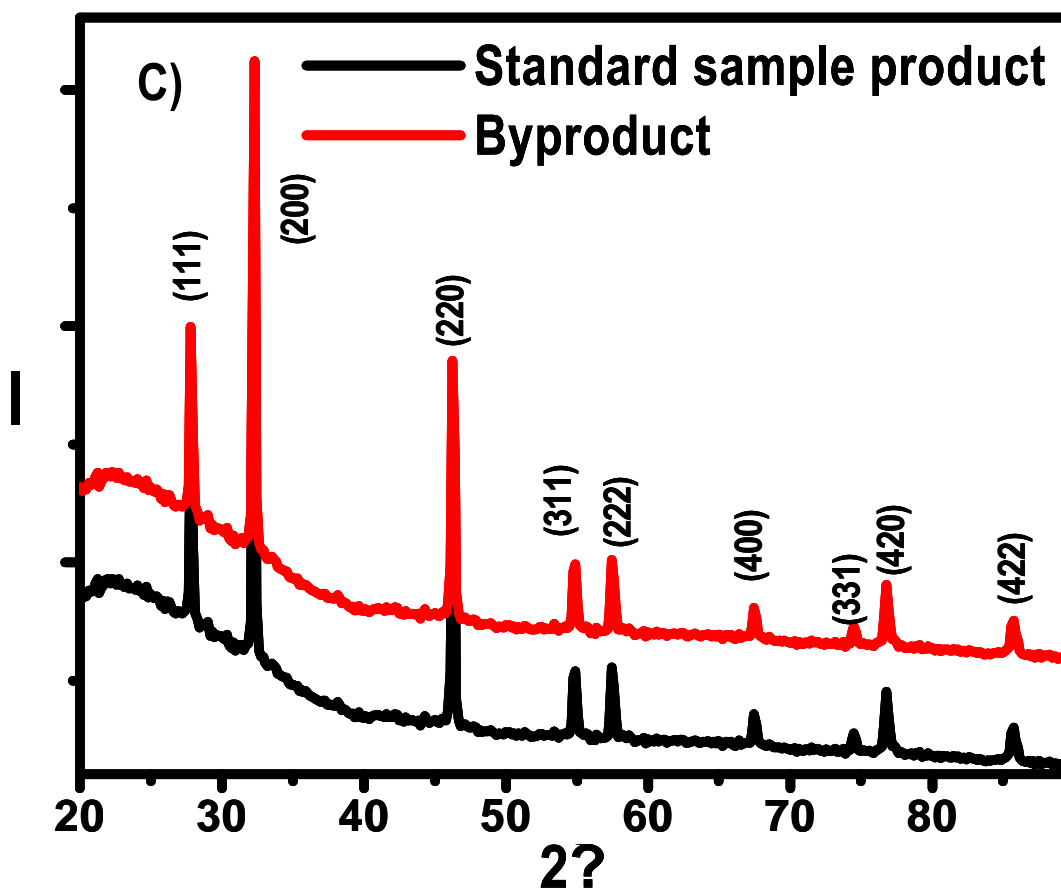


Figure S1.

- A)** I) SEM image of the byproduct during the synthesis of alloy QCs, showing the presence of 1-5 μM sized AgCl crystals, one such crystal in closer view is shown in image II).
- B)** EDAX spectrum and elemental images of the byproduct crystal (I) EDAX spectrum of the byproduct. II) SEM image of the crystal and EDAX maps using III) Ag M_{α} , (IV) Cl K_{α} , (V) O K_{α} (VI) S K_{α} , and (VII) C K_{α} are shown. Sn L_{α} and In L_{α} lines are due to the indium tin oxide substrate used. Ag:Cl atomic ratio measured is almost 1:1, which proves the presence of AgCl.
- C)** XRD patterns of the byproduct obtained during the reaction, is compared with the standard AgCl XRD patterns. Lattice planes are assigned based on JCPDS file no 85-1355. The formation of AgCl confirms that silver atoms from the cluster core are leaching out. Note that Cl^{-} is coming from the HAuCl_4 precursor used in the reaction.

S3. Supporting information 3

Comparison of crude and PAGE separated clusters

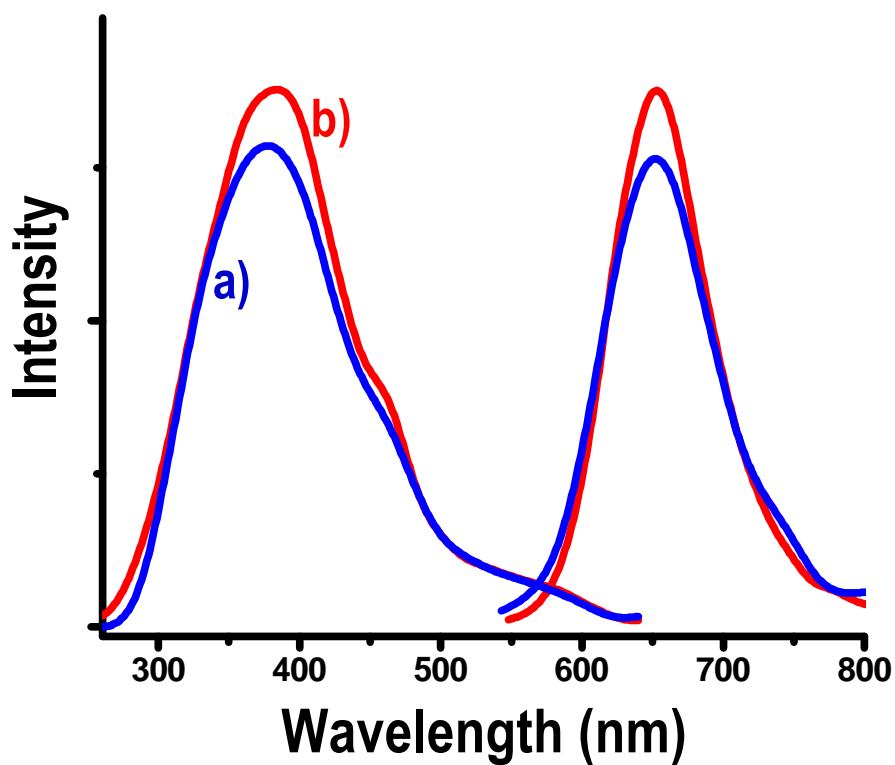


Figure S2. Luminescence spectra of the cluster in water collected at 300 K using the same concentrations. Comparison of the luminescence spectra of (a) as-synthesized cluster (before PAGE) and b) purified cluster (after PAGE).

S4. Supporting information 4

TEM, effect of electron beam irradiation images

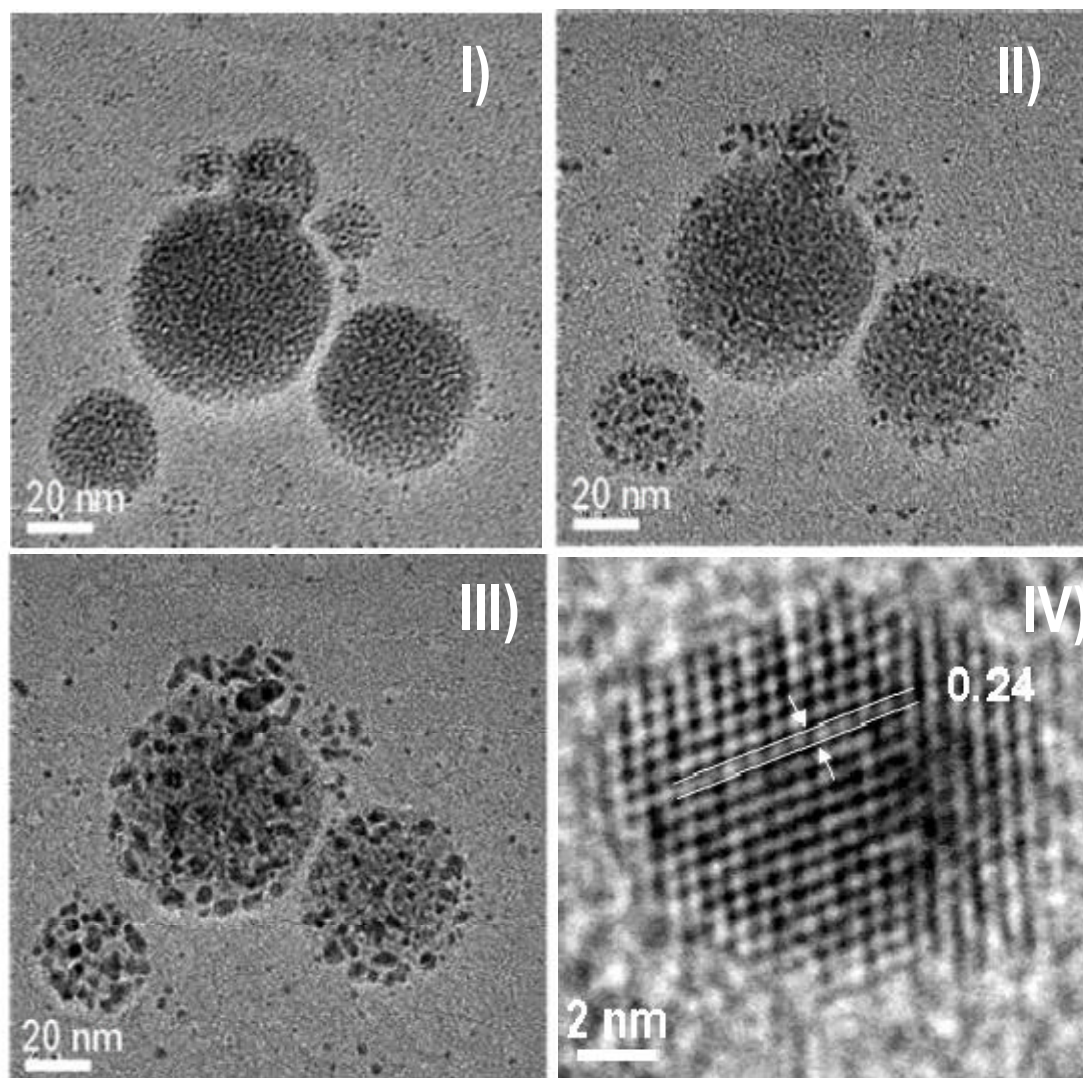


Figure S3. TEM image of Ag₇Au₆ cluster aggregates (I), which upon continuous electron beam irradiation (II) and (III) coalesce to form larger nanoparticles. The same regions of the grid are shown in the images. Image (I) is at the start of the irradiation showing small clusters, image (II) is after 10 min and image (III) is after 20 min. The contrast from the clusters is poor unlike in the case of nanoparticles. Image (IV) is of one grown particle showing the lattice (shown by lines).

S5. Supporting information 5

XPS

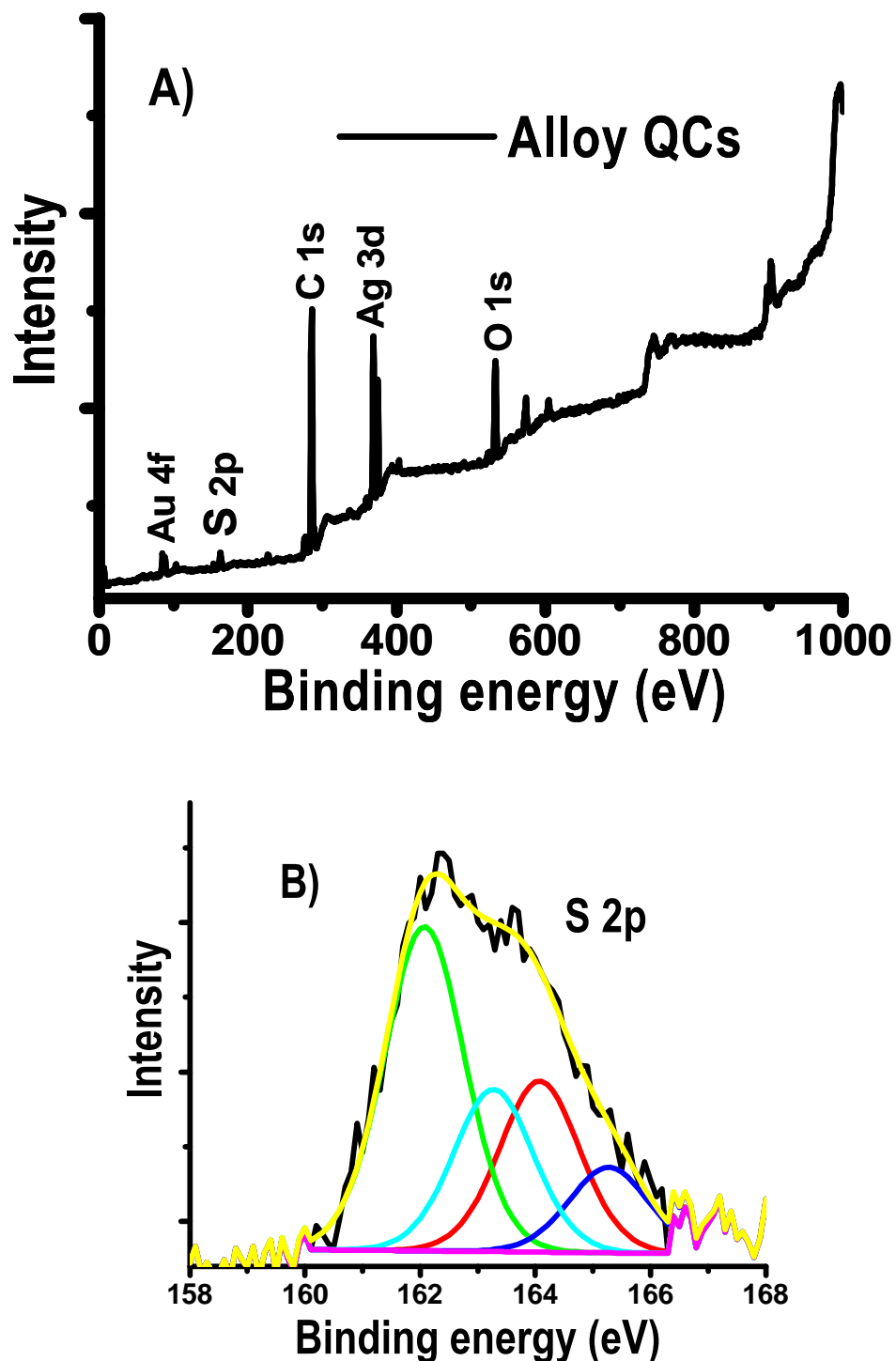


Figure S4. (A) XPS survey spectrum of the as-synthesized alloy QCs. (B) Expanded S 2p core level region. The Ag: Au: S atomic ratio is 1:0.84:1.40 whereas the expected value is 1:0.86:1.43. The S 2p_{3/2} exhibits a thiolate position of 162.0 eV and an additional S 2p_{3/2} peak at 164.1 eV observed upon peak fitting may be due to other ligand binding sites or X-ray induced damage. Total peak area was considered to get the atomic percentage of sulfur.

S6. Supporting information 6

FT-IR

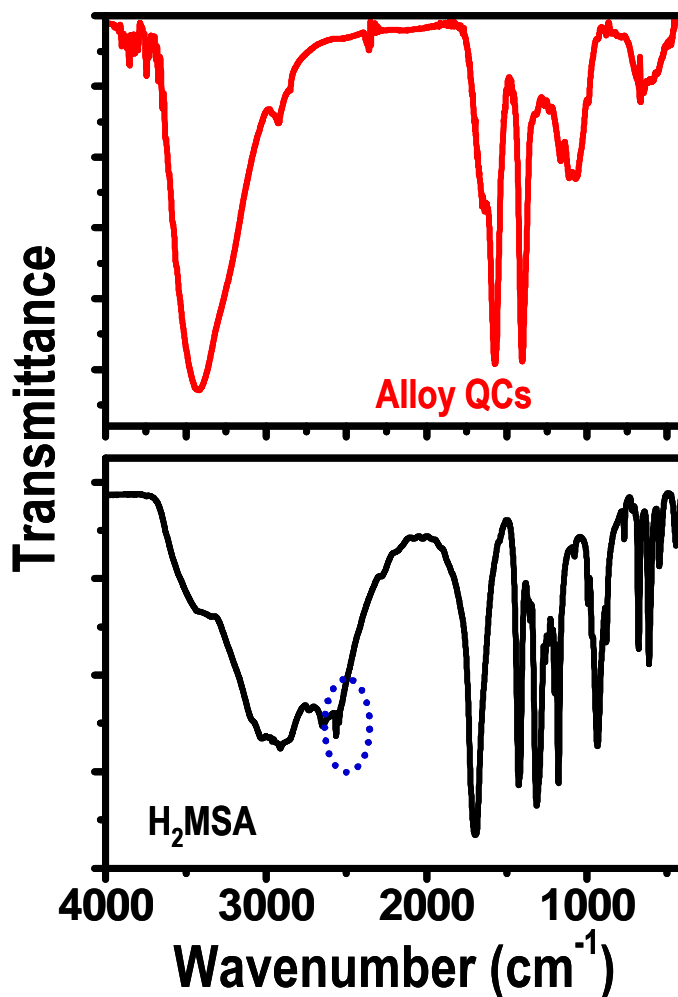


Figure S5. FT-IR spectra of pure H₂MSA, alloy QCs. The -SH stretching feature at 2552 cm⁻¹ in H₂MSA is marked by the dotted-circle is absent in the alloy QCs spectrum, in agreement with the XPS. H₂MSA features in the region of 2000-500 cm⁻¹ confirm the cluster was protected by H₂MSA. A strong band at 3435 cm⁻¹ due to the hydrated water.

S7. Supporting information 7

SEM/EDAX

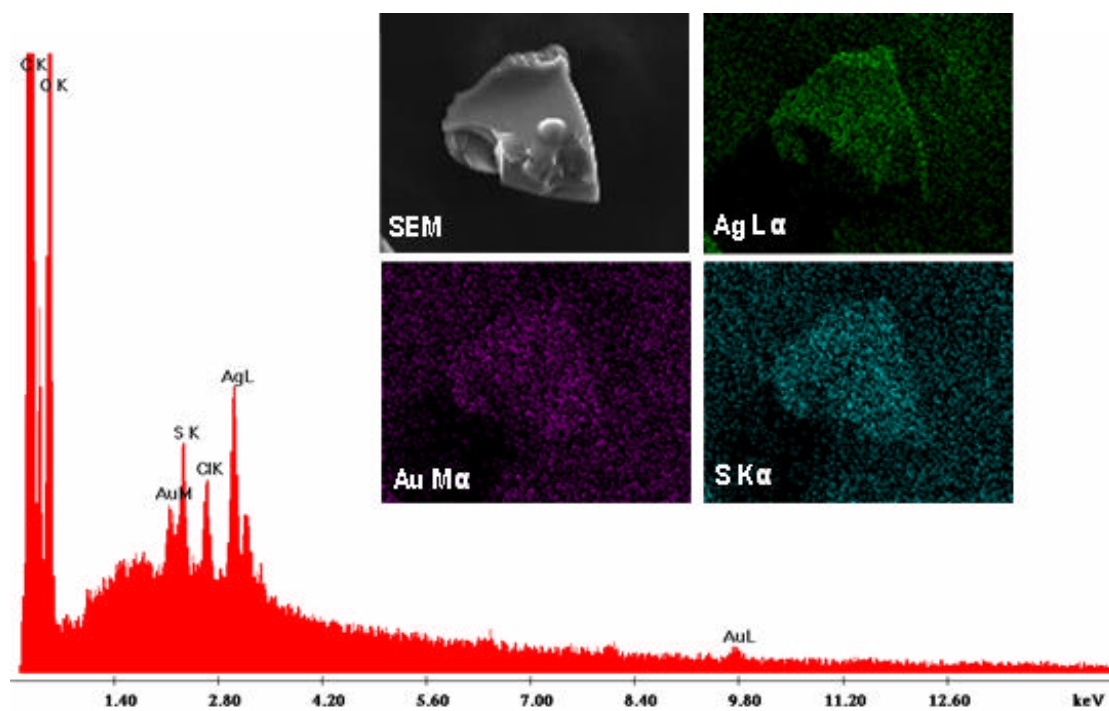


Figure S6. EDAX spectrum collected from alloy QCs. Inset showing the SEM image of the alloy QCs aggregate from which the EDAX spectrum was taken. EDAX maps using Ag L_α, Au M_α, S K_α. Ag: Au: S atomic ratio measured is 1:0.82:1.42, whereas that expected is 1:0.86:1.43.

S8. Supporting information 8

Another structure of the model cluster, $\text{Ag}_7\text{Au}_6(\text{SCH}_3)_{10}$

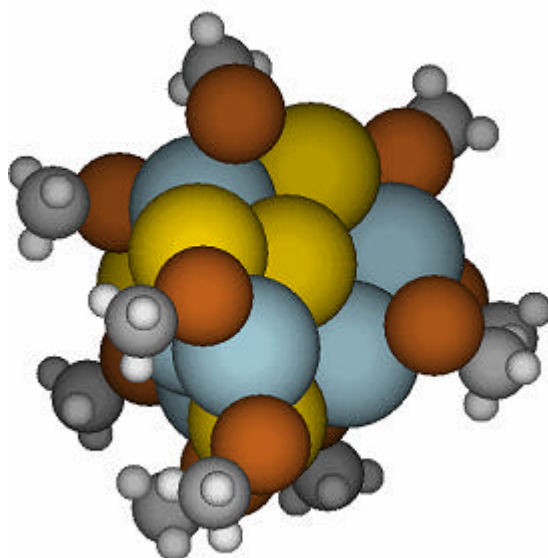


Figure S7. Another possible structure of the model cluster, $\text{Ag}_7\text{Au}_6(\text{SCH}_3)_{10}$. Ag is blue, Au is yellow and S is brown. CH_3 units are also shown.

S9. Supporting information 9

Luminescence of ligand exchanged products

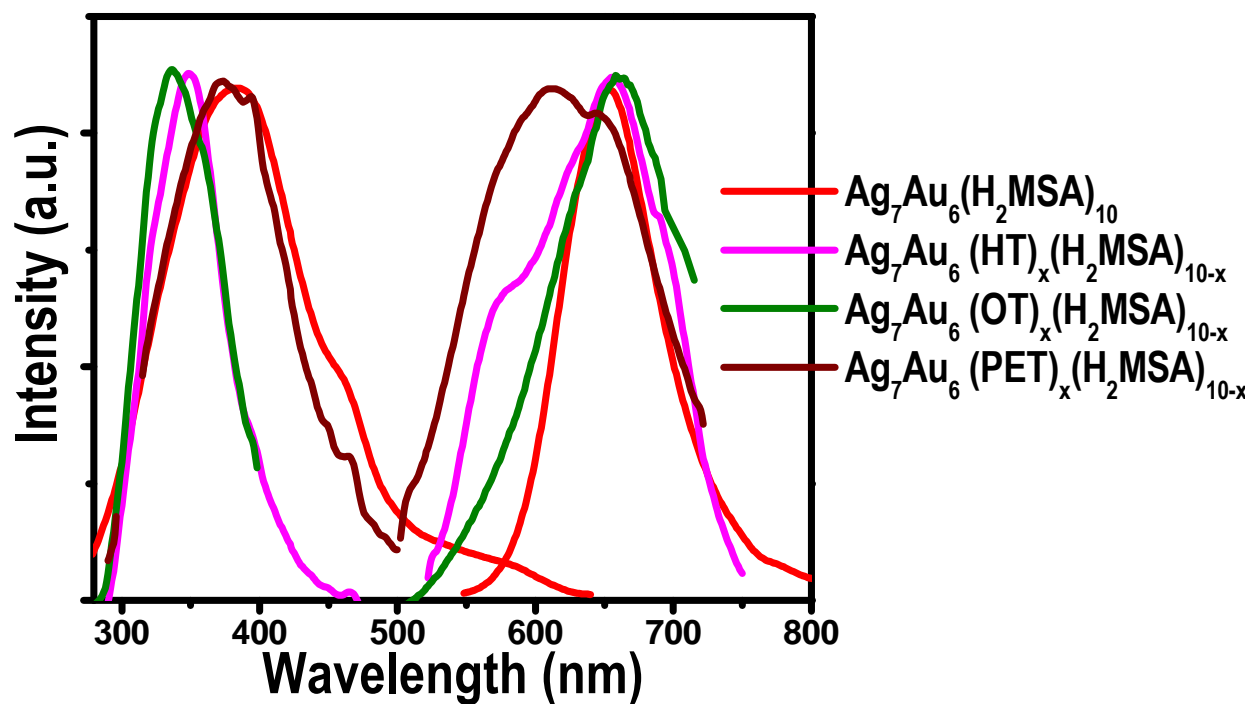


Figure S8. Luminescence spectra of the ligand exchanged cluster solution, excitation at 350 ± 30 nm and emission show a maxima of 650 ± 30 nm for Ag₇Au₆(H₂MSA)₁₀, Ag₇Au₆(HT)_x(H₂MSA)_{10-x}, Ag₇Au₆(OT)_x(H₂MSA)_{10-x} and Ag₇Au₆(PET)_x(H₂MSA)_{10-x}.

S10. Supporting information 10

ESI MS of $[\text{Ag}_7\text{Au}_6(\text{HT})_{10}]^{2+}$

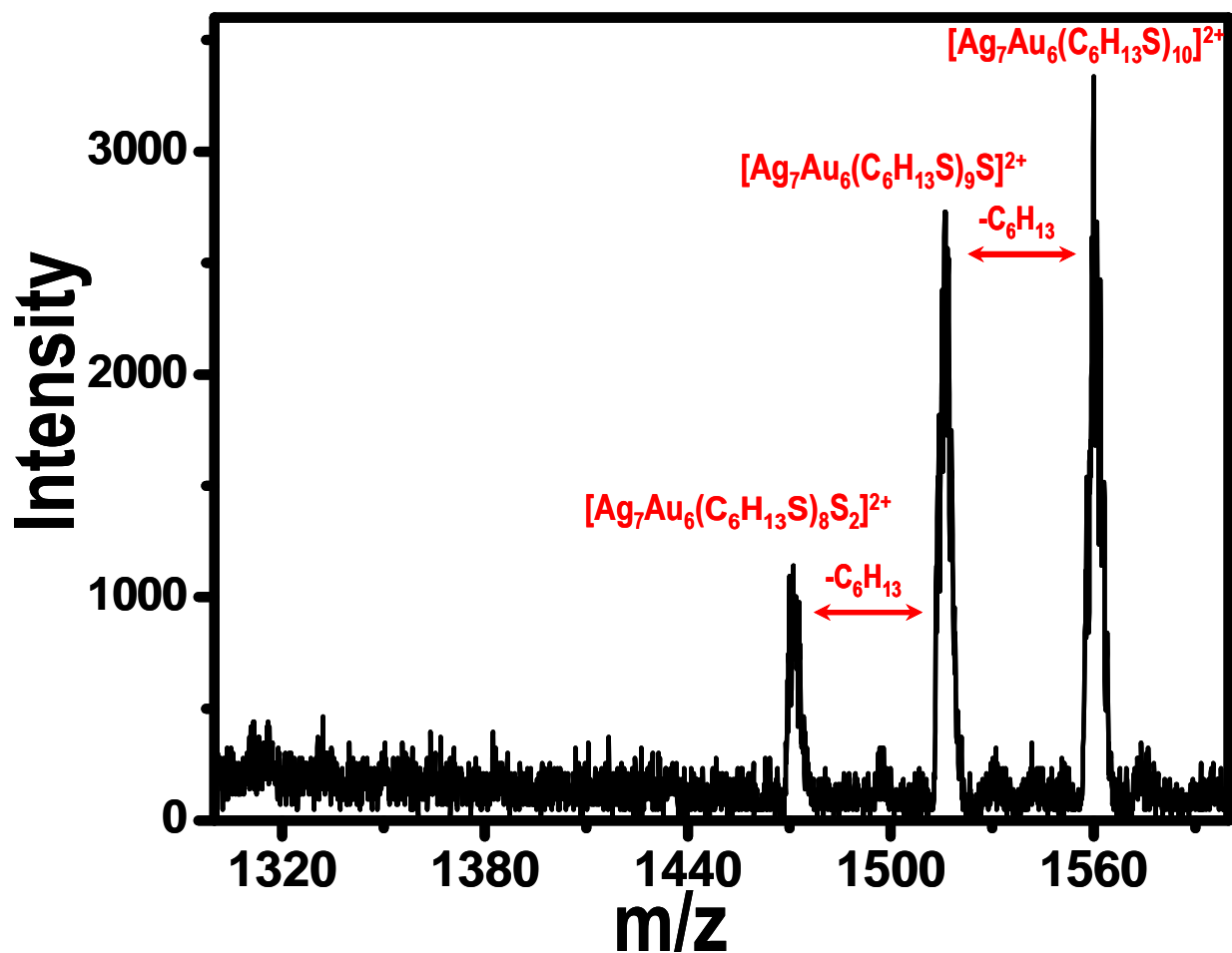


Figure S9. ESI MS of the hexane thiol exchanged cluster in the positive mode in the region of m/z 1300-1600. The ion $[\text{Ag}_7\text{Au}_6(\text{C}_6\text{H}_{13}\text{S})_{10}]^{2+}$ and its sequential $-\text{C}_6\text{H}_{13}$ losses are also seen in the spectrum. The spectrum confirms the presence of ten ligands.

S11. Supporting information 11

Luminescence spectra of $\text{Ag}_7\text{Au}_6(\text{H}_2\text{MSA})_{10}$ before and after phase transfer

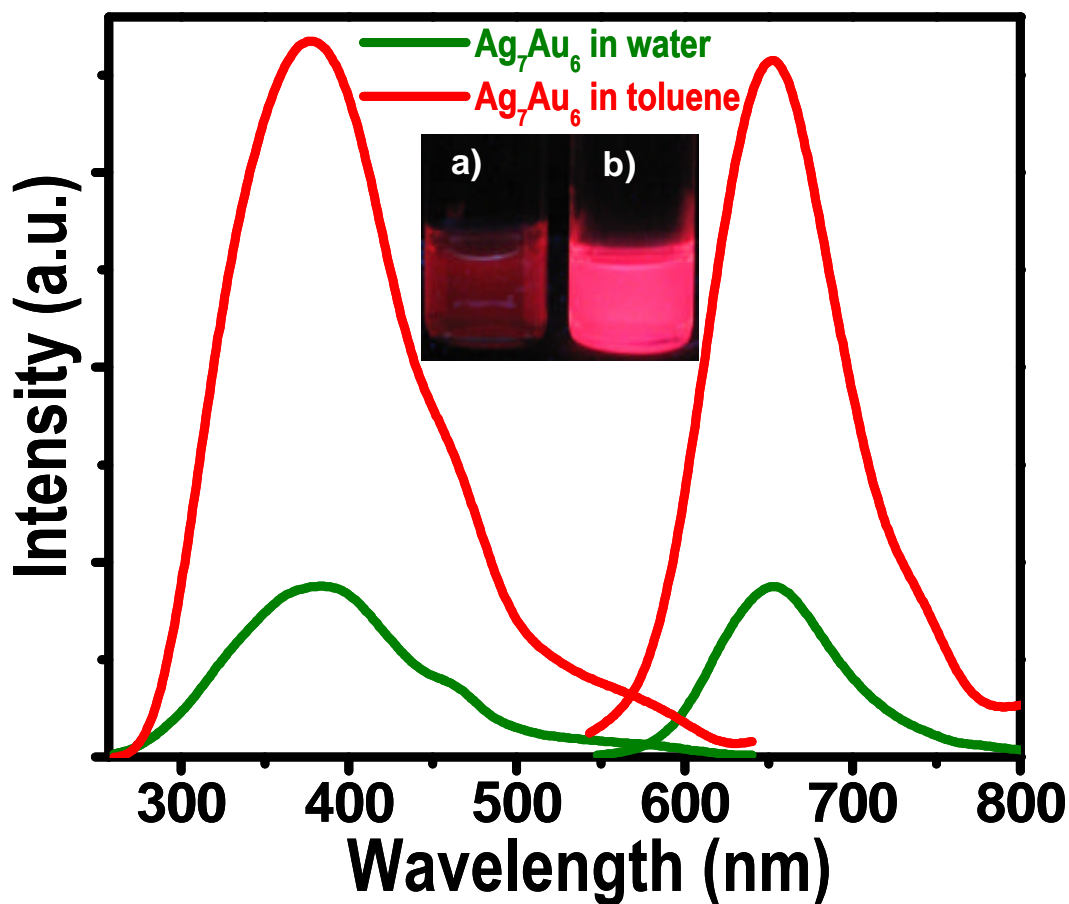


Figure S10. Luminescence spectra of $\text{Ag}_7\text{Au}_6(\text{H}_2\text{MSA})_{10}$ in water and in toluene after phase transfer. Phase transfer increases luminescence emission. Inset shows the photographs of $\text{Ag}_7\text{Au}_6(\text{H}_2\text{MSA})_{10}$ a) before (left) and b) after (right) phase transfer.

S12. Supporting information 12

Lifetime measurements

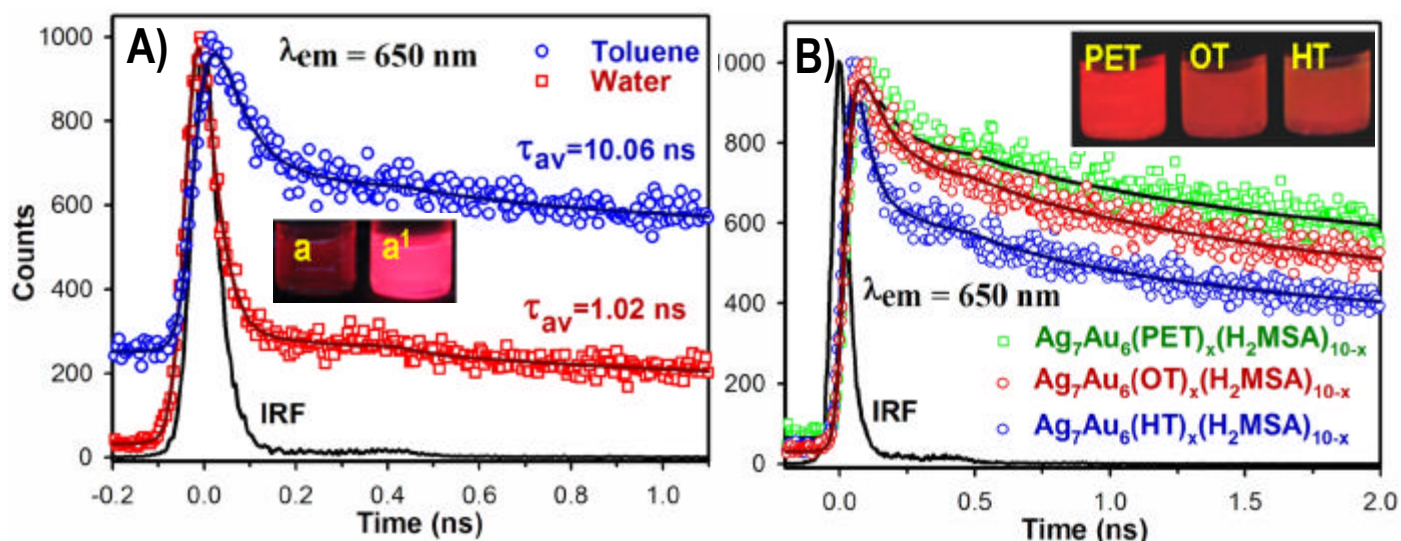


Figure S11 A) Picosecond resolved photoluminescence decay transient (excitation 409 nm and detection at 650 nm) of $\text{Ag}_7\text{Au}_6(\text{H}_2\text{MSA})_{10}$ in aqueous solution and $\text{Ag}_7\text{Au}_6(\text{H}_2\text{MSA})_{10}$ in toluene after phase transfer using tetraoctylammonium bromide. Both the decays are tri-exponential. Inset showing the photograph of the $\text{Ag}_7\text{Au}_6(\text{H}_2\text{MSA})_{10}$ before (a) and after phase transfer (a'). B) Photoluminescence decay transient (excitation 409 nm and detection at 650 nm) of $\text{Ag}_7\text{Au}_6(\text{PET})_x(\text{H}_2\text{MSA})_{10-x}$, $\text{Ag}_7\text{Au}_6(\text{OT})_x(\text{H}_2\text{MSA})_{10-x}$ and $\text{Ag}_7\text{Au}_6(\text{HT})_x(\text{H}_2\text{MSA})_{10-x}$ where PET-phenylethanethiol, HT- hexanethiol and OT- octanethiol. The numerical fitting and IRF are shown in solid lines. All the decay transients are tri-exponential. There seems to be a pattern of average lifetime which may depend on the electron donating property of the ligands. Picosecond resolved anisotropic studies would give more information. Inset shows the photographs of the $\text{Ag}_7\text{Au}_6(\text{PET})_x(\text{H}_2\text{MSA})_{10-x}$, $\text{Ag}_7\text{Au}_6(\text{OT})_x(\text{H}_2\text{MSA})_{10-x}$, $\text{Ag}_7\text{Au}_6(\text{HT})_x(\text{H}_2\text{MSA})_{10-x}$ in toluene under UV light.

Table 1: Tabulated lifetime values of the $\text{Ag}_7\text{Au}_6(\text{H}_2\text{MSA})_{10}$ cluster before and after phase transfer. Standard error in lifetime values is about 10%.

Solvent	Average lifetime(ns)	t_1 (ns)	%	t_2 (ns)	%	t_3 (ns)	%
Water	1.0	0.02	93	1.2	3	25	4
Toluene	10.0	0.08	66	1.7	13	46	21

Table 2: Tabulated lifetime values of the ligand exchange products. Standard error in lifetime values is about 10%.

	Average lifetime (ns)	t_1 (ns)	%	t_2 (ns)	%	t_3 (ns)	%
$\text{Ag}_7\text{Au}_6(\text{PET})_x(\text{H}_2\text{MSA})_{10-x}$	11.9	0.15	36	2.2	25	29	39
$\text{Ag}_7\text{Au}_6(\text{OT})_x(\text{H}_2\text{MSA})_{10-x}$	7.9	0.14	42	2.0	26	22	32
$\text{Ag}_7\text{Au}_6(\text{HT})_x(\text{H}_2\text{MSA})_{10-x}$	4.8	0.07	62	1.6	18	22	20

S13. Supporting information 13

TEM, SEM, EDAX, Optical images, Luminescence image of tubular arrangement of nanoparticles

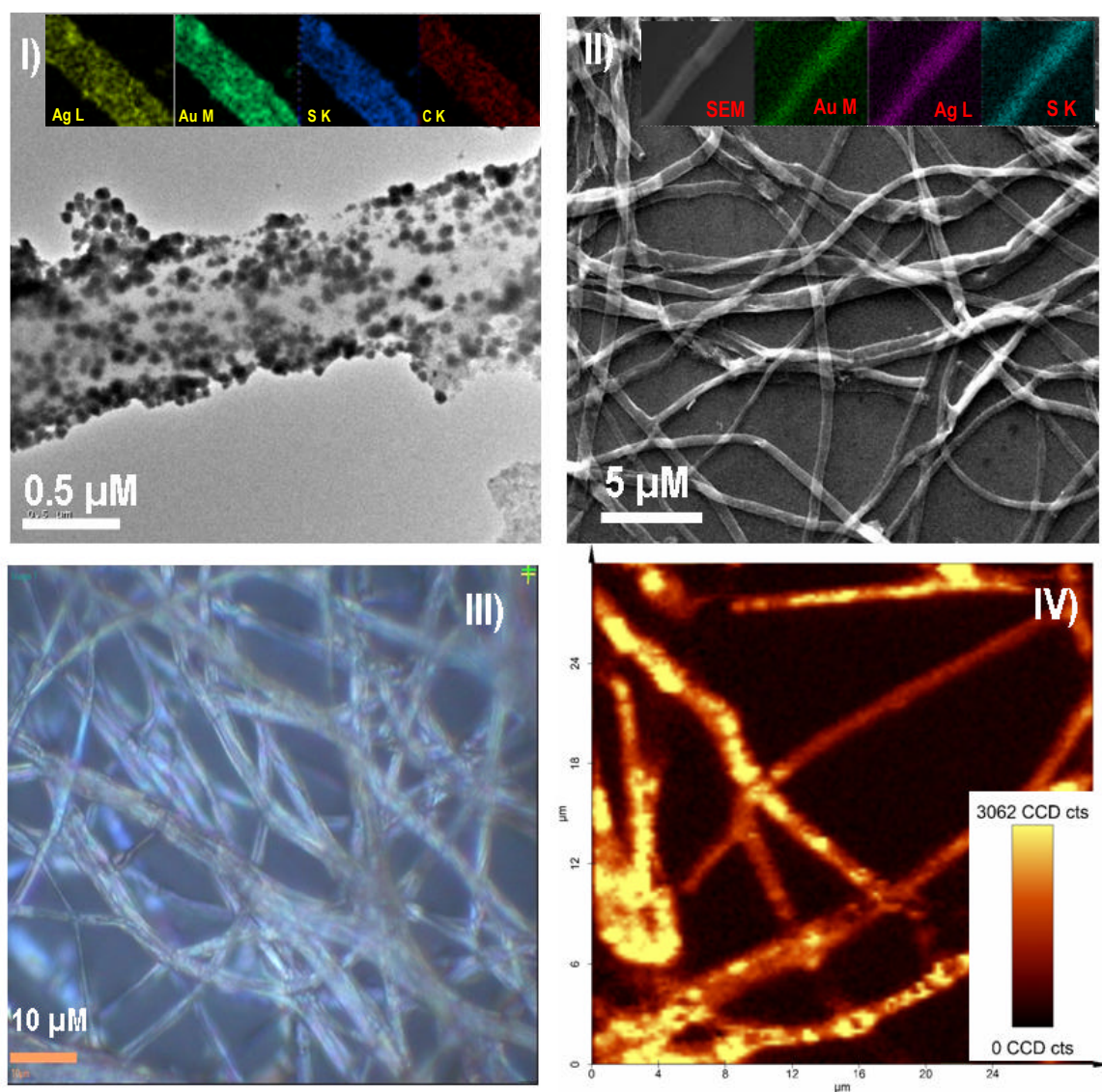


Figure S12. I) TEM images of the reaction product upon the addition of 500 μL of 10 mM HAuCl_4 to 100 μL crude silver cluster in 3 mL water. Note that here the amount of HAuCl_4 used is more than the optimized condition. Images show the presence of nanoparticles and their aggregation in a tubular manner where thiolate may be acting as a

template. Inset showing the TEM/EDAX maps of the reaction product were done using Au M_a , Ag L_a , S K_a and C K_a . II) SEM images of the product showing the presence of the tubular structures. Inset showing the SEM image of one such tube on which the EDAX maps were done using Au L_a , Ag M_a and S K_a . III) Optical image of the product showing the presence of the tubular structures. IV) Inherent solid state luminescence image of tubular structures collected by the spectroscopic mapping at an excitation wavelength of 532 nm. Regions coded bright yellow represents the pixels where the luminescence signal (used for mapping) is a maximum, the minima being represented with black. The scan area was $30 \mu\text{m} \times 30 \mu\text{m}$. Metallic nanoparticles are known to show this kind of luminescence background in Raman image.

S14. Supporting information 14

Optimizing the amount of (cluster: HAuCl_4)

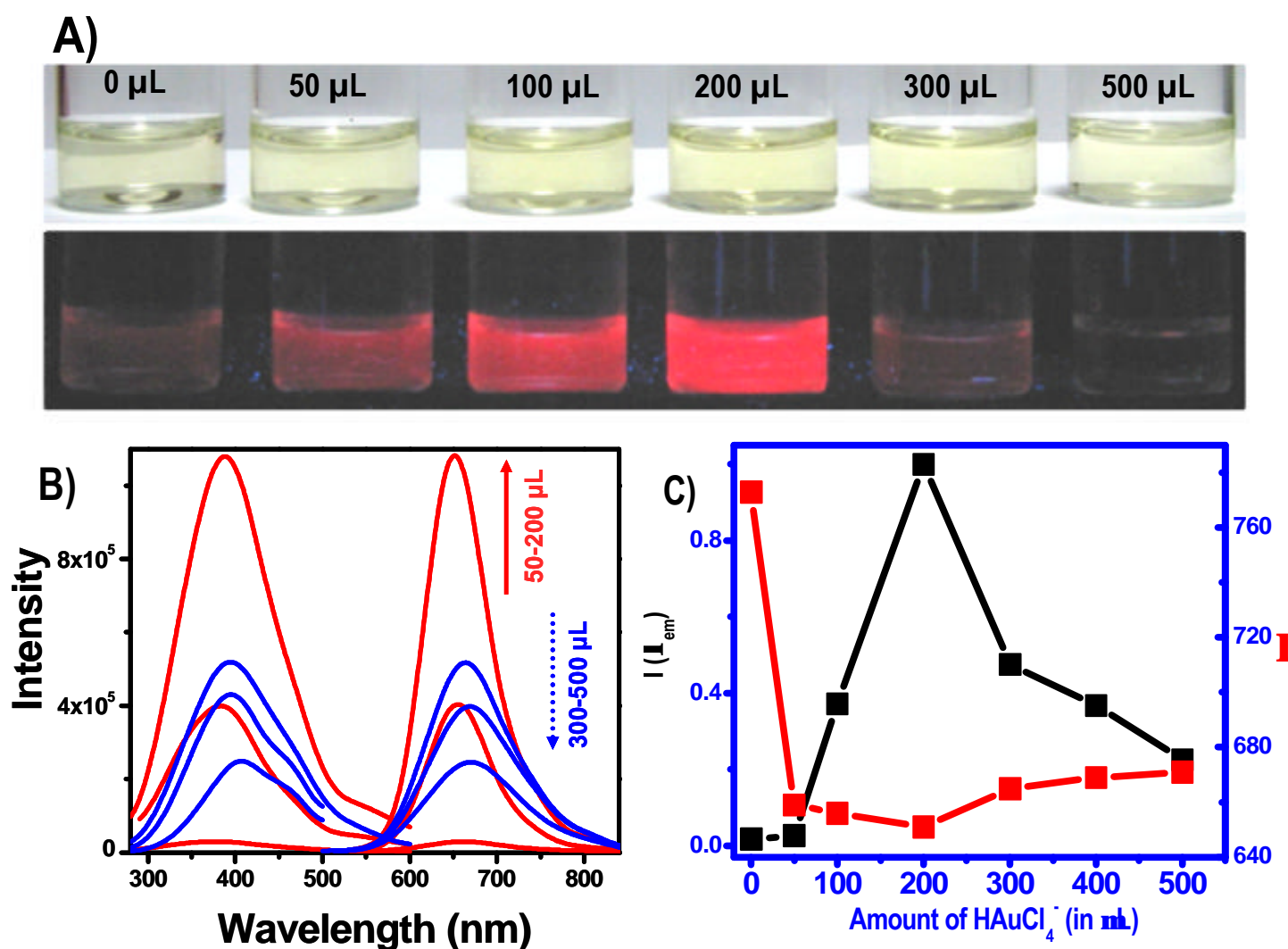


Figure S13.

- A) Reactions at various amounts of 10 mM HAuCl_4 are photographed under white light and UV light. 100 μL of crude silver cluster solution was made-up to 3.0 mL distilled water. To these solutions, 50, 100, 200, 300, 400, 500 μL of 10 mM HAuCl_4 was added and stirred for 15 min at 293 K. Volume (3.0 mL) kept constant in all these cases. At these concentrations, solutions are very dilute and the color change was not observed under ambient light, whereas the cluster solutions photographed under UV light show a drastic change in the emission of each sample. Emission of crude silver cluster was very low at room temperature. Upon the

addition of HAuCl_4 , emission got enhanced which was maximum for the addition 200 μL of HAuCl_4 . Further addition leads to decreasing luminescence emission.

- B) Changes in the luminescence emission profile during the addition of HAuCl_4 to the 100 μL of crude silver cluster in distilled water. Volume (3.0 mL) was constant in all these cases.
- C) Changes in the luminescence emission position (?) and changes in the luminescence emission intensity $[(I_{em})]$ plotted against the amount of HAuCl_4 . As-synthesized crude silver cluster showing luminescence emission at 770 nm which upon addition of 50, 100, 200, 300, 400, 500 μL of HAuCl_4 shifts to 650, 640, 630, 670, 675, 678 nm. Luminescence emission intensity was high for the reaction at 200 μL HAuCl_4 . We used these concentrations for synthesizing larger amounts.

S15. Supporting information 15

Blank reactions

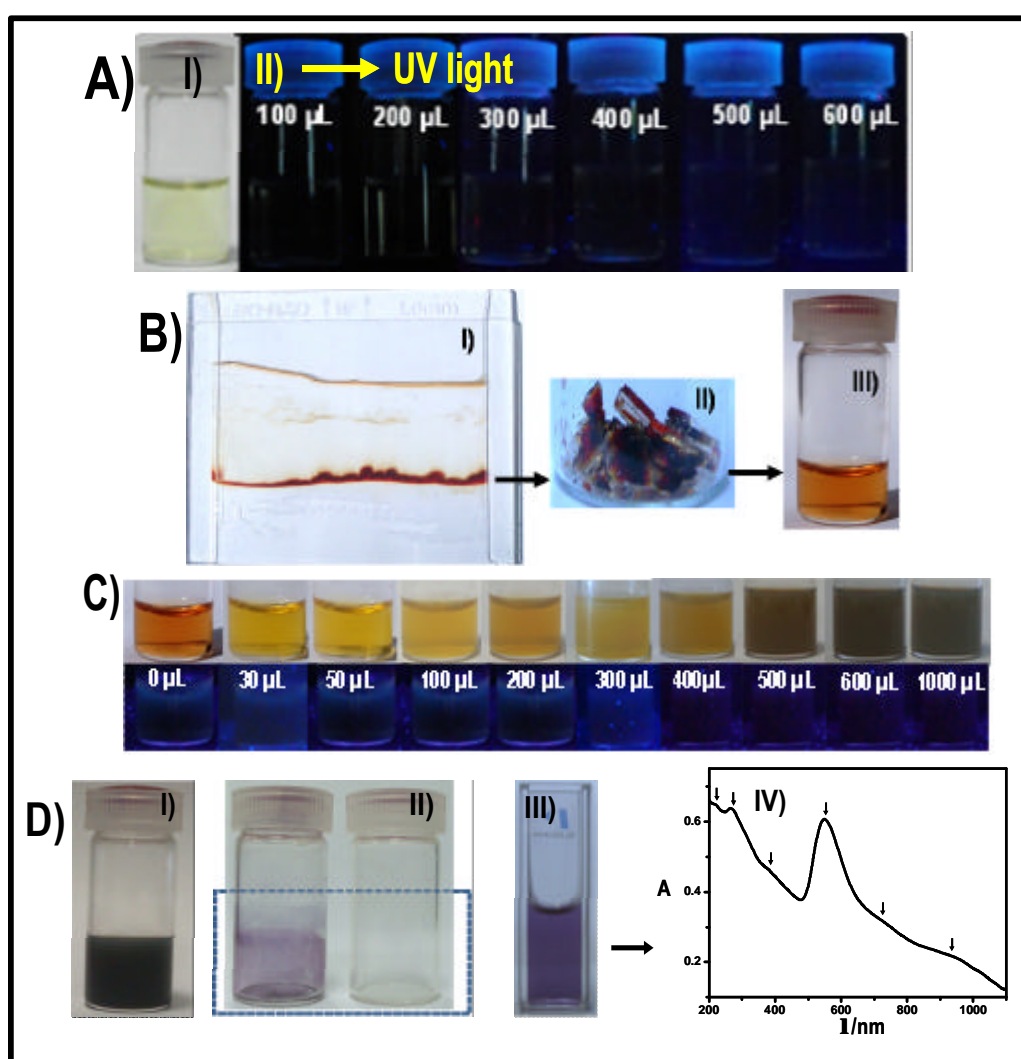


Figure S14.

- A) Photograph of 3.0 mL of oligomeric silver thiolate solution taken in a bottle (I). To this solution, 50 to 600 μL of 10 mM HAuCl_4 was added and the photographs of the corresponding solutions under UV light are shown in (II). All of them do not show any luminescence. It is noted that in contrast, addition of HAuCl_4 to crude silver cluster shows bright luminescence. It shows that the reaction involved is not a simple silver complex-gold complex interaction.

- B) (I) Photograph of the gel, containing Ag_8 cluster and selected portion of the band containing Ag_8 cluster was cut (II). Cluster was extracted into distilled water whereas gel was insoluble. Pure Ag_8 solution is of golden brown color as shown in photograph (III).
- C) HAuCl_4 was added to the pure Ag_8 cluster in various amounts and allowed the reaction for 15 min at 300 K. Photographs of the cluster in visible and UV light are shown. Amounts of solution were not the same (gradual increase from left to right) due to the increase in the amount of addition of HAuCl_4 . All of them are not showing any luminescence. This may be due to decomposition of Ag cluster and uncontrolled growth of gold after the nucleation step due to the lack of external stabilizing agent. Note that metallic nanoparticles exhibit very weak emission, not observable visibly.
- D) I) Photograph of the reaction of pure Ag_8 and 1000 μL of HAuCl_4 ; II) After removal of the solution, deep blue layer appeared on the sides of the bottle which was very clear when it was compared with an empty bottle. III) Photograph of the deep blue layer which was readily dispersible in water. IV) UV-Vis spectrum of the solution showing various peaks. It is expected that these are from differently shaped nanoscale objects (see below). Various peaks are marked.

S16. Supporting information 16

TEM images of gold-silver nanomaterials

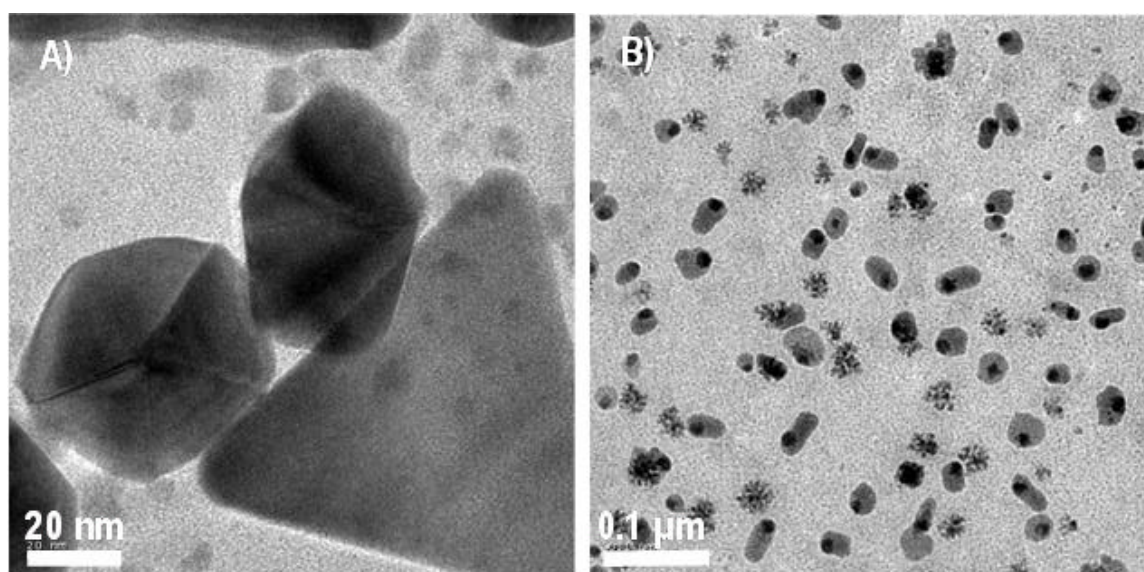


Figure S15. TEM images of the product obtained during the above mentioned reaction (S15 D, III, IV). A, B are the TEM images obtained from the same grid. 'A' shows the presence of decahedral gold nanoparticles and also gold triangles. 'B' shows the TEM images of various shaped silver-gold nanoscale objects.

S17. Supporting information 17

^1H NMR of $(\text{Ag}_m\text{Au}_n)_{\text{QC}}@SG$



Figure S16. ^1H NMR of the $(\text{Ag}_m\text{Au}_n)_{\text{QC}}@SG$ and glutathione(GSH). Peaks corresponding to the cluster become broader as compare to glutathione; especially H-7 (a-position) peak was more broadened and down field shifted due to the closer to cluster core. Inset showing the powder form of the sample collected in both visible (a) and UV light (a¹)

S18. Supporting information 18

Reactions of Au(I)MSA with $\text{Ag}_9(\text{MSA})_7$ at various conditions

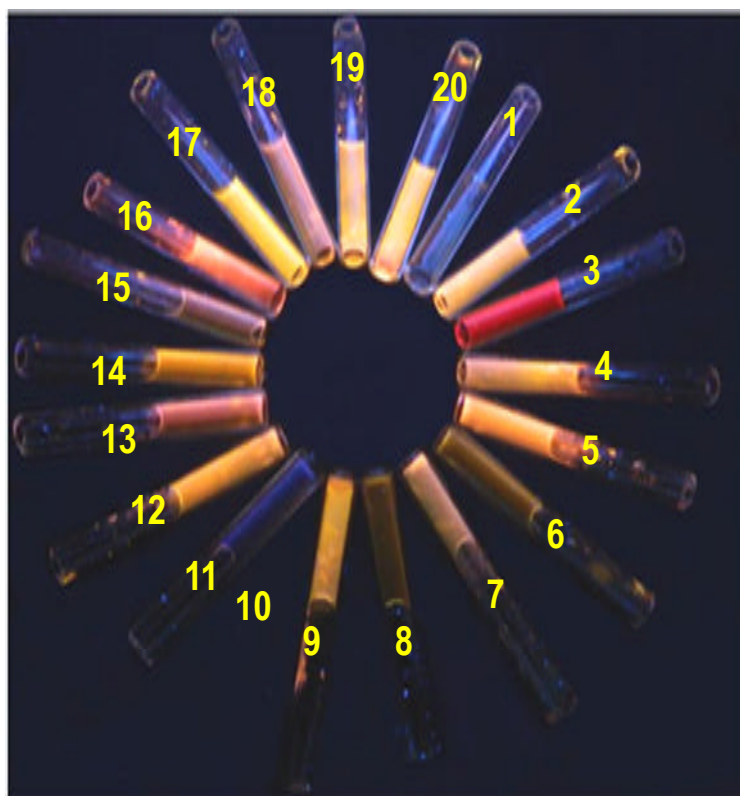


Figure S17. Photographs of the products of reaction between Au(I)MSA with $\text{Ag}_9(\text{H}_2\text{MSA})_7$ at various Au(I)MSA concentrations keeping the concentration of $\text{Ag}_9(\text{H}_2\text{MSA})_7$ the same. The photographs were taken under UV excitation. The glass sample vials were kept in a circular pattern. Image shows that alloy clusters of diverse composition and emission characteristics may be made by varying the experimental conditions.



Luminescent sub-nanometer clusters for metal ion sensing: A new direction in nanosensors

Indranath Chakraborty, T. Udayabhaskararao, T. Pradeep*

DST Unit of Nanoscience (DST UNS), Department of Chemistry, Indian Institute of Technology Madras, Chennai 600036, India

ARTICLE INFO

Article history:

Received 12 July 2011

Received in revised form 5 December 2011

Accepted 10 December 2011

Available online 19 December 2011

Keywords:

Optical properties

Clusters

Aggregation

Metal ion sensing

ABSTRACT

We describe the application of a recently discovered family of materials called quantum clusters, which are sub-nanometer particles composed of a few atoms with well-defined molecular formulae, exhibiting intense absorption and emission in the visible region in metal ion sensing, taking Ag₂₅ as an example. The changes in the optical properties of the cluster, in both absorption and emission upon exposure to various metal ions in aqueous medium are explored. The cluster can detect Hg²⁺ down to ppb levels. It can also detect 5d block ions (Pt²⁺, Au³⁺ and Hg²⁺) down to ppm limits. Hg²⁺ interacts with the metal core as well as the functional groups of the capping agents and the interaction is concentration-dependent. To understand the mechanism behind this type of specific interaction, we have used spectroscopic and microscopic techniques such as UV–vis spectroscopy, luminescence spectroscopy, Fourier transform infrared spectroscopy (FT-IR), scanning electron microscopy (SEM), high resolution transmission electron microscopy (HRTEM), and X-ray diffraction (XRD). Specific reasons responsible for the interaction of Hg²⁺ have been proposed.

© 2011 Elsevier B.V. All rights reserved.

1. Introduction

Among the synthesized nanostructures in the recent past, quantum clusters [1] (QCs) or sub-nanoclusters [2] of noble metals are exciting due to their novel optical and electronic properties. They are useful in various kinds of applications such as metal ion sensing, [3–8] catalysis [9,10] and bioimaging, [11–13]. Among all the metal ions, mercury has a specific attraction towards sulphur due to soft–soft interaction and several sensors, belonging to a broad category of technologies and materials, have been developed based on chemical interactions [14–18]. A number of fluorescence based sensors for the detection of mercury has been reported [19–22]. Mercury is one of the highly toxic heavy metals. It is equally stable in its metallic, inorganic and organic forms. Spreading of mercury into the environment is due to anthropogenic sources like combustion of solid waste, fossil fuels, gold mining, etc. [23]. Contamination of mercury in the ground water resources is one of the biggest threats for mankind. The release of mercury into water caused several public health hazards like the Minamata disease. As it has strong affinity towards sulphur, it can block the sulphhydryl group of enzymes, proteins and membranes [24]. It is also responsible for abnormal activity of the brain, liver and kidney [25]. Because of its several serious hazardous effects on mankind, there is a need to develop highly selective and sensitive sensors for detecting mer-

cury in aqueous medium. The USEPA (United State Environmental Protection Agency) has set a maximum of 2 ppb limit for mercuric ion in drinking water [26]. Gold nanoparticle [27] and gold nanorod [28] based determination of mercury has been reported. Investigation to such an extent has not been done in the case of silver. Bootharaju and Pradeep [29] have reported silver nanoparticle based Hg scavengers, which have also been used for other heavy metals.

All of these sensing studies do not give much details of the interaction of the heavy metal with the nanosystem. In this report, we have studied the sensing capability of a silver cluster as well as the detailed mechanism of interaction of Hg²⁺ under different concentrations. For the study, we have used Ag₂₅, a newly discovered cluster as the cluster of choice [30]. Distinctly different chemical species have been observed as a result of the interaction and they have been characterized with diverse instrumentation. Although there have been a few reports of metal ion sensing by quantum clusters of gold [3–8], there have been no reports on silver clusters. Applications such as the present one will be better viable with silver than gold, in view of the reduced cost. Mechanism of interaction has been studied in detail.

2. Experimental

2.1. Chemicals

We have used commercially available chemicals without additional purification. Silver nitrate (AgNO₃, 99%), glutathione

* Corresponding author. Tel.: +91 44 2257 4208; fax: +91 44 2257 0545.
E-mail address: pradeep@iitm.ac.in (T. Pradeep).

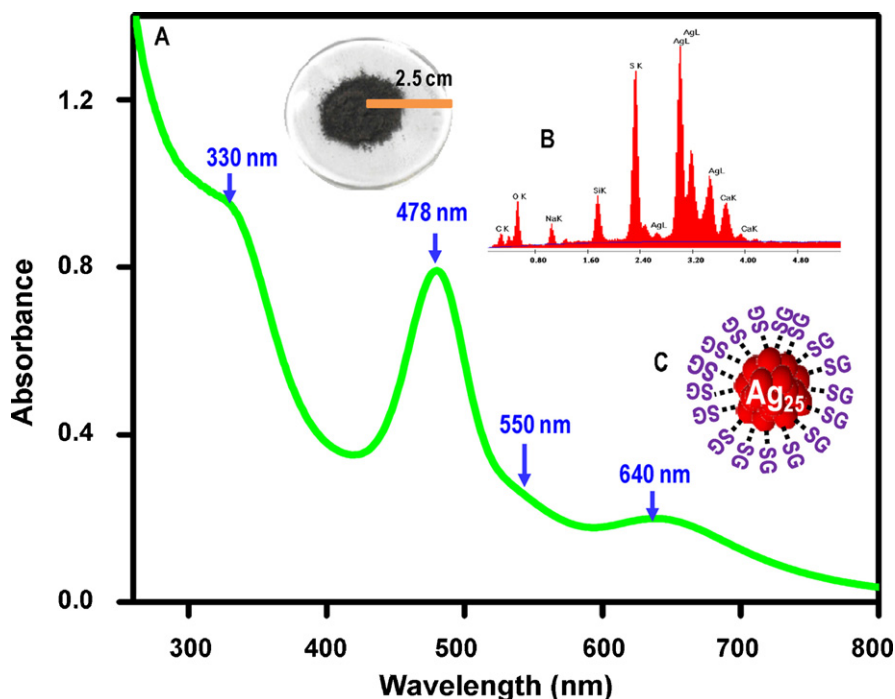


Fig. 1. (A) UV-vis spectrum of the as-synthesized Ag_{25} clusters in the aqueous medium. Inset is a photograph of the Ag_{25} powder. The peak positions are marked. (B) EDAX spectrum of the Ag_{25} aggregate. The various peaks are labeled. (C) A cartoon representation of the Ag_{25} cluster. SG corresponds to glutathione in the thiolate form.

(GSH, 97%), methanol (G.R grade), ammonium per sulphate (APS), N,N'-methylene bisacrylamide (A.R grade), acryl amide (A.R grade), N,N,N',N'-tetramethylethylenediamine (TEMED), all metal chlorides and mercuric acetates were purchased from SRL Chemicals Co. Ltd. Sodium borohydride (99.99%), ethanol (HPLC grade), methanol (HPLC grade) and tetraoctylammonium bromide (TOAB) were purchased from Sigma-Aldrich.

2.2. Synthesis of the silver cluster

Glutathione protected silver cluster (GSH exists as $-\text{SG}$, the thiolate form on the cluster) was synthesized within the polyacrylamide gel [30]. The detailed synthesis protocol is given in [Supplementary data 1](#). After the synthesis, it was further purified through filtration to remove the excess gel. Instrumentation details are presented in [Supplementary data 2](#).

2.3. Reaction of silver cluster with metal ions

In the initial experiments, Ag_{25} (20 ppm concentration) was allowed to interact with 50 ppm solutions of the metal ions (Cr^{3+} , Mn^{2+} , Fe^{3+} , Co^{2+} , Ni^{2+} , Cu^{2+} , Zn^{2+} , Pd^{2+} , Cd^{2+} , Pt^{2+} , Au^{3+} and Hg^{2+}) separately. Later experiments were done with reduced metal ion concentrations of 10 ppm for selective sensitivity study. As Hg^{2+} was sensitive at 1 ppm range, lower concentration (ppb) studies were done only with Hg^{2+} , monitored by optical absorption spectroscopy. The concentrations mentioned are those present in the final solutions, after mixing. All the experiments were carried out in room temperature. Initial studies were done with chlorides, but other salts such as acetates were also used to confirm the results. For fluorescence quenching experiment we have transfer the cluster into organic medium by using TOAB.

3. Results and discussion

3.1. Characterization of silver cluster

In the following, we present the most essential characterization of the cluster. More detailed discussion of the data is presented

in a separate work, which reported this cluster initially [30]. The as-synthesized clusters show strong quantum size effects such as multiple molecule-like transitions in their optical spectrum measured in water appearing at 330, 478 and 640 nm (Fig. 1A). A shoulder is also found at 550 nm. Absorption profile of the clusters is in agreement with the clusters reported by Cathcart and Kitaev [31], who have suggested that these clusters may be Ag_{25} from electro spray ionization mass spectrometry (ESI MS) data. LDI MS of phase transferred clusters show well defined peaks to multiply charged species of the type $(\text{Ag}_{25}\text{SG}_{18})^{q-}$, and ions corresponding to $q = 7, 8, 9, \dots, 18$ were detected which makes it possible to precisely assign the cluster [30]. Laser desorption ionization mass spectrometry (LDI MS) data of phase transferred Ag_{25} clusters in the negative mode also show well-defined peaks assignable to the cluster. The atomic ratio of Ag:S is confirmed by EDAX (Fig. 1B). Other spectroscopic characterization of the cluster such as XPS will be discussed at an appropriate place below. The cluster exists as a brown-black powder in the solid state. It is highly soluble in water giving a brown solution. The clusters can be transferred to organic medium by a phase transfer agent, TOAB. The optical absorption features of clusters are not affected as a result of phase transfer to toluene (Fig. 2A). The as-synthesized cluster does not show observable luminescence under UV lamp but upon phase transfer to the organic medium, it shows bright luminescence which can be photographed. Increase in luminescence intensity upon phase transfer is attributed to the change in the rate of non-radiative rate [8]. The excitation and emission maxima are at 480 and 630 nm at room temperature (Fig. 2B). Photographs of the phase transferred cluster, along with the aqueous phase in visible and UV light are shown in the inset of Fig. 1A.

3.2. Application in metal ion sensing

The interaction of mercury with the cluster has been investigated with the help of several spectroscopic and microscopic tools and a discussion of the data are presented below.

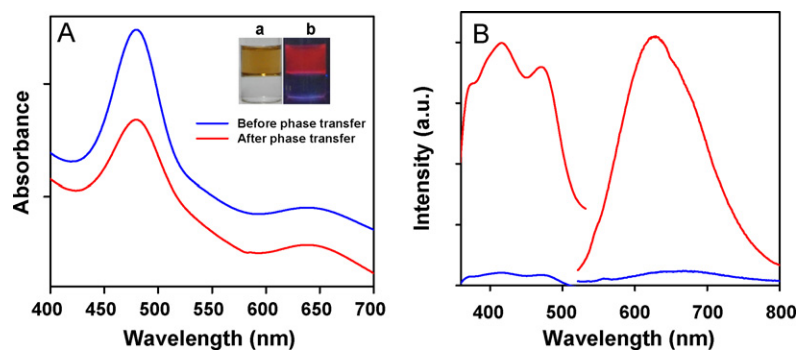


Fig. 2. UV-vis spectra of (A) as-synthesized Ag_{25} in aqueous (blue trace, before phase transfer) and organic media (red trace, after phase transfer in toluene). Peak positions in both the cases are the same. The peaks are shifted for clarity. Insets are photographs of Ag_{25} solution after phase transfer in visible light (a) and UV light (b), respectively. Aqueous layer below is colorless after complete transfer of clusters to the organic phase above. (B) This shows luminescence excitation and emission of Ag_{25} in water (blue trace, before phase transfer) and toluene (red trace, after phase transfer). The samples were excited at 480 nm and the emission maximum was at 630 nm. (For interpretation of the references to color in this figure legend, the reader is referred to the web version of the article.)

3.2.1. UV-visible spectroscopy

In the optical absorption spectrum, the characteristic peaks of Ag_{25} clusters appear at 330, 478 and 640 nm. It has been found that upon addition of metal ions into the cluster solution, there is a change in the characteristics of the cluster, depending on the metal ion. Initially the effect has been studied with 50 ppm solution of the metal ion, which was added to the cluster solution (20 ppm). UV-vis characteristics of the as-synthesized Ag_{25} cluster changed drastically for the 5d block ions (Fig. S2). The intensity of the 478 nm peak decreased for every metal ion, and the 640 nm peak nearly disappeared (Fig. S3A). Among the 5d block elements, particularly Hg^{2+} and Au^{3+} almost destroyed the UV-vis characteristics of the Ag_{25} cluster, while Pt^{2+} shows a shift in wavelength. Metal ion concentration was reduced to 10 ppm to know the metal ion specificity, keeping the cluster concentration constant. Important information to note is that Cd^{2+} is different in the UV-vis characteristics (Fig. S3B). A multiple step-like behaviour is observed at both the concentrations. For 10 ppm solution (Fig. 3A) it has been found that only Hg^{2+} solution is showing effect on UV-vis features of the cluster, rest of the ions are not manifesting changes. The 478 nm peak

is blue-shifted and a new hump is seen at 420 nm, which may be due to the Ag-Hg alloy formation [32,33]. In order to prove that anion does not have any effect, acetate salt of Hg (II) was taken (Fig. S3D). This also shows the same behaviour, which confirms that the interaction is due to Hg^{2+} only. Therefore, we conclude that at low concentration, Ag_{25} can sense Hg^{2+} in aqueous medium. Detection of Hg^{2+} with a lower limit detection of 1 ppb is possible as shown in Fig. S4. The sensing capability and limit of detection can be easily understood from Fig. 4, which shows that among all the metal ions, the sensitivity is better for Hg^{2+} and the detection limit is down to 1 ppb (see also supporting information Fig. S4).

3.2.2. Fluorescence spectroscopy

It is also possible to detect the presence of Hg^{2+} by a fluorescence quenching experiment. The phase transferred cluster in toluene shows bright fluorescence under UV light compared to cluster in the aqueous medium (Fig. 3A, inset photographs). Upon addition of Hg^{2+} , the fluorescence intensity is decreased (Fig. 3C). The excitation and emission spectra are taken for all metal ions (Fig. S5). As seen, Hg^{2+} is showing a pronounced effect in decreasing the

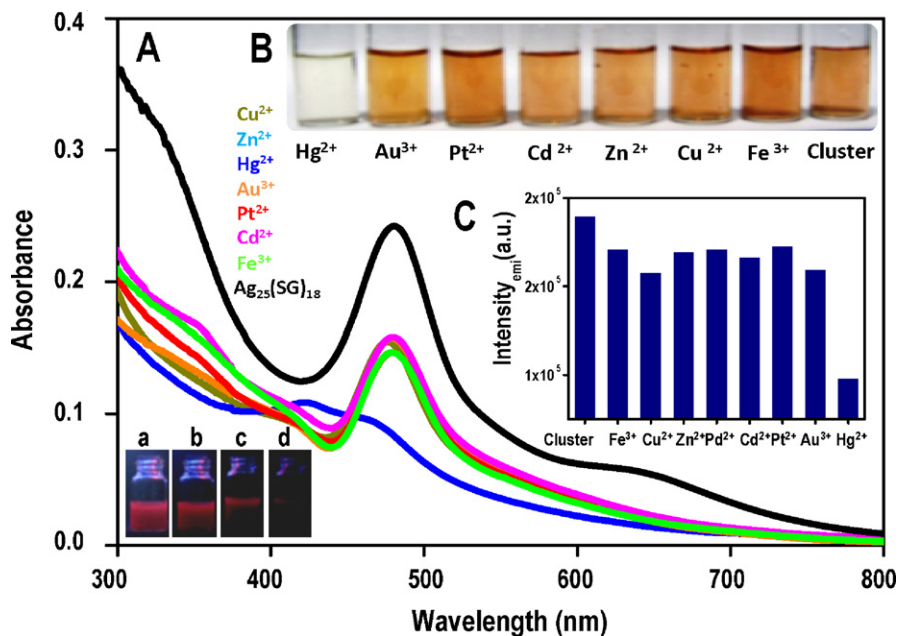


Fig. 3. UV-vis absorption spectra of various metal ions (10 ppm concentration) which are added to aqueous Ag_{25} cluster solution (A). Photographs of corresponding solutions under visible light (B). Effect of various metal ions (10 ppm) on the emission intensity of Ag_{25} cluster (C). Below the UV-vis spectra, photographs (under UV excitation) depicting fluorescence quenching are given for the phase transferred cluster (a) upon addition of, 1 ppm (b), 2 ppm (c) and 10 ppm (d) solutions of Hg^{2+} .

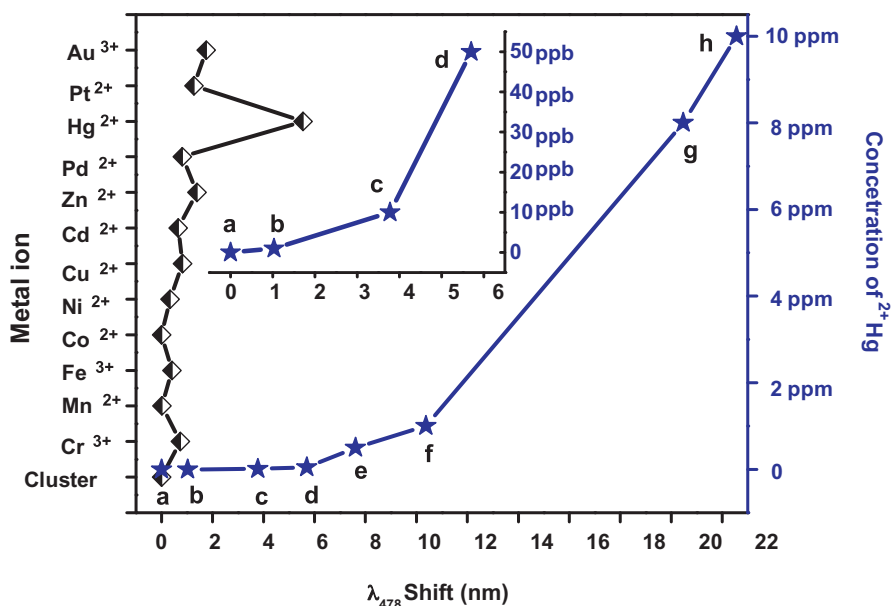


Fig. 4. The effect of various metal ions on the optical absorption peak at 478 nm. Concentration of Hg^{2+} alone is also plotted against the same (on the right side). Inset is showing an expanded portion of the same in ppb range, which shows the sensing capability of Hg^{2+} in the ppb range.

emission intensity compared to other metal ions. The parent cluster is giving a characteristic excitation at 480 nm and emission at 630 nm.

3.2.3. IR spectral analysis

We shall now discuss the details of the interaction of Hg^{2+} with Ag_{25} clusters. The IR-spectral data of parent cluster and the cluster treated with different concentrations of Hg^{2+} (10 ppb and 10 ppm) are given in Fig. 5. The cluster has characteristic bands at 3430 cm^{-1} due to O–H stretching, and at 2922 cm^{-1} due to C–H stretching. Absence of band at 2552 cm^{-1} proves the presence of the ligand in the thiolate form [30]. The band at 1658 cm^{-1} was shifted to 1643 cm^{-1} upon treatment of the cluster with Hg^{2+} solution (for both the cases, i.e. with 10 ppm and 10 ppb concentration). This

band is assigned to C=O stretching frequency of the peptide. This confirms the binding of Hg^{2+} with the carbonyl moiety of the peptide [34,35]. Band at 1397 cm^{-1} is due to the C–O stretching of the carboxylate. Absence of shift in this band has confirmed the non-attachment of Hg^{2+} to the free carboxylate group of the ligand. The C–C stretching and COO^- bending are found at 1122 cm^{-1} and 621 cm^{-1} , respectively. Therefore, from this data it can be predicted that Hg^{2+} is binding to the carbonyl moiety of the peptide in both the cases.

3.2.4. HRTEM and SEM analysis

Fig. S6 shows the HRTEM images of the cluster treated with low concentration of Hg^{2+} (10 ppb). The presence of cluster indicates that at low concentration of Hg^{2+} (10 ppb) it will not destroy the

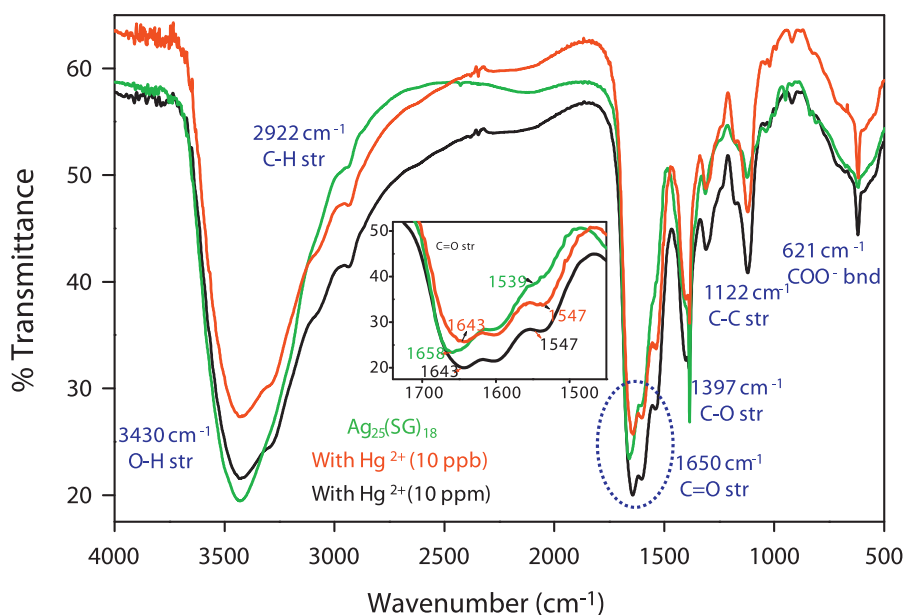


Fig. 5. FT-IR spectra of free Ag_{25} cluster (green) and the cluster with low (10 ppb, red trace) and high concentration (50 ppm, black trace) of Hg^{2+} measured in a KBr matrix. Inset is an expanded view of the carbonyl stretching region. (For interpretation of the references to color in this figure legend, the reader is referred to the web version of the article.)

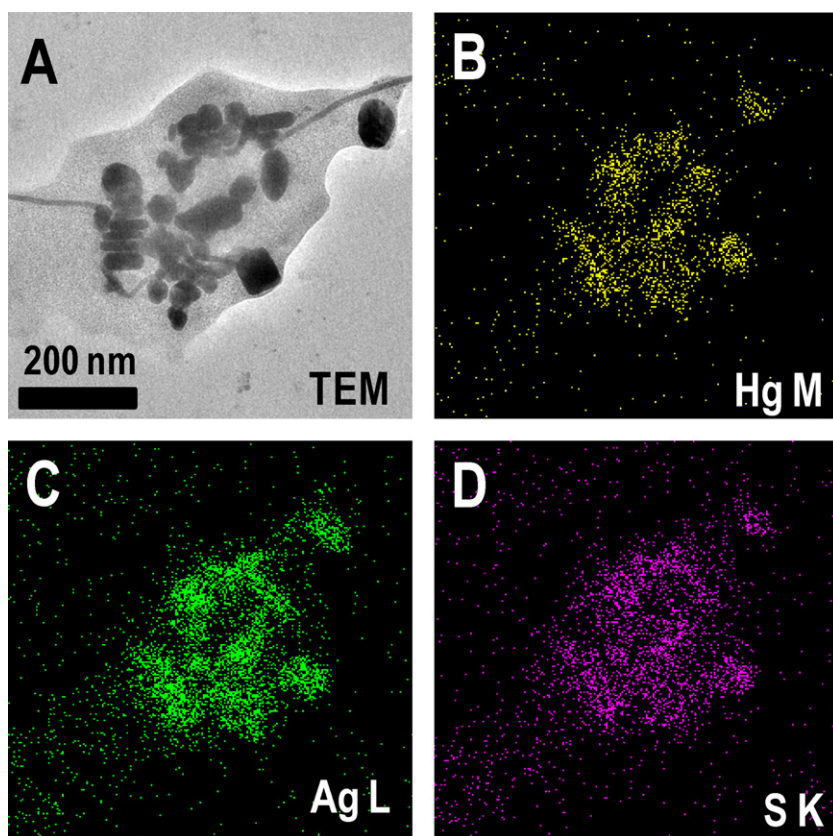


Fig. 6. TEM and EDAX images of aggregated mass formed by the addition of 10 ppm Hg^{2+} solution to the cluster solution. The TEM image and elemental maps of Hg, Ag and S are in (A, B, C and D), respectively. Various types of aggregated geometries are found.

cluster features, which is also confirmed from the IR spectral data which suggests the attachment of Hg^{2+} with the carbonyl moiety of the peptide. Low concentration is also supported from the EDAX analysis (Fig. S7) where elemental maps of Ag, Hg and S are also given.

TEM image of an aggregated mass formed after treating with 10 ppm solution of Hg^{2+} reveals a few distinctly visible clusters as well (Figs. 6 and S8B). It may be noted that clusters are highly sensitive to the electron beam. The TEM image of the aggregated mass formed by the treatment of 10 ppm Hg^{2+} shows various types of shapes such as rods, hexagons, triangles, squares, octagons (Fig. S9), etc. which are a few micrometer in dimension. These can be separated from the free clusters upon centrifugation (Fig. S10). Upon higher magnification, the lattice planes were visible which are corresponding to (0 2 1) plane of paraschachnerite or Ag_3Hg_2 (Fig. S9H). This is also supported by XRD data given below. EDAX quantification of an isolated hexagonal shape (Fig. S11A) also supports the formation of Ag_3Hg_2 alloy during interaction of 10 ppm solution of Hg^{2+} with Ag_{25} cluster.

The composition of alloy is also supported by the SEM analysis presented earlier (Fig. 7), where the EDAX quantification data of this sample shows a composition of $\text{Ag}_{2.8}\text{Hg}_{2.1}$.

3.2.5. XRD data

The X-ray diffraction pattern of the residue formed due to the treatment of Ag_{25} cluster with 10 ppm Hg^{2+} shows peaks (Fig. 8A) corresponding to Ag–Hg alloy. The peaks are well matched with the JCPDS data of Ag_3Hg_2 or paraschachnerite having an orthorhombic crystal structure [36]. This confirms the reduction of mercury. At very low concentration (10 ppb) of Hg^{2+} it can only attach to the carbonyl moiety but at higher concentration (10 ppm) it can bind with sulphur moiety of thiolate ligand and interact with silver

surface leading to the reduction of Hg^{2+} to Hg and subsequently to the alloy. This is in accordance with the UV–vis data (Fig. S3C) where the peaks are shifted to lower wavelength. At still higher concentration, cluster gets degraded due to more and more reduction occurring on the surface of silver. XRD of the final product obtained after treating the cluster with excess Hg^{2+} is given in Fig. 8B. The product peaks are well matched with the peaks corresponding to Hg and AgCl (ID 74-0039 and 85-1355) which confirms the reduction of Hg^{2+} to Hg in the nanoscale as Ag is oxidized [29].

3.2.6. XPS study

XPS survey spectrum of the parent sample shows the expected elements (Fig. S12). Ag is in its zero valent state in XPS, with a binding energy of 368.0 eV for Ag $3d_{5/2}$. XPS and SEM give the same atomic ratio of Ag and S. The XPS survey spectrum of the cluster treated with high (100 ppm) and low (100 ppb) concentration of Hg^{2+} are given in Fig. S12. All the peaks are assigned. The presence of Na is from sodium borohydride used as the reducing agent in the synthesis. Fig. 9 shows the expanded XPS spectra of Ag and Hg for both the cases. At low concentration (100 ppb), no peaks corresponding to Hg 4f are observed (Fig. 9B) which may be due to the fact that such a low concentration is beyond the detection limit of the technique. The peak at 367.8 eV (Fig. 9A) assigned to $3d_{5/2}$ suggests the presence of silver in the zero valent state. So, at lower concentration, oxidation is not happening which proves that low concentration Hg^{2+} is not affecting the cluster core which also supports the IR data. At high concentration, the Hg $4f_{7/2}$ shows a peak at 101.6 eV corresponding to mercuric ion bonded to the carbonyl moiety of the ligands, in agreement with the IR data. The peak at 99.9 eV corresponds to metallic mercury [29]. So, reduction is happening in such a nanosystem. A peak at 367.2 eV for Ag $3d_{5/2}$ confirms the oxidation of silver during the course of the reaction.

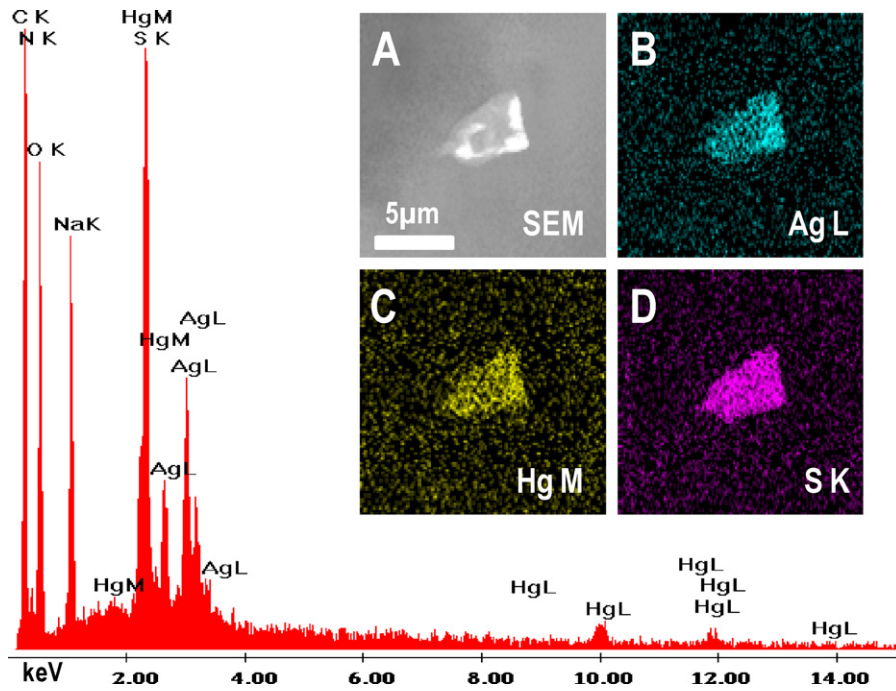


Fig. 7. EDAX spectrum of the cluster with 10 ppm Hg^{2+} . Inset shows the SEM image (A) and elemental maps of silver (B), mercury (C) and sulphur (D). Elemental analysis shows that Ag and Hg are present in 2.8:2.1 ratio in the aggregated mass.

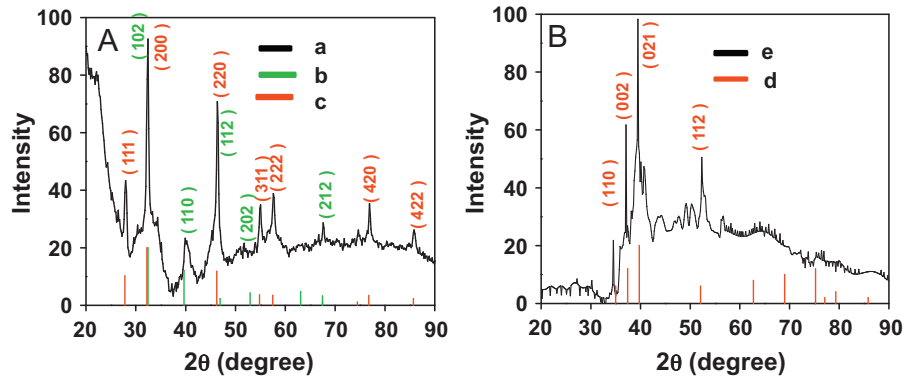


Fig. 8. X-ray diffraction patterns of cluster treated with 10 ppm concentration of Hg^{2+} . Ag_3Hg_2 type aggregated mass was formed, as shown by XRD (A). The XRD pattern of final decomposed product formed by reaction of Ag_{25} with Hg^{2+} (100 ppm) via shown in (B). With 10 ppm concentration of Hg^{2+} , JCPDS data of Ag_3Hg_2 (a), Hg (c) and AgCl (e) (ID 27-0617, 74-0039 and 85-1355, respectively) are also plotted against 2θ (the maximum intensity of the standard patterns is scaled to 20). Good agreement is seen with the experimental data.

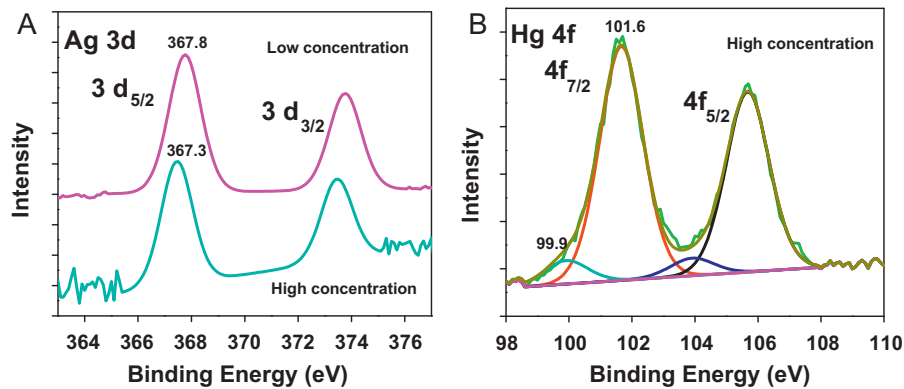


Fig. 9. XPS spectra of Ag 3d (A) and Hg 4f (B) regions from the residue obtained after reaction with mercuric ions at high (100 ppm) and low (100 ppb) concentrations. At low concentration, Hg is not detected and therefore the trace is not shown while for high concentration, distinct peaks are seen.

- [18] M. Suresh, S. Mishra, S.K. Mishra, E. Suresh, A.K. Mandal, A. Shrivastav, A. Das, Resonance energy transfer approach and a new ratiometric probe for Hg^{2+} in aqueous media and living organism, *Org. Lett.* 11 (2009) 2740–2743.
- [19] K. Harano, S. Hiraoka, M. Shionoya, 3 nm-scale molecular switching between fluorescent coordination capsule and nonfluorescent cage, *J. Am. Chem. Soc.* 129 (2007) 5300–5301.
- [20] O.T. Butler, J.M. Cook, C.F. Harrington, S.J. Hill, J. Rieuwertsd, D.L. Milesb, Atomic spectrometry update. environmental analysis, *J. Anal. At. Spectrom.* 219 (2006) 217–243.
- [21] J.V. Mello, N.S. Finney, Reversing the discovery paradigm: a new approach to the combinatorial discovery of fluorescent chemosensors, *J. Am. Chem. Soc.* 127 (2005) 10124–10125.
- [22] E.M. Nolan, S.J. Lippard, A turn-on fluorescent sensor for the selective detection of mercuric ion in aqueous media, *J. Am. Chem. Soc.* 125 (2003) 14270–14271.
- [23] Q. Wang, D. Kima, D.D. Dionysiou, G.A. Soriala, D. Timberlakeb, Sources and remediation for mercury contamination in aquatic systems – literature review, *Environ. Pollut.* 131 (2004) 323–336.
- [24] S. Homma-Takeda, M. Shinyashiki, Y. Kumagai, N. Shimojo, A new method for detection of mercury-bound protein with a combination of gel electrophoresis and one dimensional synchrotron radiation X-ray fluorescence analysis, *J. Occup. Health* 38 (1996) 118–119.
- [25] T.W. Clarkson, L. Magos, G.J. Myers, The toxicology of mercury – current exposures and clinical manifestations, *N. Engl. J. Med.* 349 (2003) 1731–1737.
- [26] Mercury Update: Impact of Fish Advisories, EPA Fact Sheet EPA-823-F-01-011, EPA, Office of Water, Washington, DC, 2001.
- [27] G.K. Darbha, A.K. Sing, U.S. Rai, E. Yu, H. Yu, P.C. Ray, Selective detection of mercury (II) ion using nonlinear optical properties of gold nanoparticles, *J. Am. Chem. Soc.* 130 (2008) 8038–8043.
- [28] M. Rex, F.E. Hernandez, A.D. Campiglia, Pushing the limits of mercury sensors with gold nanorods, *Anal. Chem.* 78 (2006) 445–451.
- [29] M.S. Bootharaju, T. Pradeep, Uptake of toxic metal ions from water by naked and monolayer protected silver nanoparticles: an X-ray photoelectron spectroscopic investigation, *J. Phys. Chem. C* 114 (2010) 8328–8336.
- [30] T.U.B. Rao, T. Pradeep, A 25 atom silver cluster made in molecular confinement, *Angew. Chem. Int. Ed.*, under revision.
- [31] N. Cathcart, V. Kitaev, Silver nanoclusters: single-stage scaleable synthesis of monodisperse species and their chiroptical properties, *J. Phys. Chem. C* 114 (2010) 16010–16017.
- [32] G.V. Ramesh, T.P. Radhakrishnan, A universal sensor for mercury (Hg, HgI, HgII) based on silver nanoparticle-embedded polymer thin film, *ACS Appl. Mater. Interfaces* 3 (2011) 988–994.
- [33] E. Sumesh, M.S. Bootharaju, S. Anshup, T. Pradeep, A practical silver nanoparticle-based adsorbent for the removal of Hg^{2+} from water, *J. Hazard. Mater.* 189 (2011) 450–457.
- [34] B.K. Singh, R.K. Sharma, B.S. Garg, Kinetics and molecular modeling of biologically active glutathione complexes with lead(II) ions, *J. Therm. Anal. Calorim.* 84 (2006) 593–600.
- [35] D.N. Kumar, B. Kumar Singh, B.S. Garg, P.K. Singh, Spectral studies on copper(II) complexes of biologically active glutathione, *Spectrochim. Acta* 59 (2003) 1487–1496.
- [36] JCPDS Data File No-27-0617.

Luminescent Sub-nanometer Clusters for Metal Ion Sensing: A New Direction in Nanosensors

Indranath Chakraborty, T. Udaya Bhaskara Rao and T. Pradeep*

DST Unit of Nanoscience (DST UNS), Department of Chemistry,

Indian Institute of Technology Madras, Chennai- 600036, India.

*Corresponding author: Fax: +91-44 2257-0545

E-mail: pradeep@iitm.ac.in

Supplementary data 1. Methods

1.1 Synthesis of Ag₂₅ cluster.

Supplementary data 2. Instrumentation

Figure S1. Photographs at different stages of reaction during synthesis of Ag₂₅ cluster.

Figure S2. UV-Vis absorption spectra of various metal ion (50 ppm) treated Ag₂₅ cluster.

Figure S3. UV-Vis features of Ag₂₅ cluster with different system and conditions.

Figure S4. UV-Vis absorption spectra of cluster with various concentration of Hg²⁺.

Figure S5. Effect of various metal ion in luminescence spectra of Ag₂₅ cluster solution

Figure S6. HRTEM image of cluster with low concentration (10 ppb) of Hg²⁺.

Figure S7. SEM image and EDAX spectrum of Ag₂₅ cluster with 10 ppb Hg²⁺ solution.

Figure S8. The EDAX spectra of Ag₂₅ cluster treated with 10ppm of Hg²⁺ ions.

Figure S9. HRTEM images of aggregated mass formed during the interaction of Ag₂₅ cluster with Hg²⁺ solution.

Figure S10. HRTEM images of aggregated mass after centrifuge.

Figure S11. TEM and EDAX images of an isolated aggregated mass.

Figure S12. XPS survey spectra of cluster treated with low (black) and high (red) concentration. Individual peaks have been assigned.

Figure S13. The S 2p, C 1s, O 1s and N 1s peaks in the XPS spectra for the residue formed while reacting with low (10 ppb) and high (100 ppm) concentration of Hg²⁺.

Supplementary data 1. Methods

1.1 Synthesis of Ag₂₅ Clusters

We have started our initial efforts of using the gel cavities for synthesis within the PAGE set-up itself. The thiolates were prepared along with the gels and NaBH₄ was taken in place of buffer. Potential was applied as usual. The reduction resulted in the formation of a colored gel from which clusters could be extracted in aqueous medium. Later on this procedure was modified and it can be synthesized in beaker only without the help of PAGE set up. For that 47 mg of AgNO₃, 150 mg of GSH and 40 mg NaOH are mixed in 1 ml of water. In a beaker 3 ml of gel (acrylamide : bisacrylamide = 47:3) solution was taken, to that 0.7 ml of above prepared thiolate solution was added and well mixed. Now to poly 40 µl of APS and 40 µl of TEMED was added to polymerize it. Then 10 ml of NaBH₄ solution (10mg/ ml) was added to reduce it. After that it was crashed and washed with methanol to remove unreacted NaBH₄ otherwise it will leads to nanoparticle. Finally it was extracted in water; clusters are coming out in solution while gel remain as such. The schematic photographs are given here (figure S1).

Supplementary data 2. Instrumentation

2.4 Instrumentation

UV-Vis spectra were collected from Perkin Elmer Lamda 25 instrument in the range of 200-1100 nm. Luminescence measurements were carried out on a Jobin Vyon Nanolog instrument. For excitation and emission the band pass was set as 2 nm. The FT-IR spectra were measured using Perkin Elmer Spectrum One instrument, KBr crystals were used as a matrix for preparing the samples. Scanning Electron Microscopy (SEM) and Energy Dispersive X-Ray Analyses (EDAX) were done in FEI QUANTA – 200 SEM. For measurements, sample were drop casted on an indium tin oxide coated

conducting glass and dried in vacuum. As a result of the substrate, the EDAX spectrum shows features due to In, Sn and Si. High resolution Transmission Electron Microscopy (HRTEM) and EDAX were carried out with a JEOL 3010 instrument. Samples were taken on carbon coated copper grids and allowed to dry in ambient conditions. Powder XRD patterns of the samples were recorded using PANalytical X'pert Pro diffractometer. The powder samples of clusters were taken on a glass plate and the X-ray diffractogram was collected for 5 to 100 degree in 2 theta using Cu K α radiation.

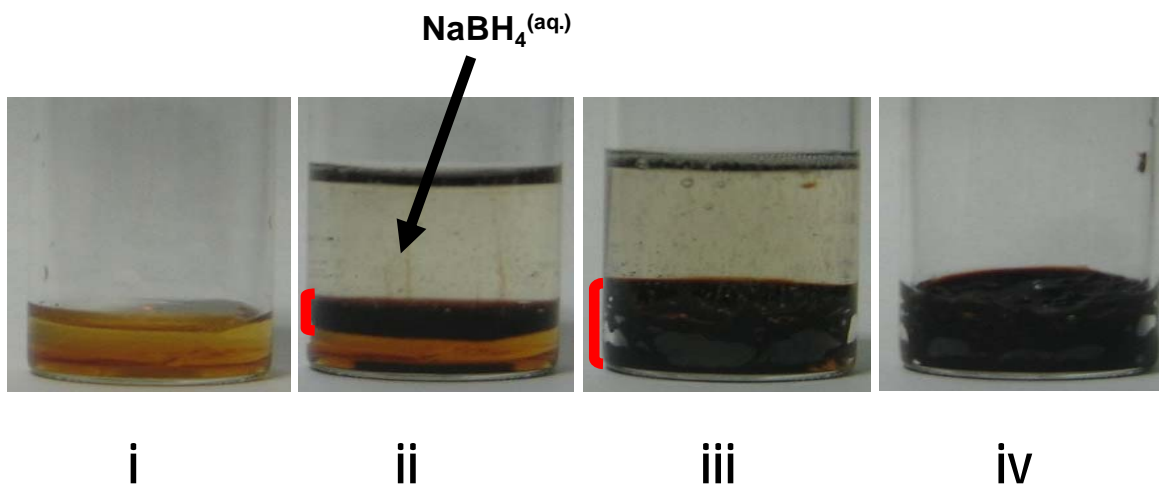


Figure S1. Photographs at different stages of reaction during synthesis of Ag_{25} cluster. i) Thiolate solution, ii) after addition of NaBH_4 , iii) after 20 minutes and iv) after removing unreacted NaBH_4 .

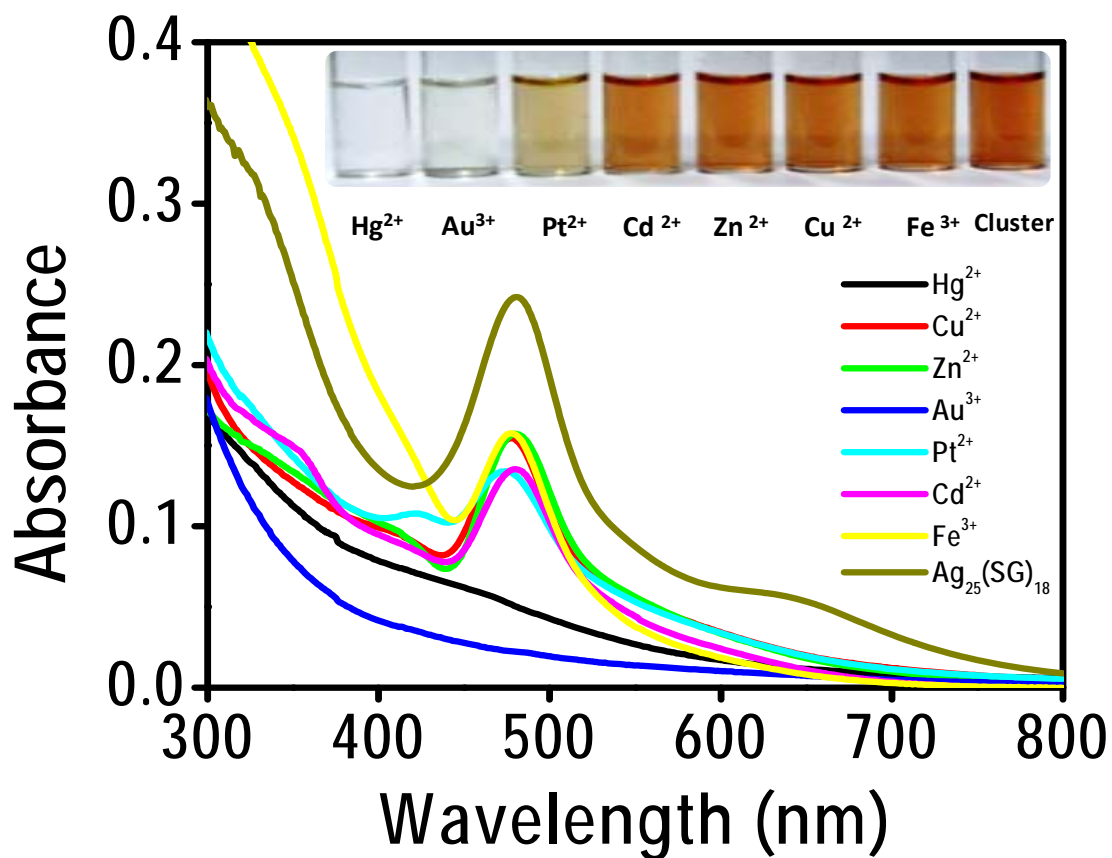


Figure S2. UV-Vis absorption spectra upon addition of various metal ions (50 ppm concentration) to aqueous Ag_{25} cluster solution. . Inset is a photograph of the corresponding solutions under visible light.

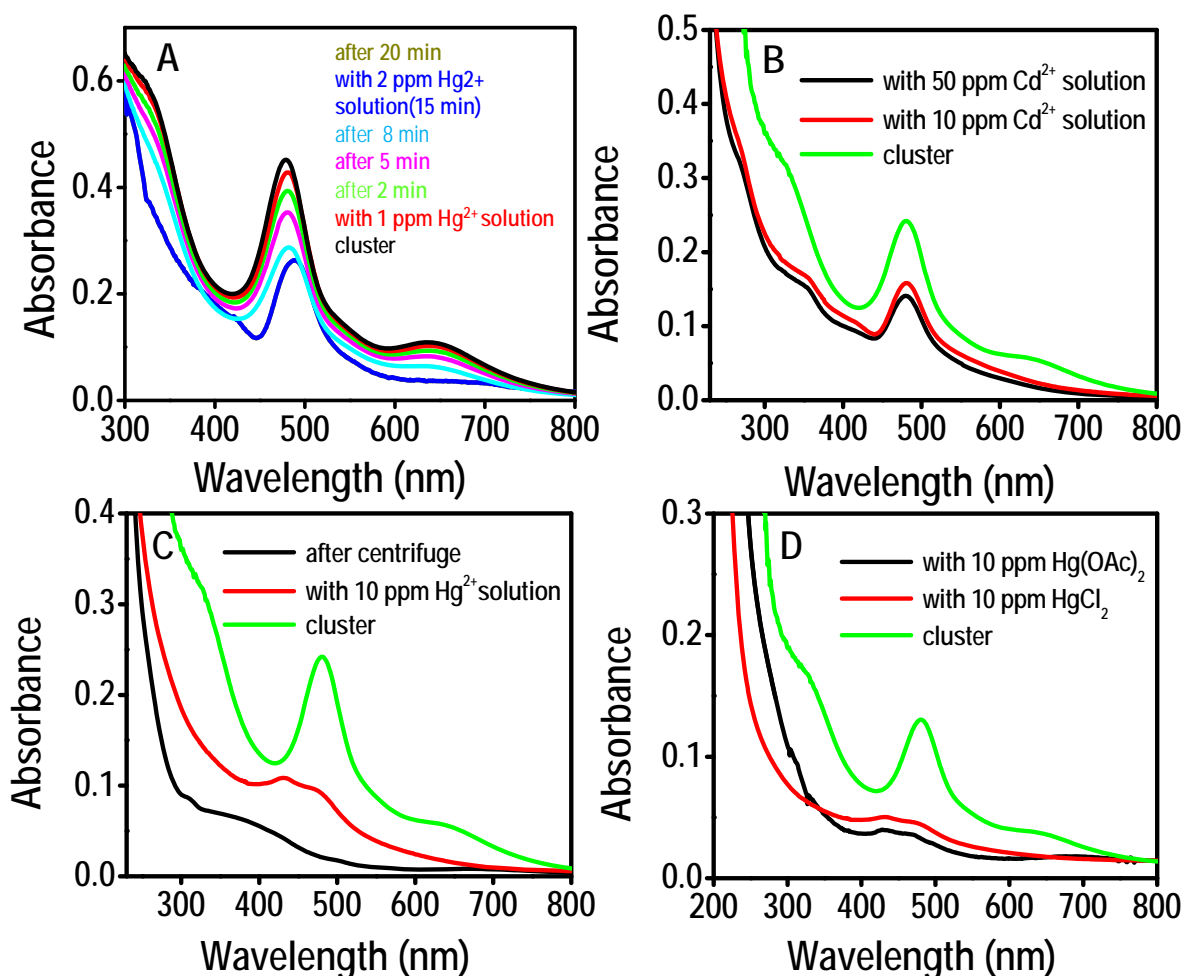


Figure S3. UV-Vis features of Ag₂₅ cluster with different system and conditions. Upon addition of Hg²⁺ the change in UV-Vis spectra with time is shown in “A”. An exceptionally different feature was observed with Cd²⁺ solution (B). Characteristic feature is also observed in C, where 10 ppm solution of Hg²⁺ added to cluster (red one), and also after centrifuging the solution, and redissolving the ppt in aqueous medium (black one). Effect of anion is given by “D”, which shows anion is not responsible for this interaction

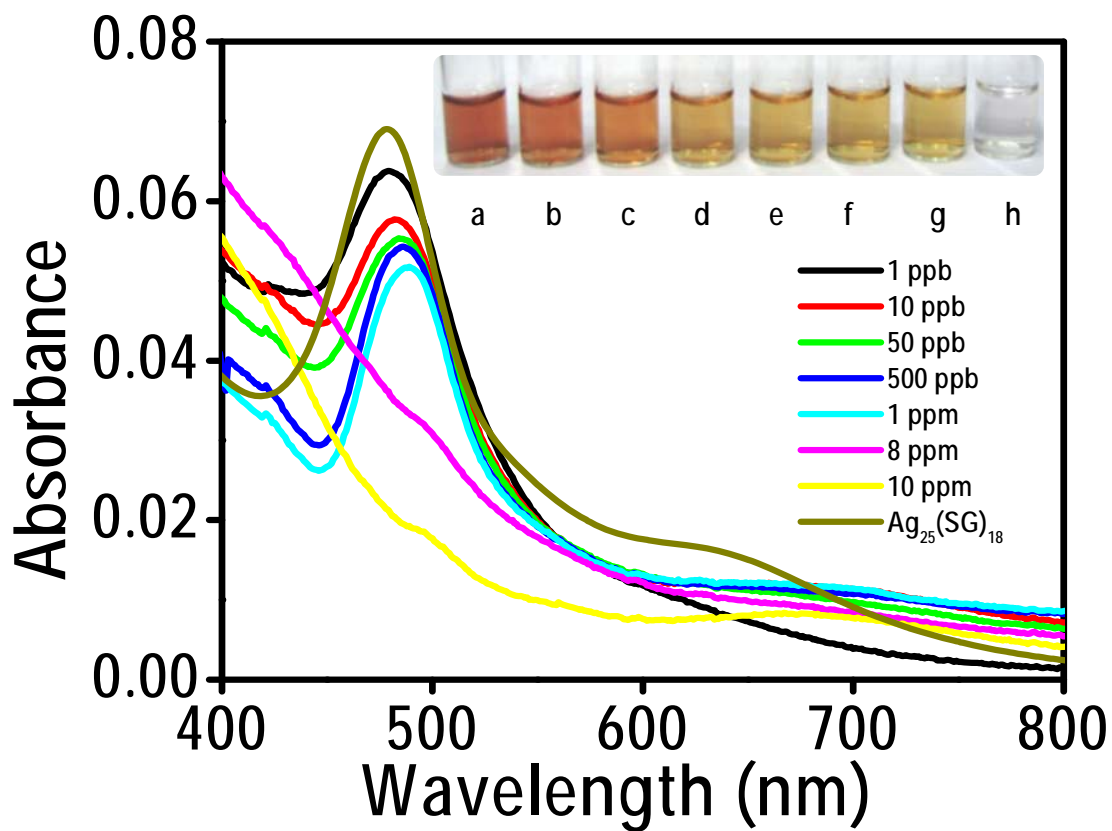


Figure S4. UV-Vis absorption spectra of various concentrations of Hg^{2+} -treated aqueous Ag_{25} cluster solutions. Inset is a photograph of corresponding solutions under visible light. The bottles a, b, ..., h correspond to pure $\text{Ag}_{25}(\text{SG})_{18}$, $\text{Ag}_{25}(\text{SG})_{18}$ + 1 ppb Hg^{2+} , ..., $\text{Ag}_{25}(\text{SG})_{18}$ + 10 ppm Hg^{2+} .

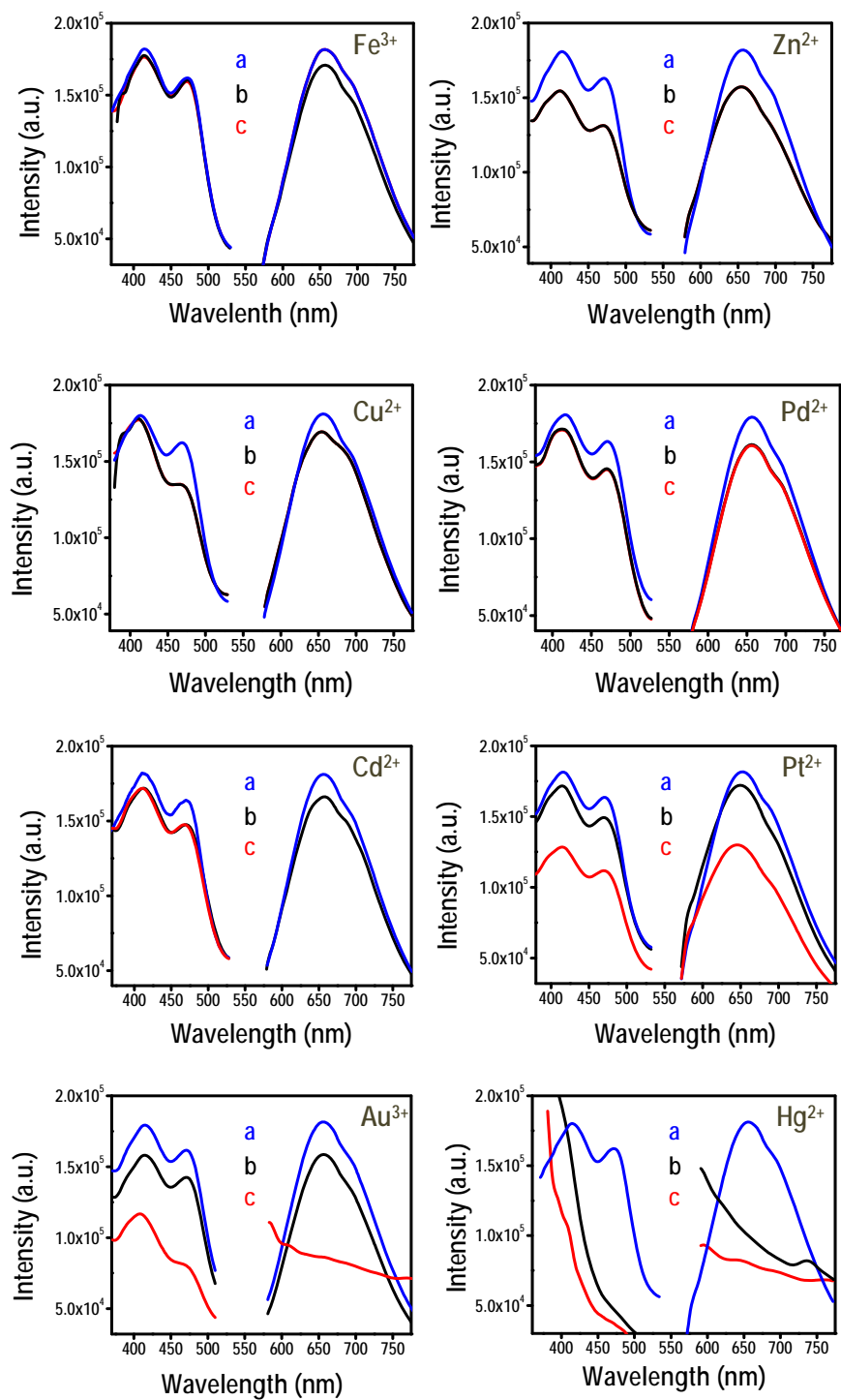


Figure S5. Effect of various metal ions on the luminescence spectra of Ag_{25} cluster solution. Trace a is showing the cluster feature whereas b and c are the cluster with 10 and 50 ppm solutions of metal ion, respectively.

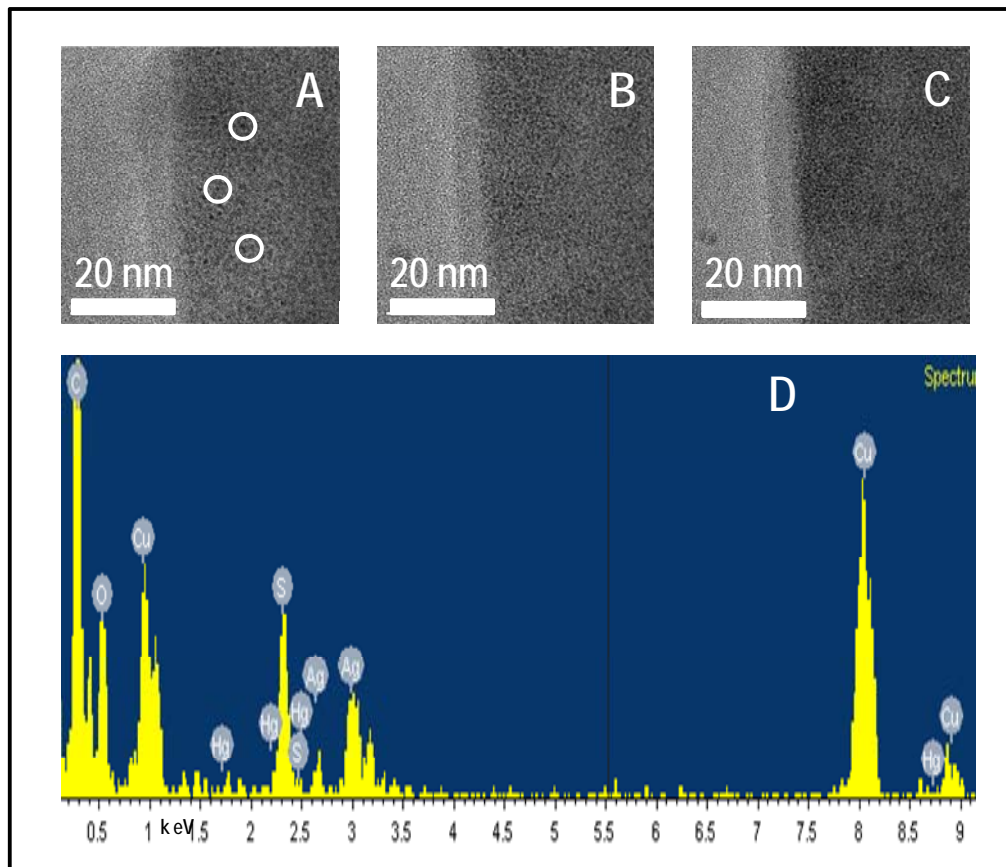


Figure S6. HRTEM image of cluster with low concentration (10 ppb) of Hg^{2+} showing the presence of cluster (A). Some of the distinct spots due to the cluster are marked with white circles. B and C are images taken after electron beam irradiation. D is showing the EDAX spectrum of corresponding sample.

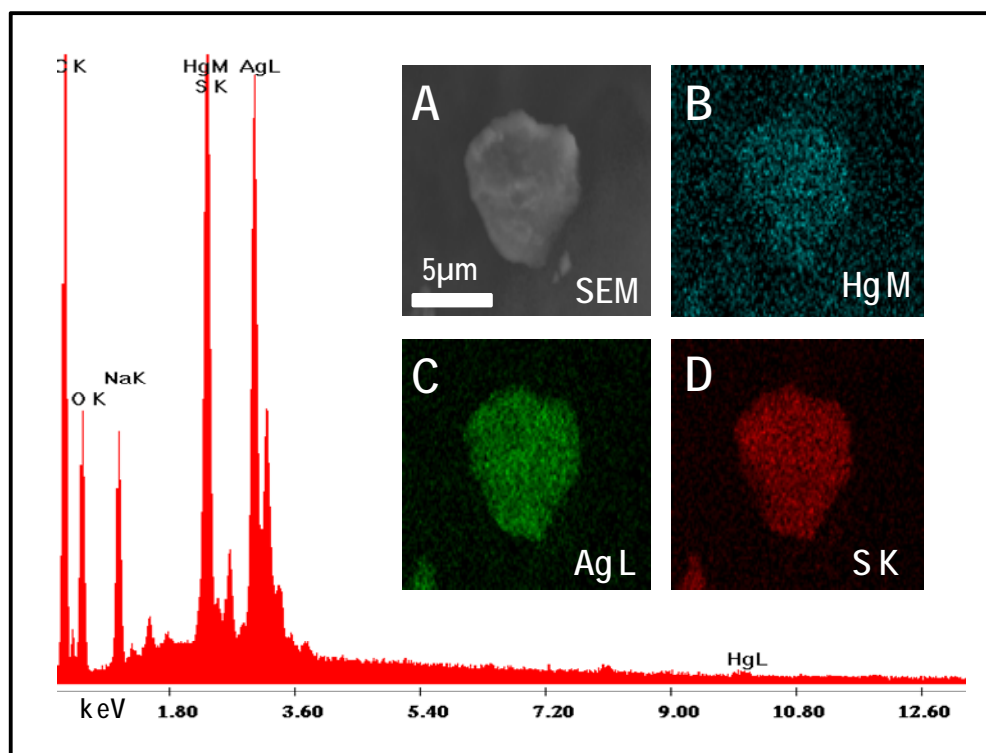


Figure S7. SEM image and EDAX spectrum of Ag_{25} cluster after exposure to 10 ppb Hg^{2+} solution. The elemental maps of Hg, Ag and S are given by B, C and D, respectively.

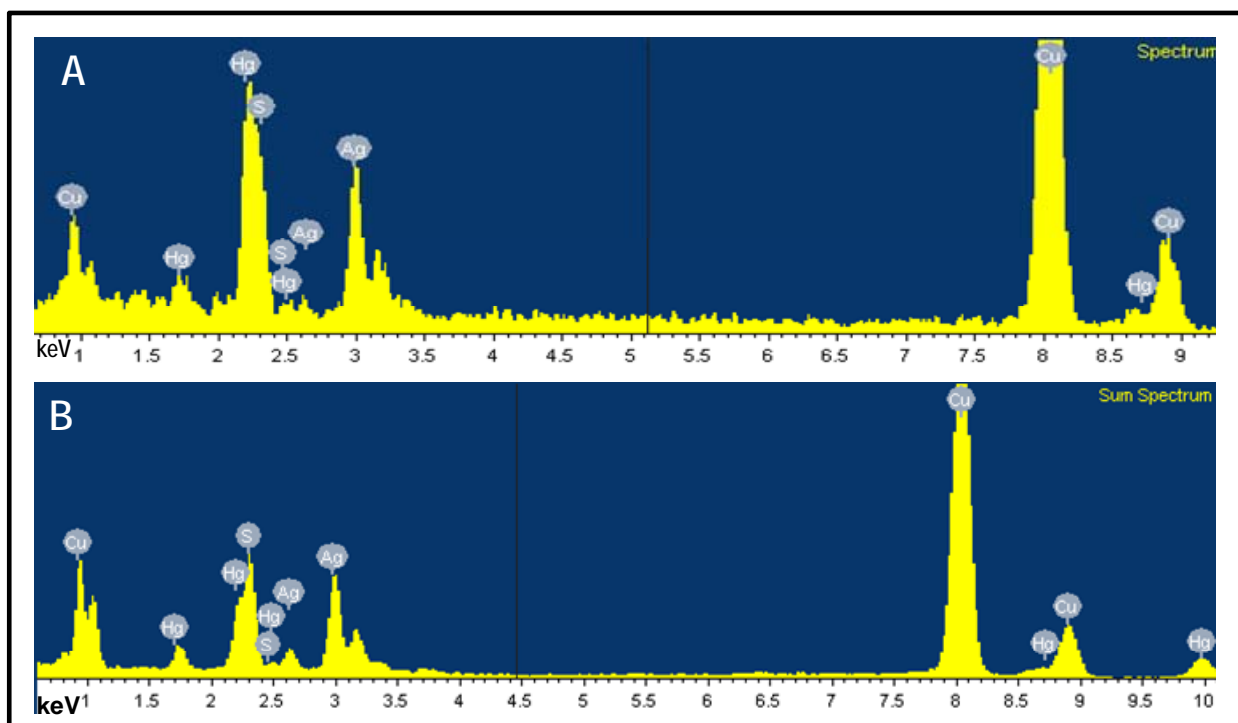


Figure S8. The EDAX spectra of Ag_{25} cluster treated with 10 ppm of Hg^{2+} . A is the corresponding EDAX spectrum of an isolated hexagonal species (Ag_3Hg_2) and B is the corresponding aggregated mass (whole area EDAX) formed during the treatment of Hg^{2+} with Ag_{25} cluster.

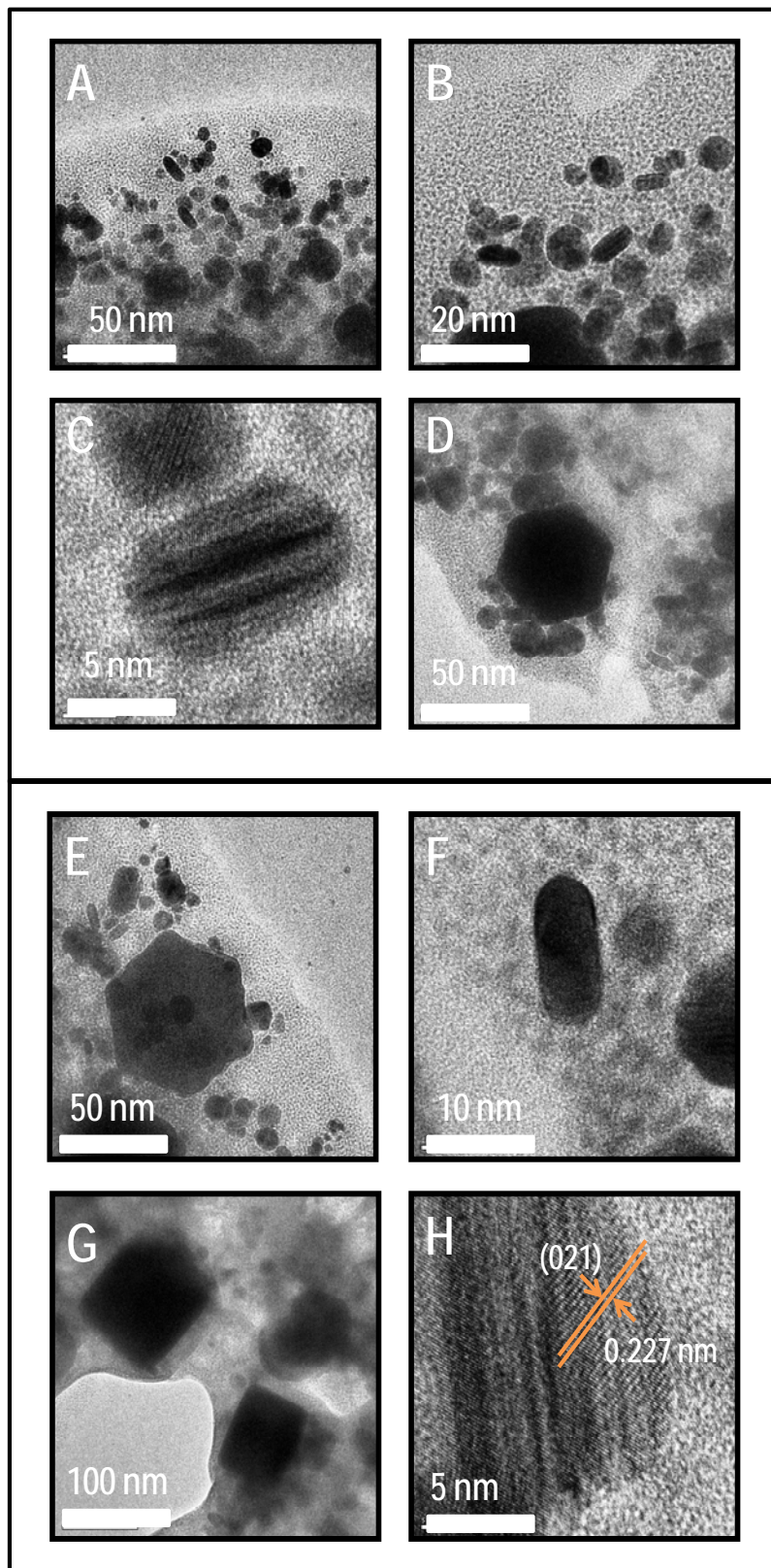


Figure S9. HRTEM images of the aggregated mass formed during the interaction of Ag_{25} cluster with Hg^{2+} solution. Various types of geometries are formed during the course of the reaction (A-G). Lattice has been found with a regular spacing of 0.227 nm (H).

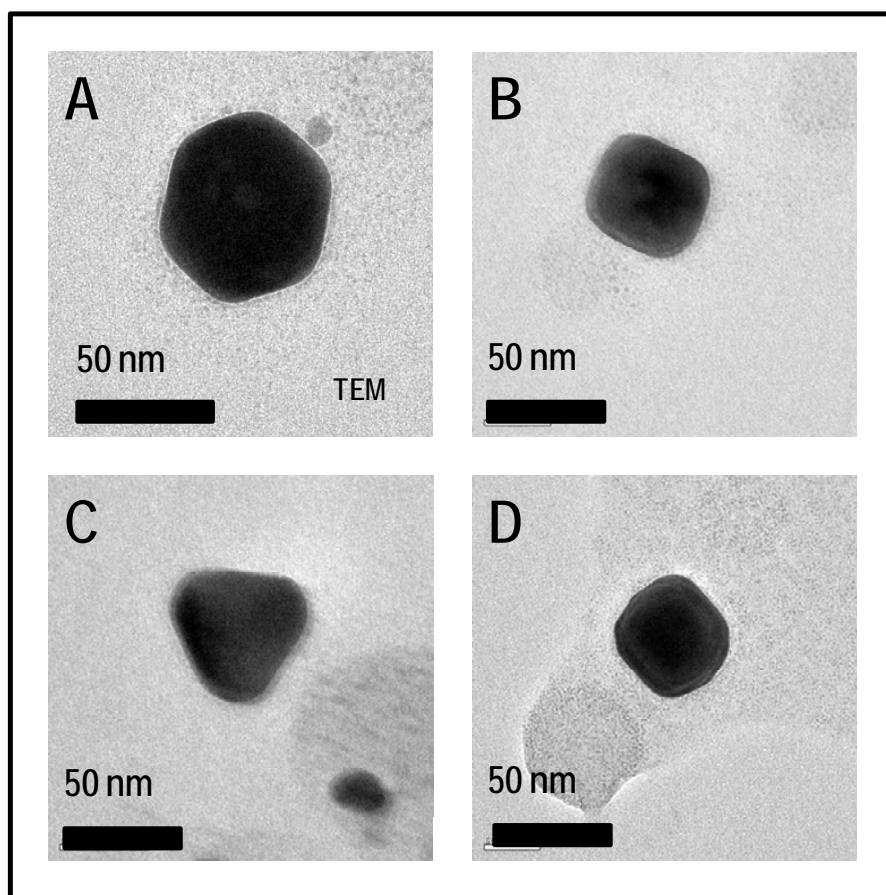


Figure S10. HRTEM images of aggregated mass after centrifugation: Hexagonal (A), square (B), triangular (C) and octagonal (D) type of geometries were observed.

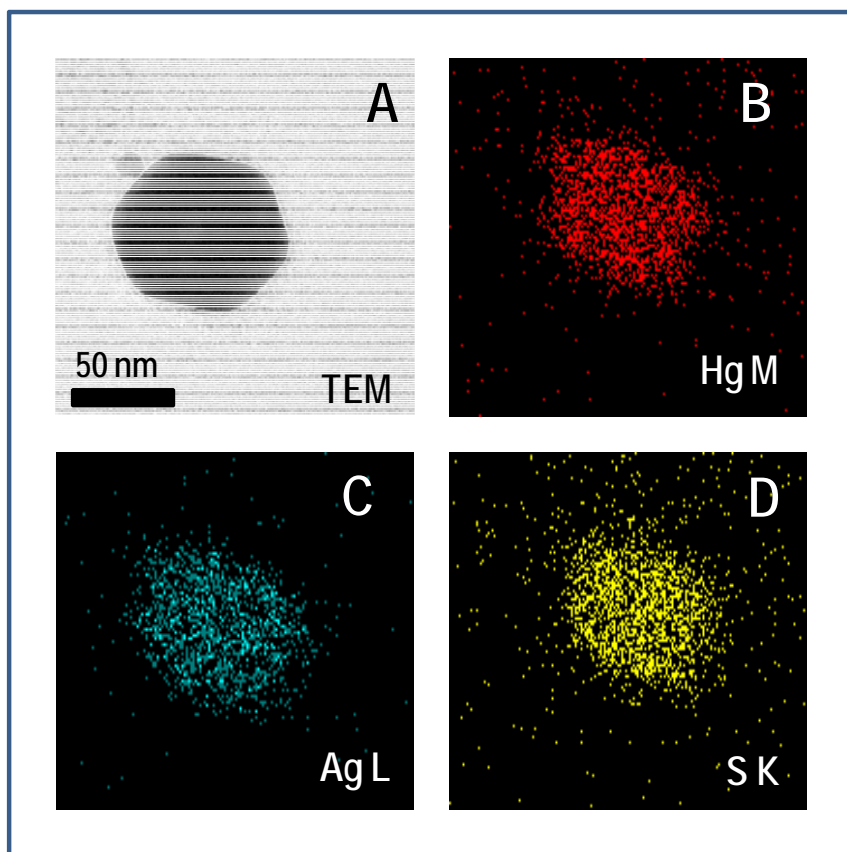


Figure S11. TEM and EDAX images of aggregated mass formed by the addition of 10 ppm Hg^{2+} solution (A) showing an isolated hexagonal object. The elemental maps of Hg, Ag and S of the particle are given in B, C and D.

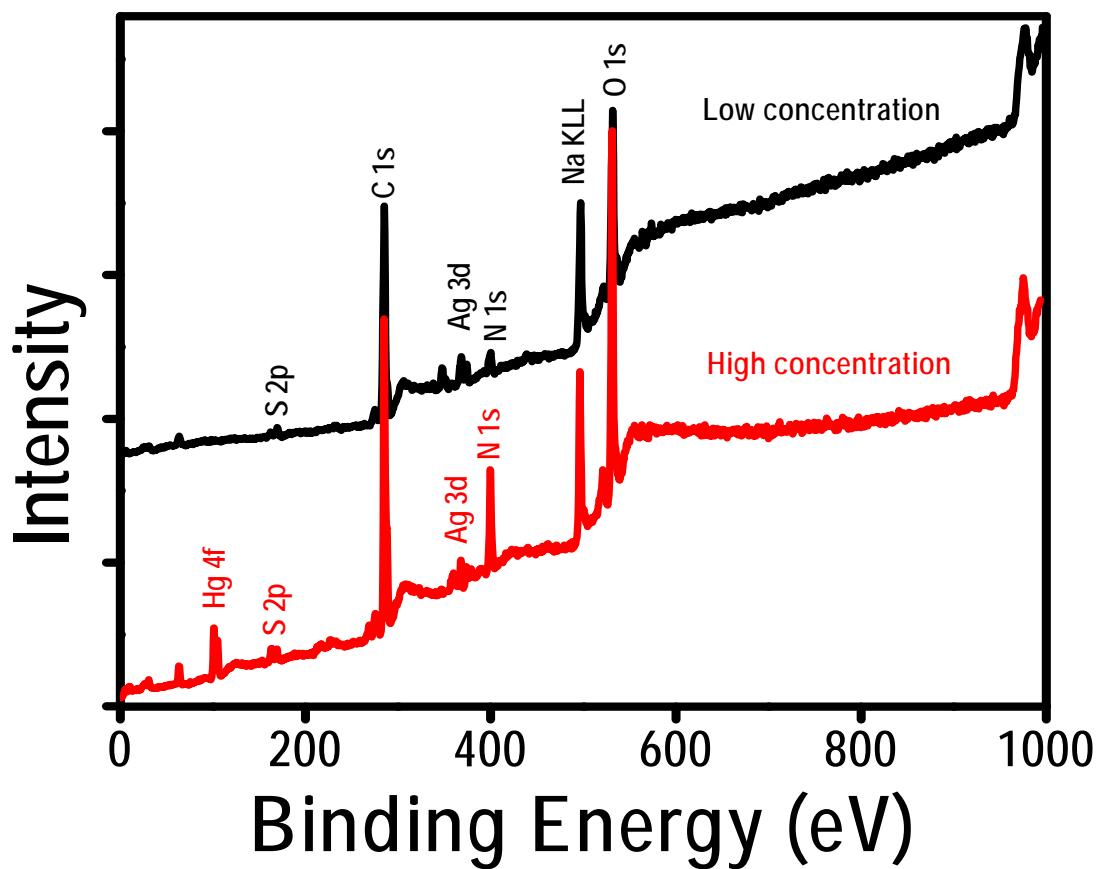


Figure S12. XPS survey spectra of cluster treated with low (100 ppb) (black) and high (100 ppm) (red) concentrations of Hg²⁺. Individual peaks are assigned.

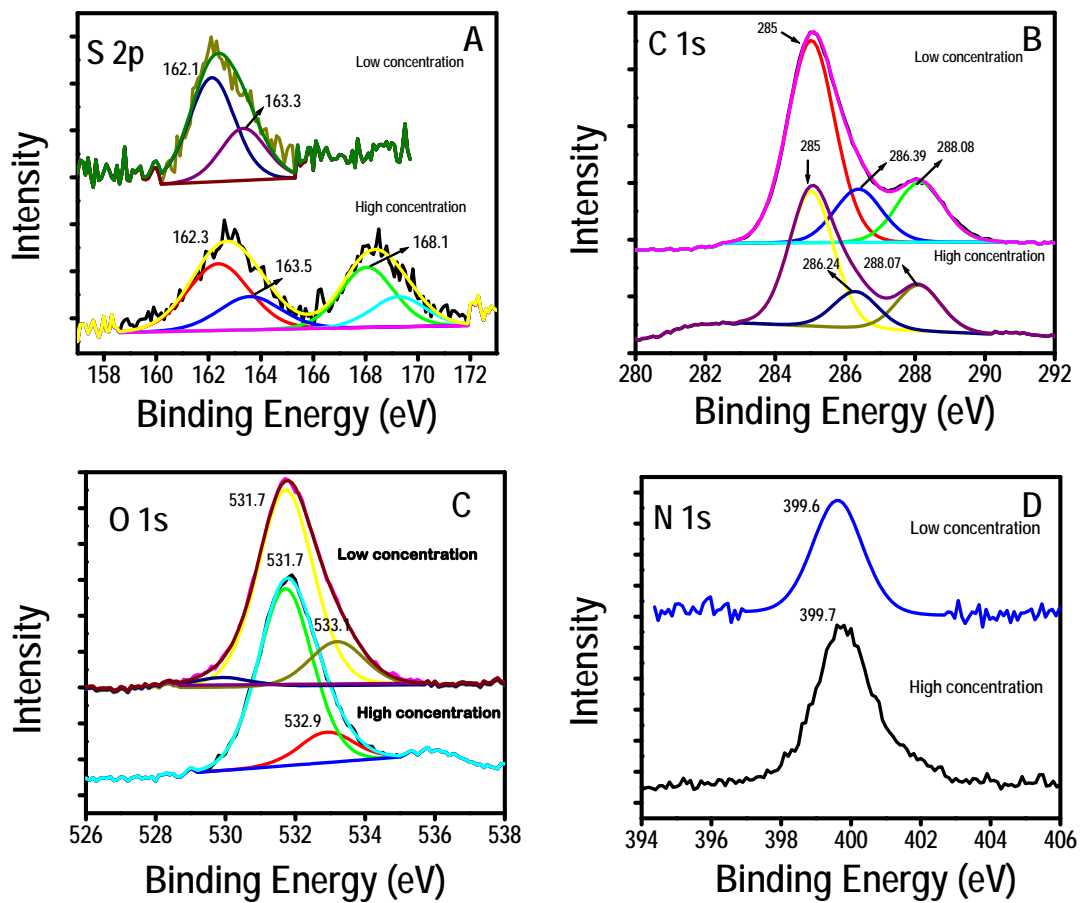


Figure S13. The S 2p, C 1s, O 1s and N 1s peaks in the XPS spectra for the residue formed after reacting with low (10 ppb) and high (100 ppm) concentrations of Hg^{2+} .

REVIEW ARTICLE

Protein-protected luminescent noble metal quantum clusters: an emerging trend in atomic cluster nanoscience

Paulrajpillai Lourdu Xavier¹, Kamalesh Chaudhari^{1,2},
Ananya Baksi¹ and Thalappil Pradeep^{1*}

¹DST Unit of Nanoscience, Department of Chemistry, Indian Institute of Technology Madras, Chennai, India; ²Department of Biotechnology, Indian Institute of Technology Madras, Chennai, India

Received: 23 November 2011; Revised: 26 December 2011; Accepted: 30 December 2011; Published: 3 February 2012

Abstract

Noble metal quantum clusters (NMQCs) are the missing link between isolated noble metal atoms and nanoparticles. NMQCs are sub-nanometer core sized clusters composed of a group of atoms, most often luminescent in the visible region, and possess intriguing photo-physical and chemical properties. A trend is observed in the use of ligands, ranging from phosphines to functional proteins, for the synthesis of NMQCs in the liquid phase. In this review, we briefly overview recent advancements in the synthesis of protein protected NMQCs with special emphasis on their structural and photo-physical properties. In view of the protein protection, coupled with direct synthesis and easy functionalization, this hybrid QC-protein system is expected to have numerous optical and bioimaging applications in the future, pointers in this direction are visible in the literature.

Keywords: *protein; peptide; noble metals; nano; quantum cluster; fluorescence*

Contents

1. **Introduction**
2. **QCs: the convergence of properties from nanoparticles downward and from atoms upward**
3. **Properties of NMQCs and the trend in the stabilizing ligands**
4. **Biom mineralization and NMQCs**
5. **Synthesis and properties of NMQCs@proteins**
6. **Evolution of gold quantum clusters in protein templates**
7. **NMQCs@peptides**
8. **Applications of NMQCs@proteins**
9. **Summary and outlook**

Acknowledgment

References



Paulrajpillai Lourdu Xavier received an M.Tech. in Nanoscience and Nanotechnology, from the National Centre for Nanosciences and Nanotechnology, University of Madras, Chennai. Currently, he is working as a Research Associate with Prof. T. Pradeep, DST UNS, Department of Chemistry, IIT Madras, Chennai. He is working on understanding noble metal quantum clusters in multifunctional macromolecules and their applications.



Kamalesh Chaudhari received an M.Sc. in Physics from the Indian Institute of Technology Kharagpur. Currently, he is pursuing a PhD in the Department of Biotechnology, Indian Institute of Technology Madras, under the guidance of Prof. T. Pradeep. He is working on understanding noble metal quantum clusters in macromolecular templates, their biological applications and study of nano-bio interactions using single particle spectroscopy.

Dramatic growth has been witnessed in the field of atomic clusters during the last few decades, due to their fascinating properties (1–12). Clusters, which are made of few atoms, can be either in the gas phase or in the condensed phase, exhibit a bridge between atomic properties and those of the bulk and have been

researched by both theoreticians and experimentalists. Arrival of nanoscience has intensified research on clusters in the condensed phase (1–3). For quite some time, anything that is evaporated or made in smaller dimension used to be referred to as clusters. The term clusters is now by and large restricted to entities distinctly smaller than nanoparticles. Quantum confined condensed phase clusters of noble metals such as gold and silver have been of recent interest due to their intriguing properties such as photoluminescence, non-photobleachability, photon anti-bunching, longer lifetime when compared to the conventional organic fluorophores and versatility in applications (4, 5). It should be mentioned that experimental studies on Pt and Cu QCs have also been emerging recently (13, 14). Here, one may remember that noble metals have always been of larger interest to materials scientists, they had been part of catalysis, organometallics and inorganic complex chemistry (10, 12, 16, 17). And what we have been currently pursuing as cluster science is closely associated with the progress in other areas (1, 10, 16). In the next few paragraphs, we have attempted to give a condensed version of the subject area of NMQCs.

QCs: the convergence of properties from nanoparticles downward and from atoms upward

Exploring the properties of matter at decreasing dimensions has been an everlasting question in science. From the ‘divided state of metal’ of Faraday, colloidal state has been explored intensely over the past one and a half century (18). Excitement in this area can be seen in three distinct categories of materials: noble metal nanosystems, semiconductor particles or quantum dots and zero, one and two dimensional systems of carbon. Synthesis of stable and well defined particles of gold in the solution state as well as in the solid state redispersible forms, with various functional attributes contributed to the expansion of research in this area. Along with the multitude of properties of free and supported nanoparticles such as catalysis and plasmonics accelerated research in this area. Use of zero dimensional materials expanded into 1, 2, 3 dimensional states of matter and each one of these specific forms have produced distinct shapes for which reproducible synthetic procedures are now available. This evolution can be best observed in the case of gold, which makes gold based nanosystem the most extensively investigated category of materials. Excitements in this category of materials are covered elsewhere in detail (19–21).

The above mentioned evolution in chemical synthesis of nanoscale matter has produced entirely new class of materials in the recent past and they belong to the sub-nanometer analogues of nanoparticles with precise number of atoms which makes them inseparable from molecules. They are also called as clusters or molecular clusters and have also been referred to as artificial atoms



Ananya Baksi received an M.Sc. in Chemistry from the Indian Institute of Technology, Kharagpur. Currently, she is pursuing a PhD under the guidance of Prof. T. Pradeep in the Department of Chemistry, Indian Institute of Technology, Madras. She is presently working on understanding the growth of noble metal quantum clusters in macromolecular templates and their applications.



Thalappil Pradeep is a professor of Chemistry at the Indian Institute of Technology Madras, Chennai, India. He earned his PhD. from the Indian Institute of Science in 1991 and had post doctoral training at the Lawrence Berkeley Laboratory, University of California, Berkeley and Purdue University, West Lafayette. He held visiting positions at many leading universities and institutes in Asia and Europe. Prof.

Pradeep's research interests are in molecular and nanoscale materials and he develops instrumentation for those studies. He has authored 250 scientific papers in journals and is an inventor in 30 patents or patent applications. He is involved in the development of affordable technologies for drinking-water purification. One of his technologies has been commercialized. He is a recipient of several awards including the Shanti Swaroop Bhatnagar Prize, BM Birla Science Prize and National Award for Nanoscience and Nanotechnology. He is a Fellow of the Indian Academy of Sciences. He is the author of the introductory textbook, *Nano: The Essentials* (McGraw-Hill) and is one of the authors of the monograph, *Nanofluids* (Wiley-Interscience). His other interests include education, popularization of science and development of advanced teaching aids. He has authored a few popular science books in Malayalam and is the recipient of Kerala Sahitya Academi Award for knowledge literature for the year 2010. For more information, please see, <http://www.dstuns.iitm.ac.in/pradeep-research-group.php>.

in the literature. From the earliest synthesis of Au₁₁, Au₁₃ and Au₅₅ in 1978 onwards (22–24) there have been numerous developments in this area. After the synthesis of thiolate protected AuNP in 1994 (25) and water soluble thiol protected clusters in 1997, this area started receiving increased attention (26). The smallest analogues of these clusters could not be observed in TEM and were examined using mass spectrometry, especially by laser desorption ionization (LDI) (26). As precise characterization was not possible, the early clusters were

characterised based on mass numbers in their name such as '28 kDa clusters' (27). Luminescence from these clusters in the NIR region, although not bright, attracted attention (28). Several of these clusters were separated by electrophoresis and their spectroscopic properties were examined in detail (29). This was the turning point of research in such materials which opened up numerous properties of the molecular state of gold (4, 6, 60, 73, 93).

Parallel to the chemical synthesis of clusters, atomically precise clusters with unusual structural stability have been explored from the very early part of cluster science. Several of these studies are natural extensions of gas phase cluster spectroscopy. Marriage of advanced mass spectrometry with laser ablation changed the course of research as any material could be evaporated under an intense laser beam. Such clusters, mass selected or otherwise, could be deposited on surfaces to explore the catalytic chemistry of reduced dimensions. In fact, deposition of atoms on surfaces to produce clusters or active catalysts, without mass selection has been practiced for a long time. Depositing and manipulating atoms using scanning probe microscopy has been the holy grail in nanoscience (1, 15, 16, 30, 31). As can be seen, the area of QCs therefore represents a convergence of matter (and the research on them too) from nanoparticle to molecules or from atoms to molecules (Fig. 1) (1–55).

Various names may be given to these systems such as clusters, molecules, nanoclusters, nanoparticles, monolayer protected clusters, artificial atoms and so forth and many of these have been used in the literature. We would like to present briefly our reasons for naming them as quantum clusters. As nanoparticles and monolayer protected clusters (MPCs) have been used to describe large nanoparticles with or without monolayers, these two terminologies do not bring out the distinct differences or make their differences apparent from the systems under discussion. Terminologies such as artificial atoms may not be appropriate, as apart from single metal clusters, there are distinct categories of mixed atom analogues which make it necessary to have 'mixed atom' or 'alloy' superatoms and such a terminology does not appear suitable. Besides, shell closing is not the only reason for their existence. While clusters bring a gas phase analogy, it also suggests that these systems may exist only in the free state, without molecular protection. On the contrary, we are discussing molecules which can be precipitated, crystallised and redispersed just as any standard molecule. Thus the two better suitable names are quantum clusters and molecules. We refer to them with the former title as the latter suggests that the whole entity such as M_mX_x where M and X are the metal atom and ligand, respectively have

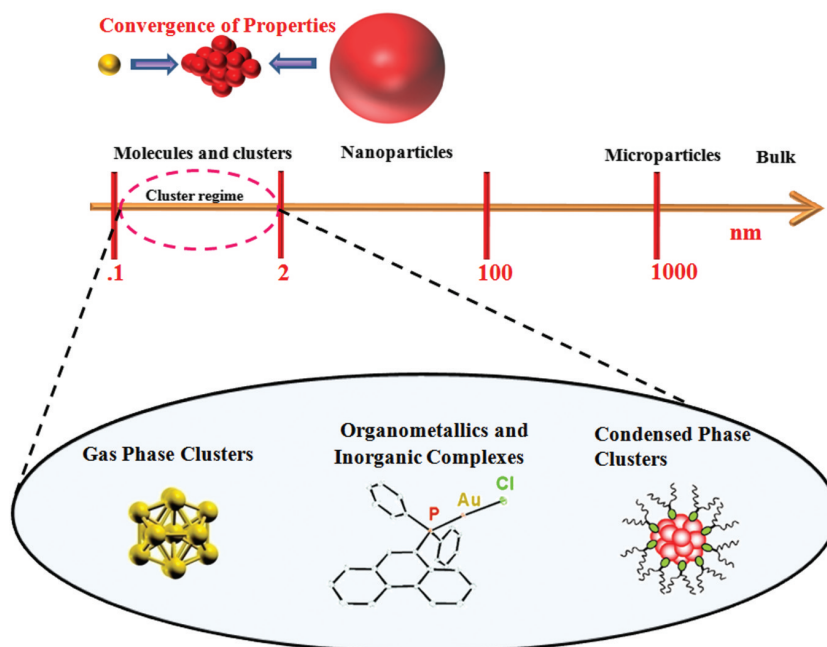


Fig. 1. Hierarchy of materials from atoms to bulk, especially in the case of noble metals. Clusters fall in-between atoms and nanoparticles. Expanded view is of the cluster regime showing diverse variety in this category: gas phase and condensed phase clusters with possible intermediate forms, the complexes. This schematic illustrates typical model nanosystems of gold but the same applies to other noble metals also. The transition of properties occurs between atoms to nanoparticles and also it illustrates the convergence of properties of colloidal nanoparticles and atoms at the scale of clusters. Schematic is for illustration purpose only and is not to scale. In the expanded view of clusters, images of naked cluster, complex and condensed phase thiol protected cluster were adapted from references 56, 57 and 58, respectively.

no separate existence. This is not true, as the core and the ligand are often two separate species with distinct features. Besides these distinct reasons, the name quantum clusters make them appear similar to quantum dots, both are intensely luminescent, one of the commonly used properties of the latter. Below we briefly discuss the properties and trend in the stabilizing ligands of these new materials.

Properties of NMQCs and the trend in the stabilizing ligands

NMQCs are sub-nanometer to 2 nm sized nanocrystal cores composed of noble metals, containing typically tens of atoms, with ligand protection and are distinctly different from nanoparticles and bulk powders in many properties (1–12). Surface plasmon is absent, since size of the cluster reaches de Broglie wavelength of the electron at the Fermi energy of the metal ($E_{\text{Fermi}} = 5.53$ eV, 4.28 eV, 5.49 eV, and 7.00 eV for Au, Pt, Ag and Cu, respectively (33)) and it can no longer support the plasmon excitation (5). Their structure is distinctly different from those of nanoparticles and bulk. For instance, the QC Au₁₃ has an icosahedral structure (6, 10). As it is known, fraction of atoms on the surface plays an important role in determining certain properties and in the case of QCs, fraction of surface atoms is high due to their extremely small core size (1). Electronic confinement occurs due to the protection of the core with the ligand shell and energy levels of the core become discrete. Further, NMQCs exhibit highly polarizable transitions which scale in size with $E_{\text{Fermi}}/N^{1/3}$ where E_{Fermi} is Fermi energy of the bulk metal and N is the number of atoms (4). Luminescence in them arise from the transitions between the $d \rightarrow sp$ interband and $sp \rightarrow sp$ intraband derived levels and these conduction electron transitions are the low-number limit of plasmons (4, 6). Hence, by manipulating the number of atoms in the core, emission wavelength can be tuned. Luminescence combined with the non-cytotoxic nature, unlike the popular semiconductor QD analogues, make them unique for biological applications. NMQCs can be magnetic and may exhibit chirality (6–8). Although physico-chemical, structural and electronic properties of NMQCs are not covered in this short review (which may be found elsewhere (1–3, 6, 10)), they pose several intriguing questions. For example, one may ask: Where does the transition from icosahedron to *fcc* start? How many atoms would be needed for plasmons to appear? When would a specific chemical property such as CO reactivity appear? In all of these properties, each atom counts.

With this abridged note, we would look at the various ligands used and the trend observed in the synthesis of NMQCs.

In the early times, groups of atoms formed by evaporation were stabilized in unreactive matrices, typically of

condensed gases (1–2, 33–34). Since these clusters are extremely reactive in nature, without a stabilizing moiety, they tend to aggregate in solution to form bigger structures, to release their higher free energy. Hence, unlike some weakly protected colloids, the role of stabilizing ligands and controlled synthesis became crucial for solution state realisation of these materials. In the beginning, by exploiting the gold-phosphine chemistry, phosphine protected clusters came into existence (22–24). Thiol based cluster synthesis was developed by Whetten and Murray (35), they introduced glutathione (GSH) as a ligand to make water soluble clusters. Tsukada and colleagues extended this method and purified the clusters (29). Initially thiol protected clusters were synthesized in the organic phase (25, 26). Thiols like phenylethanethiol, hexanethiol, octanethiol and dodecanethiol-protected clusters were also prepared by taking advantage of thiol-gold affinity (6, 35). Later, water soluble thiols like mercaptosuccinic acid (MSA), D/L penicillamine, captopril, etc. were employed (6, 38–41). Use of MSA in nanoparticle and cluster synthesis is due to Kimura (36, 37). Dickson's group synthesized gold and silver clusters in dendrimers and DNA, respectively (42, 43). Ligand exchange of as-synthesized clusters has also been demonstrated by Pradeep's group (44–46). Novel synthetic routes may be used to make these clusters directly without purification and in larger quantities (40–41, 44, 47–49, 51). Stable series of organogold clusters (gold covalently bound to carbon) protected by phenylacetylene has been synthesized recently (52). Recently, Pradeep and co workers demonstrated that direct synthesis of NMQCs in solid state is also feasible (49). In zeolite scaffolds also silver clusters were made (50). Direct conversion of colloidal silver nanoparticles to thiol passivated Ag_{QCs} has been demonstrated (51). While mass spectrometric and few other spectroscopic details of these clusters are known, very few crystal structures are available so far (53–55). An emerging trend is synthesizing clusters with proteins and peptides which are functional. This trend in change of ligands for cluster synthesis is indeed fascinating and a gradual size evolution in the protecting agent is also noticed (Fig. 2). This may be thought of as a way to add additional attributes as scientists have been looking at the proteins to mimic them, especially the functional ones such as enzymes (17). The most exciting aspect of this research is bright luminescence in such clusters (60). The bio-molecular templates add another dimension to this research, with all their functional attributes. With this short briefing, hereafter we would focus on NMQCs@proteins (the @ symbolism implies NMQCs are embedded in proteins). We hope this review would connect various aspects of science from bio-mineralization by complex proteins to quantum confined noble metal clusters.

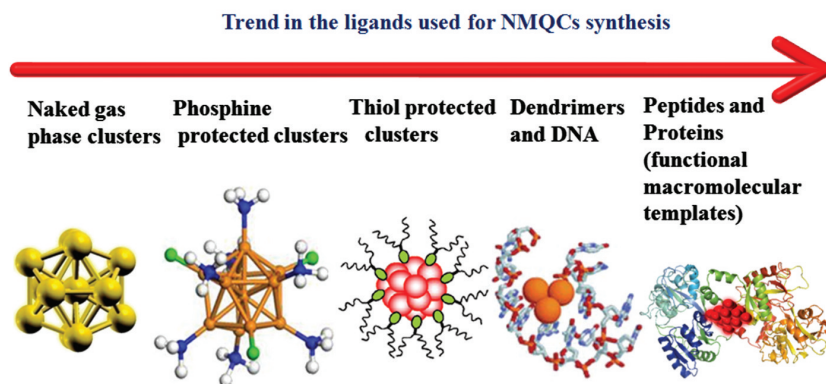


Fig. 2. The trend observed in the use of ligands for cluster synthesis, starting from gas phase unprotected analogues to phosphine protected systems to functional protein protected QCs. Representations of naked, phosphine, thiol, and DNA protected clusters were adapted from references 56, 59, 58 and 42, respectively.

Biom mineralization and NMQCs

Nature leaves one awestruck by its marvellous creations and mysteries. Biom mineralization is a natural process in which living organisms adapt to form hard structures by mineralizing metal ions through mineralizing peptides, vesicles, etc., and it is known that mineralization in many organisms occur as a mechanism to escape from ill effects of toxic metal ions or to form specific functional structures of millimeter to nanometer scale as in the case of magnetic bacteria (61). Interesting reports are available on bacterial mineralization of gold. Bacteria which are closely related to *Ralstonia metallidurans* play vital role in the formation of gold nuggets (62). Myriad of inorganic nanostructures have been formed by biom mineralization or biomimetic mineralization processes and a lot of research efforts have been made to understand these processes (61–66). While naturally formed AuNPs are reported, unfortunately, QCs are not observed so far to occur naturally, may be because of their high reactivity. The biom mineralization process has been mimicked to synthesize NMQCs too by carefully adjusting the concentration of metal ions and modifying the environment suitably. Unlike semiconductor QDs, quantum confinement effects starts only below two nanometers in NMQCs, hence, controlling the size becomes a tedious but crucial process. The captivating point is that size control is achieved by proteins very easily (60). It is likely for an NMQC to reside inside a large protein due to the former's sub-nanometer dimension or to be surrounded by more than one protein in the case of very small proteins.

Synthesis and properties of NMQCs@proteins

Mimicking biom mineralization, Narayanan and Pal have synthesized luminescent silver clusters in proteins using NaBH_4 (67). Yu et al. transferred the as-synthesized luminescent silver clusters to other biomolecular scaffolds by shuttle-based method (68) and synthesized Ag_{QCs} intracellularly in NIH 3T3 cells (69). Xie et al. (60) first

reported the direct synthesis and stabilization of Au_{QC} by a protein, bovine serum albumin (BSA) without any external reducing agent. Synthesis was done by mixing metal ion precursor with the protein and changing the environment to alkaline pH. At alkaline pH, it is reported that aromatic aminoacids donate electrons to reduce gold ions while broken disulphide bonds play major role in stabilizing the nucleated cluster (60). However, a clear understanding of the process is not yet available. Several groups have followed this procedure. Some groups have followed modified procedures like using ascorbic acid in addition to the above said mixture (70). Muhammed et al. reported the synthesis of Au_{QCs} by etching of gold nanoparticles by BSA (71) following their earlier method of etching larger nanoparticles by GSH (44). Wei et al. synthesized gold cluster with lysozyme (72). Xavier et al. had demonstrated the synthesis of Au_{QCs} in iron binding transferrin proteins such as lactotransferrin (Lf) and showed that iron saturation does not affect the cluster formation (73). But comparatively, Au_{QCs} in iron depleted protein had higher emission intensity than Au_{QCs} in iron saturated protein. This was first report to use a multifunctional metallo-protein for cluster synthesis. Recently, Le Guével et al. have synthesized gold clusters in human serum transferrin (74). Shao et al. synthesized Au_{QCs} and Ag_{QCs} on a solid platform of egg shell membrane (ESM) which consists of mixture of proteins, by soaking the separated ESM in metal ion precursor solution and illuminating the surface with UV light (75). Le Guével et al. synthesized $\text{Au}_{\text{QC}}@BSA$ and protected it with silica shell (76). Recently, Yan et al. synthesized $\text{Au}_{\text{QC}}@BSA$ and HSA using microwave assisted method in a few minutes (77). Liu et al. synthesized $\text{Au}@Ag_{\text{QCs}}$ by sonochemical method in BSA (78). Choi et al. have recently synthesized Au_{QCs} in fixed NIH 3T3 cellular matrix (79). Mathew et al. reported a red emitting fifteen atom silver cluster in BSA. However, it was less stable and the stability was enhanced by protection with poly vinyl

pyrrolidone (PVP) (80). Peptides are used to direct the synthesis of clusters using mild reducing agent and by varying the pH. Recently, electrostatically induced phase transfer method has been used to synthesize NMQCs (81). A series of silver clusters and Au₂₅ have been produced using custom peptides at alkaline pH (82, 83).

In general, from the published results so far, NIR emitting Au_{QCs}@proteins in general possess two excitation maxima (λ ex. max = ~ 370 nm and 510 nm) and one emission maximum in the NIR region (λ em. max = ~ 650–670 nm (Fig. 3B) (70–73). They have higher quantum yield ~6% when compared to their monolayer protected counterparts (60, 70–74). Upon excitation at 370 nm, an emission around 450 nm is seen. This is attributed to protein's intrinsic fluorescence by a few groups and due to Au₈ by other groups (60, 73, 75, 84). NMQCs@protein exhibit strong stability across a wide range of pH and is stable in higher ionic strength (Fig. 3C) (60, 73). Long lifetime component values, usually above 100 ns, have been reported for Au_{QCs}@proteins (73, 74, 84). Recently, Kawasaki et al. reported blue and green emitting Au_{QCs} synthesized at different pH with high quantum yield using pepsin (85). Compared to their monolayer protected counterparts, QCs@proteins have

several fold enhanced luminescence. The reason for the enhancement of luminescence is still not completely understood, albeit the nature of the ligands bound to the cluster is important in this (86). In addition, the emission from the complex and how the emission from the intrinsic fluorophores of protein is contributing to the enhanced luminescence are also not properly understood. Earlier, it was suggested that there is a possibility of FRET between protein's fluorophores and the cluster; however, other studies on this have not been reported (73). The newly generated modified fluorophores during the reaction may play crucial role in addition to the ligand's role (91). While investigating the luminescence from clusters, one should be cautious about the intrinsic fluorescence of the template or ligand used and their modified products during the course of the reaction (43, 87–90).

Several groups have carried out XPS studies of NMQCs@proteins and results showed the existence of zero-valent Au and Ag indicating the presence of metallic core (60, 70–74, 80). Simms et al. studied the structural and electronic properties of Au_{QC}@BSA using X-ray absorption spectroscopy (XAS). Their analysis of the Au L(3)-edge extended X-ray absorption fine structure (EXAFS) of Au_{QC}@BSA suggested that the QC was

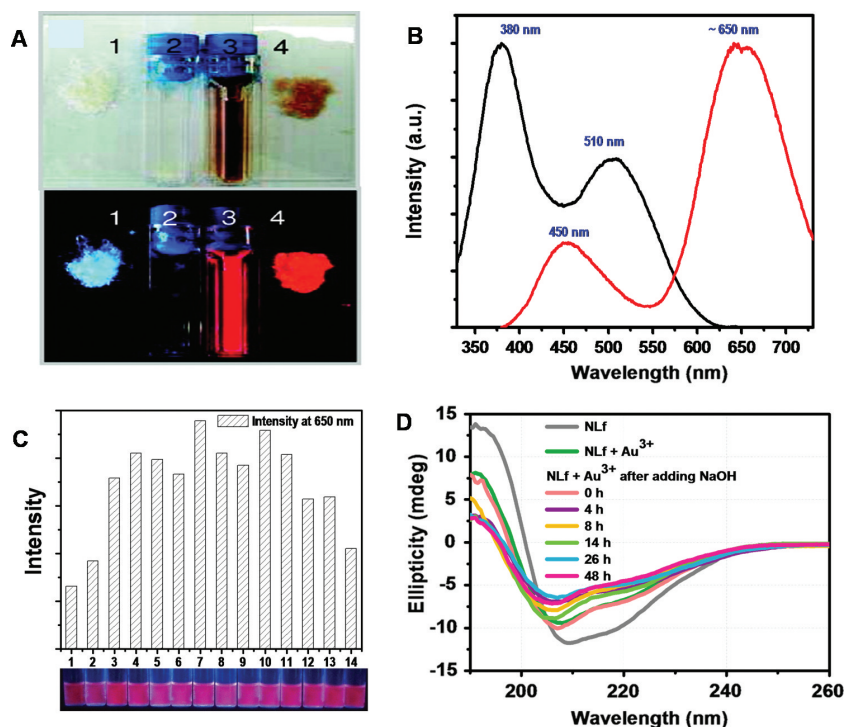


Fig. 3. (A) A photograph illustrating the luminescence of Au_{QC}@BSA. Red luminescence of the cluster solution and solid upon UV irradiation is shown, while the blue emission is from fluorophores of the protein. (B) Fluorescence spectra showing the excitation and emission maxima for a typical protein protected cluster. (C) Bar diagram showing the changes in luminescence intensity of clusters at various pH and corresponding photograph of the solutions in UV light. This indicates the significant stability of protein protected clusters over a wide range of pH. (D) CD spectra showing change in the conformation of NLf at various stages of cluster growth. A and D were adapted from references 60 & 94, respectively. B and C were adapted from reference 73.

Au₂₅ with a Au-thiolate ‘staple’ motif. Further, they used X-ray absorption near-edge structure (XANES) and Au 4f XPS to probe the electronic behavior of Au_{QC}@BSA. The Au d-electron density of Au-BSA was found to decrease by 0.047 e⁻ relative to that of the bulk. They further reported that ab-initio calculations involving local density of states (l-dos) of Au_{QC}@BSA were consistent with the experimental d-dos results (92).

Mass spectrometry (MS) has been indispensable in understanding atomic clusters (27, 29). For the QCs@protein systems also, MS plays a major role in characterizing the cluster core. But very few reports are available on specific cluster cores in proteins, such as Au₂₅@BSA, Au₃₈@BSA, Au_{13,25}@Lf, Ag₁₅@BSA (Fig. 4D) and Ag₈@BSA. Some groups have reported that mixture of several clusters must be present in the protein matrix (60, 71, 73, 74, 80, 84). The formation of clusters is highly dependent on the structural properties of a given protein, hence various proteins with clusters should be analysed separately to know about the cluster core. Cluster core was shown to be similar in case of

Au_{QC}@BSA and Au_{QC}@Lf, two larger proteins containing similar number of thiols (60, 73). Recently, Liu et al. have grown gold clusters in solution and also in insulin crystals (93) (Fig. 4A, 4B). They have reported that no mass shift was observed in the protein to characterize the nature of the cluster and suggested a reason that since insulin is a small peptide hormone, during ionization, the grown clusters detach from proteins and therefore are not identified in MS. The intact disulphide bonds observed in Raman stretching and non-formation of clusters when disulphide bonds were cut suggested an alternative growth mechanism other than that is observed for larger proteins like BSA or Lactoferrin. Recently, we also have observed similar mechanisms where the growth of QCs in small proteins does follow different mechanisms in comparison to larger proteins. We have observed that unlike larger proteins like BSA and Lf, cluster growth in lysozyme was different (Fig. 4C) (91). MS data, particularly for the cluster core protected by small proteins with less number of cysteine is not yet available. More MS oriented studies are expected in the future to understand the

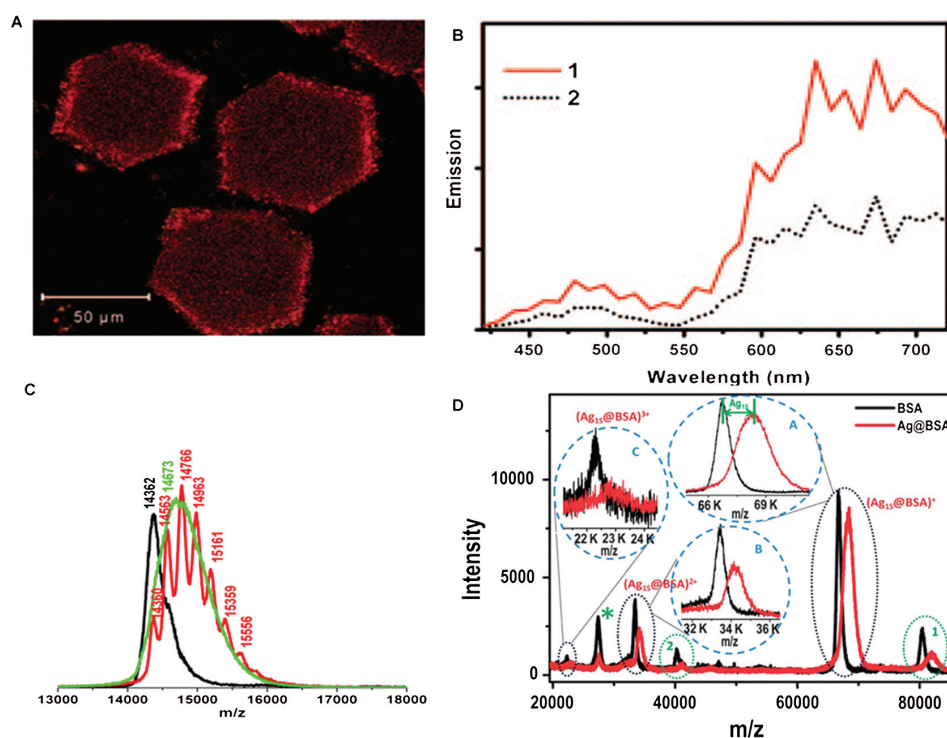


Fig. 4. (A) Two photon fluorescence image of Au_{QC}s grown in insulin crystals ($\lambda_{\text{ex}} = 800$ nm). (B) Two photon excitation of Au_{QC}s in the crystal, under different depth showing characteristic spectra of red emitting Au_{QC}@protein, Line 1 (red solid) is emission from the surface of the crystals and line 2 (black dotted) is the emission from 5.0 μm below the incident surface. (C) MALDI MS data of lysozyme at pH 7 (black), lysozyme-Au¹⁺ complex (red) at neutral pH with 2.5 mM HAuCl₄ showing binding of gold ions by the observed mass shift. After cluster formation at pH 12, the mass shift pattern of complex disappears and very little mass shift is seen (can be one or two gold atoms strongly bound to the protein) suggesting that cluster is bound by more than one protein in case of smaller proteins like lysozyme. Hence during ionization in MALDI, it is not likely to see them (Our unpublished data). (D) MALDI MS data of Ag₁₅@BSA. MALDI MS of pure BSA solution (black trace) collected in linear positive ion mode using sinapic acid as matrix and that of the as-prepared red emitting Ag₁₅@BSA (red trace). The peaks due to singly, doubly and triply charged ions of Ag₁₅@BSA are expanded in the inset marked A, B and C, respectively A and B are adapted from 93, C and D are adapted from references 80 and 91, respectively.

system well. Since well defined optical properties of cluster cores are not seen in UV-vis spectra, it becomes difficult to give more details about the cluster core. Investigations by various groups on protein's conformation upon cluster formation revealed that there is a significant conformational change (Fig. 3D) (60, 67, 73, 94). Narayanan and Pal synthesized fluorescent silver clusters in α -chymotrypsin and studied the cluster protein interaction using time resolved fluorescence studies and reported that the conformation and activity of the enzyme is affected considerably. Here, we have to note that NaBH_4 was used in their method which may independently affect the protein's activity (67). The dynamics of protein during and post synthesis of cluster is yet to be investigated. Overall, while critically assessing the NMQCs@proteins system, the synthesis part is simple but the fundamental properties like origin of enhanced emission, role of protein's intrinsic emission, fate of protein's activity and how cluster is growing are yet to be understood completely. Hence there is a need to have a relook at the present understanding of QCs@proteins.

Evolution of gold quantum clusters in protein templates

As we discussed above, the understanding of QCs@proteins and how they evolve in the protein templates is key to design next generation fluorescent functional

noble metal clusters in macromolecular templates. Though one can say it as bio-mineralization, exact mechanisms of bio-mineralization are yet to be understood properly. As from early reports, mechanisms of bio-mineralization have been the topics of hot debate (61–66). Recently, Chaudhari et al. attempted to understand the growth process using mass spectrometry and have reported the current understanding of the evolution of gold QCs in Native Lf (NLF) and BSA templates (94) (Fig. 5A). Pradeep group's initial findings are intriguing and leads to many additional questions for future research. From the MALDI MS data, they observed that immediately upon addition of gold ions (Au^{3+}) to the protein molecules, 13–14 gold atoms bind to protein and they remain in the Au^{1+} state (Fig. 5B). Once NaOH was added, the Au^0 state was observed and number of bound gold atoms increased to ~ 25 per protein suggesting the formation of Au_{25} , which was further corroborated by the commencement of red emission. In the process of cluster growth, some free protein is generated depending on the total metal ion content in the Au^{1+} complex. As far as the optical properties are concerned, in the UV-vis spectra, they did not observe any prominent Au_{25} feature, it may be due to the bulky nature of the protein molecule and its strong absorption, but after 48 h, weak features around 650 nm were seen. During the evolution, at certain time intervals, they have observed

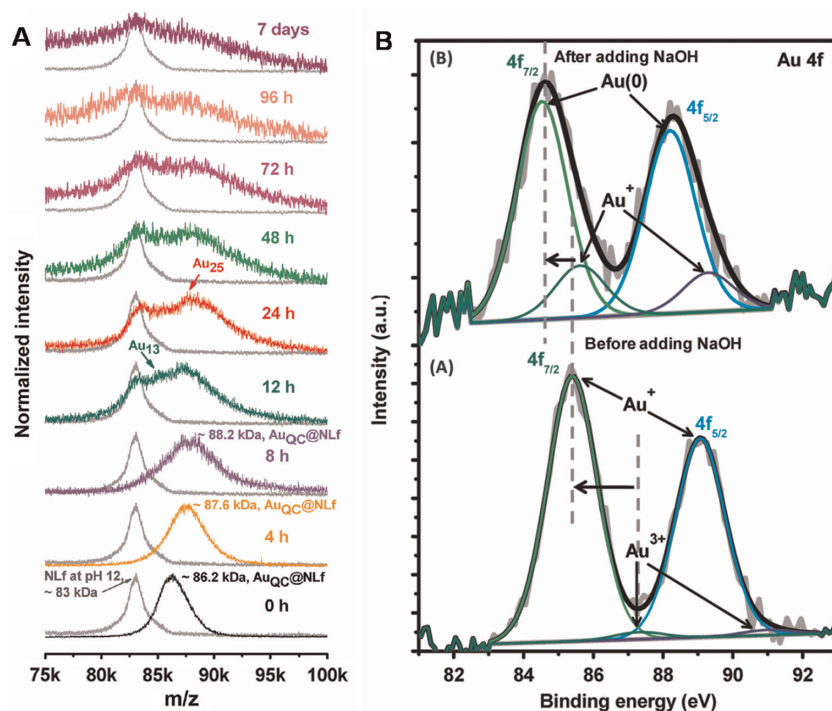


Fig. 5. (A) Time dependent MALDI MS suggesting the presence of Au_{25} and emergence of free protein from 12th hour of incubation. Initially, upon addition of Au^{3+} to Lf at pH 12, only one peak is there from which parent protein peak emerges when the clusters are nucleated. (B) XPS spectra showing the presence of Au^{1+} before the addition of NaOH and Au^0 after the addition of NaOH. A and B were adapted from reference 94.

the emergence of free protein at a specific molar ratio of protein and gold, suggesting an inter-protein metal ion transfer. This free protein was effectively utilized by providing extra gold ions at specific time intervals and they could obtain monodispersed clusters with enhanced luminescence. CD spectroscopic studies revealed that there were alterations in the secondary structure of the protein as a function of time to facilitate the cluster formation (Fig. 3D). Chaudhari et al. further demonstrated two step and multi-step approaches to utilize the free proteins generated to effectively form monodispersed clusters with enhanced luminescence. They also have hypothesized that inter-protein metal ion transfer and auriphilic interactions also play vital role in the formation of clusters in protein molecules. Li et al. has also observed free protein during cluster growth and proposed a method to remove the free protein from the as-synthesized protein cluster mixture. They have devised a simple chromatographic technique to remove the free protein by dansylating the protein and then identifying the free protein without the cluster by its green fluorescence from the red emitting cluster containing proteins (95).

NMQCs@peptides

Like peptide based nanoparticle synthesis, QCs have also been synthesized using selected peptides. Even few amino acids are used for cluster synthesis. For instance, histidine has been used to synthesize Au₁₀ (96). Banerjee et al. used modified peptides for silver cluster synthesis (97, 98). The most used peptide is glutathione GSH (Glutamic acid-Glycine- Cysteine) which is a tripeptide, present in biological systems. It has been used as a monolayer ligand for cluster synthesis from the early stage of cluster studies as mentioned before (6, 27, 29). Previously, Fabris et al. had shown peptides when bound to Au₃₈ remained in a conformationally constrained fashion (99). Target specific peptides based synthesis would be a more interesting field. Recently, Gao et al. synthesized a series of silver clusters and Au₂₅ by using a peptide containing nuclear target sequence (CCYRGRKRRQRRR) and demonstrated nuclear specific staining by Au_{QC}s (82, 83). Yuan et al. synthesized Ag_{QC}s using GSH and designed peptides (Asp-Cys-Asp, Glu-Cys-Glu, and Ser-Cys-Ser for red emitting Ag_{QC}s and Lys-Cys-Lys for blue emitting Ag_{QC}s) (81). Recently, Bellina et al. studied the isolated GSH-Au and GSH-Ag complexes, correlated their optical properties by the combination of action spectroscopy and time dependent density functional (TDDF) calculations and have reported that intense transitions are occurring within S-Ag-S motif and not within the cluster which is responsible for strong emission of silver clusters in biomolecules (100). These small peptides containing clusters may be helpful as biolabels where hydrodynamic

size of the protein protected clusters is not compatible and where smaller diameter is required.

Applications of NMQCs@proteins

NMQCs@proteins have been applied in sensing, electrochemiluminescence (ECL) and bio imaging so far and we shall discuss their applications in the above-mentioned order. Xie et al. had first shown that Au_{QC}@BSA can be used as a sensor for Hg²⁺ (101). Wei et al. and Lin et al. synthesized Au_{QC} in lysozyme and had shown its Hg²⁺ sensing application (72, 102). In general, it is reported that Hg²⁺ quenches fluorescence by interacting with the core while fluorescence quenches due to the aggregation caused by Cu²⁺ ions. Au_{QC}@Nlf was reported to be sensitive to Cu²⁺ ions other than Hg²⁺ (73). Several groups (101–105) have worked on metal ion sensing such as Hg²⁺, Cu²⁺ and Pb²⁺ using QCs@protein; simplicity in preparation makes them attractive tool for such applications (Table 1). Muhammed et al. showed metal enhanced fluorescence in case of Au₃₈@BSA, fluorescence turn off in the presence of Cu²⁺ and turn on in the presence of glutathione (71). Various other proteins containing Au_{QC}s and Ag_{QC}s have been employed for metal ion sensing such as trypsin, pepsin, ESM (75, 85, 105). Au_{QC}@horseradish peroxidase has been used to detect H₂O₂ (106). Wang et al. used Au_{QC}@BSA for the detection of glutaraldehyde in water (107) and Liu et al. used it for the detection of cyanide (108). Guo et al. synthesized red fluorescent stable silver clusters in denatured BSA and used the clusters for Hg²⁺ detection (109). Recently Goswami et al. synthesized blue emitting Cu_{QC}@BSA and showed that it can be used as a sensor for H₂O₂ and Pb²⁺. They have proposed that the additional aggregation due to Pb²⁺ ions was responsible for fluorescence quenching (110).

Apart from direct metal ion sensing, ECL based sensing has also been demonstrated. Li et al. demonstrated that ITO coated Au_{QC}@BSA exhibited ECL and reported that ITO played a significant role in enhancing ECL. They reported that in the presence of anionic co-reactant S₂O₈²⁻, ECL was enhanced and demonstrated its application to detect dopamine (111) (Fig. 6A). Fang et al. showed the generation of ECL from Au_{QC}@BSA in the presence of tetraethyl amine (TEA) and showed that ECL is differently influenced by the metal ions; here they showed it to be affected by Pb²⁺ (112) (Fig. 6B). Recently, graphene conjugated Au_{QC}@BSA has also been employed for generating ECL (113). Hun et al. recently employed Au_{QC}@BSA in chemiluminescence based experiments for the detection of lysozyme in cells (114). Antibacterial composites have also been made using NMQCs@proteins. Sreepasad et al. showed that Au_{QC}@Lf can be used to create luminescent patternable composites together with chitosan and graphene oxide. Au_{QC} in these composites were not quenched even in

Table 1. List of proteins used for NMQCs synthesis and their demonstrated applications

Protein	Metal cluster	Study and application	References
Bovine serum albumin	Au, Ag, Cu	Sensing of Hg^{2+} , Cu^{2+} , Pb^{2+} , H_2O_2 , Glutaraldehyde, and cyanide, electrochemiluminescence, cluster evolution, bio-imaging and <i>in vivo</i> imaging.	70–71, 94, 103–104, 101, 107–114, 117–121
Lysozyme	Au	Hg^{2+} sensing, antibacterial activity	72, 102, 116
Cellular retinoic acid Binding protein II	Au		72
Lactotransferrin	Au	Cu^{2+} sensing, FRET, composite with graphene cluster evolution and bio imaging	73, 94, 115, 91
Insulin	Au	Grown in crystals, bio imaging and bioactivity	93
Pepsin	Au	Hg^{2+} sensing, Blue, green and red emitting Au_{QC}	85
Trypsin	Au	Hg^{2+} sensing	105
Serum transferrin	Au	Bio imaging	74
Egg shell membrane (mixture of proteins)	Au, Ag	Hg^{2+} sensing	75
α -Chymotrypsin	Ag	Cluster-protein interaction	67
Horseradish peroxidase	Au	H_2O_2 sensing	106
Human serum albumin	Au	NO_x sensing	77
Egg white	Au	Metal ion sensing	91
Ovalbumin, papain	Au	Metal ion sensing	91
Cell matrix (nucleolin)	Au, Ag	Intracellular synthesis	69, 79

the presence of Hg^{2+} ions (115). Chen et al. reported that $\text{Au}_{\text{QC}}@$ lysozyme has enhanced antibacterial activity against resistant strains (116).

Several biological applications of the NMQCs@proteins have also been demonstrated. Retnakumari et al. showed that $\text{Au}_{\text{QC}}@$ BSA conjugated with folic acid can

be effectively used to target the folate receptors in cancer cells; this was the first report to employ QC@protein for molecular receptor specific application and in another report, they showed $\text{Au}_{\text{QC}}@$ BSA can be conjugated to monoclonal antibodies and used for targeted detection of acute myeloid leukemic cells (70, 117) (Fig. 7C).

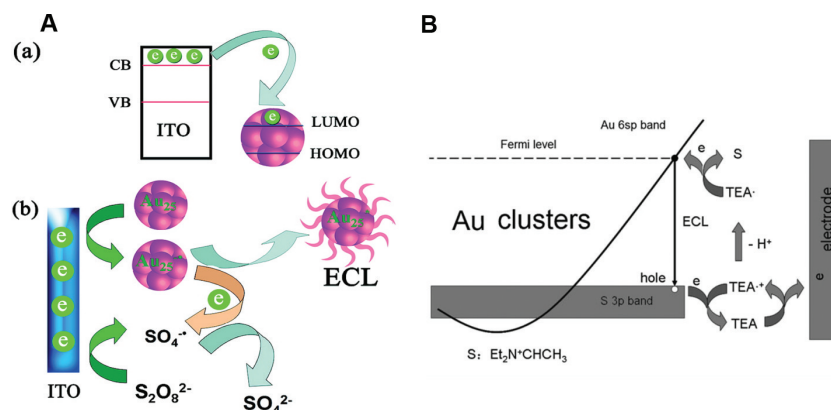


Fig. 6. Electro-chemiluminescence of (A) $\text{Au}_{\text{QC}}@$ BSA coated on ITO plate where $\text{S}_2\text{O}_8^{2-}$ was used as co-reactant. (a) Electron transfer between ITO and $\text{Au}_{\text{QC}}@$ BSA and (b) the ECL mechanism of $\text{Au}_{\text{QC}}@$ BSA in the presence of anionic co-reactant, $\text{S}_2\text{O}_8^{2-}$. (B) In another study, TEA was used as co-reactant. Figure illustrates the mechanism of ECL of $\text{Au}_{\text{QC}}@$ BSA in the presence of cationic co-reactant, TEA. A and B are adapted from references 111 and 112, respectively.

Similarly, Muhammed et al. have also shown folate receptor specific uptake of $\text{Au}_{\text{QC}}@BSA$ by human epidermoid carcinoma KB cells (71) (Fig. 7A). Recently, Wang et al. have conjugated $\text{Au}_{\text{QC}}@BSA$ to herceptin (a widely used humanized monoclonal antibody in case of breast cancer) to nuclear target Erb2 over-expressing HER2+ breast cancer cells for targeted cancer therapy. Unconjugated $\text{Au}_{\text{QC}}@BSA$ were not taken up by cells, thus demonstrated the targeting ability (118). Previously, to impart functionality one has to rely on conjugation chemistry to conjugate with biofunctional molecules, now due to the arrival of QCs@functional proteins, bio-functionality becomes intrinsic. $\text{Au}_{\text{QC}}@insulin$ has been used for bioimaging of brain cells (Fig. 7B) and as a CT contrast agent. Commercially available insulin and $\text{Au}_{\text{QC}}@insulin$ are shown to reduce the blood level glucose in a similar manner and no considerable change was observed. They suggested that the preservation of bioactivity of insulin, even after the formation of clusters in them,

is mainly due to the intact disulphide bonds. They further have shown that in undifferentiated myoblast cells having less number of insulin receptors, uptake of $\text{Au}_{\text{QC}}@insulin$ was less compared to the differentiated myoblast cells having increased number of receptors (93). Durgadas et al. recently used $\text{Au}_{\text{QC}}@BSA$ as a tool to detect intracellular presence of copper ions after treating the cells with copper solution (119) and have proposed a dialysis method to isolate circulating cancerous cells from normal cells in blood by conjugating $\text{Au}_{\text{QC}}@BSA$ with superparamagnetic nanoparticles (120). Le Guével et al. used $\text{Au}_{\text{QC}}@BSA$ protected by silica shell and $\text{Au}_{\text{QC}}@serum$ transferrin for bio imaging of A549 cells (74).

NMQCs@proteins have been used for *in vivo* imaging also. Wu et al. used $\text{Au}_{\text{QC}}@BSA$ for in-vivo imaging of cancer tissue in an animal model by exploiting the enhanced permeability and retention (EPR) effect of cancer tissue and this was the first report to use $\text{Au}_{\text{QC}}@protein$ for in-vivo imaging (121) (Fig. 7D).

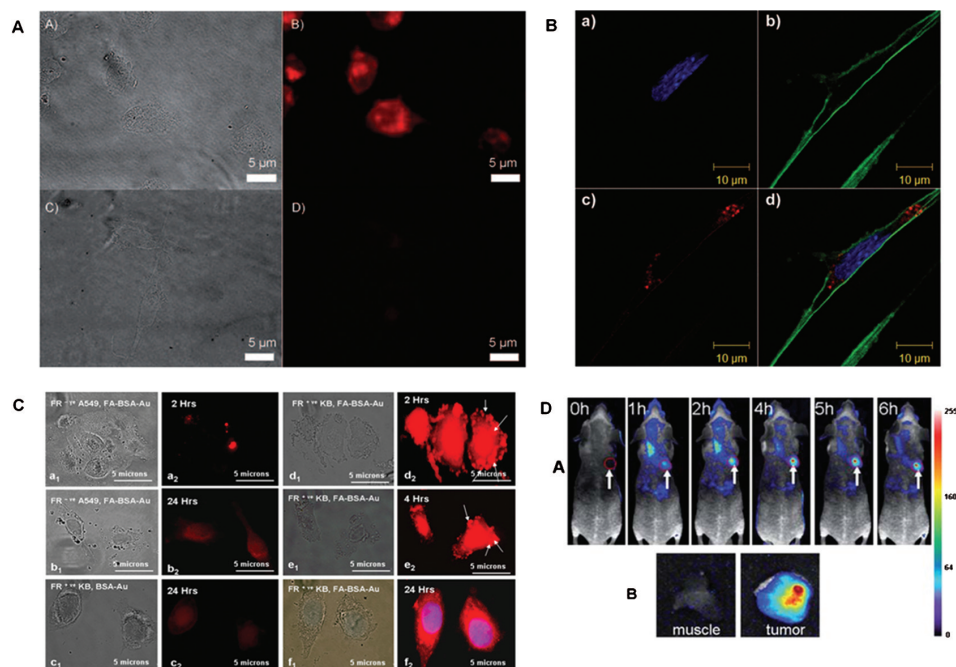


Fig. 7. Bioimaging applications demonstrated using $\text{Au}_{\text{QC}}@proteins$. (A) Uptake of FA- $\text{Au}_{\text{QC}}@BSA$ (synthesized by etching of larger nanoparticles with BSA) conjugated with folic acid Bright-field (A,C) and the corresponding fluorescence microscopy (B, D) upper panel images show the interaction of FA- $\text{Au}_{\text{QC}}@BSA$ with folate-receptorpositive KB cells with FA-conjugated $\text{Au}_{\text{QC}}@BSA$. lower panel images show FA- $\text{Au}_{\text{QC}}@BSA$ interaction with folate-receptor-negative mouse fibroblast L929 cells. (B) Microscopic observation of internalization of the $\text{Au}_{\text{QC}}@insulin$. Differentiated C2C12 myoblasts were treated with insulin- Au_{QC} for 2 h. a) Cell nucleus stained with 4',6-diamidino-2-phenylindole (DAPI, blue). b) Actin fiber stained with Alexa Fluor 488 phalloidin to confirm the cell boundary (green). c) $\text{Au}_{\text{QC}}@insulin$ exhibit red luminescence. d) Fluorescence image overlay of the three images. (C) Molecular receptor specific uptake of $\text{Au}_{\text{QC}}@BSA$ conjugated to folic acid (FA). Fluorescent microscopic images showing interaction of $\text{Au}_{\text{QC}}@BSA-FA$ with different types of cell lines: (a1)–(a2) FR^{-ve} lung carcinoma A549, (b1)–(b2) FR-depressed oral cell carcinoma, KB, (c1)–(c2) FR^{+ve} KB cells with unconjugated Au clusters, (d1)–(d2) FR^{+ve} KB cells with FA-conjugated Au clusters at 2 h, (e1)–(e2) 4 h and (f1)–(f2) 24 h of incubation. (D) In vivo imaging using $\text{Au}_{\text{QC}}@proteins$. (A) Fluorescence images of mice bearing an MDA-MB-45 tumor. Strong signal from $\text{Au}_{\text{QC}}@BSA$ was observed in the tumor (marked by the red circle) demonstrating significant passive accumulation in the tumor by the EPR effect. The arrowheads indicate the tumor. (B) Ex vivo fluorescence image of the tumor tissue and the muscle tissue around the tumor from the mice used in A. A, B, C and D were adapted from references 71, 93, 70 and 121, respectively.

Nie et al. reported controlled assembly of two gold quantumclusters in a well studied protein, ferritin. They assembled two Au_{QCs} (blue and red emitting) at the ferroxidase active sites of apo-ferritin heavy chain and showed that the resulting nanostructures (Au_{QC}@Ft) retained the intrinsic fluorescence properties of the cluster with enhanced intensity. Native structure of ferritin was intact after assembly and they used it for *in vivo* kidney targeting and bio imaging (122).

Summary and outlook

There has been an impressive growth in nanoscience and technology at the nano-bio interface. In this review, we have addressed such an interdisciplinary system where clusters of quantum confined noble metal atoms are grown by the union of materials and biology. NMQCs in protein templates are recent additions to the family of QCs with the fascinating advantage of being embedded in a functional macromolecule matrix. Increasing research interest in this system indicates an emerging trend. To mention the versatility of this approach, not-limiting to NMQCs, even doped semiconductor QDs, much bigger in size, are also synthesized in aqueous phase recently (123). It may be pointed out that nanoparticles of metals and semiconductors were synthesised by bacteria, viruses and fungi several years ago and biological synthesis is now fairly established (124–126). However, there has been very little understanding about NMQCs@protein systems. Complete structural understanding of the system is essential including how such systems evolve with time. For such an understanding, crystal structures of the intact protein protected metal clusters are necessary. Nevertheless, it can be understood to an extent by various mass spectrometric and spectroscopic tools. Clusters in liquid-protein systems would have considerable advantage in future (127). Molecular mechanics and dynamics based computational studies combined with DFT simulations would help to refine our understanding. Metallo-protein systems like ferritin, aconitase and laccase are known to have different metal cluster cores and the enzymes use the cores as functional sites. Likewise, in future, it is likely that luminescent noble metal cluster-protein systems having cluster-based active sites to function as catalysts. The cluster core at this specific size can have interesting redox properties which may affect the stability of the cluster itself. It can be viewed as a mix of bio-mimetic and bio-kleptic nanotechnology since we exploit the functionality of the protein (128). The catalytic chemistry mentioned above may be manipulated with photons to have new kinds of photocatalysis. Synthesizing clusters at physiological pH would have potential benefits in the field. Since, this system has opened a new area at the nano-bio interface; there is a need to know to what extent these proteins are modified and what exactly is modified. Considering the biological

applications of these cluster systems, despite the ongoing research efforts, there is a substantial need to know how these proteins with clusters are going to interact with the biological systems and what would be the intracellular fate of the uptaken clusters. We also should know whether these modified proteins are seen differently by the cell machinery. Proteins are fundamentally biological nanomachines. Rationally designed proteins with clusters would mean creating a permanent indicator to the nanomachines so that we can track them anytime. Thermostable templates mimicking the extremozymes where the cluster's stability is taken care of would have big impact in high temperature reactions especially as molecular beacons in PCR and in catalysis. To date, all the studies indicate the possibilities of growing clusters in organisms, if environment is suitably managed; it would not be surprising, if we get viruses growing QCs, after all it is also a protein body containing genetic material. It is up to us to identify the right protein system. In a nutshell, NMQCs in peptide and protein templates are expected to have plenty of applications in electronics, chemistry, biology and medicine over the years to come for which early signs are apparent in the recent literature.

Acknowledgements

We thank the Department of Science and Technology, Government of India for constantly supporting our research program on nanomaterials. We also thank all our research colleagues and collaborators whose names appear in the reference list.

Conflict of interest and funding

There is no conflict of interest in the present study for any of the authors.

References

1. Wurth W, Martins M. Atomic clusters: from gas phase to deposited. In: Woodruff DP, ed. The chemical physics of solid surfaces, first ed. Jordan Hill, Oxford: Elsevier; 2007, 1–626.
2. Alonso JA. Structure and properties of atomic nanoclusters. London: Imperial College Press; 2005.
3. Schmid G, editor. Clusters and colloids. Weinheim: VCH, 1994.
4. Zheng J, Nicovich PR, Dickson RM. Highly fluorescent noble-metal quantum dots. *Annu Rev Phys Chem* 2007; 58: 409–31.
5. Muhammed MAH, Pradeep T. Luminescent quantum clusters of gold as bio-labels. In: Demchenko AP, ed. *Advances in fluorescence spectroscopy*. Springer: Heidelberg, 2010. p. 333–53.
6. Jin R. Quantum sized thiolate-protected gold nanoclusters. *Nanoscale* 2010; 2: 343–62.
7. Lin CAJ, Lee CH, Hsieh JT, Wang HH, Li JK, Shen JL, et al. Synthesis of fluorescent metallic nanoclusters toward biomedical application: recent progress and present challenges. *J Med Biol Eng* 2009; 29: 276–83.
8. Shanga L, Dong S, Nienhaus GU. Ultra-small fluorescent metal nanoclusters: synthesis and biological applications. *Nano Today* 2011; 6: 401–18.

9. Diez I, Ras RHA. Fluorescent silver nanoclusters. *Nanoscale* 2011; 3: 1963–70.
10. Jin R, Zhu Y, Qia H. Quantum-sized gold nanoclusters: bridging the gap between organometallics and nanocrystals. *Chem Eur J* 2011; 17: 6584–93.
11. Choi S, Dickson RM, Yu J. Developing luminescent silver nanodots for biological applications. *Chem Soc Rev* 2012 (Advance Article). DOI: 10.1039/C1CS15226B.
12. Laguna A, Modern supramolecular gold chemistry gold–metal interactions and applications. Weinheim: WILEY-VCH Verlag GmbH & Co., KGaA, 2008.
13. Tanaka SI, Miyazaki J, Tiwari DK, Jin T, Inouye Y. Fluorescent platinum nanoclusters: synthesis, purification, characterization, and application to bioimaging. *Angew Chem Int Ed* 2011; 50: 431–5.
14. Wei WT, Lu YZ, Chen W, Chen SW. One-pot synthesis, photoluminescence, and electrocatalytic properties of sub-nanometer-sized copper clusters. *J Am Chem Soc* 2011; 133: 2060.
15. Heiz U, Schneider WD. Size-selected clusters on solid surfaces. *Crit Rev Solid State Mater Sci* 2001; 26: 251–90.
16. Heiz U, Landman U. *Nanocatalysis*. Berlin, Heidelberg: Springer; 2007.
17. Silva ND, Ha JM, Solovoyov A, Nigra MM, Ogino I, Yeh SW, et al. Bioinspired approach for controlling accessibility in calix[4]arene-bound metal cluster catalysts. *Nat Chem* 2010; 2: 1062–8.
18. Faraday M. Experimental relations of gold (and other metals) to light. *Philos Trans R Soc London Ser A* 1857; 147: 145.
19. Wang H, Brandl DW, Nordlander P, Halas NJ. Plasmonic nanostructures: artificial molecules. *Acc Chem Res* 2007; 40: 53–62.
20. Burda C, Chen X, Narayanan R, El-Sayed MA. Chemistry and properties of nanocrystals of different shapes. *Chem Rev* 2005; 105: 1025102.
21. Sajanlal PR, Sreepasad TS, Samal AK, Pradeep T. Anisotropic nanomaterials: structure, growth, assembly, and functions. *Nano Reviews* 2011; 2: 5883. DOI: 10.3402/nano.v2i0.5883.
22. Bartlett PA, Bauer B, Singer S. Synthesis of water-soluble undecagold cluster compounds of potential importance in electron microscopic and other studies of biological systems. *J Am Chem Soc* 1978; 100: 5085–9.
23. Briant CE, Theobald BRC, White JW, Bell LK, Mingos DMP, Welch AJ. Synthesis and X-ray structural characterization of the centred icosahedral gold cluster compound $[\text{Au}_{13}(\text{PMe}_2\text{Ph})_{10}\text{C}_{12}(\text{PF}_6)_3]$; the realization of a theoretical prediction. *J Chem Soc Chem Commun* 1981, 201–2.
24. Schmid G, Boese R, Pfeil B, Bandermann F, Meyer S, Calis GHM, et al. $\text{Au}_{55}[\text{P}(\text{C}_6\text{H}_5)_3]_{12}\text{Cl}_6$ – a gold cluster of an exceptional size. *Chem Ber* 1981; 114: 3634–42.
25. Brust M, Walker M, Bethell D, Schiffrin DJ, Whyman R. Synthesis of thiol-derivatised gold nanoparticles in a two-phase liquid-liquid system. *J Chem Soc Chem Commun* 1994; 7: 801–2.
26. Harkness KM, Cliffl DE, McLean JA. Characterization of thiolate-protected gold nanoparticles by mass spectrometry. *Analyst* 2010; 135: 868–74.
27. Ingram RS, Hostetler MJ, Murray RW, Schaaff TG, Khoury JT, Whetten RL, et al. 28 kDa alkanethiolate-protected Au clusters give analogous solution electrochemistry and STM coulomb staircases. *J Am Chem Soc* 1997; 119: 9279–80.
28. Huang T, Murray RW. Visible luminescence of water-soluble monolayer-protected gold clusters. *J Phys Chem B* 2001; 105: 12498–502.
29. Negishi Y, Nobusada K, Tsukuda T. Glutathione-protected gold clusters revisited: bridging the gap between gold (I) thiolate complexes and thiolate-protected gold nanocrystals. *J Am Chem Soc* 2005; 127: 5261–70.
30. Mamin JH, Guethner PH, Rugar D. Atomic emission from a gold scanning-tunneling-microscope tip. *Phys Rev Lett* 1990; 65: 2418–21.
31. Hu X, Blankenhagen PV. Nano-scale metal cluster deposition using STM. *Appl Phys A* 1999; 68: 137–44.
32. Lide DH, CRC hand book of chemistry and physics, editor. eighty fifth ed. Boca Raton: CRC Press, 2005.
33. Ozin GA, Huber H. Cryophotocustering techniques for synthesizing very small, naked silver clusters Ag_n of known size (where $n = 2-5$). The molecular metal cluster-bulk metal particle interface. *Inorg Chem* 1978; 17: 155–63.
34. Konig L, Rabin I, Schulze W, Ertl G. Chemiluminescence in the agglomeration of metal clusters. *Science* 1996; 274: 1353–4.
35. Templeton AC, Wuelfing WP, Murray RW. Monolayer-protected cluster molecules. *Acc Chem Res* 2000; 33: 27–36.
36. Chen SH, Kimura K. Water soluble silver nanoparticles functionalized with thiolate. *Chem Lett* 1999; 28: 1169–70.
37. Chen SH, Kimura K. Synthesis and characterization of carboxylate-modified gold nanoparticle powders dispersible in water. *Langmuir* 1999; 15: 1075–82.
38. Nishida N, Yao H, Ueda T, Sasaki A, Kimura K. Synthesis and chiroptical study of d/l-Penicillamine-capped silver nanoclusters. *Chem Mater* 2007; 19: 2831–41.
39. Cathcart N, Kitaev V. Silver nanoclusters: single-stage scalable synthesis of monodisperse species and their chiroptical properties. *J Phys Chem C* 2010; 114: 16010–7.
40. Rao TUB, Pradeep T. Luminescent Ag_7 and Ag_8 clusters by interfacial synthesis. *Angew Chem Int Ed* 2010; 49: 3925–9.
41. Udhayabhaskararao T, Sun Y, Goswami N, Pal SK, Balasubramanian K, Pradeep T. Ag_7Au_6 : a 13 atom alloy quantum cluster. *Angew Chem Int Ed* (2011) (In Press).
42. Petty JT, Zheng J, Hud NV, Dickson RM. DNA-templated Ag nanocluster formation. *J Am Chem Soc* 2004; 126: 5207–12.
43. Zheng J, Petty JT, Dickson RM. High quantum yield blue emission from water-soluble Au_8 nanodots. *J Am Chem Soc* 2003; 125: 7780–1.
44. Muhammed MAH, Ramesh S, Sinha SS, Pal SK, Pradeep T. Two distinct fluorescent quantum clusters of gold starting from metallic nanoparticles by pH-dependent ligand etching. *Nano Res* 2008; 1: 333–40.
45. Muhammed MAH, Shaw AK, Pal SK, Pradeep T. Quantum clusters of gold exhibiting FRET. *J Phys Chem C* 2008; 112: 14324–30.
46. Shibu ES, Muhammed MAH, Tsukuda T, Pradeep T. Ligand exchange of $\text{Au}_{25}\text{SG}_{18}$ leading to functionalized gold clusters: spectroscopy, kinetics and luminescence. *J Phys Chem C* 2008; 112: 12168–76.
47. Shibu ES, Pradeep T. Quantum clusters in cavities: trapped Au_{15} in cyclodextrins. *Chem Mater* 2011; 23: 989–99.
48. Mrudula KV, Rao TUB, Pradeep T. Interfacial synthesis of luminescent 7 kDa silver clusters. *J Mater Chem* 2009; 19: 4335–42.
49. Rao TUB, Nataraju B, Pradeep T. Ag_9 quantum cluster through a solid state route. *J Am Chem Soc* 2010; 132: 16304–7.
50. Sun T, Seff K. Silver clusters and chemistry in zeolites. *Chem Rev* 1994; 94: 857–70.
51. Dhanalakshmi L, Udayabhaskararao T, Pradeep T. Conversion of double layer charge-stabilized $\text{Ag}@$ citrate colloids to thiol passivated luminescent quantum clusters. *Chem Commun* 2012; 48: 859–61. DOI: 10.1039/C1CC15604G.

52. Maity P, Tsunoyama H, Yamauchi M, Xie S, Tsukuda T. Organogold clusters protected by phenylacetylene. *J Am Chem Soc* 2011; 133(50): 20123–5. DOI: 10.1021/ja209236n.
53. Jadzinsky PD, Calero G, Ackerson CJ, Bushnell DA, Kornberg RD. Structure of a thiol monolayer-protected gold nanoparticle at 1.1 Å resolution. *Science* 2007; 318: 430–3.
54. Heaven MW, Dass A, White PS, Holt KM, Murray RW. Crystal structure of the gold nanoparticle $[N(C_8H_{17})_4][Au_{25}(SCH_2CH_2Ph)_{18}]$. *J Am Chem Soc* 2008; 130: 3754–5.
55. Zhu M, Aikens CM, Hollander FJ, Schatz GC, Jin R. Correlating the crystal structure of a thiol-protected Au_{25} cluster and optical properties. *J Am Chem Soc* 2008; 130: 5883–5.
56. Pundlik SS, Kalyanaraman K, Waghmare UV. First-principles investigation of the atomic and electronic structure and magnetic moments in gold nanoclusters. *J Phys Chem C* 2011; 115: 3809–20.
57. Osawa M, Hoshino M, Akita M, Wada T. Synthesis and characterization of phenanthrylphosphine gold complex: observation of Au-induced blue-green phosphorescence at room temperature. *Inorg Chem* 2005; 44: 1157–9.
58. Shibu ES, Radar B, Vera PK, Harappa P, Kulkarni GU, Pal SK, et al. Functionalized Au_{22} clusters: Synthesis, characterization and patterning. *ACS App Mater Interfaces* 2009; 1: 2199–210.
59. Walter M, Akola J, Acevedo OL, Jadzinsky PD, Calero G, Ackerson CJ, et al. A unified view of ligand-protected gold clusters as superatom complexes. *Proc Natl Acad Sci* 2008; 105: 9157–62.
60. Xie J, Zheng Y, Ying JY. Protein-directed synthesis of highly fluorescent gold nanoclusters. *J Am Chem Soc* 2009; 131: 888–9.
61. Dickerson MB, Sandhage KH, Naik RR. Protein- and peptide-directed syntheses of inorganic materials. *Chem Rev* 2008; 108: 4935–78.
62. Reith F, Rogers SL, McPhail DC, Webb D. Biomineralization of gold: biofilms on bacterioform gold. *Science* 2006; 313: 233–6.
63. Heinz H, Farmer BL, Pandey RB, Slocik JM, Patnaik SS, Pachter R, et al. Nature of molecular interactions of peptides with gold, palladium, and Pd-Au bimetal surfaces in aqueous solution. *J Am Chem Soc* 2009; 131: 9704.
64. Slocik JM, Naik RR. Probing peptide–nanomaterial interactions. *Chem Soc Rev* 2010; 39: 3454–63.
65. Wei H, Wang Z, Zhang J, House S, Gao YG, Yang L, et al. Time-dependent, protein-directed growth of gold nanoparticles within a single crystal of lysozyme. *Nat Nanotechnol* 2011; 6: 93–7.
66. Panzner MJ, Bilinovich SM, Youngs WJ, Leeper TC. Silver metallation of hen egg white lysozyme: X-ray crystal structure and NMR studies. *Chem Commun* 2011; 47: 12479–81.
67. Narayanan SS, Pal SK. Structural and functional characterization of luminescent silver-protein nanobioconjugates. *J Phys Chem C* 2008; 112: 4874–9.
68. Yu J, Choi S, Dickson RM. Shuttle-based fluorogenic silver cluster biolabels. *Angew Chem Int Ed Engl* 2009; 48: 318–20.
69. Yu J, Patel SA, Dickson RM. In-vitro and intracellular production of peptide-encapsulated fluorescent silver nanoclusters. *Angew Chem Int Ed Engl* 2007; 46: 2028–30.
70. Retnakumari A, Setua S, Menon D, Ravindran P, Muhammed H, Pradeep T, et al. Molecular receptor specific, non-toxic, near-infrared emitting Au cluster-protein nanoconjugates for targeted cancer imaging. *Nanotechnology* 2010; 21: 055103.
71. Muhammed MAH, Verma PK, Pal SK, Retnakumari A, Koyakutty M, Nair S, et al. Luminescent quantum clusters of gold in bulk by albumin-induced core etching of nanoparticles: metal ion sensing, metal enhanced luminescence and biolabeling. *Chem Eur J* 2010; 16: 10103–12.
72. Wei H, Wang Z, Yang L, Tian S, Hou C, Lu Y. Lysozyme-stabilized gold fluorescent cluster: synthesis and application as Hg^{2+} sensor. *Analyst* 2010; 135: 1406–10.
73. Xavier PL, Chaudhari K, Verma PK, Pal SK, Pradeep T. Luminescent quantum clusters of gold in transferrin family protein, lactoferrin exhibiting FRET. *Nanoscale* 2010; 2: 2769–76.
74. Guével XL, Daum N, Schneider M. Synthesis and characterization of human transferrin-stabilized gold nanoclusters. *Nanotechnology* 2011; 22: 275103.
75. Shao C, Yuan B, Wang H, Zhou Q, Li Y, Guan Y, et al. Eggshell membrane as a multimodal solid state platform for generating fluorescent metal nanoclusters. *J Mater Chem* 2011; 21: 2863–6.
76. Guével XL, Hötzer B, Jung G, Schneider M. NIR-emitting fluorescent gold nanoclusters doped in silica nanoparticles. *J Mater Chem* 2011; 21: 2974–81.
77. Yan L, Cai Y, Zheng B, Yuan H, Guo Y, Xiao D, et al. Microwave-assisted synthesis of BSA-stabilized and HSA-protected gold nanoclusters with red emission. *J Mater Chem*. DOI: 10.1039/C1JM13457D(Advance Article 2012).
78. Liu H, Zhang X, Wu X, Jiang L, Burda C, Zhu JJ. Rapid sonochemical synthesis of highly luminescent non-toxic AuNCs and Au@AgNCs and Cu (II) sensing. *Chem Commun* 2011; 47: 4237–9.
79. Choi S, Dickson RM, Lee JK, Yu J. Generation of luminescent noble metal nanodots in cell matrices. *Photochem Photobiol Sci* 2011; DOI: 10.1039/C1PP05276D.
80. Mathew A, Sajanlal PR, Pradeep T. A fifteen atom silver cluster confined in bovine serum albumin. *J Mater Chem* 2011; 21: 11205–12.
81. Yuan X, Luo Z, Zhang Q, Zhang X, Zheng Y, Lee JY, et al. Synthesis of highly fluorescent metal (Ag, Au, Pt, and Cu) nanoclusters by electrostatically induced reversible phase transfer. *ACS Nano* 2011; 5(11): 8800–8. DOI: 10.1021/nn202860s.
82. Cui Y, Wang Y, Liu R, Sun Z, Wei Y, Zhao Y, et al. Serial silver clusters bio-mineralized by one peptide. *ACS Nano* 2011; 5(11): 8684–9. DOI: 10.1021/nn202566n.
83. Wang Y, Cui Y, Zhao Y, Liu R, Sun Z, Li W. Bifunctional peptides that precisely biomineralize Au clusters and specifically stain cell nuclei. *Chem Commun* 2012; 48: 871–3. DOI: 10.1039/C1CC15926G.
84. Guével XL, Hötzer B, Jung G, Hollemeyer K, Trouillet V, Schneider M. Formation of fluorescent metal (Au, Ag) nanoclusters capped in bovine serum albumin followed by fluorescence and spectroscopy. *J Phys Chem C* 2011; 115: 10955–63.
85. Kawasaki H, Hamaguchi K, Osaka I, Arakawa R. pH-dependent synthesis of pepsin-mediated gold nanoclusters with blue green and red fluorescent emission. *Adv Func Mater* 2011; 21: 3508–15.
86. Wu Z, Jin R. On the ligand's role in the fluorescence of gold nanoclusters. *Nano Lett* 2010; 10: 2568–73.
87. Wang D, Imae T. Fluorescence emission from dendrimers and its pH dependence. *J Am Chem Soc* 2004; 126: 13204–5.
88. Lee WI, Bae Y, Bard AJ. Strong blue photoluminescence and ECL from OH-terminated PAMAM dendrimers in the absence of gold. *J Am Chem Soc* 2004; 126: 8358–9.
89. Si S, Mandal TK. Tryptophan-based peptides to synthesize gold and silver nanoparticles: a mechanistic and kinetic study. *Chem Eur J* 2007; 13: 3160–8.

90. Goswami N, Makhil A, Pal SK. Toward an alternative intrinsic probe for spectroscopic characterization of a protein. *J Phys Chem B* 2010; 114: 15236–43.
91. Pradeep T, et al., MALDI MS of lysozyme-Au clusters, formation of protein's tryptophan metabolite during cluster growth, ovalbumin and papain stabilized gold clusters.
92. Simms GA, Padmos JD, Zhang P. Structural and electronic properties of protein/thiolate-protected gold nanocluster with 'staple' motif: a XAS, L-DOS, and XPS study. *J Chem Phys* 2009; 131: 214703.
93. Liu CL, Wu HT, Hsiao YH, Lai CW, Shih CW, Peng YK, et al. Insulin-directed synthesis of fluorescent gold nanoclusters: preservation of insulin bioactivity and versatility in cell imaging. *Angew Chem Int Ed* 2011; 50: 7056–60.
94. Chaudhari K, Xavier PL, Pradeep T. Understanding the evolution of luminescent gold quantum clusters in protein templates. *ACS Nano* 2011; 5(11): 8816–27. DOI: 10.1021/nn202901a.
95. Li HW, Ai K, Wu Y. Fluorescence visual gel-separation of dansylated BSA-protected gold-nanoclusters. *Chem Commun* 2011; 47: 9852–4.
96. Yang X, Shi M, Zhou R, Chen X, Chen H. Blending of HAuCl₄ and histidine in aqueous solution: a simple approach to the Au₁₀ cluster. *Nanoscale* 2011; 3: 2596–601.
97. Adhikari B, Banerjee A. Short-peptide-based hydrogel: a template for the in situ synthesis of fluorescent silver nanoclusters by using sunlight. *Chem Eur J* 2010; 16: 13698–705.
98. Roy S, Banerjee A. Amino acid based smart hydrogel: formation, characterization and fluorescence properties of silver nanoclusters within the hydrogel matrix. *Soft Matter* 2011; 7: 5300–8.
99. Fabris L, Antonello S, Armelao L, Donkers RL, Polo F, Toniolo C, et al. Gold nanoclusters protected by conformationally constrained peptides. *J Am Chem Soc* 2006; 128: 326–36.
100. Bellina B, Compagnon I, Bertorelle F, Broyer M, Antoine R, Dugourd P. Structural and optical properties of isolated noble metal-glutathione complexes. Insight into the chemistry of liganded nanoclusters. *J Phys Chem C* 2011; 115, 24549–54. DOI: 10.1021/jp207158v.
101. Xie J, Zheng Y, Ying JY. Highly selective and ultrasensitive detection of Hg²⁺ based on fluorescence quenching of Au nanoclusters by Hg²⁺-Au⁺ interactions. *Chem Commun* 2010; 46: 961–3.
102. Lin YH, Tseng WL. Ultrasensitive sensing of Hg²⁺ and CH₃Hg⁺ based on the fluorescence quenching of lysozyme type VI-stabilized gold nanoclusters. *Anal Chem* 2010; 82: 9194–200.
103. Hu D, Sheng Z, Gong P, Zhang P, Cai L. Highly selective fluorescent sensors for Hg²⁺ based on bovine serum albumin-capped gold nanoclusters. *Analyst* 2010; 135: 1411–6.
104. Chai F, Wang T, Li L, Liu H, Zhang L, Su Z, et al. Fluorescent Gold Nanoprobes for the sensitive and selective detection for Hg²⁺. *Nanoscale Res Lett* 2010; 5: 1856–60.
105. Kawasaki H, Yoshimura K, Hamaguchi K, Arakawa R. Trypsin-stabilized fluorescent gold nanocluster for sensitive and selective Hg²⁺ detection. *Analytical Sciences* 2011; 27: 591.
106. Wen F, Dong Y, Feng L, Wang S, Zhang S, Zhang X. Horseradish peroxidase functionalized fluorescent gold nanoclusters for hydrogen peroxide sensing. *Anal Chem* 2011; 83: 1193–6.
107. Wang X, Wuc P, Lv Y, Hou X. Ultrasensitive fluorescence detection of glutaraldehyde in water samples with bovine serum albumin-Au nanoclusters. *Microchemical Journal* 2011; 99: 327–31.
108. Liu Y, Ai K, Cheng X, Huo L, Lu L. Gold-nanocluster-based fluorescent sensors for highly sensitive and selective detection of cyanide in water. *Adv Fun Mat* 2010; 20: 951–6.
109. Guo C, Irudayaraj J. Fluorescent Ag clusters via a protein-directed approach as a Hg(II) ion sensor. *Anal Chem* 2011; 83: 2883–9.
110. Goswami N, Giri A, Bootharaju MS, Xavier PL, Pradeep T, Pal SK. Copper quantum clusters in protein matrix: potential sensor of Pb²⁺ ion. *Anal Chem* 2011; 83(24): 9676–80. DOI:10.1021/ac202610e.
111. Li L, Liu H, Shen Y, Zhang J, Zhu JJ. Electrogenerated chemiluminescence of Au nanoclusters for the detection of dopamine. *Anal Chem* 2011; 8: 661–5.
112. Fang YM, Song J, Li J, Wang YW, Yang HH, Sun JJ, et al. Electrogenerated chemiluminescence from Au nanoclusters. *Chem Commun* 2011; 47: 2369–71.
113. Chen Y, Shen Y, Sun D, Zhang H, Tian D, Zhang J. Fabrication of a dispersible graphene/gold nanoclusters hybrid and its potential application in electrogenerated chemiluminescence. *Chem Commun* 2011; 47: 11733–5.
114. Hun X, Chen H, Wang W. Design of ultrasensitive chemiluminescence detection of lysozyme in cancer cells based on nicking endonuclease signal amplification technology. *Biosensors and Bioelectronics* 2010; 26: 248–54.
115. Sreepasad TS, Maliyekkal SM, Krishnan D, Chaudhari K, Xavier PL, Pradeep T. Transparent, luminescent, antibacterial and patternable film forming composites of graphene oxide/reduced graphene oxide. *ACS Appl Mater Interfaces* 2011; 3: 2643–54.
116. Chen WY, Lin JY, Chen WJ, Luo L, Diau EWG, Chen YC. Gold nanoclusters as antimicrobial agents for antibiotic-resistant bacteria. *Nanomedicine* 2010; 5: 755–64.
117. Retnakumari A, Jayasimhan J, Chandran P, Menon D, Nair S, Mony U, et al. CD33 monoclonal antibody conjugated Au cluster nano-bioprobes for targeted flow-cytometric detection of acute myeloid leukaemia. *Nanotechnology* 2011; 22: 285102.
118. Wang Y, Chen J, Irudayaraj J. Nuclear targeting dynamics of gold nanoclusters for enhanced therapy of HER2+ breast cancer. *ACS Nano* 2011; 5(12): 9718–25. DOI: 10.1021/nn2032177.
119. Durgadas CV, Sharma CP, Sreenivasan K. Fluorescent gold clusters as nanosensors for copper ions in live cells. *Analyst* 2011; 136: 933–40.
120. Durgadas CV, Sharma CP, Sreenivasan K. Fluorescent and superparamagnetic hybrid quantum clusters for magnetic separation and imaging of cancer cells from blood. *Nanoscale* 2011; 3(11): 4780–7. DOI: 10.1039/C1NR10900F.
121. Wu X, He X, Wang K, Xie C, Zhou B, Qing Z. Ultrasmall near-infrared gold nanoclusters for tumor fluorescence imaging in vivo. *Nanoscale* 2010; 2: 2244–9.
122. Sun C, Yang H, Yuan Y, Tian X, Wang L, Guo Y, et al. Controlling assembly of paired gold clusters within apoferritin nanoreactor for in vivo kidney targeting and biomedical imaging. *J Am Chem Soc* 2011; 133: 8617–24.
123. Zhou W, Baneyx F. Aqueous, protein-driven synthesis of transition metal-doped ZnS immuno-quantum dots. *ACS Nano* 2011; 5: 8013–8.
124. Shankar SS, Rai A, Ankamwar B, Singh A, Ahmad A, Sastri M. Biological synthesis of triangular gold nanoprisms. *Nat Mater* 2004; 3: 482–8.
125. Nair B, Pradeep T. Coalescence of nanoclusters and the formation of sub-micron crystallites assisted by *Lactobacillus* strains. *Cryst Growth Des* 2002; 2: 293–8.

126. Xie J, Tan YN, Lee JY. Biological and biomimetic synthesis of metal nanomaterials. In: Challa Kumar, ed., Bio-mimetic and bio-inspired nanomaterials for life sciences, nanomaterials for life sciences, vol 7. Weinheim: Wiley-VCH Verlag, GmbH & Co, KGaA; 2010, 251–81.
127. Perriman AW, Ifen HC, Hughes RW, Barrie CL, Mann S. Solvent-free protein liquids and liquid crystals. *Angew Chem Int Ed* 2009; 48: 6242–6.
128. Jones R. What can biology teach us? *Nat Nanotech* 2009; 1: 85–6.

***Thalappil Pradeep**

DST Unit of Nanoscience (DST UNS)
Department of Chemistry
Indian Institute of Technology Madras
Chennai 600 036, India
Fax: +91-44 2257-0545
Email: pradeep@iitm.ac.in

Luminescent, Freestanding Composite Films of Au₁₅ for Specific Metal Ion Sensing

Anu George,[†] E. S. Shibu,[†] Shihabudheen M. Maliyekkal,^{†,‡} M. S. Bootharaju,[†] and T. Pradeep^{*,†}

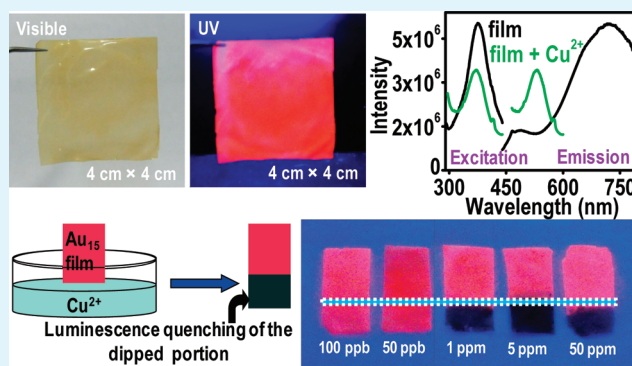
[†]DST Unit of Nanoscience (DST UNS), Department of Chemistry, Indian Institute of Technology, Madras, Chennai 600 036, India

[‡]School of Mechanical and Building Sciences, VIT University, Chennai Campus, Chennai-600 048, India

Supporting Information

ABSTRACT: A highly luminescent freestanding film composed of the quantum cluster, Au₁₅, was prepared. We studied the utility of the material for specific metal ion detection. The sensitivity of the red emission of the cluster in the composite to Cu²⁺ has been used to make a freestanding metal ion sensor, similar to pH paper. The luminescence of the film was stable when exposed to several other metal ions such as Hg²⁺, As³⁺, and As⁵⁺. The composite film exhibited visual sensitivity to Cu²⁺ up to 1 ppm, which is below the permissible limit (1.3 ppm) in drinking water set by the U.S. environmental protection agency (EPA). The specificity of the film for Cu²⁺ sensing may be due to the reduction of Cu²⁺ to Cu¹⁺/Cu⁰ by the glutathione ligand or the Au₁₅ core. Extended stability of the luminescence of the film makes it useful for practical applications.

KEYWORDS: Au₁₅ quantum cluster, luminescent films, composite, chitosan, specific metal ion sensing



INTRODUCTION

Quantum clusters of noble metals are a new category of materials with unusually intense luminescence.¹ Low cytotoxicity, excellent photostability and high quantum yield have made these materials excellent biolabels.² Sensitivity of their absorption and luminescence to parameters such as exposed metal ions,^{3–5} solvent polarity and hydrogen bonding² has been explored in the recent past. Because of the strong quantum size effect, they possess characteristic absorption and emission profiles due to intraband and interband transitions and can be distinguished from the adjacent clusters easily from these features. Metal-enhanced luminescence of such clusters has also been explored.⁶ A variety of applications in catalysis,^{7,8} electroluminescence,⁹ nanoelectronics,¹⁰ soft lithography,¹¹ bioanalysis,^{6,12} etc., are also current excitements in their research.

There are several reports in the recent past on the utilization of gold and silver quantum clusters for Hg²⁺ sensing.^{13–16} Metal ion reactivity with luminescent noble metal clusters was pioneered by our group³ and it has been shown that several Au clusters, especially Au₂₃² and Au₂₂¹¹ are especially selective. No sensitivity was seen for Ag⁺, Ni²⁺, Ca²⁺, Mg²⁺, Na⁺, Pb²⁺, Hg²⁺, and Cd²⁺ in these clusters.² Cu²⁺ is known to be toxic and its allowed level in drinking water is 1.3 ppm, set by the U.S. Environmental Protection Agency (EPA).¹⁷ Creating composite structures using quantum clusters can be directly adapted for applications.¹⁸ These materials are endowed with many important properties such as nonlinear optical properties,^{19,20}

electronic conductivity²¹ and luminescence,²² and have been suggested for use in various applications including chemical sensors,²³ electroluminescent devices, electrocatalysis,²⁴ etc.

Although these applications are important, it is necessary to demonstrate the usability of such materials in the device format. For this, it is important to have the materials fabricated in various forms such as films. A free-standing film of a composite may be used for direct applications for metal ions in solution phase, similar to a pH paper. We note that several such nanoscale materials have been prepared in the form of composites for applications of this kind.^{25,26} However, no quantum cluster has been developed hitherto in this format adaptable for applications.

One of the newest quantum clusters is Au₁₅ encapsulated in cyclodextrin (CD) cavities.²⁷ While larger clusters are etched by ligands to yield smaller clusters,²⁸ the product formed is trapped in host cavities to prevent it from further core reduction. Encapsulation allows increased chemical and thermal stability for the cluster. In the present method, Au₁₅ cluster protected with glutathione was further stabilized in cyclodextrin cavities. Encapsulation is manifested in 2-dimensional nuclear magnetic resonance (2D NMR) spectroscopy in the form of cross peaks between the protecting glutathione and the encapsulating CD molecules. The size of gold QCs is small

Received: July 2, 2011

Accepted: January 2, 2012

Published: January 2, 2012

to accommodate the cluster inside the CD cavity. The large size of gold nanoparticles limits their incorporation inside the CD cavity. In this work, we present the use of Au₁₅ cluster composites for metal ion sensing. A freestanding film of the cluster is shown to be a Cu²⁺ sensor at parts per million concentrations. The luminescence of the film was found to be quenched by Cu²⁺. Visually detectable changes of the film enable the use of these materials as a Cu²⁺ sensing paper. The extended stable luminescence of the film finds utility in practical applications. Although metal ion sensing in the solution state is known with quantum clusters, specificity to a metal and application as a practical device are demonstrated for the first time.

EXPERIMENTAL SECTION

Materials. All the chemicals were commercially available and used without further purification. HAuCl₄·3H₂O, methanol (GR grade), reduced GSH (γ -Glu-Cys-Gly, M.W. = 307), CuCl₂·2H₂O, Cu(OAc)₂·H₂O, Cu₂Cl₂·2H₂O, and CuSO₄·5H₂O were purchased from SRL Chemical Co. Ltd., India. NaBH₄ (>90%) was purchased from Sigma Aldrich. β -cyclodextrin (CD) was purchased from Wako Chemicals, Japan. Chitosan was procured from Pelican Biotech & Chemical Laboratories, India.

Synthesis of Au@SG. The nanoparticles protected with -SG ligands (Au@SG) were synthesized using the reported protocol.²⁷ To a 50 mL methanolic solution (0.5 mM) of HAuCl₄·3H₂O, 1.0 mM GSH was added (1:2 molar ratio, total volume of methanol was 50 mL). The mixture was cooled to 0 °C in an ice bath for 30 min. An aqueous solution of NaBH₄ (0.2 M, 12.5 mL), cooled to 0 °C, was injected rapidly into the above mixture under vigorous stirring. The mixture was allowed to react for another hour. The resulting precipitate was collected and washed repeatedly with methanol through centrifugal precipitation. Finally the Au@SG precipitate was dried and collected as a dark brown powder. The size of Au@SG particles made here is in the range of 2–3 nm.

Cyclodextrin-Assisted Synthesis of Au₁₅ Clusters. The above nanoparticles (50 mg) were dissolved in 40 mL of deionized (DI) water containing 1.6 mol of GSH and 2.2×10^{-4} mol of cyclodextrin. In this synthesis, GSH is used in excess as it works as an etchant. The mixture was heated at 70 °C for 48 h. The completion of the reaction was monitored by checking the red emission of the cluster under UV light. The entire solution was centrifuged at 5000 rpm for 10 min. The supernatant was transferred to a plastic vial and solution was freeze-dried to obtain a brown powder with intense red emission in the solid state. The material was washed twice with ethanol to remove excess GSH.

Preparation of Cluster Composite Film. Two grams of chitosan is dissolved with stirring in 50 mL of distilled water containing 5% glacial acetic acid. Insoluble substances are removed by filtration through a medium-pore-sized glass funnel to yield chitosan solution. Twenty milliliters of chitosan solution is poured onto plastic petri dish and dried at 40 °C for 24 h. The film so obtained is soaked in 20 mL solution of 5% trisodium citrate to enhance the strength and was washed thoroughly and dried. A free-standing film of Au₁₅ incorporated chitosan was prepared by soaking the film in Au₁₅ cluster solution for 10 min and dried. Uptake of Au₁₅ was manifested in the form of bright luminescence of the film upon UV irradiation.

Methods. Ultraviolet–visible (UV–vis) spectra were recorded using a PerkinElmer Lambda 25 spectrophotometer. The photoexcitation and luminescence (PL) studies were done using a NanoLog HORIBA JOBINYVON spectrofluorimeter. Band pass for both excitation and emission monochromators was kept at 3 nm. Scanning electron microscopic (SEM) images and energy-dispersive analysis of X-rays (EDAX) studies were obtained using a FEI QUANTA-200 SEM. Attenuated total reflection infrared spectroscopy (ATR–IR) was measured using PerkinElmer Spectrum 100 Spectrometer. Chlorides (Cu²⁺, Cu¹⁺, and Hg²⁺), sulfates, acetates (Cu²⁺), arsenates, and arsenites (Na⁺) were used for metal ion detection studies. Metal ion

detection was studied at ppm concentrations. X-ray photoelectron spectroscopy measurements were conducted using an Omicron ESCA Probe spectrometer with unmonochromatized Al K α X-rays (energy = 1486.6 eV).

RESULTS AND DISCUSSION

Au₁₅ shows a well-defined optical absorption spectrum in aqueous solution with features at 318, 458, and 580 nm, all of which are marked in Figure 1. The absorption features of

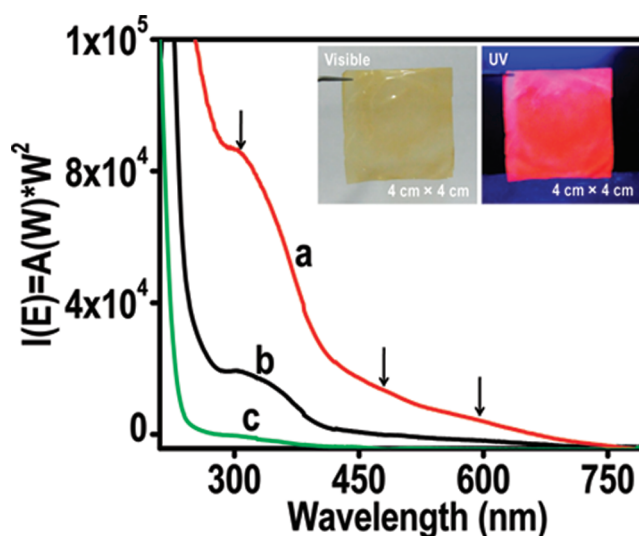


Figure 1. Time-dependent UV/vis spectra of Au₁₅ cluster solution in which the parent film was soaked. Traces a, b, and c correspond to 2, 6, and 10 min of exposure, respectively. Inset shows the photographs of the cluster incorporated film under white light and UV light.

Au₁₅@CD are not sharp, unlike in the case of QCs such as Au₂₅,²⁹ Au₂₂,¹¹ and Au₂₃.² Optical luminescence, solvent dependency, metal ion sensing, gelation are some of the reported properties of Au₁₅.²⁷ Upon exposing a freestanding film of chitosan to the Au₁₅ solution, the cluster gets loaded onto the film. The spectra of the solution after various intervals of exposure of the chitosan film are shown in Figure 1. The decrease in the intensity of the peaks shows that the cluster is getting loaded onto the film. The film after loading the cluster shows luminescence as shown in the inset of Figure 1. A time-dependent color change of the Au₁₅ solution is observed during loading. Initially the solution shows high luminescence on UV irradiation, which gradually disappears with respect to time.

A saturation uptake of the cluster was observed after ten minutes of exposure as shown in Figure 2. From the decrease in intensity of optical absorption of Au₁₅, a maximum uptake of 0.06×10^{-4} mol per sq. cm can be inferred. Beyond this, no further uptake happens as shown by the inset of Figure 2. Uptake of Au₁₅ is manifested in the form of bright luminescence of film upon UV irradiation (inset of Figure 1).

The morphology of the film was studied using SEM. A higher-magnification image of an edge of the composite film is shown in Figure 3. To study the spatial distribution of gold and sulfur in the film formed by QCs, we carried out elemental mapping using EDAX. Figure 3A shows the EDAX spectrum collected from the film. Elemental maps are given as inset a₁ and a₂ in Figure 3A. The data confirm the uniform presence of the cluster in the composite. Luminescence of the parent chitosan film appears at 500 nm, far away from the cluster emission (in the Supporting Information, discussed later). The

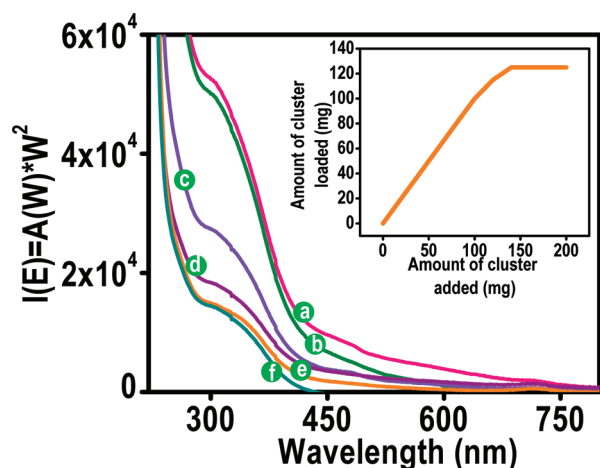


Figure 2. Time-dependent UV/vis spectra of Au₁₅ cluster solution at the saturation point. Traces a–f correspond to 0, 2, 4, 6, 8, and 10 min of exposure, respectively. Inset shows the saturation uptake of the cluster after 10 min of soaking.

photoluminescence spectrum of the Au₁₅ cluster (in solution form) used in the study is given in the Supporting Information (Figure S1). The luminescence spectrum of the composite film is shown in Figure 3. The spectrum is comparable to that of Au₁₅ in the solution phase, which shows a similar bright red luminescence on UV irradiation. Au₁₅ shows a NIR emission with a maximum of 690 nm for excitation at 375 nm. PL spectra of these quantum clusters show a large Stokes shift. Possible reason for this could be the energy cascade within the sp derived excited states, facilitated by the concomitant energy

relaxation through structural distortion and low energy excitation of the ligands. The composite film, when excited around 375 nm, shows an emission around 700 nm which resembles that of the Au₁₅ solution. This confirms the molecular nature of the cluster in the composite film. Corresponding photographs of Au₁₅ and the composite film under the UV light are shown as the inset of Figure 3B.

Attenuated total reflection infrared spectroscopy (ATR–IR) was employed to investigate the chemical affinity of Au₁₅ to the surface of the film. Figure 4 shows the ATR–IR spectra of the

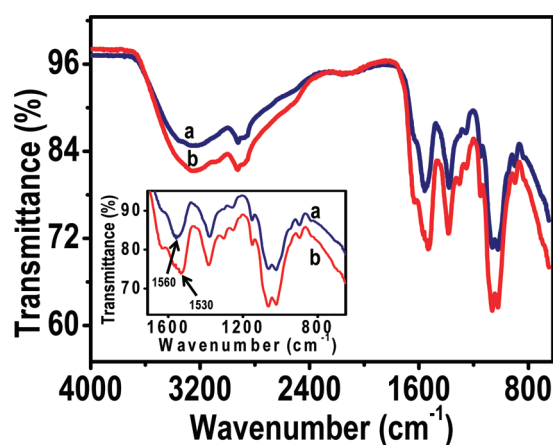


Figure 4. ATR–IR spectra of the parent film (trace a) and composite (trace b). Inset shows an expanded view of the fingerprint region of the composite.

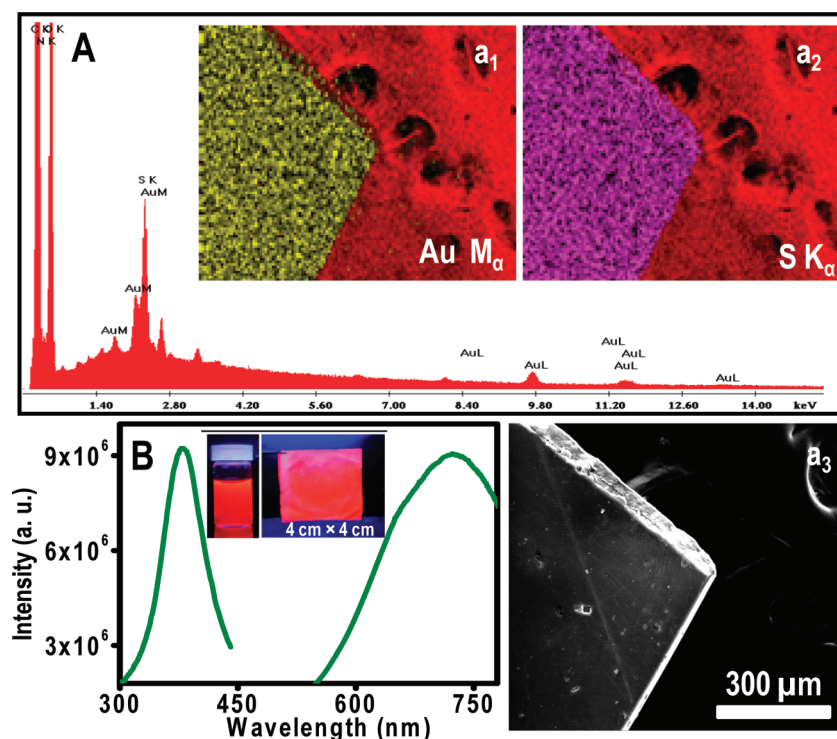


Figure 3. (A) EDAX spectrum of the composite film formed by the quantum cluster. (a₁), (a₂) EDAX mapping of the film using Au M_α and S K_α lines, respectively. The corresponding SEM image in a₃. The uniform red background in a₁ and a₂ is due to the conducting carbon tape on which the composite film was placed. (B) PL spectrum of cluster-chitosan film. Peaks in UV and visible regions correspond to excitation and emission, respectively. Inset of B shows the photographs of aqueous Au₁₅ solution and the film under the UV light.

parent chitosan film (trace a) and the composite (trace b). The characteristic absorption bands of chitosan are the bands at 1560 cm^{-1} , due to the stretching vibration of the amino group, and that at 1334 cm^{-1} , assigned to the C–H stretching vibration. Another band around 3336 cm^{-1} is due to the amine N–H symmetric vibration. The peak at 2927 cm^{-1} is the typical C–H stretching vibration. The peaks around 897 and 1154 cm^{-1} correspond to the saccharide structure of chitosan. The broad peak at 1081 cm^{-1} is due to the C–O stretching vibration. A comparison with the chitosan film shows that the band at 1560 cm^{-1} corresponding to the amino group stretching is shifted in the composite (trace b). All the other features are essentially unaltered. Therefore, we suggest that the binding of the Au_{15} to the film occurs due to the interaction of amino group (NH_3^+) on chitosan with COO^- functionalities on the cluster.

The transmittance spectra of the parent chitosan film and the cluster incorporated film were analyzed and shown in Figure 5.

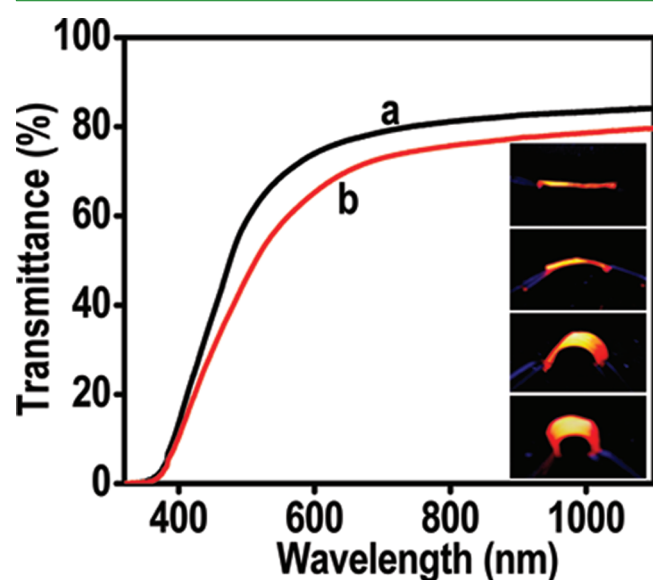


Figure 5. Transmittance of parent chitosan film (trace a) and the composite (trace b) as a function of wavelength ranging from 300 to 1100 nm. Inset shows the photographs of the composite film under UV light upon bending.

A transmittance of 80% is observed in the case of the parent film (trace a). After the loading of the cluster, the transmittance was reduced by 10% (trace b). Appreciable optical transparency to visible and near-infrared light promises its utility in making transparent, luminescent films with applications, ranging from flat panel displays to photovoltaic cells. The film is flexible and the luminescence is retained. Photographs of the film under the UV light at different extent of bending are shown in Figure 5.

The red emission from the cluster was utilized for selective metal ion detection. In the case of parent Au_{15} in solution, we could see a drastic change, such as immediate disappearance of red emission followed by the emergence of yellow emission when exposed to Cu^{2+} , and no effect was observed for several other metal ions tested.²⁷ However, the film incorporated with Au_{15} shows specific sensing for Cu^{2+} by immediate quenching of the luminescence. The detection studies were carried out at ppm concentrations. A drastic change in the emission maximum was seen in the PL spectra of the film before and after exposure of Cu^{2+} (Figure 6A, traces a and b, respectively). The quenching of luminescence in the case of Cu^{2+} is abrupt. This exposure to Cu^{2+} makes an irreversible colored stain on the film. The parent chitosan film shows a decrease in luminescence intensity and a blue shift of 7 nm in peak maximum upon exposure to 5 ppm Cu^{2+} (see Figure S2 in the Supporting Information). The composite film was exposed to several other metal ions as well (Figure 6B). Although there is a decrease in luminescence upon exposure to Hg^{2+} , As^{5+} and As^{3+} (Figure 6B, traces b, c and d, respectively), the luminescence recovers upon drying the film, unlike in the case of Cu^{2+} . A film upon exposure to pure water itself shows a decrease in luminescence, but it recovers upon drying. Thus the decrease obtained with other metal ions is due to the solvent. Traces labeled a in Figures 6A and B are due to the composite film alone.

A prototypical sensor film was fabricated which shows the effectiveness of the material. Figure 6C shows photographs of the films exposed to various concentrations of Cu^{2+} . The concentration of Cu^{2+} was varied from 50 ppb to 50 ppm. The region exposed to Cu^{2+} shows visible color change and the intensity of the color is proportional to Cu^{2+} concentration. The exposed film is stable for an extended period; the parent composite film is also stable for a long time. EDAX analysis showed that the Cu^{2+} exposed film showed uniform

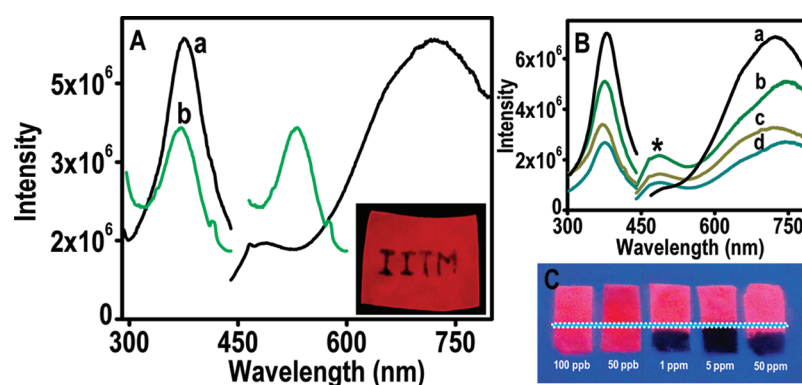


Figure 6. (A) PL spectra of the film before and after exposing to Cu^{2+} (traces a and b, respectively). Inset shows the pattern written on the film using Cu^{2+} in solution. (B) PL spectra of the film exposed to Hg^{2+} , As^{5+} and As^{3+} (traces b, c and d, respectively). Trace a is due to composite film alone. Peaks in UV and visible regions correspond to excitation and emission, respectively (both in A and B). (C) Dependence of Cu^{2+} concentration on luminescence quenching. Peaks marked with an asterisk (*) in B correspond to the emission of chitosan.

concentration of Au, Cu, S and Cl (see Figure S3 in the Supporting Information).

To understand the specificity to Cu^{2+} and also the negligible response to Hg^{2+} , we performed XPS studies. The cluster in the solution phase was treated with metal ions such as Cu^{2+} and Hg^{2+} for 10 min such that their final concentration was 5 ppm. The samples were freeze-dried and washed with methanol in order to remove the possibility of physical adsorption. The precipitate collected on washing was spotted on a molybdenum sample plate and dried in vacuum. The spectra in the required binding energy (BE) range were collected. Figure 7A shows the

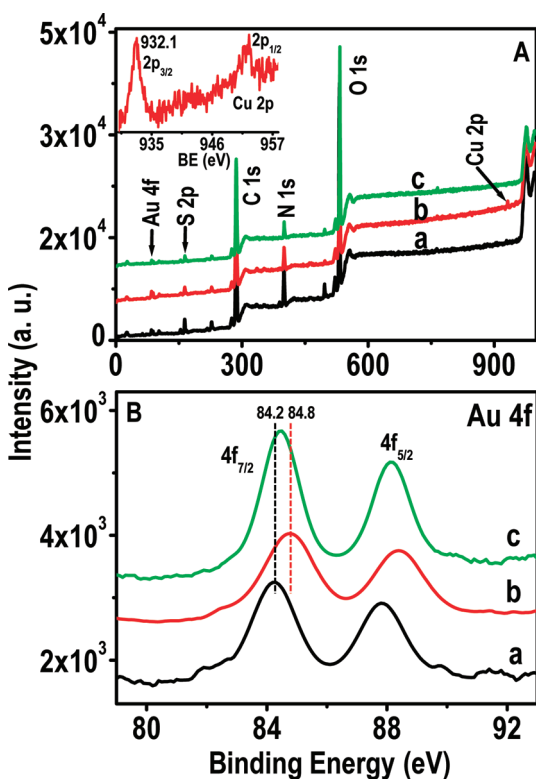


Figure 7. A and B are survey spectra and Au 4f regions, respectively of a) $\text{Au}_{15}@\text{SG-}\beta\text{CD}$, b) $\text{Au}_{15}@\text{SG-}\beta\text{CD}+\text{Cu}^{2+}$ and c) $\text{Au}_{15}@\text{SG-}\beta\text{CD}+\text{Hg}^{2+}$. Inset of A is Cu 2p region of sample b. The dotted lines in B indicate the change in BE. Minor shift in c (0.2 eV) is within the variations seen typically.

XPS survey spectra of $\text{Au}_{15}@\text{SG-}\beta\text{CD}$, $\text{Au}_{15}@\text{SG-}\beta\text{CD}+\text{Cu}^{2+}$ and $\text{Au}_{15}@\text{SG-}\beta\text{CD}+\text{Hg}^{2+}$ (traces a, b and c, respectively) and the detailed spectra are collected at a pass energy of 20 eV for specific regions (7B and inset of 7A). The presence of gold, sulfur, carbon, nitrogen, oxygen and copper is evident from the survey spectra. The Au 4f_{7/2} for both $\text{Au}_{15}@\text{SG-}\beta\text{CD}$ and $\text{Au}_{15}@\text{SG-}\beta\text{CD}+\text{Hg}^{2+}$ (Figure 7B, traces a and c, respectively) appear at 84.2 (± 0.2) eV, corresponding to the characteristic binding energy of gold in zerovalent state.³⁰ The Au 4f_{7/2} feature of copper treated sample is shifted by a significant value (+0.6 eV, Figure 7B, trace b) which shows the interaction of the cluster with copper. This supports the change in the luminescence of $\text{Au}_{15}@\text{SG-}\beta\text{CD}$. The Cu 2p region of $\text{Au}_{15}@\text{SG-}\beta\text{CD}+\text{Cu}^{2+}$ is shown as inset of Figure 7A. This shows a feature of Cu 2p_{3/2} at 932.1 eV with the absence of satellite. The absence of satellite indicates the absence of copper in the +2 state.³¹ The peak at 932.1 eV may be due to Cu^{1+} or Cu^0 as their binding energies are very close (by only 0.1–0.2 eV) and

differentiation is difficult by XPS.³¹ The reduction of Cu^{2+} to $\text{Cu}^{1+}/\text{Cu}^0$ may be due to the interaction of glutathione ligands of the cluster as glutathione is well-known to reduce Cu^{2+} to Cu^{1+} .³² The other possibility is the reduction of Cu^{2+} by Au_{15} core where redox reaction may be feasible at the size scale of quantum clusters. This change is expected to affect the luminescence greatly. The Hg 4f region of $\text{Au}_{15}@\text{SG-}\beta\text{CD}+\text{Hg}^{2+}$ is shown in Figure S4 in the Supporting Information. Mercury is not detected. This may be due to negligible/weak interactions of Hg^{2+} with glutathione ligands of the cluster. The feature observed in this binding energy region is due to Au 5s.

The sensitivity of the composite film to various salts of Cu^{2+} was also checked. All the salts of Cu^{2+} (such as chloride, sulfate and acetate) showed a similar shift in the emission wavelength (see Figure S5 in the Supporting Information). The sensitivity to Cu^{1+} in ppm concentration was also investigated which showed a shift similar to Cu^{2+} but larger in magnitude (see Figure S6 in the Supporting Information). Dependence of the emission features on the anions and valence state of copper are subtle at the concentrations tested but they suggest that these aspects are also significant.

CONCLUSION

A multifunctional freestanding film of cm^2 area composed of Au_{15} cluster was fabricated. We demonstrated the utility of the film as a practical metal ion sensor. The visually observable changes are proportional to the metal ion concentration. The sensitivity of the luminescence to various cations was investigated in which the material showed an abrupt change in the case of Cu^{2+} and there is no effect when several other ions were tested. The stability of the composite, sensitivity to lower concentration, applicability across all anions and absence of other metal ion induced changes make this system useful for practical applications. The specific sensing of Cu^{2+} is understood by XPS analysis which reveals the reduction of Cu^{2+} to $\text{Cu}^{1+}/\text{Cu}^0$ either by the glutathione ligand or the Au_{15} core.

ASSOCIATED CONTENT

Supporting Information

Excitation/emission spectrum and photograph of Au_{15} in solution phase under visible light, photoluminescence spectra of chitosan film with and without Cu^{2+} , EDAX spectrum and SEM/EDAX image of the film in the presence of Cu^{2+} , XPS of $\text{Au}_{15}@\text{SG-}\beta\text{CD}+\text{Hg}^{2+}$ sample in the Hg 4f region, PL spectra of the composite film on exposure to different compounds of Cu^{2+} and comparison of the emission spectra of the film with Cu^{1+} and Cu^{2+} . This material is available free of charge via the Internet at <http://pubs.acs.org>.

AUTHOR INFORMATION

Corresponding Author

*E-mail: pradeep@iitm.ac.in.

ACKNOWLEDGMENTS

We thank Department of Science and Technology, Government of India for constantly supporting our research program on nanomaterials.

REFERENCES

- (1) Muhammed, M. A. H.; Pradeep, T. In *Advanced Fluorescence Reporters in Chemistry and Biology II*; Demchenko, A. P., Ed.; Springer-Verlag: Berlin, 2010; Vol. 9, part 4, pp 333–353.

- (2) Muhammed, M. A. H.; Verma, P. K.; Pal, S. K.; Kumar, R. C. A.; Paul, S.; Omkumar, R. V.; Pradeep, T. *Chem.—Eur. J.* **2009**, *15*, 10110–10120.
- (3) Muhammed, M. A. H.; Pradeep, T. *Chem. Phys. Lett.* **2007**, *449*, 186–190.
- (4) Shichibu, Y.; Negishi, Y.; Tsunoyama, H.; Kanehara, M.; Teranishi, T.; Tsukuda, T. *Small* **2007**, *3*, 835–839.
- (5) Adhikari, B.; Banerjee, A. *Chem. Mater.* **2010**, *22*, 4364–4371.
- (6) Muhammed, M. A. H.; Verma, P. K.; Pal, S. K.; Retnakumari, A.; Koyakutty, M.; Nair, S.; Pradeep, T. *Chem.—Eur. J.* **2010**, *16*, 10103–10102.
- (7) Tsunoyama, H.; Sakurai, H.; Ichikuni, N.; Negishi, Y.; Tsukuda, T. *Langmuir* **2004**, *20*, 11293–11296.
- (8) Tsunoyama, H.; Sakurai, H.; Negishi, Y.; Tsukuda, T. *J. Am. Chem. Soc.* **2005**, *127*, 9374–9375.
- (9) Gonzalez, J. I.; Lee, T. H.; Barnes, M. D.; Antoku, Y.; Dickson, R. M. *Phys. Rev. Lett.* **2004**, *93*, 147402–147405.
- (10) Chen, S.; Ingram, R. S.; Hostetler, M. J.; Pietron, J. J.; Murray, R. W.; Schaaff, T. G.; Khoury, J. T.; Alvarez, M. M.; Whetten, R. L. *Science* **1998**, *280*, 2098–2101.
- (11) Shibu, E. S.; Radha, B.; Verma, P. K.; Bhyrappa, P.; Kulkarni, G. U.; Pal, S. K.; Pradeep, T. *ACS Appl. Mater. Interfaces* **2009**, *1*, 2199–2210.
- (12) Cui, Y.; Ren, B.; Jao, J. L.; Gu, R. A.; Tian, Z. Q. *J. Phys. Chem. B* **2006**, *110*, 4002–4006.
- (13) Lin, Y. H.; Tseng, W. L. *Anal. Chem.* **2010**, *82*, 9194–9200.
- (14) Wei, H.; Wang, Z.; Yang, L.; Tian, S.; Hou, C.; Lu, Y. *Analyst* **2010**, *135*, 1406–1410.
- (15) Xie, J.; Zheng, Y.; Ying, J. Y. *Chem. Commun.* **2010**, *46*, 961–963.
- (16) Bootharaju, M. S.; Pradeep, T. *Langmuir* **2011**, *27*, 8134–8143.
- (17) Su, Y. T.; Lan, G. Y.; Chen, W. Y.; Chang, H. T. *Anal. Chem.* **2010**, *82*, 8566–8572.
- (18) Sreeprasad, T. S.; Maliyekkal, S. M.; Krishnan, D.; Chaudhari, K.; Xavier, P. L.; Pradeep, T. *ACS Appl. Mater. Interfaces* **2011**, *3*, 2643–2654.
- (19) Irimpan, L.; Nampoore, V. P. N.; Radhakrishnan, P. *J. Appl. Phys.* **2008**, *103*, 094914 (1–8).
- (20) Srivastava, S.; Haridas, M.; Basu, J. K. *Bull. Mater. Sci.* **2008**, *31*, 213–217.
- (21) Gelves, G. A.; Mohammed, H.; Salehab, A.; Sundararaj, U. *J. Mater. Chem.* **2011**, *21*, 829–836.
- (22) Zhou, H.; Chen, X.; Wu, G.; Gao, F.; Qin, N.; Bao, D. J. *Am. Chem. Soc.* **2010**, *132*, 1790–1791.
- (23) Bubb, D. M.; McGill, R. A.; Horwitz, J. S.; Fitz-Gerald, J. M.; Houser, E. J.; Stroud, R. M.; Wu, P. W.; Ringeisen, B. R.; Pique, A.; Chrisey, D. B. *J. Appl. Phys.* **2001**, *89*, 5739–5746.
- (24) Zhou, Q.; Li, C. M.; Li, J.; Cui, X.; Gervasio, D. J. *J. Phys. Chem. C* **2007**, *111*, 11216–11222.
- (25) Liu, X.; Hu, Q.; Fang, Z.; Zhang, X.; Zhang, B. *Langmuir* **2009**, *25*, 3–8.
- (26) Kampalanonwat, P.; Supaphol, P. *ACS Appl. Mater. Interfaces* **2010**, *2*, 3619–3627.
- (27) Shibu, E. S.; Pradeep, T. *Chem. Mater.* **2011**, *23*, 989–999.
- (28) Shibu, E. S.; Muhammed, M. A. H.; Tsukuda, T.; Pradeep, T. *J. Phys. Chem. C* **2008**, *112*, 12168–12176.
- (29) Zhu, M.; Lanni, E.; Garg, N.; Bier, M. E.; Jin, R. *J. Am. Chem. Soc.* **2008**, *130*, 1138–1139.
- (30) Negishi, Y.; Nobusada, K.; Tsukuda, T. *J. Am. Chem. Soc.* **2005**, *127*, 5261–5270.
- (31) Ai, Z.; Zhang, L.; Lee, S.; Ho, W. *J. Phys. Chem. C* **2009**, *113*, 20896–20902.
- (32) Anwar, Z. M. *J. Chin. Chem. Soc.* **2005**, *52*, 863–871.

Supporting information

Luminescent, Freestanding Composite Films of Au_{15} for Specific Metal Ion Sensing

Anu George,[†] E. S. Shibu,[†] Shihabudheen M. Maliyekkal,^{†,‡} M. S. Bootharaju,[†] and
T. Pradeep*,[†]

[†]*DST Unit of Nanoscience (DST UNS), Department of Chemistry, Indian Institute of
Technology, Madras, Chennai 600 036, India*

[‡]*School of Mechanical and Building Sciences, VIT University, Chennai Campus,
Chennai-600 048, India*

*Email: pradeep@iitm.ac.in (T. Pradeep)

Supporting information 1

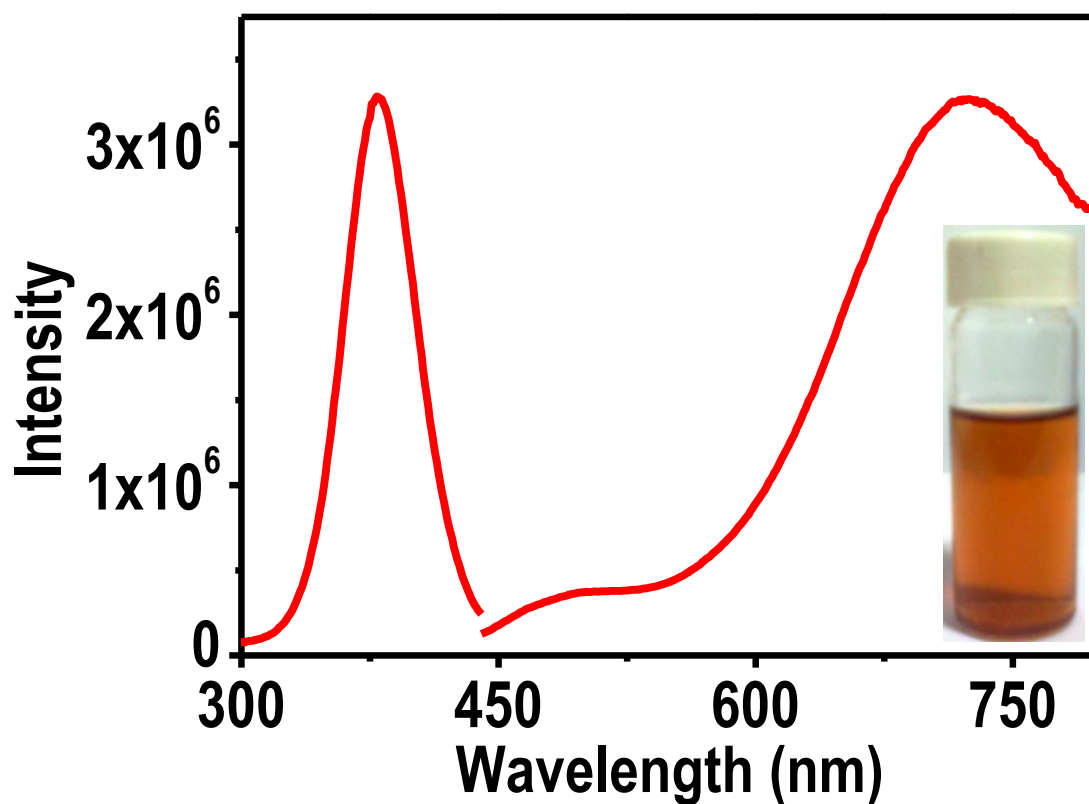


Figure S1. Excitation and emission spectra of Au₁₅ solution. Inset shows the photograph of Au₁₅ in solution phase under visible light. A photograph in UV light is given in Figure 3.

Supporting information 2

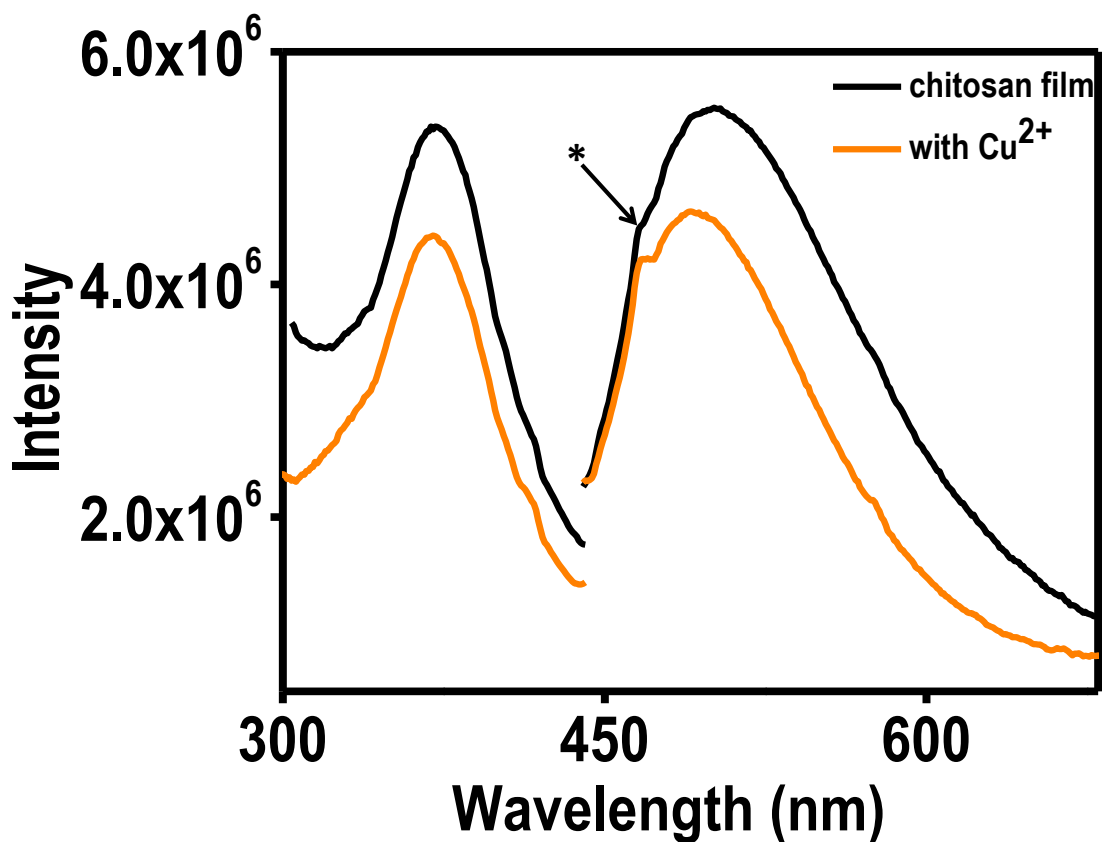


Figure S2. Photoluminescence spectra of parent chitosan film with and without Cu^{2+} ion (5 ppm). Peaks in UV and visible regions correspond to excitation and emission, respectively. The feature indicated with (*) is due to an unidentified impurity.

Supporting information 3

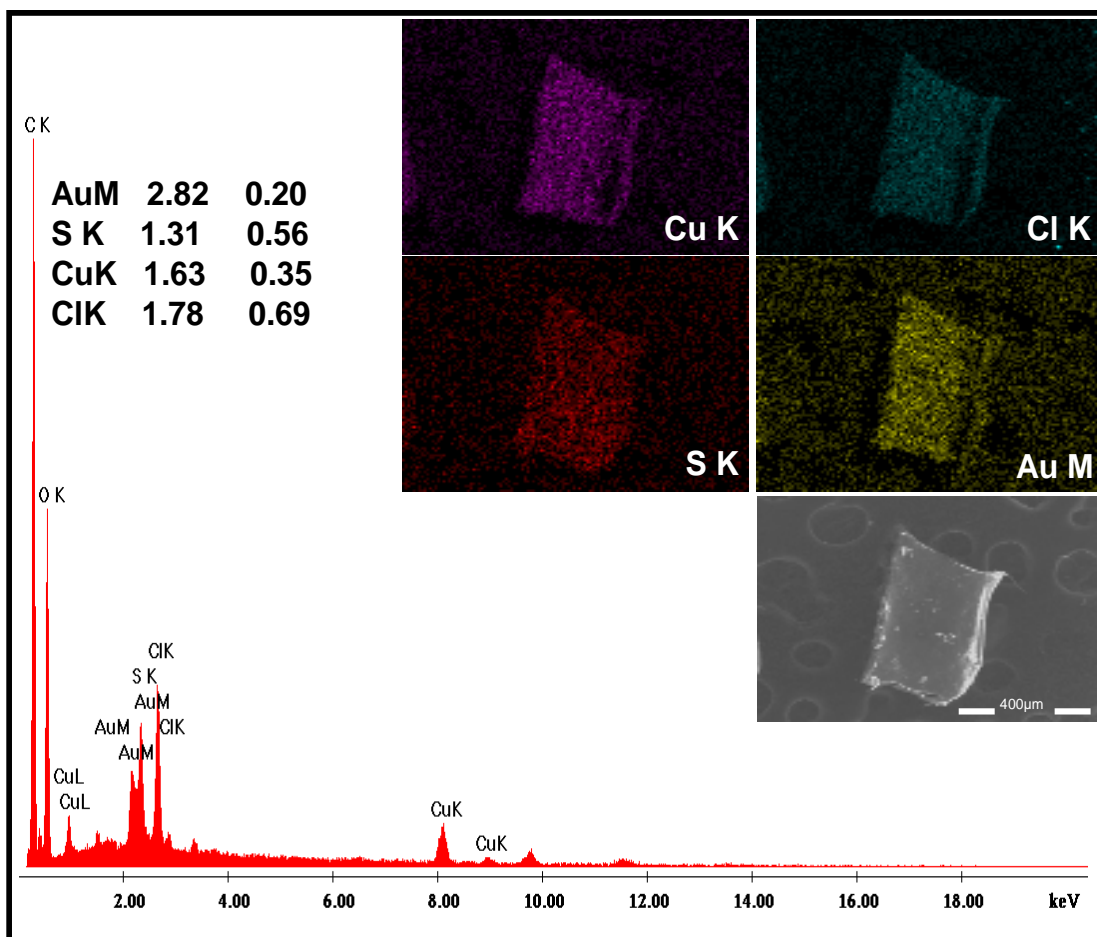


Figure S3. EDAX spectrum of the composite film exposed to CuCl_2 . Inset shows the SEM and EDAX image of the composite film which shows uniform elemental distribution of copper, gold, sulfur and chlorine in the exposed composite film.

Supporting information 4

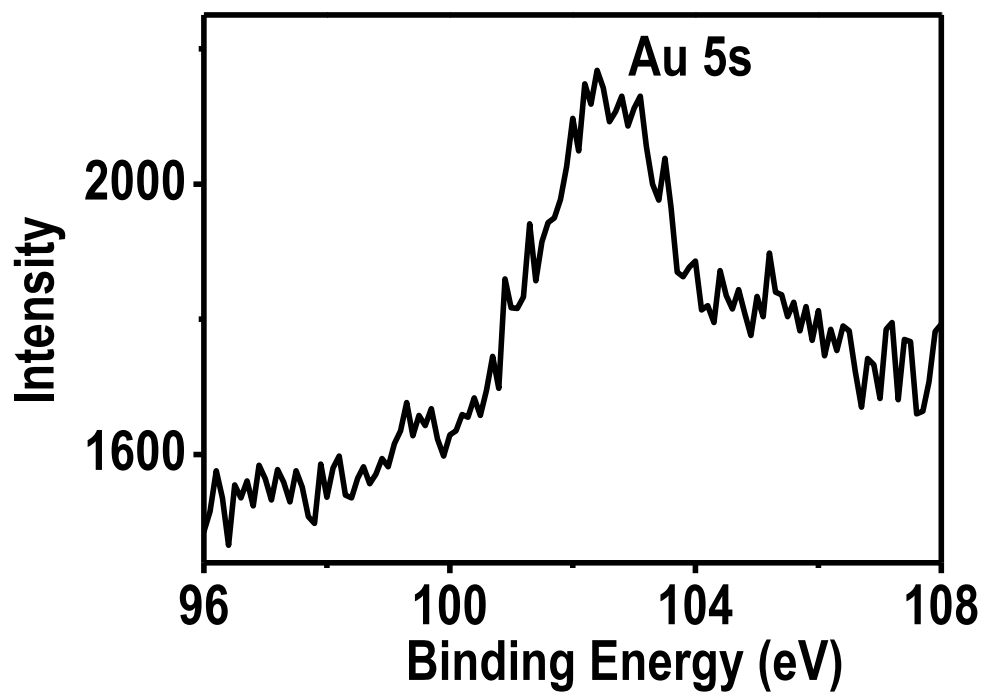


Figure S4. XP spectrum of Au₁₅@SG-βCD+Hg²⁺ sample in Hg 4f region. A peak corresponds to Au 5s is noticed whereas no Hg 4f feature is seen.

Supporting information 5

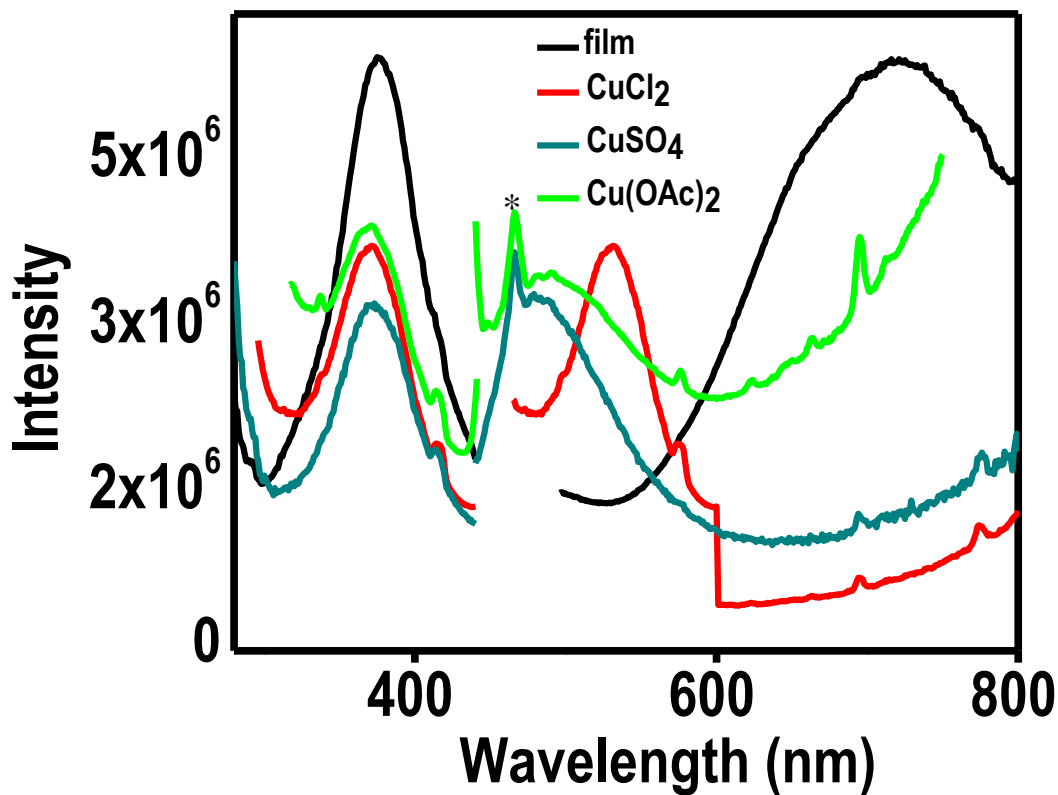


Figure S5. Photoluminescence spectra of the composite film exposed to different salts of Cu^{2+} ion in 1 ppm concentration. Peaks in UV and visible regions correspond to excitation and emission, respectively. Chloride, sulphate, acetate salts of copper shows a similar shift in their emission wavelength. The feature indicated with (*) is due to an unidentified impurity.

Supporting information 6

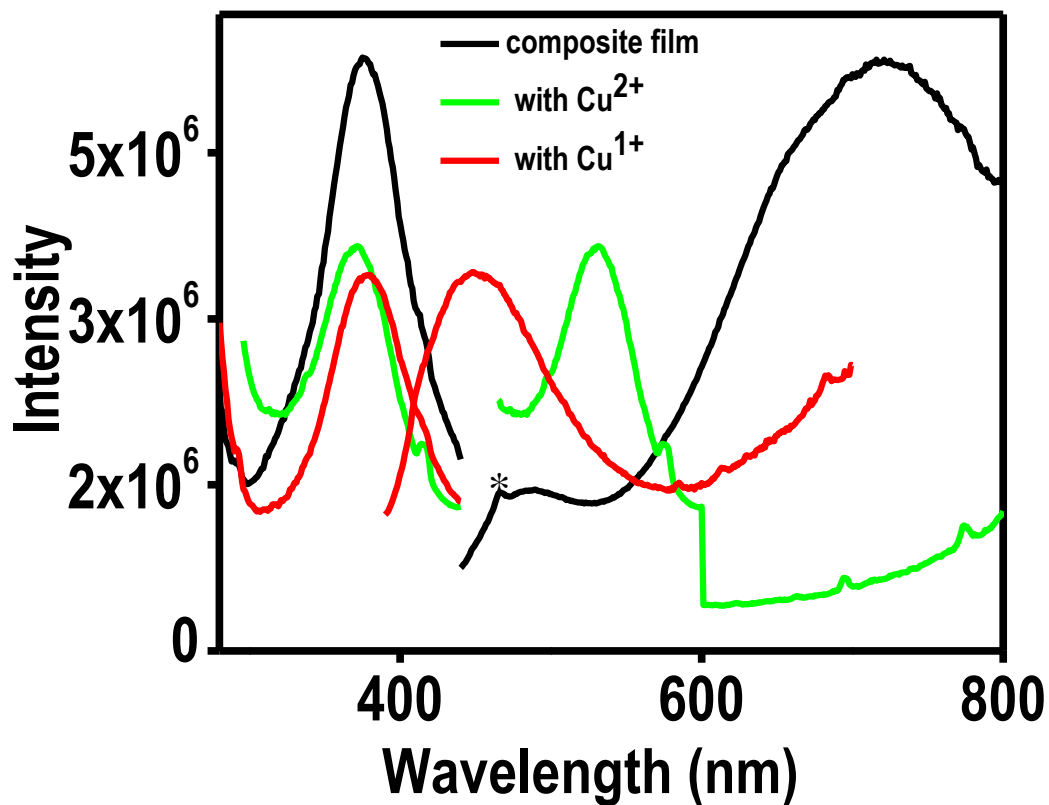


Figure S6. A comparison of the photoluminescence spectra of the composite film with chloride salt of Cu^{2+} and Cu^{1+} metal ions at 1 ppm concentration. Peaks in UV and visible regions correspond to excitation and emission, respectively. The feature indicated with (*) is due to an unidentified impurity.

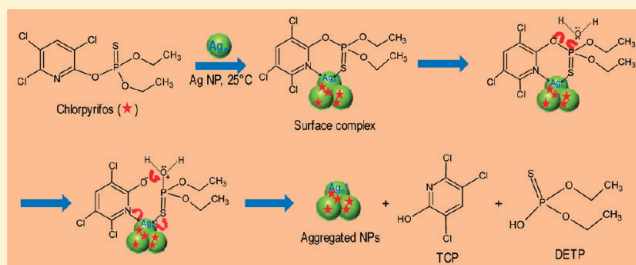
Understanding the Degradation Pathway of the Pesticide, Chlorpyrifos by Noble Metal Nanoparticles

M. S. Bootharaju and T. Pradeep*

DST Unit of Nanoscience (DST UNS), Department of Chemistry, Indian Institute of Technology Madras, Chennai-600 036, India

Supporting Information

ABSTRACT: Application of nanoparticles (NPs) in environmental remediation such as water purification requires a detailed understanding of the mechanistic aspects of the interaction between the species involved. Here, an attempt was made to understand the chemistry of noble metal nanoparticle–pesticide interaction, as these nanosystems are being used extensively for water purification. Our model pesticide, chlorpyrifos (CP), belonging to the organophosphorothioate group, is shown to decompose to 3,5,6-trichloro-2-pyridinol (TCP) and diethyl thiophosphate at room temperature over Ag and Au NPs, in supported and unsupported forms. The degradation products were characterized by absorption spectroscopy and electrospray ionization mass spectrometry (ESI MS). These were further confirmed by ESI tandem mass spectrometry. The interaction of CP with NP surfaces was investigated using transmission electron microscopy, energy dispersive analysis of X-rays, Raman spectroscopy, and X-ray photoelectron spectroscopy (XPS). XPS reveals no change in the oxidation state of silver after the degradation of CP. It is proposed that the degradation of CP proceeds through the formation of AgNP–S surface complex, which is confirmed by Raman spectroscopy. In this complex, the P–O bond cleaves to yield a stable aromatic species, TCP. The rate of degradation of CP increases with increase of temperature and pH. Complete degradation of 10 mL of 2 ppm CP solution is achieved in 3 h using 100 mg of supported Ag@citrate NPs on neutral alumina at room temperature at a loading of ~0.5 wt %. The effect of alumina and monolayer protection of NPs on the degradation of CP is also investigated. The rate of degradation of CP by Ag NPs is greater than that of Au NPs. The results have implications to the application of noble metal NPs for drinking water purification, as pesticide contamination is prevalent in many parts of the world. Study shows that supported Ag and Au NPs may be employed in sustainable environmental remediation, as they can be used at room temperature in aqueous solutions without the use of additional stimulus such as UV light.



INTRODUCTION

Modern agriculture requires tons of pesticides and insecticides worldwide to protect plants and produce from pests and insects. It is estimated that about 2 million tons of organophosphorus (OP) pesticides are used in a year throughout the world.¹ Because of indiscriminate and extensive use of pesticides, they persist in soil, ground, surface waters, air, and agricultural products.² Chlorpyrifos, *O,O*-diethyl *O*-(3,5,6-trichloro-2-pyridyl) phosphorothioate (C₉H₁₁Cl₃NO₃PS) (CP), is a well-known organophosphorothioate pesticide that is used in agricultural and nonagricultural areas.³ It is available in various formulations under the trade names such as Lorsban, Pynex, Spannit, Tricel, Dursban, Piridane, Silrifos, and Talon.⁴ In the European Community (EC) countries, 0.1 and 0.5 ppb are set as the maximum admissible quantities for individual and the total amount of pesticides, respectively, in drinking water.⁵ Exposure of CP for long periods results in serious harm to the human nervous system, respiratory tract, and cardiovascular systems.^{6,7} The effects of CP have been observed about 24 km away from the place of application.⁸ Therefore, the degradation of CP present in environment has become a public concern. The government of India has banned several chlorinated

hydrocarbon insecticides, such as dichlorodiphenyltrichloroethane (DDT), aldrin, and chlordane, and the use of CP has increased as an alternative.⁶ Corn, tree nuts, and soybeans are the major crops on which CP is used.⁹ Although reliable data of the presence of pesticides in groundwater of different parts of the world are rare, limited information is available from some regions. Studies were conducted on the contamination of soil and groundwater quality of Roorkee area, Haridwar district, India, due to intense agricultural activities. Nine organophosphorous and 17 organochlorine pesticides were present in groundwater much above the limits of Indian drinking water standards.¹⁰

The major pathways of chemical transformation of CP and its analogues like CP-methyl are oxidation, hydrolysis, and nucleophilic substitution reactions.¹¹ CP can be oxidized by various oxidizing agents, such as ozone, dinitrogen tetroxide, peracid, and chlorine, which give CP oxon after the replacement of S by oxygen in the thiophosphoryl bond (P=S).^{12–15} CP oxon is

Received: October 19, 2011

Revised: January 10, 2012

Published: January 12, 2012

substantially more toxic compared to its parent compound, as it inhibits acetylcholinesterase (AChE, an enzyme necessary for proper function of the nervous system).¹⁶ CP readily undergoes hydrolysis in basic pH,^{17,18} whereas it persists in neutral and slightly acidic conditions typical of soils, surface waters, and aquifer sediments.¹⁹ There are several methods to degrade CP in the literature, such as photolytic,²⁰ enzymatic,²¹ electro-enzymatic,²² ultrasonic,²³ and biodegradative²⁴ paths. Divalent metal ion catalyzed hydrolysis of CP has been reported in which Cu²⁺ is found to show high catalytic activity.²⁵

Nanotechnology is important in the context of environmental remediation.^{26,27} We have shown that noble metal nanoparticles cause dehalogenation of several halocarbons and the chemistry can be extended to halocarbon pesticides.²⁸ Subsequently, noble metal (especially silver and gold) nanostructures have been used in water purification applications, especially because the chemistry occurs at room temperature and at high efficiency.^{29–34} Absorption spectra of these NPs show that they are highly sensitive to toxic species present in water, such as heavy metal ions^{35,36} (Hg²⁺, Cd²⁺, and Pb²⁺, etc.) and pesticides^{37,38} (endosulfan, chlorpyrifos, and malathion, etc.). It is very much essential to understand the pathways of degradation of pesticides and the toxicity of the transformed products in order to design better nanomaterials-based remediation strategies.

In this report, we have studied the degradation of this pesticide at different concentrations by silver and gold NPs in supported (on neutral alumina) and unsupported forms. The system was chosen as a model as CP has well-defined spectroscopic, elemental, and mass spectrometric features that allow precise identification of the species involved. The degradation products of CP, 3,5,6-trichloro-2-pyridinol (TCP) and diethyl thiophosphate (DETP), have been identified. TCP is less toxic³⁹ when compared to CP, whereas other oxidation products like CP oxon are more toxic¹⁶ than parent CP. We have also studied the effects of monolayer protection, support, temperature, and pH on the degradation of CP. A mechanism has been proposed on the basis of the formation of a surface complex involving AgNP–S binding. As the preparation of Ag and Au nanoparticle-supported alumina is easy and degradation of CP in aqueous solutions occurs at room temperature by simply stirring without any additional irradiation of light, the application of noble metal nanoparticles in water purification applications is sustainable.

EXPERIMENTAL SECTION

Materials. Silver nitrate, tetrachloroauric acid trihydrate (CDH, India), trisodium citrate (TSC, Qualigens), mercaptosuccinic acid (MSA), CP (Fluka), sodium borohydride (Sigma Aldrich), and methanol were received from various vendors and used as such without further purification. Neutral alumina (60–325 mesh BSS) was supplied by SRL, India. The surface area of alumina was 900 ± 50 cm²/g and the mean particle size was 0.13 μ m. Adsorption capacity was at least 1 mg/g for *o*-nitroaniline. Pore size distribution is 50–60 Å.

Synthesis of Ag NPs. The Ag@citrate NPs were prepared according to the literature.³⁵ In this method, to a boiling 50 mL silver nitrate (1 mM) solution, 2 mL of 1 wt % trisodium citrate was added, and heating was continued further for a few minutes. The solution turned light yellow, indicating the formation of NPs. The solution was cooled in an ice bath. Later, the solution was centrifuged, and the precipitate was washed with distilled water to remove excess citrate. MSA-protected Ag NPs were prepared as follows.³⁶ About 448.9 mg of MSA was dissolved in 100 mL of methanol with stirring, at 0 °C. To this was added AgNO₃ solution (85 mg of AgNO₃ in 1.7 mL of distilled water). Then 25 mL of 0.2 M aqueous NaBH₄ was added

dropwise, and stirring was continued for 1 h. The precipitate of NPs was centrifuged and washed several times with methanol to remove excess sodium borohydride and MSA. Finally, the solvent methanol was evaporated with a rotavapor to get NPs in the powder form.

Supporting Ag NPs on Neutral Alumina. The loading of Ag@citrate NPs was done by adding NPs solution to a calculated amount of neutral alumina followed by gentle shaking. The adsorption of NPs on alumina was noticed by the disappearance of color of the supernatant. Addition of NPs solution was stopped when there was no change in color of the supernatant. This was monitored using absorption measurements of the supernatant also. The loading of Ag NPs was ~0.5 wt %. Similarly, MSA-protected Ag NPs were also loaded on alumina at ~0.5 wt % by adding a stock solution of Ag@MSA NPs.

Interaction of Supported and Unsupported Ag@Citrate NPs with CP. A 6 mL portion of Ag@citrate NPs solution was centrifuged at 10 000 rpm for 6–7 min to remove excess citrate. To the centrifugate was added the required volume of CP in a 1:1 water–methanol mixture. Typically, 5 mL of Ag@citrate–CP solutions (at 1, 10, and 50 ppm concentrations of CP) was stirred at 1500 rpm. In the case of alumina-supported Ag@citrate, 100 mg of material and 10 mL of 2 ppm CP solutions were stirred at 1500 rpm.

Instrumentation. UV–vis absorption spectra were recorded with a PerkinElmer Lambda 25 instrument in the spectral range of 200–1100 nm. High-resolution transmission electron microscopy (HRTEM) of the samples was carried out using a JEOL 3010 instrument with a UHR pole piece. TEM specimens were prepared by drop-casting one or two drops of aqueous solution to carbon-coated copper grids and allowed to dry at room temperature overnight. All measurements were done at 200 kV to minimize the damage of the sample by the high-energy electron beam. Raman spectra were measured using WiTec GmbH confocal micro Raman equipped with a CCD detector. The light source was a Nd:YAG laser of 532 nm wavelength. X-ray photoelectron spectroscopy (XPS) measurements were done using an Omicron ESCA Probe spectrometer with polychromatic Mg K α X-rays ($h\nu = 1253.6$ eV). The X-ray power applied was 300 W. The pass energy was 50 eV for survey scans and 20 eV for specific regions. Sample solution was spotted on a molybdenum sample plate and dried in vacuum. The base pressure of the instrument was 5.0×10^{-10} mbar. The binding energy was calibrated with respect to the adventitious C 1s feature at 285.0 eV. Most of the spectra were deconvoluted to their component peaks, using the software CASA-XPS. The ESI MS measurements were done in the negative and positive modes using an MDX Sciex 3200 QTRAP MS/MS instrument having a mass range of m/z 50–1700, in which the spray and the extraction are orthogonal to each other. The samples were electro-sprayed at a flow rate of 10 μ L/min and ion spray voltage of 5 kV. The spectra were averaged for 100 scans. MS/MS spectra were collected at optimized collision energies in the range of 35–45 eV.

RESULTS AND DISCUSSION

Interaction of Ag@Citrate NPs with CP. Ag@citrate³⁵ NPs show plasmon absorption at 424 nm in water (inset of Figure 1A, trace a). The absorption features of CP are seen at 229 and 289 nm in a 1:1 water:methanol mixture (inset of Figure 1A, trace b). The peaks at 229 and 289 nm may be attributed to the substituents in the pyridine ring.⁸ CP solutions of different concentrations (1, 10, and 50 ppm) were treated with Ag@citrate NPs and the absorption spectra of the solutions were recorded after 24 and 48 h (Figure 1). After 24 h, the silver plasmon peak was shifted to 436 and 650 nm in the 50 ppm case (Figure 1A, trace c), which may be due to the aggregation of NPs due to adsorption³⁸ of CP, and the intensity of the spectrum decreased drastically. The CP peak at 289 nm disappeared completely and a new peak appeared at 320 nm, which may be the product after the complete degradation of CP. In the 10 ppm CP case, a slight decrease in intensity of surface plasmon resonance of NPs is seen and a weak hump at 320 nm in CP was observed. After 48 h, a clear peak at 320 nm

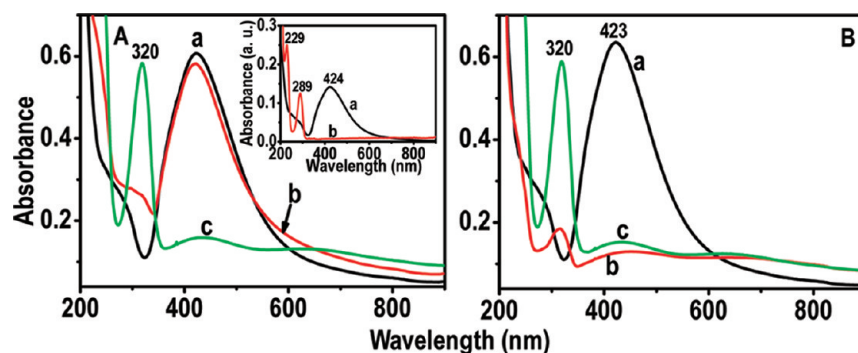


Figure 1. UV-vis absorption spectra of Ag@citrate NPs treated with 1, 10, and 50 ppm CP solutions (traces a, b, and c, respectively) after 24 and 48 h (A and B, respectively). The inset of A is UV-vis absorption spectra of Ag@citrate NPs and 1 ppm CP (a and b, respectively).

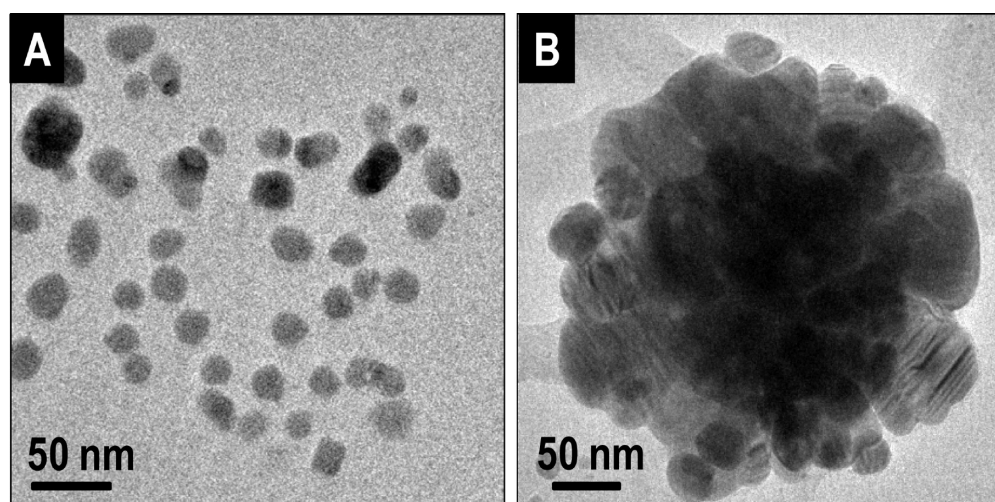


Figure 2. TEM images of Ag@citrate NPs (A) and NPs treated with 10 ppm CP solution after 48 h (B).

is seen in the 10 ppm CP case (Figure 1B, trace b) and the silver plasmon peak is shifted to 457 and 700 nm, which is due to aggregation of NPs.³⁸

To understand the red shift of surface plasmon of silver NPs after the treatment of CP, TEM analysis was performed. TEM images of the as-prepared and 10 ppm CP treated Ag@citrate NPs (after 48 h) are shown in Figure 2. A larger area TEM image of the CP-treated sample is shown in the Supporting Information (Figure S1). The average size of Ag@citrate NPs is 30 ± 10 nm (Figure 2A). Figure 2B is a small area TEM image where we can see clear aggregation of Ag NPs induced by CP.

To see the elemental composition of the surface of NPs in the aggregates, one of those aggregates was imaged as shown in Figure 3. Figure 3A is the TEM image, and parts B, C, D, and E are the elemental maps of Ag, Cl, S, and P, respectively. Part F is the TEM image of single NP, and the Ag(111) lattice (0.234 nm) is marked.⁴⁰ The presence of P confirms the presence of CP on the surfaces of the NPs. The energy dispersive analysis of X-rays (EDAX) spectrum corresponding to the image is shown in the Supporting Information (Figure S2). It shows the presence of elements Ag, S, P, and Cl.

To determine the origin of the new peak at 320 nm in the absorption spectrum, the suspension of 10 ppm CP solution and Ag@citrate was centrifuged (after 48 h) and the supernatant was analyzed using electrospray ionization mass spectrometry (ESI MS). For comparison, ESI MS of CP was also measured, and the data are shown in Figures 4 and 5. Figure 4A is the ESI MS in the positive mode. Traces a and b correspond

to parent CP and the reaction products, respectively. In trace a, the molecular ion peak of CP is at m/z 350.5. The major fragments of CP are at m/z 323, 295, and 277, which are due to losses of m/z 28 (C_2H_4), 56 ($2C_2H_4$), and 74 ($2C_2H_4 + H_2O$), respectively, from m/z 350.5 (Figure 4A, trace a). The other major specie noticed is at m/z 198, which may be due to protonated TCP. The positive mode ESI MS of the reaction product shows the disappearance of m/z 350.5, which is due to CP (Figure 4A, trace b). This confirms that CP has degraded. The major peaks are noticed at m/z 220 and 198. The m/z 198 peak may be due to TCP. To confirm this further, tandem mass spectrometry of m/z 198 was performed. The MS^2 of m/z 198 is shown in Figure 4B. In TCP, there are three chlorine atoms. Due to the existence of ^{35}Cl and ^{37}Cl isotopes, for TCP, three peaks at m/z 198, 200, and 202 are seen. The calculated mass spectral positions for TCP and the peaks in the m/z 198 region are compared in inset of Figure 4A. They are in good agreement. The peaks at m/z 198, 200, and 202 are due to $^{35}Cl_3$, $^{35}Cl_2^{37}Cl$, and $^{35}Cl^{37}Cl_2$ isotopomers of TCP, respectively. The MS^2 of m/z 198 peak (Figure 4B, trace a) gives fragments at m/z 180, 162, 144, 134, and 107, which are due to the loss of H_2O , Cl, $H_2O + Cl$, $CO + Cl$, and $CO + Cl + HCN$, respectively. Here, ^{35}Cl is lost in the fragmentation. However, in the MS^2 of m/z 200, the ion can lose ^{35}Cl or ^{37}Cl , so we see peaks separated by 2 mass units higher than all the peaks seen in trace a (Figure 4B, trace b). In MS^2 of m/z 202 there is also a possibility to lose either ^{35}Cl or ^{37}Cl (Figure 4B, trace c). All

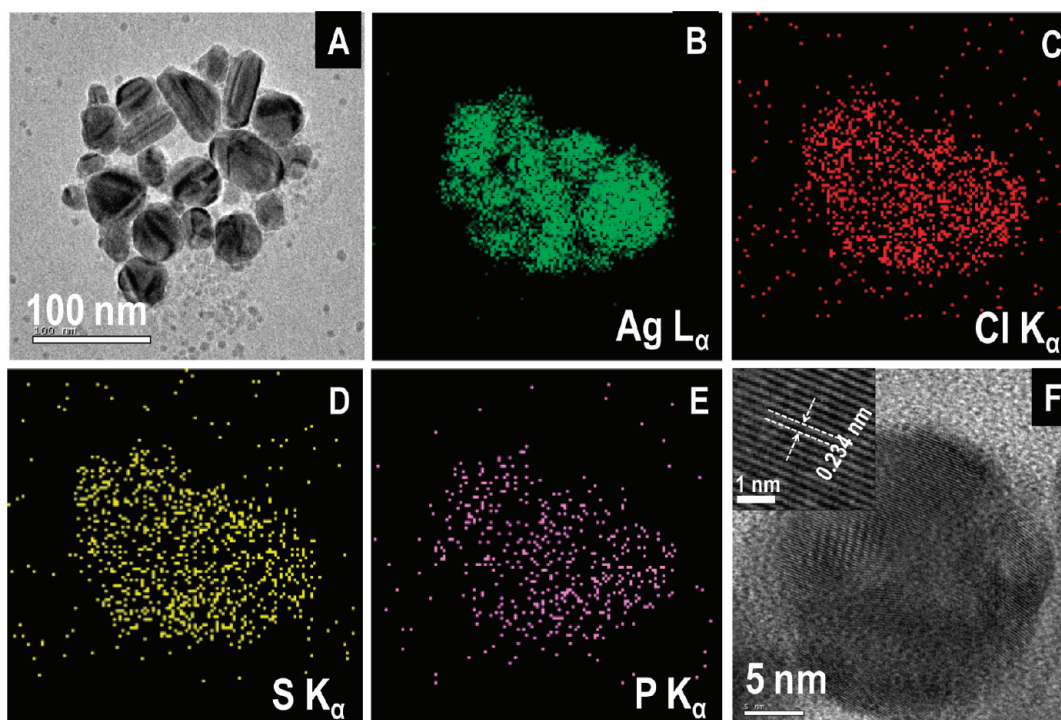


Figure 3. TEM image and elemental maps of Ag@citrate NPs after treating with 10 ppm CP solution (after 48 h). Part A is the TEM image of an aggregate. Parts B, C, D, and E are elemental maps of Ag, Cl, S, and P, respectively. Part F is the TEM image of a single NP, and the Ag(111) interplanar distance is marked in the inset. The elemental maps are rotated nearly 90° with respect to the TEM.

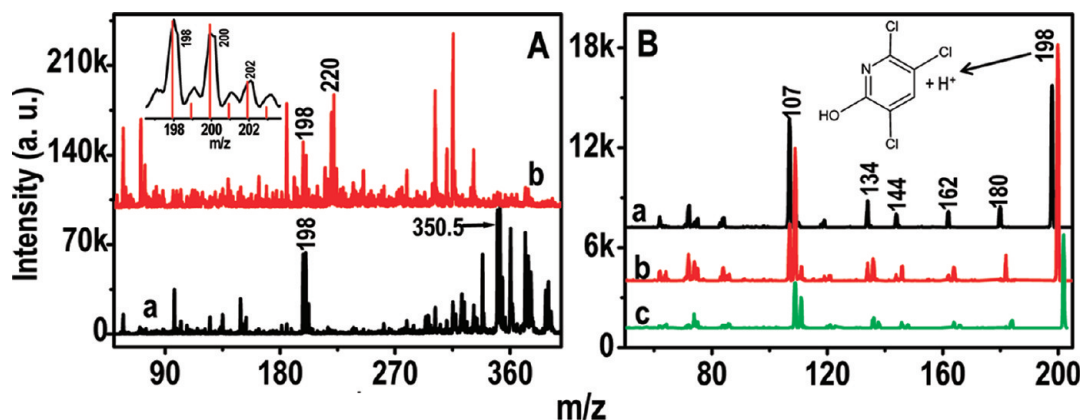


Figure 4. (A) ESI MS of CP (trace a) and supernatant of reaction mixture of Ag@citrate NPs and 10 ppm CP solution (trace b) after 48 h in positive mode. The inset of A is a comparison of calculated mass spectral positions (red trace) of protonated TCP and the experimental mass spectral region in m/z 198 (black trace). (B) MS/MS spectra of m/z 198, 200, and 202 (traces a, b, and c, respectively) in the reaction product. The chemical structure of m/z 198 is shown in B.

these losses are possible from the TCP structure, which is shown in Figure 4B. In the positive mode, the other major peak seen is at m/z 220. This may be due to the replacement of H in the $-OH$ group of the TCP structure by Na, as we used trisodium citrate in the synthesis of Ag@citrate NPs. The calculated mass spectral positions of the sodium salt of TCP and m/z 220 peak are compared, and they are in very good agreement (Supporting Information, Figure S3A). To confirm the structure of m/z 220, its MS² spectrum was measured, but we did not observe any positively charged fragments, as only Na⁺ loss occurs, giving a neutral fragment (Supporting Information, Figure S3B).

In the negative mode ESI MS of CP, the major fragment is m/z 196, due to loss of one proton from TCP (Figure 5A, trace a). The ESI MS of the product of 10 ppm CP solution

and Ag@citrate NPs shows major peaks at m/z 196 and 169 (Figure 5A, trace b). The peak at m/z 196 is assigned to the structure mentioned (shown in Figure 5A). To verify this, calculated mass spectral positions were compared with the experimental spectrum of the anion of TCP (inset of Figure 5A). Both are in good agreement. Although MS/MS analysis of m/z 196, 198, and 200 were carried out, we did not observe any negatively charged fragments (Supporting Information, Figure S4A). The other major peak is m/z 169. This may be due to the anion of DETP. To check the assignment, calculated mass spectral positions were compared with the experimental spectrum of the anion of DETP (Supporting Information, Figure S4B), and they were in good agreement. To confirm the structure, MS² of m/z 169 was performed and it gives peaks at 141 and 95, which are due to the loss of C₂H₄ and 2C₂H₄ + H₂O, respectively.

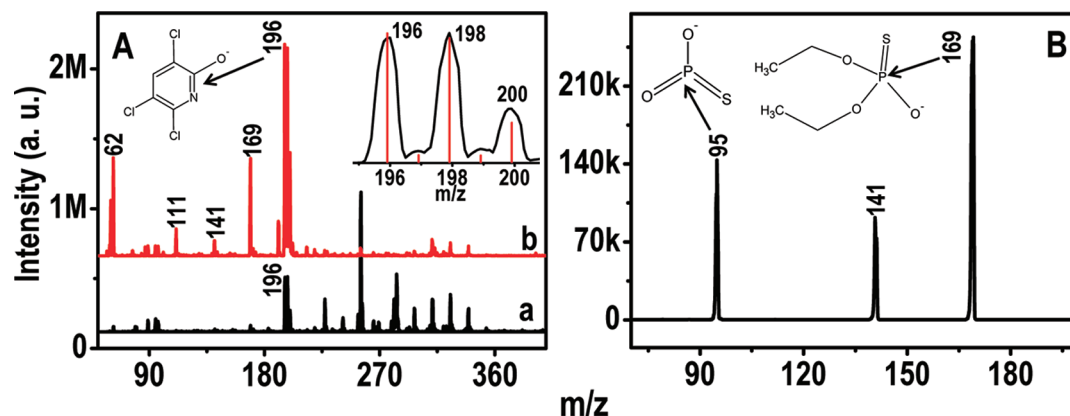


Figure 5. (A) ESI MS of CP (trace a) and supernatant of reaction mixture of Ag@citrate NPs and 10 ppm CP solution (trace b) after 48 h in negative mode. The inset of A is a comparison of the calculated mass spectral positions (red trace) of TCP and experimental mass spectral region in the m/z 196 range (black trace). (B) Tandem mass spectrum of m/z 169 of the reaction product. The chemical structures of m/z 196, 169, and 95 are also shown.

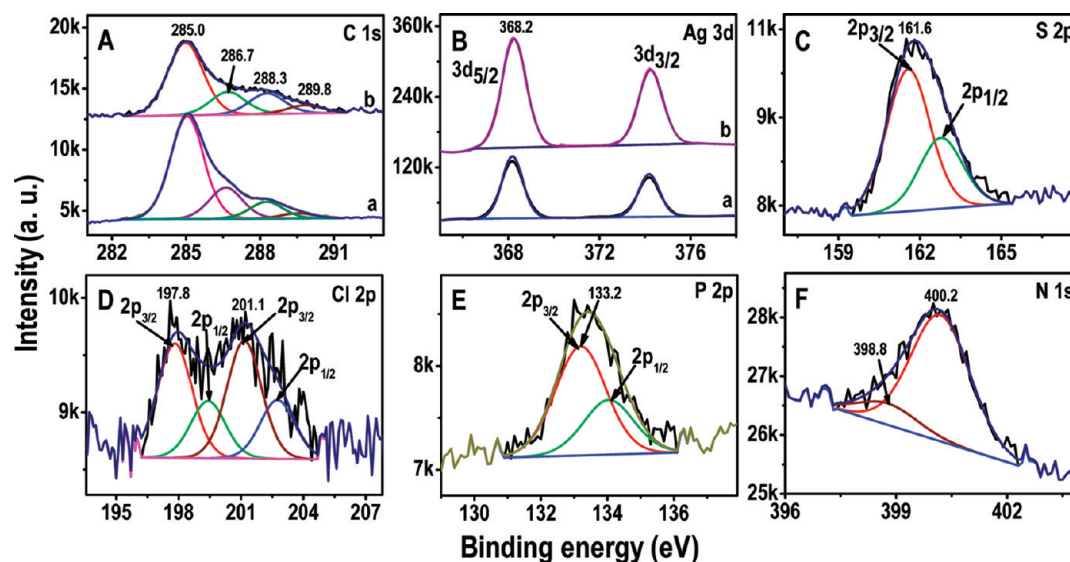
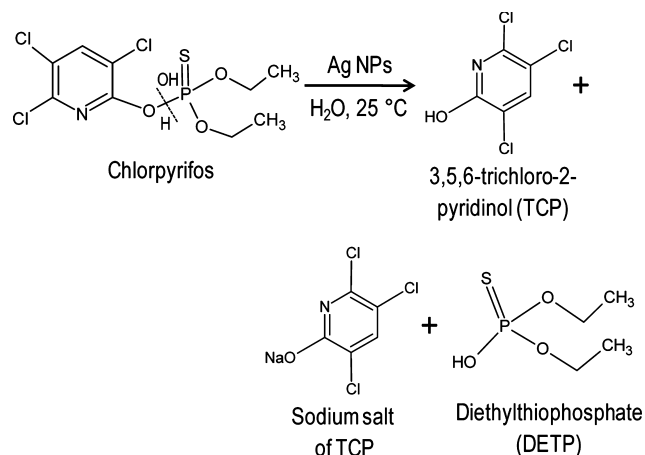


Figure 6. XPS of Ag@citrate NPs and the sample treated with 10 ppm CP solution for 48 h. Parts A, B, C, D, E, and F are C 1s, Ag 3d, S 2p, Cl 2p, P 2p, and N 1s regions, respectively. Traces a and b (in A and B) are before and after treatment of CP, respectively.

The chemical structures of m/z 169 and 95 are shown in Figure 5B. On the basis of these assignments, we can postulate an equation for the degradation of CP in presence of Ag@citrate as follows:



After the treatment of CP, NPs were subjected to XPS analysis to see whether there is a change in oxidation state of silver

in Ag@citrate NPs due to the degradation of CP. The XPS data of 10 ppm CP treated and untreated Ag@citrate NPs are shown in Figure 6. The C 1s features of as-synthesized Ag@citrate NPs are seen at 285.0, 286.7, 288.5, and 289.6 eV, which may be due to C–C, C–O, O–C–O, and O=C–O carbons, respectively (Figure 6A, trace a).⁴¹ The Ag 3d_{5/2} peak is observed at 368.2 eV, assigned to silver in the zerovalent state (Figure 6B, trace a). After the treatment of CP, the features of C 1s and Ag 3d_{5/2} are unaltered (traces b in Figures 6A and B, respectively). They indicate that after the conversion of CP there is no change in carboxylate protection and oxidation state of silver. As noticed in TEM analysis, the adsorption of CP on NPs is confirmed by XPS also. A peak of S 2p_{3/2} is observed at 161.6 eV, which may be due to chemisorbed⁴² CP or metal sulfide⁴³ as shown in Figure 6C. The Cl 2p region is shown in Figure 6D, where the distinct features are deconvoluted and labeled. The 2p_{3/2} peaks at 197.8 and 201.1 eV may be due to different chemical environments. The latter peak may be due to organic chlorides,⁴³ which may be from adsorbed CP. The P 2p_{3/2} peak is seen at 133.2 eV, which can be assigned to organophosphate species⁴⁴ (Figure 6E). The N 1s features are

observed at 398.8 and 400.2 eV (Figure 6F). The latter peak may be due to the organic N 1s signal, due to adsorbed CP.⁴² The former peak may be due to the involvement of N in the formation of a surface complex.

To understand the mechanism of interaction of CP with Ag NPs surface, Raman spectroscopy was performed. Raman spectra of CP and Ag@citrate NPs treated with 10 ppm CP solution are shown in Figure 7 (traces a and b, respectively).

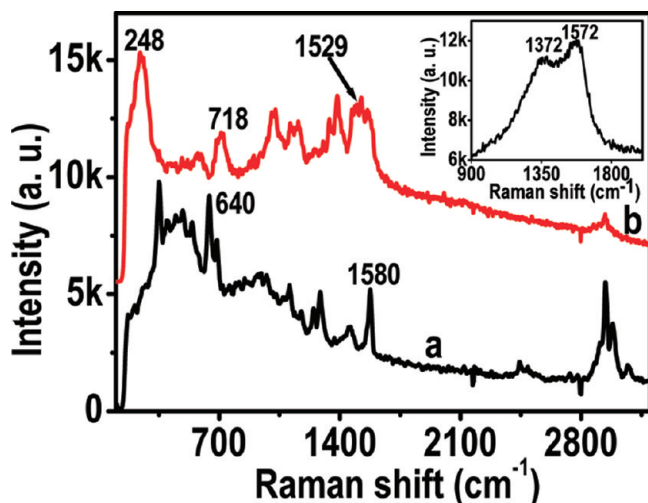


Figure 7. Raman spectra of CP and Ag@citrate NPs treated with 10 ppm CP solution for 1 day (traces a and b, respectively). The inset is the Raman spectrum of Ag@citrate NPs.

Major Raman features of CP are noticed at 640 and 1580 cm^{-1} . The former is due to C–Cl and the latter is due to P=S vibrations, respectively.³⁸ Parent Ag@citrate NPs exhibit Raman peaks at 1372 and 1572 cm^{-1} , which are due to carbonaceous species such as citrate (inset of Figure 7).²⁸ NPs treated with 10 ppm CP solution show all the Raman features of CP. The P=S and C–Cl features are broadened and shifted (Figure 7, trace b), which confirm the adsorption of CP on NPs, leading to aggregation. This is also confirmed by TEM and XPS. A new peak at 248 cm^{-1} is noticed that may be assigned to AgNP–S interaction, possibly in the form of an $\text{Ag}_n^+ \leftarrow \text{S}$ complex.^{45–47}

Effect of Temperature on the Degradation of CP. For this study, 5 mL of 10 ppm CP solution (in 1:1 methanol:water) was treated with the centrifugate obtained after centrifuging 5 mL of Ag@citrate NPs (at 10 000 rpm for 6–7 min) at 15, 25, and 35 °C. After 12 h, solutions were centrifuged at 6000 rpm and supernatants were analyzed using UV–vis absorption spectroscopy. In 35 °C solution, NPs were precipitated, whereas in 25 and 15 °C solutions, no precipitation of NPs was seen. The data are shown in the Supporting Information (Figure S5). For a given concentration of NPs and CP, the rate of degradation was increased with an increase of temperature. After 12 h, at 15 and 25 °C, 50 and 68% of CP was degraded, respectively (traces b and c, respectively in Supporting Information, Figure S5). At 35 °C, complete degradation of CP was noticed, as indicated by the presence of a peak at 320 nm (Supporting Information Figure S5, trace d).⁴⁸ In all cases, the red shift of surface plasmon of NPs due to aggregation was seen.³⁸

Interaction of Alumina Supported Ag@Citrate NPs with CP. In applications, it is necessary to use supported nanoparticles. Alumina-supported Ag@citrate NPs were treated

with CP (in 1:1 methanol + water). The samples were analyzed with UV–vis, ESI MS, and XPS techniques. Ten mL of 2 ppm CP solution was treated with 100 mg of alumina-supported Ag@citrate NPs, and the solution was analyzed with absorption spectroscopy as a function of time (Figure 8). After 5 min, only

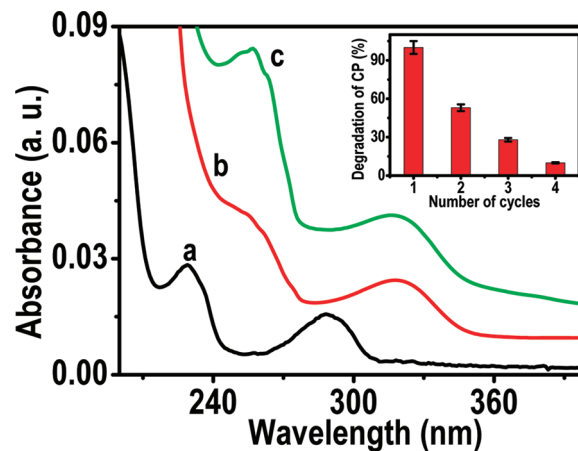
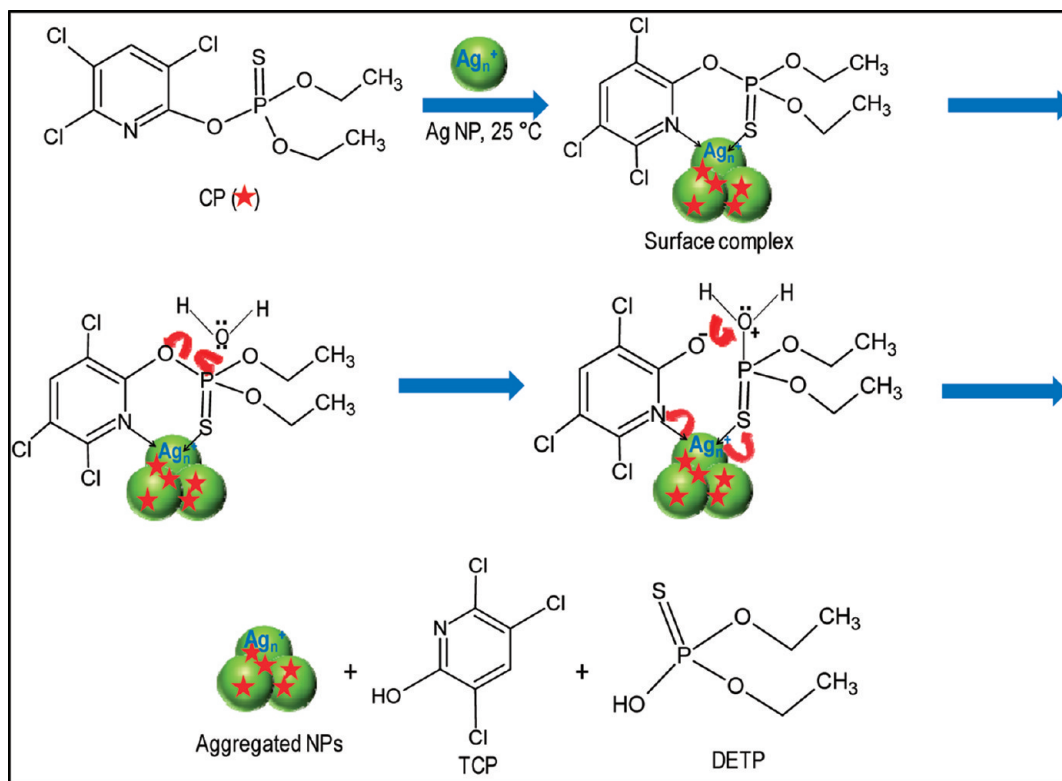


Figure 8. UV–vis absorption spectra of solutions of 2 ppm CP treated with alumina-supported Ag@citrate NPs after 5, 180, and 240 min of exposure (traces a, b, and c, respectively). Inset shows the percentage of degradation of CP in each cycle. The error bar is 4%.

features of CP (229 and 289 nm) are seen (Figure 8, trace a). After 3 h, a new peak appeared at 320 nm, which is due to the formation of TCP, and the 289 nm peak due to CP almost disappeared (Figure 8, trace b).⁴⁸ After 4 h, complete disappearance of the CP peak was seen (Figure 8, trace c). The rise in background of absorption may be due to the presence of nanoscale particulates of alumina (even in the centrifuged sample).

Recycling of Alumina Supported Ag@Citrate NPs. Reuse of NPs supported on alumina (100 mg) for the degradation of 2 ppm CP solution (10 mL) was studied for four cycles. In each cycle, reaction was done for 4 h by stirring at 1500 rpm. After the reaction, material was centrifuged in each cycle at 8000 rpm for 6–7 min, and the resulting centrifugate was washed with methanol two times to remove any adsorbed CP or degraded product of CP. The percentage of degradation of CP was calculated using the area under the peak at 289 nm in the absorption spectrum of the supernatant. In the first cycle, complete degradation was seen and it decreased to 53, 28, 10% in the second, third, and fourth cycles, respectively (inset of Figure 8). The decrease in percentage of decomposition of CP may be due to the coverage of CP on the nanoparticle surface, which was not removed even after washing twice.

The ESI MS analysis of supernatant solutions in the first cycle revealed the formation of TCP and DETP as products of degradation of CP (data not shown). The XPS data of alumina-supported Ag@citrate NPs treated with 2 ppm CP solution for 4 h are shown in the Supporting Information: parts A, B, C, and D of Figure S6 are C 1s, Ag 3d, O 1s and Al 2p regions, respectively. Traces a and b correspond to alumina-supported Ag@citrate NPs before and after treatment of CP, respectively. The C 1s peaks at 285.0, 286.0, 288.5, and 290.0 eV may be due to C–C, C–O, O–C–O, and O=C–O carbons, respectively⁴¹ (Supporting Information, Figure S6A, trace a). After treatment of CP, C 1s peaks are noticed at the same positions, which indicate no change in citrate protection

Scheme 1. Representation of Degradation of CP on Ag NPs^a

^aAdsorbed CP molecules are shown with red stars.

(Supporting Information, Figure S6A, trace b). The peak of Ag 3d_{5/2} is noticed at 368.3 eV before and after treatment of CP (traces a and b, respectively, in Supporting Information, Figure S6B) due to silver in the zerovalent state. The O 1s peaks are noticed at 529.3, 531.2, and 532.8 eV before and after treatment of CP (traces a and b, respectively in Supporting Information, Figure S6C). The peaks at 529.3, 531.2, and 532.8 eV may be assigned to oxygen of alumina, hydroxyl groups of citrate, and oxygen of carboxylate groups, respectively.³⁵ The Al 2p peak at 74.6 eV due to alumina appears before and after treatment of CP (traces a and b, respectively of Supporting Information, Figure S6D).

Mechanism of Decomposition. A mechanism is proposed on the basis of results obtained from UV–vis absorption, ESI MS, TEM, XPS, and Raman measurements and is depicted in Scheme 1. The NP can bind with sulfur and nitrogen atoms to form a surface complex,²⁵ as they have a lone pair of electrons. The formation of the Ag_n⁺←S bond is confirmed by Raman spectroscopy (Figure 7).⁴⁵ Due to the electron polarization in the proposed surface complex, the side chain link to the pyridine ring may get weakened.²⁵ The P–O bond may cleave, which results in the attack of water (nucleophile) at the electrophilic phosphorus site.¹⁹ Since TCP is a stable aromatic compound, nitrogen will withdraw electrons from a coordination bond (to Ag_n) to produce TCP. Then, DETP, which is also a stable molecule, may form after withdrawing sulfur electrons from the coordination bond. Aggregation of Ag NPs due to adsorption of CP molecules was confirmed by TEM images and the red shift of the UV–vis spectra. The adsorbed CP molecules are shown with a star symbols in the scheme. Presence of adsorbed species has been confirmed by elemental mapping and various spectroscopic studies.

Effect of pH on the Degradation of CP. CP is known to undergo degradation to give TCP and DETP at basic pH.¹⁹ The results shown above are at neutral pH. The same degradation is also noticed at basic pH, in the presence of supported nanoparticles. However, unsupported Ag NPs are unstable at high basic pH. In the acidic pH range, NPs leach into the solution, resulting in a decrease in the rate of degradation compared to basic pH (data not shown).

Reaction of CP with Au@Citrate NPs. Au@citrate NPs were synthesized³⁸ similar to Ag@citrate NPs. A 5 mL solution of as-synthesized Au@citrate NPs was centrifuged at 10 000 rpm for 6–7 min to remove excess citrate. To the residue, 5 mL of 10 ppm CP solution (in 1:1 water:methanol mixture) was added and the mixture was stirred at 1500 rpm. The absorption spectra of the reaction mixtures were collected at different times and data are shown in Figure 9A. The absorption feature of NPs at 522 nm got shifted to 530 and 690 nm, which may be due to aggregation. The red color of Au NPs turned to blue. The background of the spectra increased with time, which may be due to aggregation of NPs leading to the formation of turbidity in the solution. After 7 h (trace b), a hump at 320 nm is noticed that may be due to TCP.⁴⁸ A very small conversion of CP to TCP was noticed as parent CP was still observed even after 6 days, whereas in the case of Ag NPs, conversion was complete in 2 days. The ESI MS data also revealed the presence of CP in the solution after 6 days (data not shown). Aggregation of NPs was confirmed by TEM analysis after reaction for 7 h. A large-area TEM image is shown in Figure 9B. Small-area TEM images of Au@citrate NPs before and after treatment of 10 ppm CP solution for 7 h are shown in the Supporting Information (Figure S7, parts A and B, respectively).

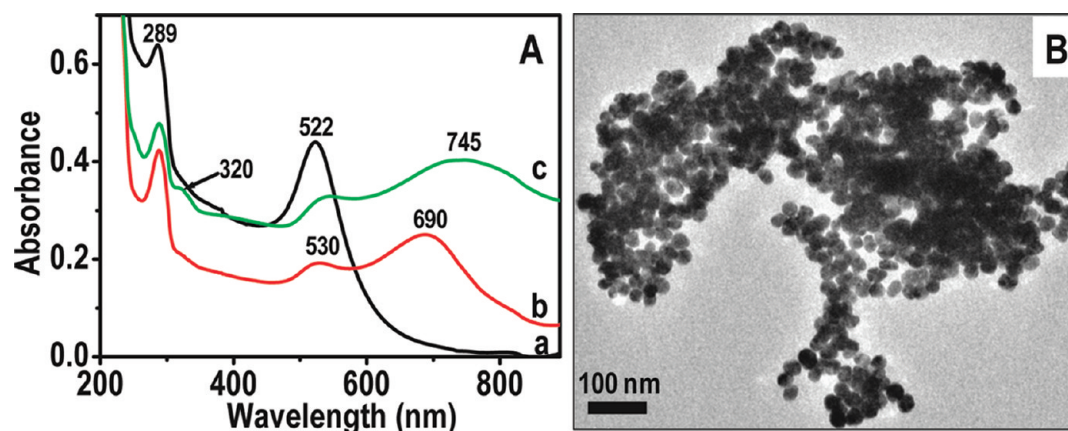


Figure 9. UV-vis absorption spectra (A) of Au@citrate NPs + 10 ppm CP reaction mixture at different times. Traces a–c are at 5 min, 7 min, and 150 h, respectively. B is the large-area TEM image of above reaction mixture after 7 h.

Control Experiments. To prove the degradation of CP in the presence of NPs, several control experiments were performed. The possibility of degradation of CP at room temperature in 1:1 water:methanol mixture was checked by measuring the absorption spectrum of CP with time. No change in the absorption spectrum was seen, even after 5 days at room temperature (Supporting Information, Figure S8A). The effect of alumina substrate on the degradation of CP was also checked using 3 ppm CP solution. The absorption spectrum of CP after 24 h showed a small ($\sim 10\%$) conversion to TCP (Supporting Information, Figure S8B, trace b). Unprotected NPs were synthesized by reducing silver nitrate with ice-cold sodium borohydride, which show surface plasmon absorption at 390 nm (data not shown). As-synthesized Ag NPs were immediately loaded on neutral alumina and were used for the degradation of 1 ppm CP. CP was completely degraded to give a peak at 320 nm in the absorption spectrum after 24 h (Figure S8B, trace c). Monolayer-protected Ag@MSA NPs were synthesized according to the literature³⁶ and loaded on alumina. These NPs were used for degradation of CP (2 ppm). After 3 h, the TCP peak at 320 nm was seen in the absorption spectrum (Supporting Information, Figure S9, trace c).⁴⁸ After 5 h, the CP peak at 289 nm disappeared completely, indicating the complete degradation of CP (Supporting Information, Figure S9, trace e). All these studies were done at neutral pH. The importance of NPs is verified by using bulk silver powder (black in color), which was obtained by reducing AgNO_3 with sodium borohydride. In this case, only $\sim 5\%$ of CP was converted to TCP even after 2 days (data not shown). All these control experiments revealed that Ag NPs, both unprotected and monolayer-protected, in supported and unsupported forms, help in the degradation of CP.

CONCLUSIONS

The degradation of CP by Ag and Au NPs was investigated at room temperature. The degradation products, TCP and DETP, were confirmed using tandem ESI MS. A mechanism of degradation of CP was proposed based on TEM, EDAX, XPS, and Raman results. To the best of our knowledge, this is the first report on the chemistry of Ag NPs for the degradation of CP. Unsupported Ag and Au@citrate NPs show aggregation after adsorption of CP, leading to the red shift of surface plasmon of NPs. The activity of Ag NPs is greater than that of Au NPs in the degradation of CP. Unprotected and monolayer-protected Ag NPs are also found to show degradation of CP.

Supported Ag and Au NPs can be used to degrade CP efficiently, because these may be reused, as aggregation of particles is avoided. The rate of degradation of CP can be increased with an increase of temperature and pH of the solution. However, the fact that degradation occurs at room temperature and on supported NPs is important, as these allow the utilization of such materials for water purification. In such applications, it is necessary that there is a postdegradation step to remove the degradation products by adsorbents such as activated carbon. The degraded products may undergo subsequent chemistry with nanoparticles, and this aspect needs to be explored. It is also necessary to extend this work to other pesticides of relevance so that viable technologies are developed.

ASSOCIATED CONTENT

Supporting Information

TEM images, EDAX, ESI MS, UV-vis, and XPS data of Ag NPs and reaction products of CP. This material is available free of charge via the Internet at <http://pubs.acs.org>.

AUTHOR INFORMATION

Corresponding Author

*E-mail: pradeep@iitm.ac.in.

Notes

The authors declare no competing financial interest.

ACKNOWLEDGMENTS

We thank the Department of Science and Technology (DST), Government of India, for constantly supporting our research program on nanomaterials. M.S.B. thanks the CSIR for a research fellowship.

REFERENCES

- (1) Zhang, K.; Mei, Q. S.; Guan, G. J.; Liu, B. H.; Wang, S. H.; Zhang, Z. P. *Anal. Chem.* **2010**, *82*, 9579–9586.
- (2) Sharma, D.; Nagpal, A.; Pakade, Y. B.; Katnoria, J. K. *Talanta* **2010**, *82*, 1077–1089.
- (3) Kamel, A.; Byrne, C.; Vigo, C.; Ferrario, J.; Stafford, C.; Verdin, G.; Siegelman, F.; Knizner, S.; Hetrick, J. *Water Res.* **2009**, *43*, 522–534.
- (4) Murillo, R.; Sarasa, J.; Lanao, M.; Ovelleiro, J. L. *Water Sci. Technol.* **2010**, *10*, 1–6.
- (5) Garcia-Reyes, J. F.; Gilbert-Lopez, B.; Molina-Diaz, A.; Fernandez-Alba, A. R. *Anal. Chem.* **2008**, *80*, 8966–8974.

- (6) Sinha, S. N.; Pal, R.; Dewan, A.; Mansuri, M. M.; Saiyed, H. N. *Int. J. Mass Spectrom.* **2006**, *253*, 48–57.
- (7) Farag, A. T.; El Okazy, A. M.; El-Aswed, A. F. *Reprod. Toxicol.* **2003**, *17*, 203–208.
- (8) Devi, L. G.; Murthy, B. N.; Kumar, S. G. *J. Mol. Catal. A* **2009**, *308*, 174–181.
- (9) Eaton, D. L.; Daroff, R. B.; Autrup, H.; Bridges, J.; Buffler, P.; Costa, L. G.; Coyle, J.; McKhann, G.; Mobley, W. C.; Nadel, L.; Neubert, D.; Schulte-Hermann, R.; Spencer, P. S. *Crit. Rev. Toxicol.* **2008**, *38*, 1–125.
- (10) Agarwal, A.; Joshi, H. *Rec. Res. Sci. Technol.* **2010**, *2*, 51–57.
- (11) Wu, T.; Jans, U. *Environ. Sci. Technol.* **2006**, *40*, 784–790.
- (12) Berkelhammer, G.; Dauterman, W. C.; O'Brien, R. D. *J. Agric. Food Chem.* **1963**, *11*, 307–8.
- (13) Bellet, E. M.; Casida, J. E. *J. Agric. Food Chem.* **1974**, *22*, 207–211.
- (14) Ohashi, N.; Tsuchiya, Y.; Sasano, H.; Hamada, A. *Jpn. J. Toxicol. Environ. Health* **1994**, *40*, 185–192.
- (15) Duirk, S. E.; Tarr, J. C.; Collette, T. W. *J. Agric. Food Chem.* **2008**, *56*, 1328–1335.
- (16) Wu, J. G.; Laird, D. A. *Environ. Toxicol. Chem.* **2003**, *22*, 261–264.
- (17) Faust, S. D.; Gomaa, H. M. *Environ. Lett.* **1972**, *3*, 171.
- (18) Macalady, D. L.; Wolfe, N. L. *J. Agric. Food Chem.* **1983**, *31*, 1139–1147.
- (19) Smolen, J. M.; Stone, A. T. *Environ. Sci. Technol.* **1997**, *31*, 1664–1673.
- (20) Barcelo, D.; Durand, G.; Bertrand, N. D. *Toxicol. Environ. Chem.* **1993**, *38*, 183–99.
- (21) Li, X.; He, J.; Li, S. *Res. Microbiol.* **2007**, *158*, 143–149.
- (22) Tang, T.; Dong, J.; Ai, S.; Qiu, Y.; Han, R. *J. Hazard. Mater.* **2011**, *188*, 92–97.
- (23) Zhang, Y.; Xiao, Z.; Chen, F.; Ge, Y.; Wu, J.; Hu, X. *Ultrason. Sonochem.* **2010**, *17*, 72–77.
- (24) Anwar, S.; Liaquat, F.; Khan, Q. M.; Khalid, Z. M.; Iqbal, S. *J. Hazard. Mater.* **2009**, *168*, 400–405.
- (25) Mortland, M. M.; Raman, K. V. *J. Agric. Food Chem.* **1967**, *15*, 163.
- (26) Warner, C. L.; Addleman, R. S.; Cinson, A. D.; Droubay, T. C.; Engelhard, M. H.; Nash, M. A.; Yantasee, W.; Warner, M. G. *ChemSusChem* **2010**, *3*, 749–757.
- (27) Campelo, J. M.; Luna, D.; Luque, R.; Marinas, J. M.; Romero, A. *ChemSusChem* **2009**, *2*, 18–45.
- (28) Nair, A. S.; Pradeep, T. *Curr. Sci.* **2003**, *84*, 1560–1564.
- (29) Pradeep, T.; Anshup. *Thin Solid Films* **2009**, *517*, 6441–6478.
- (30) Gupta, R.; Kulkarni, G. U. *ChemSusChem* **2011**, *4*, 737–743.
- (31) Nair, A. S.; Pradeep, T. U. S. Patent 7,968,493B2, 2011.
- (32) Nair, A. S.; Pradeep, T. Indian Patent 200767.
- (33) Das, S. K.; Das, A. R.; Guha, A. K. *Langmuir* **2009**, *25*, 8192–8199.
- (34) Ratliff, J. S.; Tenney, S. A.; Hu, X.; Conner, S. F.; Ma, S.; Chen, D. A. *Langmuir* **2009**, *25*, 216–225.
- (35) Bootharaju, M. S.; Pradeep, T. *J. Phys. Chem. C* **2010**, *114*, 8328–8336.
- (36) Sumesh, E.; Bootharaju, M. S.; Pradeep, A. T. *J. Hazard. Mater.* **2011**, *189*, 450–457.
- (37) Nair, A. S.; Tom, R. T.; Pradeep, T. *J. Environ. Monit.* **2003**, *5*, 363–365.
- (38) Nair, A. S.; Pradeep, T. *J. Nanosci. Nanotechnol.* **2007**, *7*, 1871–1877.
- (39) Richardson, S. D. *Anal. Chem.* **2007**, *79*, 4295–4323.
- (40) Zhang, F. X.; Guan, N. J.; Li, Y. Z.; Zhang, X.; Chen, J. X.; Zeng, H. S. *Langmuir* **2003**, *19*, 8230–8234.
- (41) Bootharaju, M. S.; Pradeep, T. *Langmuir* **2011**, *27*, 8134–8143.
- (42) Pemberton, J. E.; Buck, R. P. *Anal. Chem.* **1982**, *54*, 1355–62.
- (43) Domazetis, G.; Raoarun, M.; James, B. D.; Liesegang, J.; Pigram, P. J.; Brack, N.; Glaisher, R. *Energy Fuels* **2006**, *20*, 1556–1564.
- (44) Zhang, X. F.; Shu, C. Y.; Xie, L.; Wang, C. R.; Zhang, Y. Z.; Xiang, J. F.; Li, L.; Tang, Y. L. *J. Phys. Chem. C* **2007**, *111*, 14327–14333.
- (45) Imai, Y.; Tamai, Y.; Kurokawa, Y. *J. Sol-Gel. Sci. Technol.* **1998**, *11*, 273–278.
- (46) Liu, B.; Han, G.; Zhang, Z.; Liu, R.; Jiang, C.; Wang, S.; Han, M. Y. *Anal. Chem.* **2012**, *84*, 255–261.
- (47) Sanchez-Cortes, S.; Domingo, C.; Garcra-Ramos, J. V.; Aznarez, J. A. *Langmuir* **2001**, *17*, 1157–1162.
- (48) Dilling, W. L.; Lickly, L. C.; Lickly, T. D.; Murphy, P. G.; McKellar, R. L. *Environ. Sci. Technol.* **1984**, *18*, 540–543.

Supporting information

Understanding the degradation pathway of the pesticide, chlorpyrifos by noble metal nanoparticles

M. S. Bootharaju and T. Pradeep*

DST Unit of Nanoscience (DST UNS), Department of Chemistry,

Indian Institute of Technology Madras, Chennai - 600 036, India

*E-mail: pradeep@iitm.ac.in

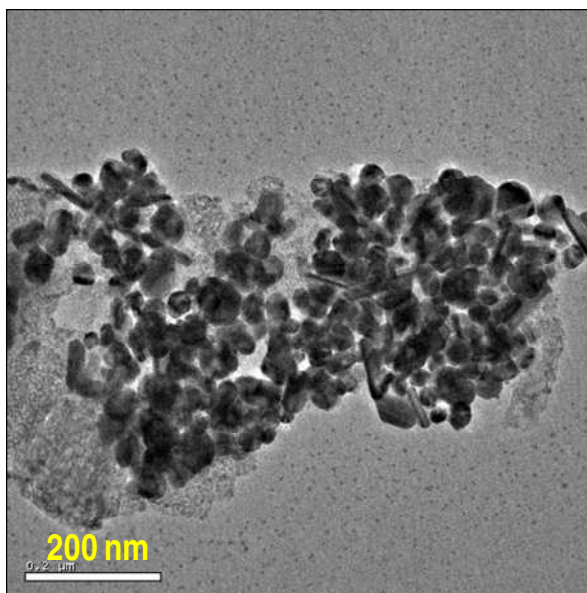


Figure S1. Large area TEM image of Ag@citrate NPs treated with 10 ppm CP for 48 h.

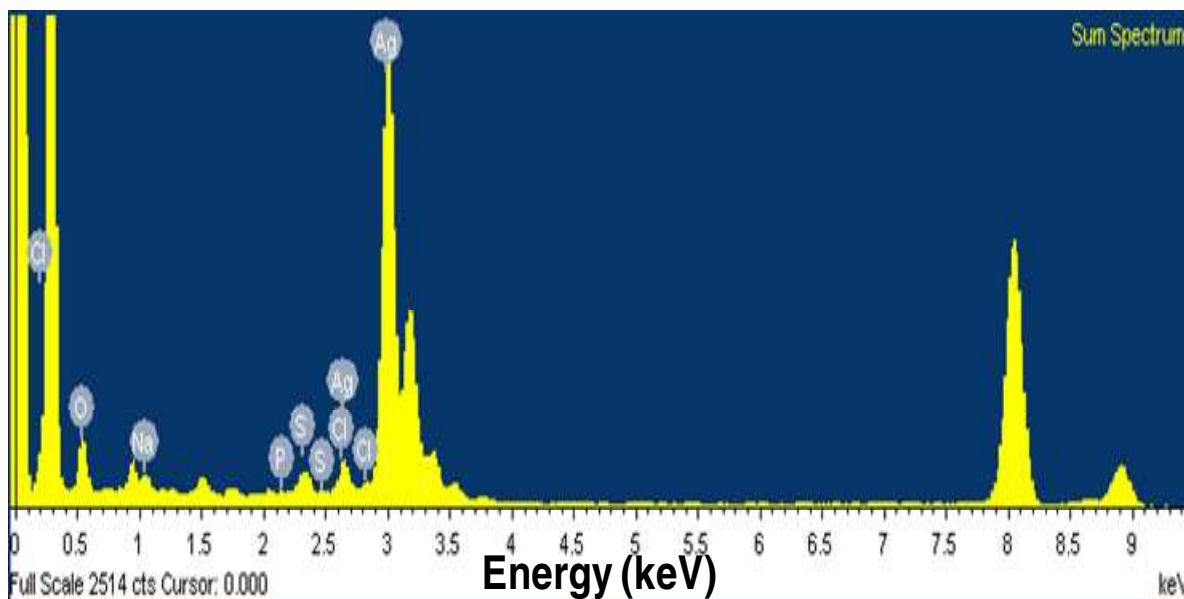


Figure S2. TEM-EDAX spectrum of Ag@citrate NPs treated with 10 ppm CP for 48 h.

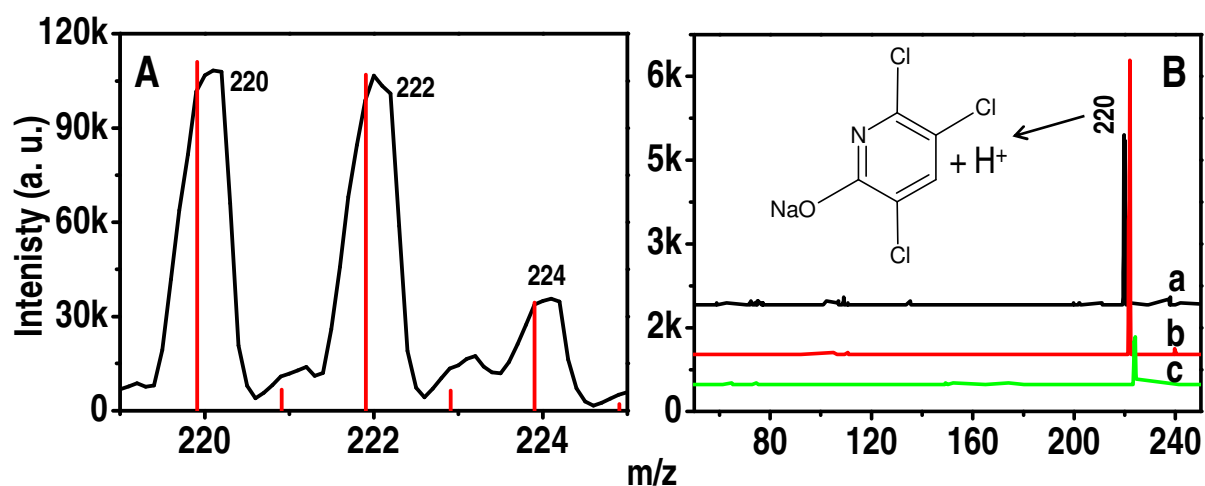


Figure S3. A) Comparison of the calculated mass spectral positions (red trace) of sodium salt of TCP and ESI MS of CP degradation product (black trace) in the m/z 220 region, in positive mode. B) ESI MS² of m/z 220, 222 and 224 (traces a, b and c, respectively) of degradation product of CP, in positive mode. The chemical structure of protonated sodium salt of TCP is also seen.

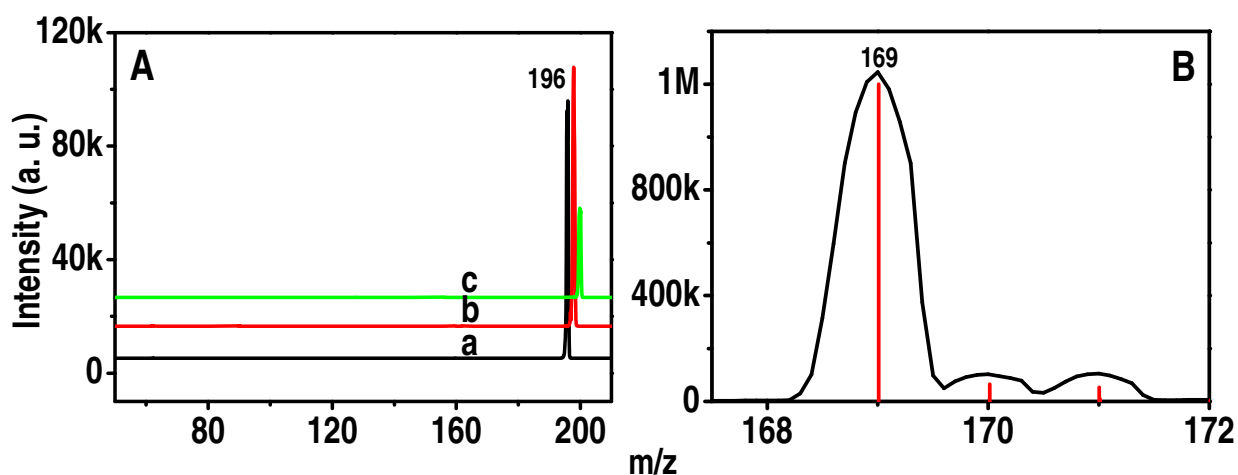


Figure S4. A) ESI MS² of m/z 196, 198 and 200 (traces a, b and c, respectively) of degradation product of CP, in negative mode. B) Comparison of the calculated mass spectral positions (red trace) of the anion of DETP and ESI MS of degradation product of CP (black trace) in the m/z 169 region, in negative mode.

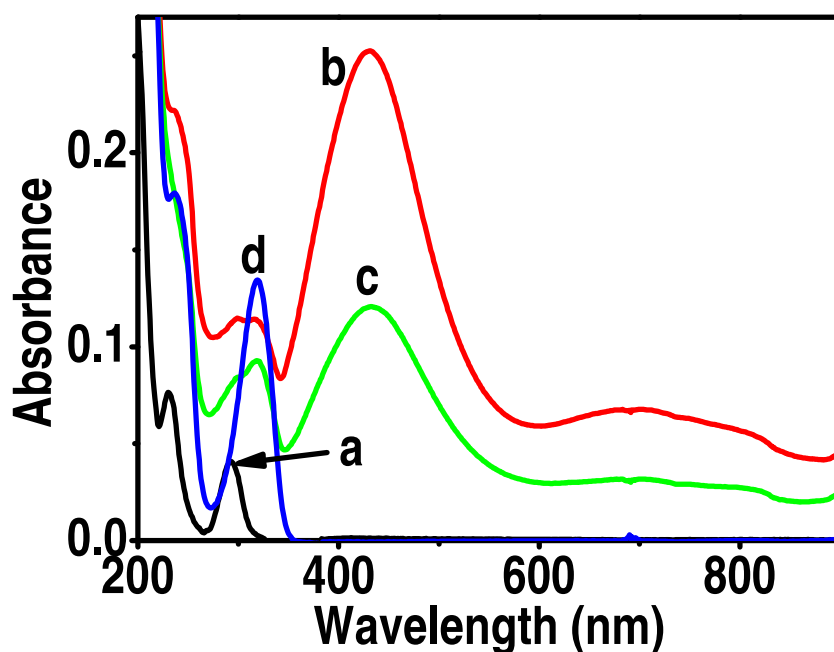


Figure S5. UV-vis absorption spectra Ag@citrate NPs treated with 10 ppm CP at 15, 25 and 35 °C (traces b, c and d, respectively). Absorption spectrum of 2 ppm CP (trace a) is shown for comparison.

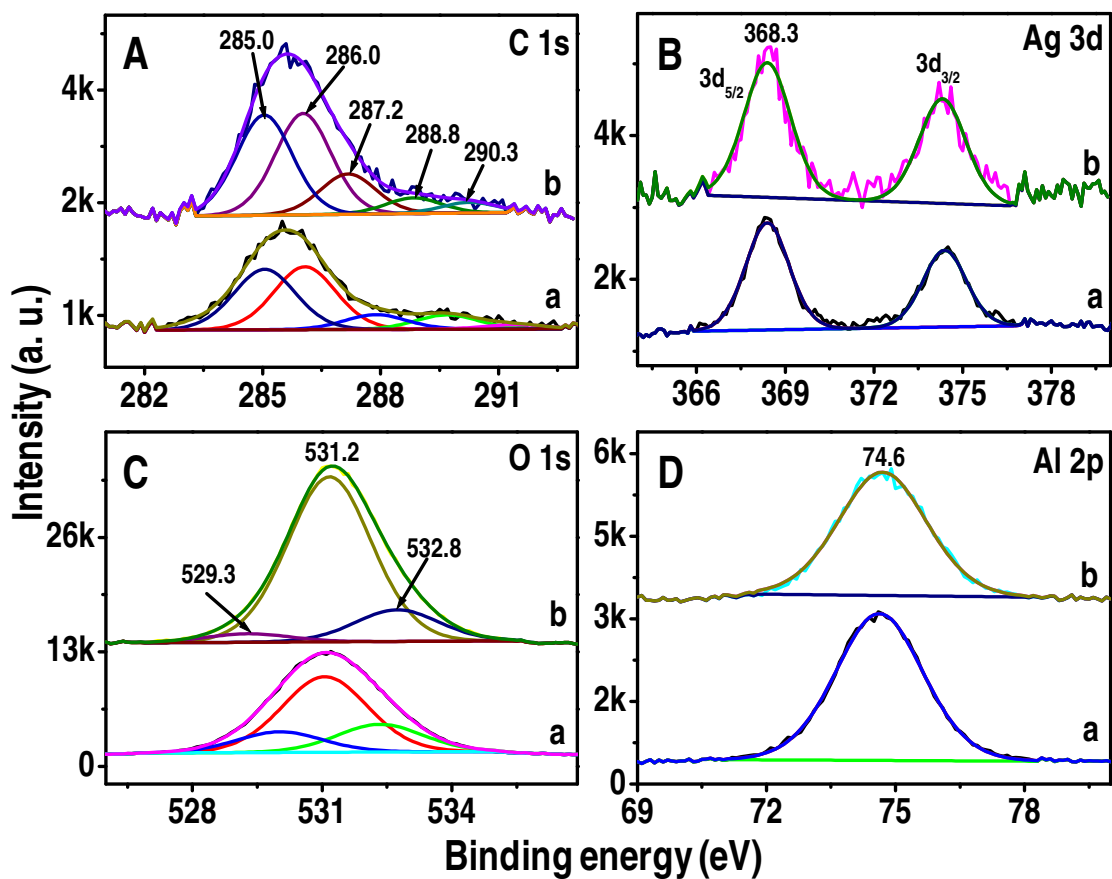


Figure S6. XPS spectra of alumina supported Ag@citrate NPs treated for 4 h with 2 ppm CP (traces b) in C 1s, Ag 3d, O 1s and Al 2p regions (A, B, C and D, respectively). Traces a correspond to parent alumina supported Ag@citrate NPs.

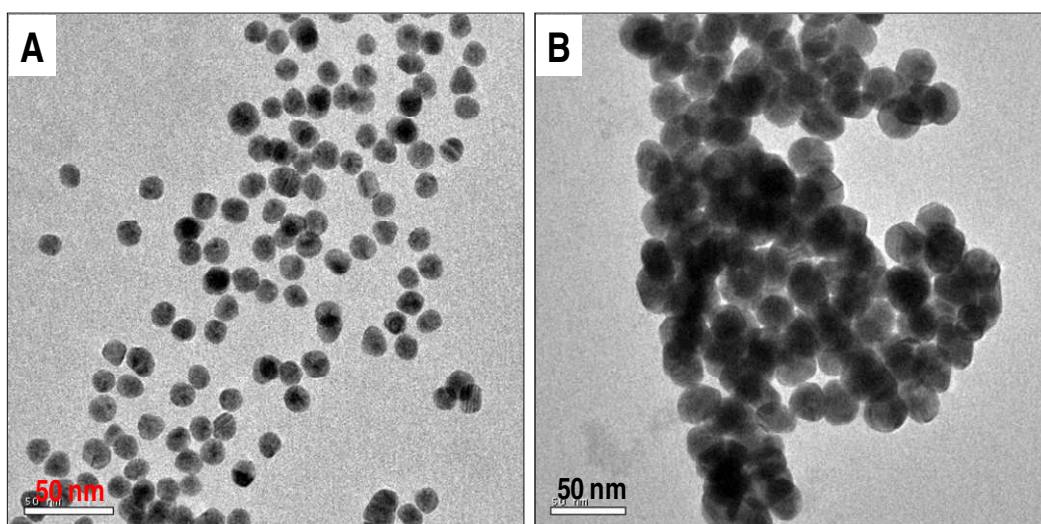


Figure S7. TEM images of as-synthesized Au@citrate (A) and reaction mixture of Au@citrate NPs and 10 ppm CP after 7 h (B).

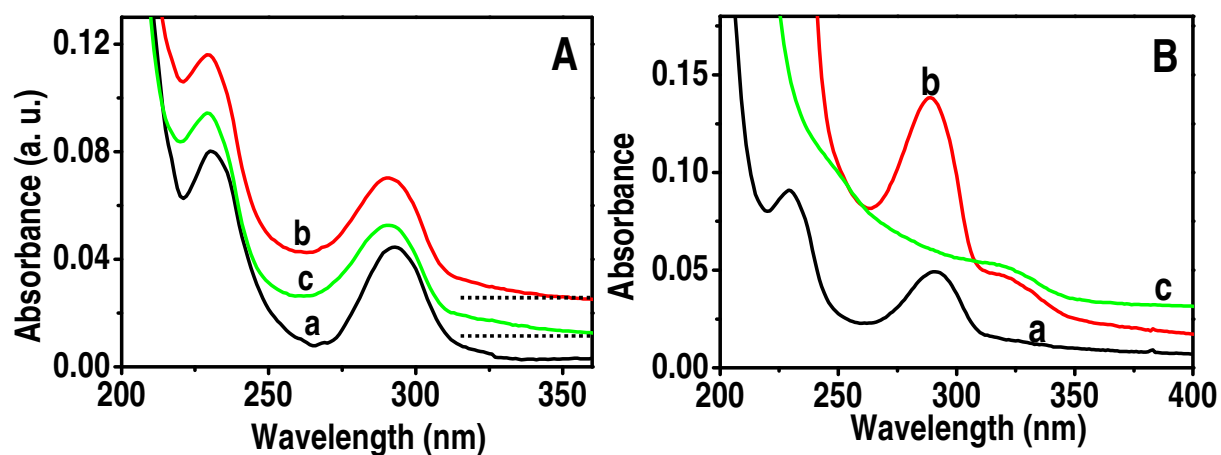


Figure S8. A) UV-vis absorption spectra of 1 ppm CP in 1:1 water + methanol mixture after 1, 3 and 5 days (traces a, b and c, respectively) at room temperature. Traces b and c are vertically shifted for clarity. B) UV-vis absorption spectra of 1 ppm CP and 1 ppm CP treated with unprotected Ag NPs supported on alumina (traces a and c, respectively). Trace b is the absorption spectrum of 3 ppm CP treated with alumina. In B all measurements were done after 24 hours.

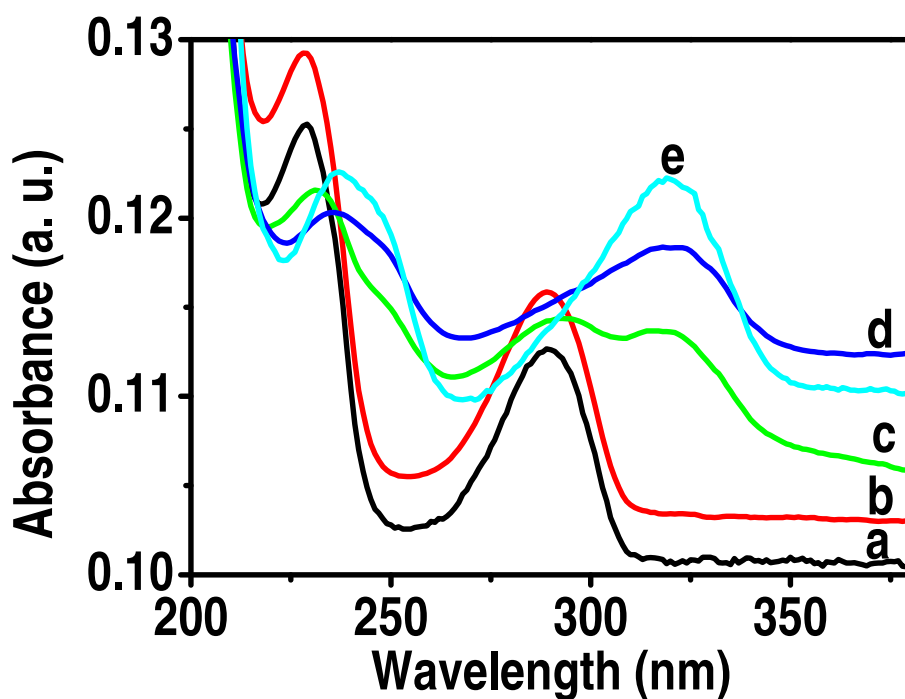


Figure S9. Absorption spectra of 2 ppm CP treated with Ag@MSA NPs loaded on alumina after 1, 2, 3, 4 and 5 hours (traces a, b, c, d and e, respectively). The rise in background of absorption spectrum in trace c is due to the presence of alumina particulates.

Cite this: *Nanoscale*, 2012, **4**, 3427

www.rsc.org/nanoscale

Functional hybrid nickel nanostructures as recyclable SERS substrates: detection of explosives and biowarfare agents†

P. R. Sajanlal and T. Pradeep*

Received 7th March 2012, Accepted 14th March 2012

DOI: 10.1039/c2nr30557g

We present the synthesis of highly anisotropic nickel nanowires (NWs) and large area, free-standing carpets extending over cm² area by simple solution phase chemistry. The materials can be post-synthetically manipulated to produce hybrid tubes, wires, and carpets by galvanic exchange reactions with Au³⁺, Ag⁺, Pt²⁺, and Pd²⁺. All of these structures, especially the hybrid carpets and tubes, have been prepared in bulk and are surface enhanced Raman scattering (SERS) active substrates. Molecules of relevance such as dipicolinic acid (constituting 5–15% of the dry weight of bacterial spores of *Bacillus anthracis*), dinitrotoluene, hexahydro-1,3,5-triazine (RDX), and trinitrotoluene at nanomolar concentrations have been detected. An enhancement factor of $\sim 10^{10}$ was observed for the Ni–Au nanocarpets. The reusability of the Ni–Au nanocarpets for SERS applications was tested 5 times without affecting the sensitivity. The reusability and sensitivity over large area have been demonstrated by Raman microscopy. Our method provides an easy and cost effective way to produce recyclable, large area, SERS active substrates with high sensitivity and reproducibility which can overcome the limitation of one-time use of traditional SERS substrates.

1. Introduction

Detection of trace amounts of explosives and chemical warfare agents is an important task in view of national security and defense. Potentially harmful materials such as disease causing bacterial spores, viruses, and toxins have to be identified at low concentrations quickly and accurately for the safety and well-being of the population. Though various detection techniques are available, systematic efforts have been ongoing to develop better analytical techniques to detect a multitude of hazardous materials in a cost-effective, rapid, and reliable manner. Anisotropic micro-/nanomaterials with well-defined physiochemical properties are of great interest to materials chemists in view of their morphology-, size-, and crystallinity-dependent intrinsic properties as well as attractive applications in the fields of catalysis, sensing, electronics, and bio-related applications.^{1–3}

Surface enhanced Raman scattering (SERS)^{4–10} is a phenomenon, exhibited by certain nanoparticles (NPs), which enables the rapid detection of molecules down to single molecule level, under ambient conditions. Highly anisotropic NPs such as triangles,^{11,12} stars,¹³ flowers,⁴ etc.^{4–9,11,14} are well-known for their

excellent SERS activity and related applications.¹⁵ Nanoparticle assemblies such as superlattices¹⁶ also show similar enhancement, enabling them for sensing applications.¹⁷ Theoretical predictions of field enhancement around various anisotropic nanostructures have been reported.^{13,18,19} However, cost-effective production of a robust, reusable, large-area, and homogeneous SERS substrate with high sensitivity and reproducibility still remains an important issue. In view of making appropriate and affordable SERS substrates, synthesizing SERS active nanomaterials by making a thin coating of Au or Ag on prefabricated, cheap substrates gained popularity.^{20,21} A periodic array of SERS active nanostructures can also be fabricated over a large area by nanosphere lithography techniques.²² Most of these techniques have the major disadvantage of being very time consuming with high production costs. Solution based synthesis of most of the anisotropic nanomaterials requires various surfactants such as cetyltrimethylammonium bromide (CTAB) and sodium dodecyl sulfate (SDS) and polymers such as poly(*N*-vinyl-2-pyrrolidone) (PVP) and polyamines. The presence of such organic coating may reduce the efficiency and sensitivity of these NPs towards SERS activity.

The galvanic displacement reaction^{23–28} is an easy way to make SERS active nanomaterials from a pre-fabricated NPs template. The galvanic displacement reaction has advantages over the other methods in synthesizing nanostructures since no surfactant or coordinating molecules are involved in the synthesis which can yield clean surfaces, and is an important attribute for surface enhanced spectroscopies. Here, we report the synthesis of thorny nickel nanowires (NWs) and nanocarpets (NCs) *via* a simple

DST Unit of Nanoscience (DST UNS), Department of Chemistry, Indian Institute of Technology Madras, Chennai 600 036, India. E-mail: pradeep@iitm.ac.in; Fax: +91-44 2257-0545

† Electronic supplementary information (ESI) available: SEM and EADX data of various materials such as Ni NC and NWs and their hybrid forms, SEM image of branched Ni NWs, XPS spectra of O 1s of various nanomaterials, Raman data showing higher detection limit and reusability of Ni–Au NCs. See DOI: 10.1039/c2nr30557g

chemical reduction route and their subsequent use as sacrificial templates for making highly SERS active, hybrid anisotropic materials such as Au–Ni NCs, NWs and nanotubes through the galvanic displacement reaction. Nickel NPs are very good candidates to use as sacrificial templates for making SERS active noble metal nanomaterials, as Ni is relatively cheap and has lower reduction potential (0.25 V for Ni^{2+}/Ni (vs. standard hydrogen electrode (SHE))) than noble metal ions (0.99 V for $\text{AuCl}_4^-/\text{Au}$, 0.76 V for $\text{PtCl}_4^{2-}/\text{Pt}$, and 0.59 V for $\text{PdCl}_4^{2-}/\text{Pd}$). Such hybrid materials show enhanced oxidation-resistance and stability, which make them useful for certain biological applications, catalysis and SERS.^{29–31} Various other nanosystems like Ni–Pd nanotubes, Ni–Pt and Ni–Ag NWs were also made to demonstrate the viability of our method to make various hybrid nanomaterials. Reusability and utility of the Ni–Au NCs in the detection of biomolecules, explosives, and an explosive surrogate at very low concentrations have been demonstrated using Raman spectroscopy and microscopy. Synthesis of such inexpensive, free standing, recyclable, large area SERS substrates by a fast chemistry without the aid of templates or surfactants is advantageous for developing applications.

2. Experimental

2.1. Materials

$\text{NiCl}_2 \cdot 6\text{H}_2\text{O}$, $\text{HAuCl}_4 \cdot 2\text{H}_2\text{O}$, PdCl_2 , and hydrazine monohydrate were purchased from SD Fine Chemicals, India (AR grade). Hexachloroplatinic acid ($\text{H}_2\text{PtCl}_6 \cdot 6\text{H}_2\text{O}$), dipicolinic acid (DPA), and 2,4-dinitrotoluene (DNT) were purchased from Sigma Aldrich. Trinitrotoluene (TNT) and hexahydro-1,3,5-triazine (RDX) were gifts from Indira Gandhi Centre for Atomic Research, Kalpakkam, India. All chemicals were used as such without further purification. Triply distilled water was used throughout the experiments.

2.2. Synthesis of nickel nanowires and nanocarpets

Ni NWs were synthesized by the reduction of nickel chloride in water using concentrated aqueous hydrazine hydrate (HyH) solution as the reducing agent. In a typical synthesis, 1 mL of 250 mM aqueous solution of nickel chloride was added to 9 mL of water at 80 °C to get 25 mM solution of Ni^{2+} . After about one minute, 1 mL of HyH solution was added drop-wise into the solution. No stirring was done during this process. After the addition of HyH, NCs were formed gradually inside the wall of the glass beaker as a silverish film after 5 min. These NCs measuring an area of $\sim 5 \text{ cm}^2$ were then peeled carefully off the beaker. Ni NWs were formed simultaneously inside the solution as a black network-like residue, which was separated by forceps. The NCs and NWs were washed carefully with distilled water and subsequently with alcohol, to remove excess of hydrazine and the other unreacted ions. The methodology could be scaled to get larger quantities of these materials of the order of grams.

2.3. Making of hybrid Ni nanotubes and wires

About 4 mg of the Ni NWs, synthesized as per the above procedure, were immersed inside 500 μL of 10 mM HAuCl_4 or H_2PdCl_4 solution in a vial. This solution was shaken gently for

5 min. After that, as formed Ni–Au and Ni–Pd nanotubes were separated out from the solution using a bar magnet. They were then washed carefully with distilled water and subsequently with alcohol, to remove unreacted ions.

In order to make hybrid Ni–Ag and Ni–Pt NWs the aforementioned experiment was conducted using 500 μL of 25 mM H_2PtCl_6 or AgNO_3 in place of Au and Pd precursors.

2.4. Ni–Au nanocarpets

Thin films of nickel NCs (4 mg, $\sim 2 \text{ cm}^2$) were immersed inside 500 μL of 10 mM of HAuCl_4 in a vial for about 5 min. A visible change from silverish to light brown color indicates the formation of Ni–Au NCs. The Ni–Au NCs were separated out carefully from the solution using forceps, washed with distilled water and subsequently with alcohol and dried. This material was later used for SERS measurements.

In all the abovementioned cases of synthesis of hybrid nanostructures, varying quantities of metal ions were added to the Ni nanostructures to deposit the required amount of metals on them.

3. Instrumentation

Scanning electron microscopy (SEM) imaging and energy dispersive analysis of X-ray (EDAX) studies were done with a FEI QUANTA-200 scanning electron microscope. Raman measurements were done with a WiTec GmbH, Alpha-SNOM CRM 300 instrument having a 633 nm laser with a maximum power of 35 mW. During the Raman measurements, the laser power has been adjusted so as to get a good Raman spectrum. The material was carefully transferred onto a cover glass, and required amounts of analyte solution of finite concentrations were mixed with it. It was then mounted onto the sample stage of the Raman spectrometer. For the SERS measurements, the backscattered light was collected using a 60 \times liquid immersion objective at an integration time of 1 s. For Raman imaging of Ni–Au nanotubes and Ni–Au NC, the backscattered light was collected using 100 \times and 20 \times objectives, respectively, at an integration time of 50 ms. A super notch filter placed in the path of the signal effectively cuts off the excitation radiation. The signal was then dispersed using a 600 grooves per mm grating, and the dispersed light was collected by a Peltier cooled charge coupled device (CCD). Raman enhancement factors were calculated as discussed in earlier reports.³² XPS measurements were done with an Omicron ESCA Probe spectrometer with unmonochromatized Al $K\alpha$ X-rays ($h\nu = 1486.6 \text{ eV}$).

4. Results and discussion

Highly thorny NWs and NCs of Ni were synthesized by following the procedure mentioned in the Experimental section and their morphology was studied using SEM. The NCs were separated as thin films which were several centimetres in length and width (Fig. 1). The surface of the NCs attached onto the wall of the glass beaker appeared silverish and was relatively smooth in appearance (photograph is given in Fig. 6). The other side of the NC which was not attached to the glass wall (in contact with the solution) was highly thorny in nature and appeared black (photograph in Fig. 6). The thorns, which were projecting

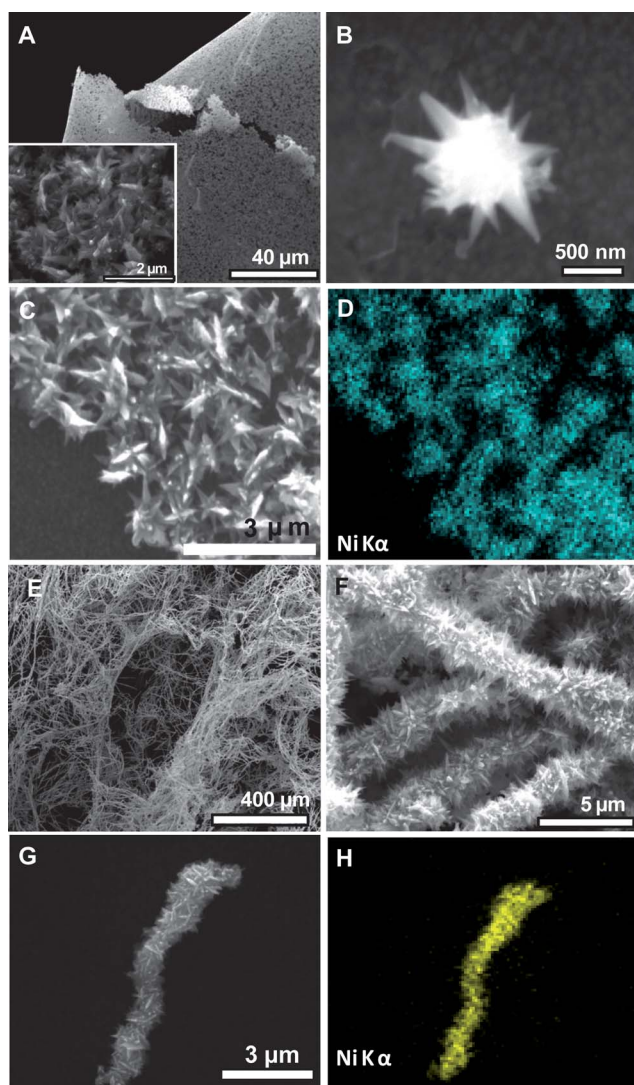


Fig. 1 SEM image of Ni NC (A) and a single nanoflower (B). Inset of (A) is an enlarged view of the Ni NC showing the presence of thorny projections. (C) and (D) are the SEM and corresponding Ni K α -based EDAX images of Ni NCs. (E) and (F) are the SEM images of thorny Ni NWs taken at various magnifications. (G) and (H) are the SEM and corresponding EDAX images of Ni NWs.

outward from the surface (the inset of Fig. 1A), gave a carpet-like appearance to these films. SEM analysis revealed that these NCs were formed by the self-assembly of several flower-shaped Ni NPs of around 1 μm size, as shown in Fig. 1B.

Since the constituent nanoflowers were not packed densely, the NC appeared highly porous in nature (Fig. 1A). The chemical composition of the Ni NCs was characterized using EDAX (Fig. 1C and D). They are mainly composed of Ni along with some amount of oxygen, probably formed due to the surface oxidation of Ni (ESI, Fig. S1 \dagger). While carpets were formed as films, Ni NWs 2 μm in diameter and length up to several hundred microns (Fig. 1E and F) were formed in the solution as a black mass within 10 min. These were separated from the solution using forceps. Closer examination revealed that these wires were highly anisotropic, constructed with a large number of thorns with a length of 100–300 nm (Fig. 1F). The NWs were highly

stable. Even long time (30 min) ultrasonication could not break them, indicating that the thorn-like building blocks had fused together.

The chemical composition of the NW was examined using EDAX (Fig. 1G and H). In addition to nickel, small amounts of oxygen were also present which might be attributed to the surface oxidation of nickel due to the high reactivity of elemental nickel (ESI, Fig. S2 \dagger).

The temperature dependence of the surface structure of these NWs has been studied. We found that the surface of the thorny NWs (Fig. 2A) became fairly smooth when the reaction was carried out at elevated temperatures in ethylene glycol as solvent. The synthesis yielded Ni NWs with an average diameter of ~ 200 nm in very large quantity without any other NPs of different morphology (Fig. 2A and B). The amount of HyH also plays an important role in determining the surface structure of the NW. At low concentration of HyH (100 μL), sphere-like NPs were formed and NWs were not seen (Fig. 2C). Some of these particles tend to self-assemble to form chain-like structures. As the amount of HyH increases (500 μL), an increase in the number of thorns present on the NW surface was observed (Fig. 2D). Further increase of the reducing agent (1 mL) resulted in the formation of highly thorny Ni NWs (Fig. 2E). The number of thorns was found to decrease when excess amount of reducing agent (5 mL) was added (Fig. 2F). At an elevated temperature and at a high concentration of the reducing agent, reduction of

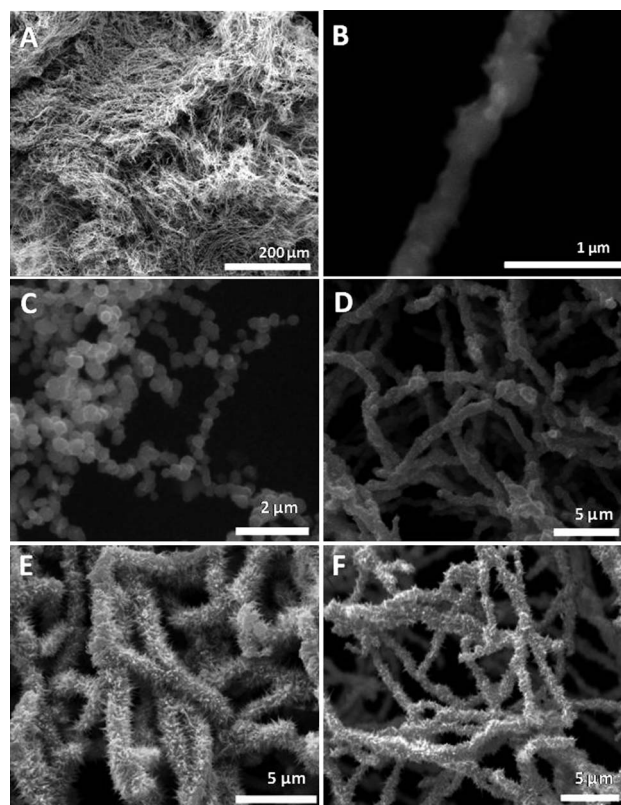


Fig. 2 Large area (A) and enlarged (B) SEM images of the Ni NWs formed when ethylene glycol was used as a solvent at 130 $^{\circ}\text{C}$. (C)–(F) are the SEM images of the nanostructures synthesized using various amounts of HyH such as 0.1, 0.5, 1.0, and 5.0 mL, respectively, keeping other parameters the same.

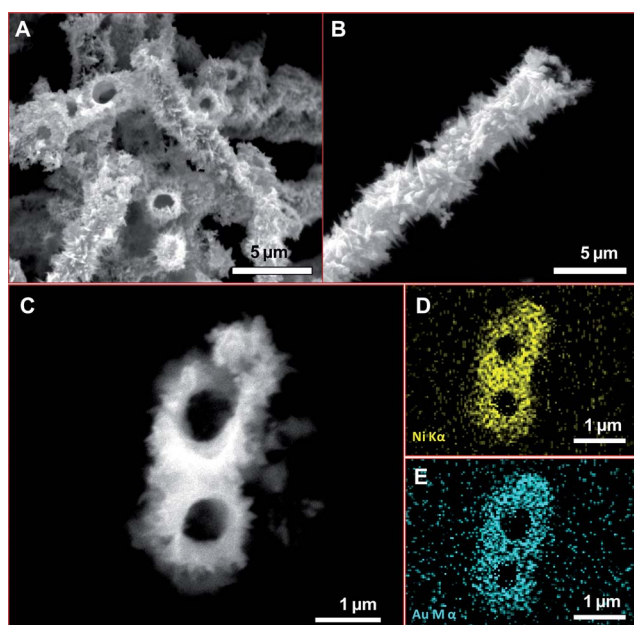


Fig. 3 SEM images (A–C) of the sample A_1 taken in various magnifications. (D) and (E) are Ni $K\alpha$ and Au $M\alpha$ based EDAX maps of the tip of a nanowire shown in (C).

metal ions may happen at a faster rate, resulting in the formation of a smooth surface. Though thorny NPs and NWs of Ni were seen earlier with the assistance of a surfactant and an external magnetic field,^{33–38} our synthetic protocol is very simple, which does not require any surfactant or magnetic field. It is proposed

that at the initial stage of the reaction, $NiCl_2$ undergoes complexation with HyH. In the subsequent step, this complex is reduced by excess HyH to form smaller Ni nuclei. These nanocrystals could serve as seeds as well as provide catalytic surfaces for further growth of larger particles. Further reduction of Ni ions happens at these seed surfaces in all directions to form spherical NPs.

Since the circumferential edges have higher free energies,³⁹ further reduction may preferentially occur at these relatively more active sites which lead to the formation of a spiky surface. The high reducing capacity of HyH at higher temperatures⁴⁰ enhances the reduction rate of Ni ions. At elevated temperatures, these spiky nanospheres may tend to join each other to reduce surface energy. Subsequently, these nickel crystals would connect to form hierarchical nickel NWs. Reduction in the surface energy by the elimination of the interface during this process may facilitate NW formation. In the following steps, further deposition of Ni ions continues at these spear-like nickel stems, which grow longer toward different directions until all of the nickel ions are consumed. Continuous heating of the reaction mixture for about 30 min resulted in the formation of branched NWs (ESI, Fig. S3†). In the case of NC formation, the assembly of smaller nanoflowers may happen laterally in all directions which results in sheet-like structures.

4.1. Galvanic replacement reaction

Since nickel has a relatively lower reduction potential than noble metals, the Ni NCs and NWs have been used as sacrificial templates for the galvanic displacement reaction^{23–26} to make

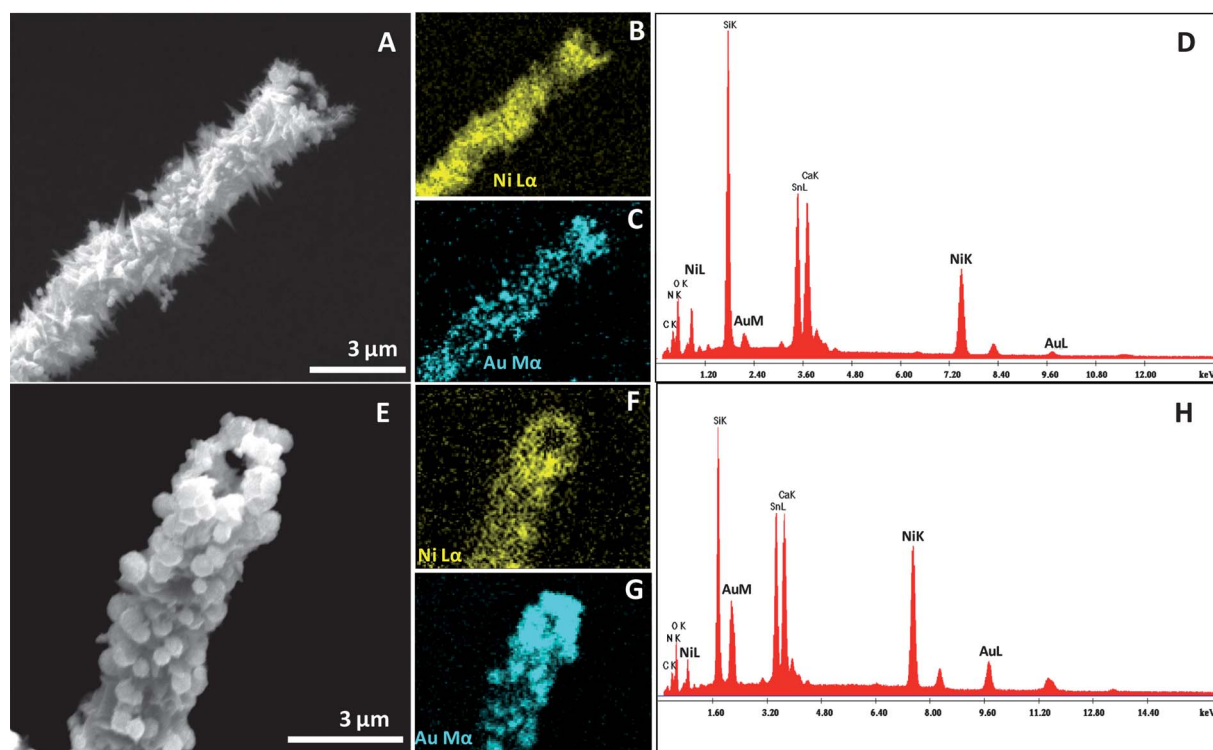


Fig. 4 (A) and (E) are the SEM images of the sample A_1 and A_2 , respectively. Corresponding EDAX images and spectra are also given. The elements Ca, Sn and Si are due to the ITO conducting glass substrate used.

hybrid systems with Au, Ag, Pt, and Pd. In such experiments, the metal nanocrystal will get oxidized by the noble metal ion which has a more positive reduction potential. In the case of Ni NWs, after the addition of Au^{3+} , interestingly we found that the NWs get converted to nanotubes. The resultant Ni–Au nanotubes were characterized using SEM (Fig. 3). Almost all the NWs underwent the galvanic displacement reaction and converted to nanotubes (Fig. 3A). Fig. 3B reveals the tubular nature of these hybrid nanomaterials. From the SEM images, it is clear that the tips of the NWs undergo reaction easily resulting in nanotubes with holes, mostly at the center of the tip which could be attributed to the high reactivity of the tip of such one dimensional NWs.⁴¹ After the addition of Au^{3+} into the Ni NWs, the displacement reaction happens at sites of relatively high surface energies such as point defects, stacking fault, steps, *etc.*⁴² During the reaction, Ni atoms diffused to the surface of the NCs and Au atoms diffused into the structure. More Ni atoms on the NW surface will get displaced by Au atoms as etching creates Ni surfaces with higher surface energies. At the same time, epitaxial growth of Au results in the formation of thin films at the surface of Ni NWs and subsequent etching will happen at the interior of the NWs, newly formed high energy Ni surfaces are now abundant. This could lead to the formation of nanotubes. The Kirkendall effect⁴³ is also expected to play a significant role in the formation of such nanotubes.

The chemical composition of these hybrid nanotubes was further confirmed by EDAX (Fig. 3C–E), which shows the presence of Ni and Au. Well-defined nanotubes as shown in Fig. 3 were obtained in 5 min when 500 μL of 10 mM of Au^{3+} was added into 4 mg of the Ni NWs (we refer to this sample as A_1). Upon increasing the concentration of Au^{3+} from 10 mM to 25 mM (referred to as A_2), a greater amount of gold was deposited onto the Ni NWs after 5 min and the NW surface was decorated with nearly spherical gold nanobeads.

SEM images and corresponding EDAX data showing the variation in the elemental compositions of the Ni–Au nanotubes with increasing concentration of Au^{3+} are given in Fig. 4. Ni–Au nanotubes formed after 5 min of addition of 500 μL of 10, 15, and 25 mM of Au^{3+} into 4 mg of Ni NWs are shown in ESI (Fig. S4†). As the reaction proceeds, a greater amount of Au was deposited onto the NW surface.

A similar approach was followed to make various hybrid nanomaterials such as Ni–Pd nanotubes, Ni–Pt, and Ni–Ag NWs. For Pd, by the addition of 500 μL of 25 mM Pd^{2+} solution, the Ni NWs were converted to Ni–Pd nanotubes as in the case of Ni–Au nanotubes (Fig. 5A and B) whereas the nanotube formation was not observed for the same amount of Ag or Pt ions. At this particular concentration of metal ions, instead of forming nanotubes, Ag and Pt got deposited onto the Ni NW surface to form hybrid Ni–Ag and Ni–Pt NWs, respectively. The

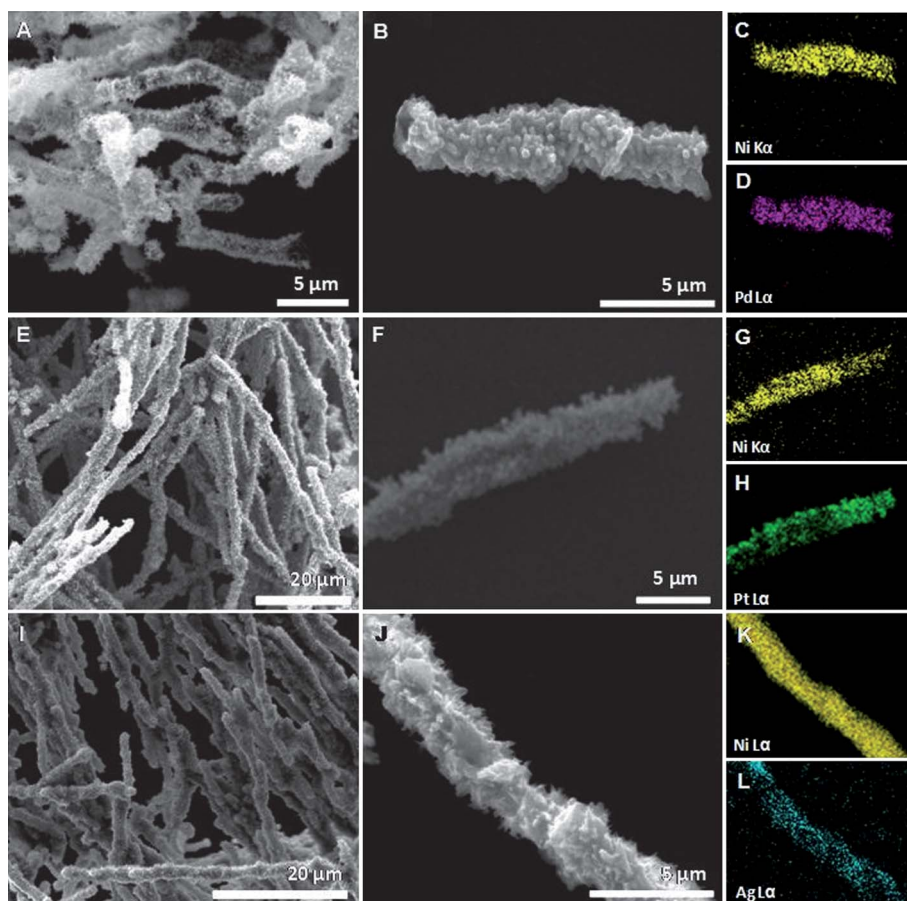


Fig. 5 (A), (E), and (I) are large area SEM images of Ni–Pd nanotubes, and Ni–Pt and Ni–Ag NWs, respectively. Single particle SEM images (B, F, and J) and corresponding EDAX images (C, D, G, H, K, and L) of these nanostructures are also given.

large area and corresponding single particle SEM images of Ni–Pd nanotubes as well as Ni–Pt and Ni–Ag NWs are given in Fig. 5. The chemical composition of these hybrid nanostructures was characterized using EDAX (Fig. 5C, D, G, H, K, and L).

We also made bimetallic Ni–Au NCs *via* the galvanic displacement reaction by the addition of Au^{3+} into the Ni NCs. By the addition of 500 μL of 10 mM of Au^{3+} into 4 mg of Ni NCs, we could make ~ 4 mg of Ni–Au bimetallic NCs (this sample is referred to as **B**₁ with 2 cm² surface area, having almost the same morphology as the parent Ni NCs (Fig. 6E)). After the deposition of Au, the sharpness of the thorns reduced slightly compared to that of Ni NCs (Fig. 6D). The inset of Fig. 6E shows a magnified SEM image of the bimetallic NCs in which the thorns are projecting outward from the surface. Photographs of a large-area Ni NC before and after treatment with Au^{3+} solution are shown in Fig. 6A–C.

As all the Au^{3+} added were not reacted with Ni atoms in the replacement reaction, a significant amount of Ni remained inside the nanocarpets (see ESI, Fig. S5†). As the reactivity at the tip of each thorn is high, the displacement reaction happened to a greater extent at the tip and a greater amount of Au was deposited at the tip. EDAX data suggested that the ratio of atomic percentage of Au and Ni in **B**₁ is $\sim 1 : 4$ (ESI, Fig. S5†). A greater amount of Au was deposited by increasing the concentration of Au^{3+} from 10 mM to 15 mM. The nanothorns present on the NCs were converted to spherical NPs with roughened surfaces of around 500 nm diameter, and the carpet was looking like a film made by the assembly of spheres as shown in Fig. 6F. Again when the concentration of Au increased to 25 mM (referred to as **B**₂), a greater amount of Au^{3+} was deposited and the size of the spheres increased from ~ 500 nm to ~ 3 μm (Fig. 6G). Even after the galvanic displacement reaction, these

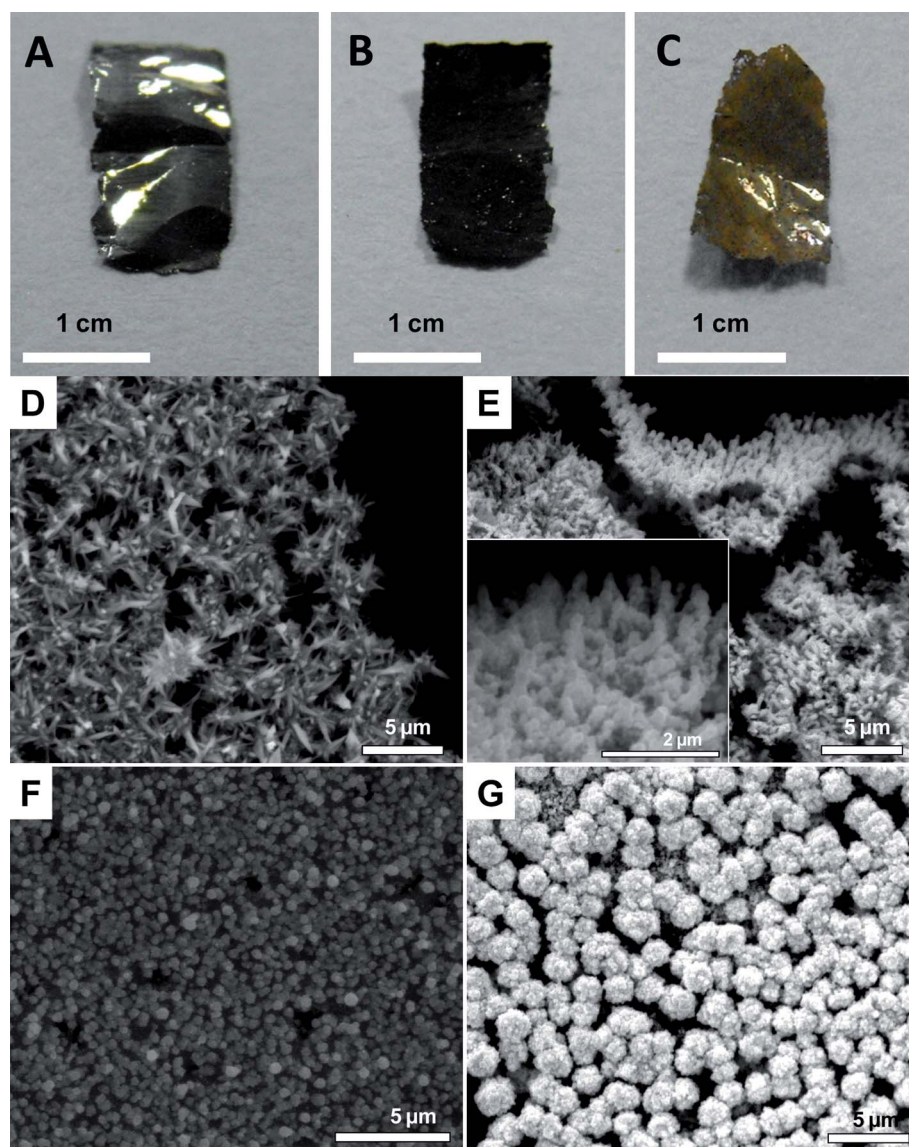


Fig. 6 Photographs of the Ni NC before (A (the side attached to the glass beaker is facing the viewer) and B (the side in contact with the solution)) and after (C) treatment with Au^{3+} solution. (D) SEM image of Ni NC showing a large number of spiky projections before the galvanic displacement reaction. (E)–(G) are Ni–Au NCs formed by the addition of 500 μL of 10, 15, and 25 mM of Au^{3+} , respectively, into 4 mg of Ni NCs.

NCs were not completely fragmented or disassembled, but existed as a film.

The chemical compositions of NCs and NWs of Ni and hybrid Ni–Au NCs and nanotubes were characterized by using X-ray photoelectron spectroscopy (XPS). The wide scan XPS spectra of NCs and NWs of Ni and bimetallic Ni–Au NCs and nanotubes are given in Fig. 7A. The enlarged scan of Ni 2p of Ni NCs and NWs showed $2p_{3/2}$ at ~ 855.5 eV and $2p_{1/2}$ at ~ 873.5 eV (Fig. 7B). At the same time, the Ni 2p region of Ni–Au NCs showed $2p_{3/2}$ at ~ 855.3 eV and $2p_{1/2}$ at ~ 873.3 eV (Fig. 7C). In the case of Ni–Au nanotubes, Ni $2p_{3/2}$ and $2p_{1/2}$ were observed at ~ 855.4 eV and at ~ 873.1 eV, respectively. The observed shift in the Ni 2p peaks in all the above mentioned cases toward the higher binding energy region compared to Ni(0) (852.6 eV) can be due to the possible existence of Ni²⁺ in the form of oxide coating on the surface of these Ni nanosurfaces. The presence of satellite peaks found in the high-binding energy region confirms the existence of Ni in its divalent state.^{44–46} Poor intensity of the satellite features indicates that the extent of surface oxidation at the surface of Ni nanostructures is small. The O 1s peaks found around 531.4 eV in all the cases (see ESI, Fig. S6†) again confirm the presence of O²⁻. The 4f region of Au in Ni–Au NCs and nanotubes is given in Fig. 7D. The spectra showed the presence of Au 4f_{7/2} and Au 4f_{5/2} peaks at ~ 84.1 and ~ 87.8 eV, respectively, confirming the existence of gold in its metallic form, due to galvanic exchange.

4.2. SERS measurements

Noble metal NPs with sharp edges and corners exhibit an enhanced electric field around these locations capable of enhancing the intensities of Raman signals of molecules present there.^{4,8,9,47,48} In our case, these spiky Ni–Au bimetallic nanotubes and NCs with highly roughened surfaces, devoid of any surfactants or organic species, exhibited very good SERS activity. The SERS activity of the nanomaterials has been studied using crystal violet (CV) as the analyte. For the SERS study, we selected four different substrates such as Ni–Au nanotubes (A₁ and A₂) and Ni–Au NCs (B₁ and B₂).

Samples A₁ and B₁ corresponding to reaction with 10 mM Au³⁺ showed much better SERS activity compared to the other two using a higher concentration of Au³⁺. The SERS spectra collected from various nanomaterials and corresponding SEM images are given in Fig. 8. From a detailed study, we found that the sample B₁ can detect CV up to a concentration of 10⁻¹¹ M (ESI, Fig. S7†) with an enhancement factor^{49,50} of the order of $\sim 10^{10}$. Even at a concentration of 10⁻¹¹ M, we got characteristic Raman features of CV adsorbed on Ni–Au NC. The high SERS activity of Ni–Au NCs and nanotubes can be attributed to the presence of the spiky tips as well as highly corrugated surfaces acting as hot spots. Comparatively less SERS activity of the other two systems (A₂ and B₂) can be due to the absence of the sharp thorns (due to the deposition of a greater amount of Au³⁺, spiky thorns were converted into nearly spherical particles). However, they also showed SERS activity with an EF of the order of $\sim 10^7$, attributed to the presence of a highly roughened surface. Apart from this, the junction between the adjacent nanospheres in the self-assembled film or wires can also act as hot spots, capable of enhancing the intensity of Raman signals. Recently, Mirkin *et al.* have shown that very long range SERS is

possible in a nickel NW separated by a pair of gold nanodisks by the excitation of the surface-plasmon resonance from the gold nanodisk pair.⁵¹ A Raman image of a Ni–Au nanotube created by integrating the spectral intensities of adsorbed CV molecules

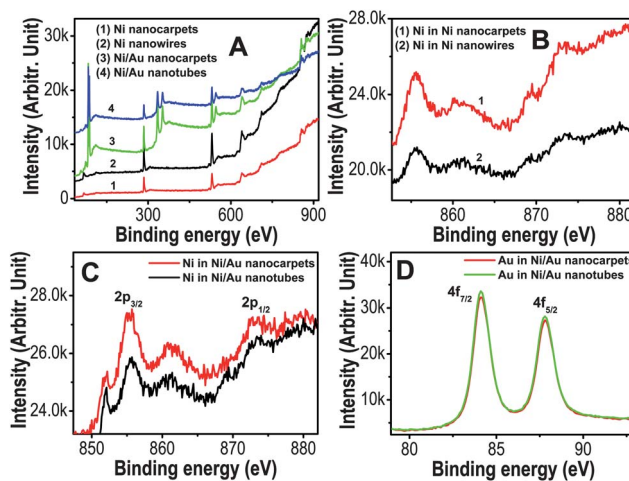


Fig. 7 (A) Wide scan XPS spectra of NCs and NWs of Ni and bimetallic Ni–Au NCs and nanotubes. (B) The Ni 2p region of Ni NCs and NWs. (C) The Ni 2p region of Ni–Au NCs and nanotubes. (D) The Au 4f region of Ni–Au NCs and nanotubes.

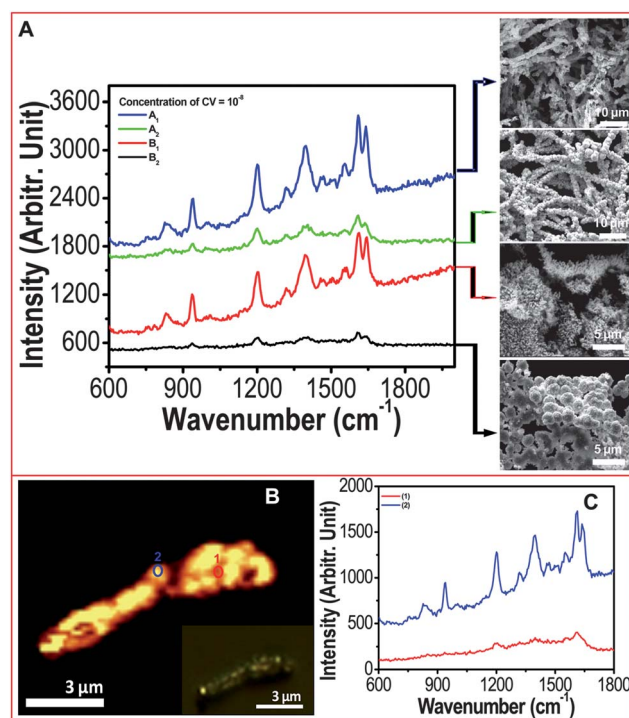


Fig. 8 (A) Raman spectra collected from A₁, A₂, B₁, and B₂ upon exposure to 10⁻⁸ M CV. Representative large area SEM images of each Ni–Au nanosubstrate are shown along with the spectra. (B) Raman image of a Ni–Au nanotube created by integrating the spectral intensities of adsorbed CV between 1200 and 1700 cm⁻¹. The inset shows the optical image of the nanotube used for Raman imaging. (C) Raman spectra collected from the two regions marked in the Raman image shown in (B).

(10^{-8} M) between the 1200 and 1700 cm^{-1} window is shown in Fig. 8B. From the Raman image, it is clear that the enhancement of the Raman features is not uniform throughout the nanotubes.

The spectra collected from various regions of the nanotube showed varying intensities at different regions (Fig. 8C). This can be due to the uneven distribution of gold at the surface of the nanotubes. The more SERS active Au rich region (spot 2) showed higher intensities compared to the Ni rich areas (spot 1) which is not as good as Au in terms of its SERS activity. This result confirms that the deposition of Au onto the Ni NW during the galvanic displacement reaction is not uniform; hence there will be slight differences in the intensities of SERS signal at different points.

Taking advantage of the high SERS activity of sample **B₁**, we demonstrated the utility of this material as an SERS substrate for the detection of certain analytes such as DPA, a molecule which constitutes 5 to 15% of the dry weight of the bacterial spore of *Bacillus anthracis*, the explosives TNT and RDX and an explosive surrogate, DNT. In our study, first we took the Ni–Au NCs on a glass substrate and 20 μL of the analyte solutions of different concentrations were drop-casted. The substrate was subjected to an SERS test in ambient air. The back-scattered light was collected using a 60 \times liquid immersion objective with an integration time of 1 s. The enhancement factors (EFs) were calculated in all the cases for a lower detection limit. We could detect the characteristic Raman features of DNT and TNT up to a concentration of 10^{-7} M (EF $\approx 10^6$) (Fig. 9). In the case of DPA, the detection limit was 10^{-8} M (EF $\approx 10^7$). We could get distinct Raman features up to 10^{-6} M (EF $\approx 10^5$) for RDX. In all the cases, the resulting Raman features were comparable with the standard solid samples. The multi-analyte detection capability of our SERS substrate makes it highly promising for defense- or diagnostics-related applications.

4.3. Reusability of Ni nanocarpet

Further, to demonstrate the reusability of the Ni–Au NCs after each Raman measurement, the substrate was subjected to a sequence of cleaning procedures. Each cycle of cleaning includes washing of the substrate with deionized water (after the SERS measurements) followed by gentle sonication with acetone for about 1 min. The substrate was then kept at 300 $^{\circ}\text{C}$ for 30 min in a furnace to remove volatile organic components and the resulting substrate was used for further SERS measurements. Even after heat treatment, the surface morphology of the NCs remained almost unchanged. Fig. 10A and B show the SEM

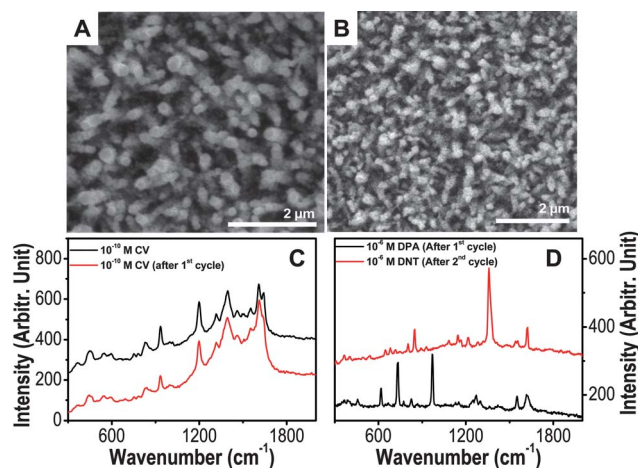


Fig. 10 SEM images of the sample **B₁** before (A) and after (B) the first cycle of cleaning. (C) Raman spectra of 10^{-10} M of CV collected from **B₁** before (black trace) and after 1st cycle of cleaning (red trace). (D) Raman spectra of 10^{-6} M of DPA and DNT adsorbed on **B₁** after 1st and 2nd cycles of cleaning.

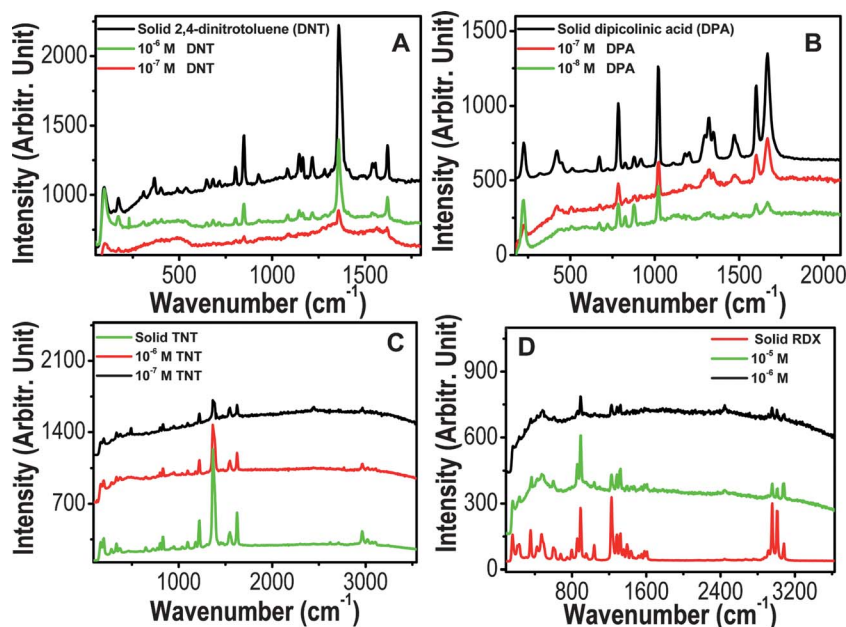


Fig. 9 Raman spectra of DNT (A), DPA (B), TNT (C) and RDX (D) solutions of various concentrations adsorbed on **B₁**. The traces are given in the same intensity scale, but shifted vertically for clarity.

images of the Ni–Au NCs before and after heat treatment. The resultant substrate was devoid of any Raman features of CV (ESI, Fig. S8†). Even though there is a possibility of oxidation of Ni during heat treatment, it did not affect the SERS activity of

the Ni–Au NC as gold is mainly responsible for the SERS enhancement which was quite stable at that temperature. However, it is to be noted that the adsorption strength of the analyte may also play a role in the reusability of this material.

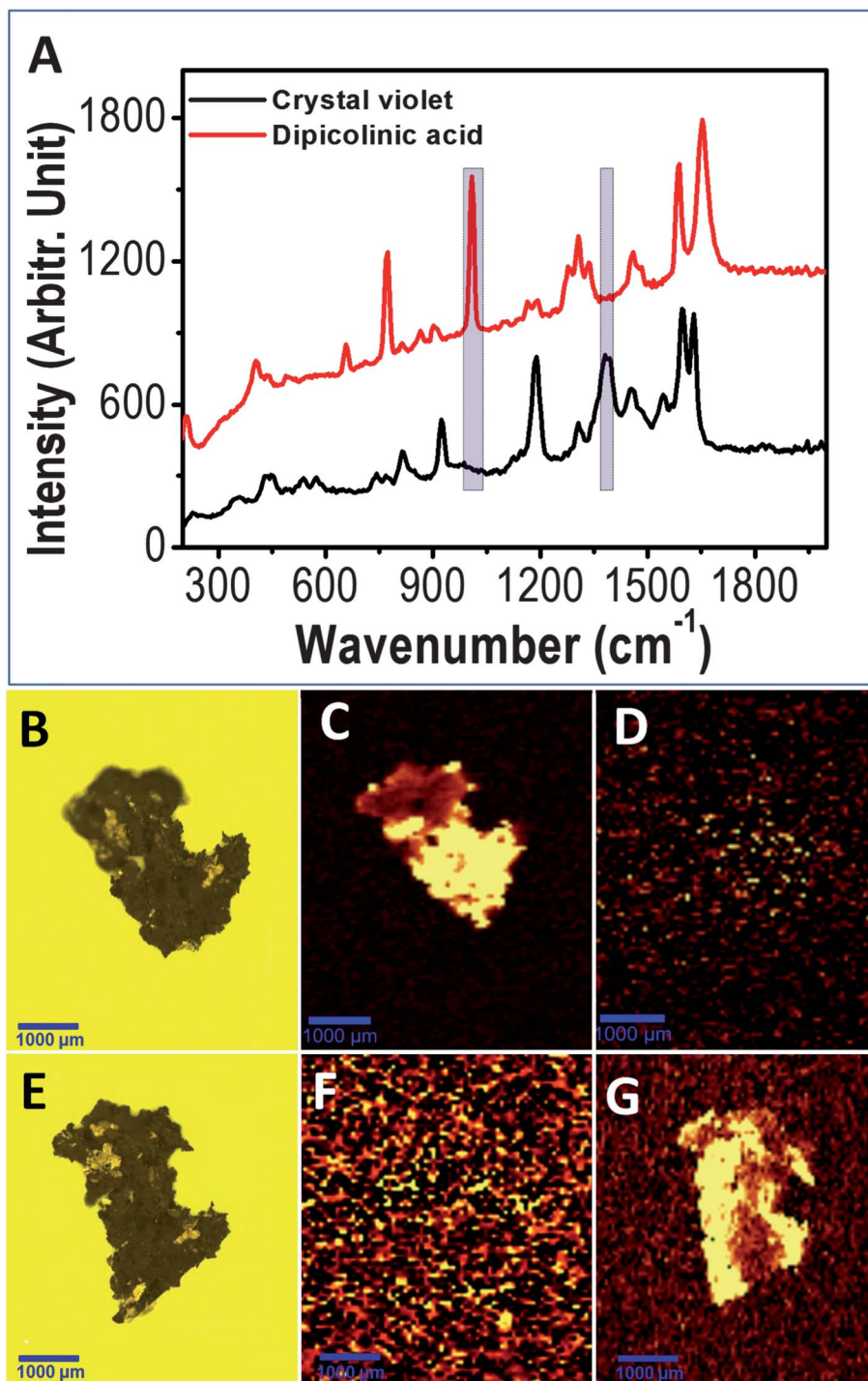


Fig. 11 (A) Raman spectrum of 10^{-6} M of CV (black trace) collected from **B**₁ before the 1st cycle of cleaning. Red trace shows the Raman spectrum of 10^{-6} M of DPA adsorbed on the same sample **B**₁ after the 1st cycle of cleaning. (B) and (E) are the optical images of **B**₁ before and after the 1st cycle of cleaning, respectively. (C) and (D) are the Raman images of **B**₁ acquired by collecting the Raman intensities of the peaks in the range of 1375–1382 and 995–1002 cm^{-1} , respectively. 10^{-6} M of CV was used as analyte for the Raman imaging. (F) and (G) are the Raman images of **B**₁ (after the first cycle of cleaning) acquired by collecting the Raman intensities of the peaks in the range of 1375–1382 and 995–1002 cm^{-1} , respectively. Here, DPA (10^{-6} M) was used as analyte for the Raman imaging.

Some molecules may have to be heated well above 300 °C for complete desorption. So there is a chance of structural transformation of the NCs which may affect its sensitivity.

After the first cycle of cleaning, the same substrate was used for SERS measurements. The substrate showed similar Raman spectra of CV at a concentration of 10^{-10} M, with its characteristic Raman features with almost the same intensity (Fig. 10C). The distance between the substrate and the microscope objective was adjusted so as to get maximum Raman intensity. We checked the reusability of the substrate by measuring the Raman spectra after subsequent washing and cleaning processes many times. After each cycle of cleaning, we verified the efficiency of the substrate by collecting the spectra of adsorbed CV. The results obtained using recycled substrates were comparable to the Raman spectra recorded using fresh substrates. The Raman spectra of 10^{-9} M CV collected from the Ni–Au NC after it was subjected for five cycles of cleaning showed almost all the characteristic features of CV (ESI, Fig. S9†). The SERS sensitivity was found to be decreased upon further use of the same substrate.

To test the sensitivity of the reprocessed substrates, we conducted the same procedure with different molecules, one after the other on the same substrate. For that, first we used the sample **B₁** after the first cycle of the cleaning process (previously used for the SERS measurement with CV solution) and drop casted DPA solution of 10^{-6} M concentration. The spectrum collected showed the Raman features of DPA molecule (Fig. 10D). The same substrate was subjected to a second cycle of the cleaning process and again used for the SERS study with a DNT solution of 10^{-6} M. Using that substrate, we could get the distinct Raman features of DNT (Fig. 10D).

The sensitivity of the recycled Ni–Au NCs towards its SERS activity was further verified by collecting the Raman image of a large area film, before and after recycling, using various analytes such as CV and DPA. We selected two different regions of 1375–1382 and 995–1002 cm^{-1} for imaging due to the reason that CV shows an intense *N*-phenyl stretching¹⁶ band at 1379 cm^{-1} , which is absent in DPA. At the same time, DPA shows an intense symmetric ring breathing mode⁵² at 998 cm^{-1} which is almost absent or weak (appears at 992 cm^{-1} as a weak band) in the case of CV. Fig. 11C and D show Raman images of the Ni–Au NC (before recycling) acquired by collecting the Raman intensities of the adsorbed CV in the range of 1375–1382 and 995–1002 cm^{-1} , respectively. The optical image of the Ni–Au NC selected for the Raman imaging is shown in Fig. 11B. The Raman image of the Ni–Au NC in (C) appeared bright and there was no such image in Fig. 11D. After the Raman measurements, we carefully cleaned the substrate without any serious damage to the material, treated it with 10^{-6} M of DPA, and collected the Raman image. In this case, we could get the Raman image using intensities in the range of 995–1002 cm^{-1} . But, there was no such image found for the 1375–1382 cm^{-1} range. This indicates that the adsorbed CV molecules were completely removed from the NC after the first cycle of cleaning. The Raman study shows that we can successfully regenerate the NC substrate without losing its sensitivity after recycling.

5. Conclusions

A facile and cost-effective way to make reusable, highly SERS active, and free-standing large area nanocarpet, extending over

cm^2 area, has been developed through a galvanic replacement reaction, starting from prefabricated Ni NCs. Using the same approach we made highly SERS active nanotubes from Ni NWs. We demonstrated the viability of our method to make several hybrid nanosystems such as Ni–Pd nanotubes and Ni–Pt and Ni–Ag NWs in an easy manner by following the same procedure. The high SERS activity of these hybrid materials has been utilized to detect molecules such as dipicolinic acid, dinitrotoluene, trinitrotoluene, and RDX at very low concentrations. We verified that the Ni–Au NC can be reused multiple times as SERS substrates without significant loss of its activity. Compared with other conventional SERS substrates, reusable and highly SERS active, large area Ni–Au NCs made by a cost-effective method may be a perfect choice for making large area sensors in many practical applications.

Acknowledgements

We thank the Department of Science and Technology, Government of India for constantly supporting our research program on nanomaterials.

References

- M. E. Stewart, C. R. Anderton, L. B. Thompson, J. Maria, S. K. Gray, J. A. Rogers and R. G. Nuzzo, *Chem. Rev.*, 2008, **108**, 494–521.
- S. R. Nicewarner-Pena, R. G. Freeman, B. D. Reiss, L. He, D. J. Pena, I. D. Walton, R. Cromer, C. D. Keating and M. J. Natan, *Science*, 2001, **294**, 137–141.
- R. Narayanan and M. A. El-Sayed, *J. Am. Chem. Soc.*, 2004, **126**, 7194–7195.
- J. P. Xie, Q. B. Zhang, J. Y. Lee and D. I. C. Wang, *ACS Nano*, 2008, **2**, 2473–2480.
- C. Wang, Y. Chen, T. Wang, Z. Ma and Z. Su, *Adv. Funct. Mater.*, 2008, **18**, 355–361.
- J. B. Jackson, S. L. Westcott, L. R. Hirsch, J. L. West and N. J. Halas, *Appl. Phys. Lett.*, 2003, **82**, 257–259.
- R. J. Banholzer, J. E. Millstone, L. Qin and C. A. Mirkin, *Chem. Soc. Rev.*, 2008, **37**, 885–897.
- C. G. Khoury and T. Vo-Dinh, *J. Phys. Chem. C*, 2008, **112**, 18849–18859.
- P. R. Sajanlal and T. Pradeep, *Nano Res.*, 2009, **2**, 306–320.
- L. A. Lyon, C. D. Keating, A. P. Fox, B. E. Baker, L. He, S. R. Nicewarner, S. P. Mulvaney and M. J. Natan, *Anal. Chem.*, 1998, **70**, 341R–361R.
- P. R. Sajanlal and T. Pradeep, *Adv. Mater.*, 2008, **20**, 980–983.
- J. E. Millstone, S. Park, K. L. Shuford, L. Qin, G. C. Schatz and C. A. Mirkin, *J. Am. Chem. Soc.*, 2005, **127**, 5312–5313.
- F. Hao, C. L. Nehl, J. H. Hafner and P. Nordlander, *Nano Lett.*, 2007, **7**, 729–732.
- P. R. Sajanlal and T. Pradeep, *Langmuir*, 2010, **26**, 8901–8907.
- L. J. Sherry, S.-H. Chang, G. C. Schatz, D. R. P. Van, B. J. Wiley and Y. Xia, *Nano Lett.*, 2005, **5**, 2034–2038.
- E. S. Shibu, K. Kimura and T. Pradeep, *Chem. Mater.*, 2009, **21**, 3773–3781.
- E. S. Shibu, J. Cyriac, T. Pradeep and J. Chakrabarti, *Nanoscale*, 2011, **3**, 1066–1072.
- P. R. Sajanlal, C. Subramaniam, P. Sasanpour, B. Rashidian and T. Pradeep, *J. Mater. Chem.*, 2010, **20**, 2108.
- D. P. Fromm, A. Sundaramurthy, P. J. Schuck, G. Kino and W. E. Moerner, *Nano Lett.*, 2004, **4**, 957–961.
- L. Chen, X. Han, J. Yang, J. Zhou, W. Song, B. Zhao, W. Xu and Y. Ozaki, *J. Colloid Interface Sci.*, 2011, **360**, 482–487.
- O. Peron, E. Rinnert, T. Toury, M. Lamy de la Chapelle and C. Compere, *Analyst*, 2011, **136**, 1018–1022.
- J. A. Dieringer, A. D. McFarland, N. C. Shah, D. A. Stuart, A. V. Whitney, C. R. Yonzon, M. A. Young, X. Zhang and D. R. P. Van, *Faraday Discuss.*, 2006, **132**, 9–26.

- 23 L. Au, X. Lu and Y. Xia, *Adv. Mater.*, 2008, **20**, 2517–2522.
- 24 X. Lu, H.-Y. Tuan, J. Chen, Z.-Y. Li, B. A. Korgel and Y. Xia, *J. Am. Chem. Soc.*, 2007, **129**, 1733–1742.
- 25 L. Au, Y. Chen, F. Zhou, P. H. C. Camargo, B. Lim, Z.-Y. Li, D. S. Ginger and Y. Xia, *Nano Res.*, 2008, **1**, 441–449.
- 26 S. E. Skrabalak, J. Chen, Y. Sun, X. Lu, L. Au, C. M. Cobley and Y. Xia, *Acc. Chem. Res.*, 2008, **41**, 1587–1595.
- 27 A. J. Chung, Y. S. Huh and D. Erickson, *Nanoscale*, 2011, **3**, 2903–2908.
- 28 Y. Lai, W. Pan, D. Zhang and J. Zhan, *Nanoscale*, 2011, **3**, 2134–2137.
- 29 V. V. Hardikar and E. Matijevic, *J. Colloid Interface Sci.*, 2000, **221**, 133–136.
- 30 T. Bala, S. D. Bhamre, P. A. Joy, B. L. V. Prasad and M. Sastry, *J. Mater. Chem.*, 2004, **14**, 2941–2945.
- 31 T. Bala, S. K. Arumugam, R. Pasricha, B. L. V. Prasad and M. Sastry, *J. Mater. Chem.*, 2004, **14**, 1057–1061.
- 32 P. R. Sajanlal and T. Pradeep, *J. Nanosci. Nanotechnol.*, 2009, **9**, 5283–5287.
- 33 M. Zhang, J. Deng, M. Zhang and W. Li, *Chin. J. Catal.*, 2009, **30**, 447–452.
- 34 D.-P. Wang, D.-B. Sun, H.-Y. Yu and H.-M. Meng, *J. Cryst. Growth*, 2008, **310**, 1195–1201.
- 35 X. Ni, J. Zhang, Y. Zhang and H. Zheng, *J. Colloid Interface Sci.*, 2007, **307**, 554–558.
- 36 G. Zhang, T. Zhang, X. Lu, W. Wang, J. Qu and X. Li, *J. Phys. Chem. C*, 2007, **111**, 12663–12668.
- 37 D. Liu, S. Ren, H. Wu, Q. Zhang and L. Wen, *J. Mater. Sci.*, 2008, **43**, 1974–1978.
- 38 S. Sarkar, A. K. Sinha, M. Pradhan, M. Basu, Y. Negishi and T. Pal, *J. Phys. Chem. C*, 2011, **115**, 1659–1673.
- 39 Y. Wang, Q. Zhu and H. Zhang, *Mater. Res. Bull.*, 2007, **42**, 1450–1456.
- 40 L. Bai, F. Yuan and Q. Tang, *Mater. Lett.*, 2008, **62**, 2267–2270.
- 41 T. S. Sreepasad, A. K. Samal and T. Pradeep, *Langmuir*, 2007, **23**, 9463–9471.
- 42 Y. Sun, *Nanoscale*, 2010, **2**, 1626–1642.
- 43 H. J. Fan, U. Gösele and M. Zacharias, *Small*, 2007, **3**, 1660–1671.
- 44 A. F. Carley, S. D. Jackson, J. N. O’Shea and M. W. Roberts, *Phys. Chem. Chem. Phys.*, 2001, **3**, 274–281.
- 45 P. F. Luo, T. Kuwana, D. K. Paul and P. M. A. Sherwood, *Anal. Chem.*, 1996, **68**, 3330–3337.
- 46 S. K. Sharma, V. Zaporozhchenko, J. Zekonyte, A. Buettner, S. Deki and F. Faupel, *J. Mater. Sci.*, 2004, **39**, 6291–6297.
- 47 E. N. Esenturk and W. A. R. Hight, *J. Raman Spectrosc.*, 2009, **40**, 86–91.
- 48 L. Rodriguez-Lorenzo, R. A. Alvarez-Puebla, I. Pastoriza-Santos, S. Mazzucco, O. Stephan, M. Kociak, L. M. Liz-Marzan and d. A. F. J. Garcia, *J. Am. Chem. Soc.*, 2009, **131**, 4616–4618.
- 49 (a) G. V. P. Kumar, S. Shruthi, B. Vibha, B. A. A. Reddy, T. K. Kundu and C. Narayana, *J. Phys. Chem. C*, 2007, **111**, 4388–4392; (b) E. C. Le Ru, E. Blackie, M. Meyer and P. G. Etchegoin, *J. Phys. Chem. C*, 2007, **111**, 13794–13803; (c) G. Upender, R. Satyavathi, B. Raju, K. Shadak Alee, D. Narayana Rao and C. Bansal, *Chem. Phys. Lett.*, 2011, **511**, 309–314.
- 50 K. Kim, H. J. Jang and K. S. Shin, *Analyst*, 2009, **134**, 308–313.
- 51 W. Wei, S. Li, J. E. Millstone, M. J. Banholzer, X. Chen, X. Xu, G. C. Schatz and C. A. Mirkin, *Angew. Chem., Int. Ed.*, 2009, **48**, 4210–4212.
- 52 A. A. Kolomenskii and H. A. Schuessler, *Spectrochim. Acta, Part A*, 2005, **61**, 647–651.

Cite this: *Nanoscale*, 2012, **4**, 4255

www.rsc.org/nanoscale

PAPER

Luminescent, bimetallic AuAg alloy quantum clusters in protein templates†

Jyoti Sarita Mohanty,^a P. Lourdu Xavier,^a Kamalesh Chaudhari,^{ab} M. S. Bootharaju,^a N. Goswami,^c S. K. Pal^c and T. Pradeep^{*a}

Received 26th March 2012, Accepted 3rd May 2012

DOI: 10.1039/c2nr30729d

We report the synthesis of luminescent AuAg alloy quantum clusters (QCs) in bovine serum albumin (BSA), for the first time, with experimentally determined atomic composition. Mixing of the as-synthesized protein-protected Au and Ag clusters resulted in the formation of alloy AuAg clusters within the BSA. Mass spectrometric analysis of the product of a 1 : 1 molar ratio reaction mixture of Au_{QC}@BSA and Ag_{QC}@BSA suggested that the alloy clusters could be Au_{38-x}Ag_x@BSA. Further analyses by standard techniques revealed that the alloy cluster core of ~1.2 nm diameter is composed of nearly zero valent Au and Ag atoms that exhibit distinctly different steady state and time resolved excited state luminescence profiles compared to the parent clusters. Tuning of the alloy composition was achieved by varying the molar ratio of the parent species in the reaction mixture and compositional changes were observed by mass spectrometry. In another approach, mixing of Au³⁺ ions with the as-synthesized Ag_{QC}@BSA also resulted in the formation of alloy clusters through galvanic exchange reactions. We believe that alloy clusters with the combined properties of the constituents in versatile protein templates would have potential applications in the future. The work presents interesting aspects of the reactivity of the protein-protected clusters.

1. Introduction

Atomically precise molecules of noble metals with quantum confined phenomena have been some of the most fascinating materials in molecular cluster science in the recent past.¹⁻⁶ They are groups of atoms with a sub-nanometer sized core, considered to be the missing link between atoms and nanoparticles, and we refer to them as quantum clusters (QCs). Intense luminescence, unusual photo-stability, novel catalytic properties and several other phenomena have caused excitement in this branch of science. Because of the sp → sp intraband and sp → d interband transitions occurring in them, they are luminescent and their luminescence can be tuned by controlling the number of atoms in the core. Clusters of Au and Ag have been among the most studied clusters in the solution phase.¹⁻⁴ Several methods in the solution phase,¹ as well as in the solid state,⁷ have been used to synthesize metallic clusters. From the characterization point of view, among the different techniques, mass spectrometry has

been an indispensable analytical tool to understand the atomic composition of metallic clusters.⁶ The possibility of manipulating their properties through precise variations in composition has prompted the exploration of alloy clusters. Recently, monolayer-protected alloy clusters like AuAg₁₄₄ and AuAg₃₈, Pd-doped Au clusters and AuAg alloy clusters stabilized by chitosan in the solid state have been demonstrated.⁸⁻¹¹ A recent example of manipulation in alloy composition is the creation of a stable 13-atom AuAg alloy of such clusters by our group.¹² The most recent category of these new materials is their analogues in protein templates such as Au₂₅@BSA, Au₃₈@BSA, Au_{13,25}@NLF, Ag₁₅@BSA and Au₁₆@BSA.¹³⁻¹⁷ The bright emission of clusters in protein and peptide templates has been exploited for bio-labelling.^{3,14,18} Various bio-medically important functional proteins such as lactotransferrin¹⁵ and insulin²¹ have been used to synthesize such clusters and the latter is shown to retain bioactivity.^{3,19,20} Hence, these new analogues hold huge potential in the bio-medical field. While intense luminescence, bio-compatibility and facile targeting capability have been demonstrated with these systems, structural properties and the precise compositional manipulation of the cluster core are still being explored.^{3,22,23} The creation of such a cluster goes through multiple steps involving metal ion uptake in an intermediate valance state and its subsequent reduction involving concomitant inter-protein metal transfer.²³ While various questions concerning the growth, structural and optoelectronic properties of clusters in protein templates have yet to be answered, their intense luminescence has resulted in several applications. In this

^aDST Unit of Nanoscience, Department of Chemistry, Indian Institute of Technology Madras, Chennai-600 036, India. E-mail: pradeep@iitm.ac.in

^bDepartment of Biotechnology, Indian Institute of Technology Madras, Chennai-600036, India

^cUnit for Nanoscience and Technology, Department of Chemical, Biological and Macromolecular Sciences, Satyendra Nath Bose National Centre for Basic Sciences, Block JD, Sector III, Salt Lake, Kolkata 700 098, India

† Electronic supplementary information (ESI) available: XPS, SEM EDAX, UV-Vis, PL and FTIR measurements. See DOI: 10.1039/c2nr30729d

paper, we explore the precise compositional manipulation of cluster cores leading to AuAg alloys across the entire compositional window. This becomes feasible in the AuAg alloy system as they form solid solutions in the entire compositional range. The results propose that stoichiometric reactions are possible in the case of clusters within proteins, which suggests a dynamic interaction between the cluster core and the medium. Such compositional changes occur on fast timescales, implying chemistry analogous to molecular systems. The cluster core is susceptible to galvanic chemistry leading to etching.¹² This supports the existence of cluster nuclei within them with larger electrochemical potential compared to the parent bulk metal, allowing facile electron transfer to isolated ions. Applications of alloy cluster systems in electronics, catalysis and in medicine have enormous potential. The longer lifetime possessed by these non-photobleachable luminescent clusters becomes an attractive option in fluorescence life-time imaging.⁴

2. Experimental

2.1. Reagents and materials

Tetrachloroauric acid trihydrate ($\text{HAuCl}_4 \cdot 3\text{H}_2\text{O}$) was purchased from CDH, India. Silver nitrate (AgNO_3) and sodium hydroxide (NaOH) were purchased from Rankem, India. BSA was purchased from the Sisco Research Laboratory. Sodium borohydride (NaBH_4) was purchased from Spectrochem, India. Sinapinic acid was used as the matrix for matrix assisted laser desorption ionization mass spectrometry (MALDI MS). All chemicals were used as received without further purification.

2.2. Instrumentation

UV-Vis spectra were collected using a PerkinElmer Lambda 25 instrument in the range of 200–1100 nm. Luminescence measurements were carried out on a Jobin Yvon NanoLog instrument. The band pass for excitation and emission was set as 3 nm. Picosecond-resolved fluorescence decay transients were measured by using a commercially available spectrophotometer (Life Spec-ps, Edinburgh Instruments, UK) with 60 ps instrument response function (IRF). The observed fluorescence transients were fitted by using a nonlinear least squares fitting procedure to a function ($X(t) = \int_0^t E(t')R(t-t')dt'$) comprising of the convolution of the IRF ($E(t)$) with an exponential sum ($R(t) = A + \sum_{i=1}^N B_i e^{-t/\tau_i}$) with pre-exponential factors (B_i), characteristic lifetimes (τ_i) and a background (A). The relative concentration in a multi-exponential decay was finally expressed as: $c_n = \frac{B_n}{\sum_{i=1}^N B_i} \times 100$. The quality of the curve fitting was evaluated by a reduced χ -squared analysis and residual data. It should be noted that with our time resolved instrument, we can resolve at least one quarter of the instrument response time constants after the de-convolution of the IRF. X-Ray photoelectron spectroscopy (XPS) studies were conducted with an Omicron ESCA probe spectrometer with polychromatic Mg K_{α} X-rays ($h\nu = 1253.6$ eV). The samples were spotted as drop-cast films on a sample stub. A constant analyser energy of 20 eV was used for the measurements. MALDI MS studies were conducted using a Voyager DE PRO Biospectrometry Workstation from

Applied Biosystems. A pulsed nitrogen laser of 337 nm was used for the MALDI MS studies. Mass spectra were collected in linear positive mode and were averaged for 100 shots. Scanning electron microscopy (SEM) and energy dispersive analysis of the X-ray (EDAX) images were collected using an FEI QUANTA-200 SEM. For the SEM and EDAX measurements, samples were spotted on an indium tin oxide (ITO) conducting glass substrate and dried in ambient conditions. High resolution transmission electron microscopy (HRTEM) was performed with a JEOL 3010, 300 kV instrument equipped with an ultra high resolution (UHR) pole piece. Samples were prepared by dropping the dispersion on carbon coated copper grids for HRTEM. Solid-state FTIR spectra were measured with a PerkinElmer instrument. KBr crystals were used as the matrix for preparing the samples. Far-UV circular dichroism (CD) spectra were measured with a Jasco 815 spectropolarimeter.

2.3. Alpha-helix calculation

The alpha helix content from the obtained CD spectra was calculated by the formula proposed by Chen *et al.*²⁴ α -helix (%) = $-(\theta + 3000)/39\,000$, where $\theta = \text{MRW} \times \theta_{222}/10lc$, where MRW is mean residual weight, l is path length of the cell and c is the concentration of the sample used for the measurement. The MRW of BSA is 114, the concentration of the protein used for the measurements was 2×10^{-7} g mL^{-1} and the path length of the cell used was 1 cm.

2.4. Synthesis

Au and Ag QCs were synthesized in protein templates as reported previously.^{12,16} Briefly, $\text{Au}_{\text{QC}}@BSA$ was synthesized by mixing solutions of BSA and HAuCl_4 to get final concentrations of 169.0 μM and 4.4 mM, respectively (the molar ratio of the protein to Au^{3+} was 1 : 26), along with the addition of 100.0 μL 1.0 M NaOH to make the final volume 1.1 mL. Then the mixture was stirred vigorously for 8 h until the solution turned golden brown in colour. Similarly, $\text{Ag}_{\text{QC}}@BSA$ was also synthesized by mixing the protein and AgNO_3 solutions to get a final concentration of 169.0 μM and 4.4.0 mM, respectively (1 : 26 molar ratio) and 100.0 μL of 1.0 M NaOH was added to make the final volume ~ 1.1 mL. 1.0 μL of 0.05 M freshly prepared NaBH_4 was added to the reaction mixture and stirred for ten minutes until the solution turned golden brown. Note that here the final molarities of Au^{3+} and Ag^+ used for the individual Au and Ag cluster synthesis were kept the same in order to carry out further alloy cluster synthesis reactions. The as-synthesized $\text{Au}_{\text{QC}}@BSA$ and $\text{Ag}_{\text{QC}}@BSA$ were mixed together and stirred for 4 h to form alloy clusters in different v/v ratios. In a second approach, to the as-synthesized $\text{Ag}_{\text{QC}}@BSA$, different volumes (10, 25, 50 and 80 μL) of 100 mM HAuCl_4 were added to make a different final concentration of Au^{3+} in the reaction mixture and stirred vigorously for 8 h. All the samples were directly taken from the reaction product for the MALDI MS and for time dependent measurements, samples were collected at appropriate time intervals.

3. Results and discussion

3.1. Formation of the alloy cluster through QC–QC interaction

Isolated gold and silver clusters protected with proteins, especially BSA, have been characterised in detail.^{3,13,16} At specific molar ratios of metal ions to proteins, they produce well defined clusters exhibiting sharp peaks in the MALDI MS spectra. These mass shifts from the parent protein give the size of the metal cluster nucleus and it also implies the presence of a specific cluster within a single protein.^{12,23} We chose to make Ag and Au clusters ($\text{Ag}_{\text{QC}}@BSA$ and $\text{Au}_{\text{QC}}@BSA$) with ~ 31 and ~ 38 atoms, respectively in the core, although other cluster nuclei are possible by incubating varying concentrations of the metal ions. Fig. 1 is the comparison of the MS spectra of the Au, Ag and AuAg alloy clusters formed in BSA. The formation of the alloy clusters ($\text{AuAg}_{\text{QC}}@BSA$) can be inferred from the occurrence of a mass spectral feature in between the parent Au and Ag clusters with the simultaneous absence of both the parent clusters. Along with these, there is an emergence of the BSA feature confirming the appearance of the free protein²³ (Fig. 1). The alloy formation leads to a distinct change in photoluminescence, as seen from the inset photographs in Fig. 1a–d. It may be noted that MALDI MS is quantitative and can be used to determine the relative concentration of species, however, the peak intensities do not reflect the true concentrations of the species in the sample due to differences in their ionization efficiencies.

The calculated mass difference between the monocation peak of QC@protein and intact protein suggests the number of atoms in the cluster core. BSA in NaOH has a peak at m/z 66 500, which is shifted by 300 to lower m/z when compared to the protein at neutral pH (m/z 66 800). This can be attributed to the concomitant modifications occurring due to the breakage of disulfide

bonds or deamidation at extreme pH. $\text{Au}_{\text{QC}}@BSA$ has a peak at $m/z \sim 73$ 900 and $\text{Ag}_{\text{QC}}@BSA$ has a peak at m/z 69 900. The calculated mass difference between $\text{Au}_{\text{QC}}@BSA$ and BSA is ~ 7.5 kDa, indicating the formation of Au_{38} (Fig. 1). The possibility of the formation of $\text{Au}_{38}@BSA$ has already been reported by our group.¹⁴ The difference between $\text{Ag}_{\text{QC}}@BSA$ and BSA was ~ 3.4 kDa, suggesting the formation of $\sim \text{Ag}_{31}$. Finally, the difference between $\text{AuAg}_{\text{QC}}@BSA$ and the protein was ~ 5.9 kDa, suggesting the formation of $(\text{AuAg})_{38}$. Since the atomic ratio (in Au and Ag) used was 1 : 1, the composition could be $\text{Au}_{19} : \text{Ag}_{19}$. Since a definite understanding of the mechanism of cluster–cluster interaction is not yet available, several other possibilities of composition may also be possible. It is almost impossible to determine the exact mass from the mass spectra due to the inherent uncertainty at this high mass. The possibility of the formation of $(\text{AuAg})_{38}$ nanomolecules in the case of monolayer-protected clusters has been demonstrated recently.⁹ It is likely that such a system could also be synthesized in protein templates. It is important to note that the parent cluster peaks do not exist in the reaction product; however, the peak corresponding to the free protein appears and this has been probed further (see below).

HRTEM analysis showed that the cluster cores are ~ 1.2 nm in size (Fig. 1 inset). TEM is not an appropriate tool, unlike MS, to investigate the clusters, since electron beam induced growth of the clusters²⁵ would give an exaggerated cluster size. However, it is useful to know the approximate size and rule out the possibility of the presence of bigger plasmonic nanoparticles. Here, it is clear that the emission shown in the inset photographs of Fig. 1 comes from non-plasmonic particles. It is important to confirm that plasmonic particles are not formed in solution due to cluster–cluster interactions.

Alloy clusters of one specific composition ($(\text{AuAg})_{38}$ obtained by mixing clusters at a 1 : 1 molar ratio) were investigated in detail to understand the variation in their properties in comparison to the parent clusters. These studies revealed systematic changes in the cluster properties. For example, the absorption spectra are almost the same in all the cases and no distinct features were observable, unlike in the case of monolayer-protected clusters^{8–10,12,13} (Fig. 2A). However, broad peaks of poor intensity in between 300 and 600 nm were observed in the case of the Ag clusters. $\text{Au}_{38}@BSA$ did not show any absorption peak, as in the case of other protein-protected gold clusters,^{13,14,23} and the lack of prominent absorbance features in such systems is under investigation. In the case of the alloy, although broad peaks from $\text{Ag}_{\text{QC}}@BSA$ were faintly visible initially, the spectrum became featureless with time. This change in the optical spectra could be due to the alloy cluster formation, as suggested by the MALDI MS. As no spectral features of the parent clusters were seen in the MALDI MS after the reaction, the new peak is attributed to the alloy. Here we have to note that the reason for the absence of distinct optical peaks in such clusters, quite unlike monolayer-protected clusters, is still under investigation. The presence of such peaks would have allowed the cluster core size to be deciphered. The luminescence emission maximum of the alloy cluster shifts to red (~ 707 nm) at this composition compared to the Au (~ 660 nm) and Ag (~ 670 nm) clusters (Fig. 2B) when excited at 370 nm. Multiple excitation peaks were observed as expected for QCs in proteins due to the cluster core

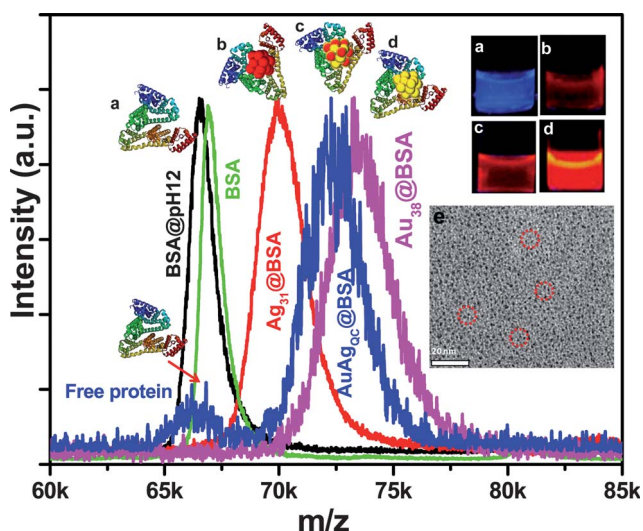


Fig. 1 MALDI MS data showing the formation of the alloy cluster. Positive ion mass spectra of BSA (green solid line), BSA at pH 12 stirred for 12 h (solid black line), $\text{Au}_{\text{QC}}@BSA$ (solid magenta line), $\text{Ag}_{\text{QC}}@BSA$ (solid red line) and $\text{AuAg}_{\text{QC}}@BSA$ (solid blue line). Cartoons above the mass spectra show the different clusters formed. Insets: photographs under UV-light of (a) BSA, (b) $\text{Ag}_{\text{QC}}@BSA$, (c) $\text{AuAg}_{\text{QC}}@BSA$ and (d) $\text{Au}_{\text{QC}}@BSA$. (e) TEM image of $\text{AuAg}_{\text{QC}}@BSA$ shows a core size of ~ 1.2 nm. The scale bar in the TEM image is 20 nm.

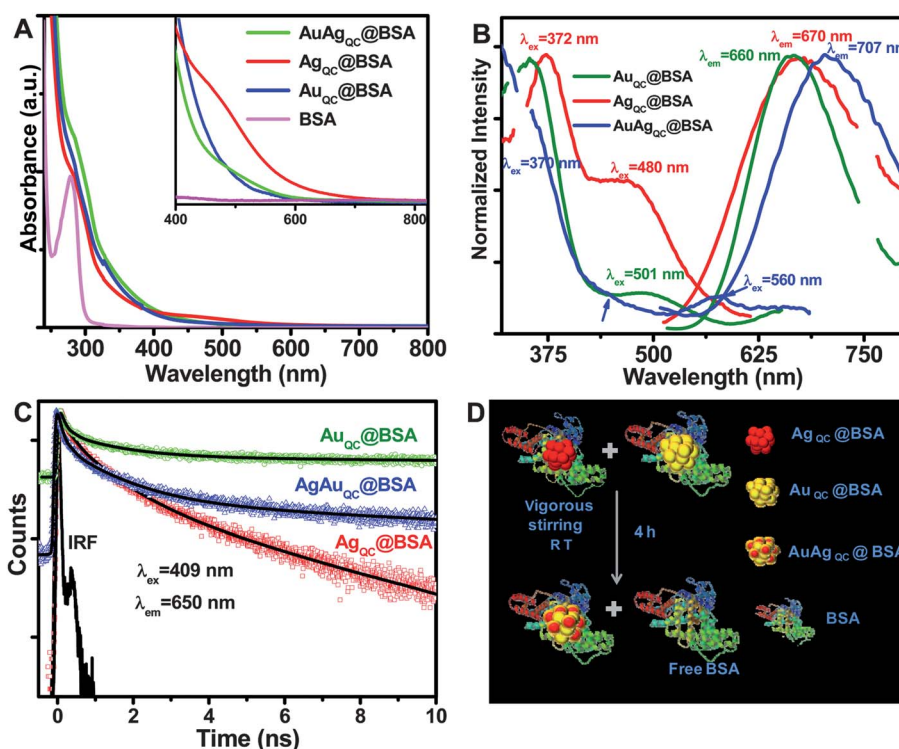


Fig. 2 (A) UV-Vis spectra of BSA, Au_{QC}, Ag_{QC}, and AuAg_{QC}@BSA. (B) PL spectra of Au_{QC} (green line), Ag_{QC} (red line), and AuAg_{QC} (blue line) @BSA. Emission spectra were collected for all the three clusters by exciting them at 370 nm. (C) Picosecond-resolved fluorescence transients of Au_{QC} (green), Ag_{QC} (red), AuAg_{QC} (blue) @BSA. (D) Schematic of the synthesis of AuAg@BSA alloy clusters through QC-QC interaction.

as well as the protein.²³ Au_{QC}@BSA has two excitation maxima at ~370 and 504 nm and Ag_{QC}@BSA has excitation peaks at ~370 and 480 nm, as previously reported.¹⁴⁻¹⁶ AuAg_{QC}@BSA showed excitation peaks at ~370, 470 and 560 nm. Time resolved measurements revealed tri-exponential decay for all the clusters and gave the following lifetime values: Ag₃₁@BSA – 0.16 ns (55%), 0.96 ns (33%) and 3.9 ns (12%); Au₃₈@BSA – 0.14 ns (64%), 1.30 ns (24%) and 32.9 ns (12%); (AuAg)₃₈ – 0.12 ns (71%), 1.20 ns (22%) and 11.8 ns (7%) (Fig. 2C and Table 1). From the above data, it is evident that the lifetime of the alloy cluster is distinctly different from its parent clusters. It should be mentioned that we have tried to fit the decay profile of the alloy clusters to different combinations of the lifetimes of the Au and Ag QCs, however, none of these combinations fitted well, revealing the presence of a new emitting species. The calculated quantum yield values for Au_{QC}@BSA, Ag_{QC}@BSA and AuAg_{QC}@BSA were 6.8, 1.9 and 2.8%, respectively, with rhodamine 6G as the reference.

Immediately upon addition of Au_{QC}@BSA to Ag_{QC}@BSA, both the parent cluster peaks vanished and a new peak at *m/z* ~72 600 appeared, implying a fast QC-QC interaction (Fig. 3).

Table 1 Lifetime components of the parent Au, Ag and alloy clusters in the protein template. The numbers in the parentheses indicate relative weights (standard error 10%)

QC system	τ_1 (ns)	τ_2 (ns)	τ_3 (ns)	τ_{av} (ns)
Ag ₃₁ @BSA	0.16 (55%)	0.96 (33%)	3.9 (12%)	0.51
Au ₃₈ @BSA	0.14 (64%)	1.30 (24%)	32.9 (12%)	3.40
(AuAg) ₃₈ @BSA	0.12 (71%)	1.20 (22%)	11.8 (7%)	0.85

Although the chemical interaction between the clusters is fast, there are distinct time dependent changes, as expected for such large molecular systems. The time evolution of the MALDI MS spectra over the course of one day revealed the gradual emergence of the free BSA peak, along with the alloy nucleation. Until the second hour of incubation, the peak remained at the same position and from the fourth hour of incubation, the mass increased and the peak was around *m/z* 73 600, coinciding with the emergence of the free protein. This increase in mass is attributed to the incorporation of metal ions released from the parent clusters in the initial stages of the reaction. Slow reduction and metal incorporation is seen in such systems.²³ The alloy clusters are not as stable as their parent analogues. As Fig. 3 shows a similar position for the parent protein, it is clear that cluster-containing proteins do exchange metal ions between them, and concomitantly free protein emerges. Protein based synthesis procedures involve highly dynamic structural changes in the protein's secondary structure as a function of time to facilitate the cluster synthesis. Here, we have to note that amino acid metal ion interaction is also dynamic.^{23,26} These data imply a chemical substitution reaction retaining a similar number of core atoms, as metal atom transfer from the protein during cluster incubation is feasible.²³ Similar processes may be facile in fully grown clusters as well. The wrapping of a single metal cluster non-covalently, with multiple thiol groups anchored on the cluster surface by a single large organic molecule, is possible where the flexible conformations are feasible.²⁷ Similarly, it is likely that a high molecular weight protein with a large number of thiols could completely wrap metallic clusters with multiple-thiol anchoring points. Dynamic light scattering (DLS) studies

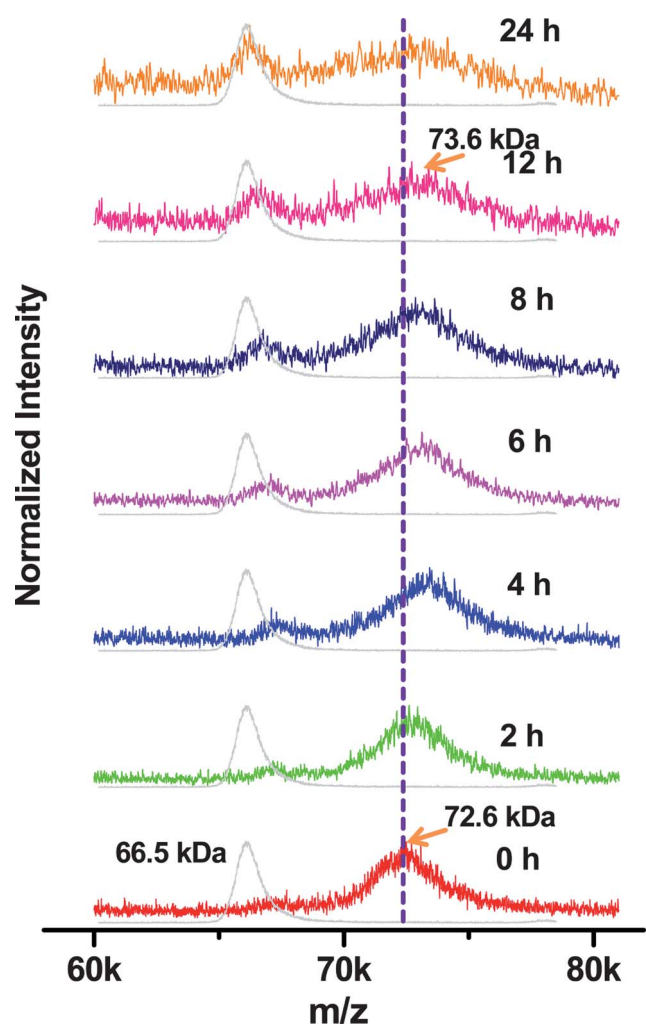


Fig. 3 Time-dependent MALDI MS data of AuAg_{QC}@BSA show the emergence of the free protein and also the shifting of the cluster-containing protein peak from *m/z* 72 600 (0 h) towards *m/z* 73 600 (12 h) as a function of time.

have shown the absence of any aggregate other than a slightly larger sized protein, supporting the presence of a cluster within.^{13,19}

The existence of the alloy is confirmed using elemental analysis by SEM-EDAX and XPS. In the specific case of a 1 : 1 alloy, EDAX confirms the composition of the alloy cluster to be 1 : 1 in Au : Ag (Fig. S1†). The presence of the alloy cluster has been further strengthened by the observations made in the XPS analysis, which indicated the presence of a metallic core and hence rules out the possibility that the presence of complexes to be the reason for the observed MS pattern and the cause of the emission. In XPS, the Au 4f and Ag 3d regions support the zero-valent state for both the elements (Inset of Fig. 4). The Au 4f_{7/2} and Ag 3d_{5/2} peaks appear at 84.1 and 368.2 eV, respectively, close to the metallic values. These are the same positions seen in metal clusters protected with monolayers and proteins.^{12–16} The S 2p_{3/2} and 2p_{1/2} peaks occurred at 162.1 and 163.3 eV, respectively (Fig. S2†), which are the characteristic features of thiolate.²⁸ Thus, it is evident that the cluster core is stabilized by the thiol groups of the protein (predominantly from the cysteine residues,

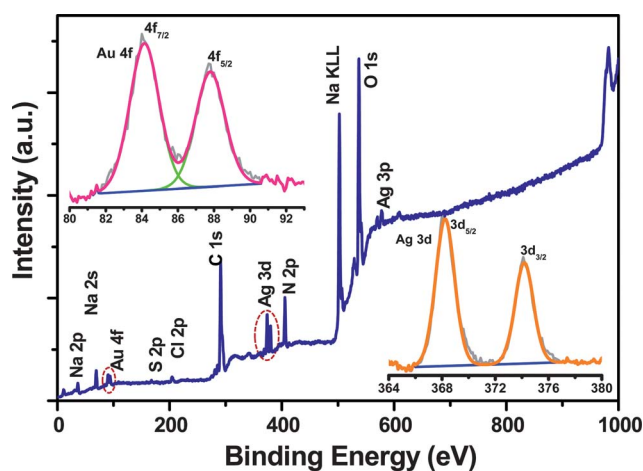


Fig. 4 XPS survey spectrum of AuAg_{QC}@BSA showing the presence of metallic Ag and Au (dotted pink circles). Inset: expanded and fitted spectral regions of Au 4f (magenta line) and Ag 3d (orange line).

since they are highly reactive) in view of the large affinity of S to noble metals. The atomic Au : S and Ag : S ratios suggested one cluster per intact protein with excess thiol–thiolate groups. The other possibility for excess sulfur may be free protein molecules. In the SEM-EDAX analysis, the atomic S : Au : Ag ratio was 2 : 1 : 1. The excess content of sulfur can be attributed to the available 34 cysteine residues per protein, which is higher than the required (SR₂₄ for (AuAg)₃₈) to stabilize the cluster in one

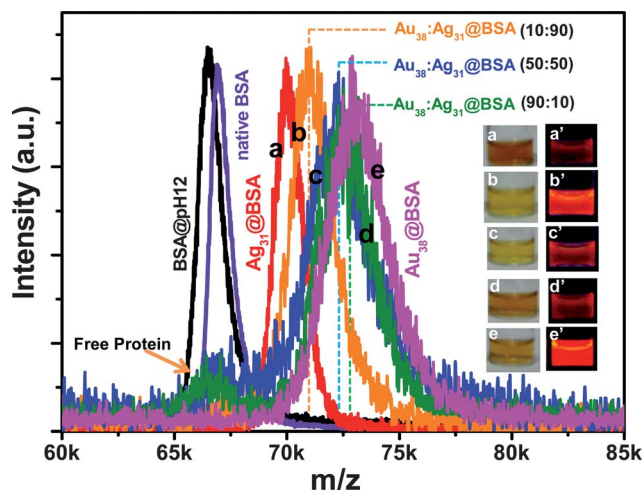


Fig. 5 MALDI MS data shows the tunability of the composition of the AuAg alloy clusters in protein templates. MS of native BSA (violet) and BSA at pH 12 (black). The products of 900 μ L Ag_{QC}@BSA + 100 μ L Au_{QC}@BSA (90 : 10) peak at *m/z* 71 100 (orange trace), 500 μ L Ag_{QC}@BSA + 500 μ L Au_{QC}@BSA (50 : 50) peak at *m/z* 72 300 (blue trace) and 100 μ L Ag_{QC}@BSA + 900 μ L Au_{QC}@BSA (10 : 90) peak at *m/z* 72 800 (olive trace) lie between Ag_{QC} (red trace) and Au_{QC}@BSA (magenta trace), suggesting compositional variation in the alloys. Inset photographs: (a) Ag_{QC}@BSA, (b) Au_{QC} : Ag_{QC}@BSA (10 : 90), (c) 50 : 50 Au_{QC} : Ag_{QC}, (d) Au_{QC} : Ag_{QC} (90 : 10) and (e) Au_{QC}@BSA under visible light (left) and UV light (right). The ratio mentioned here is v/v, which can also be considered as a molar ratio since Au and Ag solutions of the same molarity were used.

protein, since they may not all participate in the stabilization process. Another sulfur-containing amino acid, the less reactive methionine (~ 5 per BSA molecule) is also present. All the other elements in the XPS survey spectrum are due to the protein. The presence of Na and Cl is due to the by-products derived from the reagents (Fig. 4).

As AuAg alloys are possible across the entire compositional window, we tried to create clusters of varying composition by mixing appropriate amounts of the as-prepared clusters. The mass spectra of the mixture of clusters (Fig. 5) showed well defined compositions with complete tunability, suggesting the formation of $Au_{1-x}Ag_x$ clusters across the entire compositional window. No parent clusters are seen in the mass spectra. All these clusters are luminescent and the photophysical properties of the alloy clusters formed from the interactions of different ratios of Au_{QC} and Ag_{QC} are currently under investigation. The final composition in the product need not be the same as in the starting materials. The emergence of free protein may indicate that inter-protein metal ion transfer facilitates alloy formation.

3. 2. Alloy cluster through galvanic exchange

In another approach, we have synthesized the alloy clusters through galvanic exchange reactions. While the Au and Ag clusters react, a similar reactivity is possible between the cluster core and the Au ions, especially when a galvanic reaction is facile. Reduction of Au^{3+} by an Ag cluster is a possible way to form

alloy clusters, as we have shown before.¹² To test this hypothesis with protein-protected clusters, we added varying amounts of Au^{3+} to the Ag cluster. The mass spectra showed a systematic shift in which the composition of the core continuously altered (Fig. 6A). The initial measurements around one hour showed a mass shift for all the different volumes of 100 mM Au^{3+} added, although the observed mass shift may not represent the alloy cluster formed, since XPS only showed the Au^0 state after 4 h. Hence, we carried out time dependent MS studies for the volume of 25 μL Au^{3+} added to $Ag_{QC}@BSA$. These changes, although observed immediately after mixing, continued for a longer timescale as shown in Fig. 6B. Such clusters are also luminescent, as shown in the ESI (Fig. S3[†]) and the existence of the alloy was confirmed by EDAX (Fig. S4[†]). The galvanic nature of this reaction is shown from the formation of AgCl crystallites with well defined morphology in the SEM and EDAX images (Fig. S5[†]).¹² Note that Cl^- is in solution. In agreement with this, systematic changes in the valence state of gold are seen in the XPS data. While Au^{3+} is taken up as Au^{1+} due to the interaction of the protein, it gradually transforms to Au^0 as time progresses. The Au $4f_{7/2}$ at 85.6 eV due to Au^{1+} decreases in intensity and a peak at 84.0 eV due to Au^0 evolves gradually (Fig. 6D). There is no drastic change seen in the Ag 3d region, as Ag^0 and Ag^+ are similar in binding energy (Fig. 6 D).

There have been a number of reports of reactions of quantum dots, especially reactions such as cation/anion exchange. These exchange reactions are also facile in nanowires, especially in

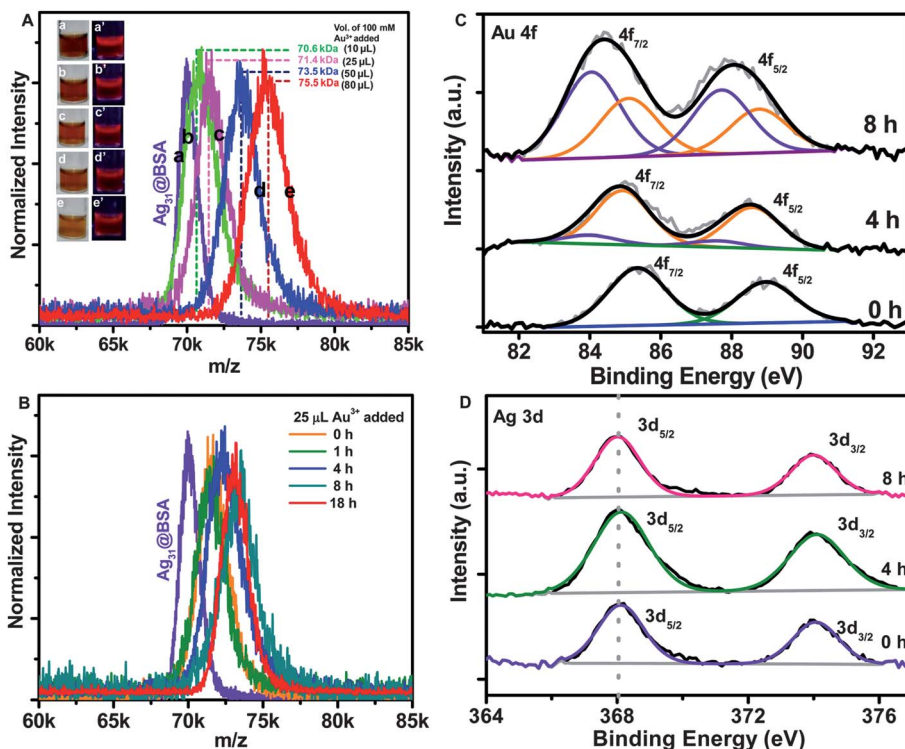


Fig. 6 (A) MALDI MS data of (a) $Ag_{QC}@BSA$ (violet trace), reaction products obtained around one hour after the addition of different volumes of $H AuCl_4$: (b) 10 μL (green trace), (c) 25 μL (magenta trace), (d) 50 μL (blue) and (e) 80 μL (red trace) of Au^{3+} . Inset photographs: the reaction products of $Ag_{QC}@BSA$ with different volumes of Au^{3+} under visible (a–e) and UV (a'–e') light. (B) Time-dependent MALDI MS data of $Ag_{QC}@BSA$ interacting with Au^{3+} ions to form $AuAg_{QC}@BSA$. Time-dependent XPS spectra of (C) the Au 4f region showing the emergence of zero-valent state and (D) the Ag 3d region.

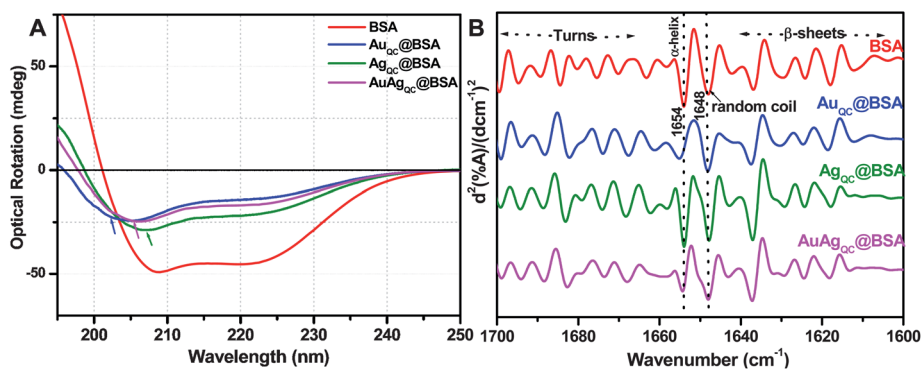


Fig. 7 (A) CD spectra of BSA (red), Ag_{QC}@BSA (green), Au_{QC}@BSA (blue) and AuAg_{QC}@BSA (magenta). (B) Second derivative FTIR spectra of amide I region of BSA (red), Au_{QC}@BSA (blue), Ag_{QC}@BSA (green) and AuAg_{QC}@BSA (magenta).

shape-conserving transformations.^{29,30} Compositional changes leading to core/shell systems are also reported in the literature. Thus, the creation of alloy clusters in protein templates is not surprising. However, the nearly identical nuclearity across the entire compositional window is unprecedented. We assume that it is observed due to the intact protein structure with specific locations of the binding residues. Possibly such restrictions preserve a given cluster's nucleus.

3.3. Conformational changes in the protein

Such metal atom substitution reactions may lead to changes in the protein conformation. These are reflected in the CD spectra where the alloy cluster-containing protein solution exhibits intermediate peaks in comparison to the parent clusters. The calculated data showed the alpha helix content to be 64.5%, 13.8%, 16.5% and 20.7% for BSA, Au_{QC}@BSA, AuAg_{QC}@BSA and Ag_{QC}@BSA, respectively (Fig. 7A). The formation of the three different clusters showed a significant loss of alpha helix content. While Ag_{QC} showed minimum and Au_{QC} showed maximum losses, AuAg_{QC} showed an intermediate loss. These results are also supported by vibrational spectroscopic studies, especially IR studies. FTIR has been one of the widely used techniques to probe the changes of the protein's secondary structure. The shifting of bands to higher frequency and the broadening of the bands are the features seen in general. The FTIR spectra showed the expected bands for the protein such as amide I, amide II, amide III and amide A, in the 1600–1690, 1480–1575, 1229–1301 and ~3300 cm⁻¹ regions, respectively^{15,31,32} (Fig. S6†). The IR second derivative spectra, which are more sensitive to changes, showed that the alpha helix content (indicated by the peak at 1654 cm⁻¹) of the protein decreased to a greater extent in Au_{QC}@BSA and to a lesser extent for Ag_{QC}@BSA. For AuAg_{QC}@BSA, the changes were intermediate between the former two (Fig. 7B). These results were corroborated by the CD data, which also suggests that the changes in the structure of the protein observed in AuAg_{QC}@BSA are intermediate to those of Au_{QC}@BSA and Ag_{QC}@BSA. These are related to the intermediate conformational changes occurring in the protein molecules due to the alloy cluster.

4. Conclusion

We have demonstrated the synthesis of AuAg alloy quantum clusters with tuneable compositions in a BSA template starting from Au and Ag clusters. MALDI MS suggested the presence of the alloy cluster in BSA. XPS analysis revealed the presence of both Au and Ag in the alloy cluster in the zero-valent state. The rapid interaction between the parent QCs@proteins and the evolution of the compositionally isotropic alloy clusters with a complete absence of the parent clusters is unusual. Inter-protein metal ion transfer leading to the formation of the new hybrid cluster and the concomitant emergence of free protein is apparent from this study. While many questions remain unanswered regarding clusters in proteins, the creation of new materials in the macromolecule template is evident. A complete understanding of protein-protected cluster systems would require several additional experiments like high resolution MS of electrophoretically/chromatographically separated entities and in particular, X-ray crystallography of intact QC@proteins. Efforts are being made in this direction. Such alloy systems with their luminescence and tuneable composition would have interesting applications in the field of catalysis, electronics and medicine. The synthesis of other alloy systems following a similar method using various proteins and metals is likely and the topic is being explored currently.

Acknowledgements

We thank the Department of Science and Technology, Government of India for constantly supporting our research programme on nanomaterials. J.S.M. thanks T. Udayabhaskararao for helpful discussions. N.G. thanks CSIR, India, for a fellowship. Partial equipment support to S.K.P. was provided by the DST (SR/SO/BB-15/2007).

References

- 1 R. Jin, *Nanoscale*, 2010, **2**, 343–362 and the references cited therein.
- 2 M. A. H. Muhammed and T. Pradeep, in *Advanced Fluorescence Reporters in Chemistry and Biology II*, ed. A. P. Demchenko, Springer, Berlin, Heidelberg, 2010, pp. 333–353.
- 3 P. L. Xavier, K. Chaudhari, A. Baksi and T. Pradeep, *Nano Rev.*, 2012, **3**, 14767, DOI: 10.3402/nano.v3i0.14767 and the references cited therein.
- 4 L. Shang, S. Dong and G. U. Nienhaus, *Nano Today*, 2011, **6**, 401.

-
- 5 J. Zheng, P. R. Nicovich and R. M. Dickson, *Annu. Rev. Phys. Chem.*, 2007, **58**, 409–431.
 - 6 K. M. Harkness, D. E. Cliffler and J. A. McLean, *Analyst*, 2010, **135**, 868–874.
 - 7 T. U. B. Rao, B. Nataraju and T. Pradeep, *J. Am. Chem. Soc.*, 2010, **132**, 16304–16307.
 - 8 C. Kumara and A. Dass, *Nanoscale*, 2011, **3**, 3064–3067.
 - 9 C. Kumara and A. Dass, *Nanoscale*, 2012, DOI: 10.1039/c2nr11781a.
 - 10 Y. Negishi, K. Igarashi, K. Munakata, W. Ohgake and K. Nobusada, *Chem. Commun.*, 2012, **48**, 660–662.
 - 11 A. Murugadoss, N. Kai and H. Sakurai, *Nanoscale*, 2012, **4**, 1280–1282.
 - 12 T. Udayabhaskararao, Y. Sun, N. Goswami, S. K. Pal, K. Balasubramanian and T. Pradeep, *Angew. Chem., Int. Ed.*, 2012, **51**, 2155–2159.
 - 13 J. Xie, Y. Zheng and J. Y. Ying, *J. Am. Chem. Soc.*, 2009, **131**, 888–889.
 - 14 M. A. H. Muhammed, P. K. Verma, S. K. Pal, A. Retnakumari, M. Koyakutty, S. Nair and T. Pradeep, *Chem.–Eur. J.*, 2010, **16**, 10103–10112.
 - 15 P. L. Xavier, K. Chaudhari, P. K. Verma, S. K. Pal and T. Pradeep, *Nanoscale*, 2010, **2**, 2769–2776.
 - 16 A. Mathew, P. R. Sajanlal and T. Pradeep, *J. Mater. Chem.*, 2011, **21**, 11205–11212.
 - 17 Y. Yue, T. Y. Liu, H. W. Li, Z. Liu and Y. Wu, *Nanoscale*, 2012, **4**, 2251–2254.
 - 18 A. Retnakumari, S. Setua, D. Menon, P. Ravindran, M. A. H. Muhammed, T. Pradeep, S. Nair and M. Koyakutty, *Nanotechnology*, 2010, **21**, 055103–12.
 - 19 X. L. Guével, N. Daum and M. Schneider, *Nanotechnology*, 2011, **22**, 275103.
 - 20 S. S. Narayanan and S. K. Pal, *J. Phys. Chem. C*, 2008, **112**, 4874.
 - 21 C. L. Liu, H. T. Wu, Y. H. Hsiao, C. W. Lai, C. W. Shih, Y. K. Peng, K. C. Tang, H. W. Chang, Y. C. Chien, J. K. Hsiao, J. T. Cheng and P. T. Chou, *Angew. Chem., Int. Ed.*, 2011, **50**, 7056–7060.
 - 22 H. Liu, X. Zhang, X. Wu, L. Jiang, C. Burda and J. J. Zhu, *Chem. Commun.*, 2011, **47**, 4237–4239.
 - 23 K. Chaudhari, P. L. Xavier and T. Pradeep, *ACS Nano*, 2011, **5**, 8816–8827.
 - 24 Y. H. Chen, J. T. Yang and K. H. Chau, *Biochemistry*, 1974, **13**, 3350–3359.
 - 25 P. Ramasamy, S. Guha, E. Shibu, T. S. Sreepasad, S. Bag, A. Banerjee and T. Pradeep, *J. Mater. Chem.*, 2009, **19**, 8456–8462.
 - 26 H. Wei, Z. Wang, J. Zhang, S. House, Y. G. Gao, L. Yang, H. Robinson, L. H. Tan, H. Xing, C. Hou, I. M. Robertson, J. M. Zuo and Y. Lu, *Nat. Nanotechnol.*, 2011, **6**, 93–97.
 - 27 D. Thompson, J. P. Hermes, A. J. Quinn and M. Mayor, *ACS Nano*, 2012, **6**, 3007.
 - 28 G. J. Ashwell, B. U. Wojcik and L. J. Phillips, *Angew. Chem., Int. Ed.*, 2010, **49**, 3508–3512.
 - 29 A. K. Samal and T. Pradeep, *Nanoscale*, 2011, **3**, 4840–4847.
 - 30 X. Guo, Q. Zhang, Y. Sun, Q. Zhao and J. Yang, *ACS Nano*, 2012, **6**, 1165–1175.
 - 31 L. Shang, Y. Wang, J. Jiang and S. Dong, *Langmuir*, 2007, **23**, 2714–2721.
 - 32 A. Dong, P. Huang and W. S. Caughey, *Biochemistry*, 1990, **29**, 3303–3308.

Electronic supplementary information (ESI) for Nanoscale
This journal is © The Royal Society of Chemistry 2012

Luminescent, Bimetallic AuAg Alloy Quantum Clusters in Protein Templates†

Jyoti Sarita Mohanty,[§] P. Lourdu Xavier,[§] Kamalesh Chaudhari,^{§,†} M. S. Bootharaju,[§] N. Goswami,[†] S. K. Pal[†] and T. Pradeep^{§,*}

[§]DST Unit of Nanoscience, Department of Chemistry, Indian Institute of Technology Madras, Chennai-600036, India. *E-mail: pradeep@iitm.ac.in

[†]Department of Biotechnology, Indian Institute of Technology Madras, Chennai-600036, India [‡]Unit for Nanoscience and Technology, Department of Chemical, Biological and Macromolecular Sciences, Satyendra Nath Bose National Centre for Basic Sciences, Block JD, Sector III, Salt Lake, Kolkata 700 098, India

Electronic Supplementary Information 1

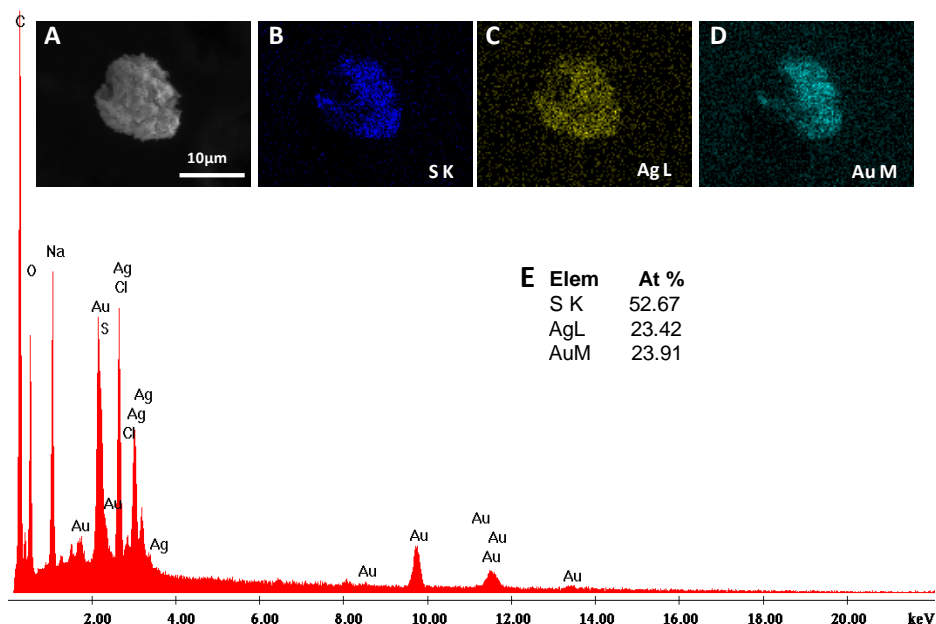


Fig. S1. SEM EDAX spectrum of the AuAg_{QC}@BSA sample. Au and Ag are in 1:1 atomic weight ratio. (B-D) EDAX images of the sample corresponding to the (A) SEM image. Quantification data (E) shows that Au:Ag ratio is matching with the expected calculated ratio.

Electronic Supplementary Information 2

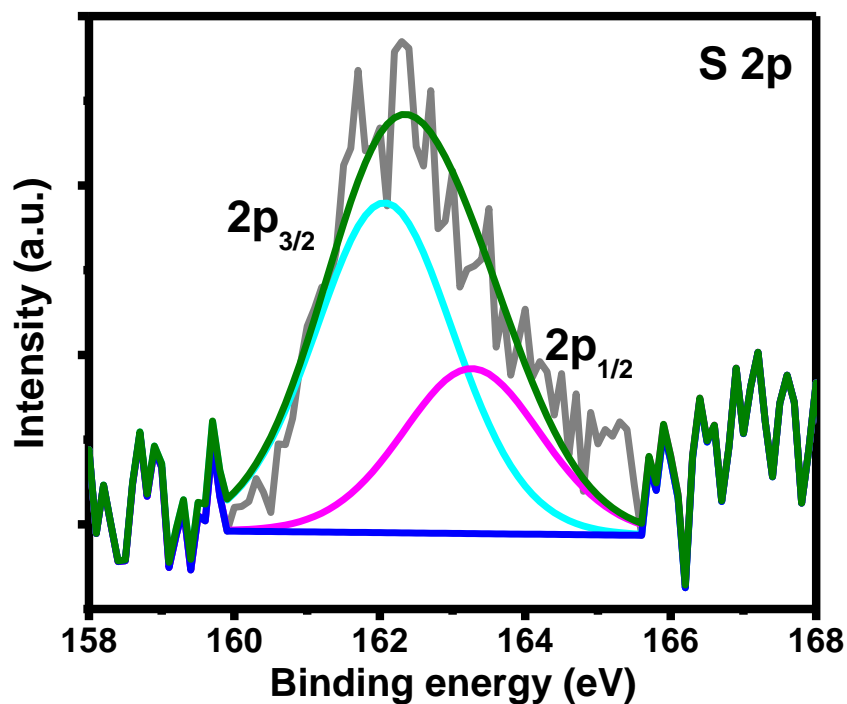


Fig. S2. XPS spectra showing the S 2p region with S 2p_{3/2} at 161.2 eV and S 2p_{1/2} at 163.3 eV.

Electronic Supplementary Information 3

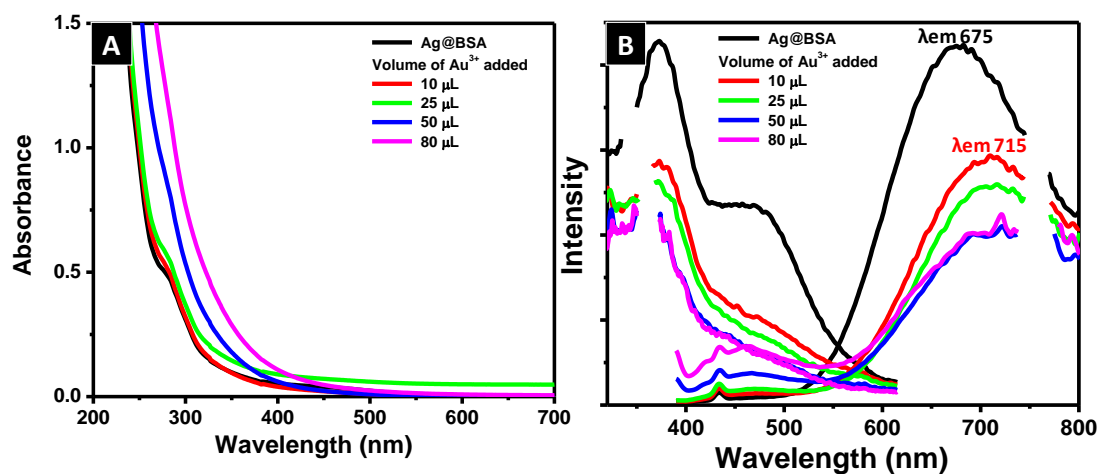


Fig. S3. (A) UV-Vis absorption spectra of Ag_{QC}@BSA and the reaction products formed after the addition of different volumes of HAuCl₄. (B) Photoluminescence spectra of Ag_{QC}@BSA (black trace) upon adding different volumes of Au³⁺. Emission spectrum got shifted to 715 nm suggesting the formation of an alloy.

Electronic Supplementary Information 4

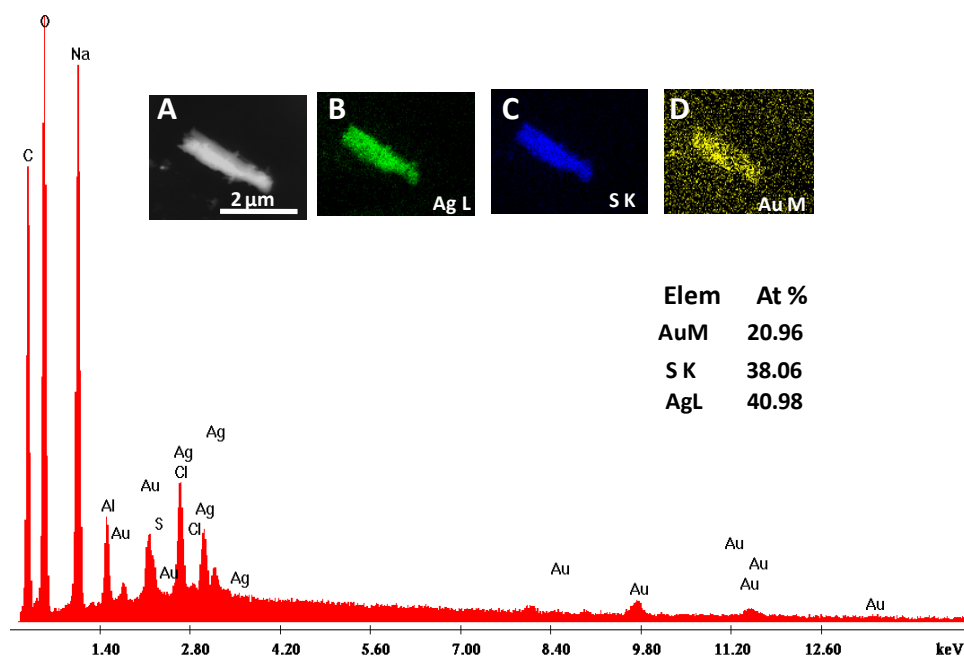


Fig. S4. SEM EDAX spectrum of AgQC@BSA after adding Au³⁺ ions along with the quantification data. (B-D) are EDAX images corresponding to the SEM image (A).

Electronic Supplementary Information 5

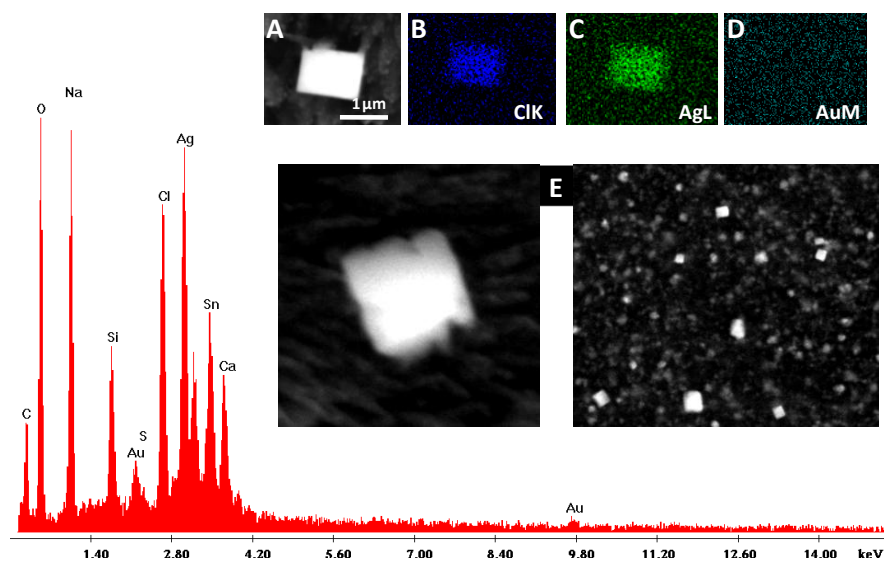


Fig. S5. SEM EDAX analysis indicating the formation of AgCl crystals due to galvanic exchange. The peaks of Si and Sn are due to the substrate (ITO) used for sample preparation.

Electronic Supplementary Information 6

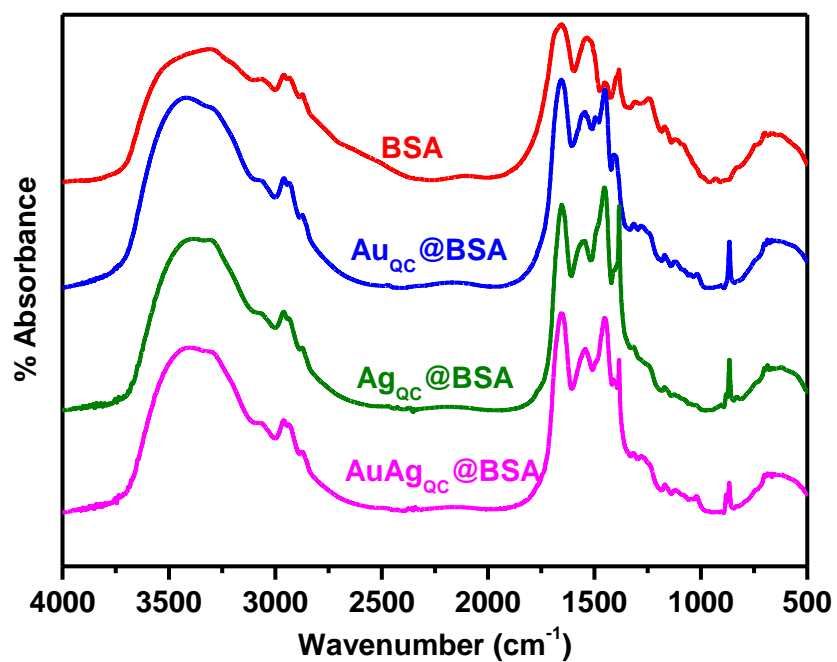


Fig. S6. Full range FTIR spectra of BSA (red), Au_{qc}@BSA (blue), Ag_{qc}@BSA (olive) and AuAg_{qc}@BSA (magenta).

Cite this: *Chem. Commun.*, 2012, **48**, 6788–6790

www.rsc.org/chemcomm

High temperature nucleation and growth of glutathione protected $\sim \text{Ag}_{75}$ clusters[†]

Indranath Chakraborty, Thumu Udayabhaskararao and Thalappil Pradeep*

Received 27th March 2012, Accepted 8th May 2012

DOI: 10.1039/c2cc33099g

We report the first high temperature solution state synthesis of glutathione (–SG) protected atomically precise silver clusters. Noble metal cluster synthesis from metal ions generally requires ice cold temperatures as they are extremely sensitive and high temperature routes are used only for core reduction methods, starting from nanoparticles. The clusters formed by the new route have distinct features in their absorption profile and they exhibit red luminescence. They are characterised by other spectroscopic and microscopic techniques and a tentative formula of $\text{Ag}_{75}(\text{SG})_{40}$ has been assigned.

Noble metal quantum clusters^{1–8} belong to a new category of materials with well defined optical absorption features and intense luminescence. While studies of atomically precise clusters with specific nuclearities such as Au_{25} , Au_{38} and Au_{102} have progressed considerably,^{9–15} their silver analogues are yet to be synthesized. In view of their reduced stability, novel routes are needed to make such relatively unstable clusters. As most of the clusters are metastable, nucleation at low temperature and rapid protection by covalent chemistry are the desired steps used in their synthesis.¹⁶ As a result, reducing agents such as NaBH_4 are used around 0 °C in a solution containing high concentration of the protecting agent.^{16–20} Relatively high temperature etching of pre-formed metallic nanoparticles can also produce such clusters.^{11,21} However, direct high temperature synthetic routes for clusters in solution, starting from ions, are yet to be reported. In this communication, we show that direct synthesis of atomically precise clusters is possible even at a high temperature of 70 °C. This study suggests that such clusters are likely to be stable even at elevated temperatures which expands the possibility of cluster research.

These clusters were synthesized by a new method which involves the mixing of 20 mL of 5.88 mM AgNO_3 with 20 mL of 2.034 mM GSH and the mixture was stirred for 5 min at 70 °C followed by the addition of 20 mL of 0.0112 mM formic acid (all in water). Temperature was kept constant throughout the reaction. The color of the solution changed with time

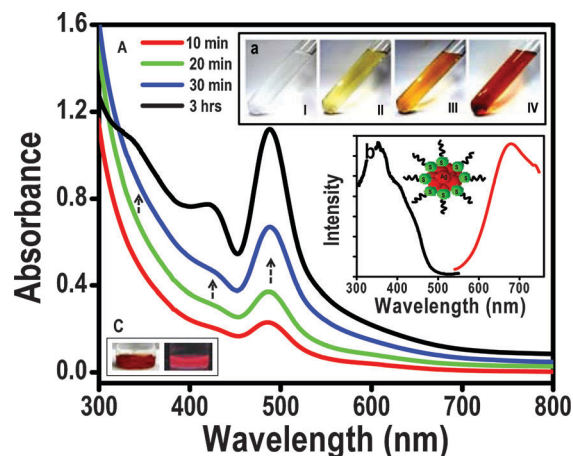


Fig. 1 UV-vis absorption spectra of the growth of clusters with time (A). Gradual increase in the intensity of the 350, 420 and 478 nm peaks is seen. The growth was complete in 3 h and no further increase in the intensity of the absorption bands occurred. Insets: (a) Photographs of the reaction mixture during synthesis at 0 min (I), 10 min (II), 20 min (III) and 3 h (IV); (b) luminescence excitation and emission spectra (black and red respectively) of as-synthesized clusters which emit at 670 nm upon excitation at 400 nm and (c) photographs of clusters under visible and UV light, respectively. Inset of inset (b) is a cartoon representation of the cluster.

indicating the nucleation and growth of clusters. After 3 h, no further color change was observed although stirring was continued for 24 h, which shows that the reaction was completed in 3 h. The final solution was reddish-brown. Photographs of time dependent reaction products are given in Fig. 1a and Fig. S1 (ESI[†]). The nucleation and growth of these clusters was monitored by UV-vis spectroscopy (Fig. 1A). Even at the initial stages of the reaction, emergence of a peak at 478 nm and shoulder peaks at 350, 420, 540 and 625 nm was observed. We ruled out the possibility of the 420 nm peak to be due to plasmonic nanoparticles as this kind of shoulder peak was observed for some glutathione protected silver clusters as well.^{5,22} Besides, no nanoparticles were seen in TEM (see below). Our recent work on silver clusters also clarifies that the new peaks belong to a cluster with molecular behaviour.²³ The shoulder peak at 625 nm disappeared upon continuation of the reaction. A prominent feature at 478 nm and shoulder peaks at 540, 420 and 350 nm were observed after completion of growth. This solution was highly stable for

DST Unit of Nanoscience (DST UNS), Department of Chemistry, Indian Institute of Technology Madras, Chennai, 600 036, India. E-mail: pradeep@iitm.ac.in; Fax: +91-44-2257 0545

[†] Electronic supplementary information (ESI) available. See DOI: 10.1039/c2cc33099g

several months even at higher temperatures. Even if we heat the clusters at 70 °C, a couple of months after synthesis, the solution was found to retain its optical properties. However, all the reported silver clusters are less stable and do not exist above 50 °C in solution.^{24,25} The band gap of the cluster is estimated to be 1.73 eV (a plot of absorbance against energy in eV is given in Fig. S2, ESI†). The cluster exhibits emission at 670 nm. The excitation spectrum gives three band maxima at 360, 400 and 430 nm (Fig. 1b) and each of these excitations give the same emission. Multiple excitation maxima are seen in QCs such as Au₂₅.¹⁴ The cluster solution shows bright red luminescence (Fig. 1c) under UV light as expected from its emission wavelength. During the synthesis, emission intensity got increased and became stable after 3 h (Fig. S3, ESI†), in concordance with the UV-vis observation. Quantum yield was measured to be 4×10^{-3} , comparable to silver clusters synthesized by core etching.²¹

As the reaction proceeds, pH of the solution changes from 5.8 to 2.4. This may be due to the production of H⁺ in the reaction medium while formic acid reduces silver ions to form silver clusters. In view of this, the following reaction for the decomposition of formic acid is suggested.



The E° of this half cell (HCOOH/CO₂, H⁺) at 298 K is -0.25 V [with respect to $E^\circ(\text{H}^+, \frac{1}{2}\text{H}_2)$], which is quite negative, but higher reaction temperature may make the reduction facile ($-T\Delta S$). It may also be noted that the electrochemical potential of a cluster ($\text{Ag}_n \rightarrow \text{Ag}_n^+ + \text{e}^-$) is substantially lower than that of bulk silver ($\text{Ag}_{\text{bulk}} \rightarrow \text{Ag}_{\text{bulk}}^+ + \text{e}^-$). This would enable the reduction of silver ions to silver clusters.

Control experiments were carried out by varying the glutathione concentration, keeping the silver concentration constant. In the absence of glutathione, nanoparticles (of 10–15 nm in diameter) were formed (Fig. S4, ESI†). With increase in concentration of GSH, clusters started to nucleate but after some concentration, thiolates were formed which precipitated in the test tube and formic acid was not able to reduce them. Extension of the reaction to gold clusters was also tried (Fig. S5, ESI†). After complete reaction, clusters showed UV-vis peaks at 350 and 680 nm. The solution exhibited strong red luminescence under UV exposure. We tried to get the material in the solid state but only a blackish powder, insoluble in water, could be obtained. It is known that it is not possible to get powders out of citrate capped gold nanoparticles²⁶ but it is very much feasible for monolayer protected gold or silver clusters.^{24,25} This suggests that the clusters may be charged.

The ¹H NMR spectrum of the cluster was recorded. The sample was prepared in D₂O and the resonances were compared with those of pure GSH (Fig. 2). All the peaks corresponding to the protons are broadened and weakened in the cluster. It should be noted that a strong peak at around 4.75 ppm arises from residual H₂O and HDO in D₂O. The resonances are labelled in the spectra. The strong singlet for H-9 (inset of Fig. 2) at 3.92 ppm, and a multiplet for H-3 and H-4 at 2.11 and 2.44 ppm, respectively, resemble closely the spectra of GSH. C-10, C-8, C-5, and C-1 do not bear hydrogen. As both H-6 (β position) and H-7 (α position) are very close to the silver core, it is likely that these protons are significantly shifted

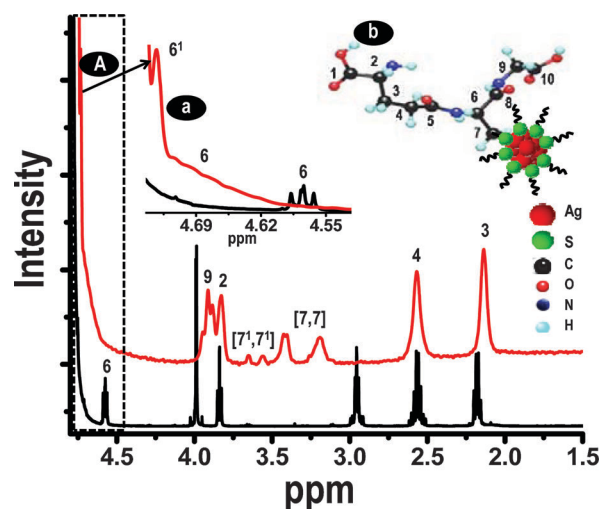


Fig. 2 (A) ¹H NMR spectra of Ag@SG clusters (red) and GSH (black) taken in D₂O. For clarity, the 4.5 ppm region was expanded in (a). All the protons are marked, along with a schematic of the cluster. Downfield shift of H-6 and H-7 confirms the binding of GSH with Ag. The inset shows the structure of GSH attached with the cluster.

downfield. There are a set of broad peaks in the range of 3.0–3.8 ppm, assigned to H-7. These peaks can be compared with the data of Au₂₅(SG)₁₈^{11,27,28} and can be discussed in the light of the different types of ligands present on the cluster surface. QCs in general are composed of two types of ligands. There are six numbers of $-\text{[SR}_C\text{-Au-SR}_B\text{-Au-SR}_C\text{-]}$ units decorating the Au₁₃ core giving the Au₂₅(SG)₁₈ composition, where SR_C and SR_B are core-linked and bridged thiolates, respectively. ¹H NMR of Au₂₅(SG)₁₈ shows two peaks in the 2:1 ratio with different chemical shifts for SR_C and SR_B, respectively.^{27,28} Each peak is again split by chirality of the cluster, making four peaks (one pair with equal intensity). In our case, a similar situation arises. Here the number of core-linked thiolates is more, as expected in the case of a larger core.¹⁴

Mass spectrometric analysis of the cluster in aqueous medium was not successful so far using electrospray ionisation (ESI) and matrix assisted laser desorption ionisation (MALDI). Due to that reason, we choose an alternative way to find the molecular formula of the cluster. As-synthesised clusters were phase transferred to the organic (toluene) medium using phenylethanethiol (PET). MALDI MS of these clusters gave distinct features (Fig. 3A). From the previous studies, it is known that *trans*-2-[3-(4-*tert*-butylphenyl)-2-methyl-2-propenylidene]malononitrile (popularly called DCTB) gives a good mass spectrum for clusters protected with PET.^{29,30} Even after ligand exchange, all absorption bands are present in the PET protected cluster which proves that the cluster core is the same as in the case of GSH (Fig. 3B). Ligand exchange without core change is known in several cases.^{11,31} The slight broadening of the absorption peak in the exchanged product is due to the overlap of two peaks (at 420 and 480 nm). In MALDI MS, the PET exchanged Ag cluster gives a molecular ion peak at 13.7 kDa at a threshold (nominal) laser intensity of 2850. Below this intensity, no cluster was detected. Peak position depends on the laser intensity. From lower (2850) to higher (3950) laser intensity, peaks were shifted to the low mass region (13.7 to 10.3 kDa). This can be understood from the gradual fragmentation of the cluster, as expected at higher

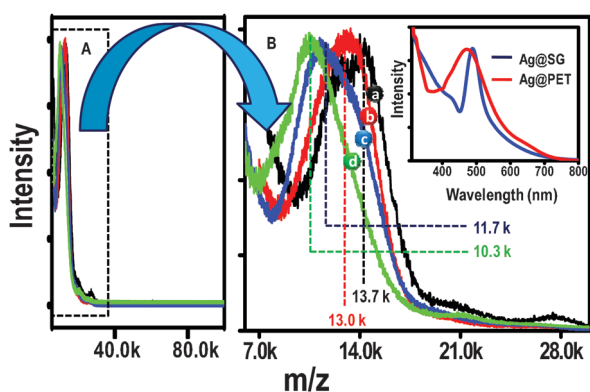


Fig. 3 MALDI MS data of ligand exchanged Ag@SG clusters in the negative mode (A). It shows a molecular ion peak at 13.7 kDa (black color). The expanded view of the molecular peaks (B). Fragmentation occurs with increase in laser intensity. The traces a, b, c, and d are at laser intensities of 2850, 2910, 3174, and 3974, respectively (numbers refer to instrument settings and not laser power). Inset of B shows the UV-vis spectra of as-synthesized clusters and PET exchanged clusters. It shows that cluster is intact even after ligand exchange.

laser intensities (Fig. 3B). It is important to note that the MALDI MS feature is broader than that of a well-defined Au cluster such as Au₂₅(SG)₁₈. We believe that the weaker Ag–S bond strength in comparison to Au–S makes ligand desorption more probable in the silver analogues, making the spectrum broad.

As the core dimension is small, these clusters do not appear well in TEM.²⁴ Upon longer electron beam irradiation, they aggregate to form nanoparticles.²¹ HRTEM images confirm the formation of the cluster with an average diameter of 0.85 nm (Fig. S6, ESI[†]). HRTEM images of PET exchanged silver clusters are given in Fig. S7 (ESI[†]). GSH protected clusters show increased aggregation (Fig. S6, ESI[†]).

The XPS survey spectrum of the as-synthesized silver cluster sample shows the expected elements (Fig. S8, ESI[†]). The expanded spectrum shows a state closer to Ag(0) with a binding energy (BE) of 368.2 eV (Fig. S8, ESI[†]). Note that between Ag(I) and Ag(0) states, there is not much difference in BE, unlike in the case of Au. S 2p exists at 162.5 eV, corresponding to thiolate. Peaks corresponding to O 1s, C 1s and N 1s appeared at the expected positions (Fig. S9, ESI[†]). The Ag to S ratio is 1.87 : 1.

Based on this information and the MALDI MS data, probable composition of our cluster is Ag₇₅(SG)₄₀. SEM/EDAX data given in Fig. S10 (ESI[†]) showing an Ag : S ratio of 1.83 : 1 also support this composition (close to the ratio in XPS). As the cluster could not be made into a free flowing powder, CHNS analysis was not performed.

The Ag@SG cluster shows optical chirality in its circular dichroism (CD) spectrum (Fig. S11, ESI[†]). It appears to arise from the cluster core as the ligand (GSH) does not show peaks in that region.

In conclusion, formic acid mediated high temperature synthesis of glutathione protected silver clusters is reported for the first time, starting from Ag⁺. A molecular mass of 13.7 kDa was confirmed from MALDI MS data of the ligand exchanged cluster. In conjunction with XPS and SEM-EDAX, a probable cluster composition of Ag₇₅(SG)₄₀ was assigned.

The cluster exhibits chirality in the solution state. As all reagents are bio-compatible, this cluster may be useful in biological applications.

We thank the Department of Science and Technology, Government of India, for financial support. Thanks are due to SAIF, IIT Madras, for the NMR data.

Notes and references

- Y. Negishi, N. K. Chaki, Y. Shichibu, R. L. Whetten and T. Tsukuda, *J. Am. Chem. Soc.*, 2007, **129**, 11322.
- M. A. Habeeb Muhammed and T. Pradeep, *Advanced Fluorescence Reporters in Chemistry and Biology II*, Springer-Verlag, Berlin, Heidelberg, 2010, vol. 9, part 4, 333, and references cited therein.
- P. L. Xavier, K. Chaudhari, A. Baksi and T. Pradeep, *Nano Rev.*, 2012, **3**, 14767.
- K. Chaudhari, P. L. Xavier and T. Pradeep, *ACS Nano*, 2011, **5**, 8816.
- S. Kumar, M. D. Bolan and T. P. Bigioni, *J. Am. Chem. Soc.*, 2010, **132**, 13141.
- L. D. Menard, S.-P. Gao, H. Xu, R. D. Twisten, A. S. Harper, Y. Song, G. Wang, A. D. Douglas, J. C. Yang, A. I. Frenkel, R. G. Nuzzo and R. W. Murray, *J. Phys. Chem. B*, 2006, **110**, 12874.
- I. Diez, M. Pusa, S. Kulmala, H. Jiang, A. Walther, A. S. Goldmann, A. H. E. Müller, O. Ikkala and R. H. A. Ras, *Angew. Chem., Int. Ed.*, 2009, **48**, 2122.
- M. A. Habeeb Muhammed and T. Pradeep, *Chem. Phys. Lett.*, 2007, **449**, 186.
- Y. Shichibu, Y. Negishi, T. Tsukuda and T. Teranishi, *J. Am. Chem. Soc.*, 2005, **127**, 13464.
- Y. Shichibu, Y. Negishi, H. Tsunoyama, M. Kanehara, T. Teranishi and T. Tsukuda, *Small*, 2007, **3**, 835.
- E. S. Shibui, M. A. H. Muhammed, T. Tsukuda and T. Pradeep, *J. Phys. Chem. C*, 2008, **112**, 12168.
- M. Zhu, E. Lanni, N. Garg, M. E. Bier and R. Jin, *J. Am. Chem. Soc.*, 2008, **130**, 1138.
- M. W. Heaven, A. Dass, P. S. White, K. M. Holt and R. W. Murray, *J. Am. Chem. Soc.*, 2008, **130**, 3754.
- P. D. Jadzinsky, G. Calero, C. J. Ackerson, D. A. Bushnell and R. D. Kornberg, *Science*, 2007, **318**, 430.
- Y. Pei, Y. Gao and X. C. Zeng, *J. Am. Chem. Soc.*, 2008, **130**, 7830.
- N. Cathcart and V. Kitaev, *J. Phys. Chem. C*, 2010, **114**, 16010.
- O. M. Bakr, V. Amendola, C. M. Aikens, W. Wenseleers, R. Li, L. Dal Negro, G. C. Schatz and F. Stellacci, *Angew. Chem., Int. Ed.*, 2009, **48**, 5921.
- Z. Wu, E. Lanni, W. Chen, M. E. Bier, D. Ly and R. Jin, *J. Am. Chem. Soc.*, 2009, **131**, 16672.
- N. Nishida, H. Yao and K. Kimura, *Langmuir*, 2008, **24**, 2759.
- K. V. Mrudula, T. U. Bhaskara Rao and T. Pradeep, *J. Mater. Chem.*, 2009, **19**, 4335.
- L. Dhanalakshmi, T. Udayabhaskararao and T. Pradeep, *Chem. Commun.*, 2012, **48**, 859.
- X. Yuan, Z. Luuuo, Q. Zhang, X. Zhang, Y. Zheng, J. Y. Lee and J. Xie, *ACS Nano*, 2011, **5**, 8800.
- I. Chakraborty, T. U. B. Rao and T. Pradeep, *J. Hazard. Mater.*, 2012, **211–212**, 396.
- T. U. B. Rao, B. Nataraju and T. Pradeep, *J. Am. Chem. Soc.*, 2010, **132**, 16304.
- T. Udaya Bhaskara Rao and T. Pradeep, *Angew. Chem., Int. Ed.*, 2010, **49**, 3925.
- J. Turkevich, P. C. Stevenson and Hillier, *Discuss. Faraday Soc.*, 1951, **11**, 55.
- Z. Wu, C. Gayathri, R. R. Gil and R. Jin, *J. Am. Chem. Soc.*, 2009, **131**, 6535.
- Z. Wu and R. Jin, *Nano Lett.*, 2010, **10**, 2568.
- S. Knoppe, A. C. Dharmaratne, E. Schreiner, A. Dass and T. Bürgi, *J. Am. Chem. Soc.*, 2010, **132**, 16783.
- S. M. Reilly, T. Krick and A. Dass, *J. Phys. Chem. C*, 2009, **114**, 741.
- T. Udayabhaskararao, Y. Sun, N. Goswami, S. K. Pal, K. Balasubramanian and T. Pradeep, *Angew. Chem., Int. Ed.*, 2012, **51**, 2155.

Supporting Information

High temperature nucleation and growth of glutathione protected ~Ag₇₅ clusters

Indranath Chakraborty, Thumu Udayabhaskararao and Thalappil Pradeep*

*DST Unit of Nanoscience (DST UNS), Department of Chemistry, Indian Institute of Technology
Madras, Chennai 600 036, India; Fax: 91-44-2257 0545;

E-mail: pradeep@iitm.ac.in

S. No.	Description	Page No.
1	Experimental section and instrumentation	2
2	Photographs during synthesis	3
3	Plot of absorbance with respect to energy	4
4	Time dependent emission spectra	5
5	Control experiment with different concentration of GSH	6
6	UV-visible spectrum of the Au@SG cluster	7
7	HRTEM images of the cluster	8
8	HRTEM images of the ligand exchanged cluster	9
9	XPS survey spectrum	10
10	Expanded XPS of C 1s, S 2p, N 1s, and O 1s	11
11	EDAX spectrum of the Ag@SG cluster	12
12	CD Spectra of the Ag@SG cluster	13

Supplementary information

Experimental section

Materials

All the chemicals were commercially available and were used without further purification. Silver nitrate (AgNO₃, 99%), glutathione (GSH, 97%), and formic acid (HCOOH, 99%) were purchased from Aldrich.

Instrumentation

UV/Vis spectra were measured with a Perkin Elmer Lambda 25 instrument in the range of 200- 1100 nm. Luminescence measurements were carried out on a Jobin Yvon NanoLog instrument. The band passes for excitation and emission were set as 2 nm. X-ray photoelectron spectroscopy (XPS) measurements were conducted using an Omicron ESCA Probe spectrometer with polychromatic MgK α X-rays ($h\nu=1253.6$ eV). The samples were spotted as drop-cast films on a sample stub. Constant analyzer energy of 20 eV was used for the measurements. High resolution transmission electron microscopy of clusters was carried out with a JEOL 3010 instrument. The samples were drop casted on carbon-coated copper grids and allowed to dry under ambient conditions. Matrix-assisted desorption ionization mass spectrometry (MALDI MS) studies were conducted using a Voyager-DE PRO Bio-spectrometry Workstation from Applied Bio-systems. A pulsed nitrogen laser of 337 nm was used for the MALDI MS studies. Mass spectra were collected in negative ion mode and were averaged for 100 shots. ¹H NMR were measured with a 500 MHz Bruker Advance III spectrometer operating at 500.13 MHz and equipped with a 5 mm triple-resonance PFG probe. Solutions were made in 99.98 % D₂O (Aldrich) and sealed immediately. The signal of the solvent served as the reference for the field frequency lock. All experiments were performed at a temperature of 25 °C. Standard Bruker pulse programs (Topspin 2.1) were employed throughout. Scanning electron microscopic (SEM) and energy dispersive X-ray (EDAX) analyses were done in a FEI QUANTA-200 SEM. For measurements, samples were drop casted on an indium tin oxide coated conducting glass and dried in vacuum.

S1. Supplementary information 1

Photographs during synthesis

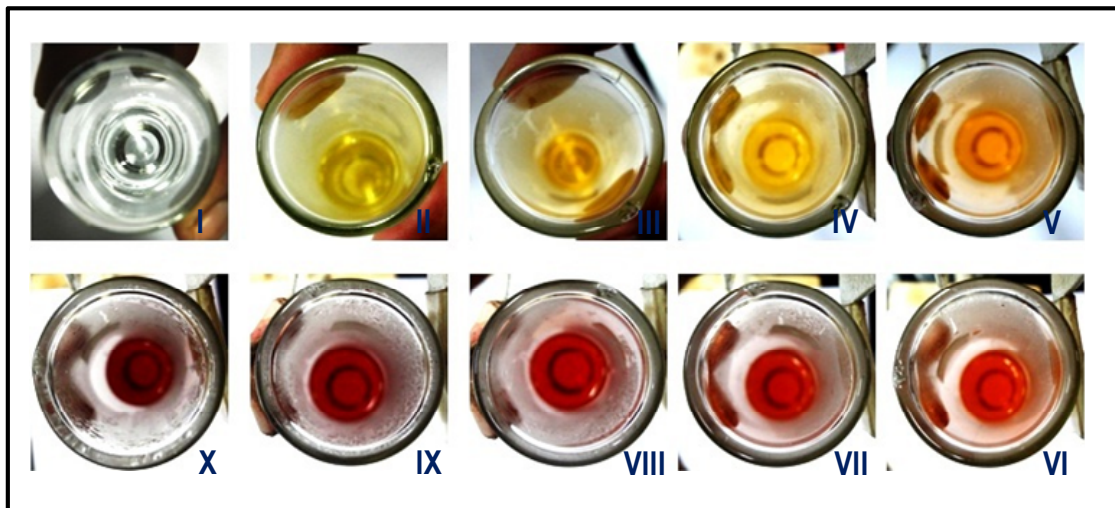


Fig. S1. Top views of the sample tubes during the synthesis of the cluster in different intervals of time, starting from 0 min to 3 hrs. Time was counted after the addition of formic acid.

S2. Supplementary information 2

Plot of absorbance with respect to energy

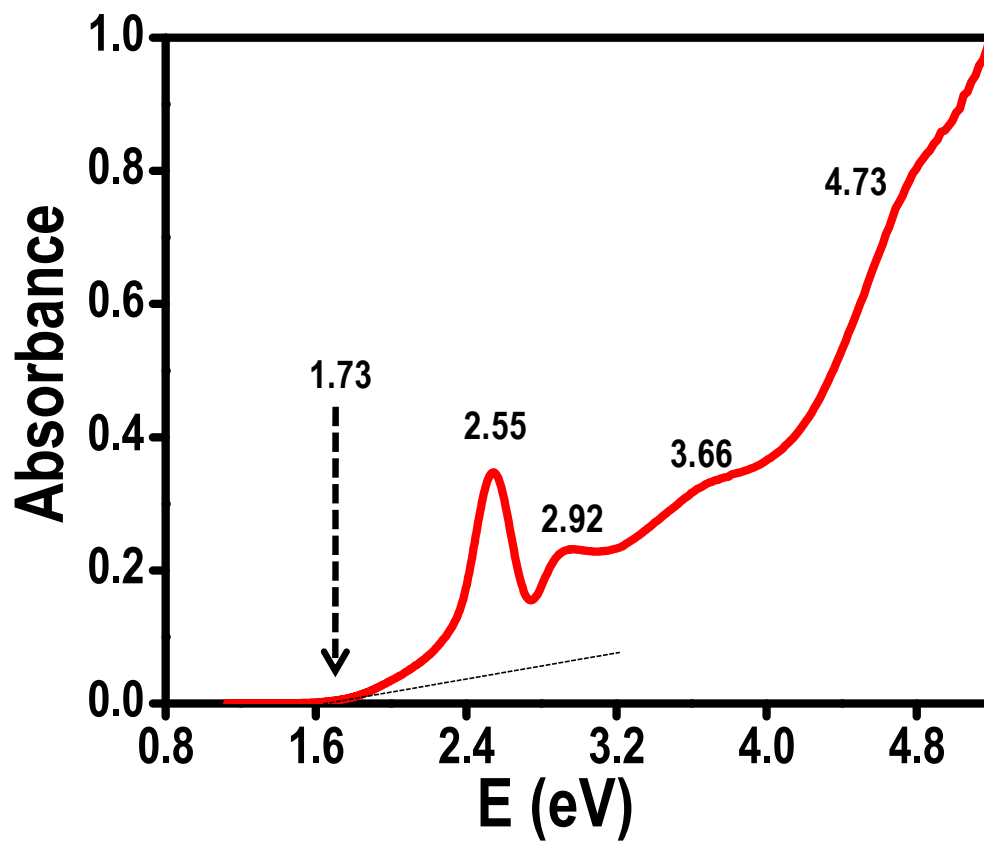


Fig. S2. The absorption spectrum is plotted in energy (eV) axis. Peaks are labeled. The spectrum shows a band gap of 1.73 eV on extrapolation.

S3. Supplementary information 3

Time dependent emission spectra

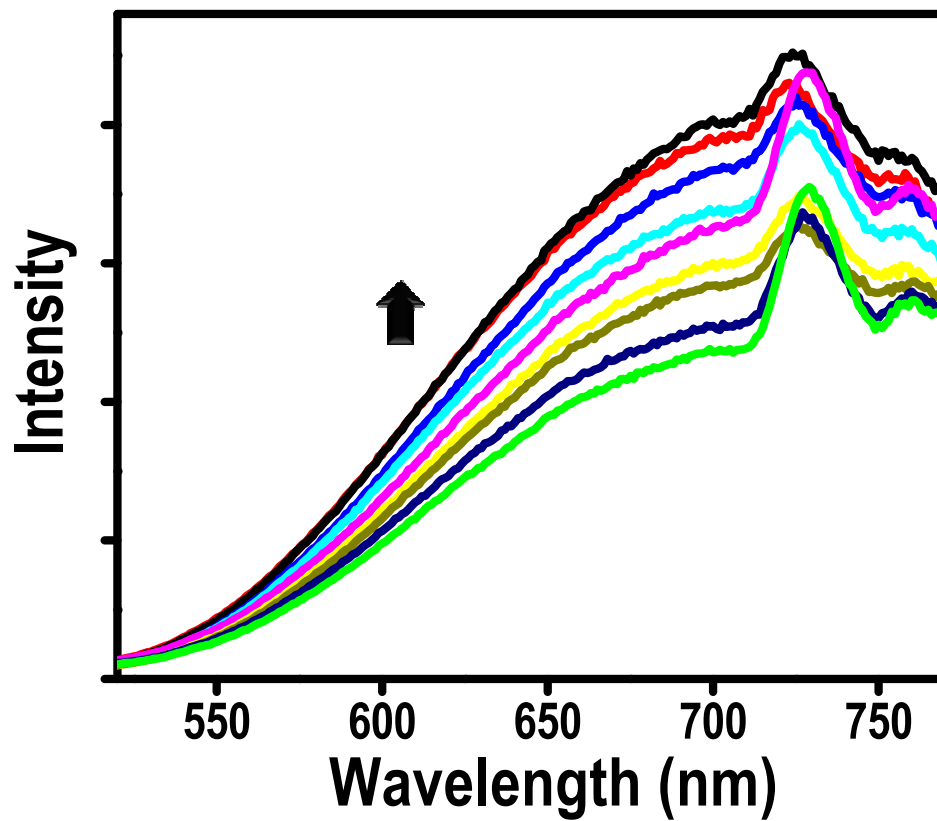


Fig. S3. The time dependent luminescence spectra of as-synthesized Ag@SG cluster that shows gradual increase in emission intensity with time till complete nucleation. It was excited with 400 nm wavelength.

S4. Supplementary information 4

Control experiment with different concentration of GSH

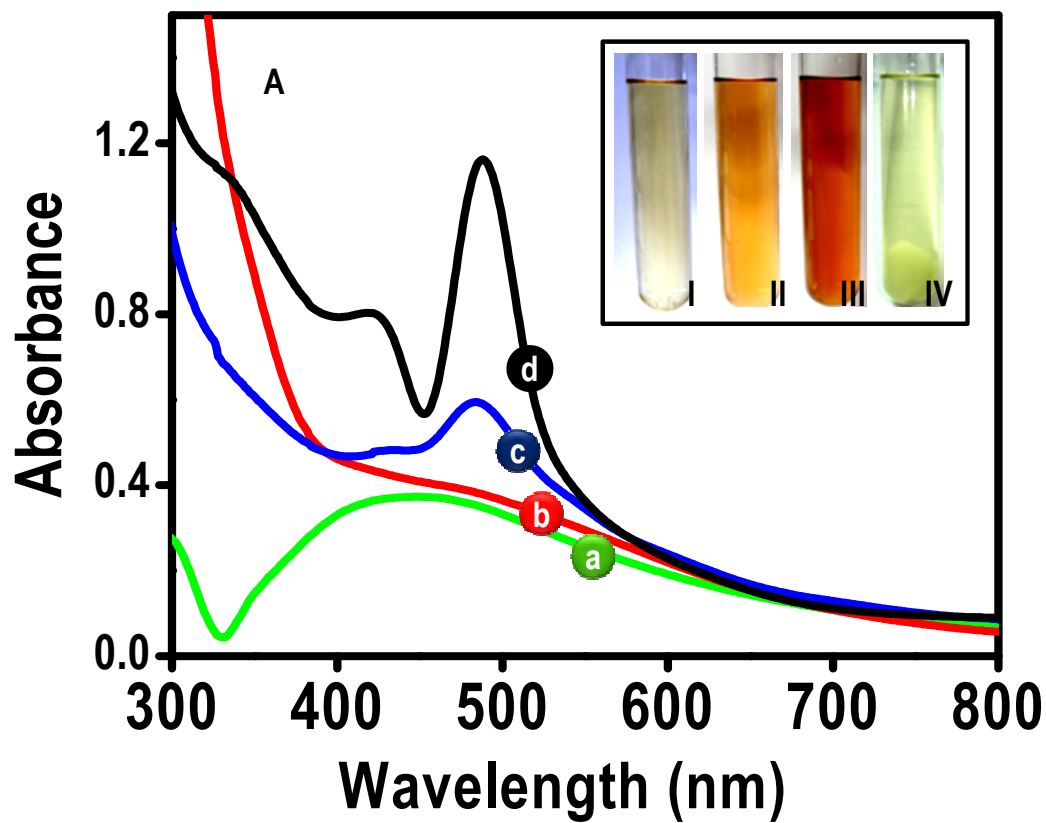


Fig. S4. UV-vis spectra of materials obtained at different concentrations of glutathione keeping the silver nitrate concentration fixed. Traces a, b, c, and d are the spectra associated with 0, 0.1, 0.275 and 0.675 mM of glutathione. Insets are the photographs of the materials formed with 0 (I), 0.1 (II), 0.675 (III) and 1 (IV) mM, respectively.

S5. Supplementary information 5

UV-visible spectrum of the Au@SG cluster

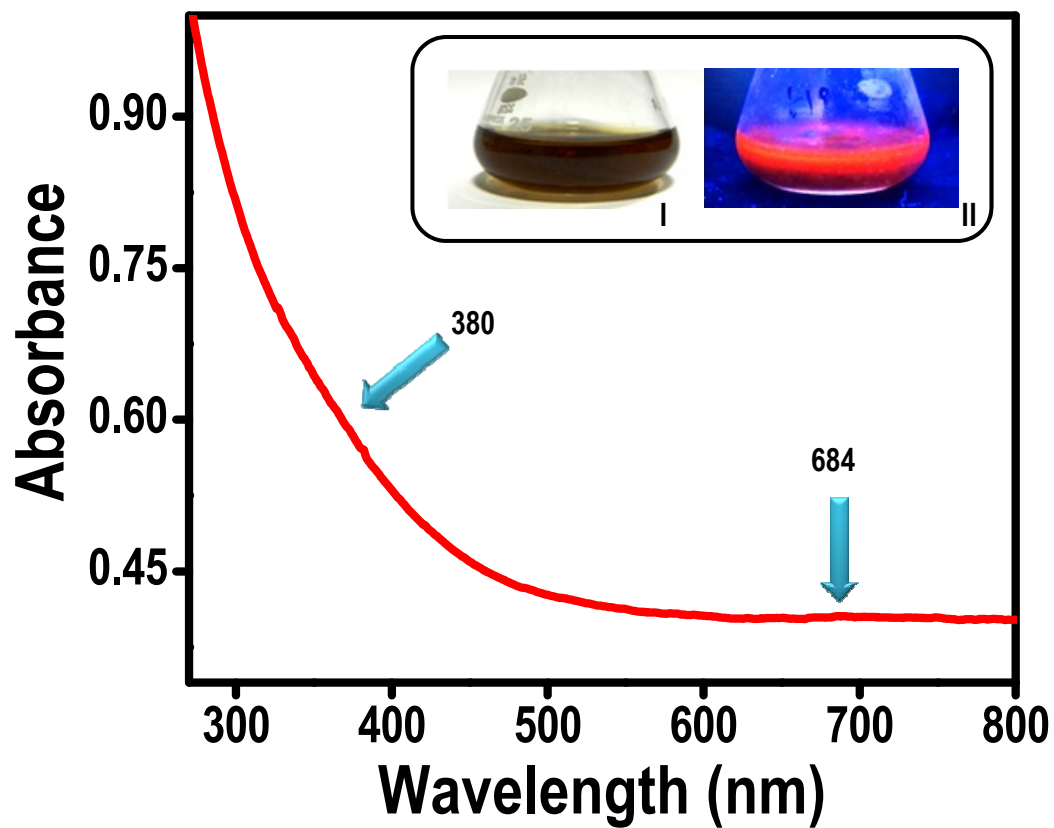


Fig. S5. The absorption spectrum of the Au@SG cluster synthesized using the same reducing agent. Two characteristics humps were observed at 684 nm and 380 nm. Inset is showing photographs under visible and UV light.

S6. Supplementary information 6

HRTEM images of the cluster

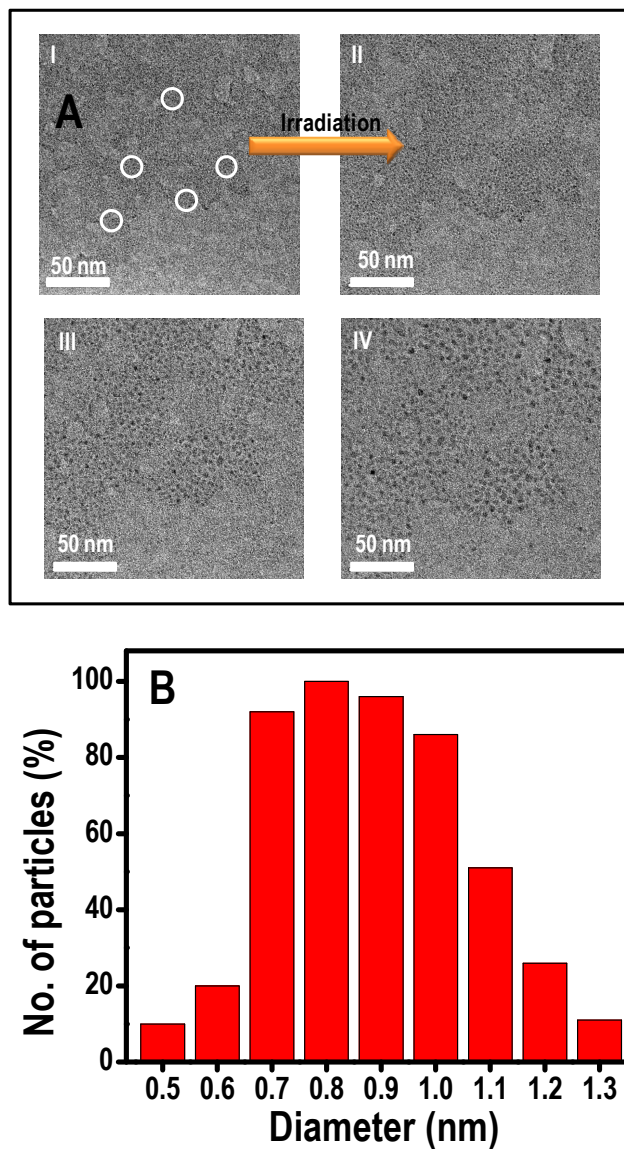


Fig. S6. A (I) HRTEM images of Ag@SG cluster, some areas are marked. II, III and IV are the effect of electron beam irradiation of the same area at a definite time interval (60 sec). It shows gradual increase in cluster size as time progresses. B is the size distribution plot for Ag@SG cluster which is ranging from 0.5 to 1.3 nm with an average diameter of 0.85 nm.

S7. Supplementary information 7

HRTEM images of the ligand exchanged cluster

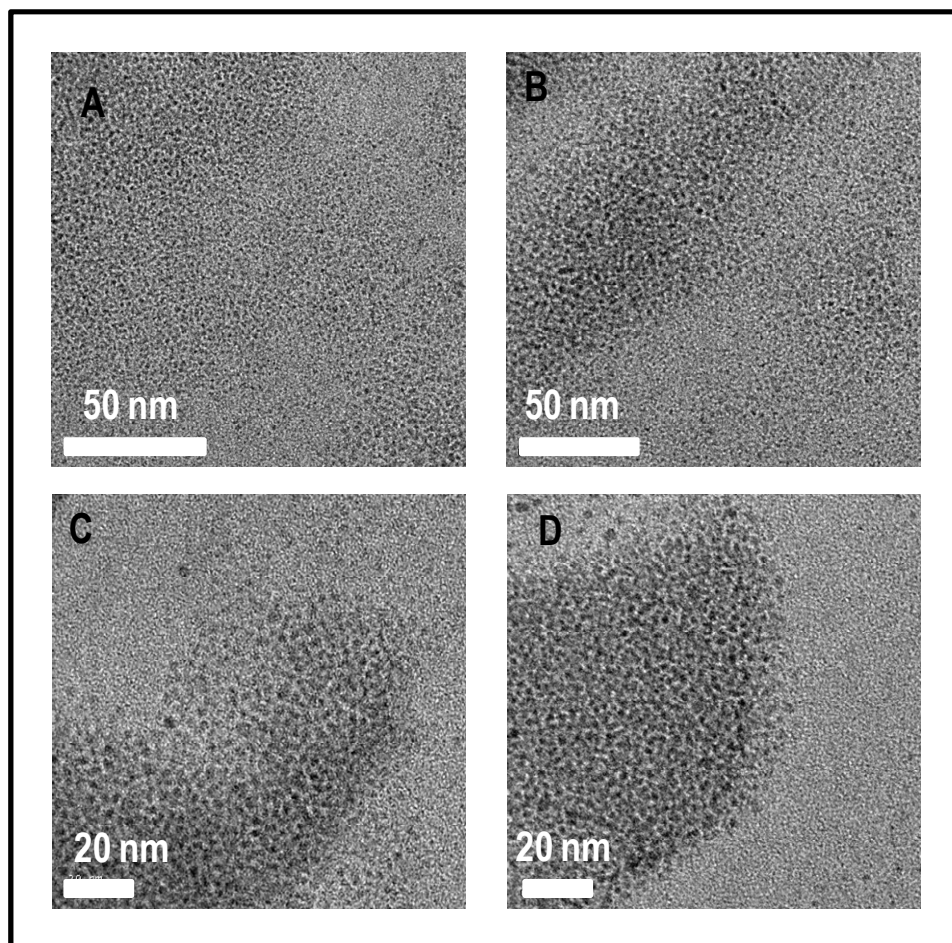


Fig. S7. HRTEM images of Ag@PET clusters. Average diameter of the clusters is almost the same. A, B, C, and D are the different regions taken from the grid.

S8. Supplementary information 8

XPS spectrum of Ag@SG

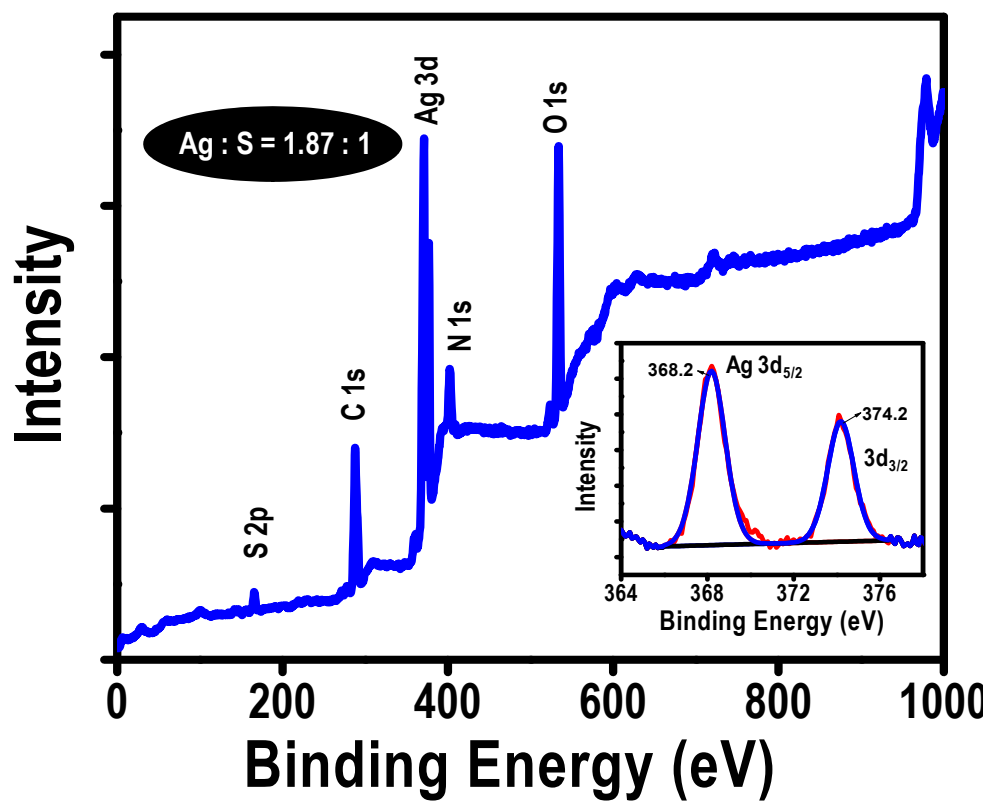


Fig. S8. The XPS survey spectrum of Ag@SG cluster. Individual elements are assigned in the spectrum. Inset is showing the expanded spectrum of Ag 3d. All peaks are labeled.

S9. Supplementary information 9

Expanded XPS of elements C 1s, S 2p, N 1s, and O 1s

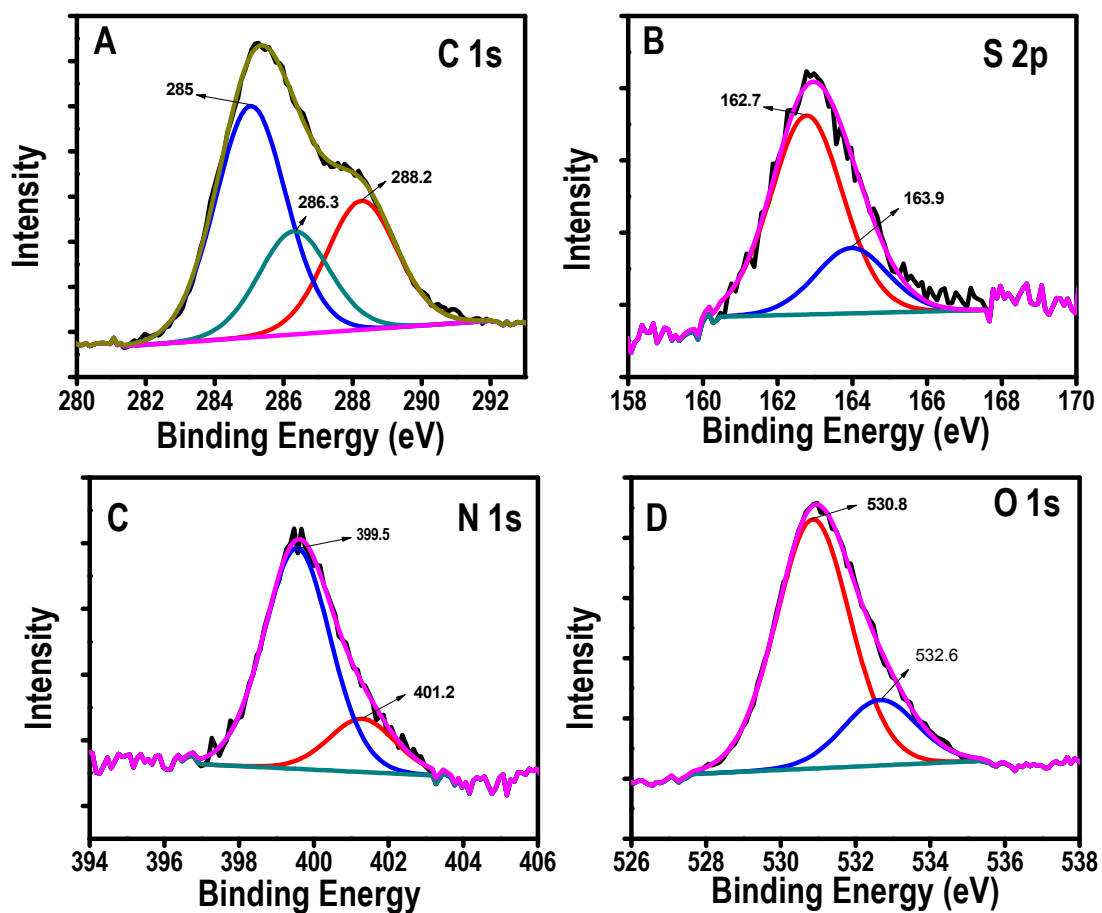


Fig. S9. A, B, C, and D are the expanded regions, C 1s, S 2p, N 1s, and O 1s, respectively. All the spectral features have been fitted into the different chemical species expected.

S10. Supplementary information 10

EDAX spectrum of the Ag@SG cluster

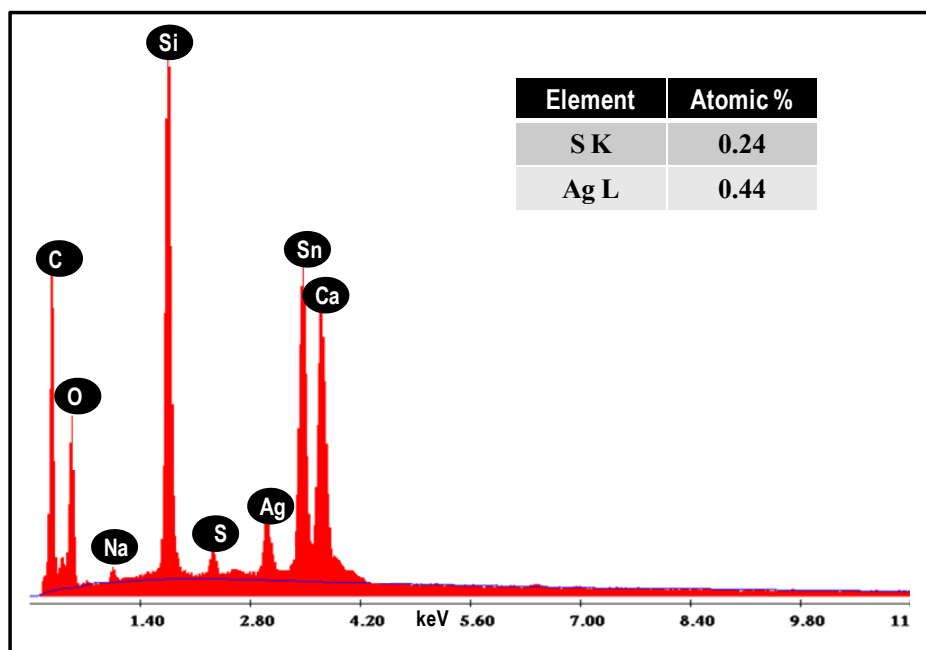


Fig. S10. SEM EDAX spectra of the as-synthesized cluster. Inset is a table showing individual elemental percentages. Elements such as Si and Sn in the spectrum are from the substrate.

S11. Supplementary information 11

CD spectra of the Ag@SG cluster

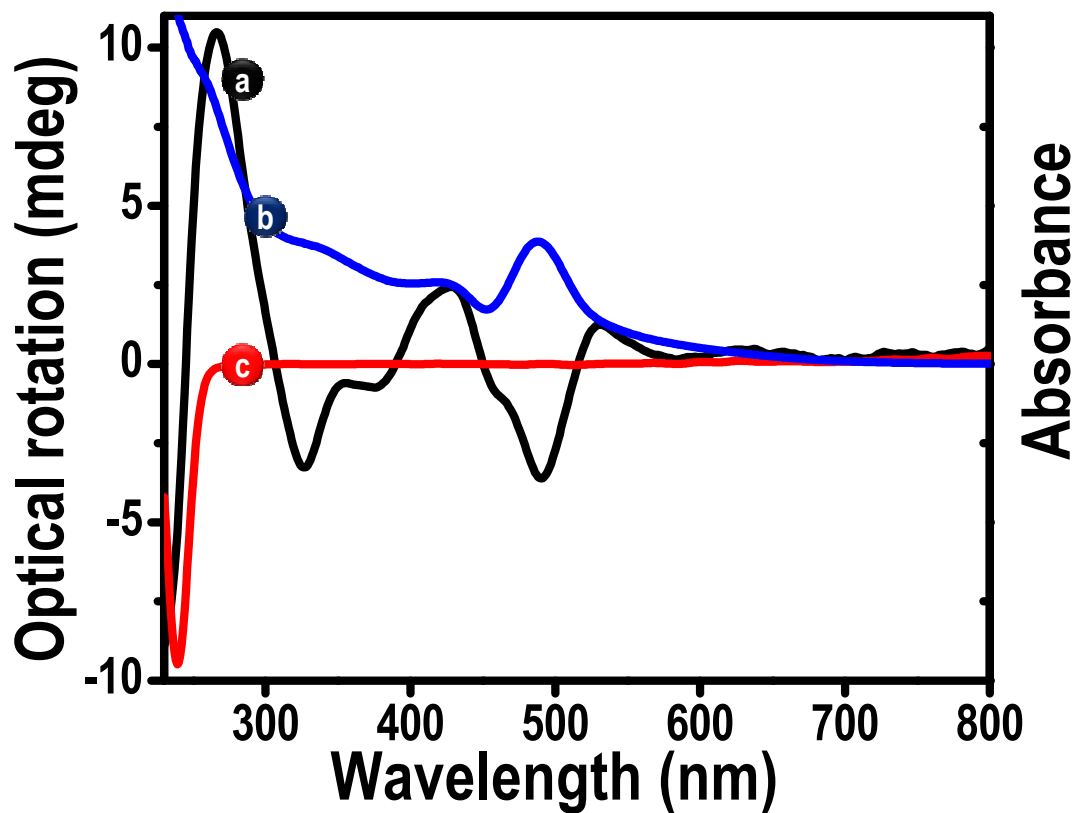


Fig. S11. CD spectra of as-synthesized Ag@SG cluster (a) and GSH ligand (c) which shows that the chirality of the cluster is from its silver core. For comparison, the absorption spectrum of the cluster is also plotted (b).

Cite this: *Nanoscale*, 2012, **4**, 4537

www.rsc.org/nanoscale

PAPER

Heterojunction double dumb-bell Ag_2Te – Te – Ag_2Te nanowires†

Anirban Som and T. Pradeep*

Received 26th March 2012, Accepted 15th May 2012

DOI: 10.1039/c2nr30730h

Growth of isolated axial heterojunction nanowires by a solution phase growth process is reported. The dumb-bell shaped nanowires contain two silver telluride sections at the extremes joined by a tellurium section. Reaction of silver nitrate with tellurium NWs in aqueous solution at a molar ratio of 1 : 1 leads to the formation of amorphous partially silver reacted Te NWs. Low temperature (75 °C) solution phase annealing of these silver deficient NWs results in phase segregation producing crystalline Ag_2Te and Te phases with clear phase boundaries along the wire axis. Structural characterization of these dumb-bell shaped NWs was performed with different microscopic and spectroscopic tools. Solution phase silver concentration over the course of annealing indicated leaching of silver into the solution during the formation of biphasic NWs. Similar Ag : Te ratios were observed in both partially silver reacted Te NWs and phase segregated Ag_2Te – Te – Ag_2Te NWs and this was attributed to redeposition of leached silver on the amorphous NW tips which eventually resulted in complete phase segregation. Successful integration of different chemical components in single NWs is expected to open up new application possibilities as physical and chemical properties of the heterostructure can be exploited.

Introduction

Integration of two or more chemically distinct phases into a single nanostructure to make hybrid materials has been a focal point of nanoscale research in recent years as such structures offer new or improved properties in comparison to a mixture of single component systems.^{1,2} These properties open up new avenues for the application of hybrid nanomaterials in various fields such as thermoelectrics,^{3–6} photocatalysis,^{7–10} battery applications,¹¹ sensors,¹² data storage,¹³ *etc.* Interest in one dimensional (1D) nanostructures has grown considerably over the years as they act as better model systems for studying nanoscale structure–property correlations and effects of quantum confinement.^{14,15} Semiconductor nanowires (NWs) offer exciting size dependent optical and electronic properties which make them suitable as the building blocks for semiconductor devices.¹⁶ Tellurium, a narrow band semiconductor

with a band gap of 0.3 eV, has a very strong tendency towards anisotropic growth. In its crystal structure, Te atoms are believed to be bound together through Van der Waals interactions in a hexagonal lattice which leads to preferential formation of 1D structures.¹⁷ This unique property has been exploited by several groups to synthesize several 1D nanostructures like rods,^{18,19} wires,^{17,20–22} tubes,^{23–26} *etc.* These 1D Te nanostructures have further been utilised as a template for synthesizing different metal telluride nanostructures.^{27–33} While several of these single phase NWs have been synthesized, recent efforts have been directed towards the facile synthesis of heterostructured NWs though reports have been very few.³⁴ These 1D hetero-nanostructures belong to multiple types. In core–shell structures, the multiple phases are uniform all through the nanowire axis. Zhang *et al.* synthesized Te–Bi and Te– Bi_2Te_3 core–shell NWs through precursor mediated solution phase reactions.⁶ In the category of multiple heterostructure NWs, two phases co-exist in segments in a given NW. Formation of Te– Bi_2Te_3 ³⁵ and Te– CdTe ³⁶ segmented NWs were observed by solid state annealing of supersaturated $\text{Bi}_{0.26}\text{Te}_{0.74}$ and $\text{Cd}_{0.28}\text{Te}_{0.72}$ alloy NWs, respectively. This suggests that non-stoichiometry induces phase separation in NWs. A one pot solution phase synthesis of Bi_2Te_3 –Te nanoplate–nanorod³⁷ heteronanostructures grown on tips of Te nanorods was reported recently by Wang *et al.*, possibly the only report of an axial heterojunction tellurium–metal telluride nanostructure, although such ‘nanobarbells’ don’t represent a 1D structure. An initial report from our group was on Ag_5Te_3 – HgTe – Ag_5Te_3 nanowires formed through partial cation exchange,³⁸ a method earlier reported by Robinson *et al.*³⁹ Development of novel methods, especially in the solution phase

DST Unit of Nanoscience (DST UNS), Department of Chemistry, Indian Institute of Technology Madras, Chennai 600 036, India. E-mail: pradeep@iitm.ac.in; Fax: +91-44-2257-0545/0509; Tel: +91-44-2257-4208

† Electronic supplementary information (ESI) available: size distribution of Te and Ag_2Te NWs, HRTEM and XRD of Te and Ag_2Te NWs, EDS of Ag_2Te NWs, TEM image and EDS spectra of partially silver reacted Te and the dumbbell shaped NWs, HRTEM, PXRD and solid state annealing data of partially silver reacted Te NWs, variation of diameter along the length of dumb-bell shaped NW, HRTEM images of heterojunction, TEM images and EDS spectra showing the time dependent growth of biphasic NWs, TEM images showing bending and breaking of biphasic system on further annealing, temperature dependence of the growth of biphasic NWs and tuning the length of Te and Ag_2Te sections in biphasic NWs. See DOI: 10.1039/c2nr30730h

is important as this enables faster scale-up and development of applications.

Silver telluride, a narrow band semiconductor at room temperature, has attracted considerable interest in recent times due to its various interesting properties. Ag_2Te exhibits a phase change from its low temperature monoclinic phase ($\beta\text{-Ag}_2\text{Te}$) to its high temperature fcc phase ($\alpha\text{-Ag}_2\text{Te}$) at ~ 423 K, where it is a superionic conductor.⁴⁰ It is also known to show large magnetoresistance^{41,42} and magnetothermopower.⁴³ Ag_2Te exhibits high electron mobility and low thermal conductivity, and is desirable for its high figure of merit (ZT) for thermoelectric applications.⁴⁴ These properties become richer when studied at the nanoscale due to the confinement of electronic states and a maximum Seebeck coefficient of $-170 \mu\text{V K}^{-1}$ was observed in NWs.⁴⁵

In the present work, an extremely efficient method to form isolated and dispersible axial heterojunction $\text{Ag}_2\text{Te}\text{-Te}\text{-Ag}_2\text{Te}$ NWs is reported. The morphology of these heterojunction NWs resembles that of dumbbells due to the larger diameter of the Ag_2Te sections compared to Te. Till now dumbbell like hybrid nanostructures have been achieved either by selective growth of the second component on the tips of nanorods^{37,46-48} or by preferential etching of core-shell nanorods.⁴⁹ These techniques require special seeds, surfactants and experimental conditions. Our synthetic procedure is a combination of the reaction between silver and tellurium NWs and subsequent annealing of those partially silver reacted NWs as shown in the schematic. Both the steps were carried out in the aqueous phase (see the experimental section). By carefully adjusting the annealing conditions, rod shaped Ag_2Te sections were grown at both ends of Te NWs. To the best of our knowledge, this is first time report of rod shaped secondary structures grown along the wire axis to produce dumbbell shaped heterostructures of tellurium in solution.

Experimental section

Sodium dodecyl sulfate (SDS, $\text{C}_{12}\text{H}_{25}\text{O}_4\text{SNa}$, 99%) was obtained from RANKEM, India. Tellurium dioxide (TeO_2 , 99.9%) powder was purchased from Alfa Aesar. Silver nitrate (AgNO_3) and hydrazine monohydrate ($\text{N}_2\text{H}_4\cdot\text{H}_2\text{O}$, 99–100%) were purchased, respectively from SD Fine Chemicals and Fisher Scientific, India. All the chemicals were used as obtained without any further purification. Deionized water was used throughout the study.

Preparation of $\text{Ag}_2\text{Te}\text{-Te}\text{-Ag}_2\text{Te}$ involves three steps as described below:

Te NWs were prepared by the chemical method; originally reported by Chang *et al.*¹⁷ In a typical procedure, 24 mg of TeO_2 powder was slowly added to a beaker containing 10 mL of hydrazine monohydrate. The reaction was allowed to continue at room temperature under constant magnetic stirring. The powder dissolved completely and the color of the solution changed from colorless to blue indicating the formation of Te NWs. After 1 h, the solution was diluted 10-fold with 10 mM SDS, in order to control the length of the NWs. The as-prepared solution was purified by centrifugation at 8000 rpm for 5 minutes. The residue was redispersed in deionized water. The centrifugation–redispersion cycle was repeated twice to remove the unreacted species and excess surfactant.

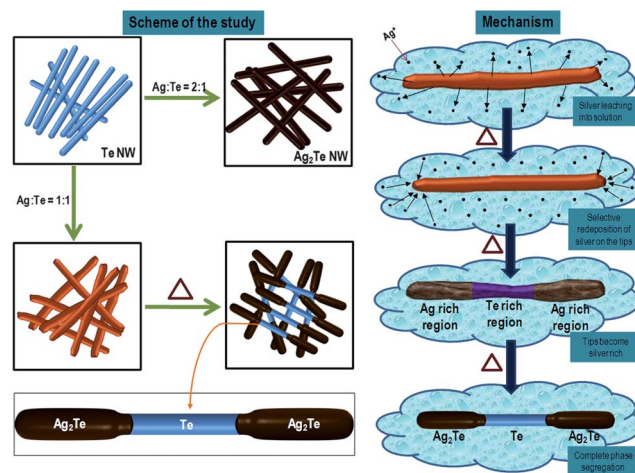
Cleaned Te NWs were used as a template for the synthesis of Ag_2Te NWs. In a typical synthetic procedure, 3 mL of 10 mM AgNO_3 solution was added to a dispersion of 10 mL Te NWs (~ 1.5 mM with respect to tellurium) under constant magnetic stirring. The color of the suspension changed from blue to dark brown within a few minutes indicating the formation of Ag_2Te NWs. Stirring was continued for 6 h and finally clean nanowires were obtained after centrifugation at 6000 rpm for 5 minutes which were redispersed in deionized water. Partially silver reacted Te NWs, used as the starting material for synthesizing the $\text{Ag}_2\text{Te}\text{-Te}\text{-Ag}_2\text{Te}$ dumbbell shaped nanowires, were prepared following the same protocol as for the Ag_2Te NWs; only change was that the amount of AgNO_3 (10 mM) added was 1.5 mL.

Formation of $\text{Ag}_2\text{Te}\text{-Te}\text{-Ag}_2\text{Te}$ heterojunction nanowires were observed upon annealing these partially silver reacted Te NWs. Annealing was done at 75°C for 24 h in aqueous solution. Outline of the experiments is shown schematically in Scheme 1. An EYELA organic synthesizer was used to ensure that the same temperature was maintained throughout the study.

Supernatant for ICP-OES measurements was collected from the heated suspension at different time intervals by centrifugation of the suspension at 18 000 rpm for 3 minutes.

Instrumentation

UV-visible extinction spectra for all the samples were recorded on a PerkinElmer Lambda 25 spectrophotometer. High-resolution transmission electron microscopy (HRTEM) was performed on a JEOL 3010 (JEOL Ltd.), 300 kV instrument equipped with a UHR polepiece. Energy dispersive X-ray spectroscopy (EDS) was carried out with an Oxford EDAX housed in the TEM. Samples for TEM analysis were prepared by dropping the dispersion on carbon coated copper grid and drying in ambient condition. X-Ray diffraction (XRD) data were collected with a Bruker AXS, D8 Discover diffractometer using $\text{Cu-K}\alpha$ ($\lambda = 1.54 \text{ \AA}$) radiation. All the peaks were assigned and compared with the database published by the Joint Committee on Powder Diffraction Standards (JCPDS). X-Ray photoelectron



Scheme 1 Schematic representation of the solution phase growth of dumbbell shaped $\text{Ag}_2\text{Te}\text{-Te}\text{-Ag}_2\text{Te}$. The proposed mechanism for the formation of biphasic nanowires is also shown.

spectroscopy (XPS) measurements were done using an Omicron ESCA Probe spectrometer with polychromatic Mg K α X-rays ($h\nu = 1253.6$ eV). The X-ray power applied was 300 W. The pass energy was 50 eV for survey scans and 20 eV for specific regions. Sample solution was spotted on a molybdenum sample plate and dried in vacuum. The base pressure of the instrument was 5.0×10^{-10} mB. The binding energy was calibrated with respect to the adventitious C 1s feature at 285.0 eV. ICP-OES data for determining silver concentration in the supernatant was collected on a PerkinElmer Optima 5300 DV spectrometer.

Results and discussion

Ag₂Te NWs were made starting from tellurium NWs.²⁸ The blue color of the dispersion of Te NWs turned dark brown upon their almost instantaneous transformation to Ag₂Te NWs. This is also manifested by the disappearance of two distinct peaks in the UV-visible extinction spectrum of tellurium NWs and simultaneous appearance of a broad band (Fig. 1A). Upon this transformation, a 15% increase in length and 33% increase in the diameter of the NWs ($\sim 103\%$ volume increase) was observed which can be seen from the length and diameter distributions of Te and Ag₂Te NWs (Fig. S1†). This is on par with the volume increase reported by Moon *et al.*³³ The EDS spectrum of Ag₂Te NWs (Fig. S2†) showed a Ag : Te ratio $\sim 2 : 1$. The slight bending observed in some of the Ag₂Te NWs is possibly a consequence of large strain, induced by volume change. Both the NWs were found to be crystalline from HRTEM and powder XRD (PXRD) analyses (Fig. S2†). No Te⁴⁺ phases were observed in the PXRD pattern indicating no disproportionation of Te into Te⁴⁺ and Te²⁻. No significant structural changes were observed upon heating the Ag₂Te NWs in solution up to 24 hours.

However, addition of lesser amount of Ag⁺ so as to produce an Ag : Te ratio of $\sim 1 : 1$ causes significant changes in the morphology (Fig. 1D). The UV-visible extinction spectrum of these partially silver reacted NWs (trace c, Fig. 1A) shows two distinct features, one broad band around 570 nm which is red shifted compared to the one for Ag₂Te at 470 nm, but blue shifted compared to peak II of Te NWs (at 796 nm) and another at 288 nm which is slightly blue shifted compared to peak I of Te NWs (at 293 nm). Incorporation of silver in the NWs was confirmed from the EDS spectrum (Fig. S3†) and it shows a Ag : Te atomic ratio of 1 : 0.96 in the formed NWs. Presence of any crystalline phase is not indicated in both HRTEM and PXRD (Fig. S4†). Although the AgTe phase is reported in the literature, it does not form under normal atmospheric conditions and is known to be metastable.⁵⁰

Solution phase annealing of these silver deficient NWs at 75 °C for 24 hours leads to the formation of dumbbell shaped NWs (Fig. 1E) predominantly. A definite contrast difference between the end segments and the middle one is observable in the TEM image of a single NW (Fig. 1F) and it hints towards the presence of two different components in those sections. The UV-visible extinction spectrum of these NWs (trace d, Fig. 1A) shows three dominant features. The peaks at 290 and 682 nm can be correlated with peak I and peak II of Te NWs of shorter length and the other appears as a band in-between these two peaks with a maximum around 370 nm. Presence of three bands in the UV-visible spectrum indicated towards the successful integration

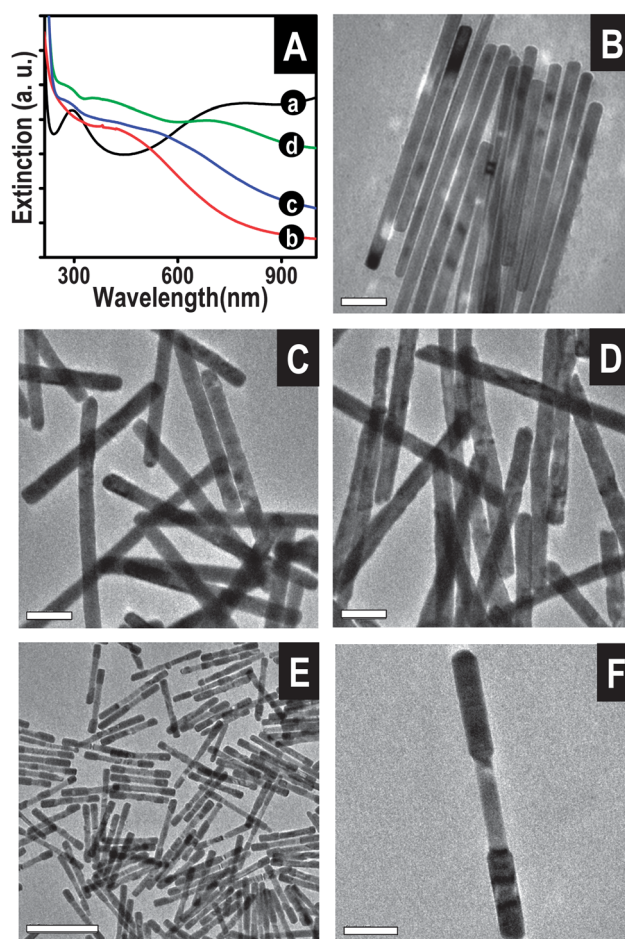


Fig. 1 (A) UV-vis extinction spectra of partially silver reacted Te nanowire dispersion before (trace c) and after (trace d) 24 h annealing at 75 °C. Spectra of Te and Ag₂Te nanowires (traces a and b, respectively) are shown for comparison. (B) TEM image of Te nanowires showing their straight morphology. (C) TEM image of Ag₂Te nanowires which are slightly bent compared to the parent Te nanowires. The increase in diameter is evident. (D) Large area TEM image of partially silver reacted tellurium nanowires, changes in nanowire morphology from Te nanowire are observable. (E) Large area TEM image of the nanowires formed after solution phase annealing. (F) TEM image of a single nanowire formed upon annealing; its morphology resembles that of a dumbbell. The scale bar in E is 500 nm and is 100 nm in the other images.

of Te and Ag–Te phases within the same nanowire. The average diameter of the middle and two end sections of the NWs (Fig. S5†) also indicated the presence of Te and Ag–Te phases in those sections of the NWs. Average diameter of the middle section was 32 nm (same as the average diameter of the parent Te NWs) and that of the end sections was 44 nm (very much comparable with the average diameter of Ag₂Te and partially silver reacted Te NWs).

EDS and HRTEM analyses of the NWs clearly reveal their biphasic nature. EDS intensity maps of Te and Ag (Fig. 2C and D, respectively) show the presence of Te throughout the length of the NW whereas Ag is limited within two end segments of the NW. Moreover, the EDS spectrum collected from area 2 (Fig. 2F) in Fig. 2A indicated the presence of only Te whereas that from area 1 (Fig. 2E) indicated it to be a compound with an atomic ratio of 66% Ag and 34% Te, which is close to the

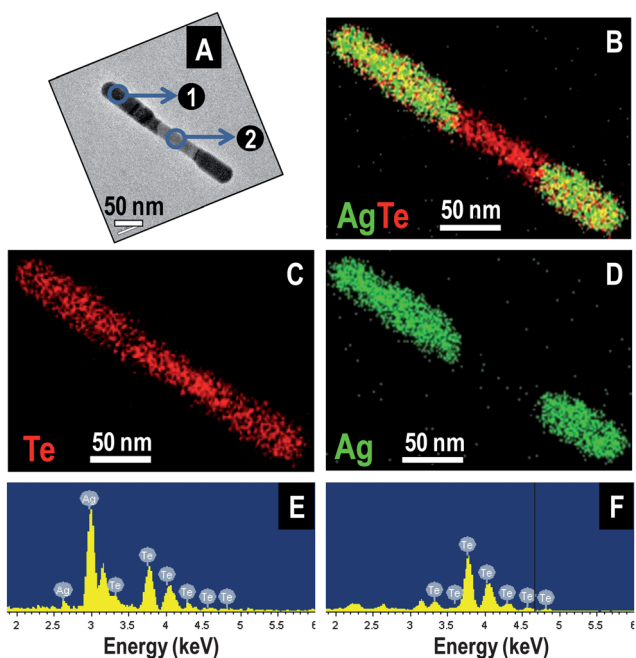


Fig. 2 EDS analysis to prove the biphasic nature of the dumbbell shaped nanowires. (A) TEM image of the dumbbell shaped nanowire chosen for EDS analysis. (B) Combined intensity maps for Ag and Te for the nanowire. (C) Te $L\alpha$ intensity map across the length of the dumbbell shaped nanowire. Note that the intensity in the middle region is higher than from the tips. (D) Ag $L\alpha$ intensity map showing that silver is limited only to both the ends. (E) EDS spectrum collected from area 1 in A showing the presence of both Ag and Te in the atomic ratio of 2 : 1. (F) EDS spectrum from area 2 in A, showing the presence of only Te in the middle section.

stoichiometry of Ag_2Te , the low temperature equilibrium phase in the Ag–Te phase diagram.⁵⁰

Lattice mismatch between two components in heterostructures generally leads to a large number of crystal defects in them. Nanowire geometry is known to facilitate the formation of defect free crystal structures required for the fabrication of high efficiency devices, as the strain induced due to lattice mismatch is relaxed at the NW side walls.⁵¹ A HRTEM image of one of the modified NWs shows the presence of perfectly crystalline Te and Ag_2Te regions (Fig. 3A) which are shown separately in the insets. Inset in Fig. 3B shows a low resolution image of a biphasic nanowire and a high resolution image from the marked area clearly indicates the presence of a definite interface across Te and Ag_2Te phases in the biphasic NWs. Detailed HRTEM analysis of the heterojunction for the same area covering the entire diameter of NW is shown in Fig. S6†.

Presence of crystalline Te and $\beta\text{-Ag}_2\text{Te}$ phases in the same nanostructure was also confirmed from the PXRD pattern of the NWs, shown in Fig. 4A. All the peaks can be indexed to either the hexagonal phase of Te or monoclinic phase of Ag_2Te . The transformation of Te NW to Ag_2Te NW is known to be topotactic where (100) directed hexagonal Te phase converts into (110) directed monoclinic Ag_2Te phase.³³ This results in the large increase in the lateral dimension of Ag_2Te phase. Strain along the c -axis of Te NW is minimized in this process which in turn helps in the formation of defect free biphasic NW system. The JCPDS patterns of Te (JCPDS: 36-1452) and Ag_2Te (JCPDS: 34-0142) are shown in the inset and they match with the data. XPS spectra in the Te 3d region for the biphasic NWs along with those of Te and Ag_2Te NWs are shown in Fig. 4B. The spectra indicate that the tellurium phase does not oxidise to Te^{4+} during the annealing

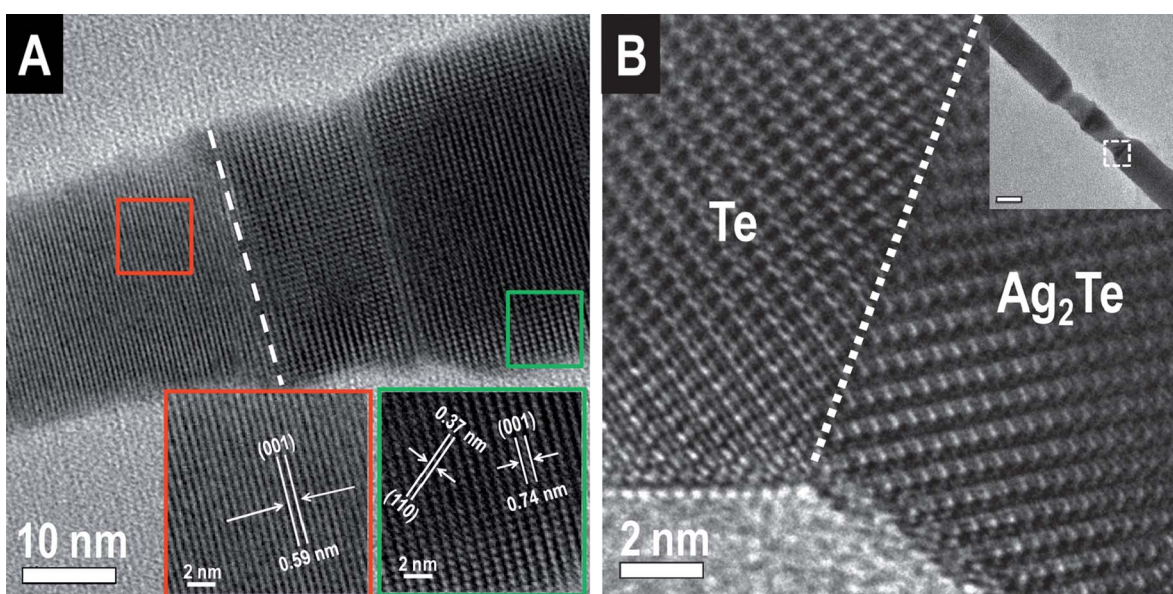


Fig. 3 HRTEM analysis of the biphasic nanowires. (A) Lattice resolved TEM image of a dumbbell shaped nanowires showing the presence of both hexagonal Te and monoclinic Ag_2Te phases (areas marked by red and green boxes, respectively) in the same nanowire. Corresponding lattice planes are marked in expanded views of those areas, shown in the insets. (B) HRTEM image showing the presence of a well defined phase boundary in the nanowire. Inset of the image shows a low magnification image of the nanowire. Area corresponding to the high resolution image is marked. Scale bar for the inset image is 100 nm.

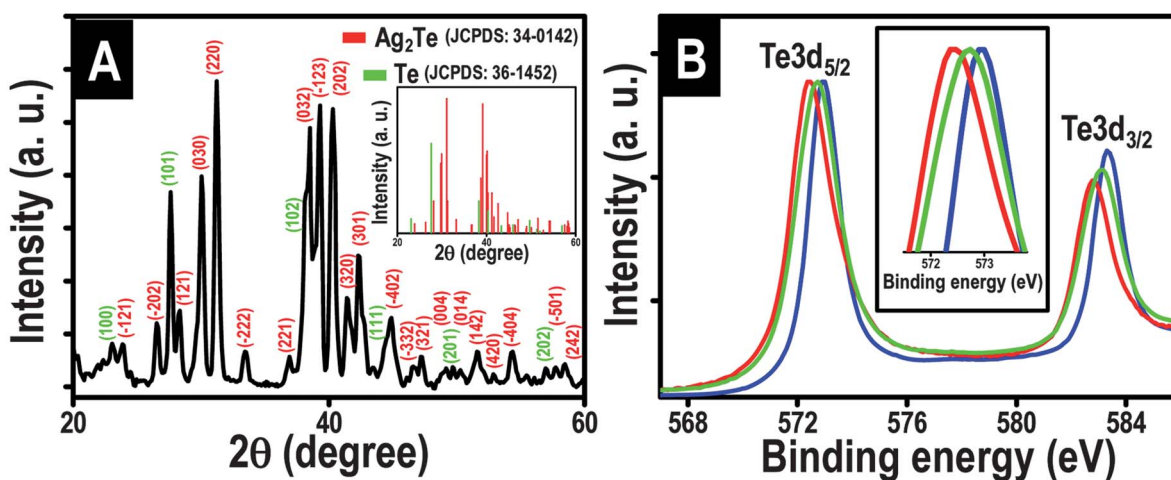


Fig. 4 (A) XRD pattern of the biphasic nanowires. All the peaks have been assigned to Te (indexed in green) and β - Ag_2Te (indexed in red). JCPDS file number and corresponding pattern for Te and Ag_2Te phases are given in the inset. (B) XPS spectra of Te 3d region of the biphasic NWs (green trace) in comparison with Te and Ag_2Te NWs (blue and red traces, respectively). No Te (IV) phases were observed. Inset in B shows a zoomed in view of Te $3d_{5/2}$ region for the three NWs.

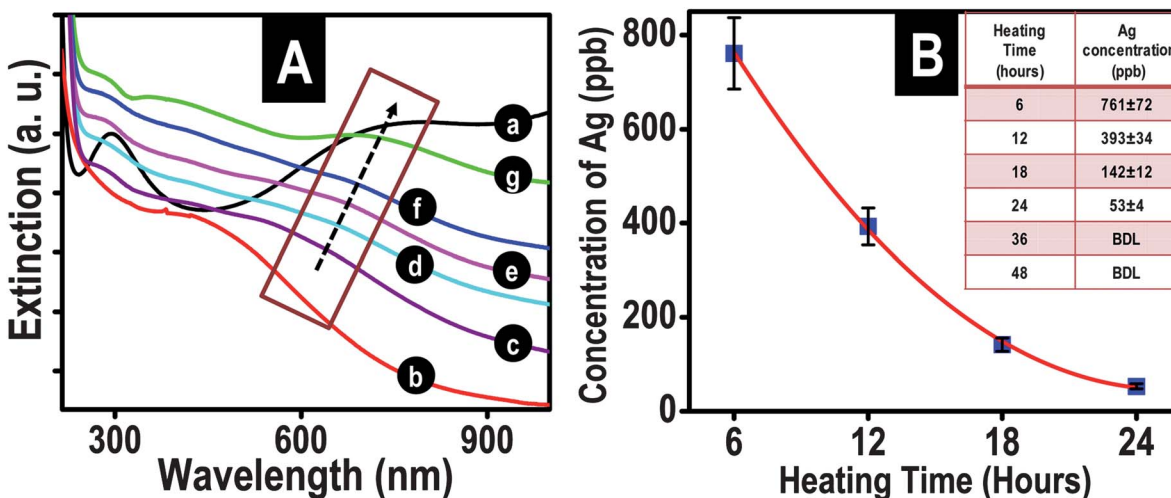


Fig. 5 Growth of biphasic nanowires with annealing time monitored with UV-visible spectroscopy. Traces d–g represent UV-visible spectra of the nanowires after 6, 12, 18 and 24 hours of annealing. Spectra for Te, Ag_2Te and partially Ag reacted Te NWs (traces a, b and c, respectively) are given for comparison. Emergence of peaks to Te NWs is evident with annealing. (B) Solution state measurement showing the decreasing concentration of silver with annealing time. Inset of the figure shows the concentrations. BDL means below detection limit.

process which correlate with the XRD data. This is another advantage of this solution state annealing process as Te can oxidise during solid state annealing in the presence of air. Residual hydrazine present creates a reducing environment in the solution and inhibits the oxidation process. Te $3d_{5/2}$ binding energies of Te and Ag_2Te NWs appear at 573.1 and 572.5 eV and it is at 572.8 eV for the biphasic NWs. The peaks for biphasic NWs appear significantly broad which most likely is due to the presence of both Te(0) and Te^{2-} phases. This corroborates with the other observations.

Formation of these biphasic NWs with increasing heating time was monitored with UV-vis spectroscopy and transmission electron microscopy. Fig. 5A represents a change in the extinction spectrum of NWs with heating time which has been compared with the spectrum of the parent Te (trace a) and Ag_2Te

(trace b) NWs. A gradual red shift (shown by an arrow) in the band maxima of partially silver reacted NWs with annealing time was seen; attributed to growth and increase in length of the Te region in the NW body.¹⁷ The observation predicted from the UV-vis data was confirmed from the TEM images taken by stopping the reaction at different time intervals during solution phase annealing (Fig. S7†).

Kinetic control of crystallization is often known to produce an amorphous phase initially which can be non-stoichiometric and is prone to phase transformations.⁵² This corroborates with the amorphous nature of the partially silver reacted Te NWs. Phase segregation and crystallization observed in these NWs upon annealing possibly originates from the fact that only phase transformation in the NWs would lead to the formation of a metastable AgTe phase. For a better understanding of the

mechanism of formation of the biphasic crystalline NWs from amorphous partially silver reacted NWs, solution phase concentration of silver was measured with annealing time (Fig. 5B). The data show a high concentration of silver in the dispersion. The silver detected in the solution is bound to originate from the silver reacted Te NWs upon annealing as no unreacted silver in the solution was detected following the addition of AgNO_3 into Te NWs. This suggests an important role for the solubility product of the system in the transformation. High solubility of partially silver reacted Te nanowires indicates that the transformation occurs directly from the amorphous phase and does not include transformation into metastable crystalline AgTe phase. The solubility product of a nanoscale solid is given by the following equation:³³

$$\log K_{\text{sp}}^* = \log K_{\text{sp,bulk}} + 2\gamma A_{\text{m}}/[3\log(RT)] \quad (1)$$

where K_{sp} , γ and A_{m} are the solubility product, surface tension and the molar surface area of the solute, respectively. As for a nanoscale solid, molar surface area increases several fold compared to its bulk counterpart; the solubility product and hence solubility increases. The amorphous phase of a solute can often be highly soluble over its crystalline counterpart. For instance, amorphous calcium carbonate (ACC) is highly soluble compared to its crystalline counterparts like calcite, vaterite, *etc.*⁵² Temperature is a basic parameter to manipulate the solubility of ionic solids and in most of the cases, solubility increases with temperature. In the case of partially Ag reacted Te NWs, silver comes out into solution at a higher solution temperature and redeposits onto the NWs. We did not observe the presence of any Te species in the supernatant which makes us conclude that only silver leaches from the NWs into the solution during the annealing process. Redeposition of silver happens preferentially on the NW tips which is most likely a result of higher reactivity of the tips than the body as may be proposed from the gold growth on Te NWs.⁵³ This is also well-known for 1D anisotropic systems like gold nanorods. It is due to the higher energy surfaces at the tips or due to poor surfactant stabilization there. In a few of the biphasic NWs, the Ag_2Te section does not form exactly at the end which possibly results from the presence of high energy defect sites on the side faces of NWs which act as re-deposition sites for silver. TEM images taken at different annealing times (Fig. S7†) indicate smoothing of the tips of the NWs upon annealing compared to the irregular nature of the tips of partially silver reacted Te NWs (Fig. 1D) and this possibly results from the deposition of silver on the tips. EDS spectra taken from the middle and end sections of the NWs after different annealing times (Fig. S8†) also support this formation mechanism. The process of silver coming out into solution and redeposition goes on at high solution temperature and results in gradual enrichment of silver content around the tips of the NWs whereas middle sections become depleted in silver. The formation process is shown in Scheme 1. This process stops once complete phase segregation is achieved and Ag_2Te -Te- Ag_2Te NWs are formed which show a very similar Ag : Te ratio to the Ag reacted Te NWs and dumbbell shaped Ag_2Te -Te- Ag_2Te NWs (Fig. S3†).

Formation of Ag_2Te may well be the driving force for the phase segregation observed. Enthalpy of mixing reaches a minimum for a ratio of 2 : 1 of silver and tellurium across the

whole range of atomic percentages⁵⁰ and this possibly facilitates the formation of the Ag_2Te phase. The basic nature (pH \sim 14) of the dispersion arising out of the presence of excess hydrazine used in the Te NW preparation may also lead to exclusive formation of Ag_2Te as the Ag-Te phase.^{13,54} On the other hand, because of the high thermodynamic stability of the monoclinic β -phase at low temperatures, it has a low solubility product and so once the Ag_2Te phase is formed, the reaction stops. Remember that no morphological changes were observed upon annealing of Ag_2Te NWs under the same conditions.

Formation of heterojunction NWs from partially silver reacted NWs by annealing was found to be solely a solution state process as solid state annealing at the same temperature was ineffective to bring out changes in the nanowire morphology (Fig. S4†). On further annealing beyond 24 hours in solution, initially bending and then breaking of the NWs was observed (Fig. S9†). The effect of annealing temperature on the growth of biphasic NWs was also probed through both UV-visible spectroscopy and TEM (Fig. S10†). When the annealing temperature was maintained at 50 °C, a change in the morphology of tips was observed but no distinct phase separation was obtained. Upon keeping the annealing temperature at 70 °C, the NWs produced had a dumbbell shape but complete phase segregation was not observed in HRTEM after 24 hours. Annealing at a higher temperature (90 °C) leads to the formation of aggregated products. These aggregates contain some silver telluride particles along with some bent wire-like structures. Though wire-like structures were rich in tellurium, presence of silver in them proves that the structures break down before complete phase segregation is achieved (Fig. S10†). This possibly is a result of higher thermal energy put into the system which makes the system more prone towards bending and breaking.

Conclusions

In summary, we have demonstrated a new methodology for the fabrication of axial heterojunction nanowires in which two ends of the Ag_2Te segments are connected through a Te section through low temperature solution phase annealing. Silver comes out into the solution at 75 °C and re-deposits on the tips of partially silver reacted Te NWs. This leads to the formation of a stable monoclinic Ag_2Te phase around the tips while the middle section gradually becomes Te rich and finally the hexagonal Te phase is formed. The morphology of resulting NWs resembles dumbbells which were characterized by UV-vis spectroscopy, TEM, EDS, PXRD and XPS. The presence of the semi-conducting Te phase between Ag_2Te regions in the biphasic NWs would reduce the lattice thermal conductivity by blocking scattering of phonons along the wire axis and this could result in the enhancement of the thermoelectric efficiency over Ag_2Te NWs. Tuning the length of Ag_2Te sections is also possible by controlling the amount of AgNO_3 added (Fig. S11†). It may also be possible to prepare other heterojunction nanostructures following this route. We are pursuing research in these directions.

Acknowledgements

We thank the Department of Science and Technology (DST), Government of India, for constantly supporting our research

program on nanomaterials. A.S. thanks the CSIR for a research fellowship.

References

- 1 R. Costi, A. E. Saunders and U. Banin, *Angew. Chem., Int. Ed.*, 2010, **49**, 4878–4897.
- 2 G. Zhu and Z. Xu, *J. Am. Chem. Soc.*, 2011, **133**, 148–157.
- 3 Y. Zhang, H. Wang, S. Kräemer, Y. Shi, F. Zhang, M. Snedaker, K. Ding, M. Moskovits, G. J. Snyder and G. D. Stucky, *ACS Nano*, 2011, **5**, 3158–3165.
- 4 R. J. Mehta, C. Karthik, B. Singh, R. Teki, T. Borca-Tasciuc and G. Ramanath, *ACS Nano*, 2010, **4**, 5055–5060.
- 5 A. Purkayastha, Q. Yan, M. S. Raghuvver, D. D. Gandhi, H. Li, Z. W. Liu, R. V. Ramanujan, T. Borca-Tasciuc and G. Ramanath, *Adv. Mater.*, 2008, **20**, 2679–2683.
- 6 G. Zhang, W. Wang and X. Li, *Adv. Mater.*, 2008, **20**, 3654–3656.
- 7 L. Amirav and A. P. Alivisatos, *J. Phys. Chem. Lett.*, 2010, **1**, 1051–1054.
- 8 C. Harris and P. V. Kamat, *ACS Nano*, 2010, **4**, 7321–7330.
- 9 Y. Shemesh, J. E. Macdonald, G. Menagen and U. Banin, *Angew. Chem., Int. Ed.*, 2011, **50**, 1185–1189.
- 10 A. Vaneski, A. S. Susha, J. Rodríguez-Fernández, M. Berr, F. Jäckel, J. Feldmann and A. L. Rogach, *Adv. Funct. Mater.*, 2011, **21**, 1547–1556.
- 11 W. Zhou, C. Cheng, J. Liu, Y. Y. Tay, J. Jiang, X. Jia, J. Zhang, H. Gong, H. H. Hng, T. Yu and H. J. Fan, *Adv. Funct. Mater.*, 2011, **21**, 2439–2445.
- 12 L. L. Xing, S. A. Yuan, Z. H. Chen, Y. J. Chen and X. Y. Xue, *Nanotechnology*, 2011, **22**, 215501.
- 13 S. K. Batabyal and J. J. Vittal, *Chem. Mater.*, 2008, **20**, 5845–5850.
- 14 Y. N. Xia and P. D. Yang, *Adv. Mater.*, 2003, **15**, 351.
- 15 M. Law, J. Goldberger and P. Yang, *Annu. Rev. Mater. Res.*, 2004, **34**, 83–122.
- 16 C. M. Lieber and Z. L. Wang, *MRS Bull.*, 2007, **32**, 99–108.
- 17 Z.-H. Lin, Z. Yang and H.-T. Chang, *Cryst. Growth Des.*, 2008, **8**, 351–357.
- 18 Z. Liu, Z. Hu, J. Liang, S. Li, Y. Yang, S. Peng and Y. Qian, *Langmuir*, 2004, **20**, 214–218.
- 19 Z. Liu, Z. Hu, Q. Xie, B. Yang, J. Wu and Y. Qian, *J. Mater. Chem.*, 2003, **13**, 159–162.
- 20 Y.-J. Zhu, W.-W. Wang, R.-J. Qi and X.-L. Hu, *Angew. Chem., Int. Ed.*, 2004, **43**, 1410–1414.
- 21 Q. Lu, F. Gao and S. Komarneni, *Langmuir*, 2005, **21**, 6002–6005.
- 22 Q. Lu, F. Gao and S. Komarneni, *Adv. Mater.*, 2004, **16**, 1629–1632.
- 23 B. Mayers and Y. Xia, *Adv. Mater.*, 2002, **14**, 279–282.
- 24 X.-L. Li, G.-H. Cao, C.-M. Feng and Y.-D. Li, *J. Mater. Chem.*, 2004, **14**, 244–247.
- 25 P. Mohanty, T. Kang, B. Kim and J. Park, *J. Phys. Chem. B*, 2006, **110**, 791–795.
- 26 A. Qin, Y. Fang, P. Tao, J. Zhang and C. Su, *Inorg. Chem.*, 2007, **46**, 7403–7409.
- 27 A. K. Samal and T. Pradeep, *J. Phys. Chem. C*, 2010, **114**, 5871–5878.
- 28 A. K. Samal and T. Pradeep, *J. Phys. Chem. C*, 2009, **113**, 13539–13544.
- 29 H.-W. Liang, S. Liu, Q.-S. Wu and S.-H. Yu, *Inorg. Chem.*, 2009, **48**, 4927–4933.
- 30 G. Zhang, Q. Yu, Z. Yao and X. Li, *Chem. Commun.*, 2009, 2317–2319.
- 31 G. Zhang, B. Kirk, L. A. Jauregui, H. Yang, X. Xu, Y. P. Chen and Y. Wu, *Nano Lett.*, 2012, **12**, 56–60.
- 32 H. Fan, Y. Zhang, M. Zhang, X. Wang and Y. Qian, *Cryst. Growth Des.*, 2008, **8**, 2838–2841.
- 33 G. D. Moon, S. Ko, Y. Xia and U. Jeong, *ACS Nano*, 2010, **4**, 2307–2319.
- 34 J. Hu, Y. Bando and D. Golberg, *J. Mater. Chem.*, 2009, **19**, 330–343.
- 35 W. Wang, X. Lu, T. Zhang, G. Zhang, W. Jiang and X. Li, *J. Am. Chem. Soc.*, 2007, **129**, 6702–6703.
- 36 W. Wang, G. Zhang and X. Li, *Chem. Lett.*, 2008, **37**, 848–849.
- 37 W. Wang, J. Goebel, L. He, S. Aloni, Y. Hu, L. Zhen and Y. Yin, *J. Am. Chem. Soc.*, 2010, **132**, 17316–17324.
- 38 A. K. Samal and T. Pradeep, *Nanoscale*, 2011, **3**, 4840–4847.
- 39 R. D. Robinson, B. Sadtler, D. O. Demchenko, C. K. Erdonmez, L.-W. Wang and A. P. Alivisatos, *Science*, 2007, **317**, 355–358.
- 40 M. Kobayashi, K. Ishikawa, F. Tachibana and H. Okazaki, *Phys. Rev. B*, 1988, **38**, 3050.
- 41 R. Xu, A. Husmann, T. F. Rosenbaum, M. L. Saboungi, J. E. Enderby and P. B. Littlewood, *Nature*, 1997, **390**, 57–60.
- 42 I. Chuprakov, *Appl. Phys. Lett.*, 1998, **72**, 2165.
- 43 Y. Sun, *Appl. Phys. Lett.*, 2003, **82**, 1440.
- 44 M. Fujikane, K. Kurosaki, H. Muta and S. Yamanaka, *J. Alloys Compd.*, 2005, **393**, 299–301.
- 45 F. Li, C. Hu, Y. Xiong, B. Wan, W. Yan and M. Zhang, *J. Phys. Chem. C*, 2008, **112**, 16130–16133.
- 46 M. Kirsanova, A. Nemchinov, N. N. Hewa-Kasakarage, N. Schmall and M. Zamkov, *Chem. Mater.*, 2009, **21**, 4305–4309.
- 47 D. Seo, C. I. Yoo, J. Jung and H. Song, *J. Am. Chem. Soc.*, 2008, **130**, 2940–2941.
- 48 K. Park and R. A. Vaia, *Adv. Mater.*, 2008, **20**, 3882–3886.
- 49 X. Guo, Q. Zhang, Y. Sun, Q. Zhao and J. Yang, *ACS Nano*, 2012, **6**, 1165–1175.
- 50 I. Karakaya and W. T. Thompson, *J. Phase Equilib.*, 1991, **12**, 56–63.
- 51 W. L. Magnus, B. W. Jakob, W. Mathias, H. Paul, E. F. Linus, S. Lars and L. R. Wallenberg, *Nanotechnology*, 2007, **18**, 015504.
- 52 H. Cölfen and S. Mann, *Angew. Chem., Int. Ed.*, 2003, **42**, 2350–2365.
- 53 Z.-H. Lin, Y.-W. Lin, K.-H. Lee and H.-T. Chang, *J. Mater. Chem.*, 2008, **18**, 2569–2572.
- 54 F. Xiao, G. Chen, Q. Wang, L. Wang, J. Pei and N. Zhou, *J. Solid State Chem.*, 2010, **183**, 2382–2388.

Electronic Supplementary Information

Heterojunction double dumb-bell Ag_2Te -Te- Ag_2Te nanowires

Anirban Som *and* T. Pradeep*

DST Unit of Nanoscience (DST-UNS), Department of Chemistry, Indian Institute of Technology Madras, Chennai - 600 036, India.

*E-mail: pradeep@iitm.ac.in

Table of contents

Number	Description	Page No.
S1	Size distribution of Te and Ag_2Te NWs	2
S2	HRTEM and XRD of Te and Ag_2Te NWs, EDS of Ag_2Te NWs	3
S3	TEM image and EDS of partially silver reacted Te and the biphasic NWs	4
S4	HRTEM, PXRD and solid state annealing data for partially silver reacted Te NWs	5
S5	Diameter distribution in the middle And end sections in dumb-bell shaped NWs, variation of diameter along a single dumb-bell shaped NW	6
S6	HRTEM images of heterojunction covering the NW diameter	7
S6	TEM images showing the time dependent growth of biphasic NWs	8
S7	EDS showing time dependent growth of biphasic NWs	9
S8	Bending and breaking of biphasic system on annealing	10
S9	Temperature dependence of the growth of biphasic NWs	11
S10	Tuning the length of Te and Ag_2Te sections	12

S1. Supporting information 1

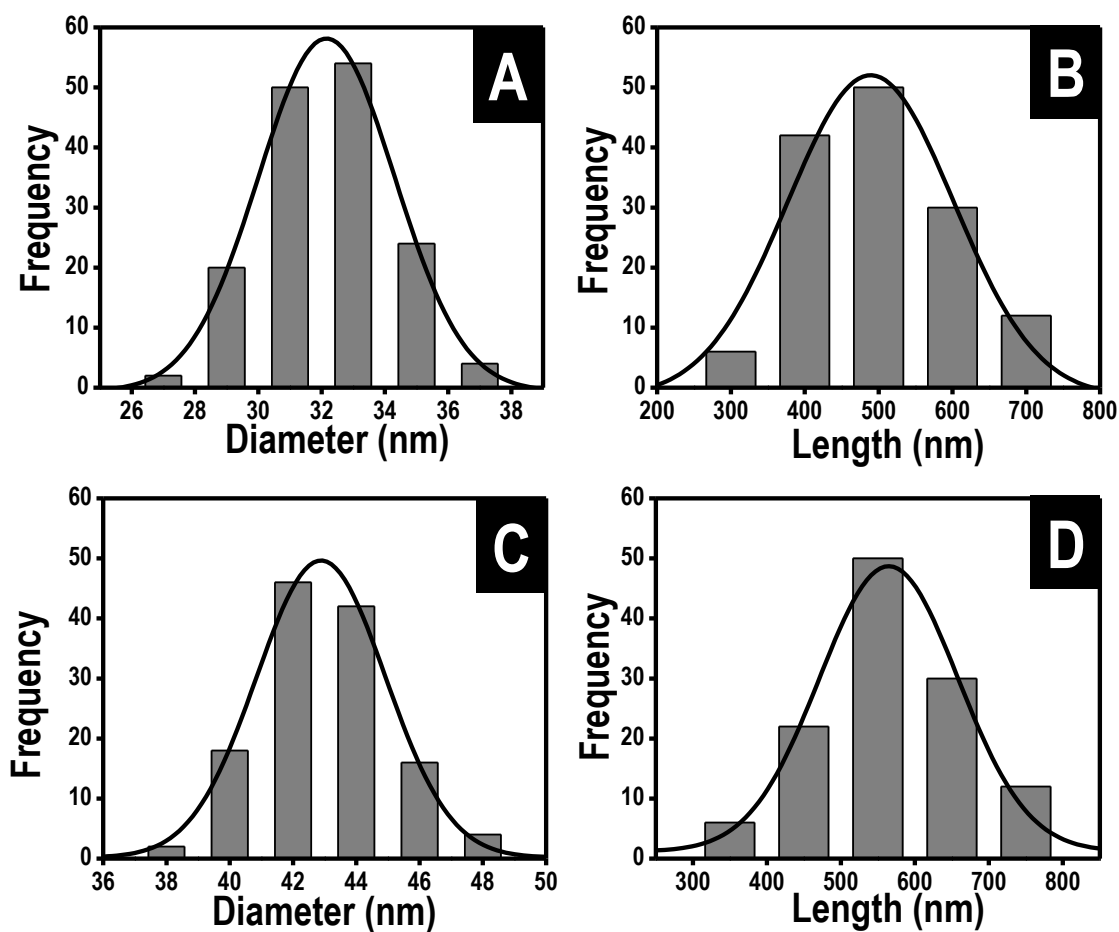


Fig. S1 Size distribution of Te and Ag₂Te NWs. (A) Diameter and (B) length distribution of Te NWs. (C) and (D) Corresponding distributions in Ag₂Te NWs. Average length and diameter were 488 and 32.2 nm, respectively in Te NWs and 561 and 42.8 nm, respectively in Ag₂Te NWs, which correspond to 15% increase in length and 33% increase in diameter upon chemical transformation.

S2. Supporting information 2

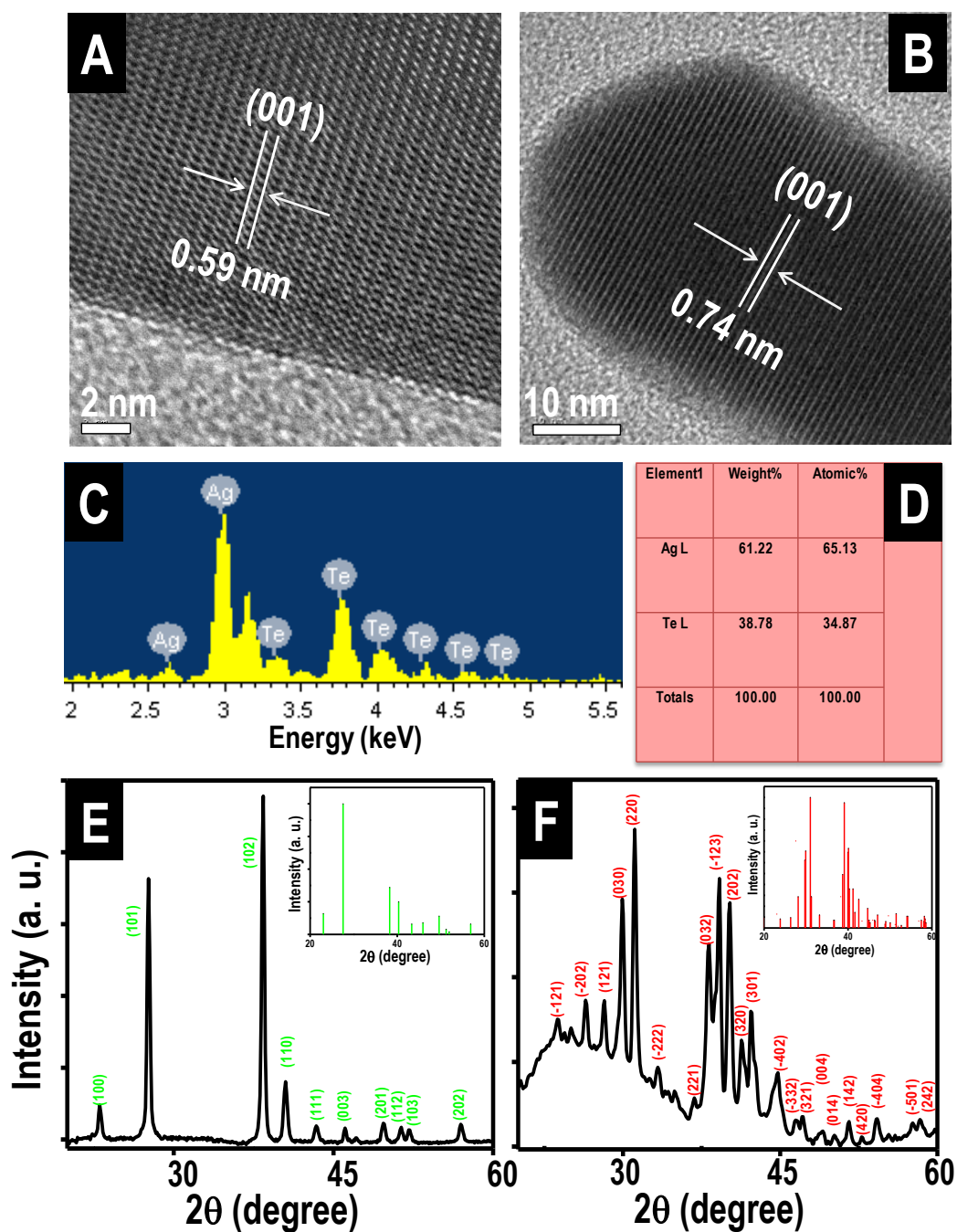


Figure S2. (A) Lattice resolved TEM image of a single hexagonal Te nanowire. (B) High resolution TEM image of a monoclinic Ag_2Te nanowire. (C) EDS spectrum of Ag_2Te nanowires showing the presence of both Ag and Te. (D) Elemental quantification corresponding to the spectrum, shows an atomic ratio of $\sim 2:1$ for Ag and Te. (E) PXRD pattern of Te NWs. All the peaks are assigned to hexagonal phase of Te (JCPDS No. 36-1452). (F) PXRD pattern of Ag_2Te NWs. Pattern matches with the pattern of monoclinic phase of Ag_2Te (JCPDS No. 34-0142). Corresponding JCPDS patterns are shown in the insets of E and F.

S3. Supporting information 3

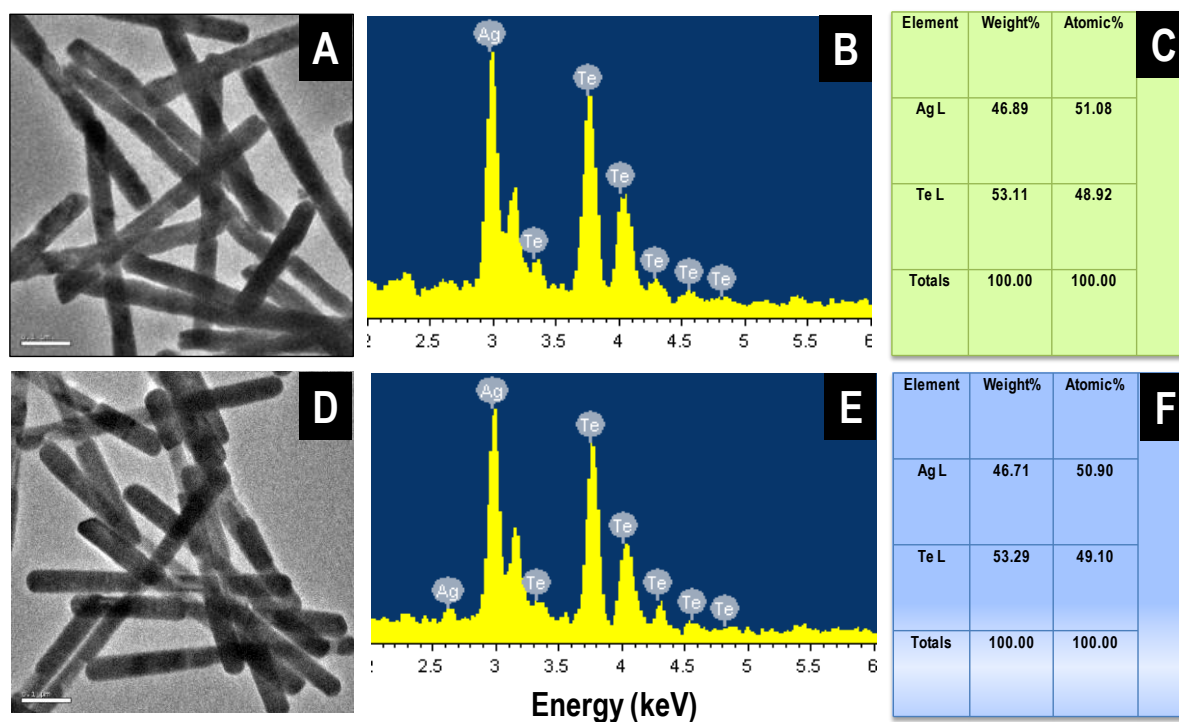


Figure S3. (A) Large area TEM image of partially silver reacted Te NWs. (B) EDS spectrum taken from the same area showing incorporation of silver in the nanowires. (C) EDS elemental quantification for Ag and Te in partially silver reacted Te nanowires. (D) Large area TEM image of phase segregated Ag_2Te -Te- Ag_2Te nanowires. (E) EDS spectrum of Ag_2Te -Te- Ag_2Te nanowires. (F) Quantification of total Ag and Te in Ag_2Te -Te- Ag_2Te NWs. Both the NWs show similar Ag:Te ratio and indicates no silver loss during the annealing process in solution. Scale bar in both TEM images is 100 nm.

S4. Supporting information 4

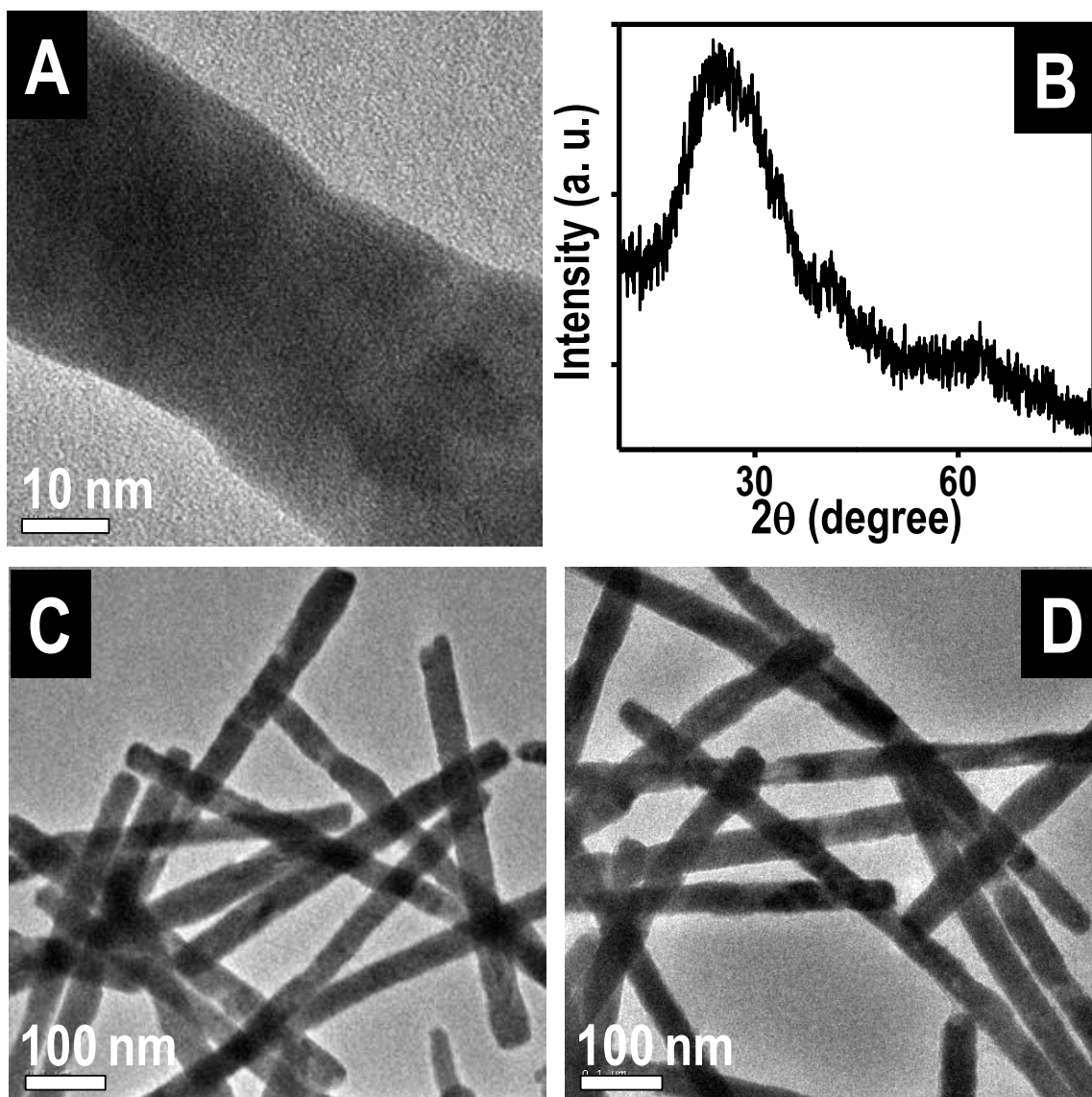


Figure S4. (A) High magnification TEM image of partially silver reacted Te nanowires. (B) XRD pattern of the partially silver reacted Te nanowires. Representative TEM images taken from these nanowires (C) before and (D) after solid state annealing at 75°C for 24 hours. Change in nanowire morphology was not observed.

S5. Supporting information 5

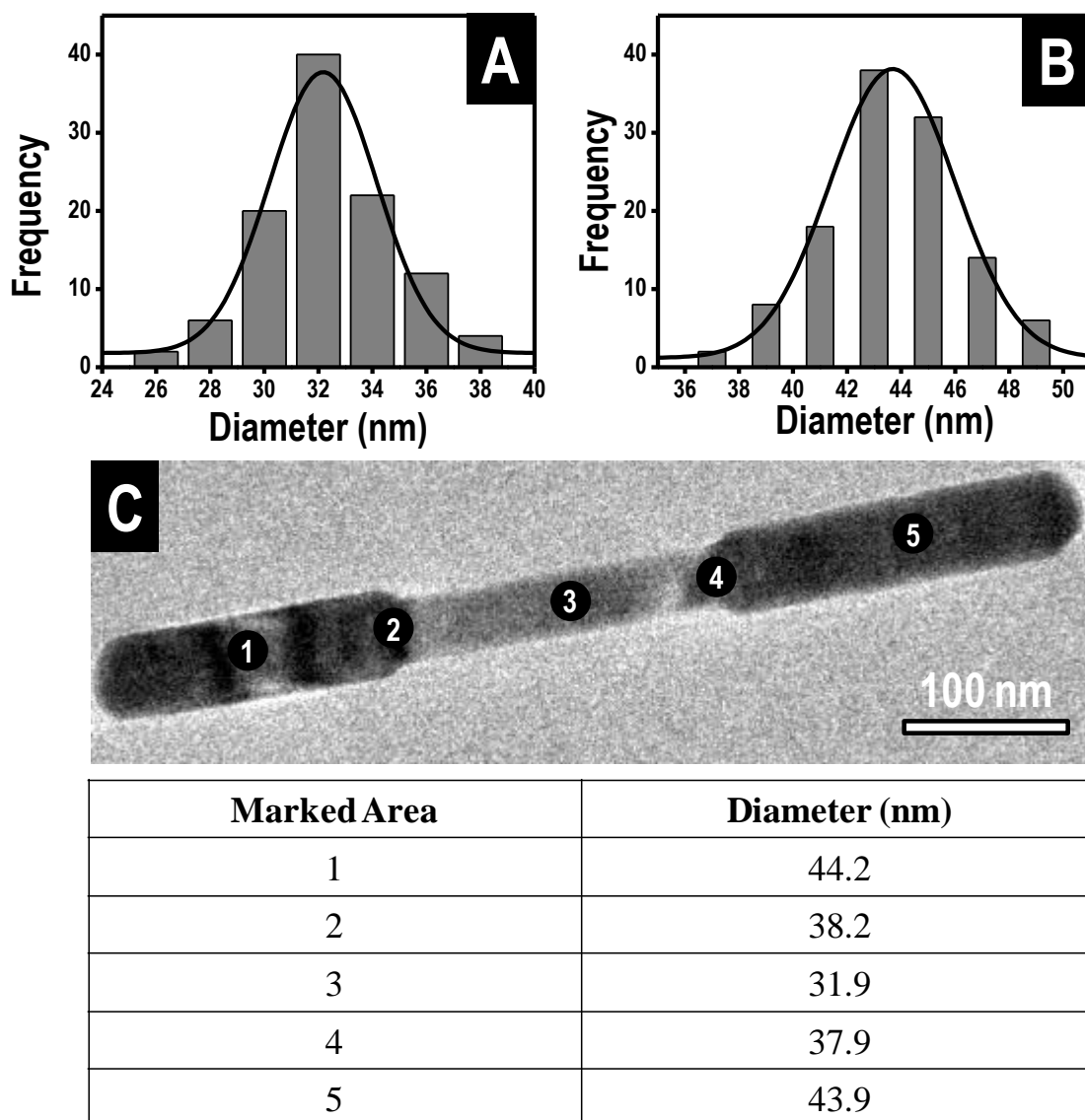


Fig. S5 (A) Diameter distribution in the middle section of dumb-bell shaped NWs. (B) Diameter distribution in the two end segments of the NWs. (C) Variation of diameter across the length of a biphasic NW. Diameters from the marked areas are shown in a tabular form.

S6. Supporting information 6

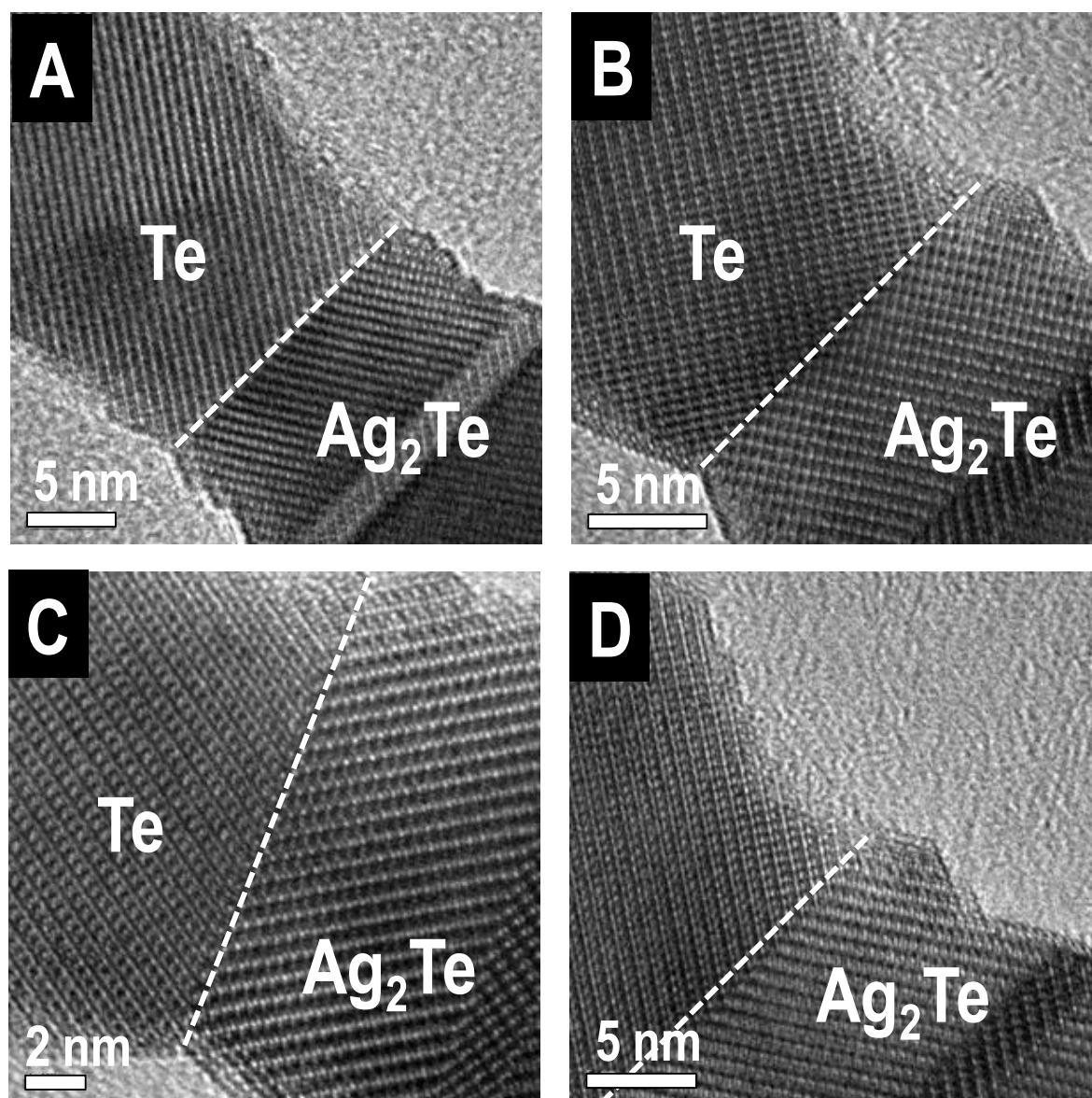


Fig. S6 HRTEM images of the heterojunction shown in Fig. 3B. (A), (B) and (C) show HRTEM of the heterojunction covering the entire diameter of the NW at different magnifications. (D) HRTEM of other half of the NW (across the diameter).

S7. Supporting information 7

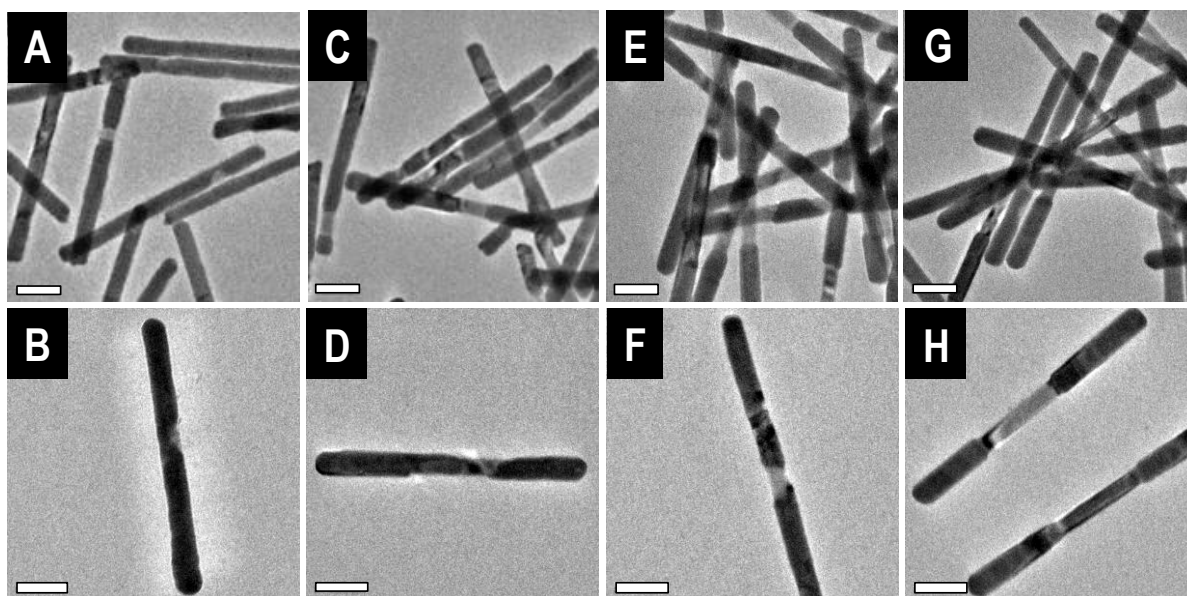


Figure S7. Morphological changes leading to biphasic dumb-bells during annealing of partially silver reacted Te nanowires. TEM images taken after (A,B) 6 h, (C,D) 12 h, (E,F) 18 h and (G,H) 24 h annealing treatment of the nanowires in solution. Scale bar is 100 nm in all the images.

S8. Supporting information 8

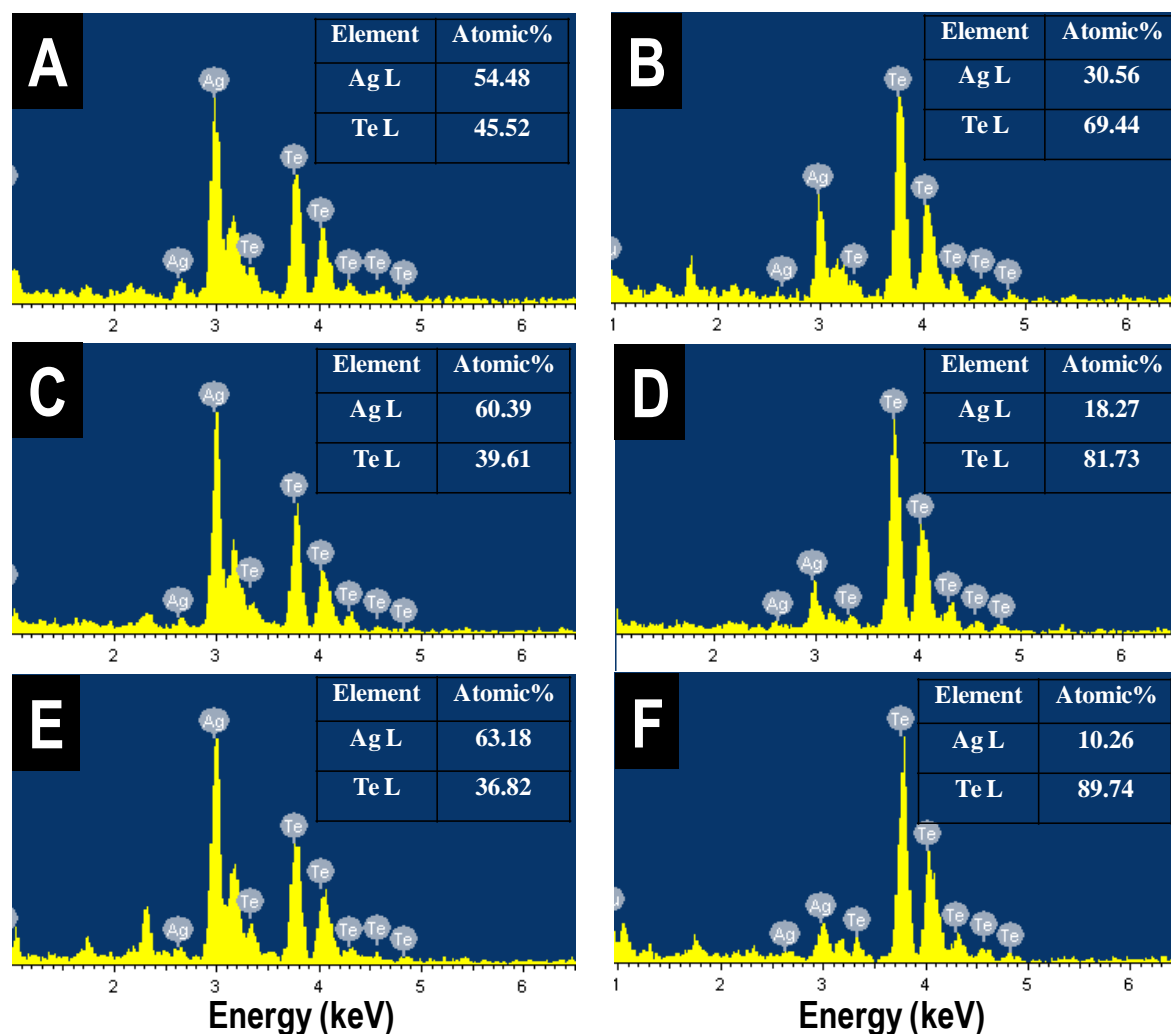
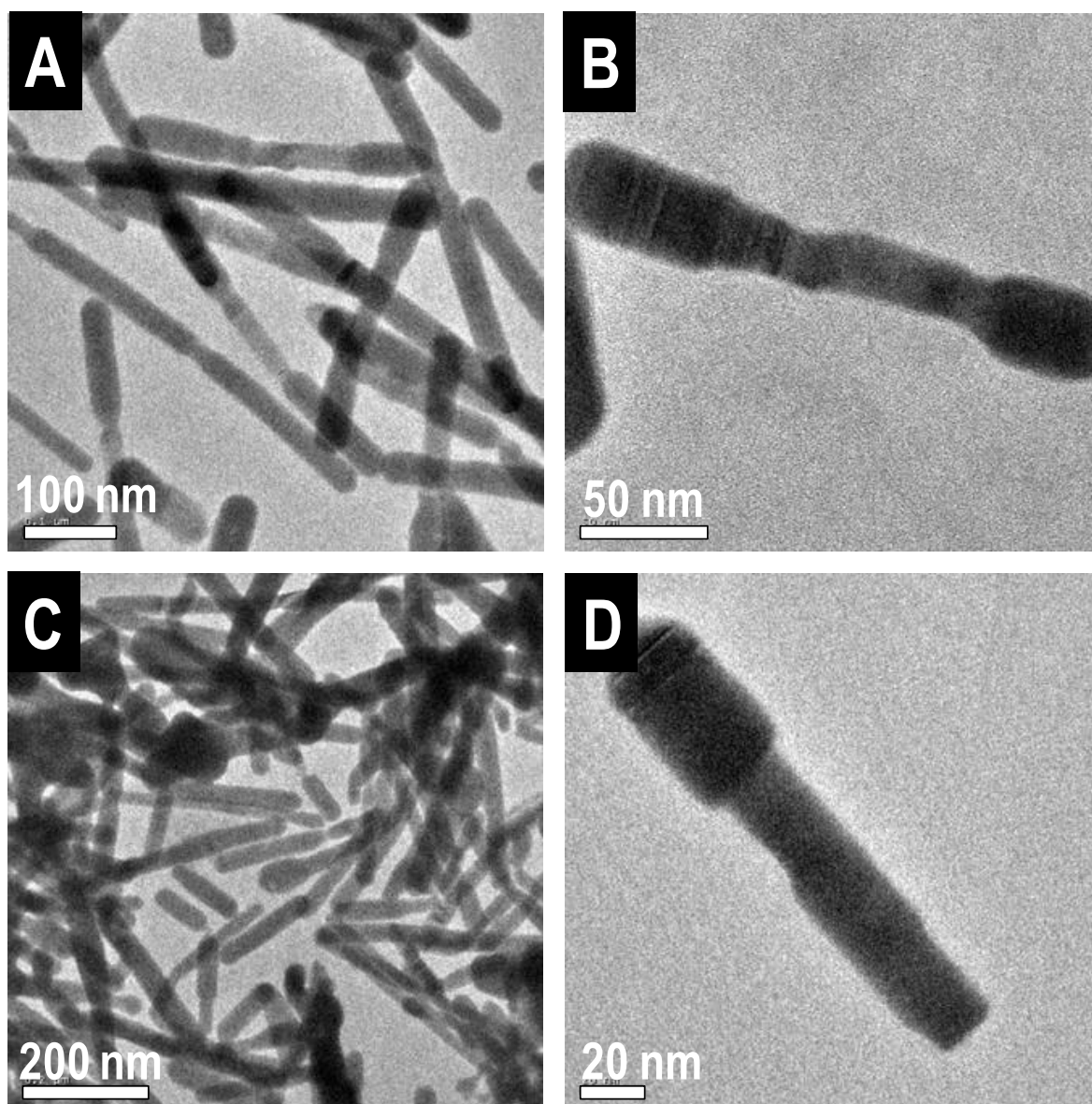


Fig. S8 EDS spectra showing changes silver concentration at the tip and the middle section of the NWs during the annealing process. (A) Tip, after 6 h; (B) middle, after 6 h; (C) tip, after 12 h; (D) middle, after 12 h; (E) tip, after 18 h and (F) middle, after 18 h. Ag:Te atomic ratios are given in the tables. While the tips become silver rich with annealing time, the middle section become depleted in silver.

S9. Supporting information 9



I

Figure S9. Bending and breaking observed in nanowires upon further annealing, once $\text{Ag}_2\text{Te}-\text{Te}-\text{Ag}_2\text{Te}$ nanowire is formed after 24 hours. (A) Large area TEM image taken from sample annealed for 36 h. (B) TEM image of a single nanowire after 36 h of annealing. (C) Large area image showing the presence of broken nanowires after 48 hours of annealing. (D) TEM image of a single broken nanowire after 48 h.

S10. Supporting information 10

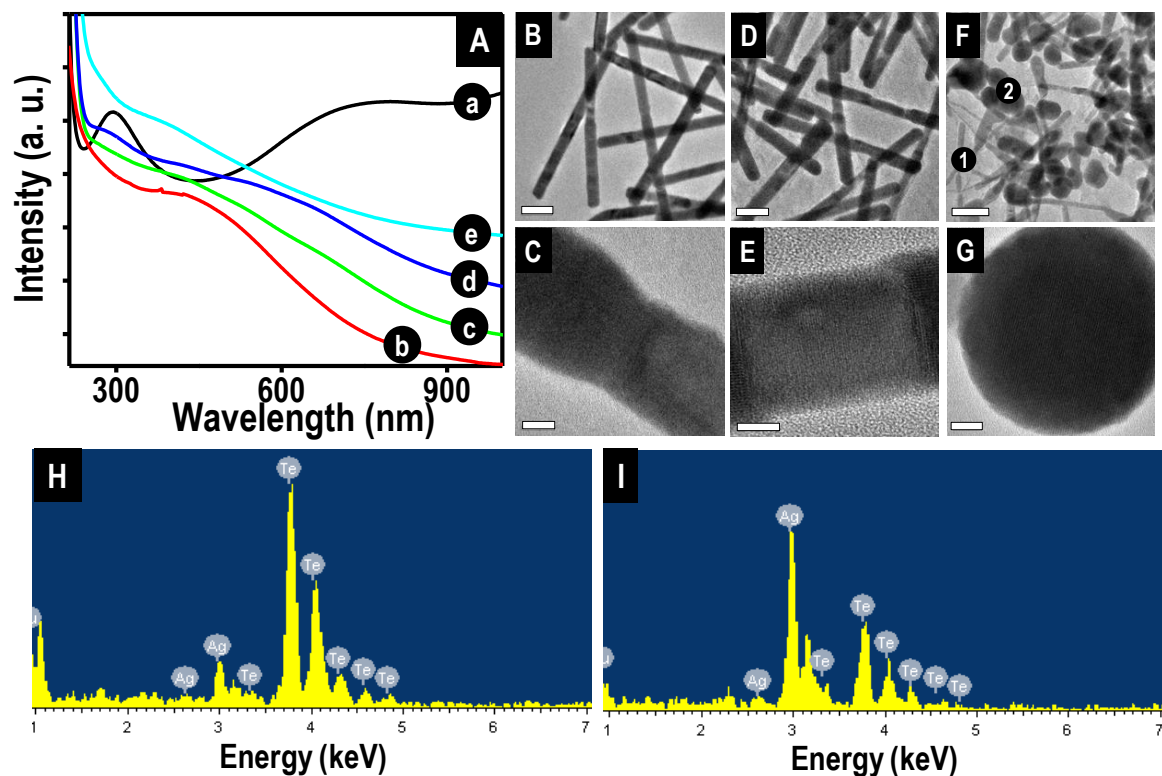


Figure S10. Effect of annealing temperature on nanowire morphology. (A) Traces c, d, e represent UV-visible extinction spectra for the partially silver reacted Te nanowires annealed at 50°, 70° and 90°C for 24 h. Traces a and b are spectra for Te and Ag₂Te nanowires. Large area and high magnification TEM images of nanowires obtained after 24 h of annealing at different temperatures; (B,C) 50°C, (D,E) 70°C and (F,G) 90°C. Scale bars in large area and high magnification TEM images are 100 and 10 nm, respectively. (H) and (I) represent the EDS spectrum taken from areas 1 and 2 in image (F), respectively.

S11. Supporting information 11

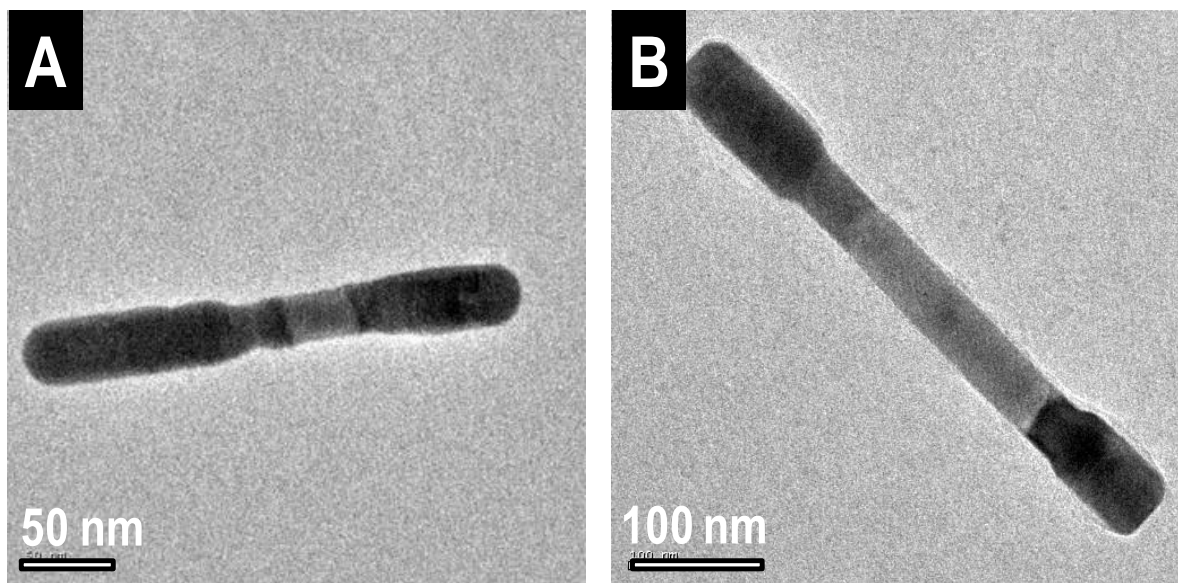


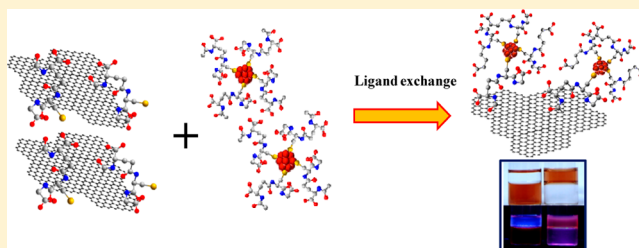
Fig. S11 Tuning the length of Te and Ag_2Te sections. (A) NW with large Ag_2Te sections obtained by annealing of NWs with Ag:Te ratio greater than 1. (B) NW with small Ag_2Te sections obtained by annealing of NWs with a Ag:Te ratio less than 1.

Luminescent Silver Clusters with Covalent Functionalization of Graphene

Aditi Chandrasekar[†] and T. Pradeep^{*,‡}[†]Indian Institute of Science Education and Research-Kolkata, Mohanpur, Nadia, West Bengal 741252, India[‡]DST Unit of Nanoscience (DST UNS), Department of Chemistry, Indian Institute of Technology Madras, Chennai 600036, India

S Supporting Information

ABSTRACT: Brightly luminescent, atomically precise sub-nanometer clusters of silver protected by glutathione were covalently functionalized by solution phase thiolated graphene using ligand exchange. A hybrid molecule was formed, which was obtained in a nearly pure form by phase transfer from the aqueous to the organic phase. The resulting hybrid exhibited properties of both of these nanoscale materials. UV-vis, luminescence, XPS, EDAX, TEM, and Raman spectroscopy were used to characterize the hybrid structure, which showed the spectroscopic characteristics of both the constituents. The luminescence of the cluster was retained in the hybrid, along with features characteristic of graphene. Atomically precise clusters with covalently linked graphene will be useful for new applications in the areas of drug delivery, sensors, and catalysis.



INTRODUCTION

Graphene, the two-dimensional analogue of carbon, has been the most fascinating material of the recent past.^{1–3} Quantum clusters (QCs) are the emerging category of noble metal based materials with atomically precise cores and well-defined features in optical absorption and emission.^{4–13} QCs contain only a few atoms in their core, which leads to discrete energy levels in them rather than continuous density of states, making them brightly luminescent with distinct emission features.⁸ The fascinating properties of both of these materials have made them important candidates for applications in diverse areas ranging from chemistry to biology.^{14,15} The large surface areas of graphenic materials allow them to capture active molecules and clusters.^{16,17} Noble metal QCs, due to their luminescence, are excellent reporters of chemical and physical changes of the medium.^{18,19} As a result, creation of a covalently bonded hybrid of the two would enhance the properties of both these nanoscale materials. Analogous structures have been made in the case of large plasmonic nanoparticles to create new reporter species.²⁰ In this article, we report the first synthesis of such a QC-graphene hybrid molecule exhibiting the characteristic features of both the constituents. Functionalization of QCs with diverse molecules has been achieved to impart additional properties such as fluorescence resonance energy transfer (FRET),^{19,21} receptor mediated transfer²² and antigen-antibody interaction.⁸ This functionalization chemistry, extending to graphene and such other carbon forms will extend the scope of cluster research.

Ag and Au atoms have been well-known to have an affinity toward sulfur,²⁰ and hence, solution phase graphene, which typically contains the carboxylic acid group, was functionalized to form thiolated graphene. Thiol protected Ag QCs were

bound to this by ligand exchange of thiol functionalities to form a covalently bound graphene cluster hybrid molecule. The hybrid was characterized in the aqueous phase and was later phase transferred to toluene to separate unbound graphenes from the hybrid.

EXPERIMENTAL SECTION

Synthesis of Solution Phase Graphene. The synthesis of graphite oxide from graphite powder was achieved by a method originally proposed by Kovtyukhova et al.²³ The pure, ion-free dispersion of graphite oxide (GO) obtained by this method was reduced to graphene (GRN) by a hydrothermal reduction technique first reported by Loh and colleagues,²⁴ which avoids the possibility of interferences due to chemical reduction at a later stage (see Supporting Information S1 for experimental details). The absorption spectrum of GO shows a raise in background at 1000 nm, but no distinct UV peaks were seen (Figure S2A in the Supporting Information).

Synthesis of Glutathione Functionalized Graphene (GRN-GSH). To 10 mL of 0.05% graphene dispersion, 5 mg of 1-(3-(dimethylamino)propyl)-3-ethyl-carbodiimide hydrochloride (EDC) was added and stirred for 6 h, to activate the carboxylate groups on the chemically synthesized graphene sheets. To this mixture, an equimolar quantity of reduced glutathione (GSH) was added and stirred overnight. A black precipitate of the functionalized graphene settled at the bottom of the reaction tube. The product was centrifuged around 12 000 rpm and washed several times with triply distilled water to

Received: April 30, 2012

Revised: June 4, 2012

Published: June 6, 2012



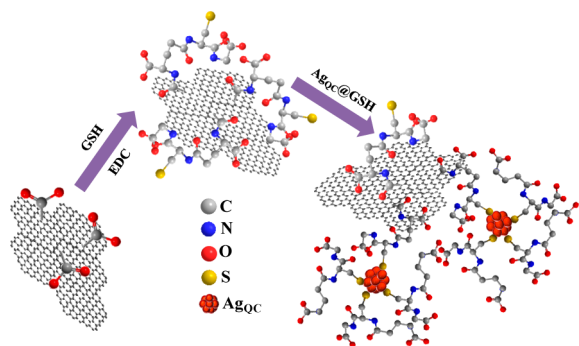
remove excess EDC and unreacted glutathione. After several washing steps, the black product was redispersed in water to make a 0.05% dispersion of GRN-GSH, which shows the characteristic feature of graphene (Figure S2A in the Supporting Information).

Synthesis of Silver QCs. Silver quantum clusters (Ag_{QC}) protected with glutathione (GSH) was synthesized by a gel mediated route proposed by Chakraborty et al.²⁵ In this method, the silver precursor was uniformly dissolved in the liquid form of the gel, which was left undisturbed until it was set. Once the gel was formed, sodium borohydride solution was added to reduce the Ag precursor, and the clusters were formed within the gel matrix. These were washed and extracted from the gel and used in further experiments (see S1 in Supporting Information for details of the synthesis).

Synthesis of Graphene Protected Ag_{QC} . Clusters were protected with GRN-GSH by stirring 1 mL of its solution with 4 mL of the cluster solution for 4 h at room temperature, followed by the addition of methanol to precipitate the clusters. The GRN-GSH attached clusters, formed through ligand exchange via their thiol functionalities, precipitated, and settled at the bottom. This mixture was centrifuged at a low speed of 1500 rpm, and the supernatant was discarded. The precipitate containing graphene functionalized Ag_{QC} , referred to as hybrid molecules (GRN- Ag_{QC}), was dried and suspended in water.

The procedure involved in synthesizing the GRN- Ag_{QC} hybrid molecule is shown in Scheme 1.

Scheme 1. (From Left to Right) Solution Phase Graphene Sheets with Free Carboxylate Groups, Coupled via Amide Linkage to GSH Forming Thiolated Graphene, Which Are Attached to Ag_{QC} s by Ligand Exchange Yielding Graphene-Cluster Hybrid Molecules; Relative Sizes of Atoms Are Not to Scale



A method of directly coupling the carboxylate groups on functionalized graphene with the glutathione on the clusters was not used because the coupling agent EDC used to facilitate the formation of the amide linkage between the amine and acid is available as a hydrochloride salt, which completely hydrolyses to form an ionic solution. When added in the presence of clusters, this can cause aggregation and instability of the cluster solution. Further, centrifugation and repeated washing is required to remove excess EDC and HCl. Clusters might not retain their inherent properties to their full extent after this process.

RESULTS AND DISCUSSION

Figure II(a) shows the absorption spectrum of $\text{Ag}_{25}\text{SG}_{18}$ (SG, glutathione thiolate) synthesized by the proposed method. The

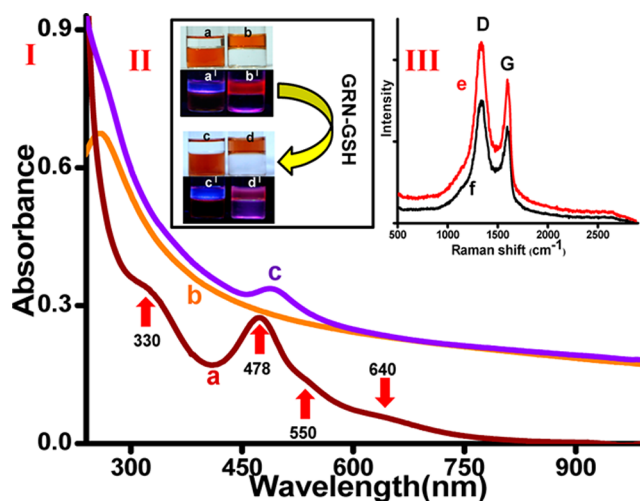


Figure 1. (I) Absorbance spectrum of (a) freshly prepared Ag_{QC} in aqueous phase, (b) GRN-GSH, and (c) GRN- Ag_{QC} . (II) Photographs of Ag_{QC} in aqueous phase and in toluene phase, respectively (a and b). Images a' and b' are the corresponding photographs under UV-light. Similar photographs of GRN- Ag_{QC} before and after phase transfer (c, d and c', d', respectively). The top layer is toluene and the bottom layer is water. (III) Raman spectra of (d) GRN and (e) GRN-GSH.

spectrum shows well-defined features due to the molecular transitions of the cluster, quite unlike plasmonic nanoparticles. The absorption spectrum of GRN-GSH in Figure II(b) shows the graphene feature at 258 nm. The spectrum is characterized by large scattering due to the suspended sheets, which manifests as a raise in background at 1000 nm. Figure III(e,f) (e,f) is the Raman spectra of graphene and GRN-GSH under 633 nm excitation. The spectra show D and G bands characteristic of the solution phase functionalized graphenes. There is no shift in either of these peaks when graphene is functionalized with thiol. Figure III shows photographs of Ag_{QC} in the aqueous phase and toluene phase, respectively (a and b). Photographs a' and b' are the corresponding images under UV irradiation. Cluster in the aqueous phase does not exhibit visible emission, and the emission intensity enhances upon phase transfer to organic phase.¹³ This makes it possible to capture the red emission. Photographs c and d are of GRN- Ag_{QC} before and after phase transfer, respectively, and c' and d' are the corresponding images under UV irradiation. GRN- Ag_{QC} shows photoluminescence under UV irradiation in both the aqueous and organic phases; however, the luminescence intensity was reduced compared to the parent Ag_{QC} . As in the case of the parent cluster, the luminescence is not observable visibly in the aqueous phase. Luminescence of Ag_{QC} was quenched as graphene binds to the clusters and transfers to the organic phase.

The absorption spectrum of GRN- Ag_{QC} (Figure II(c)) shows the features of both the clusters and GRN-GSH. The characteristic band of the cluster at 478 nm exists in the hybrid but is red-shifted. The 330 and 550 nm bands are observable as shoulders but the 640 nm band is not seen. This band is highly sensitive to chemical transformations. The presence of GRN is apparent in the absorption spectrum as the baseline shifted up significantly along with the presence of the feature at 260 nm, as in the case of the parent graphene and GRN-GSH.

The addition of graphene does not quench cluster fluorescence until high concentrations of graphene are added.

Figure 2I shows the quenching of cluster luminescence by the addition of GRN–GSH. In this measurement, the concen-

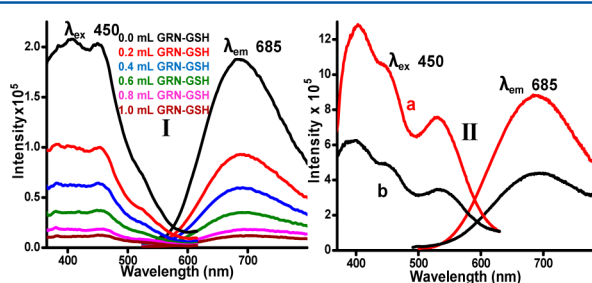


Figure 2. (I) Luminescence spectra of Ag_{QC} with increasing concentration of GRN–GSH. Cluster concentration is kept constant. (II) (a and b) Luminescence spectra of phase transferred Ag_{QC} and GRN– Ag_{QC} , respectively.

tration of clusters was kept constant, while the concentration of GRN–GSH was increased stepwise. The luminescence intensity decreases with the increase of GRN–GSH, but no peak shift is observed. Luminescence spectra of Ag_{QC} and graphene, as well as Ag_{QC} and GRN–GSH mixtures with concentrations of the two varied systematically are shown (Figure S3 in the Supporting Information). Figure 2II(a,b) shows the luminescence spectra of phase transferred Ag_{QC} and GRN– Ag_{QC} , respectively; the spectrum on the left side being the corresponding excitation spectra. Luminescence intensity of GRN– Ag_{QC} is decreased compared to the intensity of emission from Ag_{QC} , consistent with the quenching observed in Figure 1I. There is no shift seen in the emission maximum; however, the addition of excess TOABr during phase transfer can often cause a red shift in the emission spectrum by almost 10 nm, when compared with the emission peak of the cluster in the aqueous phase. This must not be mistaken as the formation of a different cluster while transferring to the organic phase. At similar ratios of graphene and Ag_{QC} in the two phases, quenching was a little more in the aqueous phase. This could be attributed to the presence of some unbound GRN–GSH before phase transfer. Low concentrations of composite were used in luminescence measurements and inner filter effect can be assumed to have only minimal effect on quenching (see also below).

In the method of cluster synthesis used, size tuning of clusters has not been reported yet. Hence, the effect of changing the size of the clusters has not been explored. However, with regard to cluster concentration, a higher concentration of the clusters (with respect to graphene) increases the intensity of fluorescence emission in a regular manner. There is no significant difference when graphene is bound at the same Ag_{25} /graphene ratio. The graphene sheet surface is covered by the clusters as seen from the TEM image. It is also equally likely that the clusters attach to either side of the sheets. Therefore, it is more probable that the clusters on the graphene surface will absorb the incident light at 450 nm as they are covering the surface and they have a higher absorption coefficient at the excitation wavelength. Moreover, in the aqueous phase there is a larger background arising due to graphene. This might also be due to the presence of unbound graphene sheets as they have not been separated. After phase transfer to toluene, this background in the absorption spectrum is negligible (Figure S2B, Supporting Information). Though the absorption and scattering of graphene sheets cannot be

completely avoided, they may be neglected for the reasons mentioned above.

Despite careful separation of unbound graphenes by precipitation through low speed centrifugation, there might still be a possibility that unbound GRN–GSH might be present with the clusters due to the high binding ability of graphene sheets. In order to eliminate this possibility, phase transfer of the functionalized graphene–cluster hybrid was done, from aqueous to organic phase, to ensure that the unbound free graphene is separated from GRN– Ag_{QC} . This was done by stirring GRN–GSH with the cluster solution for 4 h, followed by phase transfer of the material into toluene via the phase transfer reagent, tetra-octyl-ammonium bromide (TOABr). The phase transfer occurred within a few minutes of stirring with TOABr, just as in the case of clusters,¹³ and was marked by the organic layer turning orange due to the color of the clusters that have transferred from the aqueous phase. GRN–GSH when stirred in the absence of clusters does not transfer to the organic phase by this method even after several hours of vigorous stirring. This control experiment was validated by taking the Raman spectrum of the organic phase after stirring the aqueous GRN–GSH with TOABr in toluene overnight. No graphene signature was seen in the Raman measurement of the toluene phase. If the interaction between the graphenes and Ag_{QC} s was electrostatic, there would have been an equal chance of detecting organic phase graphene in the control study. Moreover, Ag atoms are known to have a strong affinity toward sulfur as opposed to oxygen due to soft–soft interaction of Ag and S. In the event of electrostatic binding, there would be no preferential binding of Ag_{QC} s to GRN–GSH compared to graphene sheets having carboxylate functionalities used in the control. Although standard techniques for the observation of covalent functionalization such as infrared and Raman spectroscopies were used, these were not successful in showing the distinct presence of a new functionality. This is expected as glutathione and graphene have the very same functionalities (such as amide, C–S, etc. bonds). Thus, indirect evidence was obtained through XPS, EDAX, TEM, and Raman characterization.

Figure 3I shows the X-ray photoelectron survey spectrum of the phase transferred GRN– Ag_{QC} , and the inset (Figure 3II) is an expanded view of the silver 3d region. Bromine is present in the sample due to the use of TOABr during phase transfer. From the XPS spectra, it is seen that there is a large amount of carbon in the phase transferred sample, strongly indicating that GRN–GSH has been transferred to the organic phase. It is therefore likely that the GRN–GSH is covalently bound to the clusters. Figure 3II shows the transmission electron microscopic (TEM) image of GRN– Ag_{QC} , phase transferred to toluene (method of phase transfer will be discussed later). Ag_{QC} are preferentially anchored on the edge of the GRN–GSH sheet (marked by the rectangles) where a larger density of dots due to the clusters can be seen. The clusters anchored on the graphene sheets are less susceptible to electron beam-induced aggregation unlike in the case of unbound clusters, which aggregate easily during TEM measurements.^{26,27} Clusters may come out from the hybrid molecule during electron impact, which may get aggregated.

Figure 4I shows the energy dispersive analysis of X-rays (EDAX) of phase transferred GRN– Ag_{QC} . The elemental analysis of the sample shown in its inset gave the following: silver (0.35%), sulfur (0.31%), and a large amount of carbon (78%) due to the presence of graphene sheets. The Ag/S

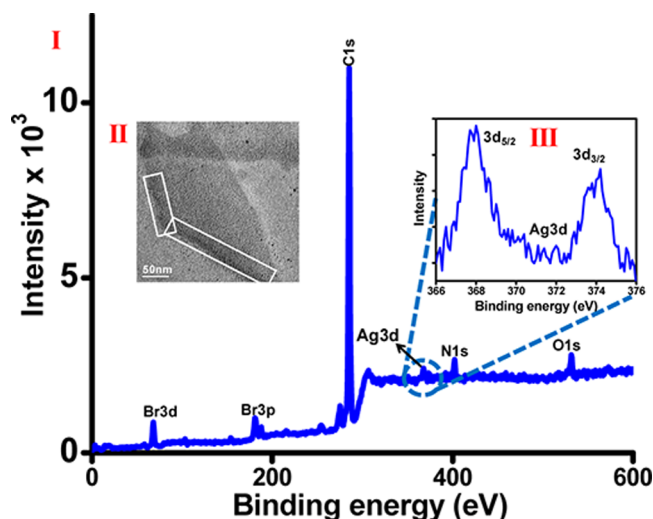


Figure 3. (I) XPS survey spectrum of the phase transferred GRN–Ag_{QC} hybrid. (II) TEM image of a GRN–GSH sheet, with Ag_{QC}s preferentially anchored on the edge (marked by the rectangles). (III) Expanded XPS spectrum showing the Ag 3d features.

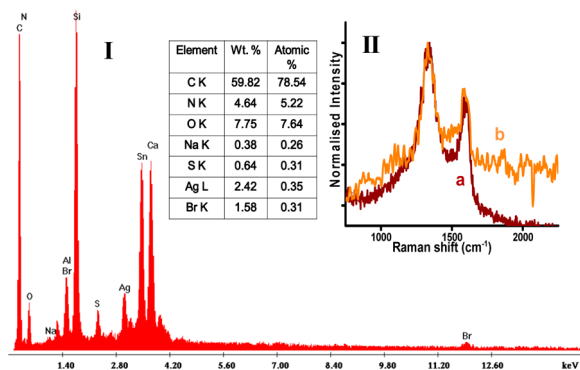


Figure 4. (I) EDAX spectrum of phase transferred GRN–Ag_{QC}. The inset table gives the elemental analysis data. Si, Ca, Al, and Sn are impurities from the substrate. (II) Raman spectra of GRN–Ag_{QC} in the aqueous phase (a) and after phase transfer to toluene (b).

atomic ratio expected for Ag₂₅SG₁₈ is 1.39, while the observed is 1.12. The increased sulfur content, due to GSH functionalization of graphene and the presence of such free GSH (unbound to clusters) are the possible reasons for this reduced ratio. Si, Ca, Al, and Sn are signatures of the substrate on which the sample was drop casted for the measurement, and these can be disregarded. From both the XPS and EDAX spectra, it is seen that there is a large amount of carbon in the organic phase. The Raman spectrum of the phase transferred sample was measured to confirm that this is the graphene that is bound to the clusters. The spectrum of the organic phase was compared with the spectrum before phase transfer (Figure 4II). Both the spectra contain the D (1350 cm⁻¹) and G (1580 cm⁻¹) bands characteristic of the graphene sheets, confirming that GRN–GSH was bound to the clusters and was transferred to the organic phase. All Raman spectra were obtained with 633 nm laser excitation, in order to minimize the fluorescence emission from the clusters present in the sample. The spectrum under 532 nm excitation shows the emission feature of the cluster as expected (Figure S4 in the Supporting Information). Ligand exchange of clusters without core change has been reported in several cases.^{7,28} The exact matching of the luminescence

features before and after phase transfer and the absence of phase transfer of the parent GRN–GSH indicate that the GRN–Ag_{QC} hybrid with its inherent properties has been phase transferred. While the presence of glutathione in GRN–GSH could be confirmed by electrospray ionization mass spectrometry (ESI MS) shown in Figure S5 in the Supporting Information, the integral GRN–Ag_{QC} hybrid could not be observed. Integral features of the clusters are difficult to be seen even in soft ionization methods.⁸

CONCLUSIONS

We report for the first time the attachment of silver quantum clusters to graphene through a covalent linker. The luminescence of the cluster is retained even after attachment to the graphene sheets. The resulting water-dispersible hybrid molecule can act as a multimodal material exhibiting the characteristics of both graphene and the cluster. Variation in the functional groups, length, and properties of the linker molecules can potentially lead to an array of different nanocomposite structures. With variation in this linker molecule, the optical properties of the hybrid can be changed by the nature of the bonds the linker makes, as this will affect the ligand field and hence the energy states. Composites of this kind could be used in drug delivery applications. Graphene has been shown to be biocompatible in past reports. Due to its high adsorption property, it can act as a carrier and the attached luminescent cluster is an in-built tracking system for locating the drug within the bloodstream. Clusters bound to graphene could potentially be catalysts in metal catalyzed reactions involving organics or biomolecules as the composite is suspendable in both organic and aqueous phases. Luminescence of the QCs is sensitive to the physical and chemical changes in their medium. This property enables this hybrid to be useful in sensor applications. Our results provide a gateway for further experimental and theoretical exploration on the electronic, optical, catalytic, and biological properties of this new material.

ASSOCIATED CONTENT

Supporting Information

All experimental details and other results presented in the text. This material is available free of charge via the Internet at <http://pubs.acs.org>.

AUTHOR INFORMATION

Corresponding Author

*E-mail: pradeep@iitm.ac.in.

Notes

The authors declare no competing financial interest.

ACKNOWLEDGMENTS

We thank the Department of Science and Technology (DST), Govt. of India, for constantly supporting our research program on nanomaterials. A.C. thanks IISER Kolkata and the INSPIRE Program of DST.

REFERENCES

- (1) Rao, C. N. R.; Sood, A. K.; Subrahmanyam, K. S.; Govindaraj, A. *Angew. Chem., Int. Ed.* **2009**, *48*, 7752–7777.
- (2) Tkachev, S. V.; Buslaeva, E. Y.; Gubin, S. P. *Inorg. Mater.* **2011**, *47*, 1–10.

- (3) Allen, M. J.; Tung, V. C.; Kaner, R. B. *Chem. Rev.* **2010**, *110*, 132–145.
- (4) Negishi, Y.; Takasugi, Y.; Sato, S.; Yao, H.; Kimura, K.; Tsukuda, T. *J. Am. Chem. Soc.* **2004**, *126*, 6518–6519.
- (5) Judai, K.; Abbet, S.; Wörz, A. S.; Heiz, U.; Henry, C. R. *J. Am. Chem. Soc.* **2004**, *126*, 2732–2737.
- (6) Shichibu, Y.; Negishi, Y.; Tsukuda, T.; Teranishi, T. *J. Am. Chem. Soc.* **2005**, *127*, 13464–13465.
- (7) Muhammed, M. A. H.; Pradeep, T. In *Advanced Fluorescence Reporters in Chemistry and Biology II*; Demchenko, A.P., Ed.; Springer-Verlag: Berlin, Germany, 2010; Vol. 9, part 4, pp 333–353 and references cited therein.
- (8) Xavier, P. L.; Chaudhari, K.; Baksi, A.; Pradeep, T. *Nano Rev.* **2012**, *3*, 14767–14783.
- (9) Diez, I.; Pusa, M.; Kulmala, S.; Jiang, H.; Walther, A.; Goldmann, A. S.; Muller, A. H. E.; Ikkala, O.; Ras, R. H. A. *Angew. Chem., Int. Ed.* **2009**, *48*, 2122–2125.
- (10) Jin, R. *Nanoscale* **2010**, *2*, 343–362.
- (11) Udayabhaskararao, T.; Sun, Y.; Goswami, N.; Pal, S. K.; Balasubramanian, K.; Pradeep, T. *Angew. Chem., Int. Ed.* **2012**, *51*, 2155–2159.
- (12) Rao, T. U. B.; Nataraju, B.; Pradeep, T. *J. Am. Chem. Soc.* **2010**, *132*, 16304–16307.
- (13) Rao, T. U. B.; Pradeep, T. *Angew. Chem., Int. Ed.* **2010**, *49*, 3925–3929.
- (14) Muhammed, M. A. H.; Verma, P. K.; Pal, S. K.; Kumar, R. C. A.; Paul, S.; Omkumar, R. V.; Pradeep, T. *Chem.—Eur. J.* **2009**, *15*, 10110–10120.
- (15) Sreeprasad, T. S.; Maliyekkal, S. M.; Krishnan, D.; Chaudhari, K.; Xavier, P. L.; Pradeep, T. *ACS Appl. Mater. Interfaces* **2011**, *3*, 2643–2654.
- (16) Sreeprasad, T. S.; Maliyekkal, S. M.; Lisha, K. P.; Pradeep, T. *J. Hazard. Mater.* **2011**, *186*, 921–931.
- (17) Gao, W.; Majumder, M.; Alemany, L. B.; Narayanan, T. N.; Ibarra, M. A.; Pradhan, B. K.; Ajayan, P. M. *ACS Appl. Mater. Interfaces* **2011**, *3*, 1821–1826.
- (18) George, A.; Shibu, E. S.; Maliyekkal, S. M.; Bootharaju, M. S.; Pradeep, T. *ACS Appl. Mater. Interfaces* **2012**, *4*, 639–644.
- (19) Xavier, P. L.; Chaudhari, K.; Verma, P. K.; Pal, S. K.; Pradeep, T. *Nanoscale* **2010**, *2*, 2769–2776.
- (20) Daniel, M. C.; Astruc, D. *Chem. Rev.* **2004**, *104*, 293–346.
- (21) Muhammed, M. A. H.; Shaw, A. K.; Pal, S. K.; Pradeep, T. Quantum Clusters of Gold Exhibiting FRET. *J. Phys. Chem. C* **2008**, *112*, 14324–14330.
- (22) Retnakumari, A.; Setua, S.; Menon, D.; Ravindran, P.; Muhammed, H.; Pradeep, T.; Nair, S.; Koyakutty, M. *Nanotechnology* **2010**, *21*, 055103–055114.
- (23) Kovtyukhova, N. I.; Ollivier, P. J.; Martin, B. R.; Mallouk, T. E.; Chizhik, S. A.; Buzaneva, E. V.; Gorchinskiy, A. D. *Chem. Mater.* **1999**, *11*, 771–778.
- (24) Zhou, Y.; Bao, Q.; Tang, L. A. L.; Zhong, Y.; Loh, K. P. *Chem. Mater.* **2009**, *21*, 2950–2956.
- (25) Chakraborty, I.; Rao, T. U. B.; Pradeep, T. *J. Hazard. Mater.* **2012**, *211–212*, 396–403.
- (26) Ramasamy, P.; Guha, S.; Shibu, E.; Sreeprasad, T. S.; Bag, S.; Banerjee, A.; Pradeep, T. *J. Mater. Chem.* **2009**, *19*, 8456–8462.
- (27) Shibu, E. S.; Muhammed, M. A. H.; Tsukuda, T.; Pradeep, T. *J. Phys. Chem. C* **2008**, *112*, 12168–12176.
- (28) Sun, Y.; Balasubramanian, K.; Rao, T. U. B.; Pradeep, T. *J. Phys. Chem. C* **2011**, *115*, 20380–20387.

Supporting Information for the paper:

Luminescent Silver Clusters with Covalent Functionalisation of Graphene

Aditi Chandrasekar[§] and T. Pradeep^{%,*}

[§]Indian Institute of Science Education and Research- Kolkata, Mohanpur, Nadia, West Bengal 741252, India

[%]DST Unit on Nanoscience (DST-UNS), Department of Chemistry and Sophisticated Analytical Instrument Facility, Indian Institute of Technology Madras, Chennai 600 036, India

*E-mail: pradeep@iitm.ac.in

Table of contents:

Number	Description	Page number
S1	Experimental	2
S2	Characterisation by absorption spectroscopy	6
S3	Characterisation by luminescence spectroscopy	8
S4	Characterisation by Raman spectroscopy	11
S5	Characterisation by ESI mass spectrometry	12

S1: Supporting information 1

Experimental

Materials

Natural graphite was purchased from Active Carbon India Pvt. Ltd., India. Sulfuric acid (H_2SO_4 , 95-98%) and hydrochloric acid (HCl , 36%) were purchased from Ranbaxy Chemicals, India. Phosphorus pentoxide (P_2O_5), hydrazine monohydrate ($\text{N}_2\text{H}_4 \cdot \text{H}_2\text{O}$, 99-100%), hydrogen peroxide (H_2O_2), were purchased from SD Fine Chemicals, India. Potassium persulphate ($\text{K}_2\text{S}_2\text{O}_8$) was purchased from Sisco Research Laboratories Pvt. Ltd., India. Potassium permanganate (KMnO_4) was purchased from Merck.

Silver nitrate (AgNO_3 , 99%), glutathione (GSH, 97%) and methanol (G.R grade), ammonium per sulphate (APS), N,N' methylene bisacrylamide (A.R grade), acryl amide (A.R grade), and N,N,N',N' -tetramethylethelenediamine (TEMED), were purchased from SRL Chemicals Co. Ltd. Sodium borohydride (99.99%), methanol (HPLC grade) and tetra-octyl-ammonium bromide (TOAB) were purchased from Sigma Aldrich. 1-(3-(dimethylamino) propyl)-3-ethyl-carbodiimide hydrochloride (EDC) was purchased from Sigma Aldrich.

Synthesis of solution phase graphene

The synthesis of graphite oxide from graphite powder was achieved by a two-step oxidation. Graphite powder (2 g) was treated with phosphorous pentoxide (1 g), and potassium persulphate (1 g) in conc. sulphuric acid (8 mL). This partial oxidation gave pre-oxidised graphite. These were mixed together with stirring at 80 °C. The reaction was allowed to cool, distilled water was added carefully, and the product was filtered over vacuum. The light grey powder was allowed to dry overnight. Pre-oxidised graphite (2 g) was further subjected to strong oxidation by potassium permanganate (6 g) in ice cold concentrated sulphuric acid (46 mL). This was done over an ice bath. KMnO_4 crystals were added to the reaction very slowly and the temperature of the reaction mixture was maintained below 20°C throughout the addition. After the complete dissolution of KMnO_4 , the reaction was stirred for 2 hours at 35 °C. The resulting brown powder was washed with 500 mL of 1:10 HCl to remove metal ions. The resultant solid

was dried and 1 % (w/w) dispersion was prepared in distilled water. This dispersion was dialyzed for 3 weeks through a semi-permeable cellulose membrane to remove all unwanted contaminants like salts and acid. De-ionized water was used for dialysis and was changed every 3-4 hours. The dispersion was later diluted to 0.05 % (w/w).

Reduction of the dialysed graphite oxide was done by a hydrothermal method. 15 mL of 0.05% w/v graphite oxide dispersion was poured into a hydrothermal bomb. The reaction was maintained at 180 °C for 6 hours. A black dispersion of the graphene was obtained, which is stable to centrifugation at moderate speeds.

Synthesis of silver quantum clusters

Silver quantum cluster (Ag_{QC}) was prepared by the following procedure. AgNO_3 (47 mg) and GSH (150 mg) were dissolved in a solution of NaOH (45 mg in 1 mL) at room temperature and the mixture was vigorously stirred and sonicated to make a uniform yellow solution of Ag(I)thiolate complexes. This precursor was added at the time of gel preparation (see below). For the preparation of the gel, acrylamide (T)/ bisacrylamide(C) (51% T, 7.8% C) 50 μL of 0.1% ammonium persulfate were first mixed and 1 mL of the above prepared silver thiolate solution was added and stirred. With the addition of 50 μL N,N,N',N'-tetramethyl-ethane-1,2-diamine (TEMED), polymerization leading to the gel formation occurred. The above gel was allowed to set for 20 minutes at room temp. It was then transferred to a cold temperature for 10 min. 10 mL of ice cold NaBH_4 solution (10 mg/mL) was added on top of the gel and the mixture was stored undisturbed for 30 min. The colour of the gel changed from light yellow to dark brown from top to bottom indicating the formation of clusters within the gel. The NaBH_4 solution on top of the gel was removed. The gel was crushed and washed with methanol 5 to 6 times to remove excess NaBH_4 and other soluble impurities. Free clusters were extracted into water from the crushed gel (the gel was insoluble in water). The cluster solution obtained was used in further reactions. Previous studies indicated that the clusters have a composition of $\text{Ag}_{25}\text{SG}_{18}^1$.

Analytical procedures

UV-vis spectroscopy

Perkin Elmer Lambda 25 UV-vis spectrometer was used for the measurements. Spectra were typically measured in the range of 200-1100 nm.

Luminescence spectroscopy

Luminescence measurements were carried out using HORIBA JOBIN VYON Nano Log instrument. The band pass for excitation and emission was set as 5 nm.

X-ray photoelectron spectroscopy

The photoelectron spectra of the samples were obtained using an ESCA probe/TPD of Omicron Nanotechnology. Sample in water was spotted on a Mo plate and allowed to dry in vacuum. The size of the analyzed area was about 3 mm². In view of the sensitivity of the sample, surface cleaning was not attempted. Al K_α radiation was used for excitation; a 180° hemispherical analyzer and a seven-channel detector were employed. The spectrometer was operated in the constant analyzer energy mode. Survey and individual regions were collected using pass energies of 50 and 20 eV, respectively. The pressure in the analyzer chamber was in the low 10⁻¹⁰ mbar range during spectrum collection. Binding energies of the core levels were calibrated with C 1s BE, set at 284.7 eV.

Raman spectroscopy

A Witec GmbH confocal Raman spectrometer, equipped with a helium- neon laser at 633 nm was used as the excitation source to collect the luminescence images. The laser was focused onto the sample using a 100X objective with the signal collected in a back scattering geometry. The signal, after passing through a super notch filter, was dispersed using a 150 grooves/mm grating onto a Peltier-cooled charge coupled device (CCD), which served as the detector. Some data were collected with 532 nm excitation also.

Mass spectrometry

All the ESI mass spectra have been acquired using a triple quadrupole mass spectrometer (3200 QTrap) from AB Sciex between the mass range of m/z 50 – 1700 in negative ion mode.

The glutathione functionalised graphene was dispersed in 1:1 water- methanol solution. This was centrifuged at around 8000 rpm for 10 minutes to allow the undissolved particle, if any, to settle and to avoid clogging of the electrospray capillary of the apparatus. The samples were electrosprayed at a flow rate of 10uL/min. The spectra were averaged for 60 scans.

Energy dispersive X-ray analysis

Energy dispersive X-ray (EDAX) analyses were done in a FEI QUANTA-200 SEM. For measurements, samples were drop-casted on an indium tin oxide coated conducting glass and completely dried before the measurement.

Transmission electron microscopy

TEM images were collected using a JEOL 3010 microscope. A diluted solution was spotted on carbon coated copper grid and was dried in the laboratory ambience. Images were collected at 200 keV, to reduce beam induced damage of the clusters.

S2: Supporting information 2

Characterisation by absorption spectroscopy

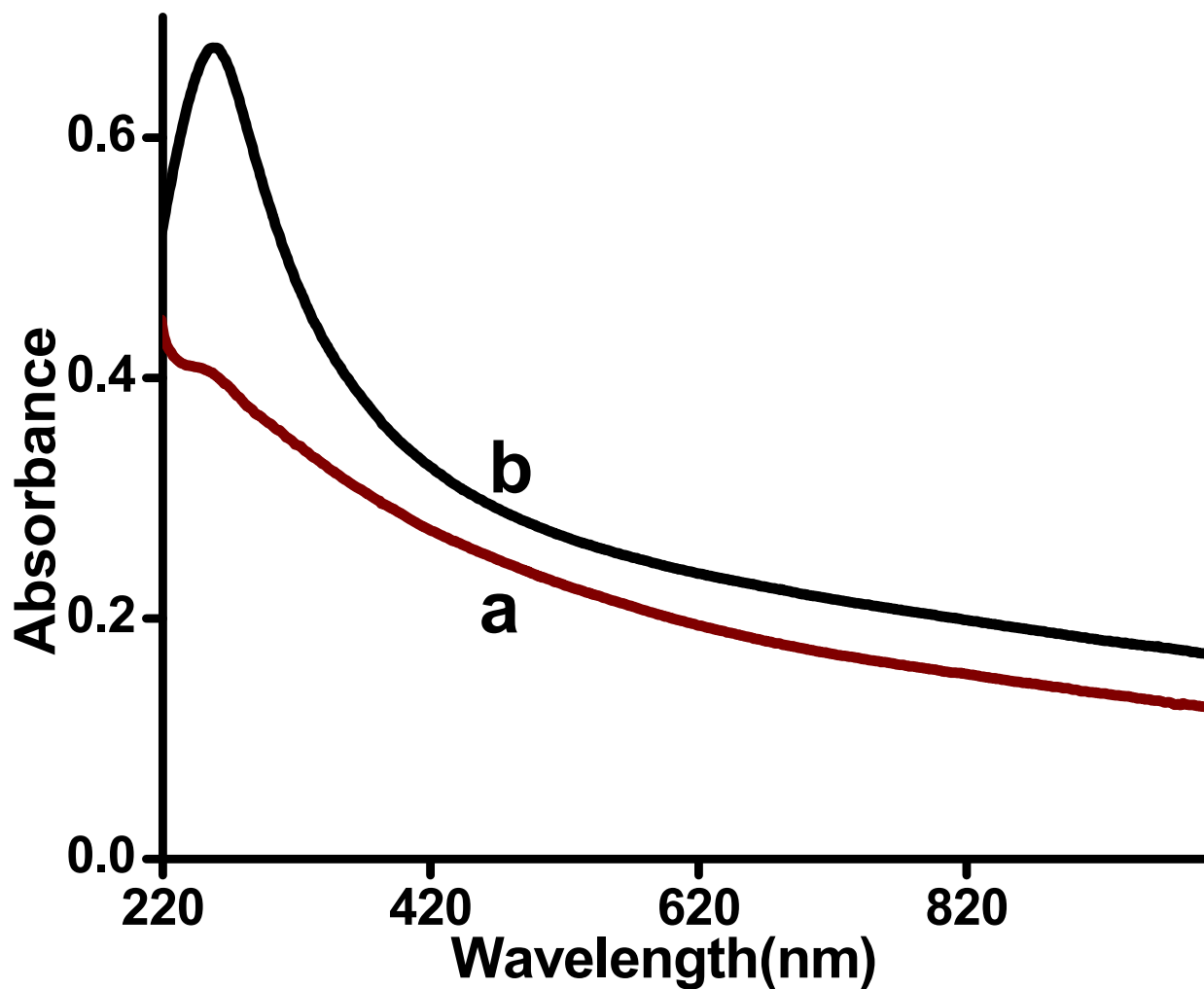


Figure S2 (A): Absorption spectra of (a) GSH functionalised graphite oxide and (b) graphene. The peak at 253 nm is a standard feature of chemically synthesised graphene due to a secondary $\pi \rightarrow \pi^*$ transition in the graphene ring system.

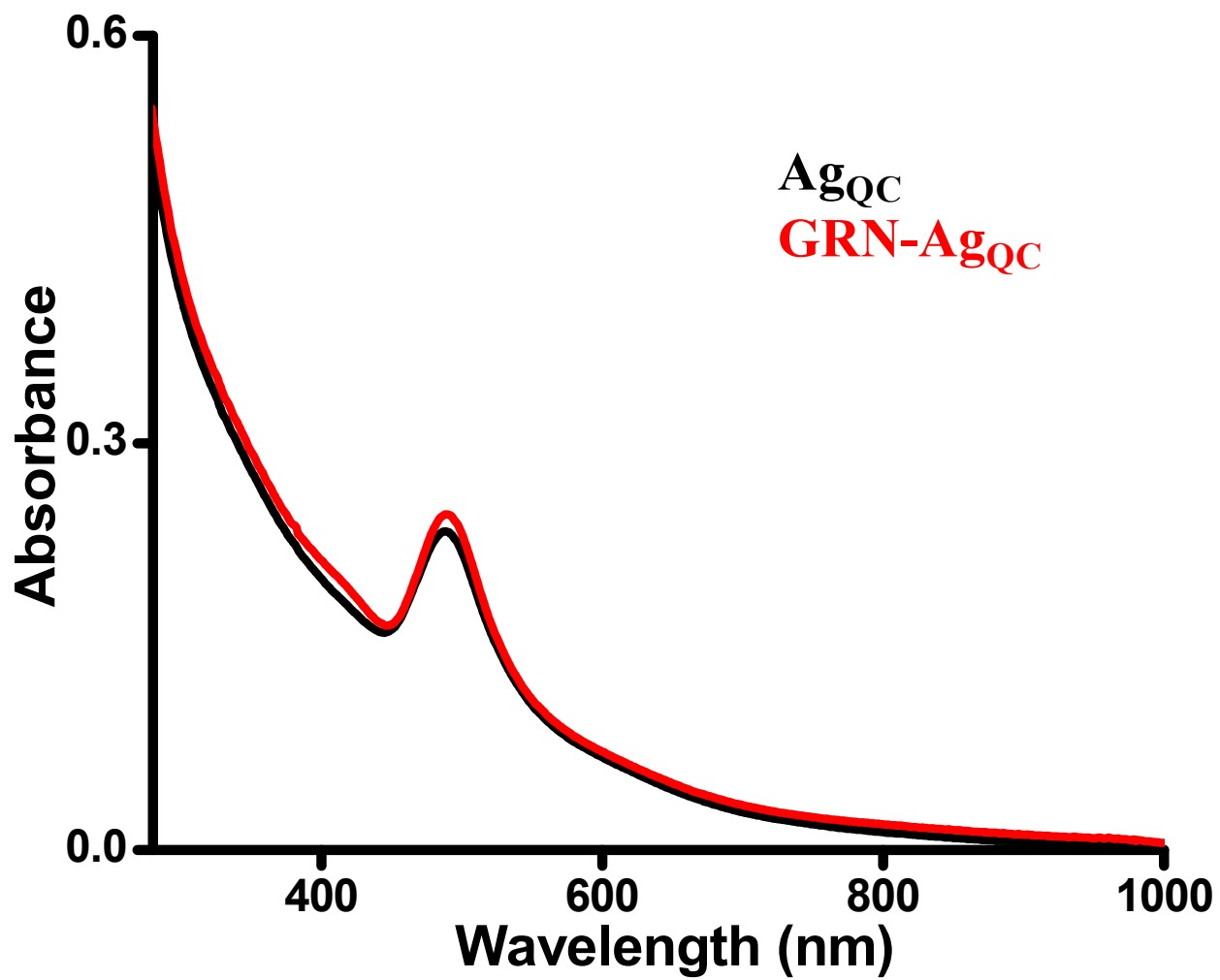


Figure S2 (B): Absorbance spectrum of AgQC and GRN-AgQC after phase transfer to toluene.

S3: Supporting information 3

Characterisation by luminescence spectroscopy

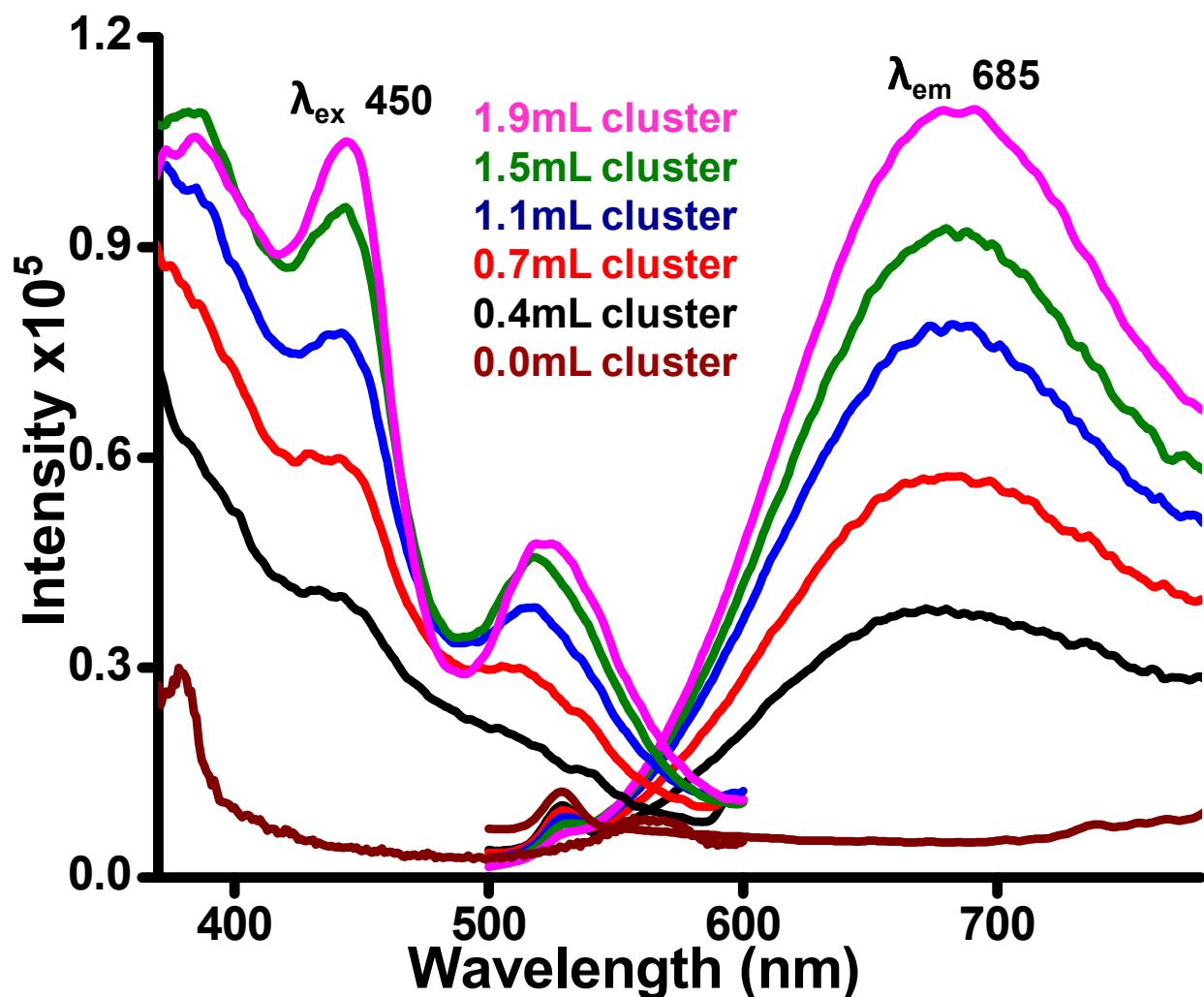


Figure S3 (A): Overlaid luminescence spectra showing change in cluster luminescence with increase in cluster concentration. GRN-GSH concentration was kept constant. GRN-GSH showed no emission and the features seen are due to impurity lines from the excitation or second order lines from the excitation.

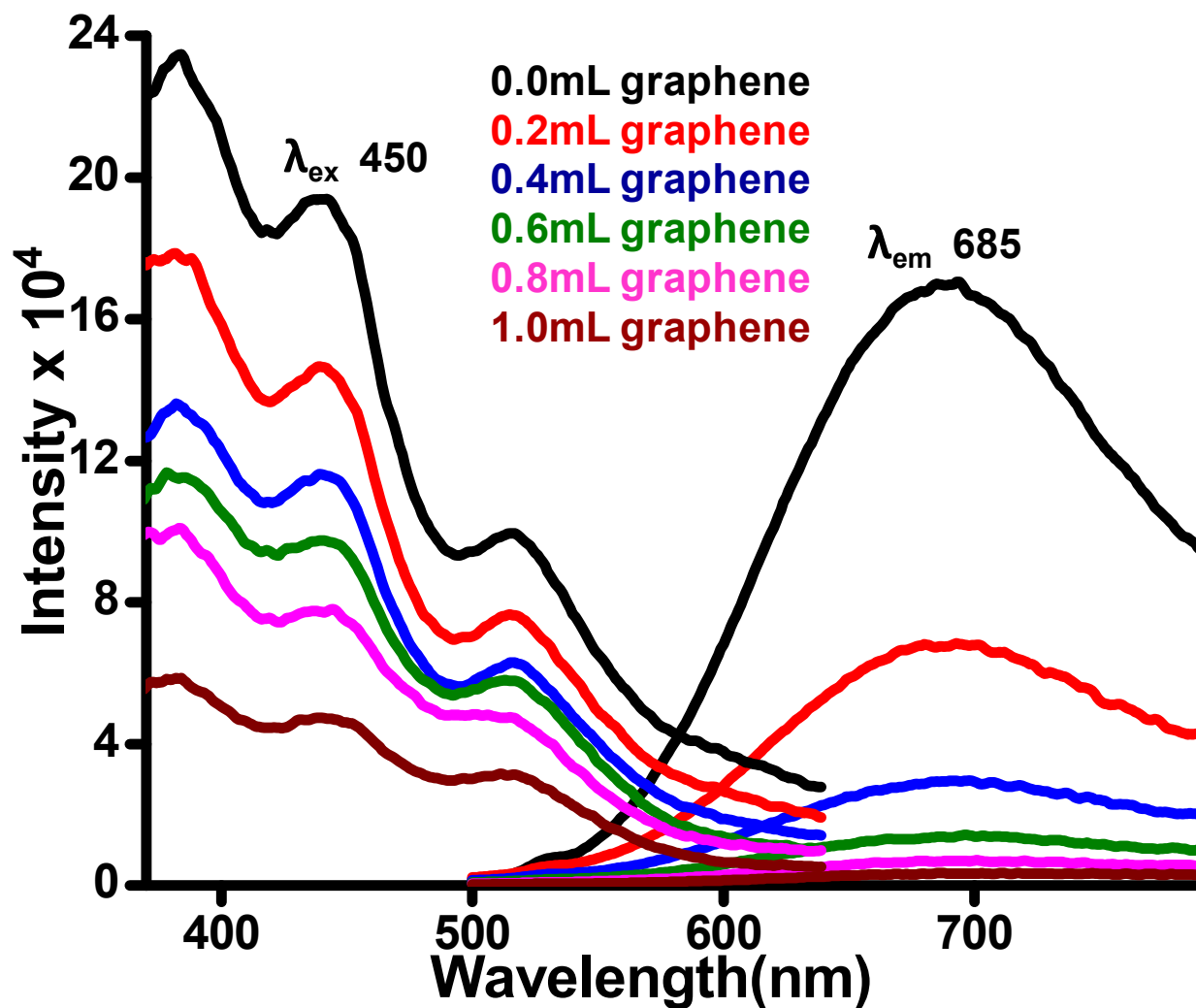


Figure S3 (B): Luminescence spectra of cluster and graphene mixtures showing change in cluster luminescence with increase in graphene concentration. Cluster concentration was kept constant and graphene concentration was varied. No peak shift was observed.

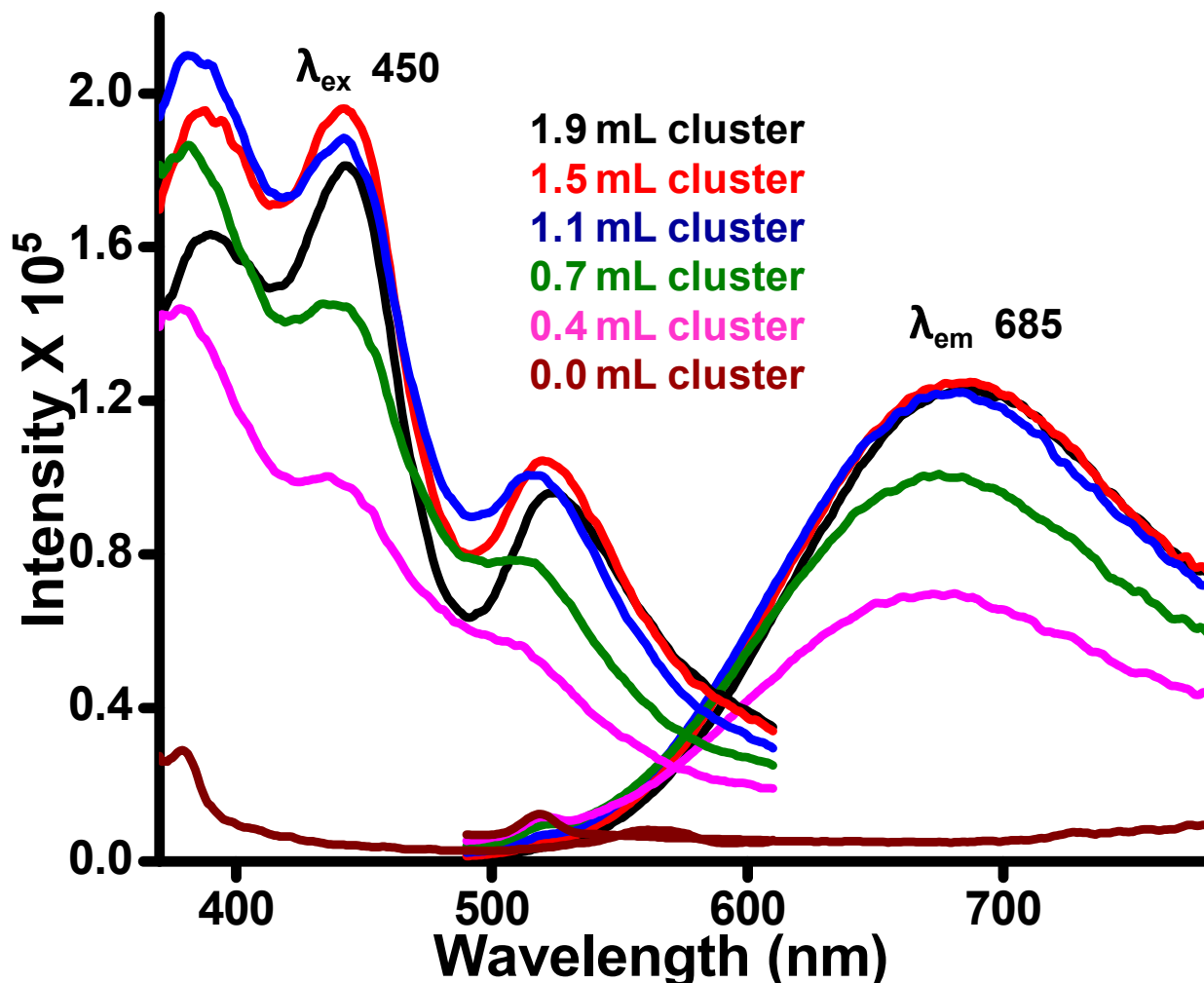


Figure S3 (C): Overlaid luminescence spectra showing change in cluster luminescence with increase in cluster concentration. Graphene concentration was kept constant. No spectral shifts were obtained. Graphene showed no emission and the features seen are due to impurity lines from the excitation or second order lines from the excitation.

S4: Supporting information 4

Characterisation by Raman spectroscopy

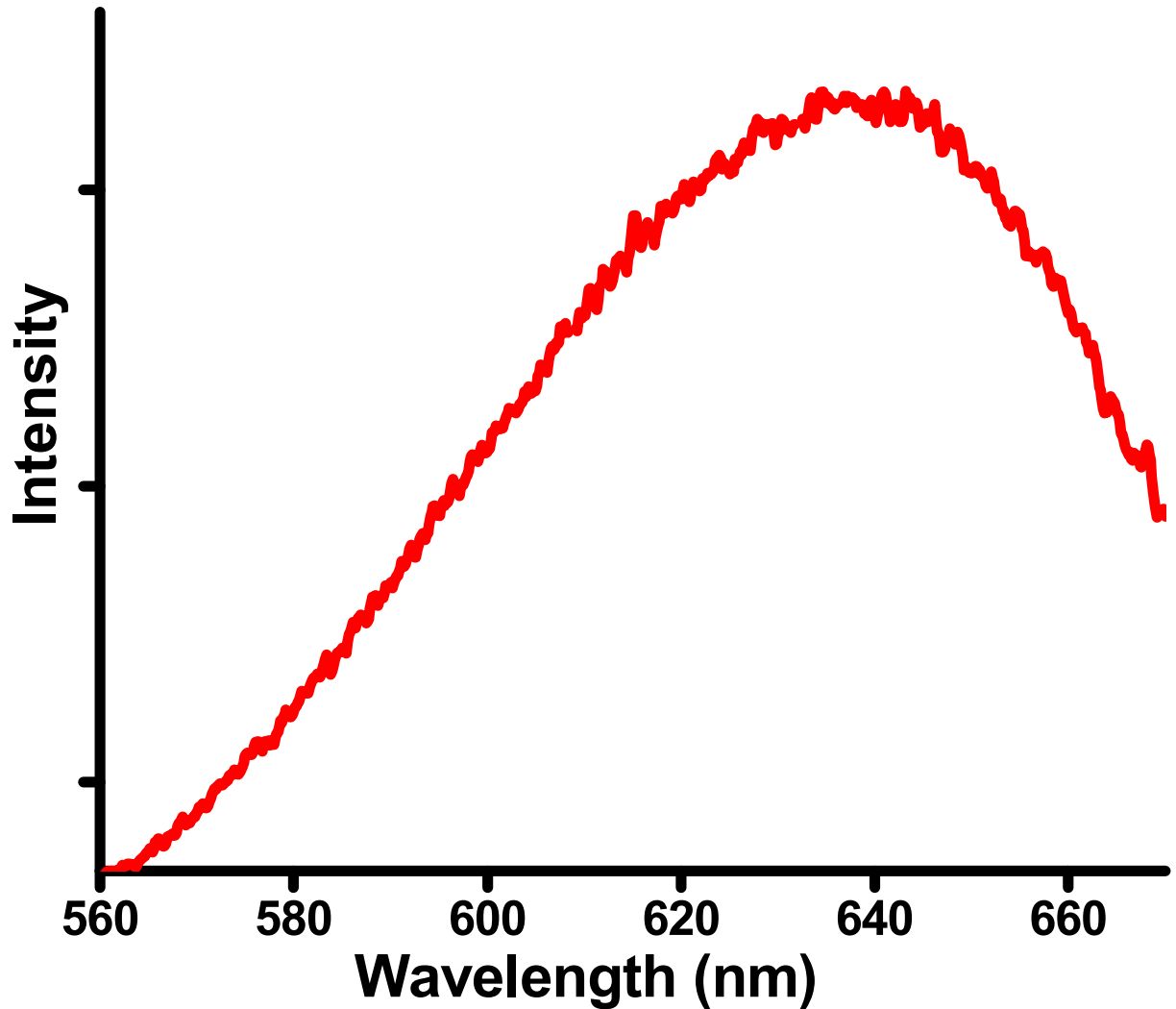


Figure S4: Raman spectrum of the phase transferred GRN-Ag_{QC} under 532 nm excitation. Raman shift (cm^{-1}) is converted to wavelength (nm) and plotted on the x-axis. The fall in intensity above 640 nm is due to the poor detector response. The data suggest the existence of the bound clusters which are luminescent.

S5: Supporting information 5

Characterisation by ESI mass spectrometry

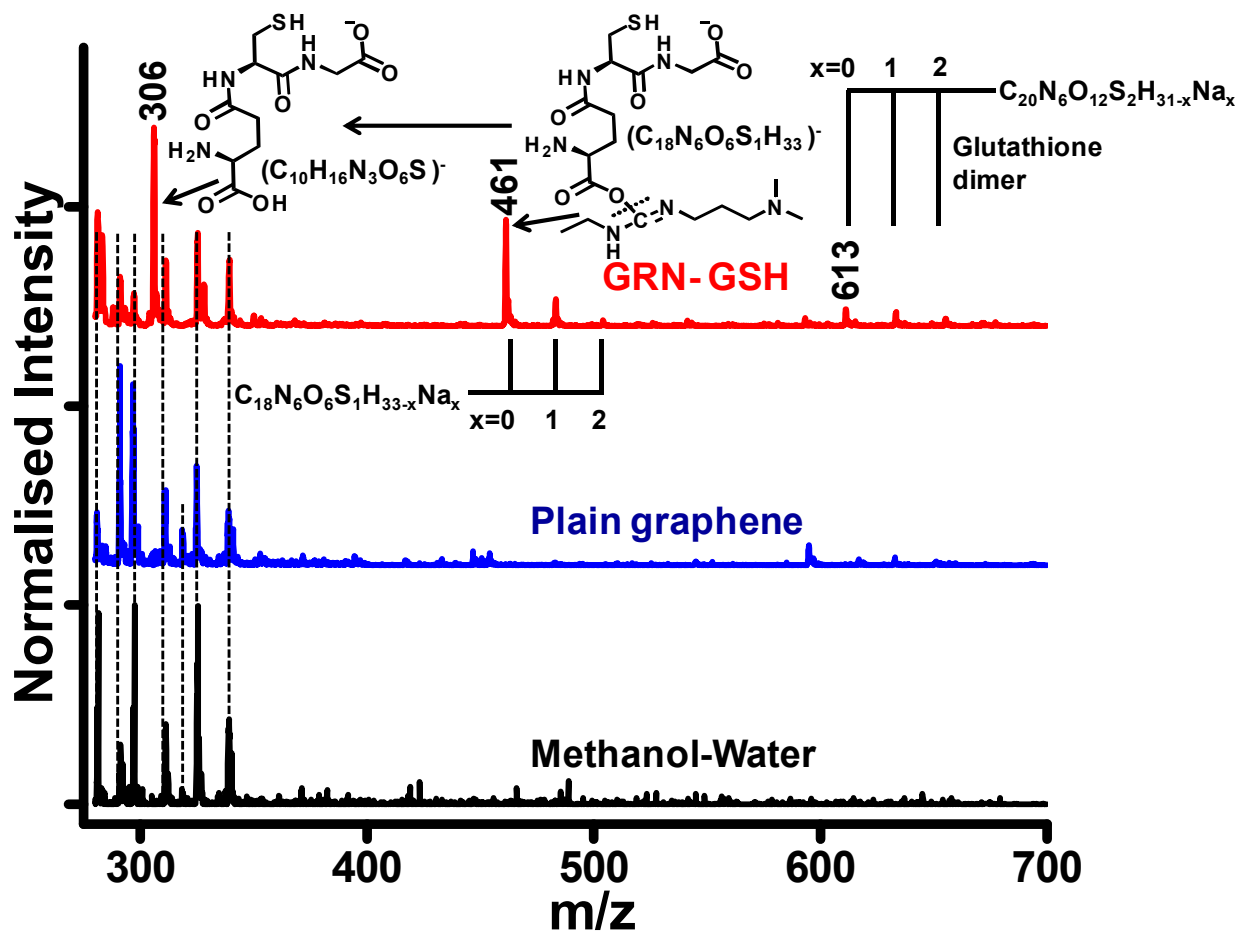


Figure S5: Electrospray ionisation mass spectrum of GRN-GSH, graphene and plain methanol: water (solvent). The spectrum of GRN-GSH shows the GSH peak at m/z 306 and an EDC bound GSH peak at m/z 461. The peak at m/z 613 is the GSH dimer formed via the sulphur-sulphur linkage. The peaks with a spacing of m/z 22 a.m.u arise due to the exchange of protons with sodium.

Reference:

1. Chakraborty, I.; Rao T. U. B.; Pradeep, T. Luminescent Sub-Nanometer Clusters for Metal Ion Sensing: A New Direction in Nanosensors. *J. Haz. Mater.* **2012**, 211– 212, 396– 403

Protein-Directed Synthesis of NIR-Emitting, Tunable HgS Quantum Dots and their Applications in Metal-Ion Sensing

Nirmal Goswami, Anupam Giri, Shantimoy Kar,
Megalamane Siddaramappa Bootharaju, Robin John,
Paulrajpillai Lourdu Xavier, Thalappil Pradeep,* and Samir Kumar Pal*

The development of luminescent mercury sulfide quantum dots (HgS QDs) through the bio-mineralization process has remained unexplored. Herein, a simple, two-step route for the synthesis of HgS quantum dots in bovine serum albumin (BSA) is reported. The QDs are characterized by UV-vis spectroscopy, Fourier transform infrared (FT-IR) spectroscopy, luminescence, Raman spectroscopy, transmission electron microscopy (TEM), X-ray photoelectron spectroscopy (XPS), circular dichroism (CD), energy dispersive X-ray analysis (EDX), and picosecond-resolved optical spectroscopy. Formation of various sizes of QDs is observed by modifying the conditions suitably. The QDs also show tunable luminescence over the 680–800 nm spectral regions, with a quantum yield of 4–5%. The as-prepared QDs can serve as selective sensor materials for Hg(II) and Cu(II), based on selective luminescence quenching. The quenching mechanism is found to be based on Dexter energy transfer and photoinduced electron transfer for Hg(II) and Cu(II), respectively. The simple synthesis route of protein-capped HgS QDs would provide additional impetus to explore applications for these materials.

1. Introduction

In the past decade, semiconductor quantum dots (QDs) have become well-established photoluminescent platforms for many scientific and industrial applications.^[1–3] For example, QDs are highly sensitive to charge/energy transfer, which can alter their optical properties, thus generating interest in charge/energy-transfer-based bio-sensing.^[1,4] Among all the semiconducting QDs, mercury chalcogenide QDs are

one of the least studied families because of the toxicity and volatility of corresponding organo-mercury compounds. Such materials are highly attractive for infrared sensing, optoelectronics, as well as for the more fundamental studies of their optical properties. Luminescence across the visible spectral region with mercury chalcogenide is extremely difficult, while it is common for zinc- and cadmium-based chalcogenides. Despite the potential toxicity of mercury and the restricted application in biology, it would be of great interest to develop

N. Goswami, A. Giri, S. Kar, Dr. S. K. Pal
Department of Chemical
Biological & Macromolecular Sciences
S. N. Bose National Centre for Basic Sciences
Block JD, Sector III, Salt Lake, Kolkata 700 098, India
E-mail: skpal@bose.res.in

M. S. Bootharaju, R. John, P. L. Xavier, Prof. T. Pradeep
Department of Chemistry
Indian Institute of Technology Madras
Chennai 600 036, India
E-mail: pradeep@iitm.ac.in

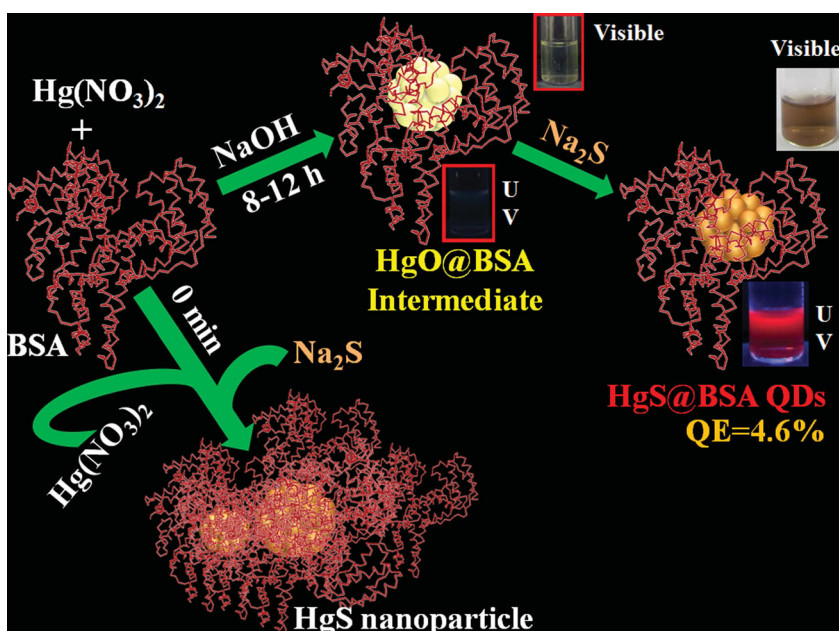


DOI: 10.1002/smll.201200760

mercury chalcogenide QDs with tunable luminescence as there is immense potentiality in their application in chemical sensing, infrared detection, and in the development of electrical devices.^[2,5,6]

Of all the mercury chalcogenides, HgTe is widely studied, having various synthetic routes leading to high-quality materials based on both aqueous- and organic-based chemistries. Recently, Keuleyan et al.^[7] prepared colloidal HgTe QDs having narrow photoluminescence tunable across the near and mid-IR regions. In contrast, there have been very few detailed studies on HgS QDs. Wichiansee et al.^[8] have successfully prepared HgS QDs based on an organic route, using trioctylphosphine oxide (TOPO) as the capping agent. Higginson et al.^[9] have synthesized HgS QDs exhibiting narrow, size-dependent transitions between 500 and 800 nm for sizes ranging from 1 to 5 nm in diameter. Typically, in most cases, HgS QDs were synthesized via thermal decomposition of organo-metallic precursors in organic solvents and/or in the presence of surfactants.^[8,10,11] However, unlike them, the use of a biomolecule as template or scaffold for the synthesis possesses many advantages due to their inherent biocompatibility and ease of functionalization. Thus, novel synthetic strategies for the preparation of HgS QDs using biomolecules that yield extremely stable, water-soluble QDs with tunable luminescence in the visible and near IR (NIR) region would be highly desirable.

Among many biological systems that could participate in biomineralization and be incorporated into bio-nanomaterials, proteins have been the subject of particular attention due to their nanoscale dimensions, distinctive molecular structures and functionalities, and their capability to control the size of inorganic crystals during nucleation and growth to a remarkable degree due to their bulky nature. For example, bovine serum albumin (BSA) and several other proteins have been used to synthesize sub-nanometer luminescent metal clusters.^[12–18] Recently, an aqueous, protein-driven synthesis of transition-metal-doped ZnS QDs has also been reported by Zhou et al.^[19] Akin to the bio-mineralization process, herein, we have developed a facile approach to prepare water-soluble, highly stable NIR-luminescent HgS QDs, which are protected and stabilized by the protein matrix. We have also used the HgS QDs formed as a fluorometric sensor for the detection of Hg(II) and Cu(II). Uses of the QDs in metal-ion sensing by exploiting their luminescence properties is not new and have been reported before.^[20,21] The mechanisms of luminescence quenching involving inner-filter effects, nonradiative recombination pathways, and electron transfer processes have also been reported. However, the quenching mechanisms addressing the specific interaction of detected ions with the sensor QDs are sparse in the existing literature. The reason for quenching relies on the metallophilic interaction between Hg(II)/Cu(II) and Hg(II) present



Scheme 1. Schematic illustration of the synthesis of HgS QDs through the bio-mineralization process mediated by the BSA protein.

on the surface of the HgS QDs. We have used time-resolved luminescence methods to study the mechanism of excited-state reactivity, which reveals that both Hg(II) and Cu(II) can reduce the lifetime of the HgS QDs. After considering all kinds of excited-state deactivation mechanisms, we have found that Dexter energy transfer is the reason in the case of Hg(II)-induced quenching whereas photoinduced electron transfer dominates in the case of Cu(II)-induced quenching. In several control experiments, we have also ruled out other possibilities for the quenching mechanisms, including aggregation and Förster resonance energy transfer (FRET).

2. Results and Discussion

The process for synthesizing the HgS QDs is simple and involves two steps (see Experimental Section for details). The various stages of synthesis are shown in **Scheme 1**. In the first step, addition of mercury nitrate solution to aqueous BSA causes the mercury ions to be coordinated with the various functional groups of BSA such as $-SH$ and $-NH$. The pH of the solution was adjusted to ~ 9 by the addition of NaOH followed by vigorous stirring at room temperature. After 8–12 h, the color of the solution changes from colorless to a pale yellow intermediate, which we have analyzed by Raman spectroscopy (see later in text) and found it to be HgO@BSA. Photographs of the intermediate under UV and visible light are shown in **Scheme 1**. In the last step, Na_2S is added and the color changes from pale yellow to light brown (**Scheme 1**), which indicates the formation of HgS QDs. **Figure 1A** illustrates the UV–vis absorption spectra of HgS@BSA QDs. In particular, **Figure 1A** gives the plot of the natural logarithm of the Jacobian factor (details in Experimental Section) versus wavelength of the QDs, to show the features more clearly. Well-defined absorption

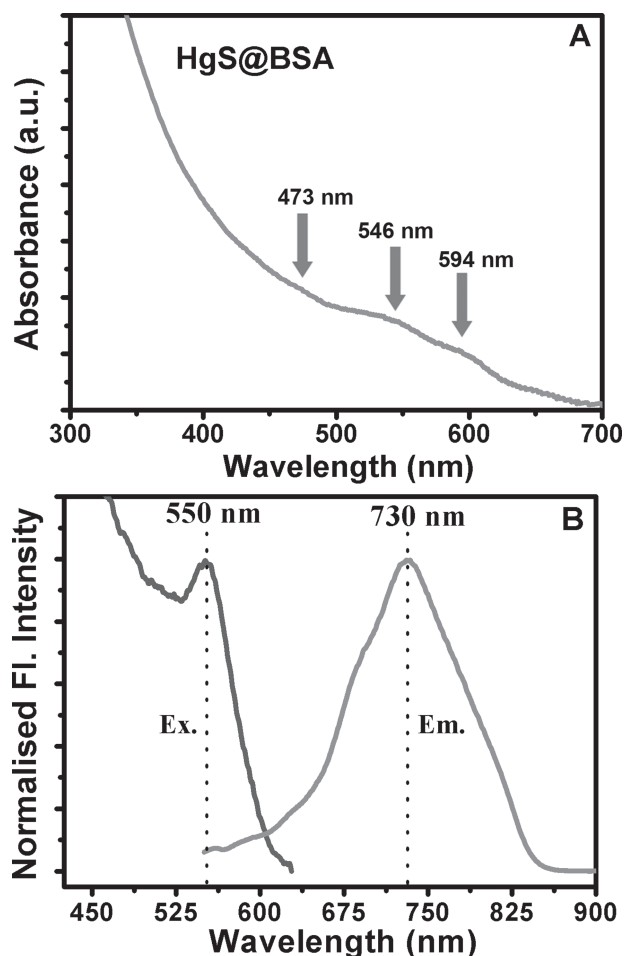


Figure 1. A) UV-Vis absorbance spectrum of HgS@BSA. B) Excitation and emission spectrum of HgS@BSA. Excitation spectrum is taken by monitoring at 730 nm. Luminescence spectrum is collected with 450 nm excitation.

features are marked with arrows. Three distinct excitonic absorption shoulders of the HgS QDs are found at 473 (2.62), 546 (2.27), and 594 nm (2.09 eV), which indicate the presence of differently sized QDs. The bandgaps calculated for UV features at 2.62, 2.27, and 2.09 eV are 2.02, 1.94 and 1.90 eV, respectively, which are very much blue-shifted from the average bandgap of bulk β -HgS (-0.2 to 0.5 eV)^[8] due to a high quantum confinement effect. Figure 1B shows the luminescence profile of the as-prepared QDs. A clear excitation maximum at 550 nm and a luminescence peak at around 730 nm is evident from Figure 1B. Note that, similar to the absorption spectrum, the luminescence spectrum is also broad and can be fitted into three different peaks having maxima at 680 (1.82), 733 (1.69), and 803 nm (1.54 eV) (Figure S1, Supporting Information (SI)). Photographs of QDs under

UV and visible radiations are shown in Scheme 1. As a control study, we have performed the reaction in the absence of Na_2S ; however, no such luminescent material is obtained even after 48 h (Figure S2, SI). This result reveals that external sulphur is required for the growth of QDs. It has to be noted that direct addition of mercury nitrate and Na_2S with protein solution leads to the formation of nonluminescent HgS nanomaterial, which provides evidence that the formation of the yellow intermediate is necessary to obtain the luminescent QDs (Figure S3, SI). The photoluminescence quantum yield of the HgS@BSA is ~4.6%, estimated using 4-(dicyanomethylene)-2-methyl-6-(*p*-dimethylaminostyryl)-4H-pyran (DCM) as a reference with a 450 nm excitation wavelength. The obtained HgS QDs are found to be very stable, showing the same luminescence spectra after almost seven days of being stored at room temperature (Figure S4, SI). The luminescence is maximum at neutral pH, however, relatively less stable in acidic and basic pH as shown in Figure S5 (SI). In order to investigate the thermal stability of the QDs, temperature-dependent luminescence of HgS@BSA has been monitored. It can be seen from Figure S6 (SI) that luminescence of the HgS@BSA in the aqueous solution decreased significantly upon increase in temperature. The reason may be the increase in hydrophilicity around the HgS QDs as protein is perturbed at higher temperature.

By varying the experimental conditions, e.g., Hg/S ratio, we achieved variations in the diameter of the QDs, resulting in the tunability of their luminescence (Figure 2A). As shown in Figure 2B, a variation of excitation peak maxima is clearly observed, pointing to the presence of QDs having different sizes. In the photoluminescence spectra the peak maxima varied from 680 to 800 nm, which corresponds to a QD diameter varying from 4 to 10 nm according to our dynamic light scattering (DLS) results (Figure 2C).

A high-resolution transmission electrom microscopy (HR-TEM) image confirmed the presence of nearly spherical

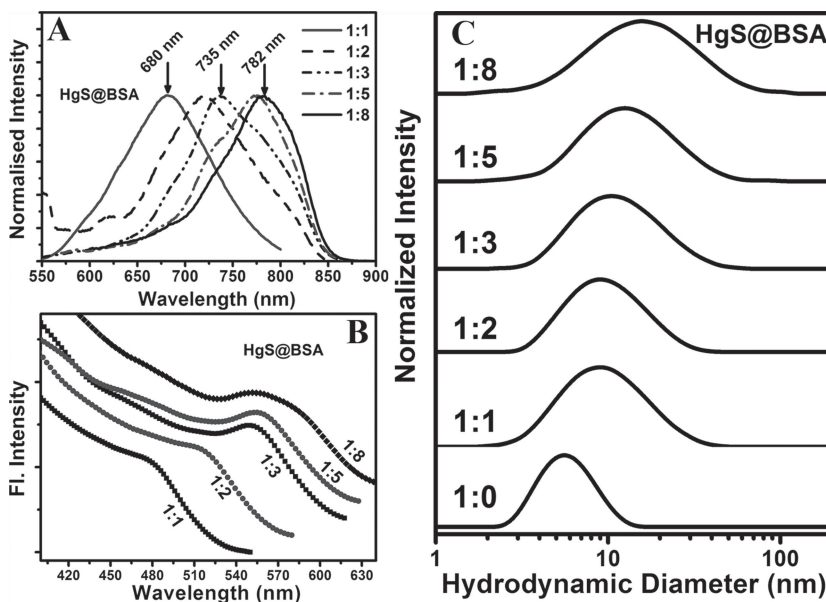


Figure 2. Normalized spectra. A) Luminescence, B) excitation, and C) dynamic light scattering spectra for HgS@BSA QDs with different Hg/S molar ratios.

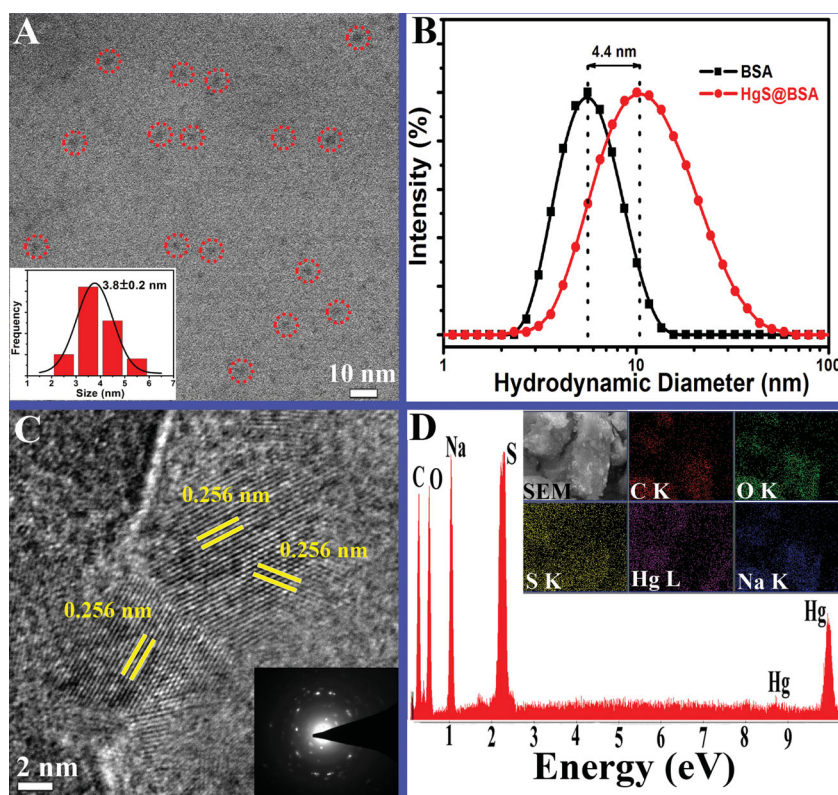


Figure 3. A) Typical TEM images of HgS QDs. The size distribution of HgS@BSA is shown in the inset. B) Dynamic light scattering spectra of BSA and HgS@BSA in aqueous solution at pH \sim 9. The swelling of the protein size by 4.4 nm has also been assigned. C) High-resolution TEM image of HgS QDs. SAED pattern in an area including HgS QDs is shown in the inset. D) EDX spectrum collected for HgS@BSA. Inset showing the SEM image of the HgS@BSA sample from which the EDX spectrum was taken. EDX maps obtained using the C K, O K, S K, Hg L, and Na K lines are also shown in the inset.

nanocrystals having a size of 3.8 ± 0.2 nm (Figure 3A). As shown in Figure 3B, the characteristic hydrodynamic diameter of BSA is shifted from $5.6(\pm 0.6)$ nm to $9.3(\pm 0.6)$ nm according to DLS after the formation of HgS QDs. This observation is consistent with the fact that QDs are formed within the protein matrix. Again, the size obtained from the TEM study is roughly comparable to the swelling of the protein size ($\sim 4.4 \pm 0.6$ nm), as revealed from our DLS measurements. The HR-TEM image of the HgS QDs is shown in Figure 3C. The distance between two adjacent planes is 0.29 nm, corresponding to the (200) lattice plane of cubic β -HgS (International Centre for Diffraction Data (ICDD), Reference no: 00-002-0453). The distinct fringe spacing and the corresponding selected-area electron diffraction (SAED) pattern (inset of Figure 3C) reveal the reasonably good crystallinity of the as-prepared HgS QDs. Moreover, the elemental composition of the HgS QDs is confirmed from X-ray diffraction (XRD) data (Figure S7, SI), energy dispersive X-ray analysis (EDX), and elemental mapping of the scanning electron microscopy (SEM) image. Figure 3D demonstrates the EDX spectrum of the HgS@BSA. SEM image of the HgS@BSA and EDX maps using the C K, O K, S K, Hg L, and Na K lines are shown in the inset of Figure 3D.

X-ray photoelectron spectroscopy (XPS) of the intermediate, HgO@BSA, and the final product, HgS@BSA, were

carried out to verify the oxidation state of Hg and the elemental composition. Survey spectra of HgO@BSA and HgS@BSA show the expected elements, C, N, O, S (from protein and QDs), and Hg (from QDs) (Figure S8, SI). The Hg 4f regions of the above samples are compared with the synthesized bulk HgO and HgS in Figure 4. The Hg 4f_{7/2} peaks of bulk HgO and HgS appeared at 100.6 and 100.1 eV, respectively, whereas in HgO@BSA and HgS@BSA, they are at 101.4 and 100.6 eV, respectively. These higher-energy peaks in the nanoparticles confirms the presence of mercury in +2 state in all the samples. The shift of the Hg 4f_{7/2} peak to a higher binding energy in both HgO@BSA and HgS@BSA samples indicate the functionalization of HgO and HgS by protein and the difference from the corresponding bulk systems. The presence of S 2p_{3/2} in bulk HgS, which results in peaks at 161.2 and 168.0 eV, is due to sulphide and partially oxidized species, such as sulphate, respectively (Figure S9A, SI). The formation of HgS in the protein sample was confirmed by the presence of S 2p_{3/2} around 161.2 eV (Figure S9B, trace b, SI). The presence of other sulphur species such as disulphides and sulphates (due to X-ray induced damage which is expected in protein samples)^[16] are observed in the HgO@BSA and HgS@BSA samples (S 2p_{3/2} peaks at 163.3 and 167.8 eV).

Raman spectroscopic measurements were performed on the HgS QDs formed and the reaction intermediate to elucidate the reaction mechanism. The spectra of bulk HgO, bulk HgS, HgO@BSA, HgS@BSA, and BSA are compared in Figure 5A. Bulk HgO has a main band centered at 334 cm^{-1} whereas the intermediate has a red-shifted feature at 330 cm^{-1} ; which originates from the oxygen interchain mode of the HgO with A_g symmetry.^[22] These features are highlighted using a dotted circle in Figure 5A. The Raman spectrum of the HgS QDs shows a slightly blue-shifted peak around 262 cm^{-1} , in comparison to bulk HgS which has a feature at 254 cm^{-1} (dashed circle) originating from a mode of A₁ symmetry.^[23] BSA has several Raman features corresponding to the detailed structure of the protein including the amide signatures as given in Table S1 (SI).^[24] It should be noted that several of these features are retained in the Raman spectra of the reaction intermediate and the QDs, confirming the formation of HgO and HgS, respectively, in the protein. In the case of HgO@BSA, the amide regions of the protein are more distorted (or several features could be merged) than in the case of HgS@BSA.

Fourier Transform infrared (FT-IR) spectroscopy has been one of the most common methods to investigate the structure of proteins by probing their functional group signatures. Amide I, II, and III bands provide information about

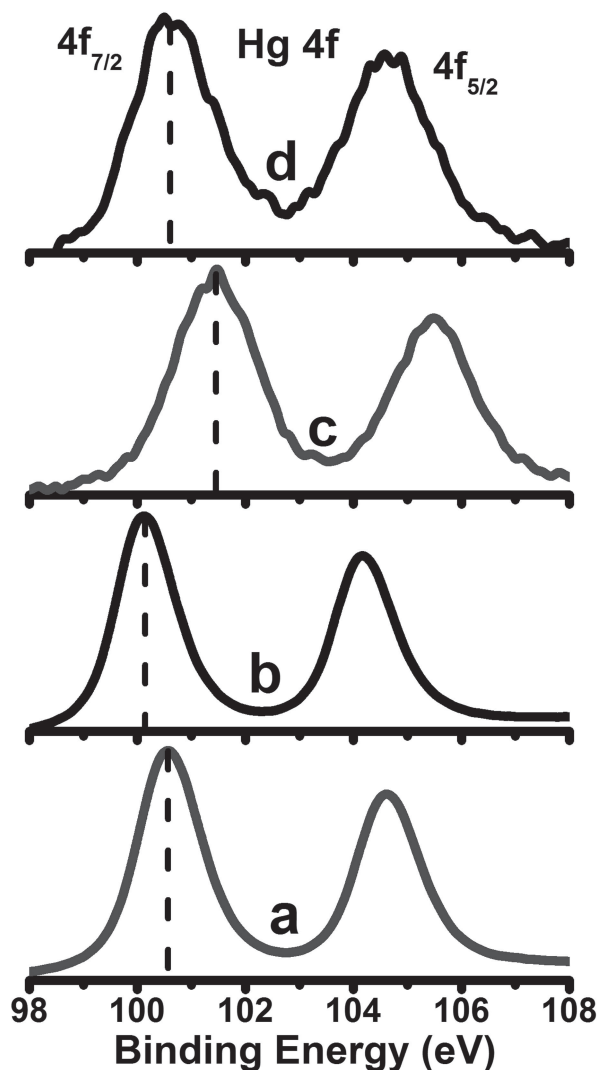


Figure 4. XPS spectra in the Hg 4f region of a) bulk HgO, b) bulk HgS, c) HgO@BSA, and d) HgS@BSA. The vertical dotted lines represent the Hg $4f_{7/2}$ binding energies.

the secondary structural changes in proteins.^[25–27] Solid-state IR analysis results suggested, in general, that the bands were broadened and shifted to a higher frequency, indicating perturbation of the secondary structure. Spectral regions within or near 1600–1690, 1480–1575, 1229–1301, and 3300 cm^{-1} have been assigned as amide I, amide II, amide III, and amide A, respectively (Figure 5B). The increase in the intensity and decrease in the peak width is seen around 1399 cm^{-1} , which is attributed to the C=O stretching of COO^- , suggests that the COO^- groups are more influenced by the formation of HgO and HgS or could be associated with the Hg in the protein matrix. Regions within 1651–1658, 1618–1642, 1666–1688, and 1650 \pm 1 cm^{-1} have been assigned as α -helix, β sheets, turns, and unordered structures, respectively.^[27] The band appearing around 700 cm^{-1} can be assigned to $-\text{NH}_2$ and $-\text{NH}$ wagging, and the band around 2960 cm^{-1} can be attributed to C–H vibrations. The band near 1400 cm^{-1} is due to the C=O stretching of COO^- , and that at 1468 cm^{-1} can be assigned as the C–H deformation of $>\text{CH}_2$, and that at 3500 cm^{-1} is

due to O–H stretching.^[25,27] In the second-derivative spectra, compared to native BSA, in HgO@BSA and HgS@BSA, the α -helix content decreased significantly as indicated by the prominent band at 1655 cm^{-1} disappearing, and the amount of β -turns increased as indicated by the 1662–1688 cm^{-1} region. In case of HgO@BSA, comparatively the β -turn content was higher than in native BSA and HgS@BSA, suggesting more perturbation in the intermediate form. A new band around 1651 cm^{-1} may be attributed to the increased in random coil structures. This observation is corroborated by observation made in Raman measurements.

Circular dichroism (CD) has been employed to study the conformational behavior of BSA before and after the formation of the HgS QDs. Native BSA displays CD features with minima at 208 and 222 nm, corresponding to the secondary structure of the protein (Figure 5C). Figure 5C shows the decrease of molar ellipticity in the presence of Hg(II), which describes more structural perturbation. From Figure 5C, it is also reflected that there is an insignificant perturbation of the secondary structure of the protein after the addition of Na_2S . The observation clearly signifies that addition of Na_2S has minimal effect on the secondary structure of the protein.

The optical responses of HgS QDs towards metal ions such as Hg(II), Ca(II), Cu(II), Co(II), Zn(II), Ni(II), Cd(II), Mg(II), Na(I), and K(I) have been investigated. Among these ions, only Cu(II) and Hg(II) can quench the luminescence of the as-prepared HgS QDs. **Figure 6** demonstrates the high optical selectivity and sensitivity of the QDs towards Cu(II) and Hg(II) over other biologically relevant metal ions, and can be seen with the naked eye (Figure 6, lower panel). The mechanism to be proposed below is due to the following reasons: A number of sulphur and Hg(II) (having $5d^{10}6s^0$ electronic configuration) are present on the surface of the HgS QDs. Addition of metal ions to the HgS QD solution therefore generates two possibilities: either it will interact with sulphur or with mercury. Moreover, sulphur has an affinity towards other metal ions including Hg(II), Cu(II), Zn(II), and Cd(II). Thus, if the quenching of the luminescence of QDs occurs through the interaction with sulphur, then all of the above mentioned metal ions are expected to reduce the luminescence of HgS@BSA. However, the almost insignificant changes in the QDs luminescence spectrum observed with Zn(II) and Cd(II) (Figure 6), clearly rules out the possibility of luminescence quenching through the interaction with sulphur. Recent theoretical studies suggest that metal centres with a d^{10} electronic configuration have a strong affinity towards other closed-shell metal ions with similar electronic configuration.^[28] In particular, this phenomenon associated with strong d^{10} – d^{10} interactions is known as metallophilic interaction.^[29] This interaction originates due to dispersive forces which are further augmented by relativistic effects.^[29] In the case of the mercury ion ($5d^{10}6s^0$), a number of examples of such interactions are present in the literature, even in the absence of protecting ligands.^[13,14,30] Our study suggests that luminescence quenching of HgS QDs in the presence of Hg(II) is due to the same $5d^{10}$ – $5d^{10}$ metallophilic interaction (**Scheme 2**). In the case of Cu(II), luminescence quenching could occur through the $5d^{10}$ – $3d^{10}$ metallophilic interaction

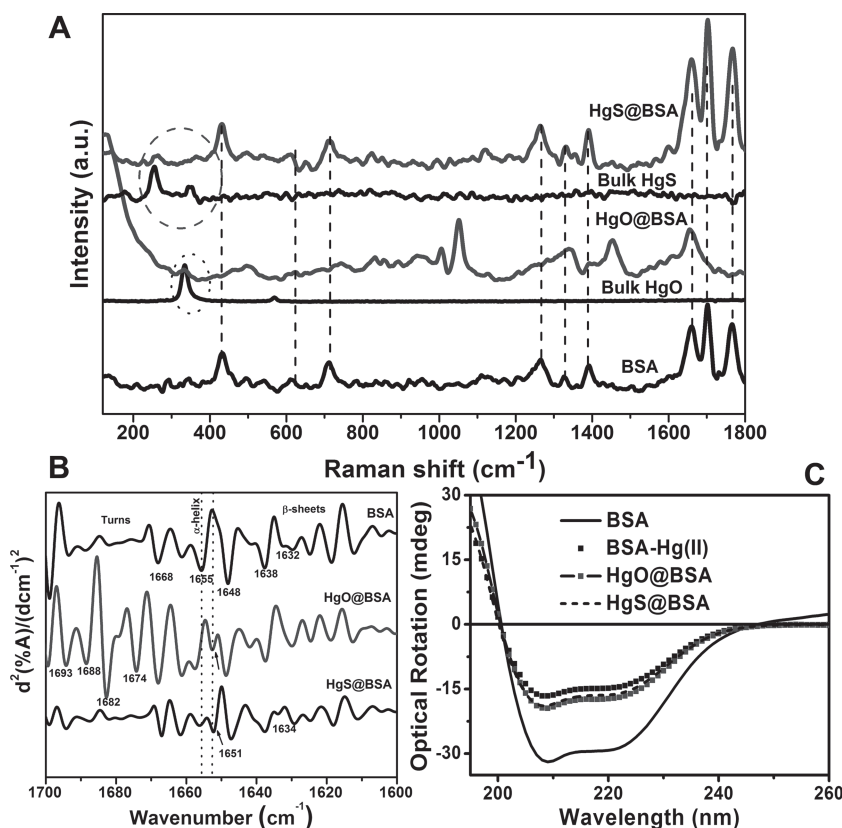


Figure 5. A) Raman spectra of BSA, bulk HgO, HgO@BSA, bulk HgS, and HgS@BSA in solid state collected using a 633 HeNe laser. The dotted marking highlights the presence of features due to A_g oxygen interchain mode in HgO and HgO@BSA as well. The dashed marking highlights the presence of HgS vibrations (A₁ mode of the sulfur atom in HgS) in the NIR-emitting HgQD, confirming the product to be HgS@BSA. B) Second-derivative spectra of amide I region of BSA, HgO@BSA, and HgS@BSA. C) Circular dichroism spectra of BSA, BSA-Hg(II) complex, HgO@BSA, and HgS@BSA.

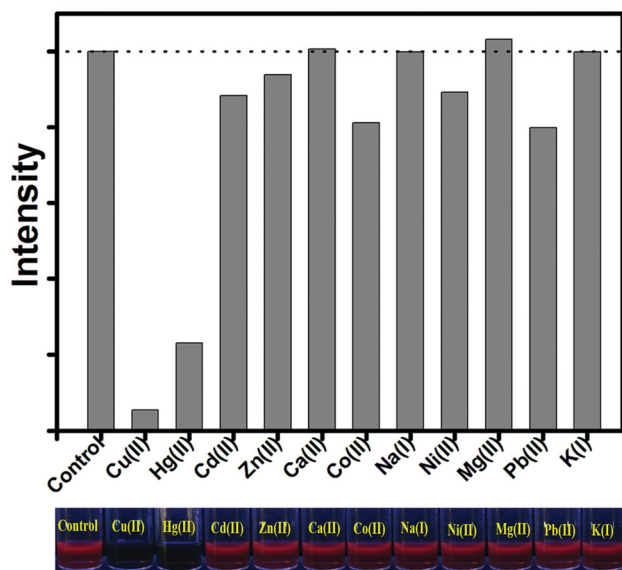
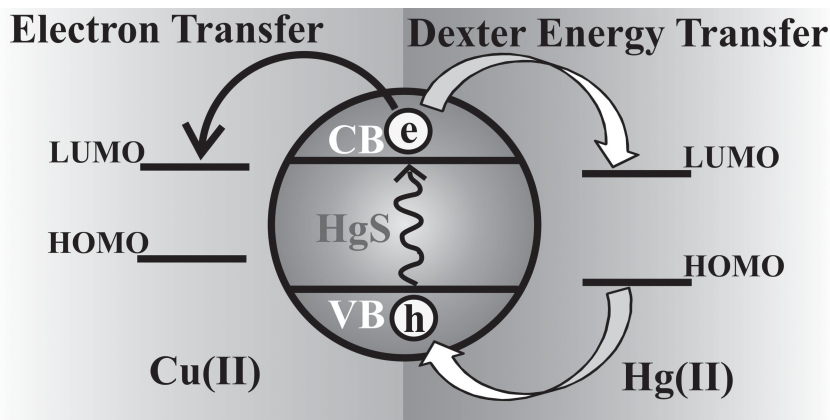


Figure 6. Upper panel: Selectivity of the HgS@BSA to different metal ions. The luminescence intensities are recorded at 730 nm. For all cases, the final metal ion concentrations are 50 ppm. Dotted line refers to see the change of luminescence with respect to the control one. Lower panel: Photographs of the HgS@BSA solution under UV light after addition of 50 ppm of various metal ions.

(Scheme 2) as in the protein environment Cu(II) is reduced to Cu(I).^[31] In order to evaluate the sensing efficiency of the HgS QDs, we have added different concentrations of Hg(II) and Cu(II) to a fixed concentration (2 mg/mL) of QD solution (see Figure S11, SI). As shown in Figure S11, the luminescence of HgS QDs is reduced as a result of increasing either metal ion concentration. In order to unravel the consequence of the metallophilic interaction, a series of systematic picosecond-resolved photoluminescence studies were performed. The shorter excited-state lifetime of the HgS/Hg(II) and HgS/Cu(II) with respect to that of the free HgS QDs are clearly noticeable from **Figure 7A,B**. Details of the fitting parameters of the time-resolved decays are tabulated in **Table 1**. As evidenced from our study, the nature of the quenching of the QD lifetime by metal ions is dynamic.

There are two possible types of dynamic quenching mechanisms through which a metal ion center can induce the nonradiative deactivation of QD luminescence: electron transfer or energy transfer. As far as the electron-transfer mechanism is concerned, it can occur between species in intimate contact. Energy transfer, which involves deactivation of an electronic excited state of the donor and concomitant formation of an excited state of the acceptor, can occur via through-space (Förster) or through-bond (Dexter) mechanisms.^[32] The Förster mechanism^[33] requires direct donor-acceptor spectral overlap and arises from the Coulombic interaction between the donor and acceptor electric fields. However, in case of HgS-Cu(II)/HgS-Hg(II), the probability of such energy transfer is usually negligible due to the lack of absorption of the unsupported metal ions (Cu and Hg). Dexter transfer^[34] is identical to the Förster mechanism but does not require significant oscillator strength on the part of the acceptor. It requires direct donor-acceptor orbital overlap; and has an exponential-distance dependence with a range of ~1 nm.

In the present study, both the possibilities, i.e., electron transfer or Dexter energy transfer can account for Hg(II) and Cu(II) inducing the lifetime quenching of the HgS QDs. To investigate the electron transfer dynamics from the HgS QDs upon excitation, we studied the complexation of the HgS QDs with an organic molecule, benzoquinone (BQ), which is well-known as an electron acceptor^[35] and efficiently accepts excited electrons from the surface of semiconductor quantum dots.^[36] As revealed from the inset of Figure 7B, in the presence of BQ a very sharp decay (monitored at 730 nm) is observed, which is associated with the transfer of excited electrons from the conduction band (CB) of the HgS QDs into the lowest unoccupied molecular orbital



Scheme 2. Schematic representation of the excited-state quenching mechanism for the Cu(II) and Hg(II) ion. HOMO and VB represents highest occupied molecular orbital and valence band, respectively.

(LUMO) of the BQ molecules. It can be seen from Table 1 that the HgS/BQ system exhibits an ultrafast time component of 55 ps with a majority (86%) of the excited electrons following this path. The similar faster decay component, i.e., 30 ps (82%) in the presence of Cu(II) as compared to HgS/BQ system at the same excitation of 409 nm may be indicative of favorable electron transfer from the HgS QDs to the Cu(II) rather than Dexter energy transfer. However, the possibility of such an energy transfer cannot be completely ruled out.

After the addition of Hg(II) solution to the HgS@BSA, although the decay is faster compared to the HgS@BSA, no such ultrafast time constant with a majority like HgS/BQ system was found, which reveals the electron transfer is not associated with this process. Assuming the formation of a

Hg(II)–Hg(II) metallophilic bond, the filled $5d_z^2$ and empty $6s$ orbital of each Hg(II) would overlap with each other,^[37] which then give rise to bonding and anti-bonding orbitals.^[38] Reorganization of these orbitals would therefore lead to new energy-accepting levels on the Hg(II), which provides the basis of a double electron exchange process (Dexter). We have also estimated the rate of energy transfer (k_{ET}) and energy transfer efficiency (E) by using the following equations:

$$k_{ET} = 1/\tau_q - 1/\tau_u \quad (1)$$

$$E = 1 - \tau_q/\tau_u \quad (2)$$

where τ_q is the “quenched” lifetime, here 1.5 ns; and τ_u is the “unquenched” lifetime, here 5 ns. From our time-resolved study, the rate of energy transfer (k_{ET}) and energy transfer efficiency (E) are found to be $4.7 \times 10^8 \text{ s}^{-1}$ and 72%, respectively.

Additionally, we performed DLS study to determine the effect of aggregation on the luminescence of as-prepared HgS@BSA. As shown in Figure S12 (SI), the addition of Hg(II) to the HgS@BSA solution has an insignificant effect

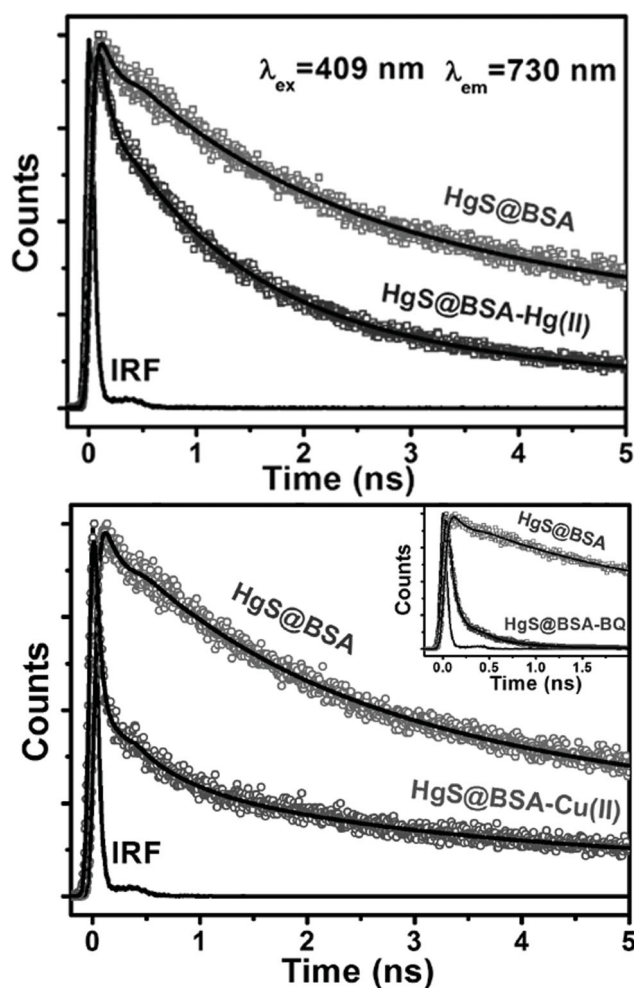


Figure 7. A) The picosecond time-resolved fluorescence transients of HgS QDs, in the absence and in the presence of acceptor Hg(II). B) The picosecond time-resolved fluorescence transients of HgS QDs, in the absence and in the presence of acceptor Cu(II). Inset showing the analogous data of HgS QDs, in the absence and in the presence of benzoquinone.

Table 1. Picosecond time-resolved luminescence transients of HgS@BSA in the absence and presence of Hg(II) and Cu(II). Lifetime values of the HgS@BSA system in presence of the well-known electron accepting agent, benzoquinone, is also shown. The luminescence of HgS QDs (maximum wavelength, $\lambda_{max} = 730 \text{ nm}$) was detected with a 409 nm excitation laser. Numbers in parentheses indicate relative weightage.

System	τ_1 [ps]	τ_2 [ps]	τ_3 [ns]	τ_4 [ns]	τ_{av} [ns]
HgS@BSA	-	120(0.23)	1.8(0.40)	12.5(0.36)	5.2
HgS@BSA_Hg(II)	-	105(0.43)	1.2(0.42)	6.5(0.15)	1.5
HgS@BSA_Cu(II)	30(0.82)	430(0.07)	2.5(0.07)	17.0(0.04)	1.0
HgS@BSA_BQ	55(0.86)	320(0.12)	1.2(0.02)	-	0.1

on the size of HgS QDs, which rules out the possibility of luminescence quenching due to QDs aggregation.^[16] In the case of HgS@BSA solution containing Cu(II), the DLS peak at ~9 nm remains unaltered; however, a new peak around 150 nm appeared which is consistent with the aggregation of the free protein in solution.^[16] To further confirm the aggregation effect by Cu(II) and Hg(II), a control experiment was carried out with ethylenediaminetetraacetate (EDTA). EDTA can chelate both the metal ions in a 1:1 ratio and Cu(II) has more affinity towards EDTA than BSA.^[39] If the metal ion induces the aggregation of the HgS@BSA, then, in the presence of EDTA, the metal ion would be chelated and should result in the recovery of its luminescence. However, no such recovery effect was observed even in a 1:2 (metal ion):EDTA ratio (data not shown), which further corroborates the direct interaction between the QDs with Cu(II) and Hg(II) ions. Attempts were also made to separate the metal ions from the protein-capped QDs by extensive dialysis against Milli-Q water. However, no evidence of the dissociation of the metal ions resulting the recovery of the QD luminescence was observed.

3. Conclusion

We have developed a simple straightforward bio-mineralization process for the synthesis of HgS QDs using a model protein, BSA. These QDs are extremely stable, luminescent-tunable from 685–800 nm, and highly quantum efficient. The luminescence of as-prepared QDs can be used for a highly sensitive and selective sensing system for the detection of Hg(II) and Cu(II). The sensing mechanism is demonstrated to be based on the formation of a metallophilic bond between Hg(II)/Cu(II) and Hg(II) present on the surface of the HgS QDs. In the excited state, the metallophilic bond facilitates the Dexter energy transfer to the Hg(II) and electron transfer to the Cu(II) over other processes associated with dynamic quenching. The synthetic approach and the metal-ion sensing with the proper mechanism described herein may be extended to other types of protein–semiconductor conjugates with tailored properties for diverse applications.

4. Experimental Section

Materials: BSA, sodium sulphide, HgNO₃ as well as the nitrates and chlorides of various metal ions were obtained from Sigma. The electron-accepting BQ was obtained from Alfa-Aesar. Milli-Q (from Millipore) water was used throughout the experiments. All the chemicals were used as received without further purification.

Synthesis of Protein-Stabilized HgS QDs: It involves two steps. In the first step, the nonluminescent HgO nanoparticles were prepared in a vial by dissolving 5 mL of 5 mM HgNO₃, H₂O, and 5 mL BSA (15 mg/mL) solution in MQ water under vigorous stirring with final pH value of ~9 (adjusted by 1 M NaOH solution carefully). Then, the solution was allowed to stir for 8–12 h. The final color of the solution was pale yellow, indicative to the formation of HgO@BSA nano-bioconjugates. In the second step, 4 mL of 20 mM Na₂S was added to 10 mL of as-synthesised HgO@BSA nano-bioconjugates, and

the solution was stirred for 15 min. Completion of the reaction was observed visibly by color changes from pale yellow to light brown. Such a color transition is indicative of the formation of HgS QDs.

Synthesis of Bulk HgO: Bulk HgO samples were prepared in a vial by dissolving 5 mL of 50 mM HgNO₃, H₂O, and 1 mL of 2.5 M NaOH solution. Then, the solution was allowed to stir for 15 min to obtain the yellow precipitate of HgO. Subsequently, the precipitate was centrifuged and washed with additional MQ water several times before measurements.

Synthesis of Bulk HgS: About 70 mg of HgNO₃, H₂O, and 70 mg Na₂S powder were dissolved in 5 mL MQ water under vigorous stirring. The reaction mixture was stirred for 30 min. The resulting precipitate was collected and repeatedly washed with MQ water by centrifugal precipitation. Finally, the bulk HgS precipitate was dried in an incubator to obtain a dark brown powder.

UV–Vis Absorption Spectroscopy: Optical absorption spectra of the solutions were measured with a Shimadzu spectrophotometer using a quartz cuvette of 1 cm path length. The experimentally obtained spectral data, $I(w)$, which are functions of wavelength, were converted to energy-dependent data, $I(E)$, according to the following relation,

$$I(E) = I(w) / (\delta E / \delta w) \propto I(w) \times w^4 \quad (3)$$

where $\delta E / \delta w$ represents the Jacobian factor.

Photoluminescence (PL) Spectroscopy: The PL spectra were recorded on a Jobin Yvon Fluoromax-3 fluorometer.

DLS: DLS measurements were performed with Nano S Malvern instrument employing a 4 mW He-Ne laser ($\lambda = 632.8$ nm) equipped with a thermostated sample chamber. All the scattered photons are collected at 173° scattering angle. The scattering intensity data are processed using the instrumental software to obtain the hydrodynamic diameter (d_H) and the size distribution of the scatterer in each sample. The instrument measures the time-dependent fluctuation in the intensity of light scattered from the particles in solution at a fixed scattering angle. d_H of the proteins is estimated from the intensity autocorrelation function of the time-dependent fluctuation in intensity. d_H is defined as:

$$d_H = \frac{k_b T}{3\pi\eta D} \quad (4)$$

where k_b is the Boltzmann constant, T is the temperature, η is the viscosity, and D is the translational diffusion coefficient. In a typical size distribution graph from the DLS measurement, the X-axis shows a distribution of size classes in nanometers, while the Y-axis shows the relative intensity of the scattered light.

XPS: XPS measurements were conducted using an Omicron ESCA Probe spectrometer with unmonochromatized Al K α X-rays (energy = 1486.6 eV). The X-ray power applied was 300 W. The pass energy was 50 eV for survey scans and 20 eV for specific regions. The base pressure of the instrument was 2.2×10^{-10} mB. The binding energy was calibrated with respect to the adventitious C 1s feature at 285.0 eV.

Raman Spectroscopy: Raman spectroscopic investigations were carried out using a confocal Raman microscope (CRM α 300 S) purchased from WITec GmbH, Germany. The spectral acquisition was done in a back scattered geometry using a dispersion grating of 600 grooves/mm. Detector was a peltier cooled charge coupled device which was maintained at -60 °C. The QDs were excited

with a HeNe 633 nm laser source. Each spectrum is an average of 100 hardware spectra, each of which is integrated over 1 s. Raman spectra were measured for BSA, HgO@BSA, and HgS@BSA in solid state, obtained after lyophilizing the corresponding solutions.

TEM: TEM images were taken using a FEI TecnaiTF-20 field-emission high-resolution transmission electron microscope operating at 200 kV. Samples for TEM imaging were prepared by placing a drop of as-prepared QDs solution on a carbon-coated Cu grid, and the solvent was evaporated under a bulb.

SEM: SEM images were taken using a FEG-SEM (FEI, Helios 600) operated at 20 kV.

Time-Correlated Single-Photon Counting: Picosecond-resolved fluorescence decay transients were measured by using a commercially available spectrophotometer (Life Spec-ps, Edinburgh Instruments, UK) with 60 ps instrument response function (IRF). The observed fluorescence transients were fitted using a nonlinear least-square fitting procedure to a function $X(t) = \int_0^t E(t')R(t-t')dt'$ comprising convolution of the IRF $E(t)$ with a sum of exponential $R(t) = A + \sum_{i=1}^N B_i e^{-t/\tau_i}$ with pre-exponential factors (B_i), characteristic lifetimes (τ_i) and a background (A). Relative concentration in a multiexponential decay was finally expressed as: $c_n = \frac{B_n}{\sum_{i=1}^N B_i} \times 100$. The quality of the curve fitting was evaluated by reduced chi-square and residual data. It has to be noted that with our time-resolved instrument, we can resolve at least one-fourth of the instrument response time constants after the de-convolution of the IRF.

CD Spectroscopy: The CD spectra were measured in a Jasco 815 spectropolarimeter with a Peltier setup for the temperature-dependent measurements. The cell path length was 10 mm.

FT-IR Spectroscopy: FT-IR spectra were measured with a Perkin Elmer Spectrum One instrument. KBr crystals were used as the matrix for sample preparation. Powder samples of BSA, HgO@BSA, and HgS@BSA (which were collected after lyophilization) were measured.

Quantum Yield Calculations: The quantum yield was calculated according to the following equation:^[40]

$$Q = Q_R \left(\frac{I}{I_R} \right) \left(\frac{OD_R}{OD} \right) \left(\frac{n^2}{n_R^2} \right) \quad (5)$$

where Q and Q_R are the quantum yield of the protein and reference (DCM in methanol), I and I_R are the integrated fluorescence intensities of the protein and reference, OD and OD_R are the optical densities of the protein and reference at the excitation wavelength, and n and n_R are the refractive indices of the protein and reference solutions. The absolute quantum yield of DCM in methanol^[41] was taken to be 0.43.

Supporting Information

Supporting Information is available from the Wiley Online Library or from the author.

Acknowledgements

N.G. and S.K. thank CSIR, India, for fellowships. A.G. thanks UGC, India, for a fellowship. We thank DST for a financial grant (SR/SO/

BB-15/2007). Equipment support to T.P. was provided by the Nano Mission of DST, Government of India.

- [1] I. L. Medintz, M. H. Stewart, S. A. Trammell, K. Susumu, J. B. Delehanty, B. C. Mei, J. S. Melinger, J. B. Blanco-Canosa, P. E. Dawson, H. Mattoussi, *Nat. Mater.* **2010**, *9*, 676.
- [2] L. Wu, B. Quan, Y. Liu, R. Song, Z. Tang, *ACS Nano* **2011**, *5*, 2224.
- [3] M. K. So, C. J. Xu, A. M. Loening, S. S. Gambhir, J. H. Rao, *Nat. Biotechnol.* **2006**, *24*, 339.
- [4] P. Yang, Y. Zhao, Y. Lu, Q. Z. Xu, X. W. Xu, L. Dong, S. H. Yu, *ACS Nano* **2011**, *5*, 2147.
- [5] M. F. Frasco, N. Chaniotakis, *Sensors* **2009**, *9*, 7266.
- [6] M. Razeghi, Y. Wei, A. Gin, G. J. Brown, *Mater. Res. Soc. Symp. Proc.* **2002**, *692*, 99.
- [7] S. Keuleyan, E. Lhuillier, P. Guyot-Sionnest, *J. Am. Chem. Soc.* **2011**, *133*, 16422.
- [8] W. Wichiansee, M. N. Nordin, M. Green, R. J. Curry, *J. Mater. Chem.* **2011**, *21*, 7331.
- [9] K. A. Higginson, M. Kuno, J. Bonevich, S. B. Qadri, M. Yousuf, H. Mattoussi, *J. Phys. Chem. B* **2002**, *106*, 9982.
- [10] Y. G. Yang, H. G. Liu, L. J. Chen, K. C. Chen, H. P. Ding, J. Hao, *Langmuir* **2010**, *26*, 14879.
- [11] T. Ren, S. Xu, W. B. Zhao, J. J. Zhu, *J. Photochem. Photobiol. A* **2005**, *173*, 93.
- [12] A. Mathew, P. R. Sajanlal, T. Pradeep, *J. Mater. Chem.* **2011**, *21*, 11205.
- [13] J. P. Xie, Y. G. Zheng, J. Y. Ying, *Chem. Commun.* **2010**, *46*, 961.
- [14] C. L. Guo, J. Irudayaraj, *Anal. Chem.* **2011**, *83*, 2883.
- [15] S. S. Narayanan, S. K. Pal, *J. Phys. Chem. C* **2008**, *112*, 4874.
- [16] N. Goswami, A. Giri, M. S. Bootharaju, P. L. Xavier, T. Pradeep, S. K. Pal, *Anal. Chem.* **2011**, *83*, 9676.
- [17] A. V. Singh, B. M. Bandgar, M. Kasture, B. L. V. Prasad, M. Sastry, *J. Mater. Chem.* **2005**, *15*, 5115.
- [18] P. L. Xavier, K. Chaudhari, A. Bakshi, T. Pradeep, *Nano Reviews* **2012**, *3*, 14767.
- [19] W. Zhou, F. Baneyx, *ACS Nano* **2011**, *5*, 8013.
- [20] Y. Long, D. Jiang, X. Zhu, J. Wang, F. Zhou, *Anal. Chem.* **2009**, *81*, 2652.
- [21] B. B. Campos, M. Algarra, B. Alonso, C. M. Casado, J. C. G. Esteves da Silva, *Analyst* **2009**, *134*, 2447.
- [22] T. Zhou, U. Schwarz, M. Hanfland, Z. X. Liu, K. Syassen, M. Cardona, *Phys. Status Solidi b* **1996**, *198*, 411.
- [23] S. V. Gotoshia, L. V. Gotoshia, *J. Phys. D: Appl. Phys.* **2008**, *41*, 115406.
- [24] B. A. Bolton, J. R. Scherer, *J. Phys. Chem.* **1989**, *93*, 7635.
- [25] A. Dong, P. Huang, W. S. Caughey, *Biochemistry* **1990**, *29*, 3303.
- [26] P. L. Xavier, K. Chaudhari, P. K. Verma, S. K. Pal, T. Pradeep, *Nano-scale* **2010**, *2*, 2769.
- [27] L. Shang, Y. Wang, J. Jiang, S. Dong, *Langmuir* **2007**, *23*, 2714.
- [28] P. Pyykko, *Angew. Chem. Int. Ed.* **2004**, *43*, 4412.
- [29] S. Sculfort, P. Braunstein, *Chem. Soc. Rev.* **2011**, *40*, 2741.
- [30] M. Kim, T. J. Taylor, F. P. Gabbai, *J. Am. Chem. Soc.* **2008**, *130*, 6332.
- [31] K. J. Wiechelmann, R. D. Braun, J. D. Fitzpatrick, *Anal. Biochem.* **1988**, *175*, 231.
- [32] G. D. Scholes, K. P. Ghiggino, A. M. Oliver, M. N. Paddonrow, *J. Am. Chem. Soc.* **1993**, *115*, 4345.
- [33] T. Forster, *Discuss. Faraday Soc.* **1959**, *27*, 7.
- [34] D. L. Dexter, *J. Chem. Phys.* **1953**, *21*, 836.
- [35] N. Goswami, A. Makhal, S. K. Pal, *J. Phys. Chem. B* **2010**, *114*, 15236.
- [36] C. Burda, T. C. Green, S. Link, M. A. El-Sayed, *J. Phys. Chem. B* **1999**, *103*, 1783.

- [37] A. Gorling, N. Rosch, D. E. Ellis, H. Schmidbaur, *Inorg. Chem.* **1991**, *30*, 3986.
- [38] C.-K. Li, X.-X. Lu, K. M.-C. Wong, C.-L. Chan, N. Zhu, V. W.-W. Yam, *Inorg. Chem.* **2004**, *43*, 7421.
- [39] M. A. H. Muhammed, P. K. Verma, S. K. Pal, A. Retnakumari, M. Koyakutty, S. Nair, T. Pradeep, *Chem. Eur. J.* **2010**, *16*, 10103.
- [40] J. Chen, S. L. Flaugh, P. R. Callis, J. King, *Biochemistry* **2006**, *45*, 11552.
- [41] H. Du, R.-C. A. Fuh, J. Li, L. A. Corkan, J. S. Lindsey, *Photochem. Photobiol.* **1998**, *68*, 141.

Received: April 7, 2012
Revised: June 13, 2012
Published online:

Selective Visual Detection of TNT at the Sub-Zeptomole Level**

Ammu Mathew, P. R. Sajanlal, and Thalappil Pradeep*

Dedicated to Professor P. T. Manoharan on the occasion of his 77th birthday

Realizing the limits of sensitivity, while maintaining selectivity, is an ongoing quest. Among the multitude of requirements, national security, early detection of diseases, safety of public utilities, and radiation prevention are some of the areas in need of ultralow detection.^[1] Structural, functional, and electronic features of nanomaterials are used to develop reliable analytical methods.^[2] Several kinds of surface-enhanced spectroscopy, surface-enhanced Raman in particular, can be used for such applications;^[3] the technique may be further enhanced by spatially separating the analyte and the active plasmonic nanostructure with an insulator, a method known as shell-isolated nanoparticle-enhanced Raman spectroscopy (SHINERS).^[4] Creating uniform anisotropic structures with nanoscale attributes by simple solution chemistry and combining analyte-selective chemistry on such surfaces enables ultrasensitive and selective detection methods.^[5] Noble metal quantum clusters (QCs),^[6] a new family of atomically precise nanomolecules with intense luminescence, along with their protein protected analogues,^[6c] are highly sensitive and selective for specific analytes.^[7] Anchoring such QCs on mesoscale (100 nm to a few μm) particles leads to surface-enhancement of their luminescence^[7c] and can create a new platform for ultrasensitive detection, especially when combined with the use of optical microscopy. Gold mesoflowers (MFs) are anisotropic materials with unique five-fold symmetric stems^[8] containing surface-enhancing nanoscale features. An entire MF is only a few micrometers in size, and its distinct shape allows for unique identification by optical microscopy; thus, changes in the properties of an MF can be used for the immediate and efficient detection of analytes. Herein, we demonstrate the selective detection of 2,4,6-trinitrotoluene (TNT) at the sub-zeptomole level (10^{-21} moles) through a combination of these strategies on a mesostructure.

Our method involves anchoring silver clusters,^[9] which are comprised of fifteen atoms and embedded in bovine serum albumin (BSA), on silica-coated Au MFs, termed

$\text{Au@SiO}_2\text{@Ag}_{15}$ MFs, and using this system for analyte detection. Syntheses of the various components are described in the experimental section. The Au@SiO_2 MFs have a tip-to-tip length of ca. 4 μm (Supporting Information, Figure S1 a). The BSA-protected silver cluster (Ag_{15}), is a red luminescent water-soluble QC prepared by a previously reported procedure (see Figure S2 for essential characterization data).^[9] Apart from a high quantum yield (10.7%) in water, it is stable over a wide pH range and exhibits emission in the solid state. We exposed varying concentrations of TNT to $\text{Au@SiO}_2\text{@Ag}_{15}$ MFs and found that even a concentration of less than one zeptomole of TNT per mesoflower quenches the luminescence of the composite mesoflowers within 1 min. The simultaneous disappearance of the luminescence of Ag_{15} on the MF and the appearance of the luminescence of another embedded fluorophore allows for easy identification of the analyte. Characterization data for the various composite MFs used in this study are presented in the Supporting Information.

The hybrid structures, $\text{Au@SiO}_2\text{@Ag}_{15}$ MFs, with unique structural attributes are observable under an optical microscope (see Figure S3 for a schematic of the setup used). Dark field microscopic images of these MFs show their well-defined features; they are star-shaped in a two dimensional projection (Figure 1 A). The fluorescence image of the same MF (ca. 490 nm excitation, emitted light was passed through a triple-pass filter and imaged) shows a characteristic red emission owing to the QCs anchored on its surface (Figure 1 A). Unlike with other spherical single particle sensors, which are difficult to locate and distinguish by light-based microscopy, the well-defined shapes of the MFs ensure that the desired particles alone are analyzed. Furthermore, the analyte adsorption capacity of the MFs is enhanced by the thin inert layer of silica employed as a base. Au core/silica shell structures of this type can provide enhanced fluorescence and Raman scattering. The better stability of the QCs on the silica layer, along with a reduction in the luminescence quenching of the QCs on the MF surface and ease of functionalization are among the added advantages of this material (see the Supporting Information).

Exposure of the $\text{Au@SiO}_2\text{@Ag}_{15}$ MFs to TNT (2.5 μL) at a concentration of one part per trillion (ppt) decreases the luminescence intensity slightly without affecting the optical image (Figure 1 B), whereas at one part per billion (ppb) of TNT the luminescence feature disappears completely (Figure 1 C; note that the MFs shown in Figure 1 A–C are different in each case). For spectral intensity data collected from the surface of these MFs, see the Supporting Information, Figure S4. The quenching of cluster luminescence is due to the formation of a Meisenheimer complex^[5c,11] by the

[*] A. Mathew, Dr. P. R. Sajanlal,^[†] Prof. T. Pradeep
DST Unit of Nanoscience (DST UNS), Department of Chemistry,
Indian Institute of Technology Madras
Chennai 600036 (India)
E-mail: pradeep@iitm.ac.in

[†] Current address: Laser Dynamics Laboratory, School of Chemistry
and Biochemistry, Georgia Institute of Technology
Atlanta, GA 30332-0400 (USA)

[**] We thank the Department of Science and Technology, Government
of India for constantly supporting our research program on
nanomaterials. A.M. thanks CSIR for a research fellowship.

Supporting information for this article is available on the WWW
under <http://dx.doi.org/10.1002/anie.201203810>.

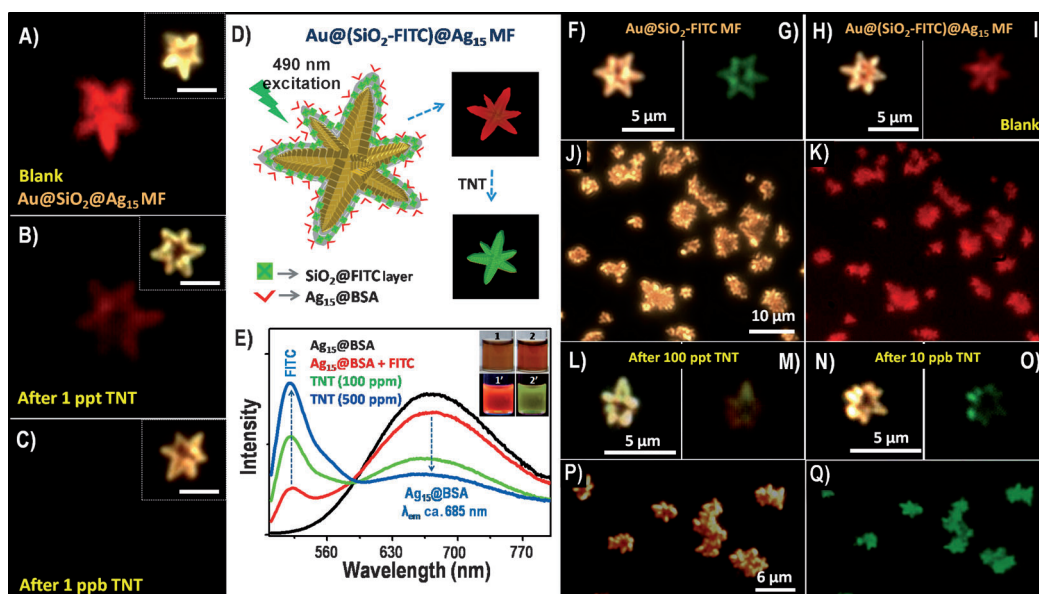


Figure 1. A–C) Fluorescence images (ca. 490 nm excitation) of Au@SiO₂@Ag₁₅ MFs taken using a dark field fluorescence microscope. Insets show the optical images corresponding to the fluorescence images; scale bars are 3 μm. Conditions under which the images are taken are specified on the figures, see the Experimental Section for details. D) Illustration of the sensor and the TNT detection approach; insets depict the sensing particle before (red) and after exposure to TNT (green). E) Effect on the emission spectra of the bare cluster upon mixing with FITC dye and subsequent exposure to TNT solutions of varying concentrations; inset shows photographs of a solution containing a mixture of FITC dye and Ag₁₅ clusters before and after TNT addition, taken under visible (1 and 2) and UV light (1' and 2'), respectively. The cluster emission (red) and FITC emission (green) are clearly observable. F–I and L–O) Optical and fluorescence images of Au@SiO₂-FITC MFs before (F,G) and after (H,I) cluster functionalization, as well as after exposure to TNT at concentrations of 100 ppt (L,M) and 10 ppb (N,O). J,K,P,Q) Large-area optical (J,P) and fluorescence (K,Q) images before (J,K) and after (P,Q) 10 ppb TNT exposure, respectively.

chemical interaction between TNT and the free amino groups in BSA. The solution turned dark red and the formation of the complex was confirmed by the emergence of features at 340, 450, and 525 nm in the UV absorption spectra (Figure S5). The specificity of the Meisenheimer complexation makes the cluster selective for TNT; closely related molecules, such as 2,4-dinitrotoluene (2,4-DNT), cyclotrimethylenetrinitramine (RDX), and 4-nitrotoluene do not quench its luminescence at this concentration (Figures S4 and S5). Note that no change in absorption features was observable when the concentration of TNT was < 10 ppm in bulk solution phase measurements (Figure S5), thus indicating the limit of TNT detection by Ag₁₅ clusters in solution. However, at the single particle level a spectral change occurred even at 1 ppt, as shown in the inset in Figure S4A. Luminescence spectra at identical concentrations (100 parts per million (ppm)) both in the solution phase and at the single particle level are compared in Figure S4B. Although the presence of tryptophan in BSA gives it an intrinsic blue fluorescence with excitation and emission maxima at 295 and 332 nm, respectively, it showed only a slight quenching in presence of TNT (Figure S4C). This poor response of the tryptophan fluorescence to the interaction of the protein with TNT may be due to the distance between the former and the free amine groups in the same protein subdomain. In the case of Ag₁₅, drastic quenching in the cluster luminescence was observed. This may either be attributed to the anionic σ complex formed and the subsequent sensitivity of the cluster to its immediate environment,

or as a result of the fluorescence resonance energy transfer between the cluster core and the protein.

For ease of visual detection, a change in the luminescence color in the presence of an analyte is a more desirable indicator than the disappearance/quenching of luminescence. Therefore, a TNT-insensitive fluorophore with the same excitation energy, but with a different emission wavelength, was pre-coated on the Au@SiO₂ MFs prior to cluster functionalization. An illustration of the procedure and the detection approach is shown in Figure 1D. We used fluorescein isothiocyanate (FITC) as the dye, which resulted in a bright green emission from the Au@SiO₂-FITC MFs (Figure 1G). The fluorescence spectrum collected from such a single particle is shown in Figure S4D. The emission observed around 540 nm clearly indicates the adsorption of FITC onto the Au@SiO₂ MFs. After further functionalization with Ag QCs, the Au@(SiO₂-FITC)@Ag₁₅ MFs showed a red emission (Figure 1I) wherein the FITC emission is suppressed. Upon exposure to 10 ppb TNT, a green emission from the underlying FITC was observed (Figure 1O), as the red luminescence from the cluster had been completely quenched. Even at 100 ppt, an observable color change was evident (Figure 1M). Large area images of the MFs before (Figure 1J and K) and after TNT exposure (Figure 1P and Q) confirm that the change occurs uniformly on all MFs. This uniformity is important in the development of a reliable method. The observation of green luminescence is in agreement with the solution phase data, wherein the disappearance

of cluster emission and the emergence of FITC emission are observed upon TNT exposure (Figure 1E).

Combining several analytical methods at the single particle level makes the detection more foolproof. Owing to their highly anisotropic nature, MFs can act as highly sensitive probes for surface-enhanced Raman spectroscopy (SERS). Bimetallic Ag-coated Au MFs (Au/Ag MFs)^[12] are yet another type of MF (see the Experimental Section for synthetic details), which allow for ultrasensitive Raman detection, as compared to bare MFs. When coated directly on Au/Ag MFs, Ag QCs result in unique metal-enhanced luminescence^[13] (Figures S3a and S6). Upon exposure to TNT, luminescence from the QCs on the MFs are lost and the Raman features from TNT (at 1209, 1361, 1535, 1619 and 2960 cm^{-1}) are detectable on the particle at 633 nm excitation. The gradual evolution of the Raman features of TNT as the concentration of TNT increases is shown in Figure 2A. The appearance of specific TNT features (Figure S7) ensures that

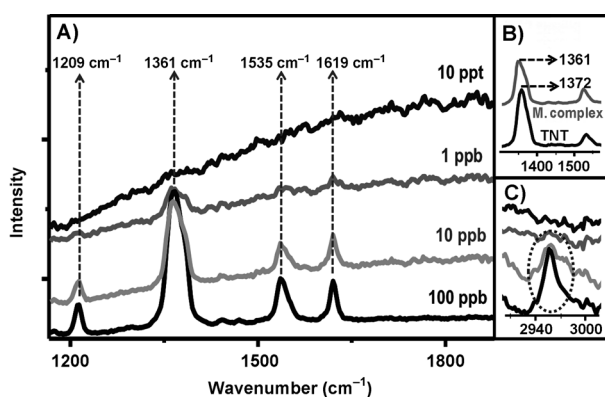


Figure 2. A) Raman spectra showing the gradual evolution of TNT features as the concentration of TNT added to Au/Ag@Ag₁₅ MFs increases. B) Comparison of the symmetric and asymmetric NO₂ stretching bands in the SERS spectra of TNT before (black) and after Meisenheimer complex formation (gray). C) The gradual appearance of a Raman band at 2960 cm^{-1} .

the observed changes are exclusively due to this analyte. Such changes were not observable with other analytes (Figure S7). The Meisenheimer complex formation was confirmed by comparing the SERS spectra of TNT before and after complexation (Figure 2B). After complexation, the symmetric and asymmetric stretching bands of the NO₂ group, observed in TNT at 1372 and 1545 cm^{-1} , respectively, were shifted to 1361 and 1535 cm^{-1} , respectively. This marked decrease in the vibrational frequencies can be attributed to electron delocalization in the ring and a post-complexation reduction in symmetry. The emergence of a peak at 2960 cm^{-1} (Figure 2C) may also be attributed to the Meisenheimer complex formed (NH₂ symmetric stretch),^[5c] but the same region also corresponds to the C–H stretching and CH₂ asymmetric stretching vibrations of TNT, which makes an exact assignment difficult. By combining the high sensitivity and selectivity offered by SERS with our sensing method, we enhance the accuracy and reliability of the detection technique.

As both the measurements are conducted at the single particle level, the number of molecules actually responsible for the observed changes is very small. Taking the dimension of a single MF as 4 μm , the volume of the analyte solution required to completely wet the MF surface can be taken as 34 femtoliters. For a 100 ppt TNT solution, this volume amounts to 0.015 zeptomoles, or ca. nine molecules of TNT. Thus, detection at far below the zeptomole level is demonstrated with this strategy. As two methods of analysis are combined at the single particle level, it is unlikely that false positives are possible. The principal advantage of this method is that only a single particle is required for the detection of an analyte, allowing for the miniaturization of devices. The amount of gold required to make one MF with a 4 μm edge length is ca. 0.288 ng, and it can be recovered and reused. Although the molecular details of the detection chemistry are complex, the procedure itself is simple.

A similar strategy can be employed for metal ion sensing. QCs are known for the selective sensing of Hg²⁺ ions in solution.^[14] The interaction of mercury with the metal core of the QCs has been proposed as a possible reason for this effect. In this case, Hg²⁺ ions were selectively visually detected at the zeptomole level among other metal ions such as Pb²⁺, Ni²⁺, Cd²⁺, and Cu²⁺ (Figure S8). Even though the luminescence of the Ag₁₅ cluster was quenched for both Cu²⁺ and Hg²⁺ ions upon treatment of a 100 ppm solution of metal ions with the cluster solution (Figure S8A), at the single particle level, a ca. 99% quenching of cluster luminescence was observed only for Hg²⁺ ions (Figure S8C–H). Spectral intensity data collected from the surface of the MFs in each case are shown in Figure S8I. Ag₁₅ clusters showed selective luminescence quenching in the presence of Hg²⁺ ions when treated with a mixture of metal ions (Figure S8B). A bar diagram illustrating the relative variation in the luminescence intensity in the solution phase and at the single particle level at 100 ppm of metal ions is shown in Figure 3G. Here, the relative intensities are comparable, except for Cu²⁺ and Hg²⁺, where the quenching of cluster luminescence at the single particle level was much more pronounced, especially for the latter. At still lower concentrations (<10 ppm) we did not observe any quenching for Cu²⁺ ions, whereas luminescence from the MF was completely quenched for Hg²⁺, even at 1 ppb (Figure 3C). Data collected from the surface of the MFs showed a decrease in spectral intensity from that collected from blank Au@SiO₂@Ag₁₅ MFs, up to a 10 ppt concentration of Hg²⁺ (Figure S8J). The gradual disappearance of the luminescence intensity from the MF surface upon exposure to Hg²⁺ of varying concentrations (10 ppt–1 ppb) is depicted in Figure 3A–C. Though a distinct color change (red to yellow) was observable even at a Hg²⁺ concentration of 500 ppt (Figure 3E), the MF appeared green at 1 ppb (Figure 3F). The yellow color observed may be due to the additive effect of the unquenched red luminescence of the cluster on the MF surface and the underlying green luminescence of FITC-incorporated silica shell. This easily observable color change (red to green) in the presence of Hg²⁺ in solution enables the visual detection of such ions at the ppt level by our hybrid single particle sensor. When 2.5 μL of a 500 ppt Hg²⁺ solution (ca. 2 picograms) is used to wet the

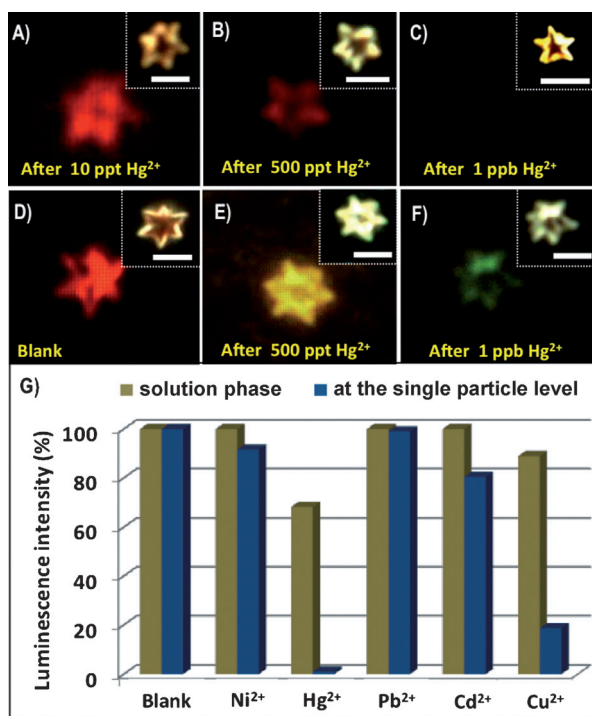


Figure 3. A–C) Dark field fluorescence images of Au@SiO₂@Ag₁₅ MFs showing the gradual disappearance of luminescence intensity as the concentration of Hg²⁺ ions increases. D–F) Fluorescence images showing variation in color during the addition of Hg²⁺ ion solutions of different concentrations to Au@SiO₂-FITC@Ag₁₅ MFs. Insets in all images show the corresponding optical images of the MFs; scale bars are 3 μm. G) Bar diagram illustrating the relative variation in the luminescence intensity of the solution phase (cluster solution) and at the single particle level upon addition of metal ions (100 ppm).

MFs, each MF will come into contact with 27 zeptograms (0.1 zeptomoles) of mercury ions. Thus, the detection of Hg²⁺ at the sub-zeptomole level is possible by this approach.

In conclusion, we have demonstrated a simple and reliable strategy for detection of two analytes of social interest, TNT and Hg²⁺, at the sub-zeptomole level in solution. The selectivity of the Ag QCs towards these analytes has been exploited and the very same methodology could be extended to other QCs with brighter luminescence, which could be protected with more specific ligands that may also enhance their chemical stability. Such functionalization of QCs also opens up numerous applications in catalysis, bioimaging, and other areas where novel devices based on the properties of both the constituents can be visualized, merged, and tailored. Studies are underway to develop a device that employs the above methodology. This approach can be considered a single-particle, single-molecule detection technique which is, probably, the ultimate in ultra-trace sensitivity.

Experimental Section

Tetrachloroauric acid trihydrate (HAuCl₄·3H₂O), cetyltrimethylammonium bromide (CTAB), ascorbic acid, and AgNO₃ were purchased from CDH, India. Fluorescein isothiocyanate (FITC), 2,4-dinitrotoluene (DNT) and 4-nitrotoluene (4-NT) were purchased from

Sigma Aldrich. Sodium hydroxide (NaOH) was purchased from Rankem, India. Bovine serum albumin (BSA) was purchased from Sisco Research Laboratories. Sodium borohydride (NaBH₄) was purchased from Spectrochem, India. 2,4,6-trinitrotoluene (TNT) and hexahydro-1,3,5-trinitro-1,3,5-triazine (RDX) were gifts from Indira Gandhi Centre for Atomic Research, Kalpakkam, India. All chemicals were of analytical grade and were used without further purification. Triply distilled water was used throughout the experiments.

Au@SiO₂ and Au@(SiO₂-FITC) mesoflowers: Au MFs were synthesized as per our earlier report.^[8] An ammonia solution (1.5 mL, 33% (w/w)), and tetraethyl orthosilicate (TEOS; 120 μL) were added under rapid stirring to a suspension of Au MFs (2 mg) dispersed in isopropanol (10 mL) and allowed to react for 1 h. The supernatant was then removed to arrest the self-nucleation of silica particles in the solution. The residue was cleaned twice by rinsing with isopropanol followed by centrifugation, and then redispersed in water. This procedure yields a uniform coating of SiO₂ of approximately 25 nm thickness on the MFs.

To produce FITC-functionalized mesoflowers, Au@(SiO₂-FITC) MFs, FITC (100 μL, 25 mM) was added to the reaction medium prior to the addition of TEOS in the above procedure.

Synthesis of Ag₁₅@BSA-loaded hybrid mesoflowers: Ag₁₅@BSA^[9] and Au/Ag MFs^[12] were synthesized as per our reported procedures. 3-aminopropyltrimethoxysilane (APTMS; 0.5 mL) was added to a suspension of MFs (2 mg) dispersed in distilled water (1 mL), and left for 15 min. The solution was washed repeatedly with water to remove excess APTMS and centrifuged. Ag₁₅@BSA solution (1 mL) was added to the residue and incubated for 30 min. The solution was again centrifuged and the residue was washed with water; this process was repeated to ensure the removal of unbound clusters from the solution. The sample was then spotted on a cover slip, dried and observed using a dark field microscope.

Detection of analytes: A stock solution containing each composite MF (2 mg) dispersed in water (2 mL) was prepared. For each analysis, this dispersion (10 μL) was drop-casted and dried on a glass slide. Analyte solutions (2.5 μL; TNT in acetonitrile or metal ions in water) of various concentrations were added on the prepared glass slide and dried under airflow after 1 min exposure. The number of analyte molecules/ions in contact with the MF is calculated from the molarity of the solution used. The molar concentrations of 100 ppt TNT (MW 227.1) and 500 ppt Hg²⁺ (as mercuric acetate; MW 318.7) are 4.403 × 10⁻¹⁰ and 2.492 × 10⁻⁹ M, respectively. The sample was covered with a cover slip and imaged using a dark field fluorescence microscope.

Received: May 17, 2012

Published online: August 22, 2012

Keywords: hybrid material · mesoflowers · nanoparticles · quantum clusters · sensors

- [1] a) M. E. Germain, M. J. Knapp, *Chem. Soc. Rev.* **2009**, *38*, 2543; b) G. Aragay, J. Pons, A. Merkoci, *Chem. Rev.* **2011**, *111*, 3433.
- [2] a) K. Saha, S. S. Agasti, C. Kim, X. Li, V. M. Rotello, *Chem. Rev.* **2012**, *112*, 2739; b) C. M. Copley, J. Chen, E. C. Cho, L. V. Wang, Y. Xia, *Chem. Soc. Rev.* **2011**, *40*, 44; c) F. P. Zamborini, L. Bao, R. Dasari, *Anal. Chem.* **2012**, *84*, 541; d) K. K. Kartha, S. S. Babu, S. Srinivasan, A. Ajayaghosh, *J. Am. Chem. Soc.* **2012**, *134*, 4834.
- [3] a) J. P. Camden, J. A. Dieringer, J. Zhao, R. P. Van Duyne, *Acc. Chem. Res.* **2008**, *41*, 1653; b) R. S. Golightly, W. E. Doering, M. J. Natan, *ACS Nano* **2009**, *3*, 2859; c) L. Rodríguez-Lorenzo, R. A. Álvarez-Puebla, I. Pastoriza-Santos, S. Mazzucco, O. Stéphan, M. Kociak, L. M. Liz-Marzán, F. J. García de Abajo, *J. Am. Chem. Soc.* **2009**, *131*, 4616; d) W. E. Smith, *Chem. Soc.*

- Rev. **2008**, *37*, 955; e) X. Huang, I. H. El-Sayed, W. Qian, M. A. El-Sayed, *Nano Lett.* **2007**, *7*, 1591.
- [4] J. F. Li, Y. F. Huang, Y. Ding, Z. L. Yang, S. B. Li, X. S. Zhou, F. R. Fan, W. Zhang, Z. Y. Zhou, Y. WuDe, B. Ren, Z. L. Wang, Z. Q. Tian, *Nature* **2010**, *464*, 392.
- [5] a) M. Li, Q. Wang, X. Shi, L. A. Hornak, N. Wu, *Anal. Chem.* **2011**, *83*, 7061; b) K. Zhang, H. Zhou, Q. Mei, S. Wang, G. Guan, R. Liu, J. Zhang, Z. Zhang, *J. Am. Chem. Soc.* **2011**, *133*, 8424; c) S. S. R. Dasary, A. K. Singh, D. Senapati, H. Yu, P. C. Ray, *J. Am. Chem. Soc.* **2009**, *131*, 13806.
- [6] a) S. Choi, R. M. Dickson, J. Yu, *Chem. Soc. Rev.* **2012**, *41*, 1867; b) M. A. H. Muhammed, T. Pradeep in *Advanced Fluorescence Reporters in Chemistry and Biology II, Vol. 9* (Ed.: A. P. Demchenko), Springer, Berlin, **2010**, part 4, pp. 333–353, and references therein; c) P. L. Xavier, K. Chaudhari, A. Baksi, T. Pradeep, *Nano Rev.* **2012**, *3*, 14767; d) T. U. B. Rao, B. Nataraju, T. Pradeep, *J. Am. Chem. Soc.* **2010**, *132*, 16304; e) T. Udayabhaskararao, Y. Sun, N. Goswami, S. K. Pal, K. Balasubramanian, T. Pradeep, *Angew. Chem.* **2012**, *124*, 2197; *Angew. Chem. Int. Ed.* **2012**, *51*, 2155; f) I. Díez, M. Pusa, S. Kulmala, H. Jiang, A. Walther, A. S. Goldmann, A. H. E. Müller, O. Ikkala, R. H. A. Ras, *Angew. Chem.* **2009**, *121*, 2156; *Angew. Chem. Int. Ed.* **2009**, *48*, 2122.
- [7] a) M. A. Habeeb Muhammed, T. Pradeep, *Chem. Phys. Lett.* **2007**, *449*, 186; b) Y. H. Lin, W. L. Tseng, *Anal. Chem.* **2010**, *82*, 9194; c) W. Y. Chen, G. Y. Lan, H. T. Chang, *Anal. Chem.* **2011**, *83*, 9450; d) X. Yuan, T. J. Yeow, Q. Zhang, J. Y. Lee, J. Xie, *Nanoscale* **2012**, *4*, 1968; e) M. A. Habeeb Muhammed, P. K. Verma, S. K. Pal, A. Retnakumari, M. Koyakutty, S. Nair, T. Pradeep, *Chem. Eur. J.* **2010**, *16*, 10103.
- [8] P. R. Sajanlal, T. Pradeep, *Nano Res.* **2009**, *2*, 306.
- [9] A. Mathew, P. R. Sajanlal, T. Pradeep, *J. Mater. Chem.* **2011**, *21*, 11205.
- [10] a) O. G. Tovmachenko, C. Graf, D. J. van den Heuvel, A. van Blaaderen, H. C. Gerritsen, *Adv. Mater.* **2006**, *18*, 91; b) A. R. Guerrero, R. F. Aroca, *Angew. Chem.* **2011**, *123*, 691; *Angew. Chem. Int. Ed.* **2011**, *50*, 665.
- [11] a) L. Yang, L. Ma, G. Chen, J. Liu, Z.-Q. Tian, *Chem. Eur. J.* **2010**, *16*, 12683; b) D. Gao, Z. Wang, B. Liu, L. Ni, M. Wu, Z. Zhang, *Anal. Chem.* **2008**, *80*, 8545; c) Y. Engel, R. Elnathan, A. Pevzner, G. Davidi, E. Flaxer, F. Patolsky, *Angew. Chem.* **2010**, *122*, 6982; *Angew. Chem. Int. Ed.* **2010**, *49*, 6830; d) Y. Xia, L. Song, C. Zhu, *Anal. Chem.* **2011**, *83*, 1401.
- [12] P. R. Sajanlal, T. Pradeep, *Langmuir* **2010**, *26*, 8901.
- [13] K. Aslan, J. R. Lakowicz, C. D. Geddes, *J. Phys. Chem. B* **2005**, *109*, 6247.
- [14] a) J. Xie, Y. Zheng, J. Y. Ying, *Chem. Commun.* **2010**, *46*, 961; b) C. C. Huang, Z. Yang, K. H. Lee, H. T. Chang, *Angew. Chem.* **2007**, *119*, 6948; *Angew. Chem. Int. Ed.* **2007**, *46*, 6824.

Supporting Information

© Wiley-VCH 2012

69451 Weinheim, Germany

Selective Visual Detection of TNT at the Sub-Zeptomole Level**

*Ammu Mathew, P. R. Sajanlal, and Thalappil Pradeep**

anie_201203810_sm_miscellaneous_information.pdf

Table of contents

Number	Description	Page no.
	Instrumentation	2
SI-1	Characterization of various MFs and their hybrid forms	3-4
SI-2	Characterization of Ag ₁₅ @BSA	5
SI-3	Dark field microscopic study of various MFs functionalized with Ag ₁₅	6-7
SI-4	Effect of TNT on the luminescence of Ag ₁₅ in solution phase and at single particle level	8
SI-5	Effect of varying TNT concentration and other compounds on the absorption spectra of Ag ₁₅ in solution	9
SI-6	Variation of intensity of emission of Ag ₁₅ @BSA in solution with the addition of equal amounts of various MFs	10
SI-7	Raman spectra of solid TNT and effect of addition of other compounds to luminescent Au/Ag@Ag ₁₅ MF	11
SI-8	Effect of luminescence of the cluster with various metal ions in solution phase and at on single particles	12

Instrumentation

Scanning electron microscopic (SEM) images and energy dispersive analysis of X-ray (EDAX) images were obtained using a FEI QUANTA-200 SEM. For the SEM and EDAX measurements, samples were spotted on a carbon tape and dried in ambient condition. Luminescence measurements were carried out on a Jobin Yvon NanoLog instrument. The bandpass for excitation and emission was set as 5 nm. Raman measurements were done with a WiTec GmbH, Alpha-SNOM CRM 200 confocal Raman microscope having a 633 nm laser as the excitation source. This excitation source (instead of 532 nm) was used to suppress the cluster emission. For Raman studies, the material was carefully transferred onto a cover glass and dried in ambience. Then the MF-coated glass plates were mounted on the sample stage of the confocal Raman microscope. A supernotch filter placed in the path of the signal effectively cuts off the excitation radiation. The signal was then dispersed using a 600 grooves/mm grating, and the dispersed light was collected by a Peltier cooled charge coupled device (CCD). Matrix assisted laser desorption ionization mass spectrometric (MALDI MS) studies were conducted using a Voyager DE PRO Biospectrometry Workstation (Applied Biosystems) matrix assisted laser desorption ionization time-of-flight mass spectrometer (MALDI TOF MS). UV-vis spectra were recorded using Perkin Elmer Lambda 25 UV-vis spectrometer. Spectra were typically measured in the range of 200-1100 nm.

Dark-field microscopy/spectroscopy of the gold mesoflowers

Dark-field imaging of the gold MFs was done using an Olympus BX-51 microscope and 100 W quartz halogen light source on a CytoViva microscope set-up. Here, a broadband white light was shown on the particles from an oblique angle via a dark field condenser. The scattered/emitted light from the particle was collected by a 100x oil immersion objective and imaged by a true-color charge-coupled device (CCD) camera or by a spectrophotometer. Each spectrum shown (in Figure S3H, for example) is collected from a single pixel and is approximately 64 nm in size. Spectral analysis was performed with hyperspectral image analysis software. For fluorescence imaging, a mercury lamp light source is used. Light after passing through specific excitation (bandpass) filter falls on the sample. The emitted light was passed through a 460-500 nm band pass filter and fluorescence (if any) emitted by the particle was imaged or the spectrum was collected with a spectrometer.

Supporting information 1

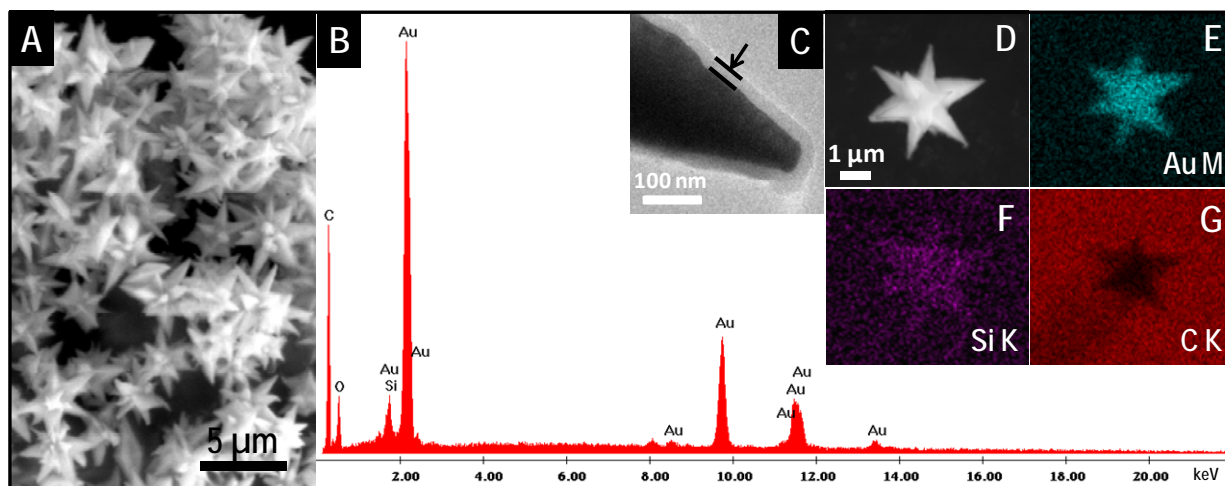


Figure S1a. (A) Large area SEM image and (B) EDAX spectrum of Au@SiO₂ MFs, (C) a magnified TEM image of the tip of the MF showing the uniform silica coating on its surface (shown with an arrow) and (D-G) SEM and corresponding EDAX images of a single MF showing the presence of Au M α , and Si K α on the MF. Carbon is from the substrate used for measurement.

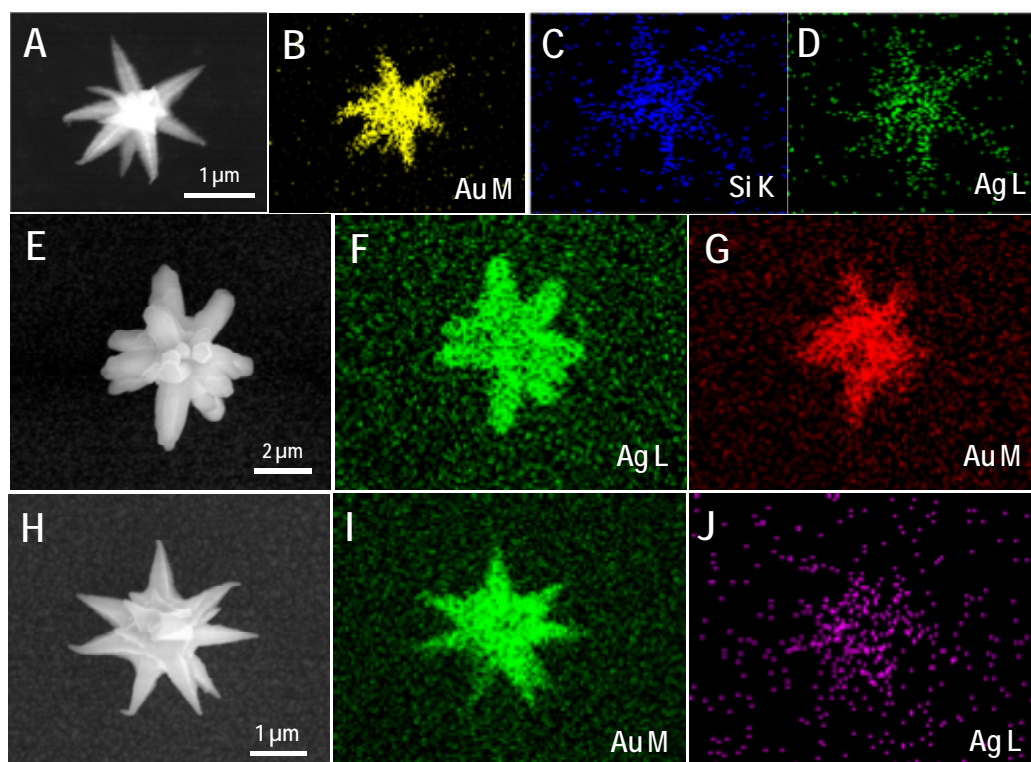


Figure S1b. SEM and EDAX characterization of the various cluster-loaded hybrid MFs used in this study, (A-D) Au@SiO₂@Ag₁₅ MF, (E-G) Au/Ag@Ag₁₅ MF and (H-J) Au@Ag₁₅MF. Coating of cluster on the MF surface is evident from the EDAX map of Ag L on the MFs.

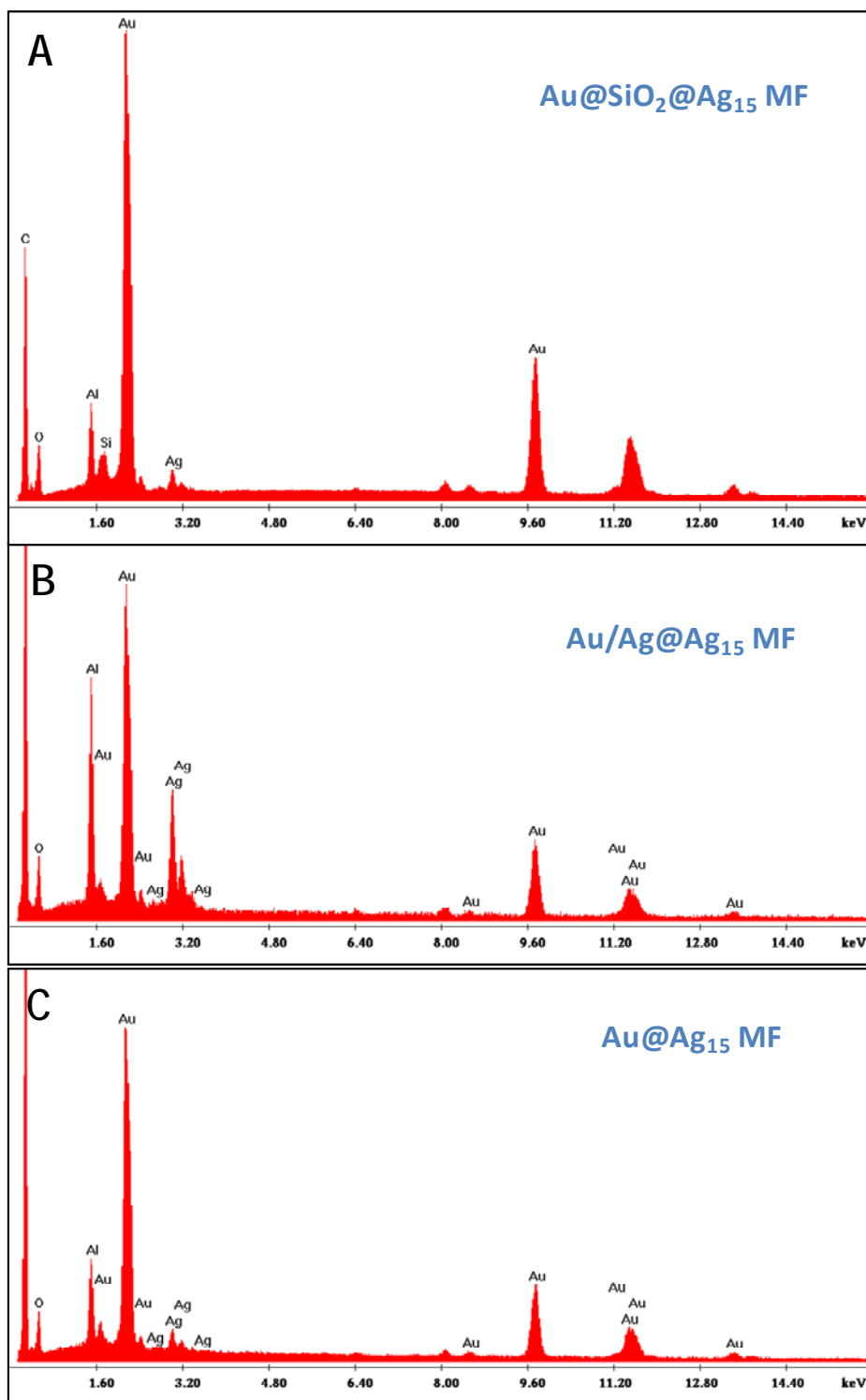


Figure S1c. EDAX spectra of the various cluster-loaded MFs (A) Au@SiO₂@Ag₁₅ MF, (B) Au/Ag@Ag₁₅ MF and (C) Au@Ag₁₅ MF. Carbon and aluminium are from the substrate used for the measurement.

Supporting information 2

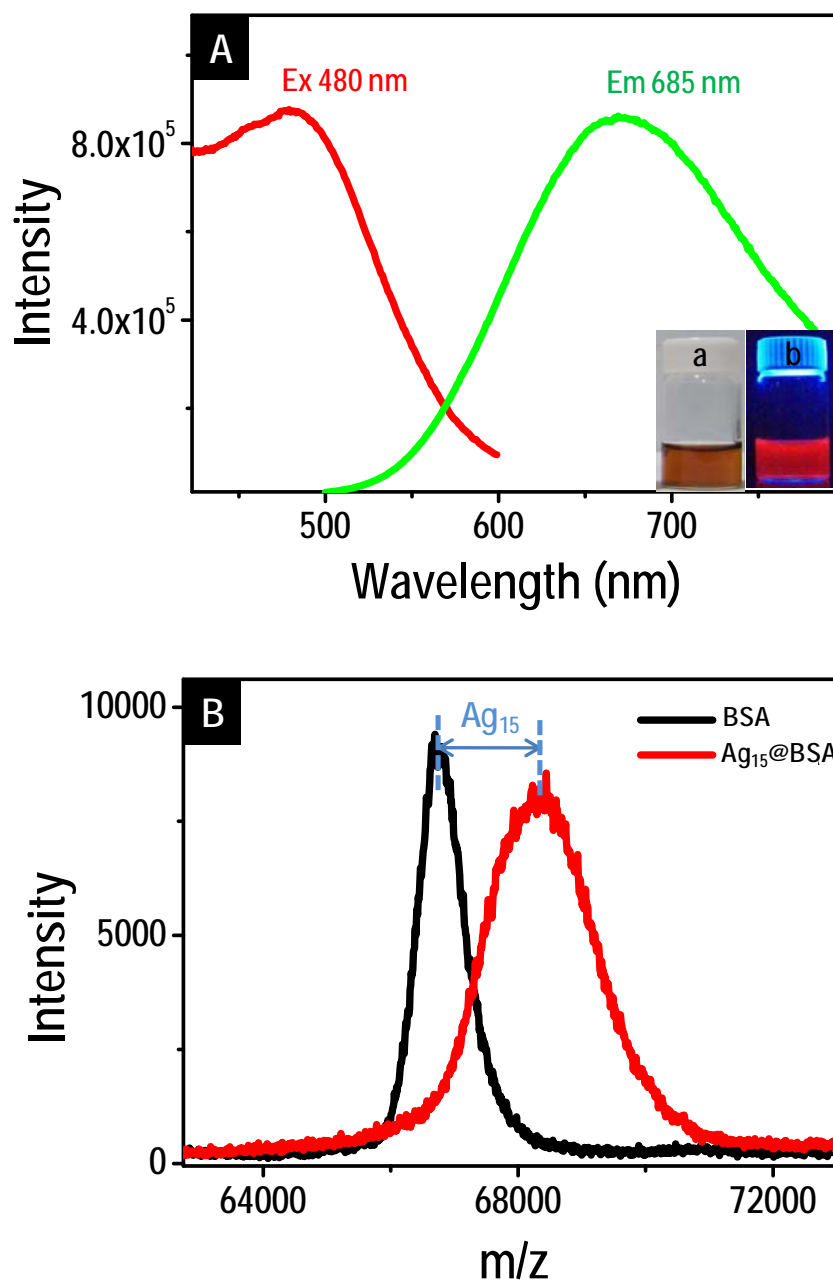


Figure S2. (A) Luminescence profile of cluster solution (Ag₁₅@BSA). Inset shows photographs of the cluster solution under visible light (a) and UV light (b). (B) MALDI MS of BSA (black trace) and cluster collected in linear positive ion mode using sinapic acid as the matrix (red trace). A mass difference corresponding to 15 atoms of silver was observed in case of cluster compared to that of bare protein and the cluster was assigned as Ag₁₅@BSA. The cluster was stable and had a bright red luminescence (as shown in the figure) at room temperature with a quantum yield of 10.7%.

Supporting information 3

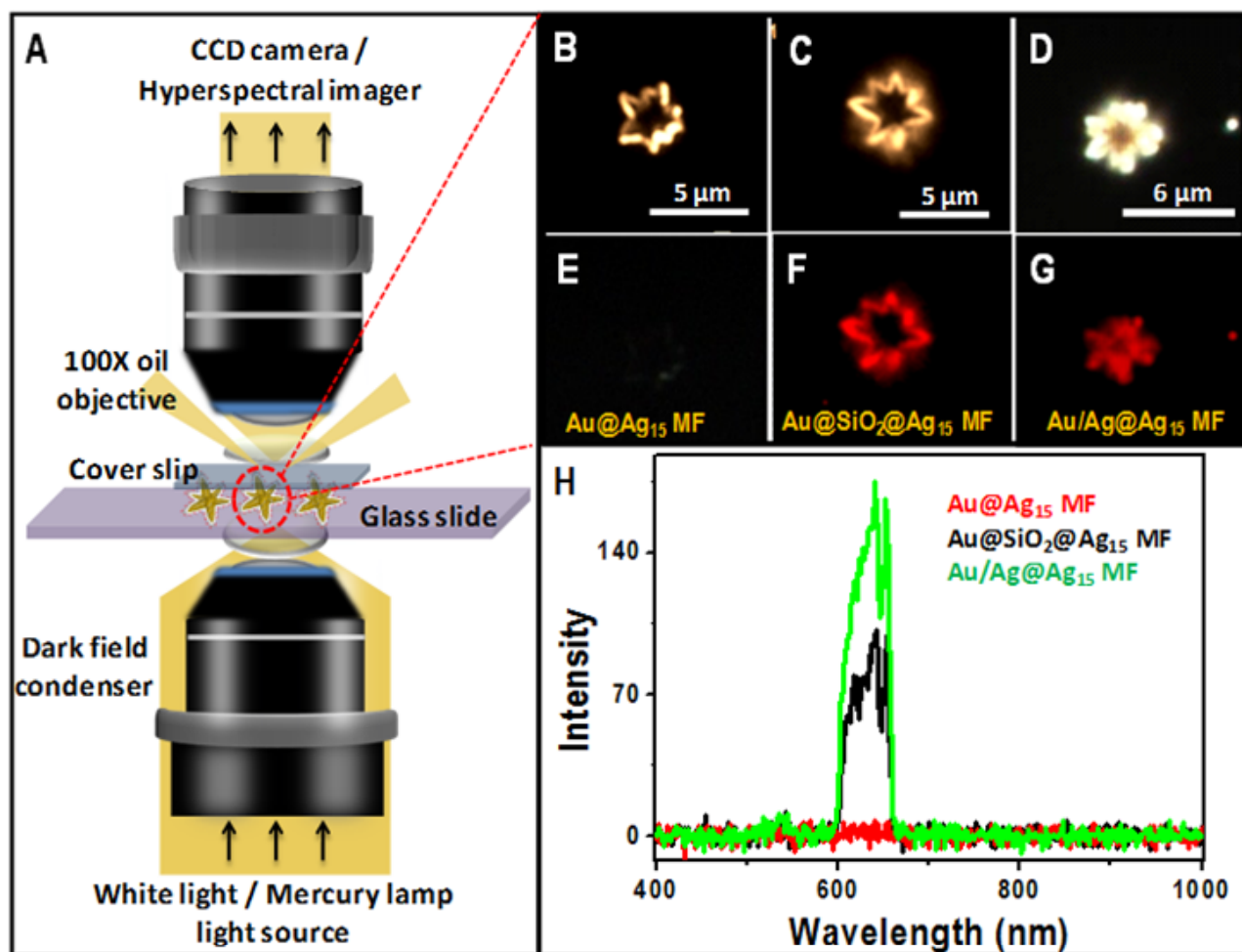


Figure S3a. (A) Schematic of the hyperspectral microscopic set-up used for collecting the images of the MFs. Optical and fluorescence images of (B, E) Au@Ag₁₅ MF, (C, F) Au@SiO₂@Ag₁₅ MF and (D, G) Au/Ag@Ag₁₅ MF obtained using a dark field fluorescence microscope, respectively. Corresponding spectra collected from the surface of the MF in each case is also shown in (H). The emitted light passes through a triple pass filter which cuts off the excitation light. SEM and EDAX characterization of the three types of MFs shown above is given in Figure S1b and c. The luminescence of Ag₁₅ is completely quenched on bare Au MF.

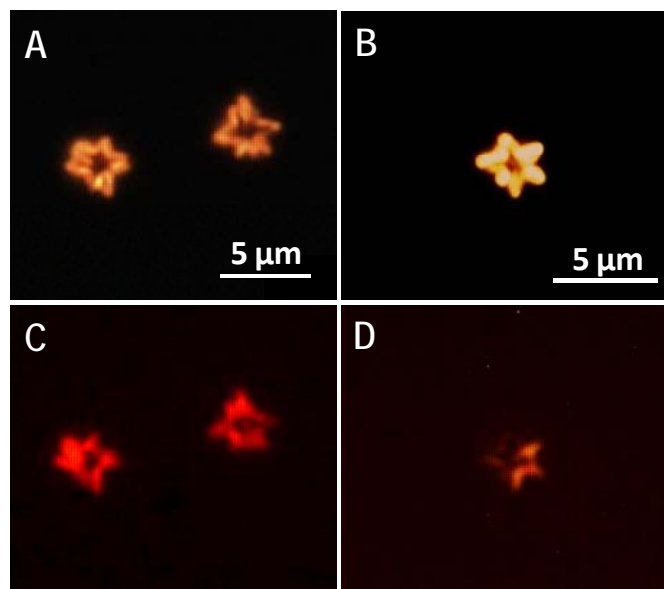


Figure S3b. (A, C) White light and fluorescence images of the as-prepared Au@SiO₂@Ag₁₅ MFs. (B, D) Images collected from the same glass slide after 1 month in ambient conditions. The enhanced stability of the otherwise easily oxidised silver clusters (under laboratory conditions) could be attributed to them getting embedded in the silica layer. Note that different particles are imaged in A and B.

Supporting information 4

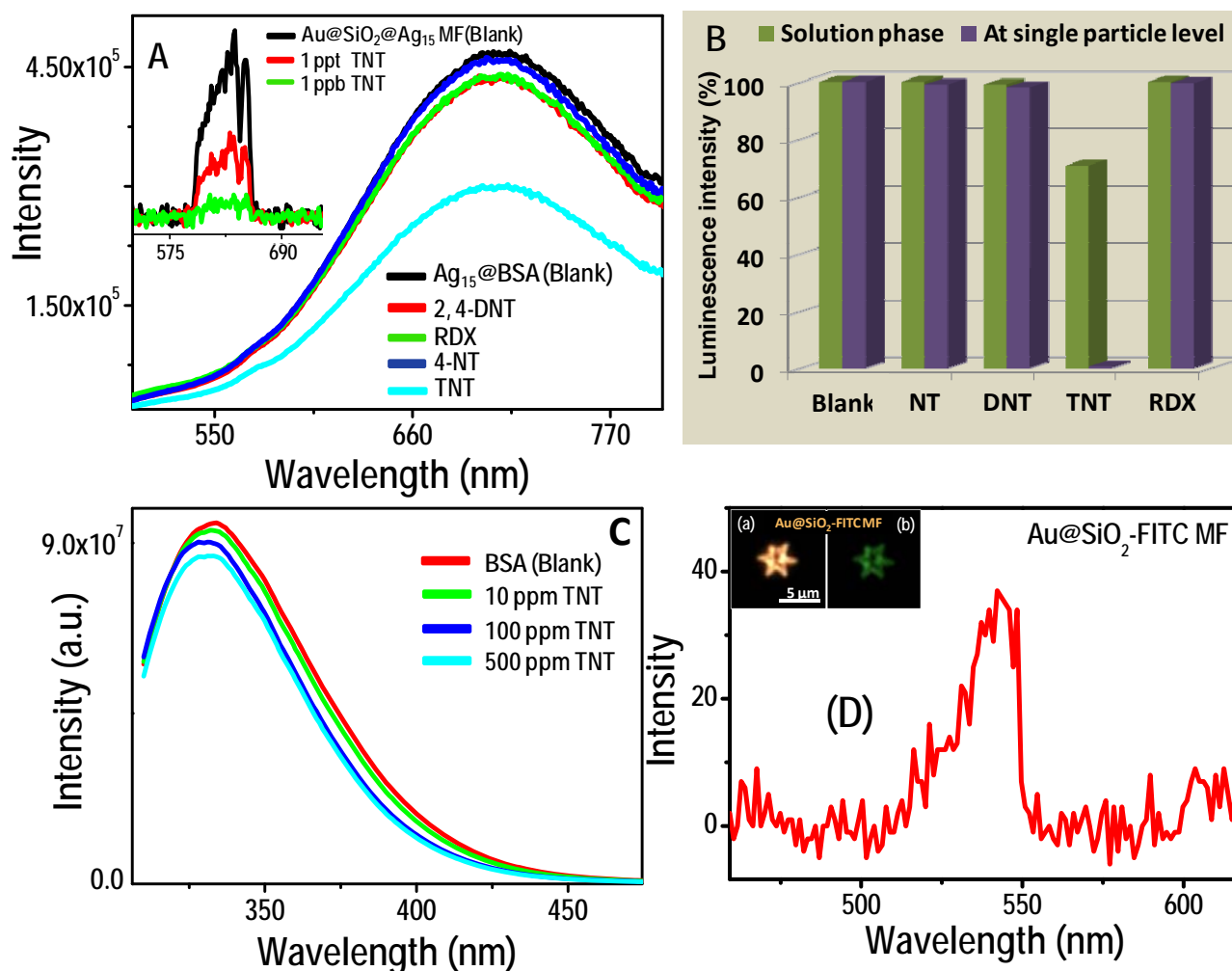


Figure S4. (A) Luminescence spectra collected after adding 100 ppm of various compounds into the Ag₁₅ cluster solution. Inset shows the luminescence spectra collected from Au@SiO₂@Ag₁₅ MF upon exposure to various concentrations of TNT. (B) Bar diagram shows the comparison of luminescence quenching phenomena at solution phase and single particle level upon exposure to various analytes (all at 100 ppm). (C) Emission spectra illustrating the effect of bare protein, BSA, with 0.1 mL of various concentrations of TNT solution indicated in the figure. Absence of any significant quenching of protein luminescence in presence of TNT indicates the importance of the cluster utilised. (D) The luminescence spectrum collected from Au@SiO₂-FITC MF. The emission is from the FITC molecules attached on Au@SiO₂ MF. Inset shows the optical (a) and fluorescence images (b) of Au@SiO₂-FITC MF.

Supporting information 5

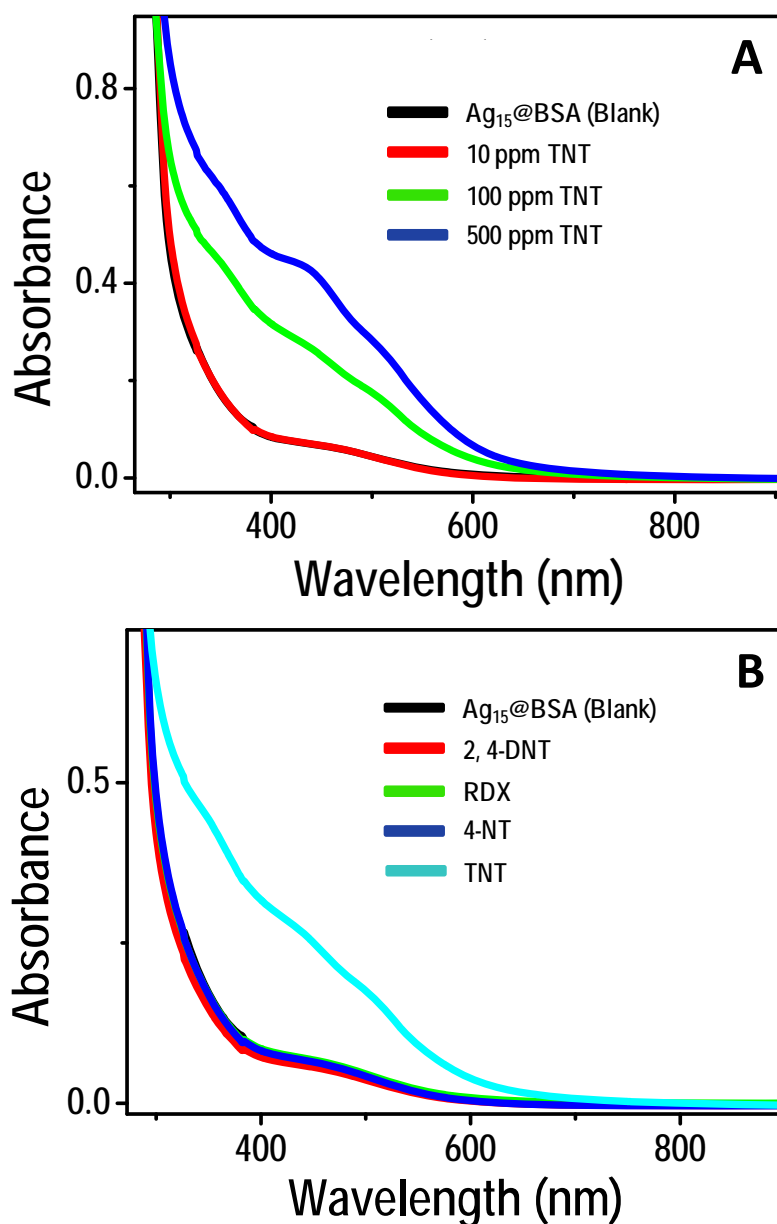


Figure S5. UV-vis absorption spectra showing the effect of cluster solution with (A) various concentrations of TNT solution and (B) various nitro compounds and RDX. Spectral features appearing at 340, 450 and 525 nm in case of higher concentration of TNT is due to the formation of the Meisenheimer complex and the resultant solution turned dark red in color. No such changes were observed for 2, 4-DNT, RDX and 4-NT.

Supporting information 6

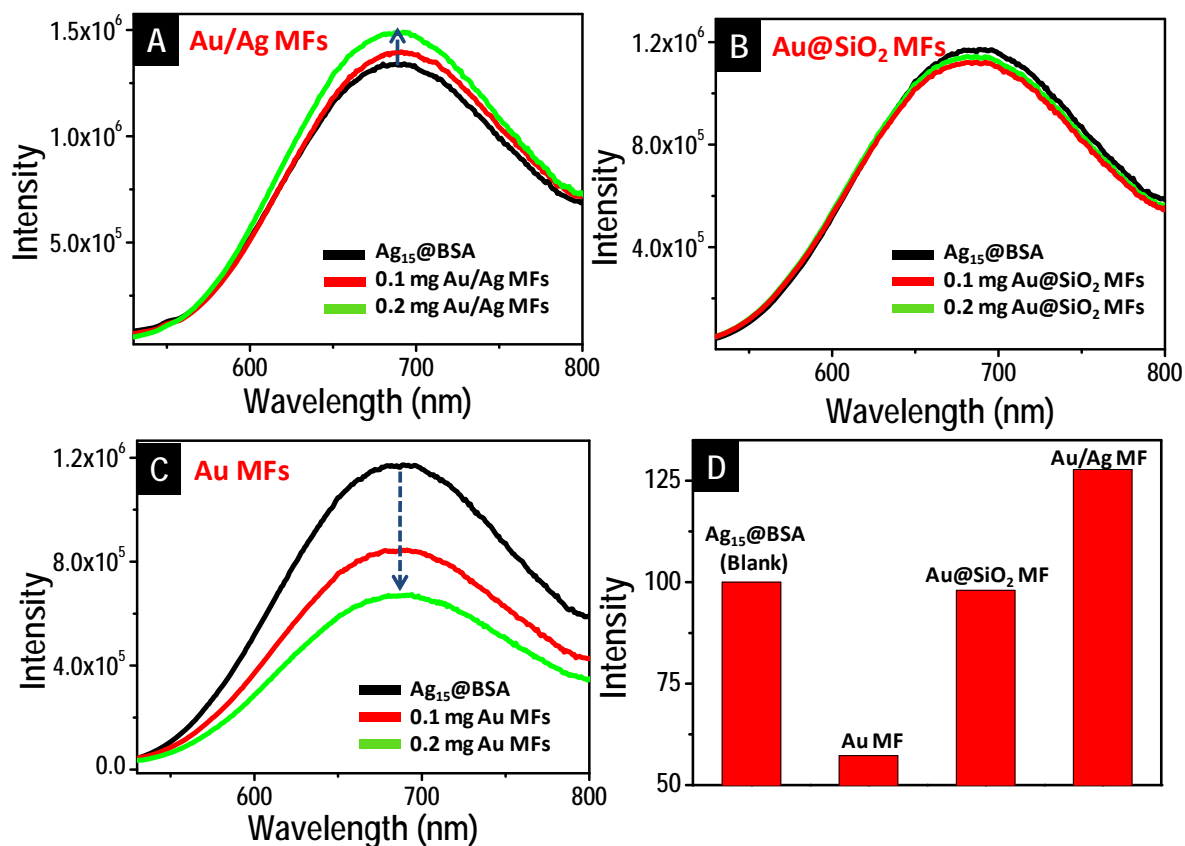


Figure S6. (A-C) Variation of emission spectra of the $\text{Ag}_{15}@BSA$ solution upon addition of equal amounts of various MFs. (D) Bar diagram showing the relative effect of luminescence intensity of the cluster solution with 0.2 mg of various MFs. While luminescence quenching was observed in the case of Au MFs, retention of the luminescence intensity of cluster solution was demonstrated by Au@ SiO_2 MFs due to the silica layer on the MF surface which acts as a spacer between the Au surface and the cluster. Bimetallic Au/Ag MFs showed an enhancement of luminescence intensity of the cluster solution due to metal enhanced luminescence.

Supporting information 7

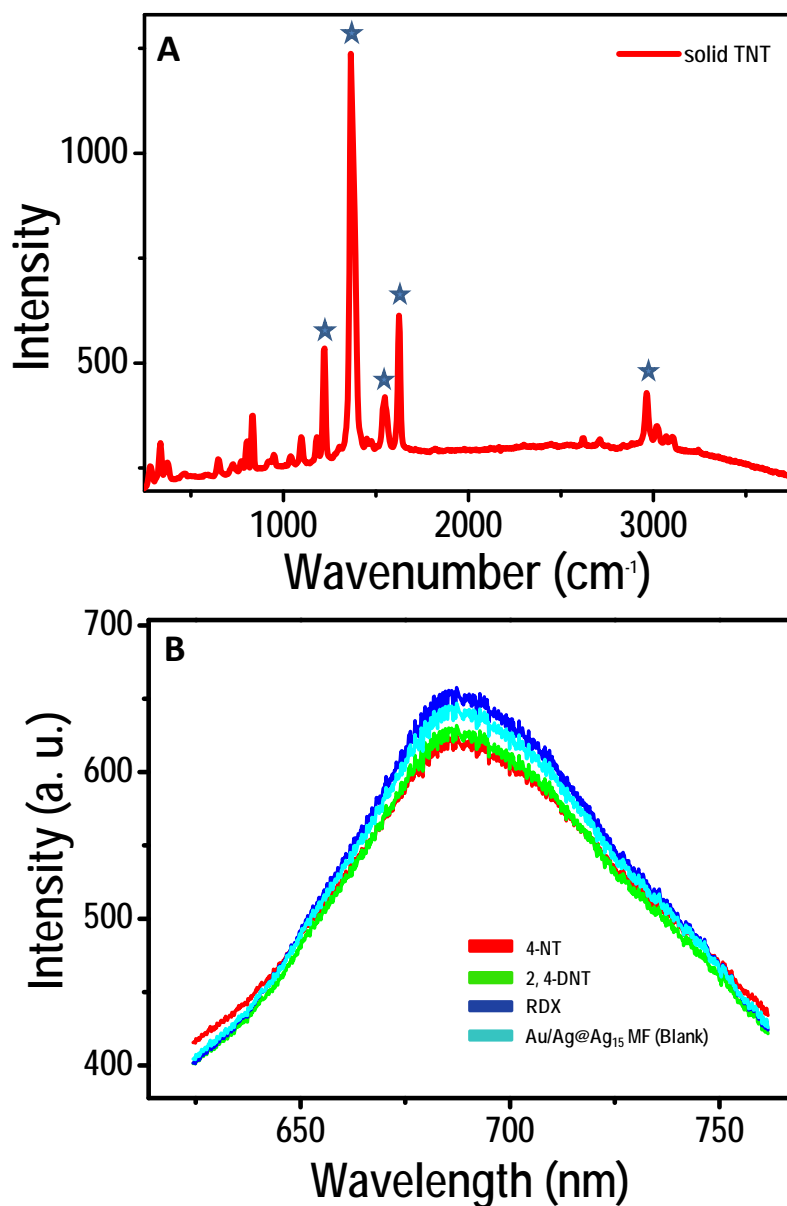


Figure S7. (A) Raman spectra of solid TNT. Prominent features of TNT due to C₆H₂-C vibration [1218 cm⁻¹], -NO₂ symmetric stretching vibration [1366 cm⁻¹ (strong)], NO₂ asymmetric stretching vibration [1545 cm⁻¹ (weak)], C=C aromatic stretching vibration [1629 cm⁻¹] and C-H stretching and CH₂ asymmetric stretching [2965 cm⁻¹] are marked on the spectra. (B) Raman spectra showing the effect of addition of 4-nitrotoluene (4-NT), 2,4-dinitrotoluene (2,4-DNT) and RDX to the luminescent Au/Ag@Ag₁₅ MFs. A broad background due to the luminescence from the cluster on the MF surface was only observed.

Supporting information 8

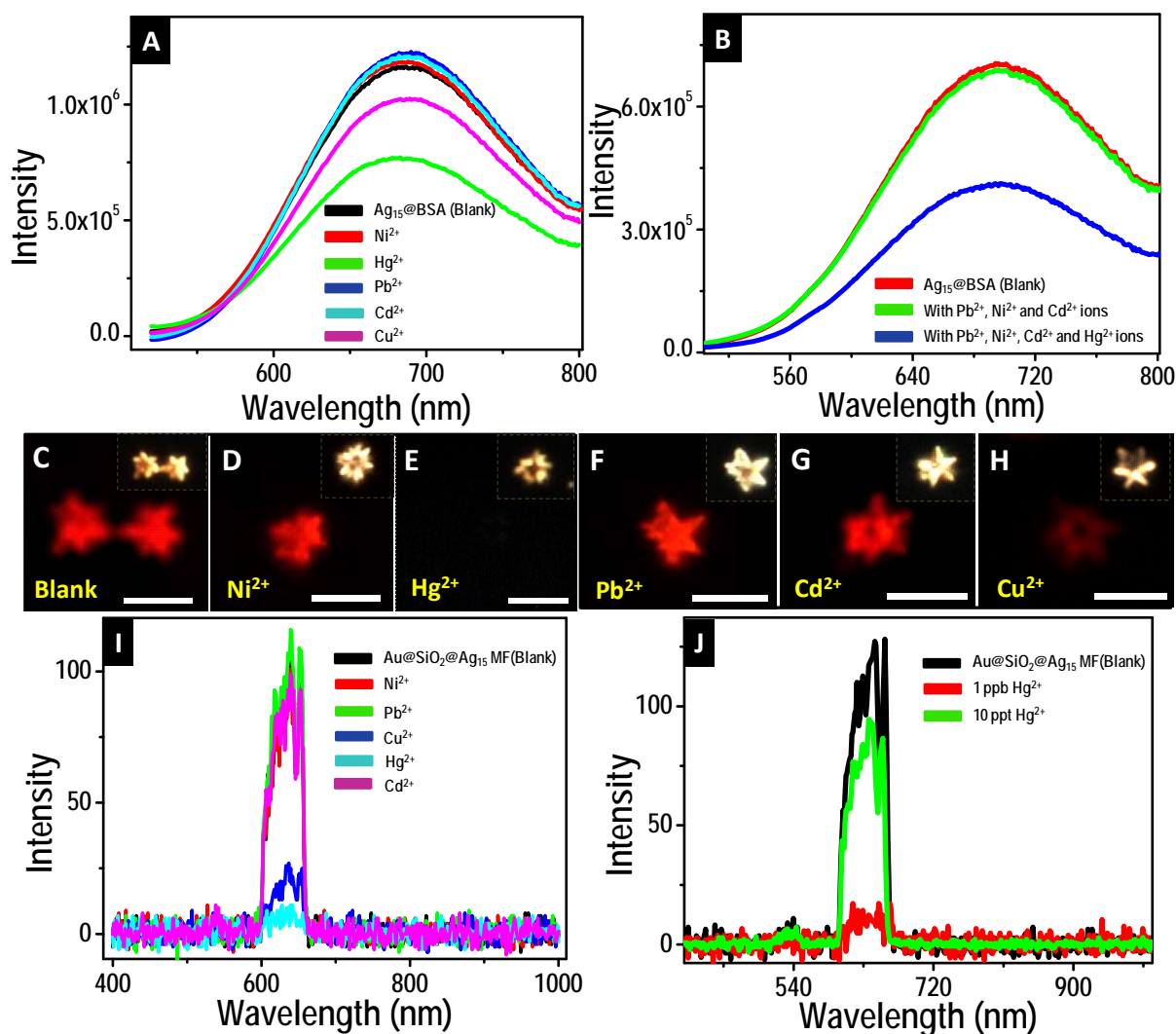


Figure S8. Effect of cluster luminescence in solution with 100 ppm concentration of each metal ion (A) and (B) with a solution containing mixture of metal ions. (C-H) Luminescence images of $\text{Au}@SiO_2@Ag_{15}$ MFs upon exposure to 100 ppm of various metal ions (indicated in each image). Corresponding optical images are shown as the inset of each figure. Scale bars in the images correspond to 5 μm . Corresponding spectra collected from the surface of the MF for 100 ppm concentration of each metal ions is shown in (I). (J) Variation of luminescence intensity of the $\text{Au}@SiO_2@Ag_{15}$ MF after treatment of 1 ppb and 10 ppt concentrations of Hg^{2+} ions. The emitted light passes through a triple pass filter which cuts off the excitation light.

Graphene from Sugar and its Application in Water Purification

Soujit Sen Gupta,[†] Theruvakkattil Sreenivasan Sreepasad,[†] Shihabudheen Mundampra Maliyekkal,[‡] Sarit Kumar Das,[§] and Thalappil Pradeep^{†,*}

[†]DST Unit on Nanoscience, Department of Chemistry, Indian Institute of Technology Madras, Chennai 600 036, India

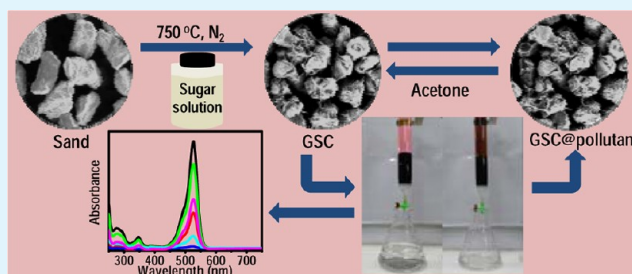
[‡]School of Mechanical and Building Sciences, VIT University, Chennai Campus, Chennai 600 048, India

[§]Department of Mechanical Engineering, Indian Institute of Technology Madras, Chennai -600036, India

S Supporting Information

ABSTRACT: This paper describes a green method for the synthesis of graphenic material from cane sugar, a common disaccharide. A suitable methodology was introduced to immobilize this material on sand without the need of any binder, resulting in a composite, referred to as graphene sand composite (GSC). Raman spectroscopy confirmed that the material is indeed graphenic in nature, having G and D bands at 1597 and 1338 cm^{-1} , respectively. It effectively removes contaminants from water. Here, we use rhodamine 6G (R6G) as a model dye and chloropyrifos (CP) as a model pesticide to demonstrate this application. The spectroscopic and microscopic analyses coupled with adsorption experiments revealed that physical adsorption plays a dominant role in the adsorption process. Isotherm data in batch experiments show an adsorption capacity of 55 mg/g for R6G and 48 mg/g for CP, which are superior to that of activated carbon. The adsorbent can be easily regenerated using a suitable eluent. This quick and cost-effective technique for the into a commercial water filter with appropriate engineering.

KEYWORDS: graphene, composites, adsorption, water purification, nanotechnology, environmental remediation



INTRODUCTION

One of the most socially relevant aspects of nanotechnology is in the field of environmental remediation. Diverse applications of nanomaterials in decontamination of air, water and soil are intensely pursued in the recent past.¹ The availability of large surface area and unusual electronic structure imparts new properties to nanomaterials. One of the early applications of such materials is the halocarbon decomposition and the use of this technology in pesticide removal.² Numerous other applications of noble metal nanoparticles have been reported in the literature.³ Chemical interaction at noble metal nanoparticle surfaces often led to charge transfer and subsequent cleavage of chemical bonds, the most often encountered is reductive dehalogenation.⁴ Enhanced surface chemistry leading to faster kinetics is reported on noble metal nanoparticles.⁵

Carbon has been the most versatile material used for water purification in history.^{6,7} Very early account of the use of charcoal in water purification is found in the *Vedic* literature.⁸ It is believed that people of Indus valley civilization used carbon and porous materials, such as earthen vessels, for filtering and storing drinking water. The most widely used material for water purification today is activated carbon (AC)^{9–13} derived from plant sources. It has the best possible surface area and could be produced at low cost, making it the most affordable adsorption medium in diverse applications. A number of other forms of carbon have appeared with very large adsorption capacities.¹⁴ Advanced techniques such as membrane filtration, reverse

osmosis and ion-exchange can be used in treatment and removal of contaminants from water.^{15,16} However, higher cost limits the large scale application of such treatment techniques in developing countries.

One of the fascinating new additions into the carbon family is graphene,¹⁷ the one-atom thick sheets of carbon. Carbon materials, such as activated carbon,¹⁸ charcoal, carbon nanotubes,^{19,20} have been used extensively in water purification²¹ and, hence, are indispensable components of all commercial water technologies.^{22,23} It is natural to look at the application of graphene in various aspects of environmental remediation. Several aspects, such as high thermal and electrical conductivity, electronic properties, quantum hall effect, and application in drug delivery²⁴ and DNA sensing,^{25,26} have been investigated in the recent past. We and others^{27,28} have shown that chemically synthesized graphene, as well as graphene oxide, can be anchored onto the surfaces of river sand to make effective adsorbents that remove heavy metal ions,^{29–34} pesticides,³⁵ and natural dyes.^{36–39} Such materials show higher adsorption capacity in comparison to activated carbon when equal masses of carbon are compared. When used as a stationary adsorbent material in a flowing water stream, it is necessary to anchor the nanoscale adsorbent onto inexpensive and reliable substrates.^{40,41} This is to

Received: May 17, 2012

Accepted: July 12, 2012

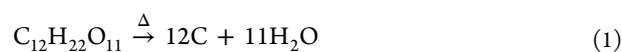
Published: July 12, 2012

Scheme 1. Upper Frame Shows a Schematic Diagram of the Preparation of Graphene–Sand Composite^a

^aLower frame shows photographs of pristine sand and GSC.

overcome engineering issues like solid–liquid separation and pressure drop.^{42,43} There have been other approaches to attach graphene on sand surfaces with the help of suitable binder such as chitosan²⁸ or by functionalizing the sand surface.²⁷

Utilization of such technologies in people-oriented applications requires the materials to be affordable. In this regard, biologically derived carbon is perhaps the most affordable and chemically most versatile. Materials derived from plant sources may even be more eco-friendly than those from fossil source⁴⁴ such as petroleum. Among the simplest of natural sources of carbon are sugars,⁴⁵ which upon dehydrogenation get converted completely to elemental carbon, leaving only water to escape. For example,



Similar reactions are applicable to decomposition of sugars of various kinds. This transformation is simple and effective. The carbon so obtained could be anchored on inorganic surfaces, and a subsequent chemical treatment could transform it to graphenic carbon (GC). Activation of newly formed surfaces may produce highly effective adsorbents.

In this paper, we report in situ creation of graphenic material anchored onto the surfaces of river sand without the need of any additional binder. We also report the application of this material in water purification. The material shows strong adsorption capability. It could completely decolorize, for example, some of the colored commercial soft drinks. The extension of this chemistry to diverse sugars and carbohydrates in general could contribute to the creation of inexpensive and efficient adsorbents.

MATERIAL AND METHODS

The raw materials used for the synthesis were common sugar, river sand, and sulfuric acid. River sand (~0.2 mm particle size) and sugar were obtained from the local market. Sulfuric acid and acetone were procured from local suppliers, rhodamine 6G chloride ($\text{C}_{27}\text{H}_{29}\text{ClN}_2\text{O}_3$) and chlorpyrifos (CP) (HPLC assay 99.9%) were from Sigma Aldrich and soft drink (Coca Cola) was from Hindustan coca-cola beverages Pvt. Ltd. No additional purification was done and the solvent generally used was water unless otherwise mentioned.

Instrumentation. UV–vis spectra were recorded using a Perkin-Elmer Lambda 25 spectrophotometer. Raman spectra were collected using a confocal Raman spectrometer (WiTec GmbH CRM 200) with a 532 nm Nd:YAG laser as the light source. XPS measurements were done

with Omicron ESCA Probe spectrometer with unmonochromatized Mg K_{α} X-rays ($h\nu = 1253.6$ eV). Most of the spectra were deconvoluted to their component peaks using the software CasaXPS. The energy resolution of the spectrometer was set at 0.1 eV at a pass energy of 20 eV. Binding energy was corrected with respect to C 1s at 284.5 eV. Surface morphology, elemental analysis, and elemental mapping studies were carried out using a scanning electron microscope (SEM) equipped with an energy dispersive analysis of X-rays (EDAX) facility (FEI Quanta 200, Czechoslovakia). High-resolution transmission electron microscopy (HRTEM) of the samples was carried out using a JEOL 3010 instrument with a UHR pole piece. For mass analyses, an Applied Biosystems Voyager DE Pro LDI MS instrument was used. A pulsed nitrogen laser of 337 nm was used for desorption/ionization.

Preparation of the Composite. Common sugar (sucrose crystals) was used as the carbon source. At first, the sugar was dissolved in water and then, the solution was mixed with requisite amount of sand (river sand). Calculated amounts of sugar and sand were taken to make different loading ratios. In each case, the mixture was dried at ~95 °C in a hot air oven for about 6 h with constant stirring. The sugar-coated sand was then placed in a silica crucible and heated in a furnace in N_2 atmosphere. The furnace temperature was programmed as follows: (a) from room temperature to 100 °C in 30 min, (b) 100–200 °C in 30 min (c), held at 200 °C for 1 h (to melt sugar to form a uniform coating; melting point of sucrose is around 186 °C), (d) ramped to 750 °C in 1 h, and (e) held for 3 h at 750 °C (to ensure complete graphitization of sugar). The furnace was switched off and the material was cooled to room temperature. The temperature of 750 ± 5 °C was chosen as the final temperature after optimization through several experiments. No special care was taken in controlling the cooling rate. The black sample was named graphene sand composite (GSC). For activation, 5 g of the composite was treated with 10 mL of concentrated sulfuric acid and kept undisturbed at room temperature for 30 min. The mixture was then filtered and dried at 120 °C. The activated GSC is labeled as GSC₇₅₀. The lower frame of Scheme 1 shows the photographs of sand (before coating) and GSC.

Adsorption Experiments. Time-dependent adsorption capacity of the as-synthesized composite was investigated in a batch reactor of 25 mL capacity. The working volume and the adsorbent dose were maintained as 10 mL and 100 mg, respectively. Water was spiked with the required concentration of rhodamine 6G (R6G) and kept with GSC for stirring at room temperature (30 ± 2 °C). The solid–liquid separation was done by filtration. The filtrate was analyzed for R6G using UV–vis spectrophotometer. The target molecules in the aqueous phase were quantified using the absorbance at 527 nm. All the experiments were conducted in duplicate and the samples were analyzed immediately. Similar experiments were done with CP, which has an absorbance peak at 297 nm.

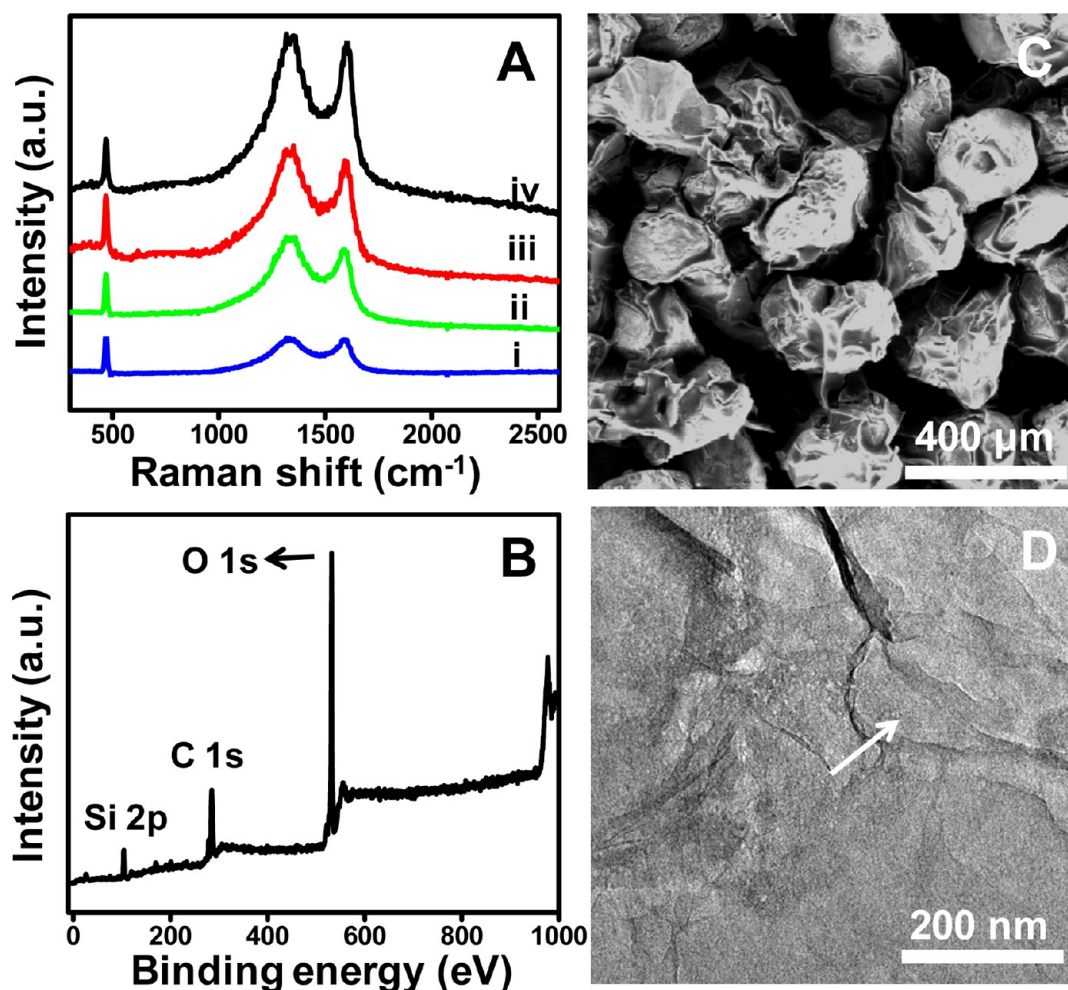


Figure 1. (A) Raman spectra of composites prepared under different conditions: (i) 250 °C in O₂ atmosphere, (ii) 450 °C in N₂ atmosphere, (iii) 600 °C in N₂ atmosphere, (iv) 750 °C in N₂ atmosphere. (B) XPS survey spectrum of GSC. (C) SEM images of graphene sand composite and (D) TEM image of extracted graphenic sheets.

To measure the adsorption capacity, a fixed-bed column was operated under down flow mode at a feed flow rate of 2.19 cm³/cm²/min and feed (R6G) concentration of 1 mg/L. The column was made by packing GSC₇₅₀ to different depth in a transparent glass tube with a length of 50 cm and an internal diameter of 8 mm. The performance of the column was evaluated as a function of time at room temperature. Residual concentration of the pollutant in the effluent samples was determined using UV–vis spectrophotometry. Similar column was packed for decolorizing colored matters from soft drinks. The column bed after exhaustion with pollutant was regenerated using acetone as eluent and was reused for three cycles.

RESULTS AND DISCUSSION

The experimental protocol is outlined in Scheme 1. After the sugar solution was dried on sand and slow carbonization at 200 °C, the material was rapidly heated to 750 °C, to ensure complete graphitization. This results in the formation of a strongly adhering char deposit on the sand surface. Washing with concentrated sulphuric acid produces the composite with higher adsorption sites. In Figure 1, we show the Raman spectrum of the 1 wt % GC loaded composite. We see the evolution of D and G bands as a function of carbonization temperature. The increase in peak intensity with increase in temperature suggests that the formation of graphenic material is better at higher temperatures. The occurrence of sharp G band at 1597 cm⁻¹ suggests complete graphitization of the material. The D band at 1338 cm⁻¹ suggests

the presence of defect sites needed for adsorption. No 2D feature was observed as typical of such chemically synthesized analogues of graphene.^{28,45} The optimum temperature is around 750 °C (N₂ atmosphere), where maximum peak intensity is observed. Upon heating the same material at 800 °C, adhesion to the surface becomes poor and the adsorption capacity decreases (see Figure S1A in Supporting Information). The optimum heating time was found to be 6 h. On increasing the heating time beyond 6 h, there was no further improvement in adsorption capacity (Supporting Information: Figure S1B). The peak at 470 cm⁻¹ is due to sand (SiO₂) present in the material, validating the name given (GSC). The peak corresponding to silica is completely masked at higher weight percent of carbon loading, as expected. Raman spectra of sand and sugar-coated sand are shown in Figure S2 of the Supporting Information.

The graphenic morphology is evident in the SEM images: thin sheets of carbon are protruding outward, as seen in Figure 1C. Thicknesses of these sheets are in nanometer regime. After sonicating GSC for 2 h in ethanol, the TEM images of the supernatant solution was taken. Now the images show the presence of nanometer-sized thin sheets (Figure 1D). Also seen are a few wrinkles at the edges which are characteristic of graphene-like material.^{32,43} An AFM image shows few layered graphenic material (Supporting Information, Figure S3A), the

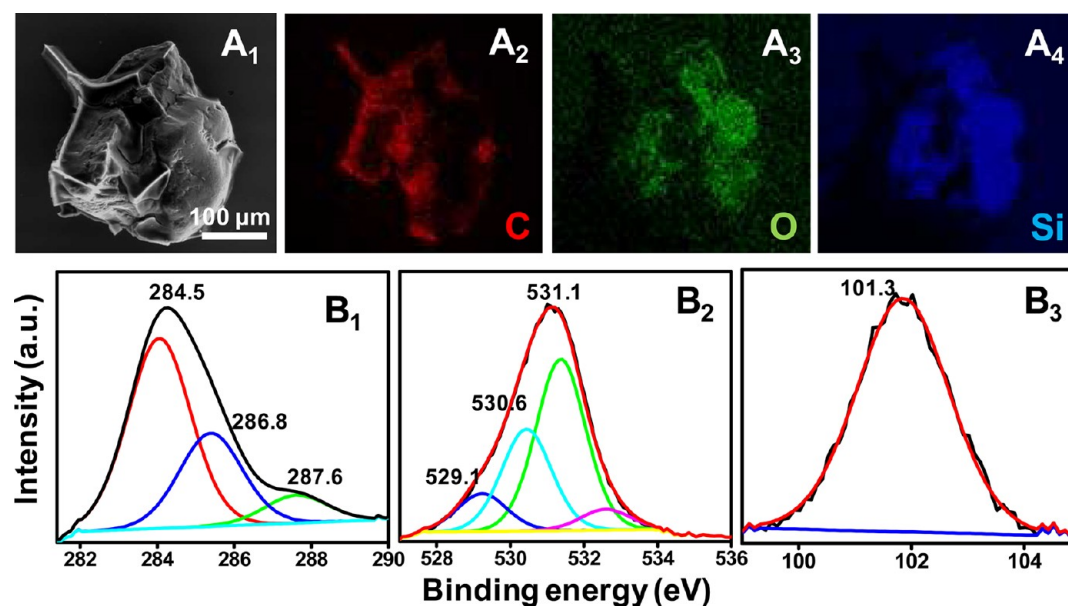


Figure 2. A₁ shows the SEM image of a single GSC particle. A₂, A₃ and A₄ are carbon, oxygen, and silicon maps of GSC. B₁, B₂, and B₃ show the deconvoluted XPS of carbon, oxygen and silicon, respectively.

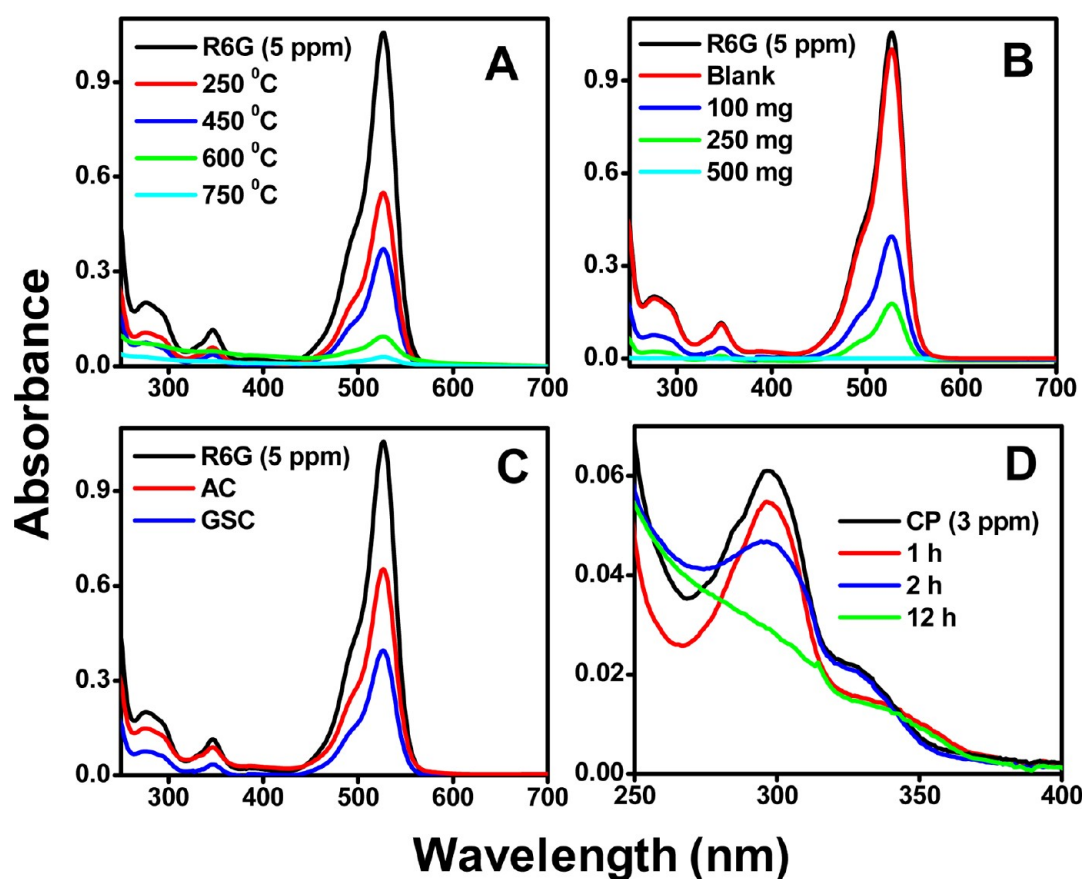


Figure 3. UV-vis spectra showing, (A) the extent of removal of R6G by different composites that were prepared by heating at different temperatures, (B) removal capacity, when different amounts of GSC₇₅₀ composite were added, (C) comparison of removal capacity among GSC₇₅₀ and AC, and (D) removal capacity of GSC₇₅₀ when CP was used as the contaminant.

height profile shows that the average thickness of the layers is 0.8 nm (Supporting Information, Figure S3B).

The physical appearance of the sand changes completely upon carbon loading (Scheme 1). The deposition of GC and its growth is visible in SEM images. The growth of carbon on SiO₂ surface is

evident on the elemental mapping. The elemental maps of GSC (Figure 2, A₁ to A₄) confirm the presence of C, O and Si. XPS is especially useful in understanding the chemical functionality of the material. For GSC, it shows all the expected elements: carbon, oxygen and silicon, as shown in the survey spectrum of

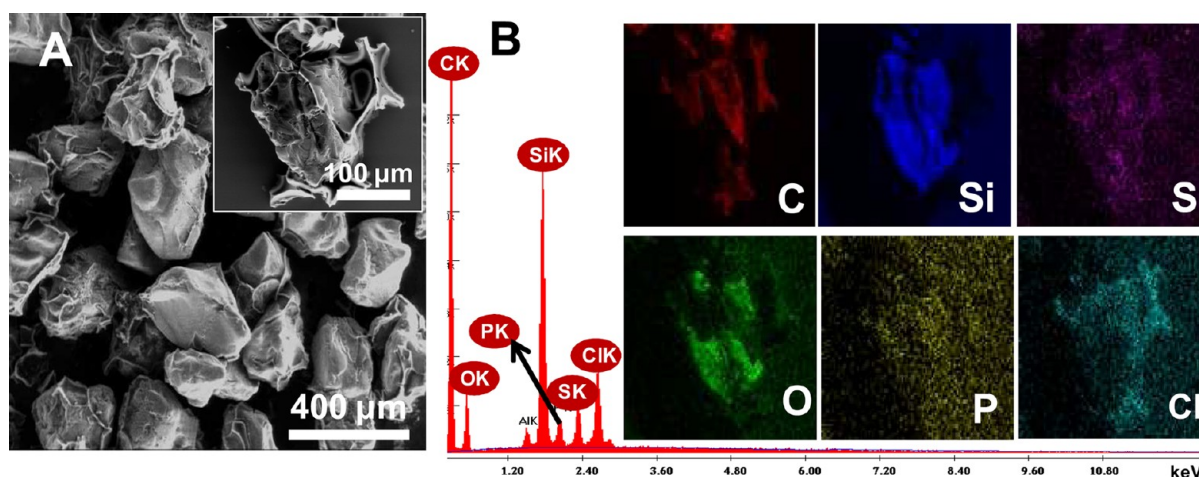


Figure 4. (A) SEM image of CP adsorbed on GSC₇₅₀. The inset shows the image of a single particle. (B) Elemental mappings of CP-adsorbed GSC₇₅₀.

the composite (Figure 1B). The existence of various functionalities is evident in the XPS spectrum. Figure 2 (B₁ to B₃) shows the deconvoluted peaks corresponding to carbon, oxygen and silicon in the spectrum. The presence of high percentage of nonoxygenated C 1s (peak centered at 284.5 eV) is a sign of extended carbon backbone. Oxygenated C as C–O (peak at 286.8 eV) is due to the presence of oxygen functionality. The presence of functional oxygen group is responsible for adsorption.^{46–48} Deconvolution of the O 1s spectrum gives three components: the first component centered around 531.1 eV, the second around 530.6 eV and the third around 529.1 eV, corresponding to C–O, C=O and O–C=O entities, respectively. The Si 2p peak is weak, as expected in view of the surface coverage. The peak is centered at 101.3 eV, expected for SiO₂. Similar features are observed at varying coverages (Figure S4 of the Supporting Information).

Batch experiment was conducted to assess the adsorption capacity of the material. As discussed earlier, the main focus of this work is effective and economically feasible removal of contaminants present in water. GSC turned out to be an excellent adsorbent for removal of such contaminants. To demonstrate this, we took R6G as the model dye and CP as the model pesticide. Figure 3A shows the removal capacity of composites prepared at different temperatures. Four different preparations were taken: Composites heated at (i) 250 °C in O₂ atmosphere, (ii) 450 °C, (iii) 600 °C, and (iv) 750 °C (all three in N₂ atmospheres). It was noticed that with equal amount of composite (500 mg) and GC loading (1 wt %), the sample prepared at 750 °C in N₂ atmosphere turned out to be the best adsorbent. So, we took this sample for further activation using sulphuric acid treatment to get GSC₇₅₀. The SEM image and elemental mapping of GSC₇₅₀ are shown in Figure S5 in Supporting Information. Previous studies have reported that the mechanism of dye adsorption on graphene is mainly π – π interaction.⁴⁹ The pollutant-removal capacity of the composite increases after activation. This conclusion was drawn after performing batch experiments with equal amounts of samples to remove R6G (5 ppm) (Figure S6 in Supporting Information). Figure 3B shows the adsorption capacity when different amounts of GSC₇₅₀ were used. It was seen that, for 500 mg, the sample completely removes R6G (5 mg/L) from 10 mL of solution in 2 h. A blank test was performed with river sand (500 mg) alone heated at 750 °C in nitrogen atmosphere which showed negligible removal capacity. Upon quantitative analysis (depicted

in Figure 3C), the adsorption capacity of GSC₇₅₀ for R6G was measured to be 55 mg/g, which is superior to that of activated carbon (32 mg/g). As AC cannot bind to the sand surface by itself, we used chitosan as a binder. The maximum adsorption capacity for R6G for AC was 44.7 mg/g under optimized condition, as found in the literature.⁵⁰ Figure 3D shows the removal capacity of GSC₇₅₀ when CP is used as the contaminant. 100 mg of the composite removes CP (3 ppm) completely from 10 mL of the solution in 12 h. CP has a characteristic absorption peak at 297 nm. The gradual decrease of intensity with time indicates that CP is being removed from water.

Adsorption of pollutant is evident from SEM results. Experiments were conducted with CP. SEM images (Figure 4A) show that the morphology of the substances does not change significantly after adsorption. Inset in Figure 4A shows a single particle on which elemental mapping was performed. From the mappings (Figure 4B), in CP-adsorbed composite, we see the presence of P and Cl, besides those present in original GSC₇₅₀ (shown in Supporting Information in Figure S5). This observation confirms that adsorption on GSC had indeed taken place. The P and Cl images overlap with Si and C images due to GSC₇₅₀.

The retention of the adsorbed species in the molecular form on the surface of GSC₇₅₀ is supported by laser desorption ionization mass spectrometry (LDI MS). The spectrum suggests the existence of the adsorbate in an integral form. No chemical transformation is observed. There was no prominent peak originating from the GSC₇₅₀, either in positive or negative mode (Figure S(i)). In Figure S(ii), the peak at m/z 444, observed for R6G adsorbed on GSC₇₅₀, represents the integral molecular ion, C₂₈H₃₁N₂O₃⁺. The other peak at m/z 415 corresponds to a fragmented product formed during LDI analysis by elimination of an ethyl group from R6G. The spectrum in the negative mode of LDI MS of CP adsorbed on GSC₇₅₀ has some characteristic peak at m/z 196 and 95 corresponding to C₃HCl₃NO[−] and (O₂PS)[−], respectively. The peak at m/z 324 is the fragmented product due to the elimination of C₂H₄ from the molecular ion peak at m/z 352. The peaks at m/z 587 and 613 are due to some fragmented dimers of CP. The structures of these most common fragments are shown in Figure 5. The XPS analysis of sample after adsorption of R6G is shown in Supporting Information in Figure S7, which shows that nitrogen due to R6G is present on the material. The N 1s features observed around 397.9 and 399.9 eV are due to two different chemical environments, under-

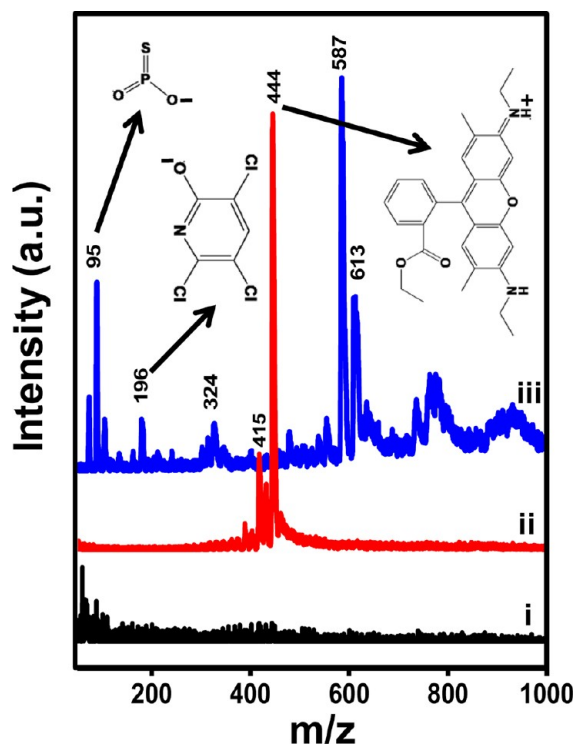


Figure 5. LDI MS spectra of (i) GSC₇₅₀, (ii) R6G-adsorbed GSC₇₅₀, and (iii) CP-adsorbed GSC₇₅₀. The structures of some of the ions detected are shown.

standable from the structure of R6G. The nitrogen peak for R6G adsorbed on GSC₇₅₀ was masked by the intense carbon peak in EDAX.

Performance of the material was tested in the column experiment as well. Figure 6 shows the photographs of two

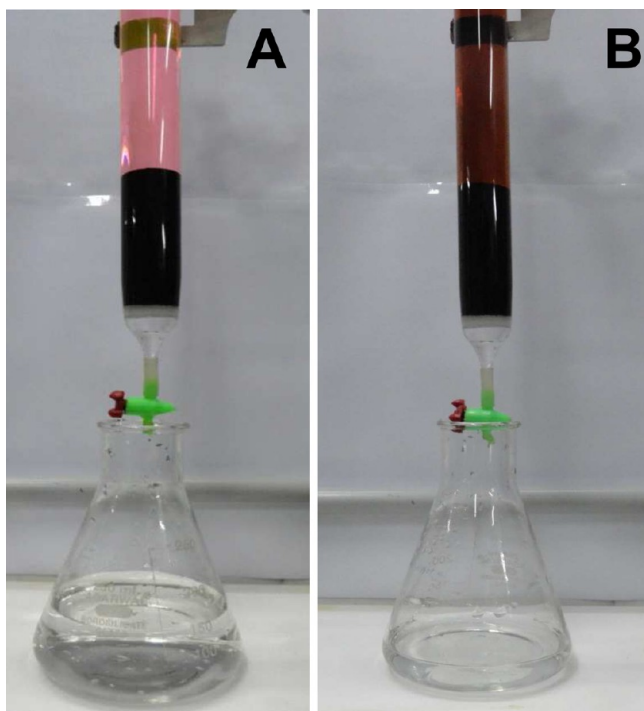


Figure 6. Photographs of adsorption columns using GSC₇₅₀ for separating (A) R6G from an aqueous solution and (B) coca cola.

columns packed with GSC₇₅₀ (1 wt % GC loading). The columns had a diameter of 2 cm and the bed height was 6 cm. Complete removal of the colored matter is evident from decolorization of the filtrate when the column was run with R6G and coca cola. Analysis of mass spectrum of the filtrate was carried out to confirm the presence/absence of R6G. No characteristic peaks of R6G fragments were seen. This observation ensures the complete removal of R6G.

The interaction between R6G and the adsorbent composite was investigated as a function of time using 100 mg of the adsorbent and 10 mL of 1 ppm R6G solution. The data are shown in Figure 7. From the results, it is apparent that the

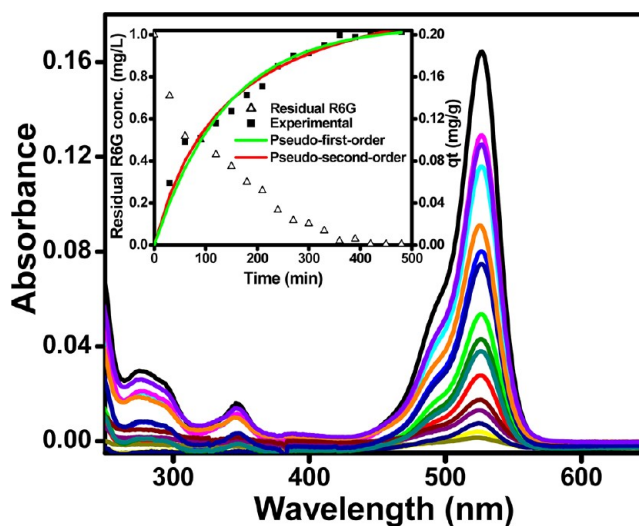


Figure 7. Kinetic study of the adsorption of R6G by GSC₇₅₀ in a batch experiment, time interval was 30 min. Inset shows the pseudofirst and pseudosecond order model fits (secondary axis); the primary axis of the inset figure shows the kinetic data obtained from the experiment.

composite could remove R6G completely in 8 h of contact time starting from the commencement of the adsorption process. During time-dependent study, the characteristic absorption peak at 527 nm corresponding to R6G was monitored. As a function of time, the intensity of the peak for the treated solution initially decreases rapidly and then the change in intensity slows down. This is because of the decreasing number of unoccupied adsorption sites with increasing time. After 8 h, the characteristic peak is absent, which emphasizes the complete removal of R6G from the solution. Thus, the equilibrium time was fixed at 8 h. The kinetic data were described by Lagergren pseudo-first-order^{51,52} and Ho's pseudo-second-order kinetic models.⁵³ The mathematical representations of these models are given elsewhere.⁵⁴ A nonlinear method was used to find the best-fitting model and kinetic parameters, which were found by trial and error method by means of Microsoft's spreadsheet, Excel software package using solver add-in option. The plots of model equation along with the experimental data are given in the inset of Figure 7. The suitability of the models to describe the data was examined using the chi square (χ^2) value. Smaller χ^2 value indicates better curve fitting. The analysis showed that a pseudo second-order equation is more appropriate in describing the experimental data.

Continuous Flow Experiments. Continuous flow experiments were conducted as a function of adsorbent bed depth to test the adsorption capacity and service time of the bed in removing R6G from water. The performance of the bed was

evaluated using the breakthrough curves (Figure 8A). The data obtained from the study are summarized in Table 1. As evident

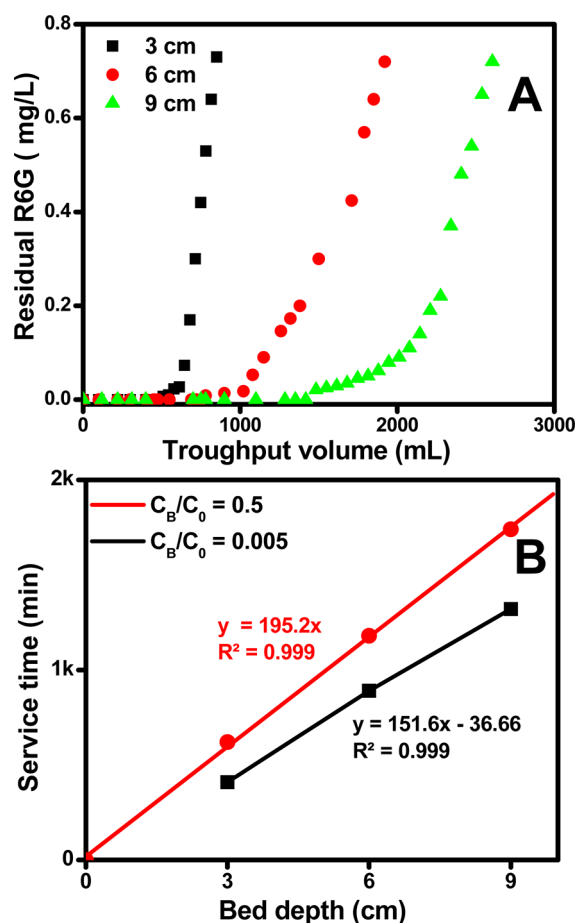


Figure 8. (A) Break through curve and (B) bed depth service time plots for the adsorption of R6G by GSC₇₅₀ in columns.

Table 1. Performance of Columns Packed with Graphene-Sand Composites at Different Bed Depths

bed depth, Z (cm)	empty bed contact time, t_{EB} (min)	breakthrough time, t_B (min)	throughput volume, V_{TB} (mL)	adsorption capacity (mg/g of carbon)
3	1.37	450	860	23.45
6	2.74	960	1950	24.55
9	4.11	1452	2706	26.63

from the figures, adsorption was affected by change in bed depth. Increase in bed depth increases the volume of treated water because of higher contact time and availability of more adsorption sites. At lower bed depths, the curve became steeper showing the quicker exhaustion of the fixed bed. A Bed Depth Service Time model (BDST) model, a successful method of analyzing data from column tests,⁵⁵ is generally used for predicting the performance of the adsorbent columns. The model gives a linear relationship between the time required to reach the desired breakthrough concentration (t_B) and the bed depth (Z), represented as

$$t_B = \frac{N_0}{C_0 U_0} Z - \frac{1}{K_{BD} C_0} \ln \left(\frac{C_0}{C_B} - 1 \right) \quad (2)$$

Here, N_0 is the saturation concentration per unit volume of bed (mg/L), C_0 is influent solute concentration (mg/L), C_B is the desired concentration of solute at breakthrough (mg/L), U_0 is the linear flow velocity (cm/min), and K_{BD} is the adsorption rate constant L/(mg min).

Figure 8B shows the plots of service time versus bed height for the adsorbent packed in column. From the results, it is clear that variation of service time with bed depth is linear, suggesting that this model is valid for predicting column performance at breakthrough point. The BDST parameters, namely, K_{BD} and N_0 , are 144.62 mg/cm³ and 0.33 cm³/mg/min, respectively ($C_B/C_0 = 0.005$). The corresponding N_0 value for 50% saturation points ($C_B/C_0 = 0.5$) is 0.43 cm³/mg/min. It is also evident that the calculated adsorption capacity at 50% saturation is greater than that at 0.5% saturation.

Regeneration and Reuse. Any adsorption process is economically more viable if the adsorbent can be regenerated and reused many times. Regeneration study will also give an insight into whether the material after use is safe for disposal or not. The present study focuses on developing a proper regeneration protocol for exhausted composite as well. For this, adsorption study was carried out with the as-synthesized adsorbent using 1 mg/L of R6G solution at neutral pH. The R6G-loaded GSC₇₅₀ was regenerated in situ in the columns using acetone as the eluent. The regenerant (acetone) was passed through the column at a flow rate of 1 mL/min. Nearly 30 bed volumes of acetone were passed through the column in down-flow mode. Samples of eluted acetone-R6G solution and the aqueous wash liquid were collected and analyzed for determining the concentrations of R6G as function of time. After complete desorption, the bed was purged with hot air (hair dryer was used for this purpose) to remove residual acetone in the bed. In order to test the feasibility of repeated use of the adsorbent bed, three consecutive adsorption/desorption cycles were performed. For a 3 cm column, the adsorption capacity was 23.45 mg/g (Table 1) for the first run, 22.78 mg/g for the second run and 22.07 mg/g for the third run. Note that the capacity given is from the column data which are generally lower than the equilibrium adsorption capacities derived from batch data. These results indicate that the material could be reused for several cycles without the performance of the material being adversely affected. SEM images of bare sand and the regenerated GSC₇₅₀ after first cycle are given in Supporting Information (Figure S8), which show that the morphology of GSC₇₅₀ does not change after regeneration.

CONCLUSION

We have established the synthesis of sugar-derived graphenic material supported on sand. Complete conversion of sugar to graphenic carbon suggests a green methodology for the creation of an active adsorbent material. We used R6G as the model dye and CP as the model pesticide, to show the adsorption capacity of the material. The batch experiment shows an adsorption capacity of 50–55 mg/g for R6G. The best capacity determined for R6G for AC under optimized condition was 44.7 mg/g.⁵⁰ The performance validates the use of this material as an active medium for commercial applications. The utilization of this material for water purification is evident from the data presented. The large adsorption capacity, green methodology and the availability of the materials across the world enables it to be used in different parts of the world. Materials of this kind are expected to contribute to developing affordable solutions for drinking water.

■ ASSOCIATED CONTENT

■ Supporting Information

UV-vis spectra pertaining to the optimization of heating time and temperature, Raman spectra of sand and sugar coated sand, AFM image and height profile of the graphenic material, XPS of GSC at different carbon loading, SEM and EDAX of GSC after acid wash, UV-vis spectrum showing GSC after acid wash, XPS analyses of R6G-adsorbed GSC₇₅₀ and SEM image of sand and GSC₇₅₀ after regeneration. This information is available free of charge via the Internet at <http://pubs.acs.org/>.

■ AUTHOR INFORMATION

Corresponding Author

*E-mail: pradeep@iitm.ac.in. Fax: 91-44-2257-0545/0509.

Notes

The authors declare no competing financial interest.

■ ACKNOWLEDGMENTS

We thank the Nanoscience and Nano Mission of the Department of Science and Technology (DST), Government of India, for supporting the research program. SSG thanks the UGC for a research fellowship.

■ REFERENCES

- (1) Litter, M. I.; Choi, W.; Dionysiou, D. D.; Falaras, P.; Hiskia, A.; Li Puma, G.; Pradeep, T.; Zhao, J. *J. Hazard. Mater.* **2012**, *211*–212, 1–2.
- (2) Pradeep, T.; Anshup. *Thin Solid Films* **2009**, *517*, 6441–6478.
- (3) Gupta, R.; Kulkarni, G. U. *ChemSusChem* **2011**, *4*, 737–743.
- (4) Matheson, L. J.; Tratnyek, P. G. *Environ. Sci. Technol.* **1994**, *28*, 2045–2053.
- (5) Bootharaju, M. S.; Pradeep, T. *Langmuir* **2012**, *28*, 2671–2679.
- (6) Zhang, S.; Li, X.-y.; Chen, J. P. *Carbon* **2010**, *48*, 60–67.
- (7) Novoselov, K. S.; Geim, A. K.; Morozov, S. V.; Jiang, D.; Zhang, Y.; Dubonos, S. V.; Grigorieva, I. V.; Firsov, A. A. *Science* **2004**, *306*, 666–669.
- (8) Anonymous. *Lancet* **1912**, *180*, 1025–1026.
- (9) Adams, B. A. *Lancet* **1932**, *219*, 724–724.
- (10) Kämpf, H. J. *Water Res.* **1972**, *6*, 493–494.
- (11) Goyal, M.; Bhagat, M.; Dhawan, R. *J. Hazard. Mater.* **2009**, *171*, 1009–1015.
- (12) Hager, D. G. *Environ. Sci. Technol.* **1967**, *1*, 287–291.
- (13) Ghosh, P. K.; Philip, L. J. *Environ. Sci. Health, Part B* **2005**, *40*, 425–441.
- (14) Zhang, H.; Zhu, G.; Jia, X.; Ding, Y.; Zhang, M.; Gao, Q.; Hu, C.; Xu, S. *J. Environ. Sci.* **2011**, *23*, 1983–1988.
- (15) Semião, A. J. C.; Schäfer, A. I. *J. Membr. Sci.* **2011**, *381*, 132–141.
- (16) Al-Rifai, J. H.; Khabbaz, H.; Schäfer, A. I. *Sep. Purif. Technol.* **2011**, *77*, 60–67.
- (17) Geim, A. K.; Novoselov, K. S. *Nat. Mater.* **2007**, *6*, 183–191.
- (18) Demirbas, A. *J. Hazard. Mater.* **2009**, *167*, 1–9.
- (19) Duran, A.; Tuzen, M.; Soylak, M. *J. Hazard. Mater.* **2009**, *169*, 466–471.
- (20) Yang, S.; Li, J.; Shao, D.; Hu, J.; Wang, X. *J. Hazard. Mater.* **2009**, *166*, 109–116.
- (21) Ruparelia, J. P.; Duttgupta, S. P.; Chatterjee, A. K.; Mukherji, S. *Desalination* **2008**, *232*, 145–156.
- (22) Zabihi, M.; Ahmadpour, A.; Asl, A. H. *J. Hazard. Mater.* **2009**, *167*, 230–236.
- (23) Matsui, Y.; Fukuda, Y.; Inoue, T.; Matsushita, T. *Water Res.* **2003**, *37*, 4413–4424.
- (24) Artiles, M. S.; Rout, C. S.; Fisher, T. S. *Adv. Drug Delivery Rev.* **2011**, *63*, 1352–1360.
- (25) Balapanuru, J.; Yang, J.-X.; Xiao, S.; Bao, Q.; Jahan, M.; Polavarapu, L.; Wei, J.; Xu, Q.-H.; Loh, K. P. *Angew. Chem., Int. Ed.* **2010**, *49*, 6549–6553.

- (26) Min, S. K.; Kim, W. Y.; Cho, Y.; Kim, K. S. *Nat. Nanotechnol.* **2011**, *6*, 162–165.
- (27) Gao, W.; Majumder, M.; Alemany, L. B.; Narayanan, T. N.; Ibarra, M. A.; Pradhan, B. K.; Ajayan, P. M. *ACS Appl. Mater. Interfaces* **2011**, *3*, 1821–1826.
- (28) Sreeprasad, T. S.; Maliyekkal, S. M.; Lisha, K. P.; Pradeep, T. *J. Hazard. Mater.* **2011**, *186*, 921–931.
- (29) Chandra, V.; Kim, K. S. *Chem. Commun.* **2011**, *47*, 3942–3944.
- (30) Chandra, V.; Park, J.; Chun, Y.; Lee, J. W.; Hwang, I.-C.; Kim, K. S. *ACS Nano* **2010**, *4*, 3979–3986.
- (31) Imamoglu, M.; Tekir, O. *Desalination* **2008**, *228*, 108–113.
- (32) Mishra, A. K.; Ramaprabhu, S. *Desalination* **2011**, *282*, 39–45.
- (33) Zabihi, M.; Ahmadpour, A.; Asl, A. H. *J. Hazard. Mater.* **2009**, *167*, 230–236.
- (34) Li, J.; Guo, S.; Zhai, Y.; Wang, E. *Electrochem. Commun.* **2009**, *11*, 1085–1088.
- (35) Yang, S.; Luo, S.; Liu, C.; Wei, W. *Colloids Surf., B* **2012**, DOI: 10.1016/j.colsurfb.2012.03.007.
- (36) Ayhan, D. *J. Hazard. Mater.* **2009**, *167*, 1–9.
- (37) Bradder, P.; Ling, S. K.; Wang, S.; Liu, S. *J. Chem. Eng. Data* **2010**, *56*, 138–141.
- (38) Wang, C.; Feng, C.; Gao, Y.; Ma, X.; Wu, Q.; Wang, Z. *Chem. Eng. J.* **2011**, *173*, 92–97.
- (39) Soylak, M.; Unsal, Y. E.; Yilmaz, E.; Tuzen, M. *Food Chem. Toxicol.* **2011**, *49*, 1796–1799.
- (40) Stankovich, S.; Dikin, D. A.; Dommett, G. H. B.; Kohlhaas, K. M.; Zimney, E. J.; Stach, E. A.; Piner, R. D.; Nguyen, S. T.; Ruoff, R. S. *Nature* **2006**, *442*, 282–286.
- (41) Gu, H.; Yu, Y.; Liu, X.; Ni, B.; Zhou, T.; Shi, G. *Biosens. Bioelectron.* **2012**, *32*, 118–126.
- (42) Maliyekkal, S. M.; Lisha, K. P.; Pradeep, T. *J. Hazard. Mater.* **2010**, *181*, 986–995.
- (43) Sreeprasad, T. S.; Maliyekkal, M. S.; Deepti, K.; Chaudhari, K.; Xavier, P. L.; Pradeep, T. *ACS Appl. Mater. Interfaces* **2011**, *3*, 2643–2654.
- (44) Ruan, G.; Sun, Z.; Peng, Z.; Tour, J. M. *ACS Nano* **2011**, *5*, 7601–7607.
- (45) Ruiz-Hitzky, E.; Darder, M.; Fernandes, F. M.; Zatile, E.; Palomares, F. J.; Aranda, P. *Adv. Mater.* **2011**, *23*, S250–S255.
- (46) Warta, C. L.; Papadimas, S. P.; Sorial, G. A.; Suidan, M. T.; Speth, T. F. *Water Res.* **1995**, *29*, 551–562.
- (47) Yu, F.; Ma, J.; Wu, Y. *J. Hazard. Mater.* **2011**, *192*, 1370–1379.
- (48) Derylo-Marczewska, A.; Buczek, B.; Swiatkowski, A. *Appl. Surf. Sci.* **2011**, *257*, 9466–9472.
- (49) Liu, F.; Chung, S.; Oh, G.; Seo, T. S. *ACS Appl. Mater. Interfaces* **2011**, *4*, 922–927.
- (50) Annadurai, G.; Juang, R.-S.; Lee, D.-J. *J. Environ. Sci. Health, Part A* **2001**, *36*, 715–725.
- (51) Lagergren, S. *K. Sven. Ventenskapsakad. Handl.* **1898**, *24*, 1–39.
- (52) Yuh-Shan, H. *Scientometrics* **2004**, *59*, 171–177.
- (53) Ho, Y. S.; McKay, G. *Water Res.* **2000**, *34*, 735–742.
- (54) Lisha, K. P.; Maliyekkal, S. M.; Pradeep, T. *Chem. Eng. J.* **2010**, *160*, 432–439.
- (55) Hutchins, R. A. *Chem. Eng. J.* **1973**, *80*, 133–138.

Supporting information

Graphene from Sugar and its Application in Water Purification

Soujit Sen Gupta¹, Theruvakkattil Sreenivasan Sreeprasad¹, Shihabudheen Mundampra Maliyekkal², Sarit Kumar Das³ and Thalappil Pradeep^{1}*

*¹DST Unit on Nanoscience, Department of Chemistry,
Indian Institute of Technology Madras, Chennai - 600 036, India*

*²School of Mechanical and Building Sciences,
VIT University, Chennai Campus, Chennai-600 048, India*

*³Department of Mechanical Engineering,
Indian Institute of Technology Madras, Chennai - 600036, India*

**Email: pradeep@iitm.ac.in; Fax: 91-44-2257-0545/ 0509*

Supporting information 1

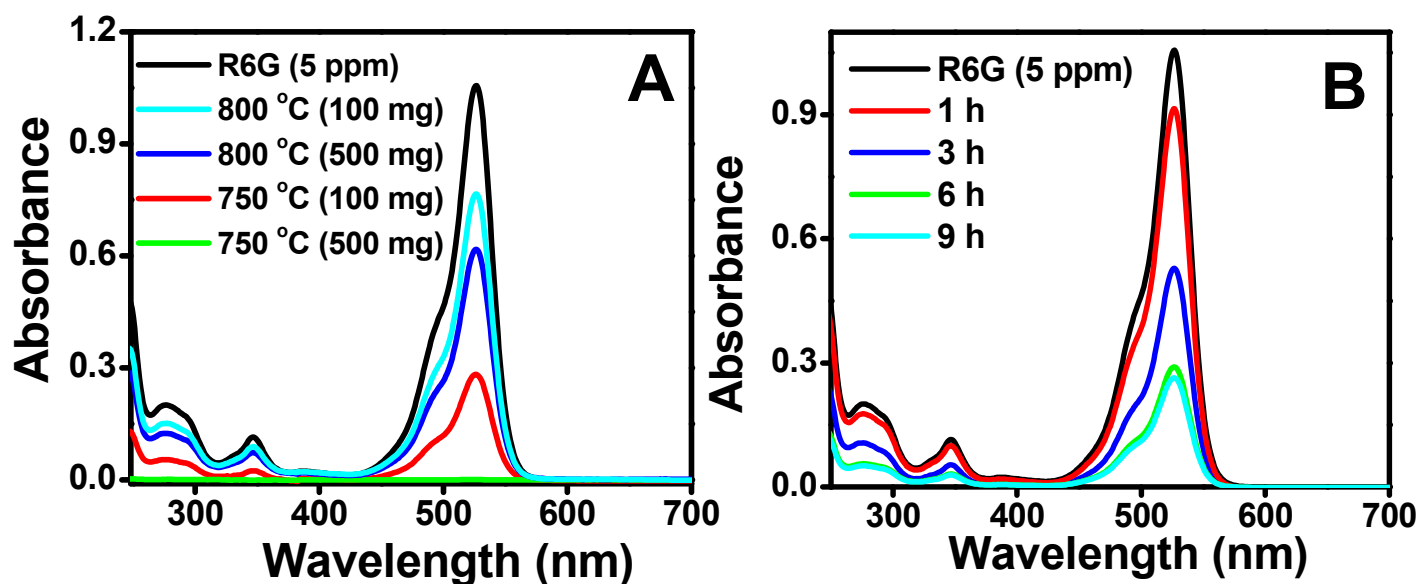


Figure S1: A) Optimization of heating temperature. B) Optimization of heating time.

The prepared material (GSC) shows better adsorption capacity at 750 °C, as shown in Figure 3A in the manuscript. Further heating this material to 800 °C, reduces its adsorption capacity. In this Figure S 1A, it can be seen that 500 mg of GSC₇₅₀ removes 5 ppm of R6G completely, whereas, the same amount of sample prepared at 800 °C is unable to do so. Therefore, the optimum temperature is taken as 750 °C. During preparation of the material GSC₇₅₀, heating time was important to optimize. In the Figure S 1B, it can be seen that the adsorption capacity increases when the time for graphitization is increases from 1 h to 3 h and further increases for sample heated for 6 h, but there is no significant change in adsorption capacity when the material was heated for 9 h. Therefore, the optimum heating time was concluded to be 6 h.

Supporting information 2

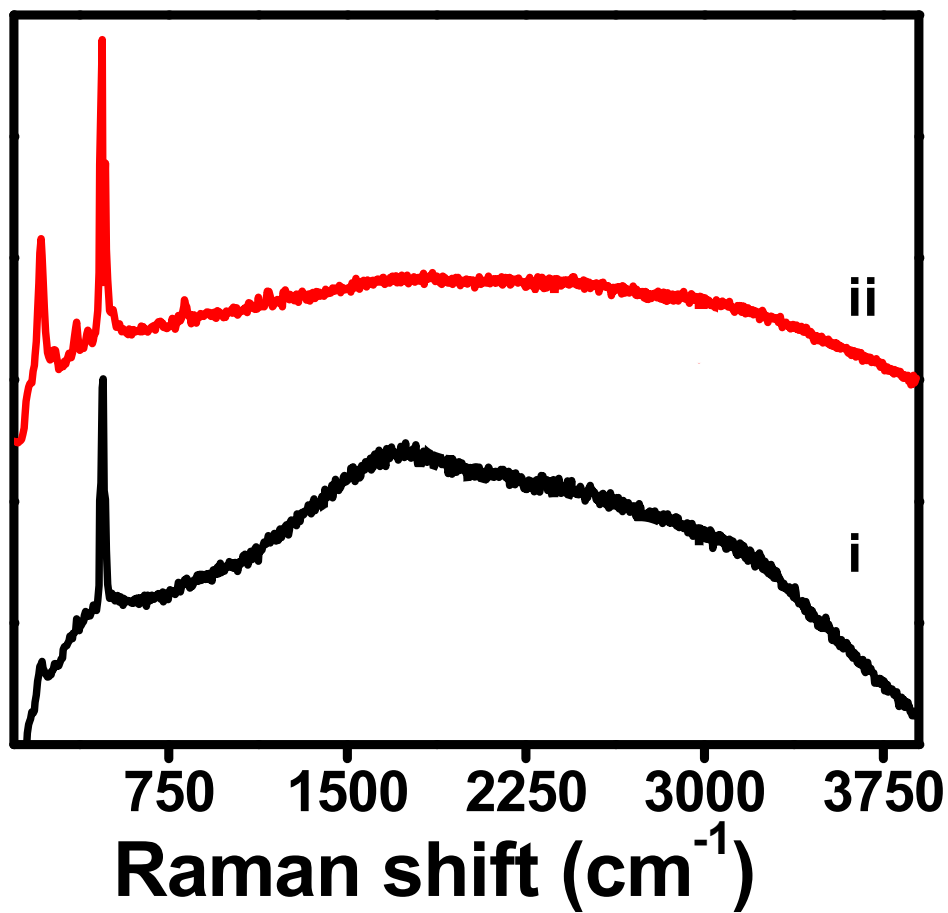


Figure S2: Raman spectra of (i) sand and (ii) sugar coated sand showing an intense peak at 470 cm^{-1} corresponding to Si-O stretching.

Supporting information 3

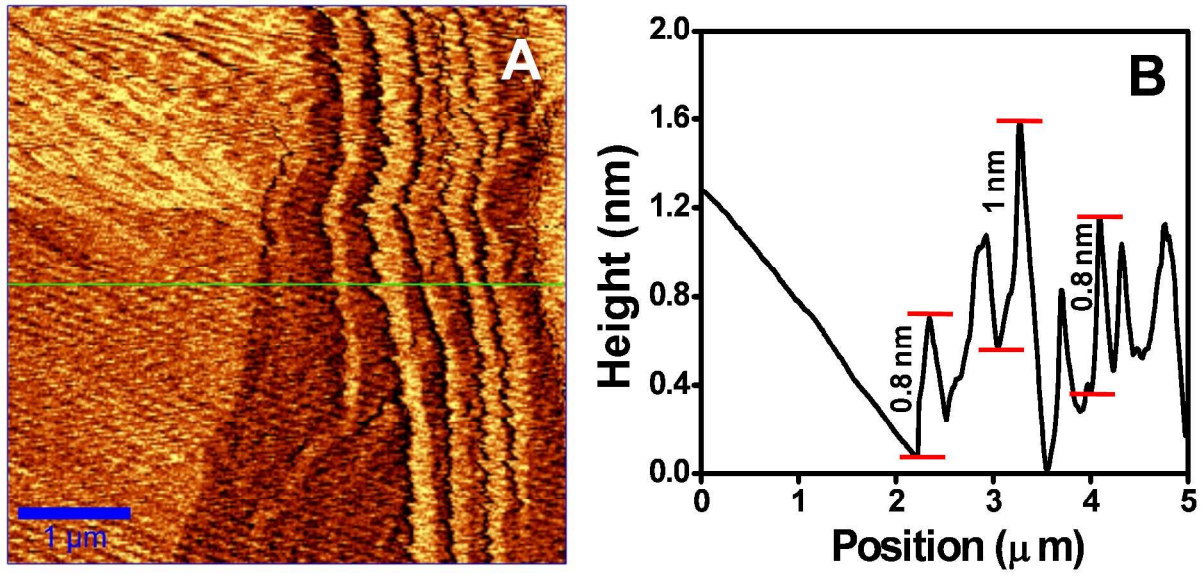


Figure S3: A) AFM image of extracted graphene and B) the height profile showing few layered graphene.

Supporting information 4

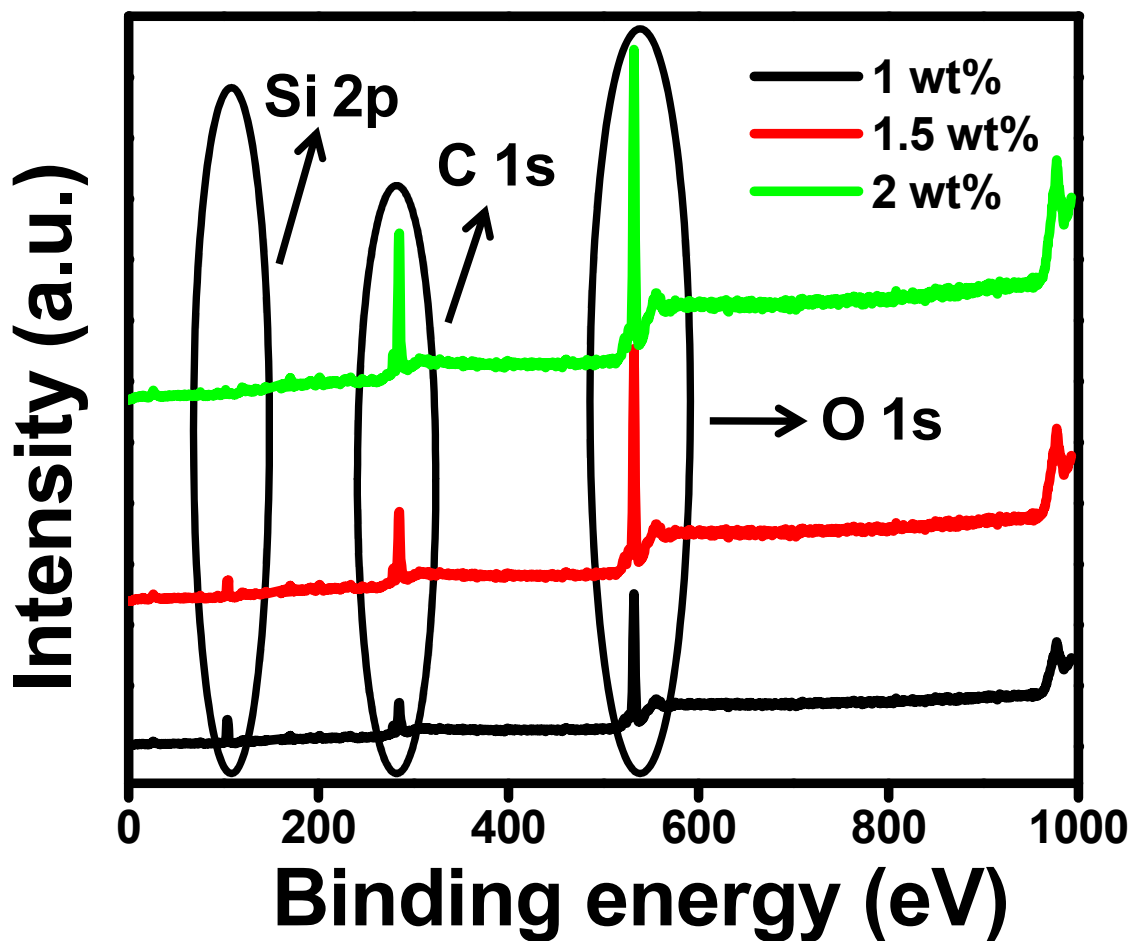


Figure S4: XPS of GSC at different carbon loadings. With the increase in the loading from 1% to 2%, it is clearly seen that the C 1s and O 1s peak intensities increase, whereas, the intensity of Si 2p peak decreases. The disappearance of Si 2p peak at 2% loading indicates complete masking by carbon.

Supporting information 5

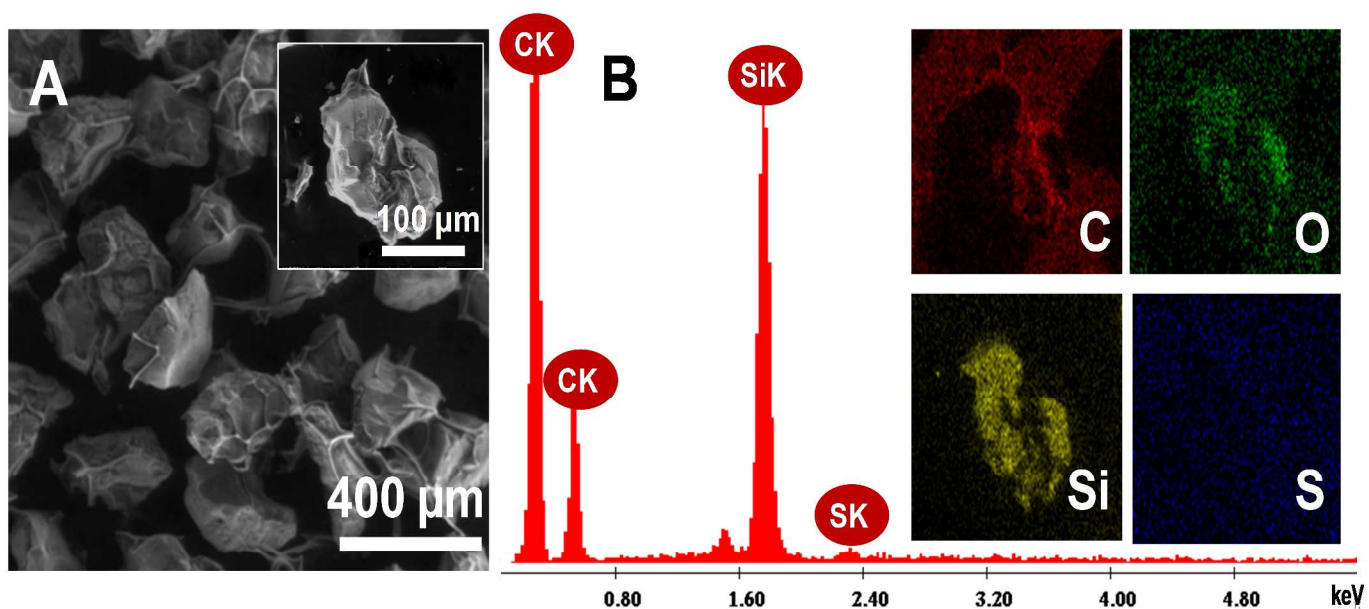


Figure S5: (A) SEM image of GSC after acid wash. Inset shows the image of a single particle.
(B) EDAX and elemental mappings.

On comparing Figure S 5A with Figure 1C, we see that there is no change in morphology after treatment with concentrated sulphuric acid. A small amount of sulphur is incorporated into the sample after acid wash which probably leads to activation of the sample.

Supporting information 6

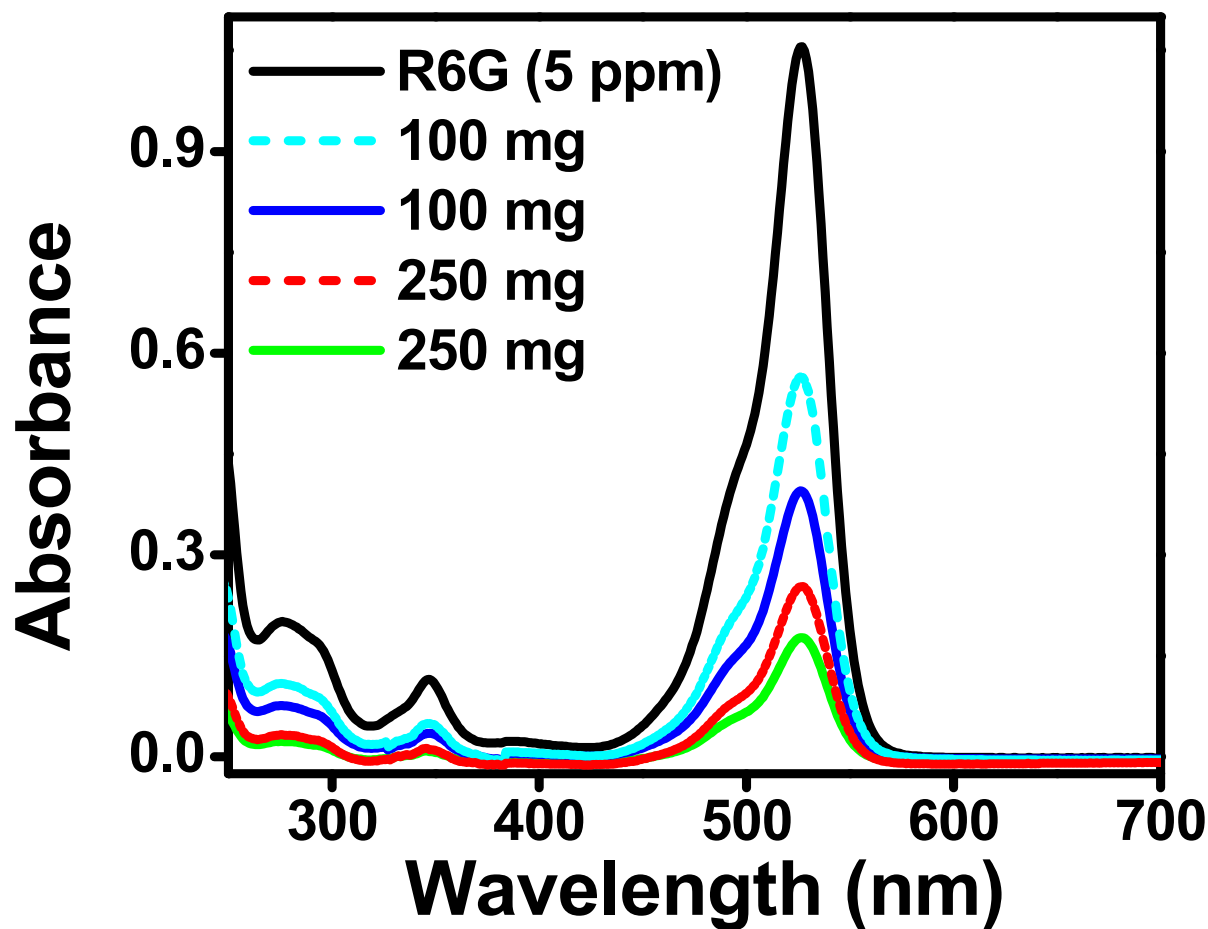


Figure S6: UV/Vis. absorption spectra of R6G left in solution after treating the test solution with GSC. Dotted lines: After treatment with as-prepared GSC. Solid lines: After treatment with acid-washed GSC. Black line: The test solution before treatment. We infer that the adsorption capacity of GSC improves after acid wash.

Supporting information 7

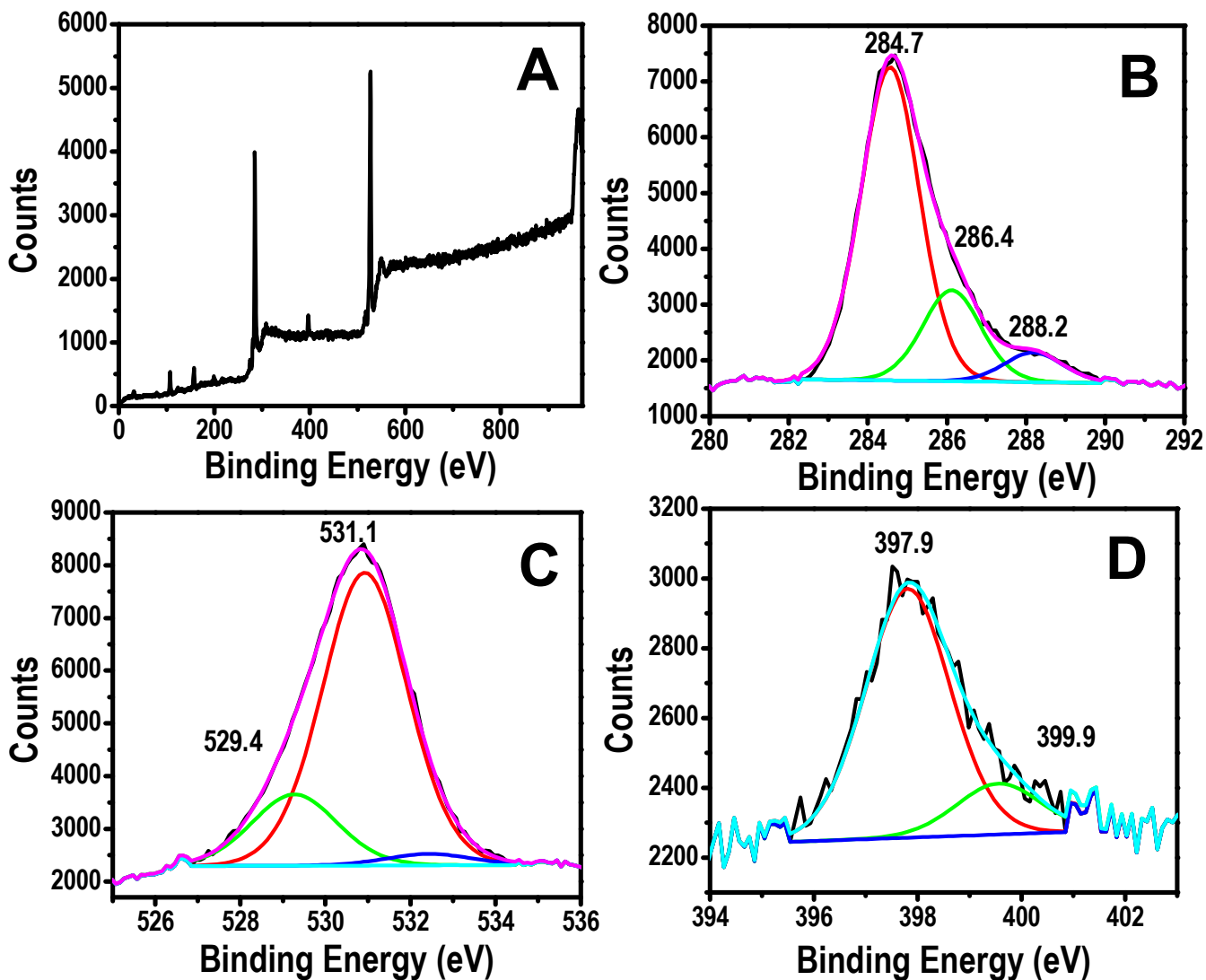


Figure S7: XPS analyses of R6G-adsorbed GSC₇₅₀. (A) shows the survey spectrum. B, C and D show the deconvoluted XPS of C 1s, O 1s and N 1s regions, respectively. N 1s is absent in the parent material, see for example Figure 1B.

Supporting information 8

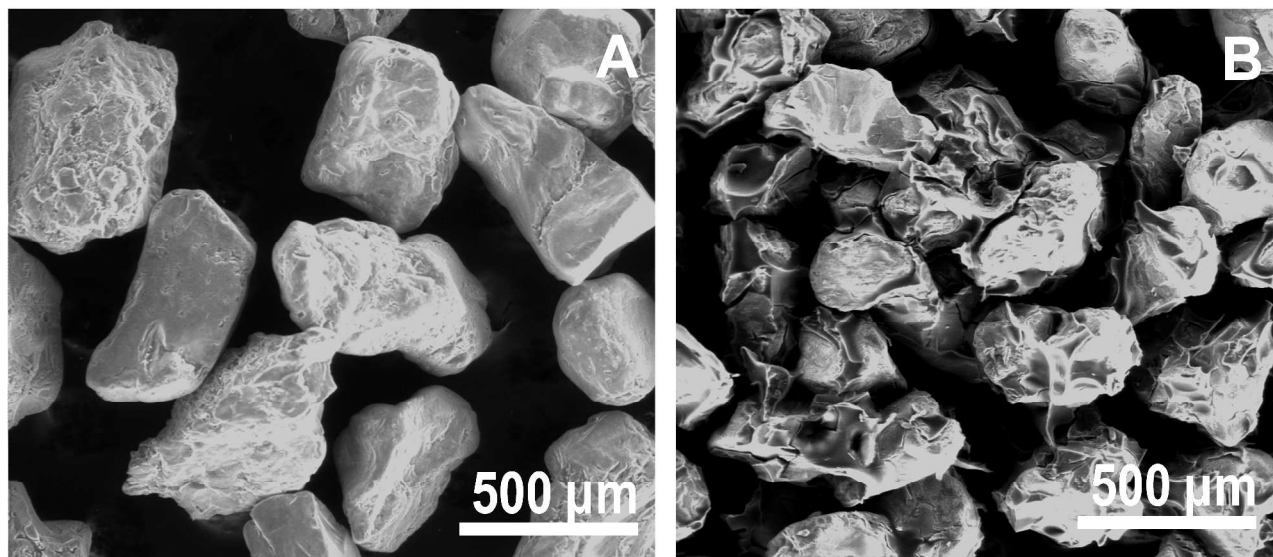


Figure S8: SEM images of (A) sand and (B) GSC₇₅₀ after removal of R6G by treatment with acetone.

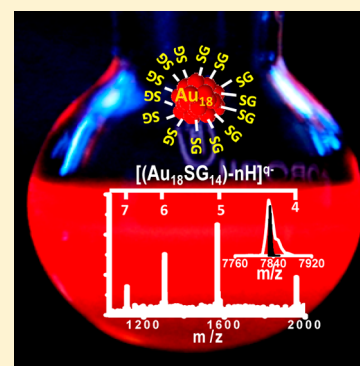
One-Step Route to Luminescent $\text{Au}_{18}\text{SG}_{14}$ in the Condensed Phase and Its Closed Shell Molecular Ions in the Gas Phase

Atanu Ghosh, Thumu Udayabhaskararao, and Thalappil Pradeep*

DST Unit of Nanoscience (DST UNS) Department of Chemistry, Indian Institute of Technology Madras, Chennai 600 036, India

S Supporting Information

ABSTRACT: We report a one-step route for the synthesis of highly luminescent and water-soluble $\text{Au}_{18}\text{SG}_{14}$ (SG- glutathione in thiolate form) in nearly pure form using a slow reduction process. The cluster shows step-like behavior in its absorption profile. It emits red light in both aqueous and solid state under UV illumination. Quantum yield of the cluster is 0.053, nearly 25-fold higher than that of $\text{Au}_{25}\text{SG}_{18}$. The cluster exhibits distinct features corresponding to multiply charged ions in electrospray ionization mass spectrometry. This composition is also confirmed from MALDI MS along with other quantitative analyses. The cluster makes closed shell molecular ions in the gas phase. The possibility of making clusters of different core sizes is also demonstrated. The simplicity of this method and identification of the cluster with exact composition may facilitate the exploration of experimental and theoretical research on this material.



SECTION: Physical Processes in Nanomaterials and Nanostructures

Development of noble metal quantum clusters (QCs) of atomically precise composition^{1–10} is necessary to explore their new applications in diverse areas such as catalysis,^{11–15} biomedicine,^{16–19} and nanoelectronics.²⁰ As properties of QCs vary with each atom added, it is important to obtain samples with high purity. However, several synthetic methods produce mixtures of clusters, and subsequent purification is necessary in order to separate a specific QC.²¹ Direct synthesis of clusters of specific nuclearity in macroscopic quantities is important to understand their unique properties. Impressive achievements have been accomplished to obtain $\text{Au}_{25}\text{SG}_{18}$ (SG, glutathione thiolate) clusters directly by a variety of methods.^{2,22,23} As a result, it is the most intensely studied cluster in this category.^{22–28} However, single-step methods to make sizable quantities of specific Au_nSG_m ($n = 10, 15, 18, 29, 33$) clusters are yet to be developed so that their properties can be explored. Herein, we report a one-step route for the synthesis of an atomically precise cluster, $\text{Au}_{18}\text{SG}_{14}$ in the hundreds of milligrams scale. Besides characterizing the clusters by diverse tools, we examine their closed shell molecular ions in the gas phase. We show that the cluster ions with their monolayers behave similarly to closed-shell systems.^{29,30}

We use the concept that the core sizes of the clusters are generally determined by the relative rates of nucleation and growth, controlled by the reducing capability of the reagent used. In organic synthesis, sodium cyanoborohydride (NaBH_3CN) is used as a mild and selective reducing agent, whereas the typical reagent, NaBH_4 , is strong and less selective.³¹ A mild and selective reducing agent can help slow down nucleation and retard the growth of the nuclei, which may result in the direct formation of smaller Au:SG QCs.

Following this idea, an aqueous solution of NaBH_3CN was injected rapidly into a methanolic solution of Au^{+} -SG polymers (details in the methods section). The resulting precipitate was collected and washed repeatedly with methanol to remove the remaining starting precursors, yielding a clear solution showing well-defined optical absorption features (Figure 1A) and characteristic color (Figure 1B). Excitation and emission spectra of the solution are shown in the inset of Figure 1A. The solution was freeze-dried to get a pale red powder (insets of Figure 1B), characterized as $\text{Au}_{18}\text{SG}_{14}$. Purity of the cluster is the most important aspect of this direct synthesis.

Polyacrylamide gel electrophoresis (PAGE, details in the methods section) of the cluster showed principally one band (Figure 1C), which confirmed the formation of a single cluster. To ensure the absence of other clusters, high-resolution PAGE was performed with 35% gel concentration. However, we did not observe any additional band, suggesting that no other cluster was formed in detectable quantities. The formula, $\text{Au}_{18}\text{SG}_{14}$, and the purity of the QC were confirmed based on mass spectrometry (MS), including electrospray ionization (ESI) and matrix-assisted laser desorption ionization (MALDI) methods (presented below). The as-synthesized cluster is stable for months in the solid state as well as in the aqueous medium at ice-cold temperatures. The synthetic method is highly robust and is reproduced without adhering to stringent conditions of temperature, purity of materials, and so forth (which are

Received: June 7, 2012

Accepted: July 12, 2012

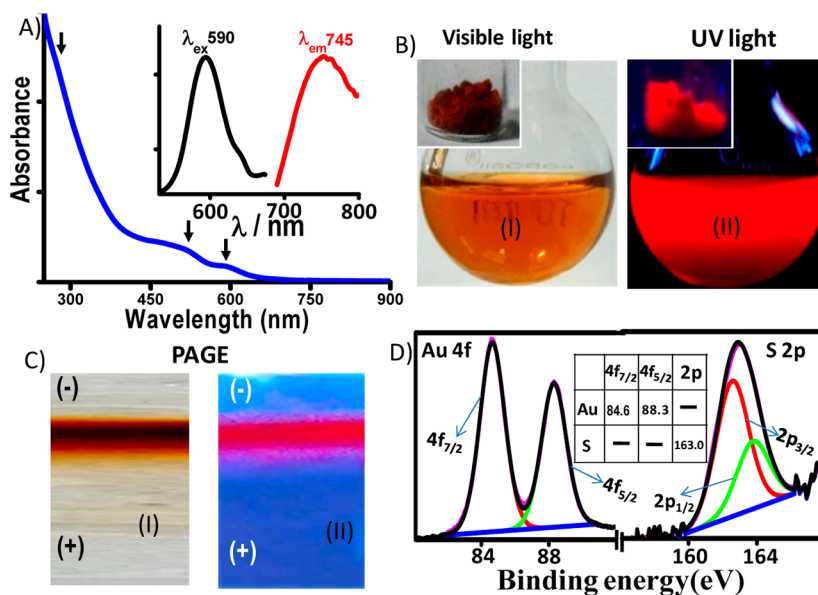


Figure 1. (A) UV-vis spectrum of the as-synthesized cluster. The spectrum shows dominant step-like behavior. Arrows indicate the well-defined optical features of the cluster. Inset: Luminescence spectrum (excitation and emission) of the cluster in water at 25 °C. (B) (I) photographs of the cluster solution in water and solid powder obtained by lyophilization of the solution (inset), in visible light, and (II) the same photographs under UV light. (C) (I) PAGE band of the cluster showing the presence of a single band, and (II) the same under UV light. The pink shade on either side of the band is due to the band edges with reduced concentration and not due to another cluster. (D) Photoelectron spectra of Au and sulfur with multiple components due to spin-orbit splitting. Peaks are fitted after background subtraction. Insets: Table presenting the BE values of gold and sulfur.

important in several QCs). The yield of the cluster in terms of Au is 61%, starting from 150 mg of $\text{HAuCl}_4 \cdot 3\text{H}_2\text{O}$. Note that the synthesis involves a lower Au:GSH (1:2.5) ratio than the standard (1:4) used to make a mixture of clusters.²² The optical absorption spectrum of the as-prepared cluster shown in Figure 1A shows a step-like, multiple-band spectrum, which is usual for gold QCs. The most prominent absorption band is centered at 590 nm (2.1 eV); additional spectral features include a broad band at 515 nm (2.4 eV) and another band in the UV region at 290 nm (4.2 eV); all of these match with the recent results of Tlahauc and Garzon, who reported first-principle calculations on $\text{Au}_{18}\text{SG}_{14}$, according to which the Au_8 core is decorated by two $-\text{[S-Au-S-Au-S-Au-S]}-$ and two $-\text{[S-Au-S-Au-S]}-$ staples in the lowest energy structure.³² The molecular orbitals responsible for optical transitions are not purely from the Au_8 core but formed due to the combination of atomic orbitals of Au_{core} , S, and $\text{Au}_{\text{staple}}$.³² The higher wavelength peak at 590 nm is blue-shifted compared to Au_{25} ,² Au_{23} ,³³ Au_{22} ,⁹ and Au_{20} ,⁸ which show absorptions in the range of 600–800 nm, as expected from its smaller core size. Cluster in aqueous medium shows excitation at 590 nm (matching with the absorption maximum) and emission at 745 nm (insets of Figure 1A). $\text{Au}_{18}\text{SG}_{14}$ exhibits observable luminescence in the aqueous medium as well as in the solid state (images in Figure 1B). Cluster in the aqueous medium exhibits enhanced luminescence as compared to bigger QCs such as Au_{25} , where emission is difficult to be photographed in the aqueous medium. The measured quantum yield of the cluster is 5.3×10^{-2} at room temperature, using rhodamine 6G as the reference. This is ~ 25 -fold higher than that of $\text{Au}_{25}\text{SG}_{18}$ (quantum yield, 1.9×10^{-3}).⁹

All the expected elements are present in the cluster, which is confirmed from the XPS survey spectrum (Figure S1, Supporting Information). The binding energy (BE) is calibrated with respect to C1s at 284.6 eV. The photoelectron spectra in the Au 4f and S 2p regions are presented in Figure

1D. The expected Au 4f_{7/2} BEs of the Au(I)-thiolate complex and Au(0) film are 86.0 and 84.0 eV, respectively. The measured Au 4f_{7/2} BE of the cluster is 84.6 eV. This suggests the presence of a nearly Au(0) core, which is expected for smaller gold clusters.^{9,21} The S 2p_{3/2} BE is 163.0 eV, characteristic of thiolate ligand. It is important to note that the luminescent Au_{18} thiocrown ether and similar systems are different from the present cluster, and they belong to the category of metal complexes.^{34,35} Au_{18} thiocrown gave absorption features at 328 and 346 nm and emission at 500 nm.³⁴ As the core dimension is small, the clusters appear as tiny dots of <1 nm and are barely observable in transmission electron microscopy (TEM). Upon longer electron beam irradiation, they aggregate to form nanoparticles (Figure S2), which is already known in the case of clusters.^{36,37}

For finding the molecular formula of the cluster, we used ESI MS. A 50% (v/v) water/methanol solution of the as-prepared cluster with a concentration of 0.1 mg/mL was used for ESI. At higher capillary temperatures, dissociation of the intact cluster into smaller fragments occurred, and species such as $[\text{Au}(\text{SG})\text{-H}]^{1-}$ and $[\text{Au}_2(\text{SG})_2\text{-H}]^{1-}$ were observed. In order to obtain the spectrum, an optimized capillary temperature (ca. 150 °C) was applied so that efficient solvent evaporation took place, leading to the formation of desolvated clusters in larger numbers.²¹ Detailed mass analyses were conducted with ESI MS to know the composition of the cluster. It is known that Au:SG cluster contains negative charge in the aqueous state since most of the carboxyl groups of the GSH ligands tend to be dissociated. The acid dissociation constants of the two carboxyl groups of free GSH are 2.56 and 3.50.³⁸ As expected, the negative-ion ESI mass spectrum is comprised of a series of peaks associated with multiply charged anions due to the presence of the cluster (Figure 2). From an analysis of the mass spectrum, a chemical composition of $[\text{Au}_{18}\text{SG}_{14}\text{-nH}]^{q-}$ could be assigned for the molecular species obtained in this synthesis,

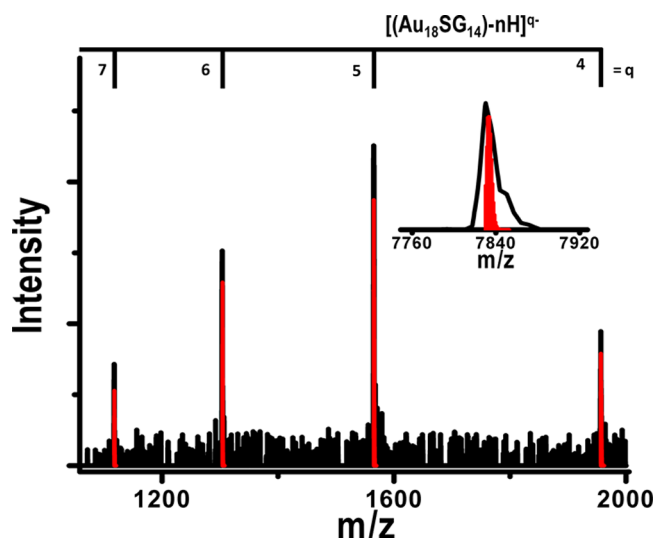


Figure 2. ESI MS spectrum of $\text{Au}_{18}\text{SG}_{14}$ in the negative mode, in the region of m/z 1000–2000. The peaks observed are due to $[\text{Au}_{18}\text{SG}_{14-n}\text{H}]^{q-}$, where n is the number of protons ionized from the carboxylic acid groups. The label q is the charge carried by the cluster. Red lines represent the calculated values for the given charge states. Inset shows the deconvoluted spectrum based on the multiply charged species observed. Besides the molecular ion feature at m/z 7830, it shows higher mass number shoulders due to sodium addition. In the spectra, the red spectrum in the inset gives the expected isotope distribution.

where n represents the number of dissociated protons, and q represents the charge of the cluster. Experimental distribution of multiply charged peaks matches perfectly with the expected pattern. Mass spectral peaks appear at the calculated positions. For example, the peaks due to $[\text{Au}_{18}(\text{SG})_{14-n}\text{H}]^{q-}$ are at m/z 1956.2, 1565.2, 1304.3, and 1117.4 for $q = 4, 5, 6$ and 7 , respectively. The peaks match with the calculated isotope pattern as well, although the instrumental resolution is not adequate to resolve the components of the multiply charged structure (Figure S3A). Deconvoluted spectrum shown in the inset of Figure 2 matches with the mass of $\text{Au}_{18}\text{SG}_{14}$. The deconvoluted spectrum of the whole mass spectrum is shown in Figure S3B, which also proves that only $\text{Au}_{18}\text{SG}_{14}$ is formed in the crude. No other clusters were detected. Deconvoluted spectrum was obtained using MagTran software.

MS analysis was carried out using MALDI as well. The matrix α -cyano-4-hydroxycinnamic acid (CHCA) was used. The spectrum collected in the positive mode shows a bunch of peaks with m/z values ranging from 100 to 10 000 (Figure S4A). Peaks at low m/z regions are very intense with huge background signals compared to those at higher m/z values. There is a pattern of peaks between m/z 1800 and 5400, and another pattern from m/z 5500 to 10 000. The second set of peaks is attributed to clustering of ions detected in the lower m/z values. Clustering of clusters is observed in MALDI MS studies of clusters.³⁹ The mass spectrum is composed of several groups of peaks with spacing of m/z 197 or 229 between the major peaks, as shown in Figure S4B. These correspond to the loss of Au (197) or AuS (229). The m/z spacing between isolated peaks is 32 on account of sulfur (Figure S4C). These results are consistent with the earlier reports of laser-desorption MS of gold QCs protected with thiolates.^{9,33,40} Each bunch of peaks can be assigned as $[\text{Au}_m\text{S}_n]^+$. Since laser irradiation, especially at high laser powers can cleave the S–C bond of the ligands, we observe only peaks due to Au_m cores covered with

S, and not the entire ligand. The mass spectrum showed a highest intense peak at m/z 3962. The peak matches with $\text{Au}_{18}\text{S}_{13}^+$ showing the presence of the Au_{18} core. In laser desorption experiments, some ligand loss (especially the bridged ones) is expected as in the case of Au_{25} , apart from the S–C bond cleavage, and as a result, $\text{Au}_{25}\text{S}_{12}$ is seen as the maximum intense feature in the spectrum of $\text{Au}_{25}\text{SG}_{18}$.²³ Intact molecular ions are difficult to see in water-soluble clusters, unlike in the case of organic soluble ones.

The Au:S ratio in the as-synthesized cluster powder using energy-dispersive analysis of X-rays (EDAX) (1:0.76) further supports the assignment of $\text{Au}_{18}\text{SG}_{14}$ (expected Au:S = 1:0.78) (Figure S5). The ligation of glutathione in the form of thiolate (SG) attached to the Au core was confirmed by the absence of the thiolate stretching peak at 2526 cm^{-1} in the Fourier transform infrared (FT-IR) spectrum of the cluster (Figure S6).

¹H NMR spectra of GSH and $\text{Au}_{18}\text{SG}_{14}$ were measured in D_2O , and the spectra are shown in Figure S7. The strong signal at 4.75 ppm arises due to the presence of residual water in D_2O . The H-7 (α - CH_2) and H-6 (β - CH_2) protons are very close to the gold core. For this reason, these proton signals shifted more downfield. The signal for H-7 became very broad (and not resolvable) and the signal corresponding to H-6 merged with the strong water signal.²³

While exploring the mass spectrum of $\text{Au}_{18}\text{SG}_{14}$, one aspect of its electronic stability became apparent. Many of the ions observed are closed shell electron species as in the case of $[\text{Au}_{18}\text{SG}_{14}]^{4-}$. Increased stability of closed shell ions is exhibited in the mass spectrometry/mass spectrometry (MS/MS) studies of many of the charged species. Table 1 below lists all the ions satisfying the above case. MS/MS of $\text{Au}_{25}(\text{SCH}_2\text{CH}_2\text{Ph})_{18}$ was reported earlier.⁴¹

MS/MS of m/z 1956 (4– charge) gave fragment ion peaks with a separation of m/z 32.5. Therefore, the actual mass loss is $32.5 \times 4 = 130$. The only possibility to have this loss is the fragmentation of glutathione, which is a tripeptide of glutamic acid, cysteine, and glycine. There are two possibilities for it to fragment, namely, at the two peptide bonds. Among them, the

Table 1. All the Ions Formed during (MS/MS) Analysis^a

cluster formula	m	n	q	$m - n + q$
$[\text{Au}_{18}\text{SG}_{14}]^{4-}$	18	14	4	8
$[\text{Au}_{18}\text{SG}_{13}\text{SG}_F]^{4-}$	18	14	4	8
$[\text{Au}_{18}\text{SG}_{13}\text{SG}_F\text{-H}_2\text{O}]^{4-}$	18	14	4	8
$[\text{Au}_{18}\text{SG}_{12}(\text{SG}_F)_2]^{4-}$	18	14	4	8
$[\text{Au}_{18}\text{SG}_{12}(\text{SG}_F)_2\text{-H}_2\text{O}]^{4-}$	18	14	4	8
$[\text{Au}_{18}\text{SG}_{11}(\text{SG}_F)_3]^{4-}$	18	14	4	8
$[\text{Au}_{18}\text{SG}_{11}(\text{SG}_F)_3\text{-H}_2\text{O}]^{4-}$	18	14	4	8
$[\text{Au}_{18}\text{SG}_{10}(\text{SG}_F)_4]^{4-}$	18	14	4	8
$[\text{Au}_{18}\text{SG}_{10}(\text{SG}_F)_4\text{-H}_2\text{O}]^{4-}$	18	14	4	8
$[\text{Au}_{17}\text{SG}_{13}]^{4-}$	17	13	4	8
$[\text{Au}_{17}\text{SG}_{12}(\text{SG}_F)]^{4-}$	17	13	4	8
$[\text{Au}_{16}\text{SG}_{12}]^{4-}$	16	12	4	8
$[\text{Au}_{16}\text{SG}_{11}(\text{SG}_F)]^{4-}$	16	12	4	8
$[\text{Au}_{15}\text{SG}_{11}]^{4-}$	15	11	4	8
$[\text{Au}_{14}\text{SG}_{10}]^{4-}$	14	10	4	8
$[\text{Au}_{12}\text{SG}_8]^{4-}$	12	8	4	8

^aTotal electron count ($m - n + q$) shows that all the ions contain $8e^-$, i.e., they are forming closed shell molecular ions in the gas phase. Here m , n , and q represent the number of gold atoms, thiolated ligands, and charges on the ligand. The electron counting rule includes the charges on the ligand also.

fragmentation between glutamic acid and cysteine is facile. Cleavage at C_{glutamic acid}—N_{cysteine} produces two fragments of m/z 130 (C₅H₈O₃N) and 176 (C₅H₈O₃N₂S). The fragment m/z 176 contains the thiol group, and therefore it got attached with the cluster and the other leaves. The C₅H₈O₃N₂S fragment is labeled SG_F.



There was systematic loss of C₅H₈O₃N as the collision energy was increased (Figure 3). Along with each fragmented peak,

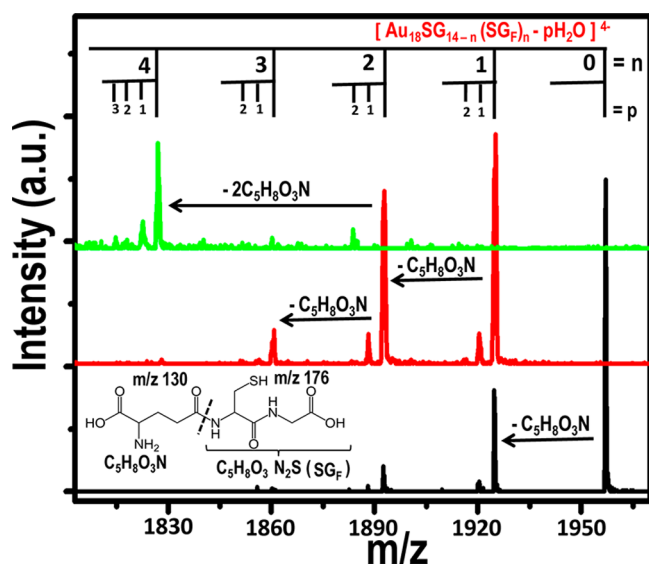


Figure 3. MS/MS spectra of $[\text{Au}_{18}\text{SG}_{14}]^{4-}$ with increasing collision energy. Here n represents the number of glutathione ligands fragmented and p represents the number of water losses. Inset shows the fragmentation channel of glutathione. The mass spectra from bottom to top are with increasing collision energy.

one more peak with m/z 4.5 loss was also observed. This loss ($4.5 \times 4 = 18$) corresponds to H₂O, as shown in Figure 3, indicating that glutathione existed as an anhydride at the cluster surface (a schematic of anhydride formation is shown in Figure S8). With increasing collision energy, the fragments so formed, derived from amide bond cleavage of glutathione, further lose water, producing a series of $p\text{H}_2\text{O}$ losses ($p = 1, 2, \dots$).

It was observed that there was no water loss from the unfragmented ion, $[\text{Au}_{18}\text{SG}_{14}]^{4-}$. After fragmentation of one glutathione group, it forms $[\text{Au}_{18}\text{SG}_{13}(\text{SG}_F)]^{4-}$, from which water loss started. It is likely that after fragmentation, some structural change happens on the cluster surface, which assisted the water loss. At higher collision energy, a loss of 4 C₅H₈O₃N is observed.

At the same time, we have observed weak peaks at m/z 503 and 1006, which are due to the loss of AuSG (197 + 306) and Au₂SG₂ (197 × 2 + 306 × 2) (Figure S8). The ion Au₂SG₂ is prominent at a certain collision energy. The resultant peak upon loss of AuSG and Au₂SG₂ from $[\text{Au}_{18}\text{SG}_{13}\text{SG}_F]^{4-}$ (m/z 1924.3) gives ions at m/z 1799.0 and 1674.1, respectively corresponding to $[\text{Au}_{17}\text{SG}_{12}\text{SG}_F]^{4-}$ and $[\text{Au}_{16}\text{SG}_{11}\text{SG}_F]^{4-}$. A peak at m/z 1704.9 appeared due to the formation of $[\text{Au}_{16}\text{SG}_{12}]^{4-}$ from $[\text{Au}_{18}\text{SG}_{14}]^{4-}$ (Figure S9). This is contrary to the data at low collision energies, where fragmentation happened from the already fragmented species $[\text{Au}_{18}\text{SG}_{13}\text{SG}_F]^{4-}$; but it happened from the parent cluster

$[\text{Au}_{18}\text{SG}_{14}]^{4-}$ itself in the present case. The same trend was continued for higher collision energies also. No other fragments with other charge species except 4⁻ were observed in the MS/MS spectrum. All these species observed correspond to $m - n + q = 8$, where m is the number of gold atoms, n is the number of thiolate ligands, and q is the charge on the ligand. This increased stability of 8e⁻ fragments is seen if we start from other ions as well, which are not 8e⁻ species to begin with. For example, $[\text{Au}_{18}\text{SG}_{14}]^{5-}$ produces a 4⁻ species upon increasing the collision energy (Figure S9). Similar “charge stripping” is seen with other anions as well, as shown in Figures S10 and S11. This kind of ion formation suggests increased stability of the tetra anion. We believe that these results closely resemble the increased stability of the Jellium core.³⁰ However, in the present case, the electron count includes the charges on the ligands as well. Table 1 in the Supporting Information presents the calculated and experimental masses of the ions observed, and Table 2 presents the calculated mass of the cluster based on the ion masses.

Variation of the concentration of NaBH₃CN in the synthesis produces other clusters. For example, Figure S12 compares the UV spectra of three different samples prepared by the addition of different concentrations of NaBH₃CN to Au(I) glutathione solution at a Au:GSH molar ratio of 1:2.5. It is clear that various concentrations of the reducing agent can give different QCs of gold, although optimization is necessary to make one specific core. Close inspection of Figure S12 shows that the absorption band maxima associated with the Au 6sp intraband transitions are shifted systematically with change in core size.

In summary, a novel route to produce Au₁₈SG₁₄ is reported. We have made a highly pure and stable material, in large quantities by the appropriate choice of synthetic parameters. Since these clusters are highly fluorescent and biocompatible due to the lower metallic content, they hold great promise as ultrabright, biocompatible biolabels and light-emitting sources at the nanoscale. These clusters can be readily conjugated with several biological molecules, which further enhances their application potential. We believe that essential properties of Au₁₈SG₁₄ reported here will generate further interest in this class of materials. One-step synthesis of this material in large quantities will enable the exploration of its properties. We performed MS/MS of Au₁₈SG₁₄, which confirms that the observed ions in the gas phase satisfy the model of closed electronic shell. We show that it is possible to make several other clusters of well-defined composition by the same route. The factors responsible for selective formation of Au₁₈SG₁₄ need additional studies.

■ ASSOCIATED CONTENT

📄 Supporting Information

Figures S1–S12 and Tables 1–2. This material is available free of charge via the Internet at <http://pubs.acs.org>.

■ AUTHOR INFORMATION

Corresponding Author

*E-mail: pradeep@iitm.ac.in.

Notes

The authors declare no competing financial interest.

■ ACKNOWLEDGMENTS

We thank the Department of Science and Technology, Government of India, for constantly supporting our research program on nanomaterials.

■ REFERENCES

- (1) Jadzinsky, P. D.; Calero, G.; Ackerson, C. J.; Bushnell, D. A.; Kornberg, R. D. Structure of a Thiol Monolayer-Protected Gold Nanoparticle at 1.1 Å Resolution. *Science* **2007**, *318*, 430–433.
- (2) Shichibu, Y.; Negishi, Y.; Tsukuda, T.; Teranishi, T. Large-Scale Synthesis of Thiolated Au₂₅ Clusters via Ligand Exchange Reactions of Phosphine-Stabilized Au₁₁ Clusters. *J. Am. Chem. Soc.* **2005**, *127*, 13464–13465.
- (3) Nimmala, P. R.; Dass, A. Au₃₆(SPh)₂₃ Nanomolecules. *J. Am. Chem. Soc.* **2011**, *133*, 9175–9177.
- (4) Zheng, J.; Petty, J. T.; Dickson, R. M. High Quantum Yield Blue Emission from Water-Soluble Au₈ Nanodots. *J. Am. Chem. Soc.* **2003**, *125*, 7780–7781.
- (5) Wu, Z.; MacDonald, M. A.; Chen, J.; Zhang, P.; Jin, R. Kinetic Control and Thermodynamic Selection in the Synthesis of Atomically Precise Gold Nanoclusters. *J. Am. Chem. Soc.* **2011**, *133*, 9670–9673.
- (6) Rao, T. U. B.; Nataraju, B.; Pradeep, T. Ag₉ Quantum Cluster through a Solid-State Route. *J. Am. Chem. Soc.* **2010**, *132*, 16304–16307.
- (7) Levi-Kalishman, Y.; Jadzinsky, P. D.; Kalishman, N.; Tsunoyama, H.; Tsukuda, T.; Bushnell, D. A.; Kornberg, R. D. Synthesis and Characterization of Au₁₀₂(p-MBA)₄₄ Nanoparticles. *J. Am. Chem. Soc.* **2011**, *133*, 2976–2982.
- (8) Zhu, M.; Qian, H.; Jin, R. Thiolate-Protected Au₂₀ Clusters with a Large Energy Gap of 2.1 eV. *J. Am. Chem. Soc.* **2009**, *131*, 7220–7221.
- (9) Shibu, E. S.; Radha, B.; Verma, P. K.; Bhyrappa, P.; Kulkarni, G. U.; Pal, S. K.; Pradeep, T. Functionalized Au₂₂ Clusters: Synthesis, Characterization, and Patterning. *ACS Appl. Mater. Interfaces* **2009**, *1*, 2199–2210.
- (10) Shibu, E. S.; Pradeep, T. Quantum Clusters in Cavities: Trapped Au₁₅ in Cyclodextrins. *Chem. Mater.* **2011**, *23*, 989–999.
- (11) Arenz, M.; Landman, U.; Heiz, U. CO Combustion on Supported Gold Clusters. *Chem. Phys. Chem.* **2006**, *7*, 1871–1879.
- (12) Liu, Y.; Tsunoyama, H.; Akita, T.; Tsukuda, T. Efficient and Selective Epoxidation of Styrene with TBHP Catalyzed by Au₂₅ Clusters on Hydroxyapatite. *Chem. Commun.* **2010**, *46*, 550–552.
- (13) Leelavathi, A.; Bhaskara Rao, T.; Pradeep, T. Supported Quantum Clusters of Silver as Enhanced Catalysts for Reduction. *Nanoscale Res. Lett.* **2011**, *6*, 1–9.
- (14) Zhu, Y.; Qian, H.; Drake, B. A.; Jin, R. Atomically Precise Au₂₅(SR)₁₈ Nanoparticles as Catalysts for the Selective Hydrogenation of α,β -Unsaturated Ketones and Aldehydes. *Angew. Chem., Int. Ed.* **2010**, *49*, 1295–1298.
- (15) de Silva, N.; Ha, J.-M.; Solovoyov, A.; Nigra, M. M.; Ogino, I.; Yeh, S. W.; Durkin, K. A.; Katz, A. A Bioinspired Approach for Controlling Accessibility in Calix[4]arene-Bound Metal Cluster Catalysts. *Nat. Chem.* **2010**, *2*, 1062–1068.
- (16) Polavarapu, L.; Manna, M.; Xu, Q.-H. Biocompatible Glutathione Capped Gold Clusters As One- and Two-Photon Excitation Fluorescence Contrast Agents for Live Cells Imaging. *Nanoscale* **2011**, *3*, 429–434.
- (17) Habeeb Muhammed, M. A.; Verma, P. K.; Pal, S. K.; Retnakumari, A.; Koyakutty, M.; Nair, S.; Pradeep, T. Luminescent Quantum Clusters of Gold in Bulk by Albumin-Induced Core Etching of Nanoparticles: Metal Ion Sensing, Metal-Enhanced Luminescence, and Biolabeling. *Chem.—Eur. J.* **2010**, *16*, 10103–10112.
- (18) Gobin, A. M.; Lee, M. H.; Halas, N. J.; James, W. D.; Drezek, R. A.; West, J. L. Near-Infrared Resonant Nanoshells for Combined Optical Imaging and Photothermal Cancer Therapy. *Nano Lett.* **2007**, *7*, 1929–1934.
- (19) Ray, P. C.; Khan, S. A.; Singh, A. K.; Senapati, D.; Fan, Z. Nanomaterials for Targeted Detection and Photothermal Killing of Bacteria. *Chem. Soc. Rev.* **2012**, *41*, 3193–3209.
- (20) Sivaramkrishnan, S.; Chia, P.-J.; Yeo, Y.-C.; Chua, L.-L.; Ho, P. K. H. Controlled insulator-to-metal transformation in printable polymer composites with nanometal clusters. *Nat. Mater.* **2007**, *6*, 149–155.
- (21) Negishi, Y.; Nobusada, K.; Tsukuda, T. Glutathione-Protected Gold Clusters Revisited: Bridging the Gap between Gold(I)–Thiolate Complexes and Thiolate-Protected Gold Nanocrystals. *J. Am. Chem. Soc.* **2005**, *127*, 5261–5270.
- (22) Shibu, E. S.; Muhammed, M. A. H.; Tsukuda, T.; Pradeep, T. Ligand Exchange of Au₂₅SG₁₈ Leading to Functionalized Gold Clusters: Spectroscopy, Kinetics, and Luminescence. *J. Phys. Chem. C* **2008**, *112*, 12168–12176.
- (23) Wu, Z.; Gayathri, C.; Gil, R. R.; Jin, R. Probing the Structure and Charge State of Glutathione-Capped Au₂₅(SG)₁₈ Clusters by NMR and Mass Spectrometry. *J. Am. Chem. Soc.* **2009**, *131*, 6535–6542.
- (24) Parker, J. F.; Fields-Zinna, C. A.; Murray, R. W. The Story of a Monodisperse Gold Nanoparticle: Au₂₅L₁₈. *Acc. Chem. Res.* **2010**, *43*, 1289–1296.
- (25) Habeeb Muhammed, M. A.; Pradeep, T. Au₂₅@SiO₂: Quantum Clusters of Gold Embedded in Silica. *Small* **2011**, *7*, 204–208.
- (26) Hamouda, R.; Bellina, B.; Bertorelle, F.; Compagnon, I.; Antoine, R.; Broyer, M.; Rayane, D.; Dugourd, P. Electron Emission of Gas-Phase [Au₂₅(SG)₁₈-6H]⁷⁻ Gold Cluster and Its Action Spectroscopy. *J. Phys. Chem. Lett.* **2010**, *1*, 3189–3194.
- (27) Kumar, S. S.; Kwak, K.; Lee, D. Amperometric Sensing Based on Glutathione Protected Au₂₅ Nanoparticles and Their pH Dependent Electrocatalytic Activity. *Electroanalysis* **2011**, *23*, 2116–2124.
- (28) Shichibu, Y.; Negishi, Y.; Tsunoyama, H.; Kanehara, M.; Teranishi, T.; Tsukuda, T. Extremely High Stability of Glutathione-Protected Au₂₅ Clusters Against Core Etching. *Small* **2007**, *3*, 835–839.
- (29) de Heer, W. A. The Physics of Simple Metal Clusters: Experimental Aspects and Simple Models. *Rev. Mod. Phys.* **1993**, *65*, 611–676.
- (30) Hakkinen, H. Atomic and Electronic Structure of Gold Clusters: Understanding Flakes, Cages and Superatoms from Simple Concepts. *Chem. Soc. Rev.* **2008**, *37*, 1847–1859.
- (31) Borch, R. F.; Bernstein, M. D.; Durst, H. D. Cyanohydrinoborate Anion as a Selective Reducing Agent. *J. Am. Chem. Soc.* **1971**, *93*, 2897–2904.
- (32) Tlahuice, A.; Garzon, I. L. On the Structure of the Au₁₈(SR)₁₄ Cluster. *Phys. Chem. Chem. Phys.* **2012**, *14*, 3737–3740.
- (33) Muhammed, M. A. H.; Verma, P. K.; Pal, S. K.; Kumar, R. C. A.; Paul, S.; Omkumar, R. V.; Pradeep, T. Bright, NIR-Emitting Au₂₃ from Au₂₅: Characterization and Applications Including Biolabeling. *Chem.—Eur. J.* **2009**, *15*, 10110–10120.
- (34) Lee, T. K.-M.; Zhu, N.; Yam, V. W.-W. An Unprecedented Luminescent Polynuclear Gold(I) μ 3-Sulfido Cluster with a Thiocrown-like Architecture. *J. Am. Chem. Soc.* **2012**, *134*, 17646–17648.
- (35) Yam, V. W.-W.; Yip, S.-K.; Yuan, L.-H.; Cheung, K.-L.; Zhu, N.; Cheung, K.-K. Synthesis, Structure, and Ion-Binding Properties of Luminescent Gold(I) Alkynylcalix[4]crown-5 Complexes. *Organometallics* **2003**, *22*, 2630–2637.
- (36) Udaya Bhaskara Rao, T.; Pradeep, T. Luminescent Ag₇ and Ag₈ Clusters by Interfacial Synthesis. *Angew. Chem., Int. Ed.* **2010**, *49*, 3925–3929.
- (37) Ramasamy, P.; Guha, S.; Shibu, E. S.; Sreeprasad, T. S.; Bag, S.; Banerjee, A.; Pradeep, T. Size Tuning of Au Nanoparticles Formed by Electron Beam Irradiation of Au₂₅ Quantum Clusters Anchored within and outside of Dipeptide Nanotubes. *J. Mater. Chem.* **2009**, *19*, 8856–8462.
- (38) Takehara, K.; Ide, Y.; Aihara, M.; Obuchi, E. An Ion-Gate Response of the Glutathione Monolayer Assembly Formed on a Gold Electrode: Part 1. The Effect of pH, K⁺ and Ca²⁺. *Bioelectrochem. Bioenerg.* **1992**, *29*, 103–111.

(39) Cyriac, J.; Rajeev Kumar, V. R.; Pradeep, T. Gas Phase Aggregates of Protected Clusters. *Chem. Phys. Lett.* **2004**, *390*, 181–185.

(40) Schaaff, T. G. Laser Desorption and Matrix-Assisted Laser Desorption/Ionization Mass Spectrometry of 29-kDa Au:SR Cluster Compounds. *Anal. Chem.* **2004**, *76*, 6187–6196.

(41) Angel, L. A.; Majors, L. T.; Dharmaratne, A. C.; Dass, A. Ion Mobility Mass Spectrometry of Au₂₅(SCH₂CH₂Ph)₁₈ Nanoclusters. *ACS Nano* **2010**, *4*, 4691–4700.

One-step Route to Luminescent Au₁₈SG₁₄ in the Condensed Phase and its Closed Shell Molecular Ions in the Gas Phase

*Atanu Ghosh, Thumu Udayabhaskararao and Thalappil Pradeep**

DST Unit of Nanoscience (DST UNS) Department of Chemistry, Indian Institute of Technology Madras, Chennai 600 036, India

*E-mail: pradeep@iitm.ac.in

Number	Description	Page number
1	Experimental section and methods	2
2	XPS	4
3	TEM, effect of electron beam irradiation	5
4	ESI MS	6
5	MALDI MS	7
6	SEM EDAX	8
7	FT-IR	9
8	NMR	10
9	MS/MS of [Au ₁₈ SG ₁₄] ⁴⁻	11
10	MS/MS of [Au ₁₈ SG ₁₄] ⁵⁻	12
11	MS/MS of [Au ₁₈ SG ₁₄] ⁶⁻	13
12	MS/MS of [Au ₁₈ SG ₁₄] ⁷⁻	14
13	Calculated and experimental masses of the ions observed and mass of the cluster calculated from ion masses	15
14	UV spectra of different clusters	16

S1. Supporting information 1

Experimental Section

Chemicals: All the chemicals are commercially available and used without further purification. $\text{HAuCl}_4 \cdot 3\text{H}_2\text{O}$, methanol (GR grade) and GSH (γ -Glu-Cys-Gly, M.W. 307.13) were purchased from SRL Chemical Co. Ltd., India. NaBH_3CN was purchased from Sigma Aldrich.

Synthesis of $\text{Au}_{18}\text{SG}_{14}$: To 1.2 mL methanolic solution, containing 150 mg of $\text{HAuCl}_4 \cdot 3\text{H}_2\text{O}$, 1.8 mL water was added. 300 mg of glutathione was added to it. The solution was sonicated to dissolve glutathione. During sonication, the color of the solution changed from yellow to almost colorless. It was diluted to 96 mL by methanol. The solution was then stirred for 10 min. 4.5 mL aqueous solution of NaBH_3CN (220 mM) was added to it. After 30 min of vigorous stirring, the precipitate was collected and washed repeatedly with methanol through centrifugal precipitation to remove the remaining precursors. The precipitate was dissolved in water and centrifuged to remove unreacted thiolate. Finally, the solution was freeze dried to obtain $\text{Au}_{18}\text{SG}_{14}$ as a pale red powder.

Polyacrylamide gel electrophoresis (PAGE): PAGE separation of the clusters was performed as per the procedure given below.

A gel electrophoresis unit with 1 mm thick spacer (Bio-rad, Mini-protein Tetra cell) was used to process the PAGE. The total contents of the acrylamide monomers were 28% (bis(acrylamide:acrylamide) = 7:93) and 3% (bis(acrylamide:acrylamide) = 6:94) for the separation and condensation gels, respectively. The eluting buffer consisted of 192 mM glycine and 25 mM tris(hydroxymethylamine). The clusters, as a pale red powder, obtained in the reaction were dissolved in 5% (v/v) glycerol-water solution (0.5 mL) at a concentration of 20 mg/mL. The sample solution (1.0 mL) was loaded onto a 1 mm gel and eluted for 6 h at a constant voltage of 120 V to achieve separation shown in Figure 1.

We also performed high resolution electrophoresis using increased contents of acrylamide monomers of 35% and 3% for the separation and condensation gels, respectively. But, we did not observe any additional bands.

Analytical procedures

A. UV-vis spectrometer

UV/Vis spectra were measured with a Perkin Elmer Lambda 25 instrument in the range of 200- 1100 nm.

B. Luminescence spectroscopy

Luminescence measurements were carried out using HORIBA JOBIN VYON Nano Log instrument. The band pass for excitation and emission was set as 3 nm.

C. Transmission electron microscopy (TEM)

TEM images were collected using a JEOL 3010 microscope. A diluted solution was spotted on carbon coated copper grid and was dried in ambience. Images were collected at 200 keV, to reduce beam induced damage of the clusters. Our earlier studies had shown that small clusters are highly sensitive to electron beam and undergoes aggregation.

D. Fourier-transform infrared (FT-IR) spectra

FT-IR spectra were measured with a Perkin Elmer Spectrum One instrument. For sample preparation KBr crystals were used as the matrix.

E. SEM and EDX analyses

Scanning electron microscopic (SEM) and energy dispersive X-ray (EDX) analyses were done in a FEI QUANTA-200 SEM. For measurements, samples were drop-casted on an indium tin oxide coated conducting glass and dried in vacuum. After drying it is used for analysis.

F. X-ray photoelectron spectroscopy

The photoelectron spectra of the samples were obtained using an ESCA probe/TPD of Omicron Nanotechnology. Sample in water was spotted on Mo plate and allowed to dry in vacuum. The size of the analyzed area was about 3 mm². In view of the sensitivity of the sample, surface cleaning was not attempted. Al K α radiation was used for excitation; a 180° hemispherical analyzer and a seven-channel detector were employed. The spectrometer was operated in the constant energy analyzer mode. Survey and high-resolution spectra were collected using pass energies of 50 and 20 eV, respectively. The pressure in the analyzer chamber was in the low 10⁻¹⁰ mbar range during spectrum collection. Binding energies of the core levels were calibrated with C 1s B.E, set at 284.9 eV.

G. Electrospray ionization (ESI) mass spectrometry

The ESI mass spectrometric measurements were done in the negative mode using LTQ XL, with a mass range of m/z 150-2000, in which the spray and the extraction are orthogonal to each other. The clusters, obtained after freeze drying were dispersed in 1:1 water-methanol solution and used for mass spectrometric measurements. The samples were electrosprayed at a flow rate of 10 μ L/min at a temperature of 150°C. The spectra were averaged for 75 scans.

H. MALDI TOF MS

The mass spectrometric studies were done using a Voyager Biospectrometry Workstation (Applied Biosystems) MALDI TOF MS instrument. A pulsed nitrogen laser of 337 nm was used for desorption ionization and TOF was operated in the delayed extraction mode. For MALDI MS study, α -cyano-4-hydroxycinnamic acid (CHCA) matrix in 0.1% trifluoroacetic acid (TFA) was mixed with cluster in water (2mg/1mL) in 2:1 ratio and soincated for 15 minute and directly spotted on the target plate. Typical delay times employed were of the order of 75–150 ns. The mass spectra were collected in positive mode and were averaged for 200 shots. Most of the measurements were done in the reflectron mode.

2. Supporting information 2

XPS

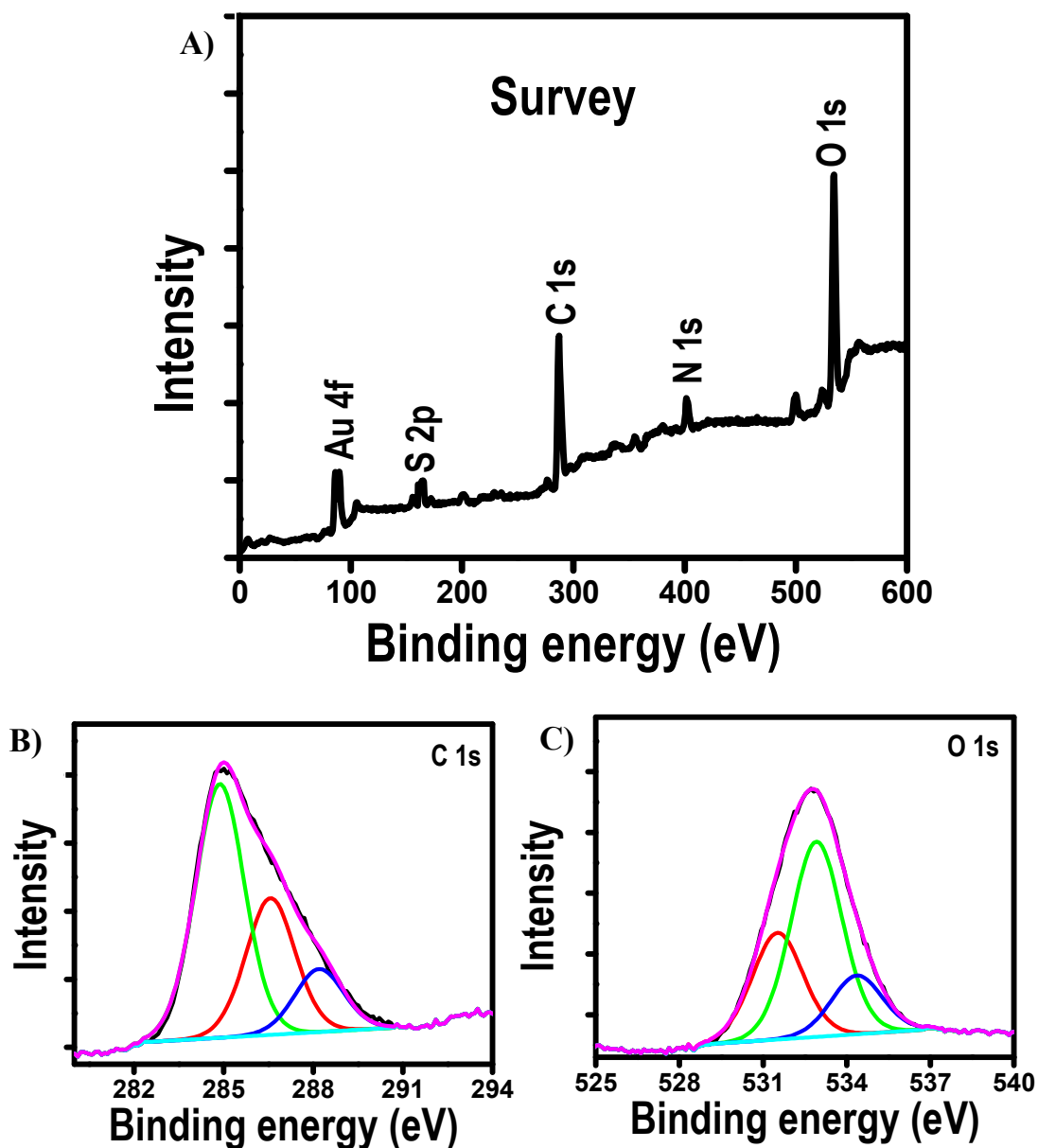


Figure S1. (A) XPS survey spectrum of the as synthesized $\text{Au}_{18}(\text{SG})_{14}$. B, C, are the expanded C 1s and O 1s core level regions, respectively. The multiple components are fitted. The peaks are assigned. The components in the C 1s and O 1s regions can be understood from the structure of the ligand.

3. Supporting information 3

TEM, effect of electron beam irradiation

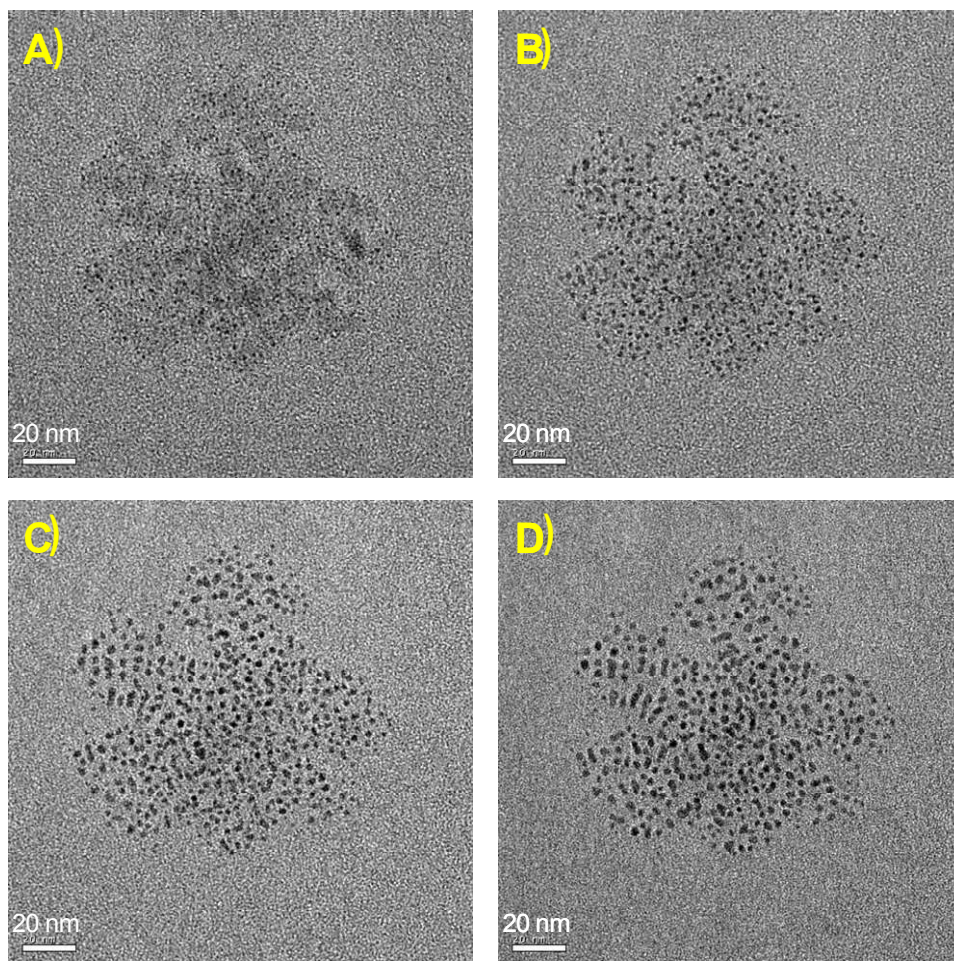


Figure S2. (A) TEM image of Au₁₈SG₁₄; particles were observable only faintly. (B-D) The systematic conversion of the clusters into bigger nanoparticles upon the irradiation with the electron beam. TEM images were taken from same area after 5, 10 and 15 minutes of irradiation in B, C and D, respectively.

4. Supporting information 4

ESI MS

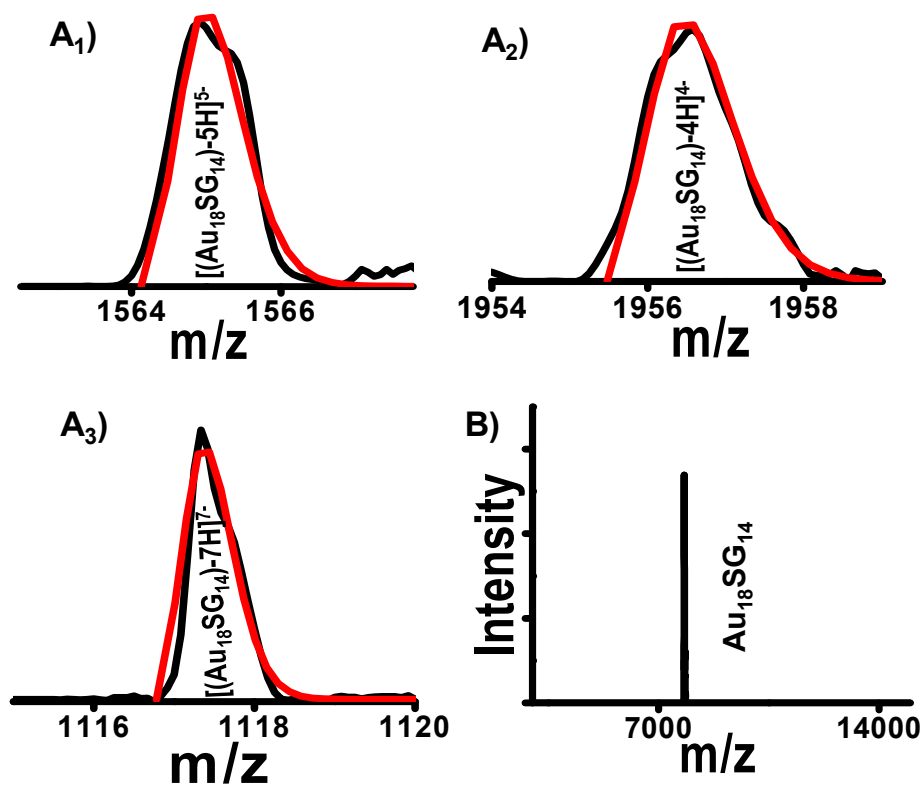


Figure S3. (A) A₁, A₂ and A₃ showed expanded views of 4-, 5- and 7- charges (black line) with simulated values (red line) and (B) the deconvoluted mass spectrum based on all the multiply charged species observed.

5. Supporting information 5

MALDI MS

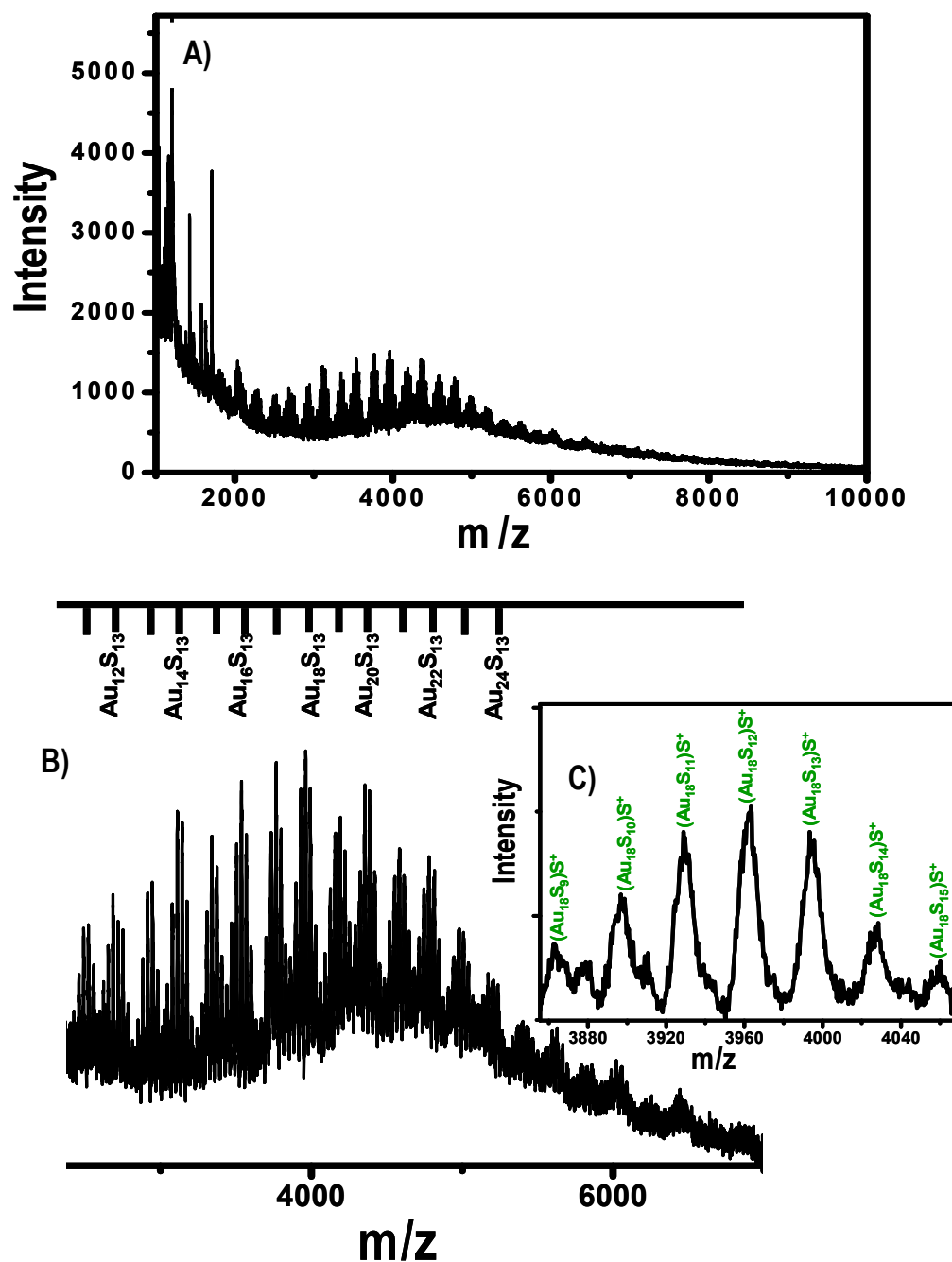


Figure S4. (A) MALDI MS in positive mode of the crude product using the matrix α -cyano-4- hydroxycinnamic acid (CHCA). (B) Expanded view giving the most intense peak at m/z 3962, well matched with Au₁₈S₁₃⁺ showing the likely presence of the Au₁₈ core and (C) expanded view of the intense peak (Au₁₈S₁₃⁺) showing a separation of m/z 32 due to sulfur. Laser induced fragmentation and reaction in the plasma complicate the spectrum.

6. Supporting information 6

SEM/EDAX

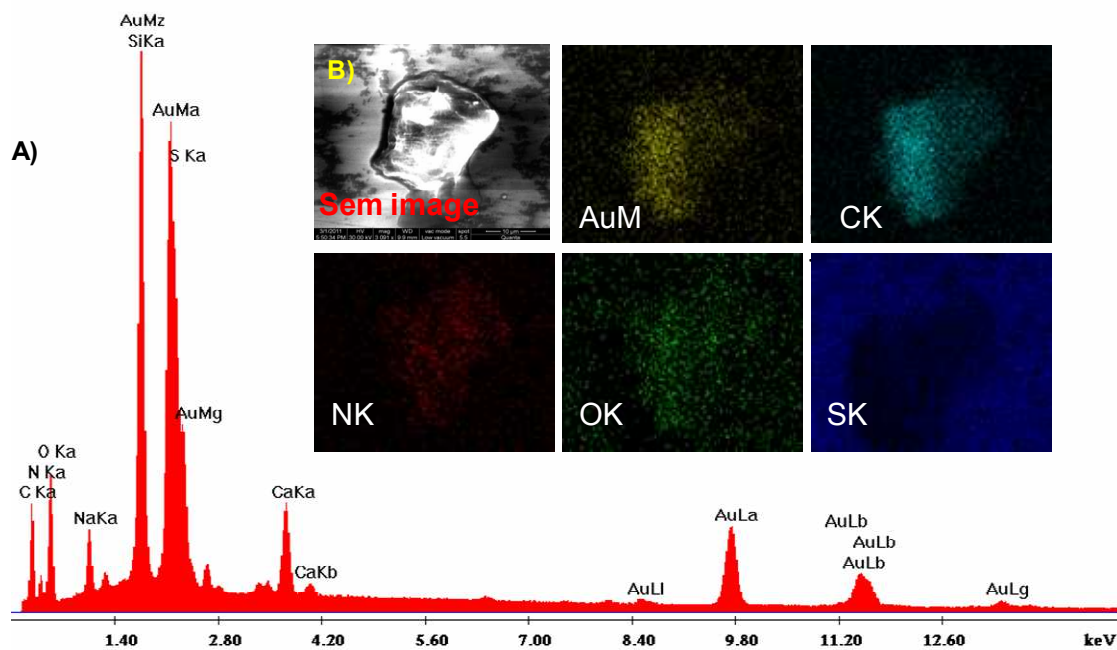


Figure S5. (A) EDAX spectrum of $\text{Au}_{18}\text{SG}_{14}$ and (B) SEM image of $\text{Au}_{18}\text{SG}_{14}$ aggregate from which the EDX spectrum was taken. Au:S atomic ratio measured is 1:0.76, as expected (actual is 1:0.78).

7. Supporting information 7

FT-IR

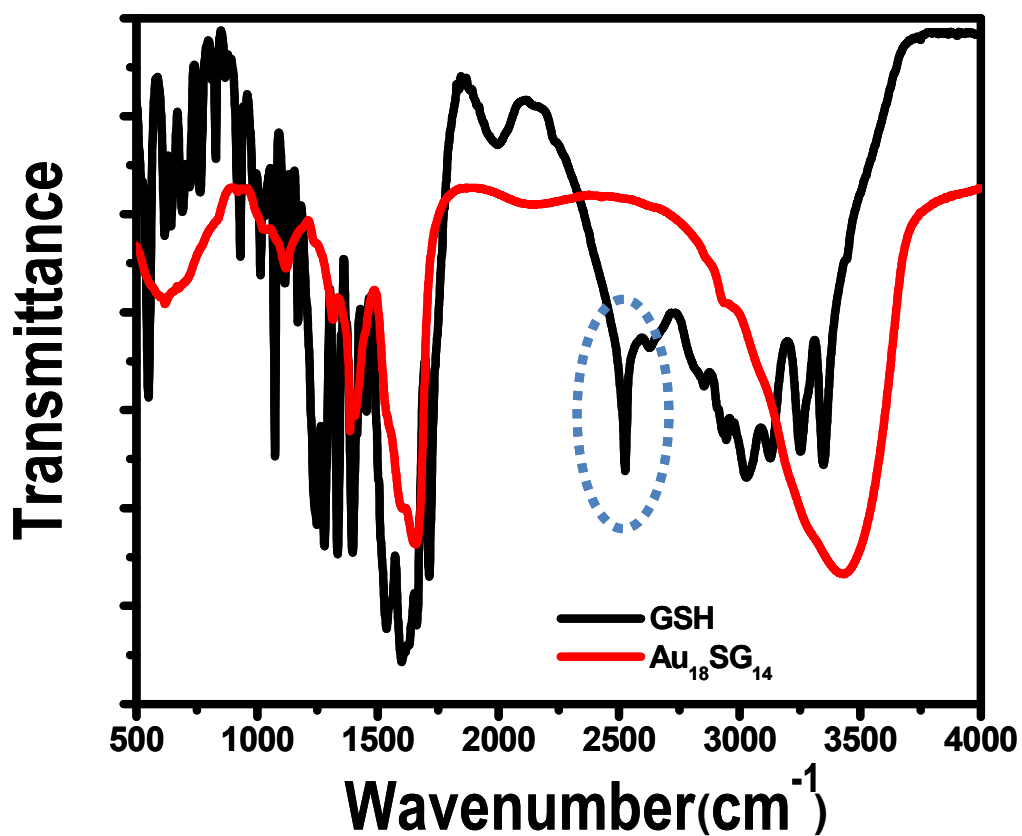


Figure S6. Expanded FT-IR of GSH and Au₁₈SG₁₄; the disappearance of the peak at 2526 cm⁻¹ for Au₁₈SG₁₄ indicated that the S-H bond was absent in it. This proved that sulphur is connected to the metal in Au₁₈SG₁₄ in the thiolate form.

8. Supporting information 8

NMR

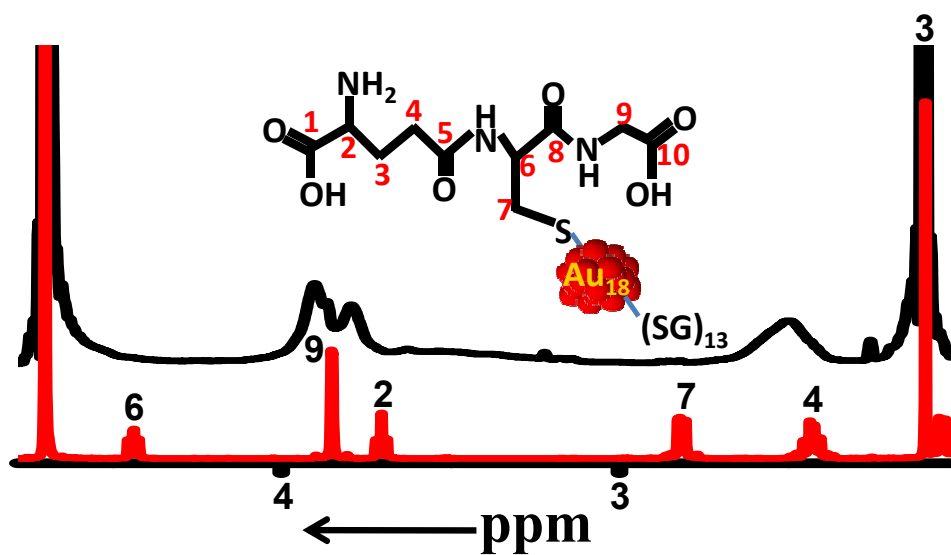


Figure S7. ¹H NMR spectra of GSH (red) and Au₁₈SG₁₄ (black). Structure of glutathione linked to Au core is shown wherein the assignment is indicated.

9. Supporting information 9

MS/MS of $[\text{Au}_{18}\text{SG}_{14}]^{4-}$

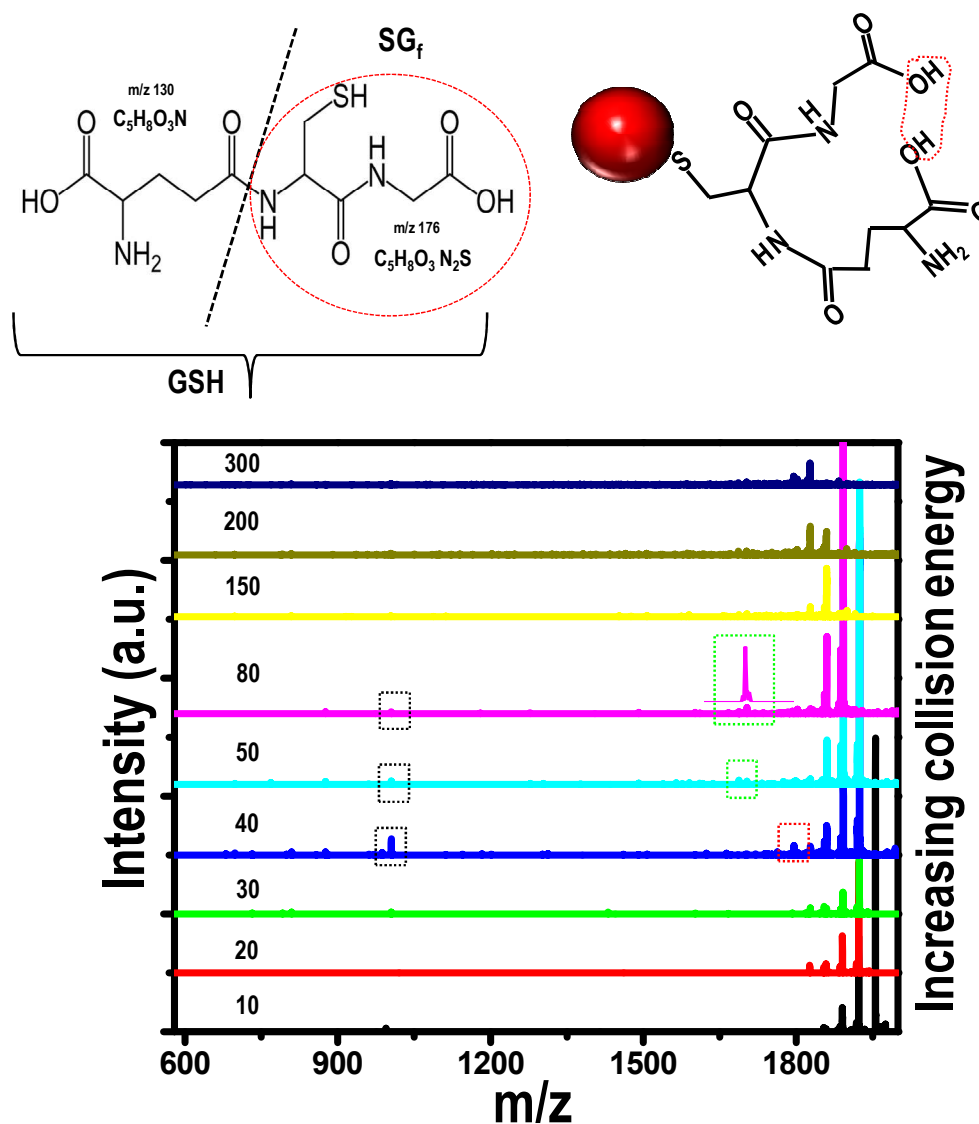


Figure S8. MS/MS spectra of the $[\text{Au}_{18}\text{SG}_{14}]^{4-}$ with increasing collision energy. Schematic diagram on the top of the figure showing the cleavage of bond and loss of water molecule in glutathione ligand. The red boxes show the peak corresponding to $[\text{Au}_{17}\text{SG}_{12}\text{SG}_f]^{4-}$ formed due to loss of AuSG from $[\text{Au}_{18}\text{SG}_{13}\text{SG}_f]^{4-}$. The green boxes show the peak corresponding to $[\text{Au}_{16}\text{SG}_{11}\text{SG}_f]^{4-}$ formed due to the loss of Au_2SG_2 from $[\text{Au}_{18}\text{SG}_{13}\text{SG}_f]^{4-}$ and the black boxes present the peak corresponding to Au_2SG_2 .

10. Supporting information 10
MS/MS of $[\text{Au}_{18}\text{SG}_{14}]^{5-}$

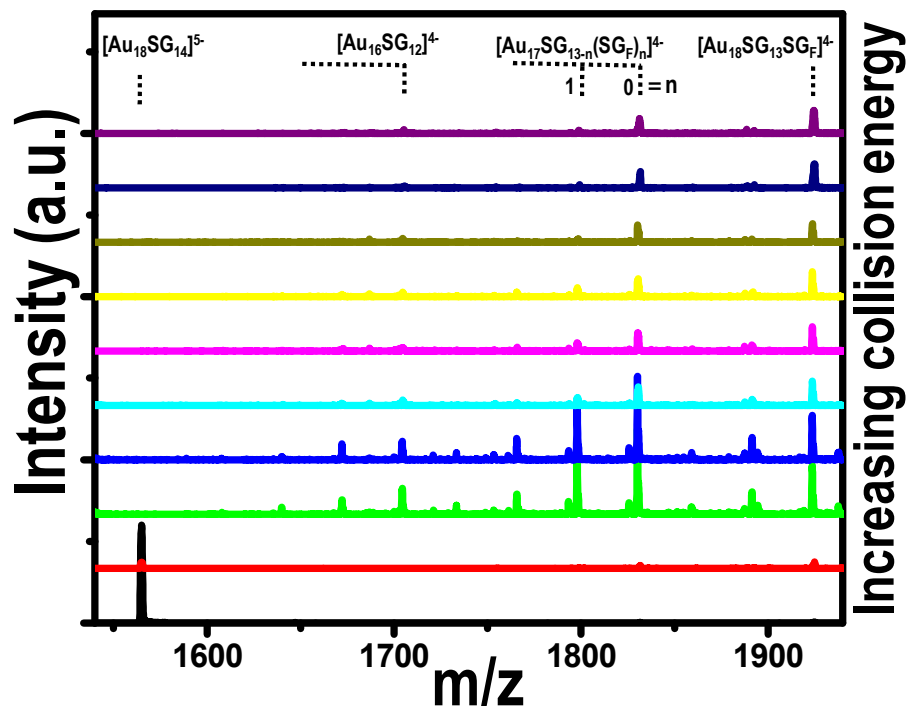


Figure S9. MS/MS spectra of the $[\text{Au}_{18}\text{SG}_{14}]^{5-}$ with increasing collision energy. At lower collision energy, peak corresponding to $[\text{Au}_{18}\text{SG}_{14}]^{5-}$ alone is present (bottom-most trace). With increasing collision energy, fragmentation of $[\text{Au}_{18}\text{SG}_{14}]^{5-}$ happened which gave ions containing 4- charge at higher m/z . Corresponding peaks are marked on the figure.

11. Supporting information 11
MS/MS of $[\text{Au}_{18}\text{SG}_{14}]^{6-}$

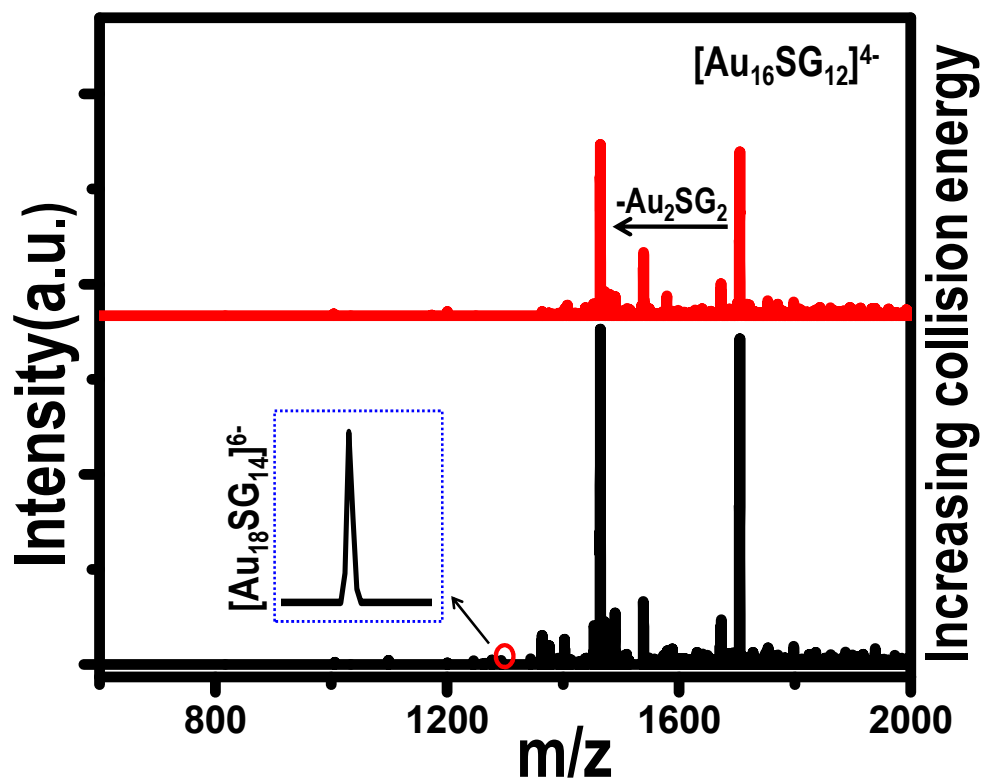


Figure S10. A) MS/MS spectra of $[\text{Au}_{18}\text{SG}_{14}]^{6-}$ (m/z 1304.3) with increasing collision energies. Corresponding peaks are marked on the above figure. Fragmentation of $[\text{Au}_{18}\text{SG}_{14}]^{6-}$ gave ions containing 4- charge. The ion, $[\text{Au}_{16}\text{SG}_{12}]^{4-}$, formed due to fragmentation, undergoes Au_2SG_2 loss to form $[\text{Au}_{14}\text{SG}_{10}]^{4-}$. The parent ion region is expanded.

12. Supporting information 12
MS/MS of $[\text{Au}_{18}\text{SG}_{14}]^{7-}$

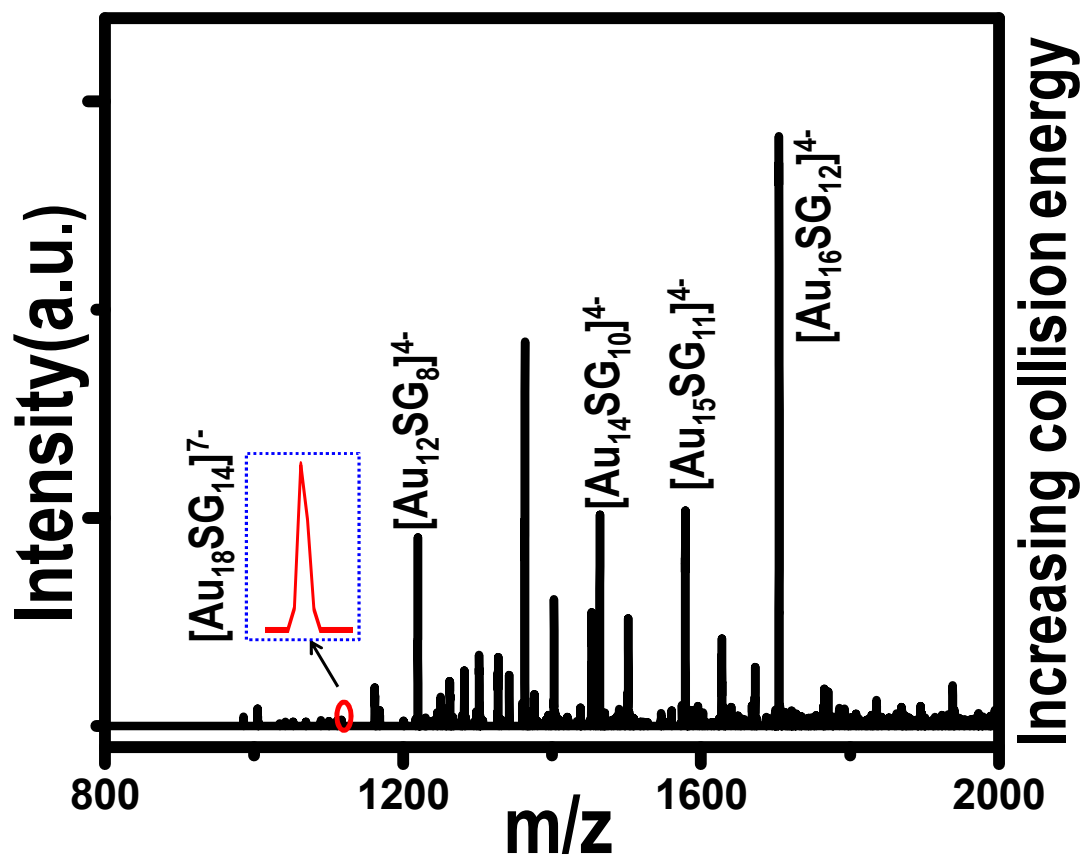


Figure S11. A) MS/MS spectrum of $[\text{Au}_{18}\text{SG}_{14}]^{7-}$. At higher collision energy $[\text{Au}_{18}\text{SG}_{14}]^{7-}$ undergoes fragmentation and produced ions containing 4- charge. All the ions formed in the above figure exhibited the $8e^-$ rule. The parent ion is expanded.

13. Supporting information 13

Table 1. Calculated and experimental masses of the ions observed

Cluster formula	Calculated mass	Experimental mass
$[\text{Au}_{18}\text{SG}_{14}]^{4-}$	1956.5	1956.2
$[\text{Au}_{18}\text{SG}_{14}]^{5-}$	1565.0	1565.2
$[\text{Au}_{18}\text{SG}_{14}]^{6-}$	1304.0	1304.3
$[\text{Au}_{18}\text{SG}_{14}]^{7-}$	1117.5	1117.4
$[\text{Au}_{18}\text{SG}_{13}(\text{SG}_F)]^{4-}$	1924.6	1924.3
$[\text{Au}_{18}\text{SG}_{13}(\text{SG}_F)\text{-H}_2\text{O}]^{4-}$	1920.0	1920.3
$[\text{Au}_{18}\text{SG}_{12}(\text{SG}_F)_2]^{4-}$	1892.5	1891.9
$[\text{Au}_{18}\text{SG}_{12}(\text{SG}_F)_2\text{-H}_2\text{O}]^{4-}$	1888.0	1887.6
$[\text{Au}_{18}\text{SG}_{11}(\text{SG}_F)_3]^{4-}$	1860.5	1860.1
$[\text{Au}_{18}\text{SG}_{11}(\text{SG}_F)_3\text{-H}_2\text{O}]^{4-}$	1856.0	1855.7
$[\text{Au}_{18}\text{SG}_{10}(\text{SG}_F)_4]^{4-}$	1828.5	1828.3
$[\text{Au}_{18}\text{SG}_{10}(\text{SG}_F)_4\text{-H}_2\text{O}]^{4-}$	1824.0	1824.1
$[\text{Au}_{17}\text{SG}_{12}(\text{SG}_F)_1]^{4-}$	1799.3	1799.0
$[\text{Au}_{16}\text{SG}_{11}(\text{SG}_F)_1]^{4-}$	1673.6	1674.1
$[\text{Au}_{16}\text{SG}_{12}]^{4-}$	1705.0	1704.9
$[\text{Au}_{14}\text{SG}_{10}]^{4-}$	1453.5	1453.6

Table 2. Mass of the cluster calculated from ion masses

Formula of ions	Mass of ions	Mass of cluster
$[\text{Au}_{18}(\text{SG})_{14}\text{-4H}]^{4-}$	1956.2	$(1956.2 \times 4 + 4) = 7828.8$
$[\text{Au}_{18}(\text{SG})_{14}\text{-5H}]^{5-}$	1565.2	$(1565.2 \times 5 + 5) = 7831.0$
$[\text{Au}_{18}(\text{SG})_{14}\text{-6H}]^{6-}$	1304.3	$(1304.3 \times 6 + 6) = 7831.8$
$[\text{Au}_{18}(\text{SG})_{14}\text{-7H}]^{7-}$	1117.4	$(1117.4 \times 7 + 7) = 7828.8$

14. Supporting information 14

UV spectra of different clusters

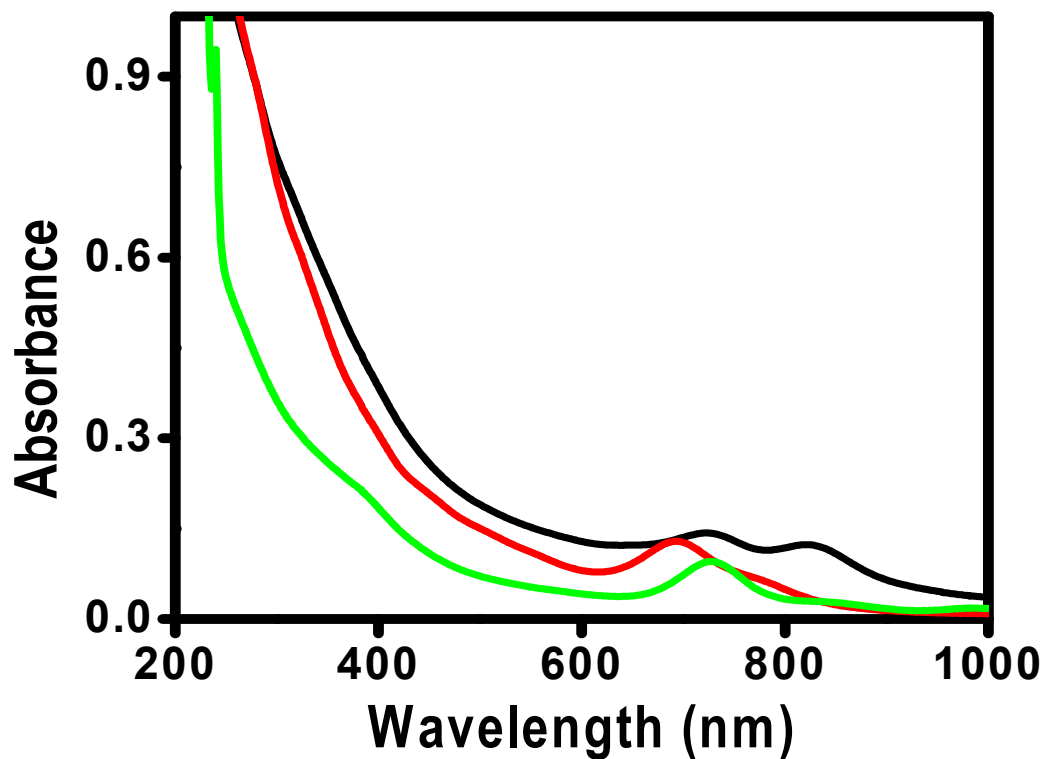


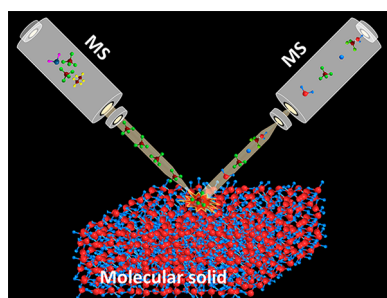
Figure S12. UV feature of different clusters synthesized by changing the ratio of glutathione and the reducing agent. The red line is almost matching with the previously reported Au₂₅ cluster. This suggests that optimization of synthetic conditions can get other specific clusters.

Low-Energy Ionic Collisions at Molecular Solids

 Jobin Cyriac,^{†,‡,⊥} T. Pradeep,^{*,†} H. Kang,[§] R. Souda,^{||} and R. G. Cooks^{*,‡}
[†]DST Unit of Nanoscience, Department of Chemistry, Indian Institute of Technology Madras, Chennai 600 036, India

[‡]Department of Chemistry, Purdue University, West Lafayette, Indiana 47907, United States

[§]Department of Chemistry, Seoul National University, Gwanak-gu, Seoul 151-747, Republic of Korea

^{||}International Center for Materials Nanoarchitectonics, National Institute for Materials Science, 1-1 Namiki, Tsukuba, Ibaraki 305-0044, Japan


CONTENTS

1. General Overview	5356
1.1. Fundamental Principles	5358
1.1.1. Electron Transfer	5359
1.1.2. Reactive Collisions	5360
1.1.3. Soft Landing	5360
2. Surfaces for Ion/Surface Collisions	5362
3. Instrumentation for Ion/Surface Collision Experiments	5364
3.1. First-Generation Instruments	5364
3.2. Newer Instruments	5364
3.3. Instrumentation for Ion Soft Landing	5367
3.4. Ionization Methods	5369
3.5. Some Ion Transfer Optics	5370
3.5.1. Static Quadrupole Bending Lens	5370
3.5.2. Octapole/Hexapole Ion Guide	5370
3.5.3. Ion Funnel	5370
4. Postcollision Surface Analysis	5371
5. Polyatomic Ion/Surface Collisions	5373
5.1. Aromatic Hydrocarbon Ions	5373
5.2. Aliphatic Hydrocarbon Ions	5374
5.3. Simple Organic Ions	5375
5.4. Organic Reactions at Surfaces	5375
5.4.1. Surface Polymerization by Ion-Assisted Deposition	5376
5.4.2. Cross-Linking Reactions	5377
5.5. Reactions of Metal-Containing Ions	5377
5.6. Some Miscellaneous Ions	5379
6. Soft Landing and Related Phenomena	5382
6.1. Separation and Protein Array Formation	5382
6.2. Peptide Immobilization by Soft Landing	5382
6.3. Retention of Biological Activity	5383
6.4. Soft Landing of Organometallics	5383
6.5. Preparation of Catalytic Surfaces	5384
6.6. Nanopatterning	5385
6.7. Fluorinated Surfaces	5386

6.8. Ambient Ion Soft Landing and Electrospray Deposition	5387
6.9. Other Uses of Soft Landing	5387
7. Collisions at Condensed Molecular Solids	5387
7.1. Reactive Scattering and Sputtering	5387
7.2. Surface Composition and Structure	5389
7.3. Transport Properties	5391
7.4. Acid–Base Chemistry	5392
7.5. Chemical Reactions	5392
8. SIMS Analysis of Condensed Molecular Solids	5396
8.1. Phase Changes	5396
8.2. Solvation (Hydration)	5398
8.3. Intermixing	5399
8.4. Dewetting	5399
8.5. Molecular Interactions	5400
8.6. Chemical Reactions	5400
8.7. Understanding SIMS as Relevant to Biological Analysis	5400
9. Summary and Perspectives	5401
Author Information	5402
Corresponding Author	5402
Present Address	5402
Notes	5402
Biographies	5402
Acknowledgments	5403
Abbreviations	5403
References	5403

1. GENERAL OVERVIEW

The roots of mass spectrometry (MS) can be traced to the early 20th century when in the Cavendish Laboratory at Cambridge University, U.K., J. J. Thomson performed his first experiments using the “parabola spectrograph”. F. W. Aston, a student of Thomson’s, contributed greatly to the technique with his originality in instrumentation and innovative applications.^{1–3} A contemporary of Aston, Arthur Dempster, at the University of Chicago, Illinois, seeded the technique of MS across the Atlantic Ocean.⁴ The Second World War and the postwar era accelerated innovation in scientific instrumentation, and this affected the pioneers in MS as well. The latter part of the 20th century saw enormous advances in MS. Mass spectrometry is no longer a discipline confined to the basic sciences; it has expanded into many areas of science, engineering, medicine,

Received: October 5, 2011

Published: August 22, 2012

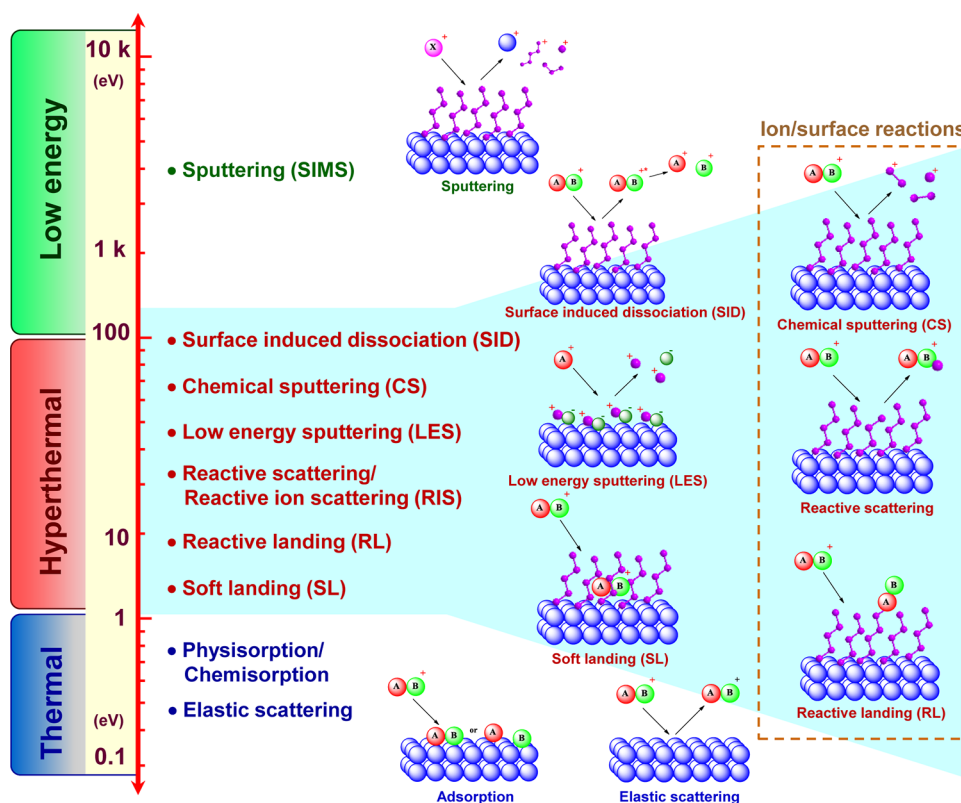


Figure 1. Important processes occurring during ion/surface collisions and the corresponding energy regimes.

agriculture, and quality control and has become a preferred tool for molecular analysis. The subject of this review, low-energy ion/surface interactions, portrays innovations in surface science and preparative methods associated with MS.

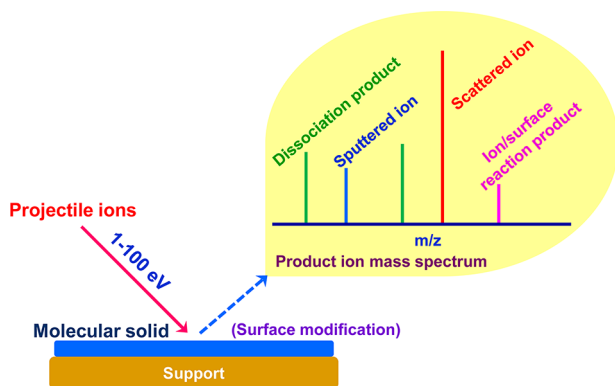
Ion-induced ejection of secondary species from a surface was known from J. J. Thomson's "Kanalstrahlen" experiments.⁵ However, Arnot and Milligan's investigation (in 1936) of the secondary ion yield and energy distribution of negative ions induced by colliding positive ions with surfaces is considered as the genesis of MS-based ion/surface experiments.^{6–8} The method was later termed secondary ion mass spectrometry (SIMS), in which bombardment of kiloelectronvolt (keV) energy primary ion beams at a condensed-phase interface releases charged atomic and molecular species which are then mass analyzed. Early SIMS experiments were used mostly for elemental analysis in a *dynamic* mode of operation.⁹ In the 1970s Benninghoven and co-workers showed the use of low-ion dose *static* SIMS experiments for the essentially nondestructive analysis of molecular surfaces, including organic materials.^{10–13} During the 1980s, SIMS emerged as a major surface molecular and elemental characterization tool as it was able to provide improved surface sensitivity and greater chemical specificity than electron spectroscopies, although it lacked the quantitative performance of the latter.

Subsequently, SIMS was developed to study chemisorption, adsorbate structure, surface reactivity, organic surfaces, and extended to biological samples.^{12,14–16} Now, apart from *static and dynamic* SIMS, other alternatives are available: *imaging* SIMS, where a highly focused ion beam provides chemical imaging with high spatial resolution, and *cluster bombardment* SIMS, in which low-damage cross sections and enhanced ion yields are achieved.^{16–21} At about the same time, surface-induced dissociation (SID) experiments emerged as a

molecular activation tool in MS. In this method, molecular ions collide at a surface (typically in the ion kinetic energy range of 20–200 eV), leading to fragmentation due to internal energy uptake occurring in competition with neutralization.^{22,23} This is a powerful method and is complementary to collision-induced dissociation (CID), the most common activation technique in tandem mass spectrometry (MS/MS), where the primary ions are activated through gaseous collisions. Recent work by Wysocki and co-workers has shown SID to be the preferred method of structural characterization of protein complexes.²⁴

In the late 1980s, data from SID in conjunction with the already established and rich area of gas-phase ion chemistry led to ion/surface collisions being performed at molecular surfaces rather than at metal surfaces. The activation of ions at these surfaces not only caused effective fragmentation of projectile molecular ions, which of course provides structural information, but also minimized neutralization and facilitated chemical reactions at these surfaces. As a consequence, the ion/surface collision procedure can provide information on the chemical nature of molecular surfaces and can alter them by forming covalent bonds with surface atoms or groups. The activation and reactive processes are fundamentally a hyperthermal energy counterpart of SIMS. The more important processes are designated as chemical sputtering (CS) and a similar process, low-energy sputtering (LES), ion/surface reactions, reactive scattering, reactive landing (RL), and soft landing (SL) (see Figure 1). Scheme 1 represents ion/surface collision events and the resulting product ion mass spectrum due to a number of these processes. Competition between these processes depends on the collision energy and the nature of the collision partners. For example, the elastic collision process of ion soft landing competes with the inelastic process in which the ion dissociates

Scheme 1. Ion/Surface Collision Event and the Resultant Product Ion Mass Spectrum^a



^aThe product mass spectrum consists of ions due to various events occurring during ion/surface collision.

upon collision (SID) and also with the several types of reactive collision processes. In CS, surface species are ejected as ions due to charge transfer between the impinging ion and the adsorbate at the surface. In the closely related LES experiment, pre-existing ions are ejected from the surface. As will become evident, these very low energy processes have recently been recognized as increasingly important, with CS proving to be a powerful new tool in the characterization of ice surfaces.

New chemical bonds are formed or broken in ion/surface reactive scattering or reactive collisions. The exchange of atoms or groups of atoms between the projectile ion and the molecular surface and/or charge exchange occur in reactive collisions. It is possible to direct gas phase generated molecular ions or clusters, possessing appropriate chemical functionality, with a few electronvolts of kinetic energy at a surface and to achieve (i) covalent immobilization of mass-selected projectile ions onto the molecular surface (termed RL) or nondestructive deposition of polyatomic ions on a condensed-phase interface (termed SL).

Extreme sensitivity to the outermost atomic layer makes the hyperthermal low-energy ion/surface collision a unique tool for surface analysis and controlled surface modification. From a molecular perspective, the surface phenomena occurring at molecular materials are applicable to gas–liquid interfaces and are important for fundamental understanding of heterogeneous processes occurring at gas–liquid as gas–solid interfaces. This makes hyperthermal or low-energy ion/surface interactions broadly applicable to research in chemistry and physics and a method that encompasses the interface between materials and biology. While the ion/surface scattering method based on elastic scattering has been used to perform elemental and structural analysis of surfaces, the use of reactive ions opens a variety of channels: dissociation of molecular ions, transfer of an atom or molecule, soft landing, ion/surface charge exchange, etc.

Various aspects of hyperthermal energy ion/surface interactions have been reviewed.^{12,22,23,25–37} Reviews devoted to ion/surface collisions at ice surfaces are also available.^{38–40} The goal of this review is to provide the current status of instrumentation and understanding of the processes and applications of ion/surface interactions at various molecular surfaces. We have limited the coverage to molecular surfaces and associated chemical processes occurring during impact of a hyperthermal energy ion. Most of the discussion will be on

polyatomic ions. One topic that is excluded is the inelastic ion/surface collision process, SID, as good overviews on this subject are available.^{41,42} Literature until June 2011 has been considered for this review.

The term “molecular solid” comprises the wide range of molecular materials that may be used in ion/surface collision experiments. Such surfaces include self-assembled monolayers (SAMs; in the text these are abbreviated in terms of their end group functionality), graphitic surfaces, polymers, liquids of low volatility, adsorbed molecules on substrates, etc. Apart from room temperature surfaces, the surfaces of interest include the condensed phases of simple molecules as well, condensed phases that are generally called “ices”. All the aforesaid molecular materials are considered as molecular solids in the discussion.

The energy regime that we consider lies in an intermediate range; a realistic lower limit of kinetic energy is ~ 1 eV, and the higher limit is on the order of a few hundred electronvolts (~ 300 eV) (see Figure 1). Primary ion energies of several kiloelectronvolts (1–15 keV), which is used in a typical SIMS experiment, have been considered in the case of condensed molecular solids to allow correlation with the results of CS or other LES experiments.

1.1. Fundamental Principles

Energy transfer in the course of an ion/surface collision can be simplified as

$$E_{\text{total}} = E_{\text{tr}} + E_{\text{int}} + E_{\text{surf}} = E'_{\text{tr}} + E'_{\text{int}} + E'_{\text{surf}}$$

(E_{tr} = translational energy of the incident projectile, E_{int} = its initial internal energy, E_{surf} = initial energy of the surface, E'_{tr} = translational energy of the product ion, E'_{int} = internal energy of the ion after surface collision, and $E'_{\text{surf}} - E_{\text{surf}}$ = energy adsorbed by the surface).²⁸ Many physical and chemical processes can occur during the collision event (see Figure 1 and Scheme 1). The occurrence of several elementary processes—elastic, inelastic, and reactive collisions in the low-energy range—assures a wide scope for this subject.

A series of complex interactions occur in the course of elastic or inelastic collisions. If sufficient energy transfer occurs in a collision cascade, secondary ions and/or neutrals are emitted, and the process is known as sputtering. Measurement of mass distributions of the secondary ions and the observation of associated chemical processes is done in SIMS. No single mechanism aptly accommodates all facts observed in studies of sputtering. Atomic SIMS can be explained by binary atomic sputtering theory, which provides a good physical model and is often used in the analysis of metals, semiconductors, and simple inorganic salts.¹² Ionization adds a considerable complication to this model. In molecular SIMS (studies of molecular surfaces by SIMS), an energetic collision cascade alone is unlikely to eject intact molecules and cannot account for ionization. Therefore, most molecular SIMS models have incorporated a translational or vibrational component into the mechanism.¹² Ion emission is initiated by a momentum transfer process followed by release of translationally and vibrationally excited target components. The translational energy distribution of the sputtered particles is broad and peaks at low energy, well below 10 eV. A fraction of the desorbed species may have sufficient internal energy to fragment in the gas phase, giving mass spectra showing both intact molecular and fragment ions.

SID takes place by transferring a fraction of the ion kinetic energy into internal energy, which in turn controls the ion's

dissociation into various fragment ions.²³ The extent of fragmentation depends upon the total internal energy content of the excited ion and the time scale, which is determined by velocity and the experimental conditions. Typically, the process occurs on the picosecond time scale, and 5–35% of the ion kinetic energy is converted into internal energy. Collisions with neutrals can further modify the ion internal energy of the sputtered ions. The basic processes can be difficult to discern since SID is accompanied by competing reactions at the surface (ion/surface reactions) involving different interaction potentials.²³ Simulations suggest that projectile ions are first excited via impulsive collisions with the surface and inelastically scattered from the surface and that they then dissociate unimolecularly some distance from the surface.⁴³ The initial ion kinetic energy, the nature of the incoming ion,^{44,45} the nature of the surface—most often SAMs, the surface roughness,⁴⁶ and the angle of collision⁴⁷ affect the energy transferred.

The internal energy distribution $P(E)$ of the surface excited ions can be estimated by studying the dissociation of “thermometer molecules” such as metal carbonyl radical cations, which have known energetics of fragmentation.^{22,48} In a specific example, the extent of surface activation of $\text{Cr}(\text{CO})_6^+$ ions in 70 eV collisions at an H-SAM surface has been calculated. The percentages of energy transferred into internal modes, E_{int} , into the surface, E_{surf} , and as final translational energy, E_{tr} , were found to be 9%, 81%, and 10%, respectively.⁴⁹ Modeling based on Rice–Ramsperger–Kassel–Marcus (RRKM) kinetics has been developed for determining the percentage of $\text{T} \rightarrow \text{V}$ transfer during SID of large molecules such as peptides.⁴⁵ For a singly protonated octapeptide, des-Arg¹-bradykinin, the average energy deposited into the ion was found to increase from H-SAM (10.1%) to LiF (12.0%), diamond (19.2%), and F-SAM (20.5%) mainly due to mass effects. However, the width of the internal energy distribution is controlled by surface stiffness and followed the order H-SAM < F-SAM < LiF < diamond. Collision energy resolved SID of des-Arg¹- and des-Arg⁹-bradykinin shows that there is a sharp transition in fragmentation behavior.⁵⁰ Both ions produce very few SID fragments at low collision energies (15–25 eV), but with increasing collision energy above 30 eV, the number of fragments in the spectrum increases dramatically. This must be due to access to a variety of dissociation pathways. Time-resolved studies support the fact that most of the high-energy fragments are formed directly from the excited precursor ion but could not be attributed to consecutive dissociation of primary fragment ions.⁵⁰

A number of reactive processes such as electron transfer, fragmentation, atom abstraction, oxidation, and RL can occur in low-energy ion/surface collision events. Most often, the relative collision energy of an ion is of the same order of magnitude as chemical bond energies. Hence, the ion/surface interaction is large enough to lead to bond dissociation and to bond formation (which normally requires substantial activation energy). The observed chemical processes are strongly influenced by the chemical nature of the projectile ion as well as the electronic structure and chemical nature of the surface. A brief account of various reactive processes is given below.

1.1.1. Electron Transfer. Several possibilities fall under this heading. Electron transfer that leads to ion neutralization is often the most probable event. The electron is lost from either the adsorbate or the metal surface to which the adsorbate is bound, and the surface gains a charge, while the projectile ion is neutralized. The efficiency of such electron transfer processes is

determined by the difference between the electron affinity of the ion (i.e., its recombination energy) and the work function of the metal surface. Aside from thermochemical factors, the kinetics of electron tunneling also varies strongly with the distance of the closest encounter between the projectile ion and the surface. Fluorocarbon SAMs (F-SAMs) and long chain alkyl SAMs (H-SAMs) are found to reduce the neutralization of projectile cations relative to bare metals. Comparatively high ionization energies and the underlying large distances between the impinging ion and metal surface reduce the neutralization of projectile ions.^{51–53} A doubly charged molecular ion may undergo charge exchange to form singly charged ions, which can be easily identified and detected.^{54–56} The singly charged intermediates formed may decompose further. For example, collisions of multiply charged fullerene cations C_{60}^{n+} ($n = 1–5$) at steel surfaces result only in singly charged scattered ions and dissociation products formed by loss of sequential C_2 units.^{32,57} The extent of fragmentation is determined by the collision energy. A possible explanation for this process may be the immediate neutralization of the incoming ions followed by autoionization due to thermally activated electron emission.⁵⁷

Apart from these simple electron transfer processes, charge inversion may occur by double electron transfer ($\text{M}^+ \rightarrow \text{M}^-$) or charge stripping ($\text{M}^- \rightarrow \text{M}^+$), where the incident positively charged ions are converted into negatively charged ions (and vice versa).⁵⁸ Most charge inversion reactions have been performed in the kiloelectronvolt energy range, mainly because at these energies electron stripping and electron transfer reaction have sufficiently high cross-sections. Projectile ions can lose electrons by charge stripping with liberation of free electrons, and often these reactions are accompanied by dissociation when the nascent product is sufficiently excited. Charge inversion is frequently observed in gas-phase processes^{59,60} and has proven to be of considerable value in the determination of thermochemical properties of gaseous ions.^{61,62} Doubly charged cations derived from benzene and toluene in collisions at highly oriented pyrolytic graphite (HOPG) surfaces were found to produce only singly charged products.^{56,63} An important process in the collisions of dications is evidently single-electron charge transfer between the surface and the projectile with formation of singly charged intermediates which may further decompose to lower mass fragments.⁶⁴

Charge transfer can lead to another important process, closely related to projectile ion neutralization, which is referred to as chemical sputtering (CS). This has great potential value in industrial processing of materials, where it is also referred to as ion-assisted erosion or ion-assisted etching.³⁰ In CS, ions are released as a result of a chemical reaction, not momentum transfer. During the collision event, charge exchange occurs between the surface (surface adsorbate) and the impinging projectile ion, causing ionization of the surface molecules and their release from the surface.⁶⁵ CS is distinct from the momentum transfer events that underlie physical sputtering in kiloelectronvolt collisions. CS may occur with or without further fragmentation depending on the difference in ionization energies (or other appropriate thermochemical properties, e.g., proton affinity) of the projectile and the target. The mass spectrum of the desorbing ionized species carries information on the nature of the outermost layers of the surface.

A study aimed at understanding the formation of sputtered neutrals showed that abundant neutral species released from the surface are due to sputtered adsorbate rather than

collisional neutralization of hyperthermal precursor ions.⁶⁶ A fraction of the sputtered molecules and neutralized precursor species will have kinetic energies in the hyperthermal range so that they can be reionized by a second surface collision.⁶⁶

1.1.2. Reactive Collisions. In reactive collisions, the colliding ion beam itself acts as a chemical reagent, forming new bonds with surface groups or abstracting atoms or groups of atoms from the surface. In these processes, thermodynamically favored reactions that lead to the formation of new chemical bonds will be favored. One of the most extensively studied ion/surface reactions is atom or group abstraction from SAMs.^{23,34,52,67–73} Figure 2 shows a good example of ion/

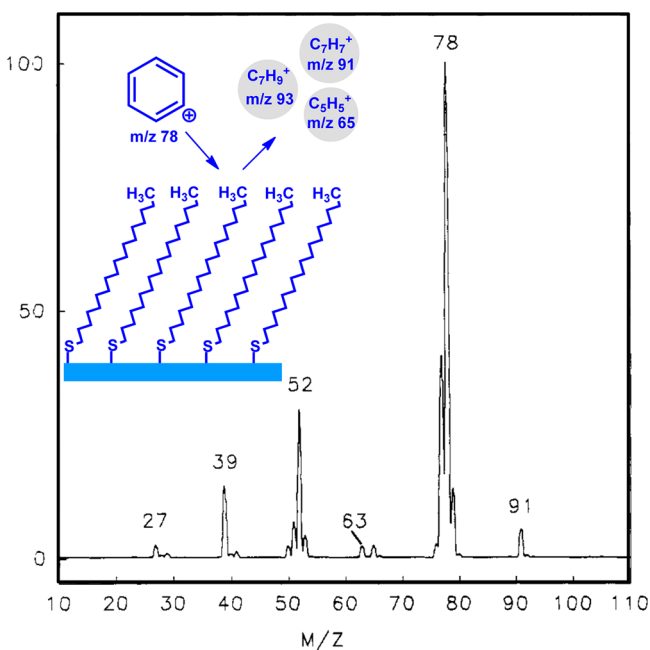


Figure 2. Ion/surface collision spectrum recorded after collision of 30 eV benzene molecular ions at an H-SAM surface. The ion at m/z 91 corresponds to the addition of a methyl group followed by loss of H_2 and that at m/z 65 to further loss of C_2H_2 . The peak at m/z 79 is due to a H atom abstraction reaction. The inset shows the collision process and some reaction products. Reprinted from ref 72. Copyright 1993 American Chemical Society.

surface reactions upon 30 eV collisions of benzene radical molecular ions at an H-SAM surface. The peaks at m/z 91, 79, and 65 are due to ion/surface reactions. Many similar examples involve the exchange of atoms or groups of atoms between the ionic projectile and the molecular surface.^{74,75} The abstraction of single hydrogen atoms from hydrocarbon surfaces was observed to occur with impinging radical cations containing heteroatoms, while multiple hydrogen atom abstraction occurs in highly unsaturated ions.^{76,77} The abstraction of whole adsorbate molecules or functional moieties can occur during hyperthermal Cs^+ reactive scattering at surfaces.^{78–80}

Reactions between incident gas molecules and surfaces are generally classified into two broad types of mechanisms, nonequilibrium Eley–Rideal (ER) and equilibrium Langmuir–Hinshelwood (LH) mechanisms. Most ordinary (non-ionic) reactions at the gas–surface interface occur via the LH mechanism in which the reagents are chemisorbed and equilibrated at the surface and the product translational energy is independent of the incident reagent. During the ER process, an incident gaseous ion reacts directly with a surface adsorbate

and leaves with a significant fraction of its translational energy. Low-energy ion/surface reactions are believed to proceed in a single scattering event with an estimated interaction time that falls in the nonequilibrium ER regime. For a typical example of the pickup of surface hydrocarbon fragments by naphthalene projectiles, calculations show that the time scale is on the order of 100 fs.⁸¹ Many convincing arguments favoring the ER mechanism in ion/surface reactions have been subsequently reported. Abstractions of O atoms from oxidized Si and Al surfaces by O^+ and NO^+ ions and C atoms from a graphite surface by low-energy N^+ ions strongly support the ER mechanism.^{82–86} Evidence for the ER mechanism in ion/surface collisions of Cs^+ with various adsorbate species has been demonstrated theoretically and experimentally.^{87–89} Formation of endohedral fullerenes produced by the collision of Cs^+ at a fullerene surface suggests that the reaction proceeds through a single collision event.^{90–92} Fragments such as $Cs@C_{50}^+$ or C_{44}^+ can be formed during their flight from the surface via a sequential emission of C_2 units either from the endohedral product or from the sputtered fullerene.^{90–92}

While it seems evident that low-energy ion/surface reactions occur during a single scattering event under nonequilibrium condition, speculations continue on whether the reactions actually occur at the surface or in the gas phase near the surface and so involve the desorbing species.^{93,94} For example, reactive collision processes of Cs^+ ions were initially considered to occur by the latter mechanism, collisional desorption of the adsorbates followed by Cs^+ –molecule association in the gas phase, when the phenomenon was first observed with chemisorbed species.^{78,95,96} In later experiments with physisorbed molecules, however, a much higher (up to $\sim 100\%$) yield was observed for the abstraction of the adsorbates by Cs^+ ,^{80,87,97} and classical molecular dynamics (MD) simulations^{88,98} suggested that this abstraction process actually occurs in a one-step mechanism classified as an ER reaction. It may be possible to view the early experimental observations with chemisorbed molecules also as a direct ER process. Reactive collision events with chemisorbed molecules may belong to a special case of the ER reaction which occurs with low efficiency, because the ion/surface collision geometry and the energy transfer must be very precisely controlled to achieve the collisional desorption of strongly adsorbed species and also the Cs^+ –molecule association reaction.⁸⁸ In the scattering of alkali-metal ions, the effect of ion neutralization at the surface is insignificant. However, when polyatomic organic ions collide with hydrocarbon-covered surfaces, the incident ions can be neutralized during the low-energy collisions (except in the SL case),³³ and protons are often sputtered as a result of these collisions.⁹⁹ For such events, it was proposed that the association reaction occurs between the neutral projectiles and sputtered protons near the surface to form protonated molecular ions (a sputtered ion mechanism).⁹⁹ A few intermediate mechanisms have been proposed that fall between these two extremes.^{100,101}

1.1.3. Soft Landing. At low energies on the order of 10 eV, polyatomic ions can be deposited intact onto surfaces.¹⁰² The process is referred to as SL, in which the intact capture of hyperthermal polyatomic ions at surfaces is achieved. The term SL refers specifically to those deposition events in which the species does not lose its molecular connectivity. In the strictest sense, the ion is not neutralized, but this distinction is often not made. Neutralization can occur by electron or proton transfer to (or from) the adsorbate. The landing species must dissipate

its kinetic energy during impact without breaking covalent bonds. The energy is distributed into vibrational and electronic degrees of freedom of the projectile and the surface. What distinguishes SL from other methods of preparing materials is the unique purity (chemical, isotopic, structural) of the selected projectile and the control that can be exerted over the nature of the deposition process exercised simply through kinetic energy (KE) selection.

One of the most fascinating aspects of the SL process is its charge retention.¹⁰² Properties such as organization, density, and steric constraints of the monolayers in which SL occurs and the orientation of the end groups of the monolayers are critical factors determining the trapping efficiency of the surface and the degree of neutralization experienced by the ions. The charge associated with a soft-landed ion can be preserved for hours or even days in matrices such as SAMs and other functionalized molecular surfaces.^{35,36} The contrast between clean metal surfaces, where image forces capture and neutralize slow ions, and self-assembled monolayers which act as leaky dielectrics precluding charge buildup (and associated repulsion of arriving ions) is that the latter do not provide the option for facile ion/electron recombination that is available at clean metal surfaces. A reviewer has commented that it is not an exaggeration to state that investigating SAM surfaces has enabled a number of breakthroughs in understanding and applications of soft landing. H-SAMs provide relatively soft matrices for collisions resulting in less fragmentation, so favoring SL of labile ions.¹⁰³ The ions are strongly held inside the SAM matrix by electrostatic interactions between the soft-landed ions and their induced electric dipoles in the substrate. The ions in a well-protected matrix (such as an F-SAM) can develop a significant potential on an insulating surface.¹⁰⁴ The attractive potential between the ion and the surface, which is a function of distance, determines the efficiency of trapping of ions at the surface. Also it is found that intact SL is more successful with closed-shell rather than open-shell ions due to the ease of neutralization and fragmentation of the latter.^{102,103,105}

Charge retention by soft-landed protonated bradykinin and gramicidin S was followed by examining fragmentation patterns recorded using SIMS spectra to interrogate the surface after SL.^{106–109} Multiply protonated peptide ions soft-landed onto F-SAM surfaces retain both doubly and singly protonated peptides, whereas H-SAM surfaces preserve only singly protonated species.^{106,107} Doubly charged species convert to singly charged species on the H-SAM surface. Complete neutralization of the same species was observed on the COOH-SAM surface.^{106,107} Ions are well protected in the F-SAM matrix compared to the H-SAM matrix, presumably due to the larger polarity and polarizability of the former.¹¹⁰ Charge retention decreases in the order F-SAM > H-SAM > COOH-SAM, indicating much increased neutralization efficiency of the hydrophilic COOH-SAM surface relative to the inert H-SAM and F-SAM surfaces. The desorption kinetics of ions and neutral peptide molecules retained on different surfaces support these observations (see Figure 3).¹⁰⁸ In Figure 3, the decrease of doubly protonated signal is attributed to the formation of a singly charged ion by proton exchange ($k = 10^{-2} \text{ min}^{-1}$). By contrast, the singly charged species mainly decays by the thermal desorption pathway ($k = 6 \times 10^{-4} \text{ min}^{-1}$) as proton loss from this ion is very slow ($k = 10^{-5} \text{ min}^{-1}$). In contrast again, the neutral species formed by instantaneous neutralization of the singly protonated ion upon collision with the surface

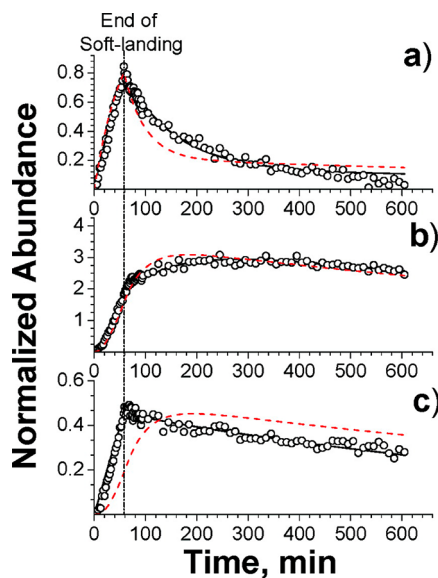


Figure 3. Kinetic plots obtained for the (a) $[\text{gramicidin S} + 2\text{H}]^{2+}$ ion, (b) $[\text{gramicidin S} + \text{H}]^{+}$ ion, and (c) neutral gramicidin S molecules on a surface: experimental data (O) and the results of the kinetic modeling with (solid lines) and without (red dashed lines) the instantaneous charge loss by ions upon collision being taken into account. Reprinted from ref 108. Copyright 2007 American Chemical Society.

shows a linear increase during ion deposition and an almost linear decrease after SL. In another experiment, it was shown that neutralization of a soft-landed $\text{M}^{\text{III}}(\text{salen})^{+}$ complex of Mn and Co deposited on F-SAM was very slow compared to that on H-SAM, where it occurs readily.¹¹¹

The second pathway for neutralization, through electron transfer, was observed in the case of SL of such molecular cations as rhodamine B or Jacobsen's catalyst. Metal, semiconductor, and F-SAM surfaces neutralize the ions, as expected, by instantaneous electron transfer, and the insulator surface (SiO_2 and Teflon) retains the charges for several days after SL of the molecular ions. Protonated species could discharge on the metal oxide (e.g., iron oxide) surface by proton transfer.¹¹² It is argued that this proton transfer is coupled with protonated oxide reduction (e.g., $\text{Fe}^{3+} \rightarrow \text{Fe}^{2+}$) by electron transfer from the conduction band of the bulk metal.

A projectile ion may sometimes undergo RL or dissociative soft landing depending upon its kinetic energy and the nature of the surface. Projectiles that react readily with atoms or functional groups present at the surface will tend to undergo RL rather than simple SL.^{105,112–114} In dissociative landing, the fragments resulting from dissociation of the projectile ion in the course of the surface collision are trapped within the surface rather than being scattered away as in SID. This process may occur with cleavage and elimination of groups and successive recombination of the landed species. For example, rhodamine (B and 6G) undergoes fragment deposition,¹¹⁵ and 1,3-divinyltetramethyldisilazane forms an inorganic silicocarbonitride film at collision energies¹¹⁶ above 100 eV. These processes do not necessarily overwhelm simple SL, so for example, the intact deposition of peptide ions onto F-SAM is feasible even at collision energies on the order of 150 eV.¹¹⁰ Because F-SAM surfaces have greater effective mass (interaction with the CF_3 group vs the CH_3 group in an H-SAM), they are more effective at converting laboratory KE into internal energy and hence in

promoting dissociation, both in dissociative SL and in the competitive inelastic collision process of SID.

2. SURFACES FOR ION/SURFACE COLLISIONS

Collisions of simple atomic and diatomic ions at clean metal surfaces have been the subject of a series of experiments since the late 1960s.^{27,117–122} Molecular materials are interesting compared to bare metals since they change the work function, functionality, and energy transfer characteristics of the surface. Well-defined highly ordered surfaces are good choices for fundamental studies. One of the best choices is the SAMs,¹²³ most often alkanethiolate SAMs on gold (Au–SAMs). The relatively low surface energy of the Au–SAMs results in low levels of surface contamination, and these surfaces are stable in ultra-high-vacuum (UHV) conditions.

Most significantly, alterations in the terminal atoms or functional groups in SAMs expose a wide variety of surface species for interaction with the projectile beam. Development of new technologies such as molecular and biodevices using organic thin films is attractive and adds importance to the study of ion/surface collisions at SAMs and other surfaces. SAMs, especially F-SAMs, are ideal choices for SID applications as they have reduced neutralization efficiencies compared to metal surfaces. Scattering from SAM surfaces results in a narrower internal energy distribution of the scattered ions (narrower, for example, than that of Au(111) surfaces), making them excellent for SID experiments.¹²⁴ However, typical SAM surfaces impart less energy to the internal modes of the scattered ions as they represent a more easily deformable target than a metal surface. The energy transfer to the surface is dependent on the masses of both partners in the collision.¹²⁵ Increased translational energy to internal energy ($T \rightarrow V$) conversion and decreased neutralization of projectile ions occurs at fluorinated surfaces relative to hydrocarbon-terminated surfaces.^{45,126–129} F-SAMs are attractive when maximum energy transfer is required as in SID experiments, and it is probable that its more massive terminal group is implicated. Compared to a F-SAM surface, an H-SAM has a lower ionization energy (IE) (13.38 eV for C_3F_8 and 10.94 eV for C_3H_8), which likely facilitates neutralization (the C–H bond energy is 98 kcal/mol in C_2H_6 , and the C–F bond energy is high, 130 kcal/mol, in C_2F_6).¹³⁰ Increased neutralization might be an advantage in SL (where it avoids charge buildup) but not in SID (where it reduces the fragment ion current).

The ion/surface reaction efficiency varies with the orientation of the atom or group present at the monolayer terminus.¹³¹ Reactive collisions involving fluorine addition to the benzene molecular ion showed even and odd carbon chain alternation ascribed to angular orientation of the terminal CF_3 group relative to the surface plane.⁷³ The intensity of the products of hydrogen and methyl addition to the pyrazine ion upon collisions at an H-SAM also vary for odd versus even chain lengths.¹³¹ This difference can be explained readily by taking fluorine addition to the benzene molecular ion as an example. The intensity of the fluorine abstraction peak is greater for odd-numbered chains than for even-numbered chains. The last fluorine atom of odd-numbered chains extends substantially above the plane defined by the outermost carbon atoms.¹³² However, in even-numbered chains, all three fluorine atoms lie slightly above the plane defined by the outermost carbon atoms. In the former case, the exposed fluorine atom would appear to be relatively accessible to the projectile ion for abstraction.

It is also clear that the surface molecular species themselves can undergo ion-beam-induced reactions or fragmentation. Ion-induced processes on H-SAM surfaces appear to lead to dissociation of C–H and C–C bonds in the chain. More than 10 eV of energy can be transferred to the surface in a typical 25 eV collision event, more than enough to break the 2–4 eV bonds of the SAMs.⁵³ Many of the species formed by ion bombardment are likely to spontaneously desorb at 300 K. The threshold incident energy for the release of ionic fragments from surface molecules is typically ~ 20 eV and was found to be independent of the nature of incident molecular ions derived from furan, pyridine, and thiophene.¹³³

Structurally rigid F-SAM surfaces and flexible perfluoropolyether (PFPE) chains show similar $T \rightarrow V$ conversion efficiencies. The reaction/fragmentation behavior of $C_6H_6^+$ at Teflon suggests correlation between this surface and F-SAM surface.¹³⁴ Similar behavior is also observed in the case of perfluorinated Langmuir–Blodgett (LB) films and F-SAM surfaces.¹³⁵ These observations clearly indicate that only the topmost surface layers take part in the hyperthermal energy collision event. Interestingly, experimental observations show quantitative similarities in energy transfer between hydrocarbon and semiconductor Si surfaces.⁴⁸ When the energy is increased (>10 keV Ga^+ primary ion), formation of Au–S and Au–adsorbate cluster ions starts to occur in the product ion spectra just as occurs in SIMS under kiloelectronvolt conditions.^{136,137}

Ionic liquids, polymer oils, graphitic surfaces, and polymer surfaces are other interesting targets. Room temperature ionic liquids are compatible with UHV conditions. The liquid surfaces have the obvious additional advantage that the surfaces are molecularly flat and are renewed after each collision because of the high mobility of molecules in liquid compared to SAMs. Glycerol-based liquids have been used in SL experiments to preserve the biological activity of the soft-landed proteins.^{138,139} The limitations of using a high-vapor-pressure liquid in high-vacuum applications were mitigated by the addition of polyols or sugars.¹⁴⁰

HOPG substrates provide an excellent SL surface for fullerene ions^{141–145} and a good surface for SID in general.¹⁴⁶ Atomic defects such as vacancies and interstitials have been produced at HOPG surfaces by low-energy ion collisions, and these atomic defects are further etched into nanoscopic pits and channels via O_2 oxidation of the surface.^{147,148} HOPG can act as a good hydrophobic surface for condensed molecular solids. Above 120 K, water forms 2D islands as a result of surface diffusion.¹⁴⁹ Another carbonaceous surface, fullerene, produces $Cs@C_{60}$ or $Cs@C_{70}$ endohedral fullerene ions upon reactive collision of hyperthermal energy Cs^+ ions.^{90,92}

Size-selected metal clusters have been soft landed onto HOPG and metal oxide substrates as a result of interest in the chemical reactivity of the deposited clusters.^{150–156} Depending on the kinetic energy of the cluster, they can undergo pinning and implantation on the graphite substrate. Clusters which are stable at room temperature can be created using a higher collision energy (a few hundred to a few thousand electronvolts) using the pinning technique.^{157–159} The clusters can be immobilized on the substrate at the point of landing by creation of a surface defect in the uppermost graphite layer.

Changes in the physicochemical properties of a large number of polymers have been reported when they are modified by ion beams.^{160–162} Hyperthermal fluorocarbon, organosiloxane, and thiophene ions have been used successfully as an alternative to

Table 1. First-Generation Ion/Surface Collision Instruments

instrument	mass filter (first stage)	mass analyzer (second stage)	ionization	~year reported	refs
Delaware	FTMS	FTMS	EI, CI, ESI	1997	203
FOM (Amsterdam)	TOF	TOF	photoionization	1994	595
Illinois	Wien filter	Q	EI	1993	76
Innsbruck	BE (reverse geometry)	TOF	EI (Nier type)	1997	261
Marburg I	TOF	TOF	²⁵² Cf plasma	1993	596, 597
Notre Dame	Wien filter	velocity image detector	laser ionization	1992	598
POSTECH I	Wien filter	Q	EI, cold plasma	1990	170, 599
POSTECH II	none	EQ	surface ionization	2001	87, 172
Prague	B	B	EI	1998	68
Princeton	Q	Q	EI	1995	260
Purdue 0	B	Q	EI/CI	1985	171
Purdue I	BE	EQ	EI/CI	1991	167
Purdue II	Qoq	oQ	EI/CI	2002	262
Tokyo	TOF	TOF	laser ionization	1995	243, 600
VCU	Q	Q	EI	1991	168, 169

Table 2. Instrument Descriptions

instrument	layout
Delaware ²⁰³	Ions were focused into the standard dual cell of an FTMS instrument by a lens assembly. The scattered ions recoiled into the source side FTMS cell, where they were trapped and detected by FTMS. A probe potential of +2 V ensured that the fragment ions were injected into the FTMS cell efficiently.
FOM (Amsterdam) ⁵⁹⁵	Ions were accelerated in an electric field and injected into the drift tube of a TOF mass spectrometer. The original gridless reflector was replaced by one with grids in which the collision surface was mounted. The SID fragments were identified on the basis of their flight times in the second stage. The angle defined by the source, the surface, and the detector was about 6°.
Illinois ⁷⁶	Ions were accelerated to ~1 keV through a Wien filter, a velocity filter with static crossed magnetic and electric fields for mass selection, bent 3° to remove fast neutrals, and finally refocused and decelerated to the appropriate energy prior to collision with the target. A quadrupole mass spectrometer was used as an analyzer for scattered ions and to conduct TPD experiments.
Innsbruck ²⁶¹	Ions were accelerated to 3 keV by a double-focusing two-sector mass spectrometer of reverse geometry. After passing the exit slit of the mass spectrometer, the ions were refocused at the collision surface by deceleration optics. The surface normal was at 45° with respect to the incident and scattered ion beam. The second mass analyzer was a linear TOF spectrometer, and the scattered ions were extracted by pulsed extraction voltages and detected by a dual microchannel plate.
Marburg I ^{596,597,601}	A modified ²⁵² Cf plasma desorption TOF mass spectrometer was used, with mass selection of the primary ions being achieved by pulsing the deflecting voltage.
Notre Dame ⁵⁹⁸	Ions were accelerated to -200 eV, mass selected using a Wien filter, and decelerated and focused with a Menzinger lens. Scattered ions were collected with a two-dimensional velocity image detector, which was positioned along the surface normal to quantify the number of ions impinging onto its surface.
POSTECH I ^{170,599}	Preaccelerated ions were mass selected through a Wien filter, bent 12° to remove fast neutrals, and decelerated to the required energy (1–300 eV). Ions scattered from the surface were detected using a quadrupole mass spectrometer, and the ion kinetic energy was analyzed with a retarding field analyzer. Surface products were characterized by electron spectroscopy and TPD.
POSTECH II ^{87,172}	Low-energy (5–100 eV) beams of alkali-metal ions were generated from a compact surface ionization source, located close to the target inside a vacuum chamber. A quadrupole mass spectrometer with an axial energy filter was used to analyze the scattered ions. Angle-resolved ion/surface scattering experiments were done using independent rotation of the ion source and the target.
Prague ⁶⁸	Ions were accelerated to 140–300 eV, mass analyzed using a 90° permanent magnet, and decelerated to the required energy. The scattered ions from the surface passed through a detection slit and then accelerated to 1000 eV into a magnetic sector instrument equipped with a Galileo channel multiplier.
Princeton ²⁶⁰	Two quadrupole mass spectrometers were mounted in a custom Conflat flange. One quadrupole served as a mass-selective ion source, and the other quadrupole served as a scattered ion detector.
Purdue 0 ¹⁷¹	Ion beams were accelerated to 6 keV prior to mass analysis by a magnetic sector (B) and then decelerated to ground potential prior to collision at the surface. The surface was placed at 45° to intersect the ion path. A mass analyzing quadrupole was placed at 90° with respect to the incident beam. A 45° energy analyzer placed between the surface and analyzer quadrupole led to a 90° angle between the incident and emerging beams.
Purdue I ¹⁶⁷	The ion beam was focused at the exit slit of the front-end electrostatic analyzer of a double-focusing sector mass spectrometer, and a quadrupole doublet collimated the ion beam onto the surface. The second stage was composed of an EQ combination, electrically floated to provide the required low axial velocity for product ion analysis. See Figure 4 for a schematic of this instrument.
Purdue II ²⁶²	Ions were extracted from the source and transferred into a quadrupole mass filter. The static quadrupole guided the ion beam either to the electron multiplier or to be turned through a 90° angle toward the target surface. The scattered ions were mass analyzed by a quadrupole mass filter and detected by a second electron multiplier.
Tokyo ^{243,600}	Ions were decelerated along a parabolic trajectory by an electric field inside a reflectron and allowed to collide with the surface. Product ions scattered from the surface were accelerated along a parabolic trajectory and then analyzed by a TOF mass spectrometer. The angle between the surface normal and the second flight path could be varied between 0° and 4° by rotating the reflectron.
VCU ^{168,169}	Two quadrupole mass analyzers were placed at 90° to each other with a surface placed to intersect the ion optical path of the two quadrupoles.

plasma processing to grow thin films on polymer surfaces, as will be discussed in section 6.7.^{162–166}

Surface composition, phase changes, solvation, transport properties, and chemical reactions have been studied by appropriate ion/surface collision experiments involving condensed molecular solids. The unique behavior of ice surfaces in

processes which are very uncommon in liquid-phase water is

fascinating, and this topic is elaborated in sections 7 and 8.

3. INSTRUMENTATION FOR ION/SURFACE COLLISION EXPERIMENTS

The simplest ion/surface collision instrument includes an ion source followed by a mass analyzer to select ions of interest with a desired kinetic energy as the first stage of the instrument, followed by the surface of interest at which collisions leading to excitation or reactions are performed. An analyzer mass spectrometer is used in the second stage to analyze the scattered products/secondary ions. As will be obvious, in the SL experiments the second-stage mass spectrometer may not be necessary. The primary difference between the various instruments that have been built is the choice of ionization methods and the type of mass analyzer. Design considerations include the usual trade-off between resolution and transmission, with both mass and energy resolution being considerations. Not only are there intrinsic factors involved—such as access to particular conditions for particular ion/surface collision processes—but differences in the types of mass and energy analyzers affect transmission, resolution, and data acquisition speed.

The discussion in this section is divided into two parts. The instruments in operation before the year 2002 are considered first-generation instruments and are presented only briefly (see Tables 1 and 2). This choice of time span is made to cover the developments during the past decade in more detail. Good reviews are available on the first-generation instruments.^{23,28,33,34} One cautionary statement: The performance parameters given are actual data for particular systems at the particular time they were reported on. They normally do not represent the best possible performance with the types of instruments selected. Similarly, there have been many advances in ion optics and modeling of devices such as ion funnels since these instruments were described, and the presentation does not attempt to update the original descriptions to reflect the current state of the art.

3.1. First-Generation Instruments

Early hyperthermal ion/surface reactive collision experiments were performed in the BEEQ instrument at Purdue.¹⁶⁷ This was a hybrid sector instrument with a BEEQ (B = magnetic sector, E = electric sector, and Q = quadrupole) configuration (referred to as Purdue I in the present review). The BEEQ allowed mass and energy selection of the primary ion beam (using BE) and measurement of the energy and mass (using EQ) of product ions scattered through selected scattering angles (see Figure 4). A double-focusing sector mass spectrometer was used as the first stage. At the same time, instruments at Virginia Commonwealth University (VCU),^{168,169} Richmond, VA, and at POSTECH,¹⁷⁰ Korea, were also used to perform reactive collisions at surfaces. The VCU instrument based on early Purdue BQ¹⁷¹ and QQ instruments used a simple design with two quadrupole mass analyzers placed 90° to each other. The surface of interest was placed at 45° to the ion optical path of these quadrupoles. The ion beam instrument developed at POSTECH, South Korea (referred to as POSTECH I),¹⁷⁰ used mass- and energy-selected beams of reactive ions in the range of 1–300 eV energy, and the scattered ions were detected using a quadrupole mass analyzer. A later instrument, an angle- and energy-resolved ion/surface scattering instrument (referred to as POSTECH II), was constructed and utilized to investigate the scattering dynamics of low-energy ions.^{87,172} The instrument was devoted to reactive collision experiments of alkali-metal

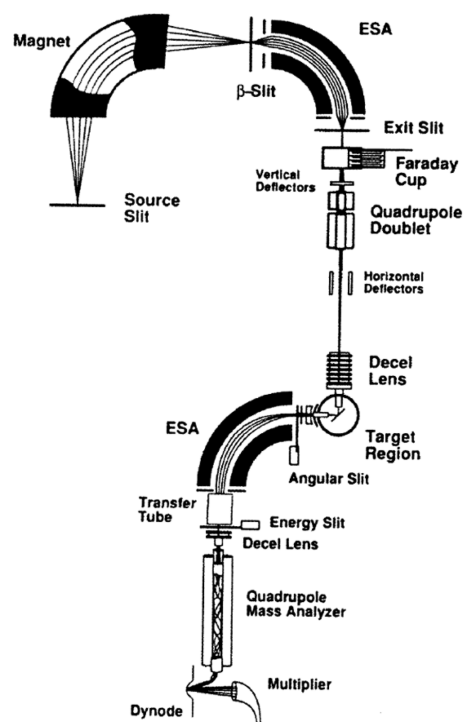


Figure 4. Schematic of the BEEQ instrument at Purdue (Purdue I). The first section of the instrument is a double-focusing (BE) mass spectrometer to select primary ions by mass and kinetic energy and deliver them to the scattering chamber, which accommodates a target and postcollision analyzer (EQ) system. The electrostatic quadrupole doublet and beam steering assembly located between the surface and BE system focus the primary beam onto the target surface. Reprinted with permission from ref 167. Copyright 1992 American Institute of Physics.

ions, particularly Cs⁺, produced from surface ionization sources (see section 7).

3.2. Newer Instruments

Newer generation instruments incorporate various high-performance state-of-the-art components as a result of a large number of innovations in instrumentation and in ionization methods. The major differences between the instruments center on the great variety of mass analyzers, the most common of which are discussed in turn (see Table 3).

Quadrupoles are widely used as mass filters since they provide adequate ion transmission and mass resolution but are compact devices (see Tables 1 and 2). There are at least three new-generation ion/surface collision instruments which use simple quadrupole mass analyzers in both the mass selection and the mass analysis stages: Arizona I,¹⁷³ Israel Institute of Technology,^{91,92} and IIT Madras^{174,175} instruments belong in this category. The Arizona I and IIT instruments (see Figure 5) adopt more or less the same design as the early VCU instrument.¹⁶⁸ These instruments consist of two quadrupoles arranged in a 90° geometry with the surface positioned at the intersection of the optical paths, producing a collision angle of 45° with respect to the surface normal. The collision energy is controlled by the potential difference between the surface and the ion source, with mass-selected singly charged ions from the first quadrupole colliding with the surface. Excellent energy resolution is reported with the IIT Madras instrument.¹⁷⁶ The measured full width at half-maximum (fwhm) of 1 eV Ar⁺ is ~62%. For 5 and 10 eV it is 10% and 4%, respectively.

Table 3. Newer Instruments

instrument	mass filter (first stage)	mass analyzer (second stage)	ionization methods	refs
Arizona I	Q	Q	EI	173
Arizona II	EB	TOF	FAB, EI	183
Arizona III	Q	TOF	ESI	177
Caltech	BQ	Q	ICP plasma	182
IIT Madras	Q	Q	EI	174
Israel Institute of Technology	Q	Q	Cs ⁺ ion gun	91, 92
Manchester	hQhQh	Q	ESI	178
Marburg II	TOF	TOF	laser ionization	190
PNNL I (also called PNNL SL I)	QQq ICR	ICR	MALDI/ESI	179, 180
PNNL II	BE	Q	EI	181
Hebrew University, Israel	TOF	TOF	ESI	189
Texas A&M	IM	TOF	MALDI	191, 192
Washington	EB	Q	EI/CI	66

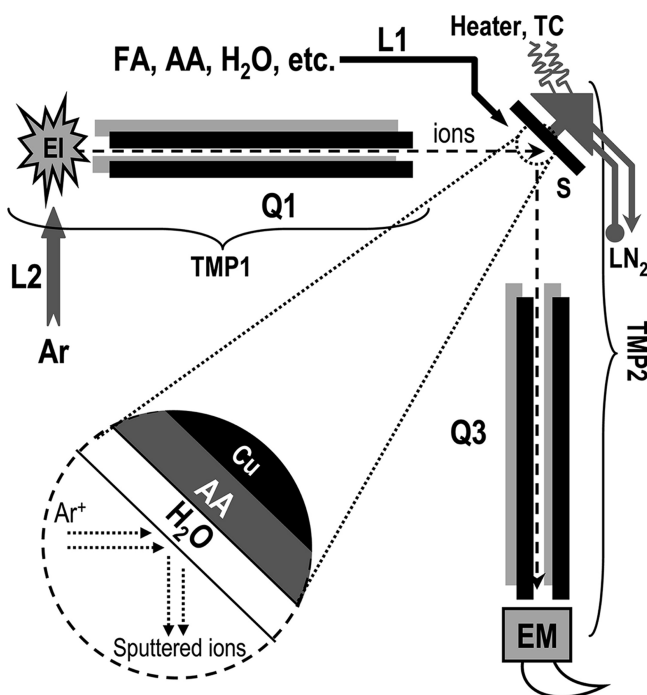


Figure 5. Schematic of the low-energy ion scattering instrument at IIT Madras, India. Q1 is the mass filter, and Q3 is the analyzer quadrupole. The substrate is represented by S, and the collision angle is 45°. Reprinted from ref 175. Copyright 2008 American Chemical Society.

Compared to these instruments, a different configuration is used in the Israel Institute of Technology instrument.^{91,92} The Cs⁺ ion gun and C₆₀ oven are held at 45° relative to the substrate, and the analyzer quadrupole is normal to the surface. The C₆₀ beam source is used to deposit fullerene ions onto the substrate, and a Cs⁺ ion gun is used for subsequent bombardment experiments to study the formation of endohedral fullerenes.

Instruments at Manchester and Arizona (called Arizona III) are composed of a tandem quadrupole mass spectrometer in the first stage.^{177,178} Both systems use modified commercial instruments (Manchester, Quattro I, Micromass; Arizona, QTOF II, Micromass). They therefore provide the advantage

of CID capabilities prior to the surface collision. One major limitation of these instruments is the loss of reflectron functionality when a time-of-flight (TOF) instrument is used as the second-stage mass spectrometer, which results in poor TOF resolution. A schematic of the Arizona III instrument is given in Figure 6. A PNNL (Pacific Northwest National Laboratory, Richland, WA) instrument (PNNL I), used for ion/surface collision studies, is composed of three quadrupoles between the ion source and the electrostatic ion guide components. These quadrupoles are used for collisional focusing (collisional quadrupole, CQ), mass resolution (resolving quadrupole, RQ), and ion accumulation (accumulation quadrupole, AQ).^{179,180} This is a triple-quadrupole arrangement, where the first two quadrupoles serve for mass resolving and accumulation followed by a third quadrupole for collisional relaxation. The resulting ions are then directed to a Fourier transform ion cyclotron resonance (FTICR) cell through an electrostatic ion optical system. The surface is introduced at the rear trapping plate of the ICR cell.

The beam scattering instrument at PNNL (PNNL II) uses a *double-focusing sector field mass spectrometer*, as in the Purdue I instrument (BEEQ).¹⁸¹ These types of mass analyzers produce stable ion beams that are precisely defined in mass and energy. PNNL II has an energy resolution of 2000–5000 at 1.25 keV compared to 1000 (10% valley) for a 3 keV ion beam for the BEEQ instrument at Purdue. The energy distribution shows a width of 1.7 eV (fwhm) at a lower energy such as 40 eV. The sector instrument at CalTech has a different arrangement: the ions are resolved using a sector magnet followed by a quadrupole doublet for ion deceleration to the desired collision energy.¹⁸² Higher resolution is achieved using a smaller exit slit. A typical energy distribution of 5–10 eV (fwhm) is achieved at a 20–1000 eV beam energy. An interesting design has been adopted for the Arizona II instrument by modifying a commercial instrument.^{173,183} The mass and energy of the precursor ion are selected using a double-focusing sector instrument (JEOL HX 110), and ions enter the TOF analyzer through the exit slit of the sector (see Figure 7). After entering the TOF chamber, the ion beam is focused by a pair of quadrupole lenses. However, this arrangement suffers from decreased mass resolution in the reflectron TOF analyzers when it is operated in the surface collision mode, but it has the convenience of rapid data acquisition. The same kind of commercial instrument is used as the first stage in the Washington instrument for surface neutralization–surface reionization mass spectrometry (so-called “ping-pong” NRMS as opposed to conventional gas-phase neutralization–reionization mass spectrometry) experiments (see Figure 8).⁶⁶ The mass resolution at full ion transmission of the JEOL instrument with all slits fully open is >1000.

Ion/surface interaction provisions can be incorporated into TOF mass spectrometers. The first of this kind was a tandem TOF instrument which was adapted for SID by placing a stainless steel surface between two orthogonal TOF regions.¹⁸⁴ The mass range and resolution of this instrument were further enhanced by incorporating an electrostatic reflectron in the second TOF stage.¹⁸⁴ This concept in SID was further pursued and improved by several research groups.^{81,183,185–188} Wysocki and co-workers used a flange-mounted surface immediately after the reflectron by removing the drift tube (used in the linear mode of operation) to convert the commercial matrix-assisted laser desorption ionization (MALDI)-TOF mass spectrometer (Proflex, Bruker Daltonics) for SID applica-

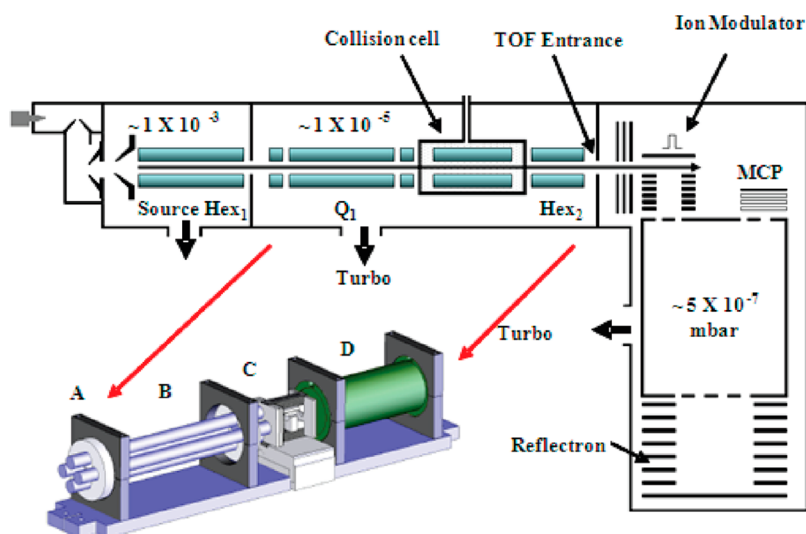


Figure 6. Schematic of the QTOF instrument at Arizona (Arizona III). An SID device was incorporated between the quadrupole analyzer Q1 and the collision cell. The collision cell of the original commercial QTOF instrument has been moved toward the TOF entrance and the hexapole ion guide (Hex₂) removed completely. Reprinted from ref 177. Copyright 2008 American Chemical Society.

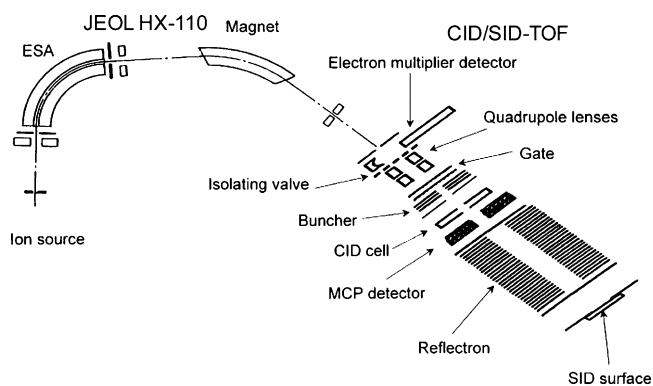


Figure 7. Schematic of the in-line JEOL sector time-of-flight instrument at Arizona (Arizona II). Reprinted with permission ref 183. Copyright 2001 Elsevier B.V.

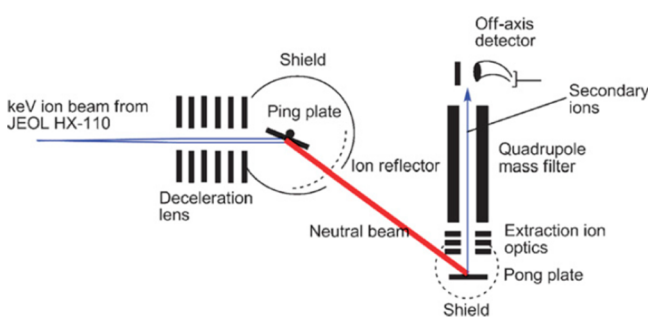


Figure 8. Schematic diagram of the ping-pong NRMS instrument at Washington. Fast neutrals formed at the “ping” surface form ions at the “pong” surface. Reprinted with permission from ref 66. Copyright 2009 Elsevier B.V.

tions.¹⁸⁷ A tandem linear TOF mass spectrometer was used for ion/surface collision studies at Hebrew University, Israel.¹⁸⁹ A primary TOF spectrometer served to prepare mass-selected cluster ion pulses of controlled and well-defined kinetic energy. Mass selection was accomplished using a pulsed ion mirror in the field-free drift region. Similarly, the new instrument at Marburg, (Marburg II) Germany, used TOF mass analyzers in

both stages.¹⁹⁰ The ions formed were transferred via the flight tube to the collision chamber. After collision at the surface, the resulting positive ions were accelerated in the electrostatic field of the reflector and reflected in the electrostatic mirror for transfer to the TOF spectrometer. By applying appropriate voltages to the lenses, the kinetic energy of the ions could be adjusted between 0 and 2 keV (nominal) with a resolution of about 100 meV. Impact of the ions at the surface occurred at normal incidence. Similar orthogonal extraction of collisionally cooled ions or fragmentation products from the surface was adopted in other instruments also, notably Texas^{191,192} and Arizona III.¹⁷⁷ In general, TOF mass analyzers have the advantages of high mass/charge range and high efficiency of product ion analysis. A crucial factor in such instrumentation is the time delay between the mass gate and the surface extraction pulses. High mass resolution requires Wiley–McLaren-type focusing to compensate for temporal, spatial, and initial kinetic energy distributions.¹⁹³

Ion mobility spectrometry (IMS) has been used for studies of hyperthermal ion/surface collisions. Combinations such as MALDI-IM-TOF MS^{191,194} and IM-TOF¹⁹² have been successfully implemented. A mobility resolution ($m/\Delta m$, fwhm) of 50–75 was obtained using a special drift cell as compared to a value of 20–30 for a conventional ion mobility (IM) drift cell. To improve the transmission and resolution efficiency, a longer periodic focusing cell¹⁹⁵ (periodic electrostatic ion guide) was used. The electrostatic potential well within the ring electrode of the IM-TOF instrument confines the scattered ions.¹⁹² The IM-TOF instrument utilizes a surface-normal incident angle for performing SID within the TOF extraction source, which helps to overcome the limitation of the small internal energy deposition associated with grazing incident angle in-line instruments.^{168,191}

Use of *Fourier transform ion cyclotron resonance mass spectrometry (FTICR MS)* for mass analysis has contributed remarkably to studies of gas-phase ion activation processes and subsequent product analysis, especially for large biomolecules, as the tool combines very high resolution and accuracy compared to other mass analyzers.^{196,197} Ion activation through surface collisions in an ICR instrument has been common since

the late 1980s.¹⁹⁸ Use of SID in ICR is considered a useful substitute for conventional ICR activation techniques such as sustained off-resonance irradiation (SORI)¹⁹⁹ collision-induced and infrared multiphoton (IRMPD) dissociation. The SID strategy was found to provide more peptide sequence coverage in FTICR for structural characterization of singly protonated peptide ions.¹⁷⁹ Ion activation by surface collisions can give results similar to those of gas-phase activation, including multiple-collision processes.^{179,200,201} However, hard surfaces such as F-SAMs and diamond give uniquely high internal energy depositions, and at high collision energies (above 30 eV), evidence for shattering of two small peptides has been observed, which results in much better sequence coverage compared to that of slow gaseous collisional activation.²⁰² Two Delaware^{203,204} instruments use FTICR mass analyzers for ion/surface studies. Also in the PNNL I instrument, the surface is placed flat on the back trapping plate of the ICR cell.^{180,201} The kinetic energy of the ions striking the surface is varied by changing the direct current (dc) offset applied to the ICR cell. A typical ion current of 50–80 pA is achieved using this configuration. The SID fragments are stored in the ICR cell using gated trapping. The collision energy is defined by the difference in the potential applied to AQ and the potential applied to the rear trapping plate and the target surface.

3.3. Instrumentation for Ion Soft Landing

Several instruments have been designed explicitly for SL (Table 4). Recent devices aim at control of ion deposition parameters as well as in situ characterization of the modified surface. The first instrument used to demonstrate the SL phenomena

Table 4. Soft Landing Instruments^a

instrument	mass filter (first stage)	ionization method	refs
EPFL (Switzerland)	Q	sputtering	219–221
Georgia Tech	EB	LSIMS	207
Illinois	Wien filter	EI	288
Johns Hopkins University	B	laser vaporization	211
Karlsruhe (Germany) instrument	Q	EI	141
Keio (Japan)	Q	laser ionization	214
Max Plank Institute of Polymer Research	EB	MALDI	142
Max Plank Institute of Solid State Research	Q	ESI	115, 213
PNNL (Cowan)	Wien filter	plasma ionizer	245
PNNL SL I	QQq-ICR	ESI	180, 218
PNNL SL II	QQq	ESI	104
PNNL SL III	QQQ	ESI	109
Purdue SL I	QQQ	EI	217
Purdue SL II	q-LIT	ESI	236, 237
Purdue SL III	q-RIT	ESI	238
Scripps Research Institute	Q	ESI	212
University of Birmingham, U.K.	TOF	plasma sputtering	233, 234
University of California, Santa Barbara	B	magnetron sputter	209
University of North Texas	drift tube	laser ablation	231
Washington SL I	EB	ESI	206
Washington SL II		ESI	241, 242

^aSeveral other cluster SL instruments are described in section 3.3.

consisted of a plasma (Colutron) ion source and a Wien velocity filter for mass selection.²⁰⁵ The mass-selected ions were decelerated into a liquid nitrogen (LN₂) cooled copper target using a six-element decelerator.

The BEEQ instrument at Purdue was used for SL in the 1990s.^{102,103,105} The ions were decelerated to 10–20 eV energy and allowed to deposit onto the substrate. Similar sector instruments (magnetic and electrical) for SL were built in Washington²⁰⁶ (referred to as Washington SL I) and at the Georgia Institute of Technology.²⁰⁷ The Washington instrument employed an electrospray ionization (ESI) source, an ion funnel, a multichannel deceleration lens, and a multichannel array collector (see Figure 9).^{206,208} Using this instrument,

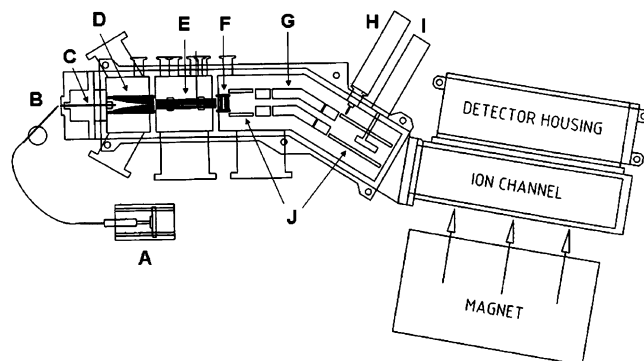


Figure 9. Schematic of the SL instrument at Washington (Washington SL I): (A) syringe pump, (B) electrospray needle, (C) glass-lined transfer capillary, (D) funnel lens, (E) octopole, (F) acceleration lens, (G) electrostatic sector with shunts, (H) movable slit mounted on a linear motion feedthrough, (I) Faraday cup ion collector mounted on a linear motion feedthrough, (J) HV-floated Faraday cages. Reprinted from ref 206. Copyright 2005 American Chemical Society.

simultaneous separation and collection of individual compounds in nanomole quantities was demonstrated successfully.²⁰⁶ The configuration of the hybrid instrument at Georgia Tech was EBqQ.²⁰⁷ The electric and magnetic sectors in this instrument were followed by a radio frequency (rf)-only quadrupole (q) collision cell and then finally a mass-analyzing quadrupole (Q). The substrate was fixed immediately after the sectors. A modified sector field tandem mass spectrometer was used at the Max Plank Institute for Polymer Research, Germany, with a custom-built MALDI source (N₂ laser 337 nm), for SL experiments.¹⁴² The ions were separated according to their *m/z* ratio in the first stage of the mass analyzer. A magnetic sector alone (with other ion optics) was used for mass selection in the cluster SL instruments at the University of California, Santa Barbara,²⁰⁹ Institut für Festkörperforschung, Jülich, Germany,²¹⁰ and Johns Hopkins University.²¹¹

Quadrupole mass filters have limitations that quickly become apparent in SL compared to ion/surface collision experiments when interest turns to biological molecules which require a higher mass range and maximum transmission efficiency. To overcome this difficulty, the mass resolution is set to as low as possible to increase the ion current to maximize transmission efficiency. The modified triple-quadrupole instruments at Scripps Research,²¹² the Max-Planck-Institute for Solid State Research, Germany,^{115,213} Karlsruhe, Germany,¹⁴¹ PNNL (PNNL SL II (see Figure 10)),¹⁰⁴ Keio, Japan,²¹⁴ and several size-selected cluster deposition instruments (see later in this section) all use quadrupole mass filters. The Scripps and Max

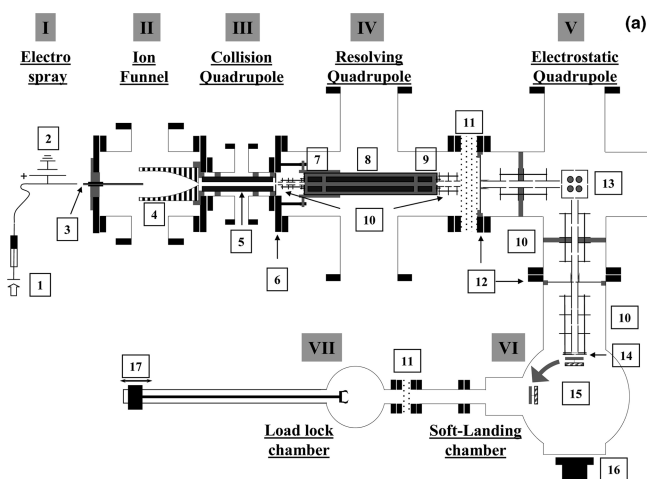


Figure 10. Schematic view of PNNL SL II: (I) ESI source, (II) ion funnel, (III) focusing stage, (IV) ion selection stage, (V) quadrupole bender, (VI) UHV chamber for SL, (VII) surface introduction stage. Some important parts are the (6) 1 mm conductance limit, (7) prefilter, (10) Einzel lenses, (11) gate valve, (12) 2 mm conductance limit, (14) deceleration area, (15) surface, (16) CCD camera, and (17) magnetic translator. Reprinted from ref 104. Copyright 2007 American Chemical Society.

Planck instruments have a similar arrangement: they are constituted by a series of quadrupole mass filters for ion focusing and mass selection. The Max-Planck-Institute for Solid State Research instrument analyzes the ions before SL using a linear TOF mass spectrometer and a retarding grid detector. The SL ion current is in the range of 1–50 pA, and the deposition energy can be varied between 1 and 80 eV. This instrument is equipped with a low-temperature scanning tunneling microscopy (STM) capability,²¹⁵ which has allowed remarkable data to be recorded for landed biomolecules. In the Keio instrument, organometallic clusters produced by laser vaporization are directed onto a surface by a sequence of ion optical elements, a quadrupole deflector, and a quadrupole mass filter.²¹⁴ The cluster cations are deposited onto a LN₂ cooled substrate using a collision energy of 20 ± 10 eV. Both the Keio and Karlsruhe instruments have a comparable total ion

current of ~ 1 nA and an fwhm of around 2–5 eV. PNNL SL II has a three quadrupole arrangement (see Figure 10).¹⁰⁴ Ions exiting collisional quadrupole (CQ) are mass selected by a resolving quadrupole (RQ) and then isolated from the fast neutrals by a quadrupole deflector. Ion beam currents for peptide SL in the PNNL SL II instruments are 60 pA, but a target placed after RQ could provide a current of 300–500 pA for mass-selected peptide ions.¹⁰⁴ A reflection–absorption infrared spectroscopy (RAIRS) capability has now been added to this instrument.²¹⁶ The latest instrument at PNNL (PNNL SL III) has a similar sequence of quadrupoles.¹⁰⁹ It has two focusing collision quadrupoles and a large 19 mm diameter quadrupole mass filter after the ion funnel interface. An in situ SIMS capability is a special advantage of this instrument.

The Purdue SL I instrument is a modified commercial triple-quadrupole instrument.²¹⁷ A movable surface was added immediately behind the detector without further mechanical changes being made to the instrument. The surface was floated, and additional voltages were applied to the final lens of the third quadrupole. The voltages applied to the conversion dynode and the electron multiplier are adjustable to pass ions through the detector housing to the surface.²¹⁷

The ICR ion/surface collision instrument at PNNL (PNNL I) is now mostly used for SL purposes (so it is referred to as PNNL SL I when used for SL).^{180,218} The energy distribution peaks around 14 eV with an fwhm of ~ 5 eV. This instrument was able to provide a 1–30 pA SL ion current for peptides, and in situ SIMS with ICR detection has been added.¹⁰⁸

A number of state-of-the-art cluster deposition instruments have been built for size-selected cluster science. The list is long, but some representative instruments are the Heiz instrument-^{224–226} and those located at EPFL, Switzerland,^{219–221} the University of Utah, Salt Lake City,²²² the Technische Universität Darmstadt, Germany,²²³ and the Universidad Autónoma de Nuevo León, Mexico.²²⁷ The listed instruments use quadrupoles in the mass selection stage. Separation is achieved using a differential mobility analyzer (DMA) at AIST, Japan,^{228,229} and Keio University, Japan,²³⁰ and using a drift tube at the University of North Texas.²³¹ Fairly uniform size clusters were prepared using these instruments. The use of mobility separation avoids complex instrumentation, and the

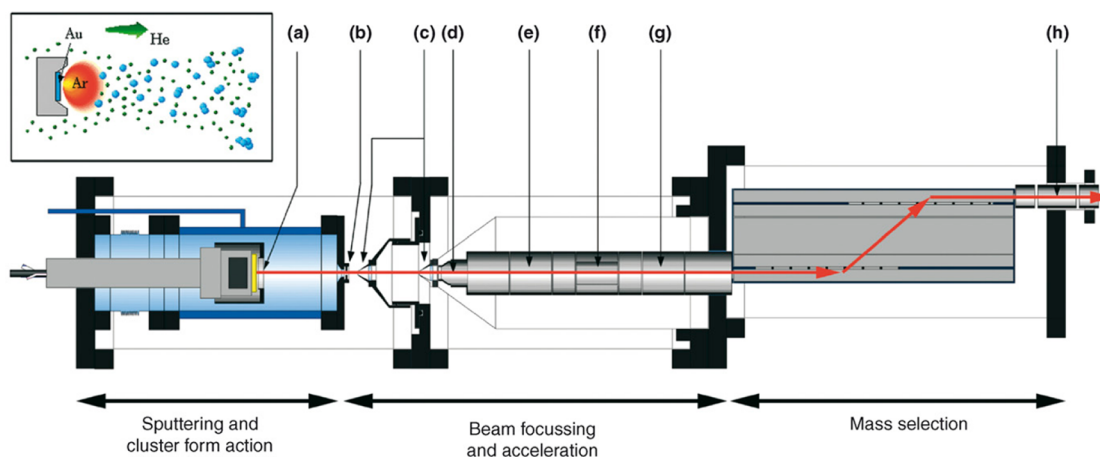


Figure 11. Size-selected cluster deposition instrument at the University of Birmingham, U.K. The instrument is equipped with a magnetron gas condensation cluster source (a) and a lateral time-of-flight mass filter: (b) adjustable-diameter nozzle, (c) skimmers, (d) high-voltage lens, (e) Einzel lens, (f) x - y deflector plates for spatial control of the cluster beam, (g, h) Einzel lenses. Reprinted with permission from ref 235. Copyright 2007 Elsevier B.V.

experiments can be performed at relatively high pressures. A distinct mass selection method, based on the TOF principle, was adopted for size-selected cluster deposition at the University of Birmingham, U.K.^{232–235} The ion beam is displaced laterally by accelerating a portion of it perpendicular to its original direction by a pulsed electric field, letting it drift for some time, and then stopping the perpendicular movement by a pulsed electric field in the opposite direction. The magnitude of the displacement is related to the magnitude and timing of the high-voltage pulse as well as the ion mass. In this way, one can select a small range from the mass distribution of the beam. An instrument using this technique is shown in Figure 11. It allows selection of the size of the ionized particle from atoms to nanoparticles ($\sim 1\text{--}70000$ in m/z). The reported mass resolution was $m/\Delta m \approx 25$, with a transmission of about 50% for a given size independent of mass. The deposition rate using this instrument was about 0.1 monolayer (ML) of Ag atoms/min.

Another type of mass analyzer used in SL instruments is the *ion trap*, viz., the two-dimensional linear ion trap (LIT) and closely related but geometrically simple rectilinear ion trap (RIT). Both of these ion trap instruments were fabricated at Purdue.^{236–238} The first one (LIT, referred to as Purdue SL II) was derived from a commercial Thermo LTQ mass spectrometer. Application of appropriate dc potentials to the electrodes enables the LIT to be used for either radial ion ejection for mass analysis or axial ejection for SL.²³⁷ Ions are trapped in the mass analyzer by using an rf field that lies in the $x\text{--}y$ plane of the analyzer. The landing surface is positioned after the LIT's back end cap. The Purdue SL III uses a home-built RIT mass analyzer instead of a commercial LIT (see Figure 12).^{238,239} The ease of RIT fabrication makes it an

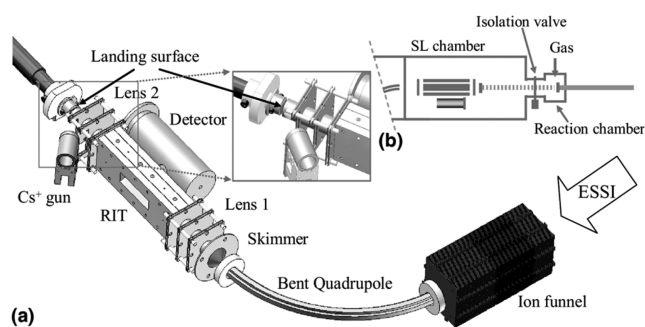


Figure 12. Schematic of the RIT-based SL instrument at Purdue (Purdue SL III) showing the bent square quadrupole and RIT (a) and SL chamber and reaction chamber (b). Reprinted with permission from ref 239. Copyright 2009 Elsevier B.V.

attractive alternative to the LIT, although with some compromise on mass resolution.²⁴⁰ The RIT is comparable in structure to a simple LIT. The instrument also has a 90° bent square quadrupole ion guide which filters fast neutrals and can also be operated as an independent and continuous mass filter for mass selection. During SL, axial ejection is employed, and to record mass spectra, the alternative radial ejection mode is used. This instrument has in situ SIMS surface analysis capabilities as well as in situ Raman analysis.^{239,619} The RIT acts in an additional role as the mass analyzer during SIMS analysis of the sputtered ions being directed into it. The LIT/RIT is advantageous for SL experiments in various ways: the device ejects ions at low kinetic energy, which is desirable for

SL, and the instrument can operate in a pulsed mode with a cycle time for ion accumulation chosen to optimize SL efficiency.

One of the important performance criteria of SL instrumentation is the ion yield. Ingenious designs can provide a non-mass-selected ion current of more than 1 nA, with 500 pA in the mass-selected mode.^{104,141,214,239} In other cases yields of $\sim 5\%$ ²⁴¹ are obtained under optimized conditions; otherwise, a 2% yield is generally achieved.¹¹³ The Washington SL II was built solely for high ion yields (at the surface) without a mass analyzer.^{241,242} These authors have reported a ~ 2 nA ion current during SL of ions derived from biomolecules.

3.4. Ionization Methods

The choice of the ionization method is dictated largely by the process of interest, the nature of the ions to be produced, and the design of the instrument (see Tables 1 and 2). The widely used ionization methods for ion/surface collision experiments in their early stages of development were electron ionization (EI), chemical ionization (CI), and laser-induced ionization. Later, the significance of complex ions which cannot be generated by these conventional vapor-phase methods led to the use of ESI and laser desorption ionization (LDI). Some groups have studied negatively charged ions in ion/surface collision experiments,^{185,189,243,244} although most studies deal with positive ions.

The stability of the ion current and the relatively small kinetic energy spread are the main advantages of EI even though the requirement of sample volatility and extensive fragmentation during ionization precludes the use of EI to generate many interesting projectile ions. The average energy spread (fwhm) of these sources is typically less than 2 eV with an ion current in the low nanoampere range. A distinct type of EI source was implemented in the PNNL (Cowin and co-workers) instrument which used a high-pressure nozzle ionizer with an expanding supersonic jet of gas crossing an electron beam (~ 100 eV) from a nearby filament to generate high ion beam currents with low energy spreads.²⁴⁵

ESI offers the ability to generate intact molecular ions of nonvolatile organic compounds, especially biomolecules; hence, it can be effective in both analytical and preparative mass spectrometry.²⁴⁶ The simple sample format, mostly aqueous solutions, and compatibility with the accessible mass range of TOF and linear ion traps are additional advantages of this ionization methodology. It is known that proteins or even enzymes can be successfully ionized by ESI, sometimes retaining at least temporarily the native structure and viability.²⁴⁷ The retention of peptide structure²⁴⁸ and enzymatic activity²³⁶ after SL has been verified. The efficiency of ion formation and transfer through the atmospheric interface are limitations of ESI, which can be overcome by using optical systems such as ion funnels in the atmospheric pressure interface.^{104,238}

Desorption ionization methods are often used for SL.^{142,179,192} In the case of size-selected metal cluster SL, high-energy sputtering/vaporization methods are widely used and ions are generated from the corresponding bulk metals.²⁴⁹ Melting points of metals and the kinetic energy of the produced clusters are the decisive factors in these sources. The list of other ion sources includes the magnetron sputter source,^{250–253} (high-power) laser vaporization,^{209,224,231,254–256} the gas condensation cluster source,^{234,257} and sputtering sources.^{221,258,259}

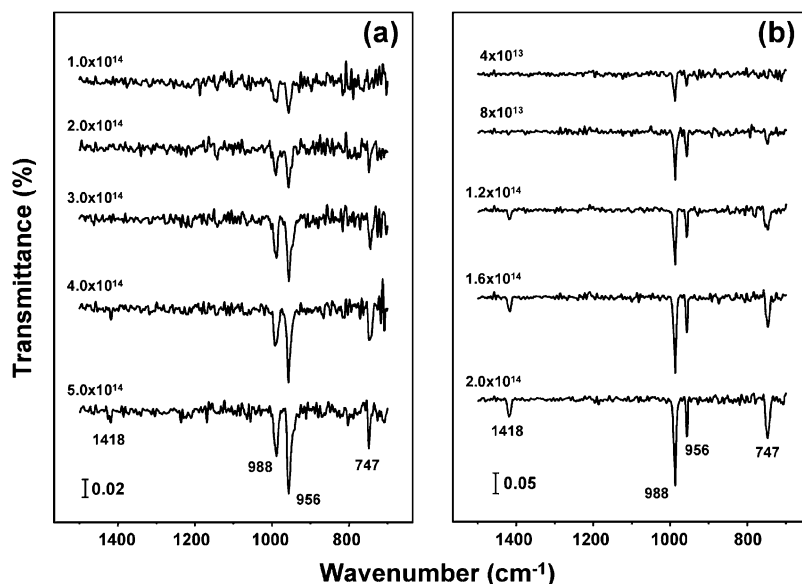


Figure 13. Comparison of the sandwich cluster SL experiment using two different substrates: (a) Au and (b) C_{18} -SAM. Temperature-dependent variation of the $V(\text{benzene})_2$ cluster after deposition of (a) 5.0×10^{14} ions onto gold and (b) 2.0×10^{14} ions onto C_{18} -SAM at 180 K as monitored using IRAS. Reprinted from ref 275. Copyright 2006 American Chemical Society.

3.5. Some Ion Transfer Optics

Ion optics are essential to achieve beams of the desired kinetic energy and cross-sectional shape. The choice of ion optics depends on the type of mass analyzer used, especially the acceleration or deceleration optics near the surface. For example, quadrupole mass filters work best at low axial ion energies, and the ion beam leaving the mass filter is not spatially focused. Simple Einzel lens assemblies can be used to control the beam geometry in such cases,^{173,174,243,260} sometimes along with deceleration optics,²⁶¹ but a situation where the ions are passed through sectors at high kinetic energy and then decelerated near the surface requires the use of a multielement deceleration lens system that is located immediately in front of the target.^{66,68,167} A few ion optical elements which have special applicability in ion/surface instruments are discussed below. Statements on the performance of these elements are based on their use in a low-energy ion/surface collision instrument. This should not be considered as representing the best current performance or general performance of the component in a commercial instrument.

3.5.1. Static Quadrupole Bending Lens. This module is also called a “quadrupole deflector” and is composed of four round electrodes (sometimes 90° quarter sections of a cylinder) where opposite electrodes are electrically connected. By selecting appropriate potentials on these electrodes, depending on the kinetic energy of the ions, the system can act as a quadrupole bending lens. Compared to ion bending through a small angle using an ion deflector,^{245,260} this type of system sometimes has a lower ion transmission efficiency, but it turns ions through 90° with adequate sensitivity and ease of operation. Apart from preventing fast neutrals or ions of opposite polarity from reaching the surface, the instrument footprint can be reduced. Several instruments, Purdue II,²⁶² PNNL SL I and II,^{104,180} Keio, Japan,²¹⁴ Karlsruhe,¹⁴¹ and Université de Lausanne, Switzerland,²²⁴ take advantage of this 90° bending lens (see Figure 10 for an instrument with a quadrupole bending lens). The University of Lyon, France,²⁶³

cluster deposition instrument uses the deflector alone for size selection.

3.5.2. Octapole/Hexapole Ion Guide. Commonly used rf-only multipole ion guides of the quadrupole,²³⁷ hexapole,¹⁷⁸ and octapole^{214,262} types are frequently used in ion/surface collision instruments. These guides generate an actual or effective potential minimum radially along the axis which produces a narrow ion beam.²⁶⁴ The flatter (pseudo)potential well in the octapole ion guide provides a higher transmission efficiency than does a hexapole ion guide, and neither ion guide shows the strong mass discrimination effects on transmission seen in quadrupoles due to node formation.²⁶² This fine spatial tuning is important when ionization is done using an external ESI ion source because the ion beam from the inlet system is spread due to mutual ion repulsion and collisions with residual air and solvent molecules. An alternative design of an octapole ion guide has been proposed.²⁶⁵ In this arrangement eight truncated cone-shaped rods are arranged in a conical geometry. This device allows focusing of Ni_{20}^+ clusters into a 2 mm diameter spot compared to a 9 mm diameter spot when a normal octapole is used in SL experiments.²⁶⁵

3.5.3. Ion Funnel. The multipole ion guides described above have limited utility in the atmospheric interface or in the higher vacuum pressure region. Ion funnels are the right choice for such situations. An ion funnel is a series of cylindrical ring electrodes of progressively smaller internal diameter which is used for collisional focusing at elevated pressures.²⁶⁶ The coapplication of rf (opposite polarity on adjacent electrodes) and dc electric fields focuses the ions efficiently and transmits them from a higher to a lower pressure region.²⁶⁷ This effectively focuses ions by reversing the Coulombically driven ion cloud expansion and transmits them through a relatively small exit aperture.^{267,268} In a typical design, the first plate has a ~ 20 mm aperture while the last plate has a 2 mm aperture through which the ion funnel delivers ions into the vacuum system ion optics.^{104,180} An advantage of this protocol, which is relevant to SL, is the gentle desolvation of protein and other biological ions and their entry into the vacuum region without

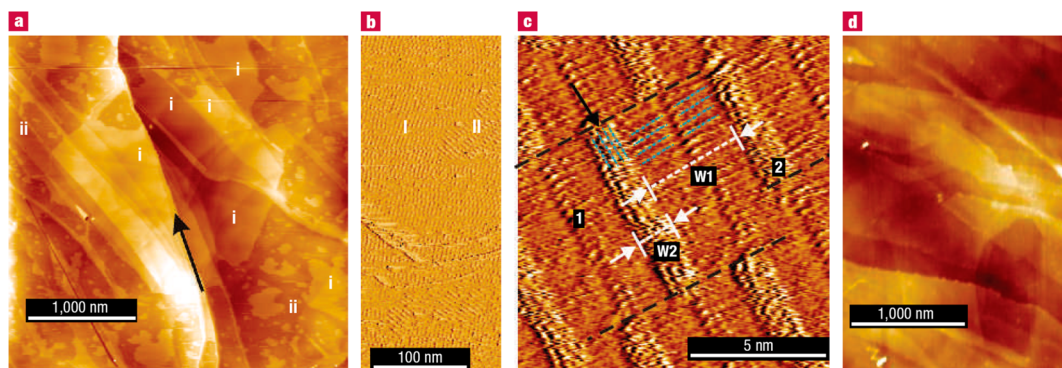


Figure 14. SFM topographical images of HOPG after SL modification (a, d) and STM images (b, c). The surfaces shown in (a)–(c) were modified using $C_{42}H_{18}$, and that shown in (d) was modified using $C_{96}H_{30}$. Polycrystalline structures composed of different domains are visible in (b), and the resulting lamellar orientation is marked. Two different types of phases (1, 2) are distinguishable from the image given in (c). Reprinted with permission from ref 142. Copyright 2006 Macmillan Publishers Ltd.

the noncovalent interactions that maintain the highly ordered structure being affected.^{104,238,242,269}

4. POSTCOLLISION SURFACE ANALYSIS

Postcollision surface analysis is essential in understanding the consequences of ion/surface collisions. In situ analysis capabilities provide potential advantages over ex situ methods by rapid characterization and elimination of possible contamination. The selection of ex situ techniques for detection is sometimes appropriate, but one should always be aware of the effect of exposure to the ambient atmosphere on the modified surface. Several experiments have followed ion/surface interactions by using in situ chemical sputtering (CS) (e.g., with 60–70 eV Xe^+ or CF_3^+)^{74,270–272} and SIMS.^{106,109,207,216,218,238,239,273,274} Some important analysis methods are now discussed briefly.

The products of RL and SL can be characterized by spectroscopic methods, particularly reflection absorption infrared spectroscopy (RAIRS or IRRAS/IRAS) or surface-enhanced Raman spectroscopy (SERS), as an alternative to MS methods. The presence and position of amide I and amide II bands originating from peptide bonds can be directly correlated to the secondary structure of the peptide.^{216,248} These studies demonstrated that SL can be used to prepare peptides on substrates in stable conformations that do not exist in solution and that covalent linkage of the peptide to the surface is feasible using appropriate SAMs.^{114,207,216,248,273} The efficiencies of SL of $V(\text{benzene})_2$ sandwich clusters onto bare gold and C_{18} -SAM surfaces were compared using IRAS experiments.^{214,275} The SAM substrate permits a higher SL efficiency than the Au surface. As shown in Figure 13, the four bands observed for each substrate, 747 cm^{-1} , C–H out-of-plane bending, 956 cm^{-1} , symmetric ring-breathing mode, 988 cm^{-1} , C–H in-plane bending mode, and 1418 cm^{-1} , asymmetric C–C stretching mode, are in good agreement with the infrared data for a neutral $V(\text{benzene})_2$ complex in an Ar matrix.²⁷⁶ The two bands at 956 and 988 cm^{-1} start to appear when approximately 1.0×10^{14} cations have been deposited onto the bare Au substrate (area $\sim 4 \text{ mm}^2$), and an additional two bands appear at 747 and 1418 cm^{-1} when the deposition number increases above 4.0×10^{14} ions. In contrast, with a C_{18} -SAM substrate, these four bands can be clearly observed at much lower deposition numbers (i.e., $<1.0 \times 10^{14}$). The cluster cations lose their charge during SL and adsorb as neutrals with the intact native sandwich structure.²⁷⁵ In another study,

esterification in the course of deposition of benzoyl cations on an HO-SAM was confirmed by ex situ RAIRS, demonstrating C–O bond formation.²⁷²

SERS^{277,278} is a promising analysis method for characterizing surface modifications by SL. The detection limits can easily be in the submonolayer coverage regime with a 10^5 – 10^6 enhancement observed for soft-landed rhodamine and crystal violet.^{279,280} The bonding of surface metal atoms to the soft-landed crystal violet species was found to be by π -coordination.²⁸⁰ SERS was utilized for characterizing soft-landed nucleosides cytidine and 2'-deoxycytidine, which even lack a chromophore for resonant excitation.²⁸⁰ This was a landmark study in which a spectroscopic method (other than MS) was used to characterize soft-landed biomolecules. SERS has been used to understand the structure of silicon ($Si_{4,6,7}$)²⁸¹ and small carbon ($C_{1,2,4}$)²⁸² clusters prepared by size-selected SL. The data suggest that Si_4 is a planar rhombus, Si_6 is a distorted octahedron, and Si_7 is a pentagonal bipyramid.²⁸¹

Temperature-programmed desorption (TPD) is helpful in providing insights into ion/surface interactions. For example, SL of $V(\text{benzene})_2$ sandwich clusters and subsequent TPD gave additional information on the interaction between SAMs and soft-landed ions.^{214,275} TPD analysis shows that the threshold for vaporization gradually increases with the chain length of the SAM, demonstrating that the soft-landed clusters are more strongly trapped by longer chain SAMs. Desorption temperatures of the clusters on all the SAM substrates are higher than that for the bare Au substrate. TPD and temperature-programmed reaction (TPR) are often used to test the catalytic reactivity of metal clusters prepared by SL of size-selected clusters.^{151,152,209} In the case of “ices”, TPD is often chosen for post ion/surface interaction investigations.^{245,283}

Hyperthermal energy ion-induced modifications of surfaces, including organic thin film growth, creation of mixed interface layers from ions, ambient neutrals, and/or surface atoms, and attachment of specific chemical functionalities, are being used in various technological processes.^{116,284,285} The morphology of soft-landed hydrocarbons $C_{42}H_{18}$ and $C_{96}H_{30}$ was investigated in air at room temperature by scanning force microscopy (SFM) and scanning tunneling microscopy (STM) (see Figure 14).^{142,286} These giant molecules exhibit a nearly homogeneous surface, characterized by several HOPG steps with sharp edges (marked with a black arrow in Figure 14) after SL. STM shows that the molecular packing occurs in layers consisting of stacks of single molecules packed “edge on”. The tilt angle is larger for

Table 5. Polyatomic Ion/Surface Collisions

projectile ion (M^+)	surface	products	refs
$C_6D_6^{+•}/C_6H_6^{+•}$	H-SAM	$[M + H/D]^+$, $[M + CH_3 - H_2(HD/D_2)]^+$	52, 68, 72, 134, 169, 260, 306
	F-SAM	$[M + F - H]^+$, $[M + F - H_2]^+$, $[M + CF_3 - H]^+$, $[M + CF_3 - H_2]^+$	72, 134, 135
	HO-SAM	$[M + CH_2OH - H_2O]^+$ (a possible reaction product)	52
$C_4H_4N_2^{+•}$ (pyrazine)	H-SAM	$M + H^+/M + CH_3^+$	67, 77
	D-SAM	$M + D^+/M + CD_3^+$	67, 77
	HD-SAM	deuterated and hydrogenated C_2 adducts; $[M + C_2H_5 - H_2]^+$, no mixed C_2 species	77
$C_4H_4N_2^{+•}$ (pyridazine)	hydrocarbon	$[M + H]^+$	260
$C_5H_5N^{+•}$ (pyridine)	C_3D_3N	$M + H^+$, $C_3D_3NH^+$, $C_3H_4N^+$	76, 308
$C_3H_3N^{+•}$	1,4-benzenedimethanethiol on Au(111)	$M + C_1-C_8$ hydrocarbon	309
	1,4-benzenedimethanethiol on Ag(111)	$M + C_1-C_4$ hydrocarbon	309
$C_5H_5N^{+•}$	HO-SAM	$M + H^+$	310
$C_5H_5N^{+•}$	CH_3CH_2O -SAM	$M + H^+$	310
	CH_3O -SAM	$M + H^+$	310
$C_5D_5N^{+•}$	H-SAM	$M + H^+$	66, 133, 602
$M^{+•}$ (naphthalene, phenanthrene)	hydrocarbon	$M + C_{1-6}H_n^+$	81
HC_2N^+	H-SAM	$M + (1-4)H^+$	25, 77
$OCNCO^+$ and $OCNCS^+$	F-SAM	transhalogenation products	361
$CD_3SOC_3^+$	H-SAM/hydrocarbon	$M + H^+$	134
$CD_3SOC_3^+$	COOH-SAM (LB film)	$M + H^+$	135
pyrene $^+$	HD-SAM	$M + C_2H_y$ and $M + C_2D_y$	77
CH_n^+ , $C_2H_m^+$	hydrocarbon-adsorbed HOPG	$C_2H_3^+/C_3H_3^+$	316, 317, 319
CH_3^+	InP	formation of a carbon film	313
$C_3H_4^{+•}$	F-SAM	CH_nF^+ ($n = 1, 2$)	321
$C_3H_n^{+•}$ ($n = 6, 8$)	HOPG	$M + H^+$	146
CH_n^+ ($n = 0-4$)	F-SAM	CF^+ , $C_2HF_2^+$ and $C_3F_3^+$	311
$C_2H_n^+$ ($n = 2, 4$)	HOPG	$M + H^+$, $M + CH_3 - H_2^+$	317
$C_7H_6^{2+}$	hydrocarbon	$C_7H_7^+$	56
$CH_3I^{+•}$	F-SAM	$IF^{+•}$	315
$CH_2Br_2^{+•}$	F-SAM	CH_2F^+ , $CHBrF^+$, CF_2Br^+	271
CCl_3^+	F-SAM	CF_2Cl^+ (surface reaction)	217
$•CH_2OCH_2^+$	F-SAM	CH_2F^+ and $FCH_2OCH_2^+$	75
$CH_3COCH_3^{+•}$	hydrocarbon	CH_2OH^+ and $(CH_3COCH_3)H^+$	322, 323
	H-SAM	$M + H^+$, $M + CH_3^+$	602
$(CH_3COCH_3)_n^+$	hydrocarbon	$(CH_3COCH_3)_nH^+$, $(CH_3COCH_3)_nCH_3CO^+$	324, 325, 603
$C_2H_5OH^+/C_2D_5OD^+$	H-SAM/COOH-SAM	$M + H^+$	129, 169
$HCOOH^+$	hydrocarbon	$HC(OH)_2^+$	329, 330
CF^+ , CF_2^+	Si, SiO_2	CF_n accumulation	313
CF_3^+	polymer	fluorinating the surface	162, 165, 421, 422
$C_3F_5^+$	polymer	fluorocarbon thin film formation	162, 165, 190, 421, 422, 424
NH_3^+	hydrocarbon surface	$M + H^+$	190

$C_{96}H_{30}$ compared to $C_{42}H_{18}$. In a different study, plasma-generated endohedral fullerene clusters were soft landed onto HOPG, and the resulting cluster-covered samples were transferred into a variable-temperature STM instrument under UHV conditions.¹⁴³⁻¹⁴⁵ Successive STM measurements revealed that $La@C_{60}$ could be mobile on an HOPG surface.¹⁴³

There are several other techniques used in postcollision surface analysis, and detailed descriptions are not made here. They include SIMS,²⁰⁷ contact angle measurements,²⁸⁷ desorption electrospray ionization (DESI),²³⁸ ESI,^{208,236,237} fluorescence,^{113,241} inductively coupled plasma mass spectrometry (ICP MS),²⁰⁷ MALDI,¹⁴² Raman spectroscopy,^{288,289} scanning electron microscopy (SEM),^{242,290} scanning/atomic force microscopy (SFM/AFM),^{164,231,280,291-296} scanning tunneling microscopy (STM),^{209,219,258,297} transmission elec-

tron microscopy (TEM),^{234,255,298,299} thermal desorption spectroscopy (TDS),¹⁴¹ TOF SIMS imaging,^{74,300} TOF SIMS,^{104,115,218,273} thermal energy atom scattering (TEAS),²²⁰ near-edge X-ray absorption fine structure (NEXAFS) spectroscopy,^{285,301} grazing incidence small-angle X-ray scattering (GISAXS),¹⁵¹ photoluminescence,^{115,166} ultraviolet photoelectron spectroscopy (UPS),^{226,285,291} X-ray absorption fine structure (XAFS) spectroscopy,³⁰² X-ray photoelectron spectroscopy (XPS),^{153,155,288,293,294,301,303,304} electron energy loss spectroscopy (EELS),²²⁶ Auger spectroscopy,²⁵¹ and quartz crystal microbalance (QCM) measurements.³⁰⁵

The next sections are focused on surface reactions and modifications performed using hyperthermal energy ions.

5. POLYATOMIC ION/SURFACE COLLISIONS

Early reports of polyatomic ion/surface reactions in the hyperthermal energy regime concerned ionic collisions with adsorbed hydrocarbons or H-SAMs.^{25,54,67,169} Abstraction of a hydrogen atom is the usual reaction when an organic radical cation impinges on a hydrocarbon surface. Abstraction of up to four hydrogen atoms or a methyl group is also observed. A brief description of these and other polyatomic ion/surface collision events is given below (see Table 5).

5.1. Aromatic Hydrocarbon Ions

Benzene molecular ion ($C_6H_6^{+\bullet}$) collisions at H-SAM and F-SAM surfaces showed peaks corresponding to H, CH_3 , F, and CF_3 additions followed by H and H_2 loss from the adducts.^{72,93} $C_6H_6^{+\bullet}$ abstracts a methyl group from H-SAM, but the product ion readily loses H_2 (see Figure 2) to form $C_7H_7^+$.^{169,306} Alternately, another thermodynamically favorable route to form $C_7H_7^{+\bullet}$ is the reaction between the sputtered $C_3H_5^+$ from the hydrocarbon surface and the neutralized benzene with elimination of C_2H_4 .⁹³ Sputtered protons are observed in the mass spectra, suggesting that the formation of protonated molecules occurs via a proton transfer mechanism.²⁶⁰ The product ion due to $C_6H_6^{+\bullet}$ collisions shows a strong inelastic scattering feature, with a maximum in translational energy distribution at 2–6 eV for a collision energy of ~ 28 eV and a maximum in angular distribution at angles of 70 – 75° , much lower than the specular angle (90°).⁶⁸

The relative concentrations of CH_3 groups in mixed CH_3 - and OH-terminated SAMs could be linked to the extent of methyl abstraction by impinging benzene molecular ions.⁵² Fragmentation and neutralization observed for benzene molecular ions increases as the percentage of OH groups present on the surface increases.⁵² This increased efficiency of the mixed monolayers with the higher fraction of OH was attributed either to the small effective mass increase in the terminal group ($CH_3 \rightarrow OH$) or to the differences in the interaction potentials between the projectile ion and the different surfaces. From Figure 15, it is evident that the relative abundance of the low-mass fragments is enhanced as the percentage of OH is increased, suggesting an increase in the internal energy transfer to the benzene projectile ion. Comparison of scattered ion intensities upon benzene molecular ion collisions at various hydrocarbon SAMs indicates that the neutralization of the ion beam that occurs for each SAM film is not a result of the presence of defect sites but is dependent on the length of the carbon chain. Unusual reaction products have been observed for the ion $C_6H_5^+$ derived from benzene when it is subjected to collision with a COOH-SAM surface pretreated with an ammonium salt to convert the terminal group to the ammonium salt.³⁰⁷ Product ions $C_6H_5CH_2^+$ and $C_6H_5CH_2CH_2^+$ were observed in the scattered ion mass spectra as a result of C–C bond formation during collision.

Compared to the benzene cation, the pyridine molecular ion ($C_5H_5N^+$) undergoes efficient pickup reactions upon surface collisions. Collision of $C_5H_5N^+$ at Ag(111) covered by C_5D_5N leads to the formation of $C_5H_5NH^+$ and $C_5D_5NH^+$ in similar yields.^{76,308} Both the projectile and the sputtered adsorbate abstract hydrogen to give these thermochemically favored product ions. It is interesting to note that no M^+ ($C_5H_5N^+$) radical cations survive the collision with the surface, even when the adsorbed pyridine coverage is varied from nominally zero to 1.1 ML. Two contributing factors control these effects: the

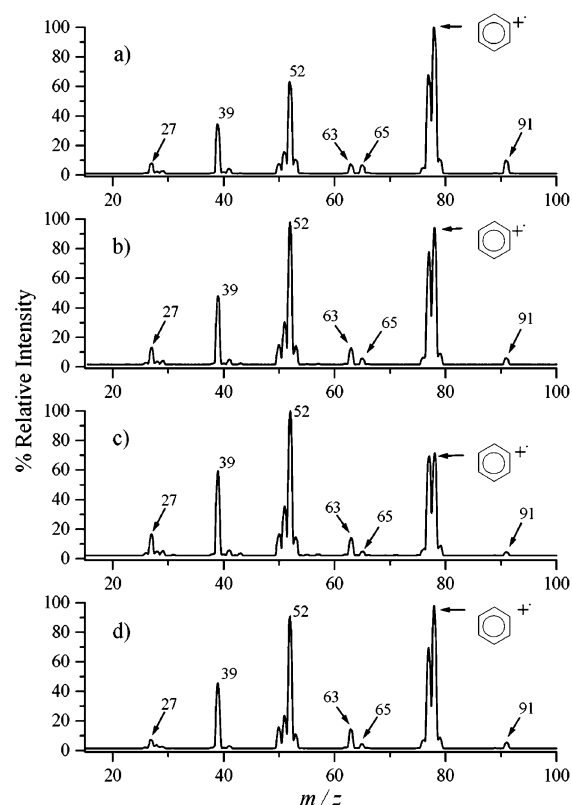


Figure 15. Product ion spectra that result from a 30 eV collision of a benzene molecular ion with a surface containing various proportions of H- and HO-SAMs: (a) 100% C_{12} /0% $C_{11}OH$, (b) 50% C_{12} /50% $C_{11}OH$, (c) 25% C_{12} /75% $C_{11}OH$, (d) unsymmetrical disulfide ($C_{12}-S-S-C_{11}OH$). Note that the relative abundance of the fragment ions is enhanced with an increase in the OH concentration (%). Reprinted from ref 52. Copyright 2003 American Chemical Society.

relative thermodynamic instability of M^+ and the ability of the surface to neutralize or protonate the projectile ions to form the stable MH^+ species. It is suggested that neutral C_5H_5NH species are not formed in the ion/surface collision process even though the C_5H_5NH radical is stable.⁶⁶

Reactive collisions of $C_5H_5N^+$ have been used in differentiating the adsorbate geometries on two different metal surfaces. 1,4-Benzenedimethanethiol chemisorbs on Au(111) and Ag(111) surfaces in two distinct geometries.³⁰⁹ At a 50 eV collision energy, $C_5H_5N^+$ picks up hydrogen to a major degree, as well as C_1 to C_8 hydrocarbon groups, from the adsorbate molecule from the 1,4-benzenedimethanethiol monolayer assembled on Au, whereas the monolayer on Ag allows abstraction of only a small portion of the molecule, C_1 to C_4 with a significantly different intensity pattern. The mass spectra show distinctive features associated with these two different substrates (Figure 16). For different isomeric oxygenated adsorbates, hydrogen atom abstraction by the $C_5H_5N^+$ ion was found to be favored at CH_3CH_2O - and CH_3O -terminated surfaces relative to the HO-terminated surface.³¹⁰

Pyrazine molecular ions ($C_4H_4N_2^+$) have been the subject of many studies and have been shown to be able to pick up hydrogen atoms, methyl radicals, and groups containing multiple carbon atoms^{67,77} (see Scheme 2). Data from isotopically mixed surfaces show that the carbon units originate from a single chain and are transferred as intact alkyl groups.⁷⁷

Ionized polycyclic aromatic hydrocarbons (PAHs) are relatively difficult to fragment in SID, but they undergo ion/

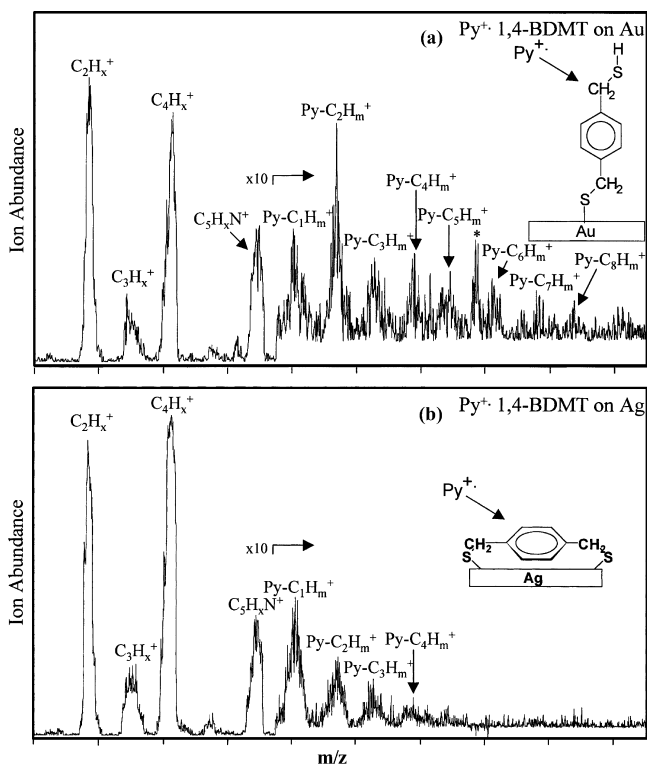
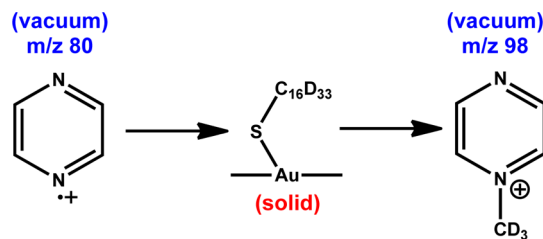


Figure 16. Product ion mass spectra due to collision of 50 eV $C_5H_5N^+$ ions at 1,4-BDMT on a Au surface (a) and a Ag surface (b). Note the difference in pickup of hydrocarbon fragments from the two surfaces. Reprinted from ref 309. Copyright 1999 American Chemical Society.

Scheme 2. Methyl Pickup Reaction of Pyrazine Ion^a



^aAdapted from ref 67. Copyright 1991 American Chemical Society.

surface reactions, picking up units with multiple carbon atoms from the adsorbed hydrocarbons. Attachment of C_1H_n – C_6H_n to naphthalene, phenanthrene, or pyrene ions has been observed.^{77,81} The multiple carbon units are likely to be derived from ion/surface reactions via a single chain as suggested by reaction at an isotopically labeled mixed SAM surface. Multiple-H abstraction from a single alkyl chain was observed, though it requires breaking of multiple bonds for each H to be added. For example, HC_2N^+ , a highly unsaturated ion derived from CH_3CN , abstracts up to four hydrogen atoms from a hydrocarbon-covered stainless steel surface.^{25,77} The removal of hydrogens from adjacent carbons on the same chain might result in the formation of a double bond, an entropically more favorable process than removal of hydrogen from the two terminal carbons.

5.2. Aliphatic Hydrocarbon Ions

We now discuss the reactions observed with short-chain hydrocarbon reagent ions (see Table 5). Collision of methane ions, CH_n ($n = 0$ – 4) with an F-SAM surface produces fluorine-

containing scattered ions, including CF^+ , $C_2HF_2^+$, and $C_3F_3^+$.³¹¹ Among these product ions, formation of CF^+ was found to be a favorable ion/surface reaction. Formation of $^{12}CF^+$ and $^{13}CF^+$ products in equal abundance at higher collision energies (≥ 60 eV), when a ^{13}C -labeled methane ion was used as the projectile ion, indicates that the mechanism involves formation of a symmetrical fluoronium collision complex; $F^{13}C-F-^{12}CF$. On a metal surface, CH_3^+ deposits as an intact methyl group below 3 eV,³¹² and above 30 eV formation of covalently bound hydrocarbon films on metal surfaces and carbon films on InP was observed.^{312,313} Collisions of CF_3^+ ions at hydrocarbon-covered surfaces generate various fluorohydrocarbons.³¹⁴ The iodomethane ion (CH_3I^+) colliding at an F-SAM surface produces IF^+ as a major product.³¹⁵ IF^+ is formed through initial fragmentation of CH_3I^+ at the surface to produce atomic iodine followed by the addition of F from the surface to yield IF^+ . The corresponding Br-containing ions are much less reactive, and the chloro analogues are virtually unreactive. This may be because CH_3I reaction did not involve charge exchange, or it may be due to the fact that formation of IF^+ is less endothermic than BrF^+ and ClF^+ .³¹⁵ However, when $CH_2Br_2^+$ ions were allowed to collide with an F-SAM surface, F was abstracted from the surface as verified by the products CH_2F^+ , $CHBrF^+$, and CF_2Br^+ ,²⁷¹ while the CCl_3^+ ion at 70 eV collision was effective in transhalogenation of an F-SAM surface.²¹⁷

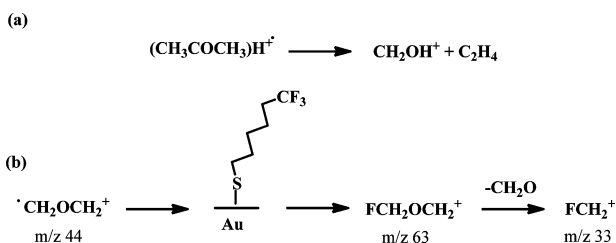
Herman and co-workers have done a series of experiments with small hydrocarbon (C_1 – C_3) projectile ions at collision energies of < 50 eV.^{146,316–319} The reaction products observed due to the collision of small hydrocarbon ions CH_n^+ and $C_2H_m^+$ and their D isotopic variants on HOPG surfaces at room temperature showed hydrogen atom transfer and carbon chain buildup reaction.^{316,317,319} The actual reactions occur between adsorbed hydrocarbons and projectile ions. Subsequent dissociation of the reaction products occurs in addition to fragmentation of the projectile ions. These reaction products disappeared when the HOPG surface was heated to 600 °C as the adsorbed hydrocarbon layer was removed by heating and elastic scattering became dominant. It was found that the hydrogen abstraction reactions and subsequent fragmentations of $C_2D_4^+$ at hydrophobic H-diamond and hydrophilic O-diamond surfaces were very similar.³¹⁹ The collision of C_3H_n ($n = 2$ – 8) ions and their deuterated analogues could not execute carbon chain buildup reactions at room temperature.¹⁴⁶ However, the radical cations $C_3H_8^+$ and $C_3H_6^+$ showed fragmentation and products of H atom transfer between the projectile ion and adsorbed hydrocarbon on the surface. The even-electron ions $C_3H_7^+$ and $C_3H_5^+$ showed only fragmentation of the incident projectile ions, consistent with thermochemical expectations. These experiments demonstrated that the inelasticity of surface collisions of smaller projectile ions was lower than that with larger polyatomic ions. Surface C–H and C–C bond cleavages have been observed with the t - $C_4H_9^+$ ion (an even-electron ion) at H-SAM surfaces, but abstraction reactions were absent, which is consistent with the result for even-electron C_3 ions.^{133,146} When the hydrocarbon cation and dication $C_7H_m^{1+/2+}$ ($m = 6, 7, 8$) generated from toluene were subjected to SID at an HOPG surface, the observed products were singly charged species due to direct dissociation of the projectiles and hydrogen abstraction products as well as dissociation of the surface-induced species, but no C adducts were observed.^{56,320} $C_3H_4^+$ ions derived from isomeric allene and propyne molecular ions collide with F-SAM surfaces and fragment as well as generate CH_nF^+ ($n = 1, 2$)

surface reaction products.³²¹ A plot of $\text{CH}_3^+/\text{CH}_2^+$ abundance ratio versus collision energy for propyne and allene reveals the isomeric differences.³²¹

5.3. Simple Organic Ions

Several ions derived from simple organic molecules have been used as projectile ions in surface collisions (see Table 5). The collisional interaction of the acetone molecular ion, $\text{CH}_3\text{COCH}_3^+$, at hydrocarbon surfaces produces the hydrogen atom abstraction product $(\text{CH}_3\text{COCH}_3)\text{H}^+$ and its unimolecular decay fragment CH_2OH^+ ^{322,323} (see Scheme 3a). In

Scheme 3. (a) Decay Path of the Protonated Ion $(\text{CH}_3\text{COCH}_3)\text{H}^+$ and (b) Reaction between the Distonic Ion and F-SAM Surface Which Involves C–F Bond Cleavage and Formation of a New Bond between the F Atom and the Reagent Ion and Subsequent Loss of Formaldehyde^a



^aPart a was adapted with permission from ref 322. Copyright 1998 Springer. Part b was adapted from ref 75. Copyright 1998 American Chemical Society.

the case of other acetone-derived projectile ions, the product ions include the stoichiometric cluster ions $(\text{CH}_3\text{COCH}_3)_n^+$, the hydrogen atom pickup reaction product $(\text{CH}_3\text{COCH}_3)_n\text{H}^+$, and the acetylated ion series $(\text{CH}_3\text{COCH}_3)_n\text{CH}_3\text{CO}^+$ ^{32,324,325}. Interaction of various molecular cluster ions of acetone, acetonitrile, and ethanol with hydrocarbon-covered steel

surfaces shows simple dissociation, intracuster ion–molecule reaction, and hydrogen atom transfer from the surface.^{326–328}

The DMSO-*d*₆ molecular ion picks up hydrogen atoms exclusively from the surface.^{134,135} The formic acid molecular ion produces protonated species and fragments in a reactive collision process.³²⁹ Both the undissociated protonated formic acid and the dissociation product CHO^+ appear in the mass spectra.³³⁰ The preferential formation of CHO^+ suggests that the protonated species exists as $\text{HC}(\text{OH})_2^+$.

The distonic ion³³¹ $\cdot\text{CH}_2\text{OCH}_2^+$ derived from 1,3-dioxalane after collision with an F-SAM surface undergoes F atom abstraction to yield CH_2F^+ and $\text{FCH}_2\text{OCH}_2^+$.⁷⁵ The presence of the product ion $\text{FCH}_2\text{OCH}_2^+$ implies a free radical abstraction reaction (see Scheme 3b). This radical-driven chemistry is confirmed using closed-shell methoxymethyl cation $\text{CH}_3\text{OCH}_2^+$ and another homologous distonic ion, $\cdot\text{C}_2\text{H}_4\text{OCH}_2^+$, at the F-SAM surface, which further indicates that the radical site plays an important role in the activation of highly inert C–F bonds.^{75,332,333} The surface collision processes are useful in characterizing aspects of the chemical nature of the ion and of the surface. Although a variety of reactions and fragmentations occur, they are readily rationalized as being constrained by well-known considerations of gas-phase organic ion reactivity and thermochemical stability.

5.4. Organic Reactions at Surfaces

Ion/surface collisions are enriched by the occurrence of a variety of organic reactions occurring in the surface-bound species (see Table 6). Hyperthermal energy collisions of $\text{C}_6\text{H}_5\text{CO}^+$ and $\text{C}_6\text{H}_5\text{CH}_2^+$ projectile ions at HO-SAM surfaces cause esterification and ether formation, respectively.²⁷² Esterification proceeds through collision of the benzoyl cation at the HO-SAM with simultaneous loss of a proton from the surface (see Figure 17b, inset). The IR bands at 1724 and 1284 cm^{-1} , corresponding to C=O and C–O stretching, respectively, agree with the formation of a benzoate-terminated

Table 6. Organic Reactions

projectile ion (M^+)	surface	products	comments	refs
$\text{C}_6\text{H}_5\text{CO}^+$	HO-SAM	C–O bond formation at the surface	reactive landing	272
$\text{C}_6\text{H}_5\text{CH}_2^+$	HO-SAM	C–O bond formation at the surface	reactive landing	272
C_6H_5^+	$\text{NH}_4^+\text{COO}^-$ -SAM	C–C bond formation reaction (Kolbe reaction)		307
C_4S_4^+	α -terthiophene (gas phase) and Si(100)	polythiophene formation on the substrate		288, 289
C_4S_4^+	<i>p</i> -terphenyl (gas phase) and Si(100)	polyphenyl formation on the surface		285, 288, 290
C_4S_4^+	gas-phase 2-methoxy-5-[(2'-ethylhexyl)oxy]-1,4-bis(4',4''-distyryl)benzene	poly(phenylenevinylene) film		291
OH^+	polystyrene	C–OH bond formation at the surface	C–OR, C=O, and COOH functionalities due to further oxidation of C–OH bonds	313, 334
H^+	dotriacontane, docosanoic acid	cross-linking reaction at the surface	selective cleavage of a C–H bond	294
H^+	poly(<i>trans</i> -isoprene)	cross-linking reaction at the surface	selective cleavage of a C–H bond	293, 294
H^+	acrylic acid oligomer	poly(acrylic acid)	cross-linking	340
H^+	H-SAM	C–C bond formation with thiol chain		343, 344
NH^+	polystyrene	C–NH ₂ , C–NHR at the surface		334
O^+	H-SAM/F-SAM	C–C bond break	abstraction product OH^-/OF^- , chemical sputtering products	347

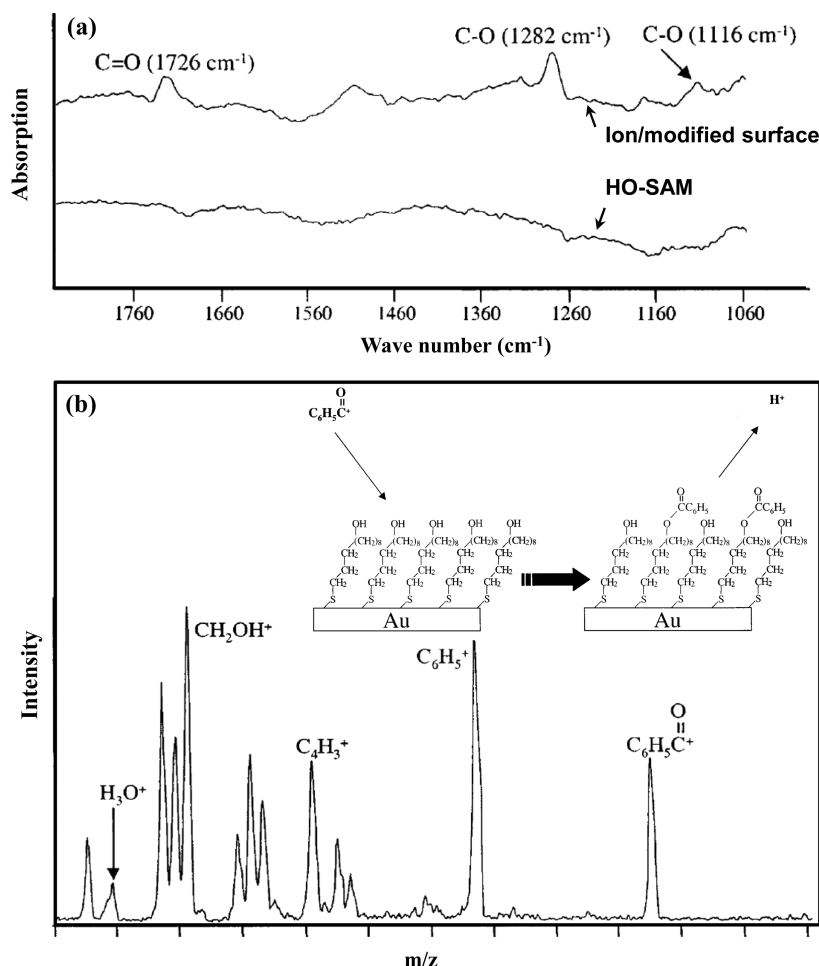
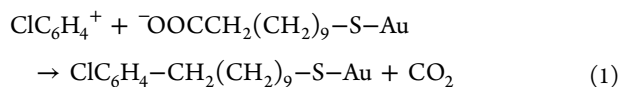


Figure 17. RAIR spectra of the HO-SAM surface modified using benzoyl cation collisions and pure HO-SAM (a). Product ion mass spectrum upon collision of CF_3^+ (at 70 eV) with the HO-SAM surface after reaction with the $\text{C}_6\text{H}_5\text{CO}^+$ ion at 15 eV for 2 h (b). This figure was compiled from Figures 1 and 4 of ref 272. Copyright 2002 American Chemical Society.

SAM surface. Comparison of RAIR spectra before and after benzoyl cation modification is made in Figure 17a. The HO-SAM does not show any $\text{C}=\text{O}$ and $\text{C}-\text{O}$ features, but the SAM surface modified using ion collisions shows features comparable to those of a surface prepared by a chemical reaction route which contains 22% benzoate-terminated molecules. The occurrence of the surface reaction was further confirmed by CF_3^+ chemical sputtering (Figure 17b). In another study, a direct chemical conversion by interfacial Kolbe reaction at a COOH-SAM made it possible to prepare an aryl-terminated surface.³⁰⁷ Similar $\text{C}-\text{C}$ bond formation was also found at lower energy (~ 10 eV) in the case of other ions such as C_6H_5^+ and BrC_6H_4^+ (see reaction 1). Additional evidence of



$\text{C}-\text{C}$ bond formation is found in the reactive scattering of C_6H_5^+ at higher collision energy (>20 eV), which produced $\text{C}_6\text{H}_5\text{CH}_2^+$.³⁰⁷ Addition of functional groups such as OH or NH_2 to the polymer surface (e.g., polystyrene) was demonstrated successfully using mass-selected hyperthermal energy OH^+ or NH^+ ions.³³⁴

5.4.1. Surface Polymerization by Ion-Assisted Deposition. Using hyperthermal ion beams, Hanley and co-workers

generated polymer thin films on various surfaces by gas-phase deposition of monomeric units. This approach is known as surface polymerization by ion-assisted deposition (SPIAD).^{288,289} Polythiophene growth on a Si(100) substrate by SPIAD was performed by combining thiophene ion (C_4S_4^+) deposition with simultaneous dosing of oligomeric α -terthiophene vapor.^{288,289} Similarly, the preparation of polyphenyl films occurred when mass-selected polyatomic thiophene ions and *p*-terphenyl neutrals were used.^{285,288,290} Addition of the neutral oligomeric species allows fast film growth and permits the production of a much wider range of film type than that available by direct polyatomic ion deposition. Successful formation of polythiophene,^{288,289} polyphenyl,^{288,290} and thin films of phenylenevinylene,²⁹¹ thiophene,¹⁶⁴ and titanylphthalocyanine³³⁵ was accomplished using SPIAD. The morphology of the film formed by ion-induced polymerization could be controlled by selecting an appropriate ion energy and ion:neutral ratio. Polymerization was found to be optimized at a 200 eV ion energy and over a narrow set of ion:neutral (e.g., 1:150) ratios.^{288,336} A high neutral flux favored surface polymerization as the dosed neutral will otherwise eventually desorb and the remaining adsorbate will be sputtered by the incoming ions. However, very high energy ions lead to excessive sputtering and so might overwhelm the polymerization event. The reaction appears to proceed via a cationic polymerization mechanism. The carbon

atom of the incident ion has enough kinetic energy to abstract hydrogen from an adjacent terthiophene molecule or directly add to terthiophene.^{336,337}

Interesting electronic properties have been found in SPIAD films. They display more electron delocalization, narrower band gaps, and reduced barriers to hole injection compared with their evaporated film counterparts.^{291,338,339} SPIAD experiments attempted with acetylene ions and titanylphthalocyanine (TiOPc) showed the formation of TiOPc dimers, bound face to face, although the overall phthalocyanine ring structure otherwise remained intact.³³⁵

5.4.2. Cross-Linking Reactions. A similar hyperthermal approach to the cross-linking of adsorbed organic molecules to form a polymer thin film was developed using low-energy proton collisions.^{294,340} The conversion of T \rightarrow V during a 10 eV H⁺ collision resulted in preferential cleavage of C–H bonds, leaving intact C–X or O–H bonds. The activated molecules created cross-links to form a polymeric film with the same chemical functionalities as the precursor molecules. The validity of this approach was previously suggested theoretically.²⁹⁴ Polymerization, cross-linking, and intact thin film formation have been found in the case of dotriacontane, docosanoic acid, poly(acrylic acid) oligomer, polystyrene, and polyisoprene.^{293,294,340,341} Cross-linking of polyisoprene or polystyrene to form cross-linked network films is found to proceed through a slightly different mechanism. The role of hyperthermal energy protons, in such cases, is to cleave C–H bonds, allowing the carbon radicals so created to initiate a polymerization chain reaction of the isoprene C=C bonds.²⁹³ This is different from the case of dotriacontane saturated hydrocarbon in which an excess fluence is required for the cleavage of more C–H bonds before enough C–C cross-linked bonds can be formed to yield a polymeric film. The effect of cross-linking extended 2 mm into the area not subjected to proton bombardment in the case of polyisoprene. The AFM images of virgin film and proton-irradiated film given in Figure 18 clearly indicate the growth of

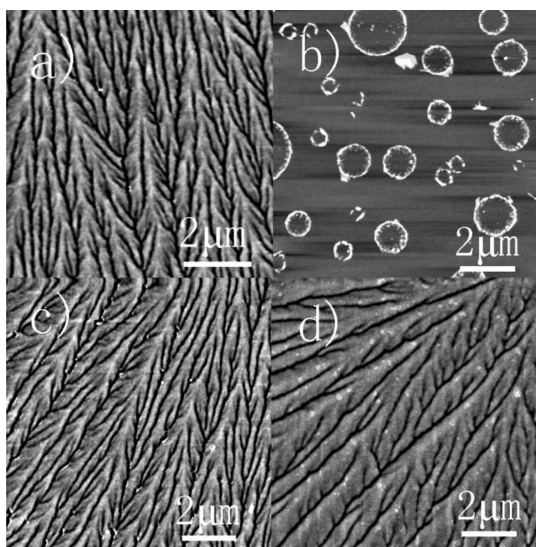


Figure 18. AFM images showing the surface morphology of (a) a virgin poly(*trans*-isoprene) film, (b) the same virgin film after 5 min of immersion in hexane, (c) the same film after irradiation with 10 eV H⁺ ions at a fluence of $2 \times 10^{16} \text{ cm}^{-2}$, and (d) the irradiated film after 5 min of immersion in hexane. Reprinted with permission from ref 293. Copyright 2006 The Royal Society of Chemistry.

dendritic structures. Cross-linking of poly(acrylic acid) oligomer with 100% retention of COOH shows the selectivity and performance of kinematically driven synthesis of cross-linked molecular films.³⁴⁰ The thicknesses of the polymer film before and after irradiation using hyperthermal protons were identical, confirming that the proton bombardment caused neither sputtering nor material loss during C–C cleavage. On the other hand, an increase in kinetic energy of the proton to 100 eV causes severe molecular damage, resulting in etching of the film.³⁴¹ The cross-linking chemistry has been applied successfully to induce interchain cross-linkage in deposited multiwalled carbon nanotubes (MWCNTs), leading to higher mechanical strength.³⁴²

Collisions of protons can preferentially cleave C–H bonds and induce cross-linking of H-SAM surfaces themselves.^{343,344} Perturbation due to C–C bond formation in the cross-linking reaction adds bond strain to the SAM chain that weakens the Au–S bond. Some molecules are lost, and some diffuse through the surface and aggregate to form nanoclusters.³⁴³ Formation of large clusters is favored by a high proton beam energy and fluence.³⁴⁴ In spite of this, atomic hydrogen collisions on thiol-SAMs can cleave the thiolate bond directly when the length of the chain is small (<12), but hydrogen atom abstraction and consequent cross-linking reactions will be dominant for longer chain thiols.^{345,346} It is found that hyperthermal O⁺ can abstract hydrogen atoms from the H-SAM surface and break C–C bonds in both the hydrocarbon and fluorocarbon SAM chains.^{347,348}

5.5. Reactions of Metal-Containing Ions

As in the case of polyatomic organic ion projectiles, information on the nature of surface groups or atoms is accessible by abstraction reactions using metal-containing ions (see Table 7). The ion/surface reactions observed with W(CO)₆⁺ and Cr(CO)₆⁺ at different surfaces clearly display “pickup” reactions.^{349–351} With fluorinated surfaces, in addition to metal fluorides, more complex species are formed which retain one or more carbon atoms or carbonyl groups. At collision energies above 30 eV, the product ion spectra after the collision of W(CO)₆⁺ at poly(tetrafluoroethylene) (PTFE) contain ions of general formula WF_m ($m = 1–5$) and W(CO)_nF_m ($n = 1, 2; m = 1, 2$).^{71,349} The peak due to chemical sputtering (CS) of the surface was abundant at higher collision energies. Gas-phase ion/molecule reactions between W(CO)₆ and single fluorocarbon chains support the occurrence of multiple-F abstraction over simple F atom extraction, a thermodynamically favored result.^{71,352}

A series of experiments has been conducted using ferrocene-SAMs. When a ferrocene-SAM was subjected to collisions of the projectile ion Cr(CO)_n⁺ ($n = 0, 2, 6$), desorption of the cyclopentadienyl (Cp) moiety was observed as Cr(C₅H₅)⁺.³⁵⁰ Product ions spectra contained both Fe(C₅H₅)⁺ and Cr(C₅H₅)⁺ when Cr⁺ was used as the impinging ion. The latter product shows that the Cr⁺ ion was able to pick up the Cp group from the surface. Formation of Cr(C₅H₅)⁺ persisted even when the projectile ion was replaced by Cr(CO)₆⁺ or Cr(CO)₂⁺, while the new product Cr(C₅H₅)CO⁺ was seen in low abundance. Other metal carbonyls, those of Fe, Mo, and W, fail to form the corresponding cyclopentadienyl adduct.³⁵⁰ The suggested mechanism for this ion/surface reaction is through the formation of a double-decker sandwich structure such as (CO)_xCr + (Cp)Fe(Cp)–surface. Besides these reactions, the ferrocene ion did not undergo reactive scattering when it was

Table 7. Reactions of Metal-Containing Ions

projectile ion (M^+)	surface	products	refs
$W(CO)_6^+$	Teflon/F-SAM	WF_m ($m = 1-5$), $W(CO)_nF_m$ ($n = 1, 2; m = 1, 2$)	71, 349
$Cr(CO)_n^+$ ($n = 0, 2, 6$)	ferrocene-SAM	$Cr(C_5H_5)^+$	350
$Cr(CO)_n^+$ ($n = 0, 2, 6$)	F-SAM	CrF^+ , CrF_2^+ , $Cr(CO)F^+$	71
$Mo(CO)_n^+$ ($n = 0, 2, 3, 6$)	F-SAM	MoF_n^+ ($n = 1-4$), $MoCF_n^+$ ($n = 1-3$)	71
$W(CO)_n^+$ ($n = 0, 3, 6$)	F-SAM	WF_n^+ ($n = 1-5$), $W(CO)_xF_y^+$, WCF_m^+	71
$Fe(Cp)_n^+$ ($n = 0-2$)	F-SAM	FeF_n^+ ($n = 1, 2$), $FeCpF^+$	71
$TiCl_n^+$ ($n = 0-4$)	F-SAM	$Ti(Cl)_xF_y^+$	71
$Ni(Cp)_2^+$	F-SAM	NiH_2^+ , $Ni(Cp)H_2^+$	355
M^+ ($M = Al, Bi, Mo, Cr, W, Sb, Te, Re$)	F-SAM	$M + F_n^+$; multiple-F abstraction efficiency, $Re^+ > W^+ > Mo^+ > Cr^+$	135, 355-357
$(CH_3)_2SiNCS^+$, $(CH_3)_2SiNCO^+$, $Si(NCO)_n^+$	F-SAM	MF^+ , MF_2^+	270, 361
$SiCl_n^+$ ($n = 0-4$)	F-SAM	MF^+	355
$SiCl_3^+$	HO-SAM	$SiCl_2OH^+$	310
$SiCl_3^+$	CH_3O -SAM	$SiCl_2OCH_3^+$	310
$SiCl_3^+$	CH_3CH_2O -SAM	$SiCl_2CH_3^+$, $SiCl_2CH_2CH_3^+$	310
$Si(CH_3)_3^+$	HO-SAM	Si-O bond formation at the surface	300, 363
BBr_n^+ ($n = 0-2$)	F-SAM	BF^+ , BF_2^+ , $BBrF^+$	130
BBr_n^+ ($n = 0-2$)	H-SAM	BH_2^+ , $BBrH$, $BBrCH_3^+$, no BH^+	130

used as the projectile ion at hydrocarbon surfaces,⁴⁸ even though ferrocene undergoes SID at both hydrocarbon and metal surfaces.^{71,353} However, Fe- or Ti-containing ions derived from the corresponding Cp derivative exhibit F abstraction reactions from fluorinated surfaces, while CS products were completely absent.⁷¹ This absence supports the suggestion that the sole mechanism for the process is oxidative addition in the course of a single collision event without electron transfer being involved. Protonated aminoferrocene and (alkylamino)-ferrocenes were used for RL modification of carboxy-functionalized multiwalled carbon nanotubes (MWCNTs) to develop improved electrochemical transducers.³⁵⁴

Mild activation of nickelocene molecular ions, $Ni(Cp)_2^+$, at an F-SAM surface leads to an interesting concerted hydrogen rearrangement reaction yielding NiH_2^+ ions.³⁵⁵ The mechanism for this reaction is likely not the direct insertion of Ni^+ into H_2 . The hydrogen abstraction is likely to be concerted with Cp ring fusion to produce $C_{10}H_8$. Collision activation could excite one of the lower vibrational modes of the nickelocenium ion by internal energy transfer, leading to Cp ring fusion and simultaneous transfer of two hydrogens to Ni^+ to form NiH_2^+ and $C_{10}H_8$ or NiH_2 and $C_{10}H_8^+$.³⁵⁵ Ferrocenium and cobaltocenium ions failed to produce the corresponding hydrides in similar experiments.

Addition of multiple F atoms was observed for Al^+ , Bi^+ , Mo^+ , Cr^+ , W^+ , Sb^+ , Te^+ , and Re^+ projectiles when a perfluorinated surface was the target.^{70,71,135,356,357} Associated processes such as F substitution reactions at the surface and CS of surface-derived ions were also observed. Multiple-F abstraction (up to 5) was abundant in many cases (see Figure 19). The reactivity of the ions toward F abstraction was observed to follow the order $Re^+ > W^+ > Mo^+ > Cr^+$.³⁵⁷ The multiple-F abstraction efficiency was pronounced for Re^+ , W^+ , and Mo^+ ions. Fluorine addition to a metal ion colliding with an LB film was investigated by using Mo^+ and Cr^+ ions as projectiles.¹³⁵ The proposed mechanism of multiple-F additions appears to involve the second $-CF_2-$ groups on the fluoroalkane chain.^{71,135} The extent of reaction is likely dependent on the penetration of the atomic metal ion to a depth so as to reach at least the first CF_2 unit below the terminal CF_3 group.⁷¹ The energy released in the course of a $C=C$ bond formation (the result of multiple-F atom abstraction from the terminal CF_3CF_2- group) helps to

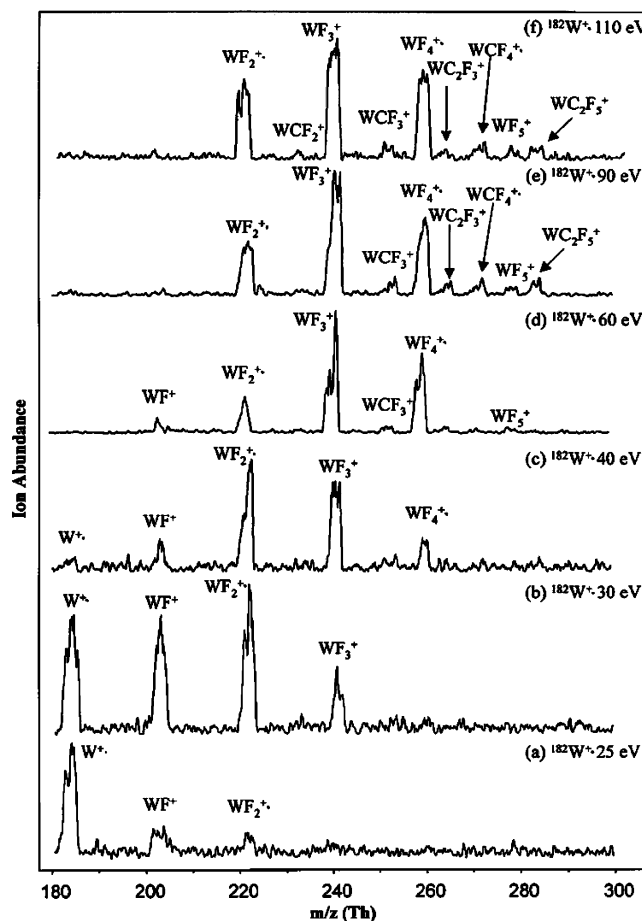


Figure 19. Reactive collisions of W^{+*} at an F-SAM surface at various incident energies. The collision energies and the ion/surface reaction products are indicated. Reprinted with permission from ref 357. Copyright 1999 John Wiley and Sons Ltd.

drive the endothermic $M^+ \rightarrow MF_n^+$ process. The reaction occurs in the course of a single scattering event at the surface rather than involving deposition of reactant at the surface and product release in a subsequent collision.³⁵⁷ Simulations show that incident ions (10–60 eV) could easily penetrate the first two to three carbon atoms of a C_6 surface.¹²⁴ Abstraction of

two F atoms is favored thermochemically by 53 kcal/mol when both F atoms originate from the same alkyl chain.⁷⁰

It is possible that the metal ion must adopt an electronic structure with available unpaired electrons to undergo atom abstraction during collision. Re^+ has a large number of unpaired electrons ($5s^2 5p^6 5d^5 6s^1$) compared to other metal ions, and this is probably the reason behind its high reactivity toward F abstraction and its ability to cleave C–C bonds readily.³⁵⁷ C–C bond activation and subsequent fluorocarbon (C_mF_n ($m = 1, 2$; $n = 1-5$)) abstraction, excluding C_xF_y formation due to CS, was found mainly with W^+ and Re^+ as projectiles.

Well-defined TiC thin films have been formed on the HOPG surface upon collision of Ti^+ , TiCl^+ , and TiCl_3^+ at higher collision energies (>100 eV).³⁵⁸ Primarily SID and dissociative scattering species were observed when the collision energy was below 100 eV, but F abstraction by these projectile ions was observed from fluorocarbon surfaces.⁷¹ From these investigations of various metal ion projectiles, predictions of abstraction reactions require consideration of such factors as the availability of the vacant orbitals, the degree of orbital overlap between the projectile and the surface species, thermochemistry, the electronic structure of the ions, and the geometry of the reactants at the surface. A detailed study of polyatomic ions (mostly Cl compounds) derived from group IIIA, IVA, VA, VIA, and VIIA element collisions at F-SAM surfaces presented by Cooks and co-workers⁷⁰ shows that all ions undergo CS and complex ion/surface reactions. Generally, it was found that polyatomic ions derived from these compounds were less reactive than the corresponding atomic projectiles.

5.6. Some Miscellaneous Ions

The ion $\text{Si}(\text{CH}_3)_3^+$ has been used as a thermometer to achieve an understanding of energy transfer during ion/surface interaction at various surfaces.^{124,359,360} The dimethylsilyl pseudo-halogen species $(\text{CH}_3)_2\text{SiNCS}^+$, $(\text{CH}_3)_2\text{SiNCO}^+$, and $\text{Si}(\text{NCO})_n^+$ undergo ion/surface reactions leading to the abstraction of one and two F atoms from the F-SAM surface together with SID processes.^{270,361} The silyl-containing species are much more reactive than carbonyl pseudo-halogen derived ions. A rich variety of reaction products appears in the product ion spectra. They range from simple SiF^+ species due to collisions of Si^+ or SiCl_n^+ projectile ions⁷⁰ at fluorinated surfaces to pseudo-halogen exchange products. The ions SiF^+ and SiH_2F^+ are the dominant species among the reaction products of dimethylsilyl pseudo-halogens.³⁶¹ Silyl ions with fewer NCO groups appear to be more reactive in F atom transfer reactions.²⁷⁰ The dimethylsilyl group was retained in projectile ions undergoing ion/surface reactions at low collision energies, suggesting that transhalogenation, namely, F-for-NCS substitution, may occur between the surface and the projectile. Hence, the halogen or pseudo-halogen transfer reactions can be exploited to introduce functional groups NCS, NCO, CH_3 , and $\text{Si}(\text{CH}_3)_2$ in the F-SAM surfaces.³⁶¹ The operating mechanism is thought to be based on Lewis acid–base reactions at the surface rather than redox or electron transfer chemistry. However, thermochemical considerations show that F abstraction may involve the unpaired electrons in the outermost orbitals of the projectile ion.²⁷⁰

Collisions (<15 eV) of the silylium cations SiCl_3^+ and $\text{Si}(\text{CH}_3)_3^+$ at various SAM surfaces resulted in covalent modification of the surface and dissociative ion/surface reactions.^{300,362} Silyl cations, including $\text{Si}(\text{CH}_3)_3^+$, $\text{Si}(\text{CD}_3)_3^+$,

$\text{Si}(\text{OCH}_3)_3^+$, $\text{Si}(\text{C}_2\text{H}_5)_3^+$, $\text{Si}(\text{CH}_3)_2\text{C}_6\text{H}_5^+$, and $\text{Si}(\text{CH}_3)_2\text{F}^+$, have been used to modify HO-SAM surfaces at low collision energies.^{300,363} Scattered ion mass spectra recorded using 70 eV CF_3^+ projectile ions serve to characterize the modified surface. Comparison of this CS spectrum with that of an authentic chemically prepared trimethylsilyl ether SAM is made in Figure 20. The notable difference between these two scattering spectra

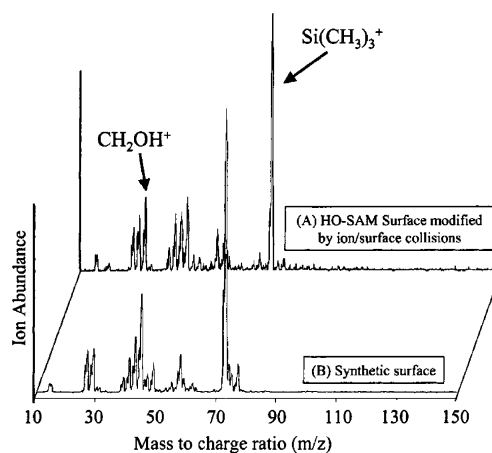


Figure 20. Scattered ion mass spectra due to the collision of CF_3^+ ions at 70 eV with (a) an HO-SAM surface modified using 15 eV $\text{Si}(\text{CH}_3)_3^+$ ion and (b) a trimethyl silyl ether SAM surface prepared by a chemical route. Reprinted from ref 300. Copyright 2002 American Chemical Society.

was the existence of OH features for the surface modified via reactive collisions. It is clear that all the surface groups have not reacted in the course of the ion/surface collision. Further characterization with XPS or re-examination after washing with simple solvents confirmed covalent bond formation between the projectile ion and the surface.³⁰⁰ Other trivalent silyl-containing projectiles were also found to be capable of surface modification by group or atom transfer ion/surface reactions.^{300,362,363}

We have seen that the extent of ion/surface collision reaction depends on the structure of the adsorbate. This fact can be used to obtain specific information on its chemical composition. An example is the reaction of SiCl_3^+ at isomeric surfaces, bearing functional groups such as HO–, CH_3O –, and $\text{CH}_3\text{CH}_2\text{O}$ –.³¹⁰ The distinctive product formation provides qualitative information about the nature of the isomeric surfaces. Scattering of SiCl_3^+ ion at 60 eV collision yields dissociative ion/surface reaction products, e.g., SiCl_2OH^+ and $\text{SiCl}_2\text{OCH}_3^+$, from the HO-terminated and CH_3O -terminated surfaces, respectively. By contrast, for the $\text{CH}_3\text{CH}_2\text{O}$ – surface, products were observed that contain alkyl groups derived from the surface such as $\text{SiCl}_2\text{CH}_3^+$ and $\text{SiCl}_2\text{C}_2\text{H}_5^+$, but none of them contained the O atom from the surface. A second example is the differentiation of isomeric chlorobenzyl mercaptan (CBM) monolayer surfaces by the reaction of Cr^+ and Cr-containing projectile ions.³⁵¹ The abundant reaction product at ~ 80 eV, $\text{C}_7\text{H}_6\text{SCr}^+$, is formed after ion/surface reaction and subsequent elimination of HCl: this species was prominent in the case of 4-CBM but not for the 2-CBM surface. By contrast, the peak due to $\text{C}_7\text{H}_5\text{Cr}^+$ was intense for the 2-CBM surface.

Among other interesting projectiles, BBr_n^+ ($n = 0-2$) ions undergo ion/surface reactions with F-SAM and H-SAM surfaces, yielding various, unique abstraction products.¹³⁰ Bare

Table 8. Soft Landing Phenomena

projectile ion/derived from	substrate	comments	refs
$C_3H_{15}OSi_2^+$	F-SAM		102
$C_3H_{14}OSi_2Cl^+$	F-SAM		102
$(CH_3)_2SiNCS^+$	F-SAM		102, 217
$ClCH_2(CH_3)SiOSi(CH_3)_2^+$	F-SAM	dissociative SL	105, 217
$C_3H_{10}OSi_2Cl^+$	F-SAM		102, 105
2,4,6-triphenylpyrylium cation	F-SAM	dissociative SL	217
<i>N,N</i> -dimethyl- <i>p</i> -toluidine, $(M - 1)^+$	H-SAM		103
<i>N,N</i> -dimethyl- <i>p</i> -toluidine, $(M - 1)^+$	F-SAM	“harder” compared to H-SAM	103
<i>m</i> -(trifluoromethyl)benzoyl ion	F-SAM		103
trypsin	Au/glycerol@Au/plasma-treated metal	retained biological activity	113, 236
lysozyme	Au/glycerol@Au	retained biological activity	113, 138, 236
streptavidin	plasma-treated metal		113
hyaluronan	steel	reactive landing	242, 379
insulin	Au		236
apomyoglobin	Au		236
DNA (160-mer ds-DNA)	nitrocellulose membrane	retained biological activity	369
bovine serum albumin (BSA)	HOPG	preferential landing onto the step edges of the substrate	213
serine	Au	serine octamer formation, chiral enrichment	371
peptide Ac-A15K	NHS-SAM	reactive landing, α -helical conformation	248, 375
cyclic peptide c-RGDfK	NHS-SAM	higher reactive landing efficiency compared to that of the linear peptide	114, 273
linear peptide GRGDSPK	NHS-SAM		273
gramicidin S + $2H^+$	F-SAM		216
dodecanediamine + H^+	NHS-SAM/COF-SAM	reactive landing (amide bond formation)	216
microperoxidase-11	Au	intact deposition	376, 377
virus (rice yellow mottle, tobacco mosaic, etc.)		retained their respective structure	212, 380
$M(\text{benzene})_2^+$ ($M = \text{Ti, Sc, Cr}$)	H-SAM, COOH-SAM, F-SAM	retains the sandwich structure, compounds produced in a molecular beam by laser evaporation	275, 383–387
$V_n(\text{benzene})_{n+1}^+$	H-SAM	retains the multidecker structure	214, 382, 383
<i>cis</i> -bis(isothiocyanato)bis(2,2'-bipyridyl-4,4'-dicarboxylato)ruthenium(II)	$TiO_2(110)$		301
mixed VO(Salen)H ⁺ and Ni(Salen)H ⁺	F-SAM	redox reaction at the surface	274
$M^{III}(\text{salen})^+$ ($M = \text{Co, Mn}$)	H-SAM, F-SAM	charge retention on F-SAM, neutralization on H-SAM	111
Jacobsen's catalyst	Si, SiO_2 , Au, SAM		238, 239
aminoferrocenes	COOH-MWCNTs	reactive landing	354
$Tu(\text{bpy})_3^{2+}/Tu(\text{bpy})_2^{2+}$	HO-SAMs	reactive landing	109, 391
Zr^{IV} - <i>n</i> -propoxide	steel	reactive landing	393
rhodamine B/6G cation	Si, SiO_2 , Au, SAMs	charge retention on insulator substrate; above 100 eV, fragment deposition	115, 239
crown ether with alkali-metal halides	Cu(100)	crown ether alkali-metal complex adsorbed flat on the surface	215
^{111}In (isotope atom)	Cu	radioactive isotope separation	604–606
Ag_n^+ ($n = 1, 17, 19$)	Pt(111)	size-selected deposition	219
Ag_3^+	Al_2O_3	propylene epoxidation	400
Ag_{309}^+ , Ag_{561}^+	C_{60} ML or BL on Au/graphite	diffusion experiments	296, 443
Ag_{1-3}	TiO_2		607
Au_{6-10}^+	alumina	partial oxidation of propene	402
Au_{1-4}	titania	CO oxidation	151
Au_n^+ ($n = 500-1000$)	HOPG		417
Au_8	HOPG	oxidation and reduction of the clusters	153
Au_{1-8}	$TiO_2(110)$	intact size-selected clusters	297
Au_{17}	graphite	immobilization of a protein molecule	406
Au_{20}	MgO	CO oxidation	152
Pt_{8-10}	porous anodized alumina	oxidative dehydrogenation of propane reaction	156
Pt clusters (2–3 nm)		self-organization	298
Pd_n^+ ($n = 1, 2, 3, 4, 7, 10, 16, 20, 250$)	$TiO_2(110)$	CO oxidation	155
Pd_{8-12} , Pd_{15-18}	amorphous alumina	oxidative decomposition of methanol	254
Al_{17}^-	HO-SAM		408
Ni_{30}	MgO, Mg	CO dissociation	154

Table 8. continued

projectile ion/derived from	substrate	comments	refs
C ⁺	Si(100), Ni(111), Ta, W, Au	C films, diamond-like structure	26
C _n ⁺ (50 ≤ n < 60, even n)	HOPG		141, 292, 415, 416
C ₅₈ H _n ⁺ (n = 0–8)	HOPG		141
C ₄₂ H ₁₈ ⁺ , C ₆₀ H ₂₄ ⁺ , C ₆₀ H ₂₄ S ₃ ⁺ , C ₉₆ H ₃₀ ⁺ , C ₂₂₂ H ₄₂ ⁺	HOPG	formation of graphene segments	142, 418–420
C ₈₀ H ₅₂ , C ₂₀₀ H ₁₃₂ , C ₃₂₀ H ₂₁₂	steel		420
La@C ₆₀ ⁺ , Ce@C ₆₀ ⁺	HOPG		143
Ce@C _n ⁺ (n = 36, 44, 50)	HOPG		144
Si ₂ NC ₈ H ₁₉ ⁺	Si	above 100 eV energy, Si–C–N-like film formation	116
Cs ⁺	thin ice films	mobility of ions through water ice	444, 445, 448
D ₃ O ⁺ /H ₃ O ⁺	thin ice (H ₂ O) films	mobility of ions through ice	444, 445
D ₃ O ⁺ /H ₃ O ⁺	n-hexane/3-methylpentane/methylcyclohexane		283, 450
D ₃ O ⁺	hydrocarbon–water–hydrocarbon sandwich structure		449

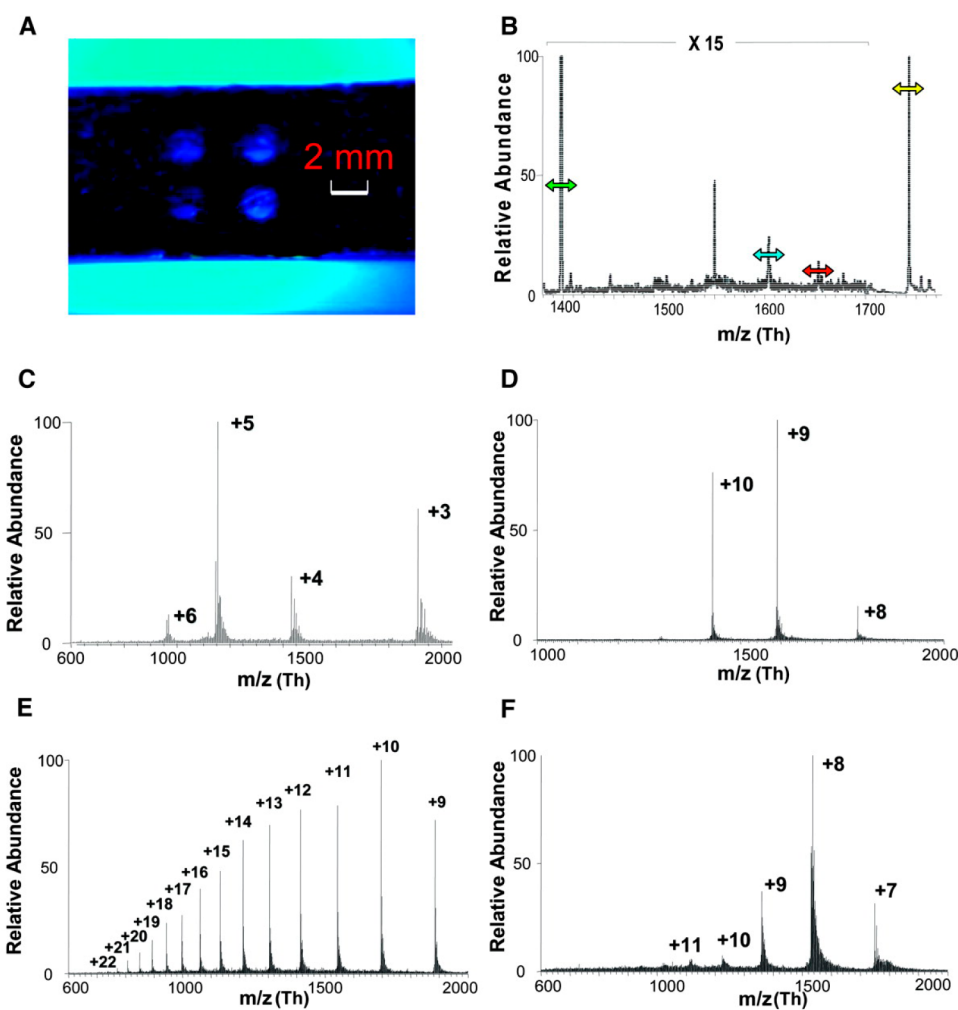


Figure 21. (A) Photograph (in blue light) of a microarray of four proteins soft-landed onto a Au substrate. Each spot is 1 mm in radius. (B) ESI mass spectrum of a mixture of 2.5 μg mL⁻¹ cytochrome *c* (molecular mass 12 360 Da), 2.5 μg mL⁻¹ lysozyme (molecular mass 14 316 Da), 2.5 μg mL⁻¹ insulin (molecular mass 5734 Da), and 2.5 μg mL⁻¹ apomyoglobin (molecular mass 16 951 Da) in methanol/water (1:1) used for soft landing. The ions of the 9 charge state of cytochrome *c* (m/z 1359), 11 charge state of lysozyme (m/z 1301), 4 charge state of insulin (m/z 1398), and 15 charge state of apomyoglobin (m/z 1135) were selected for ion SL on the basis of a window of 5 m/z units. The nominal charge landed for each protein was on the order of 10⁻⁶ C. Mass spectra of the soft-landed proteins after the spots were rinsed: (C) insulin, (D) lysozyme, (E) apomyoglobin, and (F) cytochrome *c*. Reprinted with permission from ref 236. Copyright 2003 American Association for the Advancement of Science.

B^+ ions react with the F-SAM surface, giving rise to BF_2^+ at collision energies of 25–100 eV and BF^+ at collision energies above 50 eV. The lower onset energy of BF_2^+ suggests multiple abstraction in a single step with accompanying C–C bond formation either within a chain (to give C=C) or between chains (to give C–C). As a result of the transhalogenation reaction, in the case of BBr^+ projectile ions, the abstraction product was $BBrF^+$. For the BBr_2^+ ion, the F-adduct was absent but the transhalogenation product $BBrF^+$ appears to be the major product. However, when these projectile ions were used to examine an H-SAM surface, there were no odd-electron ions, e.g., BH^+ , but other reaction products such as BH_2^+ , $BBrH^+$, and $BBrCH_3^+$ were present in the product ion spectra. The disparity between the H-SAM surface and the F-SAM surface can be explained in terms of the difference between their ionization energies, bond energies, and chain flexibility.¹³⁰

Pseudo-halogen-containing ions such as $OCNCO^+$ and $OCNCS^+$ are normally considered as “hard ions” in the SID process but are subject to transhalogenation reactions as in the case of BBr_n^+ projectile ions.³⁶¹ Evidence of reactions of an isothiocyanate group between the ion and surface, abstraction of $-F$ or $-CF_3$, and combination of bond forming and dissociations has been reported.³⁶¹ Some of the product ions are FCO^+ , FCS^+ , SF^+ , $NCSF^+$, $CNCSH^+$, and CF_2NCS^+ . The projectile $OCNCS^+$ was found to be more reactive than $OCNCO^+$, and both ions modify the F-SAM surface by leaving CO, CS, or NCS groups on the surface. State-selected NH_3^+ ions undergo a simple H atom pickup reaction and dissociation at an ammonia-adsorbed indium tin oxide (ITO) surface.¹⁹⁰

6. SOFT LANDING AND RELATED PHENOMENA

The separation of materials by the mass analysis and collection of atomic ions was an important component of the Manhattan project. *Calutron*, a type of magnetic mass spectrometer, was used to separate every atom of ^{235}U used for the production of the first atomic bomb.^{364,365} Much later work showed that, under appropriate conditions, SL is an effective method of separation and collection of molecular ions in high purity. In contrast to atomic ion collection, low collision energies must be employed. The option to explore the chemistry of highly pure reactant species is a distinguishing characteristic of SL experiments. The experiment has potential value in materials science, microelectronics, nanotechnology, biology, catalysis, and fundamental studies of ion/surface collision phenomena. We have described various instruments used for ion SL (section 3.3). See Table 8 for some important systems prepared by the ion SL method.

The concept of SL with polyatomic ions was explored by Cooks and co-workers in 1976,²⁰⁵ but did not receive much attention until the 1990s.^{102,205} An early SL experiment was the deposition of cationized organics formed after desorption ionization and landing onto a second surface.³⁶⁶ The process was demonstrated with the ions derived from trimethylsilyl isothiocyanate, hexamethyldisiloxane, 1,3-bis(chloromethyl)-tetramethyldisiloxane, *N,N*-dimethyl-*p*-toluidine, and *m*-(trifluoromethyl)benzoyl chloride, which were soft landed onto F-SAM or H-SAM surfaces.^{102,103,105,217} The projectile ions were trapped in the SAMs and released during subsequent CS experiments as intact ions.²¹⁷ Some degree of dissociation accompanying SL was also observed.²¹⁷ For smaller organic ions, the H-SAM surface shows differences in SL efficiency compared to the F-SAM surface.¹⁰³ In this context, the H-SAM surfaces act as “softer” surfaces and provide fewer fragments,

just as is the case in the SID process.^{45,126,127} The charge on the surface can be retained even after its exposure to laboratory air.^{218,239} In many situations projectiles which react readily with atoms or groups present at the surface undergo RL.¹⁰⁴

The following paragraphs discuss some applications of SL.

6.1. Separation and Protein Array Formation

Protein chips in the array format are used for the analysis of protein function as well as for drug target identification.^{367,368} Techniques based on SL should have a clear advantage in ability to separate protein species with a small mass difference, although they will be limited in the amounts of sample that can be generated. A preliminary experiment performed on a mixture of four proteins, cytochrome *c*, lysozyme, insulin, and apomyoglobin, achieved separation based on mass, and each protein was deposited at a different position on a surface using a target positioning system. A photograph of the resulting microarray is shown in Figure 21A. The landed proteins were rinsed off the surface individually using a methanol/water mixture and analyzed by ESI MS. Panels C–F of Figure 21 show the ESI spectra resulting from analysis of the rinsed solutions for each spot. These spectra contain only multiply charged ions of the corresponding protein and show no evidence of fragmentation or cross-contamination. In another experiment, Turecek and co-workers simultaneously separated five peptides from a mixture and deposited the pure compounds onto an array collector.²⁰⁸ Isolated components were found in nanomole quantities. A DNA fragment (160-mer ds-DNA) soft-landed onto a nitrocellulose membrane surface was recovered and subjected successfully to enzymatic polymerase chain reaction (PCR) amplification.³⁶⁹ SL deposition of bovine serum albumin (BSA) on an HOPG surface preferentially decorated the step edges of the substrate.²¹³ It was found that BSA assembles into two-dimensional fractal aggregates.

The amino acid serine is known to form homochiral octameric clusters in mass spectrometric ionization processes. This chiral enrichment has been studied in connection with homochirogenesis and the prebiotic conditions needed for the origin of (homochiral) life.³⁷⁰ ESI or sonic-spray ionization was used to generate protonated homochiral octamers of serine.³⁷¹ Chiral enrichment was then confirmed by SL of mass-selected protonated serine octamers. SL has also been applied for the isolation of polymeric components from a mixture. For example, monodispersed synthetic polymer from a polydisperse polymer was isolated by SL.³⁷²

6.2. Peptide Immobilization by Soft Landing

RL of proteins or peptides is a solvent-free method to immobilize biological functionality onto surfaces. Efficient covalent linkage of peptide ions to *N*-hydroxysuccinimidyl ester terminated alkanethiol (NHS-SAM) has been demonstrated.^{114,216,248,273} The primary amino groups present in the lysine side chain of the peptide or protein react with the NHS-SAM by forming amide bonds. RAIRS measurements confirm the amide bond and show that ~60% of the maximum coverage was obtained in an experiment lasting 2 h. Conformationally pure peptides could be immobilized using RL depending on the nature of the surface. The singly protonated peptide Ac-A15K, a model system that preserves its α -helical structure in the gas phase,³⁷³ was successfully transferred onto a SAM surface without losing its helical conformation.²⁴⁸ As expected, on the H-SAM surface, Ac-A15K underwent SL whereas, on NHS-SAM, it experienced RL by forming an amide bond. Compared

to the normal electrospray deposition experiment, where the peptide was dominated by the β -sheet conformation, SL of the Ac-A15K peptide shows sharp amide I and II bands in infrared reflection absorption spectra. The positions of the amide I band at 1666 cm^{-1} and the broad amide A band at 3307 cm^{-1} suggest that Ac-A15K exists in a pure α -helical conformation (see Figure 22).^{114,374} By comparison, the cyclic peptide c-

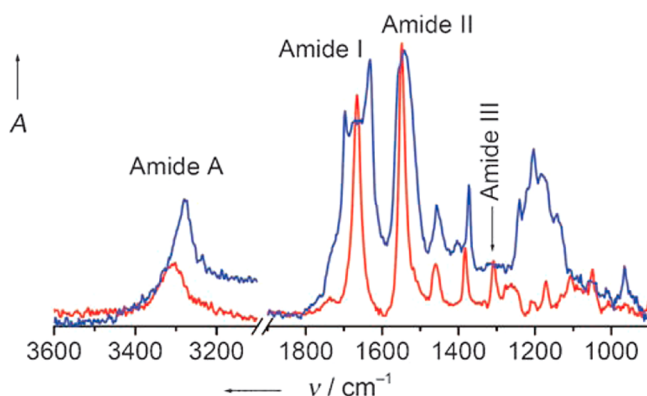


Figure 22. IRRAS spectra of the Ac-A15K layer on an H-SAM surface prepared by electrospray deposition (blue) and SL (red). The H-SAM background has been subtracted from both spectra. Reprinted with permission from ref 114. Copyright 2008 John Wiley and Sons Inc.

RGDfK, which lacks an N-terminal group, showed higher RL efficiency compared to the linear peptide GRGDSPK, which contains an N-terminal group.^{114,273} RL efficiency of peptides or proteins decreases at higher collision energy ($>100\text{ eV}$), and most likely the reaction occurs during the collision event and hence is optimum over a defined range of collision energies.²⁷³ Properties of the substrate have a strong effect on the conformations of soft-landed peptide ions. Deposition of the α -helical $[\text{Ac-A}_{15}\text{K} + \text{H}]^+$ onto H-SAMs immobilizes both the α - and 3_{10} -helical conformations.³⁷⁵ By contrast, a significant fraction of Ac-A₁₅K molecules were present as the β -sheet conformation on the F-SAMs and COOH-SAMs.

It has been shown that microperoxidase-11 (MP-11) exists in different conformations on a Au substrate depending on the charge state. MP-11 is a model compound which exhibits reversible electrochemistry of the heme $\text{Fe}^{\text{II}}/\text{Fe}^{\text{III}}$ couple.^{376,377} The redox properties of soft-landed proteins with a selected charge state were investigated using cyclic voltammetry (CV).^{376,377} Large shifts of the E^0 value for the triply charged protein were attributed to its unfolded conformation and hence its better attachment to the Au electrode surface due to the higher availability of amino groups.³⁷⁶ The lower value of the reorganization energy as well as of the electron transfer kinetic constant calculated for the unfolded conformation supports this hypothesis. Covalent immobilization of MP-11 onto MWCNT electrodes was achieved using RL.³⁷⁸ The immobilization does not seem to induce large conformational changes or denaturation of the soft-landed enzyme.

6.3. Retention of Biological Activity

Biological activity appears sometimes to be preserved during ESI, subsequent MS analysis, and SL when especially gentle (nondenaturing) conditions are used. Two enzymes, trypsin and lysozyme, separated and soft-landed on different substrates were tested for biological activity.^{113,236} The activity of trypsin (soft-landed on Au surface) was tested by digesting cytochrome *c* on the surface.²³⁶ Characteristic tryptic fragments of

cytochrome *c* were confirmed by MALDI MS. Lysozyme, an antibacterial molecule that enzymatically degrades polysaccharide components found on the cell walls of bacteria, was found to be enzymatically active after SL onto a gold substrate or into a liquid surface containing glycerol.^{138,236} The activity of lysozyme was tested with hexa-*N*-acetylchitohexaose substrate.

On plasma-treated metal surfaces, soft-landed trypsin was found to form two layers.¹¹³ The bottom layer was chemically bonded to the surface due to RL at the metal oxide surface, but the upper layer was loosely bound and could be washed away without loss of functionality.¹¹³ Molecules remaining attached to the metal oxide surface showed about 50–60% biological activity. The calculated average fraction of trypsin molecules that survived the collision without loss of enzymatic activity was 84%. In another example, the SEM images of a soft-landed polysaccharide, hyaluronan, displayed its characteristic ability to prevent platelets from adhering to the stainless steel surfaces.^{242,379} Reactively landed hyaluronan preserves the protective properties of the surface against blood platelet activation even after washing with polar solvents.³⁷⁹ It has also been shown that rice yellow mottle virus and tobacco mosaic virus retain their respective spherical and rodlike ultrastructure after ESI and subsequent mass-selected deposition.^{212,380}

6.4. Soft Landing of Organometallics

Compounds that are difficult to synthesize by solution-phase chemistry, such as some organometallic complexes, could in principle be generated by gas-phase reactions and then SL onto surfaces without structural change. Several examples of SL of gas-phase-generated metal–benzene or metal–salen complexes have been reported.^{214,381} Nakajima and co-workers prepared a series of metal–benzene complex/cluster ions by gas-phase synthesis and subsequently soft-landed them onto various substrates. $\text{V}(\text{benzene})_2^+$ and multidecker sandwich cluster ions of general formula $\text{V}_n(\text{benzene})_{n+1}$ were generated in a molecular beam by laser evaporation. The sandwich-like structure was preserved after SL.^{214,382,383} Similarly, other metal sandwich compounds, $\text{M}(\text{benzene})_2$ ($\text{M} = \text{Ti}, \text{Sc}, \text{Cr}$), were synthesized in the gas phase and captured on various SAM substrates at room temperature.^{275,287,383–387} RAIRS confirmed that clusters soft-landed into a low-temperature Ar matrix or onto a SAM surface at room temperature retain the sandwich structure.

The gas-phase-generated multidecker $\text{V}_2(\text{benzene})_3$ complex nondissociatively soft-lands onto a room temperature 1-octadecanethiol SAM substrate at kinetic energies of $<50\text{ eV}$ (see Figure 23).³⁸³ TPD results suggest that these ions undergo dissociation to $\text{V}(\text{benzene})_2$ and $\text{V}_2(\text{benzene})_2$ during landing and are trapped on the SAM substrate.³⁸³ The landed complexes were neutralized, even on F-SAM, due to charge transfer from the SAM substrate, but their native sandwich structures remained intact. The high activation energy for desorption determined using TPD suggests that the deposited metal–benzene clusters are strongly trapped inside the alkyl chains of the SAM.³⁸⁷ The threshold desorption temperature of V–benzene sandwich clusters on a C_{16} hydrocarbon SAM–Si(111) substrate was 30 K higher than that of an oxidized Si surface ($\sim 210\text{ K}$),²⁸⁷ but this desorption temperature was much lower than that on a C_{16} hydrocarbon SAM–Au(111) surface ($\sim 290\text{ K}$).²⁷⁵ SAMs prepared on silicon are less ordered and less densely packed in comparison to the well-ordered Au–SAMs, making them a less effective trapping substrate.³⁸⁸ Since the projectile ion kinetic energy was $\sim 20\text{ eV}$, the ion could

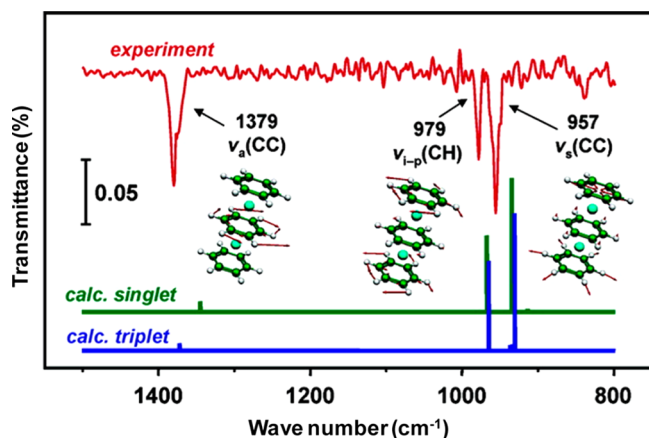


Figure 23. RAIR (IRAS) spectrum of the $V_2(\text{benzene})_3$ complex on a C_{18} -SAM, with calculated IR absorption spectra for singlet and triplet states. Reprinted from ref 383. Copyright 2007 American Chemical Society.

penetrate into the SAM matrix, which was manifested by the high desorption barrier (rather than a lower value of <100 kJ/mol, which corresponds to interaction between the methyl surface and the ion).³⁸⁹ In the case of the COOH-SAM, the hydrogen-bonding groups near the terminus create a rigid network structure. Soft-landed complexes could not penetrate into the SAM matrix but were adsorbed onto its surface.^{386,390} The desorption temperature of the soft-landed complex from the $C_{10}F$ -SAM surface increased to ~ 320 K.³⁸⁴ This difference is evidently the result of an increase in enthalpy of transition corresponding to the rotator phase of the supporting SAM matrix as a consequence of the fluorination of its molecular chains.

Another interesting difference between the F-SAM and the H-SAM surfaces in the SL of organometallic compounds was found in orientation differences. The entrapped clusters are highly oriented on the H-SAM surface with their molecular axes tilted 70 – 80° from the surface normal.^{275,385} The $Cr(\text{benzene})_2$ complexes embedded in the $C_{10}F$ -SAM matrix were oriented with their molecular axes perpendicular to the surface plane, and the complexes on the surface orient with their molecular axes slanted to the surface plane.³⁸⁴ Such preferences in orientation in the F-SAM are probably due to a repulsive interaction between the π -cloud of the capping benzene rings of the complex and the outmost CF_3 group and side chain C–F groups of the fluorocarbon axes of the F-SAM matrix. The situation in the H-SAM surface was attributed to the attractive CH– π interaction between the capping benzene rings of the cluster and the lateral methylene groups of the alkanethiolates.²⁷⁵ On the COOH-SAM surface, the $Cr(\text{benzene})_2$ complex prefers to orient its molecular axes along the surface normal direction rather than in the surface plane, presumably due to chemical interactions between the benzene ring of the complex and the carbonyl groups at the SAM surface.³⁸⁶

Reactive undercoordinated metal complexes generated in the gas phase and subsequently immobilized at SAM surfaces showed what could be catalytic activity toward gaseous reagents.^{109,391} $Ru(\text{bpy})_2^{2+}$ generated in the gas phase by CID of the corresponding $Ru(\text{bpy})_3^{2+}$ and then reactively landed onto COOH-SAMs were subsequently exposed to O_2 and C_2H_4 . The results suggested that the immobilized complex

forms an oxidized complex upon exposure to O_2 followed by deoxygenation in the presence of C_2H_4 .

A thermal atmospheric ionization method, APTDI (atmospheric-pressure thermal desorption ionization),³⁹² can provide a unique route to generate mixed-metal clusters. Ionization mixtures of $V^{IV}O(\text{salen})$, $Ni^{II}(\text{salen})$, and $Co^{II}(\text{salen})$ ($\text{salen} = N,N'$ -ethylenebis(salicylimine)) yielded mixed-metal cluster ions.³⁸¹ Normal ESI spectra of the same organometallic compounds were noticeably more complex than the APTDI mass spectra. The oligomers generated by APTDI potentially have higher reactivity than single-metal clusters and could be successfully transferred to an interface via SL. The reactivity was evident by the redox chemistry seen in the CID of Co–VO and Ni–VO mixed clusters. Evidence of the presence of reactive organometallic complexes on surfaces was obtained after selective deposition of metal–salen complexes onto F-SAM substrates. The $V^VO(\text{salen})^+$ and $[Ni^{II}(\text{salen}) + H]^+$ complexes were generated by ESI and mass-selected before being deposited onto the F-SAM. A time dependence study after ion deposition showed loss of O from $V^VO(\text{salen})^+$, forming $V^{III}(\text{salen})^+$, over a four-day period, indicating a slow interfacial reduction process.²⁷⁴ Both reduction and oxidation on the surface were observed, as seen in the loss of O from $VO(\text{salen})$ and loss of 4H from $VO(\text{salen})_2^+$. The regeneration of $V^VO(\text{salen})^+$ upon exposure to molecular oxygen and its subsequent reduction to $V^{III}(\text{salen})^+$ in vacuum completes the catalytic cycle of O_2 reduction by the immobilized vanadium–salen species. Comparison of the soft-landed $M^{III}(\text{salen})^+$ complexes of Co and Mn shows the presence of protonated $Co^{III}(\text{salen})$ features in the SIMS spectra.¹¹¹ This was likely due to the facile reduction of the complex in the SIMS plume.

RL of Zr^{IV} –1-propoxide was found to produce a zirconium oxide coating on a stainless steel substrate which can be used for selective phosphopeptide capture and subsequent analysis by desorption ionization, specifically by MALDI.³⁹³ The modified surface was found to be efficient in enriching, by a factor of 20–90, singly phosphorylated peptides in midfemtomole amounts for both synthetic peptide mixtures and a tryptic digest of α -casein.³⁹³ Similarly, RL on various surfaces showed that zirconia was superior to titania followed by hafnia in terms of phosphopeptide enrichment efficiency.³⁹⁴ The functionality of the N3 dye *cis*-bis(isothiocyanato)bis(2,2'-bipyridyl-4,4'-dicarboxylato)ruthenium(II) has been successfully transferred onto the $TiO_2(110)$ surface by SL.³⁰¹ The carboxyl groups of a bisisonicotinic acid ligand deprotonate so that its O atoms bind to Ti atoms of the substrate, and one of the thiocyanate groups binds via a S atom to an O atom of the substrate.³⁰¹

6.5. Preparation of Catalytic Surfaces

Supported subnanometer-sized metal clusters possess distinct catalytic reactivity that is not observed in their bulk analogues. Preparation of size-selected metal clusters with optimum monodispersity allows study of their size effect under catalytically realistic conditions. Several groups have prepared size-selected metal clusters of Ag, Au, Pt, and Pd by SL and investigated their catalytic activity. Some interesting chemistry is described below.

For a number of years it has been known that Ag clusters could be soft landed onto a substrate,^{219,221} and several aspects of such clusters have been studied.^{209,220,221,234,258,259,295,395–399} Size-selected Ag_3 clusters and Au nanoparticles (3.5 nm, formed by the aggregation of the trimers) on an alumina support can catalyze propylene epoxidation.⁴⁰⁰ Only a

negligible amount of CO₂ formation was observed, which is the main problem in Ag bulk metal catalysis of the same reaction. The reaction proceeded with high yields at lower temperatures. Density functional theory (DFT) calculations support the expectation that oxidized silver trimers should be more active and selective for epoxidation compared to the bulk metal surface because of the open-shell nature of their electronic structure.⁴⁰⁰

Au clusters prepared by SL were used for catalytic oxidation of CO, propene, and other substrates.^{151–153,226,255,297,401–405} Au_{6–10} clusters soft-landed onto an unconventional alumina support were active in the partial oxidation of propene.⁴⁰² Surprisingly, alumina-supported Au clusters (Au_n/Al₂O₃) were active in the presence of water vapor instead of hydrogen, which is essential to maintain the hydroxyl equilibrium at the surface.⁴⁰² Conventionally, titania is considered to be crucial for the production of •OH/•OOH radicals, which are believed to be needed for the promotion of the partial oxidation step on Au/TiO₂. The deposited Au provides unique binding sites for immobilization of protein, and the minimal contact reduces the risk of protein denaturing.^{235,406}

Naked Pt clusters are ideal model systems for fundamental catalysis investigations.^{156,255,298,299} Oxidative dehydrogenation of propane catalyzed by size-selected Pt_{8–10} clusters deposited on a high-area surface was 40–100 times more active than that on a normal Pt catalytic surface.¹⁵⁶ Moreover, the clusters were highly selective toward the formation of propylene over other products. From quantum chemical calculations, it was suggested that the highly selective activity may be due to the undercoordination of Pt in the cluster state.¹⁵⁶ The deposited Pt clusters were encapsulated by a reduced titania layer in a high-temperature (~1100 K) annealing process, resulting in a passive state of “strong metal support interaction” (SMSI) with very low catalytic activity,⁴⁰⁷ but it was found that a sputter annealing procedure transfers the Pt clusters on TiO₂(110) from their inert SMSI state into a catalytically active one for CO oxidation.¹⁵⁰ In this procedure, the sample is sputtered with Ar⁺ ions at room temperature and then annealed at the same temperature. In Figure 24, CO₂ production at the surface is shown as a function of the sample temperature when CO and O₂ reactants were pulsed alternatively onto the sample. The CO₂ production after the sputter-annealing treatment indicated that Pt nanoclusters on TiO₂(110) were transferred from their inert SMSI state to a catalytically active and thermally stable form.¹⁵⁰

The catalytic activity of size-selected Pd clusters has been studied in detail.^{226,254} A wide range of clusters of Pd (Pd_n (n = 1–25)) were deposited on a rutile TiO₂(110) surface, and the electronic structure dependence of reactivity was explored.¹⁵⁵ The reactivities of these clusters for CO oxidation were compared. The changes in electronic structure, determined by XPS, revealed that the Pd 3d binding energy varied non-monotonically with the cluster size. It is evident from the comparison of CO oxidation that the activity increased for Pd₂ and decreased slowly on going to the Pd₇ cluster. The activity increased again in a monotonic fashion before dropping again at Pd₂₅. The low activity correlated with a higher than expected Pd 3d binding energy, which was attributed to a particularly stable valence electronic structure.

Preparation and physicochemical investigations of sized-selected clusters derived from various other metals have been reported: Al,⁴⁰⁸ Cu,^{231,252} Si,²²⁸ W,⁴⁰⁹ Ni,^{154,229,410,411} Ru,²⁵⁰

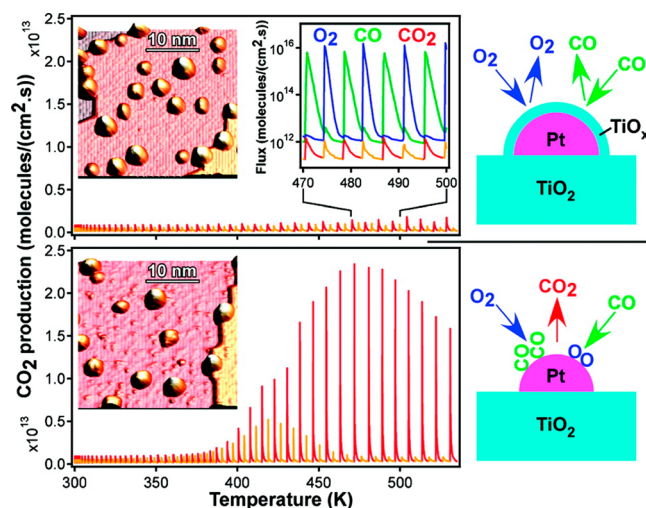


Figure 24. (a) Vanishingly small CO₂ production (red-orange) obtained on the SMSI sample displayed in the left inset upon dosing alternating pulses of O₂ (blue) and CO (green) as shown in the right inset as a function of the sample temperature and time (heating rate 1 K/s, pulse frequency 0.1 Hz). (b) High CO₂ production obtained on the sample displayed in the left inset (same preparation as in panel a), followed by Ar ion sputtering at room temperature and annealing at 1100 K for 1 h. Red and orange colors refer to the CO₂ production synchronized with CO and O₂ pulses, respectively. Reprinted from ref 150. Copyright 2011 American Chemical Society.

Mo₄S₆,²⁵¹ Mo_n/(MoO₃)_n²¹¹ Met-Cars,⁴¹² and various bimetallic clusters.^{223,263,413}

Although the results show potential value in catalysis, the challenging task of scaling up the production of size-selected clusters at surfaces for use as industrial nanocatalysts remains to be accomplished. DFT calculations predict high CO oxidation activity for ligand-protected subnanometer-sized Au clusters.⁴¹⁴ This may open up the use of ESI as an ionization source for cluster ion production. Use of high-current SL experiments could also scale up the production step considerably.

6.6. Nanopatterning

The SL approach is useful in producing ordered structures of organic macromolecules on surfaces. For example, in contrast to chemical extraction, a wide range of small endohedral fullerenes (e.g., La@C_n, Ce@C_n) are available by deposition of mass-selected cluster beams.^{143–145} A simple way to prepare alkali-metal fullerides could be to deposit a small amount of alkali metal on top of a well-defined solid C_n film at room temperature.⁴¹⁵ Subsequently, the alkali-metal atoms will diffuse into and penetrate the interstitial sites of the C_n lattice.

Besides fullerene derivatives, pure fullerenes containing fewer carbon atoms have been prepared in the gas phase and soft landed. The C_n⁺ (50 ≤ n < 60; n is even) ions, generated by EI of C₆₀ and deposited at <6 eV, produce a product with substantially higher thermal stability than a pure C₆₀ thin film.^{141,292,415,418} C_n thin film formation on HOPG surfaces proceeds initially via 2D islands followed by 3D pyramid-like structures at higher coverage on the basis of the Volmer–Weber scenario.^{415,416} Higher primary kinetic energies favor the formation of smaller and less dendritic islands.²⁹² Soft-landed C₅₈⁺ ions easily undergo reaction with residual gases to generate hydride derivatives C₅₈H_n (n = 0–8).¹⁴¹ In another study, formation of amorphous carbon films was observed when neutral C clusters were deposited on a surface.³⁰² Earlier

it was shown that the deposition of C^+ ion beams at hyperthermal energy onto metal surfaces forms diamond-like structures.²⁶ ESI of Au colloids or Au clusters onto HOPG was found to form three-dimensional agglomerates on the surface.^{213,417} These three-dimensional structures are between 250 and 640 nm in diameter and 3 and 17 nm in height and were preferentially formed at the step edges of the HOPG surfaces. The growth mechanism again follows the Volmer–Weber model, which implies a stronger interaction between the deposited particles than between the particles and the substrate.

The recent interest in graphene, due to its unique charge transfer properties, motivates grafting of surfaces with such materials. Poor solubility in common organic solvents prevents the use of surface-coating techniques. Nano-graphene segments, in other words, PAHs such as $C_{42}H_{18}$, $C_{60}H_{24}$, $C_{60}H_{24}S_3$, $C_{96}H_{30}$, $C_{222}H_{42}$, and polyphenylene-dendronized perylenes (PDPs) and several of their derivatives, were generated by laser desorption and successfully soft landed, at energies of ~ 35 eV, onto the HOPG substrate.^{142,418–420} The self-organization observed for C_{42} and C_{96} soft-landed films shows lamellar structure domains of two coexisting “edge-on” phases due to π – π stacking of the deposited molecules¹⁴² (see Figure 14 for an STM image of the soft-landed species). Large conjugated molecules containing extensively delocalized π orbitals leading to strong π -stacking and thus improved charge transport and increased charge density are ideal for electronic applications.⁴¹⁹ The dimensions of these structures range from a few nanometers to a few tens of nanometers with stacked molecule tilt angles of 18° . In the case of C_{60} and C_{222} , SL leads to the formation of two-dimensional polycrystalline molecular domains that may not be exactly edge-on phase packed.⁴¹⁸ Such self-organization is absent when other widely adopted methods of surface coating are used. The graphene segments neither fragment nor lose their structural characteristics during the deposition process. MALDI-TOF spectra of thin films formed by deposition of nano-graphene segments show the corresponding molecular ion peaks, Figure 25. The series of ions generated from PDPs $C_{80}H_{52}$, $C_{200}H_{132}$, and $C_{320}H_{212}$ and its derivatives show that SL can be successful at impact energies below 180 eV, without causing fragmentation.⁴²⁰ The yield of soft-landed material reaches its maximum value when the kinetic energy of the projectile ion lies between 50 and 100 eV.⁴²⁰

When crown ethers were electrospayed together with salts of selected alkali-metal cations (H^+ , Na^+ , or Cs^+), the resultant host–guest complexes underwent successful SL.²¹⁵ Conventional sublimation processes failed to produce such complexes at the surface. In situ low-temperature (~ 43 K) STM images showed intact SL with crown ethers adsorbed flat on a Cu(100) substrate with an ion placed centrally within the cavity (Figure 26). This example shows that SL is a versatile surface functionalization method with molecular host–guest complexes.

6.7. Fluorinated Surfaces

Organofluorine ions have been used as efficient sputtering agents in several technologically important surface modifications.^{162,163,165,284,421,422} Hyperthermal energy $C_nF_m^+$ ions have been used commonly as etching or modification agents for metal, semiconductor, or polymer surfaces.^{284,313,423} Chemical modification of the surface is strongly dependent on the ion kinetic energy and the structure of the precursor fluorocarbon ions. The deposition of fluorocarbon ions on polymer surfaces

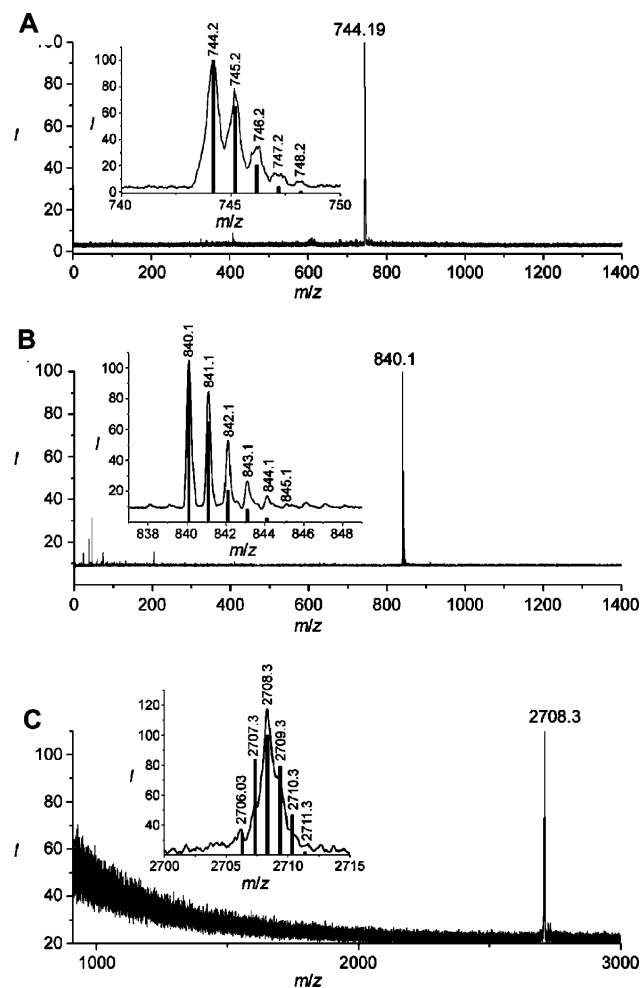


Figure 25. MALDI-TOF MS spectra of thin layers of deposited (A) $C_{60}H_{24}$, (B) $C_{60}H_{24}S_3$, and (C) $C_{222}H_{42}$. Insets: enlarged spectra of the respective molecular peaks, with simulated signals (bars) corresponding to the natural isotopic mass distribution of the individual molecules. Reprinted with permission from ref 418. Copyright 2009 John Wiley and Sons, Inc.

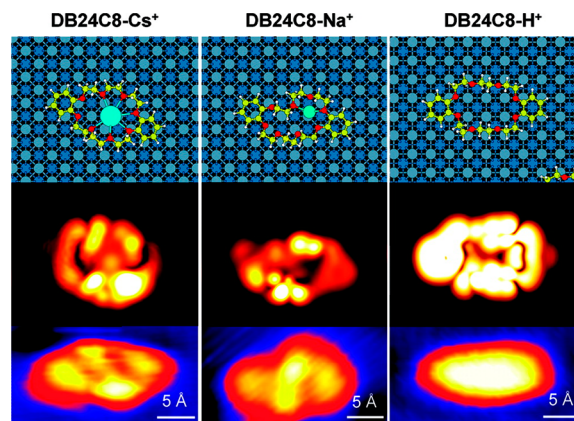


Figure 26. Top row: geometry of the DB24C8 complex at the Cu(100) surface (DB24C8– Cs^+ , – Na^+ , and – H^+). Middle row: simulated STM images according to the above structures. Bottom row: magnified STM topographs of single complexes. Reprinted from ref 215. Copyright 2010 American Chemical Society.

is a highly flexible method for nanostructure film growth or preparation of chemical gradient surfaces with a high level of

control over the process.^{164,165,284,424} $C_3F_5^+$ ions are more effective in growing fluorocarbon thin films on the surface, but CF_3^+ was successful in fluorinating polymer substrates.^{162,165,421,422} The reaction might proceed through covalently bound polyatomic precursors or fragments that can react and become incorporated within the surface materials rather than merely donating F atoms.¹⁶² The reaction channels may proceed in a different way at different collision energies; for 2–3 eV collisions, CF^+ or CF_2^+ ions are simply deposited at the Si surface, but formation of CF_2^+ and CF_3^+ was observed when the incident energy exceeded 20 eV due to impact dissociation and reaction.³¹³ No fluorocarbon species was observed at 100 eV; instead silicon carbide was formed.³¹³ Simple deposition of $C_3F_5^+$ and thiophene ions at hyperthermal energy generates thin film nanostructures on H–Si(100) with control over morphology by varying the ion energy and ion structure.¹⁶⁴ Another choice of F-containing ion for surface modification was SF_5^+ ,⁴²⁵ which was found to induce fluorination by grafting reactive F atoms formed upon dissociation.¹⁶¹ At higher collision energy, in the kiloelectron-volt range, SF_5^+ bombardment is widely used for depth profiling experiments on polymer surfaces.^{426,427} Other ions used for surface modification include SO_3^+ and the organosilane ion $Si_2O(CH_3)_5^+$.^{161,163,424}

6.8. Ambient Ion Soft Landing and Electrospray Deposition

Ion SL experiments can be performed under ambient conditions. In a typical example, ions generated by ESI are passed through a heated metal drying tube, and dry ions of selected polarity are deposited onto a substrate.^{428–430} The dry ions are used as reagent ions in heterogeneous ion/surface reactions or for surface patterning. Unlike vacuum SL, mass selection is not used in such an experiment, but the ionization conditions and reagents are optimized to provide the desired projectile ion. When the experiment is performed at atmospheric pressure (or reduced pressure) without mass selection or optimization for single-ion formation, it is sometimes termed atmospheric pressure ion deposition or electrospray deposition.^{431–440} This method has been employed to prepare arrays or patterns of nanostructures, nanotubes, fullerenes, etc.^{434,435,437,441,442} These are viable methods for the formation of nanostructure or thin films of functional materials, but they lack the molecular specificity of mass-selected ion soft-landing experiments.

6.9. Other Uses of Soft Landing

The use of the SL method in molecular separation and immobilization and in surface patterning has so far been discussed. The highly controlled and well-defined experimental conditions in SL can be utilized for several types of fundamental studies which are difficult to perform otherwise. One such example is the investigation of the mechanism of penetration of nanoparticles into thin films. A monolayer of C_{60} prepared on a Au support cannot be a good barrier for Ag_{309}^+ clusters. These clusters easily diffuse through C_{60} monolayers in a few hours.⁴⁴³ Such penetration does not occur through multilayers of C_{60} supported on a Au surface or a monolayer of C_{60} on graphite. Simple diffusion does not explain the penetration of nanoparticles through thin films or nanoscopic barriers.^{296,443} Attractive forces between the metal and metallic particles are involved. Au clusters (~350 atoms) soft-landed onto an H-SAM on a Au substrate were found to diffuse through the ML and localize at the Au–S interface.²⁹⁵ This happened as

a result of cluster implantation in the SAM followed by molecular reorganization.

It is often difficult to measure ion mobility in condensed molecular solids, but SL of ions directly onto an adsorbate can overcome many errors associated with these studies. A measure of the mobility of ions in water ice can be obtained by making Kelvin probe measurements.^{444,445} SL of hydronium (D_3O^+) ions onto ice films creates a potential difference across the ice film which was monitored using a Kelvin probe as a function of temperature.⁴⁴⁴ First, D_3O^+ and Cs^+ ions were soft landed (~1 eV) on amorphous water ice at 30 K. Upon increasing the temperature, a sharp drop in voltage occurred near 50 K, a temperature much lower than its glass transition temperature of 135 K.^{446,447} This is attributed to a dielectric response due to reorientation of dipoles of the amorphous ice film. Interestingly, SL studies show that neither Cs^+ nor H_3O^+ ions can move from the ice film surface to the interior at higher temperatures.^{445,448} These observations will be discussed in section 7.2. In a similar setup, hydronium ions were found to migrate across epitaxially grown micelle-like films of hydrocarbon/water/hydrocarbon sandwich structures (temperature range 90–150 K).⁴⁴⁹ The motion of hydronium and Cs^+ ions through simple hydrocarbon films, viz., *n*-hexane, 3-methylpentane, and methylcyclohexane, was also investigated.^{283,450} The ions were found to migrate through the amorphous version of these films as expected, and very limited diffusion was observed through crystalline films.²⁸³

7. COLLISIONS AT CONDENSED MOLECULAR SOLIDS

This section of the review is devoted to studies of low-energy ion collisions at condensed molecular solids or “ices” formed from various molecules such as water, ammonia, methane, carbon dioxide, hydrocarbons, etc. Puzzles ranging from the origin of life^{451,452} to ozone depletion⁴⁵³ propel interest in the chemistry and physics of ice surfaces. From a standpoint of physical chemistry, an ice surface has properties much different from those of liquid water or even bulk ice. Upon the phase transition from liquid to solid, the rate of reagent diffusion is reduced by several orders of magnitude. The rates of reactions are much slower at the temperature of ice. With such drastic changes, the occurrence of chemical reactions with appreciable speeds might be considered doubtful, and this expectation is generally valid in bulk ice. At the surface of ice, however, reactions may occur even at very low temperatures, sometimes at such appreciable speeds that they affect the global environment. Ice surfaces can be used as a testing ground for the investigation of water–molecule interactions, solvation phenomena, and processes in two-dimensional environments.^{38,40}

7.1. Reactive Scattering and Sputtering

For the study of ice surfaces, the projectile ion is typically used as a probe rather than as a means of modifying the surfaces. Monoatomic projectile ions such as Cs^+ and noble gas ions have been widely used.^{38,174} In particular, reactive scattering of Cs^+ has been extensively used in recent investigations of reactions at ice surfaces.^{38,39} In the original publications, the term “reactive ion scattering (RIS)” is used, but the term “reactive scattering” is used in the current review. In certain cases, ice surfaces contain pre-existing ions such as those produced by the ionization of electrolytes. These pre-existing ions can be detected by means of low-energy sputtering (LES).⁴⁵⁴ Ion desorption from surfaces can also occur by

Table 9. Hyperthermal Energy Collisions at Condensed Molecular Solids

method (projectile ion)	system	aim/observations	refs
reactive scattering and LES (Cs ⁺)	H ₂ O–D ₂ O	rate and activation energy of self-diffusion and H/D exchange of water	462, 476, 479, 496
	H ₃ O ⁺ –water ice	affinity of protons for the ice surface and proton transfer mechanism	478–480
	H ₃ O ⁺ –H ₂ O–D ₂ O	hydronium ion-mediated proton transfer at the ice surface	495
	OH [−] –H ₂ O–D ₂ O	hydroxide ion-mediated proton transfer at the ice surface	497
	HCl–water ice	molecular and ionized states of HCl on ice	457, 477
	Na–water ice	hydrolysis of Na	484
	H ₃ O ⁺ –NH ₃ –water ice	incomplete proton transfer from H ₃ O ⁺ to NH ₃ on the ice surface	454, 458
	H ₃ O ⁺ –amine–water ice	proton transfer efficiency on ice is reversed from the order of amine basicity	502
	CO ₂ –Na–water ice	CO ₂ hydrolysis is not facilitated by a hydroxide ion	463
	NO ₂ –water ice	NO ₂ hydrolysis produces nitrous acid	465
	SO ₂ –water ice	SO ₂ hydrolysis occurs through various intermediates	511
	C ₂ H ₄ –HCl–water ice	electrophilic addition reaction mechanism at the condensed molecular surface	466
	ethanol/2-methylpropan-2-ol–water ice	S _N 1 and S _N 2 mechanisms at the condensed molecular surface	505
	NH ₃ –water ice and UV irradiation	ammonium ion formation	608
	CH ₃ NH ₂ –water ice and UV irradiation	protonated methylamine formation	483
	CH ₃ NH ₂ –CO ₂ –water ice and UV irradiation	glycine and carbamic acid formation	464
NaX–water ice (X = F, Cl, Br)	surface/bulk segregation and transport properties of electrolyte ions	472–474	
reactive scattering (Cs ⁺)	CO and CO ₂ on Pt(111)	mechanism of Cs ⁺ reactive ion scattering	89
	Ar, Kr, Xe, and N ₂ on Pt(111)	adsorbate mass effect on the reactive ion scattering cross-section	609
	C ₂ H ₄ on Pt(111)	dehydrogenation mechanism of ethylene to ethynidyne	459, 610
	C ₂ D ₄ and H on Pt(111)	ethylidene intermediate in H/D exchange reaction with ethylene	80, 610
reactive scattering (H ⁺)	water ice and alcohol	H ₂ ⁺ formation	469
CS (Ar ⁺)	water ice–chloromethanes (CCl ₄ , CHCl ₃ , CH ₂ Cl ₂)	except CCl ₄ , others undergo diffusive mixing	174
	water ice–simple carboxylic acids	structural reorganization on the ice film	175
	water ice	micropore collapse in the top layers of the ice film	176
	water ice–butanol		494

means of the charge exchange processes of CS.^{174,175} Table 9 lists ice systems investigated using hyperthermal energy ions.

The Cs⁺ reactive scattering was first discovered on a Si surface with chemisorbed water molecules: Cs⁺ ions scattered from the surface picked up water molecules to form Cs⁺–water complexes.^{78,95,96} Since then, such processes have been examined on various surfaces and molecular adsorbate systems, including ice films,^{79,80,87,89,97,454–466} and the mechanism has been investigated theoretically.^{88,98,467,468} These studies clearly suggest that reactive scattering occurs via an ER-type abstraction mechanism, discussed in section 1.1.2. Figure 27 illustrates the reactive scattering mechanism with four representative snapshots of a Cs⁺ scattering trajectory in a classical MD simulation.^{39,88} The abstraction reaction is driven by the ion–dipole attraction force between the Cs⁺ ion and an adsorbate molecule. The impinging projectile first releases part of its initial energy to the surface (Figure 27b) even without direct collision with the adsorbate. Subsequently, the projectile pulls the adsorbate gently away from the surface in its outgoing trajectory (parts c and d of Figures 27 in sequence), leading to the formation of a Cs⁺–molecule complex. The velocity of the outgoing Cs⁺ must be slow enough to accommodate the inertia of the adsorbate.^{88,98} As a result, adsorbates of low mass and small binding energy are efficiently abstracted. A heavier projectile like Cs⁺ transfers more energy to the target surface, and its lower velocity in the outgoing trajectory enhances the efficiency of reactive scattering events.⁹⁵ Detailed aspects of Cs⁺

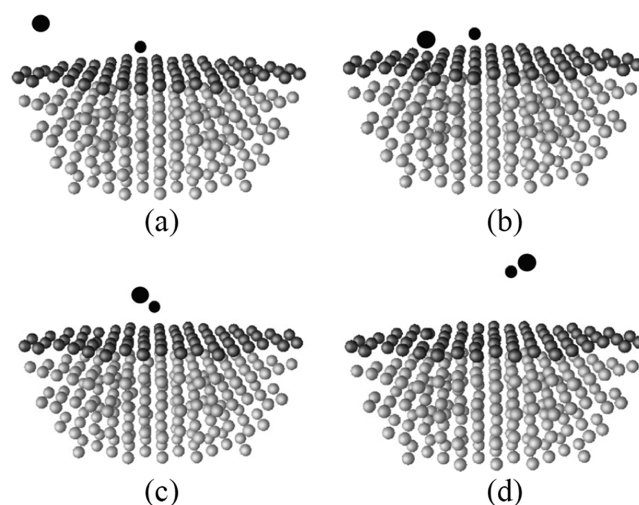


Figure 27. Illustration of the reactive scattering mechanism of a Cs⁺ ion in four snapshots of a scattering trajectory from a Pt(111) surface: (a) initial positions before impact, (b) impact of the Cs⁺ and energy release to the surface, (c) Cs⁺ pulling the adsorbate away in its outgoing trajectory, (d) slow outgoing Cs⁺ dragging the adsorbate along and forming a Cs⁺–molecule association product. Reprinted with permission from ref 88. Copyright 2004 John Wiley and Sons, Inc.

reactive scattering and its application for surface analysis have been reviewed.³⁹

Figure 28 shows an example of reactive collision mass spectra, which were obtained on a D_2O ice film exposed first to

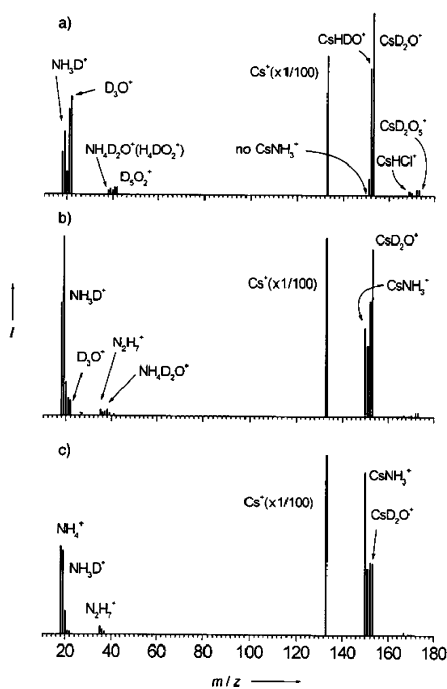


Figure 28. Cs^+ reactive scattering and LES spectra monitoring the $H_3O^+ - NH_3$ reaction on ice. The D_2O film [3–4 bilayers (BLs), 1 BL = 1.1×10^{15} water molecules cm^{-2}] was exposed first to 0.5 L of HCl to generate hydronium ions and then to NH_3 at varying exposures: (a) 0.02 L, (b) 0.3 L, (c) 0.7 L. The sample temperature was 100 K. The Cs^+ collision energy was 30 eV. Reprinted with permission from ref 454. Copyright 2001 John Wiley and Sons, Inc.

0.5 L of HCl gas and then to varying amounts of NH_3 gas at 140 K.⁴⁵⁴ The spectra show peaks at higher masses than Cs^+ (m/z 133), viz., $CsNH_3^+$ at m/z 150, $Cs(D_2O)_n^+$ ($n = 1, 2$) at m/z 153 and 173, and $CsHCl^+$ at m/z 168, indicating the presence of the corresponding molecules on the surface. The intensities of H/D-exchanged species represent their original concentrations on the surface, because H/D isotopic scrambling does not occur during the ion/surface collision time ($< 1 \times 10^{-12}$ s).

The conversion efficiency of a neutral adsorbate (X) into a gaseous ion (CsX^+) ranges from $\sim 10^{-4}$ for chemisorbed species to ~ 0.1 for physisorbed small molecules. Typical product ion signal intensities for ice film surfaces are much stronger than those for chemisorbed species. Also, it is worthwhile to point out that reactive collisions of Cs^+ are ineffective for detecting large molecules such as polymers or long-chain SAM molecules.⁴⁶¹

The mass spectra in Figure 28 also show LES signals corresponding to pre-existing ions on the surface. The hydronium ions seen are produced by the spontaneous ionization of HCl on the ice surface, and they undergo proton transfer reactions with NH_3 to generate ammonium ions. The spectra show characteristic H/D isotopomers of each species produced by H/D exchange reactions with D_2O molecules. The LES signals due to preformed hydronium and ammonium ions exhibited sputtering thresholds at Cs^+ impact energies of 17 and 19 eV, respectively.⁴⁵⁴ On the other hand, on pure H_2O and NH_3 surfaces, these ions were emitted only above ~ 60 eV

due to their formation during secondary ion emission.⁴⁵⁴ It was also found that ultra-low-energy (a few electronvolts) collision of H^+ with the ice surface can produce H_2^+ .⁴⁶⁹ The reaction proceeds more efficiently on amorphous solid water than crystalline water, reflecting differences in the surface concentration of dangling O–H bonds. Simple alkanols also behave in the same manner. The combined occurrence of reactive scattering and LES provides a powerful means to probe both neutral molecules and ions on surfaces and, therefore, to follow reactions on ice surfaces such as the ionization of electrolytes and acid–base reactions, which are described below.

7.2. Surface Composition and Structure

Impurities in ice become concentrated in the quasi-liquid layers in the surface and at grain boundary regions due to the “freeze concentration effect”, and this has important consequences for atmospheric reactions on ice surfaces.⁴⁷⁰ However, there appear to be numerous exceptions to this general trend, where the surface segregation behavior of the dissolving species and their bulk solubility are determined by thermodynamic factors specific to individual chemical species. A good example is the formation of stable bulk phases of clathrate hydrates.⁴⁷¹ Chemical specificity in the segregation phenomena can be studied by monitoring the surface populations of the dissolving species during the slow annealing of ice samples. Kang and co-workers^{472–474} examined these propensities in Na^+ and halide ions at the surface and in the interior of ice films. They ionized NaF, NaCl, and NaBr molecules on ice films by the vapor deposition of the salts, and the variation in the surface population of the ions was monitored as a function of the ice temperature for 100–140 K by using LES. As shown in Figure 29, the LES intensities of Na^+ and F^- ions decrease with an increase in temperature above ~ 120 K, whereas the Cl^- and Br^- intensities remain unchanged.^{473,474} The results indicate that Na^+ and F^- ions migrate from the ice surface to the interior at the elevated temperatures. The migration process is driven

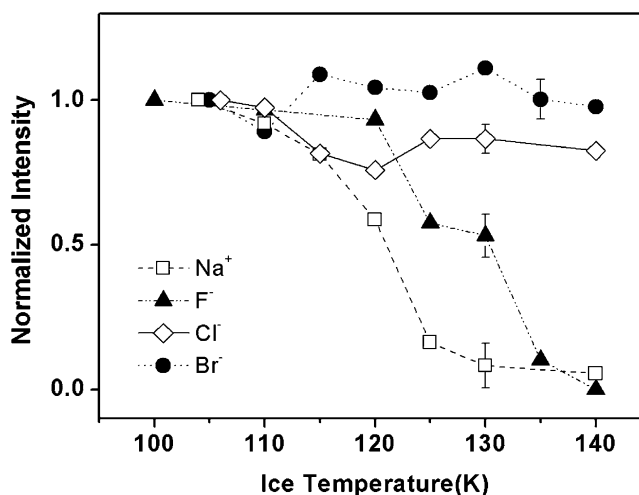


Figure 29. Surface populations of Na^+ (\square), F^- (\blacktriangle), Cl^- (\diamond), and Br^- (\bullet) ions as a function of the ice film temperature measured from LES intensities of the ions. NaF, NaCl, and NaBr were deposited for a coverage of 0.8 ML for each salt on a D_2O ice film grown at 130 K. The LES signals were measured at the indicated temperatures of salt adsorption. The LES intensities are shown on the normalized scale with the intensity at 100–105 K as a reference. The Cs^+ beam energy was 35 eV. The figure is drawn on the basis of the data in refs 473 and 474.

by the ion solvation energy, and it requires that surface water molecules have enough mobility to facilitate ion passage at temperatures above 120 K. It is worth noting that such a segregation behavior for ice agrees with the negative adsorption energy of these ions at water surfaces predicted by the Gibbs surface tension equation and MD simulations.⁴⁷⁵

An interesting property of hydronium ions observed in recent studies is that they preferentially reside at the surface of ice rather than in its interior. Evidence of this property has come from a variety of experimental observations over the past decade.^{445,476–482} The adsorption and ionization of HCl on an ice film promotes H/D exchange on the surface.⁴⁷⁶ However, vertical proton transfer to the film interior is inefficient. Continuous exposure of HCl gas on the ice film led to saturation in the hydronium ion population at the surface, and the amount of HCl uptake required for this saturation was independent of the thickness of the ice film.⁴⁷⁷ These observations suggest that protons stay at the ice surface and hardly migrate to the interior. This behavior can be attributed either to the active trapping of protons at the surface or to the lack of proton mobility to the ice interior.^{478,479}

The observation of asymmetric transport of protons at an ice surface and in its interior led to the conclusion that protons have a thermodynamic propensity to reside at the ice surface.^{478,479} The surface preference of the proton allows reinterpretation of the results for the H_3O^+ SL experiment conducted by Cowin et al.,⁴⁴⁵ who showed that H_3O^+ ions deposited onto an ice film surface remained on the surface over a wide range of temperatures (section 6.9). This observation was initially interpreted to indicate the immobility of protons through the ice films.⁴⁴⁵ However, the thermodynamic affinity of a proton for the ice surface and the proton's known mobility in the interior suggest an alternative explanation of the observation consistent with the well-known proton transport mechanism in ice and the observations of related experiments.^{471,476–479,481} More recently, the ice systems used in the H_3O^+ SL experiment were re-examined by careful control experiments,^{482,483} confirming the asymmetric transport behavior of protons.

The properties of hydroxide ions were also studied. Hydrolysis of Na atoms on an ice surface produced Na^+ and hydroxide ions at the surface.⁴⁸⁴ The LES intensity of hydroxide ions increased as the temperature was raised from 95 to 135 K. The result showed that hydroxide ions have a tendency to float on the ice surface, similar to hydronium ions. The LES intensity of Na^+ ions shows that these ions migrated to the ice interior, in agreement with the observation of the ion segregation experiments with sodium halide salts mentioned above.^{473,474}

Studies of the dissolution behavior of alkali-metal ions at liquid water surfaces show that polarizable ions such as large halide anions (Br^- and I^-) have a propensity to reside at the surface, whereas F^- and Na^+ avoid surface residence.⁴⁷⁵ These trends agree nicely with the observations made for the ice systems.^{473,474} For the cases of hydronium and hydroxide ions, their interfacial distributions for liquid water are a controversial issue in current investigations of the subject. Various experimental methods (vibrational sum-frequency generation spectroscopy, ζ potentials, and gas bubbles) and theoretical calculations report different results regarding whether water surfaces are acidic or basic relative to the interior.^{481,485}

A chemical sputtering method with hyperthermal noble gas ions has been used to probe the structural changes of

condensed molecular solid surfaces.¹⁷⁵ It is known that carboxylic acids can exist either in a chainlike crystalline form or as dimers in the solid state, depending upon the preparation temperature.^{486–488} When acetic acid is vapor-deposited onto a metal surface at 110 K, it exists in a dimeric amorphous form, but on a thin ice film, it exists as a chainlike crystalline phase at the same temperature. These two forms of acetic acid were distinguished by detecting the selective emission of acetic acid molecular cation from the amorphous phase using 30 eV Ar^+ collisions.¹⁷⁵ The crystalline form did not produce the molecular cation in the sputtering spectra; instead the formation of the CH_3CO^+ fragment was the characteristic signature of this structure. Formic acid followed a behavior similar to that of acetic acid, but propionic acid suppressed the formation of the molecular cation in the CS spectra since it existed as dimers in its crystalline form also.

Hyperthermal projectiles do not closely approach the core of individual surface atoms, but are reflected at a larger distance from the surface so they feel the surface as a relatively flat structure.⁴⁶⁷ For this reason, hyperthermal ion scattering may not be an atomistic structural probe of a surface. However, it can be used to monitor changes in the ensemble-averaged structure of surfaces. Cyriac and Pradeep¹⁷⁶ observed that the scattering of ultra-low-energy (~ 1 eV) Ar^+ ions is sensitive to the surface morphology of ice films. The Ar^+ scattering intensity from an amorphous solid water film increased by a factor of 2 as the temperature increased from 110 to 125 K (Figure 30). Such a change was absent in the case of crystalline

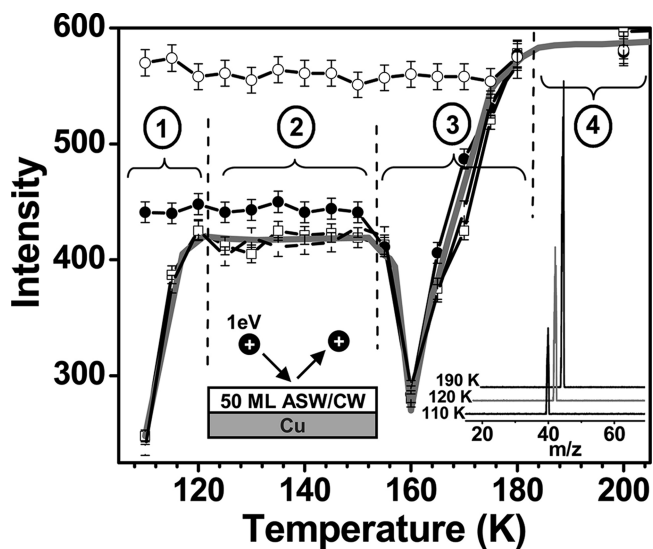


Figure 30. Scattering intensity variation of 1 eV Ar^+ collisions at bare copper (\circ), 50 ML of ASW(H_2O) (\square), 50 ML of ASW(D_2O) (\blacksquare), and 50 ML of crystalline ice (H_2O) (\bullet). The continuous gray line shows an approximate representation of the overall behavior of ASW. Inset: typical Ar^+ scattering mass spectra of 50 ML of ASW for three different temperatures and averaged for 50 scans. The collision energy was 1 eV. Reprinted from ref 176. Copyright 2008 American Chemical Society.

ice films and for other condensed molecular solids. The Ar^+ intensity dropped around ~ 160 K due to water desorption and then subsequently increased as the bare copper surface was exposed. These results suggest that an amorphous ice film undergoes a structural transformation at 110–125 K, which is below the onset temperature of the glass transition (136

K)^{489,490} and well below the appearance of quasi-liquid layers.⁴⁹¹ The observed structural change may involve the collapse of micropores in the top layers of the ice surface.

7.3. Transport Properties

Several unique reaction properties found at an ice surface compared to its liquid-phase counterpart are intimately related to the difference in molecular mobility in the two phases. Self-diffusion at ice surfaces has been studied by measuring the kinetics of the diffusional mixing of H₂O and D₂O molecules at the surface.⁴⁶² In this study, a thin H₂O ice film was prepared and then covered with a fractional layer of D₂O. The diffusion of water molecules in the top one to two molecular layers of the surface gradually changed the relative populations of H₂O and D₂O in the outermost layer and was monitored as a function of time by reactive scattering. The study indicated that the interlayer diffusion in the surface took several seconds at 140 K and about 1 h at 100 K. Temperature-dependent kinetic measurements yielded a self-diffusion activation energy (E_a^s) of 14 ± 2 kJ mol⁻¹. In comparison, the self-diffusion activation energy in bulk ice (E_a^{bulk}) was measured to be 71 ± 4 kJ mol⁻¹ in laser-induced thermal desorption experiments.⁴⁹² These studies show that surface diffusion occurs significantly faster than bulk diffusion in the temperature regime of 100–140 K, and the gap between the two diffusion rates widens exponentially as the temperature decreases due to the large difference in the activation energies.⁴⁰ This illustrates that, if reactions of ice occur at low temperatures, they will occur preferentially at the surface where molecules have a much higher mobility, rather than in the interior.

The diffusion of chloromethane molecules (CCl₄, CHCl₃, CH₂Cl₂, and CH₃Cl) through ice films has been studied by the CS method.¹⁷⁴ To show the sensitivity of CS, the CS spectra at two different temperatures (125 and 130 K) from a system prepared by depositing 50 ML of CHCl₃ followed by 250 ML of H₂O at 110 K are shown in Figure 31. The CHCl₃ concentration increases at the surface with increasing temperature. The study showed that, except for CCl₄, other

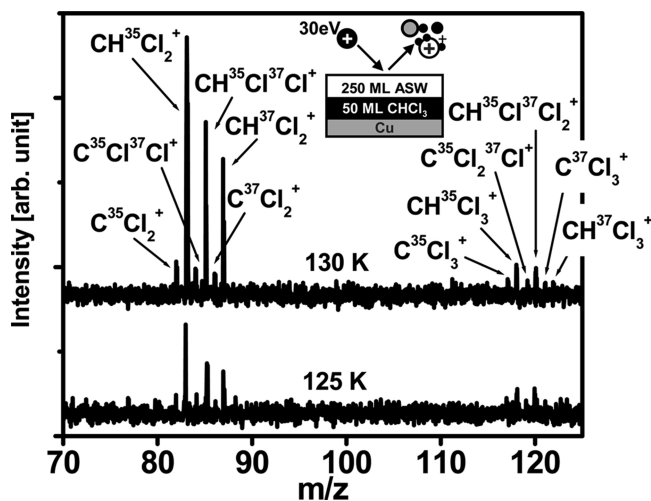


Figure 31. Intensities of the CHCl₂⁺ and CHCl₃⁺ peaks are increased due to the change in concentration of CHCl₃ on the surface with increasing temperature. The projectile ion is 30 eV Ar⁺, and the system is 50 ML of CHCl₃@250 ML of ASW. With the temperature rise from 125 K (lower trace) to 130 K (upper trace), more CHCl₃ diffuses through ice overlayers. Reprinted from ref 174. Copyright 2007 American Chemical Society.

chloromethanes investigated, viz., CHCl₃ and CH₂Cl₂, underwent diffusive mixing with amorphous solid water (ASW) in the temperature range of 100–150 K.¹⁷⁴ CCl₄ was not able to diffuse through more than four overlayers of ASW. The hydrogen bond network of the ASW film restricted the transport of CCl₄ molecules. Other molecular solids, D₂O and CH₃OH, also acted as barriers to diffusive mixing of CCl₄. The interaction energy between chloromethanes and water in the solid state was in the order CCl₄ < CHCl₃ < CH₂Cl₂ < CH₃Cl, which is the reverse order of the liquid-phase interactions.⁴⁹³ Considering that the overall interaction between chloromethanes and water is based on the atomic charge of chlorine and its molecular polarizability, replacement of a Cl atom by a H atom can have a significant effect on diffusivity in ice. Using Ar⁺ sputtering, it was found that 1-butanol undergoes diffusive mixing with water ice.⁴⁹⁴ Even after deposition of 1000 ML of ASW over solid 1-butanol, both species are observed on the surface. By contrast, water is not seen when 1-butanol is deposited over ASW. The results suggest that long-chain alcohols may act as barriers to H₂O diffusion because of their hydrophobic nature.

Proton mobility is a fundamental and important property in the physics and chemistry of ice. As discussed in section 7.2, there is a general consensus that a proton is mobile in ice at elevated temperatures.^{478,479,481} Also, a proton tends to reside at the surface of ice where it is stabilized.^{478–480,482} The hyperthermal energy ion probe offers a tool to pursue the proton transfer behavior by looking into the H/D isotopomers of water molecules and hydronium ions at ice surfaces generated by proton-induced H/D exchange reactions.^{478,479} Below 120 K, at which the rotational and diffusional motions of water molecules are frozen, a proton hopping relay (Grötthuss mechanism) is the only possible mechanism of proton transfer in ice. This is evidenced by the LES detection of H₃O⁺ at the surface of the H₂O/proton/D₂O film and also by the absence of D-substituted hydronium ions at the surface. Protons can move only across a limited distance by this mechanism, but nevertheless, this makes protons a unique mobile species in low-temperature ices, whereas water molecules and other foreign species are virtually frozen in position. Upon the activation of molecular rotations which occurs at temperatures above 125 K, the hop-and-turn process starts to occur involving the coupling of proton hopping and water molecule reorientation. All these proton transport processes can occur below the onset temperature (130 K) of water molecule diffusion near the ice surface, indicating that proton transfer can occur more easily than water self-diffusion.⁴⁷⁹

Proton transfer along the surface of ice was examined through the measurement of the H/D exchange kinetics of surface H₂O and D₂O molecules in the presence of excess protons generated from HCl ionization.^{476,495} Protons were transferred from hydronium ions mostly to the adjacent water molecules when the surface temperature was low (70 K), but the rate and propagation range of the proton transfer increased as the temperature increased above 90 K.⁴⁹⁶ This finding shows that the proton transfer process at an ice surface is thermally activated, and there exists an energy barrier of substantial magnitude (10 ± 3 kJ mol⁻¹) for the proton transfer.⁴⁹⁶ This is in agreement with the thermodynamic affinity of protons for ice surfaces, a conclusion derived from independent observations for the surface segregation of protons (section 7.2).^{478–480,482}

On a pure ice film surface in the absence of externally added protons, the H/D exchange reaction occurs slowly compared

to that observed on the proton-rich ice surface.⁴⁹⁵ The activation energy of the reaction was also higher (17 ± 4 kJ mol⁻¹) on the pure ice surface. This is because H/D exchange on this surface requires the formation of ion pairs (H_3O^+ and OH^-) which require thermal energy in addition to the occurrence of proton transfers.

Similar experiments performed with excess hydroxide ions on ice films⁴⁹⁷ showed that hydroxide ions, like hydronium ions, mediate proton transfer at an ice surface and promote the H/D exchange of water molecules. The Arrhenius activation energy of 9.4 ± 2.0 kJ mol⁻¹ was estimated for the proton transfer mediated by hydroxide ions, which is comparable in magnitude to the activation energy for the hydronium ion-mediated proton transfer. These studies indicate that proton transfer at an ice surface involves a substantial energy barrier, regardless of whether the process is mediated by hydronium ion or hydroxide ion.

7.4. Acid–Base Chemistry

Available spectroscopic tools to investigate acid–base chemistry at ice surfaces are few, for example, IR spectroscopy,^{498–500} metastable impact electron spectroscopy (MIES),⁵⁰¹ and the hyperthermal ion beam techniques described in this review. Acid–base reactions are important in ice surface chemistry because they are intimately related to two important properties of ice surfaces discussed in the previous sections: (i) thermodynamic affinity of protons and hydroxide ions for ice surfaces and (ii) unique mobility of protons in ice.

The simplest and most extensively studied example of an acid–base reaction on ice is the ionization of strong protic acids.⁴⁹⁸ Experiments performed using a hyperthermal energy Cs⁺ ion probe shows that HCl partially ionizes to hydronium and chloride ions on ice films at temperatures below 120 K and that undissociated HCl also exists.^{457,477} The presence of an undissociated HCl molecule on the surface was evident from the CsHCl⁺ signal, while hydronium ions (HD_2O^+ and D_3O^+) and hydrated clusters (HD_4O_2^+ and D_5O_2^+) represented the ionized form.⁴⁵⁷ The results indicate that, although HCl is a strong acid which ionizes completely in an aqueous solution, it acts as a weak acid on ice surfaces at low temperatures, and the degree of ionization varies with the temperature and morphology of the ice surface.

As a model case of acid–base reactions involving proton transfer on ice, Park et al.^{454,458,502} conducted detailed investigations of the reactions between the hydronium ion and amine molecules, including NH_3 . For example, the hydronium ion–ammonia system was prepared by doping a D_2O ice film with HCl followed by dosing with NH_3 gas. The ratio of proton donors to acceptor was changed by varying the NH_3 concentration. Reactive scattering spectra given in Figure 28 show the donor and acceptor species present on the surface at varying concentrations of NH_3 .⁴⁵⁴ The absence of NH_3 molecules on the surface indicates that proton transfer from hydronium ion to ammonia is complete. At a high coverage of NH_3 (spectrum b), however, the CsNH_3^+ signal shows that a substantial portion of NH_3 remains unconsumed despite the coexistence of D_3O^+ . In fact, all donor and acceptor species of the reaction (NH_3 , NH_3D^+ , D_2O , and D_3O^+) coexist even beyond the equivalence point of the titration. This shows that the acid–base reaction does not reach a true equilibrium on the ice surface due to incomplete proton transfer, in contrast with its complete occurrence in an aqueous solution at room temperature.

The extent of proton transfer was evaluated by measuring the reaction quotient (Q) of the reaction, defined by $Q = [\text{H}_2\text{O}][\text{BH}^+]/[\text{H}_3\text{O}^+][\text{B}]$, where B is an amine, as a function of amine exposure. As Figure 32 shows, the Q value on an ice

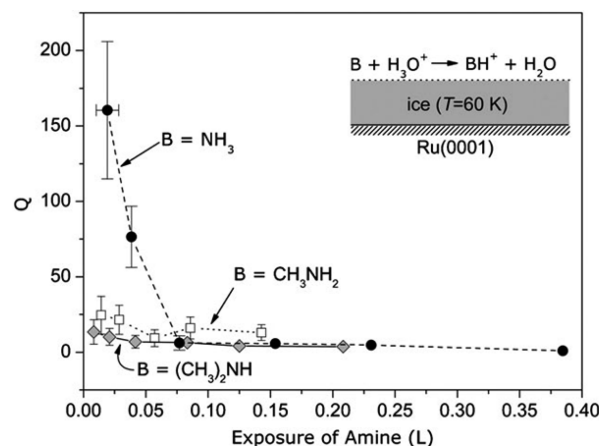


Figure 32. Reaction quotient (Q) for proton transfer from hydronium ion to NH_3 (●), CH_3NH_2 (□), and $(\text{CH}_3)_2\text{NH}$ (◆) measured as a function of amine exposure on an ice surface. The surface hydronium ions were produced by adding 0.3 L of HCl onto the ice film at 60 K and then warming it to 140 K. The donor and acceptor populations were measured from the corresponding LES and RIS signals. Reprinted with permission from ref 502. Copyright 2007 John Wiley and Sons, Inc.

surface is much smaller than the equilibrium constant of the same reaction in the gas phase or in an aqueous solution, and Q decreases with increasing amine exposure. The relative proton transfer efficiency by various amines deduced from these results follows the order $\text{NH}_3 > (\text{CH}_3)_2\text{NH} \approx \text{CH}_3\text{NH}_2$,⁵⁰² but this is opposite the trend in intrinsic basicity of amines or their basicity in aqueous solutions. Thermochemical analysis suggests that incomplete solvation of reactant and product species at the ice surface reduces the proton transfer efficiency and reverses the order of the proton-accepting abilities of amines.

The hydronium ions formed by UV irradiation of ice transfer protons to methylamine molecules adsorbed on the film surface to form methylammonium ions (CH_3NH_3^+), and the proton transfer occurs via a tunneling mechanism (hopping relay) at low temperature (50–130 K).⁴⁸³ The methylammonium ion was stable at the ice surface, in contrast with its spontaneous deprotonation to a neutral methylamine molecule in aqueous solution. Later, the study was extended to ammonium ion (NH_4^+), which was formed through UV photolysis of an NH_3 – H_2O ice mixture.⁵⁰³ The IR spectrum of NH_4^+ suggests the possibility that it is formed in interstellar ice particles and contributes to the $6.85 \mu\text{m}$ band discovered in the astronomical observations of dense molecular clouds using an infrared telescope.⁵⁰⁴

7.5. Chemical Reactions

Reactions between hydrogen halide and the alcohols ethanol and 2-methylpropan-2-ol are well-known to follow $\text{S}_{\text{N}}2$ and $\text{S}_{\text{N}}1$ pathways, respectively, in the liquid phase. The intermediate states of these reactions are protonated alcohols and carbocations, which exist only for transient times and rapidly convert to alkyl halides. However, these $\text{S}_{\text{N}}1$ and $\text{S}_{\text{N}}2$ intermediates are stabilized when the corresponding reactions occur on solid alcohol films at a low temperature.⁵⁰⁵

Specifically, HBr reacts with the ethanol surface, exclusively producing protonated ethanol species. The reaction between HBr and 2-methylpropan-2-ol resulted in protonated 2-methylpropan-2-ol and the *tert*-butyl cation in 20% and 78% yields, respectively. Importantly, alkyl bromides, which are the final products of the reactions in liquid solvents, were hardly detected on the molecular films. This indicates that the reactions on the frozen films are kinetically controlled, in contrast with the thermodynamically controlled reactions in the liquid phase. The kinetic barriers on the cold molecular surfaces stabilize the ionic intermediates (protonated alcohols and *tert*-butyl cation) and effectively block the completion of the S_N1 and S_N2 reaction pathways by impeding the diffusive encounter between the halide ion and the alcohol counterion.⁵⁰⁵

In an analogous study, the electrophilic addition reaction of ethene with HCl was investigated on frozen molecular films.⁴⁶⁶ The acid-catalyzed electrophilic addition reactions of alkenes are believed to occur through alkyl cation intermediates, but primary alkyl cations such as an ethyl cation have never been identified using spectroscopy, even for reactions in superacids.⁵⁰⁶ On a water ice film, the reaction of ethene with HCl initially produced the π complex of HCl and ethene at temperatures below about 93 K.⁴⁶⁶ LES was used to detect a $C_2H_5^+$ signal on the surface at temperatures of 80–100 K, which indicated the formation and kinetic stabilization of an ethyl cation-like species. This species dissociated into ethene and hydronium and chloride ions at high temperatures, but it did not complete the final step on the potential surface to produce ethyl chloride. The ethyl cation-like species was not formed in the reaction of ethene with hydronium ion or when the reaction of ethene with HCl occurred on a frozen ethene film, indicating that the ethyl cation-like species was formed via direct proton transfer from molecular HCl to ethene in water solvating environments. The study shows evidence that the reaction involves an intermediate species that has an ethyl-like structure with ionic character, but it remains uncertain whether this species is actually an ethyl cation or a structure intermediate between the HCl–ethene π complex and its ionized state.

Inorganic reactions studied on ice films to date include the hydrolysis of alkali-metal atoms^{484,507–509} and the reactions of simple oxide gases, viz., CO_2 ,⁴⁶³ NO_2 ,⁴⁶⁵ and SO_2 .⁵¹¹ Na^+ and OH^- ions, produced by hydrolysis of Na, were efficiently solvated by water molecules at all temperatures investigated, whereas the sodium hydroxide molecule was found to solvate only at high temperatures.⁴⁸⁴ The OH^- ions tend to reside at the film surface, whereas Na^+ ions migrate to the film interior. The adsorbed Na atoms completely reacted away without forming neutral Na clusters on the surface when the Na coverage was lower than 1 ML. These observations were complementary to the results of the TOF SIMS and metastable impact electron spectroscopy (MIES) studies of Na hydrolysis on ice films obtained under the conditions of lower temperature (15–100 K) and higher Na coverage (>1 ML) (section 8.6).^{507–509}

Reactions of acidic oxide gases at the surfaces of snow and ice particles are important to atmospheric chemistry and environmental sciences.⁵¹⁰ While CO_2 gas is unreactive to the ice films regardless of the presence or absence of excess hydroxide ions on the surfaces,⁴⁶³ SO_2 ⁵¹¹ and NO_2 ⁴⁶⁵ readily react with the ice surface to produce various chemical species even at low temperatures (80–150 K). Figure 33 shows spectra due to reactive scattering and LES from a D_2O ice film on which SO_2

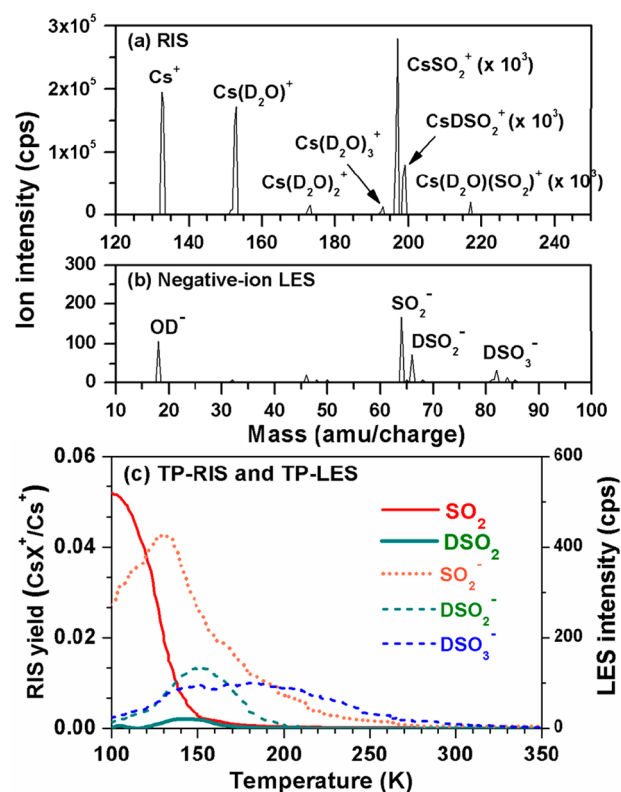


Figure 33. (a) RIS mass spectrum obtained from a D_2O ice film exposed to SO_2 gas. (b) LES spectrum of negative ions. The ice film (4 BL thickness) was exposed to 0.2 L of SO_2 at 80 K, and the RIS and LES measurements were made at 140 K. The RIS signals at masses above $m/z = 190$ amu/charge were magnified by the factors indicated. (c) Temperature-programmed RIS and LES measurements for the signals of interest detected on the surface exposed to SO_2 at 80 K. The RIS yield on the left ordinate is defined as the ratio of the RIS product to the Cs^+ signal intensity (CsX^+/Cs^+). The temperature ramping rate was 1 K s^{-1} . Data were taken from Figures 1 and 2 of ref 511. Copyright 2009 American Chemical Society.

is absorbed at 140 K. Spectrum a shows that SO_2 adsorption produces signals of $CsSO_2^+$ (m/z 197), $CsDSO_2^+$ (m/z 199), and $Cs(D_2O)(SO_2)^+$ (m/z 217) in reactive scattering experiments. The $CsSO_2^+$ and $Cs(D_2O)(SO_2)^+$ signals indicate the presence of molecular SO_2 adsorbates. Spectrum b shows the negative ion LES signals from the surface, which include OD^- (m/z 18), SO_2^- (m/z 64), DSO_2^- (m/z 66), and DSO_3^- (m/z 82). The spectra show that SO_2 is transformed into various molecular anions by hydrolysis on the surface.

When the ice film with SO_2 adsorbates was warmed slowly from 80 to 150 K, the signals of various SO_2 -related species appeared and disappeared at different temperatures (see Figure 33c).⁵¹¹ The results indicate that physisorbed SO_2 species (detected as $CsSO_2^+$) sharply decrease during the temperature increase from 100 to 140 K. In the narrow temperature range of 130–150 K, DSO_2 (detected as $CsDSO_2^+$), DSO_2^- , and DSO_3^- intensities grow at the expense of the decreasing SO_2^- intensity, indicating the conversion of SO_2^- to these species. Combined hyperthermal energy ion collision and TPD experiments indicate that the reaction of SO_2 on deuterated ice produces three types of surface species: a solvated SO_2 species with a partial negative charge, a DSO_2 species, and an anionic DSO_3^- -like species.

Table 10. SIMS Data for Condensed Molecular Solids

primary ion (keV range)	system (15–200 K)	some sputtered species	aim/observations	refs
Au ⁺	water ice	(H ₂ O) _n H ⁺ , (H ₂ O) _n ⁺ , (H ₂ O) _{n-1} OH ⁺	intensity of (H ₂ O) _n ⁺ > (H ₂ O) _n H ⁺ ~ (H ₂ O) _{n-1} OH ⁺	517
Au ₃ ⁺	water ice	(H ₂ O) _n H ⁺ , (H ₂ O) _n ⁺ , (H ₂ O) _{n-1} OH ⁺	intensity of (H ₂ O) _n H ⁺ > (H ₂ O) _n ⁺ , when <i>n</i> < 20	517
Au ₃ ⁺ , C ₆₀ ⁺	water ice	(H ₂ O) _n H ⁺ , (H ₂ O) _n ⁺ , (H ₂ O) _{n-1} OH ⁺	10 ⁴ increase in yield compared to that of Au ⁺	517
Au ₃ ⁺ , C ₆₀ ⁺	water ice	(H ₂ O) _n OH ⁻	less than 10 times compared to that of positive ions	517
Au ₃ ⁺ , C ₆₀ ⁺	water ice		depth profiling	591–593
C ₆₀ ⁺	water ice	(H ₂ O) _n H ⁺ , (H ₂ O) _n ⁺	intensity of (H ₂ O) _n H ⁺ > (H ₂ O) _n ⁺ , when <i>n</i> < 20	517
C ₆₀ ⁺	trehalose film		molecular depth profiling	520, 587
	histamine–ice		molecular depth profiling	589, 590
	LB film		molecular depth profiling	611–614
Ar ⁺ /C ₆₀ ⁺ / Ga ⁺	MX–water (MX = LiCl, KI, NaI, NaCl, etc.)	((H ₂ O) _n M [±] (M = Li ⁺ , Na ⁺ , K ⁺ , Cs ⁺ or F ⁻ , Cl ⁻ , I ⁻))	cation water clusters > anion water clusters	563, 564
He ⁺ /Ar ⁺	CF ₄ @Pt(111)	CF _x ⁺ (<i>x</i> = 0–3), F ⁺		615
He ⁺	water ice	H ⁺ , H ₃ O ⁺ , Ni(H ₂ O) ⁺	existence of quasi-liquid form and dewetting at 160 K	530, 534
	CF ₄ –D ₂ O	efficient production of (D ₂ O)D ⁺ ions	2 orders of magnitude higher than that of a pure D ₂ O film	568
	methanol–D ₂ O	(CH ₃ OH)H ⁺ , (CH ₃ OH)D ⁺ , (CH ₃ OD)D ⁺	complete intermixing above 136 K, hydrophilic hydration above 120 K, H/D exchange above 140 K, determined T _g of methanol	515, 530, 558, 565
	ethanol–D ₂ O	(C ₂ H ₅ OH)H ⁺ , (C ₂ H ₅ OH)D ⁺ , (C ₂ H ₅ OD)D ⁺ , CH ₂ OH ⁺	complete intermixing above 140 K	566
	acetic acid–D ₂ O	(CH ₃ COOH)H ⁺ , (CH ₃ COOH)D ⁺ , (CH ₃ COOD)D ⁺ , CH ₃ CO ⁺	complete intermixing above 130 K, determined T _g of acetic acid	487
	methylamine–D ₂ O	(CH ₃ NH ₂)H ⁺ , (CH ₃ NH ₂)D ⁺ , CH ₂ ND ₂ ⁺	complete intermixing above 140 K	567
	methane–D ₂ O	CH ₅ ⁺ , C ₂ H ₃ ⁺ , other common ions	complete intermixing at 15 K	568
	CO–D ₂ O	D ⁺ , D ₃ O ⁺ , C ⁺ , O ⁺ , CO ⁺ , C ₃ O ₂ ⁺	complete intermixing at 15 K	616
	CO ₂ –D ₂ O	D ⁺ , D ₃ O ⁺ , C ⁺ , O ⁺ , CO ⁺ , CO ₂ ⁺	no complete intermixing at 15 K, determined T _g of CO ₂ of 50 K	573, 616
	CD ₃ OD–methylamine	(CH ₃ NH ₂)H ⁺ , CH ₂ ND ₂ ⁺ , (CH ₃ NH ₂)D ⁺	complete intermixing above 125 K	567
	HCOOH–D ₂ O ice	(D ₂ O)H ⁺ , (D ₂ O)D ⁺ , (HCOOH)H ⁺	HCOOH stays mainly on the surface due to hydrophilic hydration, determined T _g of HCOOH	516, 572, 581
	C ₃ H ₇ OH–D ₂ O ice	C ₂ H ₃ ⁺ , (D ₂ O)D ⁺ , etc.	hydrophilic hydration at 100–145 K, hydrophobic hydration at > 145 K	516
	C ₆ H ₁₄ /C ₆ F ₁₄ –D ₂ O ice	CH ₃ ⁺ , C ₂ H ₃ ⁺ , CF ⁺ , CF ₃ ⁺ , etc.	dissolve into the bulk due to hydrophobic hydration	516
	C ₈ H ₁₈ –water ice	C ₂ H ₃ ⁺ , (D ₂ O)D ⁺ , etc.	hydrophobic hydration, incorporate into the bulk at <120 K	557
	C ₈ H ₁₈ –CH ₃ OH	C ₂ H ₃ ⁺ , (CD ₃ OD)D ⁺ , etc.	stays on the surface until 135 K	557
	pyridine–D ₂ O	(C ₅ H ₅ N)H ⁺ , (C ₅ H ₅ N)D ⁺ , C ₄ H ₄ N ⁺ , C ₃ H ₃ N ⁺ , etc.	D ₂ O dissolves in pyridine film above 110 K, pyridine stays on D ₂ O film until 180 K	559
	benzene–D ₂ O	C ₃ H ₃ ⁺ , C ₄ H ₄ ⁺ , C ₆ H ₆ ⁺ , etc.	benzene dissolves in D ₂ O film above 120 K by hydrophobic hydration, benzene stays on D ₂ O film	559
	butane–methanol	C ₂ H ₃ ⁺ , CD ₃ ⁺ , etc.	butane is incorporated into methanol below 70 K	535
	NH ₃ –HCl@water ice	NH ₄ ⁺ , Cl ⁻ , OH ⁻ , etc.	hydration of NH ₄ Cl above 100 K	560
	HCl–NH ₃ @water ice	NH ₄ ⁺ , Cl ⁻ , OH ⁻ , etc.	hydration of NH ₄ Cl and HCl above 40 K	561
	NH ₃ –HCOOH–water	HCO ⁺ , other common ions	produce NH ₄ HCO ₂ as reaction product, H/D exchange reaction above 140 K	581
	LiX–water (X = Cl, Br, I)	Li ⁺ , X ⁻	solubility increases at 160 K, evidence of deeply supercooled water	509, 538, 539, 541
	NaCl–water	Na ⁺ , Cl ⁻	Na ⁺ ion hydrated preferentially at low temperatures	542
	LiI–ethanol	(C ₂ H ₅ OH)Li ⁺ , (Li)Li ⁺ , etc.	LiI incorporated into the bulk	546
	CCl ₂ F ₂	CClF ₂ ⁺ , CCl ₂ F ⁺ , CF ⁺ , F ⁺	crystallization and dewetting at 57 K	617
	<i>n</i> -hexane	C _{<i>m</i>} H _{<i>n</i>} ⁺ (<i>m</i> = 1–6)	glass transition at 110 K, dewetting at 130 K	537
	ethylbenzene		intermixing at ~80 K, glass transition at ~118 K	618
	water, ethanol, etc. on p-Si (100)		onset of self-diffusion temperature	552–554
	Xe–water ice		Xe hydrated in the bulk of water up to 165 K	540
	D ₂ O–hexane	C ₂ H ₃ ⁺	dewetting at 165 K due to glass–liquid transition	532
	D ₂ O–dipalmitoyl- <i>sn</i> -glycero-3-phosphocholine	C ₂ H ₃ ⁺ , NCH ₃ ⁺ , etc.	hydrophobic water adsorption starts at 133 K	574, 575
	D ₂ O–bis[trifluoromethanesulfonyl]imide ([emim][Tf ₂ N])	[emim] ⁺ , C ₂ H ₅ ⁺ , CF ₃ ⁺ , [Tf ₂ N] ⁻ , F ⁻ , etc.	phase transition in water ice identified	576
	[emim][Tf ₂ N]	[emim] ⁺ , C ₂ H ₅ ⁺	crystallization at 200–220 K	536

Table 10. continued

primary ion (keV range)	system (15–200 K)	some sputtered species	aim/observations	refs
	D ₂ O–CH ₃ NH ₂	(CH ₃ NH ₂) H ⁺ , CH ₂ ND ₂ ⁺ , (CH ₃ NH ₂)D ⁺	H/D exchange reaction above 140 K	567
	CD ₃ OD–CH ₃ NH ₂	(CH ₃ NH ₂)H ⁺ , CH ₂ ND ₂ ⁺ , (CH ₃ NH ₂) D ⁺	H/D exchange reaction above 125 K	567
Ar ⁺	Cl ₂ /Cl ₂ O/ClONO ₂ –water ice	Cl _{1–5} ⁺ , Cl _{1–5} ⁺ , HOCl ⁺ , NO ⁺ , H ₂ NO ₃ ⁺ , water clusters, etc.	above 120 K, Cl ₂ undergoes reaction with ice surface to form HOCl, water, and HCl	569, 570, 583
	ClONO ₂ –HCl–water ice	Cl _{1–3} ⁺ , H ₂ OCl ⁺ , NO ₂ ⁺ , NO ₃ ⁺	formation of nitric acid at the surface	570
	Co-depositing SO ₃ –H ₂ O	(H ₂ SO ₄)H ⁺ , (H ₂ SO ₄)H ₂ O ⁺ , (H ₂ SO ₄)(H ₂ O) _{1–3} H ⁺	formation of sulfuric acid monohydrate and tetrahydrate	582

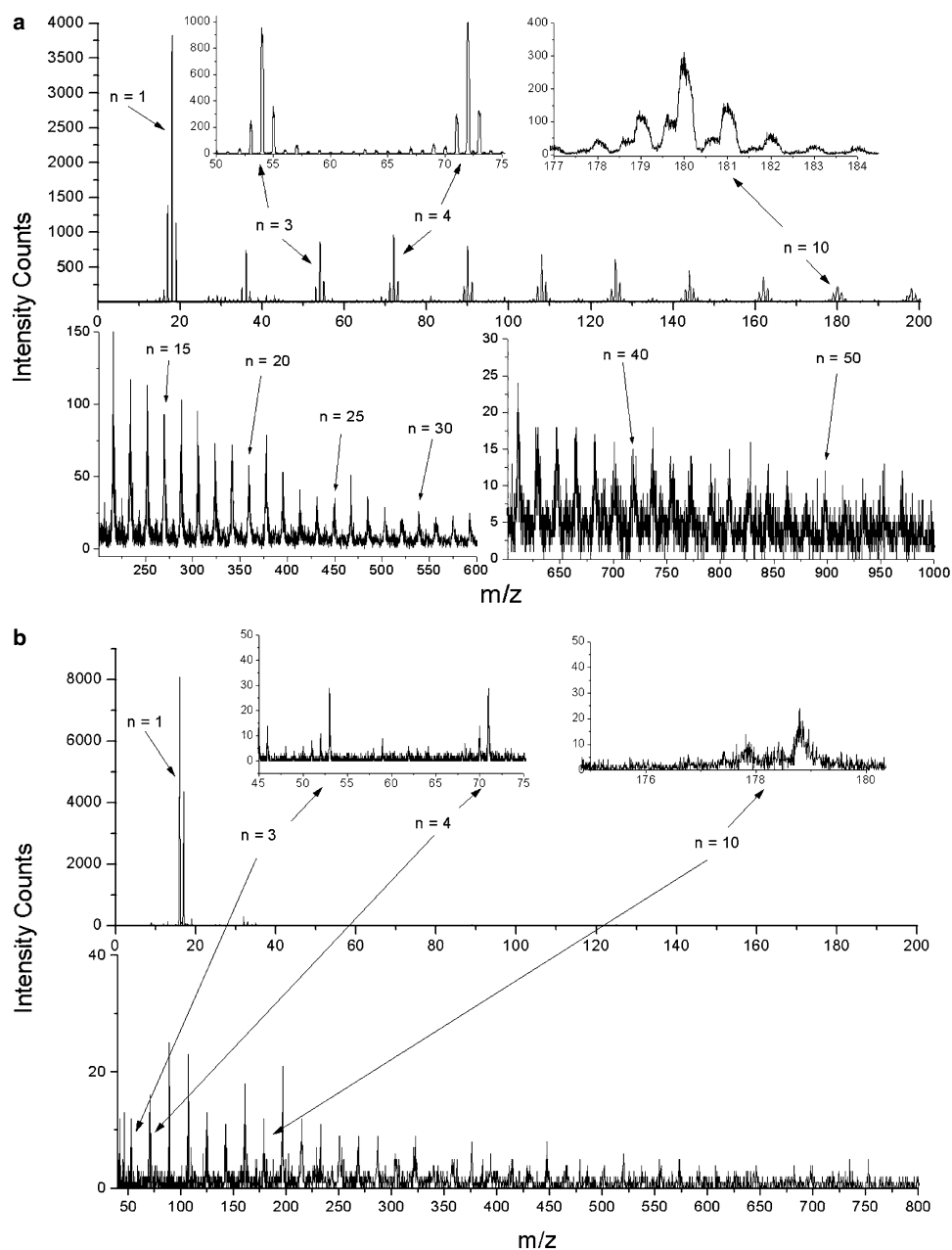


Figure 34. Positive ion SIMS spectrum of water ice using Au⁺ primary ions. Three series of cluster ions, (H₂O)_n⁺, (H₂O)_nH⁺, and (H₂O)_{n–1}OH⁺, were observed; the first one is the most intense. Reprinted from ref 517. Copyright 2010 American Chemical Society.

The study of hydrolysis of NO₂ on ice films shows that NO₂ adsorbs molecularly on the ice surface at 90 K.⁴⁶⁵ Upon heating the surface to 140 K, NO₂ adsorbates are readily converted into nitrous acid (HONO) on the surface. The implication of this

observation for the atmospheric chemistry of NO₂ is that nitrous acid gas will be formed by the heterogeneous hydrolysis of NO₂ on condensed ice surfaces even during the night

without the absorption of sunlight, which is in accordance with field observations.

The examples shown above demonstrate that ice surfaces can be used to take a “frozen snapshot” of a reaction and to capture the reaction intermediates. Characterization of reaction intermediates trapped on the ice surface using ion scattering and sputtering methods reveals important clues for the reaction mechanism. Such investigations may also be useful for understanding the corresponding reactions at gas/liquid interfaces.

8. SIMS ANALYSIS OF CONDENSED MOLECULAR SOLIDS

Although organic SIMS was an active area of research in the 1980s, the literature available on SIMS or fast atom bombardment (FAB) analysis of frozen molecular materials is mainly due to Michl and co-workers.^{512–514} More recently, SIMS has become a valued tool in low-temperature studies (see Table 10). Sputtered species and their yields from condensed-phase molecular solids provide molecular information as well as the composition for a specific chemical environment. These aspects are important in fundamental understanding related to upper atmospheric chemistry. Inclusion of temperature-programming capabilities in TOF SIMS, viz., temperature-programmed (TP) TOF SIMS, is a remarkable development in the analysis of condensed molecular solids.^{515,516} It provides unique information on compositional changes/reactions with respect to temperature. A notable number of such investigations have been carried out by Souda and co-workers.

The use of cluster ion SIMS provides higher ion yields without significant chemical damage of condensed molecular solids. In some cases, yields were 10^4 times higher compared to that of an atomic ion source.^{517,518} For example, Au_3^+ or C_{60}^+ is better than Au^+ primary ions for generating protonated clusters.⁵¹⁹ The yield was equivalent to ~ 1830 molecules per C_{60}^+ collision at 15 keV, while these numbers were ~ 1200 and 94 for Au_3^+ ion and atomic Au^+ ion projectiles, respectively. It is suggested that the C_{60}^+ sputter yield is about 3000 amu/keV for organic or ice films and 800 amu/keV for metallic targets.⁵²⁰

Protonated water clusters, $(\text{H}_2\text{O})_n\text{H}^+$, and normal water cluster ions, $(\text{H}_2\text{O})_n^+$ (n up to several tens), are abundant in the sputtering spectra of pure water ice films. See Figure 34 for the positive ion spectrum of an untreated water ice film at ~ 100 K by 15 keV Au^+ bombardment. Clusters with up to $n = 50$ have been observed.⁵¹⁷ The protonated form of the water clusters is formed predominantly with cluster ion sources C_{60}^+ and Au_3^+ when the value of n is lower than 20.^{517,519} The increased density of surface protons leads to high yields of protonated species. The case is reversed, i.e., water cluster radical ions are abundant compared to the protonated form, when n is larger. Some long-range damage to the crystal structure as a result of sputtering explains the low abundance of protonated water clusters.⁵¹⁷ Negatively charged water clusters, $(\text{H}_2\text{O})_n\text{OH}^-$, were also observed by both atomic and cluster primary ions,⁵¹⁷ but the yield is far smaller (~ 10 times) compared to that of its positive counterpart. Dosing HCl onto an ice film doubles the yield of protonated water clusters.⁵²¹ It was found that the yield of protonated water clusters is reduced significantly in the presence of adenine and alanine.⁵¹⁹ This suggests a suppression effect, with the biomolecules taking up some of the available protons that form $(\text{H}_2\text{O})\text{H}^+$ in the pure water ice.⁵¹⁸ In the case of solid methane, cluster ions C_nH_x^+ up to $n = 20$ are desorbed by low-energy He^+ ion bombardment.⁵²²

MD simulation and experimental results on the nature of the neutrals ejected; solid C_6H_6 surfaces using atomic projectiles Ar^+ and H_2^+ suggest that more than one mechanism operates.^{523–525} At submonolayer coverages of benzene molecules deposited on $\text{Ag}\{111\}$ surfaces, the kinetic energy of the ejected neutrals usually ranges from 0.25 to 1.00 eV, and these are ejected as a consequence of collisions with substrate particles.⁵²³ For multilayer coverage, the energy of the neutrals shows more of a thermal nature. A peak corresponding to extremely low kinetic energy (0.04 eV) becomes dominant. The thermal emission may be due to exothermic chemical reaction of fragments formed in a molecular collision cascade of C_6H_6 molecules. Another aspect to be considered in SIMS analysis of condensed molecular solids is the surface charge. These materials may behave similarly to insulator surfaces and charge up, but there is limited support for this so far. It is shown that the charge pattern generated using a primary ion source on frozen ($T < 188$ K) ionic liquid $[\text{emim}][\text{EtSO}_4]$ was stable and could be viewed in a negative ion map of the surface.⁵²⁶

8.1. Phase Changes

It is believed that a glass transition (T_g) of ice occurs at 136 K,⁴⁹⁰ but there are several who claim the T_g value of water be assigned as 165 K on the basis of an unusually small endotherm in the heat capacity in comparison to the T_g scaled heat capacity between water and other inorganic glasses.^{527,528} The glass transition and crystallization of ASW films can be explored on the basis of molecular diffusion, the change in film morphology, and hydration/dehydration via interactions with another molecule. All of these characteristics are accessible by TP TOF SIMS measurements. The intermixing of isotopically labeled water molecules (H_2^{16}O and H_2^{18}O) occurs at ~ 136 K, which is followed by a film morphology change at 160–165 K. These phenomena are ascribable to liquid properties.⁵²⁹ Note that these transition temperatures correspond to the conventional and reassigned T_g values of water. The methanol–water ice system has been used to probe changes occurring in the water ice film. The surface segregation of embedded methanol appears in secondary ions at the conventional T_g of 136 K.⁵³⁰ Ion intensities from the binary films prepared by deposition of 25 ML of H_2O on 25 ML of CD_3OD at 15 K are given in Figure 35a. From the figure it is clear that the H_3O^+ ion intensity dropped at 136 K whereas sputtered CD_3^+ ions from methanol increased. The penetration of methanol through water overlayers can be connected to the emergence of a liquidlike phase. The observation of $(\text{CH}_3\text{OD})\text{D}^+$ from CH_3OH (1 ML)/ D_2O (50 ML) at 136 K suggests that the transition occurred along with isotope (H/D) exchange.⁵³¹ H/D exchange was induced above the glass transition (136 K) due to the translational diffusion of water molecules. Another system used to explore the phase changes in solid water was hexane–water ice.⁵³² In contrast to methanol, n -hexane incorporated in the bulk of an amorphous water film is immobilized at the conventional T_g (136 K) despite the occurrence of translational diffusion of water molecules. The molecules are released immediately before the film morphology change at 160 K. Changes in the structure of hydrogen-bonded cages of water are thought to be responsible for this behavior. At the conventional T_g translational diffusion of water occurs without the cage structure being changed.

Similarly, the T_g of methanol has been studied using CD_3OD and water.⁵³⁰ The transition at 80 K was due to molecular

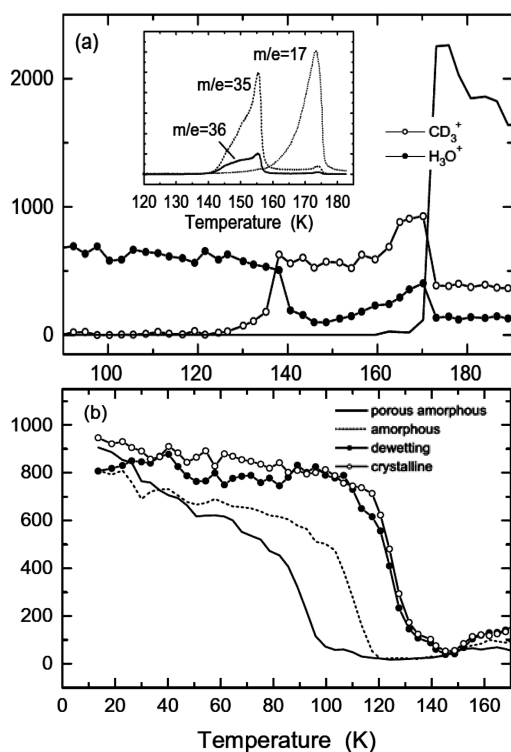


Figure 35. (a) Temperature-programmed TOF SIMS intensities of CD_3^+ ions sputtered from the film of 25 ML of H_2O grown on top of 25 ML of CD_3OD . The inset shows the TPD spectra of CD_3OD , CD_3OH , and OH from H_2O from the same film. The intensities of H_3O^+ ions sputtered from the 1 ML of H_2O molecules adsorbed on the 50 ML CD_3OD film are given in (b). The intensities are compared for the films prepared at 15 K (porous-amorphous film), heated at 120 K (amorphous film), heated at 120 K (dewetting film), and heated at 120 K for 30 min (crystalline film). This figure is reprinted with permission from Figures 2 and 3 of ref 530. Copyright 2004 American Physical Society.

diffusion, and it could be assigned to the onset of a glass transition of the vapor-deposited methanol film. The deviation from the calorimetric T_g value of 103 K reflects the difference in structure or density between the vapor-deposited and liquid-quenched glasses. Figure 35b shows the evolution of the H_3O^+ ion peak from a system prepared by depositing 1 ML of H_2O on a 50 ML CD_3OD film. Various films—porous-amorphous, amorphous, dewetting, and crystalline—were compared by monitoring the sputtered hydronium ion intensity. It is clear that the water molecule disappears from the porous amorphous methanol film below 100 K while it survives the amorphous film until 115 K. It can be inferred that long-range translational diffusion of methanol occurred at these temperatures.

In addition to water, there are many molecular solids which exhibit no apparent glass transition in calorimetric studies. Typical examples are *n*-alkanes. However, TP TOF SIMS analysis of *n*-pentane films revealed the occurrence of translational diffusion prior to crystallization at 80 K.⁵³³ Therefore, a liquidlike phase is expected to be created immediately before crystallization. Interestingly, the *n*-pentane films form droplets after crystallization, the dewetting temperature depending on the initial film thickness. This phenomenon is explainable as premelting of crystallites. In the case of *n*-butane, crystallization occurs around 60 K, but a liquidlike phase is observed at temperatures higher than 80 K along with the solid–solid phase transition.⁵³³ Liquid–crystallite coex-

istence occurred for water⁵³⁴ and methanol⁵³⁵ as well. The former is attributed to quasi-liquid formed during the phase transition of crystalline ice ($I_c \rightarrow I_h$). The uptake of water molecules deposited on a crystalline methanol film at 120 K (see Figure 35b) might also be an indication of liquid–crystallite coexistence. Crystallization of the room temperature ionic liquid 1-ethyl-3-methylimidazolium bis-[trifluoromethanesulfonyl]imide ($[\text{emim}][\text{Tf}_2\text{N}]$) occurs in the temperature range of 200–220 K as evidenced from the increased yield of the sputtered $[\text{emim}]^+$ ion.⁵³⁶

A metastable extension of normal liquid water is termed “deeply supercooled water”, but its presence is still under debate.^{527,528,537,543} The uptake of electrolytes into the bulk of glassy or crystalline water films is expected to be suppressed, and hence, one can explore the formation of deeply supercooled water from the interaction between the thin films of ASW and alkali-metal halides (e.g., LiCl , LiBr , NaCl , etc.).^{509,538–542} A metastable extension of normal liquid water with molecules having long-range translational diffusion exists above the T_g (136 K) and before crystallization.⁵⁴³ The formation of the alkali-metal halide solution could be attributed to the presence of supercooled liquid water. Using the TP TOF SIMS analysis, it was found that such a supercooled solution exists around 160–165 K.^{538–542}

In the case of glassy water, the presence of two distinct phases is confirmed experimentally, which is known as polyamorphism.⁵⁴⁴ Therefore, it is likely that ASW transforms to a low-density liquid (LDL) phase above its T_g (136 K), followed by another liquid phase, high-density liquid (HDL) or supercooled liquid, immediately before crystallization. LDL is considered to be an “ultraviscous liquid” as reflected by the poor solubility of the electrolyte. The liquid–liquid transition (LDL \rightarrow HDL) occurred at ~ 160 K as manifested by a drastic change in the solubility of the electrolyte (see Figure 36).^{538,540,541} This phenomenon can also be explained in terms of the strong-to-fragile liquid transition.^{534,545} Strong liquid (LDL) might be formed as a precursor state of the glass–liquid transition; fragile liquid (supercooled liquid water) is expected to be formed just before crystallization. The conventional T_g of water (136 K) corresponds to the strong liquid, resulting in the unusually small endotherm.⁴⁹⁰ Accurate measurement of the T_g of water (formation of supercooled liquid) can be hindered in calorimetric studies because of the huge crystallization exotherm. Very little is known about the nature of the quasi-liquid coexisting with crystallites. It might be distinct from both LDL and supercooled liquid as inferred from its strong structural correlation to crystals.⁵³⁴

Analysis of interactions of LiI and ethanol films showed the existence of at least two liquids, as in the case of water, in the deeply supercooled region.⁵⁴⁶ The viscous one was formed around T_g (97 K), where the adsorbed LiI is incorporated into the ethanol bulk. The formation of a supercooled ethanol solution occurred at 130 K. For pure ethanol, a liquidlike phase (quasi-liquid) is likely to coexist with crystallites until film evaporation, which is reflected in the continuous changes in the film morphology. The successive formation of viscous and fluidized liquid has also been observed for vapor-deposited toluene.⁵⁴⁵ These changes are inferred from the occurrence of molecular self-diffusion and dewetting, respectively, at 105 and 117 K. The presence of two liquids (strong and fragile liquids)⁵⁴⁵ explains decoupling between diffusivity and fluidity in the deeply supercooled region.⁵⁴⁷

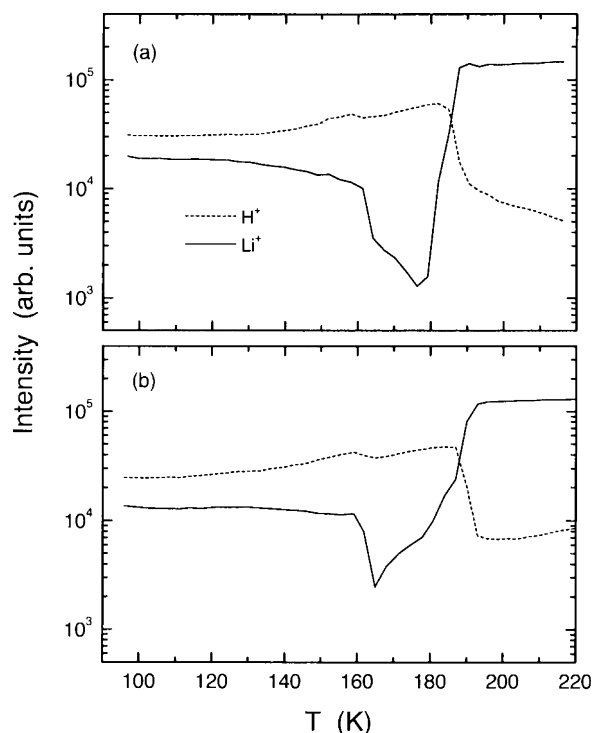


Figure 36. Intensities of the Li^+ ions sputtered from 1 ML of (a) LiCl and (b) LiI that are deposited on a 200 ML ASW film, together with those of the proton from the H_2O molecules, as a function of temperature. The Li^+ intensities are unchanged at 135 K, but they are decreased abruptly at around 160 K because of diffusion of the LiCl and LiI species into the bulk. Reprinted with permission from ref 539. Copyright 2007 American Institute of Physics.

It is expected that the T_g of thin films will be reduced relative to the bulk T_g value because of the nanoconfinement effect,^{548,549} resembling the reduction of the melting point for nanoconfined crystallites.⁵⁵⁰ The influence of substrates and the free surface on the T_g of thin ASW films has been investigated. Self-diffusion and film morphology changes of water monolayers were observed at 120 K when water was deposited on hydrophobic substrates such as quenched ionic liquid and graphite.¹⁴⁹ This phenomenon was induced by surface diffusion of water molecules and instability of the interface structure. The hydrophobicity of graphite influences the dewetting behavior of water films up to 20 ML,⁵⁵¹ but no indications of the nanoconfinement effects are recognized when the molecules are deposited on a Ni(111) substrate because an immobilized layer (a “dead layer”) is formed at the interface.

The surface mobility of condensed molecular solids has been investigated using a porous Si substrate.^{552–554} It is found that self-diffusion of water, ethanol, and 3-methylpentane in the topmost layer of thin films commences at temperatures of ca. 110, 85, and 50 K, respectively, which are considerably lower than the corresponding T_g values in the bulk.⁵⁵³ This phenomenon can be explained as the formation of 2D liquids on the free surface. Therefore, the nanoconfinement effect on reduction of the thin films’ T_g originates from the interplay between surface and volume diffusions having apparently different onset temperatures, but it can be quenched by the formation of a dead layer at the interface. The surface mobility of water appears to be unaffected by hydrogen bonds with substrates,⁵⁵³ suggesting that molecules move cooperatively via the formation of intermolecular hydrogen bonds, but the

molecules incorporated in pores might be entrapped individually at higher coordination sites by hydrogen bonds.⁵⁵⁴ For the monolayer of methanol and ethanol, the molecules tend to hop independently on the surface without formation of the 2D liquid because hydrogen bonds with the substrate prevail over intermolecular interactions.^{553,554}

8.2. Solvation (Hydration)

The ASW films deposited at temperatures below 120 K have a low density, characterized by a porous structure.^{176,555,556} It is found that polar molecules such as HCOOH and $\text{C}_3\text{H}_7\text{OH}$ stay on the surface of ASW, while nonpolar ones such as C_6H_{14} , C_6F_{14} , and C_8H_{18} are preferentially incorporated into the bulk.^{516,532,557} The difference between hydrophilic and hydrophobic hydration is the reason for this behavior. Polar molecules form hydrogen bonds with water and hence stay on the surface by facing the hydrophobic end group toward the primary ions. This situation was reflected in the reduced intensities of protons sputtered from the dangling hydroxyl bond. In the case of methanol, hydrophilic hydration occurred above 120 K followed by complete H/D exchange above 140 K.^{515,558} The nonpolar solutes were completely incorporated in the D_2O layer even below 100 K.⁵¹⁶ The molecules are entrapped at a higher coordination site and are confined in the bulk by pore collapse. The occurrence of the hydrophobic hydration in the bulk is inferred from a sharp TPD peak of confined molecules at 160–165 K along with the phase transition of water. In contrast, methanol embedded in the water film segregates to the surface around a conventional T_g of 136 K along with the self-diffusion of water.⁵³⁰ The adsorbed benzene molecules on the D_2O ice were incorporated into the bulk, but pyridine was hydrated in part on the surface at a temperature around 150 K.⁵⁵⁹

Ammonia deposited on acidic water (acidified using HCl) was converted to NH_4Cl , and the hydration of NH_4Cl starts above 100 K and is completed above 140 K.⁵⁶⁰ HCl adsorbed onto basic water (prepared by dissolving NH_3) results in hydrated HCl and the reaction product NH_4Cl above 40 K.⁵⁶¹ When HCl was deposited on a pure ice film, the ionic hydrate formed dissolved in the D_2O layer above 140 K, but some of it remained on the surface until the desorption temperature of D_2O . There also exist neutral hydrates of HCl,⁴⁵⁴ which are readily incorporated into the thin layer bulk of D_2O at temperatures well below 140 K.⁵⁶²

The solubility of the alkali-metal halides, viz., LiCl, LiBr, LiI, and NaCl, in water increased rapidly at 160 K due to the appearance of the supercooled liquid water.^{538,539,542} In the framework of polyamorphism, two distinct liquid phases exist in the deeply supercooled water region.⁵⁴⁴ They were characterized by solubility differences of LiCl in water ice as well as by interaction of a nonpolar species, Xe, and water in comparison with LiCl.^{538,540} The ultraviscous liquid (LDL) formed at $T_g = 136$ K hydrates LiCl and LiI molecularly, but they tend to stay on the surface because of amphiphilicity of the molecules.⁵³⁹ They are incorporated into the bulk at 160–165 K because cations and anions are hydrated separately by supercooled liquid (see Figure 36). The formation of aqueous LiI and LiCl solutions at 165 K is confirmed using TP TOF SIMS and RAIRS.^{539,541}

The emission of alkali-metal/halogen water cluster ions show differences with respect to their hydration.^{563,564} Cationic water clusters, $\text{M}^+(\text{H}_2\text{O})_n$ ($\text{M} = \text{Li}, \text{Na}, \text{K}, \text{Cs}$), are more efficiently formed compared to anionic ones; $\text{M}^-(\text{H}_2\text{O})_n$ ($\text{M} = \text{F}, \text{Cl}, \text{I}$).

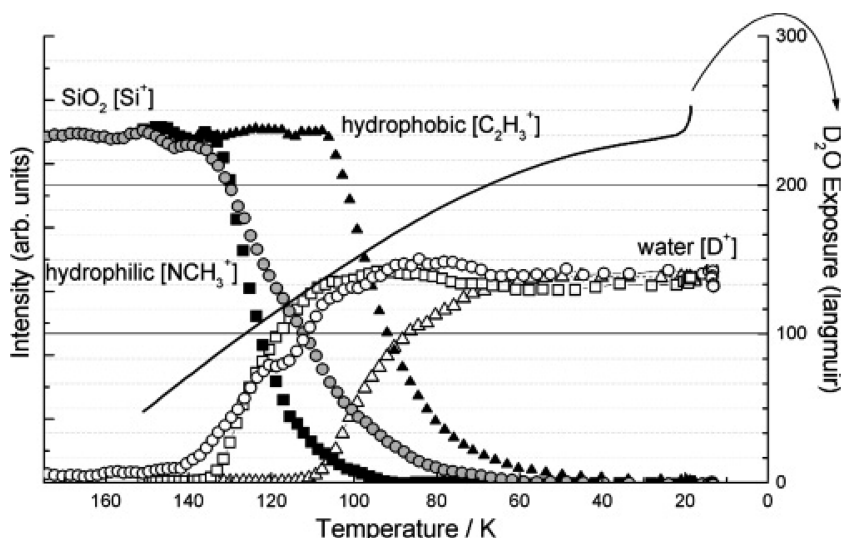


Figure 37. TOF SIMS signal from the hydrophilic and hydrophobic surfaces of the lipid DPPC film and the SiO₂/Si(100) surface exposed to a water partial pressure of 1×10^{-7} mbar as a function of the substrate temperature. The hydrophobic DPPC lipid film is represented by the C₂H₃⁺ sputter fragment, the hydrophilic film by NCH₃⁺, SiO₂ by Si⁺, and the adsorbed water by D⁺. Reprinted from ref 574. Copyright 2006 American Chemical Society.

Ar⁺ and C₆₀⁺ were used as primary ions in these cases. These experimental results were further supported by MD simulations.^{563,564} The disparity in ion emission was explained by differences in solvation structure. Complex formation readily takes place due to cation–water (through oxygen) interactions which destroy the hydrogen bonding in water, allowing the cluster to eject more easily, but anions do not disrupt the hydrogen bonding and are well trapped inside the ice matrix.

8.3. Intermixing

Intermixing of (heavy) water with molecules such as methanol,^{515,530,565} ethanol,⁵⁶⁶ acetic acid,⁴⁸⁷ methylamine,⁵⁶⁷ and methane⁵⁶⁸ has been investigated with combined TPD and TP TOF SIMS. For simple methanol–water systems (Figure 35a)⁵³⁰ the intensity change of CD₃⁺ and H₃O⁺ at 136 K is the clear indication of intermixing. For binary films in the ethanol–heavy water system, complete intermixing occurred above 140 K, due to the enhanced mobility of water molecules, where all ethanol molecules form hydrogen bonds with heavy water.⁵⁶⁶ The intermixing induced at 120 K in this case was due to increased mobility of the ethanol molecules, but it was incomplete at the molecular level as evidenced by the absence of H/D exchange. These two situations can be differentiated easily by looking at the evolution curves of CH₂OH⁺ and (C₂H₅OH)H⁺ ions relative CH₂OD⁺ and (C₂H₅OH)D⁺.⁵⁶⁶

Changes in functionality may change the solubility of molecules by altering the interaction parameters. The CH₃NH₂ molecule adsorbed on the D₂O surface undergoes a complete H/D exchange without intermixing above 140 K,⁵⁶⁷ but CH₃NH₂ undergoes H/D exchange with CD₃OD after intermixing at a lower temperature of ~125 K because these molecules can interact with each other via both their hydrophilic and hydrophobic end groups. Another system, a CH₃COOH–D₂O binary film, experienced intermixing at 130–140 K.⁴⁸⁷ Complete mixing was observed when D₂O was deposited on thin films of methane and fluoromethane at 15 K.⁵⁶⁸ A pure D₂O film could not be formed on the 20 ML methane film at a coverage up to ca. 100 ML. It is also found that heavy water undergoes complete intermixing with CO but not with CO₂ at 15 K.⁴⁸⁷ For the same reason, it was found that

D₂O molecules form nanoclusters over CO₂ films as they cannot penetrate effectively through solid CO₂.⁴⁸⁷ Systems containing Cl and water show minimum interactions in the temperature range of 90–100 K.⁵⁶⁹ A distinct layer of chlorine, with negligible interaction, was formed on solid H₂O in the temperature window of 90–100 K, but reaction occurs at higher temperatures.⁵⁶⁹ Chlorine nitrate forms a filmlike structure on water ice with a degree of polarization and desorbs simply at 130 K without undergoing any reaction.⁵⁷⁰

8.4. Dewetting

The morphological change of thin films is associated not only with the glass–liquid transition but also with crystallization as discussed in section 8.1. When crystalline ice is grown on metal surfaces such as Pt(111) or Pd(111), it favors the formation of 3D grains even at 45 ML of coverage despite the hydrophilicity of these metal substrates and their excellent lattice matching to crystalline ice.⁵⁷¹ The nonwetting growth of crystalline ice is ascribable to the properties of supercooled liquid and quasi-liquid, respectively, formed before and after crystallization^{530,534} because dewetting is characteristic of the liquidlike phase induced by surface tension rather than crystallization itself.⁵³² In fact, the adsorbed methanol or other polar molecules significantly quench the dewetting of crystalline water ice by reducing the surface tension of liquidlike layers coexisting with crystallites.^{516,565} When water is adsorbed as a monolayer on a hydrophobic substrate, such as graphite and ionic liquids, dewetting occurs in the sub-*T_g* region (120 K) because surface diffusion dominates instead of volume diffusion.¹⁴⁹

The dewetting temperature of HCOOH and CH₃COOH films was found to be 150 K.^{487,572} For ethanol films, dewetting occurs along with crystallization at 130 K,⁵⁴⁶ where the morphology change of the crystalline film continues at higher temperature and is attributable to the coexistence of a liquidlike phase or premelting. Similar dewetting behavior is observed for crystalline methanol films under isothermal conditions at 120 K.⁵³⁵ When CO₂ molecules are deposited on an ASW film, translational diffusion commences at 50 K, leading to dewetting of the monolayer CO₂ above 60 K.⁵⁷³ For *n*-pentane films, dewetting was observed after crystallization because of

premelting.⁵³³ Thus, crystallites derived from nanometer-sized thin films are so small that their properties tend to be governed by the quasi-liquid layer formed on the crystallite surface or grain boundaries.

8.5. Molecular Interactions

Water–lipid interactions were studied by taking the lipid dipalmitoyl-*sn*-glycero-3-phosphocholine (DPPC) film as a model compound.^{574,575} Two different orientations of DPPC are possible when it is adsorbed on a substrate. Either the nonpolar fatty acid chain (hydrophobic DPPC) or the polar phosphoric acid ester group (hydrophilic DPPC) can face the vacuum interface. The hydrophobic DPPC direction was monitored by choosing the $C_2H_3^+$ ion. The hydrophilic surface and adsorbed water were examined by selecting NCH_3^+ and D^+ sputtered fragments, respectively. Corresponding curves obtained when DPPC was adsorbed on a $SiO_2/Si(100)$ substrate in the temperature range of 15–170 K are given in Figure 37. The onset of water adsorption on the hydrophobic surface was observed at 106 K, approximately 30 K lower than that of the hydrophilic surface, 133 K. The different onset temperatures could be explained in terms of the longer lifetime of the adsorption precursor on the hydrophilic surface due to van der Waals interactions between the lipid polar headgroup and water.

Using thin films of room temperature ionic liquids, matrix effects on secondary ion emission have been discussed.^{576–578} The substrate effects on the kinetics of crystallization and fusion have also been investigated on the basis of temperature evolutions of sputtered secondary ion yields.⁵⁷⁶ The crystallinity of thin $[emim][Tf_2N]$ films is lower on the Ni(111) substrate than on the substrate of highly oriented pyrolytic graphite (HOPG) because the crystalline molecular alignment is disturbed by the interaction with Ni(111) at the interface. The crystal-like ordering of the $[emim][Tf_2N]$ monolayer tends to be retained at temperatures even higher than the bulk melting point on the HOPG substrate. The surface segregation study of cations and anions in binary mixtures of some room temperature ionic liquids revealed that larger and more polarizable ions tend to occupy the topmost surface layer.⁵⁷⁹

8.6. Chemical Reactions

Collision-induced proton transfer is a common process in ion/surface collisions in the low-energy regime, but a totally different proton transfer reaction (H/D exchange) can be induced thermally in a binary molecular solid system (see section 8.3 also). Earlier, such exchange reactions in ice bulk had been studied by FTIR spectroscopy.⁵⁸⁰ These reactions can be effectively monitored by SIMS. The proton transfer reaction in the water ice system is basically induced by the translational diffusion of molecules, whereas additional routes such as rotation of hydronium ions can also occur (in acidic ice).^{531,561}

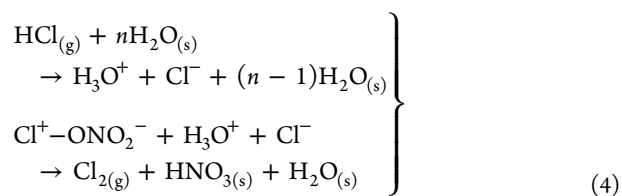
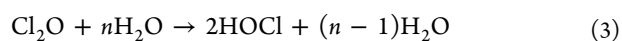
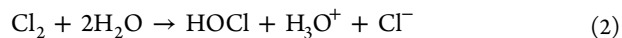
For the HCl–water ice system, HCl undergoes proton exchange reactions above 120 K, which was noticeably lower than the onset temperatures for the methanol and NH_4Cl system.⁵⁶² The presence of thermally activated ionic $H^+–Cl^-$ pairs explains the H/D exchange at lower temperatures. The hydrated HCl and NH_4Cl molecules undergo almost complete H/D exchange above 140 and 170 K, respectively.^{560,562} When pure NH_3 was adsorbed on water, the H/D exchange reaction occurred rapidly and completely at 140 K.⁵⁸¹ Similar onset temperatures for H/D exchange were reported between NH_3 and $HCOOH$.⁵⁸¹ NH_4HCO_2 appeared as a reaction product above 60 K when NH_3 and $HCOOH$ were codeposited at

lower temperatures.⁵⁸¹ CH_3NH_2 molecules undergo thermally activated H/D exchange above 140 and 125 K when adsorbed on D_2O and CD_3OD layers, respectively.⁵⁶⁷

The reaction of NH_3 molecules adsorbed on the HCl–water ice film showed a considerable difference compared with that of the pure HCl film.⁵⁶¹ The extent of NH_4Cl formation increased above 40 K for NH_3 molecules adsorbed on pure HCl. This reaction temperature was shifted to 120 K for NH_3 adsorbed on the HCl–water ice system since strongly hydrating water molecules prevent direct contact between NH_3 molecules and Cl^- ions, but for the reverse case, i.e., when HCl was adsorbed on the NH_3 –water ice system, the reaction (NH_4Cl formation) again occurred at 40 K. This establishes that NH_3 molecules are more weakly hydrated than HCl molecules.^{531,561}

Hydrolysis of an alkali metal is an interesting fundamental exothermic reaction which occurs efficiently at room temperature. The Na hydrolysis reaction occurred even at 13 K, but the reaction rate was very small until 100 K because the NaOH layer formed acted as a spacer layer to prevent the reaction between the pure water film and the metallic Na overlayer.^{507,509}

Formation of sulfuric acid hydrates was observed when H_2O and SO_3 gas were deposited in various compositions.⁵⁸² Among the chlorine-containing species, interaction of Cl_2 with the ice surface was negligible in the temperature range of 90–100 K.⁵⁶⁹ $ClONO_2$ shows some degree of polarization and interaction with water, whereas Cl_2O undergoes hydrogen-bond-like interactions with water. At about 120–130 K, Cl_2 undergoes reaction with an ice surface to form HOCl (hypochlorous acid), water, and solvated HCl.⁵⁶⁹ The possible reaction pathways suggested in the corresponding reference correspond to reaction 2. Over the same temperature range, Cl_2O produced only HOCl and H_2O upon reaction with water (reaction 3).⁵⁶⁹ $ClONO_2$ desorbs from the pure water ice surface above 130 K without leaving any signs of reaction,^{570,583} but it reacts rapidly with HCl at the ice surface. The reaction starts with the production of H_3O^+ and Cl^- ions upon contact between HCl and ice. Then it proceeds via the release of Cl_2 by the reaction between Cl^- and Cl^+ (from $ClONO_2$), which results in the formation of nitric acid at the surface (reaction 4).



8.7. Understanding SIMS as Relevant to Biological Analysis

One of the common sample preparation methods in biological SIMS is cryofixation, where the sample is frozen at liquid nitrogen temperature. Hence, water ice is a natural matrix in the analysis of biological samples, and several groups have been interested in the effect of the ice matrix on secondary ion formation. Winograd and co-workers^{16,18} and Vickerman and co-workers^{584,585} performed a noted number of experiments on frozen samples. Ice can act as an alternative source of protons.⁵¹⁹ Protonated molecular ion yields for frozen analytes have been found to be enhanced ~2 times compared to a room

temperature sample.⁵⁸⁶ Sometimes the presence of salt suppresses the ion signal in normal SIMS analysis, but this effect has been found to be reduced when the sample is frozen.⁵⁸⁶ Moreover, the addition of simple salts into an ice matrix may generate preformed ions.^{564,586}

It was found that cluster ion projectiles, especially C_{60}^+ , are effective in sputter depth profiling of organic molecules.^{519,520,587,588} In one of the experiments with histamine in an ice matrix, it was shown that signals related to both the ice and histamine are about 2 orders of magnitude higher for 20 keV C_{60}^+ projectiles than for 15 keV Ga^+ impact.^{589,590} Combined experimental and MD simulation studies on pure ice films showed an enhanced sputter yield and reduced ion escape depth for cluster ion projectiles.^{591–594} Snapshot pictures of the collision event obtained from MD simulations are given in Figure 38 for the projectiles of Au_3 and C_{60}^+ in 1, 3,

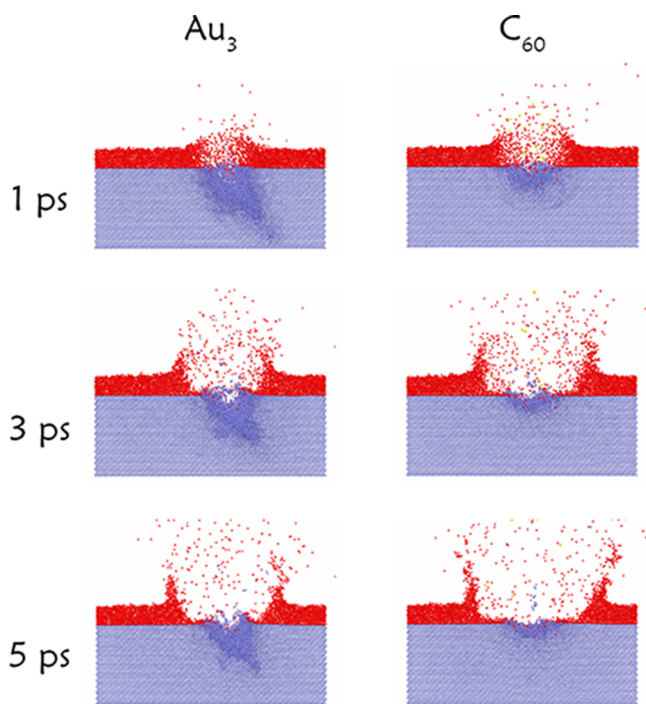


Figure 38. Snapshots of atom positions for Au_3^+ and C_{60}^+ bombardment of a 25 Å film of ice (red) on Ag (light blue). The incident angle for the impinging primary ions was 40° with a 15 keV incident energy. Reprinted with permission from ref 591. Copyright 2006 American Physical Society.

and 5 ps. Most of the water molecules near the impact point are removed from the Ag substrate in the course of collision with both projectiles. There can be very little damage accumulation during cluster ion bombardment for weakly binding molecular surfaces such as ice since the energy deposition region is confined and these projectiles are efficient in removing almost all materials close to the surface compared to their atomic ion counterparts.⁵⁹¹

9. SUMMARY AND PERSPECTIVES

Low-energy ionic collisions result in diverse ion/surface interaction phenomena. The ultrahigh purity of the probe beam, flexibility in selecting the ion and its kinetic energy, and the ensuing process control are unique advantages in these experiments. The range of ions used varies from simple organic

cations to complex proteins. The chemical reactivity of projectile ions is highlighted only at low kinetic energy. Also, kinetic energy can be used to control the reaction paths or to create new channels in the hyperthermal energy regime, which is inaccessible by a heating method. The extent to which a particular process occurs depends on a variety of factors, among which the chemical nature of the surface and of the impinging ion are most important. Specificity of a chemical reaction with spatial control provides a promising method of chemically specific surface modifications. This feature could make a contribution in the nano- or microelectronics industry. Use of soft landing for preparation of compounds and of catalytically active surfaces is encouraging, but improved yields are needed. Better instrumentation with higher throughput could solve this problem.

Central aspects of the chemistry involved in ion/surface collision events are associated with transformations of surface molecules and projectile ions. Details on these events are emerging in several cases. Time-resolved studies may help in this regard. Most of the studies look at only mass, with changes in ion kinetic energy and internal energy states not being studied. Relaxation by thermal, electron, and photon emission upon collision has not been the subject of study using low-energy ion impact. Such surface processes need additional measurements. Ab initio MD simulations of molecular ion impact at molecular solids have been performed in a number of important cases and are increasingly useful.

Ion impact at molecular solids of astrochemical relevance is an emerging area. The implications of this research to the chemical atmosphere of Jovian planets and interstellar objects need attention. Although thermal energies are far too low in space, ions impacting charged interstellar dust particles will also be accelerated by Coulombic interactions. Chemical reactivity of solids, existing as liquids and gases at normal temperatures will likely produce several surprises. Besides the implications in the origins of biological compounds that are precursors to living systems, the role of ionic collisions at ice surfaces has evident environmental implications. Associated processes at many molecular solids will be studied purely as a result of chemical curiosity.

Phase changes of molecular solids, which have so far been probed by macroscopic observables, are now accessible microscopically on the basis of static SIMS. A large advantage of this approach lies in its applicability to the effects of a free surface and a substrate interface with an extremely high sensitivity. Molecules in nanoconfined geometries are ubiquitous; their properties are expected to be distinct from those of bulk materials. For example, nanoconfined water interacting with macromolecules and biomembranes plays a decisive role in living cells, where the mobility of water molecules changes with the distance from the interface. A study of biomolecular interaction might be enabled by utilizing static SIMS in terms of hydrophilic and hydrophobic hydrations at the molecular level. However, the effects of the chemical environment on the ionization probability (matrix effects) are still poorly understood. A deeper understanding of ionization mechanisms during low-energy molecular collisions at the surface might open a new application field of SIMS and related techniques.

From the perspective of surface analysis, low-energy ion collision methods (RIS, SIMS, CS, etc.) extend extreme sensitivity and offer a means to identify and characterize molecules and functional groups on surfaces. Such capabilities are found in few other surface spectroscopic methods. In the

future, the need for surface molecular analysis is expected to continually increase in relation to the research prospects of heterogeneous catalysis, molecular nanotechnology, and biomimetic materials.

From the recent literature, it is clear that significant efforts are being made toward several of the aforementioned aspects, and breakthroughs are expected in the coming years.

AUTHOR INFORMATION

Corresponding Author

*E-mail: pradeep@iitm.ac.in (T.P.); cooks@purdue.edu (R.G.C.).

Present Address

[†]Indian Institute of Space Science and Technology, Thiruvananthapuram 695 547, India.

Notes

The authors declare no competing financial interest.

Biographies



Jobin Cyriac was born in Kerala, India, and received his Master's degree from the Mahatma Gandhi University, Kerala. He received his Ph.D. degree from the Indian Institute of Technology (IIT) Madras under the guidance of Prof. T. Pradeep. His Ph.D. research was on low-energy ion scattering at molecular solids, and he developed a spectrometer for such studies. He is currently a postdoctoral fellow with Prof. R. G. Cooks at Aston Labs for Mass Spectrometry, Purdue University. He is interested in exploring various applications of ion/surface collision phenomena and is keen on developing instrumentation for such studies.

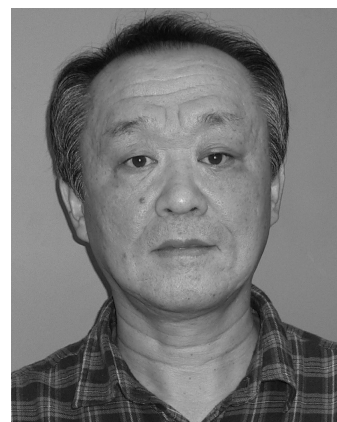


T. Pradeep earned his Ph.D. from the Indian Institute of Science in 1991 and had postdoctoral training at the Lawrence Berkeley Laboratory, University of California, Berkeley, and Purdue University,

West Lafayette, IN. He joined IIT Madras in December 1993, where he leads a research group on molecular materials and surfaces. He has held visiting positions at several universities and institutes in Asia and Europe. His research interests are in nanomaterials, molecular surfaces, monolayers, ion/surface collisions, clusters, spectroscopy, electronic structure, and instrumentation. He is committed to finding affordable solutions for drinking water for the poor. One of his technologies has been commercialized. He is the author of the introductory textbook *Nano: The Essentials* (McGraw-Hill) and is one of the authors of the monograph *Nanofluids* (Wiley-Interscience). He is a Fellow of the Indian Academy of Sciences. His other interests include education, popularization of science, and development of advanced teaching aids.

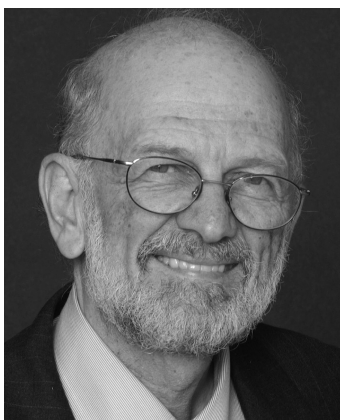


H. Kang received his B.Sc. from Seoul National University (SNU) and a Ph.D. in Physical Chemistry from the California Institute of Technology for his study of gas-phase ion chemistry in 1980–1985. After working on low-energy ion/surface interactions at the University of Houston as a postdoctoral fellow, he joined the chemistry faculty of POSTECH. There he studied reactive ion/surface collisions and developed a surface analysis method based on Cs⁺ reactive scattering. In 2001 he moved to SNU, where he leads a surface science research group and the Center for Space-Time Molecular Dynamics. His current research interest includes ice surface properties, heterogeneous reactions in the atmosphere and interstellar clouds, surface reaction dynamics, and nanoscopic investigation of electrochemical interfaces.



R. Souda was born in 1957 in Nagoya, Japan. He earned his B.S. and M.S. degrees in Physics from Nagoya University. He received his Ph.D. from the University of Tokyo in 1986. He has been at the National Institute for Research in Inorganic Materials (now the National Institute for Materials Science) since 1982. He is currently a Senior Researcher at the National Institute for Materials Science. His research interests are ion beam analysis of solid surfaces and ion/surface charge exchange mechanisms during low-energy ion and electron impacts. His current interest includes molecular-level understanding of the glass–

liquid transition and phase transition of thin films using secondary ion mass spectrometry.



R. G. Cooks received Ph.D. degrees from the University of Natal (now KwaZulu-Natal) and Cambridge University. His interests involve construction of mass spectrometers and their use in fundamental studies and applications. Early in his career, he worked on energy partitioning during metastable ion fragmentation and contributed to the concept and implementation of tandem mass spectrometry and to desorption ionization, especially matrix-based methods. His interest in minimizing sample workup and avoiding chromatography contributed to the development of the ambient ionization methods, including desorption electrospray ionization (DESI). Applications of this method in tissue imaging, forensics, and pharmaceuticals are in progress. These same interests also led to the construction of miniature ion trap mass spectrometers and their application to problems of trace chemical detection. His interests in the fundamentals of ion chemistry include inelastic ion/surface collisions, chemical sputtering, and ion soft landing. R. G. Cooks is a past President of the American Society for Mass Spectrometry and the International Mass Spectrometry Society and a Life Member of the British, Chinese, and Indian mass spectrometry societies.

ACKNOWLEDGMENTS

We acknowledge funding from the Department of Science and Technology, Government of India (T.P.), the National Research Foundation of the Korean government (MEST), Grant 2007-0056333 (H.K.), the Japan Society for the Promotion of Science through a Grant-in-Aid for Scientific Research (C), 22540339 (R.S.), the Separations and Analysis Program, Office of Basic Energy Sciences, U.S. Department of Energy, Grant DE-FG02-06ER15807, and the National Science Foundation, Grant CHE NSF 0848650 (R.G.C.). J.C. thanks T.P. and R.G.C. for their guidance and support. We acknowledge assistance from Gautam Sharma.

ABBREVIATIONS

AQ	accumulation quadrupole
ASW	amorphous solid water
CI	crystalline ice
CID	collision-induced dissociation
CQ	collisional quadrupole
CS	chemical sputtering
HDL	high-density liquid
HOPG	highly oriented pyrolytic graphite
LDL	low-density liquid
LES	low-energy sputtering
MS	mass spectrometry

RAIRS/IRAS	reflection–absorption infrared spectroscopy/ infrared reflection–absorption spectroscopy
RIS	reactive ion scattering/reactive scattering
RL	reactive landing
RQ	resolving quadrupole
SAMs	self-assembled monolayers
SID	surface-induced dissociation
SL	soft landing
SPIAD	surface polymerization by ion-assisted deposition

REFERENCES

- (1) Aston, F. W. *Philos. Mag.* **1919**, *38*, 707.
- (2) Svec, H. J. *Int. J. Mass Spectrom. Ion Processes* **1985**, *66*, 3.
- (3) Grayson, M. A. *Measuring Mass: From Positive Rays to Proteins*; Chemical Heritage Press: Philadelphia, PA, 2002.
- (4) Dempster, A. J. *Phys. Rev.* **1918**, *11*, 316.
- (5) Thomson, J. J. *Philos. Mag.* **1910**, *20*, 752.
- (6) Arnot, F. L. *Nature* **1936**, *138*, 162.
- (7) Arnot, F. L.; Milligan, J. C. *Proc. R. Soc. London, Ser. A: Math. Phys. Sci.* **1936**, *153*, 0359.
- (8) Herzog, R. F. K.; Viehbock, F. P. *Phys. Rev.* **1949**, *76*, 855.
- (9) Liebl, H. J.; Herzog, R. F. K. *J. Appl. Phys.* **1963**, *34*, 2893.
- (10) Benninghoven, A. *Z. Phys.* **1970**, *230*, 403.
- (11) Benninghoven, A.; Sichtermann, W. *Org. Mass Spectrom.* **1977**, *12*, 595.
- (12) Pachuta, S. J.; Cooks, R. G. *Chem. Rev.* **1987**, *87*, 647.
- (13) Benninghoven, A. *Surf. Interface Anal.* **2011**, *43*, 2.
- (14) *Secondary Ion Mass Spectrometry: Principles and Applications*; Vickerman, J. C., Brown, A., Reed, N. M., Eds.; Oxford University Press: Oxford, U.K., 1989.
- (15) Benninghoven, A.; Rudenauer, F. G.; Werner, H. W. *Secondary Ion Mass Spectrometry*; John Wiley and Sons, Inc.: New York, 1987.
- (16) Winograd, N.; Garrison, B. J. *Annu. Rev. Phys. Chem.* **2010**, *61*, 305.
- (17) Benninghoven, A. *Surf. Sci.* **1994**, *299*, 246.
- (18) Winograd, N. *Anal. Chem.* **2005**, *77*, 142A.
- (19) Wucher, A. *Appl. Surf. Sci.* **2006**, *252*, 6482.
- (20) Chughtai, K.; Heeren, R. M. A. *Chem. Rev.* **2010**, *110*, 3237.
- (21) Fletcher, J. S.; Lockyer, N. P.; Vaidyanathan, S.; Vickerman, J. C. *Anal. Chem.* **2007**, *79*, 2199.
- (22) Cooks, R. G.; Ast, T.; Mabud, A. *Int. J. Mass Spectrom.* **1990**, *100*, 209.
- (23) Grill, V.; Shen, J.; Evans, C.; Cooks, R. G. *Rev. Sci. Instrum.* **2001**, *72*, 3149.
- (24) Blackwell, A. E.; Dodds, E. D.; Bandarian, V.; Wysocki, V. H. *Anal. Chem.* **2011**, *83*, 2862.
- (25) Ast, T.; Mabud, M. A.; Cooks, R. G. *Int. J. Mass Spectrom. Ion Processes* **1988**, *82*, 131.
- (26) Kasi, S. R.; Kilburn, M. A.; Kang, H.; Rabalais, J. W.; Tavernini, L.; Hochmann, P. *J. Chem. Phys.* **1988**, *88*, 5902.
- (27) Jacobs, D. C. *Annu. Rev. Phys. Chem.* **2002**, *53*, 379.
- (28) Herman, Z. *J. Am. Soc. Mass Spectrom.* **2003**, *14*, 1360.
- (29) Monreal, R. C.; Flores, F. *Adv. Quantum Chem.* **2004**, *45*, 175.
- (30) Jacob, W.; Roth, J. In *Sputtering by Particle Bombardment*; Behrisch, R., Eckstein, W. E., Eds.; Springer-Verlag: Berlin, Heidelberg, 2007; p 329.
- (31) Samavat, F.; King, B. V.; O'Connor, D. J. *Surf. Rev. Lett.* **2007**, *14*, 31.
- (32) Herman, Z. *Int. J. Mass Spectrom.* **2004**, *233*, 361.
- (33) Cooks, R. G.; Ast, T.; Pradeep, T.; Wysocki, V. *Acc. Chem. Res.* **1994**, *27*, 316.
- (34) Cooks, R. G.; Jo, S. C.; Green, J. *Appl. Surf. Sci.* **2004**, *231*, 13.
- (35) Gologan, B.; Green, J. R.; Alvarez, J.; Laskin, J.; Cooks, R. G. *Phys. Chem. Chem. Phys.* **2005**, *7*, 1490.
- (36) Laskin, J.; Wang, P.; Hadjar, O. *Phys. Chem. Chem. Phys.* **2008**, *10*, 1079.

- (37) Johnson, G. E.; Hu, Q.; Laskin, J. *Annu. Rev. Anal. Chem.* **2011**, *4*, 83.
- (38) Kang, H. *Acc. Chem. Res.* **2005**, *38*, 893.
- (39) Kang, H. *Bull. Korean Chem. Soc.* **2011**, *32*, 389.
- (40) Park, S. C.; Moon, E. S.; Kang, H. *Phys. Chem. Chem. Phys.* **2010**, *12*, 12000.
- (41) Wysocki, V. H.; Joyce, K. E.; Jones, C. M.; Beardsley, R. L. *J. Am. Soc. Mass Spectrom.* **2008**, *19*, 190.
- (42) Mayer, P. M.; Poon, C. *Mass Spectrom. Rev.* **2009**, *28*, 608.
- (43) Shukla, A. K.; Futrell, J. H. *J. Mass Spectrom.* **2000**, *35*, 1069.
- (44) Schultz, D. G.; Lim, H.; Garbis, S.; Hanley, L. *J. Mass Spectrom.* **1999**, *34*, 217.
- (45) Laskin, J.; Futrell, J. H. *J. Chem. Phys.* **2003**, *119*, 3413.
- (46) Yang, Z.; Hadjar, O.; Laskin, J. *Int. J. Mass Spectrom.* **2007**, *265*, 124.
- (47) Rahaman, A.; Zhou, J. B.; Hase, W. L. *Int. J. Mass Spectrom.* **2006**, *249*, 321.
- (48) Miller, S. A.; Riederer, D. E.; Cooks, R. G.; Cho, W. R.; Lee, H. W.; Kang, H. *J. Phys. Chem.* **1994**, *98*, 245.
- (49) Song, K. Y.; Meroueh, O.; Hase, W. L. *J. Chem. Phys.* **2003**, *118*, 2893.
- (50) Laskin, J.; Bailey, T. H.; Futrell, J. H. *J. Am. Chem. Soc.* **2003**, *125*, 1625.
- (51) Rezayat, T.; Shukla, A. *J. Chem. Phys.* **2007**, *126*, 11.
- (52) Smith, D. L.; Selvan, R.; Wysocki, V. H. *Langmuir* **2003**, *19*, 7302.
- (53) Morris, M. R.; Riederer, D. E.; Winger, B. E.; Cooks, R. G.; Ast, T.; Chidsey, C. E. D. *Int. J. Mass Spectrom. Ion Processes* **1992**, *122*, 181.
- (54) Hayward, M. J.; Mabud, M. A.; Cooks, R. G. *J. Am. Chem. Soc.* **1988**, *110*, 1343.
- (55) Feketeova, L.; Grill, V.; Zappa, F.; Endstrasser, N.; Rasul, B.; Herman, Z.; Scheier, P.; Mark, T. D. *Int. J. Mass Spectrom.* **2008**, *276*, 37.
- (56) Feketeova, L.; Tepnual, T.; Grill, V.; Scheier, P.; Roithova, J.; Herman, Z.; Mark, T. D. *Int. J. Mass Spectrom.* **2007**, *265*, 337.
- (57) Biasioli, F.; Fiegele, T.; Mair, C.; Herman, Z.; Echt, O.; Aumayr, F.; Winter, H. P.; Mark, T. D. *J. Chem. Phys.* **2000**, *113*, 5053.
- (58) Cooks, R. G.; Ast, T.; Kralj, B.; Kramer, V.; Zigon, D. *J. Am. Soc. Mass Spectrom.* **1990**, *1*, 16.
- (59) Danell, A. S.; Glish, G. L. *Int. J. Mass Spectrom.* **2001**, *212*, 219.
- (60) He, M.; Emory, J. F.; McLuckey, S. A. *Anal. Chem.* **2005**, *77*, 3173.
- (61) Hayakawa, S. *J. Mass Spectrom.* **2004**, *39*, 111.
- (62) Turecek, F.; Jones, J. W.; Towle, T.; Panja, S.; Nielsen, S. B.; Hvelplund, P.; Paizs, B. *J. Am. Chem. Soc.* **2008**, *130*, 14584.
- (63) Qayyum, A.; Mair, C.; Tepnual, T.; Schustereder, W.; Scheier, P.; Mark, T. D. *Nucl. Instrum. Methods Phys. Res., Sect. B* **2003**, *205*, 714.
- (64) Mabud, A.; Dekrey, M. J.; Cooks, R. G.; Ast, T. *Int. J. Mass Spectrom. Ion Processes* **1986**, *69*, 277.
- (65) Hopf, C.; von Keudell, A.; Jacob, W. *J. Appl. Phys.* **2003**, *94*, 2373.
- (66) Hao, C. T.; Adams, L. E.; Yang, X.; Sadilek, M.; Turecek, F. *Int. J. Mass Spectrom.* **2009**, *280*, 136.
- (67) Winger, B. E.; Julian, R. K.; Cooks, R. G.; Chidsey, C. E. D. *J. Am. Chem. Soc.* **1991**, *113*, 8967.
- (68) Worgotter, R.; Kubista, J.; Zabka, J.; Dolejssek, Z.; Mark, T. D.; Herman, Z. *Int. J. Mass Spectrom.* **1998**, *174*, 53.
- (69) Feng, B.; Shen, J.; Grill, V.; Evans, C.; Cooks, R. G. *J. Am. Chem. Soc.* **1998**, *120*, 8189.
- (70) Pradeep, T.; Ast, T.; Cooks, R. G.; Feng, B. *J. Phys. Chem.* **1994**, *98*, 9301.
- (71) Pradeep, T.; Riederer, D. E.; Hoke, S. H.; Ast, T.; Cooks, R. G.; Linford, M. R. *J. Am. Chem. Soc.* **1994**, *116*, 8658.
- (72) Somogyi, A.; Kane, T. E.; Ding, J. M.; Wysocki, V. H. *J. Am. Chem. Soc.* **1993**, *115*, 5275.
- (73) Smith, D. L.; Wysocki, V. H.; Colorado, R.; Shmakova, O. E.; Graupe, M.; Lee, T. R. *Langmuir* **2002**, *18*, 3895.
- (74) Pradeep, T.; Feng, B.; Ast, T.; Patrick, J. S.; Cooks, R. G.; Pachuta, S. J. *J. Am. Soc. Mass Spectrom.* **1995**, *6*, 187.
- (75) Shen, J.; Grill, V.; Cooks, R. G. *J. Am. Chem. Soc.* **1998**, *120*, 4254.
- (76) Wu, Q. Y.; Hanley, L. *J. Phys. Chem.* **1993**, *97*, 2677.
- (77) Riederer, D. E.; Cooks, R. G.; Linford, M. R. *J. Mass Spectrom.* **1995**, *30*, 241.
- (78) Yang, M. C.; Lee, H. W.; Kang, H. *J. Chem. Phys.* **1995**, *103*, 5149.
- (79) Kang, H.; Kim, K. D.; Kim, K. Y. *J. Am. Chem. Soc.* **1997**, *119*, 12002.
- (80) Kim, C. M.; Hwang, C. H.; Lee, C. W.; Kang, H. *Angew. Chem., Int. Ed.* **2002**, *41*, 146.
- (81) Williams, E. R.; Jones, G. C.; Fang, L.; Zare, R. N.; Garrison, B. J.; Brenner, D. W. *J. Am. Chem. Soc.* **1992**, *114*, 3207.
- (82) Quinteros, C. L.; Tzvetkov, T.; Jacobs, D. C. *J. Chem. Phys.* **2000**, *113*, 5119.
- (83) Maazouz, M.; Quinteros, C. L.; Tzvetkov, T.; Maazouz, P. L.; Qin, X.; Barstis, T. L. O.; Jacobs, D. C. *Appl. Accel. Res. Ind.* **2001**, *576*, 122.
- (84) Maazouz, M.; Barstis, T. L. O.; Maazouz, P. L.; Jacobs, D. C. *Phys. Rev. Lett.* **2000**, *84*, 1331.
- (85) Deng, Z. W.; Souda, R. *J. Chem. Phys.* **2002**, *117*, 6235.
- (86) Deng, Z. W.; Souda, R. *Phys. Rev. B* **2003**, *67*, 235402.
- (87) Hahn, J. R.; Lee, C. W.; Han, S. J.; Lahaye, R.; Kang, H. *J. Phys. Chem. A* **2002**, *106*, 9827.
- (88) Lahaye, R.; Kang, H. *ChemPhysChem* **2004**, *5*, 697.
- (89) Kim, J. H.; Lahaye, R.; Kang, H. *Surf. Sci.* **2007**, *601*, 434.
- (90) Kaplan, A.; Bekkerman, A.; Tsipinyuk, B.; Kolodney, E. *J. Chem. Phys.* **2002**, *117*, 3484.
- (91) Kaplan, A.; Manor, Y.; Bekkerman, A.; Tsipinyuk, B.; Kolodney, E. *Int. J. Mass Spectrom.* **2003**, *228*, 1055.
- (92) Kaplan, A.; Manor, Y.; Bekkerman, A.; Tsipinyuk, B.; Kolodney, E. *J. Chem. Phys.* **2004**, *120*, 1572.
- (93) Hayward, M. J.; Park, F. D. S.; Phelan, L. M.; Bernasek, S. L.; Somogyi, A.; Wysocki, V. H. *J. Am. Chem. Soc.* **1996**, *118*, 8375.
- (94) Schultz, D. G.; Hanley, L. *J. Chem. Phys.* **1998**, *109*, 10976.
- (95) Yang, M. C.; Hwang, C. H.; Kang, H. *J. Chem. Phys.* **1997**, *107*, 2611.
- (96) Yang, M. C.; Hwang, C. H.; Ku, J. K.; Kang, H. *Surf. Sci.* **1996**, *366*, L719.
- (97) Shin, T. H.; Han, S. J.; Kang, H. *Nucl. Instrum. Methods Phys. Res., Sect. B* **1999**, *157*, 191.
- (98) Lahaye, R.; Kang, H. *Phys. Rev. B* **2003**, *67*, 033401.
- (99) Phelan, L. M.; Hayward, M. J.; Flynn, J. C.; Bernasek, S. L. *J. Phys. Chem. B* **1998**, *102*, 5667.
- (100) Wehner, S.; Kuppers, J. *J. Chem. Phys.* **1998**, *109*, 294.
- (101) Lanzani, G.; Martinazzo, R.; Materzanini, G.; Pino, I.; Tantardini, G. F. *Theor. Chem. Acc.* **2007**, *117*, 805.
- (102) Miller, S. A.; Luo, H.; Pachuta, S. J.; Cooks, R. G. *Science* **1997**, *275*, 1447.
- (103) Shen, J. W.; Yim, Y. H.; Feng, B. B.; Grill, V.; Evans, C.; Cooks, R. G. *Int. J. Mass Spectrom.* **1999**, *182*, 423.
- (104) Hadjar, O.; Wang, P.; Futrell, J. H.; Dessiaterik, Y.; Zhu, Z. H.; Cowin, J. P.; Iedema, M. J.; Laskin, J. *Anal. Chem.* **2007**, *79*, 6566.
- (105) Luo, H.; Miller, S. A.; Cooks, R. G.; Pachuta, S. J. *Int. J. Mass Spectrom.* **1998**, *174*, 193.
- (106) Laskin, J.; Wang, P.; Hadjar, O.; Futrell, J. H.; Alvarez, J.; Cooks, Z. G. *Int. J. Mass Spectrom.* **2007**, *265*, 237.
- (107) Hadjar, O.; Wang, P.; Futrell, J. H.; Laskin, J. *J. Am. Soc. Mass Spectrom.* **2009**, *20*, 901.
- (108) Hadjar, O.; Futrell, J. H.; Laskin, J. *J. Phys. Chem. C* **2007**, *111*, 18220.
- (109) Johnson, G. E.; Lysonski, M.; Laskin, J. *Anal. Chem.* **2010**, *82*, 5718.
- (110) Alvarez, J.; Futrell, J. H.; Laskin, J. *J. Phys. Chem. A* **2006**, *110*, 1678.
- (111) Laskin, J.; Wang, P.; Hadjar, O. *J. Phys. Chem. C* **2010**, *114*, 5305.

- (112) Volny, M.; Elam, W. T.; Ratner, B. D.; Turecek, F. *Anal. Chem.* **2005**, *77*, 4846.
- (113) Volny, M.; Elam, W. T.; Branca, A.; Ratner, B. D.; Turecek, F. *Anal. Chem.* **2005**, *77*, 4890.
- (114) Wang, P.; Hadjar, O.; Laskin, J. J. *Am. Chem. Soc.* **2007**, *129*, 8682.
- (115) Rauschenbach, S.; Vogelgesang, R.; Malinowski, N.; Gerlach, J. W.; Benyoucef, M.; Costantini, G.; Deng, Z.; Thontasen, N.; Kern, K. *ACS Nano* **2009**, *3*, 2901.
- (116) Choukourou, A.; Kousal, J.; Slavinska, D.; Biederman, H.; Fuoco, E. R.; Tepavcevic, S.; Saucedo, J.; Hanley, L. *Vacuum* **2004**, *75*, 195.
- (117) Smith, D. P. *J. Appl. Phys.* **1967**, *38*, 340.
- (118) Hochmann, P.; Miller, M. A.; Rabalais, J. W. *J. Phys. Chem.* **1985**, *89*, 2751.
- (119) Kang, H.; Kasi, S. R.; Rabalais, J. W. *J. Chem. Phys.* **1988**, *88*, 5882.
- (120) Brongersma, H. H.; Draxler, M.; de Ridder, M.; Bauer, P. *Surf. Sci. Rep.* **2007**, *62*, 63.
- (121) Samavat, F.; King, B. V.; O'Connor, D. J. *Surf. Rev. Lett.* **2007**, *14*, 31.
- (122) *Low Energy Ion-Surface Interactions*; Rabalais, J. W., Ed.; J. Wiley: Chichester, U.K., 1994.
- (123) Love, J. C.; Estroff, L. A.; Kriebel, J. K.; Nuzzo, R. G.; Whitesides, G. M. *Chem. Rev.* **2005**, *105*, 1103.
- (124) Schultz, D. G.; Wainhaus, S. B.; Hanley, L.; deSainteClaire, P.; Hase, W. L. *J. Chem. Phys.* **1997**, *106*, 10337.
- (125) Saecker, M. E.; Govoni, S. T.; Kowalski, D. V.; King, M. E.; Nathanson, G. M. *Science* **1991**, *252*, 1421.
- (126) Yang, L.; Mazyar, O. A.; Lourderaj, U.; Wang, J. P.; Rodgers, M. T.; Martinez-Nunez, E.; Addepalli, S. V.; Hase, W. L. *J. Phys. Chem. C* **2008**, *112*, 9377.
- (127) Somogyi, A.; Smith, D. L.; Wysocki, V. H.; Colorado, R.; Lee, T. R. *J. Am. Soc. Mass Spectrom.* **2002**, *13*, 1151.
- (128) Callahan, J. H.; Somogyi, A.; Wysocki, V. H. *Rapid Commun. Mass Spectrom.* **1993**, *7*, 693.
- (129) Zabka, J.; Dolejssek, Z.; Herman, Z. *J. Phys. Chem. A* **2002**, *106*, 10861.
- (130) Wade, N.; Shen, J. W.; Koskinen, J.; Cooks, R. G. *J. Mass Spectrom.* **2001**, *36*, 717.
- (131) Angelico, V. J.; Mitchell, S. A.; Wysocki, V. H. *Anal. Chem.* **2000**, *72*, 2603.
- (132) Graupe, M.; Takenaga, M.; Koini, T.; Colorado, R.; Lee, T. R. *J. Am. Chem. Soc.* **1999**, *121*, 3222.
- (133) Burroughs, J. A.; Hanley, L. *Anal. Chem.* **1994**, *66*, 3644.
- (134) Kane, T. E.; Wysocki, V. H. *Int. J. Mass Spectrom. Ion Processes* **1994**, *140*, 177.
- (135) Gu, C. G.; Wysocki, V. H.; Harada, A.; Takaya, H.; Kumadaki, I. *J. Am. Chem. Soc.* **1999**, *121*, 10554.
- (136) Wolf, K. V.; Cole, D. A.; Bernasek, S. L. *J. Phys. Chem. B* **2002**, *106*, 10382.
- (137) Wolf, K. V.; Cole, D. A.; Bernasek, S. L. *Anal. Chem.* **2002**, *74*, 5009.
- (138) Gologan, B.; Takats, Z.; Alvarez, J.; Wiseman, J. M.; Talaty, N.; Ouyang, Z.; Cooks, R. G. *J. Am. Soc. Mass Spectrom.* **2004**, *15*, 1874.
- (139) Koppers, W. R.; Beijersbergen, J. H. M.; Weeding, T. L.; Kistemaker, P. G.; Kleyn, A. W. *J. Chem. Phys.* **1997**, *107*, 10736.
- (140) Busch, K. L. *J. Mass Spectrom.* **1995**, *30*, 233.
- (141) Bottcher, A.; Weis, P.; Bihlmeier, A.; Kappes, M. M. *Phys. Chem. Chem. Phys.* **2004**, *6*, 5213.
- (142) Rader, H. J.; Rouhanipour, A.; Talarico, A. M.; Palermo, V.; Samori, P.; Mullen, K. *Nat. Mater.* **2006**, *5*, 276.
- (143) Neeb, M.; Klingeler, R.; Bechthold, P. S.; Kann, G.; Wirth, I.; Eisebitt, S.; Eberhardt, W. *Appl. Phys. A: Mater. Sci. Process.* **2001**, *72*, 289.
- (144) Klingeler, R.; Breuer, C.; Wirth, I.; Blanchard, A.; Bechthold, P. S.; Neeb, M.; Eberhardt, W. *Surf. Sci.* **2004**, *553*, 95.
- (145) Klingeler, R.; Kann, G.; Wirth, I.; Eisebitt, S.; Bechthold, P. S.; Neeb, M.; Eberhardt, W. *J. Chem. Phys.* **2001**, *115*, 7215.
- (146) Pysanenko, A.; Zabka, J.; Feketeova, L.; Mark, T. D.; Herman, Z. *Eur. J. Mass Spectrom.* **2008**, *14*, 335.
- (147) Lee, S. M.; Lee, Y. H.; Hwang, Y. G.; Hahn, J. R.; Kang, H. *Phys. Rev. Lett.* **1999**, *82*, 217.
- (148) Hahn, J. R.; Kang, H.; Lee, S. M.; Lee, Y. H. *J. Phys. Chem. B* **1999**, *103*, 9944.
- (149) Souda, R. *J. Chem. Phys.* **2008**, *129*, 124707.
- (150) Bonanni, S. B. S.; Ait-Mansour, K.; Brune, H.; Harbich, W. *ACS Catal.* **2011**, *1*, 385.
- (151) Lee, S. S.; Fan, C. Y.; Wu, T. P.; Anderson, S. L. *J. Am. Chem. Soc.* **2004**, *126*, 5682.
- (152) Harding, C.; Habibpour, V.; Kunz, S.; Farnbacher, A. N.-S.; Heiz, U.; Yoon, B.; Landman, U. *J. Am. Chem. Soc.* **2009**, *131*, 538.
- (153) Lim, D. C.; Dietsche, R.; Bubek, M.; Ketterer, T.; Gantefoer, G.; Kim, Y. D. *Chem. Phys. Lett.* **2007**, *439*, 364.
- (154) Heiz, U.; Vanolli, F.; Sanchez, A.; Schneider, W. D. *J. Am. Chem. Soc.* **1998**, *120*, 9668.
- (155) Kaden, W. E.; Wu, T. P.; Kunkel, W. A.; Anderson, S. L. *Science* **2009**, *326*, 826.
- (156) Vajda, S.; Pellin, M. J.; Greeley, J. P.; Marshall, C. L.; Curtiss, L. A.; Ballentine, G. A.; Elam, J. W.; Catillon-Mucherie, S.; Redfern, P. C.; Mehmood, F.; Zapol, P. *Nat. Mater.* **2009**, *8*, 213.
- (157) Carroll, S. J.; Pratontep, S.; Streun, M.; Palmer, R. E.; Hobday, S.; Smith, R. *J. Chem. Phys.* **2000**, *113*, 7723.
- (158) Gibilisco, S.; Di Vece, M.; Palomba, S.; Faraci, G.; Palmer, R. E. *J. Chem. Phys.* **2006**, 125.
- (159) Di Vece, M.; Palomba, S.; Palmer, R. E. *Phys. Rev. B* **2005**, *72*, 4.
- (160) Ni, B.; Andrews, R.; Jacques, D.; Qian, D.; Wijesundara, M. B. J.; Choi, Y. S.; Hanley, L.; Sinnott, S. B. *J. Phys. Chem. B* **2001**, *105*, 12719.
- (161) Ada, E. T.; Kornienko, O.; Hanley, L. *J. Phys. Chem. B* **1998**, *102*, 3959.
- (162) Wijesundara, M. B. J.; Hanley, L.; Ni, B.; Sinnott, S. B. *Proc. Natl. Acad. Sci. U.S.A.* **2000**, *97*, 23.
- (163) Hanley, L.; Fuoco, E.; Wijesundara, M. B. J.; Beck, A. J.; Brookes, P. N.; Short, R. D. *J. Vac. Sci. Technol., A* **2001**, *19*, 1531.
- (164) Hanley, L.; Choi, Y. S.; Fuoco, E. R.; Akin, F. A.; Wijesundara, M. B. J.; Li, M.; Aleksey, T. B.; Schlossman, M. *Nucl. Instrum. Methods Phys. Res., Sect. B* **2003**, *203*, 116.
- (165) Akin, F. A.; Jang, I.; Schlossman, M. L.; Sinnott, S. B.; Zajac, G.; Fuoco, E. R.; Wijesundara, M. B. J.; Li, M.; Tikhonov, A.; Pingali, S. V.; Wroble, A. T.; Hanley, L. *J. Phys. Chem. B* **2004**, *108*, 9656.
- (166) Choi, D. G.; Jang, S. G.; Yu, H. K.; Yang, S. M. *Chem. Mater.* **2004**, *16*, 3410.
- (167) Winger, B. E.; Laue, H. J.; Horning, S. R.; Julian, R. K.; Lammert, S. A.; Riederer, D. E.; Cooks, R. G. *Rev. Sci. Instrum.* **1992**, *63*, 5613.
- (168) Wysocki, V. H.; Ding, J. M.; Jones, J. L.; Callahan, J. H.; King, F. L. *J. Am. Soc. Mass Spectrom.* **1992**, *3*, 27.
- (169) Wysocki, V. H.; Jones, J. L.; Ding, J. M. *J. Am. Chem. Soc.* **1991**, *113*, 8969.
- (170) Choi, W. Y.; Kang, T. H.; Kang, H. *Bull. Korean Chem. Soc.* **1990**, *11*, 290.
- (171) Mabud, M. D. A.; Derkey, M. J.; Cooks, R. G. *Int. J. Mass Spectrom. Ion Processes* **1985**, *67*, 285.
- (172) Han, S. J.; Lee, C. W.; Hwang, C. H.; Lee, K. H.; Yang, M. C.; Kang, H. *Bull. Korean Chem. Soc.* **2001**, *22*, 883.
- (173) Fernandez, F. M.; Smith, L. L.; Kuppannan, K.; Yang, X.; Wysocki, V. H. *J. Am. Soc. Mass Spectrom.* **2003**, *14*, 1387.
- (174) Cyriac, J.; Pradeep, T. *J. Phys. Chem. C* **2007**, *111*, 8557.
- (175) Cyriac, J.; Pradeep, T. *J. Phys. Chem. C* **2008**, *112*, 1604.
- (176) Cyriac, J.; Pradeep, T. *J. Phys. Chem. C* **2008**, *112*, 5129.
- (177) Galhena, A. S.; Dagan, S.; Jones, C. M.; Beardsley, R. L.; Wysocki, V. N. *Anal. Chem.* **2008**, *80*, 1425.
- (178) Mohammed, S.; Chalmers, M. J.; Gielbert, J.; Ferro, M.; Gora, L.; Smith, D. C.; Gaskell, S. J. *J. Mass Spectrom.* **2001**, *36*, 1260.
- (179) Laskin, J.; Beck, K. M.; Hache, J. J.; Futrell, J. H. *Anal. Chem.* **2004**, *76*, 351.

- (180) Laskin, J.; Denisov, E. V.; Shukla, A. K.; Barlow, S. E.; Futrell, J. H. *Anal. Chem.* **2002**, *74*, 3255.
- (181) Shukla, A. K.; Futrell, J. H. *Rev. Sci. Instrum.* **2003**, *74*, 168.
- (182) Gordon, M. J.; Giapis, K. P. *Rev. Sci. Instrum.* **2005**, *76*, 083302.
- (183) Nikolaev, E. N.; Somogyi, A.; Smith, D. L.; Gu, C. G.; Wysocki, V. H.; Martin, C. D.; Samuelson, G. L. *Int. J. Mass Spectrom.* **2001**, *212*, 535.
- (184) Schey, K.; Cooks, R. G.; Grix, R.; Wollnik, H. *Int. J. Mass Spectrom. Ion Processes* **1987**, *77*, 49.
- (185) Beck, R. D.; Stjohn, P.; Homer, M. L.; Whetten, R. L. *Science* **1991**, *253*, 879.
- (186) Haney, L. L.; Riederer, D. E. *Anal. Chim. Acta* **1999**, *397*, 225.
- (187) Gamage, C. M.; Fernandez, F. M.; Kuppannan, K.; Wysocki, V. H. *Anal. Chem.* **2004**, *76*, 5080.
- (188) de Maaijer-Gielbert, J.; Somogyi, A.; Wysocki, V. H.; Kistemaker, P. G.; Weeding, T. L. *Int. J. Mass Spectrom.* **1998**, *174*, 81.
- (189) Christen, W.; Even, U.; Raz, T.; Levine, R. D. *J. Chem. Phys.* **1998**, *108*, 10262.
- (190) Kolling, T.; Sun, S.; Weitzel, K. M. *Int. J. Mass Spectrom.* **2008**, *277*, 245.
- (191) Stone, E. G.; Gillig, K. J.; Ruotolo, B. T.; Russell, D. H. *Int. J. Mass Spectrom.* **2001**, *212*, 519.
- (192) Sun, W. J.; May, J. C.; Russell, D. H. *Int. J. Mass Spectrom.* **2007**, *259*, 79.
- (193) Wiley, W. C.; McLaren, I. H. *Rev. Sci. Instrum.* **1955**, *26*, 1150.
- (194) Stone, E.; Gillig, K. J.; Ruotolo, B.; Fuhrer, K.; Gonin, M.; Schultz, A.; Russell, D. H. *Anal. Chem.* **2001**, *73*, 2233.
- (195) Gillig, K. J.; Ruotolo, B. T.; Stone, E. G.; Russell, D. H. *Int. J. Mass Spectrom.* **2004**, *239*, 43.
- (196) Laskin, J.; Futrell, J. H. *Mass Spectrom. Rev.* **2003**, *22*, 158.
- (197) Laskin, J.; Futrell, J. H. *Mass Spectrom. Rev.* **2005**, *24*, 135.
- (198) Williams, E. R.; Henry, K. D.; McLafferty, F. W.; Shabanowitz, J.; Hunt, D. F. *J. Am. Soc. Mass Spectrom.* **1990**, *1*, 413.
- (199) Heck, A. J. R.; Dekoning, L. J.; Pinkse, F. A.; Nibbering, N. M. M. *Rapid Commun. Mass Spectrom.* **1991**, *5*, 406.
- (200) Laskin, J.; Denisov, E.; Futrell, J. *J. Phys. Chem. B* **2001**, *105*, 1895.
- (201) Laskin, J.; Denisov, E.; Futrell, J. *J. Am. Chem. Soc.* **2000**, *122*, 9703.
- (202) Laskin, J.; Futrell, J. H. *J. Chem. Phys.* **2002**, *116*, 4302.
- (203) Zhong, W. Q.; Nikolaev, E. N.; Futrell, J. H.; Wysocki, V. H. *Anal. Chem.* **1997**, *69*, 2496.
- (204) Rakov, V. S.; Futrell, J. H.; Denisov, E. V.; Nikolaev, E. N. *Eur. J. Mass Spectrom.* **2000**, *6*, 299.
- (205) Franchetti, V.; Solka, B. H.; Baitinger, W. E.; Amy, J. W.; Cooks, R. G. *Int. J. Mass Spectrom. Ion Processes* **1977**, *23*, 29.
- (206) Mayer, P. S.; Turecek, F.; Lee, H. N.; Scheidemann, A. A.; Olney, T. N.; Schumacher, F.; Strop, P.; Smrcina, M.; Patek, M.; Schirlin, D. *Anal. Chem.* **2005**, *77*, 4378.
- (207) Geiger, R. J.; Melnyk, M. C.; Busch, K. L.; Bartlett, M. G. *Int. J. Mass Spectrom.* **1999**, *182*, 415.
- (208) Yang, X. L.; Mayer, P. S.; Turecek, F. *J. Mass Spectrom.* **2006**, *41*, 256.
- (209) Kemper, P.; Kolmakov, A.; Tong, X.; Lilach, Y.; Benz, L.; Manard, M.; Metiu, H.; Buratto, S. K.; Bowers, M. T. *Int. J. Mass Spectrom.* **2006**, *254*, 202.
- (210) Klingeler, R.; Bechthold, P. S.; Neeb, M.; Eberhardt, W. *Rev. Sci. Instrum.* **2002**, *73*, 1803.
- (211) Wepasnick, K. A.; Li, X.; Mangler, T.; Noessner, S.; Wolke, C.; Grossmann, M.; Gantefoer, G.; Fairbrother, D. H.; Bowen, K. H. *J. Phys. Chem. C* **2011**, *115*, 12299.
- (212) Siuzdak, G.; Bothner, B.; Yeager, M.; Brugidou, C.; Fauquet, C. M.; Hoey, K.; Chang, C. M. *Chem. Biol.* **1996**, *3*, 45.
- (213) Rauschenbach, S.; Stadler, F. L.; Lunedei, E.; Malinowski, N.; Koltsov, S.; Costantini, G.; Kern, K. *Small* **2006**, *2*, 540.
- (214) Judai, K.; Sera, K.; Amatsutsumi, S.; Yagi, K.; Yasuike, T.; Yabushita, S.; Nakajima, A.; Kaya, K. *Chem. Phys. Lett.* **2001**, *334*, 277.
- (215) Thontasen, N.; Levita, G.; Malinowski, N.; Deng, Z.; Rauschenbach, S.; Kern, K. *J. Phys. Chem. C* **2010**, *114*, 17768.
- (216) Hu, Q. C.; Wang, P.; Gassman, P. L.; Laskin, J. *Anal. Chem.* **2009**, *81*, 7302.
- (217) Denault, J. W.; Evans, C.; Koch, K. J.; Cooks, R. G. *Anal. Chem.* **2000**, *72*, 5798.
- (218) Alvarez, J.; Cooks, R. G.; Barlow, S. E.; Gaspar, D. J.; Futrell, J. H.; Laskin, J. *Anal. Chem.* **2005**, *77*, 3452.
- (219) Bromann, K.; Felix, C.; Brune, H.; Harbich, W.; Monot, R.; Buttet, J.; Kern, K. *Science* **1996**, *274*, 956.
- (220) Jodicke, H.; Schaub, R.; Bhowmick, A.; Monot, R.; Buttet, J.; Harbich, W. *Rev. Sci. Instrum.* **2000**, *71*, 2818.
- (221) Harbich, W.; Fedrigo, S.; Meyer, F.; Lindsay, D. M.; Lignieres, J.; Rivoal, J. C.; Kreisle, D. *J. Chem. Phys.* **1990**, *93*, 8535.
- (222) Boyd, K. J.; Lapicki, A.; Aizawa, M.; Anderson, S. L. *Rev. Sci. Instrum.* **1998**, *69*, 4106.
- (223) Turra, M.; Waldschmidt, B.; Kaiser, B.; Schafer, R. *Rev. Sci. Instrum.* **2008**, *79*, 013905.
- (224) Heiz, U.; Vanolli, F.; Trento, L.; Schneider, W. D. *Rev. Sci. Instrum.* **1997**, *68*, 1986.
- (225) Habibpour, V.; Wang, Z. W.; Palmer, R. E.; Heiz, U. *J. Appl. Sci.* **2011**, *11*, 1164.
- (226) Heiz, U.; Bullock, E. L. *J. Mater. Chem.* **2004**, *14*, 564.
- (227) Gracia-Pinilla, M.; Martinez, E.; Silva Vidaurri, G.; Perez-Tijerina, E. *Nanoscale Res. Lett.* **2010**, *5*, 180.
- (228) Seto, T.; Kawakami, Y.; Suzuki, N.; Hirasawa, M.; Aya, N. *Nano Lett.* **2001**, *1*, 315.
- (229) Sakiyama, K.; Koga, K.; Seto, T.; Hirasawa, M.; Orii, T. *J. Phys. Chem. B* **2004**, *108*, 523.
- (230) Kawabata, S.; Naono, Y.; Taguchi, Y.; Huh, S. H.; Nakajima, A. *Appl. Surf. Sci.* **2007**, *253*, 6690.
- (231) Davila, S. J.; Birdwell, D. O.; Verbeck, G. F. *Rev. Sci. Instrum.* **2010**, *81*, 034104.
- (232) von Issendorff, B.; Palmer, R. E. *Rev. Sci. Instrum.* **1999**, *70*, 4497.
- (233) Pratontep, S.; Carroll, S. J.; Xirouchaki, C.; Streun, M.; Palmer, R. E. *Rev. Sci. Instrum.* **2005**, *76*, 045103.
- (234) Palmer, R. E.; Pratontep, S.; Boyen, H. G. *Nat. Mater.* **2003**, *2*, 443.
- (235) Palmer, R. E.; Leung, C. *Trends Biotechnol.* **2007**, *25*, 48.
- (236) Ouyang, Z.; Takats, Z.; Blake, T. A.; Gologan, B.; Guymon, A. J.; Wiseman, J. M.; Oliver, J. C.; Davison, V. J.; Cooks, R. G. *Science* **2003**, *301*, 1351.
- (237) Blake, T. A.; Zheng, O. Y.; Wiseman, J. M.; Takats, Z.; Guymon, A. J.; Kothari, S.; Cooks, R. G. *Anal. Chem.* **2004**, *76*, 6293.
- (238) Peng, W. P.; Goodwin, M. P.; Nie, Z. X.; Volny, M.; Zheng, O. Y.; Cooks, R. G. *Anal. Chem.* **2008**, *80*, 6640.
- (239) Nie, Z. X.; Li, G. T.; Goodwin, M. P.; Gao, L.; Cyriac, J.; Cooks, R. G. *J. Am. Soc. Mass Spectrom.* **2009**, *20*, 949.
- (240) Ouyang, Z.; Wu, G. X.; Song, Y. S.; Li, H. Y.; Plass, W. R.; Cooks, R. G. *Anal. Chem.* **2004**, *76*, 4595.
- (241) Volny, M.; Turecek, F. *J. Mass Spectrom.* **2006**, *41*, 124.
- (242) Kitching, K. J.; Lee, H. N.; Elam, W. T.; Johnston, E. E.; MacGregor, H.; Miller, R. J.; Turecek, F.; Ratner, B. D. *Rev. Sci. Instrum.* **2003**, *74*, 4832.
- (243) Tsukuda, T.; Yasumatsu, H.; Sugai, T.; Terasaki, A.; Nagata, T.; Kondow, T. *J. Phys. Chem.* **1995**, *99*, 6367.
- (244) Stjohn, P. M.; Yeretizian, C.; Whetten, R. L. *J. Phys. Chem.* **1992**, *96*, 9100.
- (245) Biesecker, J. P.; Ellison, G. B.; Wang, H.; Iedema, M. J.; Tsekouras, A. A.; Cowin, J. P. *Rev. Sci. Instrum.* **1998**, *69*, 485.
- (246) *Electrospray Ionization Mass Spectrometry: Fundamentals, Instrumentation and Applications*; Cole, R. B., Ed.; Wiley: New York, 1997.
- (247) Ganem, B.; Li, Y. T.; Henion, J. D. *J. Am. Chem. Soc.* **1991**, *113*, 7818.
- (248) Wang, P.; Laskin, J. *Angew. Chem., Int. Ed.* **2008**, *47*, 6678.
- (249) Binns, C. *Surf. Sci. Rep.* **2001**, *44*, 1.
- (250) Nielsen, R. M.; Murphy, S.; Strebel, C.; Johansson, M.; Nielsen, J. H.; Chorkendorff, I. *Surf. Sci.* **2009**, *603*, 3420.

- (251) Lightstone, J. M.; Patterson, M. J.; Liu, P.; Lofaro, J. C., Jr.; White, M. G. *J. Phys. Chem. C* **2008**, *112*, 11495.
- (252) Gracia-Pinilla, M.; Martinez, E.; Vidaurre, G. S.; Perez-Tijerina, E. *Nanoscale Res. Lett.* **2010**, *5*, 180.
- (253) Kamalou, O.; Rangama, J.; Ramillon, J.-M.; Guinement, P.; Huber, B. A. *Rev. Sci. Instrum.* **2008**, *79*, 063301.
- (254) Lee, S.; Lee, B.; Mehmood, F.; Seifert, S.; Libera, J. A.; Elam, J. W.; Greeley, J.; Zapol, P.; Curtiss, L. A.; Pellin, M. J.; Stair, P. C.; Winans, R. E.; Vajda, S. *J. Phys. Chem. C* **2010**, *114*, 10342.
- (255) Bardotti, L.; Tournus, F.; Melinon, P.; Pellarin, M.; Broyer, M. *Phys. Rev. B* **2011**, *83*.
- (256) Vuckovic, S.; Svanqvist, M.; Popok, V. N. *Rev. Sci. Instrum.* **2008**, *79*, 073303.
- (257) Goldby, I. M.; vonIssendorff, B.; Kuipers, L.; Palmer, R. E. *Rev. Sci. Instrum.* **1997**, *68*, 3327.
- (258) Bromann, K.; Brune, H.; Giovannini, M.; Kern, K. *Surf. Sci.* **1997**, *388*, L1107.
- (259) Yamaguchi, W.; Yoshimura, K.; Tai, Y.; Maruyama, Y.; Igarashi, K.; Tanemura, S.; Murakami, J. *Chem. Phys. Lett.* **1999**, *311*, 341.
- (260) Hayward, M. J.; Park, F. D. S.; Manzella, L. M.; Bernasek, S. L. *Int. J. Mass Spectrom. Ion Processes* **1995**, *148*, 25.
- (261) Grill, V.; Worgotter, R.; Futrell, J. H.; Mark, T. D. *Z. Phys. D: At., Mol. Clusters* **1997**, *40*, 111.
- (262) Ouyang, Z.; Grill, V.; Alvarez, J.; Doerge, C. H.; Gianelli, L.; Thomas, P.; Rohrs, H. W.; Cooks, R. G. *Rev. Sci. Instrum.* **2002**, *73*, 2375.
- (263) Tournus, F.; Blanc, N.; Tamion, A.; Hillenkamp, M.; Dupuis, V. *J. Magn. Magn. Mater.* **2011**, *323*, 1868.
- (264) March, R. E.; J., T. J. F. *Quadrupole Ion Trap Mass Spectrometry*; Wiley: Hoboken, NJ, 2005.
- (265) Rottgen, M. A.; Judai, K.; Antonietti, J. M.; Heiz, U.; Rauschenbach, S.; Kern, K. *Rev. Sci. Instrum.* **2006**, *77*, 013302.
- (266) Kelly, R. T.; Tolmachev, A. V.; Page, J. S.; Tang, K.; Smith, R. D. *Mass Spectrom. Rev.* **2010**, *29*, 294.
- (267) Shaffer, S. A.; Tang, K. Q.; Anderson, G. A.; Prior, D. C.; Udseth, H. R.; Smith, R. D. *Rapid Commun. Mass Spectrom.* **1997**, *11*, 1813.
- (268) Shaffer, S. A.; Prior, D. C.; Anderson, G. A.; Udseth, H. R.; Smith, R. D. *Anal. Chem.* **1998**, *70*, 4111.
- (269) Seymour, J. L.; Syrstad, E. A.; Langley, C. C.; Turecek, F. *Int. J. Mass Spectrom.* **2003**, *228*, 687.
- (270) Shen, J. W.; Grill, V.; Evans, C.; Cooks, R. G. *J. Mass Spectrom.* **1999**, *34*, 354.
- (271) Wade, N.; Pradeep, T.; Shen, J. W.; Cooks, R. G. *Rapid Commun. Mass Spectrom.* **1999**, *13*, 986.
- (272) Wade, N.; Gologan, B.; Vincze, A.; Cooks, R. G.; Sullivan, D. M.; Bruening, M. L. *Langmuir* **2002**, *18*, 4799.
- (273) Wang, P.; Hadjar, O.; Gassman, P. L.; Laskin, J. *Phys. Chem. Chem. Phys.* **2008**, *10*, 1512.
- (274) Peng, W.-P.; Johnson, G. E.; Fortmeyer, I. C.; Wang, P.; Hadjar, O.; Cooks, R. G.; Laskin, J. *Phys. Chem. Chem. Phys.* **2011**, *13*, 267.
- (275) Nagaoka, S.; Matsumoto, T.; Okada, E.; Mitsui, M.; Nakajima, A. *J. Phys. Chem. B* **2006**, *110*, 16008.
- (276) Lyon, J. T.; Andrews, L. *J. Phys. Chem. A* **2005**, *109*, 431.
- (277) Smith, W. E. *Chem. Soc. Rev.* **2008**, *37*, 955.
- (278) Campion, A.; Kambhampati, P. *Chem. Soc. Rev.* **1998**, *27*, 241.
- (279) Cyriac, J.; Li, G.; Cooks, R. G. *Anal. Chem.* **2011**, *83*, 5114.
- (280) Volny, M.; Sengupta, A.; Wilson, C. B.; Swanson, B. D.; Davis, E. J.; Turecek, F. *Anal. Chem.* **2007**, *79*, 4543.
- (281) Honea, E. C.; Ogura, A.; Murray, C. A.; Raghavachari, K.; Sprenger, W. O.; Jarrold, M. F.; Brown, W. L. *Nature* **1993**, *366*, 42.
- (282) Haslett, T. L.; Fedrigo, S.; Moskovits, M. *J. Chem. Phys.* **1995**, *103*, 7815.
- (283) Tsekouras, A. A.; Iedema, M. J.; Cowin, J. P. *J. Chem. Phys.* **1999**, *111*, 2222.
- (284) Hanley, L.; Sinnott, S. B. *Surf. Sci.* **2002**, *500*, 500.
- (285) Tepavcevic, S.; Wroble, A. T.; Bissen, M.; Wallace, D. J.; Choi, Y.; Hanley, L. *J. Phys. Chem. B* **2005**, *109*, 7134.
- (286) Pomeroy, J. M.; Couture, A. J.; Murty, M. V. R.; Butler, E. N.; Cooper, B. H. *Rev. Sci. Instrum.* **2002**, *73*, 3846.
- (287) Matsumoto, T.; Nagaoka, S.; Ikemoto, K.; Mitsui, M.; Ara, M.; Tada, H.; Nakajima, A. *Eur. Phys. J. D* **2009**, *52*, 99.
- (288) Tepavcevic, S.; Choi, Y.; Hanley, L. *Langmuir* **2004**, *20*, 8754.
- (289) Tepavcevic, S.; Choi, Y.; Hanley, L. *J. Am. Chem. Soc.* **2003**, *125*, 2396.
- (290) Tepavcevic, S.; Zachary, A. M.; Wroble, A. T.; Choi, Y.; Hanley, L. *J. Phys. Chem. A* **2006**, *110*, 1618.
- (291) Wroble, A. T.; Wildeman, J.; Anunskis, D. J.; Hanley, L. *Thin Solid Films* **2008**, *516*, 7386.
- (292) Jester, S. S.; Loffler, D.; Weis, P.; Bottcher, A.; Kappes, M. M. *Surf. Sci.* **2009**, *603*, 1863.
- (293) Zheng, Z.; Kwok, W. M.; Lau, W. M. *Chem. Commun.* **2006**, 3122.
- (294) Zheng, Z.; Xu, X. D.; Fan, X. L.; Lau, W. M.; Kwok, R. W. M. *J. Am. Chem. Soc.* **2004**, *126*, 12336.
- (295) Lando, A.; Lauwaet, K.; Lievens, P. *Phys. Chem. Chem. Phys.* **2009**, *11*, 1521.
- (296) Duffe, S.; Irawan, T.; Bielecki, M.; Richter, T.; Sieben, B.; Yin, C.; von Issendorff, B.; Moseler, M.; Hoewel, H. *Eur. Phys. J. D* **2007**, *45*, 401.
- (297) Tong, X.; Benz, L.; Kemper, P.; Metiu, H.; Bowers, M. T.; Buratto, S. K. *J. Am. Chem. Soc.* **2005**, *127*, 13516.
- (298) Tainoff, D.; Bardotti, L.; Tournus, F.; Guiraud, G.; Boisron, O.; Melinon, P. *J. Phys. Chem. C* **2008**, *112*, 6842.
- (299) Kunz, S.; Hartl, K.; Nesselberger, M.; Schweinberger, F. F.; Kwon, G.; Hanzlik, M.; Mayrhofer, K. J. J.; Heiz, U.; Arenz, M. *Phys. Chem. Chem. Phys.* **2010**, *12*, 10288.
- (300) Evans, C.; Wade, N.; Pepi, F.; Strossman, G.; Schuerlein, T.; Cooks, R. G. *Anal. Chem.* **2002**, *74*, 317.
- (301) Mayor, L. C.; Ben Taylor, J.; Magnano, G.; Rienzo, A.; Satterley, C. J.; O'Shea, J. N.; Schnadt, J. *J. Chem. Phys.* **2008**, *129*.
- (302) Melinon, P.; Prevel, B.; Dupuis, V.; Perez, A.; Champagnon, B.; Guyot, Y.; Boudeulle, M.; Pellarin, M.; Dugourd, P.; Broyer, M. *Mater. Sci. Eng., A* **1996**, *217*, 69.
- (303) Wijesundara, M. B. J.; Zajac, G.; Fuoco, E.; Hanley, L. *J. Adhes. Sci. Technol.* **2001**, *15*, 599.
- (304) Isomura, N.; Wu, X. Y.; Hirata, H.; Watanabe, Y. *J. Vac. Sci. Technol., A* **2010**, *28*, 1141.
- (305) Bolotin, I. L.; Tetzler, S. H.; Hanley, L. *J. Phys. Chem. C* **2007**, *111*, 9953.
- (306) Mabud, M. A.; Ast, T.; Verma, S.; Jiang, Y. X.; Cooks, R. G. *J. Am. Chem. Soc.* **1987**, *109*, 7597.
- (307) Shen, J. W.; Evans, C.; Wade, N.; Cooks, R. G. *J. Am. Chem. Soc.* **1999**, *121*, 9762.
- (308) Wu, Q. Y.; Hanley, L. *J. Am. Chem. Soc.* **1993**, *115*, 1191.
- (309) Pradeep, T.; Evans, C.; Shen, J. W.; Cooks, R. G. *J. Phys. Chem. B* **1999**, *103*, 5304.
- (310) Wade, N.; Jo, S. C.; Gologan, B.; Cooks, R. G. *Int. J. Mass Spectrom.* **2003**, *230*, 151.
- (311) Ast, T.; Pradeep, T.; Feng, B.; Cooks, R. G. *J. Mass Spectrom.* **1996**, *31*, 791.
- (312) Reinke, P.; Jacob, W.; Moller, W. *J. Appl. Phys.* **1993**, *74*, 1354.
- (313) Lau, W. M.; Kwok, R. W. M. *Int. J. Mass Spectrom.* **1998**, *174*, 245.
- (314) Mair, C.; Fiegele, T.; Worgotter, R.; Futrell, J. H.; Mark, T. D. *Int. J. Mass Spectrom.* **1998**, *177*, 105.
- (315) Riederer, D. E.; Miller, S. A.; Ast, T.; Cooks, R. G. *J. Am. Soc. Mass Spectrom.* **1993**, *4*, 938.
- (316) Roithova, J.; Zabka, J.; Dolejssek, Z.; Herman, Z. *J. Phys. Chem. B* **2002**, *106*, 8293.
- (317) Jasik, J.; Zabka, J.; Feketeova, L.; Ipolyi, I.; Mark, T. D.; Herman, Z. *J. Phys. Chem. A* **2005**, *109*, 10208.
- (318) Pysanenko, A.; Zabka, J.; Herman, Z. *Collect. Czech. Chem. Commun.* **2008**, *73*, 755.
- (319) Feketeova, L.; Zabka, J.; Zappa, F.; Grill, V.; Scheier, P.; Mark, T. D.; Herman, Z. *J. Am. Soc. Mass Spectrom.* **2009**, *20*, 927.

- (320) Jasik, J.; Roithova, J.; Zabka, J.; Pysanenko, A.; Feketeova, L.; Ipolyi, I.; Mark, T. D.; Herman, Z. *Int. J. Mass Spectrom.* **2006**, *249*, 162.
- (321) Hayakawa, S.; Feng, B.; Cooks, R. G. *Int. J. Mass Spectrom.* **1997**, *167*, 525.
- (322) Mair, C.; Fiegele, T.; Biasioli, F.; Mark, T. D. *Czech. J. Phys.* **1998**, *48* (Suppl 2), 363.
- (323) Worgotter, R.; Grill, V.; Herman, Z.; Schwarz, H.; Mark, T. D. *Chem. Phys. Lett.* **1997**, *270*, 333.
- (324) Mair, C.; Fiegele, T.; Biasioli, F.; Worgotter, R.; Grill, V.; Lezius, M.; Mark, T. D. *Plasma Sources Sci. Technol.* **1999**, *8*, 191.
- (325) Mair, C.; Fiegele, T.; Biasioli, F.; Herman, Z.; Mark, T. D. *J. Chem. Phys.* **1999**, *111*, 2770.
- (326) Mair, C.; Herman, Z.; Fedor, J.; Lezius, M.; Mark, T. D. *J. Chem. Phys.* **2003**, *118*, 1479.
- (327) Mair, C.; Lezius, M.; Herman, Z.; Mark, T. D. *J. Chem. Phys.* **2003**, *118*, 7090.
- (328) Mair, C.; Fedor, J.; Lezius, M.; Scheier, P.; Probst, M.; Herman, Z.; Mark, T. D. *New J. Phys.* **2003**, *5*.
- (329) Tepnual, T.; Feketeova, L.; Grill, V.; Scheier, P.; Herman, Z.; Mark, T. D. *Int. J. Mass Spectrom.* **2005**, *244*, 164.
- (330) Sekiguchi, O.; Bakken, V.; Uggerud, E. *J. Am. Soc. Mass Spectrom.* **2004**, *15*, 982.
- (331) Stirk, K. M.; Kiminkinen, L. K. M.; Kenttamaa, H. I. *Chem. Rev.* **1992**, *92*, 1649.
- (332) Kiplinger, J. L.; Richmond, T. G.; Osterberg, C. E. *Chem. Rev.* **1994**, *94*, 373.
- (333) Amii, H.; Uneyama, K. *Chem. Rev.* **2009**, *109*, 2119.
- (334) Nowak, P.; McIntyre, N. S.; Hunter, D. H.; Bello, I.; Lau, W. M. *Surf. Interface Anal.* **1995**, *23*, 873.
- (335) Zachary, A. M.; Drabik, M.; Choi, Y.; Bolotin, I. L.; Biederman, H.; Hanley, L. *J. Vac. Sci. Technol., A* **2008**, *26*, 212.
- (336) Hsu, W. D.; Tepavcevic, S.; Hanley, L.; Sinnott, S. B. *J. Phys. Chem. C* **2007**, *111*, 4199.
- (337) Choi, Y.; Zachary, A.; Tepavcevic, S.; Wu, C. P.; Hanley, L. *Int. J. Mass Spectrom.* **2005**, *241*, 139.
- (338) Ruiz, R.; Choudhary, D.; Nickel, B.; Toccoli, T.; Chang, K. C.; Mayer, A. C.; Clancy, P.; Blakely, J. M.; Headrick, R. L.; Iannotta, S.; Malliaras, G. G. *Chem. Mater.* **2004**, *16*, 4497.
- (339) Casalis, L.; Danisman, M. F.; Nickel, B.; Bracco, G.; Toccoli, T.; Iannotta, S.; Scoles, G. *Phys. Rev. Lett.* **2003**, *90*.
- (340) Zheng, Z.; Wong, K. W.; Lau, W. C.; Kwok, R. W. M.; Lau, W. M. *Chem.—Eur. J.* **2007**, *13*, 3187.
- (341) Xu, X. D.; Kwok, R. W. M.; Lau, W. M. *Thin Solid Films* **2006**, *514*, 182.
- (342) Choi, C. Y.; Zheng, Z.; Wong, K. W.; Du, Z. L.; Lau, W. M.; Du, R. X. *Appl. Phys. A: Mater. Sci. Process.* **2008**, *91*, 403.
- (343) Xi, L.; Zheng, Z.; Lam, N. S.; Grizzi, O.; Lau, W. M. *Appl. Surf. Sci.* **2007**, *254*, 113.
- (344) Xi, L.; Zheng, Z.; Lam, N. S.; Nie, H. Y.; Grizzi, O.; Lau, W. M. *J. Phys. Chem. C* **2008**, *112*, 12111.
- (345) Gorham, J.; Smith, B.; Fairbrother, D. H. *J. Phys. Chem. C* **2007**, *111*, 374.
- (346) Kautz, N. A.; Fogarty, D. P.; Kandel, S. A. *Surf. Sci.* **2007**, *601*, L86.
- (347) Qin, X. D.; Tzvetkov, T.; Jacobs, D. C. *J. Phys. Chem. A* **2006**, *110*, 1408.
- (348) Qin, X.; Tzvetkov, T.; Jacobs, D. C. *Nucl. Instrum. Methods Phys. Res., Sect. B* **2003**, *203*, 130.
- (349) Pradeep, T.; Miller, S. A.; Cooks, R. G. *J. Am. Soc. Mass Spectrom.* **1993**, *4*, 769.
- (350) Pradeep, T.; Riederer, D. E.; Ast, T.; Cooks, R. G. *Rapid Commun. Mass Spectrom.* **1993**, *7*, 711.
- (351) Pradeep, T.; Shen, J. W.; Evans, C.; Cooks, R. G. *Anal. Chem.* **1999**, *71*, 3311.
- (352) Chen, G. D.; Hoke, S. H.; Cooks, R. G. *Int. J. Mass Spectrom.* **1994**, *139*, 87.
- (353) Kang, H.; Lee, H. W.; Cho, W. R.; Lee, S. M. *Chem. Phys. Lett.* **1998**, *292*, 213.
- (354) Pepi, F.; Tata, A.; Garzoli, S.; Giacomello, P.; Ragno, R.; Patsilinos, A.; Di Fusco, M.; D'Annibale, A.; Cannistraro, S.; Baldacchini, C.; Favero, G.; Frascioni, M.; Mazzei, F. *J. Phys. Chem. C* **2011**, *115*, 4863.
- (355) Pradeep, T.; Patrick, J. S.; Feng, B. B.; Miller, S. A.; Ast, T.; Cooks, R. G. *J. Phys. Chem.* **1995**, *99*, 2941.
- (356) Patrick, J. S.; Pradeep, T.; Luo, H.; Ma, S.; Cooks, R. G. *J. Am. Soc. Mass Spectrom.* **1998**, *9*, 1158.
- (357) Evans, C.; Pradeep, T.; Shen, J. W.; Cooks, R. G. *Rapid Commun. Mass Spectrom.* **1999**, *13*, 172.
- (358) Ada, E. T.; Lee, S. M.; Lee, H.; Rabalais, J. W. *J. Phys. Chem. B* **2000**, *104*, 5132.
- (359) Hanley, L.; Lim, H. J.; Schultz, D. G.; Wainhaus, S. B.; deSainteClaire, P.; Hase, W. L. *Nucl. Instrum. Methods Phys. Res., Sect. B* **1997**, *125*, 218.
- (360) Hanley, L.; Lim, H.; Schultz, D. G.; Garbis, S.; Yu, C. W.; Ada, E. T.; Wijesundara, M. B. *J. Nucl. Instrum. Methods Phys. Res., Sect. B* **1999**, *157*, 174.
- (361) Miller, S. A.; Luo, H.; Jiang, X.; Rohrs, H. W.; Cooks, R. G. *Int. J. Mass Spectrom. Ion Processes* **1997**, *160*, 83.
- (362) Wade, N.; Evans, C.; Pepi, F.; Cooks, R. G. *J. Phys. Chem. B* **2000**, *104*, 11230.
- (363) Wade, N.; Evans, C.; Jo, S. C.; Cooks, R. G. *J. Mass Spectrom.* **2002**, *37*, 591.
- (364) Love, L. O. *Science* **1973**, *182*, 343.
- (365) Yergey, A. L.; Yergey, A. K. *J. Am. Soc. Mass Spectrom.* **1997**, *8*, 943.
- (366) Lapack, M. A.; Pachuta, S. J.; Busch, K. L.; Cooks, R. G. *Int. J. Mass Spectrom. Ion Processes* **1983**, *53*, 323.
- (367) Zhu, H.; Bilgin, M.; Bangham, R.; Hall, D.; Casamayor, A.; Bertone, P.; Lan, N.; Jansen, R.; Bidlingmaier, S.; Houfek, T.; Mitchell, T.; Miller, P.; Dean, R. A.; Gerstein, M.; Snyder, M. *Science* **2001**, *293*, 2101.
- (368) Wong, L. S.; Khan, F.; Micklefield, J. *Chem. Rev.* **2009**, *109*, 4025.
- (369) Feng, B. B.; Wunschel, D. S.; Masselon, C. D.; Pasa-Tolic, L.; Smith, R. D. *J. Am. Chem. Soc.* **1999**, *121*, 8961.
- (370) Nanita, S. C.; Cooks, R. G. *Angew. Chem., Int. Ed.* **2006**, *45*, 554.
- (371) Nanita, S. C.; Takats, Z.; Cooks, R. G. *J. Am. Soc. Mass Spectrom.* **2004**, *15*, 1360.
- (372) Siuzdak, G.; Hollenbeck, T.; Bothner, B. *J. Mass Spectrom.* **1999**, *34*, 1087.
- (373) Kohtani, M.; Jones, T. C.; Schneider, J. E.; Jarrold, M. F. *J. Am. Chem. Soc.* **2004**, *126*, 7420.
- (374) Mandal, H. S.; Kraatz, H. B. *J. Am. Chem. Soc.* **2007**, *129*, 6356.
- (375) Hu, Q. C.; Wang, P.; Laskin, J. *Phys. Chem. Chem. Phys.* **2010**, *12*, 12802.
- (376) Mazzei, F.; Favero, G.; Frascioni, M.; Tata, A.; Tuccitto, N.; Licciardello, A.; Pepi, F. *Anal. Chem.* **2008**, *80*, 5937.
- (377) Pepi, F.; Ricci, A.; Tata, A.; Favero, G.; Frascioni, M.; Noci, S. D.; Mazzei, F. *Chem. Commun.* **2007**, 3494.
- (378) Mazzei, F.; Favero, G.; Frascioni, M.; Tata, A.; Pepi, F. *Chem.—Eur. J.* **2009**, *15*, 7359.
- (379) Volny, M.; Elam, W. T.; Ratner, B. D.; Turecek, F. *J. Biomed. Mater. Res., Part B: Appl. Biomater.* **2007**, *80B*, 505.
- (380) Fuerstenau, S. D.; Benner, W. H.; Thomas, J. J.; Brugidou, C.; Bothner, B.; Siuzdak, G. *Angew. Chem., Int. Ed.* **2001**, *40*, 542.
- (381) Peng, W. P.; Goodwin, M. P.; Chen, H.; Cooks, R. G.; Wilker, J. *Rapid Commun. Mass Spectrom.* **2008**, *22*, 3540.
- (382) Nagaoka, S.; Okada, E.; Doi, S.; Mitsui, M.; Nakajima, A. *Eur. Phys. J. D* **2005**, *34*, 239.
- (383) Nagaoka, S.; Matsumoto, T.; Ikemoto, K.; Mitsui, M.; Nakajima, A. *J. Am. Chem. Soc.* **2007**, *129*, 1528.
- (384) Nagaoka, S.; Ikemoto, K.; Matsumoto, T.; Mitsui, M.; Nakajima, A. *J. Phys. Chem. C* **2008**, *112*, 6891.
- (385) Mitsui, M.; Nagaoka, S.; Matsumoto, T.; Nakajima, A. *J. Phys. Chem. B* **2006**, *110*, 2968.

- (386) Ikemoto, K.; Nagaoka, S.; Matsumoto, T.; Mitsui, M.; Nakajima, A. *J. Phys. Chem. C* **2009**, *113*, 4476.
- (387) Nagaoka, S.; Ikemoto, K.; Fujio, K.; Hiehata, K.; Sasahara, A.; Mitsui, M.; Onishi, H.; Nakajima, A. *Eur. Phys. J. D* **2009**, *52*, 103.
- (388) Linford, M. R.; Fenter, P.; Eisenberger, P. M.; Chidsey, C. E. D. *J. Am. Chem. Soc.* **1995**, *117*, 3145.
- (389) Dubois, L. H.; Zegarski, B. R.; Nuzzo, R. G. *J. Am. Chem. Soc.* **1990**, *112*, 570.
- (390) Ferguson, M. K.; Lohr, J. R.; Day, B. S.; Morris, J. R. *Phys. Rev. Lett.* **2004**, *92*.
- (391) Johnson, G. E.; Laskin, J. *Chem.—Eur. J.* **2010**, *16*, 14433.
- (392) Chen, H.; Zheng, O. Y.; Cooks, R. G. *Angew. Chem., Int. Ed.* **2006**, *45*, 3656.
- (393) Blacken, G. R.; Volny, M.; Vaisar, T.; Sadilek, M.; Turecek, F. *Anal. Chem.* **2007**, *79*, 5449.
- (394) Blacken, G. R.; Volny, M.; Diener, M.; Jackson, K. E.; Ranjitkar, P.; Maly, D. J.; Turecek, F. *J. Am. Soc. Mass Spectrom.* **2009**, *20*, 915.
- (395) Goldby, I. M.; Kuipers, L.; vonIssendorff, B.; Palmer, R. E. *Appl. Phys. Lett.* **1996**, *69*, 2819.
- (396) Angel Gracia-Pinilla, M.; Ferrer, D.; Mejia-Rosales, S.; Perez-Tijerina, E. *Nanoscale Res. Lett.* **2009**, *4*, 896.
- (397) Harbich, W. *Philos. Mag. B: Phys. Condens. Matter: Stat. Mech., Electron., Opt. Magn. Prop.* **1999**, *79*, 1307.
- (398) Shyjumon, I.; Gopinadhan, M.; Ivanova, O.; Quasz, M.; Wulff, H.; Helm, C. A.; Hippler, R. *Eur. Phys. J. D* **2006**, *37*, 409.
- (399) Yamaguchi, W.; Yoshimura, K.; Tai, Y.; Maruyama, Y.; Igarashi, K.; Tanemura, S.; Murakami, J. *J. Chem. Phys.* **2000**, *112*, 9961.
- (400) Lei, Y.; Mehmood, F.; Lee, S.; Greeley, J.; Lee, B.; Seifert, S.; Winans, R. E.; Elam, J. W.; Meyer, R. J.; Redfern, P. C.; Teschner, D.; Schlögl, R.; Pellin, M. J.; Curtiss, L. A.; Vajda, S. *Science* **2010**, *328*, 224.
- (401) Li, H.; Pei, Y.; Zeng, X. C. *J. Chem. Phys.* **2010**, *133*, 134707.
- (402) Lee, S.; Molina, L. M.; Lopez, M. J.; Alonso, J. A.; Hammer, B.; Lee, B.; Seifert, S.; Winans, R. E.; Elam, J. W.; Pellin, M. J.; Vajda, S. *Angew. Chem., Int. Ed.* **2009**, *48*, 1467.
- (403) Thune, E.; Carpena, E.; Sauthoff, K.; Seibt, M.; Reinke, P. J. *Appl. Phys.* **2005**, *98*.
- (404) Di Vece, M.; Young, N. P.; Li, Z. Y.; Chen, Y.; Palmer, R. E. *Small* **2006**, *2*, 1270.
- (405) O'Shea, J. N.; Schnadt, J.; Andersson, S.; Patthey, L.; Rost, S.; Giertz, A.; Brena, B.; Forsell, J. O.; Sandell, A.; Bjornholm, O.; Bruhwiler, P. A.; Martensson, N. J. *Chem. Phys.* **2000**, *113*, 9233.
- (406) Leung, C.; Xirouchaki, C.; Berovic, N.; Palmer, R. E. *Adv. Mater.* **2004**, *16*, 223.
- (407) Fu, Q.; Wagner, T.; Olliges, S.; Carstanjen, H. D. *J. Phys. Chem. B* **2005**, *109*, 944.
- (408) Woodward, W. H.; Blake, M. M.; Luo, Z.; Weiss, P. S.; Castleman, A. W., Jr. *J. Phys. Chem. C* **2011**, *115*, 5373.
- (409) Hayakawa, T.; Yasumatsu, H.; Koudow, T. *Eur. Phys. J. D* **2009**, *52*, 95.
- (410) Heiz, U.; Schneider, W. D. *Crit. Rev. Solid State Mater. Sci.* **2001**, *26*, 251.
- (411) Abbet, S.; Judai, K.; Klinger, L.; Heiz, U. *Pure Appl. Chem.* **2002**, *74*, 1527.
- (412) Gao, L.; Lyn, M. E.; Bergeron, D. E.; Castleman, A. W. *Int. J. Mass Spectrom.* **2003**, *229*, 11.
- (413) Perez, A.; Melinon, P.; Dupuis, V.; Bardotti, L.; Masenelli, B.; Tournus, F.; Prevel, B.; Tuillon-Combes, J.; Bernstein, E.; Tamion, A.; Blanc, N.; Tainoff, D.; Boisron, O.; Guiraud, G.; Broyer, M.; Pellarin, M.; Del Fatti, N.; Vallee, F.; Cottancin, E.; Lerne, J.; Vialle, J. L.; Bonnet, C.; Maioli, P.; Crut, A.; Clavier, C.; Rousset, J. L.; Morfin, F. *Int. J. Nanotechnol.* **2010**, *7*, 523.
- (414) Lopez-Acevedo, O.; Kacprzak, K. A.; Akola, J.; Hakkinen, H. *Nat. Chem.* **2010**, *2*, 329.
- (415) Löffler, D.; Jester, S. S.; Weis, P.; Bottcher, A.; Kappes, M. M. *J. Chem. Phys.* **2006**, *124*.
- (416) Bottcher, A.; Weis, P.; Jester, S. S.; Löffler, D.; Bihlmeier, A.; Klopfer, W.; Kappes, M. M. *Phys. Chem. Chem. Phys.* **2005**, *7*, 2816.
- (417) Melinon, P.; Hannour, A.; Prevel, B.; Bardotti, L.; Bernstein, E.; Perez, A.; Gierak, J.; Bourhis, E.; Maily, D. *J. Cryst. Growth* **2005**, *275*, 317.
- (418) Rouhanipour, A.; Roy, M.; Feng, X. L.; Rader, H. J.; Mullen, K. *Angew. Chem., Int. Ed.* **2009**, *48*, 4602.
- (419) Tsao, H. N.; Rader, H. J.; Pisula, W.; Rouhanipour, A.; Mullen, K. *Phys. Status Solidi A* **2008**, *205*, 421.
- (420) Yang, X.; Rader, H. J.; Rouhanipour, A.; Mullen, K. *Eur. J. Mass Spectrom.* **2005**, *11*, 287.
- (421) Hsu, W. D.; Jang, I.; Sinnott, S. B. *J. Vac. Sci. Technol., A* **2007**, *25*, 1084.
- (422) Hsu, W. D.; Jang, I.; Sinnott, S. B. *Chem. Mater.* **2006**, *18*, 914.
- (423) Cunge, G.; Booth, J. P. *J. Appl. Phys.* **1999**, *85*, 3952.
- (424) Wijesundara, M. B. J.; Fuoco, E.; Hanley, L. *Langmuir* **2001**, *17*, 5721.
- (425) Ada, E. T.; Hanley, L. *Int. J. Mass Spectrom.* **1998**, *174*, 231.
- (426) Fuoco, E. R.; Gillen, G.; Wijesundara, M. B. J.; Wallace, W. E.; Hanley, L. *J. Phys. Chem. B* **2001**, *105*, 3950.
- (427) Wagner, M. S. *Surf. Interface Anal.* **2005**, *37*, 42.
- (428) Badu-Tawiah, A. K.; Wu, C.; Cooks, R. G. *Anal. Chem.* **2011**, *83*, 2648.
- (429) Espy, R. D.; Badu-Tawiah, A.; Cooks, R. G. *Curr. Opin. Chem. Biol.* **2011**, *15*, 741.
- (430) Badu-Tawiah, A. K.; Cyriac, J.; Cooks, R. G. *J. Am. Soc. Mass Spectrom.* **2012**, *23*, 842.
- (431) Saf, R.; Goriup, M.; Steindl, T.; Hamedinger, T. E.; Sandholzer, D.; Hayn, G. *Nat. Mater.* **2004**, *3*, 323.
- (432) Ju, J.; Yamagata, Y.; Higuchi, T. *Adv. Mater.* **2009**, *21*, 4343.
- (433) Tani, Y.; Kobayashi, S.; Kawazoe, H. *J. Vac. Sci. Technol., A* **2008**, *26*, 1058.
- (434) O'Shea, J. N.; Taylor, J. B.; Swarbrick, J. C.; Magnano, G.; Mayor, L. C.; Schulte, K. *Nanotechnology* **2007**, *18*, 035707.
- (435) Saywell, A.; Magnano, G.; Satterley, C. J.; Perdigao, L. M. A.; Champness, N. R.; Beton, P. H.; O'Shea, J. N. *J. Phys. Chem. C* **2008**, *112*, 7706.
- (436) Morozov, V. N.; Morozova, T. Y. *Anal. Chem.* **1999**, *71*, 3110.
- (437) Satterley, C. J.; Perdigao, L. M. A.; Saywell, A.; Magnano, G.; Rienzo, A.; Mayor, L. C.; Dhanak, V. R.; Beton, P. H.; O'Shea, J. N. *Nanotechnology* **2007**, *18*, 455304.
- (438) Rietveld, I. B.; Kobayashi, K.; Yamada, H.; Matsushige, K. *J. Phys. Chem. B* **2006**, *110*, 23351.
- (439) Rietveld, I. B.; Kobayashi, K.; Yamada, H.; Matsushige, K. *Soft Matter* **2009**, *5*, 593.
- (440) Kim, J.-S.; Chung, W.-S.; Kim, K.; Kim, D. Y.; Paeng, K.-J.; Jo, S. M.; Jang, S.-Y. *Adv. Funct. Mater.* **2010**, *20*, 3538.
- (441) Bottger, P. H. M.; Bi, Z.; Adolph, D.; Dick, K. A.; Karlsson, L. S.; Karlsson, M. N. A.; Wacaser, B. A.; Deppert, K. *Nanotechnology* **2007**, *18*.
- (442) Jayasinghe, S. N. *Physica E* **2008**, *40*, 2911.
- (443) Duffe, S.; Groenhagen, N.; Patryarcha, L.; Sieben, B.; Yin, C.; von Issendorff, B.; Moseler, M.; Hoevel, H. *Nat. Nanotechnol.* **2010**, *5*, 335.
- (444) Tsekouras, A. A.; Iedema, M. J.; Cowin, J. P. *Phys. Rev. Lett.* **1998**, *80*, 5798.
- (445) Cowin, J. P.; Tsekouras, A. A.; Iedema, M. J.; Wu, K.; Ellison, G. B. *Nature* **1999**, *398*, 405.
- (446) Johari, G. P. *J. Chem. Phys.* **1996**, *105*, 7079.
- (447) Angell, C. A. *Chem. Rev.* **2002**, *102*, 2627.
- (448) Tsekouras, A. A.; Iedema, M. J.; Ellison, G. B.; Cowin, J. P. *Int. J. Mass Spectrom.* **1998**, *174*, 219.
- (449) Wu, K.; Iedema, M. J.; Cowin, J. P. *Langmuir* **2000**, *16*, 4259.
- (450) Wu, K.; Iedema, M. J.; Tsekouras, A. A.; Cowin, J. P. *Nucl. Instrum. Methods Phys. Res., Sect. B* **1999**, *157*, 259.
- (451) Bernstein, M. P.; Dworkin, J. P.; Sandford, S. A.; Cooper, G. W.; Allamandola, L. J. *Nature* **2002**, *416*, 401.
- (452) Caro, G. M. M.; Meierhenrich, U. J.; Schutte, W. A.; Barbier, B.; Segovia, A. A.; Rosenbauer, H.; Thiemann, W. H. P.; Brack, A.; Greenberg, J. M. *Nature* **2002**, *416*, 403.

- (453) Molina, M. J.; Tso, T. L.; Molina, L. T.; Wang, F. C. Y. *Science* **1987**, *238*, 1253.
- (454) Park, S. C.; Maeng, K. W.; Pradeep, T.; Kang, H. *Angew. Chem., Int. Ed.* **2001**, *40*, 1497.
- (455) Kang, H.; Yang, M. C.; Kim, K. D.; Kim, K. Y. *Int. J. Mass Spectrom.* **1998**, *174*, 143.
- (456) Kim, K. Y.; Shin, T. H.; Han, S. J.; Kang, H. *Phys. Rev. Lett.* **1999**, *82*, 1329.
- (457) Kang, H.; Shin, T. H.; Park, S. C.; Kim, I. K.; Han, S. J. *J. Am. Chem. Soc.* **2000**, *122*, 9842.
- (458) Park, S. C.; Maeng, K. W.; Pradeep, T.; Kang, H. *Nucl. Instrum. Methods Phys. Res., Sect. B* **2001**, *182*, 193.
- (459) Hwang, C. H.; Lee, C. W.; Kang, H.; Kim, C. M. *Surf. Sci.* **2001**, *490*, 144.
- (460) Han, S. J.; Lee, C. W.; Lahaye, R.; Kang, H. *Surf. Sci.* **2003**, *538*, 184.
- (461) Shin, T.; Kim, K. N.; Lee, C. W.; Shin, S. K.; Kang, H. *J. Phys. Chem. B* **2003**, *107*, 11674.
- (462) Jung, K. H.; Park, S. C.; Kim, J. H.; Kang, H. *J. Chem. Phys.* **2004**, *121*, 2758.
- (463) Kim, Y. K.; Park, S. C.; Kim, J. H.; Lee, C. W.; Kang, H. *J. Phys. Chem. C* **2008**, *112*, 18104.
- (464) Lee, C. W.; Kim, J. K.; Moon, E. S.; Minh, Y. C.; Kang, H. *Astrophys. J.* **2009**, *697*, 428.
- (465) Kim, S.-K.; Kang, H. *J. Phys. Chem. Lett.* **2010**, *1*, 3085.
- (466) Lee, P.-R.; Lee, C.-W.; Kim, J.-K.; Moon, E.-S.; Kang, H. *Chem.—Asian J.* **2011**, *6*, 938.
- (467) Lahaye, R.; Kang, H. *Surf. Sci.* **2001**, *490*, 327.
- (468) Lahaye, R. *Surf. Sci.* **2010**, *604*, 1135.
- (469) Bag, S.; McCoustra, M. R. S.; Pradeep, T. *J. Phys. Chem. C* **2011**, *115*, 13813.
- (470) Kim, K.; Choi, W.; Hoffmann, M. R.; Yoon, H.-I.; Park, B.-K. *Environ. Sci. Technol.* **2010**, *44*, 4142.
- (471) Petrenko, V. F.; Whitworth, R. W. *Physics of Ice*; Oxford University Press: Oxford, U.K., 1999.
- (472) Park, S. C.; Pradeep, T.; Kang, H. *J. Chem. Phys.* **2000**, *113*, 9373.
- (473) Kim, J. H.; Shin, T.; Jung, K. H.; Kang, H. *ChemPhysChem* **2005**, *6*, 440.
- (474) Kim, J. H.; Kim, Y. K.; Kang, H. *J. Phys. Chem. C* **2007**, *111*, 8030.
- (475) Jungwirth, P.; Tobias, D. J. *J. Phys. Chem. B* **2002**, *106*, 6361.
- (476) Park, S. C.; Jung, K. H.; Kang, H. *J. Chem. Phys.* **2004**, *121*, 2765.
- (477) Park, S. C.; Kang, H. *J. Phys. Chem. B* **2005**, *109*, 5124.
- (478) Lee, C. W.; Lee, P. R.; Kang, H. *Angew. Chem., Int. Ed.* **2006**, *45*, 5529.
- (479) Lee, C. W.; Lee, P. R.; Kim, Y. K.; Kang, H. *J. Chem. Phys.* **2007**, *127*.
- (480) Moon, E. S.; Lee, C. W.; Kang, H. *Phys. Chem. Chem. Phys.* **2008**, *10*, 4814.
- (481) Vacha, R.; Buch, V.; Milet, A.; Devlin, P.; Jungwirth, P. *Phys. Chem. Chem. Phys.* **2007**, *9*, 4736.
- (482) Lilach, Y.; Iedema, M. J.; Cowin, J. P. *Surf. Sci.* **2008**, *602*, 2886.
- (483) Moon, E. S.; Lee, C. W.; Kim, J. K.; Park, S. C.; Kang, H. *J. Chem. Phys.* **2008**, *128*.
- (484) Kim, J. H.; Kim, Y. K.; Kang, H. *J. Phys. Chem. C* **2009**, *113*, 321.
- (485) Beattie, J. K.; Djerdjev, A. N.; Warr, G. G. *Faraday Discuss.* **2009**, *141*, 31.
- (486) Cyriac, J.; Pradeep, T. *Chem. Phys. Lett.* **2005**, *402*, 116.
- (487) Souda, R. *Chem. Phys. Lett.* **2005**, *413*, 171.
- (488) Millikan, R. C.; Pitzer, K. S. *J. Am. Chem. Soc.* **1958**, *80*, 3515.
- (489) Jenniskens, P.; Blake, D. F. *Science* **1994**, *265*, 753.
- (490) Johari, G. P.; Hallbrucker, A.; Mayer, E. *Nature* **1987**, *330*, 552.
- (491) Jenniskens, P.; Banham, S. F.; Blake, D. F.; McCoustra, M. R. *S. J. Chem. Phys.* **1997**, *107*, 1232.
- (492) George, S. M.; Livingston, F. E. *Surf. Rev. Lett.* **1997**, *4*, 771.
- (493) Holmes, N. S.; Sodeau, J. R. *J. Phys. Chem. A* **1999**, *103*, 4673.
- (494) Kumar, G. N.; Cyriac, J.; Bag, S.; Pradeep, T. *J. Phys. Chem. C* **2009**, *113*, 14258.
- (495) Moon, E. S.; Yoon, J.; Kang, H. *J. Chem. Phys.* **2010**, *133*.
- (496) Moon, E.-S.; Yoon, J.; Kang, H. *J. Chem. Phys.* **2010**, *133*.
- (497) Kim, J. H.; Kim, Y. K.; Kang, H. *J. Chem. Phys.* **2009**, *131*, 044705.
- (498) Buch, V.; Sadlej, J.; Aytemiz-Uras, N.; Devlin, J. P. *J. Phys. Chem. A* **2002**, *106*, 9374.
- (499) Everest, M. A.; Pursell, C. J. *J. Chem. Phys.* **2001**, *115*, 9843.
- (500) Marchand, P.; Riou, S.; Ayotte, P. *J. Phys. Chem. A* **2006**, *110*, 11654.
- (501) Bahr, S.; Borodin, A.; Hoffit, O.; Kempter, V.; Allouche, A. *J. Chem. Phys.* **2005**, *122*.
- (502) Park, S. C.; Kim, J. K.; Lee, C. W.; Kang, H. *ChemPhysChem* **2007**, *8*, 2520.
- (503) Moon, E. S.; Kang, H.; Oba, Y.; Watanabe, N.; Kouchi, A. *Astrophys. J.* **2010**, *713*, 906.
- (504) Russell, R. W.; Soifer, B. T.; Puetter, R. C. *Astron. Astrophys.* **1977**, *54*, 959.
- (505) Park, S. C.; Maeng, K. W.; Kang, H. *Chem.—Eur. J.* **2003**, *9*, 1706.
- (506) Olah, G. A.; Schlosbe, Rh; Halpern, Y.; Demember, J. R. *J. Am. Chem. Soc.* **1972**, *94*, 156.
- (507) Gunster, J.; Souda, R. *Chem. Phys. Lett.* **2003**, *371*, 534.
- (508) Gunster, J.; Kempter, V.; Souda, R. *J. Phys. Chem. B* **2005**, *109*, 17169.
- (509) Souda, R. *J. Chem. Phys.* **2006**, *125*, 044706.
- (510) Huthwelker, T.; Ammann, M.; Peter, T. *Chem. Rev.* **2006**, *106*, 1375.
- (511) Kim, Y. K.; Kim, S. K.; Kim, J. H.; Kang, H. *J. Phys. Chem. C* **2009**, *113*, 16863.
- (512) Magnera, T. F.; David, D. E.; Stulik, D.; Orth, R. G.; Jonkman, H. T.; Michl, J. *J. Am. Chem. Soc.* **1989**, *111*, 5036.
- (513) Jonkman, H. T.; Michl, J. *J. Am. Chem. Soc.* **1981**, *103*, 733.
- (514) Orth, R. G.; Jonkman, H. T.; Michl, J. *J. Am. Chem. Soc.* **1981**, *103*, 1564.
- (515) Souda, R.; Kawanowa, H.; Kondo, M.; Gotoh, Y. *J. Chem. Phys.* **2003**, *119*, 6194.
- (516) Souda, R. *Phys. Rev. B* **2004**, *70*, 165412.
- (517) Conlan, X. A.; Fletcher, J. S.; Lockyer, N. P.; Vickerman, J. C. *J. Phys. Chem. C* **2010**, *114*, 5468.
- (518) Conlan, X. A.; Lockyer, N. P.; Vickerman, J. C. *Rapid Commun. Mass Spectrom.* **2006**, *20*, 1327.
- (519) Conlan, X. A.; Biddulph, G. X.; Lockyer, N. P.; Vickerman, J. C. *Appl. Surf. Sci.* **2006**, *252*, 6506.
- (520) Wucher, A.; Cheng, J.; Winograd, N. *J. Phys. Chem. C* **2008**, *112*, 16550.
- (521) Donsig, H. A.; Vickerman, J. C. *J. Chem. Soc., Faraday Trans.* **1997**, *93*, 2755.
- (522) Narita, A.; Honda, M.; Hirao, N.; Baba, Y.; Yaita, T. *Appl. Surf. Sci.* **2008**, *255*, 883.
- (523) Chatterjee, R.; Riederer, D. E.; Postawa, Z.; Winograd, N. *J. Phys. Chem. B* **1998**, *102*, 4176.
- (524) Chatterjee, R.; Riederer, D. E.; Postawa, Z.; Winograd, N. *Rapid Commun. Mass Spectrom.* **1998**, *12*, 1226.
- (525) Chatterjee, R.; Postawa, Z.; Winograd, N.; Garrison, B. J. *J. Phys. Chem. B* **1999**, *103*, 151.
- (526) Ruttten, F. J. M.; Tadesse, H.; Licence, P. *Angew. Chem., Int. Ed.* **2007**, *46*, 4163.
- (527) Yue, Y. Z.; Angell, C. A. *Nature* **2004**, *427*, 717.
- (528) Velikov, V.; Borick, S.; Angell, C. A. *Science* **2001**, *294*, 2335.
- (529) Souda, R. *J. Chem. Phys.* **2004**, *121*, 8676.
- (530) Souda, R. *Phys. Rev. Lett.* **2004**, *93*, 235502.
- (531) Souda, R. *Nucl. Instrum. Methods Phys. Res., Sect. B* **2005**, *232*, 125.
- (532) Souda, R. *J. Phys. Chem. B* **2005**, *109*, 21879.
- (533) Souda, R. *J. Phys. Chem. B* **2009**, *113*, 15831.
- (534) Souda, R. *J. Phys. Chem. B* **2008**, *112*, 11976.
- (535) Souda, R. *Phys. Rev. B* **2005**, *72*, 115414.

- (536) Souda, R. *J. Phys. Chem. B* **2008**, *112*, 15349.
- (537) Souda, R. *J. Phys. Chem. B* **2008**, *112*, 12439.
- (538) Souda, R. *J. Phys. Chem. B* **2006**, *110*, 14787.
- (539) Souda, R. *J. Chem. Phys.* **2007**, *127*, 214505.
- (540) Souda, R. *J. Chem. Phys.* **2006**, *125*, 181103.
- (541) Souda, R. *J. Phys. Chem. B* **2007**, *111*, 5628.
- (542) Souda, R. *J. Phys. Chem. B* **2007**, *111*, 11209.
- (543) Smith, R. S.; Kay, B. D. *Nature* **1999**, *398*, 788.
- (544) Mishima, O.; Stanley, H. E. *Nature* **1998**, *396*, 329.
- (545) Souda, R. *J. Phys. Chem. B* **2010**, *114*, 10734.
- (546) Souda, R. *J. Phys. Chem. B* **2008**, *112*, 2649.
- (547) Debenedetti, P. G.; Stillinger, F. H. *Nature* **2001**, *410*, 259.
- (548) Keddie, J. L.; Jones, R. A. L.; Cory, R. A. *Europhys. Lett.* **1994**, *27*, 59.
- (549) Kawana, S.; Jones, R. A. L. *Phys. Rev. E* **2001**, *63*.
- (550) Jackson, C. L.; McKenna, G. B. *J. Non-Cryst. Solids* **1991**, *131*, 221.
- (551) Souda, R. *J. Phys. Chem. B* **2006**, *110*, 17524.
- (552) Souda, R. *J. Chem. Phys.* **2010**, *133*, 214704.
- (553) Souda, R. *J. Phys. Chem. C* **2011**, *115*, 8136.
- (554) Souda, R. *Surf. Sci.* **2011**, *605*, 1257.
- (555) Stevenson, K. P.; Kimmel, G. A.; Dohnalek, Z.; Smith, R. S.; Kay, B. D. *Science* **1999**, *283*, 1505.
- (556) Kimmel, G. A.; Stevenson, K. P.; Dohnalek, Z.; Smith, R. S.; Kay, B. D. *J. Chem. Phys.* **2001**, *114*, 5284.
- (557) Souda, R. *J. Phys. Chem. B* **2004**, *108*, 12159.
- (558) Kawanowa, H.; Kondo, M.; Gotoh, Y.; Souda, R. *Surf. Sci.* **2004**, *566*, 1190.
- (559) Souda, R. *J. Phys. Chem. B* **2004**, *108*, 283.
- (560) Kondo, M.; Kawanowa, H.; Gotoh, Y.; Souda, R. *Appl. Surf. Sci.* **2004**, *237*, 509.
- (561) Kondo, M.; Kawanowa, H.; Gotoh, Y.; Souda, R. *Surf. Sci.* **2005**, *594*, 141.
- (562) Kondo, M.; Kawanowa, H.; Gotoh, Y.; Souda, R. *J. Chem. Phys.* **2004**, *121*, 8589.
- (563) Wojciechowski, I. A.; Kutliev, U.; Sun, S. X.; Szakal, C.; Winograd, N.; Garrison, B. J. *Appl. Surf. Sci.* **2004**, *231*, 72.
- (564) Wojciechowski, I. A.; Sun, S. X.; Szakal, C.; Winograd, N.; Garrison, B. J. *J. Phys. Chem. A* **2004**, *108*, 2993.
- (565) Souda, R. *Phys. Rev. B* **2007**, *75*, 184116.
- (566) Souda, R. *J. Chem. Phys.* **2005**, *122*, 134711.
- (567) Souda, R. *Surf. Sci.* **2003**, *547*, 403.
- (568) Souda, R.; Kawanowa, H.; Kondo, M.; Gotoh, Y. *J. Chem. Phys.* **2004**, *120*, 5723.
- (569) Donsig, H. A.; Herridge, D.; Vickerman, J. C. *J. Phys. Chem. A* **1998**, *102*, 2302.
- (570) Donsig, H. A.; Herridge, D.; Vickerman, J. C. *J. Phys. Chem. A* **1999**, *103*, 9211.
- (571) Kimmel, G. A.; Petrik, N. G.; Dohnalek, Z.; Kay, B. D. *Phys. Rev. Lett.* **2005**, *95*, 166102.
- (572) Souda, R. *Surf. Sci.* **2006**, *600*, 3135.
- (573) Souda, R. *J. Phys. Chem. B* **2006**, *110*, 17884.
- (574) Gunster, J.; Souda, R. *Langmuir* **2006**, *22*, 6939.
- (575) Gunster, J.; Souda, R. *Phys. Rev. B* **2005**, *71*, 041407(R).
- (576) Souda, R. *J. Chem. Phys.* **2009**, *130*, 244707.
- (577) Souda, R. *J. Phys. Chem. B* **2009**, *113*, 12973.
- (578) Souda, R.; Gunster, J. *J. Chem. Phys.* **2008**, *129*.
- (579) Souda, R. *Surf. Sci.* **2010**, *604*, 1694.
- (580) Collier, W. B.; Ritzhaupt, G.; Devlin, J. P. *J. Phys. Chem.* **1984**, *88*, 363.
- (581) Souda, R. *J. Chem. Phys.* **2003**, *119*, 2774.
- (582) Fletcher, J. S.; Henderson, A.; Horn, A. B.; Vickerman, J. C. *J. Phys. Chem. B* **2004**, *108*, 5960.
- (583) Vickerman, J. C.; Oakes, A.; Gamble, H. *Surf. Interface Anal.* **2000**, *29*, 349.
- (584) Vickerman, J. C. *Surf. Sci.* **2009**, *603*, 1926.
- (585) Cliff, B.; Lockyer, N.; Jungnickel, H.; Stephens, G.; Vickerman, J. C. *Rapid Commun. Mass Spectrom.* **2003**, *17*, 2163.
- (586) Piwowar, A. M.; Lockyer, N. P.; Vickerman, J. C. *Anal. Chem.* **2009**, *81*, 1040.
- (587) Cheng, J.; Wucher, A.; Winograd, N. *J. Phys. Chem. B* **2006**, *110*, 8329.
- (588) Garrison, B. J.; Postawa, Z. *Mass Spectrom. Rev.* **2008**, *27*, 289.
- (589) Wucher, A.; Sun, S. X.; Szakal, C.; Winograd, N. *Anal. Chem.* **2004**, *76*, 7234.
- (590) Wucher, A.; Sun, S.; Szakal, C.; Winograd, N. *Appl. Surf. Sci.* **2004**, *231*, 68.
- (591) Szakal, C.; Kozole, J.; Russo, M. F.; Garrison, B. J.; Winograd, N. *Phys. Rev. Lett.* **2006**, *96*, 216104.
- (592) Szakal, C.; Kozole, J.; Winograd, N. *Appl. Surf. Sci.* **2006**, *252*, 6526.
- (593) Russo, M. F.; Wojciechowski, I. A.; Garrison, B. J. *Appl. Surf. Sci.* **2006**, *252*, 6423.
- (594) Kutliev, U. O. *Comput. Mater. Sci.* **2008**, *43*, 700.
- (595) de Maaijer-Gielbert, J.; Beijersbergen, J. H. M.; Kistemaker, P. G.; Weeding, T. L. *Int. J. Mass Spectrom. Ion Processes* **1996**, *153*, 119.
- (596) Schmidt, L.; Fritsch, H. W.; Jungclas, H. *Rapid Commun. Mass Spectrom.* **1993**, *7*, 507.
- (597) Jungclas, H.; Wieghaus, A.; Schmidt, L.; Popova, A. M.; Komarov, V. V. *J. Am. Soc. Mass Spectrom.* **1999**, *10*, 471.
- (598) Martin, J. S.; Greeley, J. N.; Morris, J. R.; Jacobs, D. C. *J. Chem. Phys.* **1992**, *97*, 9476.
- (599) Park, K. H.; Kim, B. C.; Kang, H. J. *J. Chem. Phys.* **1992**, *97*, 2742.
- (600) Terasaki, A.; Tsukuda, T.; Yasumatsu, H.; Sugai, T.; Kondow, T. *J. Chem. Phys.* **1996**, *104*, 1387.
- (601) Wieghaus, A.; Schmidt, L.; Popova, A. M.; Komarov, V. V.; Jungclas, H. *J. Mass Spectrom.* **1999**, *34*, 1178.
- (602) Kane, T. E.; Somogyi, A.; Wysocki, V. H. *Org. Mass Spectrom.* **1993**, *28*, 1665.
- (603) Mair, C.; Fiegele, T.; Biasioli, F.; Futrell, J. H.; Herman, Z.; Mark, T. D. *Int. J. Mass Spectrom.* **1999**, *188*, L1.
- (604) Laurens, C. R.; Rosu, M. F.; Pleiter, F.; Niesen, L. *Phys. Rev. Lett.* **1997**, *78*, 4075.
- (605) Laurens, C. R.; Rosu, M. F.; Pleiter, F.; Niesen, L. *Hyperfine Interact.* **1999**, *121*, 59.
- (606) Laurens, C. R.; Venema, L.; Kemerink, G. J.; Niesen, L. *Nucl. Instrum. Methods Phys. Res., Sect. B* **1997**, *129*, 429.
- (607) Benz, L.; Tong, X.; Kemper, P.; Lilach, Y.; Kolmakov, A.; Metiu, H.; Bowers, M. T.; Buratto, S. K. *J. Chem. Phys.* **2005**, *122*, 081102.
- (608) Moon, E.-S.; Kang, H.; Oba, Y.; Watanabe, N.; Kouchi, A. *Astrophys. J.* **2010**, *713*, 906.
- (609) Lee, C.-W.; Lee, P.-R.; Lahaye, R. J. W. E.; Kang, H. *Phys. Chem. Chem. Phys.* **2009**, *11*, 2268.
- (610) Kang, H.; Lee, C. W.; Hwang, C. H.; Kim, C. M. *Appl. Surf. Sci.* **2003**, *203*, 842.
- (611) Zheng, L. L.; Wucher, A.; Winograd, N. *Anal. Chem.* **2008**, *80*, 7363.
- (612) Stapel, D.; Benninghoven, A. *Appl. Surf. Sci.* **2001**, *183*, 301.
- (613) Cheng, J.; Winograd, N. *Appl. Surf. Sci.* **2006**, *252*, 6498.
- (614) Kozole, J.; Wucher, A.; Winograd, N. *Anal. Chem.* **2008**, *80*, 5293.
- (615) Souda, R. *Phys. Rev. B* **2001**, *63*, 125420.
- (616) Souda, R. *Surf. Sci.* **2004**, *551*, 171.
- (617) Souda, R. *J. Chem. Phys.* **2009**, *131*, 164501.
- (618) Souda, R. *Surf. Sci.* **2011**, *605*, 793.
- (619) Cyriac, J.; Wlekinski, M.; Li, G.; Gao, L.; Cooks, R. G. *Analyst* **2012**, *137*, 1363.

GRAPHENE FOR ENVIRONMENTAL AND BIOLOGICAL APPLICATIONS

T. S. SREEPRASAD and T. PRADEEP*

*DST Unit of Nanoscience, Department of Chemistry,
Indian Institute of Technology Madras, Chennai – 600036, India*

**pradeep@iitm.ac.in*

Received 13 October 2011

Published 16 July 2012

The latest addition to the nanocarbon family, graphene, has been proclaimed to be the material of the century. Its peculiar band structure, extraordinary thermal and electronic conductance and room temperature quantum Hall effect have all been used for various applications in diverse fields ranging from catalysis to electronics. The difficulty to synthesize graphene in bulk quantities was a limiting factor of it being utilized in several fields. Advent of chemical processes and self-assembly approaches for the synthesis of graphene analogues have opened-up new avenues for graphene based materials. The high surface area and rich abundance of functional groups present make chemically synthesized graphene (generally known as graphene oxide (GO) and reduced graphene oxide (RGO) or chemically converted graphene) an attracting candidate in biotechnology and environmental remediation. By functionalizing graphene with specific molecules, the properties of graphene can be tuned to suite applications such as sensing, drug delivery or cellular imaging. Graphene with its high surface area can act as a good adsorbent for pollutant removal. Graphene either alone or in combination with other materials can be used for the degradation or removal of a large variety of contaminants through several methods. In this review some of the relevant efforts undertaken to utilize graphene in biology, sensing and water purification are described. Most recent efforts have been given precedence over older works, although certain specific important examples of the past are also mentioned.

Keywords: Graphene oxide; functionalization; sensing; water purification; therapy.

1. Introduction

Graphene, the latest addition to the nanocarbon family, is a single atom thick extended two-dimensional (2D) sheet made up of honey comb array of carbon atoms which has become one of the hottest topics in the fields of materials science, physics, chemistry and nanotechnology. It is the building block for other allotropes such as 0D fullerene, 1D carbon nanotubes and 3D graphite. However, graphene has some special properties compared to other forms such as its unusual structural characteristics and electronic flexibility. Properties such as high planar surface area ($\sim 2630 \text{ m}^2/\text{g}$), exceptional electrical ($\sim 2000 \text{ S/cm}$) and thermal

(5300 W/mK) conductivity, transparency to visible light, exceptional mechanical strength (Young's modulus, ~ 1100 GPa) have all been expected to aid in many technological applications. However, most of the reported works in graphene related materials are concerned with catalytic or electronic processes. Two of the emerging areas of application for graphene based materials are in biology and environment.

In this review, the use of graphene (mostly the chemical analogue graphene oxide (GO) and reduced graphene oxide (RGO) and their composites for biology and water purification is outlined. Chemistry has provided many comforts and benefits to mankind. However, now we are facing the great task of cleaning the waste generated during industrial and agricultural activities, which contaminates our air and water. The search for a cheap and highly efficient adsorbent is still on. Due to its large surface area and the abundance of functional groups, graphene seems to be an ideal candidate. The recent research activities emphasize this point. Nanomaterials, due to the similarities to the size regime of biomolecules, have been interesting for applications in biotechnology. However, cytotoxicity of some of the nanomaterials is a major hindering factor when they are considered for specialized applications such as drug delivery or cellular imaging. Chemically prepared graphene, owing to the presence of large functionalities which can be functionalized as per need, put forth a new vehicle for such applications, where the biocompatibility can be modulated by easy functionalization. Hence this review focuses on the application of graphenic materials in biology and environmental remediation/sensing applications. Because of the similarities, the term "graphene" will be used commonly for both GO and RGO in some places. Efforts undertaken to use graphene or its composites for sensing and/or removing contaminants from water will be focused upon. Some application possibilities in biology which can have indirect applications in water purification will also be discussed. Graphene as a nanostructure and its biocompatibility and bio-studies also will be discussed briefly.

1.1. Graphene for environmental applications

All life forms depend on the availability of pure water. Water gets greatly affected by agricultural and industrial activities. Nanomaterials, owing to their unique properties such as high surface area and greater number of reaction sites per unit area are being considered as potential candidates for removing various contaminants from air and water. A large variety of nanosystems is being considered or is being used for this purpose now. A recent review by Pradeep and Anshup,¹ illustrates the large versatility of nanosystems for these applications. Traditionally, carbon based materials have found to be useful in water purification. Bulk carbon (activated) is a versatile adsorbent that is heavily used to remove various pollutants from the aqueous medium. Carbon in the native form and its composites has been investigated to improve the removal capacity. Recent attention has been focused on carbon based nanomaterials for decontamination and sensing contaminants from water. Nanocarbon forms like carbon nanotubes have been frequently used for this application.

Even though historically the most important and widely used application of bulk carbon is in environmental remediation, the use of graphene or their chemical counterparts, GO and RGO [also known as chemically converted graphene (CCG)] for this applications is limited. Features such as large surface area and presence of surface functional groups can make these systems highly desirable adsorbent candidates. Most applications of graphene have been reviewed. However, the use of graphenic materials for large-scale and down to earth application like water purification is limited. The difficulty in large-scale synthesis was the principal reason behind graphene not being utilized for such applications. The advent of chemical methods and self assembly approaches has assisted to overcome this difficulty. Recent literature has shown that graphene and their composites have been venturing into water purification and sensing.

2. Graphene for Sensing Applications: Contaminant and Biological Molecule Sensing

Surface modification or functionalization of graphene surface with specific receptors or functionalities is necessary for exploring sensing applications. A great deal of research activity is happening in this regard. The scope of the review does not allow a detailed description of all the events undertaken. However, a short summary of some of the most relevant efforts is given here.

Most of these efforts are concentrated on developing graphene field-effect transistors (FETs) for chemical and biological sensing. One of the pioneering work on graphene based sensors was done by Schedin *et al.* in 2007, where they detected single gaseous molecules.² The step-like changes in resistance caused by the change the local carrier concentration of graphene was used for ultrasensitive detection. Following this, a large number of people have used graphene for sensing. FET devices which are sensitive to hydrogen gas at room temperature were fabricated from RGO with different edge to plane ratios by introducing holes into the basal plane through electrochemical deposition of metal nanoparticles.³ The change in the electrical conductance of the composite as a function of gas concentration was taken as the sensor response. A mercury detection device was developed by Zhang *et al.* where they self-assembled 1-octadecanethiol monolayers on graphene.⁴ These alkanethiol modified graphene FETs were used for mercury detection. The detection of 10 ppm mercury was achieved in this method. Figure 1 shows the atomic force microscope (AFM) and scanning tunnelling microscope (STM) images of the graphene device (Fig. 1(A) and 1(B) respectively). The response of the device to 10 ppm mercury also can be seen [Fig. 1(C)]. Lu *et al.* found that under a positive gate potential (V_g), RGO device can give an instantaneous response and fast recovery for NH_3 sensing at room temperature and the sensing behavior can be modulated by controlling V_g .⁵ The V_g -dependent NH_3 sensing of RGO was mentioned to be due to the ambipolar transport of RGO and the V_g -induced change in the graphene work function. The Coulomb interaction between NH_3 and the FET might also contribute to these changes.

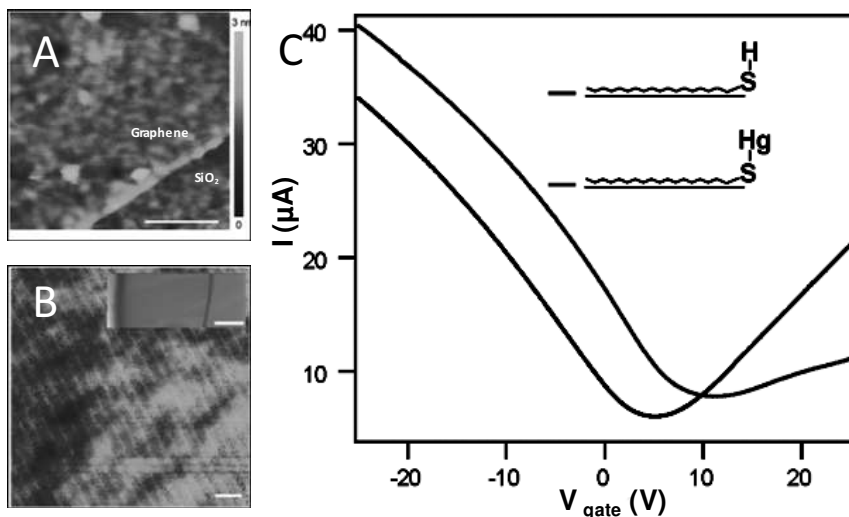


Fig. 1. (A) Tapping-mode AFM showing height and phase images of self-assembled 1-octadecanethiol nanostructures on a single-layer graphene supported on SiO₂ substrate. Scale bars, 100 nm. (B) Large-scale STM image showing configuration details of the self-assembled 1-octadecanethiol on graphene. Scale bar, 10 nm. Inset, optical image of the metal-contacted graphene. Scale bar, 20 μm. (C) Current versus back gate voltage characteristics of a modified graphene FET before (black) and after (red) contacting with 10 ppm mercury solution. Source: Adapted from Zhang *et al.* (2010).

A glucose sensor consisting of graphene platelet-glucose oxidase (GP-GOD) nanostructures, prepared through the self-assembly of GOD and chitosan (CS) functionalized GPs by simple electrostatic attraction between the positively charged CS-stabilized GP and negatively charged GOD was reported by Liu *et al.*⁶ The preparation and use of N-doped graphene for glucose bio-sensing with concentrations as low as 0.01 mM in the presence of interferences was reported by Wang *et al.*⁷ N-doped graphene was synthesized via nitrogen plasma treatment of graphene synthesized via a chemical method. Also, N-doped graphene electrode showed 400 mV shift in the reduction potential of H₂O₂ positively with around 20 times current enhancement compared with a glassy carbon electrode.⁷ Choi *et al.* reported a flexible conductive composite films made up of GO and nafion through self-assembly and directional convective-assembly in solution chemistry.⁸ These films were used for the electrochemical bio-sensing for organophosphate. The system had a sensitivity of 10.7 nA/μM and detection limit of 1.37 × 10⁻⁷ M with a response time of < 3 s.⁸ A covalent composite between biocompatible poly-L-lysine (PLL) and graphene nanosheets was used as an amplified biosensor towards H₂O₂ as well.⁹

A graphene modified electrode for the voltammetric detection of catechol and hydroquinone simultaneously was reported recently.¹⁰ A well-defined peak and significant increase of peak current were observed at the graphene modified glassy carbon electrode (GR/GCE), which clearly demonstrated that graphene could be

used as an efficient promoter to enhance the kinetics of the electrochemical process of catechol and hydroquinone. A composite film consisting of Au nanoparticles and graphene was used for highly selective and sensitive detection of Hg(II).¹¹ They concluded that the composite film greatly facilitates electron-transfer processes and the sensing behavior for Hg(II) detection, leading to a remarkably improved sensitivity and selectivity. A similar methodology was used for Cd²⁺ sensing by Li *et al.*¹² The ultrasensitive platform was fabricated by combining the nafion-graphene nanocomposite film with differential pulse anodic stripping voltameter. They found that using this platform, Cd²⁺ can be sensed from real water with good recovery.

Chemically derived GO thin film was used as a humidity sensitive coating on quartz crystal microbalances (QCMs) for humidity detection.¹³ The resultant sensors showed excellent humidity sensitivity properties with a maximum sensitivity of 22.1 Hz/% relative humidity (RH) and a linear frequency response versus RH in the wide detection range of 6.4%–93.5% RH. The frequency response of the QCMs was suggested to be dependent on water molecules adsorbed/desorbed masses on GO thin film in the low RH range, and on both water molecules adsorbed/desorbed masses on GO thin film and variations in interlayer expansion stress of GO thin film derived from swelling effect in the high RH range.¹³ A highly efficient chemical sensor for ethanol using Al₂O₃/Graphene nanocomposites was reported by Jiang *et al.*¹⁴

Through a facile, one-step process involving supercritical CO₂ (SC CO₂), Al₂O₃/Graphene nanocomposites were fabricated from GO solution. The as-prepared nanocomposite displayed high catalytic chemiluminescence (CL) sensitivity and high selectivity to ethanol gas. An appreciable response was obtained for low concentration of 9.6 mg mL⁻¹ ethanol at 200°C, pointing the promise of the fabricated nanocomposite. An RGO-quantum dots (QDs) composite for amplified electrochemiluminescence (ECL) based sensing of acetylcholine was reported by Deng *et al.*¹⁵ The structural defects of GO quenches the ECL emission of QDs coated on GO modified electrode. Due to the restoration of double bonds, RGO-QDs showed ECL emission. Two ECL biosensors for choline and acetylcholine were fabricated by covalently cross-linking choline oxidase (ChO) or ChO-acetylcholinesterase on the QDs/RGO modified electrode. This showed the linear response ranges and detection limits of 10–210 μM and 8.8 μM for choline, and 10–250 μM and 4.7 μM for acetylcholine, respectively.

Another category of sensors based on graphene utilizes Surface-enhanced Raman spectroscopy (SERS) based sensing/detection protocols. Liu *et al.* recently devised an ultrasensitive SERS based strategy for the detection of aromatic molecules.¹⁶ They fabricated Ag nanoparticle attached graphene films where GO acts as the matrix which catches the aromatic molecule and Ag nanoparticles aids in the localized surface plasmon resonance based SERS property. By using positively charged crystal violet (CV), negatively charged amaranth (a cosmopolitan genus of herbs) and neutral phosphorus triphenyl (PPh₃) as model molecules, they demonstrated the utility of the above hybrid system. A similar strategy for the detection of

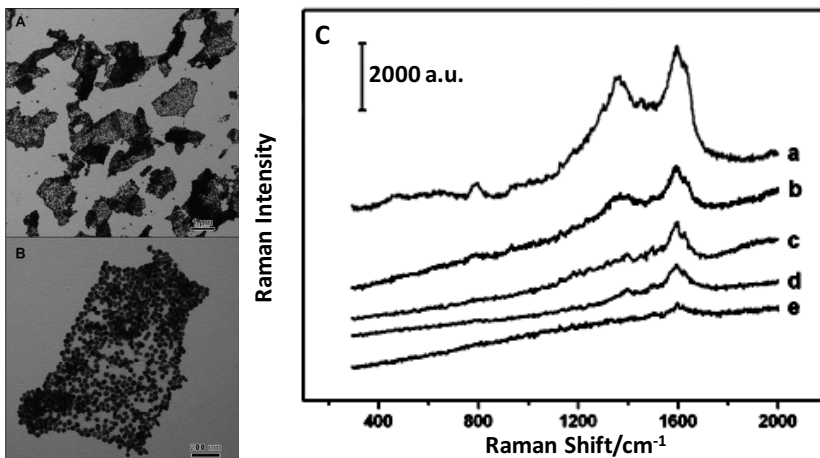


Fig. 2. (A) and (B) TEM images of the GO/PDDA/AgNPs at different magnifications. (C) SERS spectra of 9 nM folic acid obtained in the GO/PDDA/AgNP solutions with (a) 0.02 mg/mL, (b) 0.01 mg/mL, (c) 0.004 mg/mL, (d) 0.0025 mg/mL, (e) 0.002 mg/mL graphitic carbon. Source: Adapted from Ren *et al.* (2011).

folic acid was also reported recently. Through a self-assembly method with the help of poly(diallyldimethyl ammonium chloride) (PDDA) as the functional macromolecules, GO/Ag nanoparticle hybrids (GO/PDDA/AgNPs) were fabricated. Using the SERS enhancement of the hybrid, folic acid was detected with a very low detection limit of 9 nM. Figure 2 shows the TEM images (A and B) and the SERS detection capability of the formed composite.

Graphene has been used for biosensing applications as well. Li *et al.* developed a graphene-based fluorescence resonance energy transfer (FRET) biosensor which included a fluorescein amidite (FAM)-labeled ssDNA adsorbed onto GO.^{17,18} The FRET between FAM and GO, results in the rapid quenching of luminescence. However, the binding between probe ssDNA and a complementary ssDNA changes the conformation, and releases FAM-ssDNA from the GO surface, restoring fluorescence which results in the detection. Mohanty and Berry reported a graphene based bio-device which can sense single bacterium and can work as a label-free DNA sensor.¹⁹ The attachment of single-bacterium generated ~ 1400 charge carriers in a *p*-type chemically modified graphene and single-stranded DNA tethered on graphene hybridizes with its complementary DNA strand, increased the hole density by $5.61 \times 10^{12} \text{ cm}^{-2}$. Figure 3 illustrates the usefulness and accuracy of the FETs fabricated. Ohno *et al.* recently reported a graphene based FET for chemical and biological sensing application.²⁰ Single layer graphene obtained from micromechanical cleavage was used to construct FET, which can sense change in solution pH with a lowest detection limit (signal/noise = 3) of the 0.025. Using the same set up they were able to detect different charge types of biomolecules due to their isoelectric point. Jang *et al.* developed a graphene-based FRET platform that has

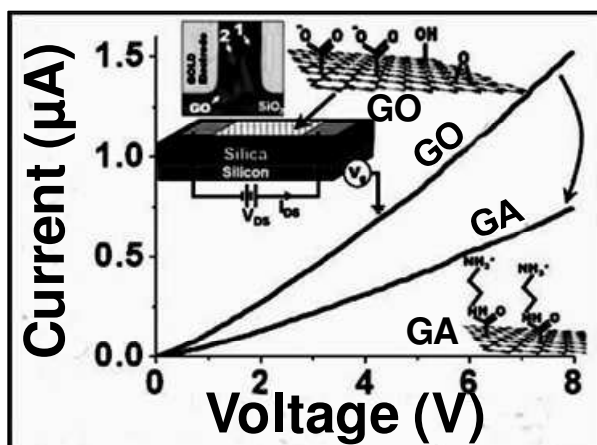


Fig. 3. Current-voltage behavior of the GO and GA devices. The insets show the device with GO/GA between gold electrodes and a schematic of the GO and GA's chemical structure. Source: Mohanty and Berry (2008).

been developed for detection of helicase-mediated unwinding of duplex DNA.²¹ Graphene-based FRET biosensors for multicolor DNA analysis was developed by He *et al.*²² Employing molecular beacons (MBs), graphene-based FRET biosensors were fabricated with enhanced sequence-specific detection of target DNA.²³ The two ends of a MB were labeled with a fluorophore and a GO/RGO. MBs did not fluoresce until they have hybridized with the target. In this study, quantum dots were used as the fluorophores owing to its broad absorption and narrow emission spectra. This FRET biosensor displayed good selectivity and high sensitivity, with a detection limit for target cyclin DNA of 12 nM.²³ GO has been used as the 'nanoquencher', with increased sensitivity and single-base mismatch selectivity for target DNA as well.²⁴ Choi *et al.* recently devised a strategy to develop a electrical sensor for DNA.²⁵ Through microwave-assisted sulfonation, highly water-soluble graphene sheets were synthesized and the complex interactions of the functionalized graphene with DNA resulted in an advanced resistive sensing platform for the electrical detection of label-free DNA.

Graphene based FET have been developed for the sensing of ion, small molecules and proteins as well. Most of these studies utilized the specific binding of aptamers towards target molecules. Wen *et al.* devised a graphene based FET containing Ag⁺-specific aptamer for the detection of Ag⁺.²⁶ Ag⁺ induces a conformational change of the aptamer which in turn leads to the recovery of FAM fluorescence. A highly selective FRET sensor for detection of bovine thrombin was developed by Chang *et al.*²⁷

The detection procedure was similar to earlier report. However, a dye-labeled aptamer probe and graphene was used in this study. Sodium dodecyl benzene sulfonate (SDBS) was used for the chemical reduction of GO to produce SDBS-graphene.

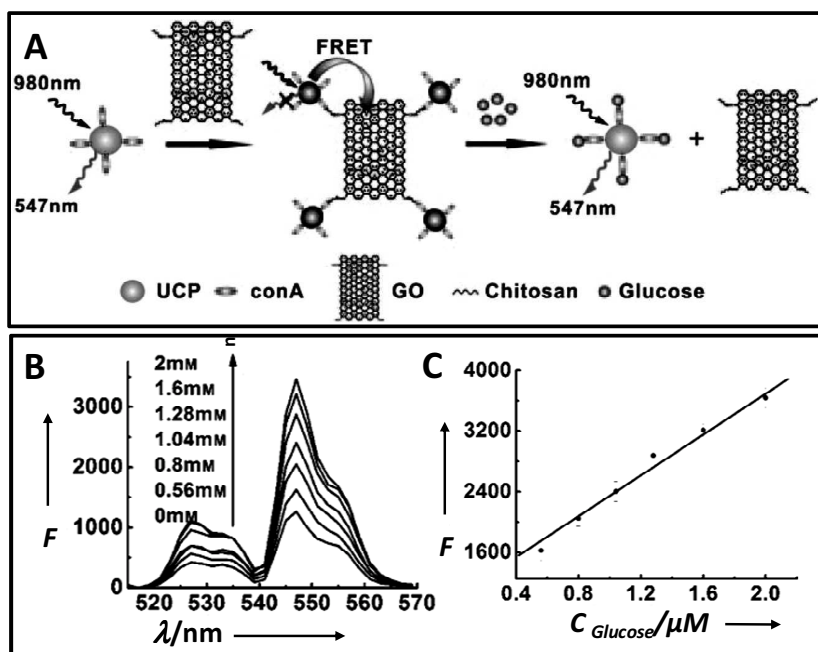


Fig. 4. (A) Schematic illustration of the UCP–GO biosensing platform and the mechanism of glucose determination. (B) Fluorescence emission spectra of GO–CS–ConA–UCP complex in the presence of different concentrations of glucose in diluted serum. (C) Linear relationship between donor fluorescence intensity and glucose concentrations. *Source:* Adapted from Zhang *et al.* (2011).

Thrombin aptamer labeled with FAM was incubated with SDBS–graphene and upon introduction of thrombin into the aptamer/graphene solution, fluorescence recovery was observed. This was used for the detection. This graphene-based FRET sensor had a sensitive detection limit for thrombin in buffer upto 31.3 pM.

Change in fluorescence has been utilized for sensing of many materials. Recently graphene based sensors utilizing the change in fluorescence have appeared. A novel sensor for glucose determination based on FRET from upconverting phosphors (UCP) to GO was devised by Zhang *et al.*²⁸ The FRET from anti-Stokes fluorophores like UCP to GO was utilized for detecting glucose directly in serum samples. They also extended the strategy for the detection of other biologically significant molecules. Figure 4 illustrates the mechanism of sensing. Xu *et al.* reported a graphene based platform for the recognition of bovine serum albumin (BSA).²⁹ They found that the binding of squaraine (SQ) dyes to RGO/GO would enhance the fluorescence response of SQ to BSA. The attachment of SQ dyes to GO surface resulted in the quenching of its fluorescence and when BSA interacts with this hybrid resulted in the triggering of large fluorescence and hence the recognition of BSA. A novel GO based fluorescent biosensor platform for the sequence-specific recognition of double-stranded DNA (dsDNA) was formulated by Wu *et al.* recently which is based upon the DNA hybridization between dye-labeled single-stranded

DNA (ssDNA) and double-stranded DNA.³⁰ FAM labeled ssDNA upon adsorption onto GO loses its fluorescence. When the target dsDNA is added, hybridization occurs between this and ssDNA by desorbing it from GO. This results in the turning on of the fluorescence of the dye. The detection limit was found to be 14.3 nM in this method.

Using a similar strategy, an intracellular protease sensor for capsase-3 was reported by Wang *et al.*³¹ Fluorescence based strategy has been extended to metal ion sensing as well. A RGO–organic dye nanoswitch for the label-free, inexpensive, sensitive and selective detection of Hg^{2+} was recently reported by Huang *et al.*³² Here, RGO functions as an effective nanoquencher and highly selective nanosorbent. Acridine orange (AO) dye was anchored onto RGO via π -stacking interactions which resulted in the effectively quenching the fluorescence of AO because of the occurrence of long range resonance energy transfer (LrRET). When Hg^{2+} selectively gets attached to RGO, the interaction between the dye and RGO will be disturbed, resulting in restoration of dye fluorescence. The detection limit for Hg^{2+} was estimated to be about 2.8 nM. Graphene-DNAzyme based biosensor for amplified fluorescence “Turn-On” detection of Pb^{2+} was also reported recently. The detection limit of the devise was found to be 300 pM.³³

3. Graphene for Water Purification Related Applications

Historically, one of the major application arenas of carbon based materials has been in water purification. Carbon based materials ranging from charcoal to activated carbon to graphite have all been used for this purpose. The emergence of carbon based nanomaterials such as carbon nanotube (either pristine or as composite) has also been used for decontamination of drinking water. Recent literature suggests that the 2D graphene (RGO/GO) is also getting into this application. Due to the high surface area this material possesses, most of these efforts have been concentrated in using this exceptional surface area and to use RGO/GO as an adsorbent. Some relevant work in this regard is summarized here. Some efforts to construct composite useful for catalytic decomposition of contaminants are described first.

Photo-catalytic decomposition of contaminants using nanomaterials has seen intense research activity in recent times. Graphene based composites showed considerable efficiency in this aspect. The photocatalytic degradation of dye over a graphene gold nanoparticle hybrid under visible light irradiation was proposed by Xiong *et al.* for the first time.³⁴ Gold nanoparticles were deposited on the graphene substrate by the spontaneous reduction of HAuCl_4 by RGO. The photoactivity of RGO–Au was evaluated using rhodamine B (RhB) under visible light irradiation. A mechanism was proposed for the degradation as well. The dye will first get excited to dye*, which is followed by an electron transfer from dye* to graphene. Then, the electron is moved to a gold nanoparticle and will be trapped by O_2 to produce various reactive oxidative species (ROSSs). The dye⁺ finally degrades either by itself and/or by the ROSSs. Zhu *et al.* reported a graphene enwrapped

Ag/AgX (X = Br, Cl) nanocomposite plasmonic photocatalyst at water/oil interface.³⁵ They used it as a stable plasmonic photocatalyst for the photodegradation of methyl orange (MO) under visible-light irradiation. The combination of Ag/AgX with GO nanosheets resulted in the increased adsorptive capacity of Ag/AgX/GO to MO molecules whereas the smaller size of the Ag/AgX nanoparticles in Ag/AgX/GO, facilitated charge transfer, and the suppressed recombination of electron-hole pairs in Ag/AgX/GO resulting in the enhanced photocatalytic activity. Graphene-semiconductor composite has also been used for decontamination of water. GO-TiO₂ composite have been regarded widely as the best photocatalyst. Akhavan *et al.* synthesized GO nanosheets on TiO₂ thin films and used them for the photoinactivation of bacteria (*E. coli*) under solar illumination.³⁶ The incorporation of GO onto TiO₂ increased the antibacterial activity by a factor of 7.5. A composite prepared by self-assembling TiO₂ nanorods on large area GO sheets at a water/toluene interface was used for the photocatalytic degradation of methylene blue (MB) under UV light irradiation.³⁷ The large enhancement of photocatalytic activity was concluded to be due to the effective charge anti-recombination and the effective absorption of MB on GO. It was also observed that the degradation rate of MB in the second cycle is faster than that in the first cycle because of the reduction of GO under UV light irradiation.

Using TiCl₃ and GO as reactants, a GO-TiO₂ composites were fabricated by Chen *et al.*³⁸ The composite could be excited by visible light of wavelength higher than 510 nm. The composite was found to be useful in visible light induced degradation of MO. A TiO₂-graphene composite for the photodegradation of volatile organic solvent in the gas phase was reported by Zhang *et al.*³⁹ A TiO₂-graphene composite was prepared using hydrothermal reaction of GO and TiO₂ in an ethanol-water solvent. The composite showed much higher photocatalytic activity and stability than bare TiO₂ toward the gas-phase degradation of benzene. Structure and photocatalytic properties of TiO₂-GO intercalated composite was reported by Zang *et al.*⁴⁰ The composite was successfully prepared at 80°C with GO and titanium sulfate (Ti(SO₄)₂) as initial reactants. The photocatalytic properties of the composite under UV light showed that the degradation rate of MO is 1.16 mg min⁻¹ g⁻¹. A similar composite was fabricated by the *in situ* growth of TiO₂ in inter-layers of expanded graphite.⁴¹ The composite was used for the photocatalytic degradation of phenol under visible and UV light. The enhanced photocatalytic performance of the composite was concluded to be due to increased charge separation, improved light absorbance and light absorption width, and high adsorptivity for pollutants.

Zhang *et al.* showed that chemically bonded TiO₂ (P25) can be anchored onto graphene surface via a hydrothermal process and can be used for the photocatalytic degradation of dyes.⁴² Liang *et al.* synthesized graphene/TiO₂ nanocrystals hybrid by directly growing TiO₂ nanoparticles on GO sheets by a two-step method.⁴³ First, TiO₂ was first coated on GO sheets by hydrolysis and then crystallized into anatase nanocrystals by hydrothermal treatment in the second step. The composite showed

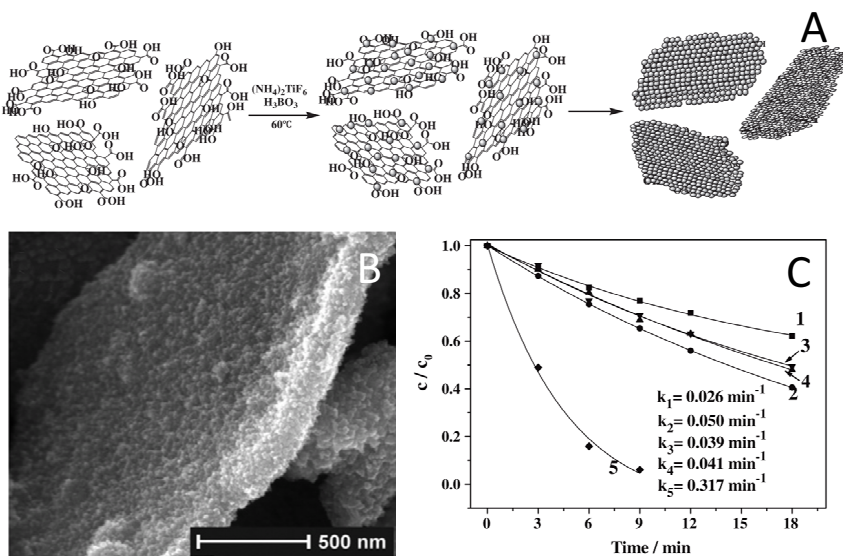


Fig. 5. (A) Schematic illustration of the assembling growth of TiO₂ nanoparticle on graphene oxide sheets. SEM image of (B) heat-treated graphene oxide/TiO₂ composites. (C) Photocatalytic degradation of 10 mg L⁻¹ methyl orange at pH 4.0 by (1) neat TiO₂, (2) mixture of neat TiO₂ and graphene oxide, (3) P25, (4) mixture of P25 with graphene oxide, and (5) the heat-treated composite of graphene oxide/TiO₂. The load of catalyst was 0.5 g L⁻¹. *Source:* Adapted from Jiang *et al.* (2011).

threefold enhancement of photocatalytic degradation efficiency over conventional TiO₂ such as P25. Figure 5 illustrate the formation of composite and its photodegradation capacity. Following this, a highly efficient photocatalyst was fabricated by *in situ* deposition of TiO₂ nanoparticles on GO nanosheets by a liquid phase deposition, followed by a calcination at 200°C recently.⁴⁴ The composite was utilized for the photocatalytic removal of pollutants. At optimum conditions of solution pH, post-calcination, and at a definite GO content, the photo-oxidative degradation rate of MO and the photo-reductive conversion rate of Cr(VI) over the composites were as high as 7.4 and 5.4 times that over P25. A photocatalyst prepared by anchoring TiO₂ nanoparticles on graphene sheets by sonochemical synthesis was used for the photocatalytic degradation of MB.⁴⁵ They found that the photocatalytic activity of the resultant graphene-TiO₂ composites containing 25 wt.% TiO₂ is better than that of commercial pure TiO₂.

The role of GO/RGO content on the photocatalytic efficiency was investigated by Nguyen-Phan *et al.*⁴⁶ They prepared TiO₂/GO composites using a simple colloidal blending method and found that the composites have superior adsorption and photocatalysis performance under both UV and visible radiation compared to pure TiO₂. They observed that gradually increasing the content of GO up to 10 wt% resulted in the increased removal efficiency and the photodegradation rate of MB.

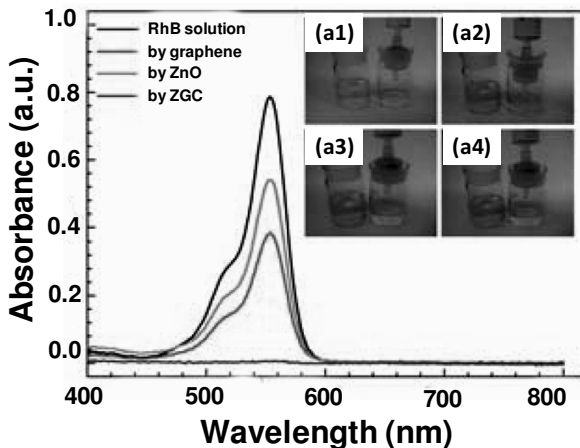


Fig. 6. The UV-visible spectra and images of (a) the original and filtered RhB solutions with graphene (inset a1), commercial ZnO (inset a2), and the ZGC (ZnO graphene composite) (insets a3 and a4). Source: Li and Cao. (2011).

The increase was attributed to synergy effects including the increase in specific surface area with GO amount as well as the formation of both π - π conjugations between dye molecules and aromatic rings and the ionic interactions between methylene blue and oxygen-containing functional groups at the edges or on the surfaces of carbon-based nanosheets. They also concluded that here, GO is working as the adsorbent, electron acceptor and photosensitizer to enhance the dye photodecomposition. Graphene-ZnO composites have also been fabricated for the photocatalytic degradation. Li and Cao recently reported a ZnO-Graphene composite which work efficiently as a photocatalyst for the degradation and filtered removal of rhodamine B (RhB).⁴⁷ Figure 6 shows the UV vis spectra and photographs of the degradation process. A graphene-MnOOH composite was prepared by solvothermal method recently.⁴⁸ The mechanism of composite formation was suggested to be dissolution-crystallization and oriented attachment. The composite showed unusual catalytic performance for the thermal decomposition of ammonium perchlorate (AP) due to the concerted effects of graphene and MnOOH. A graphene-horseradish peroxidase (HRP) composite for catalytic degradation of phenolic compounds was reported by Zhang *et al.*⁴⁹

Microbial contamination is major problem in drinking water. Graphene based solutions for this problem also has been made reported in the literature. An antibacterial brilliant blue (a common colorant)/RGO/tetradecyltriphenylphosphonium bromide composite which is highly dispersible in water and having specific targeting capability was reported by Cai *et al.*⁵⁰ The composite was found to be effective against both Gram-positive and Gram-negative bacteria. Figure 7 illustrates the antibacterial activity of the above composites. A silver-GO composite having a superior antibacterial activity towards *E. coli* due to the synergistic effect of GO and

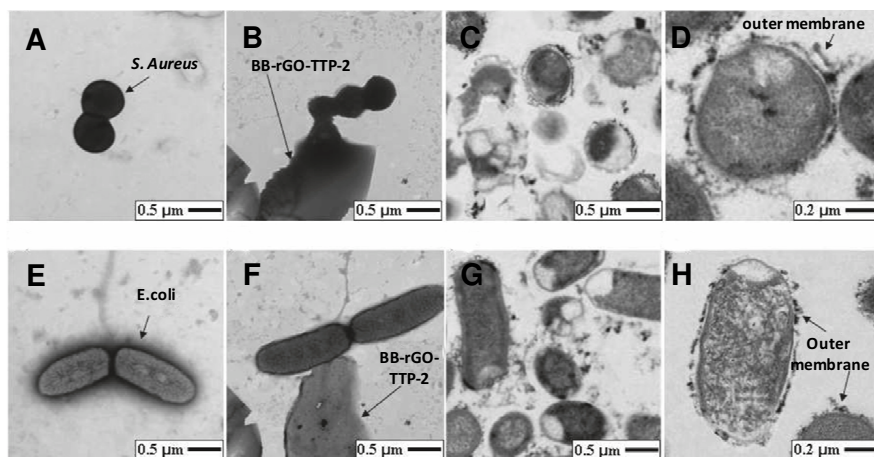


Fig. 7. (A) TEM images of normal *S. aureus* cells (A), *E. coli* cells (E), *S. aureus* cells (B), *E. coli* cells (F) treated by BB-rGO-TTP-2, the changes of *S. aureus* cells (C, D) and *E. coli* cells outer membrane (G, H). Source: Cai. (2011).

silver nanoparticles has been reported.⁵¹ A similar silver based graphene composite which can act as a bactericidal agent for water disinfection was reported by Bao *et al.*⁵² A similar monodispersed Ag nanoparticle-graphene composite having enhanced antibacterial property was reported by Liu *et al.* as well.⁵³

Utilizing the rich abundance of functional groups, a graphene based composite consisting of an antibacterial bio-polymer chitosan and a bactericidal protein was fabricated recently. The synergetic effect of different materials incorporated resulted in a highly antibacterial composite.⁵⁴ The composite showed a tendency to form self-standing films which can aid in coating this composite onto suitable substrates. The formed films can be easily imprinted with different patterns by applying compressive pressures. This pattern can be erased easily after use by simply wetting the film and new pattern can be inscribed. This points to the utility of the films in high end applications such as secure data transfer. Figure 8 illustrates the different aspects of the composite described above.

Capacitive deionization or electrosorption with porous electrodes are thought to be ideal candidates to remove various ions from aqueous solutions. Due to their good conductivity, high surface area and suitable pore size distribution, carbon based materials including activated carbon, carbon fibers, carbon aerogels and carbon nanotubes are employed as electrosorptive electrodes. Graphene also has emerged as an interesting candidate for this application. First attempt in this direction was done by Li *et al.*⁵⁵ They synthesized graphene through chemical methods and used as electrosorptive electrodes for capacitive deionization. Electrosorption experiments were conducted in NaCl solutions at low voltage (≤ 2 V) to investigate the electrosorption performance. Graphene exhibited a high electrosorption capacity of 1.85 mg/g where the electrosorption of NaCl onto graphene electrodes is driven by a

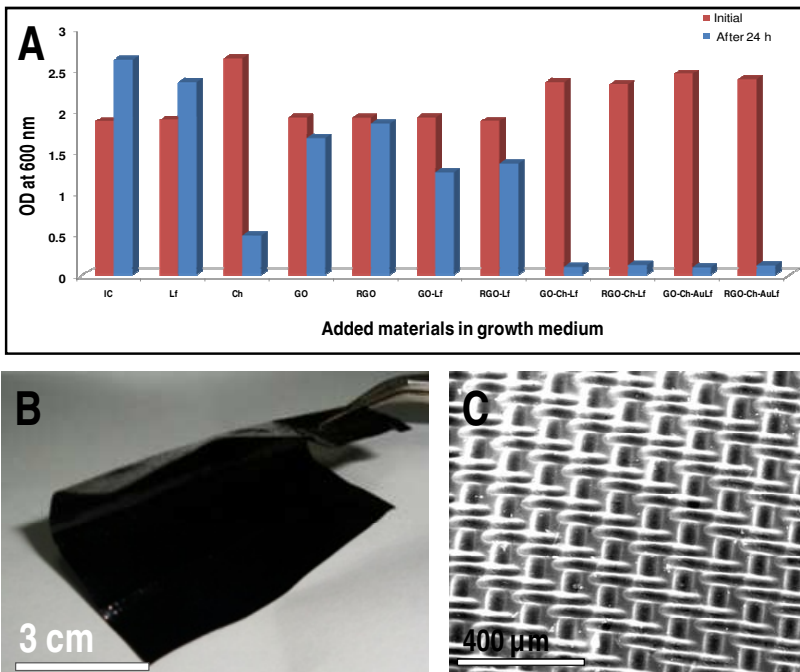


Fig. 8. (A) The plot depicting the antibacterial activity of the composites and the ingredients, (B) the photograph of the formed film and (C) SEM image of pattern imprinted on the film. Source: Sreeprasad *et al.* (2011).

physisorption process. Graphene nano-flakes (GNFs) were used as electrodes to remove ferric ions by capacitive deionization.⁵⁶ The optimum flow rate and electrical voltage were 25 ml/min and 2.0 V, respectively and the maximum equilibrium electrosorption capacity and rate constant for FeCl₃ at 2.0 V were 0.88 mg/g and 0.27 min⁻¹. The sorption experiment was repeated for different ions to quantify the selectivity and the electrosorption capacities of cations on the GNFs followed the order of Fe³⁺ > Ca²⁺ > Mg²⁺ > Na⁺.

The electrosorptive capacities of GNFs were found to be higher than activated carbon. Electrosorptive performance of GNFs electrodes with different bias potentials, flow rates and ionic strengths were measured and the electrosorption isotherm and kinetics were investigated by Li *et al.*⁵⁷ The specific electrosorptive capacity of the GNFs was 23.18 μmol/g for Na⁺ at an initial concentration of 25 mg/L, higher than activated carbon under the same experimental conditions. Figure 9 shows the schematics of graphene based capacitive deionization set up [Fig. 9(a) and 9(b)]. The utility of such a device for contaminant removal can also be seen [Fig. 9(c)]. A comparative study of electrosorptive capacities of single wall carbon nanotubes and graphene was also reported recently.⁵⁸

Graphene has recently received attention as a potentially selective material for membranes. Experimental studies and related simulations suggested the feasibility

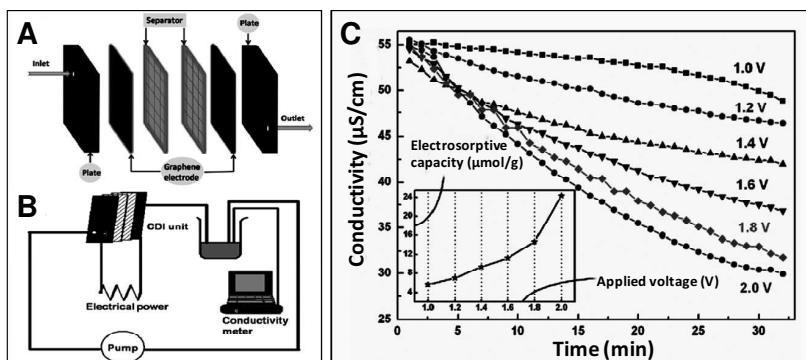


Fig. 9. (A) Schematic of electro-sorptive unit (B) cell batch-mode experiment. The CDI unit consisted of graphite plate, GNFs film, and separator. (C) The electro-sorption of Na^+ onto GNFs electrode at different bias potentials. *Source:* Adapted from Li. (2010).

of generating subnanometer pores in a controllable fashion on graphene by methods such as electron beam irradiation,⁵⁹ ion bombardment^{60,61} or by doping.⁶² The transport of ions through ~ 0.5 nm pores in graphene terminated with nitrogen or hydrogen was studied using MD simulations.⁶³ It was understood that the N-terminated pore allow the passage of metal ions such as Li^+ , Na^+ , and K^+ , while the H-terminated pore allowed Cl^- and Br^- to pass through, but not F^- . The smaller ions had the lowest passage rates due to their strongly bound hydration shells. Suk and Aluru investigated water transport through ultrathin graphene and the rate at which water molecules transport across 0.75–2.75 nm diameter pores in graphene membranes. They also compared it with 2–10 nm long carbon nanotubes (CNTs) with similar diameters. They observed that the flux through graphene pores to be a factor of two of that through CNTs and experiences a significant resistance to transport. Though the studies mentioned above pointed towards the potential of graphene membranes for water desalination with fluxes up to an order of magnitude higher than polymeric RO membranes, experimental measurements of water transport and salt rejection through them are still not realized.

Adsorption, among other technologies for removing pollutants, has proved to be most effective in removing pollutants from dilute solutions. As discussed earlier, carbon in its various forms, including composites, has been traditionally used for this application.^{64–66} However, use of graphene was not common for this application until recently. The recent research points that graphene is also highly useful as a high performance adsorbent. Graphene and the composites have proved to be an ideal candidate for the adsorption-based remediation of waste water. The adsorption of thiophene on Single-wall Nanotubes (SWNT) and graphene was investigated theoretically employing periodic boundary conditions and the van der Waals density functional (VDW-DF) and local density approximation (LDA) methodologies by Denis and Iribarne.⁶⁷ They suggested that thiophene adopts a nearly parallel configuration with respect to the graphene plane with sulfur atom 3.7 Å above

the sheet, whereas the two hydrogen atoms on carbon atoms not bonded to sulfur are 3.45 Å above it. The adsorption energy for this configuration of thiophene on graphene was calculated to be 8.9 kcal/mol. They investigated some other possible orientations and adsorption energies as well. The use of functionalized graphene prepared via fast method of electrolysis with potassium hexafluorophosphate solution as electrolyte under the static potential of 15 V was used for the adsorption of Pb(II) and Cd(II) by Deng *et al.*⁶⁸ The synthesized graphene sheets were having 30 wt.% PF₆⁻. These graphene sheets had adsorption capacities in the order of 406.6 mg/g (pH = 5.1) for Pb(II) and 73.42 mg/g (pH = 6.2) for Cd(II). A GO based solution for removing Cu²⁺ was developed by Yang *et al.*⁶⁹ They found that aggregation of GO can be induced by Cu²⁺ in aqueous solution with a huge Cu²⁺ absorption capacity. GO was found to be having 10 times absorption capacity over activated carbon. Liu *et al.* recently developed a strategy to immobilize GO and RGO on silica through covalent binding for the use of these material for solid-phase extraction (SPE).⁷⁰ The carboxy groups of GO were linked to the amino groups of an amino-terminated silica adsorbent and upon hydrazine treatment, they obtained RGO@silica.

They used these adsorbents for the removal of chlorophenols. The strategy to immobilize GO/RGO on silica is illustrated in Fig. 10(I). AFM and SEM images are also given [Fig. 10(II)]. Plot depicting the removal efficiency of the adsorbent is also given [Fig. 10(III)]. Graphene can also be produced from various sources such as high molecular petroleum fractions like asphalt or from natural sugars as well. An *in situ* strategy to synthesize and immobilize graphenic materials onto silica substrates was devised by Sreeprasad *et al.* Here, a high efficiency graphenic adsorbent was fabricated on sand particles starting from asphalt. The synthesized adsorbent was highly effective for the adsorption of dyes and pesticides from water. The material was reusable for several cycles.⁷¹ Figure 11 shows the scanning electron microscope (SEM) and energy-dispersive X-ray spectroscopy (EDX) characterization of the adsorbent. The time dependent removal a dye by the adsorbent can also be seen.

Ramesha *et al.* reported the use of GO and RGO for the removal of anionic and cationic dyes such as methylene blue, methyl violet, rhodamine B and orange G from aqueous solutions.⁷² For GO, because of the rich abundance of negatively charged functionalities, effective adsorption of cationic dyes took place while the adsorption was negligible for anionic dyes. However, RGO having high surface area is found to be very good adsorbent for anionic dyes. The removal of methylene blue by GO was studied in detail by Yang *et al.*⁷³ Absorption capacity as high as 714 mg/g was observed. For initial MB concentrations lower than 250 mg/L, the removal efficiency higher than 99% was attained and the solution turned completely colorless. Efficient adsorption of methylene blue dye from an aqueous solution by GO was studied by Zhang *et al.* as well.⁷⁴ Zhao *et al.* recently proposed the utility of sulfonated graphene for the management of aromatic pollutants taking naphthalene and 1-naphthol as model pollutants.⁷⁵ An adsorption capacity as high

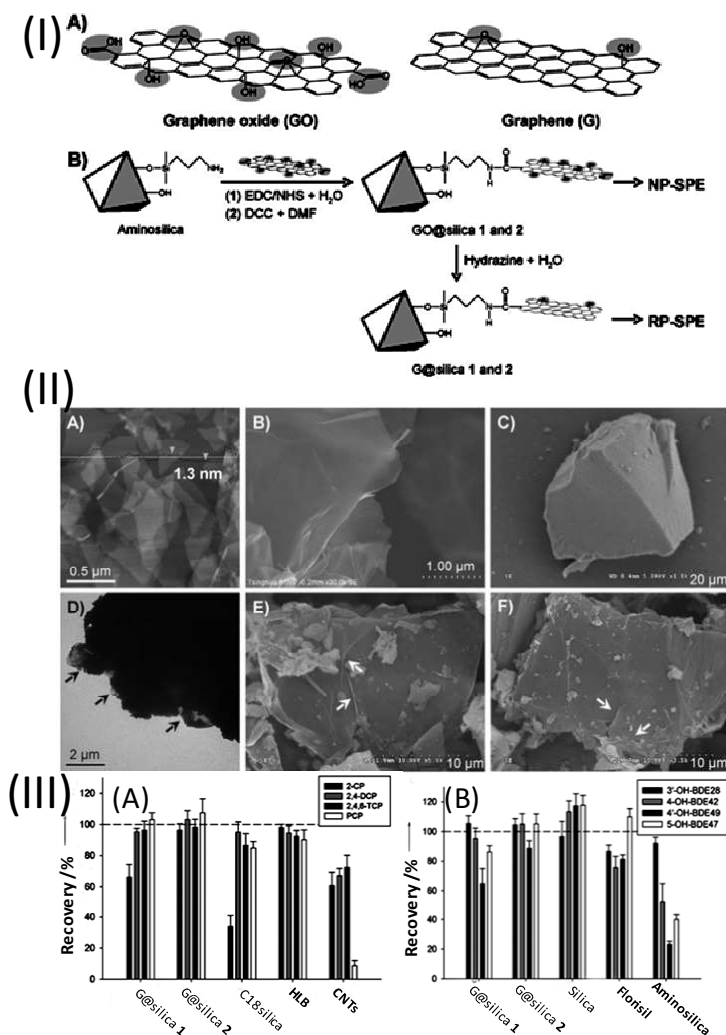


Fig. 10. (I) Chemical routes to the synthesis of GO@silica and RGO@silica. NP-SPE=normal-phase SPE, RP-SPE=reversed-phase SPE. (II) (A) AFM image of GO sheets (B) High-resolution SEM image of GO sheets. (C) SEM image of a bare silica particle. (D) TEM image of a GO@silica particle. E,F) SEM images of GO@silica 1 (E) and RGO@silica 1 (F). (III) Comparison of the analytical performance of G@silica with other adsorbents for the RP-SPE of chlorophenols (A) and GO@silica with other adsorbents for the NP-SPE (B). *Source:* Adapted from Liu *et al.* (2011).

as $\sim 2.3\text{--}2.4 \text{ mmol g}^{-1}$ for naphthalene and 1-naphthol was observed. The use of graphene as an adsorbent for fluoride from aqueous solution was demonstrated by Li *et al.*⁷⁶ Thermodynamic studies indicated that the process was spontaneous and endothermic in nature. Adsorption capacities and rates of fluoride onto graphene at different initial pH, contact time and temperature were also investigated and results revealed that the maximum adsorption capacity is up to 17.65 mg/g at

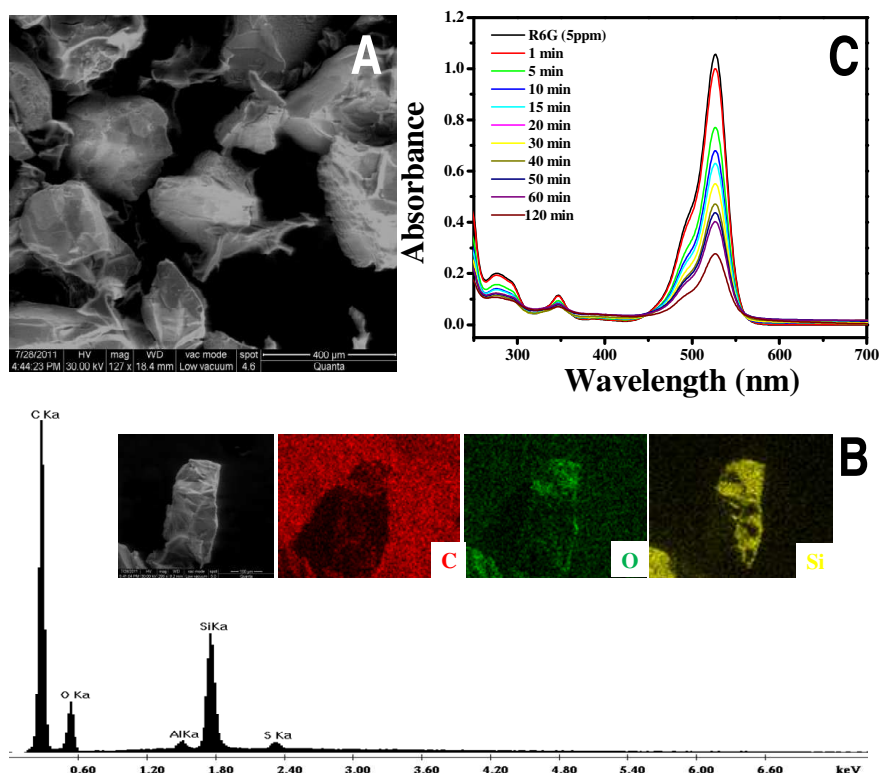


Fig. 11. (A) SEM image of the prepared adsorbent material, (B) EDAX spectrum and elemental maps and (C) Time dependent UV/Vis spectra showing the removal of rhodamine 6G. Source: Sreepasad *et al.* (2011).

initial fluoride concentration of 25 mg/L at 298 K. Graphene sheets prepared by hydrogen induced exfoliation of graphitic oxide followed by functionalization was found to be highly efficient adsorbent system for arsenic and sodium from aqueous solutions.⁷⁷ Maximum adsorption capacities for arsenate, arsenite and sodium were calculated to be 142, 139 and 122 mg/g, respectively. Recently Maliyekkal *et al.* found that RGO can function as an efficient adsorbent for pesticides.⁷⁸ The adsorption capacities of (CP), endosulfan (ES) and malathion (ML) were as high as ~1200, 1100 and 800 mg/g, respectively. RGO showed 10–20% higher affinity compared to GO, indicating that increasing surface oxygen functionality reduces the affinity of graphenic surface to pesticides. Theoretical calculations indicated that, the adsorption is dependent on the presence or absence of water molecules.⁷⁸ Figure 12 depicts the adsorbing ability of RGO towards pesticides.

Generally composites exhibit enhanced properties compared to the ingredients. A variety of graphene composites have been reported for the remediation of polluted water. One of the first attempt in this direction was from Chandra *et al.* who made water-dispersible magnetite-RGO composite and used it for arsenic removal.⁷⁹ The

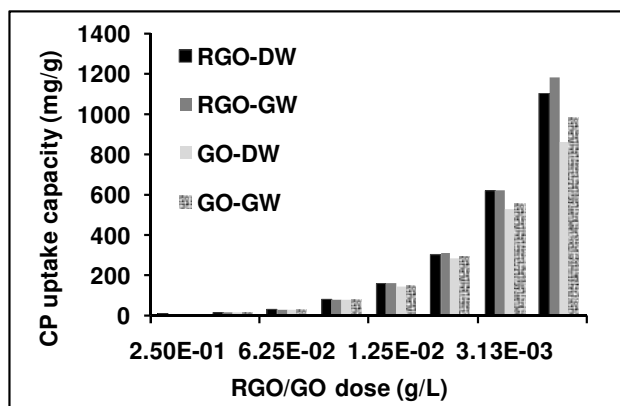


Fig. 12. Plot depicting the variation in CP uptake capacity of GO/RGO with varying dose. Source: Maliyekkal *et al.* (Unpublished). CP-chlorpyrifos, DW-distilled water, GW-ground water.

composite was prepared by chemical reduction and they observed that, compared to bare magnetite particles, the hybrids show a high binding capacity for As(III) and As(V). The composites had an added advantage that, they being superparamagnetic at room temperature, can be separated by an external magnetic field after the removal process. A versatile strategy to synthesize various metal/metal oxide graphene composite at room temperature and the utility of these composites for the removal of heavy metals were demonstrated by Sreepasad *et al.*⁸⁰ They also devised a green strategy to immobilize these composites onto cheap substrate like sand for easy post treatment handling (Fig. 13). They used an abundant and environmental friendly biopolymer, chitosan for the immobilization, thus avoiding harsh reactants and reaction conditions. The composites showed enhanced removal efficiency compared to some common adsorbents used pointing to their practical utility. Similarly, Gao *et al.* devised a strategy to anchor graphene on sand particles to create an adsorbent for water purification.⁸¹ However, the methodology used diazonium chemistry to functionalize GO and used heat treatment for the immobilization. The use of high energy processes and the use of toxic materials can hinder the use of such systems in high end applications such as water purification.

Koo *et al.* recently reported a graphene based multifunctional iron oxide sheets where needlelike iron oxide (IO) nanoparticles were grown on graphene sheets to have tunable properties.⁸² They prepared a paper-like material from the composite which showed extraordinary removal capacity and fast adsorption rates for As^V and Cr^{VI} ions in water. The removal capacities were found to be 218 and 190 mg g⁻¹ for As^V and Cr^{VI}, respectively. Porous GO/chitosan (PGOC) materials were prepared by a unidirectional freeze-drying method by He *et al.*⁸³ The metal ion absorption capacity of this composite was investigated. They found a saturated adsorption capacity of Pb²⁺ increased about 31%, up to when 5 wt% GO was incorporated in the composite. The maximum capacity obtained was 99 mg/g.

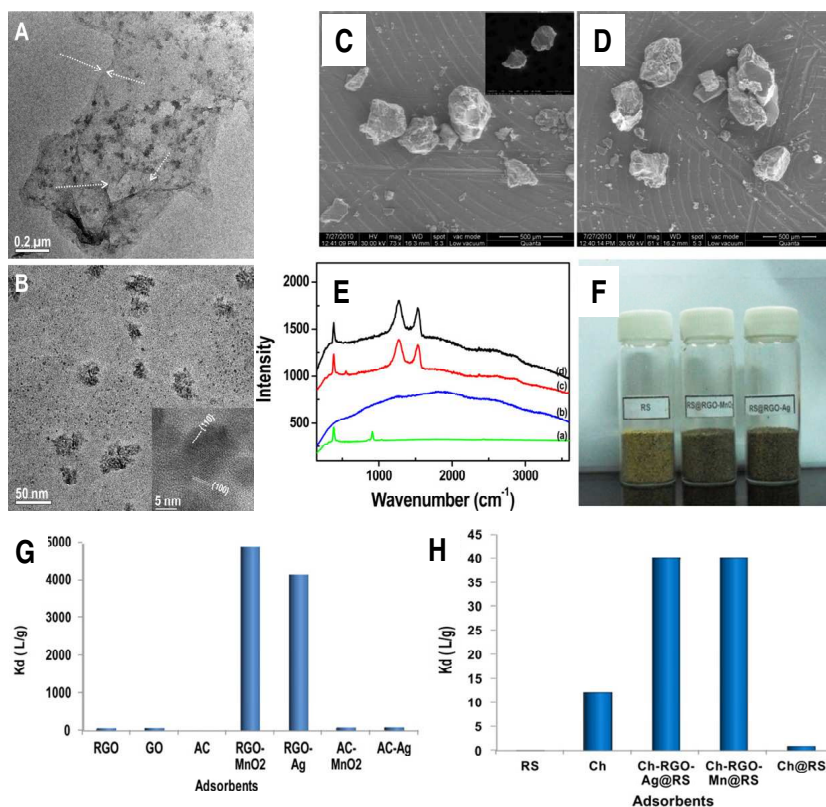


Fig. 13. (A) and (B) TEM images of RGO-MnO₂ (0.05mM) at various magnifications. SEM images of (C) Ch-RGO-Ag@RS, (D) Ch-RGO-MnO₂@RS; inset in 'C' shows a SEM image of bare sand particles, (E) Raman spectrum of (a) RS, (b) Ch, (c) Ch-RGO-MnO₂@RS, and (d) Ch-RGO-Ag@RS, (F) photograph of RS, Ch-RGO-MnO₂@RS and Ch-RGO-Ag@RS (G) unsupported RGO composites with other adsorbents (H) supported RGO composite with RS, Ch, Ch@RS. *Source:* Adapted from Sreepasad *et al.* (2011).

A polypyrrole-RGO composite, which is highly selective towards the adsorption of Hg²⁺ was also reported recently.⁸⁴ The synthesis was done through the chemical exfoliation of graphite to GO and the subsequent reduction to RGO in the presence of polypyrrole (PPy). PPy-RGO composite having 15 wt% GO loading exhibited highly selective and enhanced absorption of Hg²⁺. A high adsorption efficacy up to 980 mg g⁻¹ and an extremely high desorption capacity of up to 92.3%, showed by the composite pointed towards the repeatable applicability of the proposed composite. Zhang *et al.* also devised a strategy to make GO-ferric hydroxide composites which can be efficient for the removal of arsenate from drinking water.⁸⁵ The composite include GO cross linked with ferric hydroxide where, the amorphous ferric hydroxide was found to be homogenously impregnated onto GO. More than 95% arsenate removal was obtained for the water with arsenate concentration at 51.14 ppm, implying an absorption capacity of 23.78 mg arsenate/g of composite.

They also pointed out that the adsorption can be effective in a wide range of pH from 4 to 9. However, a decreased adsorption efficacy was exhibited for pH greater than 8.⁸⁵ A graphene-based magnetic nanocomposite for the removal of an organic dye, fuchsine from aqueous solution was reported by Wang *et al.*⁸⁶ They prepared RGO-Fe₃O₄ composite by the *in situ* chemical coprecipitation of Fe²⁺ and Fe³⁺ in alkaline solution in the presence of RGO. The study included the investigation of adsorption kinetics, capacity of the adsorbent, the effect of the adsorbent dosage and solution pH on the removal efficiency of fuchsine.

Graphene/magnetite composite synthesized by solvothermal methods were used for the removal of methylene blue from aqueous solutions.⁸⁷ Here, they achieved *in situ* conversion of FeCl₃ to Fe₃O₄ and simultaneous reduction of GO to RGO in ethylene glycol solution. This composite showed extraordinary adsorption capacity and fast adsorption rates for removal of MB. A similar method for the preparation of RGO-Fe₃O₄ was reported by Sun *et al.* as well.⁸⁸ They observed the composite to be excellent for the removal of rhodamine B (91%) and malachite green (over 94%). They also found that the removal is strongly dependent on both the loading of Fe₃O₄ and the pH value. They demonstrated that the composite can be applied in real water systems including industrial waste water and lake water. Using chemical deposition method, Mg(OH)₂-RGO composite (MGC) was synthesized by Li *et al.*⁸⁹ The formed composite had a mesoporous structure and was found to be efficient in removing MB from water. The Mg(OH)₂ nanostructures formed were highly dispersed on the RGO sheet and had high surface area. It also aided in increasing the pore volume, and to create a uniform pore width distribution. A similar Cu₂O-RGO composite (CGC) has also been reported.⁹⁰ The composite was projected for removal of dye from water and in supercapacitors. CGC exhibited a high adsorption capacity for rhodamine B (RhB), and MB. Using these composites, a reactive filtration film was assembled and was applied to remove dye from waste water.

4. Application of Graphene in Biology Other than Sensing

The discovery of ways to make graphene in bulk quantities, especially the chemical ways of preparing GO and RGO by the oxidation of graphite opened up the application of these materials in various fields. Biology being a key field where nanomaterials find tremendous application possibility, graphenic materials have been drawing interest in this area as well. Chemically prepared graphene has rich abundance of functional groups such as hydroxyl, carboxylic acid and other reactive groups which are amenable to ligand conjugation, cross-linking and other modifications, rendering GO/RGO tailored for a range of biomedical and other applications. Again, the abundance of hydrophilic functionalities renders them good biocompatibility as well. Here, a brief overview of efforts taken up to use graphene in biology is presented. The biocompatibility of graphene was investigated recently. Graphene based biocompatible paper was prepared and its biocompatibility was demonstrated by

culturing mouse fibroblast cell line (L-929).⁹¹ The cell lines were found to adhere to and proliferate on graphene papers. A sub-confluent layer of metabolically active cells were formed within 48 h of culture time. Agarwal *et al.* tested biocompatibility of RGO with rat pheochromocytoma (neuroendocrine cell, PC12) cells, human oligodendroglia (HOG) cells and human fetal osteoblast (hFOB) cells.⁹² Many efforts have been undertaken to incorporate biomaterials,^{93,94} such as DNA,^{19,95,96} protein^{97–99} to graphene.

Most of these were aimed at developing FETs or sensing. Some of these efforts have been mentioned in earlier sections. GO/RGO has tremendous ability to adsorb DNA. It can quench the luminescence from biomolecules, and can protect them from enzyme cleavage as well. Hence, GO and RGO are being utilized frequently in biotechnology and several investigations, including drug delivery, cellular imaging, real-time monitoring, cell imaging, *in vivo* targeting of ATP and *in situ* localization of mRNA. In this section, we review some of applications of graphene and graphene-based nanomaterials in live cells.

The ability of graphene to protect DNA from cleavage during cellular delivery was demonstrated by Lu *et al.* Molecular beacons (MBs) were used as oligonucleotide probes in combination with GO sheets to deliver DNA to HeLa cells, where graphene served as the protective covering for the DNA.¹⁰⁰ Wang *et al.* in 2010 designed an aptamer–carboxyfluorescein/GO nanosheet (aptamer–FAM/GO–nS) complex for *in situ* molecular analysis of ATP in JB6 Cl 41-5a mouse epithelial cells.¹⁰¹ The formed composite with the aid of a wide-field fluorescence microscope, served as a real-time sensing platform. GO/RGO was used for drug delivery vehicle as well. Liu *et al.* in 2008 was the first one to use graphene as a cargo for the delivery of water-soluble cancer drugs.¹⁰² Functionalization of GO with polyethylene glycol (PEG) to ensure better solubility of GO in aqueous solutions, as well as stability in physiological solutions. The drug delivery capacity was enhanced by anchoring SN₃₈ (a water-insoluble aromatic compound), and the composite exhibited high efficiency in carrying cancer drug to HCT-116 human colon cancer cells. Later, Zahng *et al.* found that GO conjugated with folic acid (FA) can enhance the loading efficiency and targeting ability of anticancer drugs.¹⁰³ They investigated two anticancer drugs, doxorubicin and CPT-11 onto the FA-conjugated GO (FA-GO) and found that the two anticancer drugs show specific targeting to MCF-7 human breast cancer cells. Recently Yang *et al.* utilized the strong optical absorbance of PEGylated GO in the near-infrared region to develop ultra-high *in vivo* tumor uptake of anticancer drugs, and to use them for photothermal therapy of cancer.¹⁰⁴ Some graphene based FETs for living cell detection has also been documented. A graphene-based FET was used to investigate electrogenic cells by Cohen–Karni *et al.*¹⁰⁵ They obtained FET conductance signals recorded from beating chicken embryonic cardiomyocytes yielding well-defined extracellular signals. He *et al.* used a graphene-based FET as a biosensor to detect hormonal catecholamine molecules in neuroendocrine PC12 rat adrenal medulla cells.¹⁰⁶ In

this study, a patterned GO film-based FET was constructed and it was developed into a label-free and real-time monitoring FET for catecholamine secretion from living cells.

5. Conclusions and Outlook

The fascinating properties of graphene, with respect to structures that can be modulated and surfaces that can be modified, offers some important advantages for novel applications in biotechnology and environmental science, especially in the areas of biosensors and medicine, contaminant sensing and remediation. However, the use of graphene in this field is in its infancy and many challenges remain. This review illustrated the potential of graphene or graphene based materials for applications other than catalytic or electronic processes. Recently, several efforts have been dedicated to use the extraordinary properties of graphene in fields such as sensing, biotechnology and environmental remediation. Utilizing the high surface area and the presence of a variety of functional groups, the properties of graphene can be tuned for various applications. Functionalization of graphene surface with specific target molecules can develop novel targeted sensors. By incorporating different materials, graphene can be used for FET based, voltammetric, FRET based or SERS based sensing applications. However, challenges still exist in this area. For example, even though pristine graphene (graphene obtained from physical exfoliation) has tremendous capability for FRET based application, it is highly hydrophobic which limits the application. Similarly, GO is highly hydrophilic but, its electrical conductivity is comparatively very low. Likewise, some challenges exist in the bulk production of soluble, well-defined graphene or graphene derivatives. Cytotoxicity, the cellular uptake mechanism, and the intracellular metabolic pathway of graphene and its derivatives are not known in detail. Although the initial results are promising, a thorough knowledge about these are necessary before using these systems for *in vivo* applications.

However, an area in which graphene or chemically synthesized GO/RGO is believed to make immediate impact is in water decontamination. This review clearly demonstrated the usefulness of graphenic materials in this field. Various strategies such as photocatalytic degradation, capacitive deionization, membrane separation and adsorption based removal can be used for this cause. Graphene-based materials were found to be useful in all these fields. Among these technologies, adsorption is proved to be most efficient and economically viable, especially for removing pollutants from dilute solutions. Due to the large surface area and the abundance of functional groups, GO/RGO is the best suitable candidate for low cost-high efficiency adsorbent, which is the need of the hour. The separation of graphenic adsorbent from the solution after remediation process was a challenge until recently. Researchers have found novel techniques to overcome this difficulty as well. Hence, it is believed that over the next few years, water treatment will emerge as one of the chief areas of application for graphene, especially GO/RGO.

Acknowledgment

The authors thank the Department of Science and Technology, Government of India for supporting their research program on nanomaterials.

References

1. T. Pradeep and Anshup, *Thin Solid Films* **517**, 6441 (2009).
2. F. Schedin *et al.*, *Nat. Mater.* **6**, 652 (2007).
3. H. Vedala *et al.*, *Nano Lett.* **11**, 2342 (2011).
4. T. Zhang *et al.*, *Nano Lett.* **10**, 4738 (2010).
5. G. Lu *et al.*, *Chem. Commun.* **47**, 7761 (2011).
6. S. Liu *et al.*, *Biosens. Bioelectron.* **26**, 4491 (2011).
7. Y. Wang *et al.*, *ACS Nano* **4**, 1790 (2010).
8. B. G. Choi *et al.*, *ACS Nano* **4**, 2910 (2010).
9. C. Shan *et al.*, *Langmuir* **25**, 12030 (2009).
10. H. Du *et al.*, *J. Electroanal. Chem.* **650**, 209 (2011).
11. J. Gong *et al.*, *Sens. Actuators B: Chem.* **150**, 491 (2010).
12. J. Li *et al.*, *Electrochem. Commun.* **11**, 1085 (2009).
13. Y. Yao *et al.*, *Appl. Surf. Sci.* **257**, 7778 (2011).
14. Z. Jiang *et al.*, *Chem. Commun.* **47**, 6350 (2011).
15. S. Deng *et al.*, *Biosens. Bioelectron.* **26**, 4552 (2011).
16. X. Liu *et al.*, *ACS Appl. Mater. Interfaces* Article ASAP (DOI:10.1021/am200737b) (2011).
17. W. Ren, Y. Fang and E. Wang, *ACS Nano* **5**, 6425 (2011).
18. C.-H. Lu *et al.*, *Angewandte Chemie Int. Ed.* **48**, 4785 (2009).
19. N. Mohanty and V. Berry, *Nano Lett.* **8**, 4469 (2008).
20. Y. Ohno, K. Maehashi and K. Matsumoto, *Biosens. Bioelectron.* **26**, 1727 (2010).
21. H. Jang *et al.*, *Angewandte Chemie Int. Ed.* **49**, 5703 (2010).
22. S. He *et al.*, *Adv. Funct. Mater.* **20**, 453 (2010).
23. H. Dong *et al.*, *Anal. Chem.* **82**, 5511 (2010).
24. C.-H. Lu *et al.*, *Chem. – A Euro. J.* **16**, 4889 (2010).
25. B. G. Choi *et al.*, *Nanoscale* **2**, 2692 (2010).
26. Y. Wen *et al.*, *Chem. Commun.* **46**, 2596 (2010).
27. H. Chang *et al.*, *Anal. Chem.* **82**, 2341 (2010).
28. C. Zhang *et al.*, *Angewandte Chemie Int. Ed.* **50**, 6851 (2011).
29. Y. Xu, A. Malkovskiy and Y. Pang, *Chem. Commun.* **47**, 6662 (2011).
30. C. Wu *et al.*, *Analyst* **136**, 2106 (2011).
31. H. Wang *et al.*, *Angewandte Chemie Int. Ed.* **50**, 7065 (2011).
32. W. T. Huang *et al.*, *Chem. Commun.* **47**, 7800 (2011).
33. X.-H. Zhao *et al.*, *Anal. Chem.* **83**, 5062 (211).
34. Z. Xiong *et al.*, *Chem. Commun.* **46**, 6099 (2010).
35. M. Zhu, P. Chen and M. Liu, *ACS Nano* **5**, 4529 (2011).
36. O. Akhavan and E. Ghaderi, *J. Phys. Chem. C* **113**, 20214 (2009).
37. J. Liu *et al.*, *Adv. Funct. Mater.* **20**, 4175 (2010).
38. C. Chen *et al.*, *ACS Nano* **4**, 6425 (2010).
39. Y. Zhang *et al.*, *ACS Nano* **4**, 7303 (2010).
40. Q. Zhang *et al.*, *Chin. Sci. Bull.* **56**, 331 (2011).
41. B. Jiang *et al.*, *Chem. Eur. J.* **17**, 8379 (2011).
42. H. Zhang *et al.*, *ACS Nano* **4**, 380 (2010).
43. Y. Liang *et al.*, *Nano Res.* **3**, 701 (2010).

44. G. Jiang *et al.*, *Carbon* **49**, 2693 (2011).
45. J. Guo *et al.*, *Ultras. Sonochem.* **18**, 1082 (2011).
46. T.-D. Nguyen-Phan *et al.*, *Chem. Eng. J.* **170**, 226 (2011).
47. B. Li and H. Cao, *J. Mater. Chem.* **21**, 3346 (2011).
48. S. Chen *et al.*, *J. Solid State Chem.* **183**, 2552 (2010).
49. F. Zhang *et al.*, *J. Phys. Chem. C* **114**, 8469 (2010).
50. X. Cai *et al.*, *Langmuir* **27**, 7828 (2011).
51. J. Ma *et al.*, *J. Mater. Chem.* **21**, 3350 (2011).
52. Q. Bao, D. Zhang and P. Qi, *J. Colloid Interface Sci.* **360**, 463 (2011).
53. L. Liu *et al.*, *New Chem.* **35**, 1418 (2011).
54. T. S. Sreepasad *et al.*, *ACS Appl. Mater. Interfaces* **3**, 2643 (2011).
55. H. Li *et al.*, *J. Mater. Chem.* **19**, 6773 (2009).
56. H. Li *et al.*, *Sep. Purif. Technol.* **75**, 8 (2010).
57. H. Li *et al.*, *Environ. Sci. Technol.* **44**, 8692 (2010).
58. H. Li *et al.*, *J. Electroanal. Chem.* **653**, 40 (2011).
59. A. Hashimoto *et al.*, *Nature* **430**, 870 (2004).
60. M. M. Lucchese *et al.*, *Carbon* **48**, 1592 (2010).
61. N. Inui *et al.*, *Appl. Phys. A: Mater. Sci. Process.* **98**, 787 (2010).
62. D. Wei *et al.*, *Nano Lett.* **9**, 1752 (2009).
63. K. Sint, B. Wang and P. Krail, *J. Am. Chem. Soc.* **131**, 9600 (2009).
64. M. Zabihi, A. Ahmadpour and A. H. Asl, *J. Hazard. Mater.* **167**, 230 (2009).
65. D. Ayhan, *J. Hazardous Mater.* **167**, 1 (2009).
66. S. M. Maliyekkal, K. P. Lisha and T. Pradeep, *J. Hazard. Mater.* **181**, 986 (2010).
67. P. A. Denis and F. Iribarne, *J. Mole Struct. Theochem* **957**, 114 (2010).
68. X. Deng *et al.*, *J. Hazard. Mater.* **183**, 923 (2010).
69. S.-T. Yang *et al.*, *J. Colloid Interface Sci.* **351**, 122 (2010).
70. Q. Liu *et al.*, *Angewandte Chemie Int. Ed.* **50**, 5913 (2011).
71. T. S. Sreepasad, S. S. Gupta, S. M. Maliyekkal and T. Pradeep, Unpublished (2011).
72. G. K. Ramesha *et al.*, *J. Colloid Interface Sci.* **361**, 270 (2011).
73. S.-T. Yang *et al.*, *J. Colloid Interface Sci.* **359**, 24 (2011).
74. W. Zhang *et al.*, *Bull. Environ. Contam. Toxicol.* **87**, 86 (2011).
75. G. Zhao *et al.*, *Adv. Mater.* **23**, 3959 (2011).
76. Y. Li *et al.*, *J. Colloid Interface Sci.* **363**, 348 (2011).
77. K. Mishra and S. Ramaprabhu, *Desalination* In Press, Corrected Proof (doi:10.1016/j.desal.2011.01.038) (2011).
78. S. M. Maliyekkal, T. S. Sreepasad, K. Deepti and T. Pradeep, T. Unpublished.
79. V. Chandra *et al.*, *ACS Nano* **4**, 3979 (2010).
80. T. S. Sreepasad *et al.*, *J. Hazard. Mater.* **186**, 921 (2011).
81. W. Gao *et al.*, *ACS Appl. Mater. Interfaces* **3**, 1821 (2011).
82. H. Y. Koo *et al.*, *Chem. Eur. J.* **17**, 1214 (2011).
83. Y. Q. He, N. N. Zhang and X. D. Wang, *Chin. Chem. Lett.* **22**, 859 (2011).
84. V. Chandra and K. S. Kim, *Chem. Commun.* **47**, 3942 (2011).
85. K. Zhang *et al.*, *J. Hazard. Mater.* **182**, 162 (2010).
86. C. Wang *et al.*, *Chem. Eng. J.* **173**, 92 (2011).
87. L. Ai, C. Zhang and Z. Chen, *J. Hazard. Mater.* **192**, 1515 (2011).
88. H. Sun, L. Cao and L. Lu, *Nano Res.* **4**, 550 (2011).
89. B. Li, H. Cao and G. Yin, *J. Mater. Chem.* **21**, 13765 (2011).
90. B. Li *et al.*, *J. Mater. Chem.* **21**, 10645 (2011).
91. H. Chen *et al.*, *Adv. Mater.* **20**, 3557 (2008).
92. S. Agarwal *et al.*, *Langmuir* **26**, 2244 (2010).

93. T. H. Han *et al.*, *Adv. Mater.* **22**, 2060 (2010).
94. Q. Yang *et al.*, *J. Phys. Chem. C* **114**, 3811 (2010).
95. L. A. L. Tang, J. Wang and K. P. Loh, *J. Am. Chem. Soc.* **132**, 10976 (2010).
96. J. Liu *et al.*, *J. Mate. Chem.* **20**, 900 (2010).
97. J. Zhang *et al.*, *Langmuir* **26**, 6083 (2010).
98. P. Laaksonen *et al.*, *Angewandte Chemie Int. Ed.* **49**, 4946 (2010).
99. J. Liu *et al.*, *J. Am. Chem. Soc.* **132**, 7279 (2010).
100. C.-H. Lu *et al.*, *Chem. Commun.* **46**, 3116 (2010).
101. Y. Wang *et al.*, *J. Am. Chem. Soc.* **132**, 9274 (2010).
102. Z. Liu *et al.*, *J. Am. Chem. Soc.* **130**, 10876 (2008).
103. L. Zhang *et al.*, *Small* **6**, 537 (2010).
104. K. Yang *et al.*, *Nano Lett.* **10**, 3318 (2010).
105. T. Cohen-Karni *et al.*, *Nano Lett.* **10**, 1098 (2010).
106. Q. He *et al.*, *ACS Nano* **4**, 3201 (2010).

Cite this: *Analyst*, 2012, **137**, 4559

www.rsc.org/analyst

PAPER

Rapid identification of molecular changes in tulsi (*Ocimum sanctum* Linn) upon ageing using leaf spray ionization mass spectrometry†

Depanjan Sarkar, Amitava Srimany and T. Pradeep*

Received 18th May 2012, Accepted 30th July 2012

DOI: 10.1039/c2an35655d

Tulsi or Holy Basil (*Ocimum sanctum* Linn) is a medicinally important plant. Ursolic acid (UA) and oleanolic acid (OA) are among its major constituents which account for many medicinal activities of the plant. In the present work, we deployed a new ambient ionization method, leaf spray ionization, for rapid detection of UA, OA and their oxidation products from tulsi leaves. Tandem electrospray ionization mass spectrometry (ESI-MS) has been performed on tulsi leaf extracts in methanol to establish the identity of the compounds. We probed changes occurring in the relative amounts of the parent compounds (UA and OA) with their oxidized products and the latter show an increasing trend upon ageing. The findings are verified by ESI-MS analysis of tulsi leaf extracts, which shows the same trend proving the reliability of the leaf spray method.

Introduction

Mass spectrometry is an ever growing field and is probably the most versatile amongst other analytical techniques in terms of instrumentation and methodologies. When hyphenated with other analytical tools such as liquid chromatography (LC) or gas chromatography (GC), its performance and area of applications become much broader. For example, analysis of complex mixtures derived from plant extracts has been conventionally performed by liquid chromatography-mass spectrometry (LC-MS).^{1–3} In spite of its usefulness, the main drawback of LC-MS is the time constraint associated with the method. Recently a new class of mass spectrometry, known as ambient ionization mass spectrometry,^{4–10} has emerged with the introduction of desorption electrospray ionization mass spectrometry (DESI-MS) in 2004.¹¹ Subsequently other methods like direct analysis in real time (DART)¹² and many others have been developed in this category, all aiming to achieve ionization from atmospheric pressure with minimal or no sample preparations, decreasing the time required for analysis. Until now, various ambient methods such as DESI,^{13–20} DART,^{21–23} laser ablation electrospray ionization (LAESI),^{24–26} and extractive electrospray ionization (EESI)^{27,28} have been successfully used for plant tissue analysis without or with minimal sample preparation. Leaf spray ionization,^{29,30} tissue-spray ionization³¹ or similar kinds of direct

analysis³² are basically the same in terms of operational principle as they are extended versions of paper spray ionization.^{33–36} These are also emerging ambient mass spectrometric tools for rapid identification of molecules from plant tissues.

Tulsi or Holy Basil (*Ocimum sanctum* Linn) is a very common plant (Fig. 1A) seen throughout India. It is also found in other places of the globe such as Malaysia, Australia, West Africa and several Arabian countries. The name tulsi or tulasi came from the ancient Indian language, Sanskrit, which means ‘matchless one’.³⁷ Besides its sacredness in Hindu culture, tulsi is very popular in India owing to its high medicinal activities. For this reason, it has long been used in the traditional Indian medical system called *Ayurveda*, for treatment of various diseases and modern research also suggests its medicinal activities for similar conditions.³⁸ UA and OA are two of the major constituents of tulsi leaves. They are a triterpenoid class of compounds and structurally almost similar

Department of Chemistry, Indian Institute of Technology Madras, Chennai 600036, India. E-mail: pradeep@iitm.ac.in; Fax: +91 44 2257-0545; Tel: +91 44 2257-4208

† Electronic supplementary information (ESI) available: Different categories of tulsi leaves, experimental set-up photograph, tandem mass spectra for m/z 455.5, tandem mass spectra for m/z 471.5, tandem mass spectra for m/z 487.5, expanded view of leaf spray and ESI spectra near the region m/z 487.5, and tandem mass spectra for m/z 488.3. See DOI: 10.1039/c2an35655d

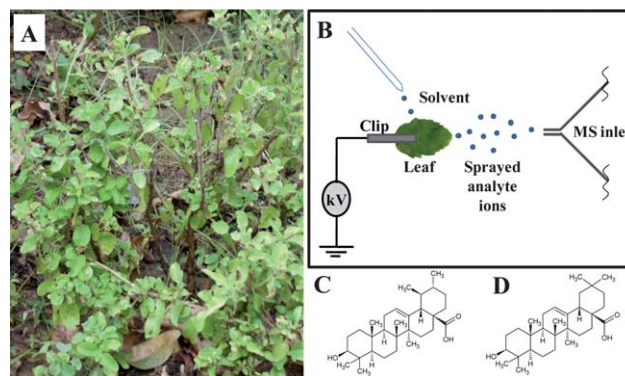


Fig. 1 (A) Photograph of a tulsi plant found in the IIT Madras campus. (B) Schematic diagram of the leaf spray experimental set-up. (C and D) Structures of ursolic acid and oleanolic acid, respectively.

(Fig. 1C and D), having the same mass. These two compounds are of major importance because of their pharmacological properties like antimicrobial,³⁹ anti-inflammatory,^{39,40} anti-HIV,⁴¹ antiulcer,⁴² *etc.* to name a few. Details of their pharmacological properties can be found in a review by Liu.³⁹

In the present study, we show the applicability of a newly developed leaf spray method to detect compounds from tulsi leaves. A schematic of the experimental set-up is shown in Fig. 1B. UA and OA, two of the major compounds present in tulsi leaves, and their oxidation products with 16 Da and 32 Da higher mass than the parent compounds have been detected. The identities of these compounds have also been established by tandem ESI-MS. A semi-quantitative approach has been adopted to monitor the changes in the total amount of the above compounds with respect to their oxidized products during ageing of the leaf by the leaf spray ionization method. The results indicate the relative increase in the oxidized product with ageing. The trend is verified by ESI-MS data from the methanol extracts of leaves.

Materials and methods

Tulsi is available everywhere in India and, for the experiments, tulsi leaves were collected from the campus of IIT Madras. In our experiments, leaves were categorized in 5 different classes. They were tender leaf (TL, just coming out from the branch, ~3 to 4 days old), young leaf (YL, after some days of maturation, ~6 to 7 days old), mature leaf (ML, after maximum growth, ~2 weeks old), old leaf (OL, after becoming yellowish, ~6 weeks old) and dried leaf (DL, after drying the mature leaves in the laboratory at 25 °C for 10 days in a Petri dish). The maturation mentioned above may vary depending on the atmospheric conditions where the plant is exposed and the season. Fig. S1† shows a photograph of all the five categories of tulsi leaves. Methanol (HPLC grade) was purchased from Standard Reagents Pvt. Ltd., Hyderabad, India. Deionized water was used for washing.

For all the mass spectrometric measurements, an ion trap LTQ XL mass spectrometer from Thermo Scientific, San Jose, CA was used. For leaf spray experiments, samples were set at a distance of approximately 5 mm from the mass spectrometer inlet in all the cases. The experimental set-up is shown in Fig. S2.† Mass spectra were acquired in negative ion mode in the mass range of m/z 150 to 500 under the following conditions: source voltage 7 kV, capillary temperature 275 °C, capillary voltage -35 V and tube lens voltage -100 V. All leaf spray ionization mass spectra presented correspond to an average of 10 scans. For the ESI experiments, methanol extracts of various tulsi leaves were prepared by dipping the leaves for 3 hours in 1.5 mL methanol, taken in a 2 mL vial separately. After the specified time, the solutions were decanted to another vial and centrifuged for 10 minutes at a speed of 10 000 rpm. These extracts were electrosprayed at a flow rate of 5 $\mu\text{L min}^{-1}$ and mass spectra were acquired in negative ion mode in the mass range of m/z 150 to 500. The following parameters were used for all the measurements: source voltage 5 kV, sheath gas (nitrogen) flow rate 8 (manufacturer's unit), capillary temperature 275 °C, capillary voltage -35 V and tube lens voltage -100 V. All ESI mass spectra presented correspond to an average of 100 scans. Tandem mass spectrometric experiments have been done with collision induced dissociation (CID).

Results and discussion

Methanol was used as a solvent in leaf spray experiments and 10 μL of it was added during each experiment. A tulsi leaf was cut in a triangular shape and connected with a clip to apply the high voltage. The spectrum of this sample is compared with that from the whole leaf (Fig. 2) which showed that a better quality of data can be obtained from the uncut leaf itself. This is possible because of the sharpness of the tip. Here the m/z 455.5 peak is due to UA and OA combined. As both of the compounds have the same mass and are structurally similar, it is difficult to distinguish them even by tandem mass spectrometry. Along with the m/z 455.5 peak, other two peaks are formed at m/z 471.5 and m/z 487.5. But in Fig. 2, the peak shown is at m/z 488.3, which will be discussed later. There is no report available in the literature about molecules with m/z 471.5 and m/z 487.5 present in tulsi. As the peaks are shifted from the peak at m/z 455.5 by 16 Da and 32 Da, respectively, it enables us to speculate that the new peaks are the oxidation products of UA and OA. Some other compounds of tulsi like rosmarinic acid and eugenol are also seen at m/z 359.3 and 163.2, respectively.

To know the structures of the two oxidized products, a tandem mass spectrometric study was conducted with the methanol extract of the tulsi leaf. ESI was used to get more signal intensity.

Fig. S3–S5† show the tandem mass spectrometry data and possible fragmentation products for m/z 455.5, 471.5 and 487.5, respectively. Concise results from this study are shown in Table 1. In the MS² spectrum of m/z 455.5, the peak is formed at m/z 407.5 with a loss of 48 Da due to the loss of neutral fragments, HCHO

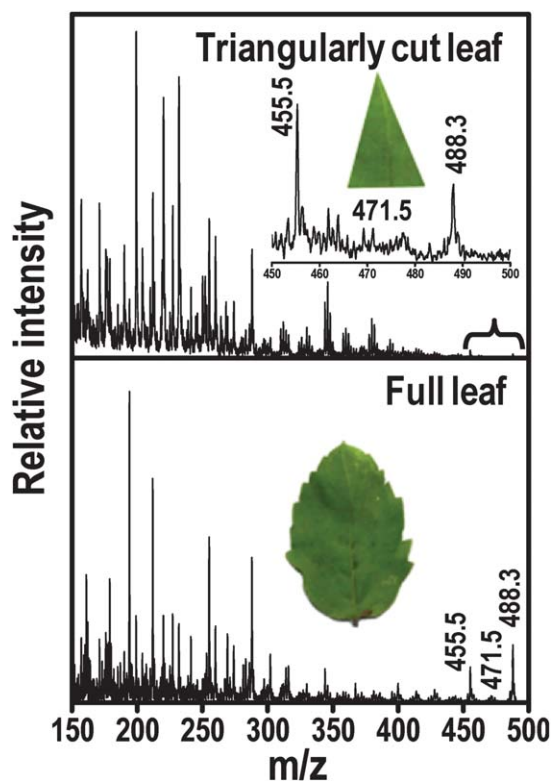


Fig. 2 Leaf spray mass spectra from a triangularly cut tulsi leaf (top) and a whole tulsi leaf (bottom). Inset of the top figure shows the expanded view from m/z 450 to 500.

Table 1 Tabulated tandem ESI-MS data from m/z 455.5, 471.5 and 487.5

m/z	MS ²	MS ³	MS ⁴
455.5	407.5	391.5 377.5	—
471.5	453.5	407.5 391.5	391.5 377.5
487.5	469.5	407.5 391.5 377.5	—

(30 Da) and H₂O (18 Da). Upon MS³ of m/z 407.5, two peaks are formed at m/z 391.5 and m/z 377.5 because of the loss of CH₄ and C₂H₆, respectively. The results are supported by a previous report in the literature.⁴³ Similar results were obtained from leaf spray data also for m/z 455.5 (data not shown). The similarity of the fragmentation peaks confirms our speculation about the new peaks at m/z 471.5 and m/z 487.5 as oxidation products of UA and OA with one and two oxygen additions, respectively. It is noteworthy to mention at this point that ambient ionization process like DESI can oxidize analyte molecules during analysis. However, it has been on totally unrelated compounds that the same sample which gives oxidized products in DESI does not give oxidized products during ESI analysis.⁴⁴ In contrast, both ESI and leaf spray give the oxidized products in the present experiments, which confirms that the observed oxidation does not occur during leaf spray ionization. Upon a close look at the ESI spectrum of tulsi leaf extract, peaks at m/z 487.5 and m/z 488.3 are

resolved properly which are not very clear in the leaf spray data where the peak at m/z 488.3 is somewhat broad (Fig. S6†). Again, tandem mass spectra of m/z 488.3 (Fig. S7†) do not reveal any similarity with other peaks. These two observations indicate that the ion at m/z 488.3 is different from that at m/z 487.5.

Five different types of leaves, *i.e.* TL, YL, ML, OL and DL (dried from OL) were collected from tulsi plants. Six sets were made from three different plants; two sets from each plant. After collection, the leaves were washed with deionized water and kept in a small closed container for 2 hours to make them uniformly moistened. The dried leaves were also moistened uniformly using the same methodology. After taking the leaves out of the container, they were wiped gently with tissue paper to remove excess water. Then 10 μ L of methanol was spotted on them using a micro-pipette and the whole leaf was attached with the clip. All other experimental parameters were the same as mentioned before. Then averages of 10 scans were taken from each sample and intensities of m/z 455.5, 471.5 and 487.5 were noted. The signal duration (time window during which electrospray occurs from the leaf) was approximately one minute in each case. Fig. 3 shows the leaf spray mass spectra of ML and DL showing prominent changes in the intensities. The intensity ratios of m/z 471.5/455.5 and m/z 487.5/455.5 were calculated and the average values were plotted for all the five types of leaves (Fig. 4). From the plot, it is clear that the combined intensity of UA and OA decreased, compared to their oxidized products, with ageing of the leaf. As the size and shape of each leaf was different, and so were their origins, it is expected that the chemical contents will

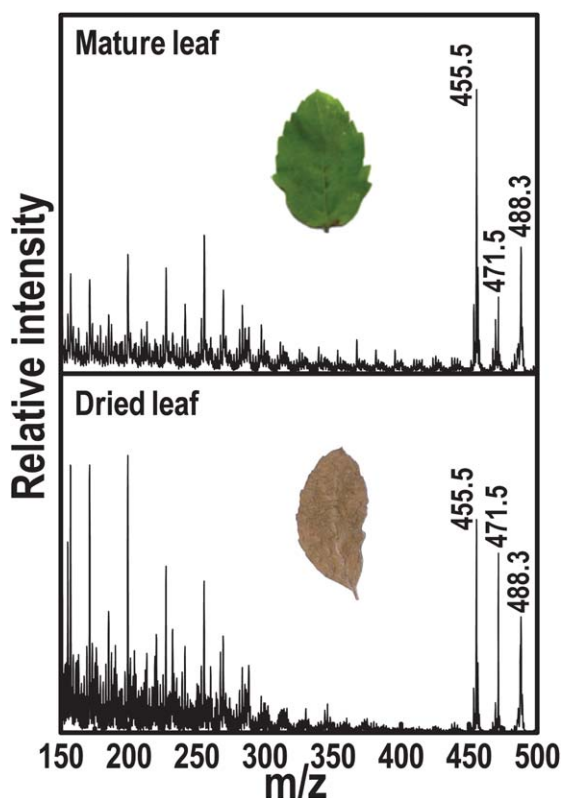


Fig. 3 Leaf spray ionization mass spectra of a mature tulsi leaf (top) and a dried tulsi leaf (bottom) using 10 μ L of methanol as a solvent.

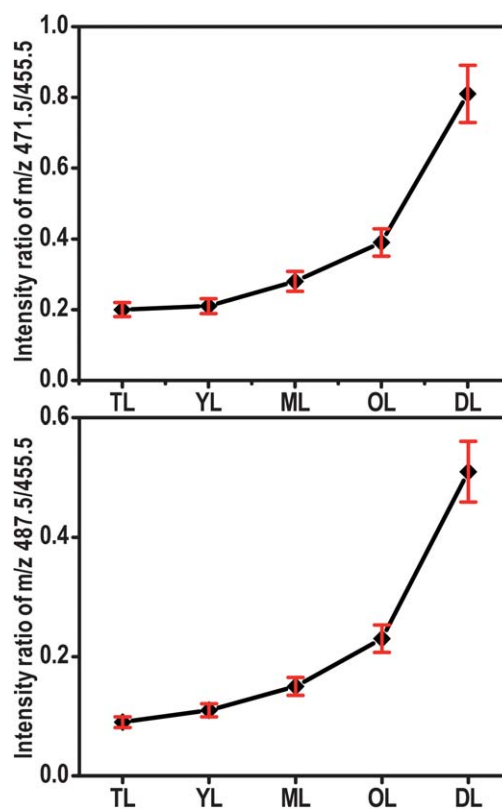


Fig. 4 Changes in intensity ratios, m/z 471.5/455.5 (top) and m/z 487.5/455.5 (bottom) with ageing of tulsi leaves, from leaf spray experiments. The error bars typically represent 10% error in absolute scale.

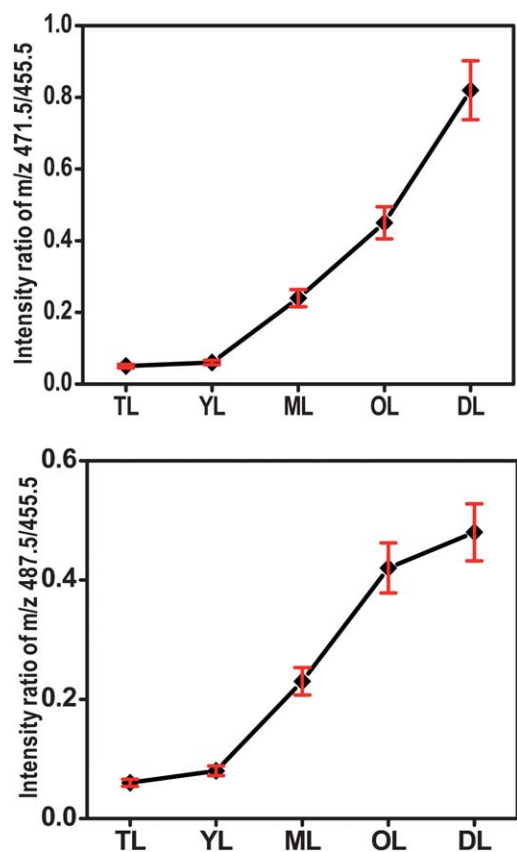


Fig. 5 Changes in intensity ratios, m/z 471.5/455.5 (top) and m/z 487.5/455.5 (bottom) with ageing of tulsi leaves from electrospray ionization experiments. The error bars typically represent 10% error in absolute scale.

also vary somewhat. This is the reason for taking the intensity ratios instead of the absolute intensities. All the six sets gave almost the same trends and the average of these is shown in Fig. 4. The same experiments were done without moistening the leaves, but they did not yield consistent results. This is also attributed to the very different nature of each leaf; *i.e.* having different degrees of moisture content. So maintaining a constant moistening condition for all of the leaves is necessary, as analyte transport is achieved by the solvent present, to get concordant datasets in experiments where comparison is needed.

The same experiments were also done with methanol extracts of tulsi leaves using ESI. Six sets of samples were made in a similar way as mentioned previously. The plots obtained from ESI are shown in Fig. 5 and are similar to those obtained from leaf spray experiments. These plots support the reliability of the data obtained from the leaf spray ionization method. In the case of ESI-MS of leaf extracts, the peak at m/z 359.3 due to rosmarinic acid occurs at high intensity whereas in leaf spray mass spectra it is poor. This enables other peaks of interest like at m/z 455.5, 471.5 and 487.5 to become prominent in the spectra and makes leaf spray ionization a better choice over ESI for studying UA, OA and their oxidation products.

Conclusions

In this work, fast detection of UA, OA and their oxidation products has been achieved by leaf spray ionization mass

spectrometry. The identity has been confirmed by tandem ESI-MS experiments. By the leaf spray ionization technique it has been shown that the total combined amount of UA and OA decreased, compared to their oxidized products, with ageing of tulsi leaves. As the above mentioned medicinally important compounds are getting oxidized, medicinal activity of tulsi leaf is reduced with ageing. It also shows the vulnerability of these compounds towards oxidation. The same trend is observed in ESI experiments. It shows the reliability of the leaf spray ionization method, which can be used for other similar applications. Leaf spray ionization could become important in the field of phytochemical research where it could become a prominent analytical tool in the near future. Additionally, this method can be implemented with handheld mass spectrometers for rapid field studies.

The exact structural identification of oxidized products (position of oxygen addition) requires several spectroscopic studies such as NMR, IR, UV-visible, *etc.* which require a reasonable amount of these compounds in their purest form. The presence of these compounds in trace quantities in tulsi leaves and their similar polarities make it almost impossible to separate them by separation techniques such as HPLC. Extensive work towards method development is underway to determine the exact structures of the oxidized products.

Acknowledgements

We acknowledge financial support from the Department of Science and Technology (DST), Government of India. Amitava Srimany thanks Council of Scientific and Industrial Research (CSIR), Government of India for a research fellowship.

References

- H. M. Merken and G. R. Beecher, *J. Agric. Food Chem.*, 2000, **48**, 577–599.
- A. Marston and K. Hostettmann, *Planta Med.*, 2009, **75**, 672–682.
- D. Steinmann and M. Ganzera, *J. Pharm. Biomed. Anal.*, 2011, **55**, 744–757.
- R. G. Cooks, Z. Ouyang, Z. Takats and J. M. Wiseman, *Science*, 2006, **311**, 1566–1570.
- G. J. Van Berkel, S. P. Pasilis and O. Ovchinnikova, *J. Mass Spectrom.*, 2008, **43**, 1161–1180.
- H. Chen, G. Gamez and R. Zenobi, *J. Am. Soc. Mass Spectrom.*, 2009, **20**, 1947–1963.
- D. R. Ifa, C. Wu, Z. Ouyang and R. G. Cooks, *Analyst*, 2010, **135**, 669–681.
- D. J. Weston, *Analyst*, 2010, **135**, 661–668.
- R. M. Alberici, R. C. Simas, G. B. Sanvido, W. Romao, P. M. Lalli, M. Benassi, I. B. S. Cunha and M. N. Eberlin, *Anal. Bioanal. Chem.*, 2010, **398**, 265–294.
- G. A. Harris, A. S. Galhena and F. M. Fernandez, *Anal. Chem.*, 2011, **83**, 4508–4538.
- Z. Takats, J. M. Wiseman, B. Gologan and R. G. Cooks, *Science*, 2004, **306**, 471–473.
- R. B. Cody, J. A. Laramée and H. D. Durst, *Anal. Chem.*, 2005, **77**, 2297–2302.
- N. Talaty, Z. Takats and R. G. Cooks, *Analyst*, 2005, **130**, 1624–1633.
- A. U. Jackson, A. Tata, C. Wu, R. H. Perry, G. Haas, L. West and R. G. Cooks, *Analyst*, 2009, **134**, 867–874.
- J. H. Kennedy and J. M. Wiseman, *Rapid Commun. Mass Spectrom.*, 2010, **24**, 1305–1311.
- A. Srimany, D. R. Ifa, H. R. Naik, V. Bhat, R. G. Cooks and T. Pradeep, *Analyst*, 2011, **136**, 3066–3068.
- T. Muller, S. Oradu, D. R. Ifa, R. G. Cooks and B. Krautler, *Anal. Chem.*, 2011, **83**, 5754–5761.

- 18 B. Li, N. Bjarnholt, S. H. Hansen and C. Janfelt, *J. Mass Spectrom.*, 2011, **46**, 1241–1246.
- 19 J. Thunig, S. H. Hansen and C. Janfelt, *Anal. Chem.*, 2011, **83**, 3256–3259.
- 20 D. R. Ifa, A. Srimany, L. S. Eberlin, H. R. Naik, V. Bhat, R. G. Cooks and T. Pradeep, *Anal. Methods*, 2011, **3**, 1910–1912.
- 21 S. D. Maleknia, T. M. Vail, R. B. Cody, D. O. Sparkman, T. L. Bell and M. A. Adams, *Rapid Commun. Mass Spectrom.*, 2009, **23**, 2241–2246.
- 22 H. J. Kim and Y. P. Jang, *Phytochem. Anal.*, 2009, **20**, 372–377.
- 23 R. Kubec, R. B. Cody, A. J. Dane, R. A. Musah, J. Schraml, A. Vattekkatte and E. Block, *J. Agric. Food Chem.*, 2010, **58**, 1121–1128.
- 24 P. Nemes and A. Vertes, *Anal. Chem.*, 2007, **79**, 8098–8106.
- 25 P. Nemes, A. A. Barton, Y. Li and A. Vertes, *Anal. Chem.*, 2008, **80**, 4575–4582.
- 26 P. Nemes, A. A. Barton and A. Vertes, *Anal. Chem.*, 2009, **81**, 6668–6675.
- 27 H. Chen, Y. Sun, A. Wortmann, H. Gu and R. Zenobi, *Anal. Chem.*, 2007, **79**, 1447–1455.
- 28 H. Chen, S. Yang, A. Wortmann and R. Zenobi, *Angew. Chem., Int. Ed.*, 2007, **46**, 7591–7594.
- 29 J. Liu, H. Wang, R. G. Cooks and Z. Ouyang, *Anal. Chem.*, 2011, **83**, 7608–7613.
- 30 F. K. Tadjimukhamedov, G. Huang, Z. Ouyang and R. G. Cooks, *Analyst*, 2012, **137**, 1082–1084.
- 31 S. L.-F. Chan, M. Y.-M. Wong, H.-W. Tang, C.-M. Che and K.-M. Ng, *Rapid Commun. Mass Spectrom.*, 2011, **25**, 2837–2843.
- 32 B. Hu, Y.-H. Lai, P.-K. So, H. Chen and Z.-P. Yao, *Analyst*, 2012, **137**, 3613–3619.
- 33 H. Wang, J. Liu, R. G. Cooks and Z. Ouyang, *Angew. Chem., Int. Ed.*, 2010, **49**, 877–880.
- 34 J. Liu, H. Wang, N. E. Manicke, J.-M. Lin, R. G. Cooks and Z. Ouyang, *Anal. Chem.*, 2010, **82**, 2463–2471.
- 35 A. Li, H. Wang, Z. Ouyang and R. G. Cooks, *Chem. Commun.*, 2011, **47**, 2811–2813.
- 36 H. Wang, N. E. Manicke, Q. Yang, L. Zheng, R. Shi, R. G. Cooks and Z. Ouyang, *Anal. Chem.*, 2011, **83**, 1197–1201.
- 37 S. Mondal, B. R. Mirdha and S. C. Mahapatra, *Indian J. Physiol. Pharmacol.*, 2009, **53**, 291–306.
- 38 P. Prakash and N. Gupta, *Indian J. Physiol. Pharmacol.*, 2005, **49**, 125–131.
- 39 J. Liu, *J. Ethnopharmacol.*, 1995, **49**, 57–68.
- 40 M. B. Gupta, T. N. Bhalla, G. P. Gupta, C. R. Mitra and K. P. Bhargava, *Eur. J. Pharmacol.*, 1969, **6**, 67–70.
- 41 Y. Kashiwada, H.-K. Wang, T. Nagao, S. Kitanaka, I. Yasuda, T. Fujioka, T. Yamagishi, L. M. Cosentino, M. Kozuka, H. Okabe, Y. Ikeshiro, C.-Q. Hu, E. Yeh and K.-H. Lee, *J. Nat. Prod.*, 1998, **61**, 1090–1095.
- 42 M. B. Gupta, R. Nath, G. P. Gupta and K. P. Bhargava, *Indian J. Med. Res.*, 1981, **73**, 649–652.
- 43 Q. Chen, Y. Zhang, W. Zhang and Z. Chen, *Biomed. Chromatogr.*, 2011, **25**, 1381–1388.
- 44 S. P. Pasilis, V. Kertesz and B. G. J. Van, *Anal. Chem.*, 2008, **80**, 1208–1214.

Supporting Information

Rapid Identification of Molecular Changes in Tulsi (*Ocimum sanctum* Linn) Upon Ageing Using Leaf Spray Ionization Mass Spectrometry

Depanjan Sarkar, Amitava Srimany and T. Pradeep*

DST Unit of Nanoscience (DST UNS), Department of Chemistry, Indian Institute of Technology Madras, Chennai 600036, India.

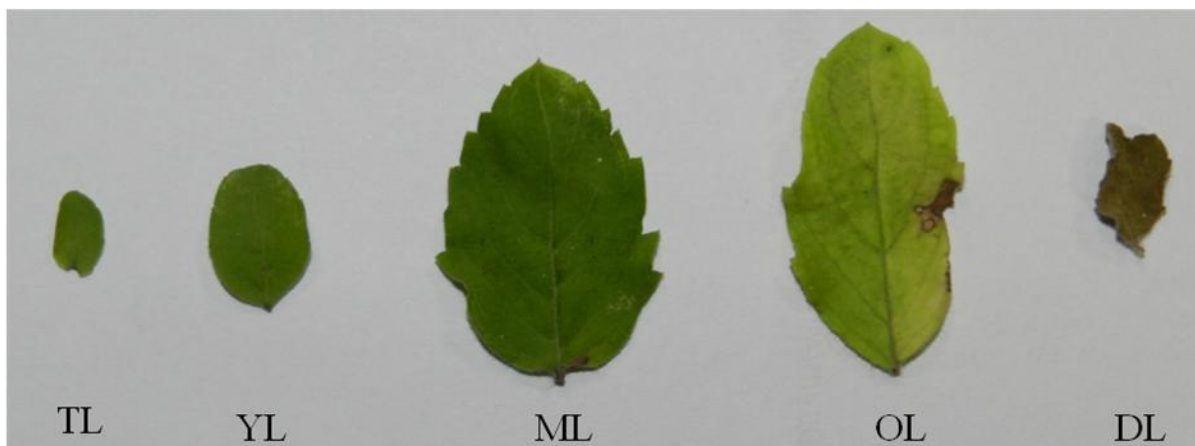


Figure S1. Five different categories of Tulsi leaves: (from left to right) tender leaf (TL), young leaf (YL), mature leaf (ML), old leaf (OL) and dried leaf (DL).



Figure S2. Experimental set-up for the leaf spray ionization showing the Tulsi leaf connected with a clip and held in front of atmospheric inlet of the mass spectrometer.

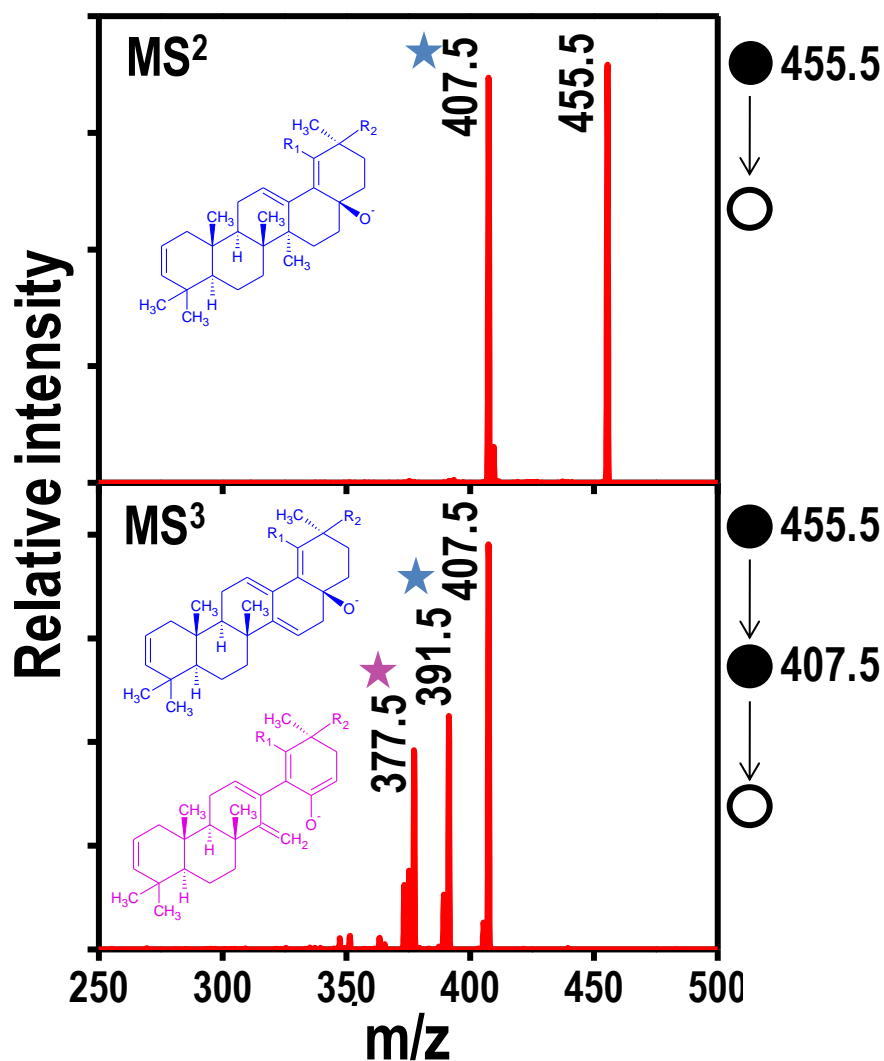


Figure S3. Tandem mass spectra for the peak at m/z 455.5. Possible structures of fragment ions at m/z 407.5, m/z 391.5 and m/z 377.5 have been incorporated. When $R_1=H$ and $R_2=CH_3$, the structures are coming from oleanolic acid fragmentations and when $R_1=CH_3$ and $R_2=H$, the structures are coming from ursolic acid fragmentations. Right side schematics show the parent ions from which fragmentations have been done.

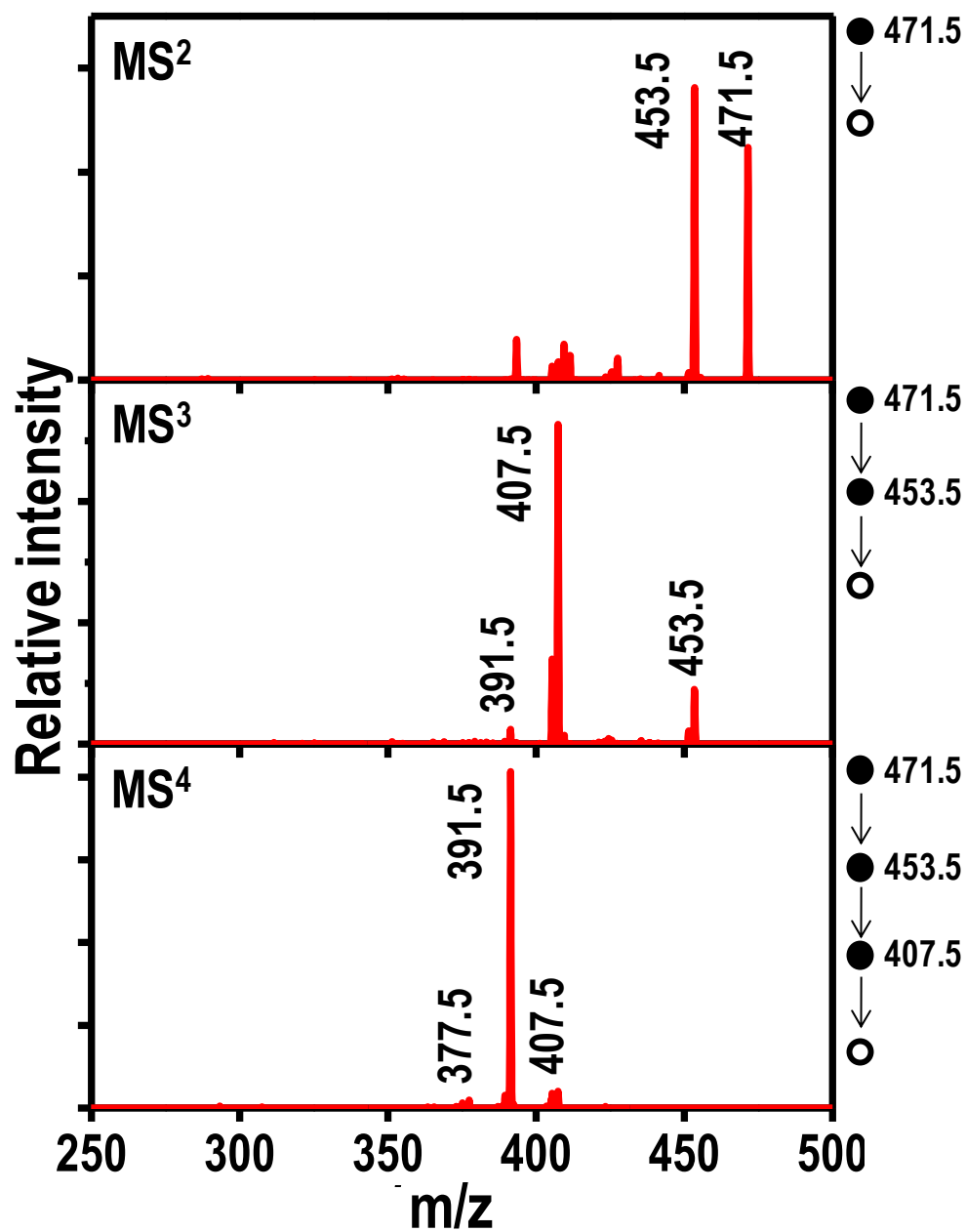


Figure S4. Tandem mass spectra for the peak at m/z 471.5. Right side schematics show the parent ions from which fragmentations have been done.

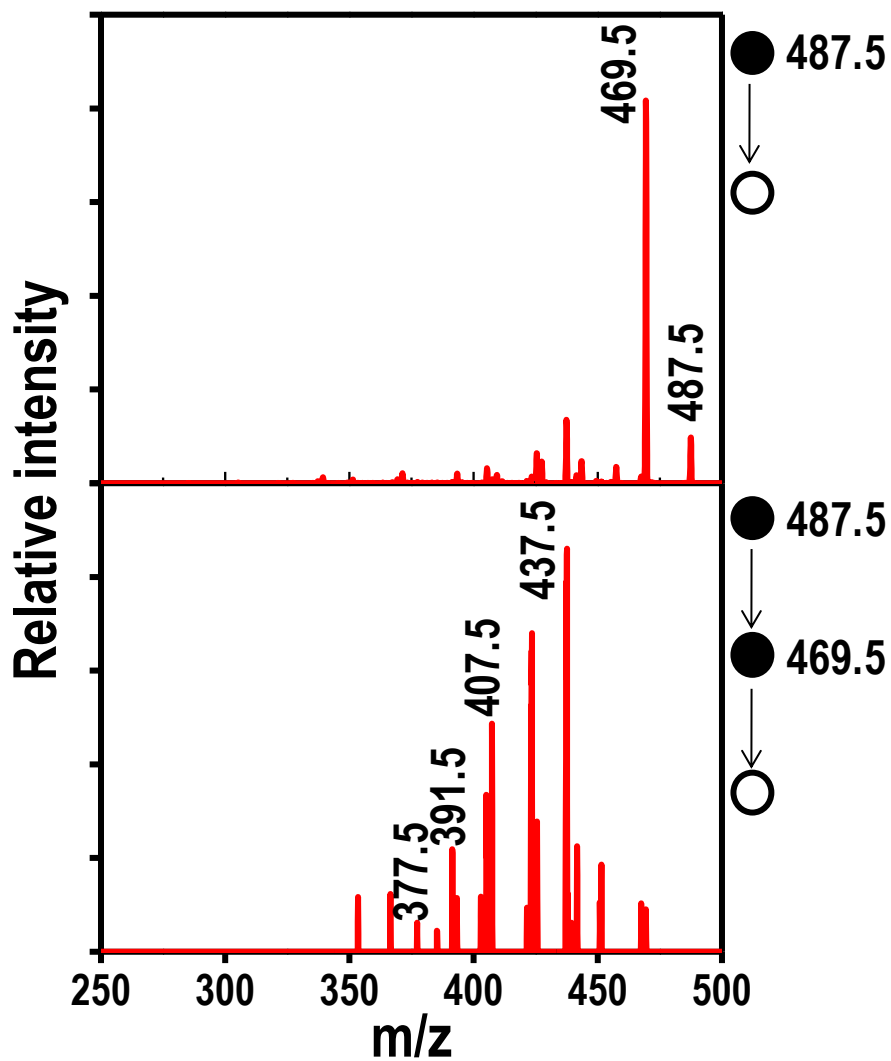


Figure S5. Tandem mass spectra for the peak at m/z 487.5. Right side schematics show the parent ions from which fragmentations have been done.

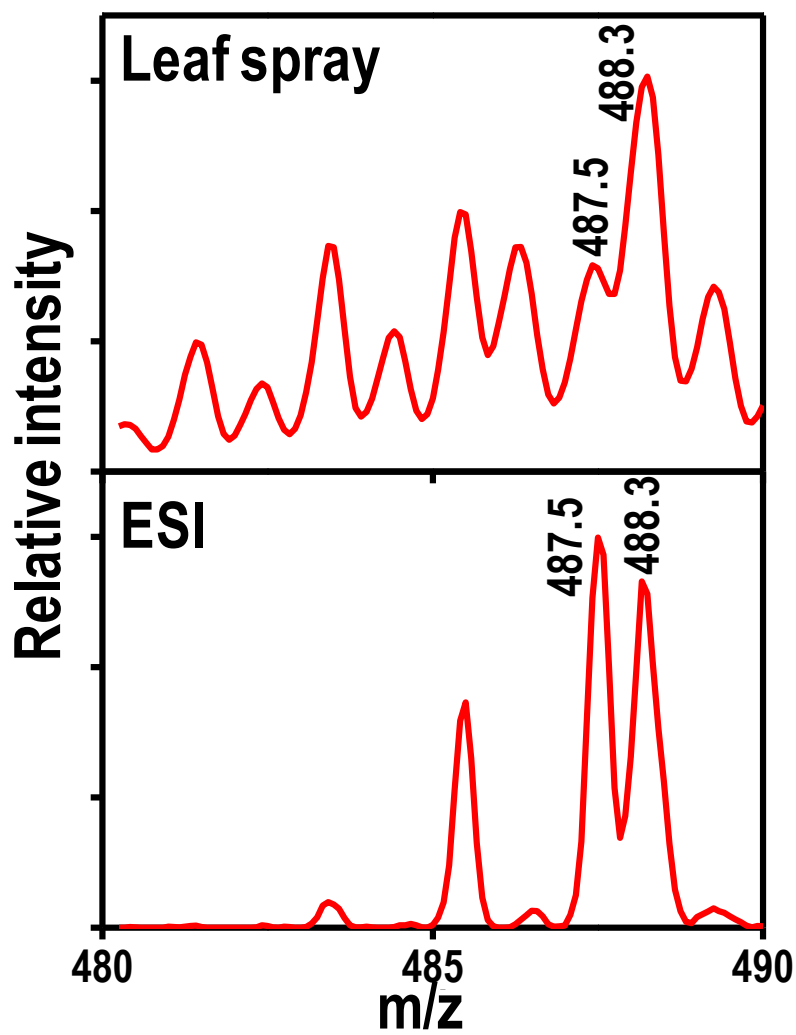


Figure S6. Expanded view of leaf spray (top) and ESI (bottom) spectra near the region at m/z 487.5.

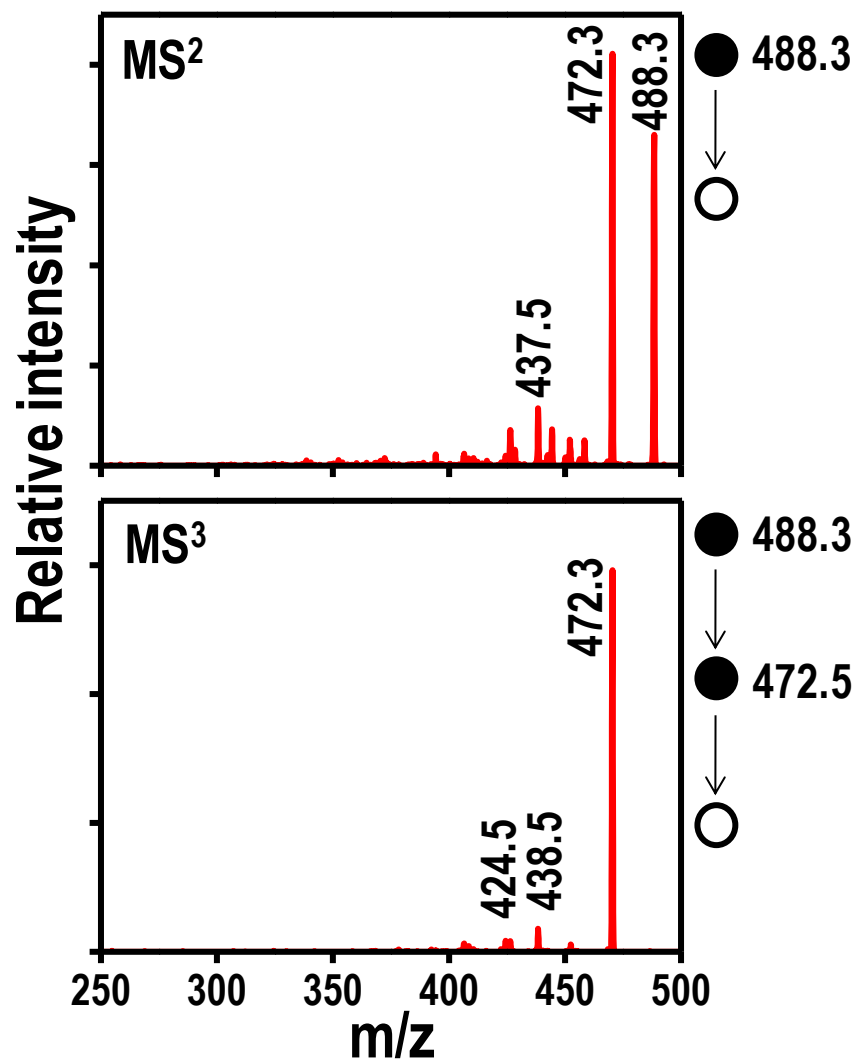


Figure S7. Tandem mass spectra for the peak at m/z 488.3. Right side schematics show the parent ions from which fragmentations have been done.

Graphene: A Reusable Substrate for Unprecedented Adsorption of Pesticides

Shihabudheen M. Maliyekkal, T. S. Sreeprasad, Deepti Krishnan, Summayya Kouser, Abhishek Kumar Mishra, Umesh V. Waghmare,* and T. Pradeep*

Unprecedented adsorption of chlorpyrifos (CP), endosulfan (ES), and malathion (ML) onto graphene oxide (GO) and reduced graphene oxide (RGO) from water is reported. The observed adsorption capacities of CP, ES, and ML are as high as ~1200, 1100, and 800 mg g⁻¹, respectively. Adsorption is found to be insensitive to pH or background ions. The adsorbent is reusable and can be applied in the field with suitable modifications. A first-principles pseudopotential-based density functional analysis of graphene–water–pesticide interactions showed that the adsorption is mediated through water, while direct interactions between graphene and the pesticides is rather weak or unlikely.

1. Introduction

Carbon and water are two vital components central to all known living systems. The adsorption capacity of several carbon forms and most importantly of activated carbon enabling affordable clean water is used extensively. The use of carbon in water purification dates back to Harappan civilization. Today, carbon has become one of the most common and

trusted means of removing contaminants like disinfection-byproduct precursors, taste and odor compounds, and synthetic organic chemicals (SOCs) such as pesticides and heavy metals from water^[1] and is the most essential component in all water purification technologies.

During the past decades, a considerable understanding of the relationship between water quality and human health has been developed. Standards of drinking water have been revised several times, and with the increased understanding of the health effects associated with several contaminants, the maximum permissible limits (MPL) of contaminants are likely to reach molecular limits in due course.^[2] Among the 92 regulated contaminant species as per the environmental protection agency (EPA) guidelines, pesticides are of major concern due to their indiscriminate use and widespread presence in drinking water. The toxicity and health hazards posed by pesticides, even at very low concentrations, have become large concerns for both developing and developed countries.^[3,4] World health organization (WHO) drinking water standards prescribe an MPL for a single pesticide as 0.1 µg L⁻¹. It is in this context that new adsorbents and new chemistry have to be developed to control these species. As a result of this tireless search for new technology to enable the efficient separation of pesticides from water, many new materials with interesting properties have been developed. We have reported the use of noble metal nanoparticles for the degradation of pesticides in water at ultra low concentrations^[5] and introduced this technology in the market.^[2]

Dr. S. M. Maliyekkal, Dr. T. S. Sreeprasad,
D. Krishnan, Prof. T. Pradeep
DST Unit on Nanoscience
Department of Chemistry
Indian Institute of Technology Madras
Chennai - 600 036, India
Fax: 91-44-2257-0545/0509
E-mail: pradeep@iitm.ac.in

Dr. S. M. Maliyekkal
School of Mechanical and Building Sciences
VIT University
Chennai Campus, Chennai-600 127, India
S. Kouser, Dr. A. K. Mishra, Prof. U. V. Waghmare
Theoretical Sciences Unit
Jawaharlal Nehru Centre for Advanced Scientific Research (JNCASR)
Jakkur, Bangalore 560 064, India
E-mail: waghmare@jncasr.ac.in



DOI: 10.1002/sml.201201125

Carbon nanotubes (CNTs) are another category of materials investigated recently for pesticide uptake.^[6–8] Studies demonstrated that CNTs are promising candidates for the adsorption of a few SOC's from water and the adsorption capacities are dependent on various factors including the specific surface area and pore volume of the CNTs, the density of oxygen-containing functionalities on CNTs, and the chemical nature of the pollutant. However, CNTs are reported to be cytotoxic,^[9,10] which may limit their utility in drinking water purification.

Since the discovery of graphene—a single atomic layer of carbon—in 2004,^[11] it has attracted overwhelming attention due to its unique chemical and physical properties and low production cost compared to other graphitic forms.^[12–14] As of now, graphene and graphene-based materials have been proposed for many applications. This includes drug delivery,^[15] solid-state gas sensors,^[16] electrochemical sensors,^[17,18] Raman scattering-based molecular sensors,^[19] hydrogen storage,^[20,21] energy storage devices,^[22] and catalysis.^[23] Recent studies show that graphene-based materials have good potential in environmental cleanup as well. Large surface area,^[24] reduced cytotoxicity,^[25] the large delocalized π electrons^[26] and tunable chemical properties^[27] make these materials perfect candidates for the adsorption of chemicals and thus the cleanup of water. The utility of graphene-based materials for arsenic removal has been proved very recently.^[28] The antibacterial properties of graphene oxide (GO) and reduced graphene oxide (RGO) have also been studied and it has been found that both are antibacterial.^[25] Sreeprasad et al. have reported a new methodology to make a series of RGO–metal and –metal oxide composites and studied their application for Hg(II) removal from water.^[29] The study also showed a simple method to immobilize GO/RGO on sand particles and demonstrated the utility of this material in heavy metal removal. Gao and co-workers also demonstrated that GO-coated sand could be used as a low-cost water purification material for developing economies.^[30] A recent investigation shows that sulfonated graphene is a good medium for the separation of naphthalene and 1-naphthol from water and the adsorption capacities were estimated to be ~ 2.3 – 2.4 mmol g⁻¹.^[31] However, no systematic effort has been done to use RGO and GO to remove complex molecules such as pesticides from water. Considering the diverse nature of pollutants in water, we believe that continuous and systematic efforts are needed to bring advanced materials like graphene for down-to-earth applications like water purification. To the best of our knowledge, no theoretical investigation is available in the literature to explain the phenomenon of organics–water–graphene interactions. Such studies may help to understand the system better and thus allow fine tuning for improved performance.

In this paper, we explore the use of RGO and GO for the removal of pesticides like endosulfan (ES), chlorpyrifos (ES), and malathion (ML) from water under different conditions. In order to delineate the removal mechanism and to comprehend the observed uptake capacity, an analysis using first-principles pseudopotential-based density functional theory (DFT) was carried out. The pesticides used in this study are widely detected in the surface and groundwaters

of many countries.^[32] While ES belongs to the organochlorine (OC) group, CP and ML belong to the organophosphate group, which are second generation pesticides developed as substitutes to OC pesticides. Although many OC pesticides are prohibited, ES is still used extensively as an insecticide in countries such as India, Pakistan, and Bangladesh under different trade names like Thiodan, Thionex, and Endosan.^[33a] Endosulfan is one of the most commonly detected pesticides in surface waters of the US (38 states).^[33b] CP (trade names: dursban, lorsban, agromil, dhanwan, dorson, dhanwan, omexan, etc.) and ML are reported to be used both for agricultural and landscape pest control and their presence in water is widely reported.^[32a,32c] The toxic effects of these pesticides are well documented.^[34]

2. Results and Discussion

2.1. Characterization of GO and RGO

The UV–vis spectral features of GO and RGO are shown in **Figure 1A**. The absorption peak at 232 nm showed the typical characteristic of GO and red shift in the peak (at 268 nm) after reduction confirmed the transformation of GO to RGO. The attenuated total reflectance infrared spectroscopy (ATR-IR) spectra of GO and RGO are shown in the inset of **Figure 1A**. GO showed characteristic peaks at 1217 (epoxy C–O), 1415 (carboxy C–O), 1614 (aromatic C=C), and 1720 (C=O in carboxylic acid), and 1035 cm⁻¹ (epoxy or alkoxy C–O). The broad band between 3200–3400 cm⁻¹ can be attributed to O–H stretching vibrations. In the case of RGO, most of the peaks due to oxygen functionalities disappeared. The peak at 1415 cm⁻¹ almost vanished after reduction. The peaks at 1575 and 1100 cm⁻¹ are due to the aromatic C=C and C–O stretching vibrations, respectively.^[35] Raman spectra of GO and RGO were also collected. As shown in **Figure 1B**, the Raman spectrum of GO showed the D-band at 1345 cm⁻¹ and G-band at 1609 cm⁻¹. After reduction, the D-band position remained the same but G-band shifted to a lower frequency region (1590 cm⁻¹), confirming the reduction of GO to RGO.^[36]

GO and RGO were characterized by X-ray photoelectron spectroscopy (XPS) as well. **Figure 1C** shows the XPS spectra of GO and RGO. GO showed four components in the C 1s spectrum. The prominent peak centered on 284.5 eV is attributed to nonoxygenated ring C 1s. Other three peaks centered around 288.8, 287.6, and 286.3 eV are ascribed to C(O)O, C=O and C–O, respectively.^[36] After the reduction of GO, the C 1s spectrum showed a major peak centered around 284.6 eV, corresponding to a non-oxygenated ring carbon. The peak centered at 288.9 eV is assigned to C(O) O. Evidently, the oxygenated peak at 286.3 eV due to C–O disappeared completely. High-resolution transmission electron microscopy (HRTEM) image of RGO sheets is shown in **Figure 1D**. An enlarged portion showing the thin folding is given in the inset. The graphenic nature of the materials can be seen from the characteristic ripples present on the sheets of GO and RGO. The edges and wrinkles were measured to

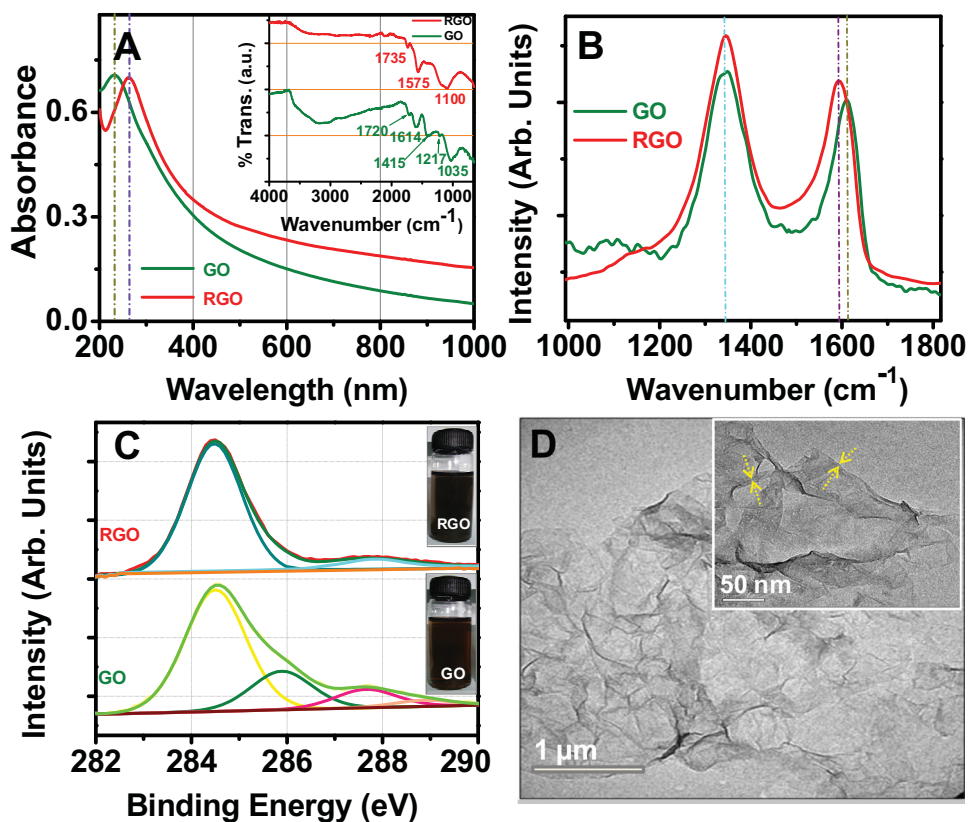


Figure 1. (A) UV-vis, (B) Raman, and (C) XPS spectra of GO and RGO. (D) HRTEM image of RGO. Inset of A shows ATR-IR of GO and RGO. Traces are shifted vertically for clarity. The shift in G-band is shown with vertical lines. Inset of (C) shows the photographs of RGO and GO dispersed in DW. Inset of (D) shows a magnified HRTEM image of RGO. The characteristic wrinkles of RGO are marked on the figure.

be around $\sim 1\text{--}1.5$ nm thick, which is close to a bilayer thickness (inset Figure 1D).^[37] RGO samples were analyzed by scanning electron microscopy and energy dispersive microscopy (SEM-EDAX) as well. A representative EDAX spectrum and elemental maps obtained are shown in Figure S3 of the Supporting Information. An SEM image of RGO from which the EDAX spectrum and maps for certain elements of relevance to pesticides were taken is also given in Figure S3. The data reveal that the sample is devoid of impurities.

2.2. Adsorption Studies

2.2.1. Comparison of GO and RGO for the Removal of Pesticides

Both GO and RGO were tested for the removal of pesticides at room temperature and neutral pH and the data for CP is shown in Figure 2. Unit uptake capacities of CP increased with decreasing RGO or GO dose. This might be due to increased mass transfer at higher adsorbate to adsorbent ratio. Better separation of RGO or GO sheets at higher dilution and thereby increased available surface area could be another reason for the significant increase in uptake capacity at lower doses. The data also revealed that RGO is a better candidate compared to GO in adsorbing CP from water. The CP uptake capacity of RGO was found to be as high as ~ 1200 mg g⁻¹, approximately 10–20% higher than that of GO. To

the best of our knowledge, no adsorbents used for the purpose are reported to have adsorption capacities of more than the weight of the adsorbate, and therefore this observation is unprecedented. Similar adsorption trends were observed for the other pesticides as well, i.e., ES and ML (Supporting Information, Figure S4). The observed capacities are several times higher than the adsorption capacities of various adsorbents investigated for the purpose.^[38–40]

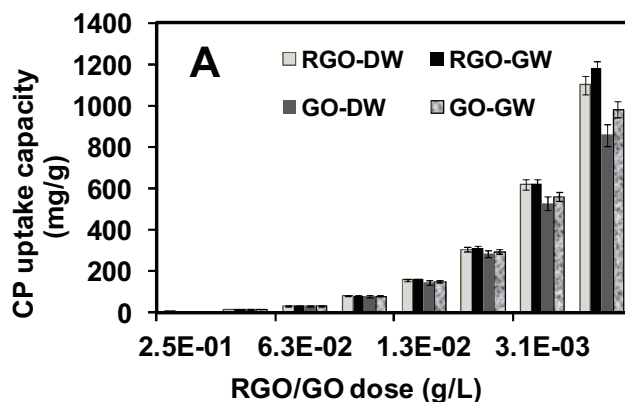


Figure 2. Adsorption of CP as a function of RGO and GO dose. Initial concentration of CP ≈ 2 mg L⁻¹, pH = 7 ± 0.2 , and temperature = 30 ± 2 °C.

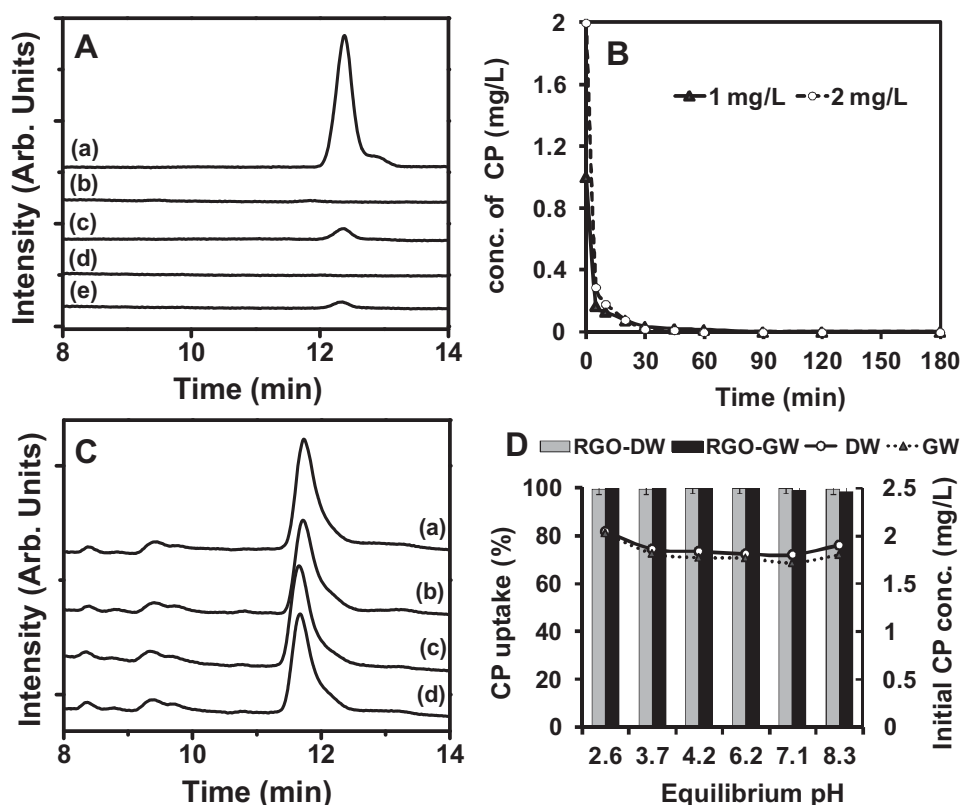


Figure 3. A) HPLC traces of (a) initial 2 mg L^{-1} of CP; (b) residual CP after contact with RGO dispersed in DW, and; (c) GO dispersed in DW; (d) residual CP after contact with RGO dispersed in GW, and; (e) GO dispersed in GW. B) Time-dependent removal of CP by RGO at two different initial concentrations of CP. C) HPLC traces of initial and desorbed CP; a, b, c, and d show initial CP and CP desorbed in three consecutive desorption cycles, respectively. D) Effect of pH on the adsorption of CP by RGO. Line diagrams (axis on the right) show the measured initial concentrations of CP at various pHs. RGO–DW indicates RGO dispersed in deionized water spiked with pesticide; RGO–GW indicates RGO dispersed in groundwater spiked with pesticide.

In order to study the interference of other ions on pesticide removal, adsorption studies were also done in groundwater spiked with pesticides. **Figure 3A** shows the High performance liquid chromatography (HPLC) trace of CP before and after contact with 0.0125 g L^{-1} of RGO. The corresponding HPLC spectra of ES and ML are given in Figure S5 of the Supporting Information. The data showed no interference, irrespective of the pesticides studied, and thus proved the possible utility of RGO and GO in purification of real waters.

2.2.2 Adsorption Kinetics

The rate of adsorption is an important factor in any adsorption process. It varies with the physical and chemical properties of the adsorbent. Here, the time dependent adsorption of CP, ES, and ML onto RGO was tested and the data for CP are given in Figure 3B. The data for ES and ML are given in Supporting Information, Figure S6. The kinetic data exhibited rapid removal of pesticides. More than 90% of the pesticide removal happened in <10 min contact time, and no traces of pesticide were detected after 30 min of contact with RGO. Control samples were also run to account for any possible volatilization and hydrolysis and they showed an insignificant effect. Concentration variation in the control was estimated to be less than 5%.

2.2.3. Regeneration and Reuse

For checking the reuse potential of RGO, successive adsorption–desorption cycles were conducted. The reuse capacity was studied for three consecutive cycles of adsorption–desorption. The HPLC spectra obtained during three desorption cycles are shown in Figure 3C. The percentage removal of CP for the corresponding adsorption cycle is shown in Figure S7 of Supporting Information. More than 90% desorption and insignificant reduction in CP uptake capacity was seen with repeated use. In the course of the study, we also observed that a good portion of RGO, which is initially dispersed in water, came to the water–hexane interface, indicating the nonpolar nature of the RGO. However, we could re-disperse the RGO effectively by ultrasonication. The UV features of the cycled RGO were also collected (Figure S7). No significant change in spectral features was seen, indicating that RGO is intact even after repeated use.

2.2.4. Effect of pH on Adsorption

The pH of the solution plays an important role in the adsorption process since it can alter the solute species as well as the surface properties of the adsorbent. At a given pH, the adsorbate and adsorbent may co-exist such that the same

or opposite charges may be present. The pesticides are susceptible to hydrolysis in aqueous media and can result in some new species, different from the parent compound. It is reported that pesticides like CP, ES, and ML hydrolyze at a faster rate in alkaline pH, whereas no effect on hydrolysis was reported at acidic pH.^[41,42] Here, RGO was tested for the pesticide uptake from water, both DW and GW, as a function of pH under batch equilibrium conditions. Figure 3D shows insignificant variation in CP uptake capacity over the pH range studied (pH \approx 3–9). Similar behavior was observed with ML and ES as well (data not shown). None of the pesticides studied are ionizable, indicating that the pesticides behave as electroneutral species. Hence, the interaction between the adsorbate and adsorbent is not expected to change with pH.^[43,44] Therefore, the interaction of a neutral molecule with a relatively electroneutral surface of RGO should show a pH-independent adsorption pattern. Analysis of the initial pesticide samples also show no evidence of the formation of hydrolysis products over the experimental time span. A study on the adsorption of diuron, a non-polar pesticide, by carbon, shows a pH-independent adsorption.^[44] The same group also reported that pesticide adsorption varies with the surface functionality of the adsorbent as well as the ionic nature of the pesticide.

The pH-independent adsorption behavior of RGO indicates that the surface functional group ($-\text{COO}^-$) present on the RGO surface is not involved in the adsorption of pesticides. This may suggest the absence of direct interactions of the pesticide with RGO in the adsorption process.^[45]

2.3. Characterization of RGO After Contact With the Pesticide Samples

The adsorption of pesticides onto RGO was also illustrated using desorption electrospray ionization (DESI) mass spectrometry measurements. CP on glass plate showed its characteristic molecular ion at m/z 352 (Supporting Information, Figure S8A). Collision-induced dissociation of this ion (in mass spectrometry/mass spectrometry (MS/MS)) confirmed the identity of the species (inset of Supporting Information, Figure S8B). RGO loaded with CP showed the characteristic molecular ion peak at m/z 352 (Figure 4A). The isotope pattern exhibited by this peak is similar to the theoretically predicted pattern, confirming the presence of CP on RGO. The MS/MS measurement further confirmed the identity of the species (Figure 4B). The fragmented ion at m/z 324 is due to the loss of C_2H_4 from the molecular ion at m/z 352. The subsequent loss of C_2H_4 from m/z 324 resulted in the ion

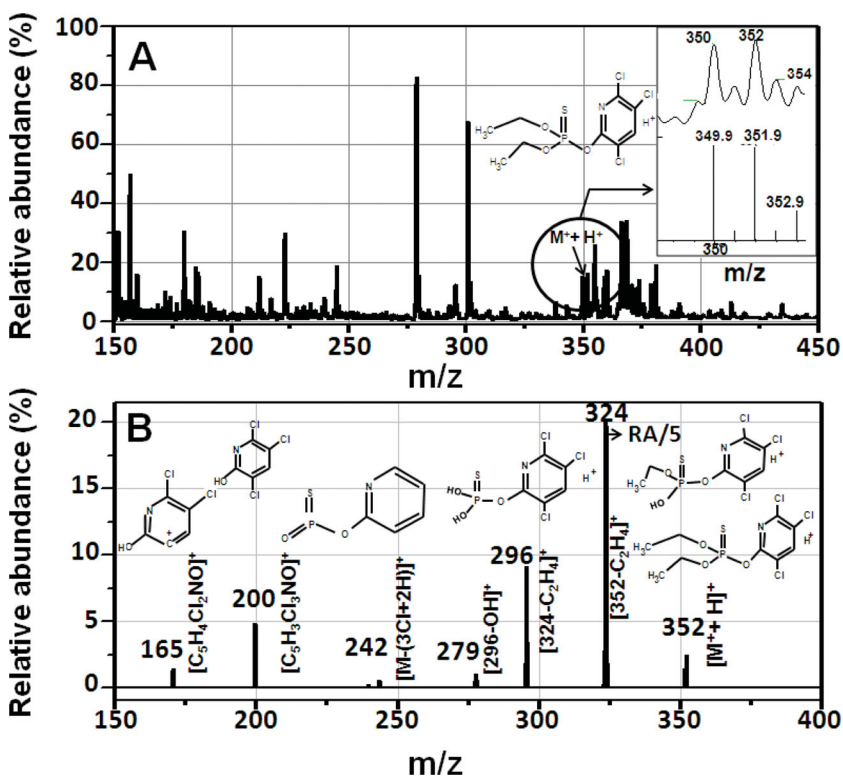


Figure 4. (A) Positive ion DESI mass spectrum of CP on RGO surface. (B) MS/MS analysis of m/z 352. Inset of A shows an expanded view of the molecular ion peak and a comparison with the theoretical isotope pattern. The m/z 324 peak intensity (RA) in B is multiplied by 1/5 to show all the ions clearly.

at m/z 296. The fragmented ion at m/z 200 was assigned to $[\text{C}_5\text{H}_3\text{Cl}_3\text{NO}]^+$.

The mass spectra of ML were also recorded and the data showed the molecular ion peak at m/z 331 (Supporting Information, Figure S9A). The theoretical and experimental isotope pattern exhibited by the molecular ion peak showed 1:1 correspondence, confirming the presence of ML on RGO (inset of Figure S9A). The MS/MS spectrum of the molecular ion is shown in Supporting Information, Figure S9B. The fragment ion masses and their molecular formulae are marked in the figure. The data established the presence of adsorbed ML on RGO.

Figures 5A and B show the TEM and SEM images, respectively, of RGO after adsorption of CP. We can see that the thickness of the sheet increased after pesticide adsorption. Similar observations were seen in the case of other pesticides as well (Supporting Information, Figure S10). However, the shape of the sheet was preserved and RGO remained in suspension without any visible aggregation. This may be explained as follows: It is known that GO prepared through reduction route can form well-dispersed aqueous colloids. The stability is attributed to electrostatic repulsion due to high surface negative charge generated as a result of ionization of the $-\text{COOH}$ and $-\text{OH}$ groups on the GO sheets.^[36] It is also known that $-\text{COOH}$ groups are unlikely to be reduced under these experimental conditions, indicating that the surface of RGO is still negatively charged. Adsorption of non-ionic species like CP, ES, and ML is unlikely to change

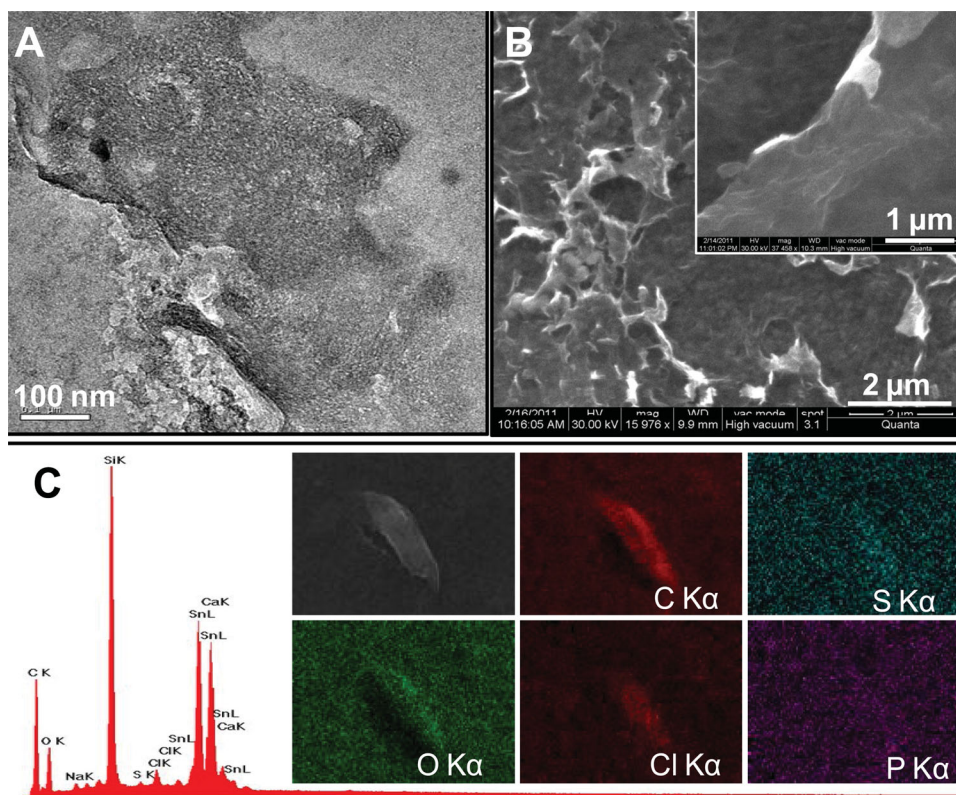


Figure 5. (A) TEM image of RGO after adsorption of CP. (B) SEM image of RGO after adsorption of CP. Inset of (B) shows a magnified SEM image. (C) EDAX spectrum of RGO loaded with CP. Inset of (C) shows the X-ray images of various elements present in RGO along with a SEM image.

the surface charge and hence the stability. On the contrary, aggregation of RGO was observed in groundwater spiked with pesticides. This may be due to the interaction of cations present in groundwater with negative functional groups on RGO, i.e., COO^- , and thereby charge neutralization and coagulation. The flocs once formed can be redispersed temporarily by ultrasonication.

2.4. First-Principles Analysis of the Graphene, Pesticide and Water Interactions

We now present results to address the following issues in the observed capacity of graphene to adsorb these pesticides at unprecedented levels: 1) Is adsorption feasible and how is it influenced by water? 2) Is such a large capacity of adsorption possible, and what may the upper limit be? 3) What are the atomistic mechanisms responsible?

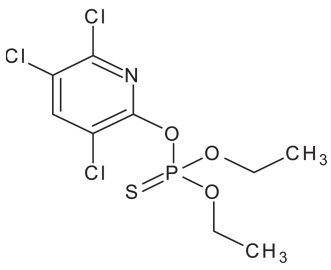
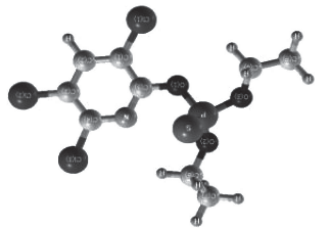
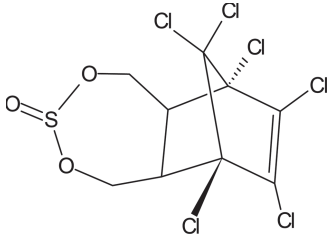
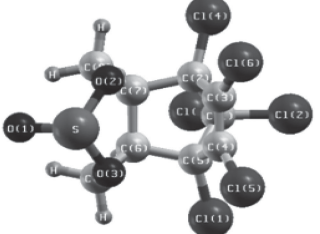
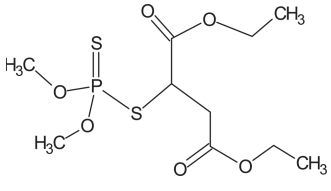
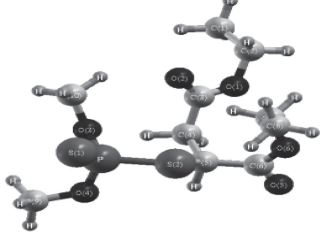
While all experiments were carried out at room temperature, the first-principles calculations provided energies at 0 K, and we used them to develop a qualitative understanding of our experiments. Although such calculations can be employed in molecular dynamics to simulate behavior at finite temperature, this approach is quite expensive and unrealistic, particularly to access the time-scales relevant to the separation of pesticides from water. However, to have some idea about entropic effects, we have considered various (8 to 10) configurations for different aggregates or complexes of

water, graphene, and each of the three pesticide molecules. To facilitate a comparative analysis of the energetics that involve different species of atoms, we first considered the following systems: a free water molecule (W), pristine graphene (G), a free pesticide molecule ($P = \text{ES}, \text{CP}, \text{or ML}$), and an aggregate of n water molecules (nW). The energy of each of these was determined through structural relaxation in a large supercell. Our optimized structure of graphene has a lattice constant of 2.45 \AA , in good agreement with the experimental value of 2.46 \AA .^[46] Using an experimental^[47] hexagonal crystal structure of $\beta\text{-ES}$ for the initial guess in our structural optimization, we found that bond-lengths of ES change by only a couple of percent during relaxation, within the typical errors of DFT calculations. Similarly, we used a monoclinic crystal structure of CP generated experimentally^[48] and found that our calculated structure is in reasonable agreement with experiment. A detailed structure of ML is not available experimentally, so we determined it from our calculations. Since our pseudopotentials and other calculational parameters accurately described the structures of ES and CP, we expect a similar level of accuracy in the structure of ML (see theoretical structures of pesticides in **Table 1**).

2.5. Adsorption of Pesticide on Graphene

Among the binary complexes, we first considered different (3–4) configurations of pesticide–graphene (P–G) complexes

Table 1. Selected properties of the pesticides used in the study.

Pesticide	Molecular Formula	Chemical Structure	Theoretical Structure (From DFT Calculations)	Mol. Wt. [g mol ⁻¹]	Water solubility [mg L ⁻¹]
Chlorpyrifos (C ₉ H ₁₁ Cl ₃ NO ₃ PS)					
Chlorpyrifos [O,O-diethyl-O-(3,5,6-trichloro-2-pyridyl)phosphorothioate]	C ₉ H ₁₁ Cl ₃ NO ₃ PS			350.59	2 (25 °C)
Endosulfan [6,7,8,9,10,10-Hexachloro-1,5,5a,6,9,9a-hexahydro-6,9-methano-2,4,3-benzodioxathiepin-3-oxide]	C ₉ H ₆ Cl ₆ O ₃ S			406.93	α-ES- 0.32 β-ES- 0.33 (22 °C)
Malathion [diethyl 2-[(dimethoxyphosphorothioyl)sulfonyl]butanedioate]	C ₁₀ H ₁₉ O ₆ PS ₂			330.36	130 (25 °C)

with different orientations of each pesticide with respect to the graphene sheet (see their relaxed structures in **Figure 6A** and **Figure S11A** of Supporting Information). To quantify the strength of the interactions between P and G, we obtained an adsorption energy, E_A defined as defined in equation 1.

$$E_A = E_{P-G} - (E_P + E_G) \quad (1)$$

where, E_{P-G} , E_P , E_G are the energies of the optimized structures of pesticide-graphene complex, isolated free pesticide molecule, and graphene supercell, respectively. Similarly, we quantify the energy of dissolution as defined in equation 2.

$$E_D = E_{W-G/P} - (E_W + E_{G/P}) \quad (2)$$

where $E_{W-G/P}$ is the energy of the water and graphene or water and pesticide complex. Our results clearly reveal that $E_A > 0$ with magnitudes from 30 to 50 kJ mol⁻¹ for ES and CP, while there is weak binding (-2 to -3 kJ mol⁻¹) for ML, and thus adsorption of these pesticides on dry graphene is unlikely or at the best very weak (Supporting Information, Table S12), and that $E_D < 0$ meaning both graphene and pesticide have an attractive interaction with water molecules (relative to free water molecules). However, we also found

that $E(nW) - nE(W) < 0$, with a magnitude comparable and even greater than that of E_D in the case of ML and CP. Thus, the adsorption of pesticides or graphene in water is limited. Experimental samples of graphene here, though, are partially functionalized which can alter the adsorption of graphene.

Finally, we turn to our results on ternary G-W-P complexes (Supporting Information, Table S13). To evaluate energetic stability, we examine the adsorption energy of the G-W-P complex (see their structural configurations in Supporting Information, Figures S11B and S14) as defined in equation 3.

$$E_{G-W-P} = E_{complex} - (E_G + E_P + nE_W) \quad (3)$$

for $n = 6$, and compare with E_A and E_D defined earlier. First of all, we find that there is an energy gain associated with binding between graphene, pesticide, and water molecules relative to any of the pair complexes: $E_{G-W-P} < E_A$ and $E_{G-W-P} < E_D$, when we consider the lowest energy configuration for each. For each pesticide, the energy of the G-W-P complex is lower by 20–40 kJ mol⁻¹ than the energy of a pair complex such as W-P or W-G or nW ($n = 6$). Thus, with respect to free graphene or free pesticide in water, it is energetically preferable for a G-W-P complex to exist. Secondly,

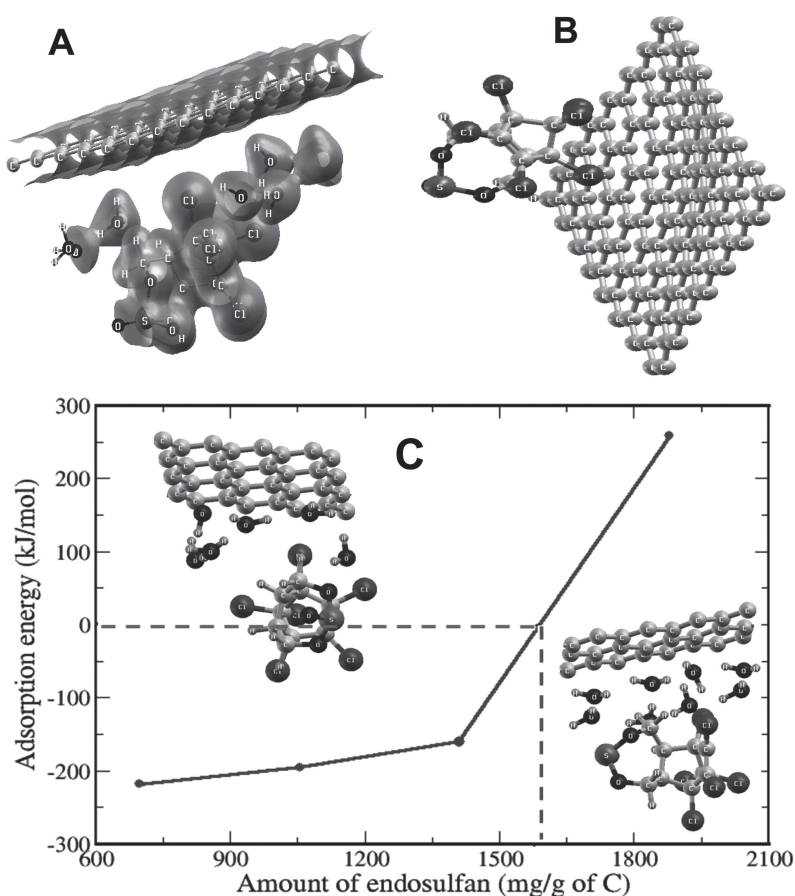


Figure 6. Relaxed structure of (A) G–W–ES complex and (B) ES–G complex. (C) Energy of adsorption of endosulfan on graphene in the presence of water molecules as a function of coverage (expressed in amount of ES per gram of graphene). The structure on the left corresponds to a 4×4 supercell and good binding in the complex, while the one on the right is for a 3×3 supercell of graphene with no binding.

the energy gain associated with the formation of a graphene–pesticide–water complex increases with n (Supporting Information, Table S15), up to a value that gives a reasonable packing of water molecules in the space available (about $n = 50$, depending on the pesticide) in the 5×5 supercell. We find that only a few bonds, particularly the polar ones, in a pesticide molecule, which are close to water molecules and graphene, change noticeably when it enters into an interaction with graphene and water. For example, while one of the P–S bonds in ML elongates and the other shortens by 1%, both P–O bonds contract by less than a percent. While a P–S bond in CP elongates by a percent, its P–O bonds are shortened by less than a percent. In ES, one of the S–O bonds becomes longer by a percent and the other contracts by half a percent. As the distance between any of the molecules and graphene is always greater than a typical bonding distance, we conclude that the origin of these structural changes and associated energetics is mainly electrostatic in nature. Visualization of the structure and charge density (Figure 6A) reveal polarity and suggest an electrostatic interaction. Naturally, water, with its polar structure, plays an important role in mediating effective interactions between graphene and a pesticide. The nature of interaction between dry graphene

and ES is slightly different, and involves some bending (by 3.2°) of graphene sheet (Figure 6B) and costs energy of the order $30\text{--}50\text{ kJ mol}^{-1}$. In this case, the S=O (double bond) bonds elongate by 1.7% and both single S–O bonds elongate by 3.5% relative to the relaxed ES molecule. On the other hand, one of the C–Cl bonds closer to the graphene sheet shortens by 1%, and the other elongates by 3.5%.

Our calculations with $n \times n$ supercell of graphene correspond to pesticide adsorption capacities ranging from 600 to 2000 mg g^{-1} (Supporting Information, Table S16). Our results for G–W–ES (Figure 6C) clearly show that there is an overall binding between ES, graphene, and water molecules for coverages lower than 1600 mg g^{-1} . Indeed, this confirms the experimental observation that a pesticide can precipitate along with graphene and water at these high coverages/capacities. Our theoretical estimate of the upper limit on pesticide adsorption capacity is slightly higher than the experimental value because it corresponds to the most stable configuration ($T = 0\text{ K}$) among the ones considered here, and DFT calculations are known to typically overestimate the binding energies.

3. Conclusion

Unprecedented water-assisted adsorption of common pesticides on graphene is demonstrated here with a combination of theory and experiment. Our work establishes that the new class of 2D carbon nanomaterials has enormous potential in water purification, in creating cheap, easily manufacturable substrates. The adsorption capacity of graphene observed to be as large as 1200 mg g^{-1} is higher than any materials investigated for the purpose. The material is also attractive due to its high specificity to the pesticides, insensitivity to changes in pH, less toxicity compared to other carbon-based nanomaterials like CNTs, and antibacterial properties (consequently unlikely accumulation of bacteria on the filter media). Besides the said merits, RGO can be easily immobilized on cheap substrates like sand and used as a filter that reduces many engineering limitations of the said material in applications like water purification. Using first-principles DFT-based analysis, we have determined the energies of adsorptive interactions between graphene and a pesticide (binary complex) as well as graphene, pesticide, and water complexes, revealing that the pesticide adsorption on graphene is thermodynamically feasible only in the presence of water molecules, and the adsorption of any of the three pesticides on dry graphene is expected to be rather weak or unlikely. Hence, the observed removal of pesticides from water by graphene is proposed to be due to the formation

and precipitation of G–W–P complexes through electrostatic interactions. The present study reveals the richness in interactions of graphene with molecular systems and opens a way for further research in this important field of environment friendly applications of graphene.

4. Experimental and Computational Details

Materials: Natural graphite was purchased from Active Carbon India Pvt. Ltd., India. Hydrochloric acid (HCl, 36%), ammonia (NH₃, 30%) and sulfuric acid (H₂SO₄, 95–98%) were procured from Rankem Chemicals, India. CP (HPLC assay 99.9%), ES (HPLC assay 99.9%, $\alpha:\beta = 1:2$), and ML (HPLC assay 96.1%) were purchased from Sigma Aldrich. Stock solutions of the pesticides were prepared in high pure ethanol (99.9%) and maintained under refrigeration until needed for testing. Phosphorus pentoxide (P₂O₅), hydrazine monohydrate (N₂H₄·H₂O, 99–100%) and hydrogen peroxide (H₂O₂), were purchased from SD Fine Chemicals, India. Potassium peroxydisulfate (K₂S₂O₈) was purchased from Sisco Research Laboratories Pvt. Ltd., India. Potassium permanganate (KMnO₄) was purchased from Merck. All chemicals were used as received without any additional purification. All solutions and suspensions were prepared using deionized water (DW).

GO and RGO Synthesis: GO synthesis from graphite powder was carried out based on the modified Hummers method.^[49] RGO synthesis was done by chemical reduction of GO as reported by Li et al.^[50] as well as through hydrothermal reduction method reported by Zhou and co-workers.^[51] The detailed procedure is given in Supporting Information S1. Various concentrations of RGO and GO were prepared by appropriate dilution using DW. The samples were dialyzed against DW to get rid of ionic impurities. After dialysis, the samples were stored in glass bottles for further use.

RGO prepared through two different reduction routes were tested for their adsorption capacity. This was done to study the influence of reduction processes on adsorption. Chemical reduction can leave reductants with graphene and its influence on adsorption was an important aspect of the investigation. The results revealed that the reduction methodologies have an insignificant effect on the adsorption process. All the experiments reported in the paper were carried out using hydrothermally synthesized RGO.

Adsorption Experiments: The pesticide uptake capacities of GO and RGO dispersions were investigated in a batch reactor (20 mL). The working volume was maintained at 10 mL. Homogeneous dispersions of GO and RGO were taken in the reactor separately and the target pesticide was added into the dispersion to get the required concentration of the contaminant. All the adsorption experiments were conducted at room temperature (30 ± 2 °C). Selected properties of the pesticides used in this are given in Table 1.

The solutions contained a small amount of ethanol (<0.5% by volume), which was added with the pesticide stock solution. The solutions were kept for stirring at ambient conditions. The solid–liquid separation was done by membrane filtration. The filtrate was analyzed to quantify the target pesticide in the aqueous phase by high pressure liquid chromatography (HPLC) (Dionex, UltiMate 3000) equipped with an UltiMate 3000 variable wave length detector and a packed column of Agilent C18, 100A. CP analysis

was carried out at a wavelength of 267 nm. An acetonitrile:water (80:20) mixture was used as the mobile phase and a total flow rate of 1 mL min⁻¹ was maintained. ES and ML were analysed at similar settings but at a wavelength of 214 nm. The effects of pH, contact time, adsorbent dose, and co-existing ions were evaluated by varying the parameters in the appropriate window. Except kinetics, all other studies were conducted by a batch equilibration method. For conducting adsorption experiments in real water, the water was simulated by spiking the required concentration of target pesticide into groundwater (GW). The water quality characteristics of the groundwater are given in Supporting Information (Table S2 of Supporting Information). Control samples were kept in all the cases to assess the removal of the pesticides by methods other than adsorption by RGO/GO. All the experiments were conducted in duplicate with proper control and the samples were analyzed immediately.

Regeneration Studies: Once used RGO was regenerated using n-hexane as the eluent. The test was restricted to CP@RGO alone (@ implies CP adsorption on RGO), since all the three pesticides studied showed similar behaviour. To begin with, CP (2 mg L⁻¹) was initially equilibrated with a dispersion of RGO (10 mL) at neutral pH and at room temperature (30 ± 2 °C). After achieving equilibrium, n-hexane (5 mL) was added to the reactor and stirred for 30 min. After 30 min, n-hexane (4 mL) was separated from the reactor carefully and the solvent was evaporated by means of rotary vaporisation. The pesticide residue was re-dissolved in equal volume of ethanol (4 mL) and analyzed using HPLC as described above. After the first cycle, the RGO was separated from the solvent and reused for the subsequent adsorption and desorption cycles.

Instrumentation: UV–vis spectra of GO and RGO were measured using a Perkin-Elmer Lambda 25 UV/Vis spectrophotometer. Attenuated total reflectance-infrared (ATR-IR) measurements were done using a PerkinElmer, Spectrum 100 spectrometer. Raman spectra of GO and RGO were collected using a confocal Raman spectroscopy (WiTec GmbH CRM 200). X-ray photoelectron spectroscopic (XPS) measurements were done with an Omicron ESCA Probe spectrometer with unmonochromatized Mg K_α X-rays (hν = 1253.6 eV). The energy resolution of the spectrometer was set at 0.1 eV at a pass energy of 20 eV. Binding energy was corrected with respect to C 1s at 284.5 eV. A high-resolution transmission electron microscope (HRTEM) with an ultra-high resolution (UHR) polepiece was used to image the samples (JEOL 3011, 300 kV). Surface morphology, elemental analysis and elemental mapping studies were carried out using scanning electron microscopy (SEM) equipped with energy dispersive analysis of X-rays (EDAX) (FEI Quanta 200, Czechoslovakia). The samples were analyzed using an electrospray ionization mass spectrometer (LTQ XL, Thermo Scientific, San Jose, CA) equipped with a 2D moving stage (Prosolia, Indianapolis, IN) desorption electrospray-mass spectrometry (DESI-MS) imaging. All the mass spectra were acquired under identical conditions of 2 mL min⁻¹ solvent flow rate, 110 psi nebulizer gas (N₂) pressure, and 5 kV spray voltage.

First-Principles DFT Analysis of Graphene, Pesticide and Water Interactions: We used Plane-Wave Self-Consistent Field (PWSCF)^[52] implementation of DFT, which is based on ultra-soft pseudopotentials^[53,54] to represent interactions between ionic cores and valence electrons and a plane-wave basis. As the densities in molecular systems change rapidly in space, we used a generalized gradient approximation (GGA) with Perdew–Burke–Ernzerhof

(PBE)^[54] form of the exchange correlation energy functional. Kohn–Sham wave functions were represented with a plane wave basis with an energy cutoff of 30 Ry and charge density with a cutoff of 180 Ry. We used periodic boundary conditions with 8×8 and 5×5 supercells of graphene to simulate different concentrations of pesticides and water molecules interacting with it, and include a vacuum up to 22 Å (minimum thickness of vacuum was 12.8 Å) in the direction perpendicular to the graphene plane to keep interactions between periodic images of molecules minimal. Integrations over the Brillouin zone (for these periodic supercells) were sampled with $3 \times 3 \times 1$ and $1 \times 1 \times 1$ uniform meshes of k-points, ensuring convergence with respect to k-points while using occupation numbers smeared with Fermi–Dirac scheme with a broadening of 0.003 Ry. We considered many structural configurations for each pesticide (β -ES, CP, and ML) obtained with different orientations and positions of the pesticides and water molecules relative to graphene, and relaxed the structure to minimize the energy until Hellman Feynman forces on atoms were less than 0.001 Ry/bohr in magnitude.

Supporting Information

Supporting Information is available from the Wiley Online Library or from the author

Acknowledgements

Authors thank the Nano Mission of the Department of Science and Technology (DST), Government of India for supporting our research program. Authors thank EWRE Division, Department of Civil Engineering, IIT Madras for providing some analytical facilities. UVW acknowledges funding from AOARD grants FA2386-10-1-4062 and FA2386-10-1-4150.

- [1] Y. Matsui, D. R. U. Knappe, K. Iwaki, H. Ohira, *Environ. Sci. Technol.* **2002**, *36*, 3432.
- [2] T. Pradeep, Anshup, *Thin Solid Films* **2009**, *517*, 6441.
- [3] A. K. Leight, R. F. Van Dolah, *Environ. Toxicol. Chem.* **1999**, *18*, 958.
- [4] S. L. Simonich, R. A. Hites, *Science* **1995**, *269*, 1851.
- [5] A. S. Nair, T. Pradeep, *Curr. Sci.* **2003**, *84*, 1560.
- [6] W. Chen, L. Duan, D. Zhu, *Environ. Sci. Technol.* **2007**, *41*, 8295.
- [7] D. Lin, B. Xing, *Environ. Sci. Technol.* **2008**, *42*, 7254.
- [8] G.-C. Chen, X.-Q. Shan, Z.-G. Pei, H. Wang, L.-R. Zheng, J. Zhang, Y.-N. Xie, *J. Hazard. Mater.* **2011**, *188*, 156.
- [9] M. L. Schipper, N. Nakayama-Ratchford, C. R. Davis, N. W. S. Kam, P. Chu, Z. Liu, X. Sun, H. Dai, S. S. Gambhir, *Nat. Nanotechnol.* **2008**, *3*, 216.
- [10] A. Magrez, S. Kasas, V. Salicio, N. Pasquier, J. W. Seo, M. Celio, S. Catsicas, B. Schwaller, L. Forró, *Nano Lett.* **2006**, *6*, 1121.
- [11] K. S. Novoselov, A. K. Geim, S. V. Morozov, D. Jiang, Y. Zhang, S. V. Dubonos, I. V. Grigorieva, A. A. Firsov, *Science* **2004**, *306*, 666.
- [12] N. Kurra, A. A. Sagade, G. U. Kulkarni, *Adv. Funct. Mater.* **2011**, *21*, 3836.
- [13] S. Stankovich, D. A. Dikin, G. H. B. Dommett, K. M. Kohlhaas, E. J. Zimney, E. A. Stach, R. D. Piner, S. T. Nguyen, R. S. Ruoff, *Nature* **2006**, *442*, 282.
- [14] A. K. Geim, *Science* **2009**, *324*, 1530.
- [15] Z. Liu, J. T. Robinson, X. Sun, H. Dai, *J. Am. Chem. Soc.* **2008**, *130*, 10876.
- [16] F. Schedin, A. K. Geim, S. V. Morozov, E. W. Hill, P. Blake, M. I. Katsnelson, K. S. Novoselov, *Nat. Mater.* **2007**, *6*, 652.
- [17] R. S. Sundaram, C. Gómez-Navarro, K. Balasubramanian, M. Burghard, K. Kern, *Adv. Mater.* **2008**, *20*, 3050.
- [18] L. Tang, Y. Wang, Y. Li, H. Feng, J. Lu, J. Li, *Adv. Funct. Mater.* **2009**, *19*, 2782.
- [19] N. Jung, A. C. Crowther, N. Kim, P. Kim, L. Brus, *ACS Nano* **2010**, *4*, 7005.
- [20] C. N. R. Rao, A. K. Sood, K. S. Subrahmanyam, A. Govindaraj, *Angew. Chem., Int. Ed.* **2009**, *48*, 7752.
- [21] G. K. Dimitrakakis, E. Tylianakis, G. E. Froudakis, *Nano Lett.* **2008**, *8*, 3166.
- [22] C. Liu, F. Li, L.-P. Ma, H.-M. Cheng, *Adv. Mater.* **2010**, *22*, E28.
- [23] D. R. Dreyer, H.-P. Jia, C. W. Bielawski, *Angew. Chem., Int. Ed.* **2010**, *49*, 6813.
- [24] Y. Zhu, S. Murali, W. Cai, X. Li, J. W. Suk, J. R. Potts, R. S. Ruoff, *Adv. Mater.* **2010**, *22*, 3906.
- [25] W. Hu, C. Peng, W. Luo, M. Lv, X. Li, D. Li, Q. Huang, C. Fan, *ACS Nano* **2010**, *4*, 4317.
- [26] J. Chen, J. Zou, J. Zeng, X. Song, J. Ji, Y. Wang, J. Ha, X. Chen, *Anal. Chim. Acta* **2010**, *678*, 44.
- [27] T. S. Sreeprasad, S. M. Maliyekkal, K. Deepti, K. Chaudhari, P. L. Xavier, T. Pradeep, *ACS Appl. Mater. Interfaces* **2011**, *3*, 2643.
- [28] V. Chandra, J. Park, Y. Chun, J. W. Lee, I.-C. Hwang, K. S. Kim, *ACS Nano* **2010**, *4*, 3979.
- [29] T. S. Sreeprasad, S. M. Maliyekkal, K. P. Lisha, T. Pradeep, *J. Hazard. Mater.* **2011**, *186*, 921.
- [30] W. Gao, M. Majumder, L. B. Alemany, T. N. Narayanan, M. A. Ibarra, B. K. Pradhan, P. M. Ajayan, *ACS Appl. Mater. Interfaces* **2011**, *3*, 1821.
- [31] G. Zhao, L. Jiang, Y. He, J. Li, H. Dong, X. Wang, W. Hu, *Adv. Mater.* **2011**, *23*, 3959.
- [32] a) J. Weber, C. J. Halsall, D. Muir, C. Teixeira, J. Small, K. Solomon, M. Hermanson, H. Hung, T. Bidleman, *Sci. Total Environ.* **2010**, *408*, 2966; b) X. Zhao, H.-M. Hwang, *Arch. Environ. Con. Tox.* **2009**, *56*, 646; c) H. Sujatha, S. M. Nair, J. Chacko, *Water Res.* **1999**, *33*, 109; d) M. Kumar, L. Philip, *Chemosphere* **2006**, *62*, 1064; e) B. K. Singh, A. Walker, J. A. W. Morgan, D. J. Wright, *Appl. Environ. Microb.* **2004**, *70*, 4855.
- [33] a) S. Memon, N. Memon, S. Memon, Y. Latif, *J. Hazard. Mater.* **2011**, *186*, 1696; b) T. Siddique, B. C. Okeke, M. Arshad, W. T. Frankenberger, *J. Agric Food Chem.* **2003**, *51*, 8015.
- [34] a) A. K. Leight, R. F. V. Dolah, *Environ. Toxicol. Chem.* **1999**, *18*, 958; b) T. Holland, G. Windham, P. Kolachana, F. Reinisch, S. Parvatham, A. M. Osorio, M. T. Smith, *Mutat. Res.-Gen. Tox. En.* **1997**, *388*, 85; c) H. Wu, R. Zhang, J. Liu, Y. Guo, E. Ma, *Chemosphere* **2011**, *83*, 599.
- [35] W. Chen, L. Yan, P. R. Bangal, *J. Phys. Chem. C* **2010**, *114*, 19885.
- [36] T. S. Sreeprasad, A. K. Samal, T. Pradeep, *J. Phys. Chem. C* **2009**, *113*, 1727.
- [37] A. J. Gil, S. Adhikari, F. Scarpa, J. Bonet, *J. Phys.: Condens. Matter.* **2010**, *22*, 145302.
- [38] P. C. Mishra, R. K. Patel, *J. Hazard. Mater.* **2008**, *152*, 730.
- [39] A. H. Yonli, I. Batonneau-Gener, J. Koulidiati, *J. Hazard. Mater.* **2012**, *203–204*, 357.
- [40] S. Kushwaha, G. Sreelatha, P. Padmaja, *J. Chem. Eng. Data* **2011**, *56*, 2407.
- [41] J. Carriger, G. Rand, *Ecotoxicology* **2008**, *17*, 660.
- [42] H. Goebel, S. Gorbach, W. Knauf, R. H. Rimpau, H. Huttenbach, *Residue Rev.* **1982**, *83*, 1.

- [43] M. Manes, in *Encyclopedia of Environmental Analysis and Remediation*, (Ed: R. A. Mayer), Wiley, New York **1998**, 26–68.
- [44] Y. Yang, Y. Chun, G. Sheng, M. Huang, *Langmuir* **2004**, *20*, 6736.
- [45] G. Lagaly, *Appl. Clay Sci.* **2001**, *18*, 205.
- [46] F. Tuinstra, *J. Chem. Phys.* **1970**, *53*, 1126.
- [47] R. G. Baughman, S. K. Jorgensen, R. A. Jacobson, *J. Agric. Food Chem.* **1978**, *26*, 576.
- [48] G. Smith, C. Kennard, K. Shields, *Aust. J. Chem.* **1977**, *30*, 911.
- [49] N. I. Kovtyukhova, P. J. Ollivier, B. R. Martin, T. E. Mallouk, S. A. Chizhik, E. V. Buzaneva, A. D. Gorchinskiy, *Chem. Mater.* **1999**, *11*, 771.
- [50] D. Li, M. B. Muller, S. Gilje, R. B. Kaner, G. G. Wallace, *Nat. Nanotechnol.* **2008**, *3*, 101.
- [51] Y. Zhou, Q. Bao, L. A. L. Tang, Y. Zhong, K. P. Loh, *Chem. Mater.* **2009**, *21*, 2950.
- [52] S. Baroni, S. de Gironcoli, A. Dal Corso, P. Giannozzi, *Rev. Mod. Phys.* **2001**, *73*, 515.
- [53] D. Vanderbilt, *Phys. Rev. B* **1990**, *41*, 7892.
- [54] J. P. Perdew, K. Burke, M. Ernzerhof, *Phys. Rev. Lett.* **1996**, *77*, 3865.

Received: May 23, 2012
Revised: August 6, 2012
Published online:

Cite this: *RSC Advances*, 2012, 2, 10048–10056

www.rsc.org/advances

PAPER

Real time plasmonic spectroscopy of the interaction of Hg²⁺ with single noble metal nanoparticles†

M. S. Bootharaju,^a Kamallesh Chaudhari^{ab} and T. Pradeep^{*a}

Received 7th July 2012, Accepted 24th August 2012

DOI: 10.1039/c2ra21384b

In this work, we use dark-field optical microscopy (DFM) and hyper spectral imaging (HSI) to study the interactions of single Ag and Au nanoparticles (NPs) with Hg²⁺ in real time, at room temperature (25 °C). NPs were immobilized on glass substrates using 3-aminopropyltrimethoxysilane (APTMS) as the anchoring agent. Red, green and blue colors were assigned to the particles in hyper spectral images on the basis of their relative scattering intensities at 640, 550 and 460 nm, where the particles showed maxima in their scattering spectra. While Ag NPs showed all the colors, Au NPs were mostly red and rarely green in DFM images. The scattering spectra of Ag NPs were more blue shifted (with an average shift of 46 nm in the case of red particles) in a given time compared to Au NPs, after passing over Hg²⁺ solution and these shifts increased with time. Depending on the extent of blue shift, the colors of the particles got modified. Red particles appeared more reactive than green and blue, as revealed from the larger extent of shifts and their time dependence. The greater reactivity of red particles is attributed to their anisotropic nature possessing reactive tips, edges and more surface area due to their large size. The effect of quality of water on the scattering spectrum was checked by passing over deionized (DI) and tap waters separately, which showed that the effect is minimal compared to the presence of Hg²⁺, when data at a given time, flow rate and temperature were compared. Solution phase interactions of NPs with Hg²⁺ were also performed for comparison. These were characterized by UV-vis absorption spectroscopy, transmission electron microscopy (TEM) and energy dispersive analysis of X-rays (EDAX). Solution phase experiments showed citrate-induced aggregation of Ag NPs and partial reduction of Hg²⁺ to Hg⁰ upon exposure to Hg²⁺. Immobilized particles cannot aggregate and they show only reduction.

Introduction

Noble metal nanoparticles (NPs) are well known to exhibit unique optical, catalytic and electronic properties which offer numerous opportunities for fundamental studies.¹ These characteristics are due to the coherent oscillations of free electrons in the conduction band of the NPs, when they are illuminated with electromagnetic radiation, a phenomenon called localized surface plasmon resonance (LSPR).^{2,3} The growing field of research of such light–metal interactions is known as ‘plasmonics’.⁴ LSPR is measured as an extinction spectrum (scattering and absorption) of these NPs which depends on various parameters such as size,⁵ shape,⁶ inter-particle spacing,⁷ composition,⁸ refractive index,⁹ local dielectric environment of the medium⁹ and

temperature.¹⁰ NPs possess extremely high absorption and scattering cross sections¹¹ compared to molecular dyes due to LSPR (for *e.g.*, fluorescein dye and 60 nm silver NPs have absorption and extinction cross sections of 3.5×10^{-16} and 2.5×10^{-10} cm², respectively)¹² which help in sensing applications. Excitation of LSPR results in wavelength-selective absorption with extremely high molar extinction coefficients ($\sim 3 \times 10^{11}$ M⁻¹ cm⁻¹).¹³ SPR can be tuned from the visible to the infrared regions¹¹ for various applications in miniaturized optical devices, chemical/biological sensing, photonic circuits as well as in medical diagnostics and therapeutics.³ In the recent past, noble metal NPs have been found to have applications in water purification by removing pesticides,^{14,15} mineralizing halogenated hydrocarbons,^{14,16} decontaminating toxic metal ions such as mercury, cadmium and lead,¹⁷ *etc.* Typically, nanoparticles in solution undergo aggregation leading to a red shift in their characteristic surface plasmon resonance upon exposure to the analyte.

The scattering properties of NPs have been used for sensing applications as extinction-based methods require relatively smaller quantities of NPs in comparison to other colorimetric reagents. Scattering intensity is highly advantageous as a single

^aDST Unit of Nanoscience and Thematic Unit of Excellence, Department of Chemistry, Indian Institute of Technology, Madras, Chennai - 600 036, India. E-mail: pradeep@iitm.ac.in

^bDepartment of Biotechnology, Indian Institute of Technology, Madras, Chennai - 600 036, India

† Electronic Supplementary Information (ESI) available: UV-vis absorption spectra and TEM images of Ag and Au@citrate NPs. EDAX spectrum, scattering spectra, FESEM and HSI images of Hg²⁺ treated NPs. See DOI: 10.1039/c2ra21384b

80 nm Au particle exhibits a light scattering power equivalent to the emission of $\sim 10^6$ fluorescein molecules.¹² Recently, a technique called single particle plasmon spectroscopy¹⁸ has evolved which measures the scattering spectrum of isolated plasmonic NPs. This spectroscopy has several advantages including greater sensitivity and smaller sample volumes than traditional methods.¹⁹ The NPs can be imaged by collecting scattered light from the particles and the image is called a hyper spectral image (HSI). This technique has been utilized for the real time study of chemical reactions,²⁰ bio-molecule binding,¹⁸ detection of conformational changes of protein,²¹ sensing of small organic molecules²² and receptors²³ as well as for DNA hybridization²⁴. The application of such a technique is necessary to understand the real time interactions of NPs with inorganic contaminants such as heavy metal ions (Hg^{2+} , Cd^{2+} , Pb^{2+} , *etc.*) and organic contaminants such as phenols, nitro aromatics, *etc.* present in water. Mercury is known to cause the minamita²⁵ disease and its permissible limit in drinking water is 2 ppb set by the US environmental protection agency (EPA).²⁶ Contamination of mercury in the environment occurs due to natural and anthropogenic processes.²⁶ Various sensors such as monolayer and protein protected noble metal quantum clusters,^{26,27} NPs,²⁸ *etc.* have been reported for mercury sensing where the interactions are ensemble averaged. Recently, functionalized single plasmonic gold NPs have been utilized for Hg^{2+} sensing.²⁹ In this paper, the mechanistic aspects of sensing are not discussed. There is no study so far on the utilization of scattering spectra of Ag NPs for understanding the real time interactions with Hg^{2+} .

In this work, we studied the interaction of immobilized Ag and Au@citrate NPs with Hg^{2+} in real time using DFM and X-ray photoelectron spectroscopy (XPS). Interactions of Hg^{2+} with mobile (solution phase) NPs were also done for comparison, which were characterized with UV-vis spectroscopy, TEM and EDAX. After interaction of immobilized NPs with Hg^{2+} , representative colors of NPs were changed with a blue shift and decrease in the intensity of the scattering. The color change and blue shifts were attributed to the redox reaction of Ag NPs and reduction of Hg^{2+} leading to the formation of Hg^0 . It may be pointed out that the particles are immobile which prevents consequent aggregation and red shift. The effect of water quality on the scattering spectrum of NPs was also studied. The decrease in silver content due to the reaction was confirmed by XPS quantification data. A visual detection limit of Hg^{2+} on the basis of color change of NPs in HSI is 1 ppm in our experimental conditions. This can be brought down further to ppb level by optimizing the experimental conditions such as decreasing the flow rate of Hg^{2+} and increasing the incubation time. Here, our objective was to understand the real time interactions of Ag NPs with Hg^{2+} spectroscopically and microscopically. Enhancing the detection limit was not an aspect of the investigation.

Experimental section

Materials

Silver nitrate, tetrachloroauric acid trihydrate (CDH, India), trisodium citrate (TSC, Qualigens), mercuric acetate (Ranbaxy), 3-aminopropyltrimethoxysilane (APTMS, Sigma-Aldrich), chloroform, hydrogen peroxide, and sulphuric acid were

purchased and used as such without further purification. For flow cell experiments, 1.1 mm thick 40 mm round glass substrates and 0.145 mm thick 30 mm round glass cover slips from Warner instruments were used. Before immobilization thorough cleaning of the substrates was done as mentioned in the section on immobilization of NPs (below). For dark-field microscopy, a type A immersion oil (Cargille) was used as received without purification.

Synthesis of Ag and Au@citrate NPs

The Ag@citrate NPs were prepared according to the literature.¹⁷ In this method, to a boiling 50 mL silver nitrate (1 mM) solution, 2 mL of 1 wt% TSC was added, and heating was continued further for a few minutes. The solution turned light yellow in color, indicating the formation of NPs. The suspension was cooled in an ice bath to allow the growth of NPs. The Au@citrate NPs (red color solution) were synthesized similar to Ag@citrate NPs according to the literature.³⁰

Immobilization of NPs on glass substrates

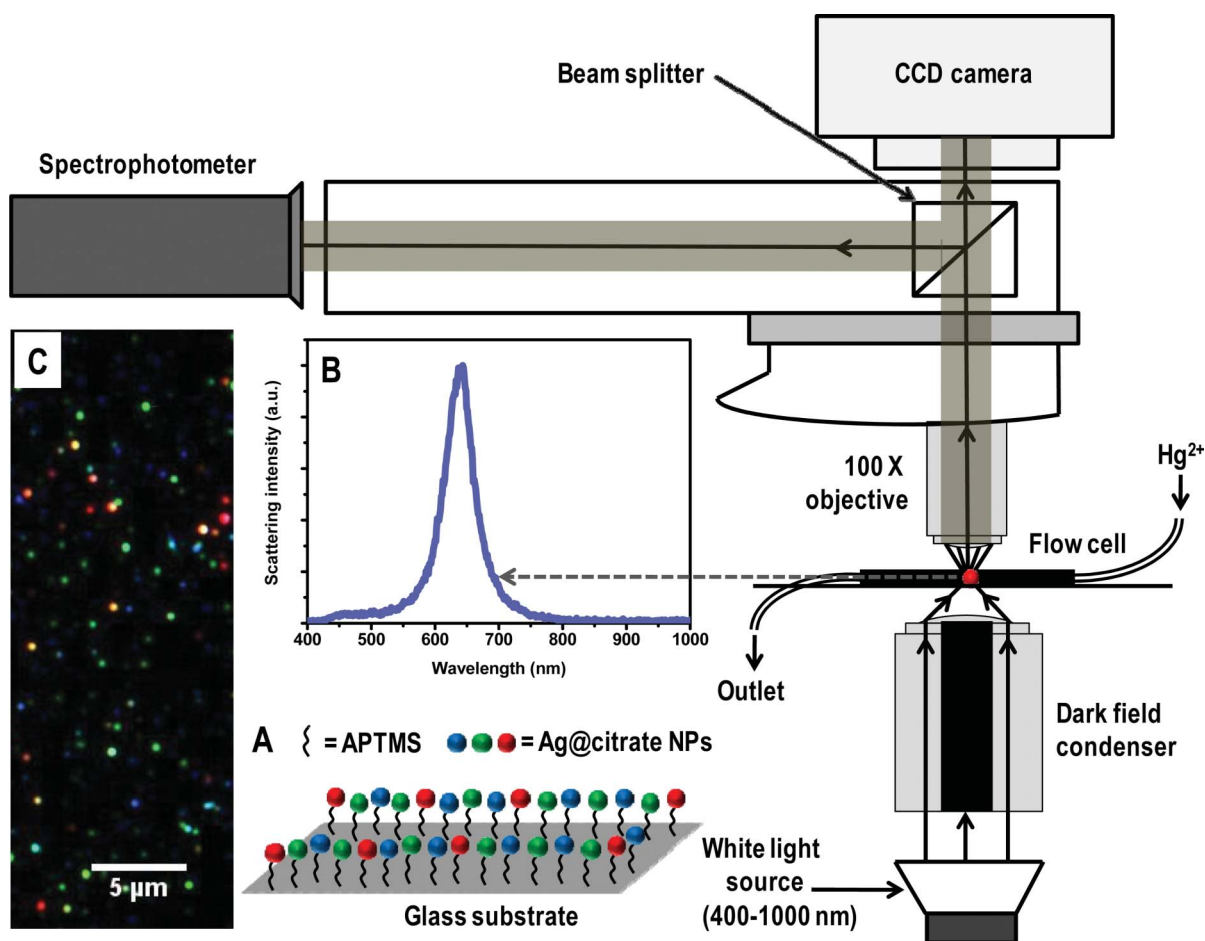
Immobilization of Ag and Au@citrate NPs (after twenty times dilution of the as-prepared particles) was done on a glass substrate in a plastic glove box in which N_2 atmosphere was maintained. Before that, it was thoroughly cleaned using aqua regia (3 : 1 volume mixture of conc. HCl and HNO_3) several times. Later, it was immersed in piranha solution (2 : 1 volume mixture of H_2SO_4 and H_2O_2) for 30 min to create Si-OH bonds. Then, the substrate was rinsed with DI water followed by drying in N_2 flow. About 100 μL of 0.3 M APTMS in chloroform was dropped on the substrate with a pipette and dried for 5 min. Then it was rinsed with excess chloroform followed by DI water to remove excess APTMS. After that, the glass substrate was dipped in the dilute NP solution for 2 min in such a way that the solution contacted only one surface. Negatively charged Ag and Au@citrate NPs bind with positively charged amino groups of APTMS through electrostatic interaction. Then it was rinsed with DI water and kept in a beaker containing DI water till it was used. Binding of NPs to APTMS is shown schematically as given below (inset A of Scheme 1).

Real time monitoring of interaction between NPs and Hg^{2+}

For this, a flow cell set-up which is shown in Scheme 1 was used. Initially, DI water was allowed to flow over the immobilized NPs for 5 min. Then, 5 ppm Hg^{2+} solution was continuously passed at a flow rate of 3.5 mL h^{-1} and HSI images from a particular area were collected at different times. In control experiments, DI and tap water were also passed to check their effect on the scattering spectrum of immobilized NPs.

Instrumentation

Hyper spectral measurements were done with the Cytoviva HSI system containing an Olympus BX-41 microscope equipped with a Dage high resolution camera and a Specim V10E spectrometer which scans in the range of 400–1000 nm, divided into 462 bands which gives a spectral resolution of ± 1.5 nm. The color of the particle was fixed on the basis of its relative scattering intensity at 640, 550 and 460 nm, assigned to red, green and blue,



Scheme 1 Schematic representation of HSI set-up. A is a representation of immobilized Ag@citrate NPs using APTMS on glass substrate. B and C are the scattering spectrum of a silver particle and HSI of Ag@citrate NPs, respectively.

respectively. UV-vis spectra were measured with a PerkinElmer Lambda 25 instrument in the range of 200 to 1100 nm. High resolution transmission electron microscopy (HRTEM) of the samples was carried out using a JEOL 3010 instrument with a UHR polepiece. TEM specimens were prepared by drop-casting one or two drops of the aqueous solution on carbon-coated copper grids and allowed to dry at room temperature overnight. All measurements were done at 200 kV to minimize the damage of the sample. X-ray photoelectron spectroscopy (XPS) measurements were conducted using an Omicron ESCA Probe spectrometer with unmonochromatized Al K α X-rays (energy = 1486.6 eV). The X-ray power applied was 300 W. The pass energy was 50 eV for survey scans and 20 eV for specific regions. The base pressure of the instrument was 2.0×10^{-10} mbar. The binding energy was calibrated with respect to the adventitious C 1s feature at 285.0 eV. Most of the spectra were deconvoluted to their component peaks using the software, CASA-XPS. Inductively coupled plasma-optical emission spectroscopic (ICP-OES) measurements were done using a PerkinElmer Optima 5300 DV instrument. Field-emission scanning electron microscopic (FESEM) measurements were carried out using an FEI Nova NanoSEM 600 instrument with a chamber pressure of 1×10^{-4} Torr, at a working distance of 3–4 mm. Instrumental conditions were optimized to avoid surface charging.

Results and discussion

Characterization of NPs

The Ag and Au@citrate NPs were characterized extensively previously^{30,31} and also in this study. We are giving here only the essential data. The Au particles show an absorption maximum at 522 nm and TEM analysis shows the size of particles as 10 ± 5 nm suggesting the narrower size distribution as shown in Fig. S1 of ESI † . As-synthesized Ag@citrate NPs show surface plasmon resonance around 417 nm as shown in Fig. S2A. The TEM image shows that they are polydispersed (Fig. S2B). Particles are mostly spherical along with some triangles, prisms, rods, pentagons, *etc.* (Fig. S3) which are expected in the case of Ag@citrate NPs.²² The sizes are in the range of 15–60 nm. XPS data suggest the presence of silver in the zero-valent state. This data will be discussed later in the text.

Immobilized particles were subjected to HSI analysis and a large area hyper spectral image is shown in Fig. 1A. It shows different representative particles in red, green and blue. The scattering spectra from single red, green and blue (traces a, b and c, respectively) particles are shown in Fig. 1B. The corresponding particles are shown in the inset of B in which particles are marked with dotted circles. In our specific case, the red, green and blue particles show maxima at 659, 540 and 470 nm,

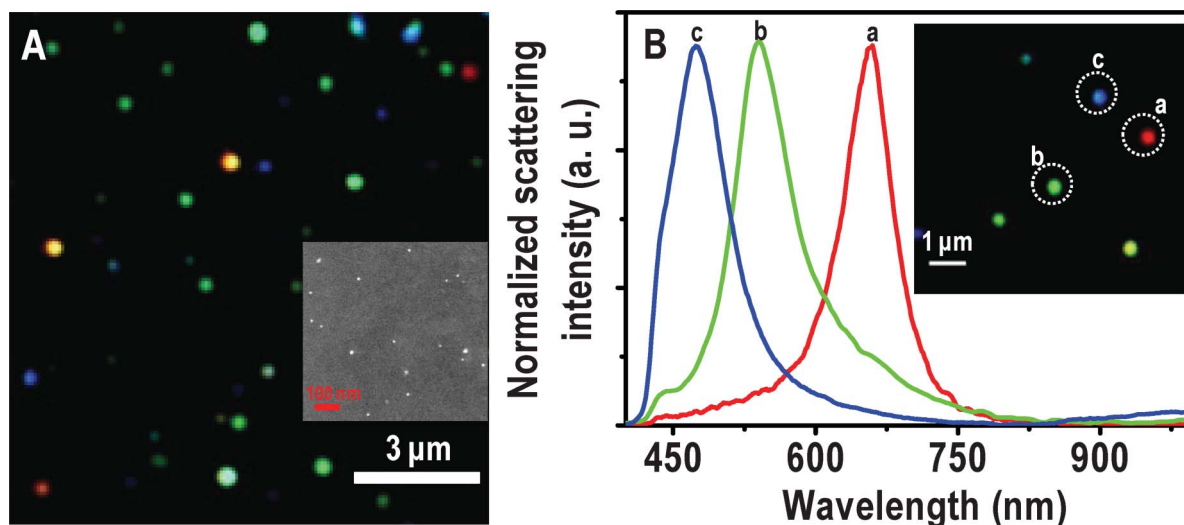


Fig. 1 (A) Large area HSI of immobilized Ag@citrate NPs. (B) Scattering spectra of Ag@citrate particles which are shown in the inset. Particles from which spectra are collected are labelled in the inset. The particles and the spectral traces have the same colors. Scale bars: 3 μm in (A) and 1 μm in the inset of (B), showing the typical distances between the particles. The sizes of the particles are exaggerated as they are imaged under the optical diffraction limit. Inset of A is an FESEM image of immobilized Ag@citrate NPs on a glass substrate.

respectively. It is reported that when Au NP monomer is converted to its dimer, a color change from green to yellow is observed with red shift in the scattering spectrum.³² Intensities of scattering spectra of blue particles are less than green and green is lesser than red. It is known that particles of high aspect ratio and larger size scatter more light than the smaller objects.²⁰ To verify the existence of isolated nanoparticles on the glass substrates, FESEM measurements were carried out on the nanoparticle-immobilized surfaces (inset of Fig. 1A). The large area FESEM image of the same sample is shown in Fig. S4A. The EDAX spectrum clearly shows the presence of silver in a single NP (Fig. S4B). FESEM images reveal that each colored particle in HSI is a single particle with polydispersity in size. The scattering position is therefore related to the size of the particle. To validate the nature of a single particle in HSI, we have compared the number of particles in HSI and FESEM in a given area. For an area of $7.2 \times 6.2 \mu\text{m}^2$, the number of particles in HSI and FESEM images are 33 ± 3 and 35 ± 3 , respectively (Fig. S5). However, as the particles appear larger in HSI images, they seem to present a larger number density.

Interaction of Ag@citrate NPs with Hg^{2+}

A Hg^{2+} solution of 5 ppm was passed over the immobilized Ag@citrate NPs in a flow cell at a flow rate of 3.5 mL h^{-1} . At different times of interaction, HSI analyses were done. The scattering spectra of all the colored particles were seen to be blue shifted simultaneously with a change in color as a function of time. The large area HSI of Ag particles before and after treating Hg^{2+} are shown in Fig. S6. The scattering spectra of almost all particles are blue shifted. One such single red particle is completely converted to green and is shown in Fig. 2A. The intermediate colors, red–yellow and yellow–green are seen after 1.5 and 2.5 h (d and f, respectively in Fig. 2A). Normalized scattering spectra of the same particle at different times are shown in Fig. 2B. The λ_{max} of the red particle at 0.0, 0.5, 1.0, 1.5,

2.0, 2.5, 3.0, 4.0 and 6.0 h of interaction with Hg^{2+} are 633, 621, 612, 607, 602, 599, 592, 588 and 585 nm, respectively (traces a–i, respectively). The peak maxima have an uncertainty of 1.5 nm. A blue shift of 12 nm within 30 min indicates a fast interaction of Ag@citrate NP with Hg^{2+} . From the HSI images, it is noted that at 3.0 h, a particular red particle is completely transformed to a green one with a λ_{max} of 592 nm (trace g). Note that the extent of blue shift varies from one red particle to another red particle. Even after an exposure for 3.0 h, no further color change is seen. But only a blue shift of 7 nm is noticed. This indicates that there could be adsorption of Hg^{2+} on the surface of NP which diminishes further interaction Hg^{2+} in solution (discussed later). The color change may be due to oxidation of Ag^0 in the process of reducing Hg^{2+} to Hg^0 and subsequent changes. At least part of the Ag^+ formed may dissolve in water. Simultaneously, the Hg^0 formed diffuses into the nanoparticles changing their composition (may lead to the formation of amalgam). Gradual conversion of another red particle is shown in Fig. S7. The λ_{max} at 0.0 and 6.0 h exposure are 632 and 605 nm, respectively (Fig. S7B). This change is reflected in a color change of deep red to red–yellow.

Similarly, conversion of a green particle to blue is shown in Fig. 3. The λ_{max} of the particle at 0.0, 0.5 and 6.0 h of passing Hg^{2+} are 528, 518 and 501 nm, respectively. The particle is almost completely converted to blue at 3.0 h (Fig. 3Ag) itself and a further blue shift of the scattering position is less than 5 nm. This indicates that similar to the red particle, there could be adsorption of Hg^{2+} followed by reduction on NPs which prevents subsequent interaction with Hg^{2+} . The HSI of the blue particle with time is shown in Fig. S8. The maxima were observed at 495, 491, 484 and 478 nm at 0.0, 0.5, 1.0 and 6.0 h of treatment of Hg^{2+} . Seemingly interaction of the blue particle with Hg^{2+} is less compared to red and green particles, under the given experimental conditions.

Interestingly, some particles (red and green) show a blue shift with decrease in scattering intensity after reacting with Hg^{2+} for

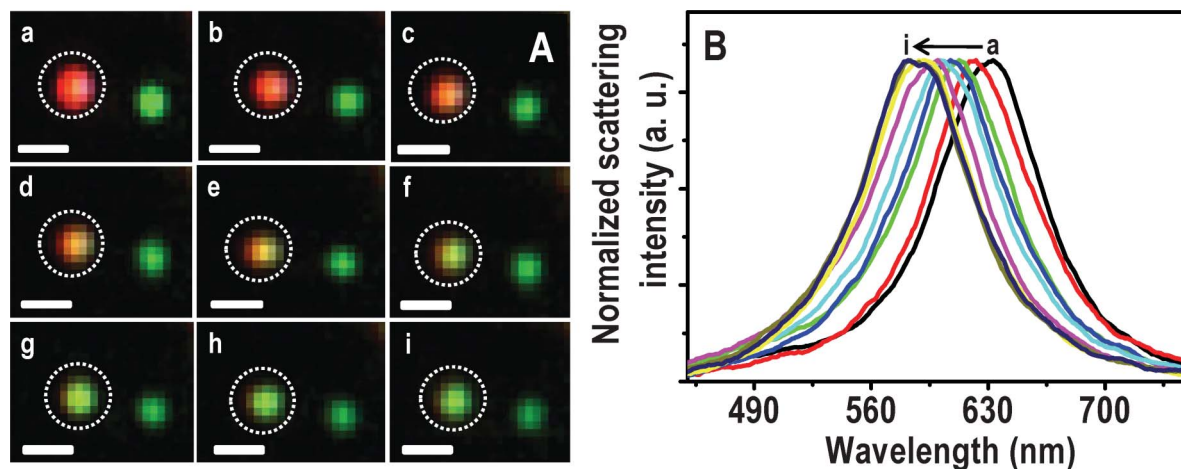


Fig. 2 HSI (A) of immobilized Ag@citrate NPs after passing 5 ppm Hg^{2+} for 0.0, 0.5, 1.0, 1.5, 2.0, 2.5, 3.0, 4.0 and 6.0 h (a–i, respectively). Scattering spectra (B) of a red particle with time (a–i). Scale bars of images in A are 500 nm. The particle from which spectra are collected is marked.

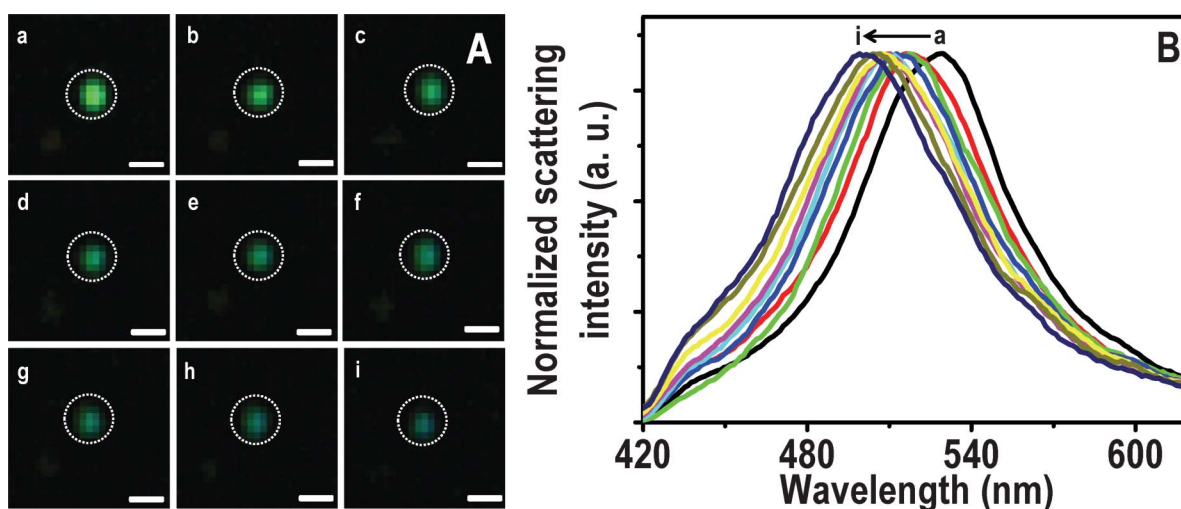


Fig. 3 HSI (A) of immobilized Ag@citrate NPs after passing 5 ppm Hg^{2+} for 0.0, 0.5, 1.0, 1.5, 2.0, 2.5, 3.0, 4.0 and 6.0 h (a–i, respectively). Scattering spectra (B) of a green particle (marked) with time (a–i). Scale bars of images in A are 400 nm.

1.5 h. These effects were attributed to a redox reaction.^{33,34} Thereafter, they show a small red shift and increase in scattering intensity up to 4.0 h (Fig. S9). These were due to the deposition of reduced mercury on partially reacted silver particles leading to a small increase in size. After 4.0 h, a small blue shift with diminishing scattering intensity was noticed which may be due to the continuous reactivity of Ag particle. The dominant blue shift (due to oxidation of Ag^0) compared to red shift (due to deposition of reduced mercury) of scattering wavelength may be due to the requirement of oxidation of two Ag^0 for reduction of one Hg^{2+} . Uptake of mercury by the particle was manifested in the EDAX spectrum of Ag@citrate particles immobilized on the functionalized glass substrate. The FESEM image of the particle from which the EDAX was taken is shown in Fig. S10 as an inset. The presence of Hg and Ag was confirmed by the EDAX spectrum collected from one of the particles (Fig. S10).

To understand the interactions better, HSI and scattering spectra of 5 particles of each color (red, green and blue) were collected. The average of shifts ($\Delta\lambda_{\text{max}}$) of each colored particle

with time of treatment with Hg^{2+} are plotted in Fig. 4. Note that the bars (I) represented in the graph are not error bars. They show the range of $\Delta\lambda_{\text{max}}$ in which all the five particles are present. Shifts are larger for red particles and smaller for green and very small for blue particles, at a given time of exposure. From this, it appears that red particles are most reactive towards Hg^{2+} in comparison to blue particles. There are two issues being discussed here. One is the larger shift of the red particles and the second is the nature of the shift itself. While the plasmon resonances are normally found to red shift upon interaction with analytes, a blue shift is observed here.

The apparent larger reactivity of red particles may be due to the following reasons. 1. As in the Ag@citrate particle system, there is a possibility of non-spherical particles to exist which possess reactive sharp edges and tips.^{35,36} Anisotropic particles are expected to scatter light of higher wavelengths due to large aspect ratios (red colored particles). Maybe due to the greater reactivity of these anisotropic particles, more of a blue shift was seen in the case of red particles. Although we looked for

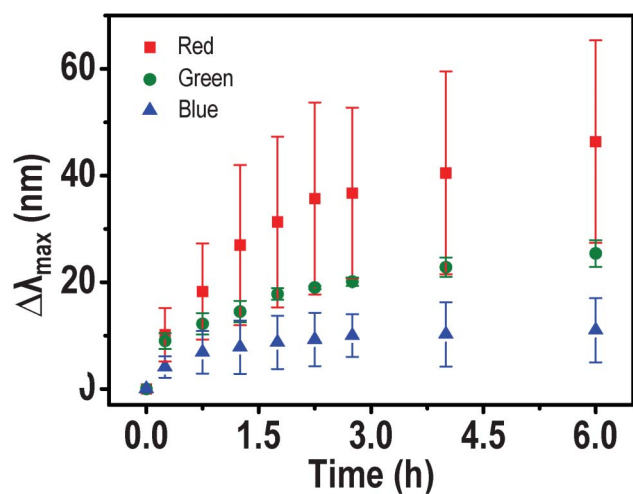


Fig. 4 A plot of average blue shift ($\Delta\lambda_{\max}$) of 5 particles of each color (red, blue and green) with time. A large shift is observed in the case of red particles and it decreases for green and blue analogues.

anisotropic particles and their shape dependent Hg^{2+} reaction leading to inhomogeneous mercury distributions on them in TEM, these effects were not detected. It could be that mercury diffusion in such nanoscale particles was fast and imaging time scale was slow to detect inhomogeneity in the distribution. 2. From the FESEM and TEM images, we know that the particles are polydispersed in size and shape. The red particles in HSI are bigger in size. Due to the greater surface area of bigger particles, a greater extent of reactivity may be expected in such red particles.

Various research groups reported the red shift of the scattering spectrum of NPs when molecules/ions interact/bind with NPs.^{18,20,37} They attributed the red shift to an increase in the local refractive index.³⁸ In our experiment, we see a blue shift which may be due to Hg^{2+} interaction with the NP core. There is the feasibility of a redox reaction which may be dominating here as particles were immobilized whereas in the mobilized case, aggregation is dominant (discussed later). The possibility of reduction of Hg^{2+} by citrate was avoided as there was a continuous flow which flushes excess citrate. The reduced Hg^{2+} may interact with the remaining silver core and change its composition leading to the formation of an amalgam, shifting the plasmon resonance. This leads to a blue shift.³⁹ The deposited Ag^+ , likely to be in the form of poorly soluble salts reduces further interaction of the core with Hg^{2+} and as a result, the shift reduces with time. The Ag^+ ions formed are partly detectable in the solution. Another reason for the blue shift is the reduction in the size of the silver particles.³³ Further support for this suggestion comes from XPS (see below). The results presented suggest that all of these events occur and the observed process is predominantly due to redox chemistry in the case of silver. However, such reduction slows down with time as Ag^+ is deposited on the surface of the particle.

Similarly immobilized Au@citrate NPs were also treated with 5 ppm Hg^{2+} . HSI images with time are shown in Fig. S11. Initially, Au particles were in green and red colors (with maxima ~ 540 and ~ 640 nm, respectively). Some of the red particles turned red–yellow after treating with Hg^{2+} . Here again the

scattering spectra were blue shifted due to reduction of Hg^{2+} leading to formation of an amalgam.³⁴ The magnitude of the shifts was less compared to Ag particles for a given time which indicates more reactivity of silver compared to gold particles in our experimental conditions. This suggests that nano silver reduces Hg^{2+} more efficiently than nano gold. Ag particles of red color show an average blue shift of 12 nm within 30 min whereas Au particles of red color show a shift of 15 nm after 2.0 h (Fig. S12). It could be due to the strong metallophilic interactions of Au^{1+} – Hg^{2+} .^{27,40} Since large shifts were seen in the case of silver, more analyses were done in this case compared to gold NPs.

XPS analysis was performed to deduce the elemental composition of immobilized Ag NPs before and after passing Hg^{2+} for 6.0 h. The XPS survey spectra and Ag 3d regions of immobilized Ag@citrate NPs are shown in Fig. 5A and B, respectively. Fig. 5A shows the presence of all possible elements C, O (from APTMS or TSC), N (from APTMS), Si (from glass substrate and APTMS) and Ag (from Ag@citrate NPs) before as well as after treatment with Hg^{2+} (traces a and b, respectively). The presence of N confirms the immobilization of NPs on APTMS. The presence of Ag 3d_{5/2} before and after treatment of Hg^{2+} at 368.2 eV suggests silver in the zero-valent state¹⁷ (Fig. 5B). But we were unable to detect the presence of mercury which may be due to its ultra low concentrations. The full width at half maximum (FWHM) of Ag 3d_{5/2} before and after passing Hg^{2+} over are 1.3 and 1.7 eV, respectively under the same conditions of XPS measurements. The increase of FWHM may be due to presence of mixed silver oxidation states (Ag^+ and Ag^0). The elemental quantification data suggest that atomic Ag% decreases with respect to Si% after treating with Hg^{2+} . The atomic ratios of Ag to Si before and after Hg^{2+} treatment were 0.09 and 0.05 as shown in Table 1. This may support a decrease in the particle size and blue shift of λ_{\max} after passing Hg^{2+} over. This could be due to the dissolution of Ag NPs as Ag^0 gives electrons for the reduction of Hg^{2+} and the ions may dissolve partially in water. Si was taken as an internal reference element because it is largely due to the glass substrate. To check the presence of Ag in the outlet of the flow cell, ICP-OES analysis was performed. An output solution of 20 mL was concentrated using a rotavapor to 2 mL in which 50 ± 7 ppb silver was detected.

Effect of water quality on the scattering spectrum

It is important that these spectral changes are compared with changes observed in real water samples. DI (specific resistance = 18.2 M Ω cm) and tap water (in which concentrations of Ca^{2+} , Mg^{2+} , Cl^- , NO_3^- , SO_4^{2-} were 52 ± 5 , 10 ± 2 , 80 ± 6 , 4 ± 1 and 31 ± 3 ppm, respectively) were separately passed over immobilized Ag@citrate NPs under the same experimental conditions as that for Hg^{2+} . HSI and scattering spectra of all colored particles were collected. The average shifts of five particles of each color were plotted at different times. The data shown in Fig. S13 suggest that DI and tap waters also cause spectral shifts. In both the cases, *i.e.* DI and tap waters (Fig. S13A and B, respectively), a maximum shift of 15 nm is observed at 6.0 h with a flow rate of 3.5 mL h⁻¹ at 25 °C. In the case of 5 ppm Hg^{2+} , a maximum shift of 46 nm was observed after 6.0 h. This indicates that under the above experimental conditions, the

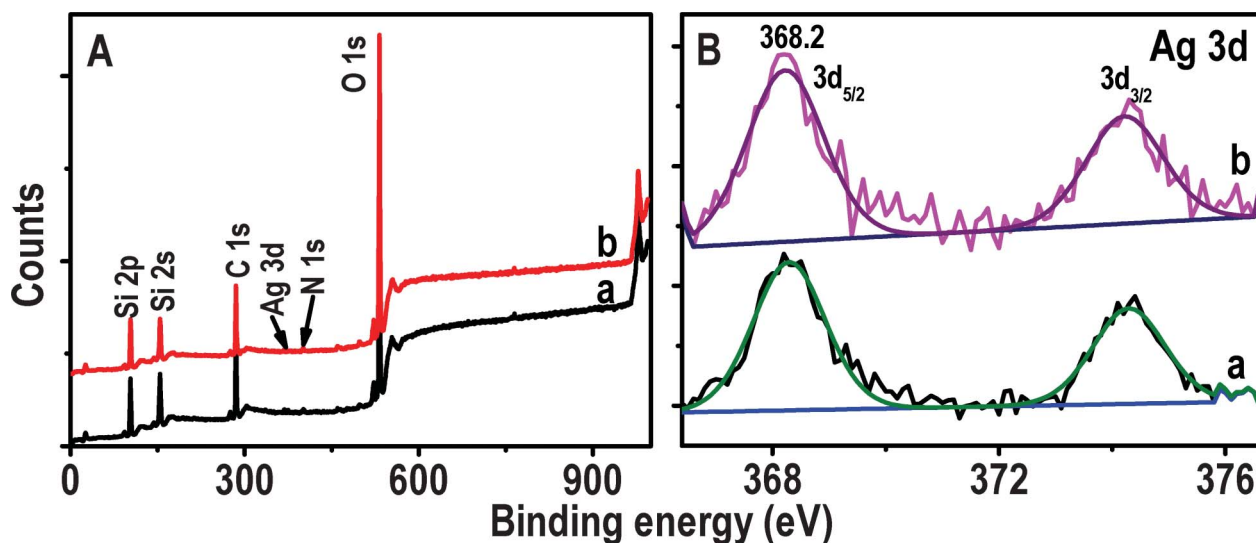


Fig. 5 XPS survey spectra and Ag 3d regions (A and B, respectively) of immobilized Ag@citrate NPs before and after passing Hg^{2+} (traces a and b, respectively). The spectra have been normalized with respect to the Si 2p feature in A and Ag 3d_{5/2} in B, but shifted vertically for clarity.

Table 1 XPS quantification data of Ag@citrate NPs before and after passing over 5 ppm Hg^{2+}

	Si(At.%)	Ag(At.%)	Atomic ratio of Ag to Si
Before	91.55	8.44	0.09
After	95.24	4.76	0.05

effect of typical ions in water on the position of the scattering spectrum is minimal.

Solution phase experiments

To understand the interactions of NPs with Hg^{2+} , solution phase reactions were performed. For this, 5 mL of as-synthesized Ag, Au@citrate NPs were centrifuged to remove excess TSC if any, and to the centrifugate, 5 mL of 5 ppm Hg^{2+} solution was added. This solution was stirred for 6.0 h at room temperature and it was analyzed with UV-vis absorption spectroscopy, XPS, TEM and EDAX. UV-vis absorption of Ag@citrate NPs (after centrifuging followed by redispersion) shows a peak at 418 nm (Fig. 6A, trace a). After 6.0 h, Hg^{2+} treated NPs show a broad peak around 464 nm with a decrease in intensity along with a hump around 384 nm (Fig. 6A, trace b). This red shift of SPR may be due to aggregation of NPs. Added Hg^{2+} interacts with carboxylate groups of citrate which leads to aggregation.¹⁷ The blue shift of SPR (similar to scattering spectra of single particles) may be due to reduction of Hg^{2+} to Hg^0 leading to the formation of an amalgam.³⁹ Formation of Hg^0 was further confirmed by XPS analysis (see below). The absorption spectrum showed dominant aggregation than reduction whereas in HSI we see only blue shift due to reduction of Hg^{2+} in a given experimental condition. It clearly indicates that in solution phase as particles were mobile, there was more chance to bring NPs closer by interlocking Hg^{2+} with the carboxylate groups present on the surface of nanoparticles. In the case of immobilized particles, interaction with the core occurred leading to the reduction of Hg^{2+} resulting in a large blue shift of the scattering wavelength.

Aggregation of NPs in the sample was confirmed by TEM analysis (Fig. S14A). The presence of mercury and silver in aggregate of NPs is supported by elemental mapping and EDAX spectrum (Fig. S14). The reaction mixture was centrifuged at 5000 rpm and the centrifugate was analyzed using XPS to deduce the oxidation states of Hg and Ag. XPS data are shown in Fig. 6B–D. Fig. 6B is the survey spectrum which shows the presence of all possible elements; C, O, Ag, Hg and Na, the last is from TSC. Peaks of Hg 4f_{7/2} are seen at 99.7 and 101.5 eV (Fig. 6C). The peak at 101.5 eV suggests that most of the mercury is present as Hg^{2+} and the peak at 99.7 eV indicates that a small percentage of Hg^0 was also formed²⁶ which supports the blue shift of UV-vis (trace b, Fig. 6A). The presence of Ag 3d_{5/2} at 368.0 eV confirms that silver is in the zero-valent state (Fig. 6D).

Time-dependent UV-vis absorption spectra of Au@citrate particles and 5 ppm Hg^{2+} solution are shown in the inset of Fig. 6A. Unlike in the case of Ag particles, no shift of plasmon peak is seen but a small decrease in the absorbance value is noticed after 6.0 h. This supports the poor interaction of Hg^{2+} with gold particles compared to silver in a given time (6.0 h) and Hg^{2+} concentration (5 ppm). The reaction mixture of Au NPs and 5 ppm Hg^{2+} (after 6.0 h) was centrifuged at 5000 rpm. The residue obtained was analyzed with XPS and data are compared with parent Au NPs (Fig. 7). Survey spectra of NPs before and after treatment of Hg^{2+} (traces a and b, respectively in Fig. 7A) show the presence of expected elements Au, C, Na and O. Gold is present in the zero-valent state (Au 4f_{7/2} at 84.1 eV) before and after treatment of Hg^{2+} (traces a and b, respectively in Fig. 7B). The Hg 4f region from Hg^{2+} treated NPs is shown as an inset in Fig. 7A. Its absence indicates that no or poor interaction of Hg^{2+} occurs with Au NPs. However, Au@citrate NPs were found to interact with mercuric ion⁴¹ at higher concentrations (~60 ppm, data not shown).

The reduction of Hg^{2+} to Hg^0 is also supported by redox potentials of Ag⁺/Ag, Hg^{2+} / Hg^+ and Hg^+ / Hg^0 systems. The standard reduction potentials of Ag⁺/Ag, Hg^{2+} / Hg^+ and Hg^+ / Hg^0

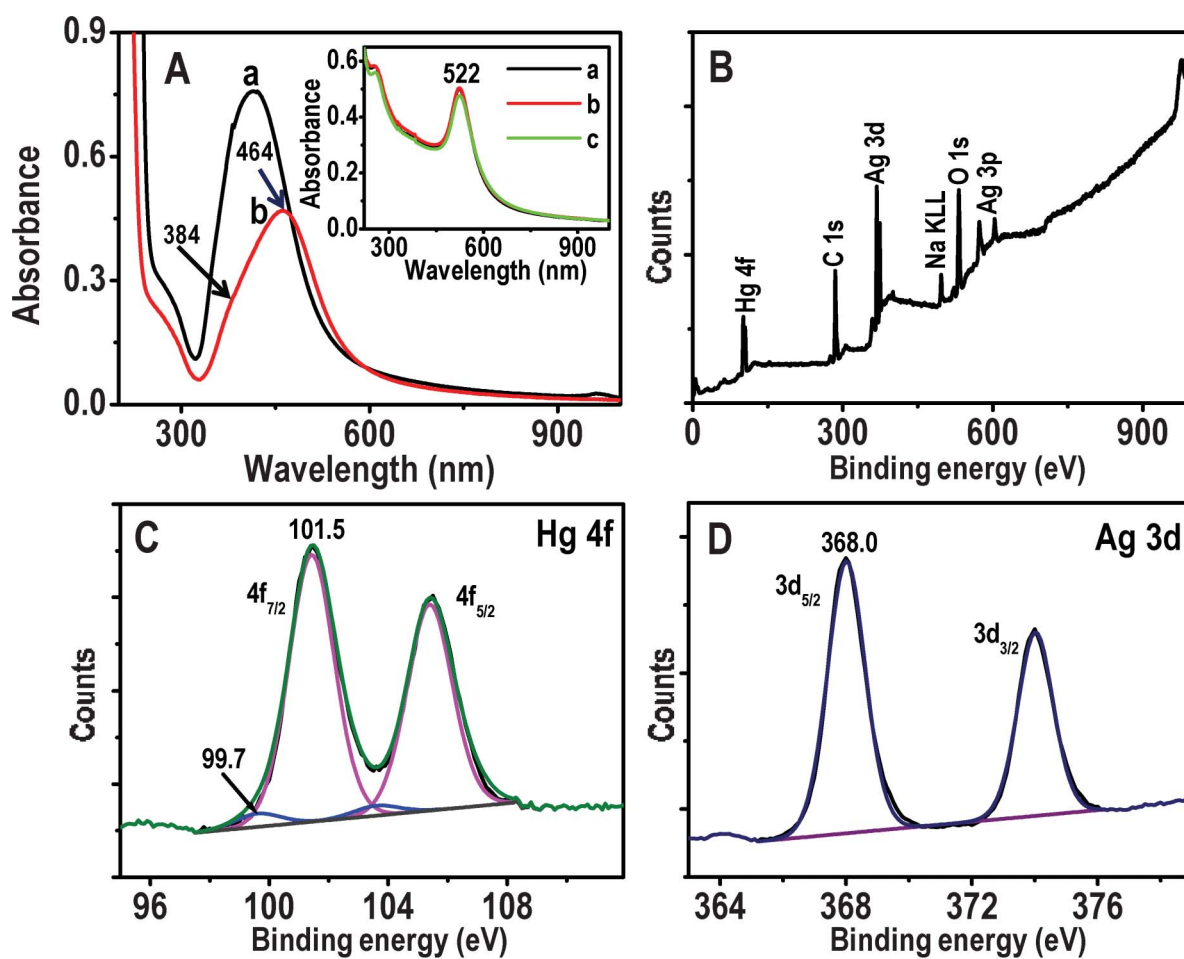


Fig. 6 A) UV-vis absorption spectra of Ag@citrate NPs before and after treatment with 5 ppm Hg^{2+} for 6.0 h (traces a and b, respectively). B–D are XPS survey spectrum, Hg 4f and Ag 3d regions, respectively of Ag@citrate NPs treated with 5 ppm Hg^{2+} for 6.0 h. Inset: UV-vis absorption spectra of Au@citrate NPs and 5 ppm Hg^{2+} after interaction for 5 min, 3.0 and 6.0 h (a, b and c, respectively).

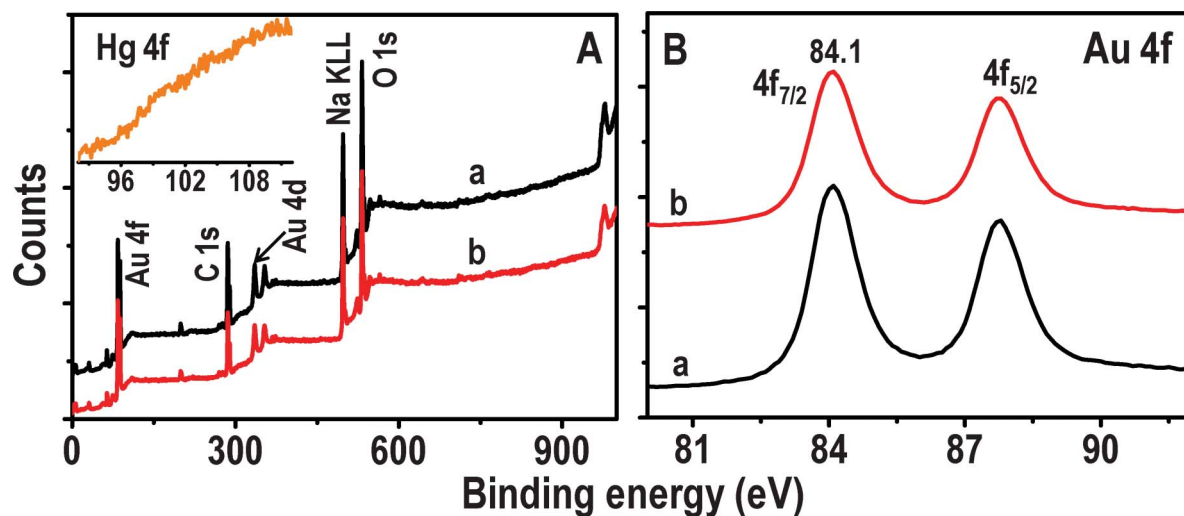


Fig. 7 XPS survey spectra and Au 4f regions (A and B, respectively) of Au@citrate NPs before and after treatment with 5 ppm Hg^{2+} for 6.0 h (traces a and b, respectively). Inset of A is the Hg 4f region of trace b.

are 0.8, 0.91 and 0.82 V, respectively. The cell emf (electromotive force) for the reactions, $\text{Ag}^0 + \text{Hg}^{2+} \rightarrow \text{Ag}^+ + \text{Hg}^+$ and $\text{Ag}^0 + \text{Hg}^+ \rightarrow \text{Ag}^+ + \text{Hg}^0$ are therefore +0.11 and +0.02 V, respectively. But at the nanoscale, the reaction may be more feasible. The lower reactivity of gold particles with Hg^{2+} may be due to the negative emf (−0.5 V) for the reduction ($2\text{Au}^0 + 3\text{Hg}^{2+} \rightarrow 2\text{Au}^{3+} + 3\text{Hg}^0$) of Hg^{2+} . Although Au^+ could be formed, this reaction is also not feasible ($\text{Au}^0 + \text{Hg}^{2+} \rightarrow \text{Au}^+ + \text{Hg}^+$, emf: −0.77 V).

Summary and conclusions

A real time study of interactions of Ag and Au@citrate NPs with Hg^{2+} was performed using hyperspectral imaging. The feasibility of the redox reaction of Ag@citrate with Hg^{2+} leads to the oxidation of silver and its dissolution. Consequently the reduced Hg interacts with the nanoparticle left behind and the amalgam formed blue shifts the scattering spectrum. It is found that red particles are more reactive compared to green and blue as they show a larger shift in the scattering spectrum upon reaction with Hg^{2+} which may be due to their larger size and consequent surface area. As NPs are immobilized, aggregation is avoided. Whereas in the solution phase, aggregation of NPs along with partial reduction of Hg^{2+} is seen, which was confirmed by XPS. The effect of ions present in tap water on the scattering spectrum of NP is minimal for a given time. Greater reactivity of silver (in the present study) compared to gold particles with Hg^{2+} in a given time is observed due to the feasibility of the redox reaction for the former. To the best of our knowledge, this is the first attempt to study real time interactions of single silver particles with mercuric ions. In terms of sensitivity, although our study reveals a visual detection limit (in HSI) of 1 ppm Hg^{2+} , the sensing capability of these NPs may be increased to detect lower mercury levels by functionalizing with thiols, increasing in incubation time, decreasing the flow rate, etc.

Acknowledgements

We thank the Department of Science and Technology (DST), Government of India, for constantly supporting our research program on nanomaterials. Thanks are also due to Prof. G. U. Kulkarni of Jawaharlal Nehru Centre for Advanced Scientific Research, Bangalore for FESEM measurements. M.S.B. thanks the CSIR for a senior research fellowship.

References

- 1 I. Pastoriza-Santos and L. M. Liz-Marzan, *J. Mater. Chem.*, 2008, **18**, 1724–1737.
- 2 J. Homola, *Chem. Rev.*, 2008, **108**, 462–493.
- 3 M. E. Stewart, C. R. Anderton, L. B. Thompson, J. Maria, S. K. Gray, J. A. Rogers and R. G. Nuzzo, *Chem. Rev.*, 2008, **108**, 494–521.
- 4 E. Ozbay, *Science*, 2006, **311**, 189–193.

- 5 M. A. El-Sayed, *Acc. Chem. Res.*, 2001, **34**, 257–264.
- 6 R. Jin, Y. Cao, C. A. Mirkin, K. L. Kelly, G. C. Schatz and J. G. Zheng, *Science*, 2001, **294**, 1901–1903.
- 7 J. Yu, H. Tao and B. Cheng, *ChemPhysChem*, 2010, **11**, 1617–1618.
- 8 E. Ringe, J. M. McMahon, K. Sohn, C. Cobley, Y. Xia, J. Huang, G. C. Schatz, L. D. Marks and R. P. Van Duyne, *J. Phys. Chem. C*, 2010, **114**, 12511–12516.
- 9 P. Mulvaney, *Langmuir*, 1996, **12**, 788–800.
- 10 S. Link and M. A. El-Sayed, *J. Phys. Chem. B*, 1999, **103**, 4212–4217.
- 11 L. Slaughter, W.-S. Chang and S. Link, *J. Phys. Chem. Lett.*, 2011, **2**, 2015–2023.
- 12 J. Yguerabide and E. E. Yguerabide, *Anal. Biochem.*, 1998, **262**, 157–176.
- 13 T. R. Jensen, M. D. Malinsky, C. L. Haynes and R. P. Van Duyne, *J. Phys. Chem. B*, 2000, **104**, 10549–10556.
- 14 T. Pradeep and S. Anshup, *Thin Solid Films*, 2009, **517**, 6441–6478.
- 15 M. S. Bootharaju and T. Pradeep, *Langmuir*, 2012, **28**, 2671–2679.
- 16 A. S. Nair and T. Pradeep, *Curr. Sci.*, 2003, **84**, 1560–1564.
- 17 M. S. Bootharaju and T. Pradeep, *J. Phys. Chem. C*, 2010, **114**, 8328–8336.
- 18 G. Raschke, S. Kowarik, T. Franzl, C. Sönnichsen, T. A. Klar, J. Feldmann, A. Nichtl and K. Kürzinger, *Nano Lett.*, 2003, **3**, 935–938.
- 19 Y. Liu, J. Ling and C. Z. Huang, *Chem. Commun.*, 2011, **47**, 8121–8123.
- 20 C. Novo, A. M. Funston and P. Mulvaney, *Nat. Nanotechnol.*, 2008, **3**, 598–602.
- 21 W. P. Hall, J. Modica, J. Anker, Y. Lin, M. Mrksich and R. P. Van Duyne, *Nano Lett.*, 2011, **11**, 1098–1105.
- 22 A. D. McFarland and R. P. Van Duyne, *Nano Lett.*, 2003, **3**, 1057–1062.
- 23 T. Huang, P. D. Nallathamby, D. Gillet and X.-H. N. Xu, *Anal. Chem.*, 2007, **79**, 7708–7718.
- 24 G. L. Liu, Y. Yin, S. Kunchakarra, B. Mukherjee, D. Gerion, S. D. Jett, D. G. Bear, J. W. Gray, A. P. Alivisatos, L. P. Lee and F. F. Chen, *Nat. Nanotechnol.*, 2006, **1**, 47–52.
- 25 E. Sumesh, M. S. Bootharaju, S. Anshup and T. Pradeep, *J. Hazard. Mater.*, 2011, **189**, 450–457.
- 26 M. S. Bootharaju and T. Pradeep, *Langmuir*, 2011, **27**, 8134–8143.
- 27 Y.-H. Lin and W.-L. Tseng, *Anal. Chem.*, 2010, **82**, 9194–9200.
- 28 C.-J. Yu and W.-L. Tseng, *Langmuir*, 2008, **24**, 12717–12722.
- 29 H. D. Song, I. Choi, Y. I. Yang, S. Hong, S. Lee, T. Kang and J. Yi, *Nanotechnology*, 2010, **21**, 145501.
- 30 A. S. Nair and T. Pradeep, *J. Nanosci. Nanotechnol.*, 2007, **7**, 1871–1877.
- 31 M. V. Cañamares, J. V. Garcia-Ramos, J. D. Gómez-Varga, C. Domingo and S. Sanchez-Cortes, *Langmuir*, 2005, **21**, 8546–8553.
- 32 B. M. Reinhard, M. Siu, H. Agarwal, A. P. Alivisatos and J. Liphardt, *Nano Lett.*, 2005, **5**, 2246–2252.
- 33 L.-X. Qin, C. Jing, Y. Li, D.-W. Li and Y.-T. Long, *Chem. Commun.*, 2012, **48**, 1511–1513.
- 34 W. Qi, Y. Wang, J. Wang and C. Huang, *Sci. China: Chem.*, 2012, **55**, 1445–1450.
- 35 R. Narayanan and M. A. El-Sayed, *J. Phys. Chem. B*, 2005, **109**, 12663–12676.
- 36 T. Mokari, E. Rothenberg, I. Popov, R. Costi and U. Banin, *Science*, 2004, **304**, 1787–1790.
- 37 T. Huang, P. D. Nallathamby and X.-H. N. Xu, *J. Am. Chem. Soc.*, 2008, **130**, 17095–17105.
- 38 J. N. Anker, W. P. Hall, M. P. Lambert, P. T. Velasco, M. Mrksich, W. L. Klein and R. P. Van Duyne, *J. Phys. Chem. C*, 2009, **113**, 5891–5894.
- 39 A. Henglein and C. Brancewicz, *Chem. Mater.*, 1997, **9**, 2164–2167.
- 40 J. Xie, Y. Zheng and J. Y. Ying, *Chem. Commun.*, 2010, **46**, 961–963.
- 41 I. Ojea-Jiménez, X. López, J. Arbiol and V. Puntes, *ACS Nano*, 2012, **6**, 2253–2260.

Electronic supplementary information

Real time plasmonic spectroscopy of the interaction of Hg^{2+} with single noble metal nanoparticles

M. S. Bootharaju, K. Chaudhari and T. Pradeep*

DST Unit of Nanoscience (DST UNS), Department of Chemistry,

Indian Institute of Technology Madras, Chennai - 600 036, India

*E-mail: pradeep@iitm.ac.in

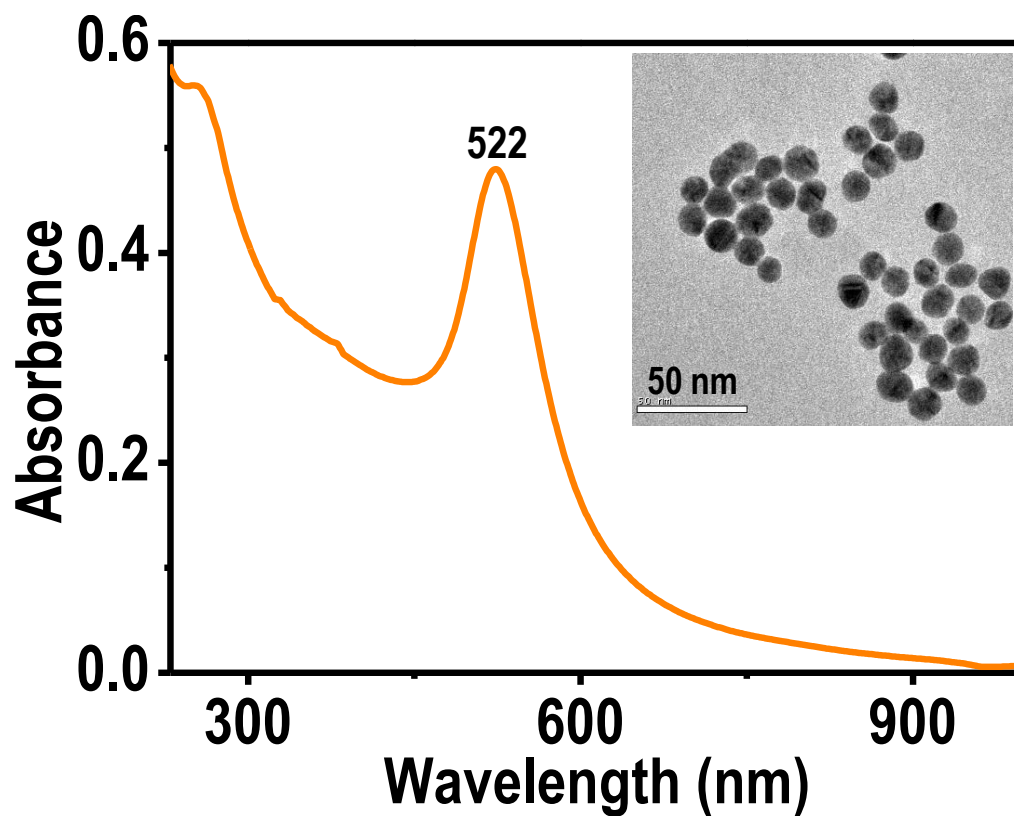


Fig. S1 UV-vis absorption spectrum of as-prepared Au@citrate NPs. Inset is the TEM image of Au@citrate NPs.

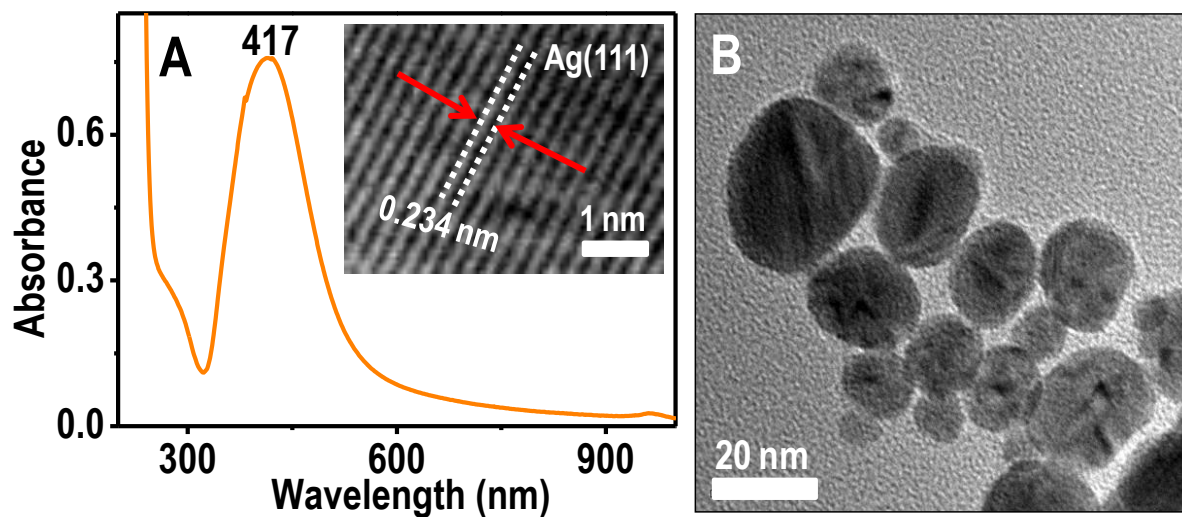


Fig. S2 UV-vis absorption spectrum (A) and TEM image (B) of as-synthesized Ag@citrate NPs. Lattice plane and inter planar distance of Ag(111) in a single NP are shown as inset of A.

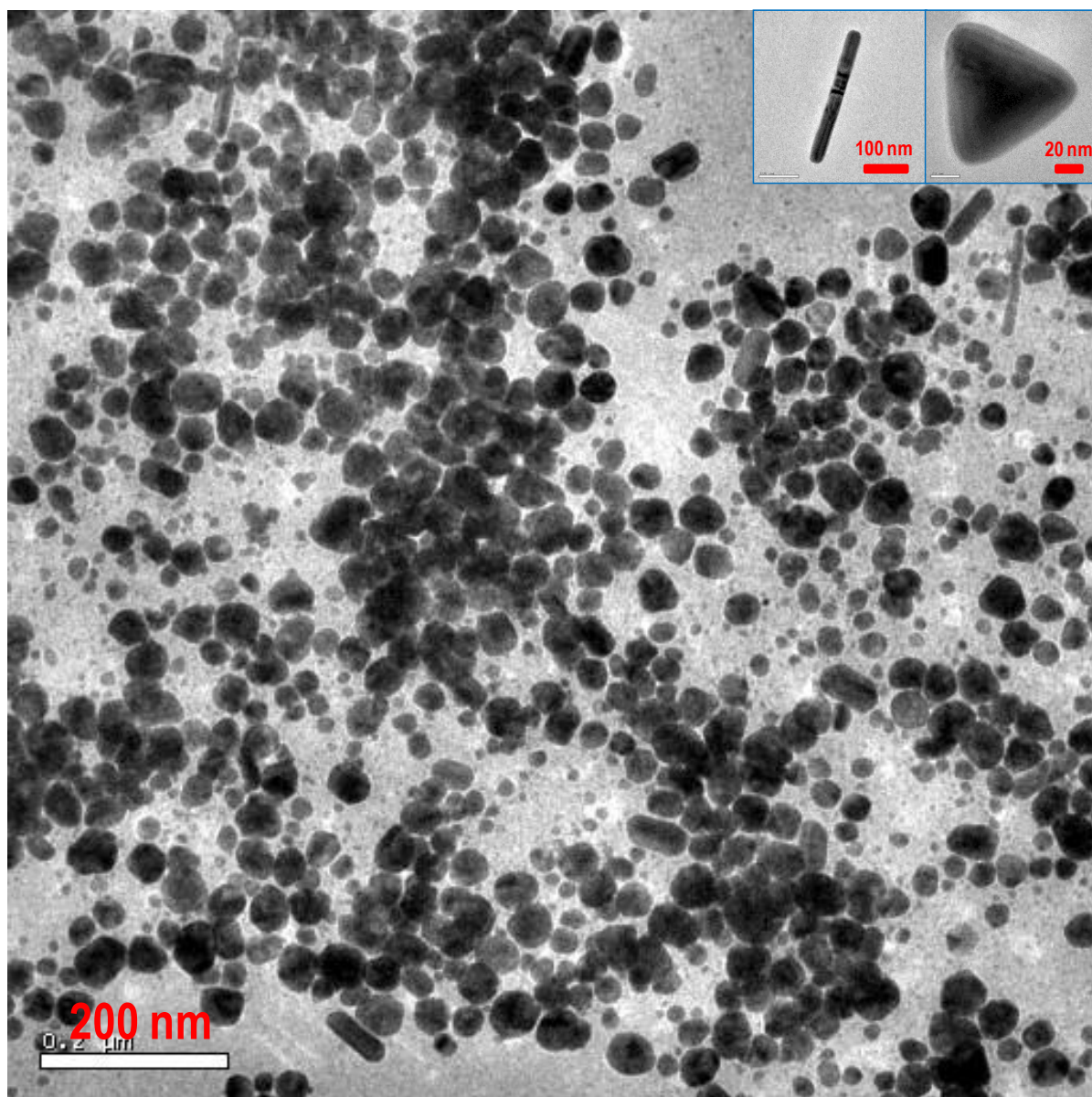


Fig. S3 Large area TEM image of as-synthesized Ag@citrate particles which shows polydispersity along with different morphologies. A single nanorod and a triangle are shown as insets.

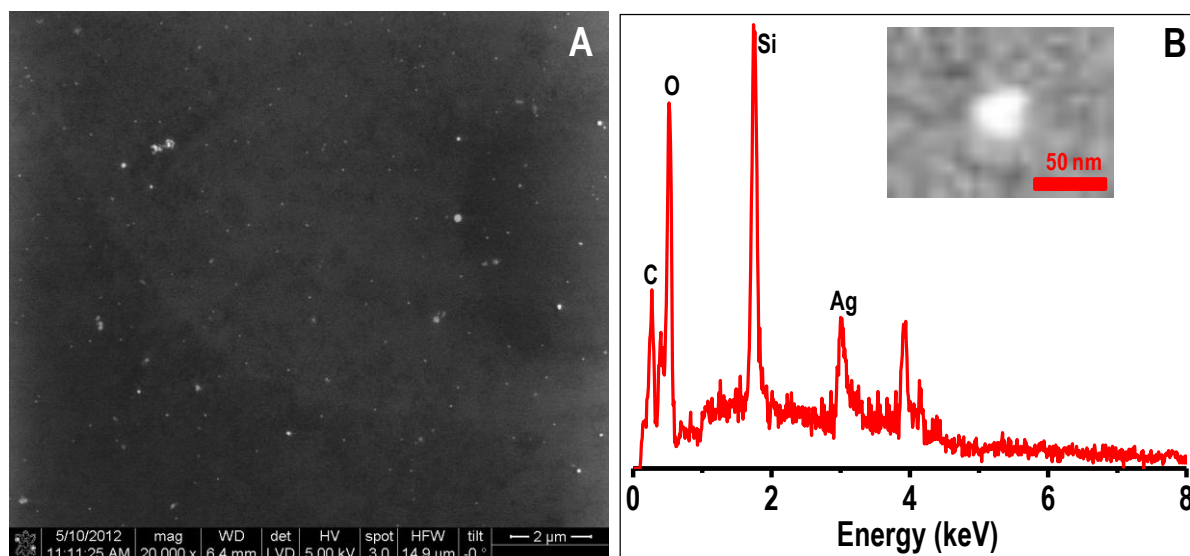


Fig. S4 A) Large area FESEM image of immobilized Ag@citrate particles on glass substrate. B is the EDAX spectrum of one of the particles (inset of B). Data indicate the presence of silver. Si is from the substrate used. O is also partly from the substrate.

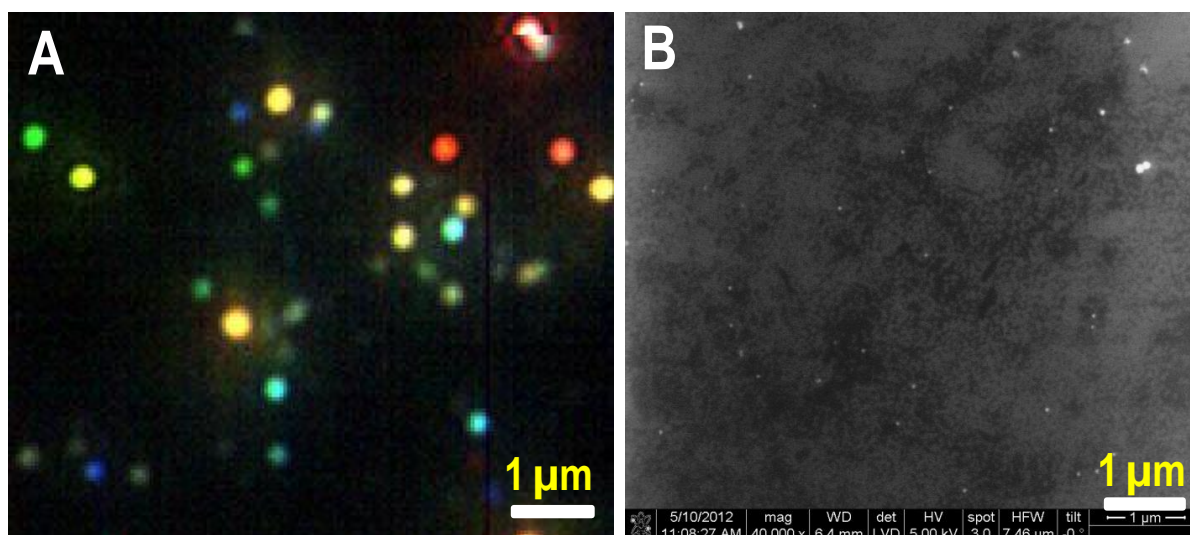


Fig. S5 Comparison of number of particles in HSI (A) and FESEM (B) images of immobilized (on glass slide) Ag@citrate nanoparticles in a given area ($7.2 \times 6.2 \mu\text{m}^2$). The number of particles in A and B are 33 ± 3 and 35 ± 3 , respectively.

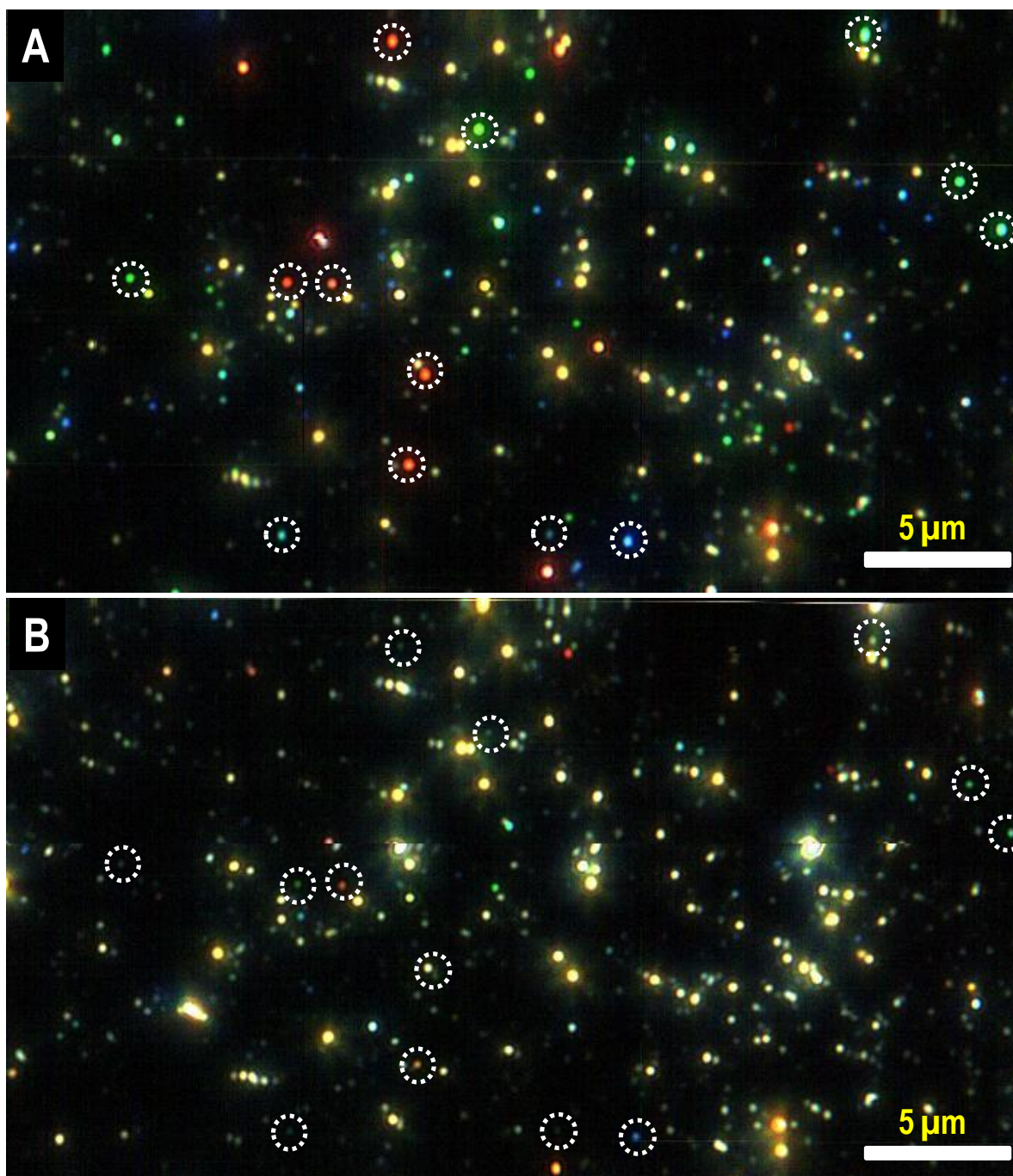


Fig. S6 Large area HSI of immobilized Ag@citrate NPs before and after treating 5 ppm Hg²⁺ for 6.0 h (A and B, respectively). Changes in colors of some of the NPs are marked with dotted circles, for comparison.

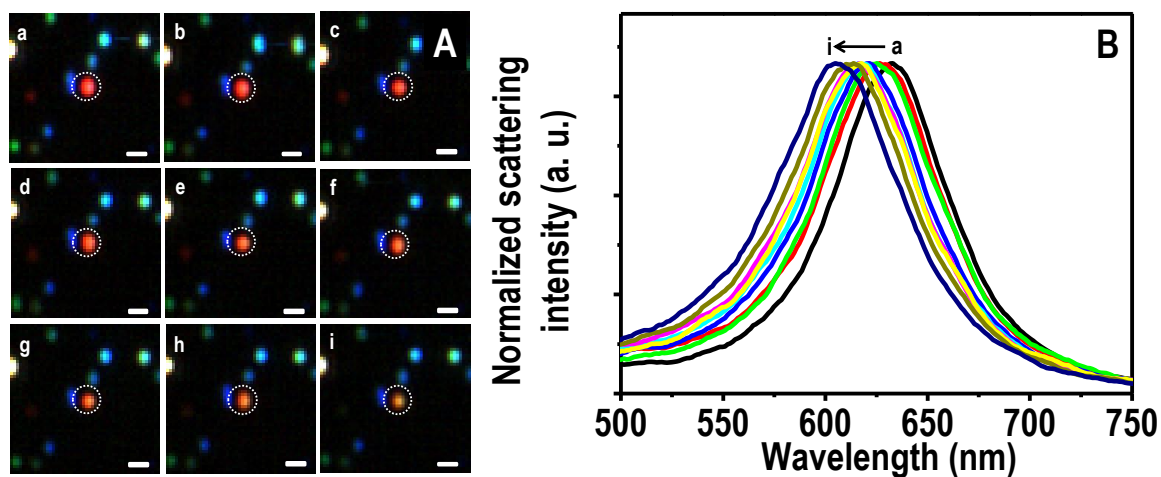


Fig. S7 HSI (A) of immobilized Ag@citrate NPs after passing 5 ppm Hg^{2+} for 0.0, 0.5, 1.0, 1.5, 2.0, 2.5, 3.0, 4.0 and 6.0 h (a-i, respectively). Scattering spectra (B) of red particle (marked with dots) with time (a-i). Scale bars of images in A are 500 nm.

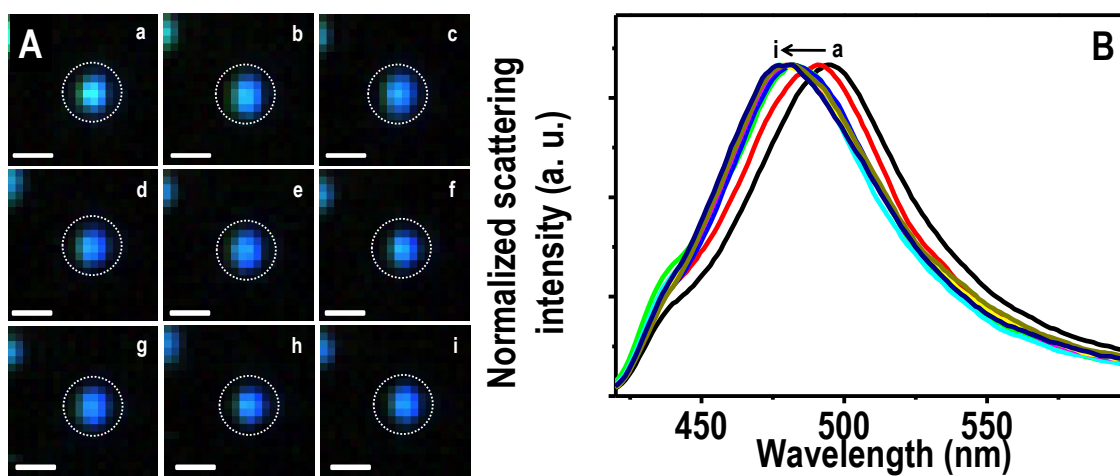


Fig. S8 HSI (A) of immobilized Ag@citrate NPs after passing 5 ppm Hg^{2+} for 0.0, 0.5, 1.0, 1.5, 2.0, 2.5, 3.0, 4.0 and 6.0 h (a-i, respectively). Scattering spectra (B) of blue particle (marked with dots) with time (a-i). Scale bars of images in A are 400 nm.

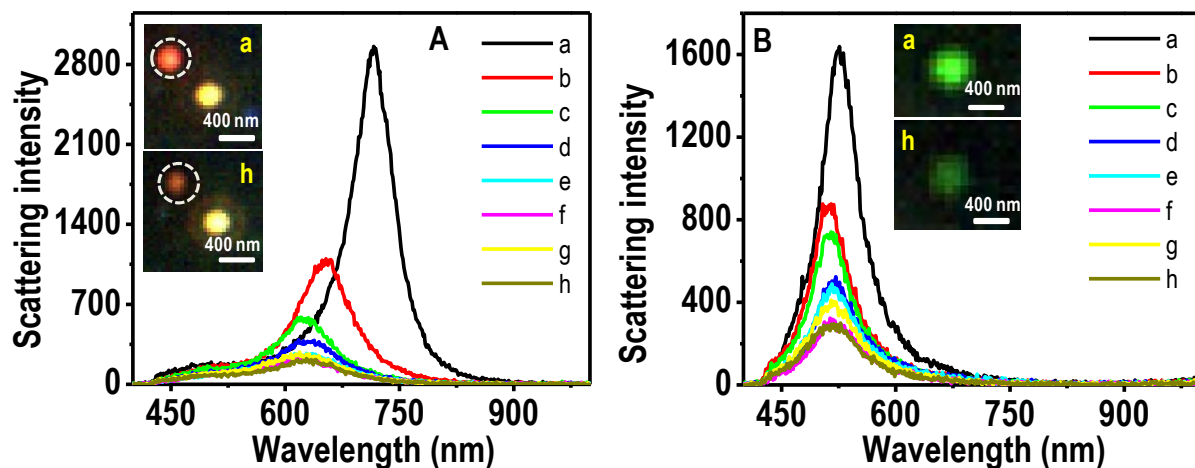


Fig. S9 Time-dependent scattering spectra of red (A) and green (B) particles. Insets of A and B are the HSI images of red and green particles after the treatment of 5 ppm Hg^{2+} for 0.5 and 6.0 h. "a-h" are the times 0.0, 0.5, 1.5, 2.0, 2.5, 3.0, 4.0 and 6.0 h, respectively.

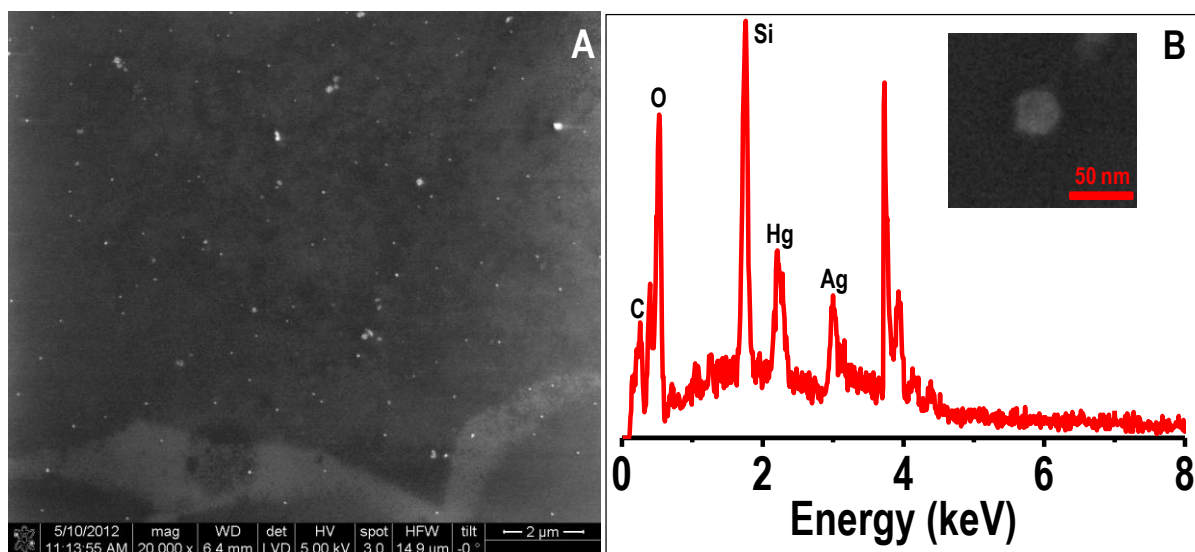


Fig. S10 A) Large area FESEM image of immobilized Ag@citrate particles after treating 5 ppm Hg^{2+} for 3.0 h on glass substrate. B is the EDAX spectrum of one of the particles (inset B) indicating the presence of silver and mercury. Si is from the substrate used. O is also partly from the substrate.

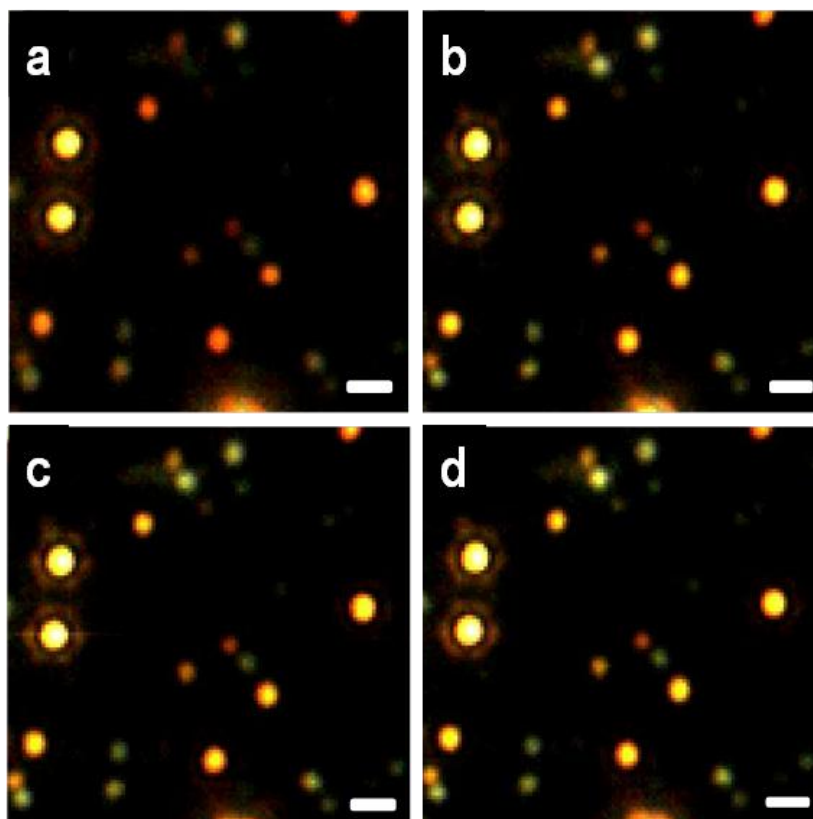


Fig. S11 HSI images of immobilized Au@citrate NPs after passing 5 ppm Hg^{2+} for 0.0, 2.0, 4.0 and 6.0 h (a-d, respectively). Scale bars in the images are 500 nm.

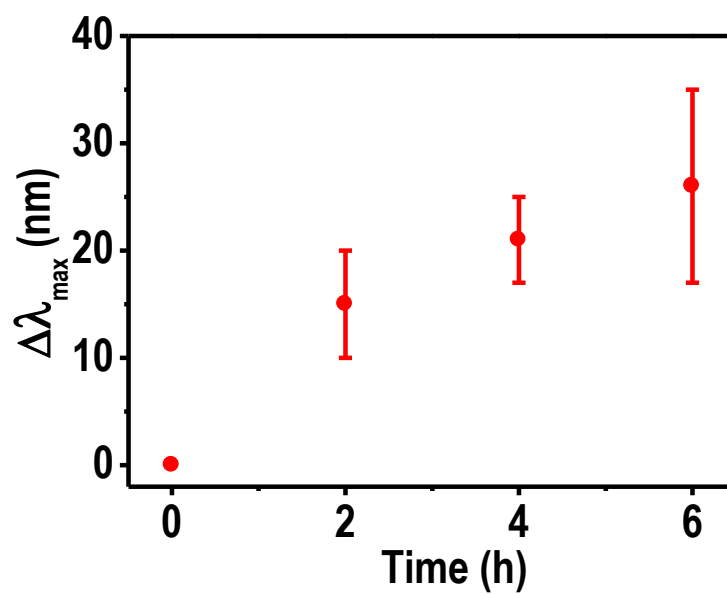


Fig. S12 A plot of average blue shift ($\Delta\lambda_{\text{max}}$) of 5 red Au@citrate particles treated with Hg^{2+} with time.

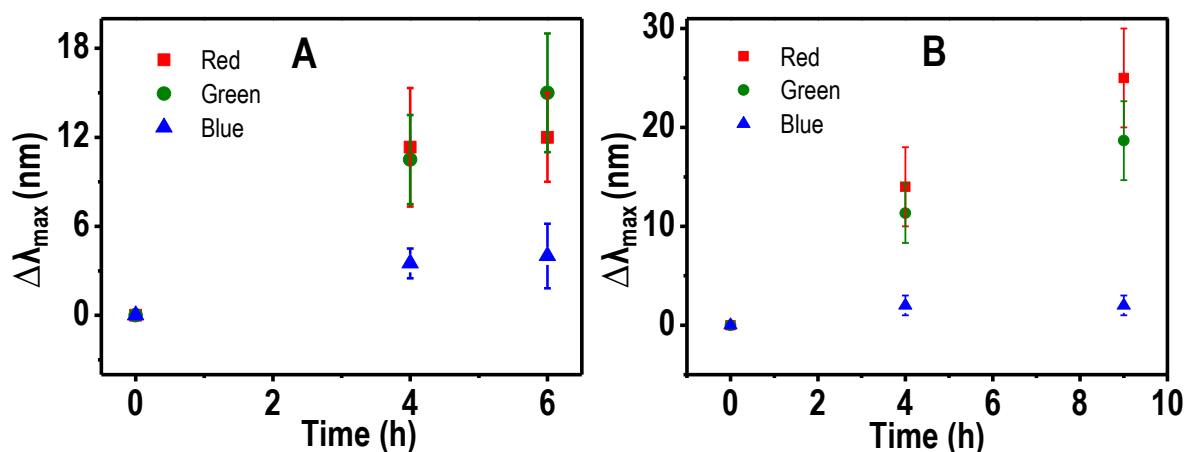


Fig. S13 Plots of average blue shift ($\Delta\lambda_{\max}$) of 5 particles of each color (red, blue and green) after passing DI and tap waters (A and B, respectively) with time.

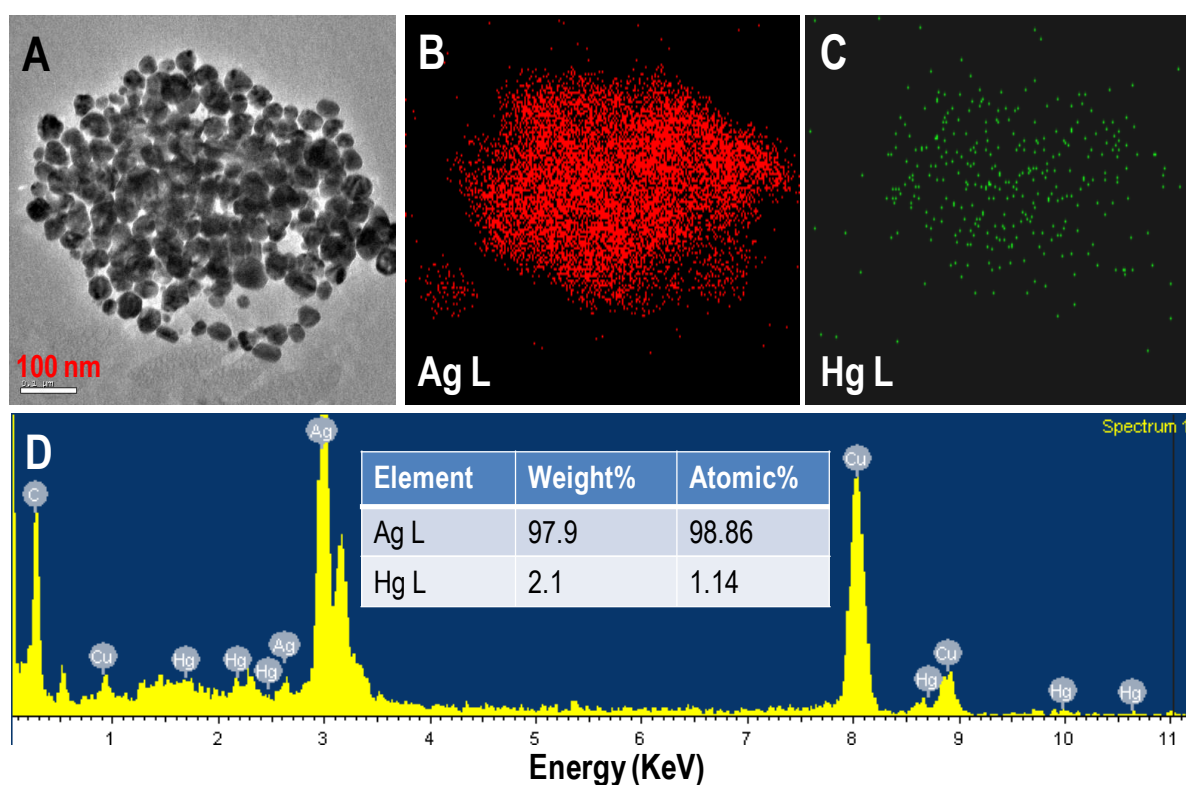


Fig. S14 TEM image (A) and elemental maps of Ag and Hg (B and C, respectively) of an aggregate of Ag@citrate NPs formed with interaction of 5 ppm Hg^{2+} for 6.0 h. D is EDAX spectrum of A in which a table of quantitation of elements is shown as inset. The EDAX image is rotated by 45° in comparison to the TEM image.

Nanoscience in India: a perspective

Anirban Som, Ammu Mathew, Paulrajpillai Lourdu Xavier and T. Pradeep*

DOI: 10.1039/9781849734844-00244

India has emerged as a leading player in the field of nanoscience and nanotechnology over the last decade. The Indian nano-endeavor got its initial push through the Nano Science and Nano Technology (NS&NT) initiative (now the Nano Mission) of the Department of Science and Technology (DST), Government of India since 2002 and has accelerated very fast since then. This article is intended to sketch a brief picture of the recent nanoscience and technology activities in India with special emphasis on synthesis of nanomaterials and emergence of new properties in them. Application of nanomaterials into the very basic needs of India like water purification and energy creation along with the recent developments at the bio-nano interface will be discussed. State of nanoscience education at educational institutions in India and nanoscience based industrial initiatives will be touched upon.

1 Introduction

Nanoscience in India is vivid, diverse and expanding as in other parts of the world. The variety and diversity of the area resemble that of India itself and therefore, precisely capturing this panoramic view in the limited space is nearly impossible. Although one can trace back the creation of nanoscale matter in India to the *Vedic* period (1700–1100 BC) as evidenced from the presence of nanoparticles in several *Ayurvedic* preparations,¹ systematic efforts to understand such materials science of the past are rare. Recent investigations into the metallurgical processing prevalent in India showed the existence of nanoscale matter in a few weaponry of 300 BC which was attributed to the extraordinary strength of these materials.^{2,3} These practices, whether in Indian medicine or in metal processing, continue to exist in several parts of the country, but there have been very limited systematic and scientific efforts to correlate the properties with the nanoscale constituents.

This article is intended to present a broad overview of the recent and emerging trends in the Indian landscape of nanoscience. Although matter at the nanoscale, called ultrafine particles then, were probed extensively in 1980's and 90's with emphasis on material science, catalysis, quasicrystals and related disciplines, a sea change in the exploration of nanoscale matter happened due to the Nano Science and Nano Technology (NS&NT) initiative of the Department of Science and Technology (DST) in 2002 (now the Nano Mission, <http://nanomission.gov.in>). Although the investment was modest in the initial years (US\$12 million for first 5 years *i.e.* 2001–2006⁴) and continued to remain small (US\$200 million during 2007–2012⁵) in comparison to other adjacent countries (*e.g.* US\$760 million in China, US\$689 million in Taiwan, US\$35 million in Malaysia, *etc.*⁵), the

DST Unit of Nanoscience, Department of Chemistry, Indian Institute of Technology Madras, Chennai 600036, India. E-mail: pradeep@iitm.ac.in

outcome has been phenomenal. Indian publications in nanoscience increased from 1412 to 3616 during 2006–2011 in comparison to 355 to 971 during 2001–2005.⁶ Large part of the investment in nanoscience went to create infrastructure necessary for the exploration of nanoscale matter. As a result, a number of Units on Nanoscience (UNS) and Centres of Nanoscience (CNS) (20 in all) got created across the length and breadth of the country. As a result, it was not necessary to wait for months together for a high resolution transmission electron micrograph or carry samples discretely on your trip abroad for a quick measurement. Several other funding agencies supported the growth of nanoscience research in India. Department of biotechnology (DBT) provides support for nanotechnology related to life sciences. Council of Scientific and Industrial Research (CSIR) and Science and Engineering Research Council (SERC) of the DST also support research projects in diverse areas of nanoscience covering both basic and applied sciences. Although there are several other agencies such as Ministry of Information Technology (MIT), Defence Research and Development Organisation (DRDO), Indian Council of Medical Research (ICMR), University Grants Commission (UGC), Board of Research in Nuclear Studies (BRNS) of the Department of Atomic Energy, Indian Space Research Organization (ISRO) and Indian Council of Agricultural Research (ICAR) have been funding research programs in the area, the efforts of DST have been the largest in fostering basic research in the country. Over 270 research projects have been funded over the period 2002–2011,⁷ producing about 670 Ph.Ds and over 4000 research papers in this window of time.⁸ Besides publications, 120 Indian and 38 foreign patents were filed in the five year term of Nano Mission of which 24 Indian and 11 foreign patents were granted.⁸ Figure 1 summarizes this rapid expansion of the science at the nanoscale in India. While this continues to fascinate scientists, it is merely 5% in the global umbrella of nanoscience and technology related activities, judged from the fraction of publications.⁶

The Indian nano endeavor continues largely in the plethora of nano-materials synthetic chemistry can unravel. As a result, chemists continue to

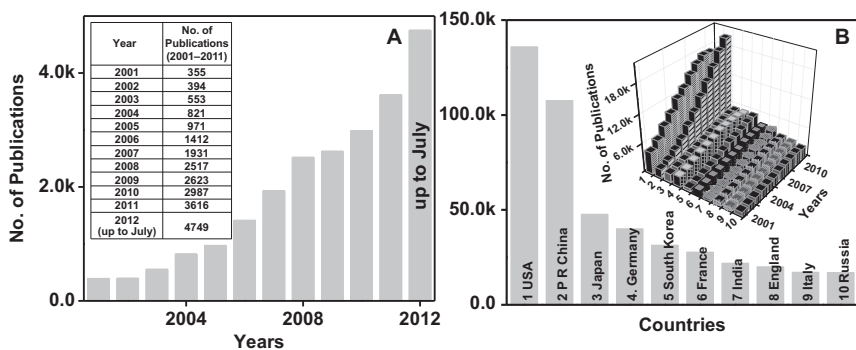


Fig. 1 (A) Increase in number of publications over the years (2001–July, 2012) in India in nanoscience and technology. Number of publications per year is shown in the inset. (B) Total number of publications in nanoscience and technology in the top 10 countries over the time span of 2001–2011. Year-wise increase in number of publications in those countries is shown in the inset.⁶

be more active in the area; chemical physics and biology complement the chemical efforts. Very few applications and devices have come about as in other parts of the world. Despite this, the early example of commercial success of nano has come from India touching upon the basic needs of India such as water.^{9,10} As a result of the close link with society, social scientists have been fascinated by the emerging implications of the area.¹¹ It has got into newspaper and public media¹² and even popular science books in regional languages.¹³

In the following, we present the recent excitements captured in materials, applications, biology and industry. Past efforts of various groups in diverse areas of their activity are collected in reviews and books. Chemistry of nanomaterials,¹⁴ carbon nanotubes,¹⁵ graphenic materials,^{16,17} nanofluids,¹⁸ nanoparticle assemblies,^{19,20} self organized structures,^{21,22} organic nanomaterials²³ polymer nanowires,²⁴ *etc.* are covered in excellent monographs and reviews. For a complete and up-to-date understanding of the nanoscience endeavor in India, it is important to consult these as well. Education in this discipline and implications to the largely young India (50% of Indian population are under the age of 25, from 2011 census) will be touched upon. We are aware that only representative work of several authors have been captured here and we are silent about the work of ~~for~~ several others. In both these instances, the readers may consult the cited reviews.

2 Nanoscience research in India

2.1 Different nanomaterials-synthesis and new properties

2.1.1 Noble metal nanomaterials. Nanoparticles have become important materials these days not only due to their excellent structural features but also by their unusual functional attributes. Due to this reason, a considerable amount of attention has been paid to discover new ways to reduce the size of the constituent particles of every material to the nanometer length scale. Following Faraday's breakthrough of the synthesis of colloidal gold,²⁵ several new nanostructured materials and synthetic protocols were developed. Based on the confinement of electronic motion along specific axes, nanomaterials are mainly divided into two categories isotropic and anisotropic particles. Synthesis of such materials involves a wide variety of strategies as careful tuning of shape and size of the particles at this length scale can result in alteration of their physiochemical and optoelectronic properties. Simple chemical reduction of metal precursors using carefully controlled variation of synthetic parameters can yield nanoparticles of varying size, shape and composition in high yield with monodispersity. Microemulsion based synthesis is another effective way for the synthesis of various nanoparticles which Ganguli *et al.* has discussed in detail elsewhere.²⁶ Anisotropic materials such as nanorods,^{27,28} nanowires, triangles,^{29,30} nanoribbons,³¹ nanoprisms,³² flowers,^{33,34} *etc.*, have been widely studied and synthetic routes such as seed-mediated synthesis, biological synthesis, polyol synthesis, galvanic displacement methods, template-mediated synthesis *etc.* have been explored.³⁵

Among the multitude of anisotropic noble metal nanomaterials synthesized, an exciting addition from the Indian context is the work by Murali

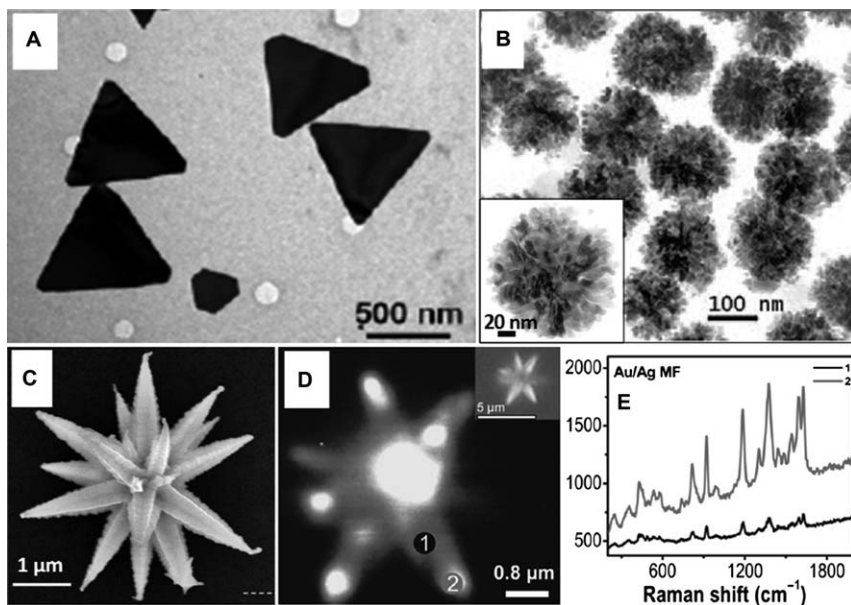


Fig. 2 (A) TEM image of gold nanotriangles synthesized by the biological reduction of HAuCl_4 solution with lemon grass extract (adapted from Ref. 325). (B) TEM image of nanostructured Au nanoparticles with marigold like morphology (nMG). Inset shows a single nMG (adapted from Ref. 326). (C) FESEM image of a gold mesoflower (adapted from Ref. 327). (D) Raman image of a single bimetallic Ag-Au mesoflower (adapted from Ref. 46). (E) Raman spectra of adsorbed crystal violet molecules on different regions of bimetallic Ag-Au mesoflower (marked in D).

Sastry *et al.* using biological templates/reducing agents. They developed a new synthetic strategy for making nanomaterials of various sizes and shapes by following biological routes.³⁶ In their pioneering work, they used the fungus, *Fusarium oxisporum*, to make gold nanoparticles.³⁷ Subsequently they made thin, flat, and single crystalline gold nanoprisms (Fig. 2A) using lemongrass (*Cymbopogon flexuosus*) extract.³² This method had a great impact in the area of anisotropic nanomaterials synthesis as it was difficult to make gold nanotriangles by a simple method in a highly reproducible manner. The method was ‘green’ as the reduction of Au^{3+} is induced by the reducing sugar (aldoses) present in the plant extract which resulted in a visible color change from pale yellow to ruby red during the reaction. Moreover, the possibilities of such bio-friendly nanotriangles in view of many bio-related applications received great attention all around the world. The other advantage of this method is that, the size of nanoprisms and thereby its longitudinal SPR band in the NIR region can be tuned by simple variation of the concentration of lemongrass extract in the reaction medium.³⁸ Several other biological systems such as tea leaves,³⁹ tamarind leaf,⁴⁰ neem seed extract,⁴¹ *Vitis vinefera* (grapes),⁴² clove buds (*Syzygium aromaticum*),⁴³ bacteria such as lactobacillus,⁴⁴ *etc.* have also been reported to make nanoparticles of noble metals.

Apart from biological synthesis, various synthetic protocols were widely used to make nanomaterials of unusual properties and applications. Jana has demonstrated that gram scale synthesis of various monodisperse

anisotropic materials of gold and silver such as nanorods, nanospheroids, platelets and cubes with controllable aspect ratios can be achieved by modified surfactant-based seed-mediated method.²⁷ Pramod and George Thomas investigated plasmon coupling in gold nanorods as a function of long-axis orientation.⁴⁵ Aligned arrays of uniform equilateral nanotriangles with NIR absorbing and SERS properties were demonstrated by Pradeep and Sajanlal, using an electric field assisted seed mediated approach.²⁹ Here, the gold seed nanoparticles (of 4 nm diameter) attached to the conducting glass surface were grown at low temperature into gold nanotriangles by applying an electric potential. Also, a highly anisotropic mesostructured material of gold, called gold mesoflowers (Fig. 2C–E), with star-shaped appearance and nanostructured stems with pentagonal symmetry was reported by the same authors.³⁴ They demonstrated that NIR-IR absorption exhibited by gold mesoflowers can capture a significant amount of heat, thereby reducing the temperature rise in an enclosure exposed to sunlight. Multiple attributes such as magnetism and Raman enhancement was achieved using bimetallic⁴⁶ and magnetic⁴⁷ mesoflowers. Jena and Raj demonstrated a seedless, surfactantless synthesis route for the synthesis of fluorescent marigold like nanoflowers (Fig. 2B).³³

Polymers have also been used to synthesize metal nanoparticles.⁴⁸ Here the polymer acts as both reducing as well as stabilizing agent and nanoparticles are formed in-situ in the polymer matrix. Recently, stable mercury nanodrops and nanocrystals were synthesized in a poly(vinyl alcohol) thin film using mild thermal annealing.⁴⁹ Various optical and nonlinear properties of such polymer encapsulated nanoparticles in view of their potential applications have been reviewed recently.⁵⁰ A mirror image relation was observed in surface plasmon coupled CD spectra of gold nanoparticles grown on D- and L-diphenylalanine nanotubes. This unique phenomenon was rationalized by Jino George and George Thomas to be a result of orientational asymmetry of GNPs driven by chiral molecules on nanotubes.⁵¹ Sharma *et al.*⁵⁴ have extensively investigated the stability, dynamics, dewetting and morphology of ultrathin nano-films and nanoparticles with a combination of theoretical, numerical and experimental techniques.²³ Catalysis using a reusable ‘Dip Catalyst’ employing silver nanoparticles embedded in a polymer thin film was demonstrated by Hariprasad and Radhakrishnan.⁵²

2.1.1.1 Noble metal quantum clusters. Chemistry of gold-sulphur interface on monolayer protected clusters (MPCs) has long attracted research interest. These materials have a nanosized metal core containing hundreds or thousands of atoms with monolayers of surfactants/ligands on its surface. The metal core made of dense packing of metal atoms forming nanocrystals with specific lattice planes on its surface.⁵³

Intensive research on thiolate protected noble metal plasmonic systems have culminated in the discovery of a new type of material, composed of a few atoms, called quantum clusters (QCs) or sub-nanoclusters. They are composed of tens to hundreds of atoms having a core size in the sub-nanometer regime. They possess discrete electronic energy levels and thereby show “molecule-like” optical transitions in absorption and emission

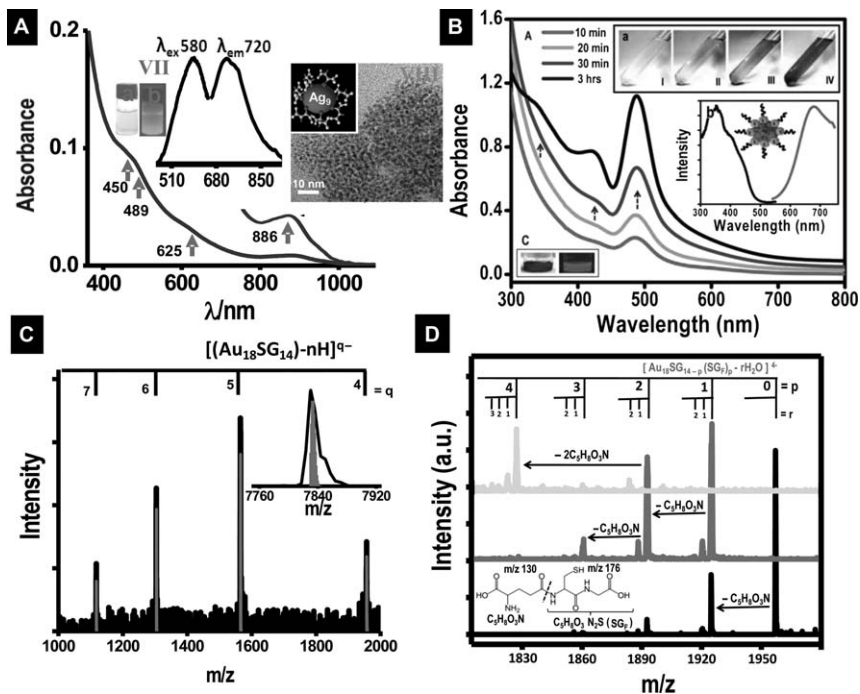


Fig. 3 (A) TEM image, UV-vis absorption spectra and luminescence spectra of $\text{Ag}_9(\text{H}_2\text{MSA})_7$ quantum clusters (adapted from Ref. 328). (B) UV-vis absorption spectra, luminescence profile of the as-synthesized $\text{Ag} \sim 75$ clusters. Photographs of the solution during various stages of reduction and that under UV light and visible light are shown in the inset (adapted from Ref. 67). (C) ESI MS spectrum of $\text{Au}_{18}\text{SG}_{14}$ in the negative mode (adapted from Ref. 62). (D) MS/MS spectra of $[\text{Au}_{18}\text{SG}_{14}]^{4-}$ with increasing collision energy.

behavior (Fig. 3A–B). Due to quantum confinement, they behave totally differently from metallic nanoparticles of the same element and are often considered to bridge the gap between atomic and nanoparticle behaviors. While theories such as Mie theory are used to describe optical properties of plasmonic nanoparticles, jellium model and time dependent density functional theory calculations explain molecule-like cluster systems more precisely. Luminescence and bio-compatibility exhibited by these systems hold great promise in biological studies.⁵⁴ Among the diverse Au:SR clusters synthesized, $\text{Au}_{25}(\text{SR})_{18}$ continues to be the most studied cluster due to its extraordinary stability and interesting optical, electronic and geometric properties. Habeeb Muhammed *et al.* observed fluorescence resonance energy transfer (FRET) between the metal core and ligand in dansyl chromophore functionalized $\text{Au}_{25}(\text{SG})_{18}$ cluster.⁵⁵ In another study, reactivity of $\text{Au}_{25}\text{SG}_{18}$ to externally added chloroaurate ions and various metal ions was investigated.⁵⁶ While addition of chloroaurate ions resulted in rapid decomposition of cluster to insoluble gold thiolate polymer, addition of metal ions did not show such an effect. Ligand exchange of $\text{Au}_{25}\text{SG}_{18}$ (SG-glutathione thiolate) was demonstrated by Shibu *et al.* for the first time.⁵⁷ Monodisperse Au_{25} clusters embedded in silica were synthesized from polydisperse glutathione-protected gold clusters (Au_mSG_n) by reaction with (3-mercaptopropyl)trimethoxysilane.⁵⁸ Dipeptide nanotubes have

been uniformly coated with glutathione protected Au₂₅ clusters and effect of electron beam irradiation on the growth of the clusters to form nanoparticles has been studied.⁵⁹ Various other clusters were also synthesized using diverse protocols. An interfacial route was developed for the synthesis of a bright-red-emitting Au₂₃ cluster from Au₂₅(SG)₁₈ via core etching, the resultant fluorescent Au₂₃ clusters were used for bioimaging of human hepatoma cells.⁶⁰ Clusters such as Au₁₅ could also be made in confined spaces such as cyclodextrin cavities (CD),⁶¹ by core etching of larger clusters and simultaneous trapping of the clusters formed inside the CD cavities. Recently a direct one step route based on slow reduction of the metal precursor was demonstrated by Ghosh *et al.* to make red luminescent Au₁₈SG₁₄ (Fig. 3C–D) in hundreds of milligram scale.⁶²

Synthesis of monolayer protected atomically precise clusters of other noble metals, especially silver, is one of the recent interests in this area. Mrudula *et al.* reported the synthesis of luminescent Ag clusters through the interfacial etching of mercaptosuccinic acid (MSA) protected silver nanoparticles, Ag@MSA, with guanine at the water-toluene interface.⁶³ Interfacial etching was also used by Uday and Pradeep to synthesize mercaptosuccinic acid (MSA) protected silver clusters such as Ag₇(MSA)₇ and Ag₈(MSA)₈ from plasmonic Ag@MSA nanoparticles.⁶⁴ A solid state route for the synthesis of Ag₉(H₂MSA)₇⁶⁵ (Fig. 3A) and Ag₅₅(SG)₃₂⁶⁶ in gram quantities has been developed. Here the reagents were mixed in the solid state which negates the effects due to diffusion of reactants in the growth step. Dhanalakshmi *et al.* synthesized a red luminescent silver cluster by the direct core reduction of the most widely studied class of silver nanoparticles, namely silver@citrate. No byproducts such as thiolates were detected during the synthesis resulting in nearly pure clusters. High temperature nucleation and growth of ~Ag₇₅SG₄₀ clusters (Fig. 3B) was reported by Indranath *et al.* recently.⁶⁷ An alloy cluster, Ag₇Au₆(MSA)₁₀ was also synthesized from the precursor, Ag₈MSA₈ using galvanic replacement of Ag atoms by Au(I).⁶⁸ A distorted icosahedral core is predicted for Ag₇Au₆(SCH₃)₁₀ from theoretical calculations.

Protein protected quantum clusters⁶⁹ are yet another category of materials which have wide variety of potential applications in optical and bioimaging areas. Such materials possess immense potential in terms of their utility for biolabelling⁵⁴ due to ease of synthesis and functionalization, biocompatibility, non-photobleaching, long fluorescence lifetimes, low toxicity, *etc.* Various noble metal clusters protected by proteins such as lactoferrin (Lf)⁷⁰ and bovine serum albumin (BSA)^{71,72} have been reported. Recently, the growth process of these clusters inside the protein templates such as Lf and BSA was investigated using mass spectrometry by Chaudhari *et al.* Yet another ‘green’ approach towards the synthesis of clusters was demonstrated by Adhikari *et al.*⁷³ by reducing silver ion encapsulated peptide hydrogel under sunlight to produce fluorescent silver nanoclusters. Luminescent quantum clusters of copper capped in BSA with Cu₅ and Cu₁₃ cores were reported recently by Goswami *et al.*⁷⁴

2.1.1.2 Nanoparticle assemblies and superlattices. Fabrication of various nanoparticles into one, two, or three dimensional assemblies can lead to

novel properties due to their inter-particle coupling resulting in exotic applications. Such self-assembled superstructures, usually synthesized by lithographic techniques or self assembly protocols, are useful in studying specific properties such as SERS, metal-insulator transition, inter-plasmon coupling, *etc.* A method for the synthesis and assembly of ultrathin nanocrystalline films of metals (gold, silver), metal chalcogenides and oxides at various liquid-liquid interfaces have been developed by Rao *et al.*⁷⁵ The inter-nanoparticle coupling observed in an ordered nanoparticle array can be tuned by the choice of the ‘linker’ molecule and its properties. Assembly and thermo-mechanical properties of various polymer grafted nanoparticles have been studied by Jaydeep *et al.*^{76,77} Furthermore, choice of the dispersing polymer medium, polymer grafting density, molecular weight, *etc.* determines their utility for realising devices. Chattopadhyay *et al.* demonstrated a new form of lithography for imprinting coloured patterns using CdS quantum dots.⁷⁸ Exposure of H₂S gas to a transmission electron microscope grid placed on a poly(vinylpyrrolidone) film leads to a yellow luminescence pattern of CdS nanoparticles on the exposed parts of the film which results in organized arrays of quantum dots in two dimensions. A 2D array of patterned Au-Ag composite nanoparticles was developed using commercially available compact disks (CDs) and digital versatile disks (DVDs) as templates.⁷⁹ Direct write techniques reduce the processing steps involved and provide better control of the properties of nanoparticles. Micro- and nanoscale patterns of various metals anions and their alloys complexed with tetraoctylammonium bromide (TOABr) was realized as direct write precursors in e-beam and soft lithography processes.⁸⁰ Here, the interaction between the anion and TOABr being mainly electrostatic, patterned regions can be easily removed by thermolysis on a hot plate in ambient air. Recently, Radha and Kulkarni developed an electrical rectifier device (diode) using Au nanoparticle array stripes employing the above direct write approach.⁸¹

Well defined arrays of monodisperse nanoparticles having long range order, called superlattices, have been studied.^{82,83} Various synthetic protocols have been reported such as digestive ripening,⁸⁴ self organization at the interface⁸⁵ *etc.* to name a few. Triangular 3D superlattices of gold nanoparticles protected by mercaptosuccinic acid and their fluorescein labeled analogues were reported.^{85,86} Shibu and Pradeep illustrated the applicability of functional gold nanoparticle superlattices⁸⁷ (Fig. 4) as good SERS substrates and these superlattices have been used for gas adsorption.⁸⁶

2.1.2 Inorganic nanostructures. For the past two decade, nanomaterials based technologies have been widely used for the construction of new devices for harvesting light energy. As the particle size decreases below the Bohr radius in a semiconductor material, an increase in the band gap energy is seen due to the confinement of electrons. Hybrid materials made of semiconducting nanomaterials provided innovative strategies for designing light harvesting systems. Various classes of semiconducting nanoparticles such as cadmium chalcogenides (CdS, CdSe, CdSeS), zinc oxides and zinc chalcogenides (ZnS, ZnSe) exhibit amazing properties in the quantum size regime. Kinetics⁸⁸ and mechanism of growth⁸⁹ of ZnO nanocrystals in

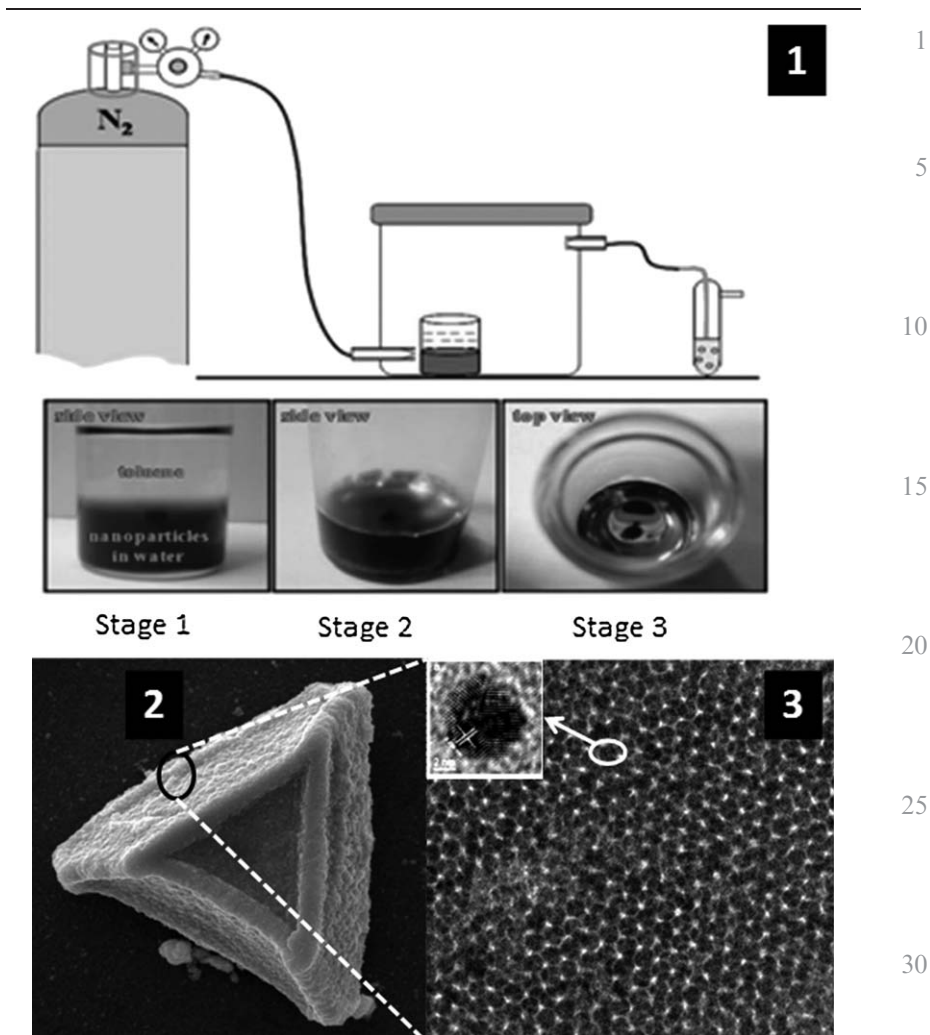


Fig. 4 (1) Cartoon representation of the setup used for the SL formation (adapted from Ref. 86). (2) SEM image of a Au NP superlattice. (3) TEM image of a corner of superlattice. Inset shows TEM image of a single nanoparticle in the superlattice (adapted from Ref. 87).

solution has been studied in detail. Size control of such systems allows tuning of their optical and electronic properties due to variation in their band gap. Doping magnetic impurities like Mn into CdS nanocrystals⁹⁰ and Zn_xCd_{1-x}S alloy nanocrystals⁹¹ allows modification of their inherent properties which can lead to new electronic, optical and magnetic devices. Quantum dot-quantum-well nanostructures having coreshell ZnS/CdSe/ZnS layers were synthesized (Fig. 5A–B) and their tunable photoluminescence was demonstrated.⁹² Reversible phase transition between wurtzite and zinc blende phases of platelet-shaped ZnS nanostructures by insertion or ejection of dopant Mn(II) ions was reported *via* a thermocyclic process.⁹³ Sarma *et al.* have reported for the first time the generation of white light from a simple Mn²⁺-doped CdS semiconducting nanocrystals (Fig. 5C), by suitably tuning the relative surface-state emissions of the

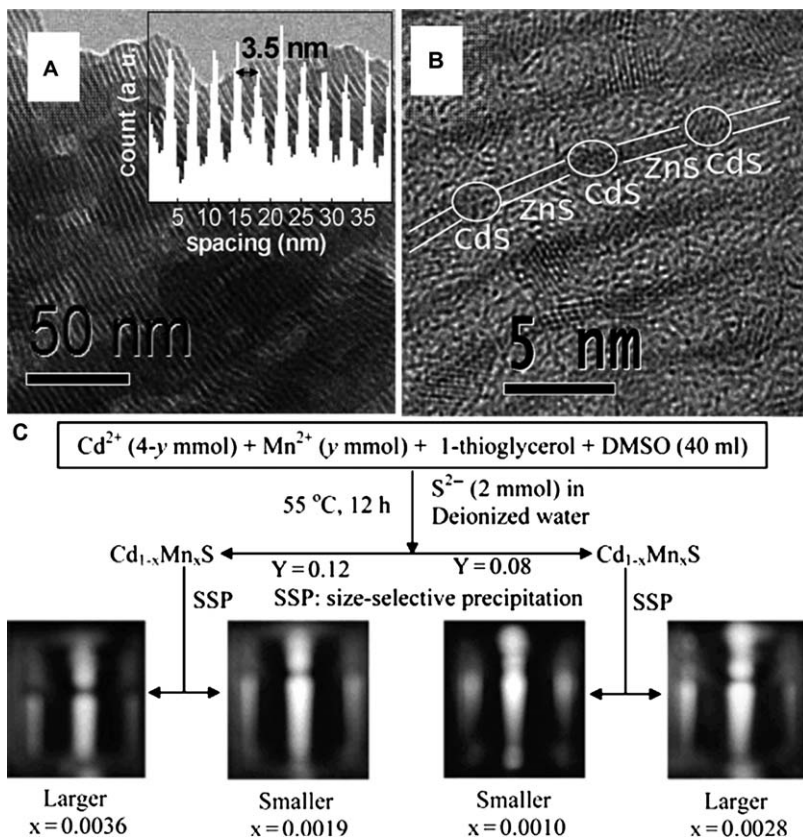


Fig. 5 (A) and (B) are the TEM images of a 2D supercrystalline parallel assembly of $(-\text{ZnS}-\text{CdS}-\text{ZnS})_n$ superlattice wires. Inset: statistical distribution of superlattices demonstrating an ultrahigh pitch density of 3.5 nm (adapted from Ref. 95). (C) Schematics of the reaction strategy for making Mn^{2+} doped light emitting CdS nanocrystals (adapted from Ref. 94). Photographs in 'C' showing 0.10 and 0.19% Mn^{2+} -doped CdS NCs producing white light upon excitation at 365 nm, whereas 0.28 and 0.36% doping produces yellow emission upon excitation at 383 nm.

nanocrystal host and the dopant emission.⁹⁴ Zero, one, and two-dimensional shape-dependent confinement in PbS nanostructures resulted in distinguishable far-field optical polarizations due to different geometries.⁹⁵ Shape dependent change in blue-green photoluminescence of ZnO nanostructures was probed by Ghosh *et al.*⁹⁶ An ultrahigh density two dimensional semiconductor superlattice array composed of periodic quantum wells with a barrier width of 5 nm by ZnS and a well width of 1-2 nm by CdS particles was synthesized *via* a general synthesis route.⁹⁷ An electrochemical DNA biosensor for the detection of chronic myelogenous leukemia was achieved using Langmuir-Blodgett monolayers of CdSe quantum dots synthesized on an indium tin oxide (ITO) coated glass substrate.⁹⁸

Intrinsically non-magnetic inorganic materials were found to exhibit room temperature ferromagnetism as their size is brought down to nanoscale. These materials include simple nonmagnetic oxides like CeO_2 , Al_2O_3 , ZnO, In_2O_3 and SnO_2 ⁹⁹ as well as complex superconducting oxides such as $\text{YBa}_2\text{Cu}_3\text{O}_7$.¹⁰⁰ Surface ferromagnetism, which arises from surface defects,

was also observed in NPs of metal nitrides and chalcogenides and is now considered to be a universal phenomenon. A detailed discussion of such systems is available in a review by Sundaresan and C. N. R. Rao.¹⁰¹ Multiferroics, which exhibit ferromagnetism as well as ferroelectricity, are another group of interesting materials. Detailed powder XRD analysis of such a nanocrystalline multiferroic, BiFeO₃, led Vijayanand *et al.* to infer that Fe₃O₄ as the magnetic impurity phase responsible for its high room temperature ferromagnetic moment.¹⁰² Antiferromagnetic coupling along S-Ni-S chain in layered nickel alkanethiolates was probed by John *et al.*¹⁰³

Chemical synthesis of graphene mimics from layered inorganic compounds and their applications is one of the emerging areas of research. Three different chemical routes for the synthesis of graphene analogues of Mo and W disulphide¹⁰⁴ and diselenide¹⁰⁵ was reported by Matte *et al.* Characteristic absence of (002) reflection and shift and broadening of the Raman bands are common feature of these materials. Synthesis of another graphene analogue of BN with control over number of layers along with its property studies was reported by Nag *et al.*¹⁰⁶ All these inorganic graphene analogues exhibit room temperature ferromagnetism. Formation of a new few layer graphene analogue, B_xC_yN_z having a composition between BCN and BC₂N, was achieved by reaction of activated charcoal, boric acid and urea.¹⁰⁷ This material possesses better CO₂ and CH₄ uptake ability than both activated charcoal and graphene. MoS₂ among these materials has been used for application in field effect transistor devices. The reason behind hysteresis observed in these devices was rationalized recently to be a combined effect of absorption of moisture combined with high photosensitivity of MoS₂.¹⁰⁸

2.1.3 Carbon nanomaterials. Carbon nanomaterials with their exciting electronic properties and application possibilities have fascinated scientists over the globe for decades. Graphene, the newest member of the nano-carbon family consisting of a single layer of hexagonally arranged carbon atom array, has caused significant stir in this pool already. Exciting new properties like quantum Hall effect at room temperature, an ambipolar electric field effect along with ballistic conduction of charge carriers, tunable band gap, and high elasticity and associated applications have come about which have turned graphene into a super-material. Indian scientists are not lagging behind to join this excitement and have contributed significantly in developing graphene based new applications.

There have been two main directions of graphene research in the country. Synthesis of graphene and graphene-composites by easy methods and from cheap sources is one of the trends.¹⁶ Other one is concerned with the discovery new properties and novel applications. John *et al.* reported the formation of single and few layer graphene on stainless steel substrates by direct thermal CVD process.¹⁰⁹ Ethanol was used as the source of carbon in this process. Dey *et al.* demonstrated a facile and rapid formation of reduced graphene oxide (RGO) sheets from graphene oxide (GO) using Zn/acid at room temperature,¹¹⁰ whereas a method for the synthesis of water soluble functionalized graphene sheets from GO was reported by Mhamane *et al.* using plant extract.¹¹¹ Production of graphene has also been achieved

by exfoliation using focused solar radiation.¹¹² Microwave irradiation induced co-reduction of graphene oxide and Pt was used to produce graphene supported Pt catalysts. Defect sites on reduced GO are found to serve as anchor points for the heterogeneous nucleation of Pt.¹⁰⁹ Graphene was recently produced from cheap starting materials like sugar¹¹³ and asphalt¹¹⁴ on silica support. This graphene coated sand was found to be very effective in water purification. A review of environmental and biological applications of graphene by Sreepasad and Pradeep was published recently.¹¹⁵

Multidimensional applications of graphene have been reported from India in the recent years. It has been used in drug delivery as an effective nanocarrier for tamoxifen citrate (TrC), a breast cancer drug.¹¹⁶ It has also been used in catalysis, for the oxidation of alcohols, by linking them with an oxo-vanadium Schiff base.¹¹⁷ Carboxyl and hydroxyl functionalized multilayered graphene, produced from multiwalled CNT has shown unique urea sensing ability.¹¹⁸ Both RGO and graphene nanoribbons (GNRs) are demonstrated to be potent infrared photodetectors.¹¹⁹ Graphene, known to be a quencher was molded into an optical bifunctional material by Gupta *et al.* by linking Eu(III) cations. Electron microscopic characterization of the material is shown in Fig. 5A–D. This material was shown to quench the luminescence of Rhodamine-B while it retained its own red emitting property. This dual nature of the material can be very useful for biosensing and optoelectronic applications.¹²⁰ Graphene has also been used for the fabrication of inexpensive and efficient solar cells. Significant improvement in organic photovoltaic (OPV) characteristics was reported in a blend of graphene quantum dots and a regioregular polymer.¹²¹ Graphene-polyvinyl fluoride polymer composite films were shown to exhibit real time strain response. Nanoscale mechanical deformation in this composite films result in change in the electrical properties of the films and enables it to act as strain sensor.¹²² Saha *et al.* synthesized graphene quantum sheet with dimensions ranging from 2–5 nm. These quantum sheets exhibited exceptional magnetoresistance which can be used in spintronic devices.¹²³ Use of graphene for hydrogen storage was demonstrated where hydrogen was found to be chemically linked with sp³-carbon.¹²⁴ A new type of gas sensor was fabricated by Pd-Pt nanoparticle-graphene composite by monitoring the change in conduction of graphene layers upon gas adsorption.¹²⁵ Graphene oxide has even been used as a carbocatalyst for Michel addition reaction.¹²⁶ Covalently linking graphene with emerging materials with functions such as quantum clusters will generate new possibilities.¹²⁷ Use of graphene for water purification and in devices are covered under sections 3.1 and 3.4, respectively.

Carbon nanotubes (CNTs), much like graphene, have been shown to exhibit novel phenomena and been used for a diverse array of applications. Voggu *et al.* reported a simple, yet effective method for the separation of metallic and semiconducting single walled CNT (SWCNT) from a solution containing potassium salt of coronene tetracarboxylic acid. Metallic tubes precipitate while semiconducting ones remain in solution, which can be used for the separation of these two varieties even without centrifugation.¹²⁸ Electrochemical unzipping of multi-walled CNT (MWCNT) to produce high quality graphene nanoribbons (GNRs) was reported by Shinde *et al.*¹²⁹

AFM and TEM images of unzipped GNRs are presented in Fig. 5G–H. 1
Similar unzipping of MWCNT was observed upon shining an excimer laser 2
also.¹³⁰ Decoration of GNRs with very small CdSe QDs was attained 3
recently by *in-situ* electrochemical unzipping of MWCNTs.¹³¹ Viscosity of a 4
floculated suspension containing of MWCNT at very low weight fractions 5
(approximately 0.5%) was found to jump sharply by four to six orders of 6
magnitude upon varying shear stress. Manipulation of mechanical strength 7
and transport properties of nanostructured composites can be achieved by 8
understanding this phenomenon.¹³² CNTs have been used for molecular 9
detection and removal of toxic chemicals. Electrochemical sensing of 10
ascorbic acid was achieved using a modified gold electrode. The electrode 11
was coated with polyaniline and carboxylated MWCNT was covalently 12
attached to ascorbate oxidase and easy detection of ascorbic acid was 13
possible.¹³³ Femtomolar detection of a herbicide, 2,4-dichlorophenoxy 14
acetic acid (2,4-D) was obtained by conductance modulation in a liquid- 15
gated field effect transistor with SWCNT as an active element.¹³⁴ Mishra 16
and Ramaprabhu fabricated a magnetite-MWCNT (Fe_3O_4 -MWCNTs) 17
nanocomposite and used the supercapacitor nanocomposite for the removal 18
of high concentration of arsenic (both arsenate and arsenite). The composite 19
was also effective for desalination of seawater.¹³⁵ Phosphonated MWCNT 20
has been used in polymer electrolyte fuel cells with polybenzimidazole with 21
enhanced efficiency.¹³⁶ Single-walled carbon nanotubes (SWCNTs) cova- 22
lently functionalized with uracil were observed to self-assemble into regular 23
nanorings with a diameter of 50–70 nm. These nanorings were formed by 24
two bundles of CNTs interacting with each other *via* uracil-uracil base-pair 25
which is most likely to find application in advanced electronic circuits.¹³⁷ 26
Acid functionalized carbon nanotubes decorated with Rh nanospheres was 27
demonstrated to have superior field emission characteristics in terms of high 28
current density at an ultra-low threshold which is better than both the 29
component structures.¹³⁸ Small interfering RNA was found to strongly bind 30
to SWCNT surface *via* unzipping its base-pairs which can be used for the 31
delivery of these SiRNAs.¹³⁹ 32

2.1.4 Organic nanostructures. Nanomaterials research in India mostly 33
used to deal with manipulation of inorganic materials until recently. 34
Organic materials, with their tunable photophysical properties are gaining 35
much more attention lately and research on soft nanomaterials like 36
assembled organic frameworks and hydro/organo-gels is growing rapidly in 37
India. Ayyappanpillai Ajayaghosh has used supramolecular chemistry of 38
functional dyes and π -conjugated systems to create nanostructured self- 39
assemblies, organogels, light-harvesting assemblies and chemosensors. 40
Formation of well defined ring and fiber shaped nanostructures through self 41
assembly approach was reported by his group.¹⁴⁰ Folding of chiral 42
 π -conjugated oligomer having alternate bipyridine and carbazole moieties 43
connected through acetylenic bonds into helical form was reported by the 44
same group. Defolding of helical conformation was observed in presence of 45
transition metal ions, while addition of EDTA helps in regaining the helical 46
conformation.¹⁴¹ Formation of self-assembled aligned fibers using supra- 47
molecular gels based on trithienylenevinylenes was demonstrated by 48

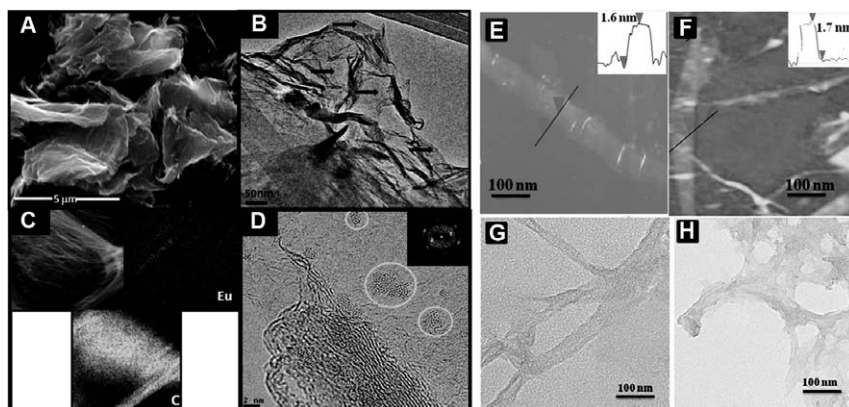


Fig. 6 (A) SEM and (B) TEM images of europium complexed graphene. (C) Eu and C EDS mapping from a selected area. (D) HRTEM image of showing hexagonal graphene lattice. FFT pattern is shown in the inset. (adapted from Ref. 120). AFM image of graphene nanoribbons synthesized by the electrochemical unzipping of MWCNT at (E) 0.7 and (F) 0.5 V. TEM images of (G) partially and (H) completely transformed MWCNT (adapted from Ref. 129).

Prasanthkumar *et al.* which highlighted the role of self assembly and gelation on the electronic property of semiconducting molecular gelators.¹⁴² AFM images and I-V characteristics of such gelators are shown in Fig. 6A–D. They also reported high metallic conductivity in oligo(thienylenevinylene) (OTV) based gelators, which are expected to be good candidates for bulk heterojunction devices.¹⁴³ Rao *et al.* reported the formation of cylindrical micelle in water. These long nanofibers formed by assembly of noncovalent donor-acceptor (D-A) pair forms hydrogel at higher concentration of D-A pair.¹⁴⁴ Concentration dependent spontaneous self-assembly formation in octupolar oxadiazole derivatives to produce spheres to fibrous gels was reported by Varghese *et al.*¹⁴⁵ They also studied the photophysical and liquid crystalline behaviour of these self organized structures.

Differences in gelation habits of organogels from derivatives of oligo(p-phenylene vinylene) (OPV) was linked to the fact that whether they can establish hydrogen bonds with adjacent OPV molecules or with the solvent.¹⁴⁶ Tunable excited-state properties of a π -acceptor- π -donor-type fluorophore with a bipyridyl moiety was exploited by Sreejith *et al.*¹⁴⁷ to respond to different analytes. Ultratrace level detection of TNT was attained very recently by a similar method which uses organogel paper strips.¹⁴⁸ Naked eye detection of fluoride ions using a fluorescent organogel was reported by Rajamalli and Prasad.¹⁴⁹ The detection process includes a reversible gel-sol transition associated with change in color in presence of fluoride ions. Vidyasagar *et al.* found that two sugar-based supergelators can congeal oils to produce highly transparent gels having low UV transmittance and high visible transmittance which make them suitable for soft optical devices.¹⁵⁰ AFM and SEM characterization of these gels is presented in Fig. 6G–H. A method for reversible shape transformation of organic waveguides to form 2D nanosheets, 1D nanotubes, and 0D nanorings was reported recently by Chandrasekhar *et al.*¹⁵¹ Both nanotubes and nanosheets act as waveguides and changes direction of incident laser light in a

shape-dependent manner. The nanosheets were turned into nanotubes and subsequently into nanorings with the addition of water to the solvent, whereas nanotubes were converted back to nanosheets through ultrasonication. CD studies revealed the induction of chirality into π -stacked dialkoxynaphthalene (DAN)-fiber made up of achiral building blocks through supramolecular co-assembly with helical naphthalenediimide (NDI)-fiber.¹⁵² Organogel-hydrogel transformation by a simple method was achieved by Kar *et al.*¹⁵³

Integration of graphene^{154,155} and other carbon nanostructures¹⁵⁵ with these organogels has been achieved. The composites formed through supramolecular interaction exhibit higher rigidity than the parent gel systems. Synergistic effects in these composites enable them to exhibit interesting optical, mechanical, thermal and electrical properties and opens up a new door of possibilities.

2.2 Theoretical and computational inputs

Computational materials science provides valuable insights into the structure and bonding in a material which in turn dictate its spectroscopic property and reactivity. In nanomaterials, where quantum confinement results in the emergence of new phenomena, theoretical and computational inputs are of larger significance for a better understanding of the systems. Computational material scientists in India have provided immense support towards understanding of experimental results which has helped in the growth of nanoscience and nanotechnology in the country.

Possibility of using few layer graphene for chemical storage of hydrogen was probed through first-principles calculations.¹²⁴ This study offers insight into the mechanism of dehydrogenation of hydrogenated graphene produced by Birch reduction. The dehydrogenation was proposed to occur through a possible reconstruction and relaxation of the hydrogenated graphene lattice, which showed the presence of sp^3 C-H bonds. First-principles simulations have also been used to determine structure, phonon dispersion, and elastic properties of graphene analogues of BN.¹⁰⁶ Metal oxide and magnetic NPs were found effective in tailoring electronic structure of graphene. First principles calculations linked charge transfer between the NPs and graphene with the change in electronic and magnetic properties.¹⁵⁶ Calculations have shown that the unusual pesticide uptake capacity of graphene is due to the interaction between the two mediated by water.¹⁵⁷

Interaction between single walled carbon nanotube (SWCNT) and α -helix was probed using classical molecular dynamics (MD) simulation by V. Subramanian *et al.*¹⁵⁸ Breakage of hydrogen bonds in the α -helix was observed, which leads to conformational transitions ($\alpha \rightarrow$ turns). His group also tried to relate the curvature of carbon nanomaterials (NMs) with their α -helix breaking tendency.¹⁵⁹ Their results show that the extent of helix breakage induced by carbon nanomaterials is inversely proportional to their curvature; *i.e.*, the tendency for helix breaking is minimum for the CNT and maximum for the graphene sheet. Srinivasu and Ghosh used *ab-initio* first-principles calculations to investigate lithium-dispersed two-dimensional carbon allotropes, viz. graphyne and graphdiyne, for lithium and hydrogen storage applications.¹⁶⁰ They have also shown that these planar carbon

allotropes can be used in nanoelectronics as tuning their band gap is possible by varying the number of acetylenic bridging units. 1

Significant effort has also been directed towards understanding the structure, bonding and reactivity of metal clusters through computational methods and tools. Most of these studies have been directed towards the study of gold clusters. Pundlik *et al.* investigated the electronic structure and magnetic moment of gold quantum clusters (Au_n ; $n = 12, 13, 24, 25$) using first-principles plane-wave density functional theory.¹⁶¹ Stability and magnetic moment in these clusters were explained in terms of degeneracies of the HOMO and LUMO levels and Jahn-Teller activity. Probing of reactivity¹⁶² and finite temperature behaviour¹⁶³ of Au_n clusters were demonstrated by Sourav Pal. Mammen *et al.* demonstrated that the morphology of gold clusters can be tuned through doping of the substrate taking Au_{20} as a model cluster.¹⁶⁴ DFT calculations showed that catalytically active planar geometry of Au_{20} is favored over its tetrahedral geometry if the MgO substrate is doped with Al. Reactivity enhancement of a closed-shell Au_8 cluster was observed by Jena *et al.* when an Au atom was replaced by a H atom.¹⁶⁵ H-doping enhances the binding efficiency of O_2 with the cluster and reduces the barrier for CO oxidation. Computational study of other metal clusters has also been reported. Size dependent reactivity of aluminium clusters with N_2 was reported by Kulkarni *et al.*¹⁶⁶ Structural stabilities of small 3d late transition metal clusters was probed by first principles DFT calculations by Datta *et al.* While Co was found to show unusual stability in hexagonal closed pack stacking, other metals prefer icosahedral structures. This structural preference was reported to be a combined effect of magnetic energy gain and s-d hybridization.¹⁶⁷ Molecular dynamics simulation has been used in understanding the clustering of ionic liquids at room temperature by Sarangi *et al.*¹⁶⁸ 15

Among other computational studies related to nanoscience, it is notable to mention the work of distance dependence of FRET by Swathi and Sebastian where they have shown non- R^{-6} type behavior in the case of graphene.¹⁶⁹ 20

3 Applications of nanomaterials 25

3.1 Environmental applications and sensing 30

Inherent properties of nanostructured materials such as large surface area and surface energy, presence of catalytic/reactive sites and modified electronic structures are used for several environmental applications. It is either enhancement of the bulk properties to increase the overall efficiency or enhancing the kinetics of a given event to make it happen at acceptable temperature or completely new phenomena at the nanoscale which can lead to applications. In the case of nanoscale matter, the quantity of material required for a given application is much smaller. Because of this, noble metal NPs, once considered impossible to be used for mundane applications such as water purification, are increasingly recognized as useful and affordable solutions. This is also due to the realization that noble metals in the bulk have been used for millennia for applications such as water disinfection and risks of toxicity are relatively less with them in comparison to 35

artificial nanomaterials. This can be illustrated with the example of silver which has been a potent antibacterial material in the ionic form. Nanoparticles of silver under favourable conditions can release silver ion (Ag^+) at a steady concentration of around 40 ppb at around 300 K.¹⁷⁰ This concentration of Ag^+ is antibacterial for a wide spectrum of bacteria, if incubated for a few hours. A practical Ag^+ releasing composition requires only 40 $\mu\text{g/L}$ or 40 mg/kL of microbially safe water. This amounts to a composition of nearly 432 mg for 3600 L of water, approximately the yearly drinking water consumption for a small family (10 L/day). Considering an effective release of 10% of silver, the consumable cost required for such a device is within the affordable limit of everyone. Combining the chemistry of diverse nanomaterials for capturing heavy metal contaminants, pesticides, organics and anions, a nanomaterials based drinking water solution is indeed possible. The advantage of such a solution is also from the point-of-use application in countries where reliable piped-water supply is not available. These solutions work in the absence of electricity, another added advantage. Although materials involved are complex in their structure and function, they can be made with simple approaches and therefore production can be decentralized. Due to all these advantages, a few such solutions have already been implemented in India with home-grown technologies.

The use of noble metal NPs in water purification for applications other than microbial disinfection was first reported in 2003.¹⁷¹ The chemistry reported can be summarized as reductive de-halogenation of chlorocarbons (halocarbons in general) in water solutions occurring at room temperature over silver nanoparticles wherein the C–Cl bond is cleaved with the formation of AgCl . UV-visible spectroscopic analysis of this reactivity is shown in Fig. 7A. A series of chemical events occur on the nanoparticle and amorphous carbon is observed as a product. This chemistry was soon extended to halogenated pesticides at high efficiency.^{172,173} A concentration of 50 ppb chlorpyrifos was reduced to less than 0.5 ppb upon passing over a filter made of supported noble metal particles which can be observed from

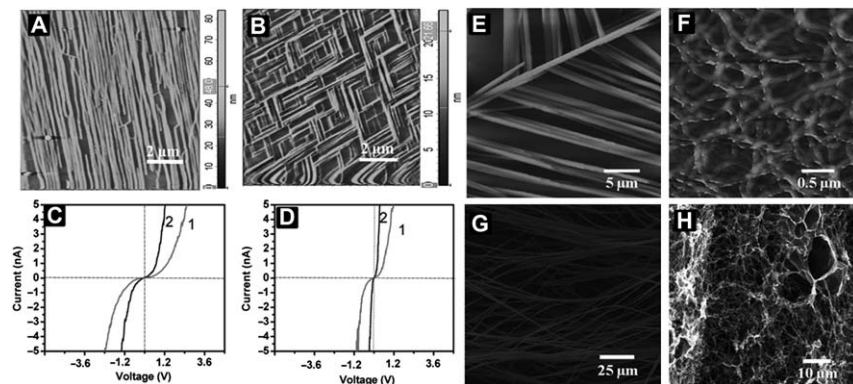


Fig. 7 AFM images of (A) TTV4 and (B) TTV5 from decane drop casted on freshly cleaved mica surface (adapted from Ref. 142). *I-V* curves of undoped (C) and doped (D) xerogels of OTV1 (1) and OTV2 (2) (adapted from Ref. 143). AFM (E and F) and SEM (G and H) of organogels formed in different organic solvents (adapted from Ref. 150).

the gas chromatogram presented in Fig. 7B. On stable supports, no NP release was observed in water. In commercial implementation of the technology, NPs are used along with activated carbon so that reaction byproducts, desorbed species, *etc.* can be removed from drinking water. A photograph of such a filter is shown in Fig. 7C. The interaction of pesticides on NPs is being explored even today from which new insights on molecular steps are available.¹⁷⁴ There are several related technologies in the market place. One involves the anchoring of NPs on cheaper substrates such as rice husk silica and to make ceramic candles. It is also worthwhile to mention the use of porous structures such as clay bricks (terracotta) for antimicrobial applications. Several filtration technologies have also come about such as polysulfone based domestic nanofilters for removing microbial contamination and ceramic filters for the removal of particulate matters (Fig. 8).

The most recent developments in this area tend to use graphene for such applications. Most of these efforts have been concentrated on using the exceptional surface area of 2D graphene (RGO/GO) to use it as an adsorbent. An *in situ* strategy to synthesize and immobilize graphenic adsorbent materials onto sand particles was recently reported by Sreepasad *et al.* starting from asphalt. The synthesized adsorbent was reusable for several cycles and it was found to be highly effective for the adsorption of dyes and pesticides from water.¹¹⁴ Sen Gupta *et al.* obtained similar graphene-sand composites using sugar as the source of graphene.¹⁷⁵ Raman spectroscopic evolution, SEM images and EDS analysis of pesticide

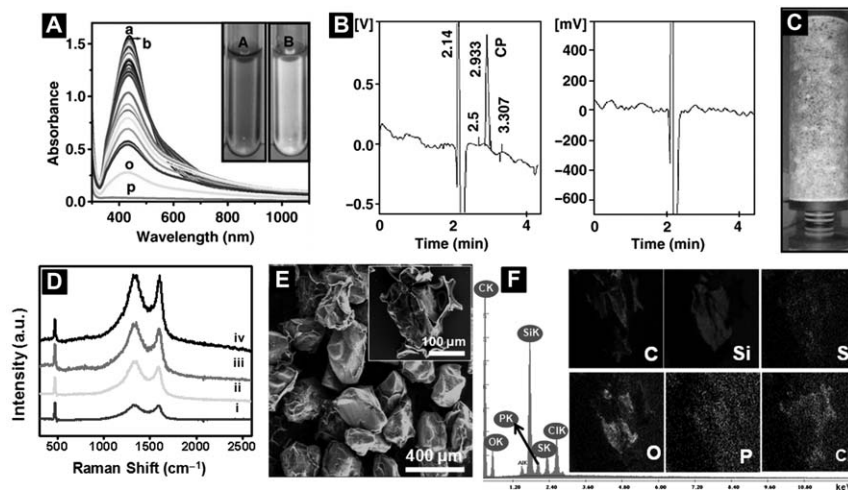


Fig. 8 (A) Variation of UV-visible absorption spectrum of Ag NP with the addition of carbon tetrachloride (adapted from Ref. 171). (B) Gas chromatogram of 50 ppb chlorpyrifos extracted in hexane before after passing through silver NPs supported on alumina. Disappearance of CP peak indicates the complete degradation of CP by Silver NPs (adapted from Ref. 173). (C) Photograph of a pesticide filter device made by using supported NPs. (D) Raman spectra of graphene-sand composite made from sugar under different heating conditions. (E) SEM image of graphene-sand composite made from sugar. Inset shows one graphene coated sand particle after absorption of chlorpyrifos. (F) EDS analysis showing adsorption of pesticide chlorpyrifos on the graphene-sand composite (adapted from Ref. 113).

adsorption by the composite are shown in Fig. 7D–F. Ramesha *et al.* demonstrated the use of GO and RGO for the removal of different anionic and cationic dyes from aqueous solutions.¹⁷⁶ Maliyekkal *et al.* found that RGO and GO can function as efficient adsorbent for pesticides and thereby can be used for the removal of pesticides from water.¹⁵⁷ The adsorption capacities reported for different groups of pesticides like chlorpyrifos (CP), endosulfan (ES) and malathion (ML) were as high as ~1200, 1100 and 800 mg/g, respectively. RGO showed 10–20% higher affinity compared to GO, indicating that increased surface oxygen functionality reduces the affinity of graphenic surface to pesticides. Theoretical calculations indicated the dependence of adsorption on the presence of water molecules. A versatile strategy for the synthesis of various metal/metal oxide graphene composite at room temperature and the utility of these composites for the removal of heavy metals were demonstrated by Sreepasad *et al.*¹⁷⁷ A green strategy was also devised to immobilize these composites onto cheap substrate like sand for easy post treatment handling. An abundant and environmental friendly biopolymer, chitosan was used for immobilization, thus avoiding harsh reactants and reaction conditions. Practical utility of these composites was showed in the form of enhanced removal efficiency over some common adsorbents. A graphene based composite consisting of antibacterial bio-polymer chitosan and a bactericidal protein was fabricated recently utilizing the rich abundance of functional groups.¹⁷⁸ The composite showed a tendency to form self-standing films which can aid in coating this composite onto suitable substrates for its practical applications in water treatment.

Water purification also requires ultrasensitive detection of ultratrace contaminants. Plasmonic noble metal nanoparticles are already known to be promising sensors for organic impurities^{172,179} and toxic metal ions.¹⁸⁰ Quantum clusters of noble metals have recently been used as nanosensors for toxic ions like Cu(II),¹⁸¹ Hg(II)¹⁸² and As(III)¹⁸³ with very high sensitivity.

Sensor research in India has extended to areas of security and safety as well. The national program on explosives utilizes nanomaterials and Microelectromechanical Systems (MEMS) based detection strategies. Ramgopal Rao has used various nanomaterials based sensors for low level detection of vapors of nitro compounds and explosives.^{184–186} Venkatramaiah *et al.* recently developed a fluoranthene based fluorescent chemosensor for ppb level detection of picric acid.¹⁸⁷ In this context, spectroscopy based sensors using self assembled nanostructures⁸⁶ and anisotropic nanomaterials^{46,188} have shown potential applications. Ajayaghosh *et al.* developed an attogram sensor for TNT using fluorescent organogelator.¹⁴⁸ Several orders of magnitude improved visual sensing of TNT was demonstrated recently using mesoflowers.¹⁸⁹

3.2 Nano and energy

Increasing demand for energy remains one of the major problems of humankind. With the limited and decreasing reserve of fossil fuels, research on clean alternate energy sources is increasing globally. A significant part of research activities have gone into exploring new ways of energy production. In a developing country like India with its huge population, demand for

energy is huge. Yet, India lags far behind in alternate and renewable energy production in comparison to developed countries and its developing neighbors. There has been some activity in the last few years in India to use nanomaterials for energy production, storage and waste energy harvesting; most of which started with the initiatives of Nano Mission of the Department of Science and Technology.

Various nanomaterials have been used in solar cells to increase their conversion efficiency. Kaniyoor *et al.* used a polyelectrolyte based soft functionalization technique to produce functionalized graphene and used it for efficient tri-iodide reduction.¹⁹⁰ Sudhagar *et al.* reported 145% increase in the performance of hierarchical nanostructured TiO₂ photoanode through N-ion implantation in a CdSe QD sensitized solar cell.¹⁹¹ Possibility of replacing Pt with cheap alternatives like graphene supported Ni NPs was reported by Bajpai *et al.*¹⁹² Guchhait *et al.* were able to increase the conversion efficiency of PbS based solar cells by several folds by the introduction of TiO₂ nanostructures.¹⁹³ Resonance energy transfer in ZnO NP-based in dye sensitized solar cell and the effect of high energy photons in solar radiation on such a cell was probed by Makhal *et al.*¹⁹⁴ Nanomaterials have also found their way into fuel cell research. Iron nitride-doped carbon nanofiber was produced by Palaniselvam *et al.* to use as cathode electrocatalyst for proton exchange membrane fuel cells. Unique cup-stake structure of this material had resulted in more number of active sites which in turn increased the oxygen reduction efficiency.¹⁹⁵ They also produced an artificially designed membrane incorporating phosphonated MWCNTs and were able to obtain 50% improved proton conductivity for polymer electrolyte fuel cell.¹⁹⁶ Ghosh and Raj produced flower-like Pt NPs supported on MWCNTs by an *in-situ* wet chemical route. The material was demonstrated to be catalytically active for both oxygen reduction and methanol oxidation.¹⁹⁷ Rao and Viswanathan observed high power density as they fabricated a membrane electrode assembly incorporating ultrasmall Pt NPs into carbon electrodes.¹⁹⁸

Nanoscale thermoelectric materials have attracted attention due to their increased conversion efficiency than the bulk counterparts. Silver chalcogenides are an interesting class of narrow band gap semiconductor for thermoelectric applications. Samal *et al.* demonstrated a room temperature solution phase method for the synthesis of Ag₂Te NWs by the direct reaction of Te NWs with AgNO₃ and examined their thermoelectric performance.¹⁹⁹ Formation of heterostructured dumb-bell shaped NWs in this system by simple post-synthetic annealing was reported by Som and Pradeep.²⁰⁰ Datta *et al.* reported the synthesis of nanocrystalline Bi₂Te₃ and Sb₂Te₃ and their alloys with spherical and flake-like morphology and examined their thermoelectric performances.²⁰¹ Paul *et al.* examined the enhancement of thermoelectric properties of PbTe through energy filtering with embedded Ag nanodots. Their study revealed that energy filtering of the carriers was facilitated by embedded Ag nanodots.²⁰²

Prakash *et al.* develop a new route to synthesize nanodimensional Li₄Ti₅O₁₂ by solution combustion method, in a single step within a minute. The Li₄Ti₅O₁₂ produced by this method were used in the lithium ion batteries with high capacity.²⁰³

Materials for the storage of hydrogen are one of the hot areas of research as hydrogen is considered as the fuel for future. The Hydrogen Energy Centre, Banaras Hindu University has been one of the pioneering centres for hydrogen storage research in the country. Their achievements in this regard can be found in a review by O. N. Srivastava and colleagues.²⁰⁴ His group showed that CNT-Mg₂Ni composite possesses higher hydrogen storage capacity as well as faster desorption kinetics than Mg₂Ni alone.²⁰⁵ CNTs²⁰⁶ and graphene nanoribbons (GNRs)²⁰⁷ were shown to be excellent catalysts for the release of hydrogen from sodium alanate. Recently few layer graphene was demonstrated to be capable of storing hydrogen by Subrahmanyam *et al.* About 5 wt% of hydrogen can be stored in the few layer graphene which is released upon UV or excimer laser irradiation.¹²⁴

3.3 Catalysis

Nanostructures possess high surface energy due to their high surface to volume ratio and presence of these high energy surfaces makes them interesting candidates for several catalytic reactions which are not observed in their bulk counterparts. Catalysis in nanoscale happens on the active sites present on the nanoparticle surfaces and their activity is governed by nanoparticle size, shape, crystal structure and support used. Metal, semiconductor and hybrid nanomaterials have been used in the recent years for catalysing various chemical reactions in India. Metal nanoparticles on oxide support are well known catalysts for various chemical reactions and microwave assisted synthesis are widely used for these catalysts. Anumol *et al.* recently shed light on the mechanism of formation of these metal NPs on oxide support considering both thermodynamic and kinetic aspects of metal ion reduction.²⁰⁸ Microwave assisted co-reduction synthesis of graphene-Pt NP was reported from the same group. This material was shown to be catalytically active for methanol oxidation and hydrogen conversion reactions.²⁰⁹ Nanoparticles have been used for the catalytic reduction and coupling of organic molecules. Tarasankar Pal successfully used Ag/Au core shell NPs for the reduction of nitroaromatics.²¹⁰ Use of monoclinic CuO nanoflowers for oxidative phenol coupling reactions was reported by the same group.²¹¹ Use of anisotropic Au NPs entrapped in mesoporous boehmite films as reusable catalysts for both inorganic and organic redox reactions was demonstrated by Jana *et al.*²¹² Magnetically recoverable copper ferrite NPs were used as catalysts for reduction of ketones into corresponding secondary alcohols with up to 99% enantiomeric excess by Lakshmikantam *et al.* These NPs were also quite effective for the asymmetric reduction of alpha and beta keto esters.²¹³ Chakravarti *et al.* demonstrated the use of highly basic MgO NPs immobilized over mesoporous carbon for the selective synthesis of sulfinamides.²¹⁴ Venkatesan and Santhanalakshmi used Au/Ag/Pd trimetallic NPs for the Sonogashira C–C coupling reaction.²¹⁵ Datta *et al.* Synthesized small (less than 7 nm) Au NPs in the channels of mesoporous carbon nitride support. These supported NPs were reported to be selective catalysts for the three-component coupling reaction of benzaldehyde, piperidine, and phenylacetylene for the synthesis of propargylamine.²¹⁶ Bej *et al.*

demonstrated the use of Pd NPs for borylation of aryl and benzyl halides which was further used for Suzuki–Miyaura coupling reaction to produce unsymmetrical biaryls and diarylmethanes in solvent free environment.²¹⁷

3.4 Device structure

India, though has become one of the leaders in nanomaterials synthesis and characterization over the span of a decade, there have been very few efforts in molding these materials in the form of devices to take advantage of their unique, yet intriguing optical and electronic properties. In the following, we point to a few recent efforts.

Top gated graphene transistor was fabricated for the first time by A. K. Sood and colleagues. A very high doping level was attained which was monitored using Raman spectroscopy.²¹⁸ Simultaneous injection of p- and n-type carriers in a bilayer graphene channel was demonstrated by Chakraborty *et al.*²¹⁹ Fabrication of ultralow noise field-effect transistor using multilayer graphene was demonstrated by Pal and Ghosh.²²⁰ Low temperature electrical transport phenomena in MoS₂ field-effect transistor devices was examined by Ghatak *et al.* with varying MoS₂ layer thickness. While 2D variable range hopping was observed at higher temperature, resonant tunneling at localized sites results in oscillatory conductivity at low temperature.²²¹ Magnetic anisotropy studies on Fe films grown on cubic GaAs and GaAs/MgO was reported by Sakshath *et al.* Pronounced uniaxial magnetic anisotropy rather than fourfold symmetry dictated by cubic crystalline symmetry of Fe was observed for a layer Fe thicknesses less than 20 monolayer.²²² An optical waveguide based sensor capable of detecting minor variations of refractive index was designed by coating Au NPs on a C-shaped polymer waveguide. This chip fabricated by Prabhakar and Mukherji utilizes localized SPR of Au NPs for detection of even minor variation in refractive index and is suitable as an affinity biosensor.²²³ A microfluidic immunosensor chip capable of visual detection and quantification of waterborne pathogens like *E. coli* and *S. typhimurium* at low concentrations was fabricated by Agrawal *et al.*²²⁴ A single polymer layer based device capable of multicolor sensing was fabricated by Gautam *et al.*²²⁵

3.5 Soft lithography

Creation of nanostructures in an organized fashion can be achieved in several ways. The traditional approach of lithography has been the dominant way but new approaches have come in the recent years. Among them the instability patterns produced by diverse physical phenomena have been extensively used by Ashutosh Sharma to create sub-micrometer structures. Using a topographically patterned stamp, Mukherjee and Sharma created instability patterns which are ordered.²²⁶ Phenomena such as dewetting have also been used to create such structures. Self-organized dewetting of ultrathin polymer film in presence of a mixture of solvents can create sub 40 nm ordered nano-droplet patterns.²²⁷ Such structures could lead to patterned organic structures as demonstrated in an earlier paper.²²⁸ Understanding such instabilities have implication to several branches of soft materials science. Therefore, it is being intensely pursued in the recent years.

Soft lithographic patterns using nanomaterials can create ultra-small structures. These structures can be of metal, alloy, oxides and nitrides using inorganic precursors as demonstrated by a recent report Kulkarni *et al.*²²⁹ Utilizing the sharp thermal decomposition of Pd-thiolates, patterned Pd₄S structures have been generated by the same group.²³⁰ Extending the very same method, it is possible to create InAs nanostructures.²³¹ Patterning can also generate femtoliter cups.²³² Electrocondensation of attoliter water droplets in such cups can be visualized by atomic force microscopy.²³³ Specific phases can be grown by methods even without the use of lithography. Kinetic control can be used in this context. A GaN NW network has been generated by this approach.²³⁴ Reduced adatom diffusion leading to supersaturation and associated dislocation have been shown to create such structures.

4 Nano-bio interface, nanomedicine and nanotoxicity

Biological organisms have adapted their best forms to survive in the conditions they live in. Cell, the best working self-replicating micro-compartment ever known, with millions of soft nanomachines dispersed in it, wandering due to Brownian motion and yet functioning precisely due to molecular recognition, sets the hardest target ever to be understood by human endeavors. As we discussed above, 'size' is the key factor which relates nanotechnology to biology and it sets biology to be an inspiration and an example for functional nanotechnology. On the other side, novel properties of nanomaterials help solve many biological/medical problems. Scientists all over the world work in both the directions at the nano-bio interface where in one direction, they try to understand, exploit or mimic, the biological molecules/structures for the development of nanoscience and technology and in the another, they try to understand the interaction of nanomaterials with biological systems and apply nanomaterials for solving biological problems. In the sub-continent too, research at the nano-bio interface has been active in both the directions mentioned above.

In the peninsula which is the second most populous in the world, nano-biology or nanobiotechnology have been of crucial importance due to, 1. rapidly growing population in need of healthcare provisions (*e.g.* according to a recent published report in *The Lancet*, around 55,000 people died in 2010 due to cancer²³⁵), 2. Multitude of issues of agriculture such as drought and floods, lands lost in vigour due to intensive use of chemical fertilizers or pesticides, increasing farmer suicides, desire to increase the quantity food produced and 3. Need to have affordable storage and transport solutions for agricultural products. The above mentioned problems as a whole or in part are a reflection of the global scenario for which nanotechnology could provide solutions. The contemporary nano-bio research areas range from investigations on 1. understanding the interaction of nanomaterials with prokaryotes, eukaryotes and biological macromolecules and their concomitant effects and 2. exploitation of nanomaterials in understanding or solving problems of biology and medicine (translational research). Below we present a brief collection of representative literature which are categorized into the themes (i) understanding the nano-biointerface, (ii) DNA nanotechnology, (iii) targeted drug and gene delivery and regenerative medicine, (iv) nano in agriculture and (v) nanotoxicity.

4.1 Understanding the nano-bio interface

Several groups in the country try to understand the nano-bio interface (especially interaction of nanomaterials with biomolecules and the mechanism of biomolecules mediated synthesis of nanomaterials) by various spectroscopic techniques such as electronic, vibrational and time resolved analysis of the macromolecule-nanoparticle interface. Pal and colleagues have worked on probing the nano-bio interactions using time resolved spectroscopic techniques²³⁶ such as quantum dot-DNA interaction, metal cluster-protein and V_2O_5 molecular magnet-protein interaction. Recently Pal and Pradeep have reported the formation HgO intermediate which is reported to be necessary during the formation of HgS quantum dots in the protein, bovine serum albumin (BSA).²³⁷ Interaction of gold nanoparticle with heme protein and the concomitant conformational changes have been studied by Pradeep's group.²³⁸ They have attempted to understand the mechanism of formation of noble metal clusters in functional proteins using MALDI MS which revealed that clusters grow *via* the initial uptake of Au^{3+} ions, which get reduced to Au^{1+} and subsequent incubation leads its reduction to Au(0) (Fig. 9). During this process, inter-protein metal ion transfer occurs with time dependent conformational changes of the protein. At the nano-bio interface, how the formation of metal nanostructures inside a protein affects the secondary structure of the

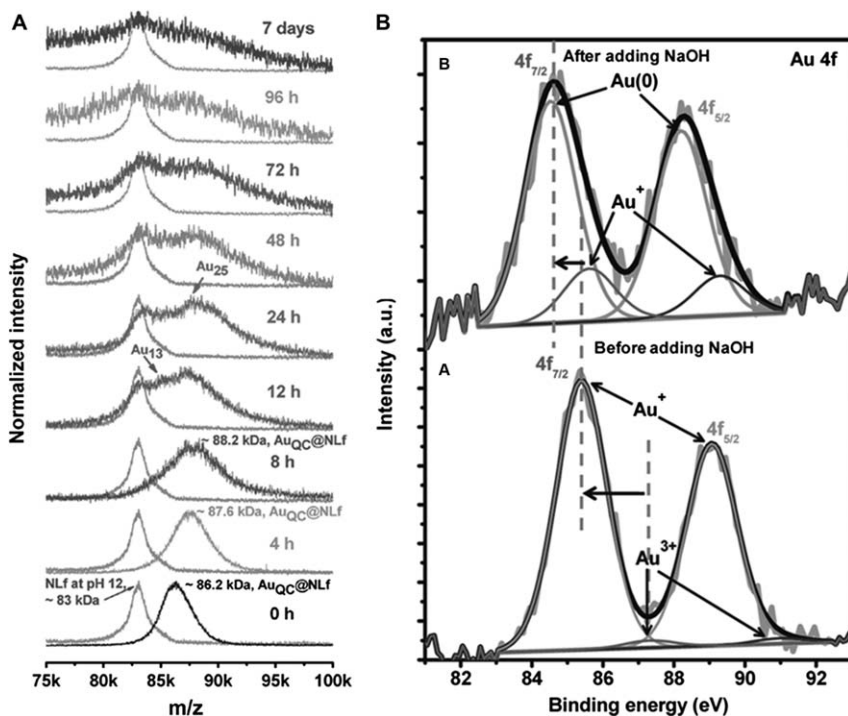


Fig. 9 A) Time dependent MALDI MS data of growth of luminescent gold quantum clusters Au_{25} in the protein lactotransferrin indicating the emergence of free protein and interprotein metal ion transfer. B) XPS spectra showing the presence of Au^{1+} state before the addition of NaOH and Au(0) after the addition of NaOH (adapted from Ref. 239).

macromolecule also has also been studied.^{70,74,239} Previously, Sastry and colleagues studied the thermodynamics of interaction of DNA and PNA bases with gold nanoparticles using isothermal titration calorimetry.²⁴⁰ Gupta *et al.* studied the mechanism of amyloid fibril disruption using biphenyl ether-conjugated CdSe/ZnS core/shell quantum dots.²⁴¹ Kundu *et al.* studied the change in bacterial size and magnetosome features for *M. magnetotacticum* (MS-1) under high concentrations of zinc and nickel.²⁴² Dasgupta and co-workers designed a colorimetric experiment based on the conformational changes induced by gold nanoparticles in a protein, and used it as a tool to sense protein conformational changes by colorimetry.²⁴³

4.2 DNA nanotechnology

Though started in 1980s in the world arena, DNA nanotechnology has been practiced only by a few people in India in recent times. Krishnan and colleagues are active in this area where they use genetic blue print material as bricks to create novel structures. One of the widely appreciated works of Krishnan is to probe the intracellular pH of cells using DNA actuators.^{244–246} Krishnan *et al.* encapsulated a fluorescent biopolymer that functions as a pH reporter within the synthetic, DNA-based icosahedral host and showed that the encapsulated cargo (FITC conjugated dextran-FD10) is up-taken by specific cells in *Caenorhabditis elegans*, a multi cellular living organism widely used in translational medicine research. Recently, together with Koushika, she was able to probe the intracellular pH of *C. elegans*.²⁴⁷ Krishnan also has worked on creating pH-toggled DNA architectures through reversible assembly of three-way junctions.²⁴⁸

4.3 Nanomedicine: targeted delivery and imaging

An Indian traditional medicine, *Jasada Bhasma* was found to contain non-stoichiometric zinc oxide nanoparticles by Bellare and co-workers thus providing the link between the ancient medicinal practices of India and nanotechnology.¹ Today we can see the influence of nanomaterials in various areas of medicine such as targeted drug/gene delivery, imaging, wound dressing and tissue engineering.²⁴⁹ Receptor mediated delivery has become another active research area.²⁵⁰ Sahoo and co-workers have extensively worked on targeted therapy, they have conjugated EGF (epidermal growth factor) antibodies to rapamycin loaded PLGA NP and used for targeted therapy of breast cancer and in another study they have treated Bcr-Abl+ leukemia cells by targeting.^{251,252} Sahoo and co-workers treated pancreatic cancer cells with herceptin (HER2)-conjugated gemcitabine-loaded chitosan NP.²⁵³ Gupta and co-workers used polyethylemine conjugated with chondritin sulfate NP for gene delivery.²⁵⁴ Chennazhi and colleagues made fibrin nano constructs and used them as a controlled and effective gene delivery agent.²⁵⁵ Sahoo *et al.* demonstrated that the paracetamol-Ag nanoparticle conjugate mediated internalization of plasmid DNA in bacteria.²⁵⁶ Dash and colleagues characterized the antiplatelet properties of silver nanoparticles and proposed it to be a potential antithrombotic agent.²⁵⁷ Sahoo *et al.* has made dual drug loaded super paramagnetic iron oxide nanoparticles for targeting human breast carcinoma cell line (MCF-7).²⁵⁸ Pramanik and co-workers made nanoconjugated vancomycin which showed

efficacy against vancomycin resistant *S. aureus*, where folic acid conjugated nanopolymer acted as effective delivery agents inside the bacterial cell.²⁵⁹ Ali *et al.* developed a dry nanopowder inhaler made of atropine sulphate and used it as antidote for organophosphorous poisoning.²⁶⁰ Maitra and colleagues made multifunctional gadolinium oxide doped silica nanoparticles for gene delivery.²⁶¹ Desmukh and colleagues made highly stable Eudragit R 100 cationic nanoparticles containing amphotericin B for ophthalmic antifungal drug delivery.^{262,263} Previously, Mittal *et al.* used PLGA nanoparticles loaded with sparflaxacin for sustained ocular drug delivery.²⁶⁴ Gupta and co-workers synthesized linear polyethylenimine (PEI) and used as efficient carrier of pDNA and siRNA both *in vitro* and *in vivo*.²⁶⁵ Pathak *et al.* used the nano sized PEI-chondritin sulphate for tumor gene therapy and evaluated their bio-distribution and resultant transfection efficiency.²⁵⁴ Jain *et al.* used mannosylated gelatin nanoparticles loaded with anti-HIV drug didanosine for organ specific delivery.²⁶⁶ Dasgupta and co-workers conjugated AuNPs to α -crystallin protein and reported that the conjugate could prevent glycation even in the presence of strong glycating agents.²⁶⁷ Wilson and co-workers used chitosan nanoparticles as a new delivery system for the anti-Alzheimer drug tacrine.²⁶⁸ Recently nanomaterials based imaging and imaging-guided therapy have become active. Surolia and co-workers probed the mechanism of biphenyl ether mediated amyloid fibril disruption by BPE-QD conjugates and also traced senile plaque in the brain of transgenic mice.²⁴¹ Sarkar and co-workers used carbon nano onions as a tool to study the life cycle of the common fruit fly, *Drosophila melanaogaster*.²⁶⁹ Pramanik and co-workers made magneto-fluorescent nanoparticles conjugated with folic acid and targeted folate receptor over expressing cancer cells and isolated them using magnetically activated cell sorting (MACS).²⁷⁰ Highly fluorescent noble metal quantum clusters have become potential imaging tools of late.^{54,271} Pradeep and co-workers conjugated streptavidin to the QC, Au₂₃ and imaged HeLa cells and in another study they have conjugated folic acid to BSA protected Au₃₈ and imaged folic acid receptor positive cancer cells.^{272,273} Manzoor and colleagues have demonstrated folate receptor specific targeted delivery and flow cytometric detection of acute myeloid leukaemia by protein protected fluorescent gold quantum clusters.^{274,275} Manzoor and co-workers have conjugated folic acid with various nanomaterials and used for targeted imaging namely with multimodal hydroxyapatite, Y₂O₃ nanocrystals based contrast agents doped with Eu³⁺ and Gd³⁺, ZnS QD and BSA protected Au_{QC}s.²⁷⁵⁻²⁷⁹ Pramanik and co-workers combined multimodal imaging, targeting and pH dependent drug delivery in a single nanosystem by conjugating folic acid methotrexate to ultra small iron oxide nanoparticles coated with N-phosphonomethyl iminodiacetic acid (PMIDA).²⁸⁰

4.4 Regenerative medicine

Very few groups in India have been doing research on this vital and lucrative topic. Mandal and co-workers has grown hydroxyapatites on physiologically clotted fibrin on gold nanoparticles.²⁸¹ Jayakumar and colleagues have made sodium alginate/ZnO/polyvinyl alcohol composite nanofibers for wound dressing.²⁸² Selvamurugan and co-workers made bio-composite scaffolds

containing chitosan/nano-hydroxyapatite/nano-copper-zinc for bone tissue engineering.²⁸³ Kalkura and co-workers synthesized hydroxyapatite nanorods by a microwave irradiation method for the treatment of bone infection.²⁸⁴ Recently Singh *et al.* used nano-biphasic calcium phosphate ceramics for bone tissue engineering and evaluated the osteogenic differentiation of mesenchymal stem cells on the substrate.²⁸⁵ Ghosh and colleagues made silk fibroin scaffolds combined with chondroitin sulfate developed with precise fiber orientation in lamellar form for tissue engineering of the annulus fibrosus part of the intervertebral disc.²⁸⁶ Sethuraman and colleagues demonstrated that aligned nanofibers of PLGA-PHT (poly (lactide-co-glycolide)-poly (3-hexylthiophene)) can be used for neural regeneration by *in vitro* cell studies.²⁸⁷ Potential applications of fibrous scaffolds containing micro and nanoscale fibers in regenerative medicine have been discussed in detail by S.V. Nair and colleagues.²⁸⁸

4.5 Agriculture

Novel strategies for plant transformation to resist flood, salinity and drought, disease and pest control, minimal and efficient use of fertilizers are few crucial needs for increased productivity for Indian agriculture, not leaving the efficient storage of agricultural products. Scientists have been promoting the use of nanotechnology in agriculture for these objectives and these are evident from various reviews and recent research.^{289–291} Samim and co-workers prepared ultra-small sized (20–50 nm diameter) calcium phosphate (CaP) nanoparticles encapsulated with a reporter gene, pCambia 1301, and transfected *Brassica juncea* L. This CaP NP method was shown to be much efficient than *Agrobacterium tumefaciens* mediated genetic transformation.²⁹² Prasad and co-workers used carbon supported gold nanoparticles as gene carrying bullets in ballistic gene transformation method. They have tested the nano bullets on *Nicotinia tobaccum*, *Oriza sativa* and *Leucaena leucocephala* and have shown that it has better gene delivery efficiency and less damage than conventional micrometer sized gold particles.²⁹³ Prasad and co-workers have shown that ZnO nanoparticles could enhance the growth and yield of ground nut (*Arachis hypogaea*) compared to the bulk ZnO counterparts.²⁹⁴ Nandy and colleagues have shown that CNTs could have beneficial role on mustard plant (*Brassica juncea*) growth.²⁹⁵ Sarkar *et al.* have shown that water soluble carbon nanotubes stimulate the growth of *Cicer arietinum*.²⁹⁶

4.6 Nanotoxicity

Nanotoxicology has become one of the active areas of research in the country in the past decade and is well promoted among biologists and toxicologists.^{297–299} Comet assay, which a simple yet sensitive visual technique for the assessment of DNA damage in cells, and an important tool in toxicity evaluation, is discussed in a recent book.³⁰⁰ Since there is a thin line between chemical toxicity and nano toxicity where the former is due to the intrinsic chemical nature of the matter and the latter is purely based on size and associated emergent properties (the size limitation for the term nano is continuously changing, at present a NM is that having size between 1 and 100 nm in its characteristic dimension), a beginner

may miss to distinguish between them. Here, we give importance to the size dependent toxicity behavior (*e.g.* carbon is non toxic while CNTs are^{301,302}) and not to chemical moiety based toxicity where chemical nature is predominant than the size, but it is also known that the stabilizing ligands also influence the toxicity of a given nanoparticle. Size does matter in the case of soft organic nanomaterials also, such as dendrimers and polymer NM for enhanced intracellular uptake which is due to the large surface area created at the nanoscale, such enhanced uptake would influence the toxicity, here the toxicity is not only due to the chemical nature of the polymer or dendrimer but size also plays a role indirectly by means of facilitating enhanced uptake. In India toxicity of nanomaterials on both prokaryotic and eukaryotic organisms has been investigated. Some of the tested nanomaterials are carbon nanostructures, metal NPs, metal oxides NPs, semiconductor QDs and polymeric particles.

4.6.1 Studies on prokaryotic and plant systems. Mukerjee and co-workers tested titanium dioxide (TiO₂) nanoparticles on two trophic levels plants *Allium cepa* and *Nicotiana tabacum*, Comet assay and DNA laddering experiments showed TiO₂ NP to be geno toxic and it was further confirmed by the presence of micronuclei and chromosomal aberrations.³⁰³ In another study, the same group showed that MWCNT are genotoxic to *Allium cepa*³⁰⁴ Mukerjee and co-workers studied the toxicity of Al₂O₃ nanoparticles on microalgae *Scenedesmus* sp. and *Chlorella* sp and concluded that inhibition of growth and decrease in chlorophyll content occurred in NP treated algae and showed enhanced toxicity for alumina.^{305,306} Manivannan and co-workers have reported that of ZnO NPs are selectively toxic towards Gram positive bacteria.³⁰⁷ Dash *et al.* investigated the toxicity of silver nanoparticles to bacteria in detail and found that bacterial death is due to cell lysis. They observed many changes in phosphotyrosine profile of putative bacterial peptide and proposed that it could have inhibited bacterial signaling and growth.³⁰⁸ While several NM are shown to be toxic to bacteria, it has a gainful side that it can be used as antimicrobial materials.³⁰⁹

4.6.2 Studies on animal systems. Testing the toxicity of NM on animal and humans are of paramount importance. Several toxicological studies dealing with *in vitro* cellular systems and *in vivo* animal studies have been performed.

4.6.2.1 In vitro cell systems. Chaudhuri and colleagues showed that Au NPs can induce platelet aggregation and platelet response increases monotonically with NP size.³¹⁰ This could provide a measure of thrombotic risk associated with nanoparticles. Dasgupta and co-workers studied the role of purinergic receptors in platelet-nanoparticle interactions and reported that pro-aggregatory effect of NPs are ADP dependent and purinergic receptors also have role to play in the observed effect. They also showed that the usage of clopidogrel can prevent NP induced thrombotic responses.³¹¹ Reddana and co-workers studied the molecular mechanism of inflammatory responses of RAW 264.7 macrophages upon exposure to Ag, Au, Al NP and carbon black. They have observed the maximum inflammatory responses such as increased IL-6, reactive oxygen species (ROS) generation,

nuclear translocation of NF- κ B, induction of cyclooxygenase-2 (COX-2) and TNF- α for Ag NP followed by Al NP while no such inflammatory response was seen for Au NP indicating the bio compatibility of Au NP.³¹² Ahmad and co-workers compared the autophagy and cytotoxicity of iron oxide NP in normal human lung fibroblast cell (IMR-90) and lung cancer cell (A549) and found that ROS generation, mitochondrial damage and increased autophagy in lung epithelial cancer cells and not in normal cells.³¹³ Dasgupta and co-workers demonstrated that Au NP can be selectively toxic to different cell lines. They reported that Au NP were toxic to A549 cells while being non toxic to BHK21 (baby hamster kidney) and HepG2 (human hepatocellular liver carcinoma) cells.³¹⁴ Rahman and co-workers reported the oxidative damage induced by MWCNT in A549 cells.³¹⁵ Manzoor and co-workers reported that carboxyl functionalization could mitigate the toxicity of pristine graphene.³¹⁶

4.6.2.2 *In vivo studies.* Palaniappan *et al.* used Raman spectroscopy as a tool to investigate the bio molecular changes occurring in TiO₂ NPs exposed zebrafish (*Danio rerio*) liver tissues.³¹⁷ Murthy and co-workers reported that repeated administration of ZnO nanoparticles on the skin of Sprague-Dawley rats lead to loss of collagen when compared to the untreated site of the skin.³¹⁸ Patravale and co-workers studied the toxicity of curcumin loaded polymeric nanoparticles of Eudragit S100 and found it to be non toxic.³¹⁹ Jain and co-workers studied the toxicity of functionalized and non functionalized fifth generation polypropylenimine (PPI) dendrimers and reported that former were non toxic and latter were severely toxic.³²⁰ Sil and co-workers recently studied the molecular mechanism of oxidative stress responsive cell signaling in Cu NP induced liver dysfunction and cell death *in vivo*. They have found that Cu NP led to increased transcriptional activity of NF- κ β , upregulation of expression of phosphorylated p38, ERK1/2 and reciprocal regulation of Bcl-2 family proteins. Disruption of mitochondrial membrane potential, release of cytochrome C, formation of apoptosome and activation of caspase 3 was also seen, conforming the role of mitochondrial signaling.³²¹

Critically looking at the present scenario, based on the published work and from the discussion above, a bright future for nano-bio in India is predictable. There are certain areas in the field of nanobio, well represented from the Gandhian land compared to certain vital areas which are less represented viz nano in medicine, artificial biomimetic structures (artificial retina for example), molecular biology of nanotoxicity, protein corona on nanoparticle surface, *in situ* real time investigation of NP-cell interaction, *etc.* Certain areas like nano based functional man-made cellular systems are yet to start, while it has already started in western countries. Nanomedicine is only at the bench level and it is yet to reach the beds, and this is expected for a new technology at its foetal stage.

5 Nano and industry

India in principle has a lot to offer towards the large and growing market of nanotechnology. Till date most of the investments to the R&D programme

on nanotechnology in India have been through governmental agencies. Availability of young professionals at cheaper price is attracting attention and investments from industries in the recent years. Whereas R&D activities in nanoscience and nanotechnology have grown larger and larger over the years, India needs more number of people with techno-managerial skills to bridge between industry and educational institutes for successful transfer of technology.

The advantages of R&D in India have already attracted giant multinational companies like GE, GM and IBM who have already set up R&D centres in India.³²² Nano-tex has set a tie-up with Madura Garments, an Indian textile major recently and has plans to set up R&D to carry out research on NPs and textiles.³²² There are several other companies in India working on the synthesis of nanomaterials like nanosilver powders for making conductive paste (Auto Fibre Craft), nano silica products (Bee Chems), CNTs and graphene (Quantum Corporation and Nanoshel), protective nano-coatings for various surfaces (Nilima Nanotechnologies), *etc.*³²³ Bilcare has developed nonClonable, a security system which uses optical and magnetic properties of NPs.³²³ Dabur Pharma is working on drug delivery using polymeric NPs which is in the advanced stages of clinical trials.³²³ Saint-Gobain Glass manufactures SGG NANO, a glass coated with multiple layers of nanoscale metallic oxides/nitrides which possesses advanced energy efficient solar control and thermal insulation properties.³²³ We have already outlined the nanotechnology efforts related to water purification earlier (section 3.1).

Lack of competent product marketing, sales and distribution skills are the major drawbacks in the Indian nano industries. Hilaal Alam, CEO of Qtech Nanosystem commented on this issue: “India has got (the) potential to become a service provider for (global) nanotechnology industry; but not a pipeline for new products. Majority of investment in India up till now has gone in services sector and into building a testing and characterization infrastructure.”³²²

6 Nano and education

Almost every institutes/universities in India has a nanotechnology programme. In most cases nanotechnology education is imparted at senior undergraduate level in the form of a completely new course or part of an existing course. At the masters level, specific nanoscience and nanotechnology programmes offering M. S. and M. Tech degrees are also available. A rather different course entitled M. Sc. Tech. is also offered by some institutions. Besides these, integrated B. Tech.-M. Tech. programmes are also initiated. A detailed discussion on the status of nanotechnology education at IITs (Indian Institute of Technologies) can be found elsewhere.³²⁴ While the first few batches from such nanotech programmes have already come out, in most of the institutions they are at advanced level of completion. As nanotechnology is diverse, most institutions have tried to specialize their degrees based on the expertise available. Nanomaterials, bionanotechnology and nanomedicine are the common specializations being offered. As industrial opportunities are limited, most of the graduates

have opted to stay with research as their career option. The steady output of PhDs in the area was commented upon earlier.

7 Future of nano-research in India

Science at the nanoscale is making numerous surprises and it is impossible to predict the future. This is true in the Indian context too. However, from the current trends, nature of investments made and the human resource available, it is expected that new materials and their modifications will continue to be the major focus in the immediate future. Applications in areas of societal relevance is getting momentum not only due to the implications but also because of the fact that it is practiceable in almost every institution as several experiments are possible with minimum infrastructure. Exciting new materials – graphene, soft materials, clusters, gels, porous materials, anisotropic nanostructures, functionally graded nanostructures, *etc.* – will continue to be active. An aspect that is apparent in current science is the greater involvement of synthetic organic chemists in nanoscience. These efforts are directed towards self organization, patterning, composites, luminescence, biology and the like.

Indian research at the nanoscale will generate new excitements if there is a greater possibility for device fabrication. These developments need not necessarily be using nanoscale patterning. In areas of sensors the range of activities in the country in national security, disease identification, environmental monitoring, water purification, *etc.* the need for demonstrable devices is large. Applications of traditional knowledge using nanomaterials will be significantly advantageous wherein new formulations are likely.

All the developments will have their ultimate impact only if materials are made and tested in quantities. There is a need to make nanomaterials of relevance to applications available to people. For this piloting facilities have to come up. Field applications and data from such studies will be possible only this way.

Society is keenly observing new breakthroughs. The nation is sensitized on this area through various media, new programmes and also due to the largely younger population. There is a realisation that a vast majority of Indians will live in the Nanotechnology-enabled society as the average age of India by 2020 is expected to be 29. The new society has to understand the benefits and risks and therefore societal relevance of nanoscience and its implications will be discussed more and more. With the availability of instrumental resources across the country, nanoscience will not only capture the imagination of people but also enable them to do something relevant. However, for this to happen sustained funding and longer term commitment is essential. Industry has to be ready to absorb the developments happening in the soil.

8 Conclusions

Nanoscience presents an explosive, diverse and highly promising science in India, just as in any part of the world. The most active area is related to the developments in materials. There is a strong overlap of computational materials science with the nanoscience activity. Although nanoscience has

not yet resulted in industrial products in several nations, early signs of applications are available in India. Surprisingly this turns out to be on one of the most pressing needs of the nation, namely water purification. The applications of nanomaterials on several of the national needs such as security, environment, health, *etc.* are visible. However, intense efforts in areas such as energy have not happened, although no area is not unrepresented. Nanoscience has got into pedagogy in several universities and the first few batches with NS&NT specialization have already come out. Nano has got into the regional language literature and the nation is pregnant with hope from this new branch of science.

Acknowledgement

The authors acknowledge financial support from the Department of Science and Technology under the Nano Mission. Thanks are due to Centre for Knowledge Management of Nanoscience and Technology (CKMNT) for providing scientometric and other data. We are thankful to the authors who sent us additional information on their work.

References

- 1 T. Bhowmick, A. Suresh, S. Kane, A. Joshi and J. Bellare, *J. Nanopart. Res.*, 2009, **11**, 655.
- 2 S. Srinivasan and S. Ranganathan, *India's Legendary Wootz Steel: An Advanced Material of the Ancient World*, National Institute of advanced studies, 2004.
- 3 M. Reibold, N. Pätzke, A. A. Levin, W. Kochmann, I. P. Shakhverdova, P. Paufler and D. C. Meyer, *Cryst. Res. Technol.*, 2009, **44**, 1139.
- 4 umconference.um.edu.my/.../189%20ShyamaRamani_NupurC.
- 5 *Nanotechnology Funding and Investments: A Global Perspective*, Centre for Knowledge Management of Nanoscience and Technology (CKMNT), 2011.
- 6 *The Emergence of India as a Leading Nation in Nanoscience and Nanotechnology*, Nanotech Insights, Centre for Knowledge Management of Nanoscience and Technology (CKMNT), 2012.
- 7 <http://nanomission.gov.in> (Accessed on July 8, 2012).
- 8 *National nanotech policy: A mirage*, Nano Digest, 2012.
- 9 K. Jayaraman, *Pesticide filter debuts in India*, Chemistry World, Royal Society of Chemistry, 2007.
- 10 D. Murali, *World's first nano-material based water filter*, Business Line, The Hindu, Chennai, 2007.
- 11 B. R. Burgi and T. Pradeep, *Curr. Sci.*, 2006, **90**, 645.
- 12 T. Pradeep, The Hindu, 2010; Nano Digest, 2011, pp. 18–19; Manorama Year Book, 2011; Deshabhimani, 2010.
- 13 T. Pradeep, *Kunjukanangalku Vasantham Nanotechnologikku Oramukham*, DC Books, 2007.
- 14 C. N. R. Rao, A. Müller and A. K. Cheetham, *The Chemistry of Nanomaterials: Synthesis, Properties and Applications*, John Wiley & Sons, 2006.
- 15 C. N. R. Rao and A. Govindaraj, *Nanotubes and Nanowires*, Royal Society of Chemistry, 2011.
- 16 C. N. R. Rao, A. K. Sood, K. S. Subrahmanyam and A. Govindaraj, *Angew. Chem., Int. Ed.*, 2009, **48**, 7752.
- 17 C. N. R. Rao, H. S. S. R. Matte and K. S. Subrahmanyam, *Acc. Chem. Res.*, 2012.

-
- 18 S. K. Das, *Nanofluids: Science and Technology*, Wiley-Interscience, 2007. 1
- 19 B. L. V. Prasad, C. M. Sorensen and K. J. Klabunde, *Chem. Soc. Rev.*, 2008, **37**, 1871.
- 20 K. Kimura and T. Pradeep, *Phys. Chem. Chem. Phys.*, 2011, **13**, 19214.
- 21 A. Ajayaghosh, V. K. Praveen and C. Vijayakumar, *Chem. Soc. Rev.*, 2008, **37**, 109. 5
- 22 A. Ajayaghosh and V. K. Praveen, *Acc. Chem. Res.*, 2007, **40**, 644.
- 23 P. Pramod, K. G. Thomas and M. V. George, *Chem. Asian J.*, 2009, **4**, 806.
- 24 A. Rahman and M. K. Sanyal, CRC Press, 2011, vol. 4, pp. 20/1.
- 25 M. Faraday, *Philosophical Transactions of the Royal Society of London*, 1857, **147**, 145. 10
- 26 A. K. Ganguli, A. Ganguly and S. Vaidya, *Chem. Soc. Rev.*, 2010, **39**, 474.
- 27 N. R. Jana, *Small*, 2005, **1**, 875.
- 28 A. Samal, T. Sreeprasad and T. Pradeep, *Journal of Nanoparticle Research*, 2010, **12**, 1777.
- 29 P. R. Sajanlal and T. Pradeep, *Advanced Materials*, 2008, **20**, 980. 15
- 30 P. R. Sajanlal, C. Subramaniam, P. Sasanpour, B. Rashidian and T. Pradeep, *Journal of Materials Chemistry*, 2010, **20**, 2108.
- 31 A. Swami, A. Kumar, P. R. Selvakannan, S. Mandal, R. Pasricha and M. Sastry, *Chemistry of Materials*, 2003, **15**, 17.
- 32 S. S. Shankar, A. Rai, B. Ankamwar, A. Singh, A. Ahmad and M. Sastry, *Nat Mater*, 2004, **3**, 482. 20
- 33 B. K. Jena and C. R. Raj, *Chemistry of Materials*, 2008, **20**, 3546.
- 34 P. Sajanlal and T. Pradeep, *Nano Research*, 2009, **2**, 306.
- 35 P. R. Sajanlal, T. S. Sreeprasad, A. K. Samal and T. Pradeep, *Nano Reviews*, 2011, **2**, 5883.
- 36 M. Sastry, A. Swami, S. Mandal and P. R. Selvakannan, *J. Mater. Chem.*, 2005, **15**, 3161. 25
- 37 P. Mukherjee, A. Ahmad, D. Mandal, S. Senapati, S. R. Sainkar, M. I. Khan, R. Ramani, R. Parischa, P. V. Ajayakumar, M. Alam, M. Sastry and R. Kumar, *Angew. Chem., Int. Ed.*, 2001, **40**, 3585.
- 38 S. S. Shankar, A. Rai, A. Ahmad and M. Sastry, *Chem. Mater.*, 2005, **17**, 566. 30
- 39 S. K. Nune, N. Chanda, R. Shukla, K. Katti, R. R. Kulkarni, S. Thilakavathy, S. Mekapothula, R. Kannan and K. V. Katti, *Journal of Materials Chemistry*, 2009, **19**, 2912.
- 40 B. Ankamwar, M. Chaudhary and M. Sastry, *Synthesis and Reactivity in Inorganic, Metal-Organic, and Nano-Metal Chemistry*, 2005, **35**, 19. 35
- 41 V. K. Shukla, R. S. Yadav, P. Yadav and A. C. Pandey, *Journal of Hazardous Materials*, 2012, **213–214**, 161.
- 42 K. Amarnath, N. Mathew, J. Nellore, C. Siddarth and J. Kumar, *Cancer Nanotechnology*, 2011, **2**, 121.
- 43 D. Raghunandan, M. D. Bedre, S. Basavaraja, B. Sawle, S. Y. Manjunath and A. Venkataraman, *Colloids and Surfaces B: Biointerfaces*, 2010, **79**, 235. 40
- 44 B. Nair and T. Pradeep, *Crystal Growth & Design*, 2002, **2**, 293.
- 45 P. Pramod and K. G. Thomas, *Adv. Mater.*, 2008, **20**, 4300.
- 46 P. R. Sajanlal and T. Pradeep, *Langmuir*, 2010, **26**, 8901.
- 47 P. R. Sajanlal and T. Pradeep, *The Journal of Physical Chemistry C*, 2010, **114**, 16051. 45
- 48 G. V. Ramesh, S. Porel and T. P. Radhakrishnan, *Chemical Society Reviews*, 2009, **38**, 2646.
- 49 G. V. Ramesh, M. D. Prasad and T. P. Radhakrishnan, *Chemistry of Materials*, 2011, **23**, 5231.
-

-
- 50 A. Patra, C. G. Chandaluri and T. P. Radhakrishnan, *Nanoscale*, 2012, **4**, 343. 1
- 51 J. George and K. G. Thomas, *J. Am. Chem. Soc.*, 2010, **132**, 2502.
- 52 E. Hariprasad and T. P. Radhakrishnan, *Chemistry—A European Journal*, 2010, **16**, 14378.
- 53 N. Sandhyarani and T. Pradeep, *International Reviews in Physical Chemistry*, 2003, **22**, 221. 5
- 54 A. P. Demchenko, M. A. H. Muhammed and T. Pradeep, in *Advanced Fluorescence Reporters in Chemistry and Biology II*, Springer Berlin Heidelberg, 2010, vol. 9, pp. 333.
- 55 M. A. H. Muhammed, A. K. Shaw, S. K. Pal and T. Pradeep, *The Journal of Physical Chemistry C*, 2008, **112**, 14324. 10
- 56 M. A. Habeeb Muhammed and T. Pradeep, *Chemical Physics Letters*, 2007, **449**, 186.
- 57 E. S. Shibu, M. A. H. Muhammed, T. Tsukuda and T. Pradeep, *The Journal of Physical Chemistry C*, 2008, **112**, 12168.
- 58 M. A. Habeeb Muhammed and T. Pradeep, *Small*, 2011, **7**, 204. 15
- 59 P. Ramasamy, S. Guha, E. S. Shibu, T. S. Sreeprasad, S. Bag, A. Banerjee and T. Pradeep, *Journal of Materials Chemistry*, 2009, **19**, 8456.
- 60 M. A. H. Muhammed, P. K. Verma, S. K. Pal, R. C. A. Kumar, S. Paul, R. V. Omkumar and T. Pradeep, *Chemistry—A European Journal*, 2009, **15**, 10110.
- 61 E. S. Shibu and T. Pradeep, *Chemistry of Materials*, 2011, **23**, 989.
- 62 A. Ghosh, T. Udayabhaskararao and T. Pradeep, *J. Phys. Chem. Lett.*, 2012, 1997. 20
- 63 K. V. Mrudula, T. U. Bhaskara Rao and T. Pradeep, *Journal of Materials Chemistry*, 2009, **19**, 4335.
- 64 B. R. T. Udaya and T. Pradeep, *Angew Chem Int Ed Engl*, 2010, **49**, 3925.
- 65 T. U. B. Rao, B. Nataraju and T. Pradeep, *Journal of the American Chemical Society*, 2010, **132**, 16304. 25
- 66 T. U. Rao, T. Pradeep and M. S. Bootharaju, 2012 (Unpublished).
- 67 I. Chakraborty, T. Udayabhaskararao and T. Pradeep, *Chemical Communications*, 2012, **48**, 6788.
- 68 T. Udayabhaskararao, Y. Sun, N. Goswami, S. K. Pal, K. Balasubramanian and T. Pradeep, *Angewandte Chemie International Edition*, 2012, **51**, 2155. 30
- 69 P. Lourdu Xavier, K. Chaudhari, A. Baksi and T. Pradeep, *Nano Reviews*, 2012, **3**, 14767.
- 70 P. L. Xavier, K. Chaudhari, P. K. Verma, S. K. Pal and T. Pradeep, *Nanoscale*, 2010, **2**, 2769.
- 71 K. Amarnath, N. Mathew, J. Nellore, C. Siddarth and J. Kumar, *Cancer Nanotechnol.*, 2011, **2**, 121. 35
- 72 M. A. Habeeb Muhammed, P. K. Verma, S. K. Pal, A. Retnakumari, M. Koyakutty, S. Nair and T. Pradeep, *Chemistry—A European Journal*, 2010, **16**, 10103.
- 73 B. Adhikari and A. Banerjee, *Chemistry of Materials*, 2010, **22**, 4364. 40
- 74 N. Goswami, A. Giri, M. S. Bootharaju, P. L. Xavier, T. Pradeep and S. K. Pal, *Analytical Chemistry*, 2011, **83**, 9676.
- 75 C. N. R. Rao and K. P. Kalyanikutty, *Accounts of Chemical Research*, 2008, **41**, 489.
- 76 S. Chandran and J. Basu, *The European Physical Journal E: Soft Matter and Biological Physics*, 2011, **34**, 1. 45
- 77 S. Chandran, S. C. K., A. K. Kandar, J. K. Basu, S. Narayanan and A. Sandy, *The Journal of Chemical Physics*, 2011, **135**, 134901.
- 78 G. Majumdar, S. K. Gogoi, A. Paul and A. Chattopadhyay, *Langmuir*, 2006, **22**, 3439.
-

-
- 79 S. K. Gogoi, S. M. Borah, K. K. Dey, A. Paul and A. Chattopadhyay, *Langmuir*, 2011, **27**, 12263. 1
- 80 B. Radha, S. Kiruthika and G. U. Kulkarni, *Journal of the American Chemical Society*, 2011, **133**, 12706.
- 81 B. Radha and G. U. Kulkarni, *Advanced Functional Materials*, 2012, n/a. 5
- 82 B. L. V. Prasad, C. M. Sorensen and K. J. Klabunde, *Chemical Society Reviews*, 2008, **37**, 1871.
- 83 K. Kimura and T. Pradeep, *Physical Chemistry Chemical Physics*, 2011, **13**, 19214.
- 84 D. S. Sidhaye and B. L. V. Prasad, *New Journal of Chemistry*, 2011, **35**, 755. 10
- 85 N. Nishida, E. S. Shibu, H. Yao, T. Oonishi, K. Kimura and T. Pradeep, *Adv. Mater. (Weinheim, Ger.)*, 2008, **20**, 4719.
- 86 E. S. Shibu, K. Kimura and T. Pradeep, *Chem. Mater.*, 2009, **21**, 3773.
- 87 E. Shibu, M. Habeeb Muhammed, K. Kimura and T. Pradeep, *Nano Res.*, 2009, **2**, 220. 15
- 88 R. Viswanatha, H. Amenitsch and D. D. Sarma, *Journal of the American Chemical Society*, 2007, **129**, 4470.
- 89 R. Viswanatha, P. K. Santra, C. Dasgupta and D. D. Sarma, *Physical Review Letters*, 2007, **98**, 255501.
- 90 A. Nag, S. Sapra, C. Nagamani, A. Sharma, N. Pradhan, S. V. Bhat and D. D. Sarma, *Chemistry of Materials*, 2007, **19**, 3252. 20
- 91 A. Nag, S. Chakraborty and D. D. Sarma, *Journal of the American Chemical Society*, 2008, **130**, 10605.
- 92 P. K. Santra, R. Viswanatha, S. M. Daniels, N. L. Pickett, J. M. Smith, P. O'Brien and D. D. Sarma, *Journal of the American Chemical Society*, 2008, **131**, 470. 25
- 93 N. S. Karan, S. Sarkar, D. D. Sarma, P. Kundu, N. Ravishankar and N. Pradhan, *Journal of the American Chemical Society*, 2011, **133**, 1666.
- 94 A. Nag and D. D. Sarma, *The Journal of Physical Chemistry C*, 2007, **111**, 13641.
- 95 S. Acharya, D. D. Sarma, Y. Golan, S. Sengupta and K. Ariga, *Journal of the American Chemical Society*, 2009, **131**, 11282. 30
- 96 M. Ghosh and A. K. Raychaudhuri, *Nanotechnology*, 2008, **19**, 445704/1.
- 97 N. Pradhan, S. Acharya, K. Ariga, N. S. Karan, D. D. Sarma, Y. Wada, S. Efrima and Y. Golan, *Journal of the American Chemical Society*, 2010, **132**, 1212.
- 98 A. Sharma, C. M. Pandey, Z. Matharu, U. Soni, S. Sapra, G. Sumana, M. K. Pandey, T. Chatterjee and B. D. Malhotra, *Analytical Chemistry*, 2012, **84**, 3082. 35
- 99 A. Sundaresan, R. Bhargavi, N. Rangarajan, U. Siddesh and C. N. R. Rao, *Phys. Rev. B*, 2006, **74**, 161306.
- 100 A. Shipra, A. Gomathi, Sundaresan and C. N. R. Rao, *Solid State Commun.*, 2007, **142**, 685. 40
- 101 A. Sundaresan and C. N. R. Rao, *Nano Today*, 2009, **4**, 96.
- 102 S. Vijayanand, H. S. Potdar and P. A. Joy, *Appl. Phys. Lett.*, 2009, **94**, 182507/1.
- 103 N. S. John, G. U. Kulkarni, A. Datta, S. K. Pati, F. Komori, G. Kavitha, C. Narayana and M. K. Sanyal, *J. Phys. Chem. C*, 2007, **111**, 1868.
- 104 H. S. S. Ramakrishna Matte, A. Gomathi, A. K. Manna, D. J. Late, R. Datta, S. K. Pati and C. N. R. Rao, *Angew. Chem. Int. Ed.*, 2010, **49**, 4059. 45
- 105 H. S. S. R. Matte, B. Plowman, R. Datta and C. N. R. Rao, *Dalton Trans.*, 2011, **40**, 10322.
-

-
- 106 A. Nag, K. Raidongia, K. P. S. S. Hembram, R. Datta, U. V. Waghmare and C. N. R. Rao, *ACS Nano*, 2010, **4**, 1539. 1
- 107 N. Kumar, K. S. Subrahmanyam, P. Chaturbedy, K. Raidongia, A. Govindaraj, K. P. S. S. Hembram, A. K. Mishra, U. V. Waghmare and C. N. R. Rao, *ChemSusChem*, 2011, **4**, 1662. 5
- 108 D. J. Late, B. Liu, H. S. S. R. Matte, V. P. Dravid and C. N. R. Rao, *ACS Nano*, 2012, **6**, 5635.
- 109 J. Robin, A. Ashokreddy, C. Vijayan and T. Pradeep, *Nanotechnology*, 2011, **22**, 165701.
- 110 R. S. Dey, S. Hajra, R. K. Sahu, C. R. Raj and M. K. Panigrahi, *Chem. Commun.*, 2011, **48**, 1787. 10
- 111 D. Mhamane, W. Ramadan, M. Fawzy, A. Rana, M. Dubey, C. Rode, B. Lefez, B. Hannoyer and S. Ogale, *Green Chem.*, 2011, **13**, 1990.
- 112 V. Eswaraiiah, S. S. Jyothirmayee Aravind and S. Ramaprabhu, *J. Mater. Chem.*, 2011, **21**, 6800.
- 113 S. S. Gupta, T. S. Sreeprasad, S. M. Maliyekkal, S. K. Das and T. Pradeep, *ACS Appl. Mater. Interfaces*, 2012. 15
- 114 T. S. Sreeprasad, S. Sen Gupta, S. M. Maliyekkal and T. Pradeep, *Unpublished (2012)*.
- 115 T. S. Sreeprasad and T. Pradeep, *Int. J. Mod. Phys. B*, 2012, **26**, 1242001.
- 116 S. K. Misra, P. Kondaiah, S. Bhattacharya and C. N. R. Rao, *Small*, 2011, **8**, 131. 20
- 117 H. P. Mungse, S. Verma, N. Kumar, B. Sain and O. P. Khatri, *J. Mater. Chem.*, 2012, **22**, 5427.
- 118 R. K. Srivastava, S. Srivastava, T. N. Narayanan, B. D. Mahlotra, R. Vajtai, P. M. Ajayan and A. Srivastava, *ACS Nano*, 2012, **6**, 168.
- 119 B. Chitara, L. S. Panchakarla, S. B. Krupanidhi and C. N. R. Rao, *Adv. Mater.*, 2011, **23**, 5419. 25
- 120 B. K. Gupta, P. Thanikaivelan, T. N. Narayanan, L. Song, W. Gao, T. Hayashi, A. Leela Mohana Reddy, A. Saha, V. Shanker, M. Endo, A. A. Mart and P. M. Ajayan, *Nano Lett.*, 2011, **11**, 5227.
- 121 V. Gupta, N. Chaudhary, R. Srivastava, G. D. Sharma, R. Bhardwaj and S. Chand, *J. Am. Chem. Soc.*, 2011, **133**, 9960. 30
- 122 V. Eswaraiiah, K. Balasubramaniam and S. Ramaprabhu, *J. Mater. Chem.*, 2011, **21**, 12626.
- 123 S. K. Saha, M. Baskey and D. Majumdar, *Adv. Mater.*, 2010, **22**, 5531.
- 124 K. S. Subrahmanyam, P. Kumar, U. Maitra, A. Govindaraj, K. P. S. S. Hembram, U. V. Waghmare and C. N. R. Rao, *Proc. Natl. Acad. Sci.*, 2011, **108**, 2674. 35
- 125 K. Rakesh, V. Deepak, B. R. Mehta, V. N. Singh, W. Zhenhai, F. Xinliang and M. I. Klaus, *Nanotechnology*, 2011, **22**, 275719.
- 126 S. Verma, H. P. Mungse, N. Kumar, S. Choudhary, S. L. Jain, B. Sain and O. P. Khatri, *Chem. Commun.*, 2011, **47**, 12673.
- 127 A. Chandrasekar and T. Pradeep, *J. phys. Chem. C*, 2012, **116**, 14057. 40
- 128 R. Voggu, K. V. Rao, S. J. George and C. N. R. Rao, *J. Am. Chem. Soc.*, 2010, **132**, 5560.
- 129 D. B. Shinde, J. Debgupta, A. Kushwaha, M. Aslam and V. K. Pillai, *J. Am. Chem. Soc.*, 2011, **133**, 4168.
- 130 P. Kumar, L. S. Panchakarla and C. N. R. Rao, *Nanoscale*, 2011, **3**, 2127.
- 131 J. Debgupta, D. B. Shinde and V. K. Pillai, *Chem. Commun.*, 2012, **48**, 3088. 45
- 132 S. Majumdar, R. Krishnaswamy and A. K. Sood, *Proc. Natl. Acad. Sci.*, 2011, **108**, 8996.
- 133 N. Chauhan, J. Narang and C. S. Pundir, *Analyst*, 2011, **136**, 1938.
-

- 134 I. P. M. Wijaya, T. J. Nie, S. Gandhi, R. Boro, A. Palaniappan, G. W. Hau, I. Rodriguez, C. R. Suri and S. G. Mhaisalkar, *Lab Chip*, 2010, **10**, 634. 1
- 135 A. K. Mishra and S. Ramaprabhu, *J. Phys. Chem. C*, 2010, **114**, 2583.
- 136 R. Kannan, P. P. Aher, T. Palaniselvam, S. Kurungot, U. K. Kharul and V. K. Pillai, *J. Phys. Chem. Lett.*, 2010, **1**, 2109. 5
- 137 P. Singh, F. M. Toma, J. Kumar, V. Venkatesh, J. Raya, M. Prato, S. Verma and A. Bianco, *Chem. Eur. J.*, 2011, **17**, 6772.
- 138 B. R. Sathe, B. A. Kakade, A. Kushwaha, M. Aslam and V. K. Pillai, *Chem. Commun.*, 2010, **46**, 5671.
- 139 M. Santosh, S. Panigrahi, D. Bhattacharyya, A. K. Sood and P. K. Maiti, *J. Chem. Phys.*, 2012, **136**, 065106. 10
- 140 S. Yagai, H. Aonuma, Y. Kikkawa, S. Kubota, T. Karatsu, A. Kitamura, S. Mahesh and A. Ajayaghosh, *Chem. Eur. J.*, 2010, **16**, 8652.
- 141 K. P. Divya, S. Sreejith, C. H. Suresh and A. Ajayaghosh, *Chem. Commun.*, 2010, **46**, 8392.
- 142 S. Prasanthkumar, A. Saeki, S. Seki and A. Ajayaghosh, *J. Am. Chem. Soc.*, 2010, **132**, 8866. 15
- 143 S. Prasanthkumar, A. Gopal and A. Ajayaghosh, *J. Am. Chem. Soc.*, 2010, **132**, 13206.
- 144 K. V. Rao, K. Jayaramulu, T. K. Maji and S. J. George, *Angew. Chem. Int. Ed.*, 2010, **49**, 4218.
- 145 S. Varghese, N. S. S. Kumar, A. Krishna, D. S. S. Rao, S. K. Prasad and S. Das, *Adv. Funct. Mater.*, 2009, **19**, 2064. 20
- 146 D. Dasgupta, S. Srinivasan, C. Rochas, A. Thierry, A. Schroder, A. Ajayaghosh and J. M. Guenet, *Soft Matter*, 2011, **7**, 2797.
- 147 S. Sreejith, K. P. Divya, T. K. Manojkumar and A. Ajayaghosh, *Chem. Asian J.*, 2010, **6**, 430. 25
- 148 K. K. Kartha, S. S. Babu, S. Srinivasan and A. Ajayaghosh, *J. Am. Chem. Soc.*, 2012, **134**, 4834.
- 149 P. Rajamalli and E. Prasad, *Org. Lett.*, 2011, **13**, 3714.
- 150 A. Vidyasagar, K. Handore and K. M. Sureshan, *Angew. Chem. Int. Ed.*, 2011, **50**, 8021.
- 151 N. Chandrasekhar and R. Chandrasekar, *Angew. Chem. Int. Ed.*, 2012, **51**, 3556. 30
- 152 M. R. Molla, A. Das and S. Ghosh, *Chem. Commun.*, 2011, **47**, 8934.
- 153 T. Kar, S. K. Mandal and P. K. Das, *Chem. Eur. J.*, 2011, **17**, 14952.
- 154 B. Adhikari, J. Nanda and A. Banerjee, *Chem. Eur. J.*, 2011, **17**, 11488.
- 155 S. K. Samanta, K. S. Subrahmanyam, S. Bhattacharya and C. N. R. Rao, *Chem. Eur. J.*, 2011, **18**, 2890. 35
- 156 B. Das, B. Choudhury, A. Gomathi, A. K. Manna, S. K. Pati and C. N. R. Rao, *ChemPhysChem*, 2011, **12**, 937.
- 157 S. M. Maliyekkal, T. S. Sreeprasad, K. Deepti, S. Kouser, A. K. Mishra, U. V. Waghmare and T. Pradeep, ~~unpublished-2012~~. 40
- 158 K. Balamurugan, R. Gopalakrishnan, S. S. Raman and V. Subramanian, *J. Phys. Chem. B*, 2010, **114**, 14048.
- 159 K. Balamurugan, E. R. A. Singam and V. Subramanian, *J. Phys. Chem. C*, 2011, **115**, 8886.
- 160 K. Srinivasu and S. K. Ghosh, *J. Phys. Chem. C*, 2012, **116**, 5951.
- 161 S. S. Pundlik, K. Kalyanaraman and U. V. Waghmare, *J. Phys. Chem. C*, 2011, **115**, 3809. 45
- 162 H. Sekhar De, S. Krishnamurty and S. Pal, *J. Phys. Chem. C*, 2010, **114**, 6690.
- 163 H. S. De, S. Krishnamurty, D. Mishra and S. Pal, *J. Phys. Chem. C*, 2011, **115**, 17278.

-
- 164 N. Mammen, S. Narasimhan and S. d. Gironcoli, *J. Am. Chem. Soc.*, 2011, **133**, 2801. 1
- 165 N. K. Jena, K. R. S. Chandrakumar and S. K. Ghosh, *J. Phys. Chem. Lett.*, 2011, **2**, 1476.
- 166 B. S. Kulkarni, S. Krishnamurthy and S. Pal, *J. Phys. Chem. C*, 2011, **115**, 14615. 5
- 167 S. Datta, M. Kabir and T. Saha-Dasgupta, *Phys. Rev. B*, 2011, **84**, 075429.
- 168 S. S. Sarangi, B. L. Bhargava and S. Balasubramanian, *Phys. Chem. Chem. Phys.*, 2009, **11**, 8745.
- 169 R. Swathi and K. Sebastian, *J. Chem. Sci.*, 2009, **121**, 777.
- 170 U. Shankar, Anshup and T. Pradeep, 2012 (Unpublished). 10
- 171 A. S. Nair and T. Pradeep, *Curr. Sci.*, 2003, **84**, 1560.
- 172 A. S. Nair, R. T. Tom and T. Pradeep, *J. Environ. Monit.*, 2003, **5**, 363.
- 173 A. S. Nair and T. Pradeep, *J. Nanosci. Nanotechnol.*, 2007, **7**, 1871.
- 174 M. S. Bootharaju and T. Pradeep, *Langmuir*, 2012, **28**, 2671.
- 175 S. Sen Gupta, T. S. Sreepasad, S. M. Maliyekkal, S. K. Das and T. Pradeep, *ACS Appl. Mater. Interfaces*—(Submitted). 15
- 176 G. K. Ramesha, A. Vijaya Kumara, H. B. Muralidhara and S. Sampath, *J. Colloid Interface Sci.*, 2011, **361**, 270.
- 177 T. S. Sreepasad, S. M. Maliyekkal, K. P. Lisha and T. Pradeep, *J. Hazard. Mater.*, 2011, **186**, 921.
- 178 T. S. Sreepasad, M. S. Maliyekkal, K. Deepti, K. Chaudhari, P. L. Xavier and T. Pradeep, *ACS Appl. Mater. Interfaces*, 2011, **3**, 2643. 20
- 179 K. P. Lisha, Anshup and T. Pradeep, *J. Environ. Sci. Health., Part B*, 2009, **44**, 697.
- 180 K. P. Lisha, Anshup and T. Pradeep, *Gold Bull.*, 2009, **42**, 144.
- 181 A. George, E. S. Shibu, S. M. Maliyekkal, M. S. Bootharaju and T. Pradeep, *ACS Appl. Mater. Interfaces*, 2012, **4**, 639. 25
- 182 I. Chakraborty, T. Udayabhaskararao and T. Pradeep, *J. Hazard. Mater.*, 2011, **211–212**, 396.
- 183 S. Roy, G. Palui and A. Banerjee, *Nanoscale*, 2012, **4**, 2734.
- 184 V. Seena, A. Fernandes, P. Pant, S. Mukherji and V. R. Rao, *Nanotechnology*, 2011, **22**, 295501/1.
- 185 V. Seena, A. Fernandes, S. Mukherji and V. R. Rao, *Int. J. Nanosci.*, 2011, **10**, 739. 30
- 186 R. S. Dudhe, H. N. Raval, A. Kumar and V. R. Rao, *Int. J. Nanosci.*, 2011, **10**, 891.
- 187 N. Venkatramaiah, S. Kumar and S. Patil, *Chem. Commun.*, 2012, **48**, 5007.
- 188 P. R. Sajanlal and T. Pradeep, *Nanoscale*, 2012, **4**, 3427. 35
- 189 A. Mathew, P. R. Sajanlal and T. Pradeep, *Angew. Chem. Int. Ed.*, 2012—(Just Accepted).
- 190 A. Kaniyoor and S. Ramaprabhu, *J. Mater. Chem.*, 2012, **22**, 8377.
- 191 P. Sudhagar, K. Asokan, E. Ito and Y. S. Kang, *Nanoscale*, 2012, **4**, 2416.
- 192 R. Bajpai, S. Roy, N. kulshrestha, J. Rafiee, N. Koratkar and D. S. Misra, *Nanoscale*, 2012, **4**, 926. 40
- 193 A. Guchhait, A. K. Rath and A. J. Pal, *Appl. Phys. Lett.*, 2010, **96**, 073505.
- 194 A. Makhal, S. Sarkar, T. Bora, S. Baruah, J. Dutta, A. K. Raychaudhuri and S. K. Pal, *J. Phys. Chem. C*, 2010, **114**, 10390.
- 195 T. Palaniselvam, R. Kannan and S. Kurungot, *Chem. Commun.*, 2011, **47**, 2910. 45
- 196 R. Kannan, P. P. Aher, T. Palaniselvam, S. Kurungot, U. K. Kharul and V. K. Pillai, *J. Phys. Chem. Lett.*, 2010, **1**, 2109.
- 197 S. Ghosh and C. R. Raj, *The Journal of Physical Chemistry C*, 2010, **114**, 10843.
-

- 198 C. V. Rao and B. Viswanathan, *J. Phys. Chem. C*, 2010, **114**, 8661. 1
- 199 A. K. Samal and T. Pradeep, *J. Phys. Chem. C*, 2009, **113**, 13539.
- 200 A. Som and T. Pradeep, *Nanoscale*, 2012, **4**, 4537.
- 201 A. Datta, J. Paul, A. Kar, A. Patra, Z. Sun, L. Chen, J. Martin and G. S. Nolas, *Cryst. Growth Des.*, 2010, **10**, 3983. 5
- 202 B. Paul and A. Kumar, V and P. Banerji, *J. Appl. Phys.*, 2010, **108**, 064322.
- 203 A. S. Prakash, P. Manikandan, K. Ramesha, M. Sathiy, J. M. Tarascon and A. K. Shukla, *Chem. Mater.*, 2010, **22**, 2857.
- 204 M. S. Leo Hudson, P. K. Dubey, D. Pukazhselvan, S. K. Pandey, R. K. Singh, H. Raghubanshi, R. R. Shahi and O. N. Srivastava, *Int. J. Hydrogen Energy*, 2009, **34**, 7358. 10
- 205 S. K. Pandey, R. K. Singh and O. N. Srivastava, *Int. J. Hydrogen Energy*, 2009, **34**, 9379.
- 206 M. S. L. Hudson, H. Raghubanshi, D. Pukazhselvan and O. N. Srivastava, *Int. J. Hydrogen Energy*, 2012, **37**, 2750.
- 207 Z. Qian, M. S. L. Hudson, H. Raghubanshi, R. H. Scheicher, B. Pathak, C. M. Araújo, A. Blomqvist, B. Johansson, O. N. Srivastava and R. Ahuja, *J. Phys. Chem. C*, 2012, **116**, 10861. 15
- 208 E. A. Anumol, P. Kundu, P. A. Deshpande, G. Madras and N. Ravishankar, *ACS Nano*, 2011, **5**, 8049.
- 209 P. Kundu, C. Nethravathi, P. A. Deshpande, M. Rajamathi, G. Madras and N. Ravishankar, *Chem. Mater.*, 2011, **23**, 2772. 20
- 210 S. Jana, S. Pande, A. K. Sinha, S. Sarkar, M. Pradhan, M. Basu, Y. Negishi, A. Pal and T. Pal, *J. Nanosci. Nanotechnol.*, 2010, **10**, 847.
- 211 M. Basu, A. K. Sinha, M. Pradhan, S. Sarkar, A. Pal and T. Pal, *Chem. Commun.*, 2010, **46**, 8785.
- 212 D. Jana, A. Dandapat and G. De, *Langmuir*, 2010, **26**, 12177. 25
- 213 M. L. Kantam, J. Yadav, S. Laha, P. Srinivas, B. Sreedhar and F. Figueras, *J. Org. Chem.*, 2009, **74**, 4608.
- 214 R. Chakravarti, A. Mano, H. Iwai, S. S. Aldeyab, R. P. Kumar, M. L. Kantam and A. Vinu, *Chem. Eur. J.*, 2011, **17**, 6673.
- 215 P. Venkatesan and J. Santhanalakshmi, *Langmuir*, 2010, **26**, 12225.
- 216 K. K. R. Datta, B. V. S. Reddy, K. Ariga and A. Vinu, *Angew. Chem. Int. Ed.*, 2010, **49**, 5961. 30
- 217 A. Bej, D. Srimani and A. Sarkar, *Green Chem.*, 2012, **14**, 661.
- 218 A. Das, S. Pisana, B. Chakraborty, S. Piscanec, S. K. Saha, U. V. Waghmare, K. S. Novoselov, H. R. Krishnamurthy, A. K. Geim, A. C. Ferrari and A. K. Sood, *Nat. Nanotechnol.*, 2008, **3**, 210. 35
- 219 C. Biswanath, D. Anindya and A. K. Sood, *Nanotechnology*, 2009, **20**, 365203.
- 220 A. N. Pal and A. Ghosh, *Appl. Phys. Lett.*, 2009, **95**, 082105.
- 221 S. Ghatak, A. N. Pal and A. Ghosh, *ACS Nano*, 2011, **5**, 7707.
- 222 S. Sakshath, S. V. Bhat, K. P. S. Anil, D. Sander and J. Kirschner, *J. Appl. Phys.*, 2011, **109**, 07C114/1. 40
- 223 A. Prabhakar and S. Mukherji, *Lab Chip*, 2010, **10**, 3422.
- 224 S. Agrawal, A. Morarka, D. Bodas and K. M. Paknikar, *Appl. Biochem. Biotechnol.*, 2012, **167**, 1668.
- 225 V. Gautam, M. Bag and K. S. Narayan, *J. Am. Chem. Soc.*, 2011, **133**, 17942.
- 226 R. Mukherjee and A. Sharma, *ACS Appl. Mater. Interfaces*, 2012, **4**, 355. 45
- 227 A. Verma and A. Sharma, *RSC Adv.*, 2012, **2**, 2247.
- 228 A. Verma and A. Sharma, *Adv. Mater.*, 2010, **22**, 5306.
- 229 B. Radha, S. Kiruthika and G. U. Kulkarni, *J. Am. Chem. Soc.*, 2011, **133**, 12706.

-
- 230 B. Radha and G. U. Kulkarni, *Adv. Funct. Mater.*, 2010, **20**, 879. 1
- 231 S. Heun, B. Radha, D. Ercolani, G. U. Kulkarni, F. Rossi, V. Grillo, G. Salviati, F. Beltram and L. Sorba, *Cryst. Growth Des.*, 2010, **10**, 4197.
- 232 T. Bhuvana and G. U. Kulkarni, *Nanotechnology*, 2009, **20**, 5.
- 233 N. Kurra, A. Scott and G. U. Kulkarni, *Nano Res.*, 2010, **3**, 307. 5
- 234 M. Kesaria, S. Shetty and S. M. Shivaprasad, *Cryst. Growth Des.*, 2011, **11**, 4900.
- 235 R. Dikshit, P. C. Gupta, C. Ramasundarhettige, V. Gajalakshmi, L. Aleksandrowicz, R. Badwe, R. Kumar, S. Roy, W. Suraweera, F. Bray, M. Mallath, P. K. Singh, D. N. Sinha, A. S. Shet, H. Gelband and P. Jha, *The Lancet*, 2012, **379**, 1807. 10
- 236 S. S. Narayanan and S. K. Pal, *The Journal of Physical Chemistry C*, 2008, **112**, 4874.
- 237 N. Goswami, A. Giri, S. Kar, M. S. Bootharaju, R. John, P. L. Xavier, T. Pradeep and S. K. Pal, *Small*, 2012,-
- 238 D. Sahoo, P. Bhattacharya, H. K. Patra, P. Mandal and S. Chakravorti, *Journal of Nanoparticle Research*, 2011, **13**, 6755. 15
- 239 K. Chaudhari, P. L. Xavier and T. Pradeep, *ACS Nano*, 2011, **5**, 8816.
- 240 A. Gourishankar, S. Shukla, K. N. Ganesh and M. Sastry, *Journal of the American Chemical Society*, 2004, **126**, 13186.
- 241 S. Gupta, P. Babu and A. Surolia, *Biomaterials*, 2010, **31**, 6809.
- 242 S. Kundu, A. A. Kale, A. G. Banpurkar, G. R. Kulkarni and S. B. Ogale, *Biomaterials*, 2009, **30**, 4211. 20
- 243 J. Bhattacharya, S. Jasrapuria, T. Sarkar, R. GhoshMoulick and A. K. Dasgupta, *Nanomedicine-Nanotechnology Biology and Medicine*, 2007 **3**, 14.
- 244 S. Modi, M. G. Swetha, D. Goswami, G. D. Gupta, S. Mayor and Y. Krishnan, *Nat Nano*, 2009, **4**, 325. 25
- 245 D. Bhatia, S. Surana, S. Chakraborty, S. P. Koushika and Y. Krishnan, *Nat Commun*, 2011, **2**, 339.
- 246 D. Bhatia, S. Sharma and Y. Krishnan, *Current Opinion in Biotechnology*, 2011, **22**, 475.
- 247 S. Surana, J. M. Bhat, S. P. Koushika and Y. Krishnan, *Nat Commun*, 2011, **2**, 340. 30
- 248 S. Saha, D. Bhatia and Y. Krishnan, *Small*, 2010, **6**, 1288.
- 249 S. K. Sahoo, S. Parveen and J. J. Panda, *Nanomedicine-Nanotechnology Biology and Medicine*, 2007, **3**, 20.
- 250 C. Mohanty, M. Das, J. R. Kanwar and S. K. Sahoo, *Current Drug Delivery*, 2011, **8**, 45. 35
- 251 S. Acharya, F. Dilnawaz and S. K. Sahoo, *Biomaterials*, 2009, **30**, 5737.
- 252 S. Acharya and S. K. Sahoo, *Biomaterials*, 2011, **32**, 5643.
- 253 G. Arya, M. Vandana, S. Acharya and S. K. Sahoo, *Nanomedicine-Nanotechnology Biology and Medicine*, 2011, **7**, 859. 40
- 254 A. Pathak, P. Kumar, K. Chuttani, S. Jain, A. K. Mishra, S. P. Vyas and K. C. Gupta, *ACS Nano*, 2009, **3**, 1493.
- 255 G. Praveen, P. R. Sreerexha, D. Menon, S. V. Nair and K. P. Chennazhi, *Nanotechnology*, 2012, **23**-
- 256 A. K. Sahoo, M. P. Sk, S. S. Ghosh and A. Chattopadhyay, *Nanoscale*, 2011, **3**, 4226. 45
- 257 S. Shrivastava, T. Bera, S. K. Singh, G. Singh, P. Ramachandrarao and D. Dash, *ACS Nano*, 2009, **3**, 1357.
- 258 F. Dilnawaz, A. Singh, C. Mohanty and S. K. Sahoo, *Biomaterials*, 2010, **31**, 3694.
-

- 259 S. P. Chakraborty, S. K. Sahu, S. K. Mahapatra, S. Santra, M. Bal, S. Roy and P. Pramanik, *Nanotechnology*, 2010, **21**. 1
- 260 R. Ali, G. K. Jain, Z. Iqbal, S. Talegaonkar, P. Pandit, S. Sule, G. Malhotra, R. K. Khar, A. Bhatnagar and F. J. Ahmad, *Nanomedicine-Nanotechnology Biology and Medicine*, 2009, **5**, 55. 5
- 261 G. Bhakta, R. K. Sharma, N. Gupta, S. Cool, V. Nurcombe and A. Maitra, *Nanomedicine-Nanotechnology Biology and Medicine*, 2011, **7**, 472.
- 262 A. Mondal, R. Basu, S. Das and P. Nandy, *J. Nanopart. Res.*, 2011, **13**, 4519.
- 263 S. Das, P. K. Suresh and R. Desmukh, *Nanomedicine-Nanotechnology Biology and Medicine*, 2010, **6**, 318.
- 264 H. Gupta, M. Aqil, R. K. Khar, A. Ali, A. Bhatnagar and G. Mittal, *Nanomedicine-Nanotechnology Biology and Medicine*, 2010, **6**, 324. 10
- 265 R. Goyal, S. K. Tripathi, S. Tyagi, A. Sharma, K. R. Ram, D. K. Chowdhuri, Y. Shukla, P. Kumar and K. C. Gupta, *Nanomedicine-Nanotechnology Biology and Medicine*, 2012, **8**, 167.
- 266 S. K. Jain, Y. Gupta, A. Jain, A. R. Saxena and P. Khare, *Nanomedicine-Nanotechnology Biology and Medicine*, 2008, **4**, 41. 15
- 267 M. S. Umashankar, R. K. Sachdeva and M. Gulati, *Nanomedicine-Nanotechnology Biology and Medicine*, 2010, **6**, 419.
- 268 B. Wilson, M. K. Samanta, K. Santhi, K. P. S. Kumar, M. Ramasamy and B. Suresh, *Nanomedicine-Nanotechnology Biology and Medicine*, 2010, **6**, 144.
- 269 M. Ghosh, S. K. Sonkar, M. Saxena and S. Sarkar, *Small*, 2011, **7**, 3170. 20
- 270 M. Das, D. Mishra, T. K. Maiti, A. Basak and P. Pramanik, *Nanotechnology*, 2008, **19**.
- 271 P. Lourdu Xavier, K. Chaudhari, A. Baksi and T. Pradeep, *Nano Rev.*, 2012, **3**, 14767.
- 272 M. A. H. Muhammed, P. K. Verma, S. K. Pal, R. C. A. Kumar, S. Paul, R. V. Omkumar and T. Pradeep, *Chem. Eur. J.*, 2009, **15**, 10110. 25
- 273 M. A. H. Muhammed, P. K. Verma, S. K. Pal, A. Retnakumari, M. Koyakutty, S. Nair and T. Pradeep, *Chem. Eur. J.*, 2010, **16**, 10103.
- 274 A. Retnakumari, J. Jayasimhan, P. Chandran, D. Menon, S. Nair, U. Mony and M. Koyakutty, *Nanotechnology*, 2011, **22**.
- 275 A. Retnakumari, S. Setua, D. Menon, P. Ravindran, H. Muhammed, T. Pradeep, S. Nair and M. Koyakutty, *Nanotechnology*, 2010, **21**. 30
- 276 A. Ashokan, D. Menon, S. Nair and M. Koyakutty, *Biomaterials*, 2010, **31**, 2606.
- 277 P. Chandran, A. Sasidharan, A. Ashokan, D. Menon, S. Nair and M. Koyakutty, *Nanoscale*, 2011, **3**, 4150. 35
- 278 K. Manzoor, S. Johny, D. Thomas, S. Setua, D. Menon and S. Nair, *Nanotechnology*, 2009, **20**.
- 279 S. Setua, D. Menon, A. Asok, S. Nair and M. Koyakutty, *Biomaterials*, 2010, **31**, 714.
- 280 M. Das, D. Mishra, P. Dhak, S. Gupta, T. K. Maiti, A. Basak and P. Pramanik, *Small*, 2009, **5**, 2883. 40
- 281 T. P. Sastry, J. Sundaraseelan, K. Swarnalatha, S. S. L. Sobhana, M. U. Makheswari, S. Sekar and A. B. Mandal, *Nanotechnology*, 2008, **19**.
- 282 K. T. Shalumon, K. H. Anulekha, S. V. Nair, K. P. Chennazhi and R. Jayakumar, *International Journal of Biological Macromolecules*, 2011, **49**, 247.
- 283 A. Tripathi, S. Saravanan, S. Pattnaik, A. Moorthi, N. C. Partridge and N. Selvamurugan, *International Journal of Biological Macromolecules*, 2012, **50**, 294. 45
- 284 R. Vani, S. B. Raja, T. S. Sridevi, K. Savithri, S. N. Devaraj, E. K. Girija, A. Thamizhavel and S. N. Kalkura, *Nanotechnology*, 2011, **22**.

-
- 285 S. Reddy, S. Wasnik, A. Guha, J. M. Kumar, A. Sinha and S. Singh, *J. Biomater. Appl.*, 2012. 1
- 286 M. Bhattacharjee, S. Miot, A. Gorecka, K. Singha, M. Loparic, S. Dickinson, A. Das, N. S. Bhavesh, A. R. Ray, I. Martin and S. Ghosh, *Acta Biomater.*, 2012. 5
- 287 A. Subramanian, U. M. Krishnan and S. Sethuraman, *J. Mater. Sci.: Mater. Med.*, 2012, **23**, 1797.
- 288 S. Srinivasan, R. Jayakumar, K. P. Chennazhi, E. J. Levorson, A. G. Mikos and S. V. Nair, in *Biomedical Applications of Polymeric Nanofibers*, eds. R. Jayakumar and S. V. Nair, Springer-Verlag Berlin, Berlin, 2012, vol. 246, pp. 1. 10
- 289 M. S. O. Rafsanjani, A. Alviri, M. Samim, M. A. Hejazi and M. Z. Abdin, *Recent Patents on Biotechnology*, 2012, **6**, 69.
- 290 A. Dey, B. Bagchi, S. Das, R. Basu and P. Nandy, *Journal of Environmental Monitoring*, 2011, **13**, 1709.
- 291 V. Ghormade, M. V. Deshpande and K. M. Paknikar, *Biotechnology Advances*, 2011, **29**, 792. 15
- 292 S. Naqvi, A. N. Maitra, M. Z. Abdin, M. Akmal, I. Arora and M. Samim, *Journal of Materials Chemistry*, 2012, **22**, 3500.
- 293 P. S. Vijayakumar, O. U. Abhilash, B. M. Khan and B. L. V. Prasad, *Advanced Functional Materials*, 2010, **20**, 2416.
- 294 T. N. V. K. V. Prasad, P. Sudhakar, Y. Sreenivasulu, P. Latha, V. Munaswamy, K. R. Reddy, T. S. Sreeprasad, P. R. Sajanlal and T. Pradeep, *J. Plant Nutr.*, 2012, **35**, 905. 20
- 295 A. Mondal, R. Basu, S. Das and P. Nandy, *Journal of Nanoparticle Research*, 2011, **13**, 4519.
- 296 S. Tripathi, S. K. Sonkar and S. Sarkar, *Nanoscale*, 2011, **3**, 1176. 25
- 297 A. Dhawan, V. Sharma and D. Parmar, *Nanotoxicology*, 2009, **3**, 1.
- 298 M. Das, N. Saxena and P. D. Dwivedi, *Nanotoxicology*, 2009, **3**, 10.
- 299 P. D. Dwivedi, A. Misra, R. Shanker and M. Das, *Nanotoxicology*, 2009, **3**, 19.
- 300 A. Dhawan, D. Anderson (Eds.), *The Comet Assay In Toxicology*, Royal Society of Chemistry, 2009.
- 301 A. K. Jain, N. K. Mehra, N. Lodhi, V. Dubey, D. K. Mishra, P. K. Jain and N. K. Jain, *Nanotoxicology*, 2007, **1**, 167. 30
- 302 J. Kayat, V. Gajbhiye, R. K. Tekade and N. K. Jain, *Nanomedicine-Nanotechnology Biology and Medicine*, 2011, **7**, 40.
- 303 M. Ghosh, M. Bandyopadhyay and A. Mukherjee, *Chemosphere*, 2010, **81**, 1253. 35
- 304 M. Ghosh, A. Chakraborty, M. Bandyopadhyay and A. Mukherjee, *Journal of Hazardous Materials*, 2011, **197**, 327.
- 305 S. Pakrashi, S. Dalai, D. Sabat, S. Singh, N. Chandrasekaran and A. Mukherjee, *Chemical Research in Toxicology*, 2011, **24**, 1899.
- 306 I. M. Sadiq, S. Pakrashi, N. Chandrasekaran and A. Mukherjee, *Journal of Nanoparticle Research*, 2011, **13**, 3287. 40
- 307 M. Premanathan, K. Karthikeyan, K. Jeyasubramanian and G. Manivannan, *Nanomedicine-Nanotechnology Biology and Medicine*, 2011, **7**, 184.
- 308 S. Shrivastava, T. Bera, A. Roy, G. Singh, P. Ramachandrarao and D. Dash, *Nanotechnology*, 2007, **18**.
- 309 A. K. Chatterjee, R. K. Sarkar, A. P. Chattopadhyay, P. Aich, R. Chakraborty and T. Basu, *Nanotechnology*, 2012, **23**. 45
- 310 S. Deb, H. K. Patra, P. Lahiri, A. K. Dasgupta, K. Chakrabarti and U. Chaudhuri, *Nanomedicine-Nanotechnology Biology and Medicine*, 2011, **7**, 376.
-

-
- 311 S. Deb, M. Chatterjee, J. Bhattacharya, P. Lahiri, U. Chaudhuri, S. P. Choudhuri, S. Kar, O. P. Siwach, P. Sen and A. K. Dasgupta, *Nanotoxicology*, 2007, **1**, 93. 1
- 312 R. P. Nishanth, R. G. Jyotsna, J. J. Schlager, S. M. Hussain and P. Reddanna, *Nanotoxicology*, 2011, **5**, 502. 5
- 313 M. I. Khan, A. Mohammad, G. Patil, S. A. H. Naqvi, L. K. S. Chauhan and I. Ahmad, *Biomaterials*, 2012, **33**, 1477.
- 314 H. K. Patra, S. Banerjee, U. Chaudhuri, P. Lahiri and A. K. Dasgupta, ~~*Nanomedicine-Nanotechnology-Biology and Medicine*~~, 2007, **3**, 111.
- 315 R. K. Srivastava, A. B. Pant, M. P. Kashyap, V. Kumar, M. Lohani, L. Jonas and Q. Rahman, *Nanotoxicology*, 2011, **5**, 195. 10
- 316 A. Sasidharan, L. S. Panchakarla, P. Chandran, D. Menon, S. Nair, C. N. R. Rao and M. Koyakutty, *Nanoscale*, 2011, **3**, 2461.
- 317 P. Palaniappan and K. S. Pramod, *Vib. Spectrosc.*, 2011, **56**, 146.
- 318 P. Surekha, A. S. Kishore, A. Srinivas, G. Selvam, A. Goparaju, P. N. Reddy and P. B. Murthy, ~~*Cutaneous and Ocular Toxicology*~~, 2012, **31**, 26. 15
- 319 P. Dandekar, R. Dhupal, R. Jain, D. Tiwari, G. Vanage and V. Patravale, ~~*Food and Chemical Toxicology*~~, 2010, **48**, 2073.
- 320 T. Dutta, M. Garg, V. Dubey, D. Mishra, K. Singh, D. Pandita, A. K. Singh, A. K. Ravi, T. Velpandian and N. K. Jain, *Nanotoxicology*, 2008, **2**, 62.
- 321 P. Manna, M. Ghosh, J. Ghosh, J. Das and P. C. Sil, *Nanotoxicology*, 2012, **6**, 1. 20
- 322 <http://www.nanotech-now.com/columns/?article=069> (Accessed on July 30, 2012).
- 323 http://www.nanowerk.com/nanotechnology/Nanotechnology_Companies_in_India.php (Accessed on July 31, 2012).
- 324 B. R. Mehta, *J. Nano Educ.*, 2009, **1**, 106. 25
- ~~325 S. S. Shankar, A. Rai, B. Ankamwar, A. Singh, A. Ahmad and M. Sastry, *Nat. Mater.*, 2004, **3**, 482.~~
- ~~326 B. K. Jena and C. R. Raj, *Chem. Mater.*, 2008, **20**, 3546.~~
- ~~327 P. Sajanalal and T. Pradeep, *Nano Res.*, 2009, **2**, 306.~~
- ~~328 T. U. B. Rao, B. Nataraju and T. Pradeep, *J. Am. Chem. Soc.*, 2010, **132**, 16304.~~ 30

35

40

45

Atomically precise silver clusters for efficient chlorocarbon degradation†

Cite this: *J. Mater. Chem. A*, 2013, **1**, 611

M. S. Bootharaju,‡ G. K. Deepesh,‡ T. Udayabhaskararao and T. Pradeep*

We describe the degradation of chlorocarbons (CCl_4 , $\text{C}_6\text{H}_5\text{CH}_2\text{Cl}$ and CHCl_3) in solution at room temperature (27 ± 4 °C) by the monolayer-protected silver quantum cluster, Ag_9MSA_7 (MSA: mercaptosuccinic acid) in the presence of isopropyl alcohol (IPA). The main degradation products were silver chloride and amorphous carbon. Benzyl chloride was less reactive towards clusters than CCl_4 and CHCl_3 . Materials used in the reactions and the reaction products were characterized using several spectroscopic and microscopic tools such as ultraviolet-visible (UV/Vis) absorption spectroscopy, Fourier transform infrared spectroscopy (FTIR), photoluminescence spectroscopy, X-ray diffraction (XRD), Raman spectroscopy, X-ray photoelectron spectroscopy (XPS), energy dispersive analysis of X-rays (EDAX) and scanning electron microscopy (SEM). We have shown that clusters are more efficient for the degradation of halocarbons than the corresponding monolayer-protected nanoparticles (Ag@MSA , particle diameter 15 ± 5 nm) at a given time and temperature. The higher reactivity of clusters is attributed to their small size and large surface area. Clusters and nanoparticles were used for reactions in supported (on neutral alumina) and unsupported forms. A possible mechanism for the reaction has been postulated on the basis of experimental results.

Received 10th September 2012

Accepted 12th October 2012

DOI: 10.1039/c2ta00254j

www.rsc.org/MaterialsA

Introduction

Research on noble metal (silver and gold) quantum clusters^{1,2} has become increasingly fascinating in the last two decades. Quantum clusters, composed of a few tens to hundreds of atoms at the core and protected with ligands, are the connecting link between nanoparticles and molecules which exhibit molecular optical properties like absorption,^{3,4} emission,^{5,6} chirality,⁷ etc. These nanosystems are very interesting because they show several applications in various fields such as catalysis,^{8,9} biology,¹⁰ environmental remediation,¹¹ etc. They are highly reactive due to their extremely small size and large surface area. They show unusual reactivity with salts.¹² Metal clusters exhibit the property of alloying with other metals.^{13,14} Clusters have been used for sensing metal ions^{15–17} and anions¹⁸ by using their luminescence property.

The environment has been contaminated by a large number of pollutants like organic halides¹⁹ (chlorofluorocarbons (CFC), C_2Cl_4 , C_2ClF_3 , CCl_4 , etc.), heavy metals²⁰ (Hg, Pb, Cd, Cr, etc. in various forms), energetic materials²¹ (hexahydro-1,3,5-trinitro-

1,3,5-triazine (RDX) and 2,4,6-trinitrotoluene (TNT)), and many others. Halocarbons are harmful trace components in water and air, either in the context of biological toxicity or due to their global warming potential or undesirable atmospheric chemistry.²² The main sources of these are cleaning solvents, lubricants, plasticizers and refrigerants. Several of these have been replaced by less harmful chemicals. However, many of them continue to be used due to economic considerations or the lack of suitable replacements. CCl_4 is a widely used solvent in industry, research laboratories, dry cleaning, etc.²³ It is carcinogenic and it can persist in ground and surface waters. Due to this, it is one of the complex contaminants. The maximum allowed level of CCl_4 in surface water is $5 \mu\text{g L}^{-1}$.²⁴ CFCs cause depletion of the ozone layer.²⁵ Various methods such as photodecomposition,²⁶ incineration,²⁷ photocatalysis^{28,29} and adsorption³⁰ are developed to eliminate halocarbons from the environment. Chlorinated halocarbons are degraded by reductive mechanisms.³¹ There are four types of reductive mechanisms: hydrogenolysis, elimination, dehydrohalogenation and hydrogenation.

Nanoparticles are increasingly used for environmental applications due to increased amount of contaminants in soil and groundwater.³² Common nanoparticles used for halocarbon degradation in the literature are iron in oxide and zero-valent forms,³¹ MgO ³³ and ZnO .³⁴ In most of the above studies, nanoparticles form corresponding metal halides as principal products at high temperatures. Recently, noble metal and oxide nanoparticles have been studied in the degradation of

DST Unit of Nanoscience (DST UNS), Department of Chemistry, Indian Institute of Technology Madras, Chennai - 600 036, India. E-mail: pradeep@iitm.ac.in

† Electronic supplementary information (ESI) available: SEM elemental analysis and photograph of supported silver clusters, UV/Vis absorption spectrum and TEM image of Ag@MSA nanoparticles, XPS, XRD, Raman and EDAX data of the products of the reaction between supported clusters and CCl_4 . See DOI: 10.1039/c2ta00254j

‡ These authors have contributed equally.

halocarbons.³⁵ Our research group has pioneered the use of noble metal nanoparticles for the removal of pesticides and halocarbons from drinking water.^{36–40}

The standard Gibbs free energy change of formation ($\Delta_f G^0$) of AgCl(s) and CCl₄(l) are -109.8 and -65.2 kJ mol⁻¹, respectively. The net free energy change for the reaction $4\text{Ag(s)} + \text{CCl}_4(\text{l}) \rightarrow 4\text{AgCl(s)} + \text{C (graphite)}$ is -374.0 kJ mol⁻¹. This indicates that the above reaction is feasible at 298 K and 1 atm pressure. The cell electromotive force (emf), E_{cell}^0 , for the reduction of CCl₄ by silver (in the above reaction) is calculated to be 0.97 V using the equation $\Delta_r G^0 = -4FE_{\text{cell}}^0$, where F is Faraday's constant (96 500 C or J/V). The reaction may be slow but it is feasible. However, by using materials at the nanoscale, particularly silver at the nano/cluster length scale, the reduction potential is expected to reduce significantly as nanoscale silver is metastable with respect to the bulk. Due to the reduced dimension, the reaction is likely to be kinetically more favorable. Therefore, we may see interesting reactivity. This motivated us to study the reaction of CCl₄ with silver quantum clusters.

In the context of environmental applications, there are only a few studies on metal clusters. A study of sensitivity of Au₂₅ clusters, one of the most studied clusters, to various metal ions was performed by Habeeb Muhammed and Pradeep.¹² Subsequently, a number of studies have shown the effect of metal ions on monolayer-protected as well as protein-protected gold clusters.^{10,15,41} Sensing experiments have been performed with silver clusters as well.^{16,17} There is a large need to develop techniques to use such materials as commercial products. Here, we utilized Ag₉ clusters protected with mercaptosuccinic acid (MSA) for the complete catalytic degradation of CCl₄, CHCl₃ and C₆H₅CH₂Cl at room temperature. The reaction products were AgCl, CCl₃COOH, amorphous carbon and acetone. We found that isopropyl alcohol (IPA), used to increase the solubility of halocarbons in water, is very important in the reaction. Mechanistic aspects of the reaction are discussed based on experimental results. We propose that Cl⁻ ions, which are formed due to the cleavage of Cl₃C–Cl, replace the thiolates on the surface of the cluster. As a result, stability of the cluster is lost which causes the interaction of silver with Cl⁻, leading to the formation of AgCl. The detached thiolates are converted to stable sulphites/sulphates in solution, the presence of which was confirmed by XPS. We demonstrate the increased efficiency of clusters for halocarbon degradation compared to analogous MSA protected silver nanoparticles. Reactions were carried out with clusters supported on alumina also, in which observations similar to unsupported clusters were noted.

Experimental section

Materials

Silver nitrate (CDH, India), mercaptosuccinic acid (MSA), sodium borohydride (Sigma Aldrich), methanol, ethanol, isopropyl alcohol (IPA), carbon tetrachloride (CCl₄), benzyl chloride (C₆H₅CH₂Cl) and chloroform (CHCl₃) (SRL Chemical Co. Ltd., India) were purchased from various sources and used as such without further purification. Neutral alumina was

supplied by SRL, India. The surface area and the mean particle size were 900 ± 50 cm² g⁻¹ and 0.13 μm, respectively.

Synthesis of silver clusters

The Ag₉MSA₇ cluster was synthesized according to the reported protocol.⁴² Briefly, 47 mg of AgNO₃(s) and 187 mg of MSA(s) were ground until the mixture turned orange due to the formation of Ag-thiolates. After that, about 50 mg of NaBH₄(s) was added to it and grinding was continued for 2–3 minutes. To this, 10 mL of distilled water was added which led to the formation of clusters. The cluster was precipitated by the addition of ethanol. The precipitate was washed several times with pure methanol to remove excess NaBH₄, MSA and thiolates. Finally, a reddish brown powder of the clusters was obtained after evaporation of methanol using a rotavapor.

Synthesis of Ag@MSA nanoparticles

Ag@MSA nanoparticles were prepared as per the previous report.²⁰ Nearly 1.7 mL of distilled water containing 85 mg of AgNO₃ was added to 100 mL of methanol containing 448.9 mg of MSA which was kept at 0–5 °C. The resulting solution was stirred at 4000 rpm. 25 mL of freshly prepared 0.2 M NaBH₄ solution was added to the above solution drop-wise. Stirring was continued for 45 minutes at 0–5 °C. The mixture containing the precipitate of nanoparticles was centrifuged and the residue was washed with methanol to remove excess MSA and NaBH₄. Finally, a black powder of nanoparticles was obtained by evaporating methanol using a rotavapor.

Preparation of supported clusters and nanoparticles on neutral alumina

Loading of clusters was done by the addition of cluster solution (known amount) to a calculated amount of alumina followed by shaking with a mechanical shaker. The color of the solution disappeared immediately, indicating adsorption of clusters on alumina. The addition of cluster solution and shaking were continued until the supernatant retained the color of the cluster solution, indicating saturation loading. The supernatant at this stage showed the absorption features of the clusters, indicating the saturation of the alumina surface with adsorbed clusters. The saturation limit was found to be 10 mg per gram of alumina. After surface saturation, the supernatant was removed by centrifugation. Supported clusters were washed with water followed by methanol to remove the excess cluster. A solvent-free material was obtained by evaporation using a rotavapor. The same method was followed to prepare Ag@MSA nanoparticles supported on neutral alumina.

Reaction of halocarbons with clusters and nanoparticles

Nearly 5 mL of CCl₄ was added to the cluster solution (25 mg in 30 mL water). To this, 10 mL of isopropyl alcohol (IPA) was added. Here, the importance of IPA was to increase the miscibility of CCl₄ in the reaction mixture (solubility of CCl₄ = 800 mg L⁻¹ in water at 298 K). The above mixture (orange red color) was stirred at 4000 rpm for 24 h at room temperature. The CCl₄ layer

disappeared and a grey colored precipitate was formed after 1.5 h. These observations indicate the occurrence of reaction between clusters and CCl_4 . Reactions were carried out in methanol and ethanol as well in place of IPA. In these cases, no reaction was seen. A probable reason is that oxidation of IPA is more facile than other alcohols (methanol and ethanol). Other halocarbons, CHCl_3 and $\text{C}_6\text{H}_5\text{CH}_2\text{Cl}$, were used in place of CCl_4 under identical experimental conditions. A precipitate was formed after 24 h in the case of benzyl chloride, indicating less reactivity. In the case of supported clusters, 500 mg of the material was used under the above experimental conditions. Similar quantities of $\text{Ag}@\text{MSA}$ nanoparticles (both unsupported and supported) were also used for the reaction of halocarbons.

Instrumentation

UV/Vis absorption spectra were recorded with a PerkinElmer Lambda 25 instrument in the spectral range of 200 to 1100 nm. FTIR spectra were recorded with a PerkinElmer Spectrum One instrument. KBr crystals were used as the matrix for preparing the samples. X-ray photoelectron spectroscopy (XPS) measurements were done using an Omicron ESCA Probe spectrometer with polychromatic $\text{Mg K}\alpha$ X-rays ($h\nu = 1253.6$ eV). Experiments were carried out at an X-ray power of 300 W and pass energies of 50 eV for survey scans and 20 eV for specific regions. The base pressure of the instrument was 5.0×10^{-10} mbar. The binding energy was calibrated with respect to the adventitious C 1s feature at 285.0 eV. Most of the spectra were deconvoluted to their component peaks using the software CASA XPS. Scanning electron microscopy (SEM) and energy dispersive analysis of X-rays (EDAX) were performed using a FEI QUANTA-200 SEM. For the SEM measurements, samples were spotted on an indium tin oxide (ITO)-coated conducting glass and dried in ambience. X-ray diffraction (XRD) data were collected with a Shimadzu XD-D1 diffractometer using $\text{Cu K}\alpha$ ($\lambda = 1.54 \text{ \AA}$) radiation. The samples were scanned in the 2θ range of 10 to

90° . The electrospray ionization mass spectrometry (ESI MS) measurements were done in the negative and positive modes using a MDX Sciex 3200 QTRAP MS/MS instrument having a mass range of m/z 50–1700, in which the spray and the extraction are orthogonal to each other. The samples were electrosprayed at a flow rate of $10 \mu\text{L min}^{-1}$ and an ion spray voltage of 5 kV. The spectra were averaged for 100 scans. MS/MS spectra were collected at optimized collision energies in the range of 25–45 eV.

Results and discussion

Starting materials: clusters, nanoparticles and supported materials

Silver nanoclusters (Ag_9MSA_7) and $\text{Ag}@\text{MSA}$ nanoparticles have been well characterized as per other reports^{20,42} and we present here only the essential data. As-synthesized silver clusters show characteristic UV/Vis absorption features at 450, 490, 626 and 886 nm (Fig. 1A). These clusters showed red emission at 726 nm when excited at 590 nm in a water–methanol mixture at 5°C (inset of Fig. 1A). These two data prove the formation of clusters. The evidence for the binding of MSA to the cluster core was obtained by FTIR analysis (Fig. 1B). Pure MSA shows a characteristic $-\text{CO}-$ of free carboxylate and $\text{S}-\text{H}$ stretching peaks at 1700 and 2566 cm^{-1} , respectively (trace (a)). In the cluster sample, carboxylate stretching mode got shifted to 1576 cm^{-1} and the $\text{S}-\text{H}$ stretching peak was absent (trace (b)). The presence of characteristic peaks of MSA in clusters (trace (b)) with a characteristic shift in peak positions in comparison to parent MSA (trace (a)) confirms the binding of MSA. The absence of the $\text{S}-\text{H}$ feature (marked in trace (a)) in the cluster sample shows the binding of MSA with the cluster through an $\text{Ag}-\text{S}$ linkage.⁴² The chemical nature of silver and sulphur was confirmed by XPS (discussed later).

Supported clusters on alumina were characterized by SEM EDAX and the data are shown in Fig. S1 of ESI.† The spectrum

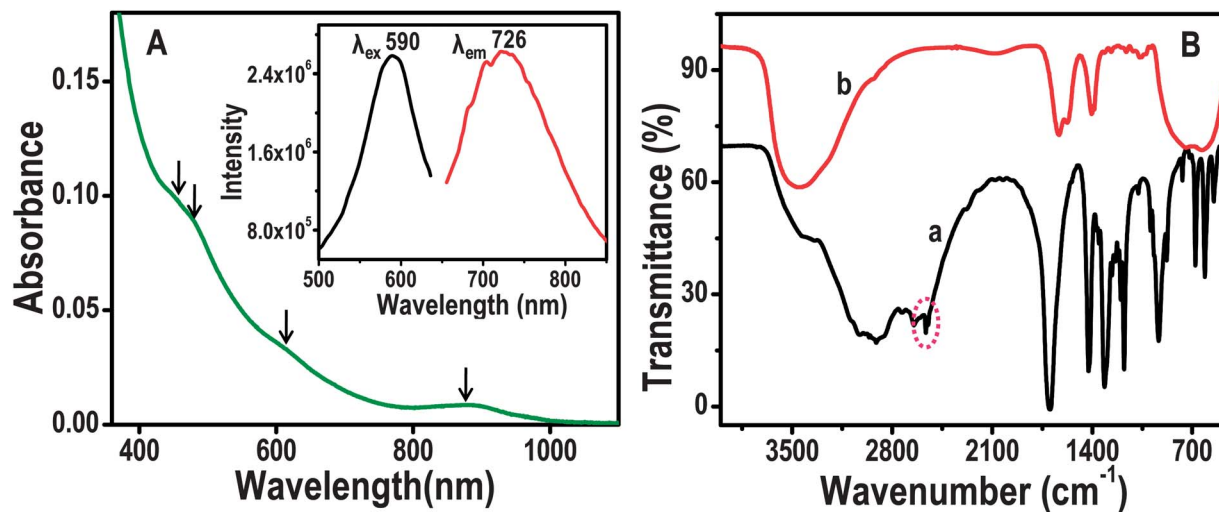


Fig. 1 (A) UV/Vis absorption spectrum of as-synthesized Ag_9MSA_7 clusters. Inset of (A) is the photoluminescence excitation and emission spectra of the clusters. They show emission at 726 nm when excited at 590 nm, at 5°C . (B) Comparison of the FTIR spectra of MSA and Ag_9MSA_7 (traces (a) and (b), respectively); the latter shows the absence of $\text{S}-\text{H}$ stretching in (b).

shows the presence of elements silver and sulphur which confirms the adsorption of clusters. Important evidence to show the presence of clusters on alumina is the red luminescence of the supported cluster kept under a UV lamp at liquid nitrogen temperature (inset of Fig. S1[†]). Bare alumina does not show any luminescence under UV lamp. The Ag@MSA nanoparticles were characterized by absorption spectroscopy. Silver nanoparticles show a surface plasmon resonance band at 392 nm which proves the formation of nanoparticles (Fig. S2[†]). TEM analysis of nanoparticles shows the average size to be 15 ± 5 nm (inset of Fig. S2[†]).

Reaction with CCl_4

We performed reactions with unsupported and supported clusters (on alumina) which are presented separately.

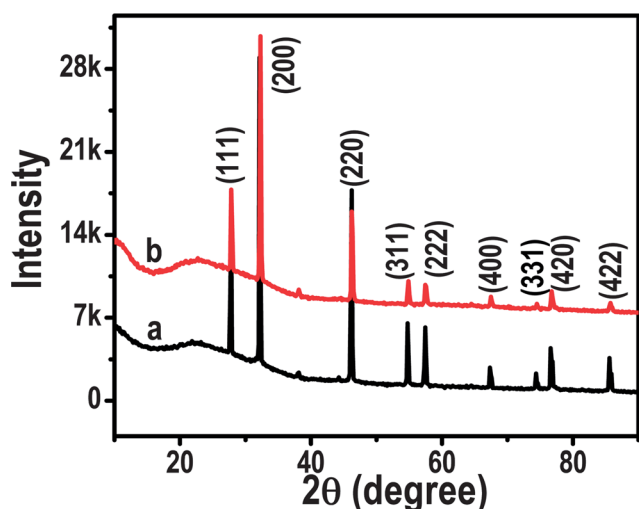


Fig. 2 XRD of as-prepared AgCl (a) and the product (b) obtained due to the reaction of Ag_9MSA_7 with CCl_4 . The data have not been corrected for the background.

A. UNSUPPORTED CLUSTERS. The reactions were performed as described in the Experimental section. We have products in the solid state and products in solution. While the former are studied by XRD, Raman, IR, *etc.*, the latter are studied by mass spectrometry. The grey colored precipitate and colorless supernatant obtained after the reaction of CCl_4 and clusters were characterized with various analytical tools. The XRD pattern of the precipitate is shown in Fig. 2. It matches exactly with as-prepared AgCl (a precipitate obtained after mixing solutions of AgNO_3 and NaCl). This observation confirms the formation of AgCl as the reaction product.

The precipitate was used for Raman analysis before and after washing with ammonia solution (Fig. 3A). The purpose of washing with ammonia was to remove AgCl as a soluble complex, $[\text{Ag}(\text{NH}_3)_2]^+\text{Cl}^-$. After that, the solution was centrifuged at 10 000 rpm. A black residue was obtained which was analyzed by Raman spectroscopy. The unwashed precipitate (trace (a)) shows the presence of peaks at ~ 1408 and ~ 1575 cm^{-1} . These are attributed to D and G bands of carbonaceous species which is due to the formation of carbon from degradation of CCl_4 .⁴³ After washing with ammonia, the peaks got shifted to ~ 1357 and ~ 1590 cm^{-1} (trace (b)). This shift may be due to the removal of impurities like AgCl which are soluble in ammonia. The red shift of the D band may be due to variation in defects (due to washing with NH_3 solution) of the graphitic structure and the blue shift of the G band is due to further amorphization of carbon due to removal of impurities.⁴⁴ Comparison of FTIR data of the reaction product (Fig. 3B) and the parent cluster (trace (a) in the inset of Fig. 3B) further supports the formation of the carbonaceous material. The stretching modes of the carboxylate group at 1576 and 1407 cm^{-1} are completely absent in the reaction product (trace (b) in the inset of Fig. 3B). This confirms the removal of a monolayer of MSA from the cluster. The peak at 1625 cm^{-1} in traces (a) and (b) is due to adsorbed water. A strong peak at 1384 cm^{-1} has emerged due to the presence of carbonaceous

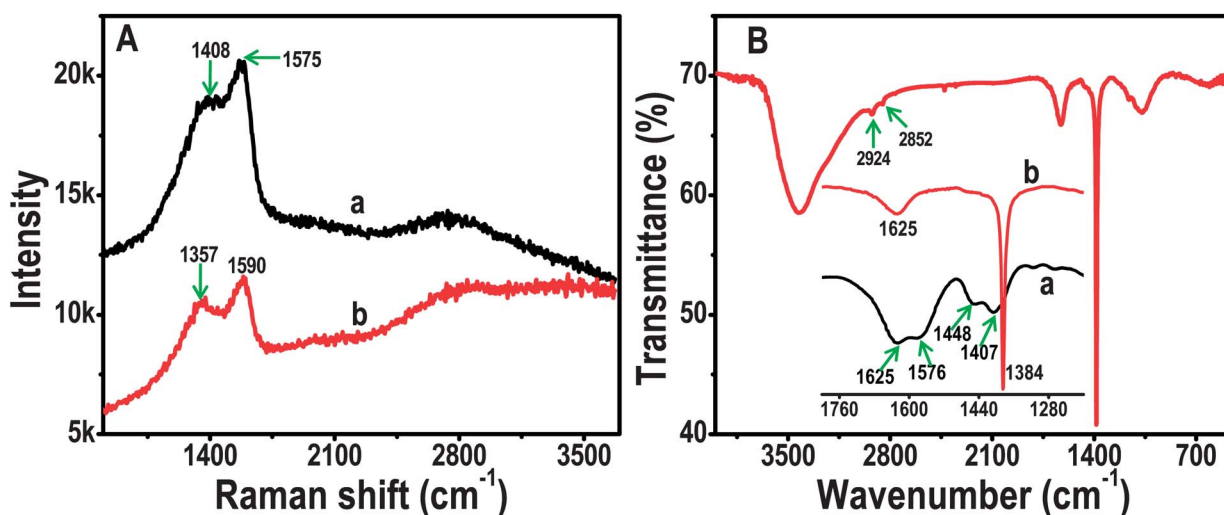


Fig. 3 (A) Raman spectra of the reaction product of Ag_9MSA_7 and CCl_4 before and after washing ((a) and (b), respectively) with aqueous ammonia. (B) FTIR spectrum of the reaction product before washing. Inset of (B) is the FTIR spectra of parent clusters (a) and the reaction product (b) in a specific region.

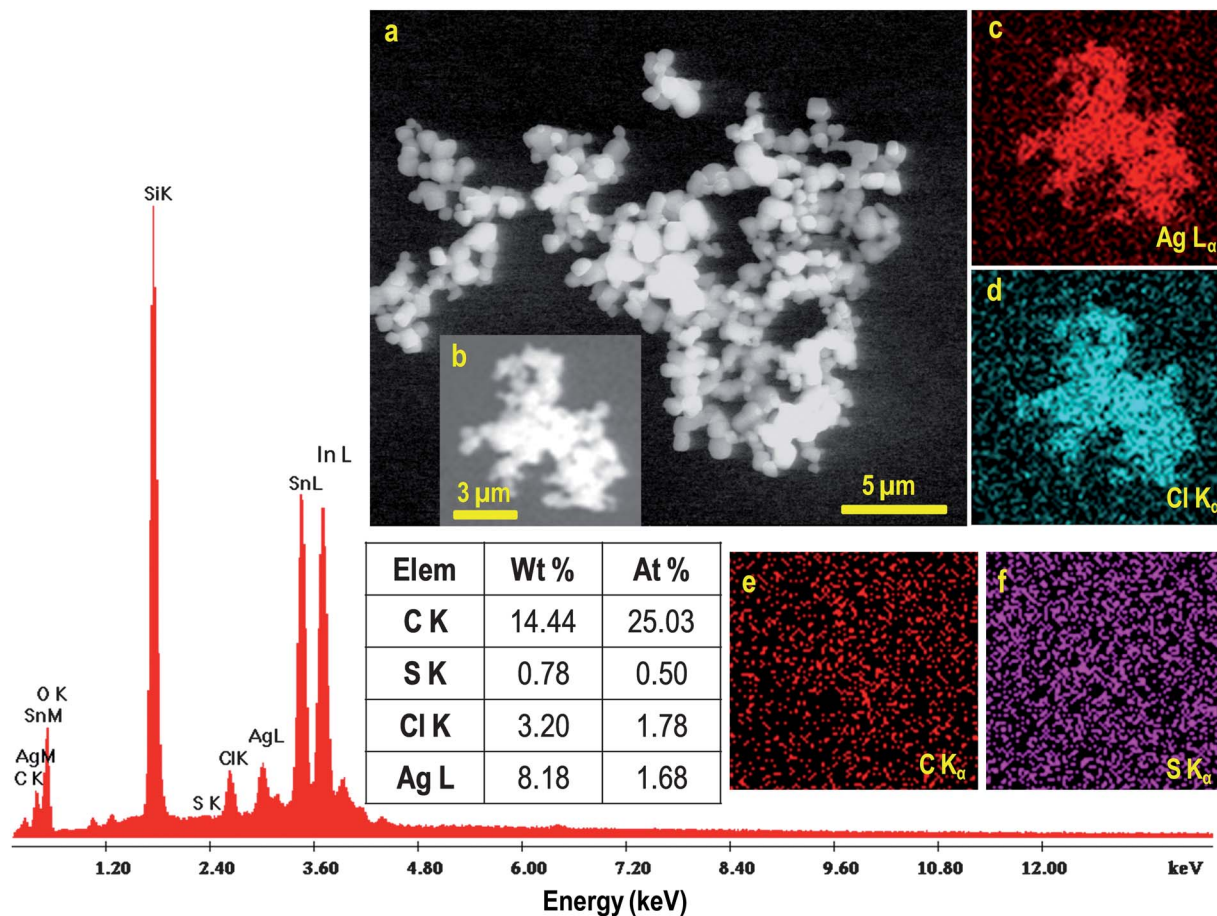


Fig. 4 EDAX spectrum of the product obtained after the reaction of the Ag₉MSA₇ cluster with CCl₄. The quantification table of elements in the EDAX spectrum is also shown. Si, In and Sn are due to the indium tin oxide substrate used. (a) and (b) are SEM images of the above sample. Elements Ag, Cl, C and S of the region shown in (b) are mapped in (c)–(f), respectively using X-ray energies of Ag L α , Cl K α , C K α and S K α .

species which confirms the formation of carbon, possibly as a graphitic product.⁴⁵ The other peaks at 2924 and 2852 cm⁻¹ in Fig. 3B are due to the C–H stretching mode in graphitic carbon. The presence of chemically transformed sulphur species (sulphite/sulphate) which are adsorbed on the reaction product and the absence of carboxylate features were confirmed by XPS (discussed later). From all these, it is evident that a monolayer of the cluster has been transformed chemically. However, the mechanism is complex and is not understood well.

SEM analysis of the precipitate is given in Fig. 4. Fig. 4a is a large area SEM image. It shows the presence of AgCl crystals. The elemental maps of the area shown in (b) are presented in (c)–(f). They clearly show the presence of elements Ag, Cl and a little amount of C. The EDAX spectrum collected from a portion of the sample is shown in Fig. 4. It shows the presence of elements Ag, Cl and trace amounts of S. The quantification table of elements of the same area (in Fig. 4) shows the presence of Ag and Cl in 1 : 1 atomic ratio which matches with AgCl composition. Also it shows the atomic percent of C and S in which sulphur was seen less in quantity.

In Fig. 5, XPS data of the precipitate (traces (b)) are compared with parent silver clusters (traces (a)). In the survey spectra of both the samples, carbon, silver, sulphur and oxygen were

present (Fig. 5A). After the reaction, a new peak around 200.0 eV appears due to the presence of chlorine. The C 1s regions of the cluster and the reaction product clearly indicate the almost complete disappearance of the peak at 288.9 eV due to the carboxylate⁴⁶ groups in the product (Fig. S3†). This observation is also supported by FTIR analysis which confirms the replacement of the ligand MSA on the cluster. The intensity of the peak at 286.5 eV (due to carbon in C–O) increased compared to the parent clusters. The Ag 3d regions of both the samples are compared in Fig. 5B. Before the reaction, Ag 3d_{5/2} appeared at 368.1 eV whereas it is at 367.6 eV after the reaction. This clearly reveals the oxidation of silver from Ag⁰ to Ag⁺ state.¹⁶ Note that in Ag, oxidation leads to shifting of binding energy to lower values.¹⁶ The S 2p region due to the monolayer of the cluster is shown in Fig. 5C. Before the reaction, S 2p_{3/2} was at 162.1 eV assigned to sulphur bound to the cluster in the thiolate form. After the reaction, it shifted to 168.5 eV. This suggests the chemical change of the monolayer due to the reaction of the cluster core. This peak is assigned to sulphate/sulphite species.⁴⁷ The Cl 2p feature (Fig. 5D) is quite broad and it is fitted into two components corresponding to two types of Cl moieties. The Cl 2p_{3/2} positions are at 198.9 and 201.1 eV. The former peak may be due to chemisorbed chloride⁴⁸ possibly

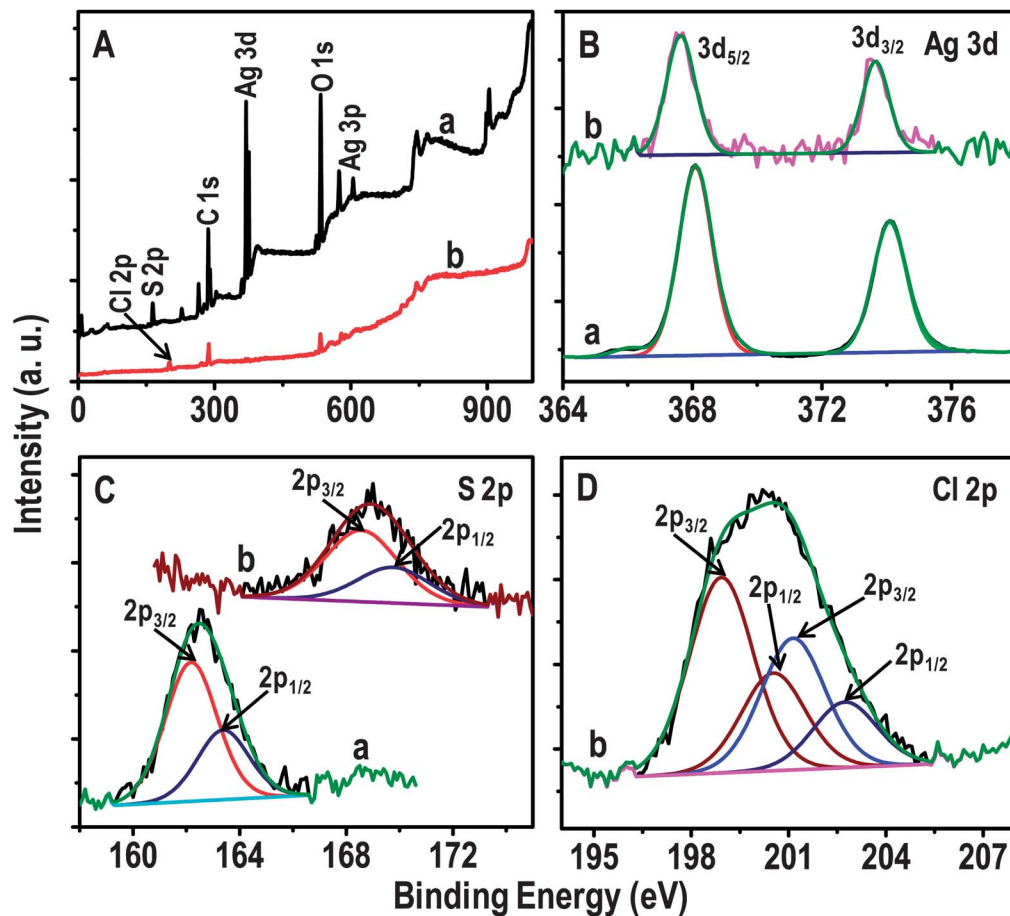


Fig. 5 XPS of parent Ag_9MSA_7 clusters (a) and the product obtained after the reaction of clusters with CCl_4 (b). (A–D) survey spectra, Ag 3d, S 2p and Cl 2p regions, respectively.

from AgCl and the latter may be due to adsorbed organic chlorine, possibly from CCl_4 .^{39,49} While all the silver got reacted in this sample, there could be some CCl_4 left behind.

During the progress of the reaction, we have followed the variation in pH of the solution with time (Fig. 6A). Initially, the pH of the reaction mixture was 5.7. The pH after 1.0, 2.0, 3.0 and

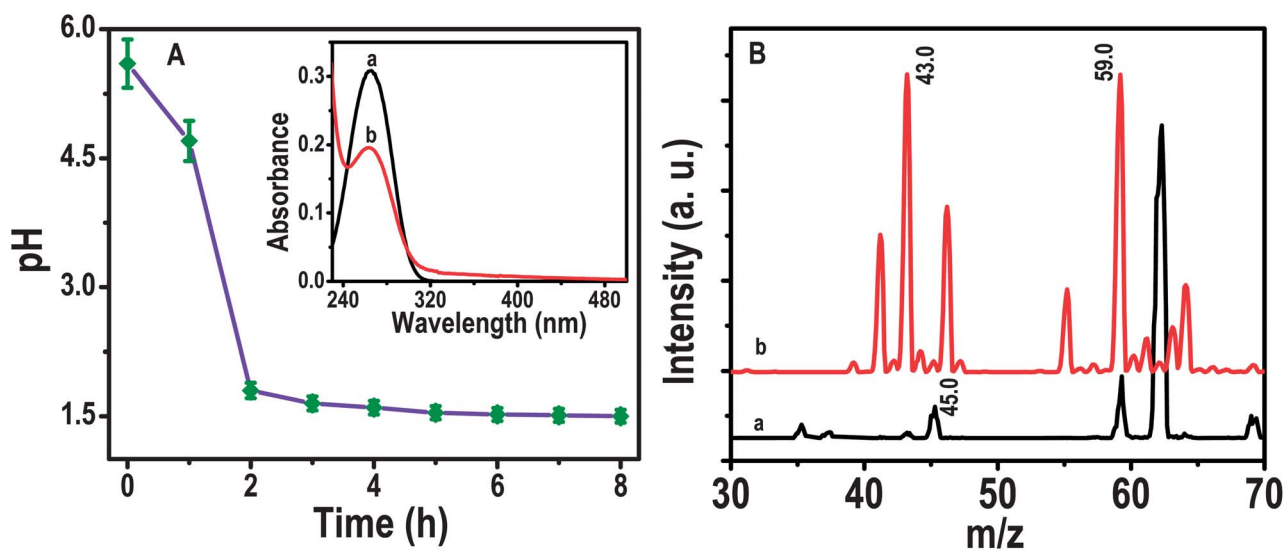


Fig. 6 (A) Plot of pH of the reaction product of $\text{Ag}_9\text{MSA}_7 + \text{CCl}_4$ with time. The estimated error is 5%. Inset is the absorbance spectra of pure acetone (a) and that of the supernatant (b) of the above reaction, after 8.0 h. (B) Comparison of positive mode ESI MS of IPA and the reaction mixture (traces (a) and (b), respectively).

4.0 h of the reaction was 4.7, 1.8, 1.6 and 1.5, respectively. This clearly indicates the increase in the acidity of the reaction mixture. The release of H^+ can be due to the oxidation of IPA to acetone during the reaction. The UV/Vis absorption spectra of the supernatant of the reaction mixture and of acetone are compared in the inset of Fig. 6A. Pure acetone (trace (a)) shows an absorption maximum in water at 265 nm due to $n-\pi^*$ transition of the carbonyl group. The presence of an identical peak at 265 nm (trace (b)) in the reaction mixture confirms the formation of acetone from IPA.⁵⁰ Formation of acetone was further confirmed by comparison of ESI MS of IPA and reaction products in solution (Fig. 6B). IPA (trace (a)) shows an intense peak at m/z 45.0 which is assigned to $\text{CH}_3\text{C}(\text{OH})\text{H}^+$. The reaction product (trace (b)) shows the disappearance of the peak at m/z 45.0 (due to IPA) with the appearance of a new peak at m/z 43.0 assigned to CH_3CO^+ . The molecular ion peak of acetone was also seen at m/z 59.0. Interestingly, ESI MS data (Fig. S4[†]) of the reaction product show the formation of CCl_3COO^- which was tentatively assigned using mass spectrometry/mass spectrometry (MS/MS) analysis. In Fig. S4A,[†] trace (a) is the positive mode ESI MS of the reaction mixture in which no MSA peak at m/z 151.0 was noticed. Trace (b) is in negative mode where the peaks

at m/z 196.0 and 161.0 are seen. The MSA peak at m/z 149.0 was not noticed here as well. The absence of parent MSA peaks after the reaction indicates the chemical transformation of detached ligands. The peak at m/z 196.0 is assigned to CCl_4COO^- . MS/MS of m/z 196.0 gives the peak m/z 161.0 due to the loss of ^{35}Cl (Fig. S4B[†]). MS^2 of m/z 198.0 gives 161.0 and 163.0 due to the loss of ^{37}Cl and ^{35}Cl , respectively. Similar losses were seen in MS^2 of m/z 200.0 and 202.0. The species CCl_4COO^- (or $[\text{CCl}_3\text{COO}]\text{Cl}^-$) may be formed by halogen attachment to CCl_3COO^- . Above assignments were again checked by comparing the calculated and experimental mass spectra for the above species which show an exact match (Fig. S4C and D[†]). Formation of CCl_3COO^- may be explained as follows. Oxidation of acetone may be continued to form CH_3COOH by active Cl species formed in the reaction (active Cl species can act as oxidizing agents) followed by the formation of chlorinated acid. However, more studies are essential to understand the formation mechanism of such species. A possible chemical equation for the above reaction can be written as follows. The changes observed in the monolayer are not included in the reaction as we do not know the exact mechanism of the chemical transformation of the ligand.

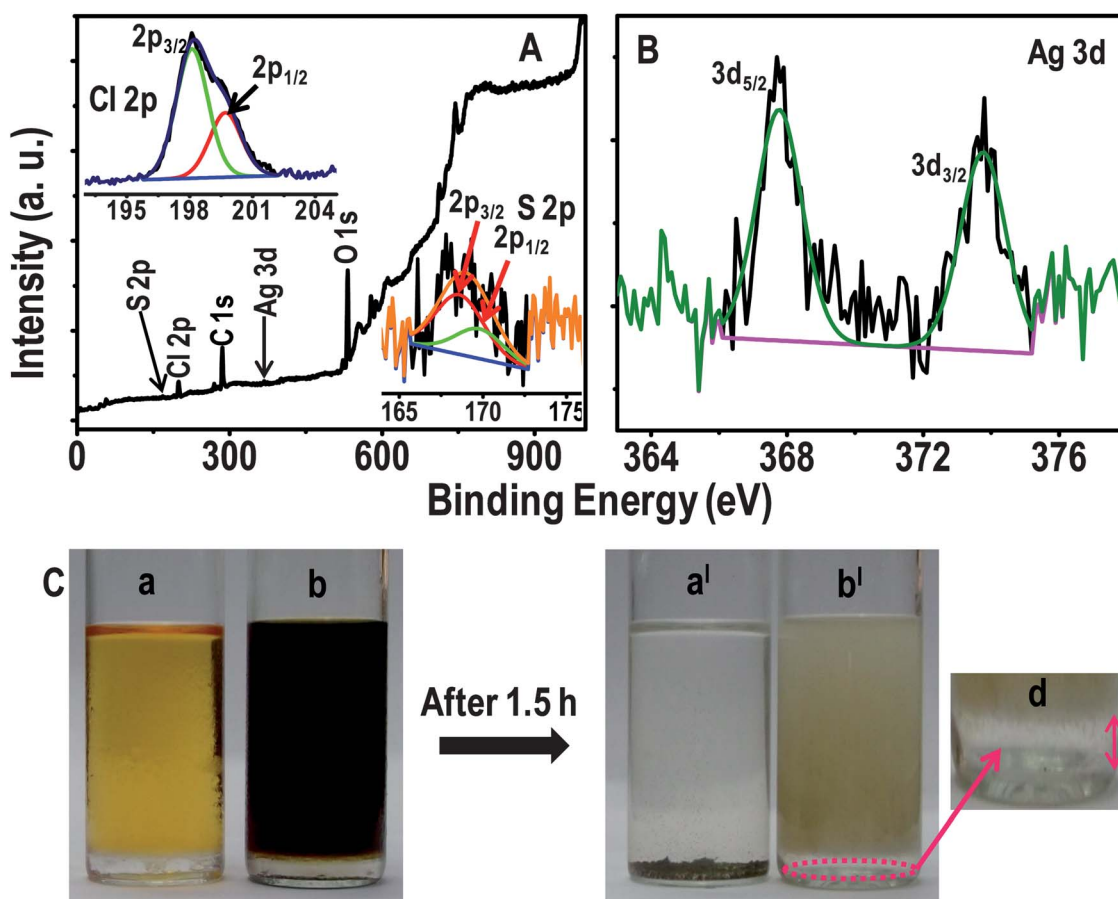
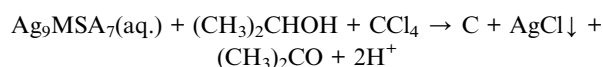


Fig. 7 (A) and (B) XPS survey spectrum and expanded Ag 3d region, respectively of the product of the reaction between Ag_9MSA_7 and benzyl chloride. Insets of (A) are Cl 2p and S 2p regions in the XPS of the same sample. (C) Photographs of the reaction mixtures of (a) $\text{Ag}_9\text{MSA}_7 + \text{CCl}_4$ and (b) Ag@MSA nanoparticles + CCl_4 initially (0.0 h). The CCl_4 layer is seen separately at the bottom. Photographs (a') and (b') are of corresponding mixtures after the reaction for 1.5 h. Unreacted CCl_4 is marked in (b'). An enlarged photograph of the marked area of (b') is shown in (d).

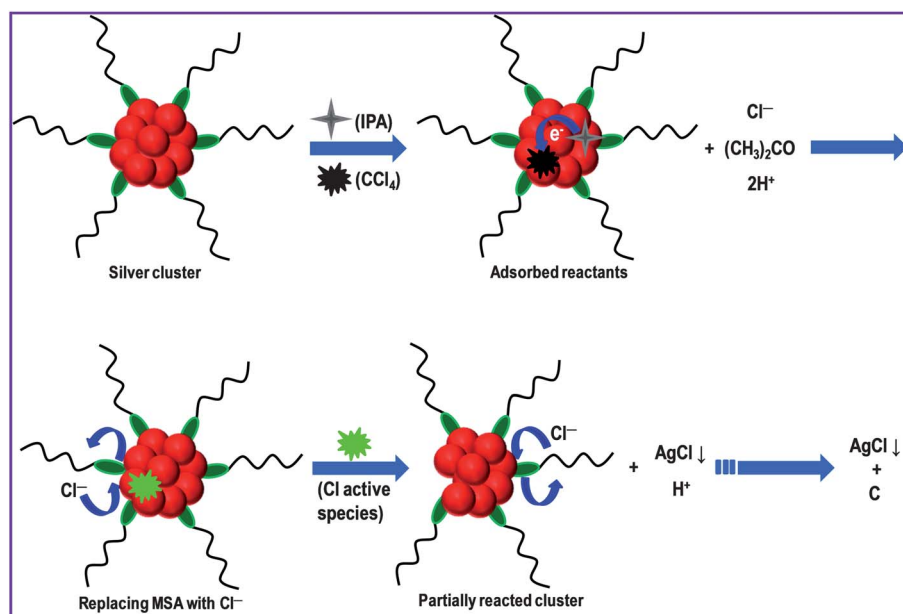
Table 1 Comparison of various nanomaterials used for the degradation of chlorocarbons

Nanomaterials	Halocarbons	Process	Conditions	Products	Remarks	Ref.
Elemental iron and zinc	CCl ₄	Reductive dechlorination	Ambient conditions	Free metal ions, CHCl ₃ and H ₂	Kinetics depends on pH, surface area, <i>etc.</i>	51
Pd/C, Rh/C, Ru/C and Pt/C	Polychlorinated biphenyls (PCBs)	Catalytic dechlorination	2-Propanol, aq. NaOH, 82 °C	Biphenyl and phenylcyclohexane	Complete dechlorination in ~2–3 h	52
TiO ₂ (30 nm) suspension	CHCl ₃ , CHBr ₃ , and CCl ₃ COO ⁻	Photocatalysis	pH > 11, H ₂ O + CH ₃ OH	CO, CO ₂ and Cl ⁻	Xe arc lamp at 910 W, 2 h irradiation	53
Subcolloidal Fe/Ag particles (<0.1 μm size)	Hexachlorobenzene (HCB)	Reductive dehalogenation	Room temperature, in water	Tetra-, tri-, and dichlorobenzenes	Complete dehalogenation in 24 h	54
Charge stabilized Ag and Au NPs (10–150 nm)	CCl ₄ , C ₆ H ₅ CH ₂ Cl, CHCl ₃ , CH ₂ Cl ₂ , <i>etc.</i>	Catalytic degradation	2-Propanol + water, 28 °C	AgCl, C and acetone	Complete destruction in 12 h	35
TiO ₂ (40 and 80 nm)	CCl ₄	Thermal decomposition	<550 °C, gaseous CCl ₄	CO, CO ₂ , COCl ₂ , Cl ₂ , C, TiCl ₄ , HCl and titanium oxychloride	Particles of size 40 nm are more reactive than 80 nm	55
Monolayer-protected Ag clusters (<1 nm size)	CCl ₄ , C ₆ H ₅ CH ₂ Cl and CHCl ₃	Catalytic degradation	2-Propanol + water, 28 °C	AgCl, C, acetone and CCl ₃ COOH	Complete destruction within 3 h	Present study



B. SUPPORTED CLUSTERS. Clusters supported on neutral alumina were also used for the study of degradation of CCl₄. Reaction products were characterized by XRD, Raman and SEM EDAX. XRD (Fig. S5A†) confirms the formation of AgCl and Raman analysis (Fig. S5B†) reveals the presence of the carbonaceous material due to the degradation of halocarbon. EDAX analysis shows clearly the presence of Cl, Ag and S (Fig. S6†). The quantification table of elements also supports the formation of AgCl which shows the silver to chlorine atomic ratio as

1 : 1 (inset of Fig. S6†). Other halocarbons like CHCl₃ and C₆H₅CH₂Cl were also degraded by unsupported and supported clusters giving silver chloride and amorphous carbon as the products (data are not shown). Time taken for complete destruction of CHCl₃ is comparable to the CCl₄ case, whereas for benzyl chloride, it was more. The possible reason is its complete immiscibility in the reaction mixture. XPS data of the reaction products of benzyl chloride and clusters are shown in Fig. 7A and B. A survey spectrum indicates the presence of elements C, O, Ag, S and Cl (Fig. 7A). The peak of Ag 3d_{5/2} at 367.7 eV confirms the presence of silver in the +1 oxidation state formed due to the reaction (Fig. 7B). The chemical change of the monolayer has been confirmed by the presence of S 2p_{3/2} at



Scheme 1 Schematic representation of the degradation of halocarbon, CCl₄, by silver clusters along with other chemical transformations. All the chemical species detected are not marked.

168.5 eV (inset of Fig. 7A). The nature of Cl has been understood from the peak of Cl 2p_{3/2} at 198.2 (inset of Fig. 7A). This is due to Cl⁻ from AgCl. It is important to recall that as the reaction was complete in this case, no unreacted chlorine feature was detected.

It is good to compare the efficiency of degradation of halocarbons by quantum clusters with the corresponding nanoparticles. For that, the same quantities (25 mg) of clusters and nanoparticles were used for the degradation of 5 mL of CCl₄ under the same experimental conditions. Surprisingly, in the case of clusters, the color of the mixture disappeared after 1.5 h accompanied by the formation of a grey colored precipitate (Fig. 7C). But, in the case of nanoparticles, reddish black color turned to pale brown. No precipitate of AgCl was seen after 1.5 h, and CCl₄ remained at the bottom, as marked in Fig. 7b¹. The color change reflects progress in the reaction. The color change and the presence of CCl₄ confirm that clusters are more efficient for the degradation reaction. Degradation of chlorocarbons by other relevant nanomaterials is compared in Table 1. This suggests that quantum clusters of silver are good candidates for efficient degradation of chlorocarbons. Other materials need light, high temperatures, *etc.* whereas in our study we show the possibility of degradation at room temperature by simple mixing.

Mechanism

We propose the following mechanism on the basis of experimental observations. After addition of IPA and CCl₄ to the cluster solution, adsorption of both would occur on the surface of the cluster. Clusters play two important roles: one in catalyzing the oxidation of IPA and the other in activating the halocarbon. Formation of acetone from IPA due to catalytic oxidation (on the surface of the cluster) has been confirmed by UV/Vis spectroscopic analysis during the reaction. The control experiment, *i.e.*, a mixture of clusters (in water) and IPA, reveals that there is no formation of acetone. Mixture of IPA and CCl₄ also does not lead to the formation of acetone with time. These observations clearly indicate the necessity of an electron acceptor for the facile formation of H⁺ as indicated by the decrease in pH of the solution. Activation of the C–Cl bond of chlorocarbon may occur on the surface of the cluster as reported previously in the case of noble metals.⁵⁶ The electrons released in the oxidation of IPA are abstracted by activated CCl₄ on the surface leading to the formation of Cl⁻ and other active Cl species which may act as oxidizing agents. The Cl⁻ formed may replace some of the MSA ligands similar to a report wherein phenylethane thiolate on Au cluster was replaced by the halide ion.⁵⁷ As MSA is replaced by Cl⁻, stability of the cluster is lost which makes silver to react to form crystalline AgCl. Once one Ag atom from a cluster is removed to form AgCl, the other silver atoms also take part in the reaction. The final pH of the reaction mixture is acidic which may also facilitate the mineralization of CCl₄. The molecules of the monolayer which are detached from the cluster surface will be oxidized in the solution to form stable sulphate/sulphite species (confirmed by XPS). The process is schematically represented in Scheme 1.

Summary and conclusions

In summary, we have studied the reaction of monolayer-protected atomically precise silver clusters and nanoparticles with halocarbons at room temperature. The presence of reaction products, silver chloride, CCl₃COO⁻ and amorphous carbon, was confirmed by various spectroscopic and microscopic tools. A possible mechanism for the reaction is proposed accounting for the observed products. The efficiency of clusters in degrading halocarbons is considerably higher than the corresponding nanoparticles. This was attributed to the smaller size and reduced nobility of silver. Control experiments and the measurement of pH were carried out to validate the proposed mechanism. A limitation of this material is the non-reusability. But the reaction product AgCl can be recovered and used to make metallic silver or silver clusters back again.

Acknowledgements

We thank the Department of Science and Technology (DST), Government of India, for constantly supporting our research program on nanomaterials. M.S.B. thanks the CSIR for a senior research fellowship.

References

- 1 R. Jin, *Nanoscale*, 2010, **2**, 343–362.
- 2 P. L. Xavier, K. Chaudhari, A. Baksi and T. Pradeep, *Nano Rev.*, 2012, **3**, 14767.
- 3 O. M. Bakr, V. Amendola, C. M. Aikens, W. Wenseleers, R. Li, N. L. Dal, G. C. Schatz and F. Stellacci, *Angew. Chem., Int. Ed.*, 2009, **48**, 5921–5926.
- 4 S. Kumar, M. D. Bolan and T. P. Bigioni, *J. Am. Chem. Soc.*, 2010, **132**, 13141–13143.
- 5 T. U. B. Rao and T. Pradeep, *Angew. Chem., Int. Ed.*, 2010, **49**, 3925–3929.
- 6 A. George, E. S. Shibu, S. M. Maliyekkal, M. S. Bootharaju and T. Pradeep, *ACS Appl. Mater. Interfaces*, 2012, **4**, 639–644.
- 7 M. Zhu, H. Qian, X. Meng, S. Jin, Z. Wu and R. Jin, *Nano Lett.*, 2011, **11**, 3963–3969.
- 8 Y. Lei, F. Mehmood, S. Lee, J. Greeley, B. Lee, S. Seifert, R. E. Winans, J. W. Elam, R. J. Meyer, P. C. Redfern, D. Teschner, R. Schloegl, M. J. Pellin, L. A. Curtiss and S. Vajda, *Science*, 2010, **328**, 224–228.
- 9 K.-I. Shimizu, R. Sato and A. Satsuma, *Angew. Chem., Int. Ed.*, 2009, **48**, 3982–3986.
- 10 M. M. A. Habeeb, P. K. Verma, S. K. Pal, A. Retnakumari, M. Koyakutty, S. Nair and T. Pradeep, *Chem.–Eur. J.*, 2010, **16**, 10103–10112.
- 11 Y. Lu and W. Chen, *Chem. Soc. Rev.*, 2012, **41**, 3594–3623.
- 12 M. M. A. Habeeb and T. Pradeep, *Chem. Phys. Lett.*, 2007, **449**, 186–190.
- 13 T. Udayabhaskararao, Y. Sun, N. Goswami, S. K. Pal, K. Balasubramanian and T. Pradeep, *Angew. Chem., Int. Ed.*, 2012, **51**, 2155–2159.
- 14 C. Kumara and A. Dass, *Nanoscale*, 2011, **3**, 3064–3067.

- 15 M. A. H. Muhammed, P. K. Verma, S. K. Pal, R. C. A. Kumar, S. Paul, R. V. Omkumar and T. Pradeep, *Chem.–Eur. J.*, 2009, **15**, 10110–10120.
- 16 M. S. Bootharaju and T. Pradeep, *Langmuir*, 2011, **27**, 8134–8143.
- 17 I. Chakraborty, T. Udayabhaskararao and T. Pradeep, *J. Hazard. Mater.*, 2012, **211–212**, 396–403.
- 18 Y. Liu, K. Ai, X. Cheng, L. Huo and L. Lu, *Adv. Funct. Mater.*, 2010, **20**, 951–956.
- 19 B. Schrick, J. L. Blough, A. D. Jones and T. E. Mallouk, *Chem. Mater.*, 2002, **14**, 5140–5147.
- 20 E. Sumesh, M. S. Bootharaju, Anshup and T. Pradeep, *J. Hazard. Mater.*, 2011, **189**, 450–457.
- 21 W. Zheng, J. Lichwa, M. D'Alessio and C. Ray, *Chemosphere*, 2009, **76**, 1167–1177.
- 22 C. Kroeze and L. Reijnders, *Sci. Total Environ.*, 1992, **112**, 269–290.
- 23 W.-Y. Xu and T.-Y. Gao, *J. Environ. Sci.*, 2007, **19**, 792–799.
- 24 G. W. Reynolds, J. T. Hoff and R. W. Gillham, *Environ. Sci. Technol.*, 1990, **24**, 135–142.
- 25 C. A. Keller, M. Hill, M. K. Vollmer, S. Henne, D. Brunner, S. Reimann, S. O'Doherty, J. Arduini, M. Maione, Z. Ferenczi, L. Haszpra, A. J. Manning and T. Peter, *Environ. Sci. Technol.*, 2011, **46**, 217–225.
- 26 C. E. Jones and L. J. Carpenter, *Environ. Sci. Technol.*, 2005, **39**, 6130–6137.
- 27 T.-K. Tseng, H. Chu and H.-H. Hsu, *Environ. Sci. Technol.*, 2002, **37**, 171–176.
- 28 Q. Xiang, J. Yu, B. Cheng and H. C. Ong, *Chem.–Asian J.*, 2010, **5**, 1466–1474.
- 29 X. Zhou, G. Liu, J. Yu and W. Fan, *J. Mater. Chem.*, 2012, **22**, 21337–21354.
- 30 O. Koper, I. Lagadic and K. J. Klabunde, *Chem. Mater.*, 1997, **9**, 838–848.
- 31 J. Farrell, M. Kason, N. Melitas and T. Li, *Environ. Sci. Technol.*, 1999, **34**, 514–521.
- 32 M. I. Litter, W. Choi, D. D. Dionysiou, P. Falaras, A. Hiskia, G. Li Puma, T. Pradeep and J. Zhao, *J. Hazard. Mater.*, 2012, **211–212**, 1–2.
- 33 I. V. Mishakov, V. I. Zaikovskii, D. S. Heroux, A. F. Bedilo, V. V. Chesnokov, A. M. Volodin, I. N. Martyanov, S. V. Filimonova, V. N. Parmon and K. J. Klabunde, *J. Phys. Chem. B*, 2005, **109**, 6982–6989.
- 34 C. L. Carnes and K. J. Klabunde, *Langmuir*, 2000, **16**, 3764–3772.
- 35 A. S. Nair and T. Pradeep, *Curr. Sci.*, 2003, **84**, 1560–1564.
- 36 A. S. Nair and T. Pradeep, *Indian Pat.*, 200767, 2006.
- 37 A. S. Nair and T. Pradeep, *U. S. Pat.*, 7,968,493B962, 2011.
- 38 A. S. Nair and T. Pradeep, *J. Nanosci. Nanotechnol.*, 2007, **7**, 1871–1877.
- 39 M. S. Bootharaju and T. Pradeep, *Langmuir*, 2012, **28**, 2671–2679.
- 40 T. Pradeep and Anshup, *Thin Solid Films*, 2009, **517**, 6441–6478.
- 41 E. S. Shibu and T. Pradeep, *Chem. Mater.*, 2011, **23**, 989–999.
- 42 T. U. B. Rao, B. Nataraju and T. Pradeep, *J. Am. Chem. Soc.*, 2010, **132**, 16304–16307.
- 43 R. John, A. Ashokreddy, C. Vijayan and T. Pradeep, *Nanotechnology*, 2011, **22**, 165701.
- 44 K. N. Kudin, B. Ozbas, H. C. Schniepp, R. K. Prud'homme, I. A. Aksay and R. Car, *Nano Lett.*, 2007, **8**, 36–41.
- 45 V. Palshin, E. I. Meletis, S. Ves and S. Logothetidis, *Thin Solid Films*, 1995, **270**, 165–172.
- 46 D. Fan, C. Zhang, J. He, R. Hua, Y. Zhang and Y. Yang, *J. Mater. Chem.*, 2012, **22**, 18564–18571.
- 47 M. S. Bootharaju and T. Pradeep, *J. Phys. Chem. C*, 2010, **114**, 8328–8336.
- 48 H. Zhang, Q. Fu, Y. Yao, Z. Zhang, T. Ma, D. Tan and X. Bao, *Langmuir*, 2008, **24**, 10874–10878.
- 49 H. Piao, K. Adib, Z. Chang, J. Hrbek, M. Enever, M. A. Barteau and D. R. Mullins, *J. Phys. Chem. B*, 2003, **107**, 13976–13985.
- 50 A. Henglein, B. G. Ershov and M. Malow, *J. Phys. Chem.*, 1995, **99**, 14129–14136.
- 51 K. D. Warren, R. G. Arnold, T. L. Bishop, L. C. Lindholm and E. A. Betterton, *J. Hazard. Mater.*, 1995, **41**, 217–227.
- 52 Y. Ukisu, S. Iimura and R. Uchida, *Chemosphere*, 1996, **33**, 1523–1530.
- 53 W. Choi and M. R. Hoffmann, *Environ. Sci. Technol.*, 1996, **31**, 89–95.
- 54 Y. Xu and W.-X. Zhang, *Ind. Eng. Chem. Res.*, 2000, **39**, 2238–2244.
- 55 G. Liu, J. Wang, Y. Zhu and X. Zhang, *Phys. Chem. Chem. Phys.*, 2004, **6**, 985–991.
- 56 H. Imai, T. Nishiguchi, M. Tanaka and K. Fukuzumi, *J. Org. Chem.*, 1977, **42**, 2309–2313.
- 57 M. Zhu, G. Chan, H. Qian and R. Jin, *Nanoscale*, 2011, **3**, 1703–1707.

Electronic supplementary information

Atomically precise silver clusters for efficient chlorocarbon degradation

M. S. Bootharaju,^a G. K. Deepesh,^a T. Udayabhaskararao and T. Pradeep*

DST Unit of Nanoscience (DST UNS), Department of Chemistry,

Indian Institute of Technology Madras, Chennai - 600 036, India

*E-mail: pradeep@iitm.ac.in

^aThese authors have contributed equally

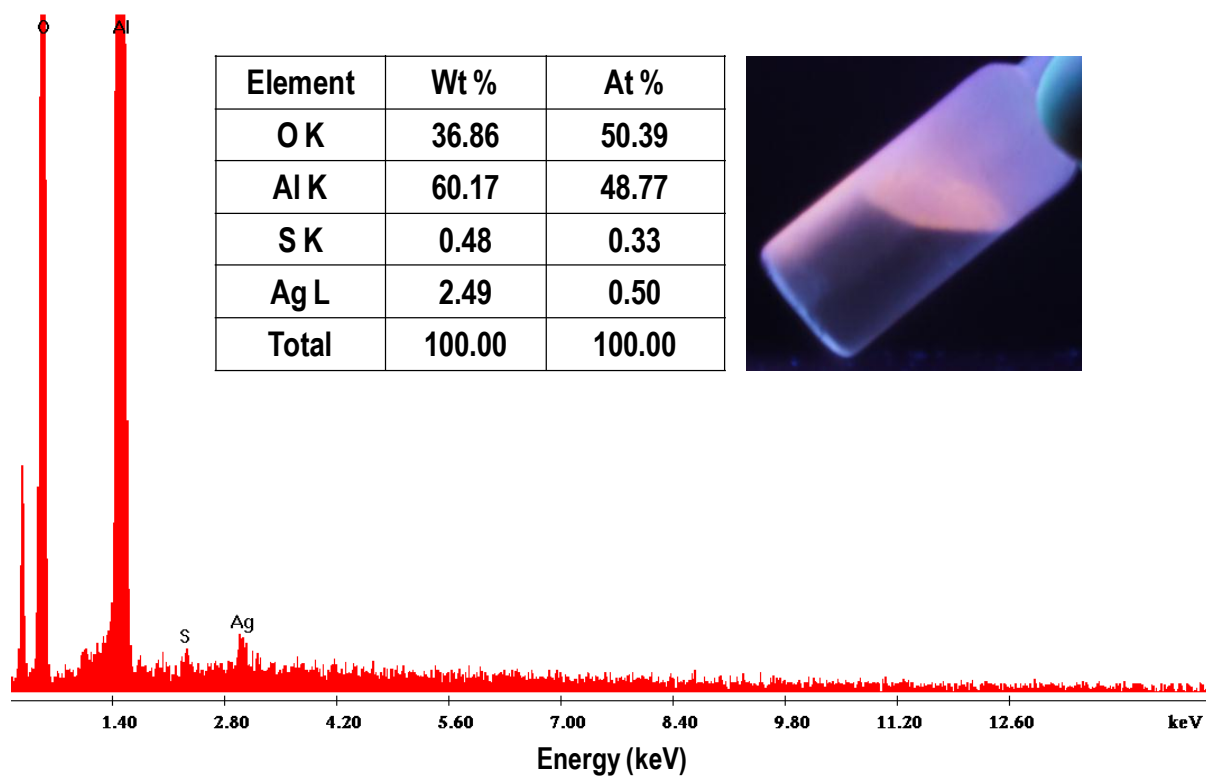


Fig. S1 EDAX spectrum of supported Ag_9MSA_7 clusters which confirms the presence of Ag and S from the cluster on alumina. Insets are the quantification table of elements and a photograph of supported Ag_9MSA_7 clusters under UV lamp. Photograph was taken after dipping the sample bottle in liquid nitrogen. The blue scattered light around the glass bottle is due to scattering from condensed moisture. The emission of the cluster is red.

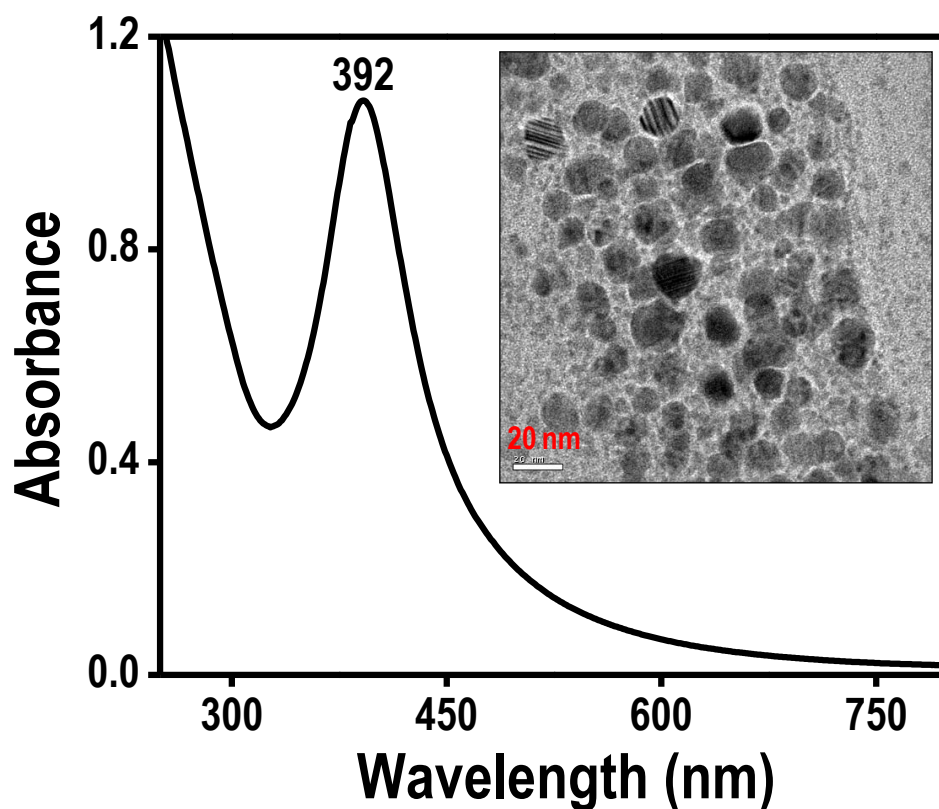


Fig. S2 UV/Vis absorption spectrum of as-synthesized Ag@MSA nanoparticles. Inset is a TEM image of Ag@MSA nanoparticles.

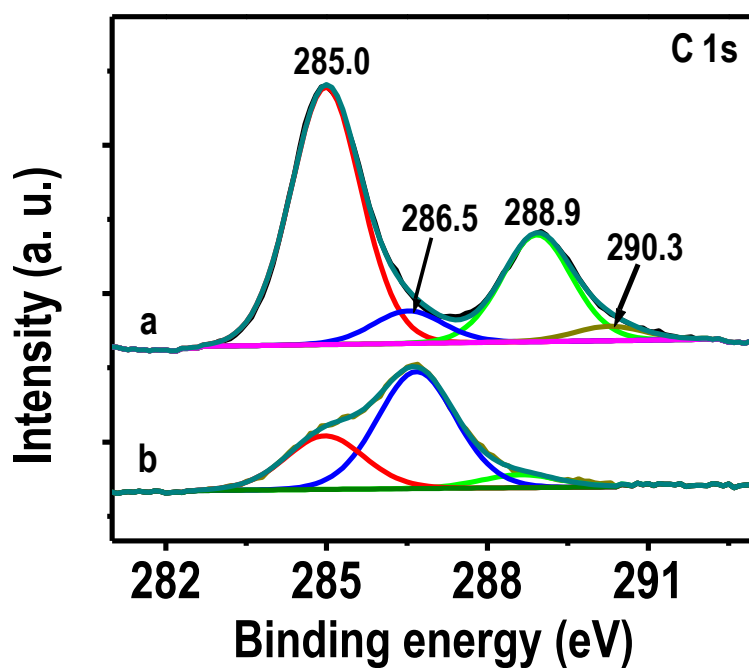


Fig. S3 C 1s region of the XPS of parent Ag₉MSA₇ clusters (a) and the product (b) obtained after the reaction of clusters with CCl₄.

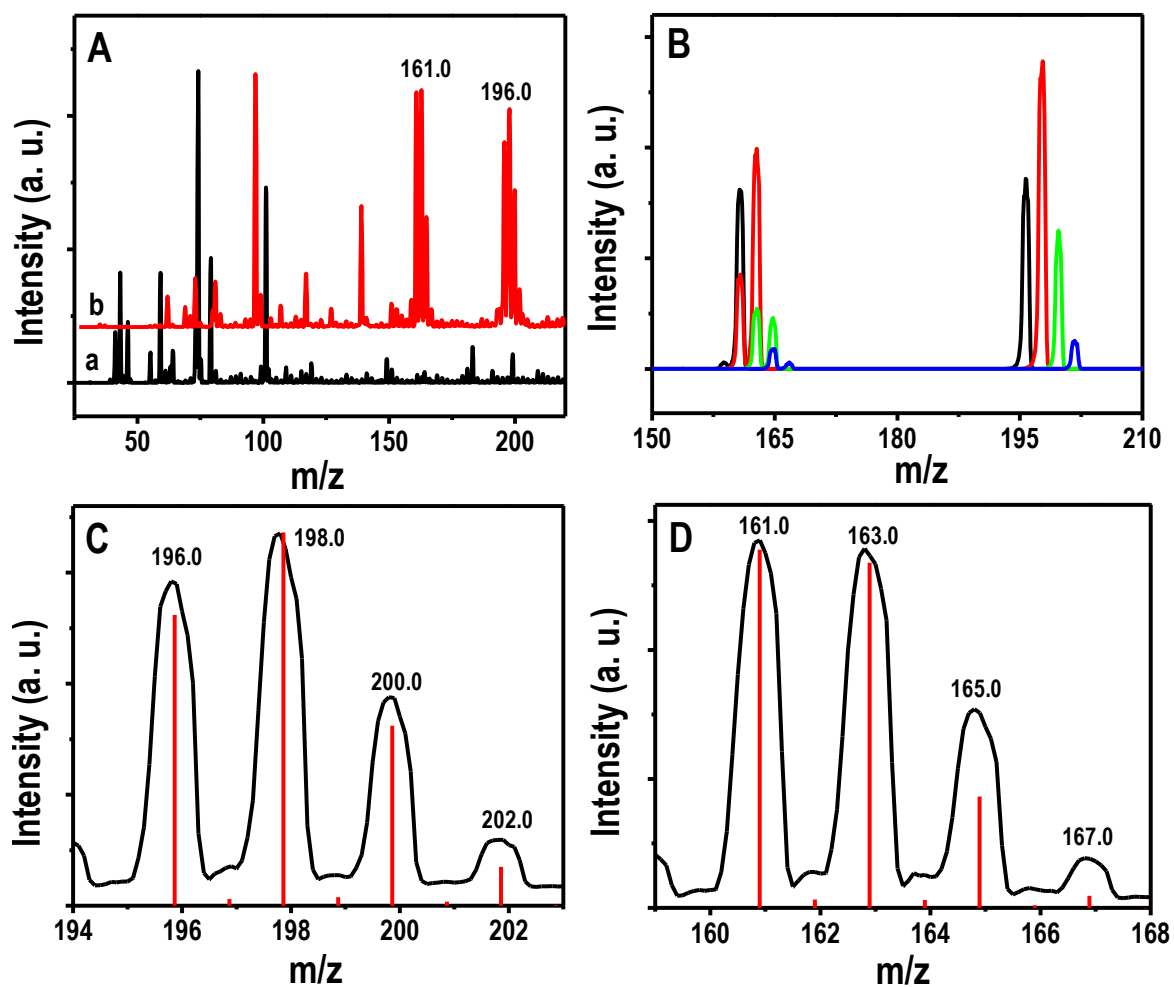


Fig. S4 A) ESI MS of reaction mixture of Ag_9MSA_7 and CCl_4 in positive and negative modes (traces a and b, respectively). B is MS/MS of m/z 196.0, 198.0, 200.0 and 202.0 in negative mode. C and D are comparisons of experimental (black traces) and calculated spectra (red traces) for species CCl_4COO^- and CCl_3COO^- , respectively.

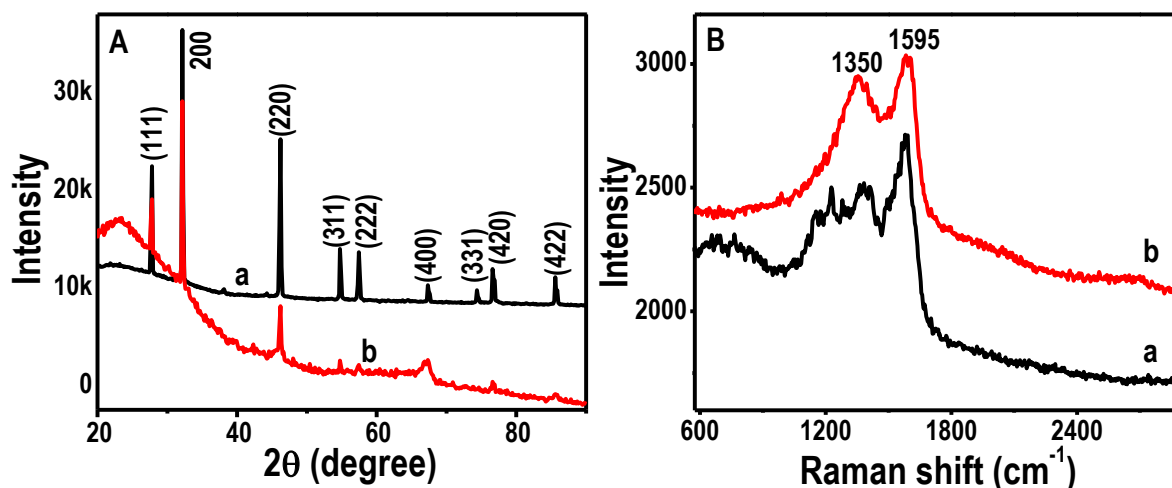


Fig. S5 A) Comparison of XRD patterns of as-prepared AgCl (a) and reaction product (b) of CCl_4 and supported clusters. B) Raman spectra of the reaction product of CCl_4 and supported clusters before (a) and after (b) washing with ammonia solution.

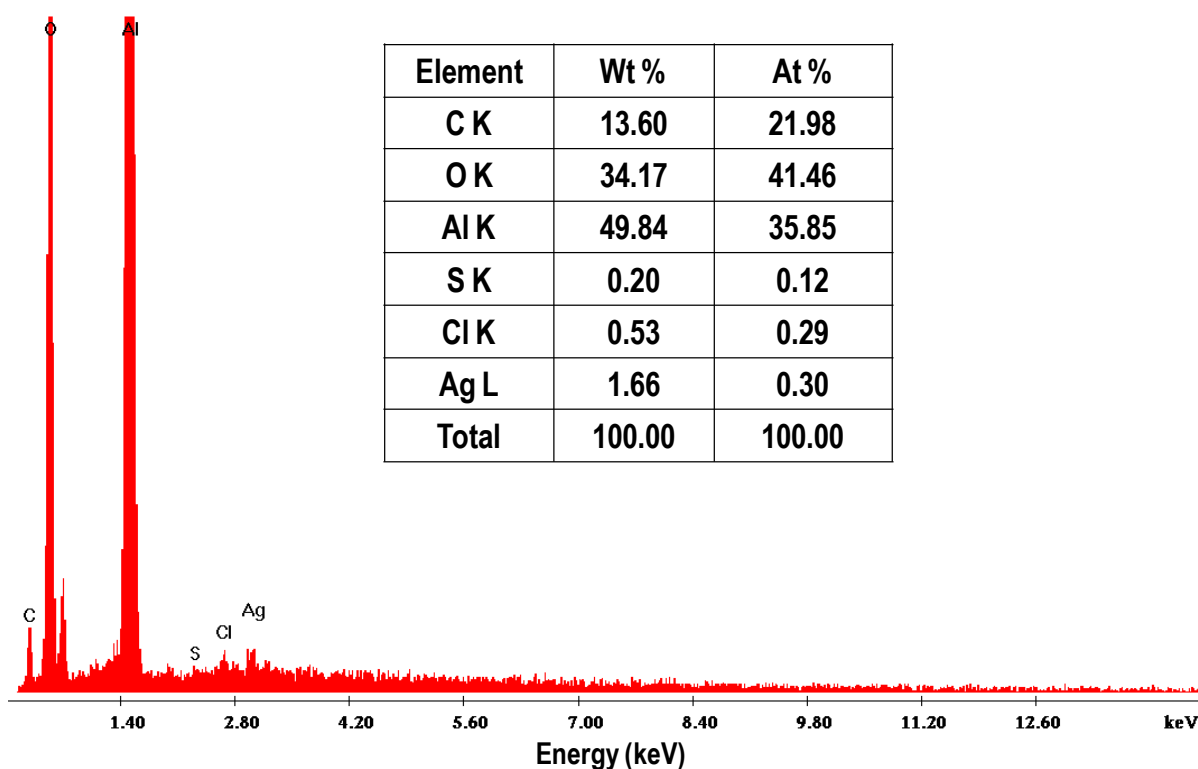


Fig. S6 EDAX spectrum of the reaction product of CCl_4 and supported clusters showing the presence of Cl, Ag and S. Inset is a quantification table of elements which shows that the atomic ratio of Ag to S is 1:1.

The Superstable 25 kDa Monolayer Protected Silver Nanoparticle: Measurements and Interpretation as an Icosahedral $\text{Ag}_{152}(\text{SCH}_2\text{CH}_2\text{Ph})_{60}$ Cluster

Indranath Chakraborty,^{†,||} Anuradha Govindarajan,^{†,||,⊥} Jayanthi Erusappan,^{†,⊥} Atanu Ghosh,[†] T. Pradeep,^{*,†} Bokwon Yoon,[‡] Robert L. Whetten,[§] and Uzi Landman[‡]

[†]DST Unit of Nanoscience (DST UNS), Department of Chemistry, Indian Institute of Technology Madras, Chennai 600036, India

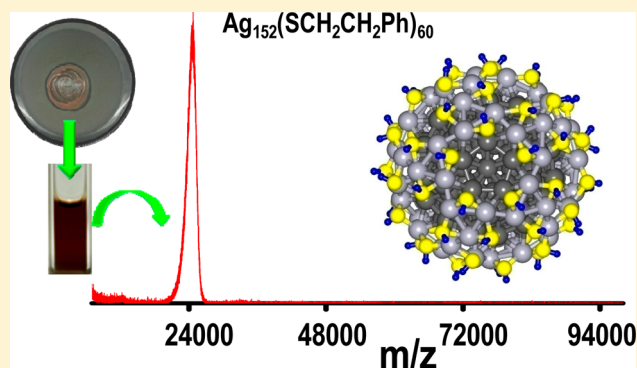
[‡]School of Physics, Georgia Institute of Technology, Atlanta, Georgia 30332-0430, United States

[§]School of Chemistry & Biochemistry, Georgia Institute of Technology, Atlanta, Georgia 30332, United States

Supporting Information

ABSTRACT: A cluster obtained in high yield from the reduction of a silver-thiolate precursor, $\text{Ag-SCH}_2\text{CH}_2\text{Ph}$, exhibited a single sharp peak near 25 kDa in the matrix-assisted laser desorption mass spectrum (MALDI MS) and a well-defined metal core of ~ 2 nm measured with transmission electron microscopy (TEM). The cluster yields a single fraction in high-performance liquid chromatography (HPLC). Increased laser fluence fragments the cluster until a new peak near 19 kDa predominates, suggesting that the parent cluster— $\text{Ag}_{152}(\text{SCH}_2\text{CH}_2\text{Ph})_{60}$ —evolves into a stable inorganic core— $\text{Ag}_{152}\text{S}_{60}$. Exploiting combined insights from investigations of clusters and surface science, a core-shell structure model was developed, with a 92-atom silver core having icosahedral-dodecahedral symmetry and an encapsulating protective shell containing 60 Ag atoms and 60 thiolates arranged in a network of six-membered rings resembling the geometry found in self-assembled monolayers on $\text{Ag}(111)$. The structure is in agreement with small-angle X-ray scattering (SAXS) data. The protective layer encapsulating this silver cluster may be the smallest known three-dimensional self-assembled monolayer. First-principles electronic structure calculations show, for the geometry-optimized structure, the development of a ~ 0.4 eV energy gap between the highest-occupied and lowest-unoccupied states, originating from a superatom 90-electron shell-closure and conferring stability to the cluster. The optical absorption spectrum of the cluster resembles that of plasmonic silver nanoparticles with a broad single feature peaking at 460 nm, but the luminescence spectrum shows two maxima with one attributed to the ligated shell and the other to the core.

KEYWORDS: Noble metals, clusters, nanoparticles, plasmon resonance, MALDI MS, first-principles electronic structure, projected electronic density of states (PDOS), superatom electronic shells



The quest to fabricate, characterize, and understand small noble metal molecules is among the outstanding challenges of contemporary materials science, as such nano-materials bridge the atomic and the bulk worlds.^{1–3} Distinct stable clusters most often arrange in concentric atomic shell structures composed of 13, 55, 147, 309, and so forth, atoms, known as Mackay icosahedra, and some of them have been synthesized through solution chemistry. Whereas reports about Au_{13} ⁴ and Au_{55} ^{5,6} are available, investigations of the corresponding silver clusters remain an open challenge. Recently, several studies pertaining to electronically stable clusters of gold and silver have appeared.^{7–16} In some of these investigations (particularly on gold clusters, starting with an early study of bare gold clusters),¹⁷ a superatom description of the enhanced stability acquired via electron shell closures at magic number sizes, that is, for clusters containing 2, 8, 18, 34, 58, 92, and so forth, delocalized electrons (see below), has been

applied with a significant measure of success; we recall here that this methodology has been formulated in the mid 1980s to explain time-of-flight mass spectrometric measurements on bare alkali-metal clusters.¹⁸ The scarcity of reports on silver clusters^{14–16,19,20} may be attributed to the high reactivity and relatively poor stability of the Ag-ligand interface. Consequently, the creation, characterization, and understanding of stable silver clusters would provide a “missing link” in this field and serve as impetus for increased research activity in this area.

In this Letter, we present the successful isolation and identification of a 25 kDa silver-thiolate cluster, **1**, which points to the existence of an Ag analogue of the familiar

Received: August 29, 2012

Revised: October 15, 2012

Published: October 24, 2012

$\text{Au}_{144/146}(\text{thiolate})_{60}$ systems.^{21–24} Optical absorption of the cluster closely resembles the plasmon resonance of silver nanoparticles and confirms that molecular excitations in such systems resemble free electron oscillations in metals.

The synthesis of **1** follows a solid state route¹⁴ in which $\text{AgNO}_3(\text{s})$ was ground with phenylethanethiol (PETH)(**1**) at 1:5.3 molar ratio in a mortar and pestle. Adding 25 mg of $\text{NaBH}_4(\text{s})$ and continued grinding completes the reaction. Immediate extraction of the excess thiol in the reaction mixture with 5 mL of ethanol and subsequent dissolution of the residue in toluene/tetrahydrofuran (THF) makes product **1** [details are in SI (S1)]. The crucial aspect of this procedure is the limited supply of water needed for the reduction, which becomes available from the laboratory atmosphere as well as from the ethanol used for subsequent washing. Extended grinding in humid air as well as repeated washing by ethanol stimulate cluster formation and subsequently nanoparticles were detected. The sample was further purified using HPLC (see Figure S2), showing a single sharp peak consistent with the formation and isolation of a unique compound.

Mass spectrometry is the key analytical technique used to obtain the molecular composition of clusters of this kind.^{23,25,26} In this case, laser desorption at threshold laser power (fluence) gives molecular ion features in MALDI MS (Figure 1), although at higher fluence dissociation is seen. The spectra shown in Figure 1 are at the lowest fluence needed to observe ion signals (data at higher fluence will be discussed below). We show here mass spectra for the unpurified (Figure 1a) as well as the HPLC-purified sample (Figure 1b). The peak in Figure 1a is centered at $m/z = 24\,600$ Da (fwhm of 1.5 kDa), where the imprecision in the mass number is ± 100 in this mass range, and therefore the composition will have corresponding uncertainty. Additionally, the doubly charged cluster (2^+ , dication) is observed (see small signal peaked at $m/z = 12\,300 \pm 30$). The negative ion mass spectra were of much lower intensity, but the features were identical. The peak of the data in Figure 1b is located at $m/z = 24\,610 \pm 80$, and it is narrower (fwhm of 1.3 kDa), exhibiting in addition a much more pronounced dication signal with a peak at $12\,320 \pm 30$. Such a sharp and solitary peak in the mass spectrum has not been observed for any other large silver cluster to date. Moreover, the above observation of a clear dication signal corroborates the unit charge assignment of the cluster molecular ion. The similarity between the results with and without HPLC purification allows us to focus in the following on measurements for the latter.

The estimated yield of the reaction was determined to be as high as 82%. These factors suggest the ubiquitous existence of an uniquely stable cluster compound lying in this particular size and composition range. A well-defined cluster was also supported by the HRTEM image (Figure 1c), which shows the presence of a core with an average diameter of ~ 2 nm. SAXS (small angle X-ray scattering) analysis in solution further confirms the homogeneity of particle size with a sharp feature at a radius of 1.395 nm (Figure S3). Some bigger particles of 3–4 nm diameter were observed in TEM (Figure 1) which are attributed to cluster aggregates or cluster coalescence which is typical in the electron microscopic analysis of clusters, especially with higher primary beam energy. Interestingly, this cluster shows a specific arrangement in HRTEM, which indicates a high propensity for crystallization. This specific arrangement was not restricted to a single place but was found almost throughout the entire grid (Figure 1c). Even the SEM images showed some crystalline behavior along with sharp faces

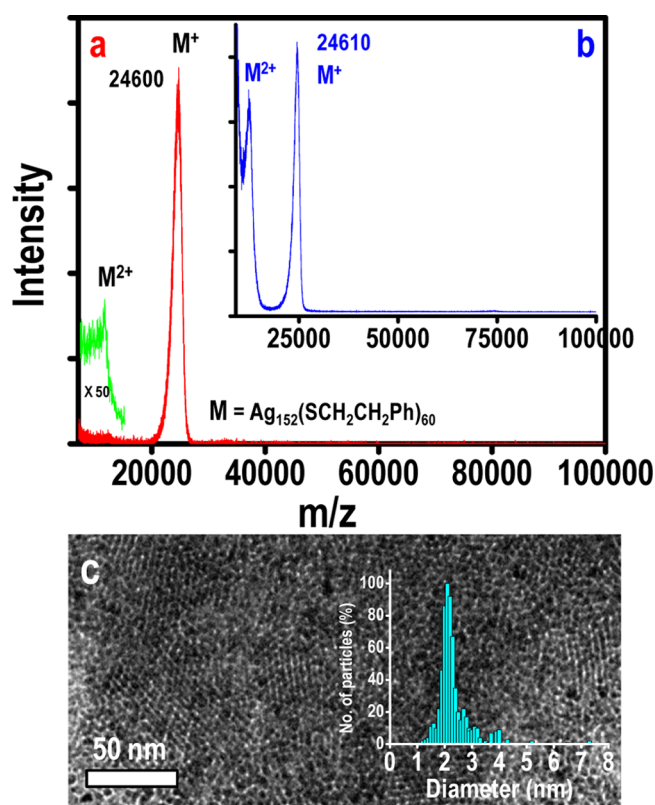


Figure 1. (a) MALDI MS mass spectrum of as-synthesized 25 kDa compound **1** (extracted in toluene) detected in the positive mode. It gives a sharp (fwhm m/z 1.5 kDa) molecular peak centered at $m/z = 24\,600 \pm 100$. A minor peak at $m/z = 12\,300 \pm 30$ was seen, due to the doubly charged species. For clarity, this was expanded 50 times in the vertical axis. (b) Same as a but for a HPLC-purified sample extracted in THF, showing a narrower peak (fwhm of 1.3 kDa) at $24\,610 \pm 80$ Da and a pronounced dication peak at $m/z = 12\,320 \pm 30$ mass. (c) HRTEM image of clusters that are drop-cast on a carbon-coated copper grid. This specific arrangement of clusters has been observed throughout the grid. Inset shows the size distribution of the clusters observed in TEM. A very narrow distribution was found with an average core diameter of ~ 2 nm.

(Figure S4) of microcrystals. Elemental analysis (Figure S5) of these crystallites showed the expected quantity of silver and sulfur.

Systematic studies of the dependence on laser fluence (f) were performed to establish the character of the molecular ion feature in the MALDI MS. Below a well-defined threshold laser fluence, f_{TH} , no ions were detected (Figure S6), and above a second threshold fragmentation commenced (Figure S7). With further increased fluence, $f = x f_{\text{TH}}$, $x > 1.04$, a new peak appears centered near $m/z = 19\,200$ (Figure 2), independent of further increase in f (Figure S7); in Figure 2 we show the behavior for a 33% (i.e., $1.04 \leq x < 1.38$) increase in the fluence. The shapes of both peaks (the one at $m/z = 24\,600$ and the other at $19\,200$) exhibit interesting features (see Figure 2, inset): (i) the former shows a steeply falling edge on the high-mass side, which may be used to estimate the total molecular weight of **1**, whereas (ii) the latter shows a steeply rising edge on its low-mass side, which may be used to identify a particularly stable inorganic (consisting of silver and sulfur) core. The midpoints of these respective features (fall and rise) occur ~ 6.3 kDa apart, that is, near 24.8 kDa and 18.5 kDa; the organic content of 60 thiolates is also 6.3 kDa (60×105 Da, the mass of PhCH_2CH_2

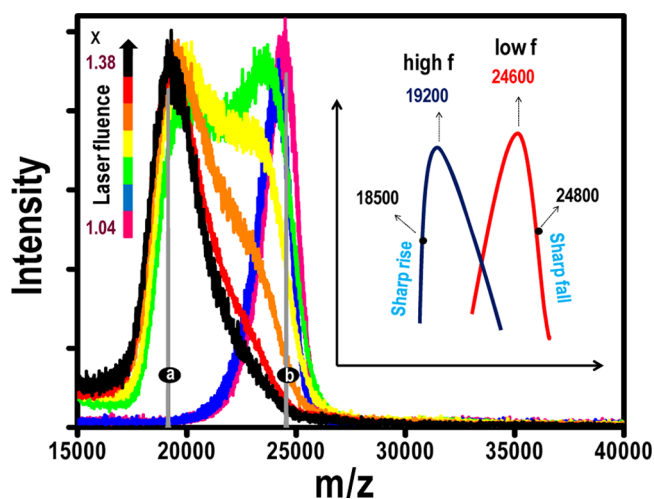


Figure 2. Laser fluence-dependent MALDI mass spectra of the Ag_{152} compound **1**. With a 33% increase in laser fluence ($1.04 < x < 1.38$), the peak position shifts from a higher mass (pink in color with m/z of 24 600, marked by “b”) to a lower mass (black in color with m/z of 19 200, marked by “a”). A further increase in the laser fluence does not change the peak position. Inset: schematic showing the sharp rise and steep fall of the mass-spectral features occurring as the laser fluence is varied.

fragment). These masses and mass-differences suggest that the composition of **1** is best described by $\text{Ag}_{152}(\text{SCH}_2\text{CH}_2\text{Ph})_{60}$ for which the inorganic core is $\text{Ag}_{152}\text{S}_{60}$. This composition is used below as a starting point to obtain a detailed theoretical study to reveal the structure of this cluster.

The toluene extract of **1** was dark brown, and it showed an absorption maximum at 460 nm (2.69 eV; Figure 3). The above band was along with an absorption onset near 1.07 eV (Figure S8), which is comparable with the findings for Au_{144} . Normally

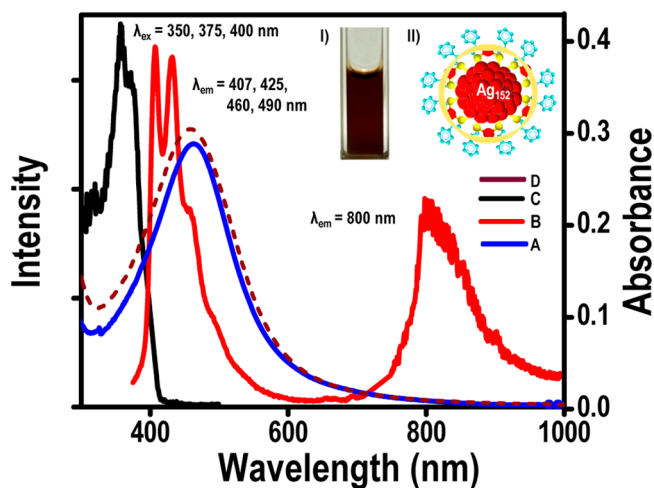


Figure 3. UV-vis absorption spectrum (A) and luminescence spectra (B and C) of compound **1**. The absorption spectrum is reminiscent of Ag nanoparticles. For comparison, the spectrum of PET protected Ag nanoparticles of the 5 nm core diameter is shown (brown dashed line). A NIR emission at 800 nm was observed when the cluster was excited at 375 nm (B). The lower wavelength emission may be due to the thiolate shell consisting of the staple motifs. The cluster extracted in toluene is deep brown in color, and a photograph taken in cuvette is shown in inset I. Inset II is a cartoon representation of the cluster. For simplicity, only one type of staple is given in the cartoon.

PET protected clusters do not show any visually observable luminescence under UV light.²⁴ However, the as-synthesized cluster emits in the near-infrared (NIR) region with an emission wavelength of 800 nm, upon excitation at 375 nm (Figure 3). This NIR emission is attributed to the silver core. The fine structure at the lower wavelength region (400–600 nm) of the emission spectrum may be due to the protective silver-thiolate network (see theory section below); this assignment is supported by the fact that the features exhibit strong structures reminiscent of metal complexes. The optical absorption spectrum of the ~ 2 nm Ag particles on which we focus here resembles the plasmon excitation of silver nanoparticles of 5 ± 2 nm core and above, protected with PET (Figure 3). A TEM image of these nanoparticles is shown in Figure S9. Beyond this core size, the spectrum does not change. It may be noted that the spectral width of the two (compound **1** and larger nanoparticles) is also comparable. The HPLC-separated cluster shows an identical optical absorption spectrum (Figure S2, inset).

The construction of the structural model for the $\text{Ag}_{152}(\text{SR})_{60}$ cluster, described above, was guided by combined experiences derived from investigations on clusters [e.g., bare metal clusters^{1,17,27,28} as well as organometallic clusters containing a metal core protected by an organic shell^{1,3,12,19,22,29}] and from recent surface science studies of self-assembled monolayer (SAM)-induced reconstruction of the surface of silver.^{30,31} We describe the concentric aufbau methodology by starting from the inner region of the silver cluster (see Figure 4) which we set up as a (hollow) 20-Ag atom dodecahedron, which is a Platonic polyhedron³² made of 12 pentagonal faces and 20 vertices, with three faces meeting at each vertex (a signature that is denoted as (5.3)). Each of the 12 pentagonal faces is then capped by an Ag atom (located above the midpoint of the face), with the capping atoms forming a regular icosahedron (Ih), which is the dual of the underlying dodecahedron (for a layer-by-layer illustration, see Figure S10). The 32-atom inner shell is encapsulated by a 60 Ag atom second shell, with all of the atoms being symmetry-equivalent, forming the Archimedean polyhedron known as a snub-dodecahedron;³² this polyhedron is made of 80 triangular faces and 12 pentagonal ones, with five faces (four triangles and one pentagon) meeting at each vertex, that is, a (3⁴.5) signature. We note here that this 60-atom shell is enantiomorphic, that is it appears in right- or left-handed forms. The (32 + 60)-Ag atom core cluster described above (see Figure 4, center column) is protected by a shell containing 120 sites that are occupied by 60 Ag atoms and 60 RS- thiolates (Figure 4, right column). This network is made of 20 (distorted) hexagonal units (each made of two unequal triangles rotated by 180° with respect to each other) with the apexes of one triangle occupied by Ag atoms and those of the other one by RS- groups (that is, going around the distorted hexagon, the locations of the metal and organic molecules alternate). The Ag sites are positioned above edges of the aforementioned 60 Ag atom snub-dodecahedron second shell, and the thiolates are located radially outward from the underlying Ag atoms of the second core shell; under first-principles relaxation of the structure, the sulfur atoms displace outward with respect to the Ag atoms in the protective network (see dash-box inset in Figure 4). All of these features—the 1:1 (Ag:RS-) stoichiometry of the protective shell, the honeycomb arrangement, and the alternating height variations of the Ag and S atoms on the puckered hexagonal rings—bear close similarities to the SAMs-induced reconstruction of the

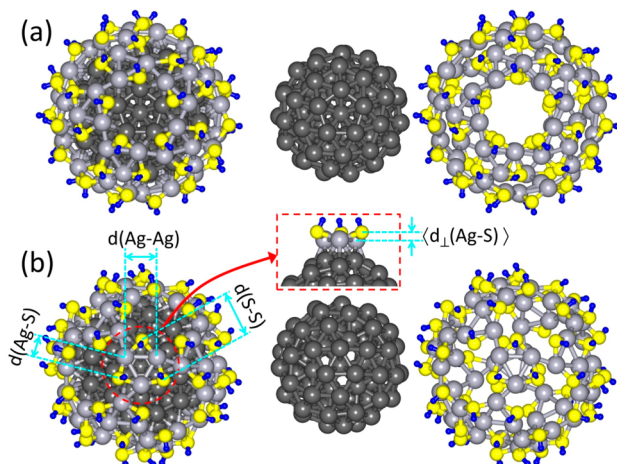


Figure 4. (Left) Optimized structure of the $\text{Ag}_{152}\text{X}_{60}$ ($\text{X} = \text{SH}$) as viewed down a 5-fold symmetry axis (top row, a) and down a 3-fold symmetry axis (bottom row, b). The structure comprises two major substructures: a 92-site core (all Ag), shown in the center column and a 120-site protective network displayed in the right column, in which Ag and S sites alternate. Across each row, the orientations described above are preserved. The encircled region (dashed in red) in the lower left frame (3-fold axis view) serves to highlight a top-view of the $(\text{Ag-S})_3$ (made of a silver, in light gray, and sulfur, in yellow, triangles), with 20 such units covering the entire surface of the structure. The central dashed rectangle (inset) shows a side view of the same six-membered ring unit. In this image, all other six-membered rings have been omitted, for clarity. Pertinent geometrical parameters: radial distances from the center of the $\text{Ag}_{152}\text{X}_{60}$ cluster: $d(20 \text{ Ag first shell}) = 3.95 \text{ \AA}$; $d(12 \text{ Ag Ih}) = 4.72 \text{ \AA}$; $d(60 \text{ Ag second shell}) = 6.48 \text{ \AA}$; $d(60 \text{ Ag protective network}) = 8.70 \text{ \AA}$; $d(60 \text{ Ag protective network}) = 9.68 \text{ \AA}$. Distances in the inset (central column): $\langle d(\text{Ag}-\text{Ag}) \rangle = 3.38 \text{ \AA}$; $\langle d(\text{Ag}-\text{S}) \rangle = 2.58 \text{ \AA}$; $\langle d(\text{S}-\text{S}) \rangle = 4.78 \text{ \AA}$; $\langle d_{\perp}(\text{Ag}-\text{S}) \rangle = 0.98 \text{ \AA}$. Color designation: S atoms are in yellow, H atoms in blue, internal silver atoms (of the 92 atom metal core) are depicted in dark gray, and silver atoms at exterior sites (the protective network) shown in light gray. The coordinates of the atoms in the optimized $\text{Ag}_{152}(\text{SH})_{60}^{2+}$ structure are given in Figure S14.

$\text{Ag}(111)$ surface.^{30,31} We note here that we found an essentially identical structure for a protected silver cluster comprised of 154 Ag atoms (see Sections S11, S12), with the two added atoms located inside the 20-atom dodecahedron (the inner core noted above); see details in sections Figure S11 and Figure S12. The radius of the protected cluster model that we described above was found to be consistent with that estimated from the SAXS measurements (i.e., $\sim 1.4 \text{ nm}$, that is, larger than the radius of the silver cluster (measured from the center to the edge of the Ag-S protecting shell) and smaller than the sum of that radius and the linear extent of the extended thiolate molecule.

Insights into the electronic structure and stability of the protected silver cluster studied here have been gained through calculations using the spin density-functional theory (SDFT)³³ in conjunction with nonlocal norm-conserving soft pseudopotentials³⁴ with the valence $4d^{10}$ and $5s^1$ electronic states of the silver atoms, as well as the valence electrons of the sulfur and hydrogen atoms of the protecting network shell, expanded in a plane-wave basis with a 62 Ry kinetic energy cutoff, and employing the Perdew–Burke–Ernzerhof (PBE) functional in the generalized gradient approximation (GGA) to the exchange-correlation corrections.³⁵

In Figure 5a,b, we display for the energy-optimized metal core Ag_{92}^{2+} (see center column in Figure 4) the projected

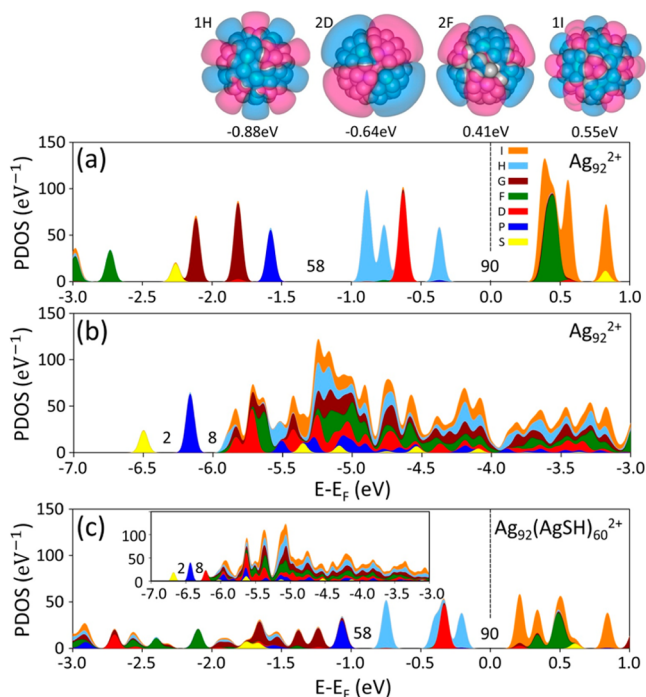


Figure 5. Calculated projected densities of states (PDOS) for Ag_{92}^{2+} (in a,b) and for $\text{Ag}_{152}(\text{SR})_{60}^{2+}$ (in c, densities for $\text{R}=\text{H}$), obtained through first-principles calculations. At the top we show images of selected (delocalized) orbitals near the top of the occupied spectrum, with their energies and angular momenta noted. (blue and pink colors correspond to opposite signs of the wave functions). In the PDOS different colors (see the color code at the right of a) correspond to the various angular momentum contributions, S (0), P (1), D (2), F (3), G (4), H (5), and I (6), which designate the irreducible representations of the full rotation group, $\text{SO}(3)$; the numbers in parentheses denote the angular momenta, $L = 0, 1, 2, \dots$, with the number of states being $2L + 1$ for a given L (that is a maximum of $2(2L + 1)$ electrons occupying states of a given angular momentum). The numbers (2, 8, 58, and 90) in the PDOS denote the number of electrons occupying superatom shells corresponding to shell closures. Note also the shell-closure-gap centered near -2.5 eV (in a) corresponding to 32-electron occupation of the superatom orbitals (with the 2S orbital shifted to the top of the gap due to deviation from spherical symmetry). While under perfect spherical, $\text{SO}(3)$, symmetry, the states corresponding to each of the angular momentum components are degenerate, they split in an environment of lower symmetry. Indeed the splitting observed in the calculated PDOS are consistent with the Ih/I point group symmetry of the 92 Ag atom core (Figure 4); see in particular the 3:4 weights of the two (split) peaks of the 1F level (with the total number of states of F symmetry being $2(3 + 1) = 7$), the 4:5 splitting of the states of 1G symmetry, and the 5:3:3 splitting of the states of 1H symmetry.

density of states (PDOS, i.e. the density of states projected onto the angular momentum components, introduced first in ref 17, see S13), along with images of representative orbitals near the top of the occupied spectrum; a vertical dashed line at $E - E_F = 0$ denotes the location of the midpoint between the highest occupied molecular orbital (HOMO) and the lowest unoccupied one (LUMO). In Figure 5c we show the PDOS for the optimized structure of $\text{Ag}_{92}(\text{AgSH})_{60}^{2+}$ (see Figure 4, left column). The first outstanding feature observed is the large HOMO–LUMO energy gap [$\Delta_{\text{HL}} = 0.73 \text{ eV}$ (0.41 eV) in

Figure 5a,c]. This large gap confers high stability to the cluster, endowing it with resistance to chemical attack.

Inspection of the electronic structure of the cluster and the orbitals' angular momentum symmetries (Figure 5) shows that, in agreement with an early proposal (introduced first in ref 17 termed as a "partial jellium" model, and used extensively in subsequent studies of protected metal clusters,³⁶ while for a wide range of energies (located at the middle of the energy spectrum) the electronic wave functions exhibit localized character (associated with Ag atomic 4d electrons), the orbitals of states with energies near the top and bottom of the electronic spectra are of delocalized character, derived from the atomic Ag 5s electrons (see representative orbital images in Figure 5a). These delocalized states can be assigned particular symmetries (determined with the use of an expansion of the calculated wave functions in spherical harmonics (see S13) following the electronic cluster-shell-model (CSM), with a (superatom) aufbau rule: $1S^2 | 1P^6 | 1D^{10} | 2S^2 | 1F^{14} | 2P^6 | 1G^{18} | 2D^{10} | 1H^{22} | 3S^2 | 1I^{26}$, and so forth, where S, P, D, F, G, H, and I, correspond, respectively, to angular momenta, $L = 0, 1, 2, 3, 4, 5,$ and 6 . In the above CSM scheme, the vertical lines denote shell-closures (magic numbers), with each closure accompanied by the opening of a stabilizing energy gap; in the above shell-structure scheme the shell closures occur at $n^* = 2, 8, 18, 34, 58, 92,$ and so forth, electrons (with the values of n^* 's called "magic numbers"). In Figure 5 the HOMO complex, consisting of 16 orbitals and holding 32 electrons, consisting of ($2D^{10} | 1H^{22}$) and corresponding to an Ag_{92}^{2+} core; note ionization of the $3S^2$ level yielding the dication. The LUMO complex consists of 21 (empty) orbitals, arising from 1I, 2F, and 3S states.

Deviations from spherical symmetry can cause certain alterations in level ordering, as well as splittings of the $(2L + 1)$ -fold level degeneracy by crystal-field effects. Such splittings are seen clearly in the PDOS for the Ag_{92}^{2+} core (see in particular Figure 5a), and they are consistent with the I_h/I point group symmetry of the core. Furthermore, we note that these splittings are maintained also in the electronic spectrum of the protected $Ag_{152}(SR)_{60}^{2+}$ cluster (see in particular the 5:3:3 splitting of the 1H states and the degeneracy of the 2D states at the top of the spectrum (compare Figure 5 a and c), attesting to the (autonomous) integrity of the protective silver-thiolate network (Figure 4, right column).

In summary, PET protected silver quantum cluster was synthesized using a solid state route. Based on MALDI MS data the cluster composition was assigned to $Ag_{152}(SCH_2CH_2Ph)_{60}$. It shows an optical absorption spectrum reminiscent of silver nanoparticles. It exhibits a NIR emission ($\lambda_{emi} \sim 800$ nm) due to the core and structured emission due to the shell. The cluster mass spectrum is sensitive to the laser fluence. Excellent periodic arrangement of the clusters was observed in HRTEM and SEM. Exploiting combined insights from investigations of clusters and surface science, a core-shell structural model was developed, with a 92-atom silver core having icosahedral-snob dodcahedral symmetry and an encapsulating protective shell comprised of 60 Ag atoms and 60 thiolates arranged in a network of six-membered rings resembling the geometry found in self-assembled monolayers on Ag(111). First-principles electronic structure calculations show the development of a ~ 0.4 eV HOMO-LUMO energy gap for the geometry-optimized structure, originating from a superatom 90-electron shell-closure and conferring stability to the cluster when in the 2^+ (dication) charge state, in correspondence with the

measured large dication intensity in the purified cluster material (see Figure 1b). Efforts are underway to crystallize the clusters.

■ ASSOCIATED CONTENT

Supporting Information

Details of experimental procedures and characterization using UV-vis (absorbance in terms of energy), SEM, EDAX, HPLC, SAXS, and MALDI MS of the 25 kDa clusters at varying laser intensities. For the theory part we report the method for calculations of the PDOS, a layer-by-layer construction of the 92-atom metal core of the cluster, and the coordinates of all the atoms in the optimized structure of the $Ag_{92}(SH)_{60}^{2+}$ cluster. This material is available free of charge via the Internet at <http://pubs.acs.org>.

■ AUTHOR INFORMATION

Corresponding Author

*E-mail: pradeep@iitm.ac.in. Fax: + 91-44 2257-0545.

Present Address

[†]Summer students from Stella Maris College, Chennai, India.

Author Contributions

[‡]These authors contributed equally.

Notes

The authors declare no competing financial interest.

■ ACKNOWLEDGMENTS

We thank the Department of Science and Technology, Government of India and IIT Madras for constantly supporting our research program on nanomaterials. Thanks to CGCRI, Kolkata for the SAXS analysis. The work of B.Y. and U.L. was supported by the Office of Basic Energy Sciences of the US Department of Energy under Contract No. FG05-86ER45234 and in part by a grant the Air Force Office of Scientific Research. Computations were made at the GATECH Center for Computational Materials Science.

■ REFERENCES

- (1) Whetten, R. L.; Khoury, J. T.; Alvarez, M. M.; Murthy, S.; Vezmar, I.; Wang, Z. L.; Stephens, P. W.; Cleveland, C. L.; Luedtke, W. D.; Landman, U. *Adv. Mater.* **1996**, *8*, 428–433.
- (2) Zheng, J.; Nicovich, P. R.; Dickson, R. M. *Annu. Rev. Phys. Chem.* **2007**, *58*, 409–431.
- (3) Jin, R. *Nanoscale* **2010**, *2*, 343–362.
- (4) Shichibu, Y.; Suzuki, K.; Konishi, K. *Nanoscale* **2012**, *4*, 4125–4129.
- (5) Schmid, G.; Meyer-Zaika, W.; Pugin, R.; Sawitowski, T.; Majoral, J.-P.; Caminade, A.-M.; Turrin, C.-O. *Chem.—Eur. J.* **2000**, *6*, 1693–1697.
- (6) Schmid, G. *Chem. Soc. Rev.* **2008**, *37*, 1909–1930.
- (7) Shichibu, Y.; Negishi, Y.; Tsukuda, T.; Teranishi, T. *J. Am. Chem. Soc.* **2005**, *127*, 13464–13465.
- (8) Shichibu, Y.; Negishi, Y.; Tsunoyama, H.; Kanehara, M.; Teranishi, T.; Tsukuda, T. *Small* **2007**, *3*, 835–839.
- (9) Shibu, E. S.; Muhammed, M. A. H.; Tsukuda, T.; Pradeep, T. *J. Phys. Chem. C* **2008**, *112*, 12168–12176.
- (10) Zhu, M.; Lanni, E.; Garg, N.; Bier, M. E.; Jin, R. *J. Am. Chem. Soc.* **2008**, *130*, 1138–1139.
- (11) Heaven, M. W.; Dass, A.; White, P. S.; Holt, K. M.; Murray, R. W. *J. Am. Chem. Soc.* **2008**, *130*, 3754–3755.
- (12) Jadzinsky, P. D.; Calero, G.; Ackerson, C. J.; Bushnell, D. A.; Kornberg, R. D. *Science* **2007**, *318*, 430–433.
- (13) Pei, Y.; Gao, Y.; Zeng, X. C. *J. Am. Chem. Soc.* **2008**, *130*, 7830–7832.

- (14) Rao, T. U. B.; Nataraju, B.; Pradeep, T. *J. Am. Chem. Soc.* **2010**, *132*, 16304–16307.
- (15) Udaya Bhaskara Rao, T.; Pradeep, T. *Angew. Chem., Int. Ed.* **2010**, *49*, 3925–3929.
- (16) Chakraborty, I.; Udayabhaskararao, T.; Pradeep, T. *Chem. Commun.* **2012**, *48*, 6788–6790.
- (17) Yoon, B.; Koskinen, P.; Huber, B.; Kostko, O.; von Issendorff, B.; Häkkinen, H.; Moseler, M.; Landman, U. *ChemPhysChem* **2007**, *8*, 157–161.
- (18) Knight, W. D.; Clemenger, K.; de Heer, W. A.; Saunders, W. A.; Chou, M. Y.; Cohen, M. L. *Phys. Rev. Lett.* **1984**, *52*, 2141–2143.
- (19) Branham, M. R.; Douglas, A. D.; Mills, A. J.; Tracy, J. B.; White, P. S.; Murray, R. W. *Langmuir* **2006**, *22*, 11376–11383.
- (20) Negishi, Y.; Arai, R.; Niihori, Y.; Tsukuda, T. *Chem. Commun.* **2011**, *47*, 5693–5695.
- (21) Schaaff, T. G.; Shafiqullin, M. N.; Khoury, J. T.; Vezmar, I.; Whetten, R. L. *J. Phys. Chem. B* **2001**, *105*, 8785–8796.
- (22) Lopez-Acevedo, O.; Akola, J.; Whetten, R. L.; GroInbeck, H.; Häkkinen, H. *J. Phys. Chem. C* **2009**, *113*, 5035–5038.
- (23) Chaki, N. K.; Negishi, Y.; Tsunoyama, H.; Shichibu, Y.; Tsukuda, T. *J. Am. Chem. Soc.* **2008**, *130*, 8608–8610.
- (24) Qian, H.; Jin, R. *Nano Lett.* **2009**, *9*, 4083–4087.
- (25) Dass, A. *J. Am. Chem. Soc.* **2009**, *131*, 11666–11667.
- (26) Dharmaratne, A. C.; Krick, T.; Dass, A. *J. Am. Chem. Soc.* **2009**, *131*, 13604–13605.
- (27) Martin, T. P. *Phys. Rep.* **1996**, *273*, 199–241.
- (28) Cleveland, C. L.; Landman, U.; Schaaff, T. G.; Shafiqullin, M. N.; Stephens, P. W.; Whetten, R. L. *Phys. Rev. Lett.* **1997**, *79*, 1873–1876.
- (29) Tran, N. T.; Powell, D. R.; Dahl, L. F. *Angew. Chem., Int. Ed.* **2000**, *39*, 4121–4125.
- (30) Parkinson, G. S.; Hentz, A.; Quinn, P. D.; Window, A. J.; Woodruff, D. P.; Bailey, P.; Noakes, T. C. Q. *Surf. Sci.* **2007**, *601*, 50–57.
- (31) Otálvaro, D.; Veening, T.; Brocks, G. *J. Phys. Chem. C* **2012**, *116*, 7826–7837.
- (32) Williams, R. *The Geometrical Foundation of Natural Structure*; Dover: New York, 1979.
- (33) Barnett, R. N.; Landman, U. *Phys. Rev. B* **1993**, *48*, 2081–2097.
- (34) Troullier, N.; Martins, J. L. *Phys. Rev. B* **1991**, *43*, 1993–2006.
- (35) Perdew, J. P.; Burke, K.; Ernzerhof, M. *Phys. Rev. Lett.* **1997**, *78*, 1396–1396.
- (36) Walter, M.; Akola, J.; Lopez-Acevedo, O.; Jadzinsky, P. D.; Calero, G.; Ackerson, C. J.; Whetten, R. L.; Groenbeck, H.; Häkkinen, H. *Proc. Natl. Acad. Sci.* **2008**, *105*, 9157–9162.

Supporting information for the paper:

The Superstable 25-*kDa* Protected Silver Nanoparticle: Measurements & Interpretation as an Icosahedral $\text{Ag}_{152}(\text{SCH}_2\text{CH}_2\text{Ph})_{60}$ Cluster

Indranath Chakraborty^{1†}, Anuradha Govindarajan^{1‡}, Jayanthi Erusappan^{1#}, Atanu Ghosh¹,
T. Pradeep^{1*}, Bokwon Yoon², Robert L. Whetten³, and Uzi Landman²

¹*DST Unit of Nanoscience (DST UNS), Department of Chemistry, Indian Institute of Technology
Madras, Chennai 600036, India.*

²*School of Physics, Georgia Institute of Technology, Atlanta, GA 30332-0430, USA*

³*School of Chemistry & Biochemistry, Georgia Institute of Technology, Atlanta, GA 30332, USA*

*E-mail: pradeep@iitm.ac.in

† Contributed equally

#Summer students from Stella Maris College, Chennai, India

Contents

Number	Description	Page number
S1	Experimental section	2-3
S2	Chromatogram of Ag_{152} cluster	4
S3	SAXS and particle size distribution	5
S4	SEM images	6
S5	Elemental mapping	7
S6	MALDI MS of the cluster at varying laser fluence	8
S7	MALDI MS of the cluster at higher laser fluence	9
S8	Absorbance in terms of energy in eV	10
S9	TEM image of $\text{Ag}@\text{PET}$ nanoparticles	11
S10	Assembly of the ideal 92 atom core	12
S11	Inner core structures of Ag_{92}^{2+} and Ag_{94}^{2+}	13
S12	Radial distances for $\text{Ag}_{152}(\text{SH})_{60}^{2+}$ and $\text{Ag}_{154}(\text{SH})_{60}^{2+}$	14
S13	Projected density of states	15
S14	Coordinates for optimized $\text{Ag}_{152}(\text{SH})_{60}^{2+}$	16-22

Supporting information 1

Materials and methods:

1. Chemicals

Silver nitrate (AgNO_3 , 99% Aldrich), sodium borohydride (NaBH_4 , 99.9%, Aldrich); 2-phenylethanethiol (PETH, 98%, Aldrich); ethanol (Changshu Yangyuan Chemical, China, AR grade), THF (MARC, HPLC grade) and toluene (Ranken, AR grade) were used in this synthesis. All the chemicals were commercially available and were used without further purification.

2. Synthesis of $\text{Ag}_{152}(\text{SCH}_2\text{CH}_2\text{Ph})_{60}$

The synthesis of Ag_{152} cluster protected by PET (2-phenylethanethiolate) involves the following processes. Initially, at room temperature (35-40°C, relative humidity-80%) 23 mg of AgNO_3 and 100 μL of PETH were ground well in a clean agate mortar using a pestle. The color of the mixture changes to pale orange showing the formation of silver thiolate. To this mixture, 25 mg of solid NaBH_4 were added and the content was mixed well. 3 mL of ethanol was added to the mixture and mixed well after which 2 mL of ethanol was added for the washing the mixture. The mixture was kept for 15-30 sec till there is a color change from pale orange to deep grey. The contents were then taken into a centrifuge tube and centrifuged at 1600 rpm. The centrifugate was removed and the residue was dissolved in 5 mL toluene/THF. The Ag_{152} clusters were obtained from the toluene extract, which was dark brown in color. The toluene extracted cluster is stable for 10 days in the laboratory conditions and in deep freezer, it is stable for one month but THF extracted cluster is stable up to 2 days. The calculated yield is 82%.

The cluster is not stable in presence of excess thiol. It is this thiol that is removed by extraction with ethanol. However, ethanol also adds water and with more water, the cluster size increases. Therefore, it is important to optimize the time of exposure of ethanol. Humidity of the laboratory air is also an important factor.

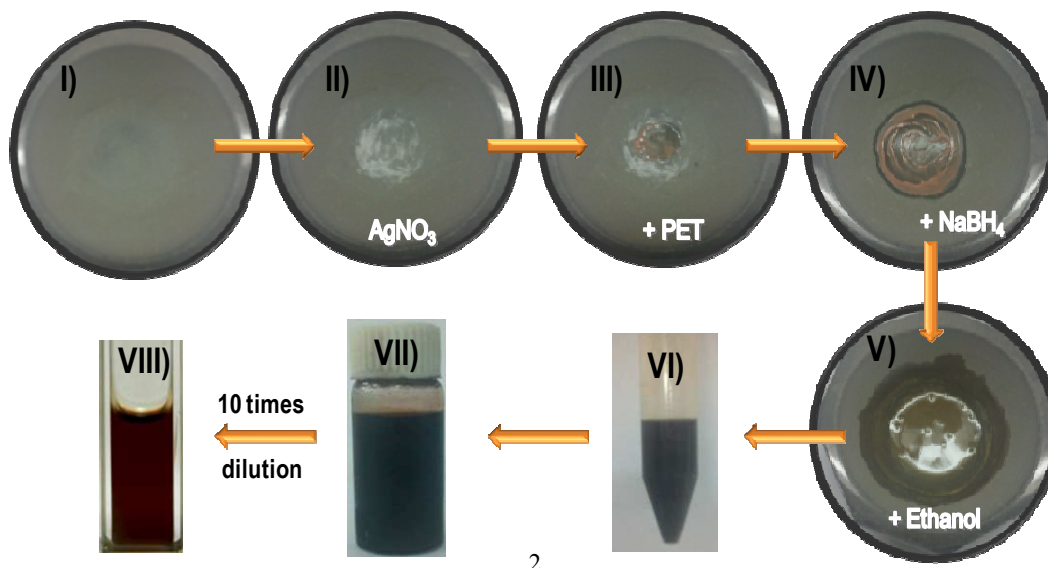


Figure S1. Photographs of various steps during the synthesis. I) Empty mortar, II) ground silver nitrate, III) addition of PETH to II, IV) addition of NaBH₄ to III, V) ethanol addition to IV, VI) reaction mixture in centrifuge tube for centrifugation, VII) residue after centrifugation, extracted in toluene and VIII) cluster in cuvette after 10 times dilution.

3. Instrumentation:

UV-Vis spectra were measured with a Perkin Elmer Lambda 25 instrument in the range of 200-1100 nm. Luminescence measurements were carried out on a Jobin Vyon NanoLog instrument. The band pass for excitation and emission was set as 2 nm. High resolution transmission electron microscopy of clusters was carried out with a JEOL 3010 instrument. The samples were drop casted on carbon-coated copper grids and allowed to dry under ambient conditions. Matrix-assisted desorption ionization mass spectrometry (MALDI MS) studies were conducted using a Voyager-DE PRO Biospectrometry Workstation from Applied Biosystems. The matrix used was DCTB (at 1:100 ratio of sample to matrix). A pulsed nitrogen laser of 337 nm was used for the MALDI MS studies. Mass spectra were collected in positive ion mode and were averaged for 200 shots. Scanning electron microscopic (SEM) and energy dispersive X-ray (EDAX) analyses were performed with a FEI QUANTA-200 SEM. For measurements, samples were drop casted on an indium tin oxide (ITO) coated glass and dried in vacuum. Transmission small angle X-ray scattering (SAXS) measurements of toluene solution of the clusters were performed with a Rigaku SmartLab X-ray diffractometer operating at 9 kW (200 mA; 45 kV) using Cu-K α radiation. A NANO-Solver programme of Rigaku was used. Nonlinear least square method was used for finding the best fit. For SAXS measurements cluster solutions were taken in a sealed silica glass capillary of 1 mm diameter. HPLC measurement was done in Shimadzu HPLC system equipped with a C18 column (Shimadzu).

Supporting information 2

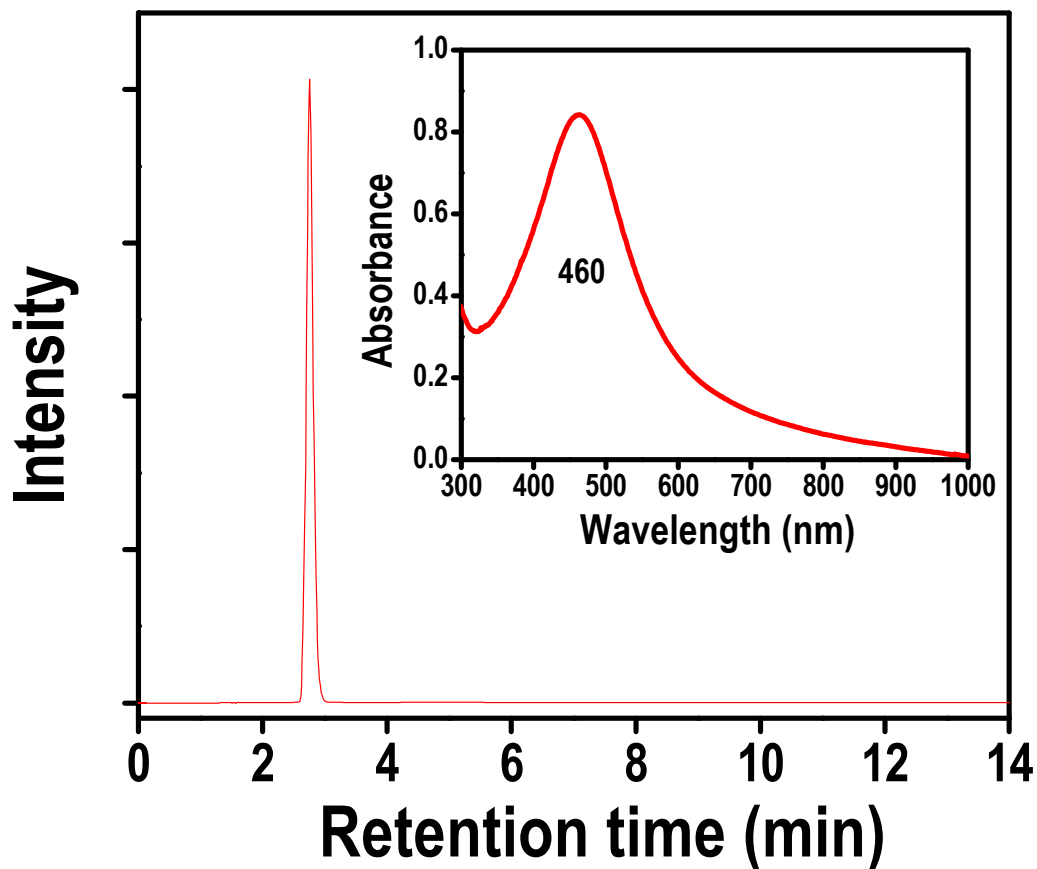


Figure S2. Chromatogram of Ag_{152} cluster extracted in THF. In this experiment, a high-performance liquid chromatography (HPLC) system equipped with a C18 column (250 X 4.6 mm) was used with a flow rate of 1 mL/min. The UV-vis absorbance detector was operated at 400 nm. The spectrum shows the presence of a single cluster. Inset: UV/Vis spectrum of the isolated cluster with a peak maximum at 460 nm.

Supporting information 3

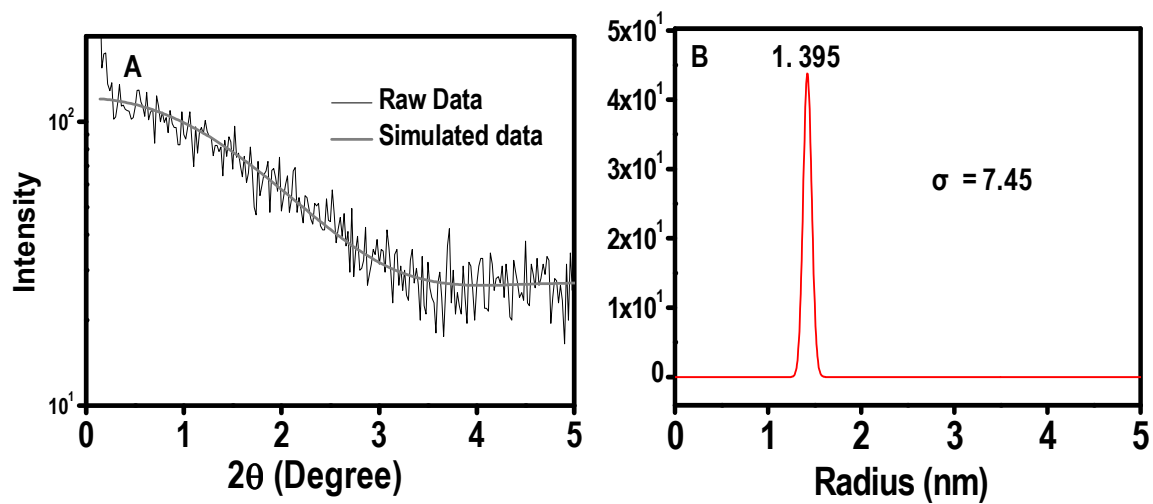


Figure S3. Small angle X-ray scattering (SAXS) analysis of the Ag_{152} cluster. Experimental and simulated (nonlinear least squares method) SAXS curves are shown in the left side (A) and the corresponding particle size distribution obtained from SAXS profile is shown in the right panel (B). Corresponding dispersion (σ) is given in the inset. It shows a great homogeneity in particle size.

Supporting information 4

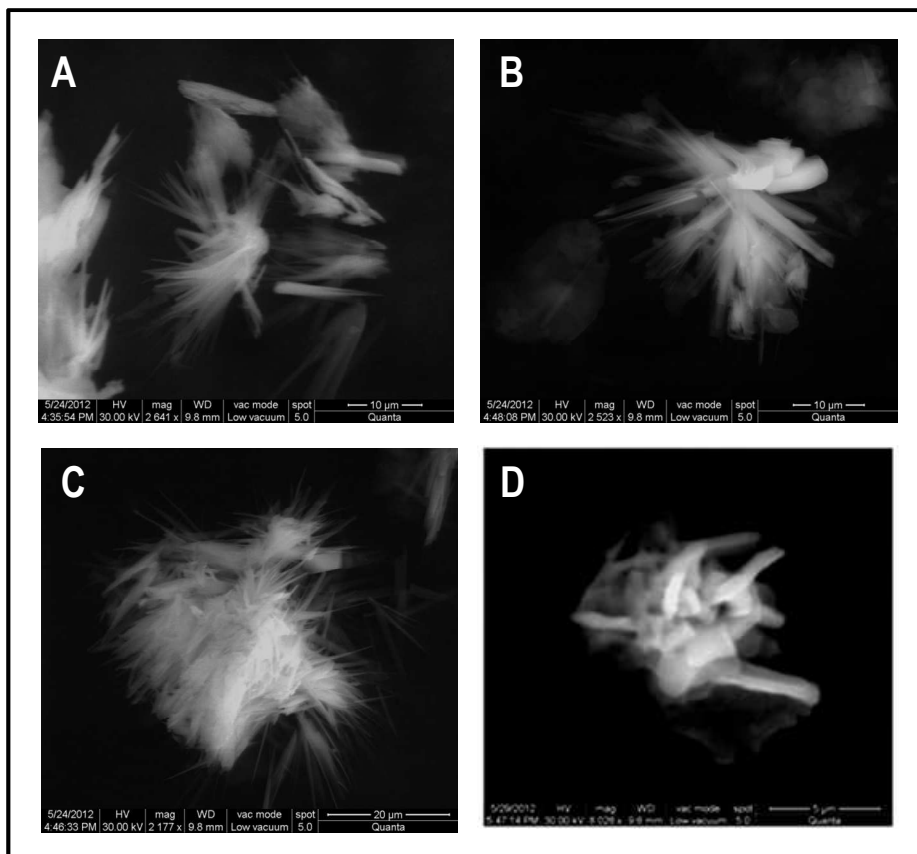


Figure S4. SEM images of as synthesized Ag₁₅₂ cluster. After removal of toluene using rotavapor, the solid mass was taken on an ITO glass plate for imaging.

Supporting information 5

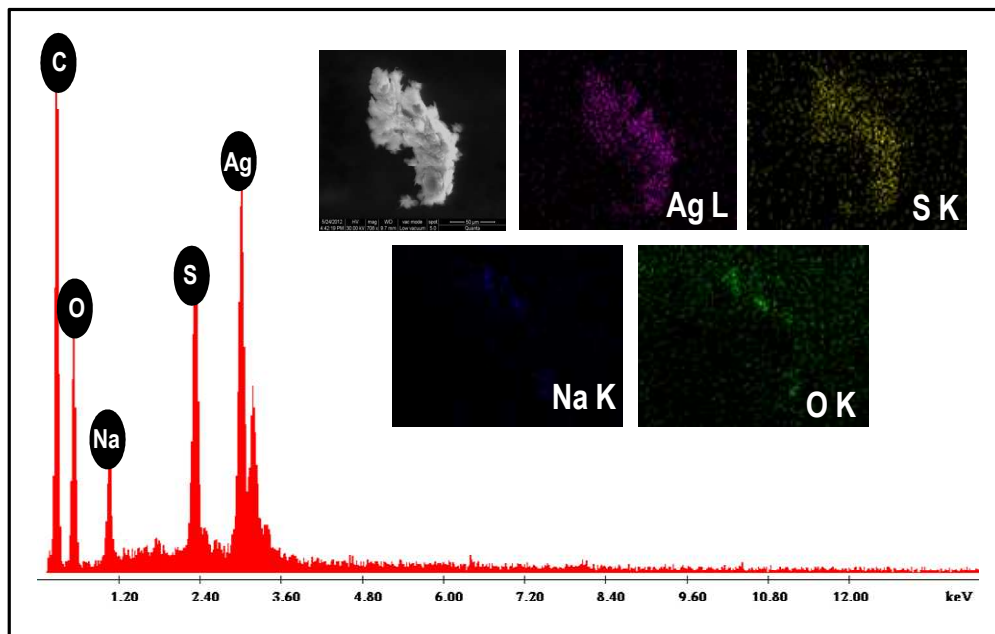


Figure S5. Elemental mapping of a specified area was taken which shows the presence of silver and sulfur at a ratio of 2.2:1. A little excess of thiol was seen compared to the expected composition (2.5:1) which may be needed for cluster stabilization in the solid state.

Supporting information 6

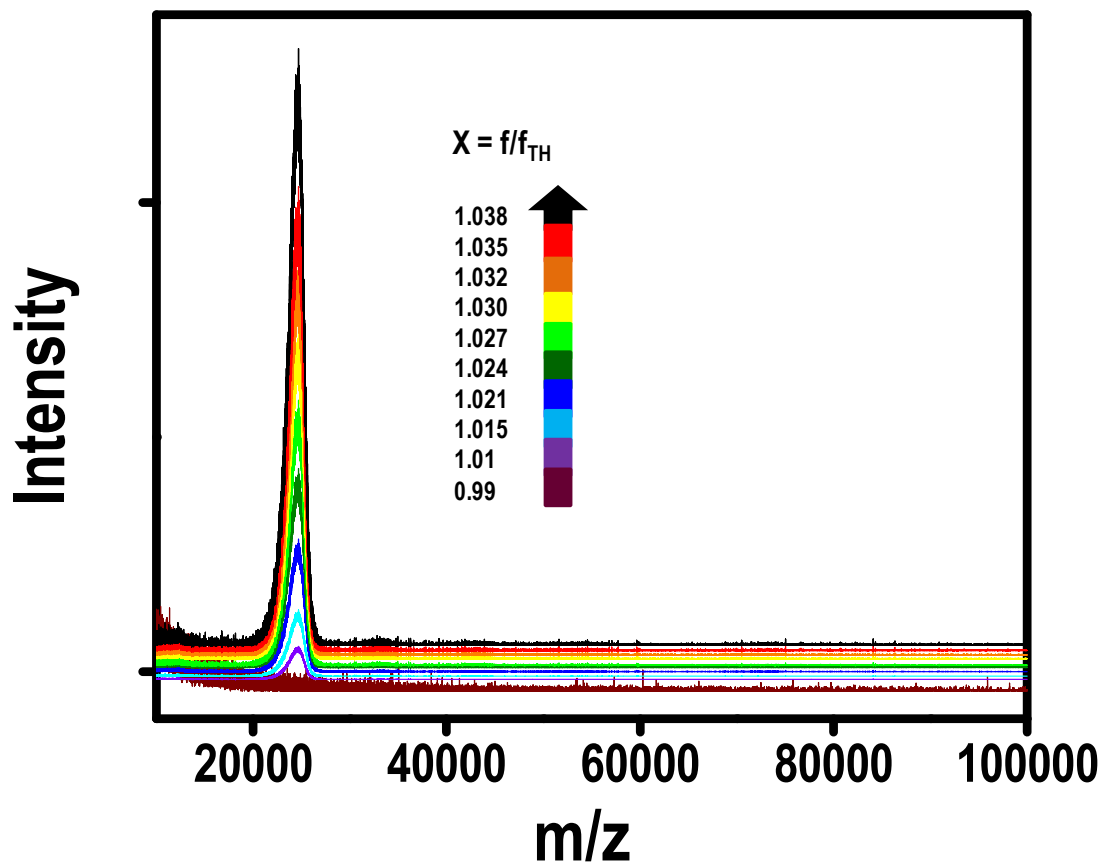


Figure S6. MALDI MS spectra for as-synthesized Ag₁₅₂ cluster measured at varying laser fluence, expressed in terms of the threshold fluence f_{TH} corresponding to the detection of ions; $f = x f_{TH}$, $x = 0.99$ to $x = 1.04$. The ion signal increases with an increase in laser fluence in this window. Subsequently, no further increase in ion intensity was observed; however, at still higher laser intensity, fragmentation commences (see Figure S7).

Supporting information 7

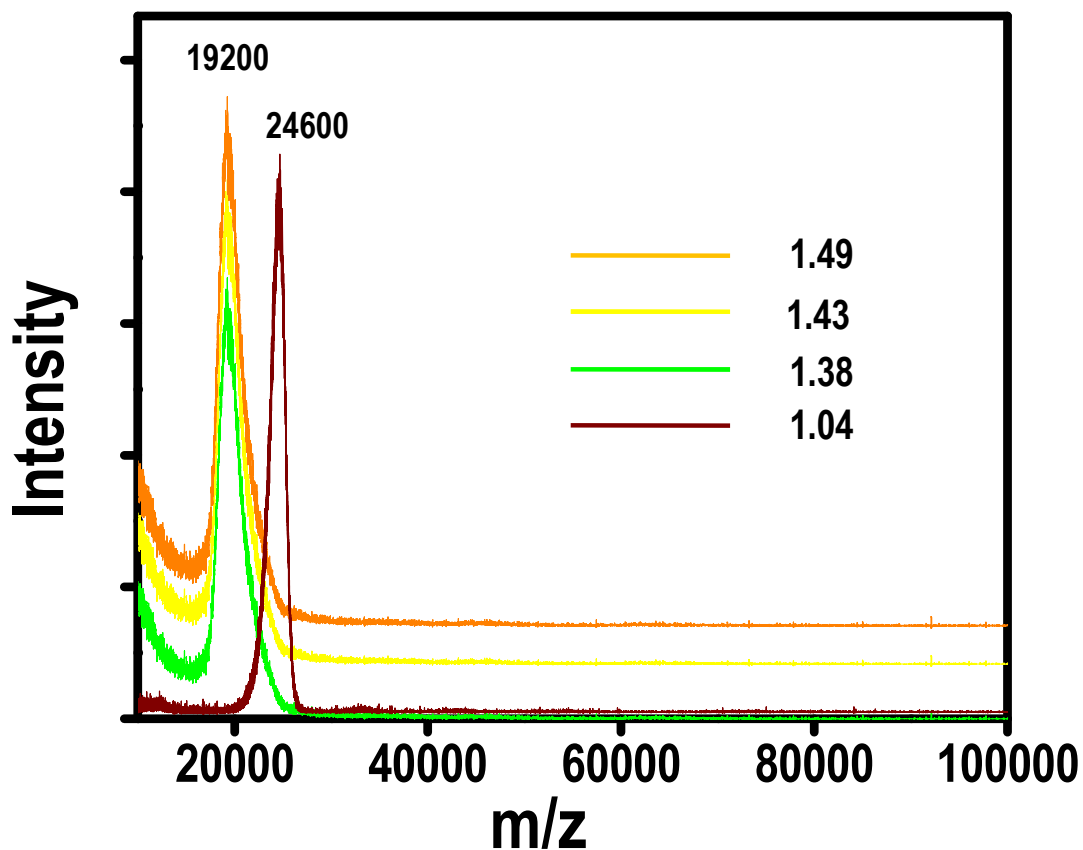


Figure S7. MALDI MS data for as-synthesized Ag_{152} cluster measured at varying laser fluence, expressed in terms of the threshold fluence f_{TH} corresponding the detection of ions; $f = x \cdot f_{\text{TH}}$, $x = 1.04$ to $x = 1.49$. In this fluence-window fragmentation occurs. The fragment-ion signal increases with increase in laser fluence (see peak at m/z 19200). Beyond a critical value no further change happens. The spectrum at a lower laser power showing the feature at m/z 24,600 is shown for comparison. Data corresponding to in-between laser intensities are shown in Figure 2 of the text.

Supporting information 8

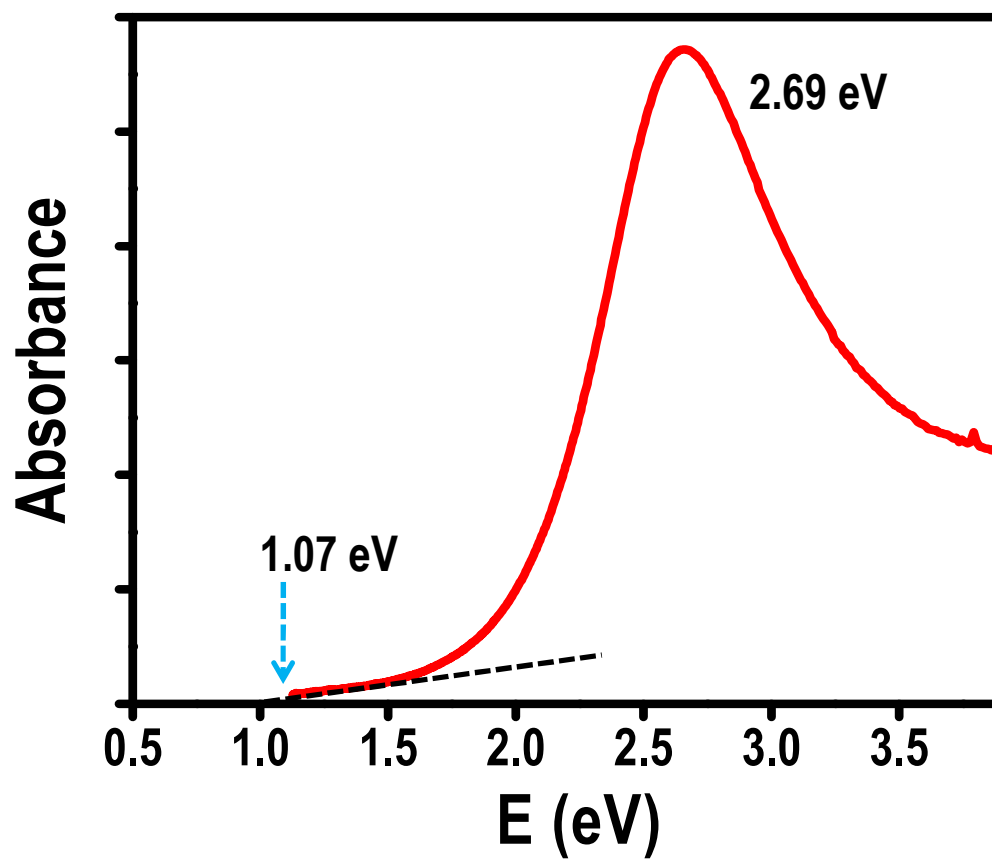
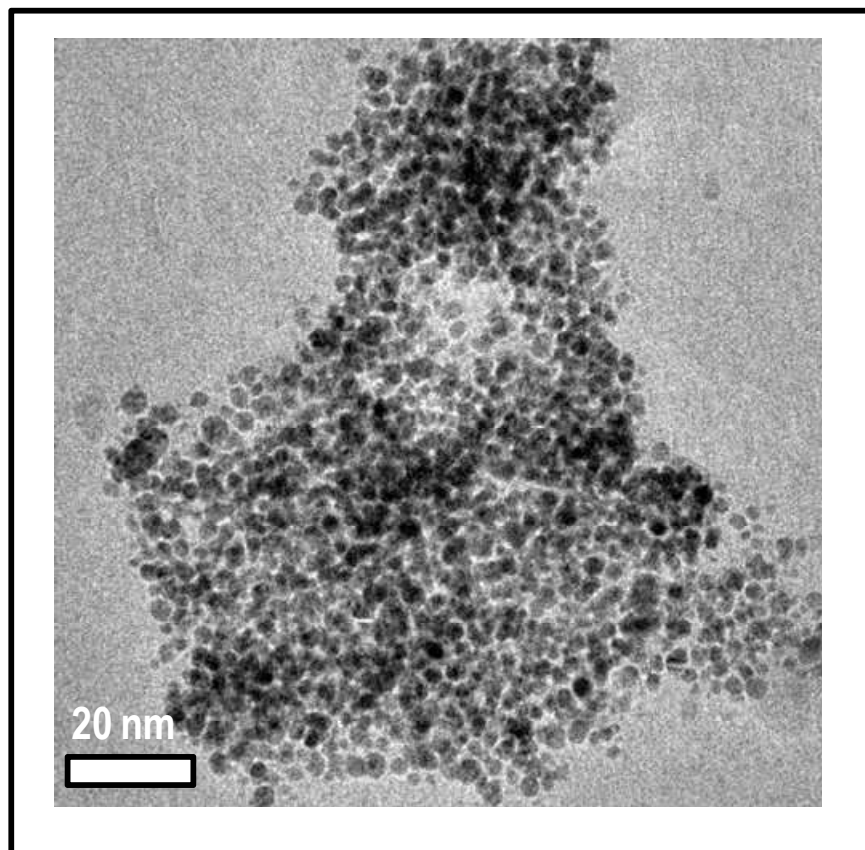


Figure S8. Absorbance spectrum in terms of energy in eV. A band at 2.66 eV was observed along with a threshold of 1.07 eV.

Supporting information 9

TEM image of Ag@PET nanoparticles



Supporting information 10
Assembly of Ag₉₂ (core) cluster

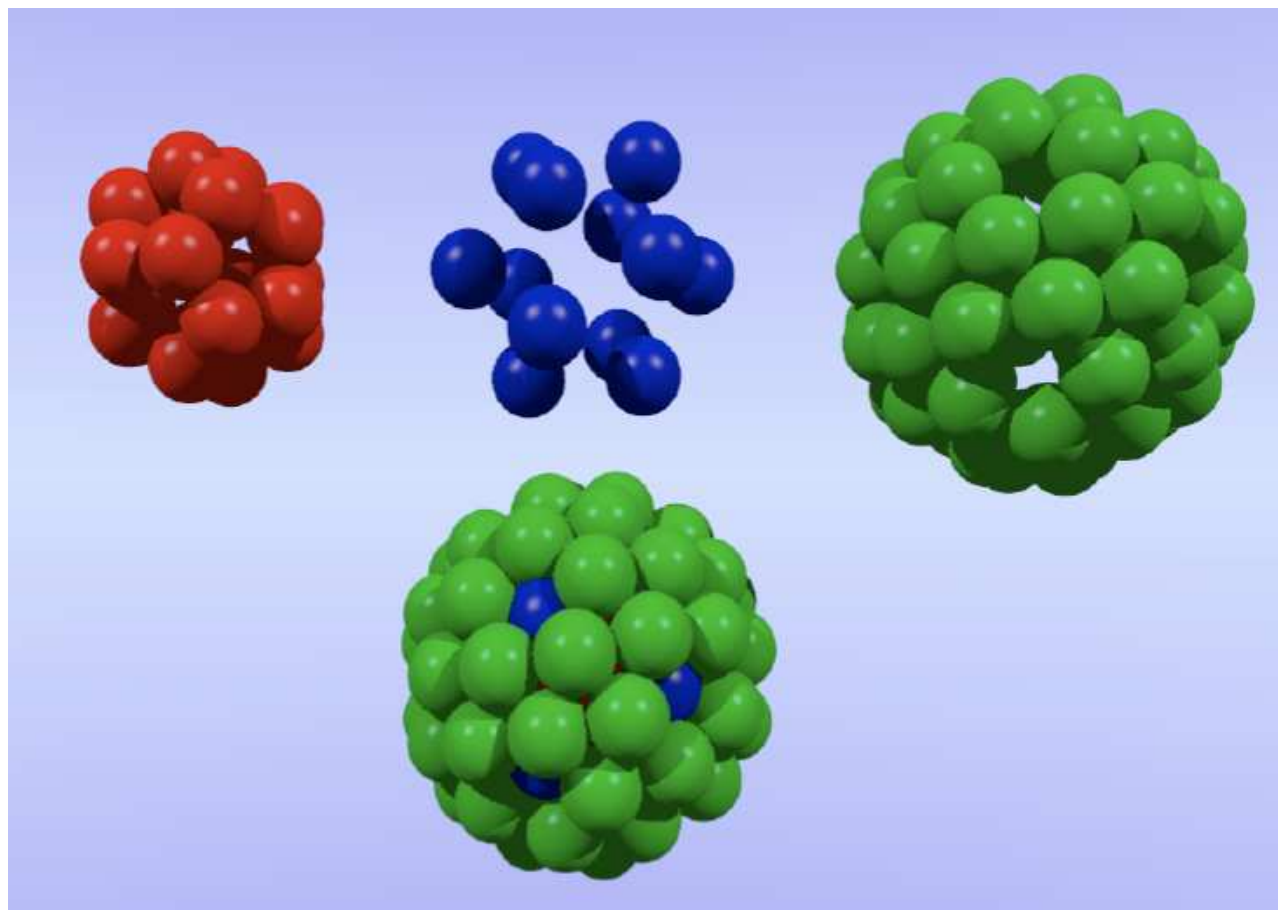


Figure S10. Schematic illustration of the assembly of the ideal 92 atom core, *Icosahedral I-92*. TOP ROW: (left, red) 20 Ag atom Pentagonal Dodecahedron and (middle, blue) surrounding 12 Ag atom Icosahedron, with the two forming the first (inner) 32 Ag atom shell; (right, green) 60 Ag atom encapsulating (second shell) Snub Dodecahedron. BOTTOM ROW: 92 Ag atom assembled Core. Source: Adapted from T. G. Schaaff, unpublished (2006).

Supporting information 11
Inner core structures of Ag_{92}^{2+} and Ag_{94}^{2+}

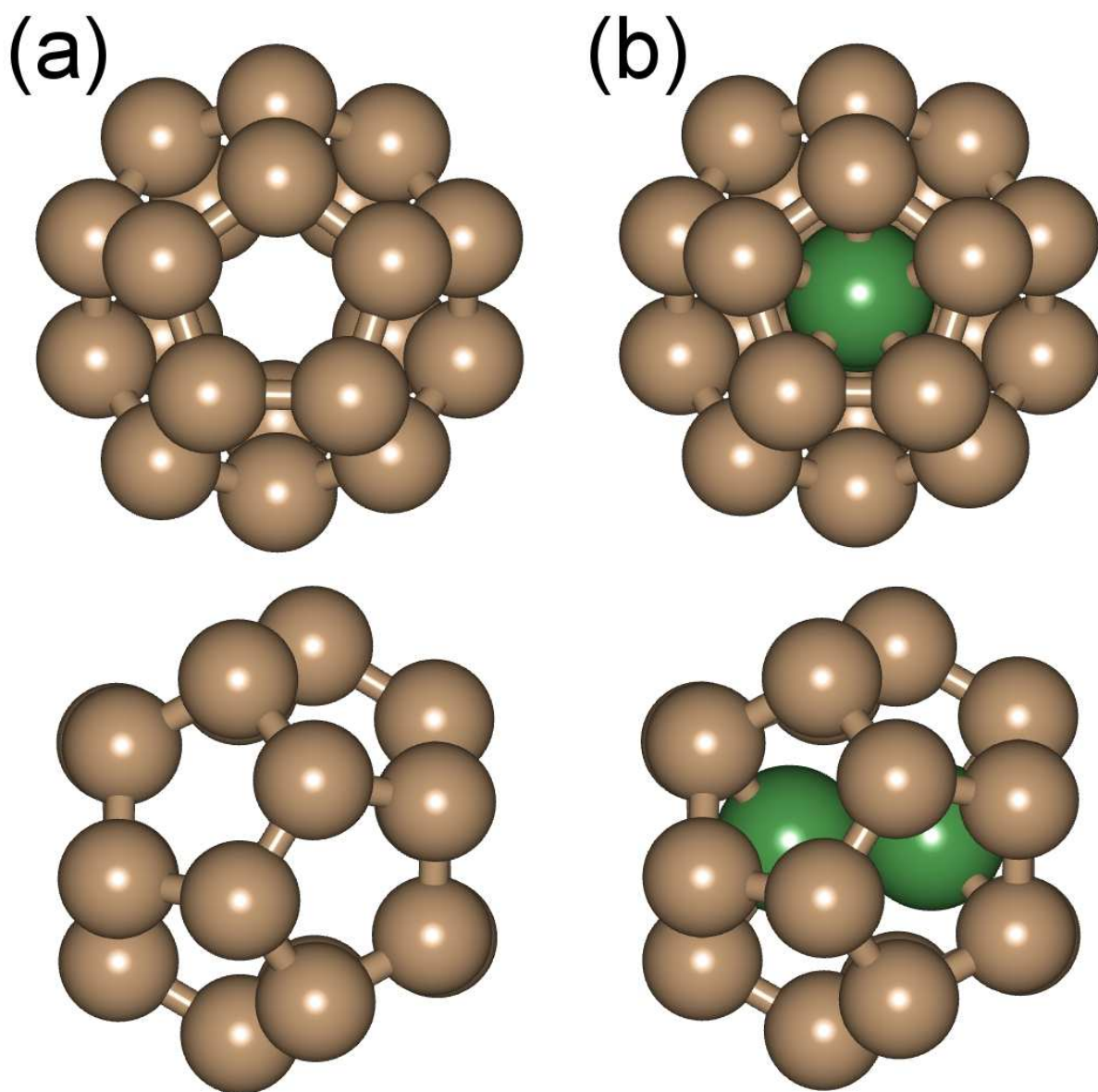


Figure S11. (a) Two views of the Pentagonal dodecahedral inner core of the relaxed Ag_{92}^{2+} cluster. (b) Two views of the Pentagonal dodecahedral inner core of the relaxed Ag_{94}^{2+} cluster. The two extra atoms inside the dodecahedron are colored green. The interatomic distance between the two inner Ag atom $d(\text{Ag}-\text{Ag}) = 2.83 \text{ \AA}$, and the mean distance between an inner Ag atom and an Ag atom on the nearest pentagonal face is 2.94 \AA .

Supporting information 12

Radial distances for $\text{Ag}_{152}(\text{SH})_{60}^{2+}$ and $\text{Ag}_{154}(\text{SH})_{60}^{2+}$

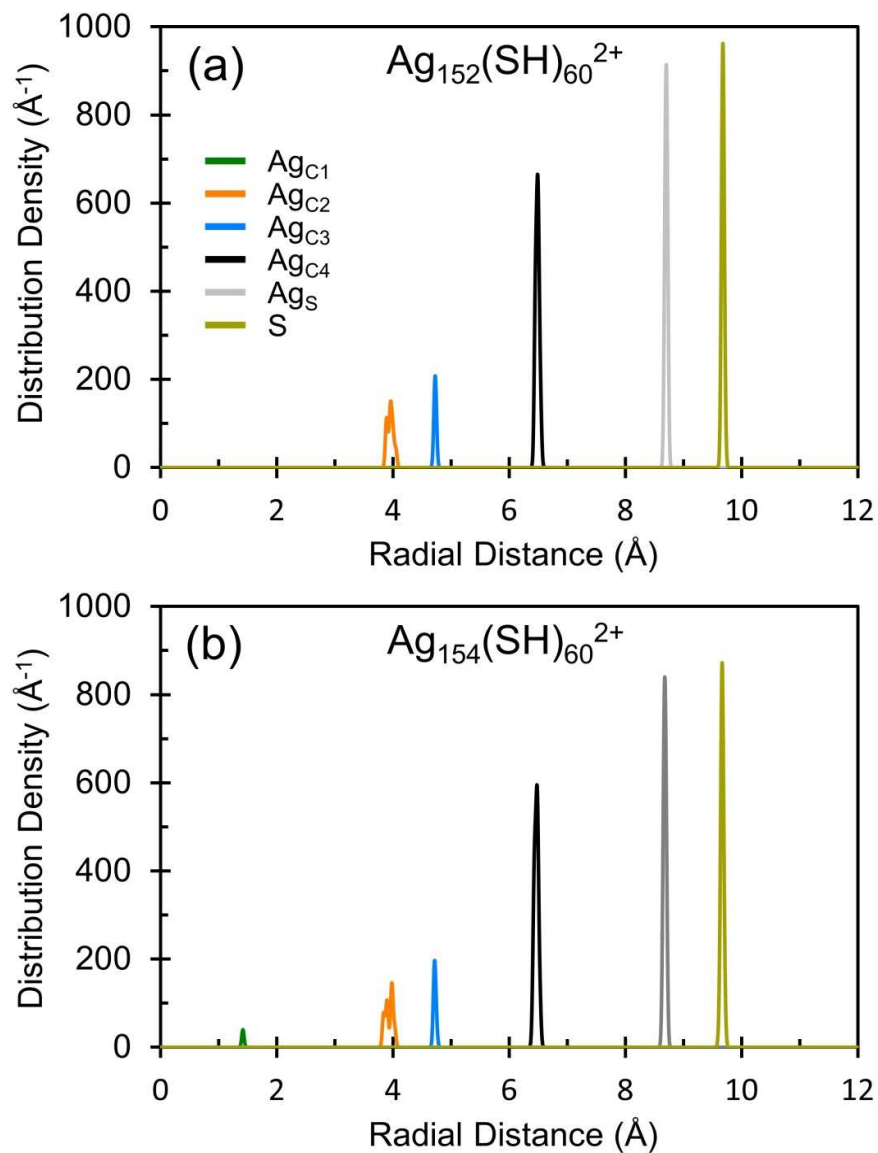


Figure S12. Radial distances for (a) $\text{Ag}_{152}(\text{SH})_{60}^{2+}$ and (b) $\text{Ag}_{154}(\text{SH})_{60}^{2+}$, measured from the center of the clusters.

Ag_{C1} : Ag dimer in the core

Ag_{C2} : 20-atom dodecahedron in the core

Ag_{C3} : 12 capping Ag atoms on the faces of dodecahedron

Ag_{C4} : 60-Ag-atom shell in the core

Ag_{S} : 60-Ag-atom outer shell

S : sulfur atoms

Supporting information 13

Projected density of states

The projected local density of states (PDOS) (1), $w_{i,l}(R_0)$ was calculated from the Kohn-Sham (KS) orbitals $\psi_i(\mathbf{r} + \mathbf{R}_{cm})$, where \mathbf{R}_{cm} is the center of mass of the cluster (taken from here on as the origin, $\mathbf{R}_{cm} = 0$), using

$$w_{i,l}(R_0) = \sum_{m=-l}^l \int_0^{R_0} r^2 dr |\varphi_{i,lm}(r)|^2$$

$$\varphi_{i,lm}(r) = \int d\Omega Y_{lm}(\Omega) \psi_i(\mathbf{r})$$

Here, Y_{lm} is the spherical harmonic function with angular momentum number l and magnetic quantum number m , and the angular momenta up to $l = 6$ (I symmetry) are included; the symmetries associated with the angular momentum numbers $l = 0, 1, 2, \dots, 6$ are denoted as S, P, D, F, G, H and I, respectively. The integration is taken in a sphere of radius R_0 , chosen as follows for Ag_{92}^{++} : $R_0 = 11.4 \text{ \AA}$ and for $\text{Au}_{92}(\text{AgSH})_{60}$: $R_0 = 7.6 \text{ \AA}$.

(1) B.Yoon *et al.* Size-Dependent Structural Evolution and Chemical Reactivity of Gold Clusters. *ChemPhysChem* **8**, 157- 161 (2007).

Supporting information 14

Coordinate file for the optimized $\text{Ag}_{152}(\text{SH})_{60}^{2+}$ cluster

Coordinates of Ag_{92}^{++} cluster (element x y z):

Ag	0.752565	2.283295	3.133637
Ag	2.357669	0.001888	3.080903
Ag	1.185169	3.646204	0.730142
Ag	-1.887624	1.398449	3.109269
Ag	3.838411	0.002623	0.716517
Ag	0.747340	-2.279548	3.132133
Ag	-1.176478	3.645008	-0.737800
Ag	3.095906	2.257852	-0.749036
Ag	-1.889690	-1.393433	3.119143
Ag	-3.095603	2.271838	0.744787
Ag	3.078952	-2.249063	-0.750801
Ag	1.182329	-3.650029	0.731682
Ag	-0.750477	2.285118	-3.146674
Ag	1.888804	1.398986	-3.114206
Ag	-3.078210	-2.257184	0.747978
Ag	-3.800016	0.002038	-0.718364
Ag	1.895171	-1.392033	-3.126091
Ag	-1.182178	-3.655543	-0.738161
Ag	-2.353206	0.000769	-3.098757
Ag	-0.742955	-2.281619	-3.136094
Ag	3.467682	2.517425	2.128473
Ag	-1.316506	4.089817	2.149922
Ag	0.021939	0.002692	4.808978
Ag	3.465158	-2.510643	2.129846
Ag	1.317465	4.089561	-2.158360
Ag	-4.248013	0.004343	2.153448
Ag	4.257215	0.003135	-2.160201
Ag	-1.308450	-4.088341	2.149553
Ag	-3.457026	2.521503	-2.138536
Ag	1.313433	-4.083525	-2.155046
Ag	-0.014006	0.003132	-4.813318
Ag	-3.456066	-2.515987	-2.137253
Ag	1.380317	2.209858	5.939215
Ag	2.539478	-0.623028	5.906376
Ag	3.983755	1.691730	4.774006
Ag	2.551184	4.280482	4.149097
Ag	-0.355265	4.335520	4.803262
Ag	-1.644978	1.991213	5.921998
Ag	0.219353	-2.588985	5.939737
Ag	2.867388	-3.282198	4.793081
Ag	4.840921	-1.065269	4.122254
Ag	5.869777	1.067690	2.463722
Ag	3.492024	5.245852	1.415309
Ag	0.815281	5.906350	2.485040
Ag	-3.277550	3.704241	4.142177
Ag	-4.188497	0.967659	4.807155
Ag	-2.369805	-0.980867	5.935834
Ag	-2.199192	-3.713279	4.802754
Ag	0.499656	-4.954496	4.148620
Ag	2.846819	-5.241823	2.472214
Ag	6.070752	-1.696460	1.409148
Ag	6.409609	0.604556	-0.420153
Ag	5.555416	3.257022	0.378086
Ag	3.918299	4.924926	-1.437916
Ag	1.398500	6.294301	-0.399647
Ag	-1.382628	6.295002	0.390958

Ag	-3.916568	4.942704	1.431590
Ag	-5.365895	2.572848	2.490832
Ag	-4.513029	-1.978574	4.148764
Ag	-4.099370	-4.319196	2.492222
Ag	0.284437	-6.305048	1.424272
Ag	2.569883	-5.912480	-0.408763
Ag	4.814106	-4.265332	0.374998
Ag	5.880936	-2.193433	-1.447088
Ag	5.373087	2.571340	-2.498196
Ag	3.279542	3.703468	-4.151868
Ag	-0.812166	5.905684	-2.492116
Ag	-3.483810	5.248730	-1.414988
Ag	-5.550348	3.263035	-0.391543
Ag	-6.389828	0.610145	0.412789
Ag	-5.874786	-2.190958	1.440724
Ag	-4.807985	-4.267857	-0.385008
Ag	-2.565062	-5.917092	0.404354
Ag	-0.267944	-6.303272	-1.420817
Ag	4.104210	-4.316433	-2.499482
Ag	4.522483	-1.977377	-4.157425
Ag	4.190690	0.968605	-4.808668
Ag	1.651083	1.988759	-5.930457
Ag	0.365861	4.334391	-4.813572
Ag	-2.540670	4.281966	-4.160821
Ag	-5.847064	1.063806	-2.463723
Ag	-6.050234	-1.686447	-1.406659
Ag	-2.832567	-5.255102	-2.474217
Ag	-0.487639	-4.955330	-4.154573
Ag	2.209467	-3.713803	-4.805810
Ag	2.374501	-0.980456	-5.940554
Ag	-1.375461	2.206283	-5.952100
Ag	-3.976530	1.687225	-4.784372
Ag	-4.835619	-1.073220	-4.132725
Ag	-2.862245	-3.286633	-4.796062
Ag	-0.208880	-2.588337	-5.938435
Ag	-2.528281	-0.627120	-5.918263

Coordinates of $\text{Ag}_{60}(\text{AgSH})_{60}^{++}$ cluster (element x y z):

Ag	0.771598	2.294144	3.177294
Ag	2.417707	0.001673	3.144356
Ag	1.201710	3.622222	0.732302
Ag	-1.892728	1.379798	3.101799
Ag	3.879332	0.012595	0.726156
Ag	0.757738	-2.280256	3.149241
Ag	-1.199948	3.616550	-0.725455
Ag	3.214630	2.326510	-0.765336
Ag	-1.944584	-1.437492	3.205171
Ag	-3.222895	2.325688	0.775359
Ag	3.098384	-2.251853	-0.747873
Ag	1.205768	-3.693893	0.745488
Ag	-0.768402	2.286000	-3.163730
Ag	1.897274	1.370939	-3.081597
Ag	-3.089166	-2.254103	0.759849
Ag	-3.868379	0.005266	-0.718883
Ag	1.946348	-1.441430	-3.190002
Ag	-1.198980	-3.706713	-0.735344
Ag	-2.421666	-0.003918	-3.149597
Ag	-0.753687	-2.289541	-3.140011
Ag	3.443167	2.480371	2.110651
Ag	-1.304446	3.997424	2.109254
Ag	0.023398	-0.005644	4.744618
Ag	3.427605	-2.477942	2.103014
Ag	1.303545	3.997684	-2.105323
Ag	-4.212575	-0.001448	2.141192
Ag	4.219636	0.000643	-2.125862
Ag	-1.285503	-4.021402	2.128641
Ag	-3.446794	2.476341	-2.101253
Ag	1.291078	-4.023941	-2.116455
Ag	-0.021789	-0.012556	-4.724414
Ag	-3.424428	-2.476297	-2.092676
Ag	1.412296	2.124128	5.977796
Ag	2.488251	-0.660141	5.963623
Ag	4.037320	1.763678	4.779885
Ag	2.628519	4.308905	4.113920
Ag	-0.423195	4.375766	4.774210
Ag	-1.579556	1.978382	5.939361
Ag	0.161116	-2.549605	5.970384
Ag	2.946769	-3.267592	4.774474
Ag	4.913933	-1.129665	4.099654
Ag	5.869587	1.120145	2.524930
Ag	3.538117	5.195445	1.405394
Ag	0.763791	5.876600	2.511916
Ag	-3.279234	3.747071	4.101023
Ag	-4.222032	0.918993	4.797415
Ag	-2.331257	-0.912127	6.018256
Ag	-2.193997	-3.810328	4.807818
Ag	0.456798	-5.001043	4.122512
Ag	2.888889	-5.219041	2.538315
Ag	6.075826	-1.761168	1.423329
Ag	6.431039	0.645220	-0.481469
Ag	5.627144	3.282152	0.472646
Ag	3.895491	5.031745	-1.478752
Ag	1.372585	6.284548	-0.467376
Ag	-1.371047	6.284833	0.461699
Ag	-3.886063	5.040505	1.484031
Ag	-5.447460	2.521285	2.588585
Ag	-4.623367	-1.971482	4.154399

Ag	-4.052244	-4.327400	2.547133
Ag	0.212111	-6.319527	1.441655
Ag	2.594091	-5.925697	-0.477129
Ag	4.807055	-4.288484	0.442830
Ag	5.916151	-2.133393	-1.449921
Ag	5.449503	2.513496	-2.580477
Ag	3.278573	3.738648	-4.089694
Ag	-0.763167	5.872165	-2.516956
Ag	-3.539064	5.194871	-1.401645
Ag	-5.635667	3.282747	-0.464553
Ag	-6.418452	0.642597	0.494845
Ag	-5.913569	-2.139257	1.450766
Ag	-4.796961	-4.290938	-0.427005
Ag	-2.585388	-5.936627	0.493854
Ag	-0.197150	-6.331459	-1.441361
Ag	4.055941	-4.324882	-2.532627
Ag	4.623503	-1.965268	-4.145772
Ag	4.225080	0.917528	-4.782964
Ag	1.582640	1.968768	-5.926951
Ag	0.427825	4.359345	-4.772804
Ag	-2.617864	4.296252	-4.103753
Ag	-5.857634	1.102339	-2.516617
Ag	-6.074093	-1.762483	-1.422845
Ag	-2.879874	-5.221679	-2.523775
Ag	-0.455120	-5.004452	-4.111056
Ag	2.194336	-3.809974	-4.799911
Ag	2.336007	-0.916256	-5.999933
Ag	-1.397955	2.126652	-5.971511
Ag	-4.027992	1.754539	-4.777375
Ag	-4.913923	-1.135371	-4.093614
Ag	-2.944226	-3.274185	-4.765411
Ag	-0.159408	-2.553825	-5.967641
Ag	-2.479007	-0.666342	-5.968993
Ag	3.390278	4.001410	6.957380
Ag	1.456422	6.507570	5.598155
Ag	0.067686	4.174048	7.614236
Ag	4.047495	1.229957	7.621216
Ag	6.660883	0.630838	5.595890
Ag	4.892354	-1.946890	6.941671
Ag	-2.757795	4.429172	6.940977
Ag	-5.667540	3.352978	5.666609
Ag	-3.926734	1.343633	7.637041
Ag	2.459162	-3.399585	7.616114
Ag	2.671895	-6.093996	5.625362
Ag	-0.352339	-5.227993	6.963301
Ag	8.018983	-0.631562	3.338610
Ag	8.606882	-1.298359	0.084006
Ag	8.408361	1.906876	1.220093
Ag	3.077018	7.395833	3.343284
Ag	0.770056	8.549110	1.233241
Ag	3.803451	7.819734	0.220997
Ag	-2.467614	-3.357012	7.646065
Ag	-4.988618	-4.473236	5.596615
Ag	-5.033303	-1.272037	6.992165
Ag	1.883146	-7.805031	3.380893
Ag	1.474156	-8.591253	0.169490
Ag	4.445939	-7.363949	1.225945
Ag	6.172763	6.154773	-0.053326
Ag	6.083286	5.192686	-3.439492
Ag	7.942893	3.381901	-1.258267
Ag	-0.736319	8.544532	-1.251412
Ag	-3.083680	7.371343	-3.369227

Ag	-3.796724	7.818075	-0.221709
Ag	-6.076614	5.209233	3.443493
Ag	-7.966038	3.336048	1.258925
Ag	-6.173294	6.158448	0.073294
Ag	-6.823402	-4.217461	3.344361
Ag	-7.684168	-4.038735	0.170274
Ag	-5.654962	-6.473209	1.281354
Ag	7.685334	-4.042038	-0.177982
Ag	6.826032	-4.215068	-3.327708
Ag	5.653645	-6.482413	-1.267099
Ag	5.675584	3.341813	-5.655561
Ag	3.922164	1.337701	-7.620917
Ag	2.754827	4.426913	-6.928457
Ag	-8.402169	1.867949	-1.223108
Ag	-8.043303	-0.626797	-3.326638
Ag	-8.599443	-1.286765	-0.098036
Ag	-1.435887	-8.597290	-0.136423
Ag	-1.866446	-7.805761	-3.382539
Ag	-4.445908	-7.347826	-1.213798
Ag	4.984035	-4.475892	-5.574073
Ag	2.471151	-3.356116	-7.638802
Ag	5.032811	-1.275032	-6.996921
Ag	-1.468800	6.460368	-5.634074
Ag	-3.373911	4.007307	-6.961513
Ag	-0.062096	4.169011	-7.615990
Ag	-2.659648	-6.096980	-5.625080
Ag	-2.458878	-3.393197	-7.608252
Ag	0.351637	-5.237039	-6.961975
Ag	-6.657527	0.623916	-5.595247
Ag	-4.891954	-1.952848	-6.925936
Ag	-4.031960	1.233913	-7.620574
S	1.946432	3.101044	8.948421
S	4.012311	6.329752	6.122828
S	-0.669456	6.618618	7.004034
S	3.588558	-0.877857	8.959094
S	6.122694	2.696972	6.990995
S	7.297447	-1.850180	6.109819
S	-2.334481	2.807836	8.962427
S	-4.775265	5.763347	6.127887
S	-6.482881	1.378113	7.041578
S	0.329933	-3.691257	8.972386
S	4.484966	-4.957844	7.000960
S	0.509818	-7.475659	6.111138
S	8.758625	1.846975	3.737892
S	9.023149	-2.703063	2.258410
S	9.582162	0.857400	-0.871639
S	5.383946	7.696714	2.310056
S	0.956361	8.858197	3.759267
S	2.141059	9.401247	-0.851942
S	-3.348766	-1.399583	8.999540
S	-3.299490	-5.768847	7.018275
S	-6.907996	-2.788619	6.167446
S	4.467837	-7.728791	3.747151
S	0.217993	-9.407415	2.308533
S	3.786969	-8.842454	-0.856707
S	8.251809	4.942473	0.823011
S	5.715520	7.439232	-2.293141
S	8.167464	3.650764	-3.777121
S	-2.115356	9.395306	0.831054
S	-0.957344	8.833362	-3.775237
S	-5.379428	7.697566	-2.310316
S	-5.700571	7.455335	2.301053

S	-8.151877	3.655041	3.779969
S	-8.241431	4.939765	-0.806279
S	-5.948659	-6.642423	3.810746
S	-8.862648	-3.102601	2.327239
S	-7.267231	-6.359750	-0.790486
S	7.268798	-6.354927	0.796436
S	8.870933	-3.095551	-2.325456
S	5.951149	-6.636315	-3.798860
S	4.779735	5.750101	-6.124922
S	6.480187	1.373139	-7.047789
S	2.334412	2.799809	-8.949266
S	-9.597890	0.850274	0.877385
S	-8.754979	1.850770	-3.741972
S	-9.022815	-2.716278	-2.259933
S	-3.771198	-8.847981	0.845693
S	-0.210225	-9.406830	-2.297163
S	-4.451977	-7.732907	-3.734311
S	6.899778	-2.788157	-6.158749
S	3.295261	-5.764223	-7.009889
S	3.344019	-1.402846	-8.997797
S	0.671406	6.616268	-7.006298
S	-4.031845	6.319960	-6.122526
S	-1.939819	3.093490	-8.955199
S	-0.494361	-7.484467	-6.097542
S	-4.475418	-4.967052	-7.004323
S	-0.328187	-3.695889	-8.963891
S	-6.115114	2.686140	-6.992409
S	-7.294838	-1.856770	-6.084962
S	-3.590325	-0.887345	-8.948496
H	2.308080	4.249805	9.608787
H	3.698763	6.976629	7.293182
H	-0.066465	6.942510	8.194998
H	4.805397	-0.909335	9.595396
H	6.654208	2.227725	8.167299
H	7.831940	-1.375220	7.282245
H	-3.309917	3.536480	9.597755
H	-5.500512	5.676351	7.290582
H	-6.625665	2.061473	8.223673
H	0.726110	-4.858822	9.576677
H	4.190411	-5.592456	8.182821
H	1.143598	-7.838364	7.274532
H	10.040974	1.357146	3.704086
H	10.314444	-2.239352	2.196371
H	10.700038	0.874076	-0.074760
H	5.382046	9.066653	2.220270
H	1.841160	9.908000	3.738538
H	2.415795	10.491718	-0.064102
H	-4.340922	-2.106259	9.634208
H	-3.966538	-5.660917	8.213766
H	-7.013840	-3.479914	7.349623
H	4.396085	-9.099264	3.703838
H	1.060926	-10.491017	2.258440
H	4.194168	-9.881854	-0.057049
H	9.141980	5.600080	0.009452
H	7.055941	7.738425	-2.253381
H	8.897892	4.813315	-3.732338
H	-2.401483	10.478594	0.037522
H	-1.818652	9.902247	-3.736906
H	-5.363194	9.068188	-2.232941
H	-7.036603	7.773592	2.268623
H	-8.883719	4.815130	3.708263
H	-9.126264	5.595083	0.015660

H	-7.281497	-6.972520	3.830569
H	-9.645347	-4.228033	2.247894
H	-8.146317	-7.041031	0.015151
H	8.142959	-7.039456	-0.011356
H	9.648057	-4.223542	-2.235359
H	7.283867	-6.966623	-3.826827
H	5.490409	5.669162	-7.297684
H	6.616091	2.053910	-8.233046
H	3.314948	3.520228	-9.586086
H	-10.721003	0.888128	0.088239
H	-10.039089	1.363885	-3.719173
H	-10.311729	-2.250187	-2.178837
H	-4.162444	-9.884856	0.034617
H	-1.069325	-10.476530	-2.246212
H	-4.370622	-9.102424	-3.675255
H	7.013789	-3.488314	-7.334839
H	3.968371	-5.654426	-8.202420
H	4.330092	-2.113397	-9.637740
H	0.072040	6.942255	-8.198235
H	-3.729361	6.993757	-7.280556
H	-2.315862	4.245437	-9.602132
H	-1.129780	-7.851674	-7.257873
H	-4.169555	-5.598178	-8.184707
H	-0.727408	-4.858990	-9.575512
H	-6.654796	2.222057	-8.167221
H	-7.827804	-1.382370	-7.258171
H	-4.806882	-0.916696	-9.584889

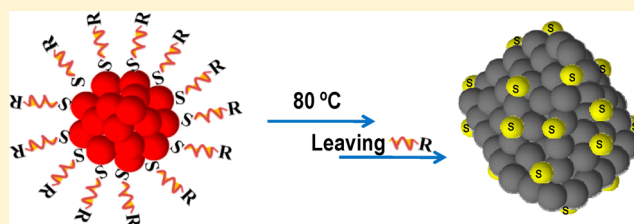
Low-Temperature Thermal Dissociation of Ag Quantum Clusters in Solution and Formation of Monodisperse Ag₂S Nanoparticles

Kadamkotte Puthenveetil Remya, Thumu Udayabhaskararao, and Thalappil Pradeep*

DST Unit of Nanoscience (DST UNS), Indian Institute of Technology, Madras, Chennai 600 036, India

S Supporting Information

ABSTRACT: We report the effect of temperature on the stability of glutathione-protected Ag₂₅ clusters. The clusters are stable up to 50 °C. Interestingly, above this temperature, they decompose to yield Ag₂S nanoparticles with an average diameter of 3 ± 1 nm, crystallizing in monoclinic acanthite polymorph. Unlike conventional methods of syntheses of Ag₂S, where a temperature of ~200 °C is needed, our study shows the possibility of synthesis of Ag₂S nanoparticles at much lower temperatures. This is in contrast with silver nanoparticles protected with thiolates, which typically give silver and alkyl/aryl disulfide upon thermal activation. The mechanism of cluster decomposition and formation of silver sulphide nanoparticles was investigated using various analytical techniques such as ultraviolet–visible spectroscopy, X-ray diffraction scanning electron microscopy, energy-dispersive analysis of X-rays, transmission electron microscopy, and electrospray ionization mass spectrometry. The monolayer of the cluster undergoes S–C bond cleavage, as revealed by mass spectrometry. This is somewhat unusual because Ag–S cleavage is expected in view of its lower bond energy.



1. INTRODUCTION

Noble-metal nanoparticles with thiolate protection^{1–4} have been extensively investigated in the past several years because of their interesting electrical, optical, and chemical properties and due to their possible applications in various fields. Their properties are highly influenced by the medium, nature of the protecting ligand, pH, temperature, and so on, of which temperature is of high importance. Thermal stability of such monolayer-protected nanoparticles, referred to as MPCs (monolayer-protected clusters), previously has been a subject of discussion.⁵ Thermal desorption of MPCs of gold results in the formation of alkyl disulfide in the gas phase and gold in the solid state, the Au–S bond being stable till 160 °C. Similar decomposition takes place in the case of silver as well.^{6–8} For example, carboxylates of silver decompose to give metallic silver and carboxylic acid derivatives or radicals upon heating.⁹ Thermal desorption of thiolate self-assembled monolayers (SAMs) on planar surfaces can also distinguish adsorption sites.^{10,5b}

Noble-metal-derived quantum clusters¹³ are exciting new materials. They exhibit unique properties due to the confinement of electrons in discrete energy levels. These subnanometer particles having a core of only a few metal atoms can be considered as the smallest analogues of MPCs. Bare cores are inherently unstable because of their high surface energy, which makes them coalesce into larger particles. Such cores could be protected and stabilized with a shell of ligands, and the system as a whole exhibits interesting optical and chemical properties. The ligand shell plays an important role in determining the properties of clusters such as their stability as well as physical and chemical properties.^{2,14,15} Study of these properties has attracted significant attention in the recent past. Study of applications of nanoclusters has been a subject of interest as well.

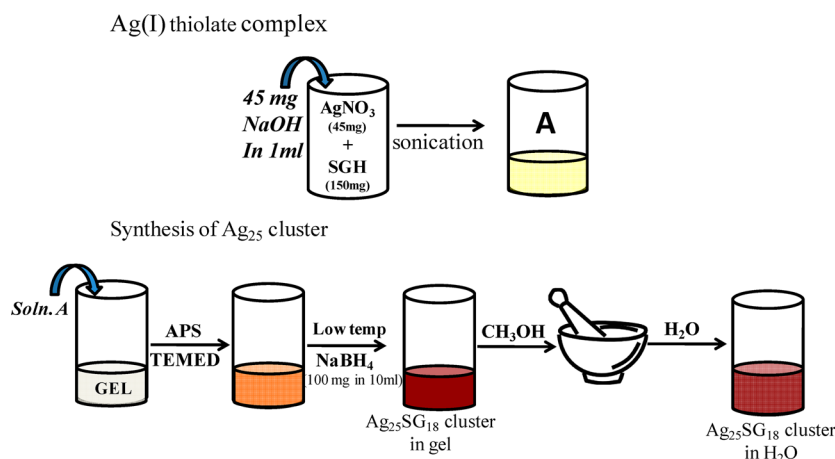
Most of the studies in this category of materials have been on gold clusters, especially Au₂₅SG₁₈. (SG is glutathione in the thiolate form, protecting the Au₂₅ core.) Silver clusters are the second most studied systems. These clusters exhibit bright fluorescence with a quantum yield up to 64%.¹⁶ Practical applications of clusters are determined by their stability under ambient conditions.¹⁷ The stability increases upon going from free to supported to passivated clusters.¹⁸ Some of the new areas of research of these materials are: (i) incorporating them in human cells¹⁹ as a diagnostic tool,^{20,21} (ii) fabrication of luminescent patterns,²² (iii) catalysis,^{23–25} (iv) metal ions sensing,^{26–28} (v) biolabeling,²⁹ and (vi) medicine.³⁰

Most of these applications would require an understanding of the thermal stability of the material of interest. We report the experimental results of our study of thermal stability of QCs, taking Ag₂₅SG₁₈ as a model. We find that these clusters undergo thiolate desorption and heterolytic bond cleavages, resulting in the formation of Ag₂S nanoparticles at low temperatures. Mechanistic aspects of the reaction were probed with several spectroscopic tools. The only related studies have been on the temperature-dependent optical properties of Au₂₅SR₁₈ in solution,¹¹ but the product of dissociation was not further investigated. It is likely to be Au(I)-thiolates. However, because the chemistry of gold clusters is quite different from that of silver, the products of thermal decomposition may vary for silver clusters. One such example is the heating of aryl-thiolated silver nanoparticles having non-plasmonic optical properties at 90 °C, leading to the formation of

Received: July 7, 2012

Revised: October 28, 2012

Published: November 7, 2012

Scheme 1. Synthetic Procedure Used to Make $\text{Ag}_{25}\text{SG}_{18}$ Clusters

nanoparticles, which show single plasmon-like resonance in their optical spectrum.¹²

Ag_2S is a direct band gap semiconductor with a narrow band gap. Its excellent optical-limiting properties and high stability, especially in nanoparticle form, enable potential applications in the field of microelectronics, IR detectors, memory devices (Giant Magneto Resistance), and so on. In general, the synthesis of Ag_2S nanoparticles requires high temperature and complex processes. Only a few reports exist on the preparation based on emulsion methods. We emphasize that our low-temperature route for the synthesis of Ag_2S nanoparticles may be explored as a general synthetic method that may be useful for preparations starting with other quantum clusters and diverse ligands.

2. EXPERIMENTAL SECTION

2.1. Materials. Silver nitrate (99%), glutathione (GSH, 97%), methanol (GR grade), acrylamide (AR grade), N,N' -methylenebisacrylamide (BIS, AR grade), ammonium persulfate, and N,N,N',N' -tetramethylethylenediamine (TEMED) were purchased from SRL Chemical, India. Other chemicals used are: (1) sodium borohydride (NaBH_4 , 99.99%, Aldrich) and (2) ethanol, methanol, and dichloromethane (all HPLC grade, Aldrich). All chemicals were used without further purification.

2.2. Synthesis of $\text{Ag}_{25}\text{SG}_{18}$. $\text{Ag}_{25}\text{SG}_{18}$ cluster was prepared by the reductive decomposition of Ag(I)SG thiolate in gel cavities following a method previously reported from our lab³¹ (Scheme 1). In brief, a mixture of AgNO_3 and GSH was (in 1:2 molar ratio) dissolved in NaOH solution (45 mg NaOH in 1 mL distilled water) at room temperature and sonicated for a few minutes. A yellow solution of Ag(I)SG complexes was obtained. It was added to 4.2 mL of gel (44 g of acrylamide and 3 g of BIS mixed with 100 mL of distilled water). To this mixture, 50 μL of 0.1% solution of ammonium persulfate and 40 μL of TEMED were added, which resulted in the formation of a gel. The gel was kept undisturbed for 20 min at room temperature and then at ice cold temperature for 10 min. A solution of 100 mg NaBH_4 in 10 mL of ice-cold water was added to the gel and kept undisturbed at 0 °C for about 0.5 h. The color of the gel changed from yellow to brown, indicating the formation of clusters within the gel. The dark-brown-colored gel was transferred to a mortar, crushed, and washed many times with methanol to remove excess NaBH_4 . The crushed gel was taken, and distilled water was added to extract the cluster into the aqueous medium. The yield of the cluster was 66% with respect to AgNO_3 .

2.3. Thermal Decomposition of the Clusters. The cluster solution was kept in a synthesizer under constant stirring at 80 °C until the color changed from reddish brown to greenish black, which took about 30 h. After cooling, it was centrifuged to get a greenish black residue. The clear supernatant solution was preserved for further characterizations.

2.4. Characterization. Optical absorption spectra were collected in the range 200 to 1100 nm. For room-temperature recordings, a Perkin-Elmer Lambda-25 spectrophotometer was used. For higher temperature recordings, another Perkin-Elmer spectrometer, with an accessory for maintaining sample temperature, was used. Luminescence spectra were recorded using a Jobin Yvon Nano Log spectrofluorimeter. Scanning electron microscopic (SEM) images and EDAX images were obtained using a FEI QUANTA-200 SEM. For measurements, samples were prepared by drop casting on an indium tin oxide (ITO)-coated glass plate and drying in vacuum. The X-ray diffractogram was collected using $\text{Cu K}\alpha$ radiation ($\lambda = 1.5418 \text{ \AA}$) in a Bruker AXS D8 Discover diffractometer. Transmission electron microscopy (TEM) measurements were carried out using a JEOL 3011 instrument. Samples for TEM were prepared by dropping the aqueous dispersions on amorphous carbon films supported on a copper grid and drying in an ambient atmosphere. Mass spectra were recorded using a QTrap 3200 instrument with electrospray ionization (ESI). Samples of 20 ppm concentration (in Ag), prepared using 1:1 mixture of CH_2Cl_2 /methanol, were electrosprayed at a flow rate of 10 $\mu\text{L}/\text{min}$ and at an ion spray voltage of 5 kV.

2.5. Results and Discussion. The absorption spectrum of freshly prepared clusters in aqueous medium (Figure S1 of the Supporting Information) confirms the formation of $\text{Ag}_{25}\text{SG}_{18}$ clusters.³¹ Unlike larger Ag nanoparticles, which show surface plasmon resonance (SPR) at $\sim 400 \text{ nm}$, Ag_{25} clusters show molecule-like transitions, as revealed in their absorption spectrum, having (i) a pronounced peak at 478 nm and (ii) two broad peaks at 330 and 640 nm. The molecular-like energy levels are mostly derived from sp orbitals of silver.¹² The optical absorption spectrum of the freeze-dried cluster sample was also taken after redispersing the dried powder in water. The features at 330, 478, and 640 nm in the UV/vis spectrum of the redispersed sample indicate the presence of the cluster (Figure S2 of the Supporting Information). The inset in Figure S1 of the Supporting Information shows the TEM image of clusters. No individual cluster is seen in the image because the core dimension is small ($< 1 \text{ nm}$). Also, such clusters are highly sensitive to electron beam

in TEM; they aggregate to form nanoparticles instantaneously upon electron beam irradiation.^{32,33}

Time-dependent absorption spectra of $\text{Ag}_{25}\text{SG}_{18}$ cluster were taken at room temperature, which show a gradual decrease in the intensities of the peaks at 330, 478, and 640 nm with time (Figure S3 of the Supporting Information). The peaks at 330 and 640 nm are more sensitive and vanish at a faster rate compared with the prominent peak at 478 nm, which shows reasonable peak intensity even after 90 days. This type of behavior in the absorption spectra is observed for previously reported thiolate-protected silver clusters.³⁴ The thermal stability of these clusters was examined by taking UV/vis spectra at several fixed temperatures in the range of 25–85 °C (Figure 1). We see that the peak position

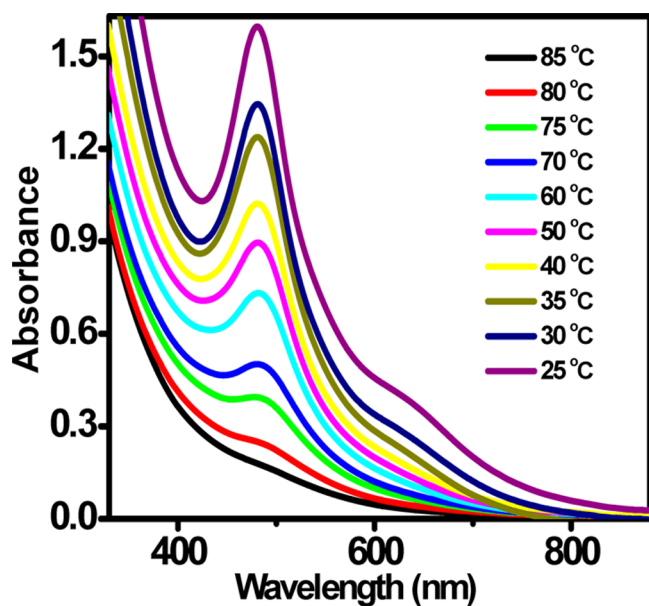


Figure 1. UV/vis spectra of $\text{Ag}_{25}\text{SG}_{18}$ clusters at various temperatures ranging from 25 to 85 °C.

remains the same, whereas peak intensities decrease with increase in temperature. Similar to the behavior in the time-dependent spectra, the peaks at 330 and 640 nm vanish very fast compared with the peak at 478 nm. Although there is a decrease in intensity with temperature, clusters seem to be almost stable up to 50 °C, as revealed by the persistence of the peak at 478 nm. Above 50 °C,

even the peak at 478 nm decreases at a faster rate, finally showing a featureless spectrum. The decomposition follows first-order kinetics, as revealed by analysis of absorption spectra, shown in Figure S4 of the Supporting Information. One of the products of decomposition is silver sulphide, the presence of which is confirmed by EDAX and XRD. (See Figures 3 and 4.)

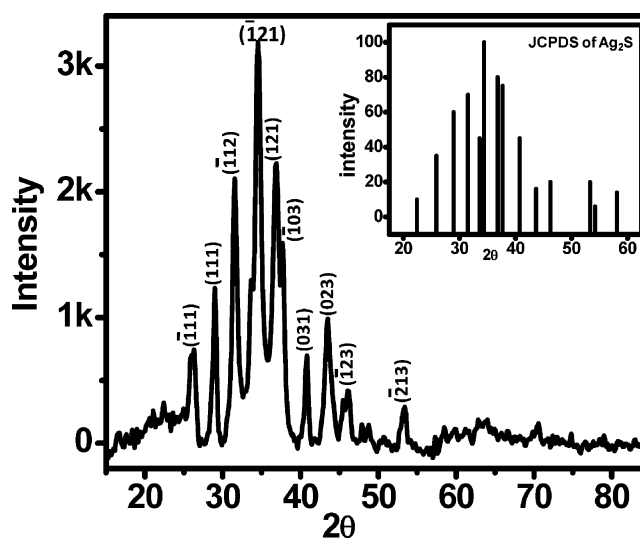


Figure 3. X-ray diffraction pattern of residue obtained after decomposition of $\text{Ag}_{25}\text{SG}_{18}$ clusters. Inset shows the standard pattern of monoclinic form of Ag_2S .

For obtaining the decomposed end product for further characterization, an aqueous solution of clusters was heated to 80 °C for 30 h with constant stirring. The resulting mixture was freeze-dried to get a greenish black solid residue. Figure 2A shows the absorption spectrum of this residue after suspending in water. We see that the peaks, characteristic of clusters, have vanished, and very broad and shallow features are observed. Starting from the beginning of heating at 80 °C, the color of the solution changed from brownish red to a reddish orange and then finally to greenish black, as shown in the photograph (Figure 2A (a–c)). The inset of Figure 2A shows the Jacobian-corrected spectrum of the greenish black residue, where absorption features at ~340 and ~770 nm are seen. To amplify less-intense absorption features, we have corrected the data with the Jacobian factor. For this, the experimentally obtained intensities in absorbance as a

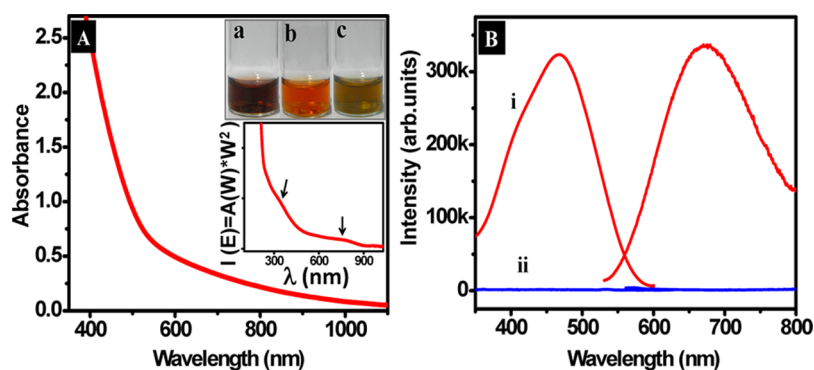


Figure 2. (A) UV/vis spectrum of product (Ag_2S) obtained by complete decomposition of $\text{Ag}_{25}\text{SG}_{18}$ clusters. The bottom inset of panel A shows the Jacobian corrected spectrum. The upper inset gives the photographs of clusters in various stages during thermal decomposition. (a) As-synthesized clusters in water. (b) After 20 h of heating at 80 °C. (c) After heating for 30 h at 80 °C. (B) Excitation and emission spectra of $\text{Ag}_{25}\text{SG}_{18}$ (i, red trace) and that of the decomposed sample in water at 25 °C (ii, blue trace).

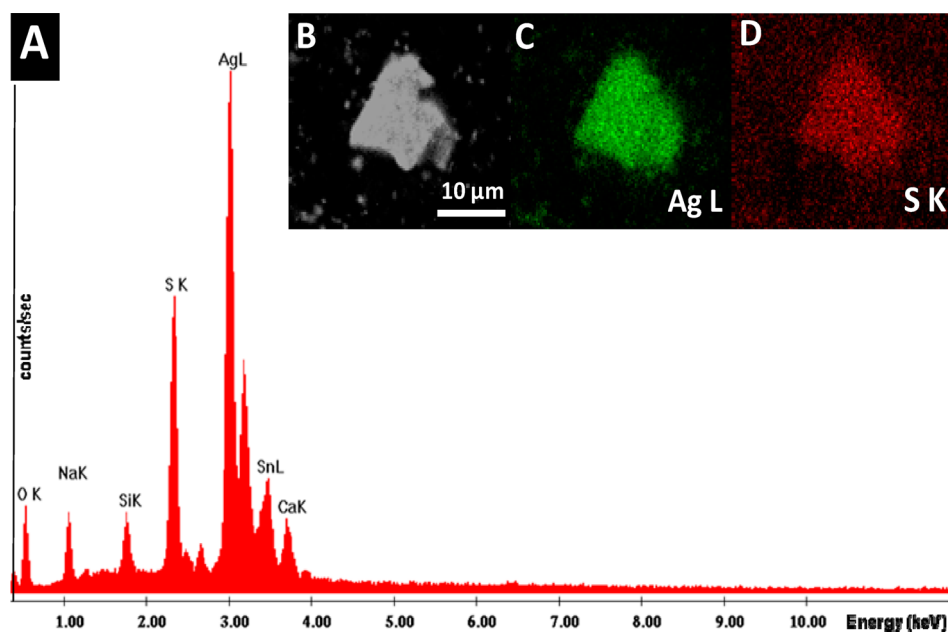


Figure 4. (A) EDAX spectrum of the residue left after decomposition of $\text{Ag}_{25}\text{SG}_{18}$ clusters. (B) Its SEM image and EDAX images collected using Ag $L\alpha$ (C) and S $K\alpha$ (D).

function of wavelength $[I(W)]$ have been converted to energy-dependent values $[I(E)]$ using the expression $I(E) = I(W)/(\partial E/\partial W) \propto I(W) \cdot W^2$, where $\partial E/\partial W$ represents the Jacobian factor against wavelength. The onset of absorption is observed at ~ 950 nm. All of these are attributed to band-edge transitions in silver sulphide nanoparticles. Similar absorption band positions and band profile are seen in the UV/vis spectrum of Ag_2S nanocrystals.^{35–37,39} The luminescence profile of the as-prepared clusters and of the decomposed sample are shown in Figure 2B. Ag_{25} clusters exhibit a red emission peaking at 650 nm when excited with 480 nm radiation. In contrast, the decomposed sample did not show luminescence for the same excitation.

Direct confirmation of the formation of Ag_2S nanoparticles is obtained from the XRD pattern (Figure 3) of the solid product. The pattern shows prominent peaks corresponding to diffraction from (111), (−111), (112), (121), (−103), (−023), (−123), and (−213) crystal planes of room temperature modification (Acanthite, monoclinic) of Ag_2S ³⁸ (JCPDS file no: 14-0072, inset of Figure 3.). Acanthite is stable at temperatures < 176 °C.^{39,40} The other phases of Ag_2S , such as body-centered cubic (argentite) and face-centered cubic (high argentite) forms, exist at high temperatures. These phases are not present in the present system. The absence of silver nanoparticles and silver thiolate is confirmed by XRD as well. This XRD taken for the decomposed sample is different from that of the parent $\text{Ag}_{25}\text{SG}_{18}$ cluster, which shows a broad peak at 36° (2θ) (Figure S5 of the Supporting Information). Slightly broader peaks observed in our diffraction pattern of the decomposed sample as compared with that of well-crystallized samples are ascribed to the smaller grain size of the former.

EDAX of the final solid (Figure 4A) shows the atomic ratio of Ag:S in the final product to be 2:1, as expected for stoichiometric Ag_2S . Figure 4B gives the SEM image of the product. Figure 4C,D is the EDAX image collected using Ag $L\alpha$ and S $K\alpha$, respectively. Peaks of other elements such as O, Si, Sn, and Ca are also present in the EDAX spectrum, which are due to elements present in the ITO-coated glass plate.

The shape and distribution of Ag_2S nanoparticles were studied by TEM (Figure 5). Monodispersed spherical nanoparticles with

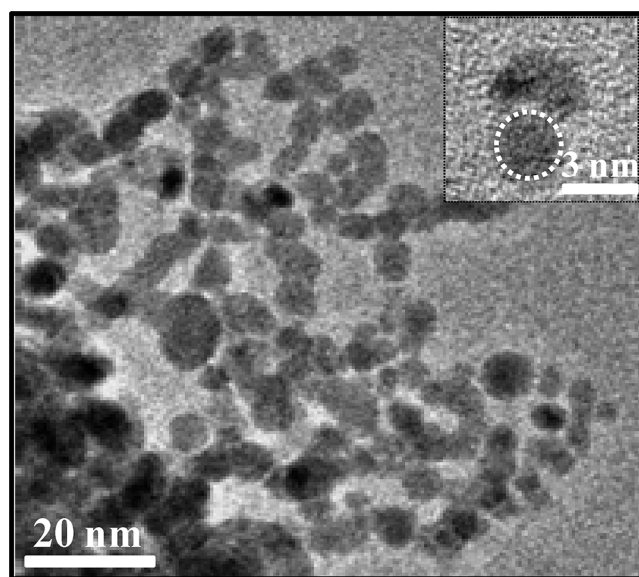


Figure 5. TEM image of the decomposed sample showing nanoparticles. Inset shows the image of a single nanoparticle at a higher magnification.

a mean diameter of 3 ± 1 nm are seen in the images. Aggregation is expected because of the lack of surface protection. The large number of aggregates seen in the image is due to high particle concentration in the solution used for analysis. The Ag_2S nanoparticles formed in the present study are very small in size in comparison with that of Ag_2S nanoparticles synthesized by previously reported methods, employing other wet chemical routes, the minimum mean diameter reported being ~ 8 nm. Although XRD revealed the presence of distinct lattice planes, TEM images did not show them because particles are very small.

Thermal decomposition of $\text{Ag}_{25}\text{SG}_{18}$ clusters at comparatively high temperatures (~ 80 °C) for long time seems to favor the breaking of sulfur–carbon bond (S–C bond) of the thiol ligand rather than the silver–sulfur bond (Ag–S bond). The organic

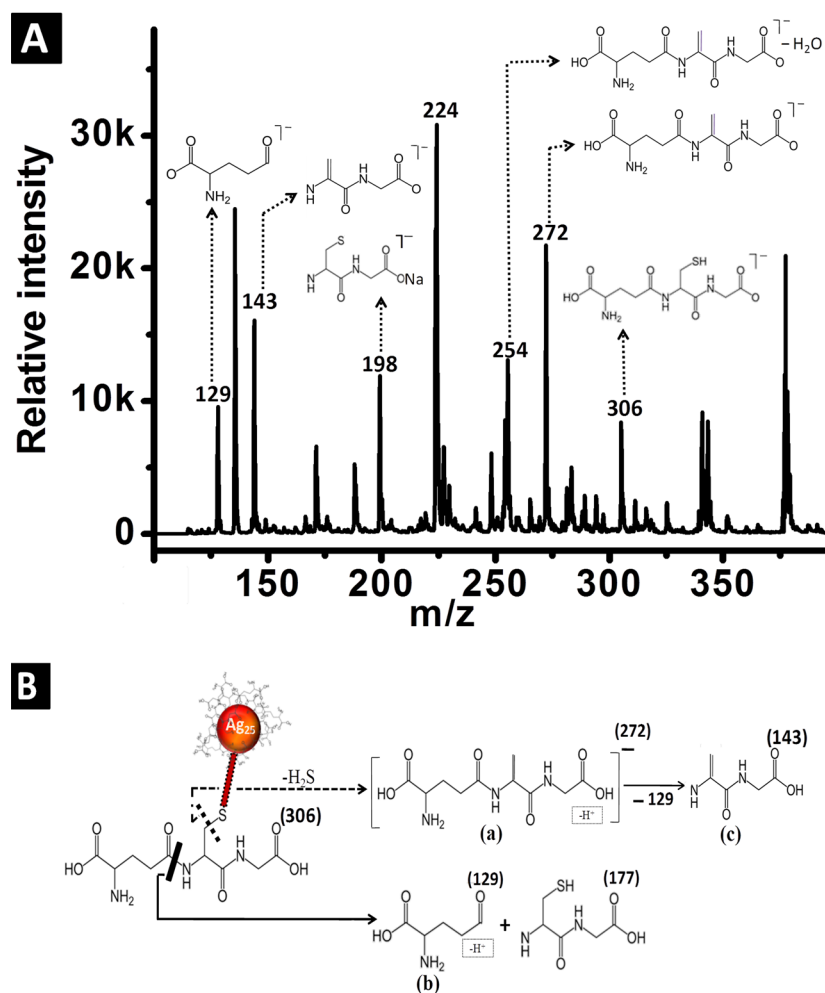


Figure 6. (A) Portion of negative ion ESI MS of the supernatant solution left after the removal of solid products obtained after decomposition of $\text{Ag}_{25}\text{SG}_{18}$. (B) Scheme showing the possible fragmentation path for glutathione molecules bonded to the Ag core.

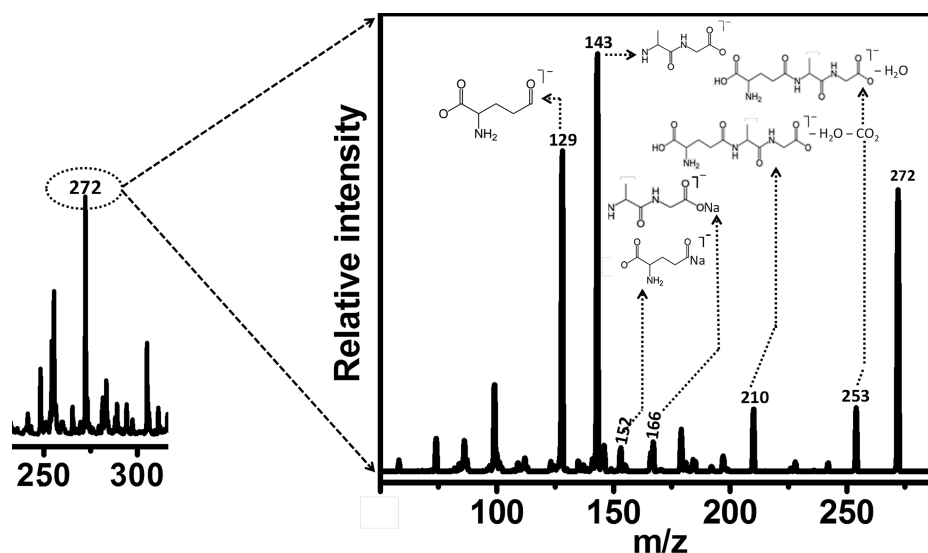
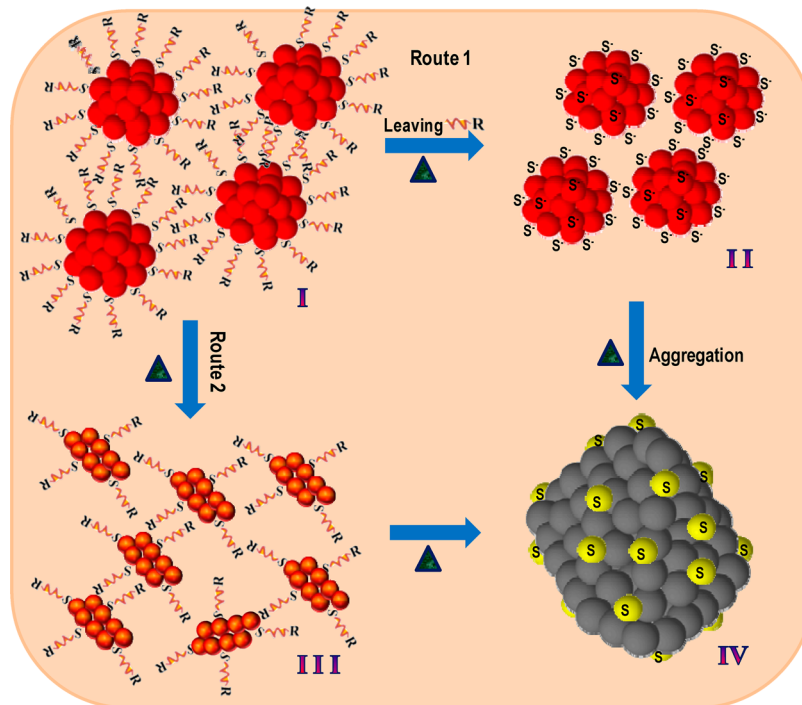


Figure 7. MS/MS of desulphurized glutathione peak at m/z 272. Spectrum on the left shows the peak selected for MS/MS analysis.

moieties formed after dissociation go to the solution, leaving stable Ag_2S . The presence of desulphurized organic entities of GSH was confirmed by ESI MS of the supernatant solution left after the removal of the solid product (Figure 6A). Only the significant portion of the mass spectrum is shown in Figure 6A.

Schematics shown in Figure 6B give the possible bond cleavage schemes of GSH upon temperature-induced decomposition application. The fragmentation results in two kinds of products: (i) a desulphurized GSH (as in scheme (a)) and (ii) two asymmetric fragments of SGH (as in schemes (b) and (c)). Mass

Scheme 2. Schematic Representation of Two Possible Routes for the Formation of Ag₂S Nanoparticles from Ag₂₅SG₁₈ Clusters^a

^a(I) Parent Ag₂₅SG₁₈ cluster before heating, (II) Ag–S moiety formed due to heating, (III) Ag(I)-thiolates formed upon heating, and (IV) the final product obtained after decomposition (Ag₂S NPs).

spectrum, taken in the negative mode, shows a peak at m/z 272, which we assign to desulphurized species. The peak at m/z 306 is assigned to reduced GSH. We can also see a number of small fragments of GSH in the mass spectrum. The formation of some prominent fragments is explained through the scheme presented in Figure 6B. Peaks appear at the calculated positions for GSH.⁴¹ For example, the peak due to the first fragment (in scheme (b)) is at m/z 129, and that at m/z 143 (in scheme (c)) can be attributed to the removal of neutral pyroglutamic acid from desulphurized species. A peak at m/z 198 (Figure 6A) is due to the presence of the second fragment in which proton is replaced by a Na⁺, that is present in the medium. The peak at m/z 254 is due to the species formed by the loss of one water molecule from the desulphurized GSH species. Along with these peaks, there are some peaks originating from a small amount of acrylamide gel still remaining in solution (for example, the peak at m/z 224). The mass spectrum in the positive ion mode also shows all of these peaks (not shown here). The mass spectrum collected for GSH alone, in the negative mode, also shows similar peaks at corresponding m/z values (Figure S6 of the Supporting Information), which further justifies our result.

Figure 7 shows the MS/MS spectrum of the peak at m/z 272. MS/MS gives major fragment peaks at m/z 129, 143, 210, and 253. The formation of these fragments is explained in Figure 6. Peaks at m/z 152 and 165 are assigned, respectively, to species formed by the replacement of protons in fragments, m/z 129 and 143 by Na⁺.

The mechanism of formation of silver sulphide nanoparticles is not well understood. Here we present our tentative suggestions for the formation of Ag₂S upon thermal decomposition of silver quantum clusters.

There are two possible routes for the dissociation of thiolates on cluster surfaces, as shown in Scheme 2. In the first case, the organic moiety, devoid of sulfur, leaves the cluster surface, resulting

in silver sulphide nuclei of the form Ag₂₅S₁₂; subsequently, these aggregate to form Ag₂S nanoparticles (Route 1). Assuming the structure of Ag₂₅SG₁₈ to be similar to that of Au analogue, there could be SG ligands directly bonded to the core along with bridged ligands. Probably, it is these bridged species that are thermally less stable,⁴³ and they get desorbed with activation. This desorption could explain the presence of anionic GSH seen in the mass spectrum of the solution. MALDI mass spectra of such clusters, where Au₂₅SR₁₂ fragments were observed, also support this view.^{42,43} Analogous entities existing in solution might have undergone thermal cleavage, leading to Ag₂₅S₁₂. We note that the Ag to S ratio, 25:12, is very close to the ideal ratio, 25:12.5, needed for the formation of stoichiometric Ag₂S. The extent of nonstoichiometry due to lower sulfur content, if it exists, would be very small. The organic moieties go to the supernatant solution as previously described. In the second case, Ag(I) thiolates are formed by thermal decomposition of the cluster and eventually Ag₂S nanoparticles formed by continuous heating (Route 2). Route 2 may be better feasible thermodynamically because the formation of thiolates is commonly seen from such clusters. Thiolates, once formed, can have two possible cleavages, namely, at the Ag–S bond (eq 1) and at the C–S bond (eq 2).



The changes in enthalpy of formation for the two reactions were calculated.

$$\Delta H_1 = \Delta_f H^\circ(\text{R-S-S-R}) + \Delta_f H^\circ(\text{Ag}) - 2\Delta_f H^\circ(\text{R-S-Ag}) \quad (1a)$$

$$\Delta H_2 = \Delta_f H^\circ(\text{R-S-R}) + \Delta_f H^\circ(\text{Ag}_2\text{S}) - 2\Delta_f H^\circ(\text{R-S-Ag}) \quad (2a)$$

These prototypical reactions represent the formation of silver nanoparticles or Ag_2S nanoparticles. The enthalpy of formation of Ag_2S is -32.6 kJ/mol. The possible entities upon heating, R-S-R and R-S-S-R, were taken to be dimethyl sulphide and dimethyl disulfide, respectively, and the corresponding values of enthalpy of formation of are -65.3 and -62.6 kJ/mol.⁴⁴ Absolute values of ΔH_1 and ΔH_2 could not be calculated because the heat of formation of R-S-Ag is not available. However, it can be seen that ΔH_2 is more negative than ΔH_1 , and hence the formation of Ag_2S is more feasible than that of Ag nanoparticles.

From the above discussion, it is clear that Ag_2S can be formed either through direct dissociation or through the thiolate intermediate. In the first, thermodynamic values of the corresponding model systems are not available to evaluate the enthalpies. In the second case, a preliminary thermodynamic evaluation supports the experimental observation.

The presence of Ag^+ and Ag nanoparticles in the mother liquor was also evaluated. Typically the presence of Ag^+ is assessed using the precipitation of AgCl upon the addition of NaCl , and that of Ag nanoparticles is assessed using their characteristic optical absorption, which is dominated by SPR at 400 nm. We did not observe any ionic Ag species in solution, nor did we have nanoparticles of silver.

3. CONCLUSIONS

In summary, temperature-dependent studies were performed on silver quantum clusters, which exhibit distinct nonplasmonic features in their absorption spectrum. Results presented here suggest that thermal decomposition of these quantum clusters follows a mechanism that is significantly different from that of their larger analogues, namely, nanoparticles. Whereas the direct desorption of disulfide, resulting in the formation of bulk silver, is seen in the case of nanoparticles, C–S bond cleavage occurs in quantum clusters, resulting in the formation of silver sulphide nanoparticles. The difference in ligand binding strength is manifested in the observed product. We have used spectroscopic studies to understand an approximate chemical reaction for the process. An extension of the study to diverse quantum clusters in different media may lead to new products of different morphologies.

■ ASSOCIATED CONTENT

● Supporting Information

Preliminary confirmation of cluster formation through UV/vis profile and a TEM image, time-dependent UV/vis spectra of $\text{Ag}_{25}\text{SG}_{18}$ quantum cluster, and kinetics of decomposition. This material is available free of charge via the Internet at <http://pubs.acs.org>.

■ AUTHOR INFORMATION

Corresponding Author

*Phone: +91-44-2257 4208. Fax: +91-44-2257 0509/0545. E-mail: pradeep@iitm.ac.in.

Notes

The authors declare no competing financial interest.

■ ACKNOWLEDGMENTS

We thank the Department of Science and Technology (DST), Government of India, for constantly supporting our research program on nanomaterials.

■ REFERENCES

- (1) Brust, M.; Walker, M.; Bethell, D.; Schiffrin, D. J.; Whyman, R. J. *Chem. Soc., Chem. Commun.* **1994**, 801–802.
- (2) Templeton, A. C.; Wuelfing, W. P.; Murray, R. W. *Acc. Chem. Res.* **2000**, *33*, 27–36.
- (3) Sandhyarani, N.; Pradeep, T. *Int. Rev. Phys. Chem.* **2003**, *22*, 221–262.
- (4) (a) Daniel, M.-C.; Astruc, D. *Chem. Rev.* **2004**, *104*, 293–346. (b) Brust, M.; Kiely, C. J. In *Colloids and Colloid Assemblies: Synthesis, Modification, and Utilization of Colloid Particles*; Wiley: Weinheim, Germany, 2004; pp 96–119.
- (5) (a) Delemarche, E.; Michel, B.; Kang, H.; Gerber, C. *Langmuir* **1994**, *10*, 4103–4108. (b) Schreiber, F. *Prog. Surf. Sci.* **2000**, *65*, 151–256. (c) Terrill, R. H.; Postlethwaite, T. A.; Chen, C.-H.; Poon, C.-D.; Terzis, A.; Chen, A.; Hutchison, J. E.; Clark, M. R.; Wignall, G.; Londono, J. D.; Superfine, R.; Falvo, M.; Johnson, C. S.; Samulski, E. D.; Murray, R. W. *J. Am. Chem. Soc.* **1995**, *117*, 12537–12548.
- (6) Nuzzo, R. G.; Korenic, E. M.; Dubois, L. H. *J. Chem. Phys.* **1990**, *93*, 767–773.
- (7) Murty, K. V. G. K.; Venkataraman, M.; Pradeep, T. *Langmuir* **1998**, *14*, 5446–5456.
- (8) Buttner, M.; Belser, T.; Oelhafen, P. *J. Phys. Chem. B* **2005**, *109*, 5464–5467.
- (9) (a) Fields, E. K.; Meyerson, S. J. *Org. Chem.* **1976**, *41*, 916–920. (b) Lee, S. J.; Han, S. W.; Choi, H. J.; Kim, K. J. *Phys. Chem. B* **2002**, *106*, 2892–2900. (c) Choi, H. J.; Han, S. W.; Lee, S. J.; Kim, K. J. *Colloid Interface Sci.* **2003**, *264*, 458–466.
- (10) (a) Pradeep, T.; Sandhyarani, N. *Pure Appl. Chem.* **2002**, *74*, 1593–1607.
- (11) (a) Devadas, M. S.; Bairu, S.; Qian, H.; Sinn, E.; Jin, R.; Ramakrishna, G. *J. Phys. Chem. Lett.* **2011**, *2*, 2752–2758. (b) Kumar, S.; Jin, R. *Nanoscale* **2012**, *4*, 4222–4227.
- (12) Bakr, O. M.; Amendola, V.; Aikens, C. M.; Wenseleers, W.; Li, R.; Negro, L. D.; Schatz, G. C.; Stellacci, F. *Angew. Chem., Int. Ed.* **2009**, *48*, 5921–5926.
- (13) (a) Branham, M. R.; Douglas, A. D.; Mills, A. J.; Tracy, J. B.; White, P. S.; Murray, R. W. *Langmuir* **2006**, *22*, 11376–11383. (b) Zheng, J.; Petty, J. T.; Dickson, R. M. *J. Am. Chem. Soc.* **2003**, *125*, 7780–7781. (c) Rao, T. U. B.; Nataraju, B.; Pradeep, T. *J. Am. Chem. Soc.* **2010**, *132*, 16304–16307. (d) Jin, R. *Nanoscale* **2010**, *2*, 343–362.
- (14) Muhammed, M. A. H.; Pradeep, T. In *Advanced Fluorescence Reporters in Chemistry and Biology II*; Demchenko, A. P., Ed.; Springer-Verlag: Berlin, 2010; Vol. 9, p 333 and references cited therein.
- (15) Muhammed, M. A. H.; Ramesh, S.; Sinha, S. S.; Pal, S. S.; Pradeep, T. *Nano Res.* **2008**, *1*, 333–340.
- (16) Diez, I.; Ras, R. H. A. *Nanoscale* **2011**, *3*, 1963–1970.
- (17) Toikkanen, O.; Carlsson, S.; Dass, A.; Rönholm, G.; Kalkkinen, N.; Quinn, M. B. *J. Phys. Chem. Lett.* **2010**, *1*, 32–37.
- (18) Lourdu Xavier, P.; Chaudhari, K.; Bakshi, A.; Pradeep, T. *Nano Res.* **2012**, *3*, 14767.
- (19) Triulzi, R. C.; Micic, M.; Giordani, S.; Serry, M.; Chiou, W. A.; Leblanc, R. M. *Chem. Commun.* **2006**, *48*, 5068–5070.
- (20) Wu, X.; He, X.; Wang, K.; Xie, C.; Zhou, B.; Qing, Z. *Nanoscale* **2010**, *2*, 2244–2249.
- (21) Zhang, X.-D.; Wu, D.; Shen, X.; Liu, P.-X.; Fan, F.-Y.; Fan, S.-J. *Biomaterials* **2012**, *33*, 4628–4638.
- (22) Shibu, E. S.; Radha, B.; Verma, P. K.; Bhyrappa, P.; Kulkarni, G. U.; Pal, S. K.; Pradeep, T. *ACS Appl. Mater. Interfaces* **2009**, *1*, 2199–2210.
- (23) Lewis, L. N. *Chem. Rev.* **1993**, *93*, 2693–2730.
- (24) Sanchez, A.; Abbet, S.; Heiz, U.; Schneider, W. D.; Häkkinen, H.; Barnett, R. N.; Landman, U. *J. Phys. Chem. A* **1999**, *103*, 9573–9578.
- (25) Zhu, Y.; Qian, H.; Drake, B. A.; Jin, R. *Angew. Chem., Int. Ed.* **2010**, *49*, 1295–1298. Leelavathi, A.; Rao, T. U. B.; Pradeep, T. *Int. J. Nanosci.* **2011**, *10*, 839–843.
- (26) Muhammed, M. A. H.; Pradeep, T. *Chem. Phys. Lett.* **2007**, *449*, 186–190.

- (27) (a) Bootharaju, M. S.; Pradeep, T. *Langmuir* **2011**, *27*, 8134–8143. (b) Liu, H.; Zhang, X.; Wu, L.; Jiang, L.; Burda, C.; Zhu, J. *Chem. Commun.* **2011**, *47*, 4237–4239.
- (28) (a) Adhikari, B.; Banerjee, A. *Chem. Mater.* **2010**, *22*, 4364–4371. (b) Liu, S.; Lu, F.; Zhu, J.-J. *Chem. Commun.* **2011**, *47*, 2661–2663.
- (29) (a) Muhammed, M. A. H.; Verma, P. K.; Pal, S. K.; ArunKumar, R. C.; Paul, S.; OmKumar, R. V.; Pradeep, T. *Chem.—Eur. J.* **2009**, *15*, 10110–10120. (b) Yu, J.; Choi, S.; Dickson, R. M. *Angew. Chem., Int. Ed.* **2009**, *48*, 318–320.
- (30) Verma, A.; Uzun, O.; Hu, Y. H.; Hu, Y.; Han, H. S.; Watson, N.; Chen, S. L.; Irvine, D. J.; Stellacci, F. *Nat. Mater.* **2008**, *7*, 588.
- (31) (a) Cathcart, N.; Kitaev, V. *J. Phys. Chem. C* **2010**, *114*, 16010–16017. (b) Chakraborty, I.; Udayabhaskararao, T.; Pradeep, T. *J. Hazard. Mater.* **2012**, *211–212*, 396–403.
- (32) Shibu, E. S.; Habeeb Muhammed, M. A.; Tsukuda, T.; Pradeep, T. *J. Phys. Chem. C* **2008**, *112*, 12168–12176.
- (33) Rao, T. U. B.; Pradeep, T. *Angew. Chem., Int. Ed.* **2010**, *49*, 3925–3929.
- (34) Cathcart, N.; Mistry, P.; Makra, C.; Pietrobon, B.; Coombs, N.; Niaraki, M. J.; Kitaev, V. *Langmuir* **2009**, *25*, 5840–5846.
- (35) Pileni, M. P.; Motte, L.; Billoudeet, F.; Mahrt, J.; Willig, F. *Mater. Lett.* **1997**, *31*, 255–260.
- (36) Leon-Velazquez, M. S.; Irizarry, R.; Castro-Rosario, M. E. *J. Phys. Chem. C* **2010**, *114*, 5839–5849.
- (37) Chen, R.; Nuhfer, N. T.; Moussa, L.; Morris, H. R.; Whitmore, P. M. *Nanotechnology* **2008**, *19*, 455604–455615.
- (38) Karimzadeh, R.; Aleali, H.; Mansour, N. *Opt. Commun.* **2011**, *284*, 2370–2375.
- (39) Aleali, H.; Sarkhosh, L.; Karimzadeh, R.; Mansour, N. *Phys. Status Solidi B* **2011**, *248*, 680–685.
- (40) Martinez-Castañón, G. A.; Sánchez-Loredo, M. G.; Dorantes, H. J.; Martinez-Mendoza, J. R.; Ortega-Zarzosa, G.; Ruiz, F. *Mater. Lett.* **2005**, *59*, 529–534.
- (41) Thakur, S. S.; Balaram, P. *J. Am. Soc. Mass. Spectrom.* **2008**, *19*, 358–366.
- (42) Wu, Z.; Gayathri, C.; Gil, R. R.; Jin, R. *J. Am. Chem. Soc.* **2009**, *131*, 6535–6542.
- (43) Wu, Z.; Jin, R. *ACS Nano* **2009**, *3*, 2036–2042.
- (44) Lide, D. R. *Handbook of Chemistry and Physics*, 80th ed.; CRC Press: Boca Raton, FL, 1999–2000; pp 5–31.

Low temperature thermal dissociation of Ag quantum clusters in solution and formation of monodisperse Ag₂S nanoparticles

*Remya K. P, Udaya Bhaskara Rao Tumu and Thalappil Pradeep**

DST Unit on Nanoscience (DST-UNS), Department of Chemistry and Sophisticated Analytical Instrument Facility, Indian Institute of Technology Madras, Chennai 600 036, India

*E-mail: pradeep@iitm.ac.in

S1. Supporting information 1

Preliminary confirmation of cluster formation through UV/Vis profile and a TEM image

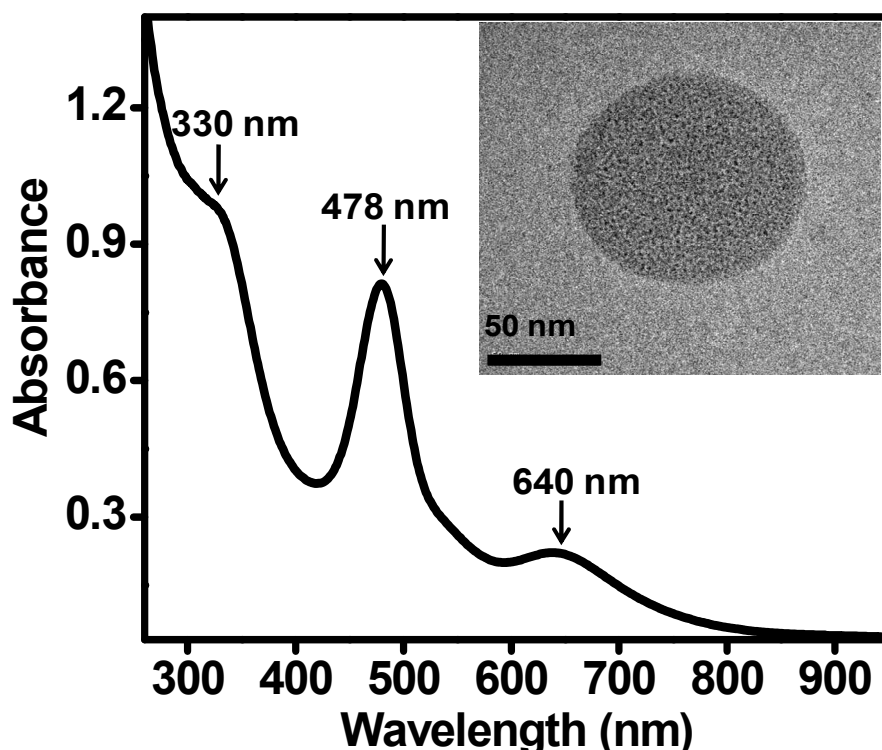


Figure S1. UV/Vis spectrum of freshly prepared $\text{Ag}_{25}\text{SG}_{18}$ quantum clusters in aqueous solution showing the characteristic absorption peaks. Inset shows the TEM image of the cluster.

S2. Supporting Information 2

Optical absorption spectrum of the freeze dried control cluster solution.

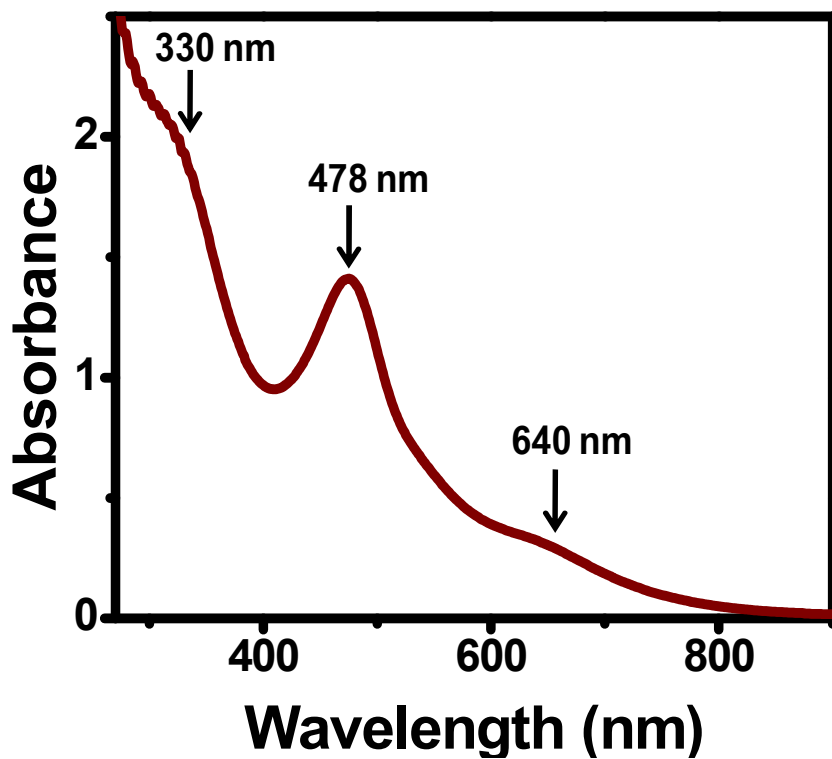


Figure S2. Shows the optical absorption spectrum of cluster after freeze drying (before subjecting to heating).

S3. Supporting Information 3

Time dependent UV/Vis spectra of $\text{Ag}_{25}\text{SG}_{18}$ quantum cluster.

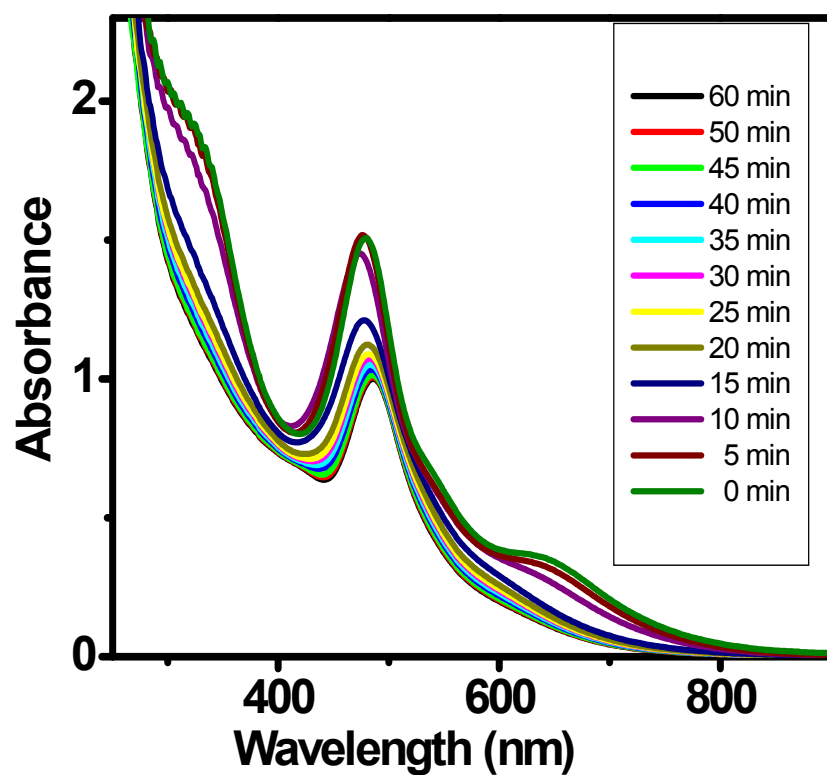


Figure S3. Time dependent UV/Vis spectra of freshly prepared $\text{Ag}_{25}\text{SG}_{18}$ clusters from 0 min-60 min at room temperature.

S4. Supporting Information 4

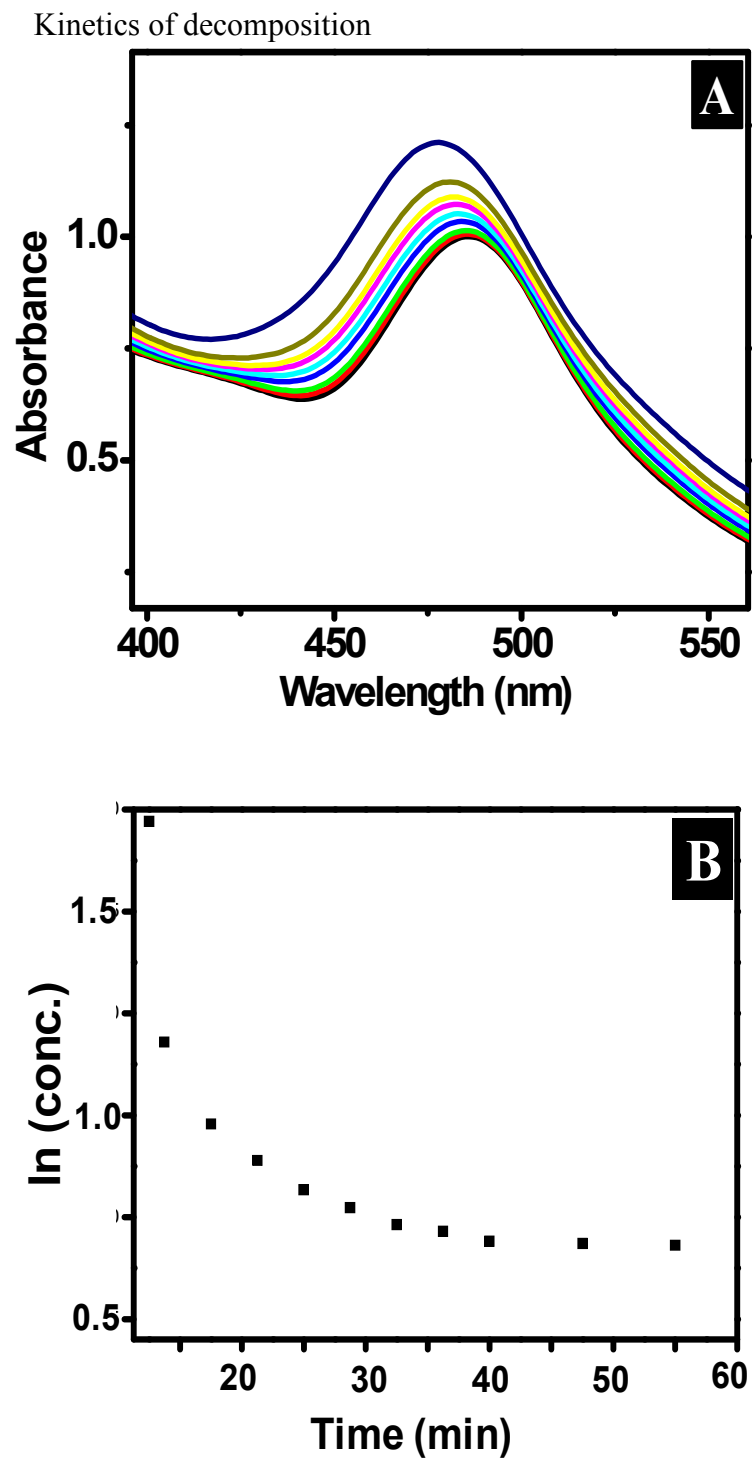


Figure S4. A) Expanded view of time-dependent variation of the 480 nm peak in the UV/Vis spectrum of clusters. B) Graph showing the decrease in the intensity of 480 nm peak with time, indicating a first order kinetics.

S5. Supporting Information 5

X-ray diffraction pattern of $\text{Ag}_{25}\text{SG}_{18}$ cluster which shows only broad peak at 36° (2θ)

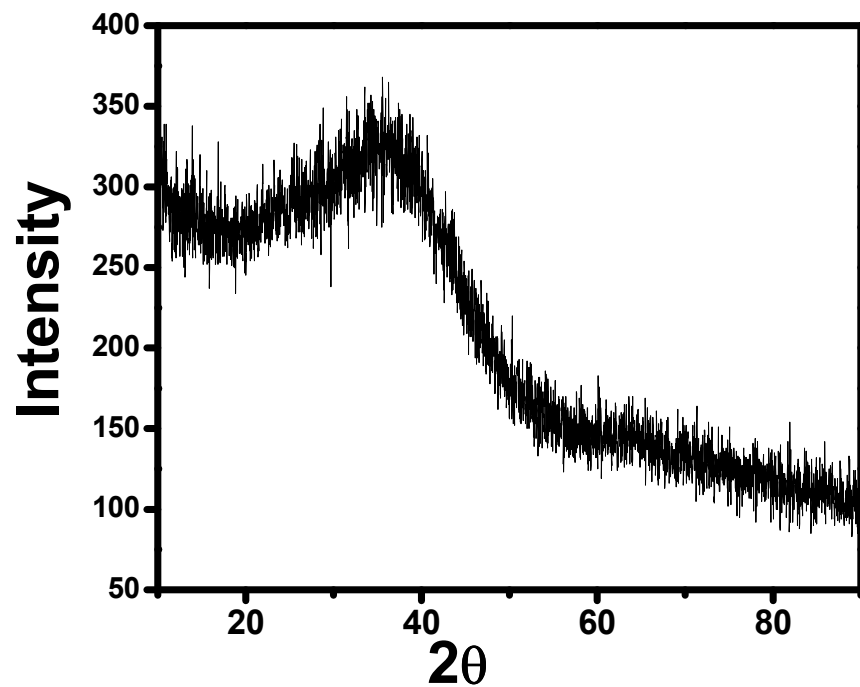


Figure S5. X-ray diffraction pattern of freshly prepared $\text{Ag}_{25}\text{SG}_{18}$ cluster.

S6. Supporting Information 6

Mass spectrum of glutathione taken in the negative mode showing fragments. The peak positions are comparable with what we obtained for the supernatant solution of the decomposed sample.

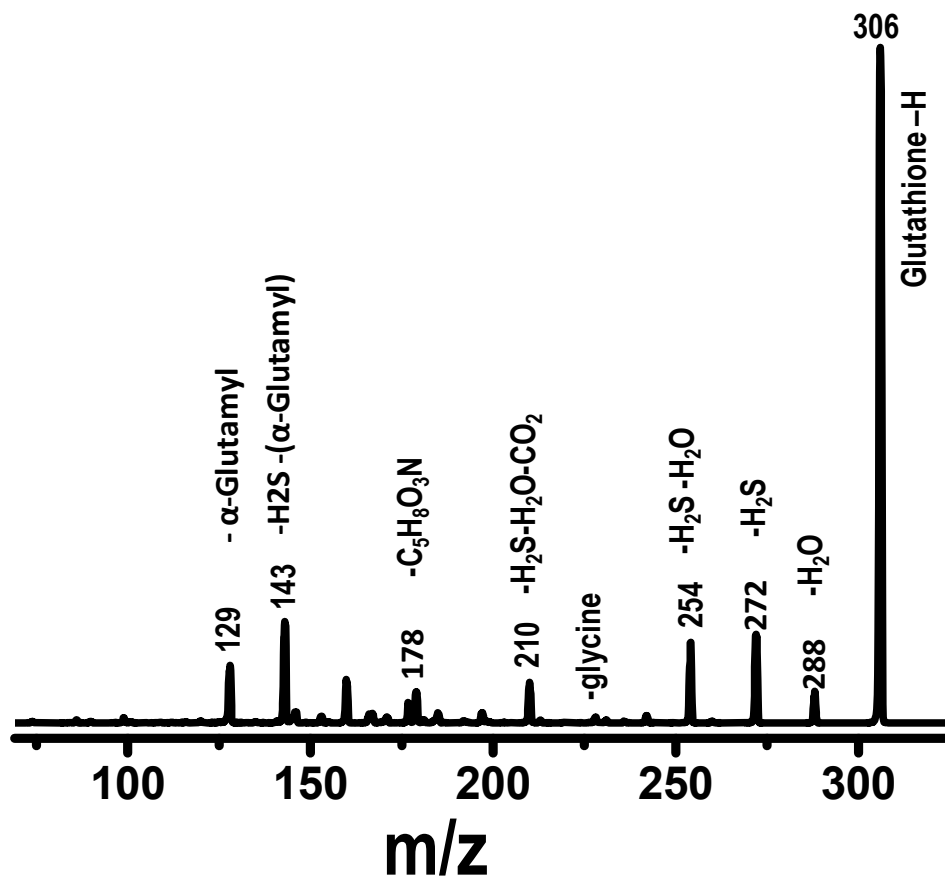


Figure S6. A portion of negative ion ESI MS of glutathione.

Emergence of Multicolor Photoluminescence in $\text{La}_{0.67}\text{Sr}_{0.33}\text{MnO}_3$ Nanoparticles

Anupam Giri,[†] Nirmal Goswami,[†] M. S. Bootharaju,[‡] Paulrajpillai Lourdu Xavier,[‡] Robin John,[‡] Nguyen T. K. Thanh,^{§,||} Thalappil Pradeep,[‡] Barnali Ghosh,[†] A. K. Raychaudhuri,[†] and Samir Kumar Pal^{†,*}

[†]Unit for Nano Science and Technology, S. N. Bose National Centre for Basic Sciences, Block JD, Sector III, Salt Lake, Kolkata 700 098, India

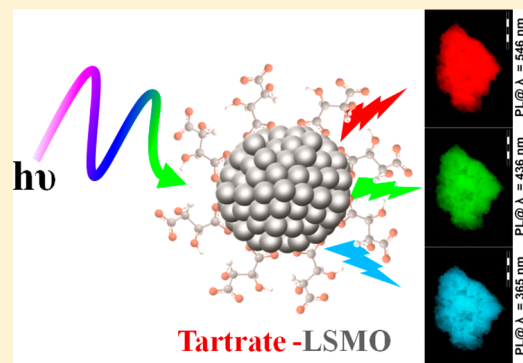
[‡]Department of Chemistry, Indian Institute of Technology Madras, Chennai 600 036 India

[§]Department of Physics and Astronomy, University College London, Gower Street, London WC1E 6BT, United Kingdom

^{||}The Davy-Faraday Research Laboratory, The Royal Institution of Great Britain, 21 Albemarle Street, London, W1S 4BS, United Kingdom

Supporting Information

ABSTRACT: Herein, we report the emergence of multicolor photoluminescence in a mixed-valence manganite nanoparticle $\text{La}_{0.67}\text{Sr}_{0.33}\text{MnO}_3$ (LSMO NP) achieved through electronic structural modification of the nanoparticles upon functionalization with a biocompatible organic ligand, sodium tartrate. From UV-vis absorption, X-ray photoelectron spectroscopy (XPS), time-resolved photoluminescence study, and Raman spectroscopic measurements, it is revealed that ligand-to-metal charge transfer transitions from highest occupied molecular orbital (HOMO, centered in tartrate ligand) to lowest unoccupied molecular orbital (LUMO, centered in $\text{Mn}^{3+/4+}$ of the NPs), and d-d transitions involving Jahn-Teller sensitive Mn^{3+} ions in the NPs plays the central role behind the origin of multiple photoluminescence from the ligand functionalized LSMO NPs.



1. INTRODUCTION

The development of nanomaterials with intrinsic photoluminescence are a key focus in nanotechnology for the rational designing of multifunctional nanoparticles and could have profound impact on many research areas ranging from fundamental physics to photoluminescence (PL) devices, catalysis, biological detections, and therapeutics. Several novel nanomaterials have recently been described including quantum dots (QDs),¹⁻⁴ magnetic nanoparticles (MNPs),^{5,6} magneto-fluorescent nanoparticle,⁷⁻⁹ and metallic NPs.¹⁰ Their unique optical, magnetic, electronic, and structural properties have addressed a broad spectrum of technological/biological applications.¹¹⁻¹⁴ Considerable efforts have also been directed toward rational surface modifications to modulate their electronic structure and complicated surface chemistry. However, despite recent advancement, much work still needs to be done to achieve hydrophilic and biocompatible NPs that are luminescent with surface chemistry adaptable to varied technological/biological applications.

In this article, we demonstrate how one can modify the electronic structure of the nanoparticles of functional mixed-valence oxides by making a hybrid with an organic molecule and thereby make the nanoparticles multicolor photoluminescent. The investigation has been done on nanoparticles (NPs)

of the perovskite manganite $\text{La}_{0.67}\text{Sr}_{0.33}\text{MnO}_3$ (LSMO), which is known to display a number of exotic properties like colossal magnetoresistance.¹⁵ The functionality of the perovskite manganites arises from mixed valence of Mn ions, which in such system as LSMO have two valence states Mn^{3+} and Mn^{4+} . Presence of Mn^{3+} ions lead to Jahn-Teller distortion around Mn ions, whereas simultaneous presence of Mn^{4+} leads to ferromagnetic double-exchange interactions and metallic behavior.

In recent times, significant efforts have been made to exploit the room temperature ferromagnetism of the perovskite manganite NPs for prospective applications in cancer therapy involving the hyperthermal effect¹⁶ and as dual imaging probes for magnetic resonance imaging and fluorescence microscopy (after tagging an external fluorescent agent).¹⁷ Several experiments have also been focused to solubilize the manganite NPs in aqueous solution by employing some biocompatible macromolecules, still, resulted only in a suspension of the NPs in solution.¹⁷⁻¹⁹ However, in a recent attempt we have functionalized individual manganite NPs with a small

Received: August 30, 2012

Revised: November 7, 2012

Published: November 9, 2012

biocompatible ligand to solubilize them into water and the functionalized NPs shows extremely high colloidal stability.²⁰

Herein, we report a new class of multifunctional nanoprobes based on $\text{La}_{0.67}\text{Sr}_{0.33}\text{MnO}_3$ (LSMO) NPs, a mixed-valent manganite where Mn present in two oxidation states, +3 and +4. We have demonstrated the novel optical properties of LSMO NPs upon interaction with sodium tartrate, a dicarboxylate ligand used to solubilized the NPs into water. UV-vis spectroscopic study of the tartrate functionalized LSMO (T-LSMO) NPs reveals that different absorption bands originated from various types of electronic transitions involving ligands-NP interaction. One of the important discovery associated with this work is the observation that the resulting changes on electronic structures (achieved by functionalization with sodium tartrate) can lead to the emergences of multiple color photoluminescence from T-LSMO NPs when it is addressed with different excitation wavelengths, where the respective excitation wavelengths have a direct correlation with the observed UV-vis absorption bands. From X-ray photoelectron spectroscopic (XPS) analysis and time-resolved photoluminescence lifetime measurements, we have acquired additional evidence supporting the proposed mechanism regarding the origin of different optical properties of T-LSMO NPs.

2. EXPERIMENTAL SECTION

Tartaric acid, citric acid, malic acid, sodium hydroxide, metal acetates, 2-amino-purine (2AP), potassium bromide (KBr), and phosphate buffer were obtained from Sigma-Aldrich (USA) and used as received without further purification. 4',6-Diamidino-2-phenylindole (DAPI), Hoechst (H33258), and ethidium bromide (EtBr) were obtained from Molecular Probes. Organic dye COUMARIN 500 (C500) was obtained from exciton.

We have synthesized the bulk LSMO nanoparticles following a reported procedure where a modified sol-gel technique has been designed especially for the preparation of complex oxide nanoparticles and the reaction mechanism was first given by Shankar et al.²¹ The structural and magnetic characterization of the as-prepared nanoparticles has also been described in the reported article.²⁰

We have solubilized the as-prepared LSMO NPs into water by using the reactivity of hydroxyl (-OH) and carboxylate (COO^-) groups of tartrate. First, we prepared 6 mL of 0.5 M tartrate solution (pH \sim 7) and then 200 mg as-prepared LSMO NPs was added to the solution followed by 6 h of extensive mixing by cyclo-mixer. Finally, the nonfunctionalized bigger sized NPs (as evident from Figure S5 of the Supporting Information, only 5–10% of as-prepared LSMO NPs were in the size range of 2–6 nm, which become solubilized by tartrate ligands) were filtered out (by a syringe driven filter of 0.22 μm diameter) and UV-vis optical absorption of the resulting greenish-yellow filtrate solution was measured.

Next, we increased the pH of the resulting greenish-yellow tartrate-LSMO solution from pH \sim 7 to pH \sim 12, by dropwise addition of NaOH. The greenish-yellow color of the solution turns to yellowish-brown (indicating conversion of surface Mn^{2+} to Mn^{3+} , as in acidic/neutral pH, Mn^{3+} ions are unstable and tend to disproportionate into Mn^{2+} and Mn^{4+} , whereas it is stabilized by the comproportionation of Mn^{2+} and Mn^{4+} in alkaline conditions²²) and the resulting solution was heated at 70 $^\circ\text{C}$ under vigorous stirring condition for 8 h. After eight hours, the solution became highly fluorescence. Photographs of the resulting solution taken under white light and UV light have

been presented in Figure 1. Optical spectra of the Tartrate-LSMO NPs solutions were taken with a Shimadzu Model UV-

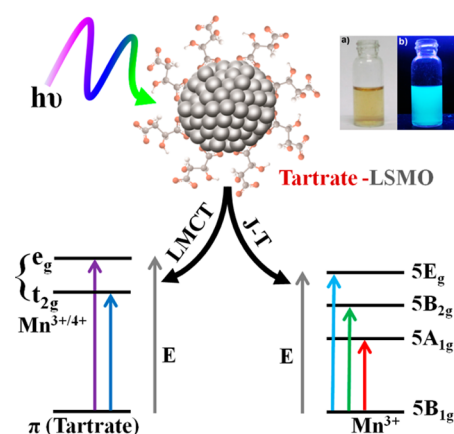


Figure 1. Schematic presentation of the most likely events occurring when a photon hits a tartrate functionalized LSMO NPs (T-LSMO): ligand-to-metal charge transfer transitions from HOMO (centered in tartrate ligand) to LUMO (centered in $\text{Mn}^{3+/4+}$ of the NP), and d-d transitions involving Jahn-Teller sensitive Mn^{3+} ions in the NP. Arrows show the transition involved upon excitation by photon of different energy. Insert shows the photographs of T-LSMO NPs under visible light (a) and under UV light (b).

2450 spectrophotometer using a quartz cuvette of 1 cm path length. The characteristic fluorescence excitation and emission spectra of tartrate-LSMO NPs solution were recorded on a Jobin Yvon Model Fluoromax-3 fluorimeter.

Fluorescence micrographs of as-prepared LSMO and T-LSMO NPs were taken using an Olympus BX51 fluorescence microscope employing 365, 436, and 546 nm excitation wavelengths generated through WBS, WGS, and WUS mirror units, respectively. During the capturing of fluorescence micrographs, in the case of all three excitations (365, 436, and 546 nm), excitation light powers and integration times were kept constant.

TEM samples were prepared by dropping sample stock solutions onto a 300-mesh carbon coated copper grid and dried overnight in air. Particle sizes were determined from micrographs recorded at a magnification of 450 000 \times using a FEI TecnaiTF-20 field-emission high-resolution transmission electron microscope operating at 200 kV.

XPS measurements were done using an Omicron ESCA Probe spectrometer with polychromatic $\text{Al K}\alpha$ X-rays ($h\nu = 1486.6$ eV). The X-ray power applied was 300 W. The pass energy was 50 eV for survey scans and 20 eV for specific regions. Sample solution was spotted on a molybdenum sample plate and dried in vacuum. The binding energy was calibrated with respect to the adventitious C 1s feature at 285.0 eV. Most of the spectra were deconvoluted to their component peaks using the software 6.

A JASCO FTIR-6300 spectrometer was used for the FTIR to confirm the covalent attachment of the tartrate molecules with the LSMO NPs. For FTIR measurements, powdered Tartrate-LSMO samples were mixed with KBr powder and pelletized. The background correction was made by using a reference blank of KBr pellet.

Raman spectroscopic investigations were carried out using a confocal Raman microscope (CRM α 300 S) purchased from WITec GmbH, Germany. The spectral acquisition was done in

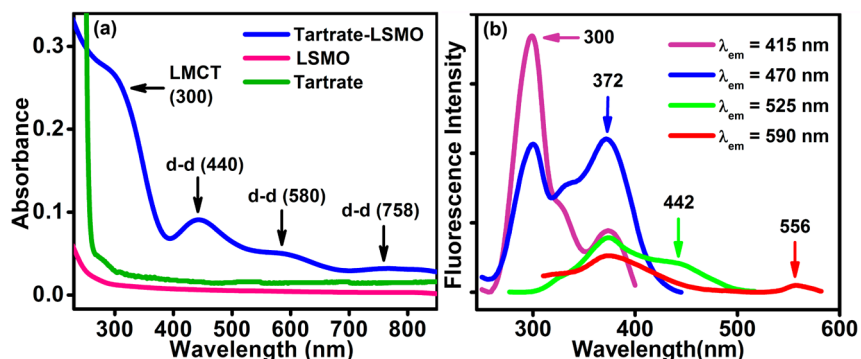


Figure 2. (a) UV-vis absorption spectra of as-prepared LSMO, tartrate, and tartrate-LSMO NPs (in aqueous solution at pH~7). (b) Photoluminescence excitation spectra of tartrate-LSMO NPs at different emission maximum (shown in part a) of 415, 470, 525, and 590 nm.

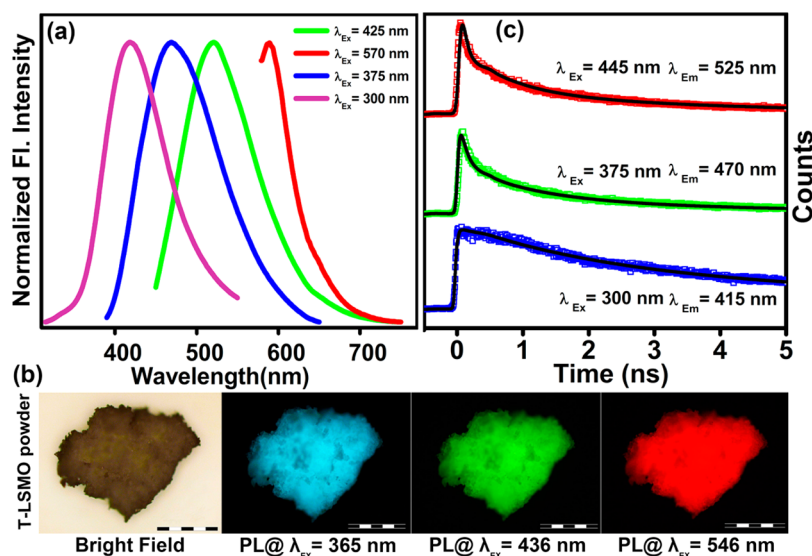


Figure 3. (a) Normalized steady-state photoluminescence spectra collected from tartrate-LSMO NPs with four different excitation wavelengths of 300, 375, 425, and 570 nm at pH ~7. (b) Fluorescence microscopic images of tartrate-LSMO NP powder under irradiation of white light (bright field) and light of three different wavelengths of 365, 436, and 546 nm. Scale bars in the figure are of 500 μm . (c) Picosecond-resolved photoluminescence decay transients of tartrate-LSMO NPs in water measured at emission wavelengths of 415, 470, and 525 nm upon excitation with laser source of 300, 375, and 445 nm wavelengths, respectively.

a back scattered geometry using a dispersion grating of 600 grooves/mm. The detector used is a peltier cooled charge coupled device, which is maintained at $-60\text{ }^{\circ}\text{C}$. The NPs were excited with a HeNe 532 nm laser source. Each spectrum is an average of 100 hardware spectra, each of which is integrated over 1 s. Raman were measured for LSMO, tartrate, and tartrate-LSMO in solid state, obtained after lyophilizing the corresponding solutions.

Squamous epithelial cells were directly collected from human mouth with proper permission from the volunteer. Prior to cell imaging, the cells were spread on glass slides in presence of PBS (phosphate buffered saline) and NP solution (at a final concentration of $3 \times 10^{-6}\text{ M}$) was added followed by 30 min of incubation at room temperature. After incubation, the cells were washed twice with PBS to remove unbound NPs. Fluorescence micrographs of the cells were taken using an Olympus BX51 fluorescence microscope employing 365, 436, and 546 nm excitation wavelengths generated through WBS, WGS, and WUS mirror units, respectively.

Magnetization curves of Tartrate-LSMO NPs were carried out in a Quantum Design hybrid superconducting quantum

interference device-vibrating sample magnetometer (SQUID-VSM) at 5, 50, 100, and 300 K with fields up to 7 T.

Picosecond-resolved fluorescence transients were measured by using commercially available spectrophotometer (Life Specs) from Edinburgh Instruments, UK for 375 nm excitation (80 ps instrument response function, IRF). And for 300 nm excitation, we have used the third harmonic laser beam of 900 nm (0.5 nJ per pulse) using a mode locked Ti-sapphire laser with an 80 MHz repetition rate (Tsunami, Spectra Physics), pumped by a 10 W Millennia (Spectra Physics) followed by a pulse-peaker (rate 8 MHz), and a third harmonic generator (Spectra Physics, model 3980). The third harmonic beam is used for excitation of the sample inside the time-correlated-single-photon-counting (TCSPC) instrument (IRF = 50 ps) and the second harmonic beam is collected for the start pulse. The observed fluorescence transients were fitted by using a nonlinear least-squares fitting procedure to a function

$$(X(t) = \int_0^t E(t')R(t-t')dt')$$

comprising of convolution of the IRF ($E(t)$) with a sum of exponential

$$R(t) = A + \sum_{i=1}^N B_i e^{-t/\tau_i}$$

with pre-exponential factors (B_i), characteristic lifetimes (τ_i), and a background (A). Relative concentration in a multi exponential decay was finally expressed as:

$$c_n = \frac{B_n}{\sum_{i=1}^N B_i} \times 100$$

The quality of the curve fitting was evaluated by reduced chi-square and residual data. It has to be noted that with our time-resolved instrument, we can resolve at least one-fourth of the instrument response time constants after the deconvolution of the IRF.

3. RESULTS AND DISCUSSION

Part a of Figure 2 illustrates the UV–vis absorption spectrum of as-prepared LSMO, tartrate, and T–LSMO NPs (at pH \sim 7). In the case of T–LSMO, it shows two peaks at 300 and 440 nm, a shoulder descending into lower energies around 580 nm and a broad band at 758 nm. The peak at 300 nm could be assigned to one of the possible high energy charge-transfer, ligand-to-metal charge transfer (LMCT) processes involving tartrate– $Mn^{3+/4+}$ interaction.²³ The other expected LMCT band²³ at around 385 nm has not been observed in the absorption spectrum presumably because the band has been masked by the more intense 300 nm absorption, however, is distinctly visible in the excitation spectrum at around 372 nm (part b of Figure 2). Other bands at 440, 580, and 758 nm are reasonably attributed to d–d transitions of Mn^{3+} in T–LSMO NPs, as the degeneracy of $5E_g$ ground state term of d^4 (Mn^{3+}) high-spin octahedral environment, has been lifted by the Jahn–Teller effect, that ultimately leads to a tentative assignment of the observed bands to the transitions $5B_{1g} \rightarrow 5E_g$, $5B_{1g} \rightarrow 5B_{2g}$, and $5B_{1g} \rightarrow 5A_{1g}$, respectively^{24,25} (Figure 1). Any absorption contribution from other metal ions (La and Sr)–tartrate interaction, tartrate ligand or as-prepared LSMO itself, in the assigned peak positions has been nullified from control experiments. Reflection of the UV–vis absorption patterns into the photoluminescence excitation spectra (shown in part b of Figure 2) of the sample has been expected and indeed observed, which further supports the assignment of the electronic excited states those give rise to multiple color photoluminescence.

Part a of Figure 3 displays the normalized photoluminescence spectra of T–LSMO NPs at room temperature. The four distinct emission bands starting from blue to red region (maximum at 418, 470, 520, and 590 nm) of the spectrum corresponding with four distinct excitation wavelengths (300, 375, 425, and 570 nm) are clearly observed. The photoluminescence as shown in part a of Figure 3 may be assigned to originate predominantly from the LMCT [tartrate $\rightarrow Mn^{3+/4+}$] excited states and ligand field excited states of the metal (Mn^{3+}) d orbitals. Photoluminescence from either an intraligand or metal to ligand charge-transfer (MLCT) excited states are considered unlikely. To represent qualitatively the relationship between emission bands, we have shown the OD normalized PL spectra of T–LSMO NPs in part a of Figure S1 of the Supporting Information. Moreover, to confirm that the lower energy emission spectra are not subsets of high energy emission tail, we have compared the similar excitation wavelength dependent fluorescence emission of a well-known

organic dye C500 having one emission maximum centered at 510 nm in water (part c of Figure S1 of the Supporting Information). From the figure, it has been observed that, unlike T–LSMO NPs, despite the change in excitation wavelengths (from 320 to 470 nm), emission maxima of C500 (at around 510 nm) remains same and so its fluorescence decay transients (part d of Figure S1 of the Supporting Information). The observation clearly indicates that the lower energy emission spectra are not subsets of high energy emission tail of T–LSMO NPs.

The above speculation regarding the origin of photoluminescence (PL) is also supported by the pH dependent PL measurements of T–LSMO NPs. As revealed from Figure S2 of the Supporting Information, upon changing the pH of the T–LSMO solution from 12 to 3, its PL intensity quenches significantly, however, almost totally recovered again, by changing the pH from 3 to 12. This phenomenon is consistent with the fact that, in acidic/neutral pH, Mn^{3+} ions are unstable and tend to disproportionate into Mn^{2+} and Mn^{4+} , whereas it is stabilized by the comproportionation of Mn^{2+} and Mn^{4+} in alkaline conditions.²² Thus, reduction potentials of Mn^{3+}/Mn^{2+} system in acidic and basic solutions ($E^{\circ}_{Mn^{3+}/Mn^{2+}} = 1.51$ V at pH 0, whereas $E^{\circ}_{Mn^{3+}/Mn^{2+}} = -0.25$ V at pH 14)²⁶ play a crucial role in understanding the pH dependent PL profile of the studied system. Tartaric acid possesses four protons (two carboxylic acid protons and two hydroxyl protons), which can be liberated depending on pH. However, because of high pK_a (11–12) values of the hydroxyl protons in comparison with the carboxylic protons ($pK_{a1} = 2.95$ and $pK_{a2} = 4.25$), they would not liberate at neutral pH and were only available at highly basic pH conditions.²⁷ Thus, at higher pH, strong co-ordination of tetravalent anionic tartaric acid with Mn^{3+} facilitates both the LMCT and J–T events resulting in a maximization of PL intensity from T–LSMO NPs. However, upon acidification a decrease in pH leads to the protonation of coordinated tartrate molecules along with disproportionation of Mn^{3+} ions and diminishes the overall PL intensity from T–LSMO NPs. Part b of Figure 3 shows the fluorescence microscopic images of T–LSMO powder under irradiation of white light (bright field) and light of different wavelengths (Figure S3 of the Supporting Information shows the fluorescence microscopic images of as-prepared LSMO powder under identical conditions). Multiple color photoluminescence arising specifically from the functionalized NPs (T–LSMO) upon different excitation are clearly evident from the photographs. Photoluminescence quantum yields (QY) of the T–LSMO NPs at pH \sim 12, were obtained by using the comparative method of Williams et al.,²⁸ which involves the use of well characterized standard samples with known QY values. Photoluminescence QY of 1×10^{-2} (for 415 nm PL), 4×10^{-3} (for 470 nm PL), 8×10^{-4} (for 520 nm PL), and 2.4×10^{-4} (for 590 nm PL) were obtained relative to the standards 2-amino-purine (2AP), 4', 6-diamidino-2-phenylindole (DAPI), Hoechst (H33258), and ethidium bromide (EtBr), respectively.

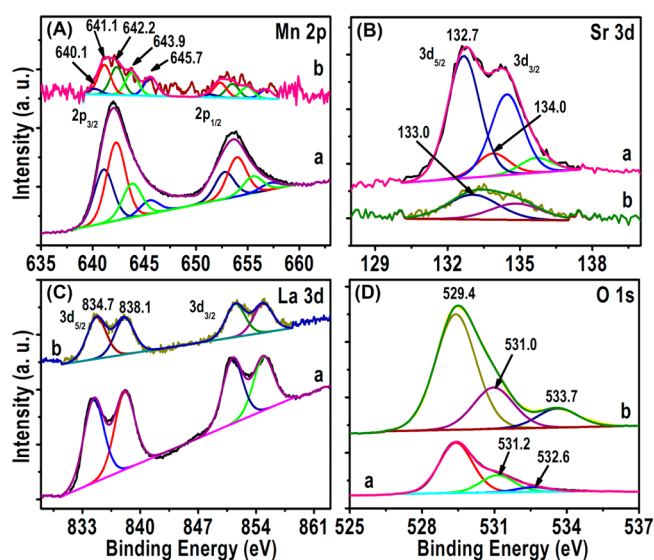
Further insights into the nature of the photoluminescence can be obtained by analyzing the luminescence lifetime decay transients of T–LSMO NPs in water measured by picosecond-resolved time-correlated single-photon counting (TCSPC) technique. Part c of Figure 3 shows the luminescence lifetime decay transients of the water-soluble NPs at three different emission wavelengths (415, 470, and 525 nm) corresponding with three different laser excitation wavelengths (300, 375, and 445 nm), respectively. Although the origin of 415 and 470 nm

Table 1. Fitted Decay Time Constants of T–LSMO NPs from Picosecond Experiments, Values in Parentheses Represent the Relative Weight Percentage of the Time Components

system	excitation wavelength, λ_{ex} (nm)	photoluminescence peak, λ_{em} (nm)	τ_1 (ps)	τ_2 (ps)	τ_3 (ps)	τ_{av} (ns)
T–LSMO NPs	300	415	1846 (45)	7565 (55)		4.77
	375	470	108 (62)	1074 (27)	4982 (11)	0.84
	445	525	56 (69)	737 (20)	4077 (11)	0.64

emission is from the LMCT excited states, luminescence lifetime of 415 nm emission is much longer ($\langle\tau\rangle = 4.77$ ns) than the 470 nm ($\langle\tau\rangle = 0.84$ ns) emission (Table 1). Substantial shortening in the luminescence lifetime of 470 nm emission and its close resemblance with the 525 nm emission lifetime ($\langle\tau\rangle = 0.64$ ns, originates from ligand field excited states of the metal d orbitals) presumably due to enhanced radiative deactivation of the excited state by the close proximity with metal d–d states.²⁹

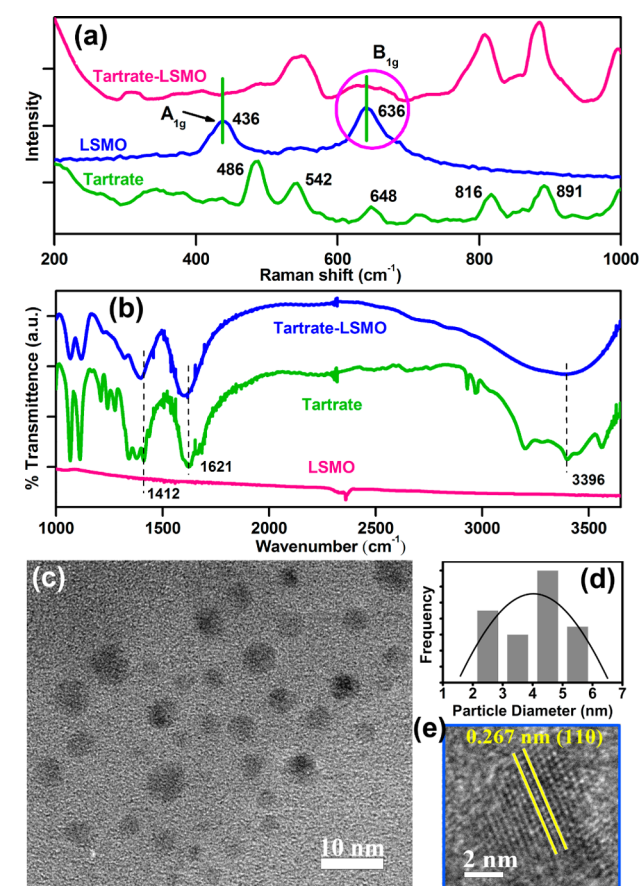
To get supporting evidence regarding the origin of different optical properties of T–LSMO NPs, XPS analysis has been carried out for LSMO NPs, before (as prepared NPs) and after (T–LSMO) functionalization with sodium tartrate (Figure S4 of the Supporting Information). Figure 4 represents the XPS

**Figure 4.** XPS analysis of LSMO NPs before and after functionalization with tartrate (traces a and b, respectively). A, B, C, and D are Mn 2p, Sr 3d, La 3d, and O 1s regions respectively of samples a and b.

data of as-prepared LSMO (traces a) and T–LSMO NPs (traces b). The Mn 2p region is shown in part A of Figure 4. The peaks of Mn 2p_{3/2} are observed at 641.1, 642.2, 643.9, and 645.7 eV in both of the samples. The Mn 2p_{3/2} features at 641.1 and 642.2 eV are attributed to oxides of Mn³⁺ and Mn⁴⁺, respectively.³⁰ The peak position at 643.9 eV may be due to the manganese in different coordination environment like other metal ions such as La³⁺ and Sr²⁺.³⁰ The peak position at 645.7 eV may be due to satellite peak.³¹ In the T–LSMO a new feature peaking at 640.1 eV is noticed, which is attributed to Mn²⁺.³⁰ The formation of Mn²⁺ could be due to reduction of some of the Mn³⁺/Mn⁴⁺ species with tartrate, as reduction of metal ions by tartrate/citrates is expected.³² The Sr 3d_{5/2} peaks at 132.7 and 134.0 eV (part B of Figure 4, trace a) are assigned to Sr²⁺ in the bulk and surface of the NPs, respectively.³³ In the case of T–LSMO, the Sr 3d_{5/2} is noticed at 133.0 eV, which is also due to Sr in the divalent (+2) state.³⁴ The peaks of La

3d_{5/2} at 834.7 and 838.1 eV are due to La³⁺ and satellite, respectively (part c of Figure 4) in both of the samples.³⁵ The O 1s peaks in LSMO NPs at 529.4 and 531.0 eV are due to lattice oxygen O²⁻ associated with Mn and surface oxygen associated hydroxyl ions, respectively.³⁰ The peak at 532.6 eV is due to the O, which is weakly bound to surface.³⁶ The peak of O 1s at 533.7 eV in T–LSMO sample is due to carboxylate oxygen from the tartrate.³⁷ So, from XPS study it is evident that, upon functionalization with tartrate a partial reduction of Mn³⁺ and Mn⁴⁺ centers in the NPs occur and resulting the formation of Mn²⁺ ions, whereas La³⁺ and Sr²⁺ centers remain unaffected.

It is argued that the change in the valence states of Mn ions will lead to a perturbation of Mn³⁺–O–Mn⁴⁺ bond. We do observe the postulated perturbation through Raman spectroscopic investigation on T–LSMO NPs, as prepared LSMO NPs and tartrate. As shown in part a of Figure 5, between the

**Figure 5.** (a) Raman spectra of as-prepared LSMO NPs, tartrate–LSMO NPs and tartrate. (b) FTIR spectra of as prepared LSMO NPs, sodium tartrate, and tartrate functionalized LSMO (tartrate–LSMO) NPs, recorded with a KBr pellet. (c) TEM image of tartrate–LSMO NPs. (d) Size distribution of the NPs in solution. (e) HRTEM image of the crystalline structure of tartrate–LSMO NPs.

two characteristic peaks of LSMO NPs at 436 and 636 cm^{-1} (corresponding with A_{1g} -like and B_{1g} -like vibrational modes involving Mn–O stretching vibration modes of MnO_6 unit, respectively),³⁸ the peak around 436 cm^{-1} completely disappeared and the 636 cm^{-1} peak becomes broadened (possibly due to mixing of tartrate features) after their functionalization with tartrate. Hence, the disappearance of A_{1g} -like stretching vibration mode that represents the extension and compression of Mn–O bond pairs and is directly correlated with Jahn–Teller distortion, provides a strong basis for the changes that occur at the level of MnO_6 octahedra which provides the physical basis for the change in the optical properties of the NPs upon functionalization.

The direct bonding of tartrate ligands to the surface of the LSMO NP has been confirmed by FTIR spectroscopy. Part b of Figure 5 represents the FTIR spectra of as-prepared LSMO NPs, tartrate, and tartrate functionalized LSMO NPs. In case of tartrate, the appearance of two strong bands at 1412 and 1621 cm^{-1} represent the symmetric and asymmetric stretching modes of $-\text{COO}^-$ ions (carboxylate), respectively.³⁹ Upon attachment with the NP surface, these two bands become red-shifted and appear sharply at 1392 and 1596 cm^{-1} respectively and clearly confirm the binding of carboxylate's oxygen with the NPs. Moreover, the significant broadening of the band representing O–H (hydroxyl) stretching vibration mode⁴⁰ at 3396 cm^{-1} for tartrate–LSMO also substantiate the involvement of hydroxyl groups during the functionalization process.

As shown in part c of Figure 5, transmission electron microscopy (TEM) revealed that T–LSMO NPs are nearly spherical in shape with an average diameter of around 4 nm (part d of Figure 5). Thus, tartrate ligands only solubilized the small sized particles out of a wide range of particle size from ~ 2 to 30 nm in the as-prepared LSMO NPs (Figure S5 of the Supporting Information). The HRTEM image (part e of Figure 5) confirms the crystalline nature of the T–LSMO NPs having interplanar distance of 0.267 nm, which corresponds to the (110) plane of the crystal lattice (as shown in part b of Figure S6 of the Supporting Information, and similar interplanar distance have also been observed in case of as-prepared LSMO NPs). Selected area electron diffraction (SAED) and energy dispersive X-ray (EDAX) pattern of LSMO and T–LSMO NPs also provided supporting evidence (Figures S6 and S7 of the Supporting Information).

Because the tartrate ligand (contains two hydroxyl and two carboxylate groups) is from the class of organic hydroxycarboxylates, we have used two more ligands which are close mimic of tartrate (trisodium citrate and sodium salt of malic acid) and of the same class, for meaningful comparisons with the data obtained from tartrate. It has been observed that both citrate and malate functionalized LSMO NPs exhibit similar UV–vis absorption pattern (part a of Figure 6 and Figure S8 of the Supporting Information, respectively) and excitation wavelength-dependent multiple photoluminescence (in case of citrate–LSMO, parts b and c of Figure 6), which further substantiate the results obtained using tartrate (spectral position of the observed absorption and photoluminescence peaks from these functionalized NPs has been listed in Table S1 of the Supporting Information). Moreover, we have observed the same pH dependent PL profile from citrate–LSMO NPs also (Figure S9 of the Supporting Information). Because of the structural similarity of tartrate and citrate, their pH dependent co-ordination behavior with the NP surface has been expected to be alike. It is revealed that the ligand field of tartrate, citrate

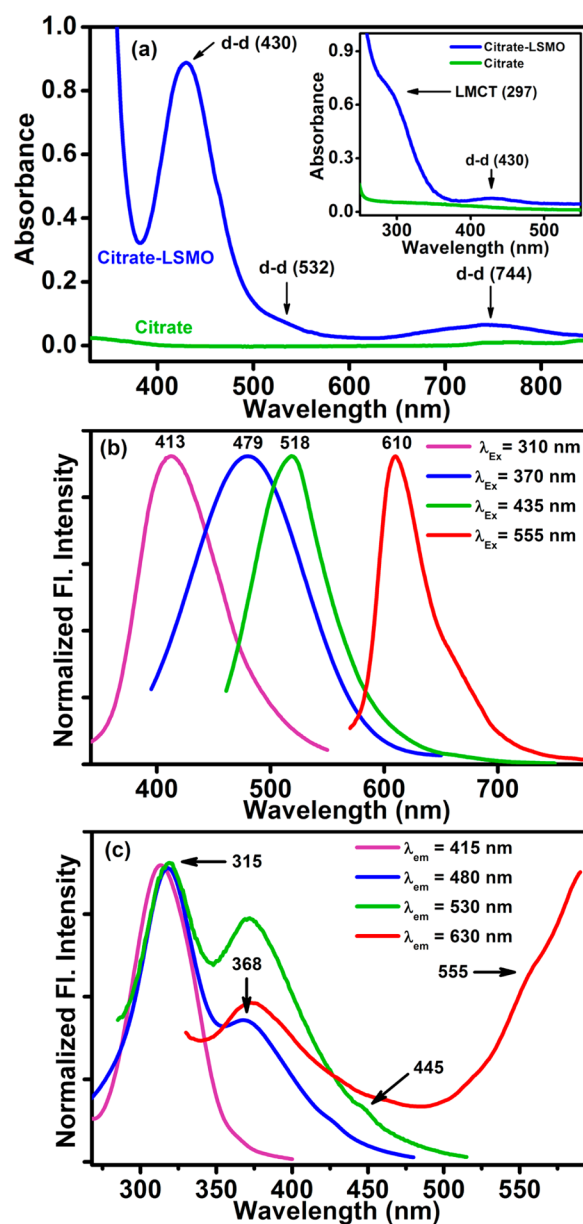


Figure 6. (a) UV–vis absorption spectra of citrate and citrate–LSMO NPs in aqueous solution at pH ~ 7 . Inset shows the absorption peak (LMCT) at around 300 nm obtained from diluted solution of citrate–LSMO NPs. Although, the entire characteristic peaks/bands are present in case of citrate–LSMO, the observed shift in their positions with respect to T–LSMO NPs could be due to the structural variations of the two ligands. (b) Normalized steady-state photoluminescence spectra collected from citrate–LSMO NPs with four different excitation wavelengths of 310, 370, 435, and 555 nm. (c) Photoluminescence excitation spectra of citrate–LSMO NPs at different emission maximum of 415, 480, 530, and 630 nm.

and malate can activate the Jahn–Teller (J–T) splitting of Mn^{3+} ions in the NPs and the corresponding d–d transitions along with ligand-to-metal charge transfer transitions (LMCT) plays the crucial role for the emergence of such novel optical properties from LSMO NPs upon functionalization.

4. CONCLUSIONS

Within the present studies, we have demonstrated the possibility of electronic structural modifications of manganites NPs (LSMO, and thus the resulting novel optical properties)

by charge transfer through functionalization with small organic ligands. The modified electronic structure notably leads to multicolor photoluminescence from the functionalized NPs when excited with different wavelength. We have also explored the mechanistic insight into the origin of multicolor photoluminescence from the T–LSMO NPs. We envision that, given the potentiality of the interaction of Mn^{2+} (easy to convert into Mn^{3+} at high pH), Mn^{3+} (J–T sensitive) and Mn^{4+} toward hydroxycarboxylates (tartrate/citrate) and the consequent origin of novel optical properties, a logical extension of this work would be the functionalization of manganese oxides and various manganese doped nanoparticles including manganese ferrites, ZnO, CdS, and so forth.

■ ASSOCIATED CONTENT

■ Supporting Information

Detailed characterization of as-prepared LSMO, T–LSMO, citrate–LSMO and malate–LSMO NPs, SQUID measurements and cell imaging study of T–LSMO NPs. This material is available free of charge via the Internet at <http://pubs.acs.org>.

■ AUTHOR INFORMATION

Corresponding Author

*E-mail: skpal@bose.res.in.

Notes

The authors declare no competing financial interest.

■ ACKNOWLEDGMENTS

The authors would like to acknowledge Mr. Sounik Sarkar and Prof. Anjan Kr. Dasgupta at Department of Biochemistry, University of Calcutta for insightful discussions. A.G. thanks UGC, India, for fellowship. N.G. thanks CSIR, India, for fellowship. We thank DST for financial grants SR/SO/BB-15/2007. The work of A.K.R. and B.G. has been supported by funding from the DST, India as UNANST-II. Equipment support to T.P. was provided by the Nano Mission of DST, India.

■ REFERENCES

- (1) Chan, W. C. W.; Nie, S. *Science* **1998**, *281*, 2016–2018.
- (2) Taylor, J. R.; Fang, M. M.; Nie, S. *Anal. Chem.* **2000**, *72*, 1979–1986.
- (3) Bonadeo, N. H.; Erland, J.; Gammon, D.; Park, D.; Katzer, D. S.; Steel, D. G. *Science* **1998**, *282*, 1473–1476.
- (4) Gao, X. H.; Nie, S. M. *Trends. Biotechnol.* **2003**, *21*, 371–373.
- (5) Pecorelli, T. A.; Dibrell, M. M.; Li, Z.; Thomas, C. R.; Zink, J. I. *Proc. SPIE* **2010**, *7576*, 75760k.
- (6) Gao, F.; Chen, X. Y.; Yin, K. B.; Dong, S.; Ren, Z. F.; Yuan, F.; Yu, T.; Zou, Z. G.; Liu, J. M. *Adv. Mater.* **2007**, *19*, 2889–2892.
- (7) Josephson, L.; Kircher, M. F.; Mahmood, U.; Tang, Y.; Weissleder, R. *Bioconjugate Chem.* **2002**, *13*, 554–560.
- (8) Kircher, M. F.; Weissleder, R.; Josephson, L. *Bioconjugate Chem.* **2004**, *15*, 242–248.
- (9) Cho, N.-H.; Cheong, T.-C.; Min, J. H.; Wu, J. H.; Lee, S. J.; Kim, D.; Yang, J.-S.; Kim, Y. K.; Seong, S.-Y. *Nat. Nanotechnol.* **2011**, *6*, 675–682.
- (10) Verma, P. K.; Giri, A.; Thanh, N. T. K.; Tung, L. D.; Mondal, O.; Pal, M.; Pal, S. K. *J. Mater. Chem.* **2010**, *20*, 3722–3728.
- (11) Petros, R. A.; DeSimone, J. M. *Nat. Rev. Drug Discov.* **2010**, *9*, 615–627.
- (12) Luo, X.; Morrin, A.; Killard, A. J.; Smyth, M. R. *Electroanalysis* **2006**, *18*, 319–326.
- (13) Chen, W. *J. Nanosci. Nanotechnol.* **2008**, *8*, 1019–1051.
- (14) Pankhurst, Q. A.; Thanh, N. T. K.; Jones, S. K.; Dobson, J. J. *Phys. D: Appl. Phys.* **2009**, *42*, 224001–224016.

(15) Rao, C. N. R.; Raveau, B. *Colossal Magnetoresistance, Charge Ordering and Related Properties of Manganese Oxides*; World Scientific: Singapore, 1998.

(16) Kim, D. K.; Amin, M. S.; Elborai, S.; Lee, S. H.; Koseoglu, Y.; Zahn, M.; Muhammed, M. *J. Appl. Phys.* **2005**, *97*, 100510.

(17) Kacemka, M.; Kaman, O.; Kotek, J.; Falteisek, L.; Cerny, J.; Jirak, D.; Herynek, V.; Zacharovova, K.; Berkova, Z.; Jendelova, P.; Kupcik, J.; Pollert, E.; Veverka, P.; Lukes, I. *J. Mater. Chem.* **2011**, *21*, 157–164.

(18) Bhayani, K. R.; Kale, S. N.; Arora, S.; Rajagopal, R.; Mamgain, H.; Kaul-Ghanekar, R.; Kundaliya, D. C.; Kulkarni, S. D.; Pasricha, R.; Dhole, S. D.; Ogale, S. B.; Paknikar, K. M. *Nanotechnology* **2007**, *18*, 345101.

(19) Rajagopal, R.; Mona, J.; Kale, S. N.; Bala, T.; Pasricha, R.; Poddar, P.; Sastry, M.; Prasad, B. L. V.; Kundaliya, D. C.; S. B. Ogale, S. B. *Appl. Phys. Lett.* **2006**, *89*, 023107.

(20) Giri, A.; Makhal, A.; Ghosh, B.; Raychaudhuri, A. K.; Pal, S. K. *Nanoscale* **2010**, *2*, 2704–2709.

(21) Shankar, K. S.; Raychaudhuri, A. K. *J. Mater. Res.* **2006**, *21*, 27–33.

(22) Takashima, T.; Hashimoto, K.; Nakamura, R. *J. Am. Chem. Soc.* **2011**, *134*, 1519–1527.

(23) Bodini, M. E.; Willis, L. A.; Riechel, T. L.; Sawyer, D. T. *Inorg. Chem.* **1976**, *15*, 1538–1543.

(24) Matzapetakis, M.; Karligiano, N.; Bino, A.; Dakanali, M.; Raptopoulou, C. P.; Tangoulis, V.; Terzis, A.; Giapintzakis, J.; Salifoglou, A. *Inorg. Chem.* **2000**, *39*, 4044–4051.

(25) Aguado, F.; Rodriguez, F.; Núñez, P. *Phys. Rev. B* **2007**, *76*, 094417.

(26) Miessler, G. L.; Tarr, D. A. *Inorganic Chemistry*, 3rd ed.; Prentice-Hall: Englewood Cliffs, NJ, 2004.

(27) Topolski, A. *Chemical Papers* **2011**, *65*, 389–392.

(28) Williams, A. T. R.; Winfield, S. A.; Miller, J. N. *Analyst* **1983**, *108*, 1067–1071.

(29) Lee, Y. F.; Kirchoff, J. R. *J. Am. Chem. Soc.* **1994**, *116*, 3599–3600.

(30) Li, F.; Zhang, L. H.; Evans, D. G.; Duan, X. *Colloids Surf., A* **2004**, *244*, 169–177.

(31) Sandell, A.; Jaworowski, A. J. *J. Electron Spectrosc. Relat. Phenom.* **2004**, *135*, 7–14.

(32) Guindy, N. M.; Basily, E. K.; Milad, N. E. *J. Appl. Chem. Biotech.* **1974**, *24*, 407–413.

(33) Cantoni, M.; Petti, D.; Bertacco, R.; Pallecchi, I.; Marre, D.; Colizzi, G.; Filippetti, A.; Fiorentini, V. *Appl. Phys. Lett.* **2010**, *97*, 032115.

(34) Ding, T. Z.; Li, J.; Qi, Q. G.; Ji, B. H.; Liu, J.; Zhang, C. Z. *J. Rare Earth.* **2003**, *21*, 453–457.

(35) Samal, A. K.; Pradeep, T. *J. Phys. Chem. C* **2010**, *114*, 5871–5878.

(36) Zou, G.; You, X.; He, P. *Mater. Lett.* **2008**, *62*, 1785–1788.

(37) Bootharaju, M. S.; Pradeep, T. *J. Phys. Chem. C* **2010**, *114*, 8328–8336.

(38) Liang, S.; Teng, F.; Bulgan, G.; Zhu, Y. *J. Phys. Chem. C* **2007**, *111*, 16742–16749.

(39) Ramakrishnan, V.; Maroor, J. M. T. *Infra. Phys.* **1988**, *28*, 201–204.

(40) Kaneko, N.; Kaneko, M.; Takahashi, H. *Spectrochim. Acta Mol.* **1984**, *40*, 33–42.

Supplementary Information

Emergence of Multicolor Photoluminescence in $\text{La}_{0.67}\text{Sr}_{0.33}\text{MnO}_3$ Nanoparticles

Anupam Giri ^a, Nirmal Goswami ^a, M. S. Bootharaju ^b, Paulrajpillai Lourdu Xavier ^b, Robin John ^b, Nguyen T. K. Thanh ^{c,d}, Thalappil Pradeep ^b, Barnali Ghosh ^a, Arup K. Raychaudhuri ^a and Samir K. Pal ^{a*}

^a*Unit for Nano Science and Technology, S. N. Bose National Centre for Basic Sciences, Block JD, Sector III, Salt Lake, Kolkata 700 098, India*

^b*Department of Chemistry, Indian Institute of Technology Madras, Chennai 600 036 India*

^c*Department of Physics and Astronomy, University College London, Gower Street, London WC1E 6BT, United Kingdom*

^d*The Davy-Faraday Research Laboratory, The Royal Institution of Great Britain, 21 Albemarle Street, London, W1S 4BS, United Kingdom*

*Corresponding Authors Email: skpal@bose.res.in

1. Magnetic study of Tartrate-LSMO NPs

In case of as-prepared LSMO NPs, simultaneous electron transfer between Mn^{3+} and Mn^{4+} ions via an oxygen ion (i.e. exchange between Mn^{3+} and Mn^{4+} ions, well known as *double exchange*) plays the key role for the origin of their room temperature ferromagnetism¹. So, any perturbation to the parallel alignment of the spins of the two adjacent cations or if the Mn^{3+} -O- Mn^{4+} bond is bent, the electron transfer becomes more difficult and the magnetic interaction decreases. The magnetization of T-LSMO NPs was measured using superconducting quantum interference device (SQUID) magnetometry and the NPs showed paramagnetic behavior at low temperature (upto 50 K), while they were diamagnetic at around room temperature (shown in Supporting Information Figure S10). Thus, upon functionalization with tartrate the magnetic behavior of LSMO NPs has been changed dramatically from room temperature ferromagnetic to diamagnetic. This flipping of magnetism could be due to small average size (~ 4 nm, see Figure 5d of main text) of the T-LSMO NPs (as tartrate only solubilized the small sized particles out of a wide range of particle size from 2 to 30 nm in the as-prepared LSMO NPs) or due to any distortion of the Mn^{3+} -O- Mn^{4+} bond.

2. Incorporation of Tartrate-LSMO NPs into human oral squamous epithelial cells

The observed phenomena that there can be multiple photoluminescence from the T-LSMO, has been utilized for investigating possible *in vitro* cells imaging. Importantly, this has been done by employing the intrinsic photoluminescent properties of T-LSMO NPs, without further grafting of any biorecognition molecules (e.g., oligonucleotides, antibodies, or peptides) onto the NP surface. In this study, a primary squamous epithelial cells collected from the inner lining of human mouth have been used. Prior to cell imaging, the cells were spread on glass slides in presence of PBS (phosphate buffered saline) and NP solution (at a final concentration of 3×10^{-6}

M) was added followed by 30 min of incubation. After incubation, the cells were washed twice with PBS to remove unbound NPs. Figure S11 demonstrates the fluorescence microscopic images of the cell labeled with T-LSMO NPs. Upper left image in the figure represent the bright-field images (black arrows indicate the nucleus of the cell) and other three images represent fluorescence images (employing 365, 436 and 546 nm excitation wavelengths respectively) of the T-LSMO NP labeled cells. Our results show that in case of NP treated cells, all fluorescence of the NPs (365, 436 and 546 nm excitation wavelength) are preferentially derived from the nuclear region of the cells. To verify the sub-cellular localization of the NPs in the cells, double labeling experiments using NPs and other fluorescent organelle marker in a single set of cell was not possible, as the excitation wavelengths of the NPs matched with that of the marker. Therefore, to circumvent this problem, we have done localization experiments with NPs and fluorescent nuclear marker (DAPI) in separate sets of cells (Figure S12). The comparative evaluation of the results from these two set of experiments suggest that the particles were indeed in the nucleus. The control image (Figure S13) shows no fluorescence from untreated squamous epithelial cells compared to those with incorporated T-LSMO NPs (Figure S11). The efficiency of cellular internalization and subsequent nuclear localization of T-LSMO NPs has also been revealed from time-dependent cellular uptake experiment (Figure S14) by monitoring (using fluorescence microscope and excitation wavelength of 365 nm) a single set of cell for 30 min after addition of the NPs. As shown in the figure, within 30 min, the NPs become enriched inside the nucleus of the cells. Although, the cellular internalization of untargeted negatively charged (due to carboxylate groups of tartrate) NPs is believed to occur through nonspecific binding on cationic sites of the plasma membrane followed by their endocytosis², the reason behind their efficient nuclear localization is unknown and needs further rigorous investigation. However,

taken together these multicolor photoluminescence and efficient nuclear localization results suggest that the T-LSMO NP has the potential for multifunctional nanoprobe in terms of biological imaging and targeted drug delivery. According to a recent study liquid extract of LSMO nanoparticles are not toxic to the cells³ and we have also found that T-LSMO NPs are nontoxic by a standard MTT cell viability assay (data not shown).

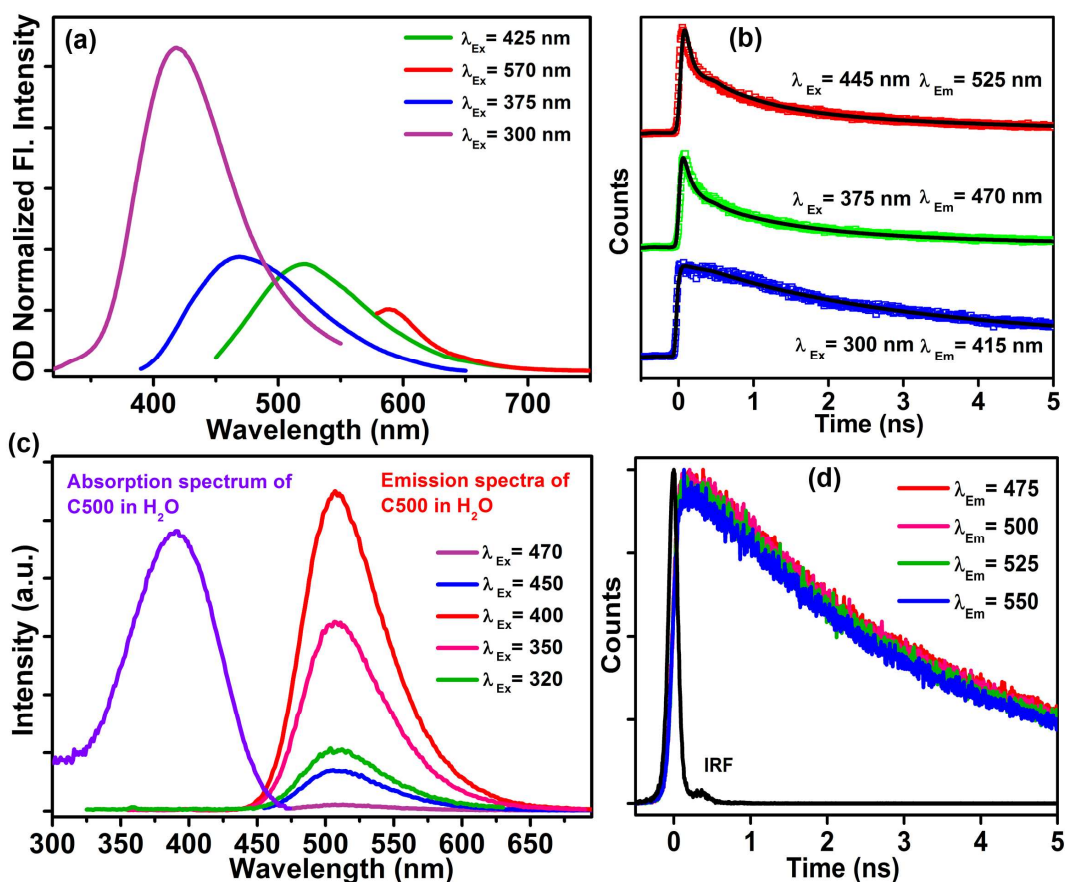


Figure S1. a) OD normalized PL spectra of Tartrate-LSMO NPs at pH~7. b) Picosecond-resolved photoluminescence decays transients of tartrate-LSMO NPs in water measured at emission wavelengths of 415, 470 and 525 nm upon excitation with laser source of 300, 375 and 445 nm wavelengths respectively. c) Absorption spectrum and excitation wavelength dependent emission spectra of C500 in water. The emission spectra show unique characteristics (position of the emission peak and spectral width) independent of the wavelength of excitation. d) Picosecond-resolved photoluminescence decays transients of C500 in water measured at emission wavelengths of 475, 500, 525 and 550 nm upon excitation with a laser source of 375 nm wavelength. The transients detected at various emission wavelengths show similar decay constants of 2.77 ns (51.61%) and 4.37 ns (48.38%).

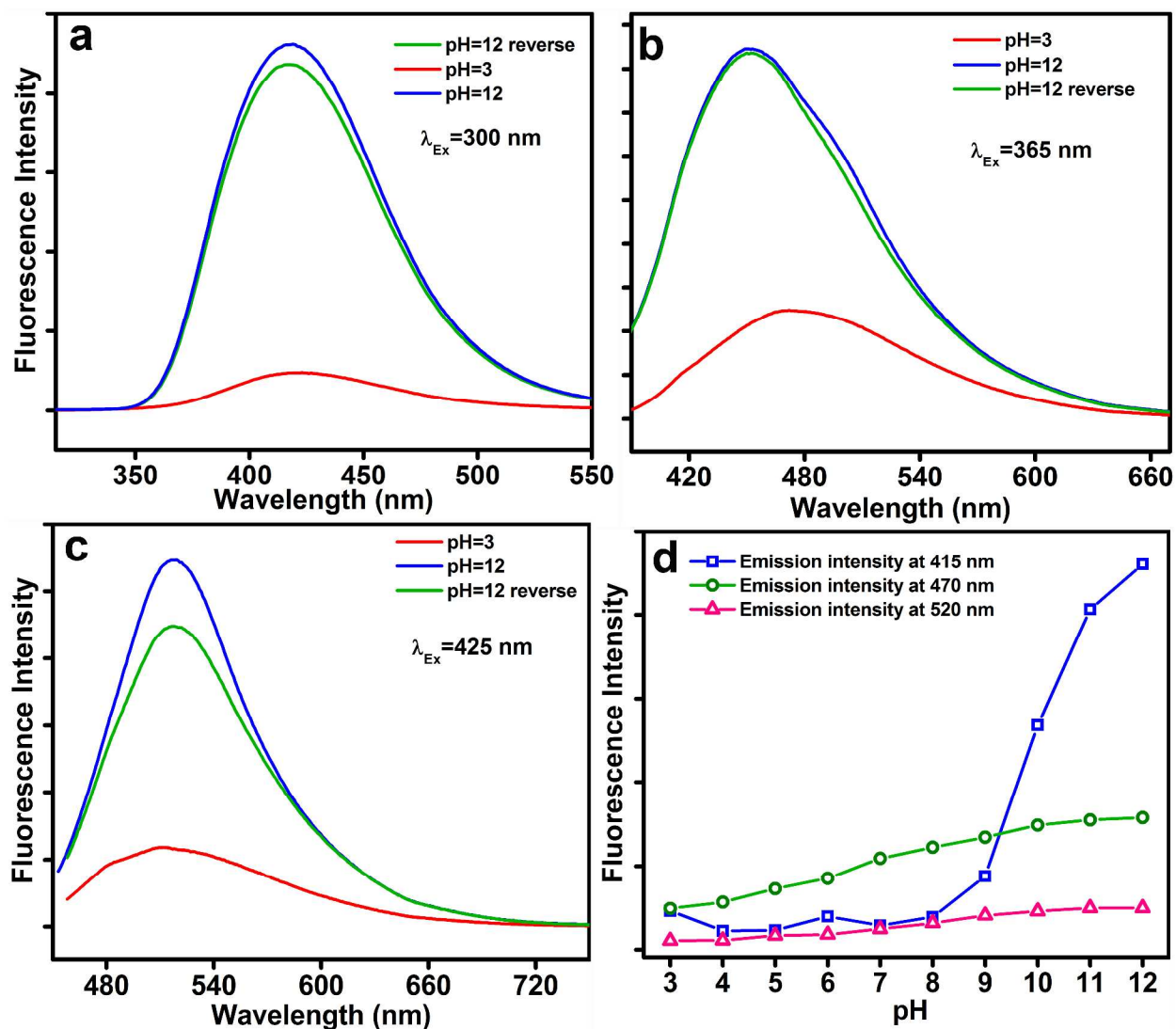


Figure S2. pH dependent photoluminescence (PL) spectra of T-LSMO NPs. a), b) and c) Represents the photoluminescence quenching and recovery of T-LSMO NPs by changing the pH of the solution from 12 (blue spectrum) to 3 (red spectrum) and again reverse back to 12 (green spectrum). d) Represents the change of PL intensity at different PL maximum with changing the pH of the solution from 12 to 3 by drop wise addition of HCl. Solid lines are a guide to the eye.

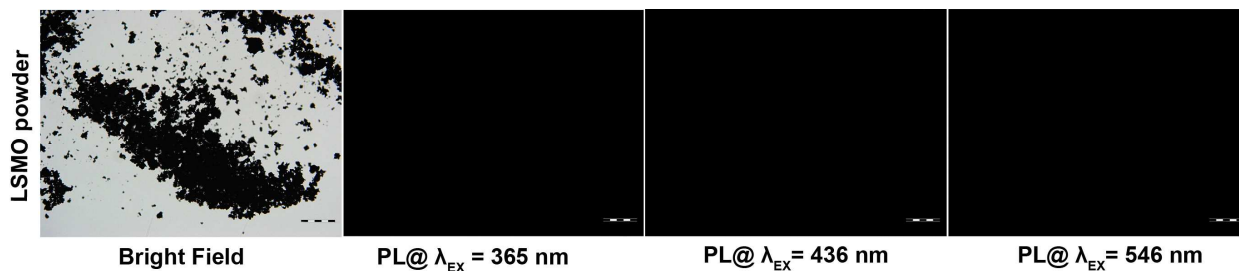


Figure S3. Fluorescence microscopic images of as-prepared LSMO NPs powder under irradiation of white light (bright field) and light of three different wavelengths of 365, 436 and 546 nm.

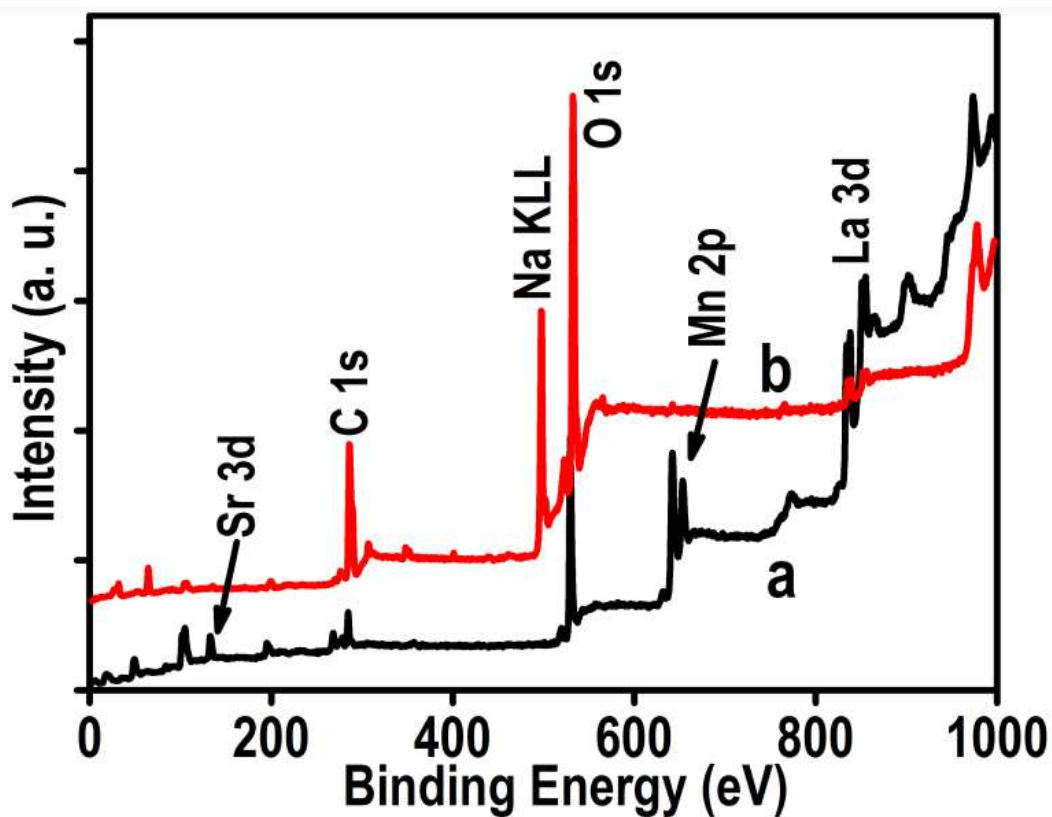


Figure S4. XPS survey spectra of LSMO NPs (traces a) and T-LSMO NPs (traces b) showing the expected elements.

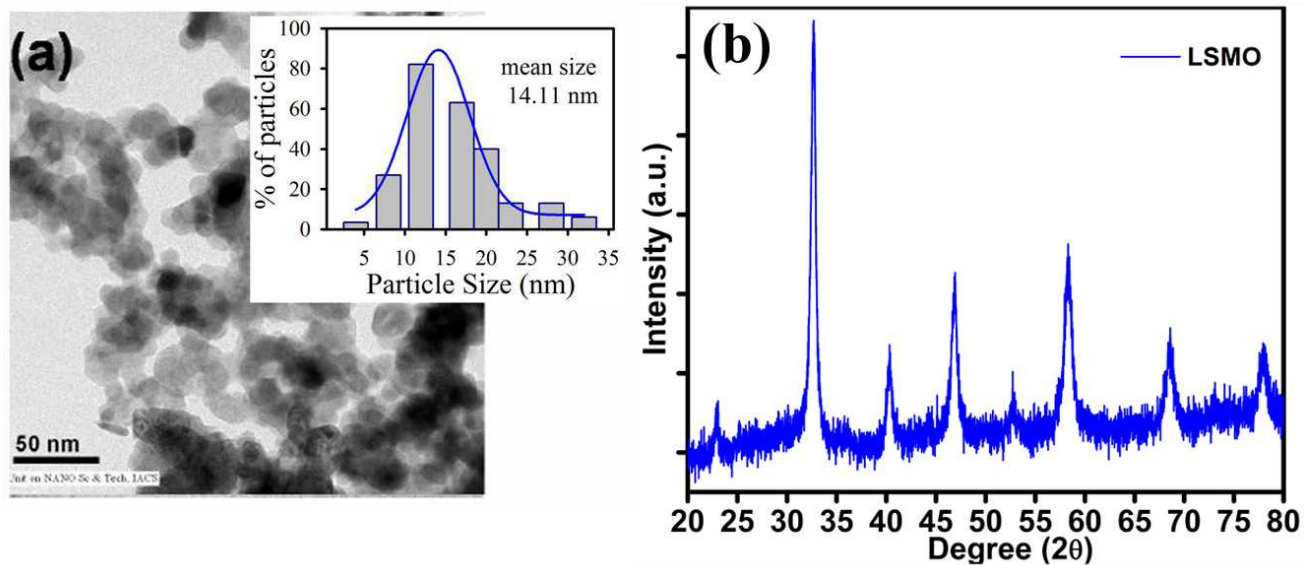


Figure S5. (a) Represents the TEM image of the as prepared LSMO NPs and the inset showing the particle size distribution. (b) Shows XRD pattern of as-prepared bulk LSMO NPs and the corresponding peak positions matched with the values reported earlier.

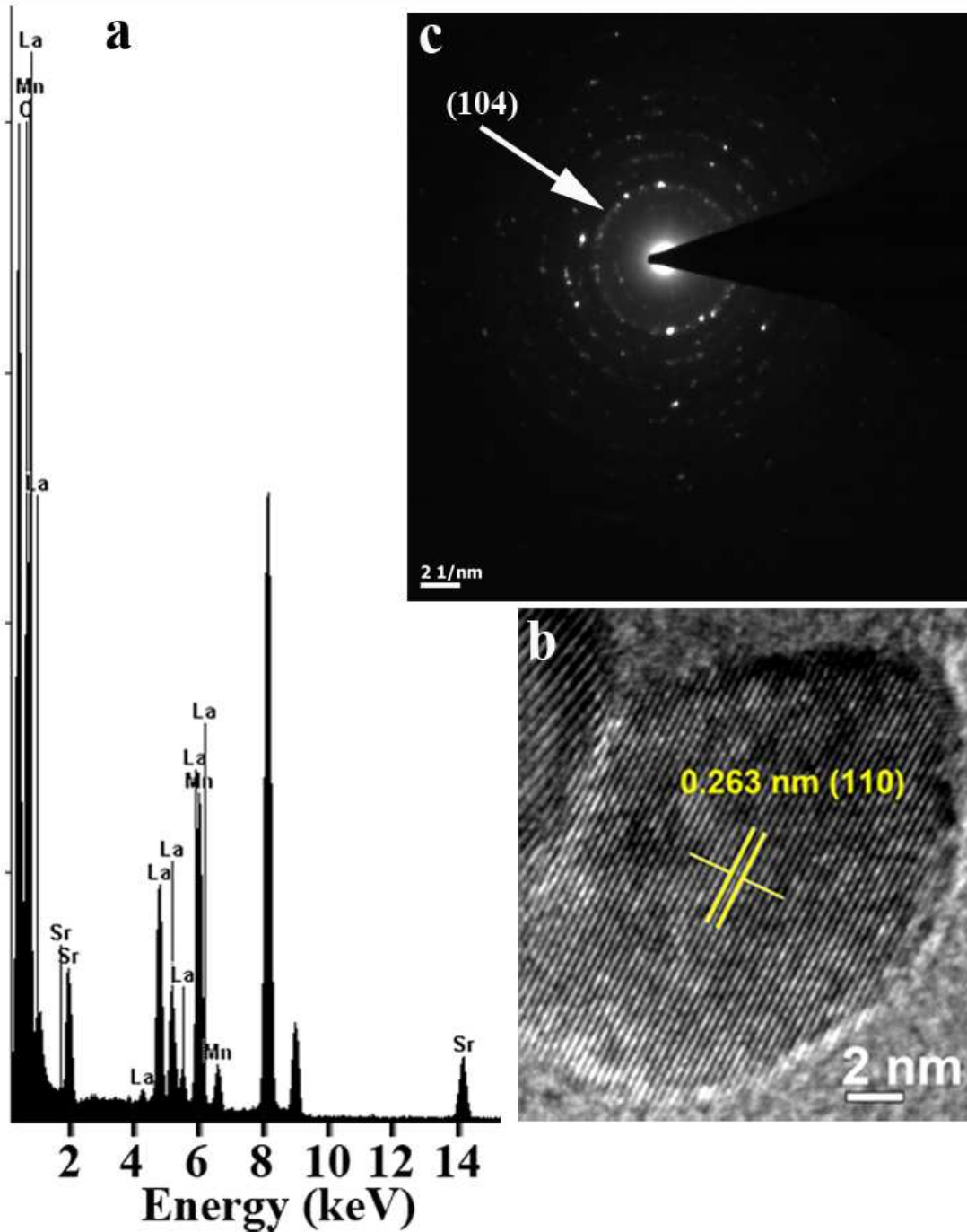


Figure S6. (a) The EDAX spectrum of as prepared LSMO NPs shows elemental composition of the NPs. (b) HRTEM image of as-prepared LSMO NPs having interplanar distance of 0.263 nm (which is similar with Tartrate-LSMO NPs shown in main text Figure 5e) corresponding to (110) plane of the crystal lattice. (c) SAED pattern of the as prepared LSMO NPs and the arrow head indicates the diffraction ring originated from (104) plane of the crystal lattice.

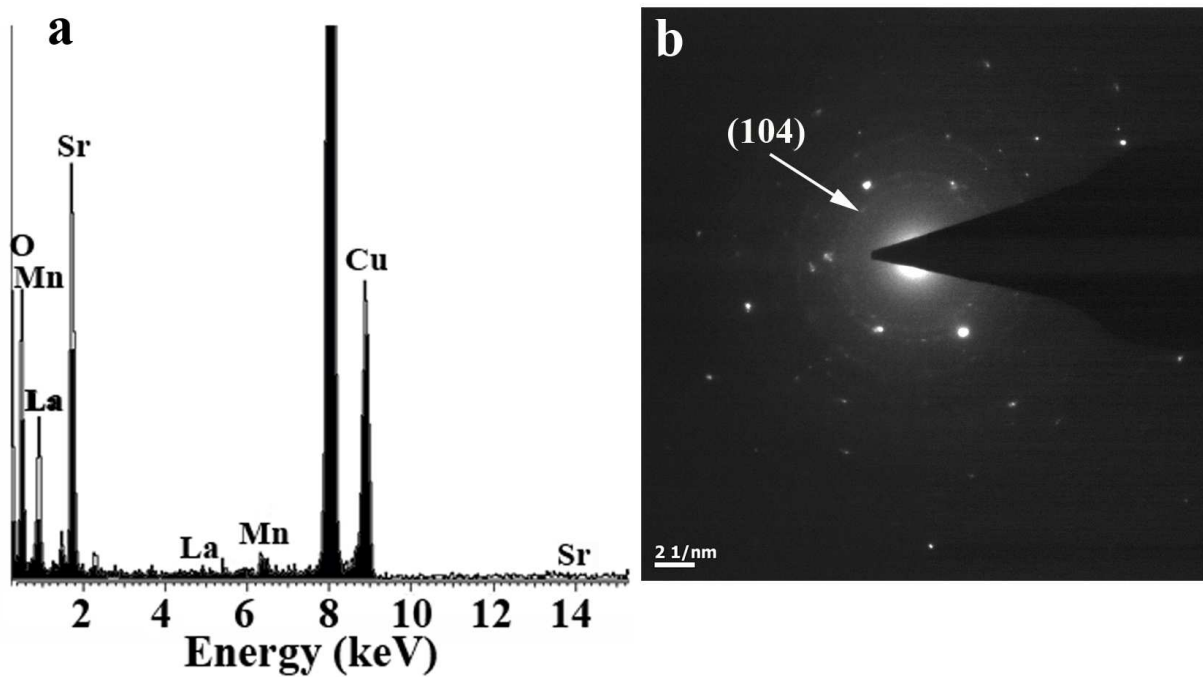


Figure S7. (a) The EDAX spectrum of Tartrate-LSMO NPs shows elemental composition of the NPs. (b) SAED pattern of the Tartrate-LSMO NPs. Arrow head indicates the appearance of diffraction ring from (104) plane, which have also been observed in case of as prepared LSMO NPs shown in Figure S6c.

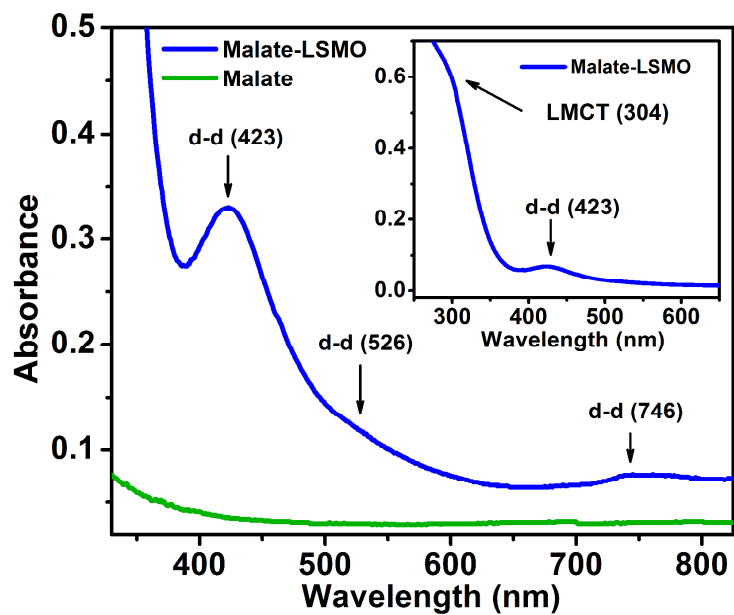


Figure S8. UV-vis absorption spectrum of malate and malate-LSMO NPs in aqueous solution at pH~7. Inset shows the absorption peak (LMCT) at around 304 nm obtained from diluted solution of malate-LSMO NPs.

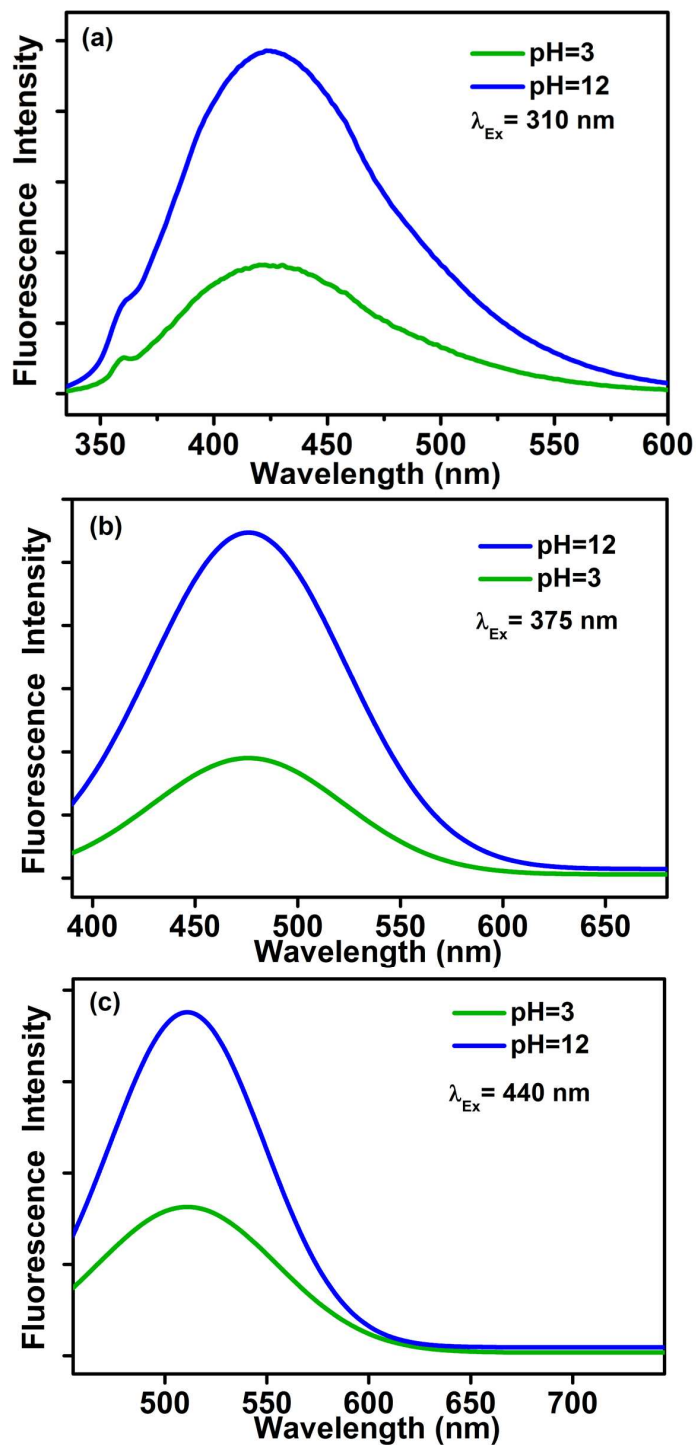


Figure S9. pH dependent photoluminescence (PL) spectra of Citrate-LSMO NPs. a), b) and c) represents the photoluminescence quenching of Citrate-LSMO NPs by changing the pH of the solution from 12 (blue spectrum) to 3 (green spectrum).

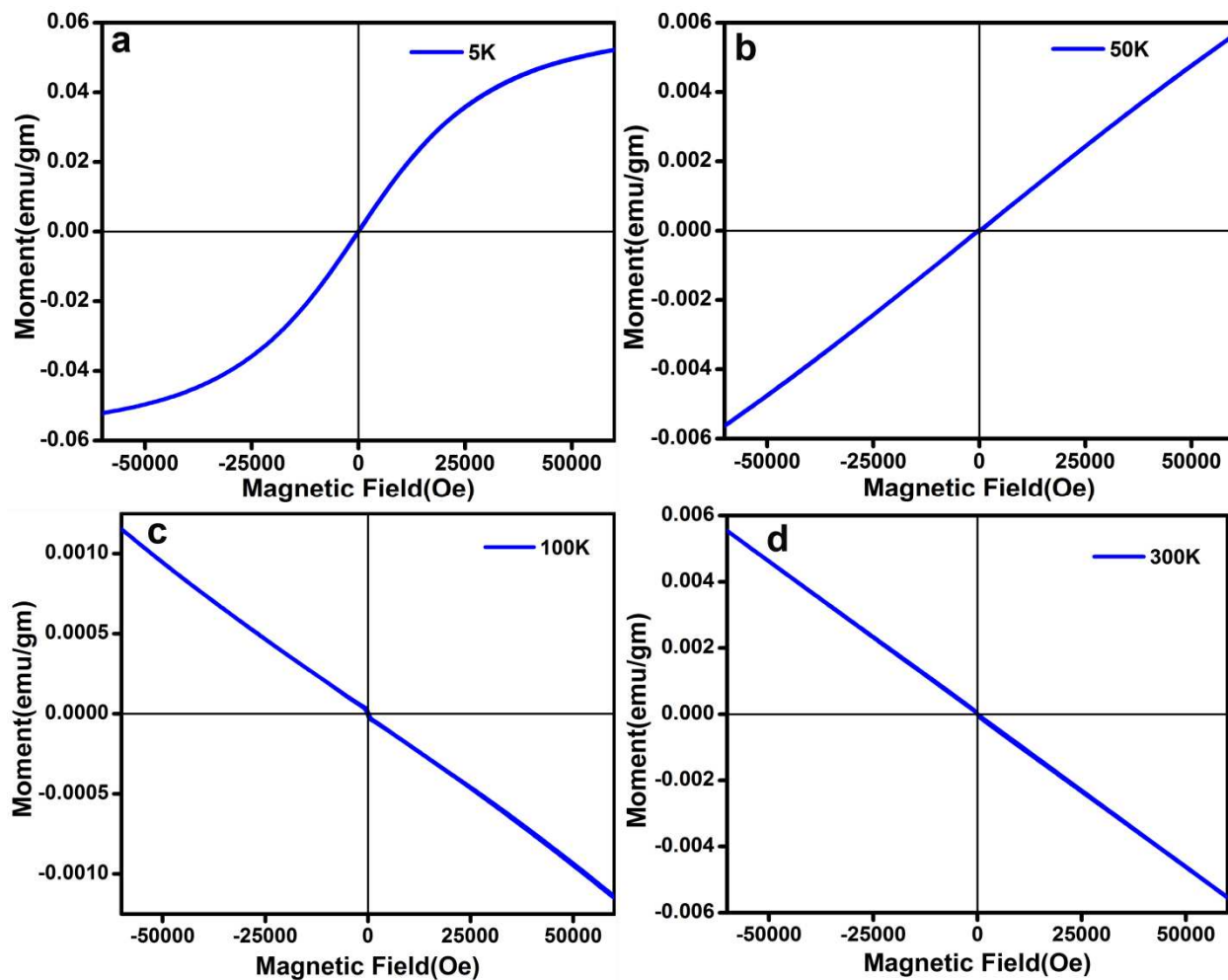


Figure S10. The M (moment)-H (magnetic field applied) magnetization plots of T-LSMO NPs at different temperature.

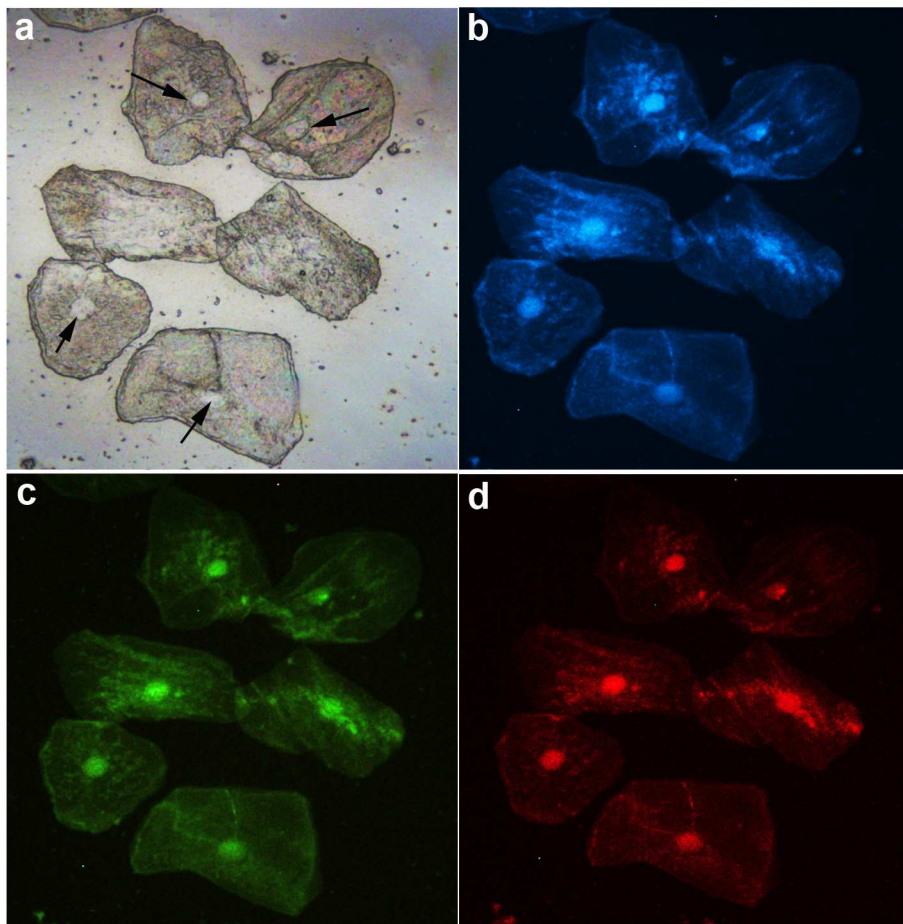


Figure S11. Representative fluorescence microscopic images of human oral squamous epithelial cells labeled with T-LSMO NPs. Upper left image corresponds to the bright-field image of the cells and the black arrows indicate the nucleus of the cells. The fluorescence images were taken using 365 (b), 436 (c) and 546 nm (d) excitations wavelengths. Selective nuclear localization of the NPs is clearly evident from the multicolor photoluminescence images of the cell.

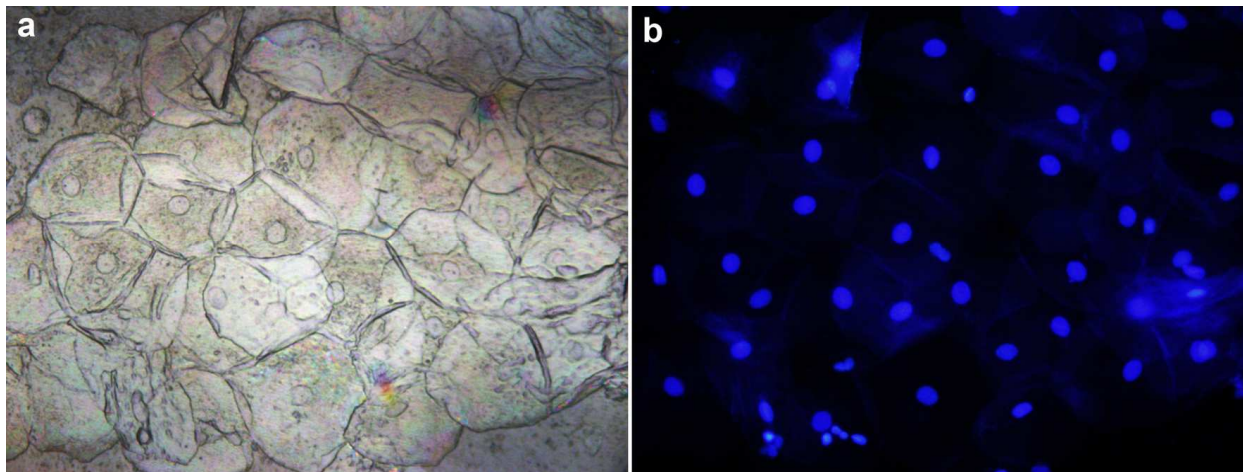


Figure S12. (a) Bright-field image of human oral squamous epithelial cells and (b) fluorescence micrographs (using an excitation source of 365 nm wavelength) of the same cells stained with DAPI.

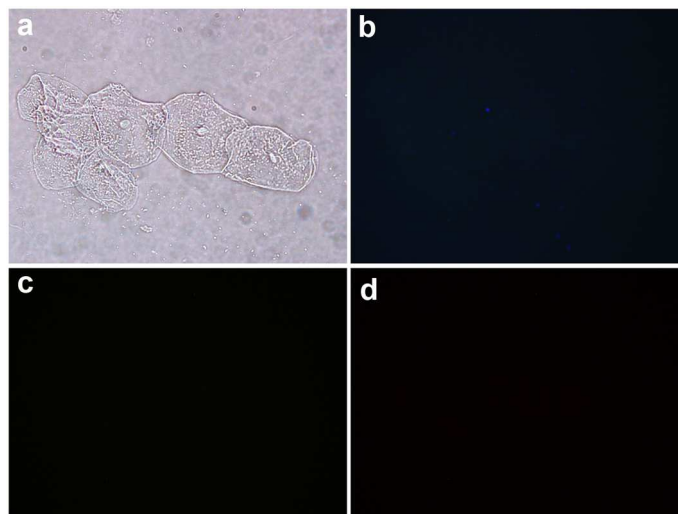


Figure S13. The fluorescence microscopic images of squamous epithelial cells non-treated with T-LSMO NPs: (a) bright field image; and fluorescence images collected upon excitation at (b) 365 nm, (c) 436 nm and (d) 546 nm wavelengths.

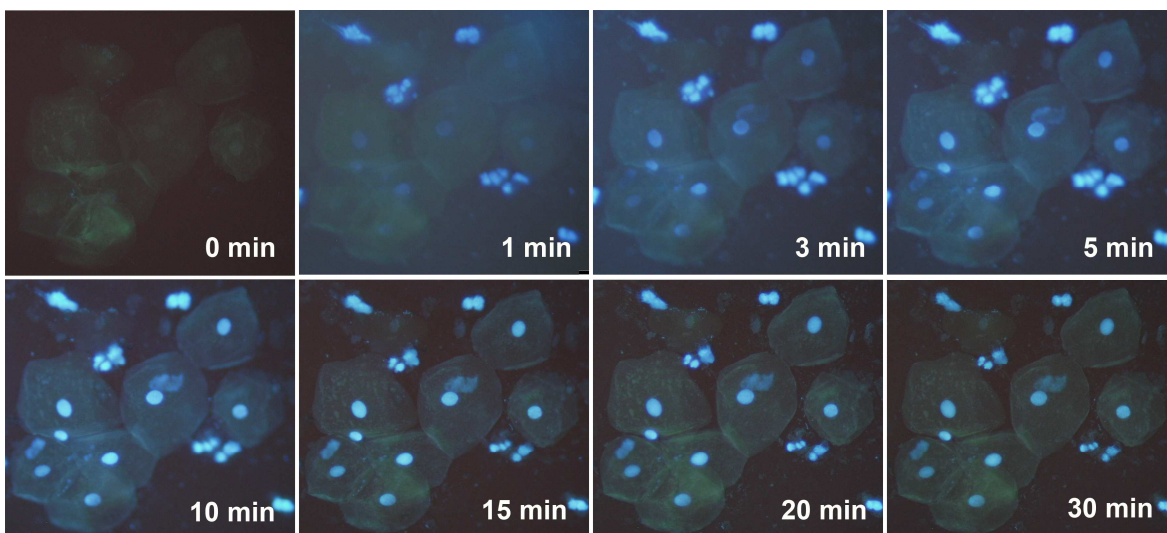


Figure S14. Time-dependent internalization of T-LSMO NPs into human oral squamous epithelial cells. Fluorescence micrographs (taken using an excitation source of 365 nm wavelength) of a single set of cells clearly indicates that the NPs become localized into to the nucleus of the cells within 30 min of addition.

Table S1: Spectral position of UV-vis absorption bands/peaks of tartrate, citrate and malate functionalized LSMO NPs along with their photoluminescence peak positions (except Malate-LSMO).

System	Positions of UV-vis absorption bands/peaks, λ_{abs} (nm)	Position of photoluminescence peaks, λ_{em} (nm)
T-LSMO	300, 440, 580 and 758	418, 470, 520 and 590
Citrate-LSMO	297, 430, 532 and 744	413, 479, 518 and 610
Malate-LSMO	304, 423, 526 and 746	Not been performed

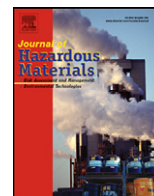
References

- (1) Coey, J. M. D.; Viret, M.; von Molnár, S. *Advances in Physics* **1999**, *48*, 167-293.
- (2) Verma, A.; Stellacci, F. *Small* **2010**, *6*, 12-21.
- (3) Daengsakul, S.; Thomas, C.; Thomas, I.; Mongkolkachit, C.; Siri, S.; Amornkitbamrung, V.; Maensiri, S. *Nanoscale Res. Lett.* **2009**, *4*, 839-845.



Contents lists available at SciVerse ScienceDirect

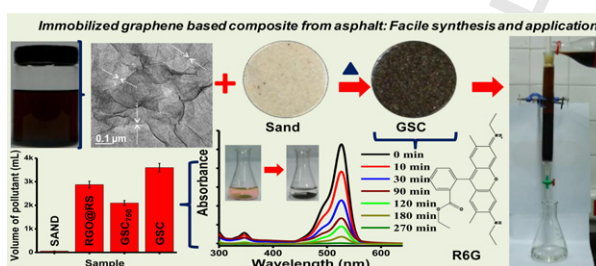
Journal of Hazardous Materials

journal homepage: www.elsevier.com/locate/jhazmat1 Immobilized graphene-based composite from asphalt: Facile synthesis and
2 application in water purification3 Q1 T.S. Sreepasad^a, Soujit Sen Gupta^a, Shihabudheen M. Maliyekkal^b, T. Pradeep^{a,*}4 ^a DST Unit on Nanoscience, Department of Chemistry, Indian Institute of Technology Madras, Chennai 600036, India5 ^b School of Mechanical and Building Sciences, VIT University, Chennai Campus, Chennai 600048, India

1 HIGHLIGHTS

- 2
-
- 3 ▶ Facile strategy to make graphenic
-
- 4 materials from cheaper precursor
-
- 5 such as asphalt.
-
- 6 ▶ Material can be made in solution also
-
- 7 as anchored on solid substrates is
-
- 8 reported.
-
- 9 ▶ The synthesized material, GSC, was
-
- 10 found to be excellent for water purification.
-
- 11 ▶ The applicability was demonstrated
-
- 12 through batch and laboratory
-
- 13 columns experiments.
-
- 14 ▶ The capacity was compared to other
-
- 15 similar adsorbents and was found to
-
- 16 be superior.
-
- 17

1 GRAPHICAL ABSTRACT



19 ARTICLE INFO

20 Article history:

21 Received 12 October 2012

22 Received in revised form 4 December 2012

23 Accepted 11 December 2012

24 Available online xxx

25 Keywords:

26 Adsorption

27 Graphene-sand composite

28 Pesticide removal

29 Water purification

30 Asphalt

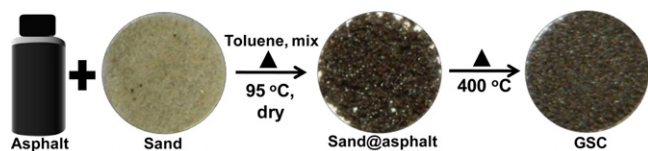
19 ABSTRACT

20 An *in situ* strategy for the preparation of graphene immobilized on sand using asphalt, a cheap carbon precursor is presented. The as-synthesized material was characterized in detail using various spectroscopic and microscopic techniques. The presence of G and D bands at 1578 cm^{-1} and 1345 cm^{-1} in Raman spectroscopy and the 2D sheet-like structure with wrinkles in transmission electron microscopy confirmed the formation of graphenic materials. In view of the potential applicability of supported graphenic materials in environmental application, the as-synthesized material was tested for purifying water. Removal of a dye (rhodamine-6G) and a pesticide (chlorpyrifos), two of the important types of pollutants of concern in water, were investigated in this study. Adsorption studies were conducted in batch mode as a function of time, particle size, and adsorbent dose. The continuous mode experiments were conducted in multiple cycles and they confirmed that the material can be used for water purification applications. The adsorption efficacy of the present adsorbent system was compared to other reported similar adsorbent systems and the results illustrated that the present materials are superior. The adsorbents were analyzed for post treatment and their reusability was evaluated.

© 2012 Published by Elsevier B.V.

32 1. Introduction

33 Graphene, a 2D sheet made up of extended carbon network, or
34 their chemical analogs are promising adsorbents [1-7] and have35 great potential in water purification due to their unique physical
36 and chemical properties including high surface area [8], antibac-
37 terial properties [9,10] and lesser cytotoxicity compared to carbon
38 nanotubes [11,12]. However, the immediate use of graphenic materi-
39 als for down-to-earth applications such as water purification
40 is limited mainly due to the difficulty in large-scale synthesis
41 and post treatment-handling, including solid-liquid separation
42 [6,13].Q2 * Corresponding author. Tel.: +91 44 2257 4208; fax: +91 44 2257 0545/0509.
E-mail address: pradeep@iitm.ac.in (T. Pradeep).



Scheme 1. Schematic illustration of the formation of GSC.

Discovery of chemical routes to produce graphenic materials by the oxidation of graphite to graphite oxide (GO) [14] and subsequent reduction to reduced graphene oxide (RGO), closely resembling graphene with extended double bonded sp^2 carbon network with edge carboxylic acid moieties [15–19] opened up the pathway for mass production of RGO. Recently, we have shown that RGO and chemically reduced graphene can be bound on cheap substrate such as river sand and such substrates are effective in contaminant removal [6]. In another effort, Gao and coworkers have demonstrated that GO-coated sand, termed as ‘super sand’, could be used as a low-cost water purification material for the developing economies [20]. The use of GO/RGO supported on silica as adsorbent for solid phase extraction was also reported recently [13]. These materials got wide publicity in the world news due to their likely utility in water purification. These composites were prepared through two-step processes that involve the preparation of graphene through relatively laborious chemical conversion of graphite to graphite oxide [14,21] and subsequent reduction of GO by hydrazine to RGO [15]. In the second step, the GO/RGO was immobilized onto sand via heat treatment [20] or by directly binding them covalently onto silica [13] or by using molecular binders [6]. However, the preparation of RGO involves the use of a variety of chemicals including hydrazine, P_2O_5 and $K_2S_2O_8$ which produces undesirable hazardous products like, P_2O_3 , SO_2 , etc. This necessitates laborious steps including post-synthesis cleaning. Developing an efficient and eco-friendly graphenic adsorbent generated from a cheaper source is desirable for water purification. Several graphene based composites with metals and metal oxides have also been demonstrated to be useful for this application. As cost is an important criterion in the success of such materials, new approaches for their production are necessary. Efforts have been made to grow graphene from diverse sources. Recent studies show that graphenic material can be synthesized from cheaper sources of carbon, like sugar [7,22] using a modified CVD process [23]. Graphene was also prepared from food, insects, and waste using a similar methodology [24]. This is necessary as chemically different carbon sources are available in different parts of the world. Among these, asphalt and various petroleum products are important to consider. A simple synthetic route is always preferable when it comes to applications such as water purification, where the use of chemicals should be avoided as much as possible.

Here, a method for the *in situ* preparation of graphenic material anchored on a solid substrate starting from a cheap and locally available material, asphalt, is discussed. A single-step strategy was used to immobilize the graphenic material on sand surface. Application of the as-synthesized material as a water purifying medium is reported using a pesticide and a dye as examples. Synthetic dyes mostly being non-biodegradable can have acute effects on exposed organisms and aquatic life. Exposure to such dyes can cause abnormal coloration and resultant reduction in photosynthetic efficiency. Pesticides, designed to induce acute effects or kill living organisms, are highly toxic to the environment and to all living forms including humans. We have used rhodamine-6G (R6G), a rhodamine dye and chlorpyrifos (CP), an organo-phosphorus pesticide in our studies. The adsorption capacity of the reported adsorbent was compared to several other adsorbents reported and the superiority of the present system is demonstrated. The simple and cost effective methodology

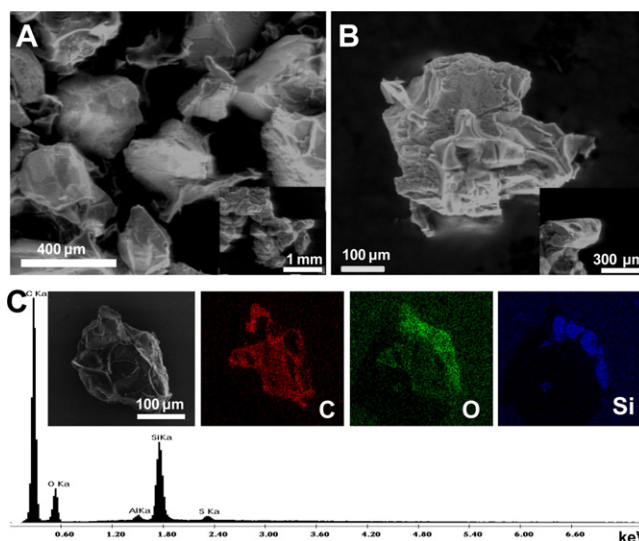


Fig. 1. (A and B) SEM images and (C) EDAX spectrum and the corresponding elemental maps of GSC (5% loading). A higher loading was used for getting a more clear observation of the film in SEM and EDAX mapping. Insets in (A) and (B) show the corresponding asphalt coated samples before heating. Clustered particles can be seen in the expanded figure.

adopted here facilitates the preparation of large-scale graphenic material and immobilization of the material on sand surface without any external chemical agents, in a single step. This may open up the practical use of graphenic materials. The solution based processability of the sample has also been demonstrated. However, additional experiments are needed to validate the applications of the material.

2. Materials and methods

Materials, *in situ* synthesis of graphene-sand composite (GSC), batch adsorption experiments, fixed-bed column experiments, instrumentation and the mechanism for the formation of graphene are given in supplementary data 1. The process of preparation of GSC starting from asphalt and sand is shown in Scheme 1.

3. Results and discussion

3.1. Characterization of the graphene-sand composite (GSC)

GSC was characterized using different microscopic techniques. Fig. 1A and B shows the SEM image of the prepared composite. The sheet-like structure covering the surface of the sand particles indicate the formation of graphenic material. Asphalt coated samples before heating had a sticky coating over the surface and formed aggregated clusters (insets in Fig. 1A and B). To understand the elemental composition of the material, the composite was analyzed using EDAX (Fig. 1C), where, we can see that the major elements present are carbon, silicon and oxygen. Inset in Fig. 1C shows the SEM image of a GSC particle and the corresponding elemental maps. Si and O features are due to sand (SiO_2). The large C feature points to the presence of graphenic material formed over the sand surface.

The (002) diffraction of graphite (002) appears at $\sim 26^\circ$ (2θ) in $CuK\alpha$ powder X-ray diffraction (XRD) and as it is getting exfoliated, due to the increase in inter-layer spacing, this feature is known to occur at lower values. Fully exfoliated graphite oxide is known to show this feature around 11° . River sand, used as a substrate in this study, also showed a feature in the same region and at lower carbon contents, no feature corresponding to graphene was observed. Graphenic material formed in the study was treated with

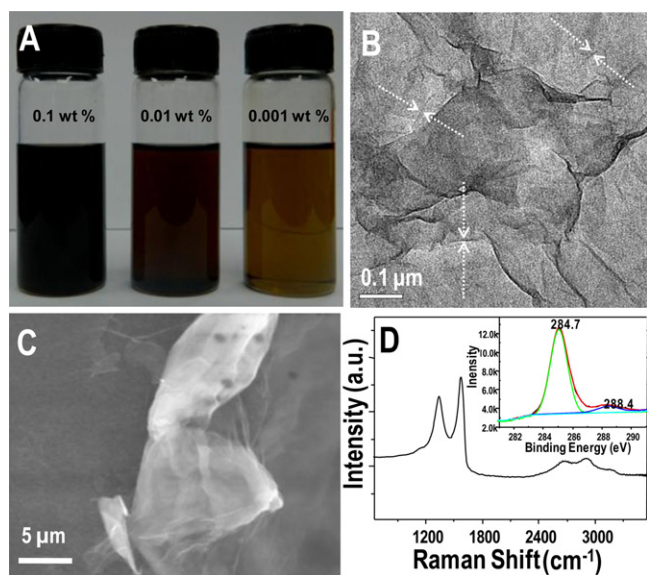


Fig. 2. (A) Photographs of the prepared graphenic material dispersed in toluene at different wt% of initial asphalt. (B) TEM and (C) SEM images of a graphenic sheet and (D) Raman spectra taken from the sample showing the D and G band. Inset shows the XPS spectrum in the C 1s region. The TEM image shows foldings of 2 nm thickness (marked).

acid and has undergone heat treatment as well. Hence, the multi-layer structures getting formed in the study are expected to have higher d-spacing compared pristine graphite. Our observations are consistent with these. A new peak was seen around 22° for GSC of 2% loading and at 24° for GSC having 5% loading. This was attributed to (002) diffraction of multilayer graphenic structures. XRD data of GSC at these two carbon loadings and a comparison with bare river sand is included in supplementary data, Fig. S2.

The possibility of producing graphenic material in dispersed phase was also investigated. The procedure employed for the preparation of GSC was carried without the presence of sand. The material obtained was suspended in N-Methyl-2-pyrrolidone (NMPs) by mild sonication, which points to the non-polar nature of the material. Hence, the presence of oxygen functionalities can be neglected [25]. This material was analyzed using microscopic and spectroscopic techniques. Fig. 2A shows the dispersibility of the material in NMP. Near perfect colloidal dispersions of the material at different weight percentages can be seen in the figure. Fig. 2B shows the TEM taken from such a sample (0.0005 wt%). We can see large sheets spread over μm^2 area. Large number of wrinkles, which characterize graphene, can be seen on the surface confirming that the material prepared is graphenic, comprising of thin sheets. However, in some areas of the grid thicker sheets were also seen. Fig. 2C shows the SEM image of such a thick film spread over μm^2 area. Hence, we can conclude that the present methodology predominantly gives multi-layer graphenic structures. The sample was analyzed using Raman and XPS as well (Fig. 2D). Raman spectrum clearly showed a prominent G band and a less intense D band at 1578 and 1345 cm^{-1} , respectively. The presence of such a peak again points to the material being graphenic in nature. The presence of D band points toward the presence of defects. We attribute these defects to structural defects other than those arising from the presence of oxygen functionalities. Moreover, most of the functionalities are unstable at 400 $^\circ\text{C}$. In the present methodology, due to the presence of multi-layers, a larger number of grains can be present, giving rise to the D-band observed. The 2D region had a broad feature similar to chemically prepared graphene (RGO). Presence of the D-band (and the associated D+D' band) and the presence multi-layer structure might be reducing the intensity of 2D band. To

confirm the absence of oxygen functionalities, the sample was analyzed using XPS. The inset of Fig. 2D, shows the deconvoluted XPS spectrum in the carbon 1s region of the prepared material. We can clearly see that the carbon is unfunctionalized, nearly completely.

As the main theme of this work being the creation of a cheap graphenic adsorbent for water purification, the supported composite was analyzed in more detail. The material was characterized using Raman and XPS extensively. Fig. 3A shows the Raman spectra at different stages of GSC preparation. Initial sand showed a prominent feature at 470 cm^{-1} (due to SiO_2). However, upon coating with asphalt, all the features disappeared (curve ii in Fig. 3A). Only a large fluorescence background due to asphalt was seen. Upon heating the particle at 250 $^\circ\text{C}$ (curve iii), a small G-band started to appear. Still, the large fluorescence background was persistent. Curve iv shows the Raman spectrum of the final GSC sample. The sample clearly showed a prominent G-band centered at 1578 cm^{-1} and a less prominent D-band at 1345 cm^{-1} pointing to the formation of graphenic material. The peak at 470 cm^{-1} confirmed the presence of sand. The resulting sample was compared with RGO supported on river-sand sample (RGO@RS) prepared through the methodology reported earlier [6]. Curve v shows the Raman spectra collected from RGO@RS. We can see that there are close similarities between the samples, indicating that the GSC prepared is closely related to the graphenic adsorbent in the literature [6,19]. On closer examination we can see that the intensity of the D band is much lesser in GSC, indicating the lesser extent of defects in the sample compared to RGO@RS. It is proposed that this may be due to the absence of oxygen functionalities in GSC. We can also see that the 2D region is more prominent in GSC compared to RGO@RS. Hence, it might be proposed that graphene formed in the present case is of better quality than RGO.

Panel B in Fig. 3 shows the XPS of GSC at different stages of synthesis. Fig. 3B a1 shows the survey spectrum of the asphalt coated sand sample. The C 1s region of the same sample is given in a2. We can see that the carbon is highly functionalized with several components other than the most prominent peak at 284.5 eV (a2). The survey spectra (b1 and c1) show that as the heating and acid treatment is done to the sample, most of the oxygen is getting removed from the sample. This is expected since the thermal stability of most of the functional groups is lesser than the temperature used and due to the use of strong dehydrating agent (H_2SO_4). Upon heating at 400 $^\circ\text{C}$, these extra features disappeared to give a single component (b2). After acid wash also only one component was seen for C 1s (c2) showing that the carbon is mostly unfunctionalized.

Carbon loading on GSC was calculated using TGA (supplementary data Fig. S3). Pristine sand did not show any weight loss when subjected to heat treatment. However, for 2 wt% asphalt loaded sand, there was a weight loss of about 0.8% indicating the removal of functional groups in asphalt leaving behind pure carbon. Using this, the exact carbon content on GSC was calculated and different sets of composites with varying loading (wt% loading) and varying sand particle size were prepared. Fig. 4 shows the SEM images of GSC having different carbon loading. The sand particles to begin with were pretty clean and had no covering on the surface (supplementary data Fig. S4). As the loading of graphene was increased, a layer was progressively visible on the surface (details are given in supplementary data 5). Similarly, GSC with different sand particle size having the same loading was also prepared (supplementary data Fig. S6).

3.2. Batch adsorption experiments

3.2.1. Parameter optimization

In this study, the R6G removal performance of the material synthesized at various conditions were tested. The variables in synthesis were carbon loading, particle size and process temperature.

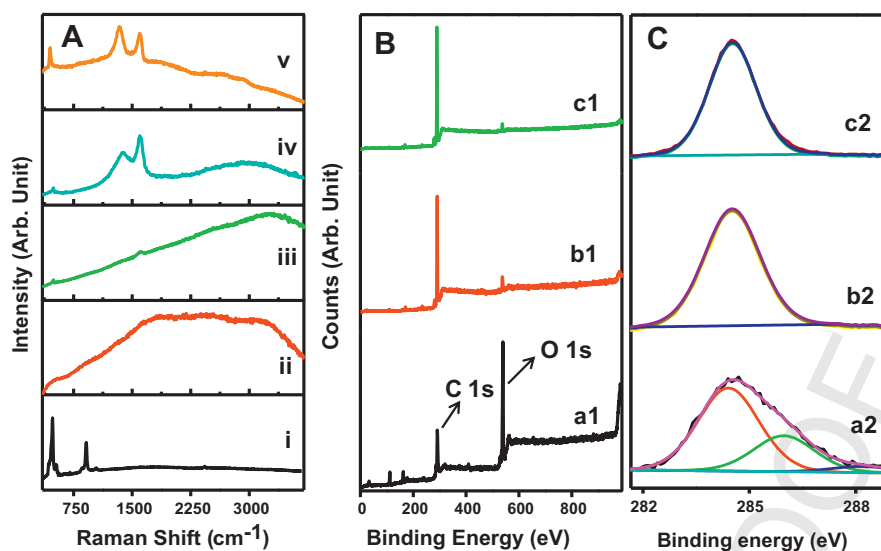


Fig. 3. (A) Raman spectra at different stages of preparation of GSC. (i) Sand, (ii) asphalt coated sand, (iii) heated at 250°C, (iv) GSC and (v) RGO@RS. (B and C) XPS analysis of GSC at different stages. a1, b1 and c1 are the survey spectra and a2, b2, and c2 are the corresponding C 1s spectra: (a1 and a2) asphalt coated sand, (b1 and b2) asphalt coated sand particles heated at 400°C before acid wash and (c1 and c2) after acid wash (GSC).

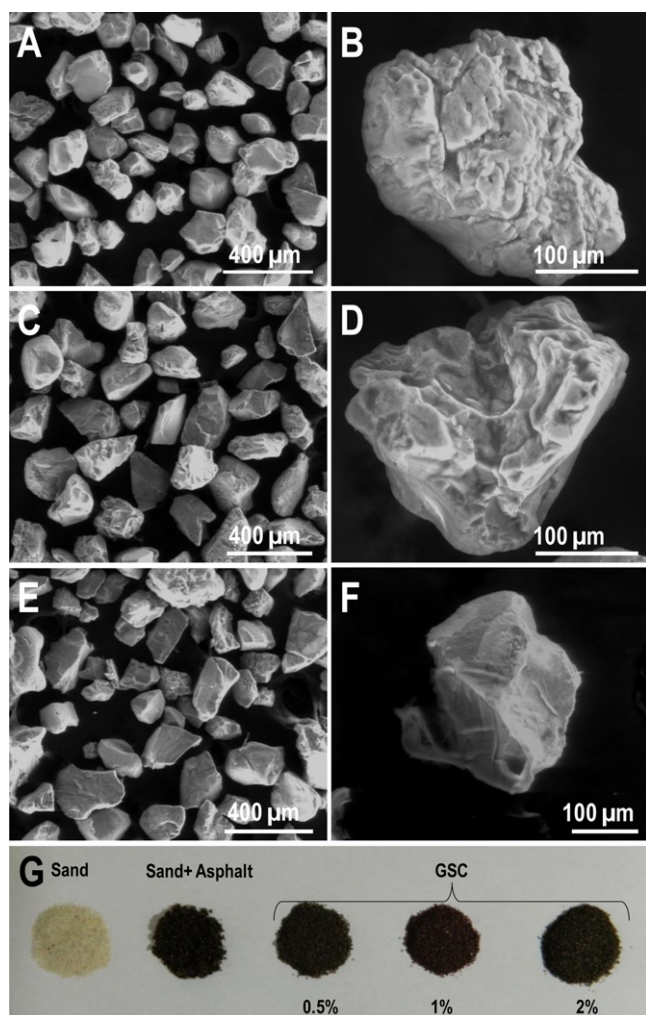


Fig. 4. SEM images (larger and smaller area) of GSC having different carbon loading (A and B) 0.2%, (C and D) 0.5% and (E and F) 1 wt% of graphenic carbon. (G) Photographs of pristine sand, sand coated asphalt and GSC of different loading.

Fig. 5A shows a direct correlation between the carbon content and adsorption capacity. The maximum uptake was observed at a loading of 1 wt% and further loading did not affect the adsorption capacity greatly. The plausible reason might be that, as the loading increases from 0.2 to 1 wt%, sand surface is progressively getting covered by graphene resulting in large increase in the effective surface area and at 1 wt%, a complete coverage occurs. Upon further increase in loading, only multi-layers are getting formed which do not increase the effective surface area significantly. Hence, no appreciable increase in uptake capacity was observed further.

The effect of sand particle size on the adsorption capacity was also tested (Fig. 5B). As expected, the data show an increase in the uptake with decrease in sand size due to the increase in effective surface area. The synthesis temperature was also optimized through several iterations and the optimum performance was achieved at 400°C. The auto-ignition temperature of the material is above 400°C, so further increase in temperature beyond 400°C in the presence of oxygen was not possible. The temperature was increased to 500°C under nitrogen atmosphere but it did not show any appreciable increase in graphene quality or adsorption efficiency. Fig. 5C shows the effect of heat treatment as a function of time. The data show an optimum heating time of 4 h and further heating did not change the uptake much. The adsorbent dose was also optimized as a function of pollutant uptake. The percentage capacities increased with increasing dose. This can be attributed to increase in adsorption sites with increasing dose. 100% removal efficiency (for the used pollutant concentration) was observed with an adsorbent dose above 50 g/L (Fig. 5D). With acid treatment, the adsorption capacity of the sample increases significantly (about 12%, supplementary data S7) possibly due to increase in the number of adsorption sites of the composite or due to some electrostatic interaction between GSC and the pollutant [27]. Our recent *ab initio* calculations have shown that adsorption is likely to be mediated by adsorbed water itself [28]. Still the adsorption mechanism is unclear as far as graphene is concerned.

The CP removal capacity of the adsorbent was also tested. CP had a prominent adsorption peak at 297 nm in the UV/vis spectrum. The change in the spectrum during exposure is shown in Fig. 6A. The kinetics was observed to be faster for the initial stages (up to 120 min) but then slows down significantly. Complete removal

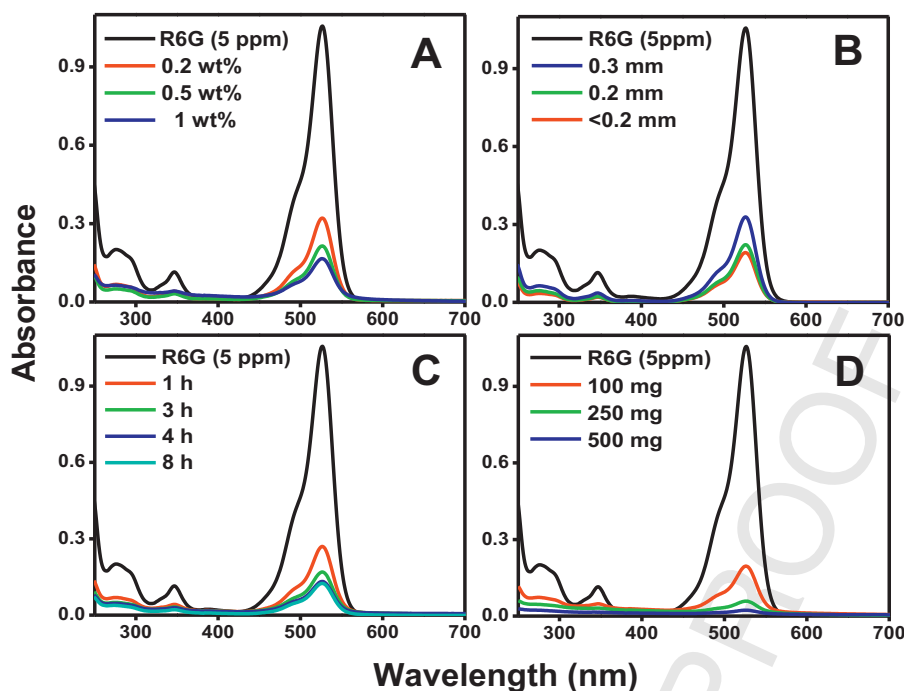


Fig. 5. Effect on adsorption capacity of the composite with change in (A) carbon loading, (B) sand size, (C) heating time and (D) adsorbent dose. The capacity is manifested in terms of the decrease in the absorbance of R6G upon exposure to GSC after an exposure of 1 h.

(below the detection limit) of CP was assumed when no peak was observed at 297 nm. About 250 mg of GSC (0.5 wt%) removes 4 ppm of CP (10 mL) completely.

The versatility of the adsorbent in removing pollutants/colored materials was further explored with the experiments conducted with Coca-cola. The original Coca-cola after dilution with water (1:20) has an adsorption peak at 274 nm. The decrease in peak height with respect to time confirms that GSC can decolorize Coca-cola as shown in Fig. 6B. Column experiments were also done to confirm the results (supplementary data video1 in S8). It was seen that the adsorption is very fast and 50 cm column of 8 cm length filled with GSC of 1% loading efficiently decolorized 200 mL Coca-cola in 20 min.

3.2.2. Kinetic study

Adsorption rate is an important parameter in designing batch or continuous adsorption process. The pollutant removal was tested as a function of time and the data are shown in Fig. 7. Here, we

used R6G as the model pollutant (10 mL) and 500 mg of 1 wt% (loading) of GSC as the adsorbent. As we can see, the kinetic data exhibited rapid removal of R6G. More than 65% of the pollutant was removed in the first 60 min and the system reached pseudo equilibrium in 240 min and further contact did not make noticeable change in the uptake. Control samples were also run to account for any possible natural attenuation and the data showed insignificant effect. Estimation of adsorption rate constants was done by fitting the experimental data with well-known adsorption kinetic models, viz. Langergren pseudo first-order kinetic model [29], and Ho's pseudo-second-order kinetic model [30-32]. The mathematical representations of these models are given in supplementary data 9. The inset in Fig. 7 shows the pseudo first and second order model fitted data along with experimental data. The data analysis and associated error measurements show that pseudo second-order model is more appropriate to describe the system and the data fitted well with more than 99% confidence level.

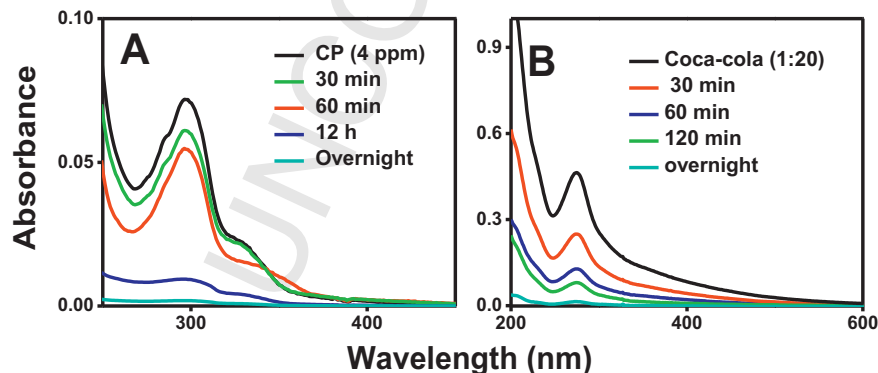


Fig. 6. (A and B) Adsorption experiments using GSC. The adsorbents were CP and Coca-cola, respectively for A and B. A standard Coca-cola sample was diluted 20 times with deionized water.

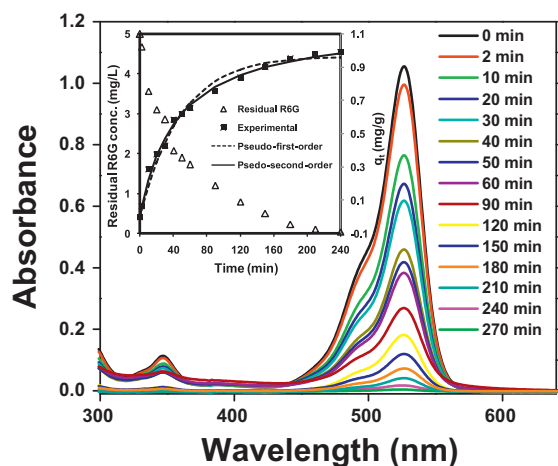


Fig. 7. UV/vis data showing time dependent removal of R6G. The inset shows the removal of R6G as function of time (primary axis). The pseudo and second order model fits are shown in secondary axis. Initial R6G concentration = 1 mg/L; flow rate = 2.3 mL/min.

Table 1 Breakthrough parameters obtained during three consecutive cycles of adsorption.

Cycle number	Bed height (cm)	Breakthrough volume (mL)	Adsorption capacity (mg/g) of carbon
1	3	3547	44.5
2	3	3260	42.3
3	3	3146	40.4

3.3. Fixed-bed column experiment

Laboratory based fixed bed adsorption studies are important in order to obtain basic engineering data for the design of any adsorption column. In this study, removal of R6G from contaminated water using columns packed with GSC was examined. The ratio of column diameter to the diameter of the particles was approximately 100, which is much above the ratio reported to overcome the premature leakage with wall effect [33,34]. Three successive cycles of adsorption and desorption were carried out *in situ* to test the reusability. After the first adsorption cycle, the bed was regenerated *in situ* by backwashing with 42 bed volume of acetone at flow rate of 2.3 mL/min followed by purging with hot air to remove the entrapped/adsorbed acetone. Fig. 8A shows the adsorption and desorption breakthrough curves and the data are summarized in Table 1. From the data it is clear that the material can be used in

multiple cycles without affecting the adsorption capacity significantly. The reduction in adsorption was found to be less than 5% at the end of the third cycle (Fig. 8B).

3.4. Comparison study

The superiority of our material over other similar adsorbents was investigated. We compared the adsorption capacity (q) of the as-synthesized material with RGO@RS, GSC₇₅₀, GO_{SAND} (also called super-sand). While the performance of RGO@RS and GSC₇₅₀ was evaluated in the lab; that of GO_{SAND} was taken from the literature [20]. RGO@RS was prepared as reported by Sreeprasad et al. [6] and GSC₇₅₀ was prepared from sugar [7], where carbon loading was fixed as 0.5 wt% in both cases. A comparison of q of GSC, GSC₇₅₀, and RGO@RS was made based on batch experiments. 100 mg of sand-composites having 0.5 wt% of carbon content were taken separately and their adsorption efficiencies were evaluated with 10 mL of 5 ppm R6G. The adsorption experiment was performed as mentioned previously and the sample was allowed to stir for a day to ensure saturation adsorption. The q value was determined from UV/Vis data (supplementary data S10A). From the standard curve, the q was calculated. The q value of RGO@RS and GSC₇₅₀ was 60 and 50–55 mg/g of carbon content, respectively. The q of our material (GSC) is 75.4 mg/g in terms of carbon content. The q of AC for R6G reported in batch experiments is 44.7 mg/g [35] which is much lower than that observed for GSC. For CP, GSC exhibited a q of 52.6 mg/g of carbon under identical conditions (supplementary data Fig. S10B).

Fixed-bed experiments were also conducted to compare adsorption efficiency. Columns of equal diameter were taken and packed with adsorbents (GSC, GSC₇₅₀, RGO@RS and sand) with equal bed height of 3 cm. Graphenic content in all the adsorbents were 0.5 wt%. R6G (1 ppm) was passed through the columns packed with the adsorbent at the flow rate of 2.3 mL/min. It was observed that while the sand got exhausted after passing 60 mL of R6G, whereas the other adsorbents had higher capacity. The column packed with GSC₇₅₀ and RGO@RS showed 35 (2.1 L) and 48-fold (2.9 L) increase in q than regular sand. GSC showed the highest q among all the adsorbents, the column got exhausted after passing 3.6 L of R6G solution, which shows a 60-fold increase in q than sand itself. Recently, Gao et al. claimed a 5-fold higher q than regular sand for 'super sand' [20]. A comparison of different adsorbents is shown in Fig. 9. These results clearly indicate that our material is superior to other adsorbents in terms of q and it has about 12 times more adsorption efficacy compared to 'super sand' and can function as

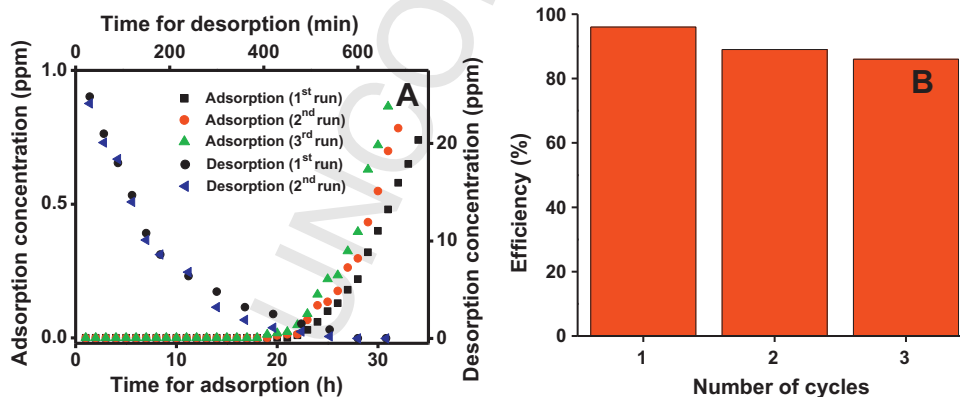


Fig. 8. (A) Breakthrough curves showing the performance of the adsorbent composite in removing R6G from water for three consecutive adsorption cycles and (B) efficiency bar (initial R6G concentration = 1.0 mg/L; pH = 7 ± 0.2; bed depth = 3 cm; loading = 0.6 wt% (carbon content), particle size = 0.2 mm and flow rate = 2.3 mL/min). (B) The amount of R6G desorbed in three consecutive cycles of desorption using acetone as the eluent.

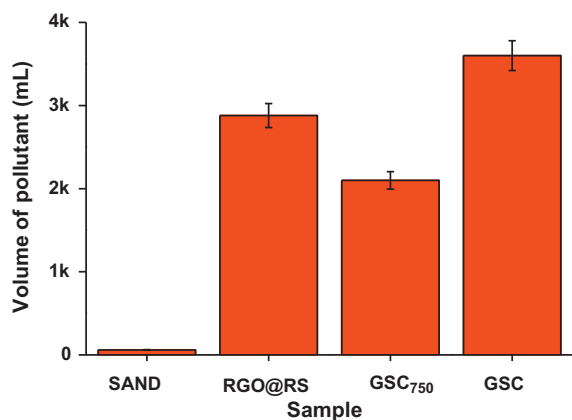


Fig. 9. Comparison of adsorption capacity with different graphenic adsorbents. Estimated error bar is 5%.

a cheaper and superior substitute. For want of a better word, we name this as 'wonder sand'.

4. Post-adsorption analysis of the adsorbent

The adsorbent was analyzed after the adsorption process to check the presence of the contaminants. Fig. 10A shows the SEM and EDAX characterization of GSC after the adsorption of chlorpyrifos. We can clearly see that the morphology of the GSC does not change during the adsorption process. However, EDAX identified signatures of P, S and Cl which was not present in the parent sample (data given earlier), which points to the presence of chlorpyrifos adsorbed on the particle. After regeneration, the sample was again analyzed using SEM and EDAX. The absence of P or Cl indicates the removal of chlorpyrifos (supplementary data S11).

In Fig. 10B, the LDI data confirms that the adsorption has taken place on the surface of GSC. There is no peak corresponding to GSC either in positive or negative mode (the data presented here is in positive mode, trace i). After the complete exhaustion of the adsorbent (R6G and CP adsorption in batch), the material was filtered and dried under N_2 atmosphere. The sample was spotted on the LDI plate. The LDI MS in positive mode of the R6G sample (Fig. 10B (ii)) shows a peak at m/z 444 corresponding to $C_{28}H_{31}N_2O_3^+$ (R6G) and the fragmented peaks at m/z 415 and 386 due to the elimination of ethyl groups from the side chain. The LDI of GSC adsorbed CP was taken in negative mode, Fig. 10B (iii) showing fragmented peaks at m/z 181, 79 and 228 corresponding to $C_5HCl_3N^-$, $(SPO_2)^-$ and $(C_5HCl_3NPO)^-$. The fragmented structures are shown in supplementary data of Fig. S12. The inset shows the isotopic distribution due the presence of three Cl groups at

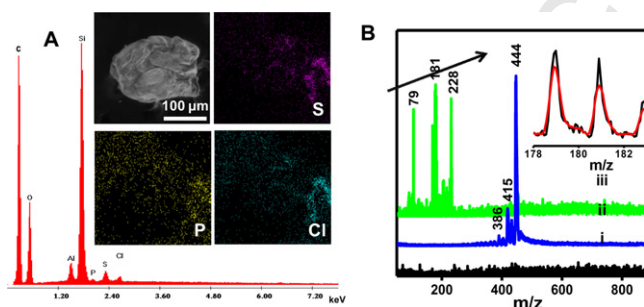


Fig. 10. (A) SEM and EDAX characterization of adsorbent after adsorption of chlorpyrifos. (B) LDI of (i) GSC, (ii) R6G adsorbed on GSC and (iii) CP adsorbed on GSC. Inset shows an expanded view of the peak at m/z 181.

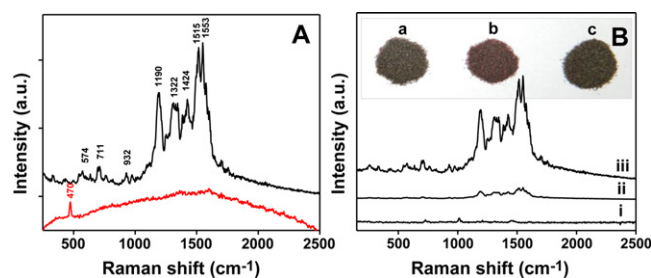


Fig. 11. (A) Red line: Raman spectrum of R6G adsorbed on GSC and black line: SERS of R6G. (B) Evaluation of the capacity of the column. SERS collected from the R6G spiked water sample after passing (i) 2 L, (ii) 3.6 L and (iii) 4.8 L through the column. The inset shows the photograph of (a) GSC, (b) R6G adsorbed GSC and (c) GSC after regeneration. (For interpretation of the references to color in this figure legend, the reader is referred to the web version of the article.)

a mass difference of two (the peak at m/z 181 is enlarged). This categorically proved the adsorption of targeted pollutants on GSC.

Unlike pesticides, the characteristic colors of the dyes can be used to identify the adsorption or desorption of these substances. The adsorption of R6G was evident from the color change (black to reddish) of the adsorbent particle (photograph in the inset of Fig. 11B). After regeneration, the adsorbent completely regained the initial color (black). Expanded photographs of the materials are presented in supplementary data S13 so that the color changes are appreciated.

However, trace amounts of R6G can be present on the adsorbent even without giving visual color. R6G being a Raman active molecule, Raman spectroscopy was employed for this analysis. Due to the inherent fluorescence of R6G, normal Raman spectrum was not able to show the characteristic features. In such cases, surface enhanced Raman spectroscopy (SERS) can be a useful technique to identify the sample. Hence, we used silver nanoparticles, which are known to be highly active SERS substrates [36,37]. We can see that the normal Raman spectrum does not have prominent features of R6G as in Fig. 11A (red trace) whereas the SERS spectrum obtained using silver nanoparticles showed all the characteristic features of R6G (Fig. 11A (black trace)). GSC before adsorption of R6G does not have the fluorescence background and the presence of this background (which masks other features) confirms the presence of R6G on GSC.

To assure complete regeneration of the adsorbent, the adsorbent was washed with acetone at a flow rate of 2.3 mL/min. The acetone extract after different wash cycles were analyzed. It was found that after 42 bed-volume of washing, no trace of R6G remained in the SERS spectra (supplementary data S14) pointing to the complete removal of R6G from the adsorbent surface. A similar strategy was used to calculate the capacity of the column. The bed height of the column was 3 cm (containing silica particle of size 0.3 μm and graphenic carbon loading of 0.6%). The filtrate was collected after different time (volume passed through the column) and was analyzed using SERS. Fig. 11B shows the SERS spectra taken from filtrate collected after passing 1 ppm of R6G solution through the column at different times (different volumes passed through the column). We can see that the evolution of peaks started after the passage of 3.6 L (1 ppm) of R6G solution through the column and appreciable features were seen when the volume passed through the column reached 4.8 L.

5. Conclusions

A facile *in situ* strategy for the synthesis of graphene-sand composite (GSC) is reported. A cheap and abundant material, asphalt was used as the carbon precursor. The synthetic strategy used here is useful to produce graphenic materials in solution phase as well

as on solid substrates. The formation of graphenic materials was confirmed by different spectroscopic and microscopic techniques. Characteristic G and D bands were observed at 1578 cm^{-1} and 1345 cm^{-1} , respectively, in the Raman spectrum. The 2D sheet-like structure with wrinkles observed in TEM and SEM confirmed the formation of graphenic materials. The as-synthesized composite, GSC, was tested for its applicability in decontaminating water. Rhodamine-6G and chlorpyrifos, a dye and a pesticide, respectively, were taken as the model pollutants. Batch experiments indicated that adsorption is highly dependent on the particle size, and carbon loading on sand particles. The suitability of the adsorbent in real time application was demonstrated through laboratory column experiments. The performance of GSC was compared to some other reported graphenic adsorbents and the results illustrated that GSC is superior in terms of strength and adsorption capacity for the contaminant tested. The adsorption capacity of GSC is 75.4 mg/g while it is 44.7 mg/g for AC in the case of R6G. The reusability of the adsorbent was demonstrated and found that the material is reusable and hence economically viable. The present study illustrates the possibility of making large quantity of graphenic materials in a cost effective manner and it is likely to be used in water purification industry.

Q3 Uncited reference

[26].

Acknowledgements

We thank the Nanoscience and Nano Mission of the Department of Science and Technology (DST), Government of India, for supporting our research program and Anirban Som for helping in taking the TEM images. SSG also thank UGC for the fellowship.

Appendix A. Supplementary data

Supplementary data associated with this article can be found, in the online version, at <http://dx.doi.org/10.1016/j.jhazmat.2012.12.022>.

References

- [1] V. Chandra, K.S. Kim, Highly selective adsorption of Hg^{2+} by a polypyrrole-reduced graphene oxide composite, *Chem. Commun.* 47 (2011) 3942–3944.
- [2] V. Chandra, J. Park, Y. Chun, J.W. Lee, I.C. Hwang, K.S. Kim, Water-dispersible magnetite-reduced graphene oxide composites for arsenic removal, *ACS Nano* 4 (2010) 3979–3986.
- [3] D. Cohen-Tanugi, J.C. Grossman, Water desalination across nanoporous graphene, *Nano Lett.* 12 (2012) 3602–3608.
- [4] F. Liu, S. Chung, G. Oh, T.S. Seo, Three-dimensional graphene oxide nanostructure for fast and efficient water-soluble dye removal, *ACS Appl. Mater. Interfaces* 4 (2011) 922–927.
- [5] A.K. Mishra, S. Ramaprabhu, Functionalized graphene sheets for arsenic removal and desalination of sea water, *Desalination* 282 (2011) 39–45.
- [6] T.S. Sreeprasad, S.M. Maliyekkal, K.P. Lisha, T. Pradeep, Reduced graphene oxide–metal/metal oxide composites: facile synthesis and application in water purification, *J. Hazard. Mater.* 186 (2011) 921–931.
- [7] S.S. Gupta, T.S. Sreeprasad, S.M. Maliyekkal, S.K. Das, T. Pradeep, Graphene from sugar and its application in water purification, *ACS Appl. Mater. Interfaces* 4 (2012) 4156–4163.
- [8] Y.W. Zhu, S. Murali, W.W. Cai, X.S. Li, J.W. Suk, J.R. Potts, R.S. Ruoff, Graphene and graphene oxide: synthesis, properties, and applications, *Adv. Mater.* 22 (2010) 5226.
- [9] W. Hu, C. Peng, W. Luo, M. Lv, X. Li, D. Li, Q. Huang, C. Fan, Graphene-based antibacterial paper, *ACS Nano* 4 (2010) 4317–4323.
- [10] T.S. Sreeprasad, M.S. Maliyekkal, K. Deepti, K. Chaudhari, P.L. Xavier, T. Pradeep, Transparent, luminescent, antibacterial and patternable film forming composites of graphene oxide/reduced graphene oxide, *ACS Appl. Mater. Interfaces* 3 (2011) 2643–2654.
- [11] M.L. Schipper, N. Nakayama-Ratchford, C.R. Davis, N.W.S. Kam, P. Chu, Z. Liu, X. Sun, H. Dai, S.S. Gambhir, A pilot toxicology study of single-walled carbon nanotubes in a small sample of mice, *Nat. Nanotechnol.* 3 (2008) 216–221.
- [12] J.W. Seo, A. Magrez, M. Milas, K. Lee, V. Lukovac, L. Forró, Catalytically grown carbon nanotubes: from synthesis to toxicity, *J. Phys. D: Appl. Phys.* 40 (2007) R109.
- [13] Q. Liu, J. Shi, J. Sun, T. Wang, L. Zeng, G. Jiang, Graphene and graphene oxide sheets supported on silica as versatile and high-performance adsorbents for solid-phase extraction, *Angew. Chem. Int. Ed.* 50 (2011) 5913–5917.
- [14] W.S. Hummers, R.E. Offeman, Preparation of graphitic oxide, *J. Am. Chem. Soc.* 80 (1958) 1339.
- [15] D. Li, M.B. Muller, S. Gilje, R.B. Kaner, G.G. Wallace, Processable aqueous dispersions of graphene nanosheets, *Nat. Nanotechnol.* 3 (2008) 101–105.
- [16] M.J. McAllister, J.L. Li, D.H. Adamson, H.C. Schniepp, A.A. Abdala, J. Liu, M. Herrera-Alonso, D.L. Milius, R. Car, R.K. Prud'homme, I.A. Aksay, Single sheet functionalized graphene by oxidation and thermal expansion of graphite, *Chem. Mater.* 19 (2007) 4396–4404.
- [17] S. Stankovich, D.A. Dikin, G.H.B. Dommett, K.M. Kohlhaas, E.J. Zimney, E.A. Stach, R.D. Piner, S.T. Nguyen, R.S. Ruoff, Graphene-based composite materials, *Nature* 442 (2006) 282–286.
- [18] S. Stankovich, D.A. Dikin, R.D. Piner, K.A. Kohlhaas, A. Kleinhammes, Y. Jia, Y. Wu, S.T. Nguyen, R.S. Ruoff, Synthesis of graphene-based nanosheets via chemical reduction of exfoliated graphite oxide, *Carbon* 45 (2007) 1558–1565.
- [19] T.S. Sreeprasad, A.K. Samal, T. Pradeep, Tellurium nanowire-induced room temperature conversion of graphite oxide to leaf-like graphenic structures, *J. Phys. Chem. C* 113 (2009) 1727–1737.
- [20] W. Gao, M. Majumder, L.B. Alemany, T.N. Narayanan, M.A. Ibarra, B.K. Pradhan, P.M. Ajayan, Engineered graphite oxide materials for application in water purification, *ACS Appl. Mater. Interfaces* 3 (2011) 1821–1826.
- [21] N.I. Kovtyukhova, P.J. Ollivier, B.R. Martin, T.E. Mallouk, S.A. Chizhik, E.V. Buzaneva, A.D. Gorchinskiy, Layer-by-layer assembly of ultrathin composite films from micron-sized graphite oxide sheets and polycations, *Chem. Mater.* 11 (1999) 771–778.
- [22] E. Ruiz-Hitzky, M. Darder, F.M. Fernandes, E. Zatile, F.J. Palomares, P. Aranda, Supported graphene from natural resources: easy preparation and applications, *Adv. Mater.* 23 (2011) 5250–5255.
- [23] Z. Sun, Z. Yan, J. Yao, E. Beitler, Y. Zhu, J.M. Tour, Growth of graphene from solid carbon sources, *Nature* 468 (2010) 549–552.
- [24] G. Ruan, Z. Sun, Z. Peng, J.M. Tour, Growth of graphene from food, insects and waste, *ACS Nano* 5 (2011) 7601–7607.
- [25] Y. Hernandez, V. Nicolosi, M. Lotya, F.M. Blighe, Z. Sun, S. De, I.T. McGovern, B. Holland, M. Byrne, Y.K. Gun'Ko, J.J. Boland, P. Niraj, G. Duesberg, S. Krishnamurthy, R. Goodhue, J. Hutchison, V. Scardaci, A.C. Ferrari, J.N. Coleman, High-yield production of graphene by liquid-phase exfoliation of graphite, *Nat. Nanotechnol.* 3 (2008) 563–568.
- [26] B. Srivastava, Review – adsorbents for pesticide uptake from contaminated water: a review, *J. Sci. Ind. Res.* 68 (2009) 839.
- [27] R. Sariri, M.S. Zakerhamidi, K. Baharpaima, A. Ghanadzadeh, The anion effect and molecular association of rhodamine dyes in isotropic and anisotropic solutions, *J. Mol. Liq.* 115 (2004) 55–61.
- [28] S.M. Maliyekkal, T.S. Sreeprasad, D. Krishnan, S. Kouser, A.K. Mishra, U.V. Waghmare, T. Pradeep, Graphene, A reusable substrate for unprecedented adsorption of pesticides, *Small* (2012), <http://dx.doi.org/10.1002/sml.201201125>.
- [29] S. Lagergren, Zur theorie der sogenannten adsorption gelöster stoffe, *K. Sven. Ventenskapskad. Handl.* 24 (1898) 1–39.
- [30] Y.S. Ho, G. McKay, The kinetics of sorption of divalent metal ions onto sphagnum moss peat, *Water Res.* 34 (2000) 735–742.
- [31] Y.S. Ho, C.C. Chiang, Y.C. Hsu, Sorption kinetics for dye removal from aqueous solution using activated clay, *Sep. Purif. Technol.* 36 (2001) 2473–2488.
- [32] K.P. Lisha, S.M. Maliyekkal, T. Pradeep, Manganese dioxide nanowhiskers: a potential adsorbent for the removal of $\text{Hg}(\text{II})$ from water, *Chem. Eng. J.* 160 (2010) 432–439.
- [33] S. Kuriakose, T.S. Singh, K.K. Pant, Adsorption of As(III) from aqueous solution onto iron oxide impregnated activated alumina, *Water Qual. Res. J. Can.* (2004).
- [34] T.S. Singh, K.K. Pant, Experimental and modelling studies on fixed bed adsorption of As(III) ions from aqueous solution, *Sep. Purif. Technol.* 48 (2006) 288–296.
- [35] G. Annadurai, R.S. Juang, D.J. Lee, Adsorption of rhodamine 6G from aqueous solutions on activated carbon, *J. Environ. Sci. Health A* 36 (2001) 715–725.
- [36] P. Hildebrandt, M. Stockburger, Surface-enhanced resonance Raman spectroscopy of rhodamine 6G adsorbed on colloidal silver, *J. Phys. Chem.* 88 (1984) 5935–5944.
- [37] A.M. Michaels, M. Nirmal, L.E. Brus, Surface enhanced Raman spectroscopy of individual rhodamine 6G molecules on large Ag nanocrystals, *J. Am. Chem. Soc.* 121 (1999) 9932–9939.

Supplementary data

Immobilized graphene-based composite from asphalt: Facile synthesis and application in water purification

*T. S. Sreeprasad¹, Soujit Sen Gupta¹, Shihabudheen M. Maliyekka²,
and T. Pradeep^{1*}*

*¹DST Unit on Nanoscience, Department of Chemistry,
Indian Institute of Technology Madras, Chennai - 600 036, India*

*²School of Mechanical and Building Sciences,
VIT University, Chennai Campus, Chennai-600 048, India*

**Email: pradeep@iitm.ac.in; Fax: 91-44-2257-0545/ 0509*

Supplementary data 1

Methods and Materials

Materials

The carbon source used for the preparation of graphene, asphalt, was procured from the local market of Chennai, India. Toluene (industrial grade) was purchased from Rankem Chemicals Pvt. Ltd., India. CP (HPLC assay 99.9%) and Rhodamine 6G chloride (R6G, $C_{27}H_{29}ClN_2O_3$) were obtained from Sigma Aldrich. Standard sand collected from Ennore, Tamilnadu was initially treated with 0.1 M nitric acid to remove impurities. Subsequently the sand was washed extensively with deionized water and dried at 100 ± 3 °C. This purified sand was sieved to obtain particles of desired size. All chemicals were used as received without additional purification. All solutions and suspensions were prepared using deionized water, unless otherwise mentioned.

In-situ synthesis of graphene-sand composite (GSC)

Asphalt was initially dissolved in toluene at a solid to solvent ratio of 1:10. The dispersed asphalt was then mixed with sand particles of size ranging from 200-500 micrometers. The carbon loading on the sand particles was varied by changing the sand to asphalt ratio. The samples were then dried in a hot air oven at 90 ± 3 °C under constant stirring for about 5 h. The dried sample was then transferred to a muffle furnace and subjected to heat treatment. The furnace was programmed as follows: a) temperature was increased from 30 to 250 °C in 30 min. b) held at 250 °C for an hour, c) again increased to 400 °C in next 1 h and d) finally held at 400 °C for next 4 h. It was then cooled to room temperature, just by switching off the power and without any control on the cooling rate. The optimum temperature was 400 ± 5 °C, which was established after several iterations. The stable carbon coating on the sand surface was evident from the characteristic black color of the sample. The pre-weighed material was then soaked in concentrated sulfuric

acid for about 30 min and filtered, washed several times with deionized water until the pH of the wash-water reaches that of the input water. The composite was then dried at 110 °C for further use. The sample was again weighed to check any weight gain or loss. This material is termed as graphene sand composite (GSC). The carbon loading (wt%) was calculated from thermo-gravimetric analysis (TGA) (Supplementary data Fig. S2).

Batch adsorption experiments

Batch experiments were carried out to evaluate the pollutant uptake capacity of the composite in 25 mL conical flasks. Calculated amount of adsorbent was added to 10 mL of the water spiked with the target pollutant (R6G or CP) and placed on a shaker at room temperature (30 ± 2 °C). The solid-liquid separation was done by filtration. The filtrate was analyzed to quantify the target molecule R6G in the aqueous phase by UV/Vis spectrophotometer based on the absorbance at 527 nm. Analysis of CP was carried out at a wavelength of 297 nm. The effect of particle size, contact time, and adsorbent dose were evaluated by varying the parameters in the appropriate window. Except kinetics, all other studies were conducted by batch equilibration method. Control samples were kept in all the cases to assess the natural attenuation of the target molecule. All the experiments were conducted in duplicate and the average values are reported.

Fixed-bed column experiments

Continuous removal of the R6G was studied in fixed-bed columns made of transparent glass with a length of 500 mm and an internal diameter of 18 mm. The columns were packed with the adsorbent to a depth of 3 cm and operated in down-flow mode at a feed flow rate of 2.3 mL/min. The performance of the column was evaluated as a function of time at room temperature. The initial R6G concentration was maintained at 1 mg/L. The residual concentration of the effluent samples were analysed as a function of time.

The R6G loaded adsorbents were regenerated *in-situ* in the columns using acetone as the eluent. The regenerant was passed through the column bed with the same flow rate of adsorption cycle. Nearly 42 bed

volumes of acetone were passed through the column in down-flow mode and followed by purging with hot air. The column was then washed to check the pollutant concentration in the wash-water. The spent regenerant and back washed water were collected and analysed for eluted concentrations of the pollutant as function of time.

Instrumentation

UV/Vis spectra were measured using a Perkin-Elmer Lambda 25 UV/Vis spectrophotometer. Raman spectra were collected using a confocal Raman spectroscope (WiTec GmbH CRM 200). High-resolution transmission electron microscopy (HRTEM) of the samples was carried out using a JEOL 3010 microscope with a UHR pole piece. X-ray photoelectron spectroscopy (XPS) measurements were done with Omicron ESCA Probe spectrometer with unmonochromatized Mg K α X-rays ($h\nu = 1253.6$ eV). The energy resolution of the spectrometer was set at 0.1 eV at pass energy of 20 eV. Binding energy was corrected with respect to C 1s at 284.5 eV. Surface morphology, elemental analysis and elemental mapping studies were carried out using scanning electron microscopy (SEM) equipped with energy dispersive analysis of X-rays (EDAX). SEM measurements used indium doped tin oxide (ITO plate), presence of Si and Sn in the images is expected. For mass analyses, an Applied Biosystems Voyager DE Pro LDI-MS instrument was used. A pulsed nitrogen laser of 337 nm was used for desorption/ionization.

Mechanism of formation of graphenic material from asphalt

The mechanism behind the formation of graphenic material is not fully understood. However, Raman and XPS evaluation suggested the loss of organic functionalities from asphalt during the process. TGA also indicated a weight loss during the process. Asphalt mainly consists of highly condensed polycyclic aromatic hydrocarbons. It is considered as a colloidal mixture with the chief component being asphaltene. Asphaltene is composed of nitrogen, oxygen and sulfur (as functional groups or adsorbates) in addition to carbon and hydrogen. Asphaltene is highly soluble in toluene. In our process, asphalt was first dissolved in toluene and hence chief fraction in the solution is asphaltene. The carbon functionalities are highly

susceptible to thermal decomposition above 300 °C [1, 2]. Hence, based on the prevailing knowledge and Raman, XPS and TGA results obtained in the study, it is proposed that at elevated temperatures, asphaltene will lose the impurities (the functional groups) and will form unfunctionalized carbon. This carbon, in presence of a solid substrate (sand particle), is believed to combine and form the graphenic materials. The substrate not being single crystalline, the formation can start from different places in different orientation. This leads to the formation of large number of structural defects in the films formed.

Supplementary data 2

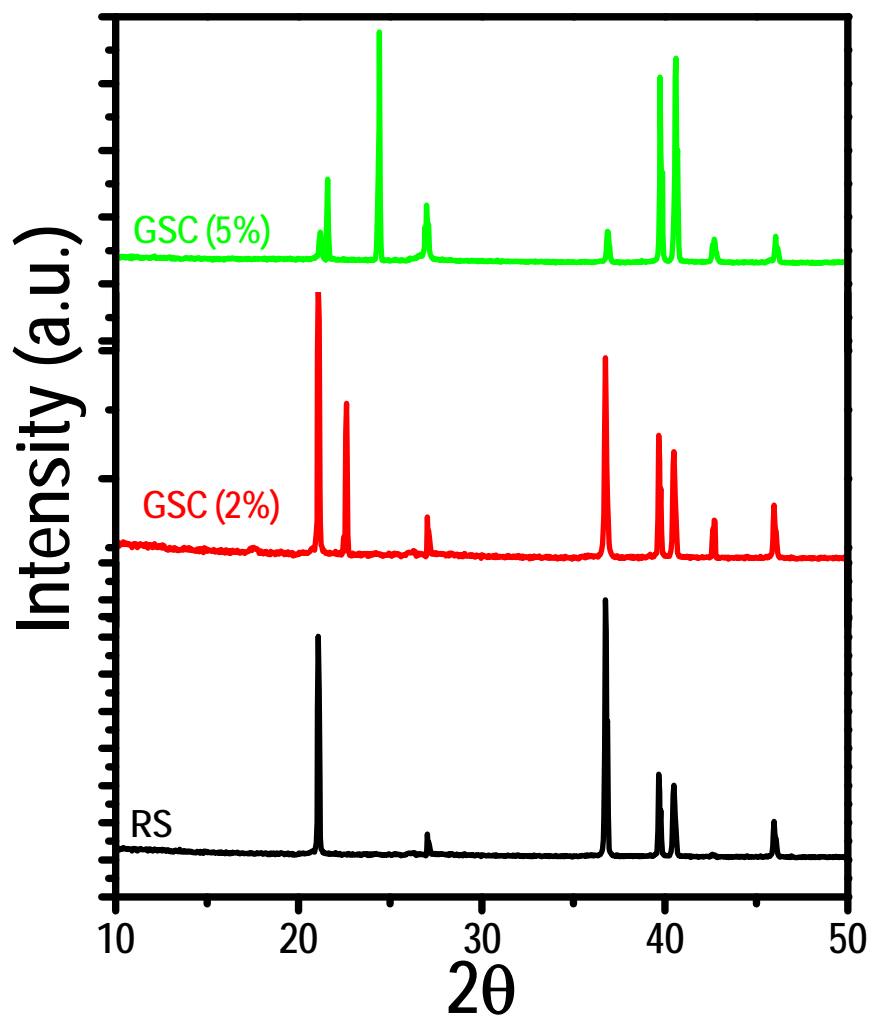


Fig S2: XRD data of bare sand (silica) and GSC at different graphenic carbon loading (2 and 5 wt%).

Supplementary data 3

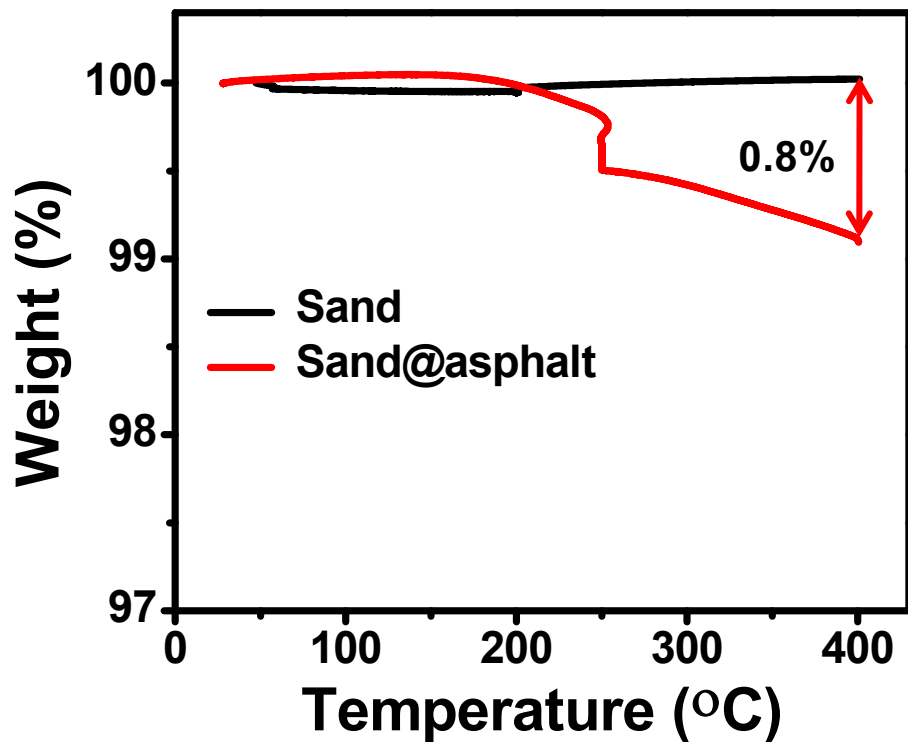


Fig. S3: TGA of sand and asphalt coated sand (2 wt%), showing weight loss of 0.8 wt%. Temperature was programmed as given in text. The initial loading is based on calculation. The temperature was not ramped above 400 °C as the auto-ignition temperature in air is above this value. However, heating up to 750 °C in N₂ atmosphere did not increase the adsorption capacity.

Supplementary data 4

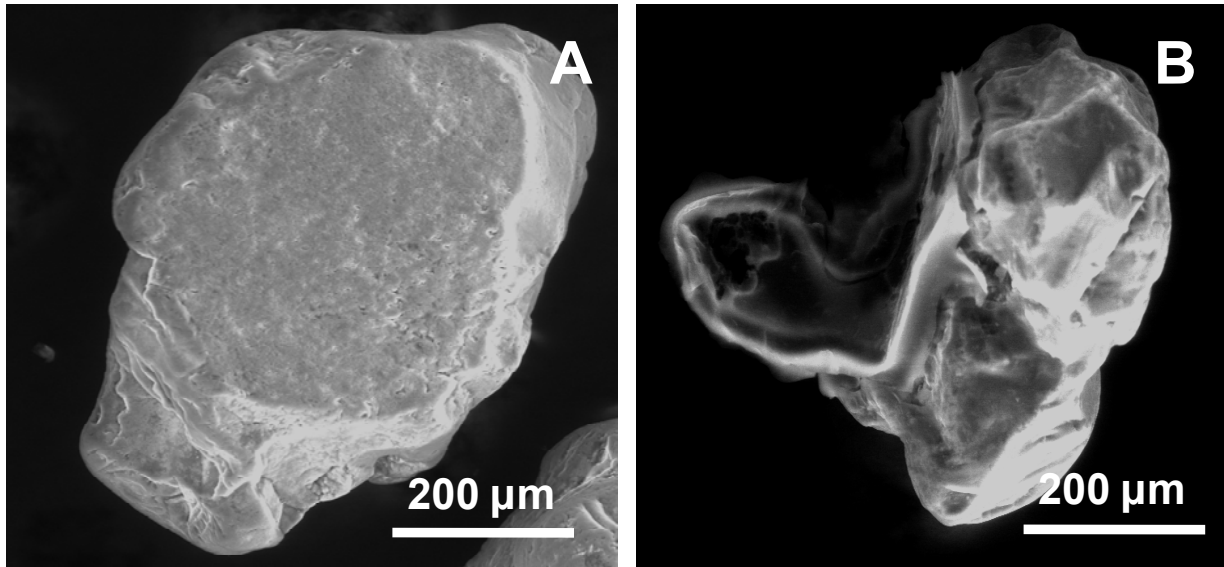


Fig. S4: SEM images of A) virgin-sand showing that the surface is plain and B) sand coated with graphene, where the surface is rougher and sheet-like structures can be seen.

Supplementary data 5

Fig. 4A and B show the SEM images of GSC with 0.2 % loading, where the surface is rougher than the pristine sand. When the loading reached 0.5%, careful observation showed more prominent surface changes. The surface looked rougher compared 0.2% loading (Fig. 4C and D). At 1% loading, a clear sheet-like structure was visible (Fig. 4E and F). Fig. 4F shows a closer view (higher magnification) of a GSC particle with 1% loading. We can see a sheet covering the surface of sand. The outward appearance (color) of the sand also changed as the loading increased. The color turned more intense as the loading increased (Fig. 4G).

Supplementary data 6

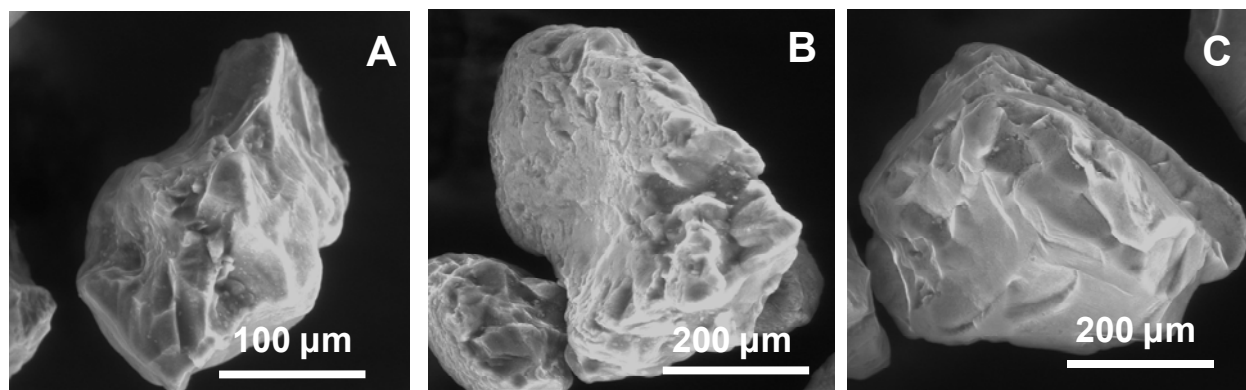


Fig. S6: SEM images of GSC with different sand particle sizes. A) Less than 0.2 mm, B) between 0.2-0.3 mm and C) more than 0.3 mm having 0.5% carbon loading.

Supplementary data 7

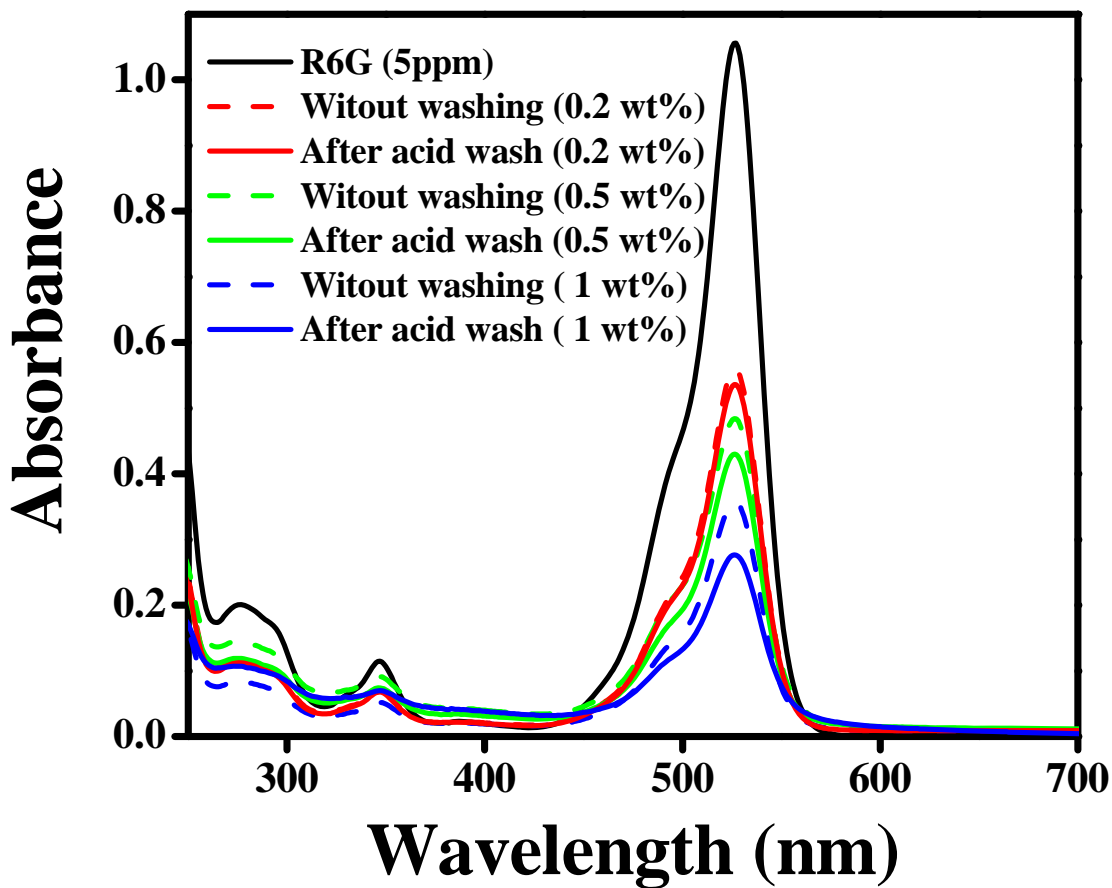


Fig. S7: UV/Vis spectrum showing an increase in efficiency of GSC after acid wash for different carbon loading.

Supplementary data 8



Video 1: Removal of Coca-cola. Bed depth was 6 cm and no special care was taken for controlling the flow-rate in this clip.

Supplementary data 9

Pseudo-first-order equation: $q_t = q_e(1 - e^{-k_1 t})$ (1)

Pseudo- second-order equation: $\frac{q_e^2 k_2 t}{1 + q_e k_2 t}$ (2)

Where q_e and q_t are the adsorption capacities at equilibrium and at time t, respectively (mg/g). k_1 is the rate constant of pseudo-first-order adsorption (L/min) and k_2 is the rate constant of pseudo-second order adsorption (g/mg min). The estimated value of k_1 and k_2 are 0.02 /min and 0.019 mg/g min, respectively.

Supplementary data 10

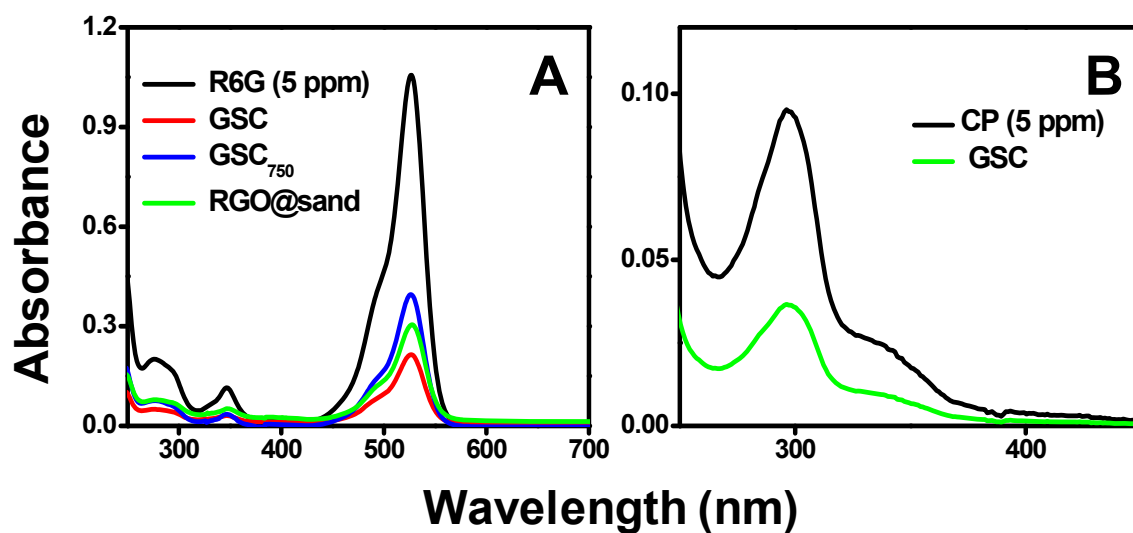


Fig. S10: UV/Vis spectrum showing A) removal of R6G with different graphenic materials as the adsorbent.

B) Removal of CP with GSC.

Supplementary data 11

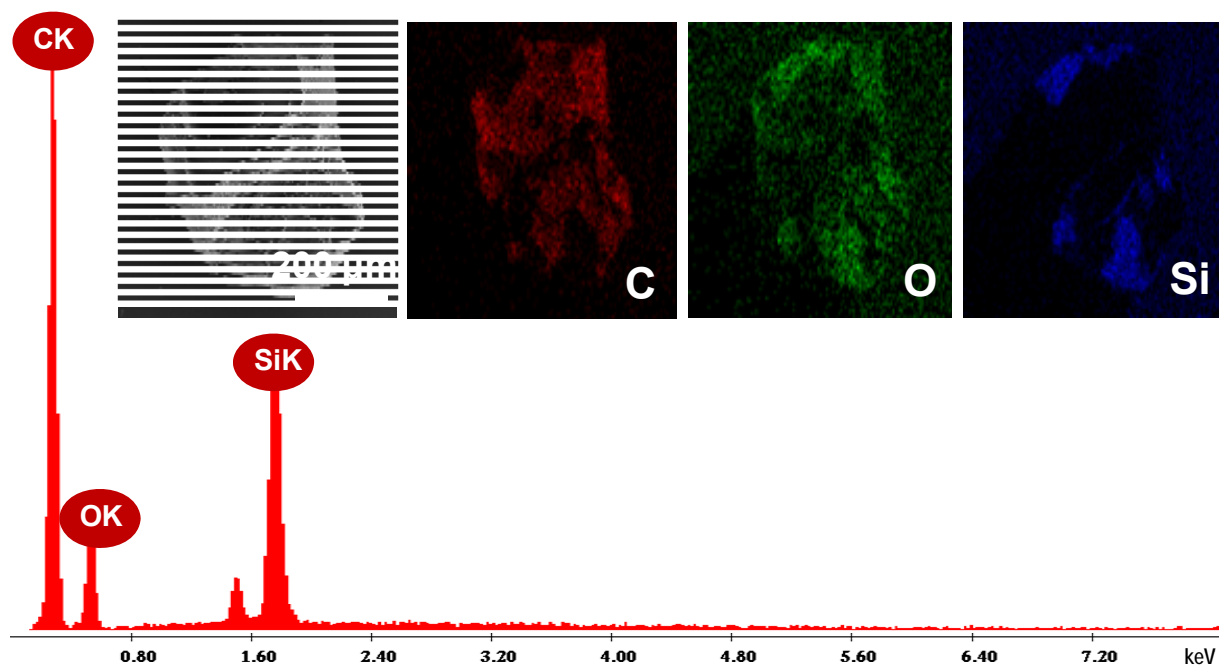


Fig. S11: SEM-EDAX of CP adsorbed GSC after regeneration. P, Cl and S are absent.

Supplementary data 12

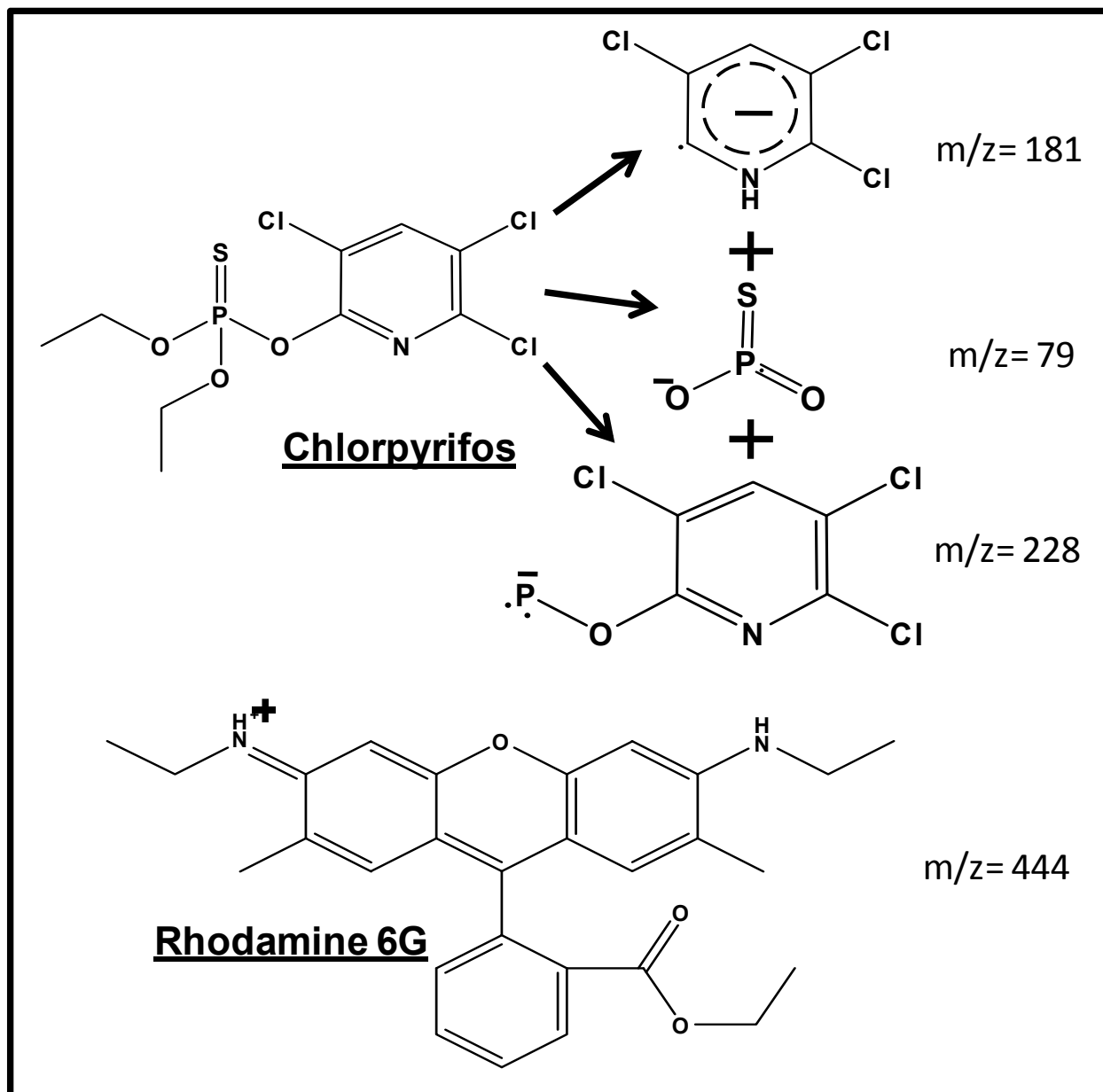


Fig. S12: Common fragments of CP and the molecular ion of R6G.

Supplementary data 13

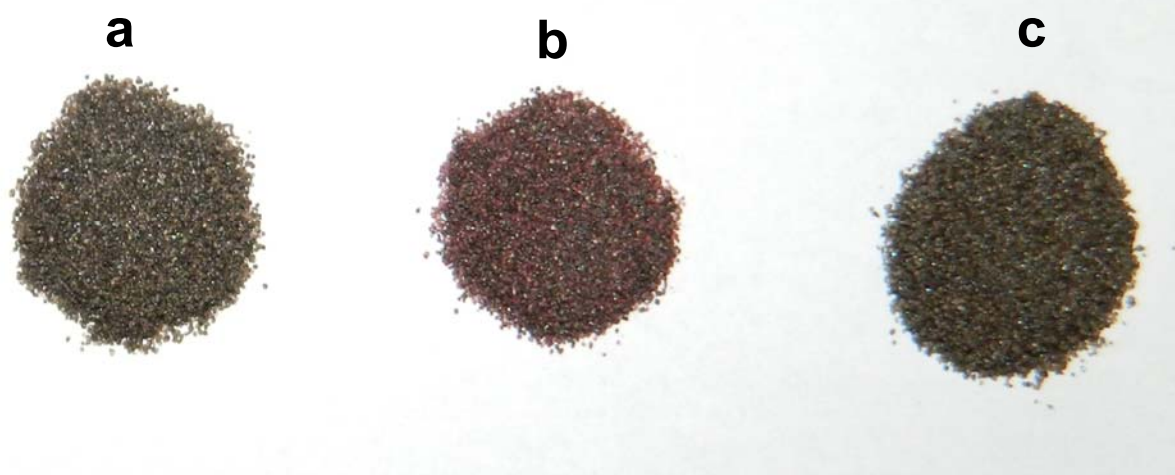


Fig. S13: Photographs of a) initial material (GSC), b) R6G adsorbed GSC and c) GSC after regeneration. The color change of the material after adsorption of R6G, from black (a) to reddish (b) can be clearly seen.

Supplementary data 14

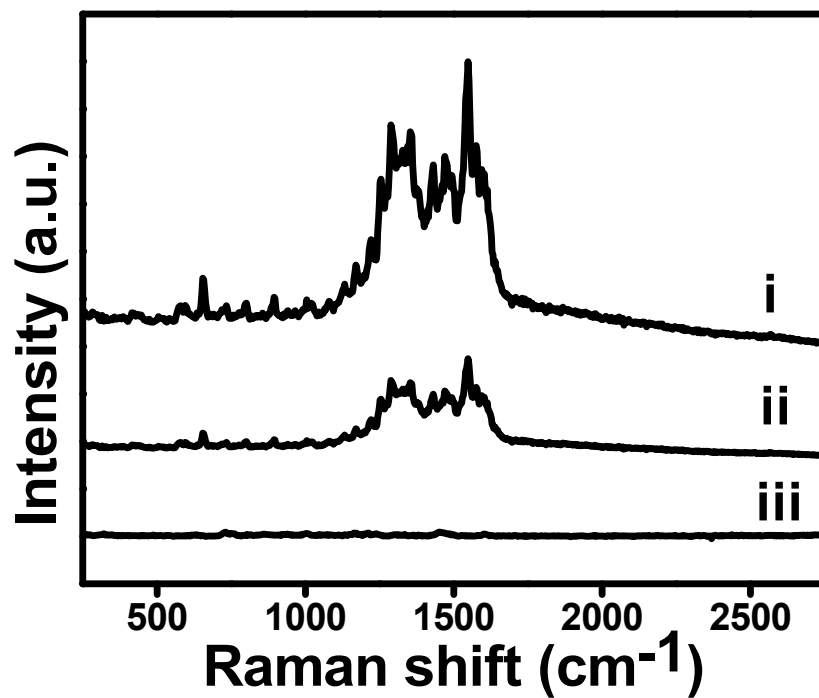


Fig. S14: SERS of the filtrate after passing different volumes of acetone during regeneration, i) after 10 bed volume, ii) after 20 bed volume and iii) 30 bed volume.

References:

- [1] G. de la Puente, J. J. Pis, J. A. Menendez, P. Grange, Thermal stability of oxygenated functions in activated carbons, *J. Anal. Appl. Pyrol.* 43 (1997), 125–138.
- [2] A. G. Vandeputte, M. F. Reyniers, G. B. Marin, Theoretical study of the thermal decomposition of dimethyl disulfide, *J. Phys. Chem. A* 114 (2010), 10531-10549.

4. Patents Filed

Only list is attached

Indian patent applications

Visible detection of quantity of water flow using quantum clusters, T. Pradeep, Leelavathi A, M. Udhaya Sankar, Amrita Chaudhary, Anshup, T. Udayabhaskararao, 1521/CHE/2012, April 17, 2012.

Luminescent graphene patterns, T. Pradeep, T. S. Sreeprasad and Shihabudheen M. Maliyekkal, 2097/CHE/2012, May 23, 2012.

Methods for selective visual detection of TNT, T. Pradeep, Ammu Mathew and P. R. Sajanlal, 3150/CHE/2012, August 1, 2012.

A method for the preparation of immobilized graphene-based composite from asphalt and its application in water purification, T. Pradeep, Soujit Sengupta, T. S. Sreeprasad and S. M. Maliyekkal, 3863/CHE/2012, September 17, 2012

PCT patent applications

A sustained silver release composition for water purification, T. Pradeep, Anshup, Amrita Chaudhary, M. Udhaya Sankar, and S.Gayathri, PCT/IB2012/001079, filed on March 25, 2012.

Luminescent graphene patterns, T. Pradeep, T. S. Sreeprasad and Shihabudheen M. Maliyekkal, PCT/IB2012/001518, August 7, 2012.

Visual detection of mercury ions, T. Pradeep, Ammu Mathew and P. R. Sajanlal, PCT/IB2012/001543, August 10, 2012.

One container gravity fed storage water purifier, Indian patent application - 1522/CHE/2011, PCT application.

US Patents

Graphene based antimicrobial composites, T. Pradeep, T. S. Sreeprasad and Shihabudheen M. Maliyekkal, Application number 13443408, filed on April 10, 2012.

5. Technologies

Arsenic filter – two community units are installed based on our technology, pictures are on the next pages.





A community unit at the actual location in West Bengal.

6. Media reports

In the following pages some of the media reports are captured.

Browse our products:

Books

» Journals

Please specify  

» Journals from A to Z

Online Submission of Manuscripts

New journals

Latest issues

Featured sites

Choose your area of interest:

Please specify  

Website Search

[\[More press releases\]](#)

Press Release

Angewandte Chemie International Edition ,
 doi: [10.1002/anie.201203810](https://doi.org/10.1002/anie.201203810)

Nr. 32/2012
August 27, 2012

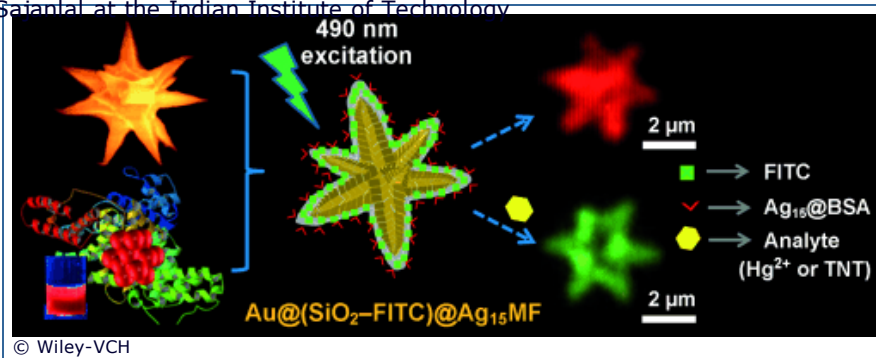
Glowing Flowers for Ultra-Trace Analysis of TNT

Selective optical TNT detection down to the sub-zeptomole level

Highly sensitive and highly selective tests are important for the early detection of disease, the detection of environmental toxins, or for the detection of explosives at airports. Increased selectivity for the target analytes helps to avoid false-positive results. In the journal *Angewandte Chemie*, Indian scientists have now introduced a specific detection method for the explosive TNT that can be used to detect even a single molecule.

Contact: [Thalappil Pradeep, Indian Institute of Technology Madras, Chennai \(India\)](#)
 Registered journalists may **download the original article** here: [Selective Visual Detection of TNT at the Sub-Zeptomole Level](#)

Thalappil Pradeep, Ammu Mathew, and P. R. Saianal at the Indian Institute of Technology



Madras use an ingenious combination of micro- and nanostructures as sensors: gold mesoflowers, flower-shaped gold particles about 4 µm in size, act as supports for silver clusters, tiny clumps of exactly 15 silver atoms embedded in the protein bovine serum albumin. When irradiated with light of the right wavelength, the silver clusters luminesce, giving off red light. The gold of the mesoflower supports intensifies the fluorescence. Their unique shape is a particular advantage, because it is easy to unambiguously identify under an optical microscope, unlike spherical particles.

If a drop of a solution containing TNT is applied, it reacts with the amino groups of the bovine serum albumin to make a Meisenheimer complex—a reaction specific to TNT. This extinguishes the red glow of the silver clusters. In order to make this reaction even more distinct, the researchers also embedded a green fluorescing dye, which was adsorbed on a silicon dioxide layer grown on the gold flowers. As long as the silver clusters glow red, the green fluorescence is suppressed. When TNT molecules switch off the red light, the green dye begins to glow. The color change from red to green can be observed with a fluorescence microscope.

A TNT concentration of one ppb (part per billion) extinguishes the

Deutsche Ausgabe

A Journal of the 

[Contact](#)

[Subscribe now!](#)

[Advertise](#)

[News](#)

05-Sep-2012

[Hot Paper: The Active Phase of Nickel/Ordered Ce₂Zr₂O_x Catalysts with a Discontinuity \(x=7–8\) in Methane Steam Reforming](#)

04-Sep-2012

[Hot Paper: Magnesium Borohydride: From Hydrogen Storage to Magnesium Battery](#)

03-Sep-2012

[Hot Paper: Photoinduced Reductive Electron Transfer in LNA:DNA Hybrids: A Compromise between Conformation and Base Stacking](#)

[more News >>](#)

By authors of *Angewandte*:



Dilar Arnes (Ed)
Modern Arene Chemistry

Concepts, Synthesis, and Applications



fluorescence, one ppt (part per trillion), reduces it markedly. The researchers supplemented their luminescence technique with a second analytical method, SERS (surface-enhanced Raman scattering), which also functions extremely well with a version of the flower-shaped sensors. "This allowed us to attain detection limits as low as the sub-zeptomole range (10^{-21} mol)," explains Pradeep. Just one "flower" is enough to operate as a sensor. It reacts when it comes into contact with as few as nine molecules. A device based on this principle is under development.

The researchers were also able to detect mercury with similar sensitivity by using the same sensor strategy. Says Pradeep: "Our concept could also be used for the ultra-trace analysis of other substances through the incorporation of specific ligands on the sensors."

(2756 characters)

About the Author

Dr. Pradeep is Professor of Chemistry at the Indian Institute of Technology Madras, Chennai, India. He heads the Thematic Unit of Excellence and the Unit of Nanoscience sponsored by the Department of Science and Technology. He is a Fellow of the Indian Academy of Sciences and is a recipient of some of the highest recognitions for scientists in India.



[Tell a friend](#)



[RSS Feeds](#)

[Print-Version](#)

[Sitemap](#)

©2012 Wiley-VCH Verlag GmbH & Co. KGaA - [Provider](#)
<http://www.wiley-vch.de> - [mailto: info@wiley-vch.de](mailto:info@wiley-vch.de)
[Data Protection](#)

From IIT-Madras, nano-scale device to detect big explosives +1

IBNS

Chennai: Researchers at the Indian Institute of Technology, Madras, (IIT-M) have developed a novel device that can visually detect even a single molecule of TNT used in the making of powerful explosives. Apart from national security, this ultra-sensitive and highly selective detection method will have applications in early identification of diseases and in radiation prevention, the IIT researchers claim.

Chemistry professor Thalappil Pradeep and his students Ammu Mathew and P.R. Sajanlal reported the principle behind this device in the online issue of the leading chemistry journal *Angewandte Chemie* on Aug 22. They are now building the device that may be put to practical use soon.

The science behind this explosive detector is rather involved and difficult to explain. In simple terms, the detector works somewhat like an alert traffic cop who spots a violator by simply looking at the traffic signal. In other words, if the suspected sample being tested is clean, the detector gives off a red glow on being irradiated with light of a particular wavelength.




 You are here: [Home](#) » [National](#) » From IIT-M, nano-scale device to detect big explosives

From IIT-M, nano-scale device to detect big explosives

Chennai, Aug 28, 2012, (IANS)

Researchers at the Indian Institute of Technology, Madras, (IIT-M) have developed a novel device that can visually detect even a single molecule of TNT used in the making of powerful explosives.

Apart from national security, this ultra-sensitive and highly selective detection method will have applications in early identification of diseases and in radiation prevention, the IIT researchers claim.

Chemistry professor Thalappil Pradeep and his students Ammu Mathew and P.R. Sajanlal reported the principle behind this device in the online issue of the leading chemistry journal Angewandte Chemie on Aug 22. They are now building the device that may be put to practical use soon.

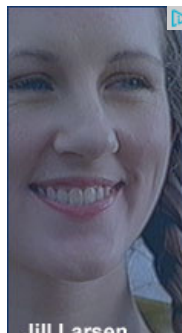
The science behind this explosive detector is rather involved and difficult to explain. In simple terms, the detector works somewhat like an alert traffic cop who spots a violator by simply looking at the traffic signal. In other words, if the suspected sample being tested is clean, the detector gives off a red glow on being irradiated with light of a particular wavelength.

But if the sample contains the explosive TNT (trinitrotoluene), the signal changes to with a fluorescence microscope has been demonstrated by the IIT team to take place in the presence of even just one molecule of TNT -- a lower limit that has not been achieved by any detector so far.

Pradeep heads IIT's nanoscience centre and naturally the TNT sensor that his team has developed uses a combination of gold and silver nano-particles, which are particles of extremely small dimensions. The entire detector system is just four millionths of a metre in size and its distinct star shape is of particular advantage because it is easy to unmistakably identify the colour change under the microscope, says Pradeep.

According to the scientists, their novel approach "can be considered a single-particle, single-molecule detection technique which is probably the ultimate in ultra-trace sensitivity".

The researchers have demonstrated that they can also detect extremely low levels of mercury - an environmental contaminant -- using the same sensor strategy. They say the concept could also be used for the detection of very low concentration of other substances by incorporating appropriate molecules called "ligands" on their sensor thereby opening up applications in catalysis, bio-imaging and other areas.



Jill Larsen
ITT Tech graduate, 2001
Richardson, TX

"When I started working with computers, I found that the more I learned the more I wanted to know."

ITT Tech
www.itt-tech.edu

> Click here to request a Free ITT Tech brochure

Ad Links

India Flowers - Florist Hyderabad
Mumbai Gurgaon Bangalore

Flowers to India, Gifts to India, Bangalore, Chennai, Goa, Hyderabad

Go to Top
Flowers to India, Flowers to Mumbai, Flowers to Hyderabad

Gifts to India, Gifts to Delhi, Gifts to Mumbai

Horoscope

- Year 2012
- Weekly
- Daily Astrospeak
- Calendar 2011

Cricket

Movie Guide



'Joker' is directed by Shirish Kunder, starring Akshay Kumar and Sonakshi Sinha in lead roles. [...]

Deccan Herald Prajavani
RATE CARD
Karnataka Advt. Tariff
Classifieds Tariff
Delhi Advt. Tariff

Related News

- ▶ Device helps paralysed walk again
- ▶ Now, device to help doctors see hard to reach body parts
- ▶ Madras Atomic Power Station to restart after shutdown
- ▶ IIT students awarded for innovations
- ▶ HC wants guidelines on vehicles in two weeks

Photo Gallery



Customers coming out of a clothing shop named 'Hitler' in Ahmadabad...

[more](#)

 E-mail this Page  Print this Page  Bookmark

Like 0

Tweet 1

0

doi:10.1038/nindia.2012.124; Published online 26 August 2012

Science news

Gold flowers to detect explosives

K. S. Jayaraman

Scientists at the Indian Institute of Technology, Madras (IIT-M) have developed an ingenious method to visually detect even a single molecule of the explosive TNT.

The technique described¹ by chemistry professor Thalappil Pradeep and his students Ammu Mathew and P. R. Sajanlal (now a postdoc at the Georgia Institute of Technology in the U.S.) may someday become a powerful tool for detectives searching for explosives at airports and terrorist hideouts.

The IIT chemists used a combination of micro- and nanostructures called 'gold mesoflowers' as sensors. These are flower-shaped gold particles about 4 μm (millionths of a meter) in size. These gold flowers act as 'supports' for silver clusters which are tiny clumps of exactly 15 silver atoms embedded in protein bovine serum albumin.

This unique detector system works as follows: when irradiated with light of right wavelength (490 nm), the silver clusters luminesce, giving off red light. The nanostructures in the gold mesoflower intensifies the fluorescence. The distinct star shape of the mesoflower is of particular advantage because it is easy to unambiguously identify it under an optical microscope, says Pradeep.

If a drop of test solution containing TNT is applied, it reacts with the free amino groups of the bovine serum albumin to make a 'Meisenheimer complex' — a reaction specific to TNT. This reaction extinguishes the red glow of the silver clusters within one minute. The disappearance of the red glow can be seen visually under a microscope and is a clear indication of the presence of TNT.

In order to make this reaction even more distinct, the researchers also embedded a green fluorescing dye called 'fluorescein isothiocyanate (FITC)', on to a silicon dioxide layer grown on the gold flowers. As long as the silver clusters glow red, the green fluorescence is suppressed. When TNT molecules switch off the red light, the green dye begins to glow. The change of colour from red to green can be observed with a fluorescence microscope.

"A TNT concentration of one ppb (parts per billion) extinguishes the fluorescence whereas one ppt (part per trillion) reduces it markedly." According to Pradeep, just one 'flower' is enough to operate as a sensor. A device based on this principle is under development at the IIT-M, he told *Nature India*. The amount of gold required to make one mesoflower with a 4 μm edge length is about 0.288 nanogram and it can be recovered and reused.

The IIT-M scientists supplemented their luminescence technique with a second analytical method called surface-enhanced Raman scattering or SERS which also functions extremely well with a version of the flower-shaped sensors. "By combining the high sensitivity and selectivity offered by SERS with our sensing method,



Researchers Ammu Mathew (front) and T. Pradeep.

we enhance the accuracy and reliability of the detection technique," the researchers said.

The researchers were also able to detect mercury with this method. Pradeep says the concept could also be used for the ultra-trace analysis of other substances through the incorporation of specific ligands (or molecules) on the sensors. This, he says, will open up applications in catalysis, bio-imaging and other areas. "This approach can be considered a single-particle, single-molecule detection technique which is, probably, the ultimate in ultra-trace sensitivity."

References

1. Mathew, A. *et al.* Selective Visual Detection of TNT at the Sub-Zeptomole Level. *Angew. Chem. Int. Ed.* doi: [10.1002/anie.201203810](https://doi.org/10.1002/anie.201203810) (2012)

Nature India EISSN 1755-3180

Header image source: Getty

About NPG
Contact NPG
Accessibility statement
Help

Privacy policy
Use of cookies
Legal notice
Terms

Naturejobs
Nature Asia
Nature Education
RSS web feeds

Search:

© 2012 Nature Publishing Group, a division of Macmillan Publishers Limited.
All Rights Reserved.

partner of AGORA, HINARI, OARE, INASP, ORCID, CrossRef and COUNTER

Tuesday, September 25, 2012

Home Classified Jobs Matrimonials Blog Archives Advertise Feedback About Us

Last Updated: 25 Sep 07:56 AM IST

The Statesman
137 YEARS IN PRINT
Because we are different.

[News](#) [Page-One](#) [World](#) [Editorial](#) [Perspective](#) [Business](#) [Sport](#) [Bengal Plus](#) [India](#) [Bengal](#) [Kolkata Plus](#)
[Features](#) [Marquee](#) [Evolve](#) [8th Day](#) [Voices](#) [North East Page](#) [NB Extra](#) [Viewpoint](#) [Notebook](#) [Campus](#) [Career](#) [Science](#)

case | **CWC:** Congress Working Committee endorses economic reforms undertaken by the government; Mrs Sonia Gandhi attacks BJP for its "negative politics", sa

Quest ONLINE BOOKING
CLASSIFIED ADS

Submit a
Letter to the Editor

e - PAPER
- READ IT ONLINE >

Internships at
The Statesman >

ANN Asia News Network
WE KNOW ASIA BETTER

SPJS The Statesman
Print Journalism School

Govt mulls IIT-made plants for arsenic-free water in Murshidabad

30 August 2012

asim pramanik

BEHRAMPORE, 30 AUG: The state government has found a low-cost option for installing anti-arsenic drinking water plants made by IIT Kharagpur and IIT Chennai in the areas not covered by the ongoing multi-crore projects meant to supply arsenic-free drinking water.

A Rs 700-crore pilot project aims to install 121 arsenic-removal plants in Murshidabad district: 117 based on underground water and four based on river water.

As the pilot project is not enough to cover all 19 arsenic-hit blocks of the district, the administration has decided to use Rs 6 crore of Rs 127 crore in minority development funds to install low-cost IIT-made plants in the left-out pockets of the district, public health engineering officials said.

The two types of arsenic-removal plants the state government plans to purchase include one devised by Professor Shirsendu Dey of the department of chemical engineering at IIT-Kharagpur, and one developed by Professor T Pradip of the department of chemistry at IIT Chennai, the officials said. Prof. Dey's product, to be purchased at the rate of Rs 20,000 per plant, can produce 40 to 50 litres of arsenic-free water per day and entails a maintenance cost of Rs 5,000 per year.

This plant will be set up initially at Ananda Ashram, a government-run home for boys at the Kadai area of Behrampore, and at Tentuliapara village of Lalgola block.

Prof. Pradip's plant, which has a market price of Rs 95,000 can dispense 80 to 90 litres of arsenic and iron-free water per hour. It will be installed initially at Shilayan, a government-sponsored after-care home for girls at the Panchanantala area of Behrampore. It requires a maintenance cost of Rs 60,000 per year.

Murshidabad district has 19 arsenic-affected blocks: Behrampore, Beldanga-I and -II, Hariharpara, Naoda, Domkal, Jalangi, Raninagar-I&II, Murshidabad-Jiaganj, Lalgola, Bhagwangola-I&II, Raghunathganj-I&II, Suti-I and -II, Samsheganj and Farakka.

Comments (0)

Other Related News

[Varsity Bill to be tabled soon](#)
[US ambassador meets Mamata](#)
[Board bungs Vidyasagar's birthday](#)
[Govt mulls new fire safety guidelines](#)
[Robbers loot four houses](#)

User Login Section

[Forgot](#)

[Password?](#) [Sign up now!](#)

[nature.com](#)[Publications A-Z index](#)

Search

[Advanced search](#)[Browse by subject](#)[My account](#)[E-alert sign up](#)[Register](#)[RSS](#)

Welcome back: Soumabha Baq

[Logout](#)

[Home](#) [Archive](#) [Our picks](#) [Jobs](#) [Events](#) [Blog](#) [Forum](#) [Special features](#) [For authors](#)

[About](#)

Articles by subject

[Biotechnology](#)
[Cell & molecular biology](#)
[Chemistry](#)
[Clinical medicine](#)
[Developmental biology](#)
[Earth & environment](#)
[Ecology & evolution](#)
[Genetics](#)
[Materials](#)
[Neuroscience](#)
[Physics](#)
[Space & astronomy](#)

Articles by keywords

[graphene](#)
[pesticides](#)

This article elsewhere

[Blogs linking to this article](#)

[Add to Connotea](#)

[Add to Digg](#)

[Add to Furl](#)

[Add to Newsvine](#)

[Add to Del.icio.us](#)

doi: 10.1038/nindia.2012.147; Published online 3 October 2012

Science news

Graphene to clean polluted water

K. S. Jayaraman

Chemists at the Indian Institute of Technology Madras have discovered the exceptional ability of graphene to remove common pesticides from water¹. The work can herald a cheap method of cleaning up sources of drinking water polluted by pesticides, a common problem worldwide.

Graphene is an 'allotrope' or a 2-dimensional form of carbon with atoms densely packed in a honeycomb fashion in a one-atom-thick sheet or layer. Scientists have found several uses for this amazing material including for making transistors, gas sensors and corrosion-resistant coatings. The IITM chemists' discovery adds one more to this list.

Toxicity and health hazards posed by pesticides, even at very low concentrations, are of concern in both developing and developed countries. The World Health Organization prescribes a maximum limit of 0.1 microgram per litre of drinking water for a single pesticide.

In their work, the team led by Thalappil Pradeep studied graphene's interaction with chlorpyrifos, endosulfan and malathion, widely detected in surface and groundwater samples in many countries.

Their study showed that graphene picks up these pesticides in very large quantities — in fact, more than its self weight. For instance one



Graphene can remove common pesticides from water sources.

© Brand X

most recent

[Sealing cracks with bacteria, nanotubes](#)
22 November 2012

[Science backs biodiversity policy](#)
21 November 2012

[Co-circulating JEV strains question vaccine efficacy](#)
20 November 2012

[Cancer research giants come together](#)
19 November 2012

[Mercury sniffing carbon nanotube](#)
19 November 2012

Naturejobs

[Senior Medical Writer](#)
Cactus Communications

[Senior Research Fellow \(SRF\) in a DBT Funded Research Project Genetic Mapping of Resistance to Stem Rot Disease in Jute](#)
Ch. Charan Singh University

[Postdoctoral Position in Cognitive Science](#)
Indian Institute of Technology Gandhinagar

[Fellowship](#)
Department of Biotechnology

[Research Associate in a DBT Funded Project Creation of Bioinformatics Infrastructure Facility](#)
Ch. Charan Singh University

gram of graphene was found to adsorb 1.2 gram of the pesticide endosulfan "higher than any material investigated for the purpose." This unusual capacity of graphene for the uptake of pesticides can be used for water clean-up, Pradeep told *Nature India*.

Carbon nanotubes (CNTs), another category of carbon, have been investigated for pesticide uptake but CNTs are reported to be cancer causing which may limit their utility in drinking water purification, he says.

"Our work establishes that the new class of 2-dimensional carbon nanomaterials has enormous potential in water purification, in creating cheap, easily manufacturable substrates", the researchers report. The material, according to the researchers, is also attractive due to its high specificity to the pesticides and insensitivity to changes in pH values of water and less toxicity than CNTs.

"Besides, reduced graphene oxide can be easily immobilized on cheap substrates like sand and used as a filter," they say. The anti-bacterial properties of graphene means bacteria is unlikely to accumulate on the filter media using graphene. The research was funded by the Nano Mission of the Department of Science and Technology (DST).

References

1. Maliyekkal, M. S. *et al.* Graphene: a reusable substrate for unprecedented adsorption of pesticides. doi: [10.1002/sml.201201125](https://doi.org/10.1002/sml.201201125) (2012)

[More science jobs](#)

[Post a job for free](#)

tools

[Send to a Friend](#)

[Reprints & Permissions](#)

[RSS Feeds](#)

[Follow us on Twitter](#)

Nature India EISSN 1755-3180

Header image source: Getty

About NPG
Contact NPG
Accessibility statement
Help

Privacy policy
Use of cookies
Legal notice
Terms

Naturejobs
Nature Asia
Nature Education
RSS web feeds

Search:

© 2012 Nature Publishing Group, a division of Macmillan Publishers Limited. All Rights Reserved.

partner of AGORA, HINARI, OARE, INASP, ORCID, CrossRef and COUNTER

Today's Paper » NATIONAL » TAMIL NADU

Published: August 29, 2012 00:00 IST | Updated: August 29, 2012 05:24 IST

IIT-M professor develops sensor to detect explosives

R. Prasad

Identifying TNT explosives present even at a very low concentration — nine molecules — has become possible with a nanostructure-sized sensor developed by T. Pradeep of the Department of Chemistry, IIT Madras. There is a complete change in luminescence from red to green when TNT is added to the sensor. All that is required to detect the change in luminescence is a fluorescence microscope. The results can be double checked by Raman spectroscopy. Raman spectrum specific to TNT gets enhanced and hence identifying the signature becomes easy. The results were published on Monday in the journal *Angewandte Chemi*.

“A false alarm can be avoided by using Raman spectroscopy,” said Prof. Pradeep. The sensor has two main components — a unique flower-shaped gold particle (mesoflower). “The unique shape of the flower is important in identifying the genuineness of the sensor,” he said.

Sitting on top of the gold mesoflower is a less than one nanometre-sized silver particle that is embedded in a protein (bovine serum albumin). The gold mesoflower together with the protein-protected silver cluster is then coated with a dye. When irradiated with a right wavelength of light, the silver cluster produces a red luminescence. But adding a very dilute solution containing TNT at concentrations of one ppb (parts per billion) can quench the red luminescence.

Work on the mesoflower started in 2008 with P. R. Sajanlal who is currently doing his postdoc. In 2010 Ms. Ammu Mathew, a doctoral student, began the work of developing the sensor.

More In: [TAMIL NADU](#) | [NATIONAL](#)

Printable version | Jan 2, 2013 10:06:17 AM | <http://www.thehindu.com/todays-paper/tp-national/tp-tamilnadu/iitm-professor-develops-sensor-to-detect-explosives/article3834375.ece>

© The Hindu

The Hindu: [Home](#) | [News](#) | [Opinion](#) | [Sport](#) | [Business](#) | [Arts](#) | [Life & Style](#) | [S & T](#) | [Education](#) | [Health](#) | [Homes & Gardens](#) | [Jobs](#) | [Classifieds](#) | [Topics](#) |

The Site: [About Us](#) | [Contacts](#) | [Archives](#) | [Subscriptions](#) | [RSS Feeds](#) | [Site Map](#)

Group Sites: [The Hindu](#) | [Business Line](#) | [Sportstar](#) | [Frontline](#) | [Publications](#) | [eBooks](#) | [Images](#) |

Disclaimer: *The Hindu* is not responsible for the content of external internet sites.

Republication or dissemination of the contents of this screen are expressly prohibited without the written consent of *The Hindu*.

Comments to: web.thehindu@thehindu.co.in Copyright© 2013, The Hindu



IN TODAY'S PAPER

- Front Page
- Nation
- Calcutta
- Bengal
- Opinion
- International
- Business
- Sports
- Entertainment
- Sudoku
- Sudoku New **BETA**
- Crossword
- Jumble
- Gallery
- Horse Racing
- Press Releases
- Travel

WEEKLY FEATURES

- 7days
- Graphiti
- Knowhow**
- Jobs
- Careergraph
- Salt Lake
- Personal TT

CITIES AND REGIONS

- Metro
- North Bengal
- Northeast
- Jharkhand
- Bihar
- Odisha

ARCHIVES

Since 1st March, 1999

THE TELEGRAPH

- About Us
- Advertise
- Feedback
- Contact Us



Front Page > KnowHOW > Story

Like { 0 } Tweet { 0 } 0

Tiny cleaners

Nanoparticles are the ticket to clean water, finds **Kavitha Shanmugam**



The research team with the purifying cartridge

It is difficult to grasp the fact that the dark liquid swirling inside a small laboratory flask is actually a solution of gold. Yet, it is indeed bits of gold that are so minuscule that they are not visible to naked eyes. The gold particles may be diminutive but their atoms are packed with properties, which display unusually strong chemical reactivity.

It is this extreme "reactive" nature of these ultra-small nanoparticles that is being tapped by Thalappil Pradeep — head of the Unit of Nanoscience at the Department of Chemistry, Indian Institute of Technology (IIT), Madras, —to rid water of harmful contaminants. A long-standing champion of using nanoparticles to purify water — an effort the scientific community at large mocked at first — this IIT professor has time and again proved that nanoparticles of gold, and silver too, are highly efficient in making water fit for drinking, cleaning up **even dissolved** pesticides.

The bearded, bespectacled Pradeep, who works out of a compact lab supported by the Department of Science and Technology, comes across as a man on a mission. The enthusiastic professor, who has penned several books on nanoscience that are now prescribed textbooks in different universities, never passes up an opportunity to wax eloquent about the "magical" properties of nanoparticles which could be harnessed for the benefit of society.

In 2001, the chemistry professor demonstrated that it is possible to completely break down halocarbons, a class of compounds to which many lethal pesticides belong, into relatively harmless carbon particles and metal compounds. What this discovery meant was that pesticides in drinking water could be removed by passing them over nanoparticles. This work led to the development of a revolutionary nanoparticle-based technology for water purification. This patented technology is currently in commercial use with Eureka Forbes, a firm specialising in water purification, marketing these filters as Silver Nano.

Recently, Pradeep's team has tweaked this technology a bit could help tackle arsenic contamination in groundwater, a serious problem that afflicts most states in eastern India, including West Bengal. A nanoparticle-based cartridge developed in the IIT lab is capable of trapping arsenic and other dissolved contaminants in drinking water.

"All over the world, the permissible limit of arsenic in drinking water is 10 parts per billion (ppb), in India it is 50 ppb. There is actually no safe limit of this toxic compound. It is highly dangerous to consume arsenic contaminated water. It can trigger several diseases, including cancer," says Pradeep.

It took Pradeep's team three years to come up with filter to remove arsenic completely from drinking water. "What was challenging was to make the know-how affordable and create something that would not recontaminate water in the surrounding," he says. Therefore, they used natural materials like biomimetic material and modified them with elements that have a natural affinity for arsenic.

What the IIT team has come up with is a 10cm "cartridge" made up of biomimetic material with nano structures embedded in them. This cartridge is capable of removing arsenic in 2,000 litres of water. To put that in context, a family of five can use the cartridge to purify its drinking water for a year. And it takes the cartridge less than a minute to purify the water — after passing through the filter, the arsenic level goes down to less than 2 ppb. "It is a product suitable for families in remote areas as it does not need electricity. It can be

fitted into any kind of existing water storage facility," points out not release any other element into the water, it will just remove



However, Pradeep is still not satisfied. He believes that more w constantly improve the use of nanomaterials to purify water. "W new sensors to detect ultra low concentration sensing in water; sustainable purifying technologies." Says Pradeep.

Here's wishing that he can make his dream of providing safe dr country a reality.

Like 0 Tweet 0 0

" "